frontiers | Research Topics

Evolution mechanism and control method of engineering disasters under complex environment

Edited by
Jianyong Han, Xiaoyu Bai, Zhongqiang Liu,
Jae-Joon Song and Pengjiao Jia

Published in
Frontiers in Earth Science



FRONTIERS EBOOK COPYRIGHT STATEMENT

The copyright in the text of individual articles in this ebook is the property of their respective authors or their respective institutions or funders. The copyright in graphics and images within each article may be subject to copyright of other parties. In both cases this is subject to a license granted to Frontiers.

The compilation of articles constituting this ebook is the property of Frontiers.

Each article within this ebook, and the ebook itself, are published under the most recent version of the Creative Commons CC-BY licence. The version current at the date of publication of this ebook is CC-BY 4.0. If the CC-BY licence is updated, the licence granted by Frontiers is automatically updated to the new version.

When exercising any right under the CC-BY licence, Frontiers must be attributed as the original publisher of the article or ebook, as applicable.

Authors have the responsibility of ensuring that any graphics or other materials which are the property of others may be included in the CC-BY licence, but this should be checked before relying on the CC-BY licence to reproduce those materials. Any copyright notices relating to those materials must be complied with.

Copyright and source acknowledgement notices may not be removed and must be displayed in any copy, derivative work or partial copy which includes the elements in question.

All copyright, and all rights therein, are protected by national and international copyright laws. The above represents a summary only. For further information please read Frontiers' Conditions for Website Use and Copyright Statement, and the applicable CC-BY licence.

ISSN 1664-8714
ISBN 978-2-8325-6071-6
DOI 10.3389/978-2-8325-6071-6

About Frontiers

Frontiers is more than just an open access publisher of scholarly articles: it is a pioneering approach to the world of academia, radically improving the way scholarly research is managed. The grand vision of Frontiers is a world where all people have an equal opportunity to seek, share and generate knowledge. Frontiers provides immediate and permanent online open access to all its publications, but this alone is not enough to realize our grand goals.

Frontiers journal series

The Frontiers journal series is a multi-tier and interdisciplinary set of open-access, online journals, promising a paradigm shift from the current review, selection and dissemination processes in academic publishing. All Frontiers journals are driven by researchers for researchers; therefore, they constitute a service to the scholarly community. At the same time, the *Frontiers journal series* operates on a revolutionary invention, the tiered publishing system, initially addressing specific communities of scholars, and gradually climbing up to broader public understanding, thus serving the interests of the lay society, too.

Dedication to quality

Each Frontiers article is a landmark of the highest quality, thanks to genuinely collaborative interactions between authors and review editors, who include some of the world's best academicians. Research must be certified by peers before entering a stream of knowledge that may eventually reach the public - and shape society; therefore, Frontiers only applies the most rigorous and unbiased reviews. Frontiers revolutionizes research publishing by freely delivering the most outstanding research, evaluated with no bias from both the academic and social point of view. By applying the most advanced information technologies, Frontiers is catapulting scholarly publishing into a new generation.

What are Frontiers Research Topics?

Frontiers Research Topics are very popular trademarks of the *Frontiers journals series*: they are collections of at least ten articles, all centered on a particular subject. With their unique mix of varied contributions from Original Research to Review Articles, Frontiers Research Topics unify the most influential researchers, the latest key findings and historical advances in a hot research area.

Find out more on how to host your own Frontiers Research Topic or contribute to one as an author by contacting the Frontiers editorial office: frontiersin.org/about/contact

Evolution mechanism and control method of engineering disasters under complex environment

Topic editors

Jianyong Han — Shandong Jianzhu University, China
Xiaoyu Bai — Qingdao University of Technology, China
Zhongqiang Liu — Norwegian Geotechnical Institute (NGI), Norway
Jae-Joon Song — Seoul National University, Republic of Korea
Pengjiao Jia — Soochow University, China

Citation

Han, J., Bai, X., Liu, Z., Song, J.-J., Jia, P., eds. (2025). *Evolution mechanism and control method of engineering disasters under complex environment*. Lausanne: Frontiers Media SA. doi: 10.3389/978-2-8325-6071-6

Table of contents

06 Editorial: Evolution mechanism and control method of engineering disasters under complex environment
Jianyong Han, Hai Li, Xiaoyu Bai, Zhongqiang Liu, Jae-Joon Song and Pengjiao Jia

11 Research on the dismantling of double-arch tunnel after long-term service—the case study of Huangmeishan Tunnel demolition project
Xinyu Kou, Xiaojun Li, Jiangning Xie, Adili Rusuli, Tao Li and Yi Rui

26 Analysis and quantitative identification of guided wave propagation mechanism in concrete
Chenhui Su, Yuhang Zhang, Lin Tang and Wenchao Zhang

36 Study on the mechanical properties and acoustic emission signal characteristics of freezing pipe
Tao Wang, Weiwei Ye and Liyuan Liu

48 Numerical study on migration of overlying strata and propogation of cracks during multi-coal seams mining
Junpeng Zou, Man Wang, Lu Bai and Chongwei Yan

61 Dynamic evolution and numerical analysis of rock deformation under impact failure based on corner correlation method
Xingui Zhou, Zhongbao Ye, Hong Miao, Wei Li, Xueru Wang and Chenfeng Li

75 Failure mechanisms and dynamic process control measures of deep buried tunnels in tectonic fracture zones under high *in-situ* stresses—a case study in Southwestern China
Keyue Zheng, Chenghua Shi, Qianjin Zhao, Mingfeng Lei, Chaojun Jia and Yili Lou

92 Slope stability analysis of coastal geotechnical structures under combined effects of earthquake and rainfall
Yuyue Jia, Shuyang Luan, Mohsen Saleh Asheghabadi, Dongliang Xing, Hang Yuan and Junwei Liu

107 Rockburst hazard assessment and prevention and control strategies in the Ruihai gold mine
Pengxiang Li, Zongwen Wang, Bingrui Chen, Jianping Peng, Bochao Zhang, Jinshuai Zhao and Houlin Xie

119 Study on bearing characteristics of super-long and super-large diameter pipe piles in silt foundation of alluvial plain of Yellow River
Sifeng Zhang, Zhicheng Ren, Yingguang Zhang, Wei Fan, Chao Li, Chao Liu and Yushuai Wang

137 Mechanical performance and failure mechanism of U-steel support structure under blast loading
Jin-Shuai Zhao, Jia-Hao Yang, Peng-Xiang Li, Xin-Hao Zhu, Chong-Feng Chen and Jian-Cong Zhang

148 Predicting rock mass rating ahead of the tunnel face with Bayesian estimation
Xiaojun Li, Ziyang Chen, Li Tang, Chao Chen, Tao Li, Jiaxin Ling, Yanyun Lu and Yi Rui

164 Research and application of macro-micro fracture correlation of heterogeneous granite
Yunjuan Chen, Jiarui Su, Tao Gao, Yi Jing, Huifu Zhang, Hongjie Duan and Wenbin Zhao

175 The impact of high temperature on mechanical properties and behaviors of sandstone
Juan Jin, Jiandong Liu, Weixi Chen, Guoping Li, Wei Cheng, Xiaowen Zhang and Yifan Luo

187 Prediction of water inflow and analysis of surrounding rock stability in unfavorable geological mountain tunnel
Yunjuan Chen, Mengyue Liu, Mengzhen Su, Mingxu Ding, Haolin Li and Yi Jing

200 Research on characteristics and geological genesis of large-scale deep-seated landslide in tuff formation
Mengqi Xue, Guangli Xu, Feixiang Yao and Zhuo Ma

212 Study on overburden failure characteristics and ground pressure behavior in shallow coal seam mining underneath the gully
Jie Zhang, Li Wang, Tao Yang, Shoushi Gao, Yifeng He and Jianjun Wu

226 Investigation on shakedown response-behavior of thawed subgrade soils under long-term traffic loading
Shujian Wang, Xiangyang Li, Yanzheng Ti, Xiaoning Zhang, Tao Yin, Ruibing Wang, Xiufeng Jiang, Zhikai Su and Jianwen Hao

234 Investigation on the failure mechanism of the collapse of the columnar jointed basalt in underground cavern
Jin-Shuai Zhao, Jian-Cong Zhang, Shu-Feng Pei, Liang Xing, Chong-Feng Chen and Guang-Duan Zhang

244 Experimental study and mechanism analysis of high-pressure water jet for mud cake cutting during shield tunneling
Fuquan Ji, Pengfei Liu, Zhao Yang, Bowei Wen and Qinxin Hu

254 Research and application of new anti-floating anchor in anti-floating reinforcement of existing underground structures
Guohui Liu, Pingsheng Jia, Jianping Sun, Zongbao Jiang, Fan Yang, Guorui Yang and Guangbiao Shao

263 Experimental study on stress and deformation characteristics of foundation pit considering excavation width using 3D printing technology
Fengzhou Liu, Xu Zhang, Maolong Xiang, Jingkang Lyu, Rui Feng and Shouhua LIU

276 Study on load-bearing behaviors of prestressed post-grouting tubular piles in the karst region of northern Fujian Province, China
Lingjun Huang, Rui Gao, Jingou Chi and Xiaocai Yan

291 Study on overburden failure characteristics and displacement rule under the influence of deep faults
Pei-Ding Zhang, Yong-Jiang Wu, Zheng-Zheng Cao, Zhen-Hua Li, Feng Du, Wen-Qiang Wang and Ming-Lei Zhai

307 Experimental study on the load bearing behavior of shored mechanically stabilized earth wall
Dongdong Pang, Xiaoyi Chen, Mengliang Gao, Chenxi Miao and Wei Zhang

320 Consolidation effects on pipe-soil interaction due to tunneling
Xu Liang, Jian Xu, Yong Huang, Li Shi, Zhiquan Zeng, Baozhu Miao, Lei Huang and Jian Wu

334 Design and application of a monitoring device for embedded foundation side friction resistance
Wei Tian, Peishuai Chen, Jiacheng Li and Fuquan Ji

349 Research on optimization of grouting treatment for underground mining goaf collapse based on 3-dimensional simulation
Lin Teng, Xiansen Xing, Changze Sun, Zujian Liu, Xiaoshuang Li and Menglong Dong

361 Analytical solution for mechanical behavior characterization of sandy dolomite tunneling
Di Sun, Zhigang Tao, Hong Yang, Haoche Shui, Xiaotian Lei, Fengnian Wang, Shusen Huo, Hang Shu, Weitong Xia, Zhaoxi Wang and Manchao He

371 Multifactor-coupled study on freeze-thaw forces of rocks in cold regions
Yonghui Zhao, Kun Hu, Deming Han, Yongxian Lang and Lin Zhang

frontiers | Frontiers in Earth Science

TYPE Editorial
PUBLISHED 19 February 2025
DOI 10.3389/feart.2025.1528278

Check for updates

OPEN ACCESS

EDITED AND REVIEWED BY
Gordon Woo,
Risk Management Solutions, United Kingdom

*CORRESPONDENCE
Xiaoyu Bai,
baixiaoyu538@163.com

RECEIVED 14 November 2024
ACCEPTED 10 February 2025
PUBLISHED 19 February 2025

CITATION
Han J, Li H, Bai X, Liu Z, Song J-J and Jia P (2025) Editorial: Evolution mechanism and control method of engineering disasters under complex environment.
Front. Earth Sci. 13:1528278.
doi: 10.3389/feart.2025.1528278

COPYRIGHT
© 2025 Han, Li, Bai, Liu, Song and Jia. This is an open-access article distributed under the terms of the Creative Commons Attribution License (CC BY). The use, distribution or reproduction in other forums is permitted, provided the original author(s) and the copyright owner(s) are credited and that the original publication in this journal is cited, in accordance with accepted academic practice. No use, distribution or reproduction is permitted which does not comply with these terms.

Editorial: Evolution mechanism and control method of engineering disasters under complex environment

Jianyong Han[1,2], Hai Li[1], Xiaoyu Bai[3]*, Zhongqiang Liu[4], Jae-Joon Song[5] and Pengjiao Jia[6]

[1]School of Civil Engineering, Shandong Jianzhu University, Jinan, China, [2]Key Laboratory of Building Structural Retrofitting and Underground Space Engineering, Ministry of Education, Shandong Jianzhu University, Jinan, China, [3]School of Civil Engineering, Qingdao University of Technology, Qingdao, Shandong, China, [4]Department of Natural Hazards, Norwegian Geotechnical Institute (NGI), Oslo, Norway, [5]Department of Energy Resources Engineering, Research Institute of Energy and Resources, Seoul National University, Seoul, Republic of Korea, [6]School of Urban Rail Transportation, Soochow University, Suzhou, China

KEYWORDS

geotechnical engineering, disaster control, disaster prevention, complex environment, numerical investigation

Editorial on the Research Topic
Evolution mechanism and control method of engineering disasters under complex environment

Introduction

Against the backdrop of expanding resource development and the utilization of underground spaces, engineering disasters (such as landslides, tunnel collapses, earthquakes, debris flows, and urban infrastructure failures) have occurred frequently, resulting in substantial economic losses and casualties. Complex environmental factors, including weak or unstable geological structures, hydraulic and atmospheric pressure effects, heavy rainfall and water level fluctuations, fluid-solid coupling, earthquakes, and external dynamic disturbances, significantly impact the strength, deformation, and stability of geotechnical materials (Han et al., 2023), thereby increasing the risk of disasters such as landslides and tunnel collapses (Liu et al., 2024; Han et al., 2018). Consequently, investigating and understanding the evolution mechanisms of engineering disasters in complex environments and developing effective disaster control methods have become critical tasks in the engineering community.

To promote research progress in disaster prevention and control and to foster communication among peers, we are honored to introduce the Research Topic, "Evolution Mechanism and Control Method of Engineering Disasters Under Complex Environment." This Research Topic aims to gather cutting-edge research findings, novel methods, case studies, and review articles, with a particular focus on studies related to disaster control methods and failure evolution mechanisms. The Research Topic has received widespread attention and numerous submissions. The project has now concluded, with a total of 29 published papers covering the analysis of disaster

evolution mechanisms, the development of control technologies, and numerical simulation methods. The research emphasis includes complex disaster scenarios such as landslides, tunnel collapses, and earthquakes. This Research Topic provides crucial support for understanding and mitigating engineering disasters in complex environments, laying a solid foundation for advancements in disaster prevention and control theories and practices.

Mechanical properties and failure mechanisms of rock masses

In complex environments, the study of the mechanical properties and failure mechanisms of rock masses is a key Research Topic in predicting engineering disasters. This research not only helps deepen our understanding of how rock materials behave under extreme conditions but also provides crucial scientific support for the safe design of engineering projects, disaster prevention, and risk management.

Zhou et al. conducted numerical analysis using the corner correlation method, systematically revealing the dynamic evolution process of rocks under impact loads. This study offers theoretical support for assessing the stability and safety of rock masses under conditions such as mining blasts and earthquakes. Jin et al. investigated the significant impact of high temperatures on the mechanical properties of sandstone, discovering that the strength and deformation behavior of sandstone change markedly under thermal conditions. This provides valuable data and guidance for geothermal energy extraction, post-fire building assessments, and other engineering projects in high-temperature environments.

In the research on heterogeneous granite, Chen et al. analyzed the correlation between macro and micro cracks, offering new insights into predicting rock mass fracture behavior. Their work is significant for preventing and addressing potential fractures and landslide risks in rock masses. Sun et al. studied the mechanical behavior of sandy dolomite tunnels under complex stress conditions and proposed analytical solutions that provide scientific guidance for the design and construction of tunnel projects.

Zhao et al. conducted an in-depth analysis of the mechanical behavior of steep rock slopes in cold regions under long-term freeze-thaw conditions. By comprehensively considering seasonal and diurnal temperature variations as well as the hydrogeological conditions of the mining area, they explored the evolution of frost heave forces under the combined influence of multiple factors, providing crucial insights for the design, construction, and operation of related engineering projects. Shao et al. (2023) examined the relationship between the material composition, pore microstructure, and macro mechanical properties of 3D-printed (3DP) rocks. This research provides advanced technical support for simulating the characteristics of natural rocks. The method allows for more precise and cost-effective rock mechanics experiments in the laboratory, reducing the complexity of field tests and promoting refined rock mechanics research.

These studies lay a solid foundation for understanding the mechanical properties and failure mechanisms of rocks under extreme conditions, providing essential technical support for disaster prevention and control in engineering projects.

Geological disasters: landslides, debris flows, and earthquakes

Geological disasters, such as landslides, debris flows, and earthquakes, pose significant challenges to engineering safety, especially under complex geological conditions. Studies have shown that these disasters are often driven by a combination of environmental and human factors, resulting in extensive and far-reaching damage.

By analyzing the characteristics and geological causes of deep-seated landslides in tuff formations, Jia et al. conducted a comprehensive analysis of the combined effects of earthquakes and rainfall, revealing how these two natural factors jointly impact slope stability, ultimately leading to landslide disasters. This research emphasizes the importance of understanding multi-hazard interactions and provides new perspectives for disaster risk management. Xue et al. provided valuable insights into the mechanisms of landslide occurrences in the region. This research not only deepened our understanding of the conditions under which landslides occur but also laid a theoretical foundation for future disaster prevention strategies.

Zhang et al. discovered that during coal seam mining, the destruction of the overburden of shallow coal seams and pressure changes directly weaken the stability of the surrounding soil, significantly increasing the risk of ground subsidence and landslides. These findings are crucial for environmental impact assessments of mining projects and the protection of regional geological stability. Zou et al. investigated the mechanisms of ground subsidence and crack expansion caused by multi-seam mining, providing scientific evidence for assessing the long-term environmental impacts of mining activities. Li et al. focused on the Ruihai Gold Mine, assessing the severity of rock bursts and proposing mitigation strategies. Through an in-depth analysis of rock burst characteristics, they provided guidance for enhancing mine safety management and reducing potential disaster risks.

Zhao et al. studied the impact of seismic activity on columnar jointed basalt, uncovering how earthquakes alter fault stability and increase the likelihood of landslides or rock mass instability. This study offers critical references for designing safer geological engineering projects. Zhang et al. further explored the characteristics of deep fractures and their impact on the destruction and displacement of overlying layers, offering new insights into understanding fault activity. The evolution of deep fractures is essential for predicting surface changes and developing effective disaster response strategies.

These studies not only advance theoretical knowledge but also offer practical support for developing strategies to prevent and respond to engineering disasters, driving further progress in the field of geological disaster prevention and control.

Tunnel collapse and underground space safety

In the study of tunnel collapses and underground space safety, multiple factors collectively influence the stability and safety of tunnel structures. Research has shown that the combination of complex geological conditions, high ground stress, water inrush

risks, and external dynamic loads often leads to significant safety hazards in tunnel engineering. To address these Research Topic, scholars have conducted extensive in-depth research and proposed various innovative solutions and control strategies.

Zheng et al. explored the failure mechanisms and dynamic control measures for tunnels located in tectonic fracture zones under high ground stress. Their research provided a detailed analysis of how crack development and stress concentration affect tunnel stability, revealing the main causes of tunnel instability in high-stress environments. They also proposed feasible dynamic control methods, offering scientific support to enhance the safety of tunnel projects in such conditions. Kou et al. conducted a stability analysis of long-serving double-arched tunnels, paying particular attention to the safety risks associated with structural decommissioning. Their findings offer critical theoretical insights for evaluating the stability of aging tunnels and formulating decommissioning or maintenance plans.

Zhao et al. focused on the impact of blast loads on the mechanical performance of U-shaped steel support structures, discovering significant changes in their mechanical properties under explosive impact. This research provides a solid scientific foundation for designing support structures that are resistant to both earthquakes and blasts. Chen et al. developed a water inflow prediction model for mountain tunnels and conducted a comprehensive assessment of surrounding rock stability. Their research offers technical support for effectively managing water inrush risks in complex geological conditions.

Ji et al. proposed an innovative solution to address the problem of mud cake formation during shield tunneling. By employing high-pressure water jet cutting technology, they successfully reduced the impact of mud cake on tunneling efficiency, significantly improving the efficiency and safety of shield construction. Liang et al. studied the consolidation effects of soil-pipeline interaction during tunnel excavation and thoroughly investigated the impact of the excavation process on surrounding soil and underground pipelines.

Their research revealed the soil settlement and stress variations induced by tunnel excavation, providing scientific guidance for safeguarding the safety of underground infrastructure.

Urban infrastructure safety and structural stability

In the field of urban infrastructure safety and structural stability, researchers have conducted numerous in-depth studies focusing on the load-bearing capacity and overall stability of infrastructure. As engineering environments become increasingly complex, the importance of ensuring the safety and stability of urban facilities has become more prominent.

Zhang et al. conducted an in-depth analysis of the load-bearing characteristics of ultra-long, large-diameter piles in the Yellow River alluvial plain. By combining field experiments and numerical simulations, they investigated the effects of various pile lengths, diameters, and eccentric conditions on vertical ultimate bearing capacity, providing crucial data to support the application of piles under complex geological conditions in this area. Huang et al. studied the load-bearing behavior of post-grouted prestressed pipe piles. By utilizing finite element simulations and on-site static load tests, they analyzed the effectiveness of end-grouting techniques. The results showed that this technique significantly enhances the bearing capacity of pipe piles and reduces settlement, confirming its feasibility and reliability under complex karst conditions.

Liu et al. also conducted experiments considering excavation width, investigating the stress and deformation characteristics of foundation pits. Using 3D printing technology to create scale models, they analyzed the mechanical response patterns of support structures under different widths, providing theoretical and practical guidance for foundation pit design and construction. Pang et al. conducted experimental research on the load-bearing performance of mechanically stabilized earth walls, providing reliable empirical evidence. Their findings further refined construction standards for stabilized earth walls, ensuring structural safety in coastal and geologically complex areas.

Liu et al. proposed a new type of anti-floating prestressed compression anchor bolt. Through a combination of field pull-out tests and numerical analysis, they demonstrated its effectiveness in reinforcing underground structures against buoyancy. This research is particularly suitable for environments with frequent water level fluctuations and provides effective technical support for the safety management of underground spaces. Wang et al. conducted freeze-thaw and cyclic triaxial tests to experimentally reveal the evolution of cumulative plastic strain behavior in thawed subgrade soils. Based on stability theory, they established classification standards for different plastic deformation limits and developed a method to calculate critical dynamic stress, providing theoretical support for the long-term safety and sustainable design of subgrades.

These research findings collectively enhance the safety and reliability of urban infrastructure, offering scientific support for future engineering practices.

Disaster control and prevention

In the field of disaster control and prevention, as well as numerical simulation and monitoring technology, numerous research projects have provided important tools and methods to enhance engineering safety and risk management.

Wang et al. conducted an in-depth study on the mechanical properties of frozen pipes and the characteristics of acoustic emission signals. They examined how temperature changes affect the strength and toughness of pipeline materials, offering scientific guidance for infrastructure design in cold regions. Su et al. developed an innovative method for real-time monitoring and structural health assessment by analyzing the propagation characteristics of guided waves in concrete and damage identification techniques. This technology allows engineers to efficiently detect structural damage and take timely preventive measures, significantly enhancing the overall safety of buildings and infrastructure. Tian et al. designed and validated an embedded monitoring device for lateral friction resistance in foundations. By integrating sensor theory with field experiments, they provided a high-precision real-time monitoring tool for infrastructure stability. Their research addressed the limitations of traditional monitoring equipment, which often suffers from low precision and challenges in long-term application, ensuring the safety of infrastructure during both construction and operation.

Li et al. applied Bayesian estimation methods to predict the rock mass grades at tunnel faces, demonstrating the practical application of data-driven predictive approaches in geotechnical engineering. This study significantly improved the accuracy of rock mass grade predictions, making the construction process safer and more efficient, while providing essential decision-making support for construction in complex geological environments. Teng et al. explored optimized strategies for grouting treatment to prevent subsidence and collapse in underground mined-out areas. They studied the effective application of grouting techniques for foundation reinforcement, proposing more efficient grouting formulations and analyzing the impact of grouting pressure, flow rate, and material properties on reinforcement outcomes. This research provides practical solutions for the safe management of underground spaces.

These research findings offer solid technical support and theoretical foundations for disaster control and engineering safety management.

Conclusion and outlook

In complex environments, the study of the evolution mechanisms and control methods of engineering disasters is crucial. By conducting in-depth analyses of disasters such as landslides, tunnel collapses, and debris flows, we have gained a preliminary understanding of their triggering mechanisms and evolutionary processes. This has laid the foundation for improving engineering safety and disaster prevention capabilities.

In the future, research will advance toward more intelligent and precise directions. The application of machine learning technology (Zhang et al., 2023) will bring new possibilities for monitoring and predicting engineering disasters (Liu et al., 2024). By analyzing vast amounts of historical data, machine learning can effectively identify potential disaster patterns and improve the accuracy of early warning systems.

At the same time, large-deformation collapse simulation will become a critical research area. Traditional simulation methods often face limitations when dealing with complex nonlinear behaviors. Therefore, developing a new generation of numerical models, particularly those capable of capturing large deformations and multi-physics coupling effects, will help more accurately reflect the dynamic processes of disaster occurrences.

Moreover, we need to strengthen interdisciplinary collaboration, integrating research findings from geotechnical engineering, computational mechanics, machine learning, and environmental science. By combining these efforts, we aim to advance disaster prevention and control technologies in complex environments, achieving significant progress in ensuring engineering safety, reducing disaster risks, and promoting sustainable development and human safety.

Author contributions

JH: Conceptualization, Formal Analysis, Funding acquisition, Investigation, Writing–original draft, Writing–review and editing. HL: Methodology, Writing–original draft, Writing–review and editing. XB: Methodology, Supervision, Writing–original draft, Writing–review and editing. ZL: Writing–original draft, Writing–review and editing. J-JS: Writing–review and editing. PJ: Writing–review and editing.

Funding

The author(s) declare that financial support was received for the research, authorship, and/or publication of this article. This work was supported by the Key Research and Development Program of Gansu Province, China (Grants 22YF7FH224) and the Doctoral Research Fund of Shandong Jianzhu University (Grants X19080Z).

Conflict of interest

The authors declare that the research was conducted in the absence of any commercial or financial relationships that could be construed as a potential conflict of interest.

Generative AI statement

The author(s) declare that no Generative AI was used in the creation of this manuscript.

Publisher's note

All claims expressed in this article are solely those of the authors and do not necessarily represent those of their affiliated organizations, or those of the publisher, the editors and the reviewers. Any product that may be evaluated in this article, or claim that may be made by its manufacturer, is not guaranteed or endorsed by the publisher.

References

Han, J., Liu, L., Zuo, C., Wang, H., Lin, F., Zhao, Y., et al. (2023). Evolution and parametric analysis of concrete temperature field induced by electric heating curing in winter. *Sustainability* 15 (10), 8337. doi:10.3390/su15108337

Han, J., Zhao, W., Jia, P., Guan, Y., Chen, Y., and Jiang, B. (2018). Risk analysis of the opening of shield-tunnel circumferential joints induced by adjacent deep excavation. *J. Perform. Constr. Facil.* 32 (1), 04017123. doi:10.1061/(asce)cf.1943-5509.0001122

Liu, B., Han, Q., Fu, C., Zhang, G., He, Y., and Li, W. (2024). Development and engineering application of intelligent management and control platform for the shield tunneling construction close to risk sources. *J. Intell. Constr.* doi:10.26599/JIC.2024.9180018

Liu, Y., Wang, Z., Liu, X., and Han, J. (2024). Study on leakage assessment and stability analysis of water level changes in tunnels near reservoirs. *Water* 16 (17), 2378. doi:10.3390/w16172378

Shao, Y., Yang, J., Kim, J., Song, J., Moon, J., and Han, J. (2023). A comprehensive experimental study on mechanical anisotropy and failure mode of 3D printed gypsum rocks: from composition and microstructure to macroscopic mechanical properties response. *Rock Mech. Rock Eng. 1* 56 (9), 6503–6528. doi:10.1007/s00603-023-03401-4

Zhang, X., Lin, X., Zhang, W., Feng, Y., Lan, W., Da, Y., et al. (2023). Intelligent recognition of voids behind tunnel linings using deep learning and percussion sound. *J. Intelligent Constr.* 1 (4), 1–18. doi:10.26599/jic.2023.9180029

frontiers | Frontiers in Earth Science

TYPE Original Research
PUBLISHED 08 November 2023
DOI 10.3389/feart.2023.1296818

Check for updates

OPEN ACCESS

EDITED BY
Jianyong Han,
Shandong Jianzhu University, China

REVIEWED BY
Jun Wu,
Shanghai Normal University, China
Xi Jiang,
Hong Kong Polytechnic University, Hong Kong SAR, China

*CORRESPONDENCE
Yi Rui,
ruiyi@tongji.edu.cn

RECEIVED 19 September 2023
ACCEPTED 23 October 2023
PUBLISHED 08 November 2023

CITATION
Kou X, Li X, Xie J, Rusuli A, Li T and Rui Y (2023), Research on the dismantling of double-arch tunnel after long-term service—the case study of Huangmeishan Tunnel demolition project.
Front. Earth Sci. 11:1296818.
doi: 10.3389/feart.2023.1296818

COPYRIGHT
© 2023 Kou, Li, Xie, Rusuli, Li and Rui. This is an open-access article distributed under the terms of the Creative Commons Attribution License (CC BY). The use, distribution or reproduction in other forums is permitted, provided the original author(s) and the copyright owner(s) are credited and that the original publication in this journal is cited, in accordance with accepted academic practice. No use, distribution or reproduction is permitted which does not comply with these terms.

Research on the dismantling of double-arch tunnel after long-term service—the case study of Huangmeishan Tunnel demolition project

Xinyu Kou[1], Xiaojun Li[1], Jiangning Xie[2], Adili Rusuli[1], Tao Li[1] and Yi Rui[1]*

[1]Department of Geotechnical Engineering, Tongji University, Shanghai, China, [2]Anhui Transportation Holding Group Co., Ltd., Hefei, China

Mountain tunnel structures are subject to a variety of diseases with increasing service life. Earlier tunnels may need to be demolished and expanded because of the poor serving capacity. But few studies of tunnel demolition projects are available. Based on the demolition project of Huangmeishan Tunnel, this paper discusses the demolition scheme of the double-arch tunnel, calculates the stability of the slope, and investigates the defects and material performance in the tunnel. The water leakage in the tunnel mainly occurred at the mid-partition wall and the drainage pipe was clogged severely. The largest width of the crack detected is 15 mm. Material performance tests indicated that the concrete material strength exceeded the design values. In the loading test, the largest displacements of the tunnel arch and haunch were 1.73 and 1.32 mm, which verified the safety of heavy vehicles in construction. Finally, suggestions are given to avoid similar phenomena in other tunnels during the design, construction, and operation phase. The novelty of this study lies in its comprehensive analysis of a tunnel demolition project. The findings of this study contribute to enhancing the knowledge and understanding of tunnel demolition and support the safe and efficient execution of future demolition projects.

KEYWORDS

tunnel demolition, water leakage, cracks, lining thickness, loading test

1 Introduction

Mountain tunnels are extensively used in mountainous regions due to their numerous advantages, such as the ability to address geographical and elevation challenges, enhance linear connectivity, reduce travel distances, and improve operational efficiency (Ding et al., 2022; Wang et al., 2022). However, long-term service of highway tunnels often gives rise to various issues, including water leakage (Lin, 2014; Hawley and Gräbe, 2022), lining cracks (Chang et al., 2021; Yike and Yu, 2021), concrete spalling (Kiwamu and Kiyoshi, 2020; Ciro and Isidoro, 2022), reinforcement corrosion (GongHe et al., 2017), and other diseases. These problems severely compromise the structural mechanical properties of the tunnels and even result in tunnel collapse (Zhang et al., 2020). Additionally, due to the escalating traffic volume, existing tunnels may fail to adequately cater to the traffic demand or adhere to current specifications in terms of size (Chen et al., 2018).

Therefore, considering the safety of tunnel operations and the demands of modern public transportation, it is necessary to widen and renovate the existing tunnel (Höllrigl Michael et al., 2015). The tunnel reconstruction scheme is generally divided into two approaches. The first approach involves retaining the existing tunnel while constructing a new tunnel parallel to it. Comprehensive real-time monitoring (Mei et al., 2010; Yang et al., 2017) of the deformation of the existing tunnel is required in this approach, and the mechanical properties of the tunnel structure are strictly required (Wang et al., 2015; Wu et al., 2022). The existing tunnel cannot be repaired or improved. This approach aims to enhance the traffic capacity of the tunnel. The second approach entails the demolition and reconstruction of the existing tunnel. Illustrative instances of such expansions and reconstructions of the existing tunnels include the Fedro's Tunnel in Switzerland (Gianpiero, 2020), the Nazzano tunnel and Montedomini tunnel in Italy (Zhu et al., 2018), the Fleet line tunnel in the United Kingdom (Bowers and Moss, 2018), and the Chongqing Tunnel in China (Eisch, 1983).

Various studies have been conducted currently relating to the expansion and reconstruction of tunnels. Lunardi (Lunardi, 2012) effectively expanded the existing tunnel without causing disruptions to traffic. They achieved this by implementing a tunnel widening traffic protection shield and the pre-fabricated active arch structures. The operational and construction areas were separated by the implementation of a traffic protection shield, ensuring uninterrupted traffic service during the construction phase. This approach has also been successful in other tunnel projects, such as the Montedomini Tunnel (Zhu et al., 2018). The reconstruction of the waterproofing and sewerage system was conducted with the requirement of ensuring the continual functionality of each lane during daylight hours. Jia et al. (2019) investigated the expansion of a single-arch tunnel to a double-arch tunnel through the model experiments and numerical simulations. The study examined the changes in stress and strain of the lining structure, the stress of the surrounding rock and the surface subsidence. Elevated stress levels were identified in the mid-partition wall lining and the surrounding rock on both sides of the mid-partition during construction. Notably, significant subsidence occurred in the surface of the right tunnel.

However, most existing studies primarily focus on analyzing traffic conditions during tunnel reconstruction and expansion. The construction of new tunnels and the traffic capacity during the construction have been the central issue of research studies. Unfortunately, the dismantling process of existing tunnels is frequently overlooked. The research on tunnel demolition is limited, and the available studies primarily focus on the context of single-arch tunnels. For instance, Han et al. (2022) conducted an analysis of deformation and stress in the lining during the conversion of a single-arch tunnel into a graben, and they also proposed a safety zoning method for the dismantling construction. Additionally, Zheng (2023) detailed the technical scheme employed for the dismantling of the Jinjishan single-arch tunnel, and described the methodology for measuring structural displacement during the dismantling process.

The demolition of existing double-arch tunnels is a complex and challenging project that requires careful planning, execution, and monitoring to ensure the safety and efficiency of the construction.

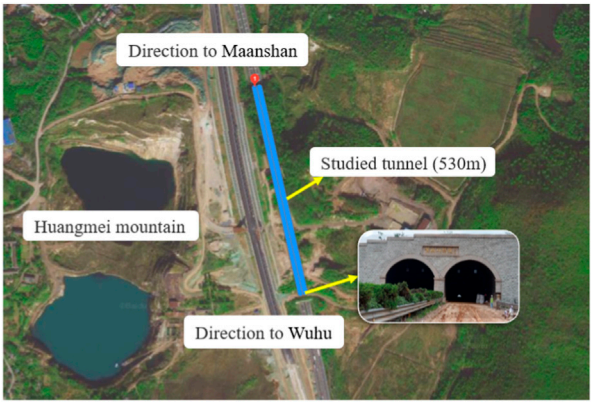

FIGURE 1
Huangmeishan Tunnel location.

The demolition project poses higher risks compared to tunnel construction due to three key aspects. Firstly, the complexity of geological formations makes it difficult to ensure the safety of tunnel construction (Jiang et al., 2021). The surrounding rock of the tunnel has already been disturbed during the construction of the existing tunnel, which will be further disturbed during the demolition process (Bai et al., 2022). The stability and self-supporting capacity of the surrounding rock are reduced and engineering risks are increased (Yan et al., 2021). Secondly, the structure of the existing tunnels may exhibit damages after years of operation (Jiang et al., 2022), such as the failure of the segment lining (Wang et al., 2019). The demolition of the tunnel negatively impacts the safety of the remaining tunnel structure. The safety risk of the project is heightened (Ding et al., 2014). Thirdly, double-arch tunnels are vulnerable to damage due to their large span and weak joints between the main tunnel and mid-partition wall (Tang et al., 2023). The structural of double-arch tunnels are subjected to complex forces, and there are limited engineering cases available that specifically address the demolition of double-arch tunnels. As a result, the unknown risks associated with the demolition of double-arch tunnels are amplified. Therefore, a detailed investigation into the dismantling of existing tunnels is necessary.

In the current research, Huangmeishan Tunnel was used as an example to introduce the demolition scheme of the double-arch tunnel. The demolition scheme included the construction of a construction platform and the demolition of the vault, sidewalls, and the remainder of the tunnel. Several studies were also carried at the same time including oblique photography, research on major diseases, material performance tests, and the loading test. The distribution of defects such as water leakage, cracks, and lining defects in tunnels after long-term operation were revealed. The mechanical strength of materials including concrete and rebar was also tested during demolition. The safety of the heavy vehicle traffic in construction was verified. This study aims to provide experience reference for similar projects and ensure the construction organization and safety of demolition construction. In addition, the current study could support the evaluation of the structural capability of tunnel in the future work.

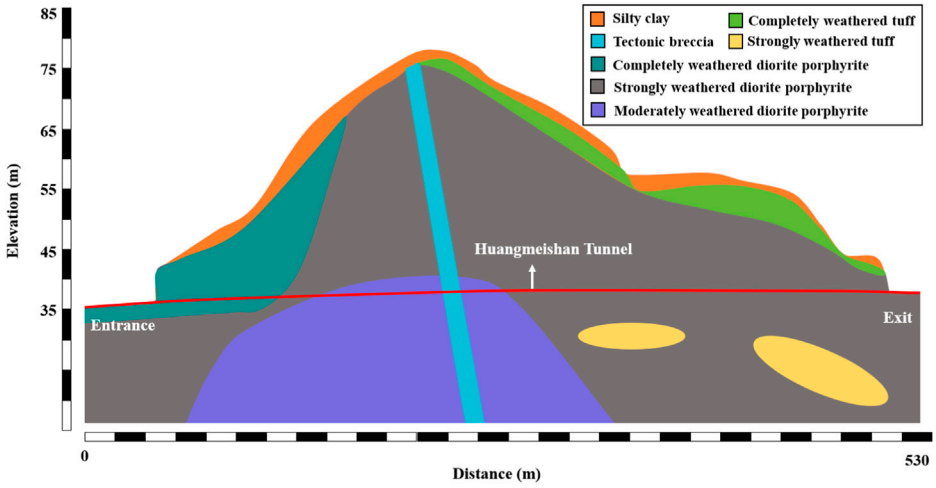

FIGURE 2
Geological structure of Huangmeishan Tunnel.

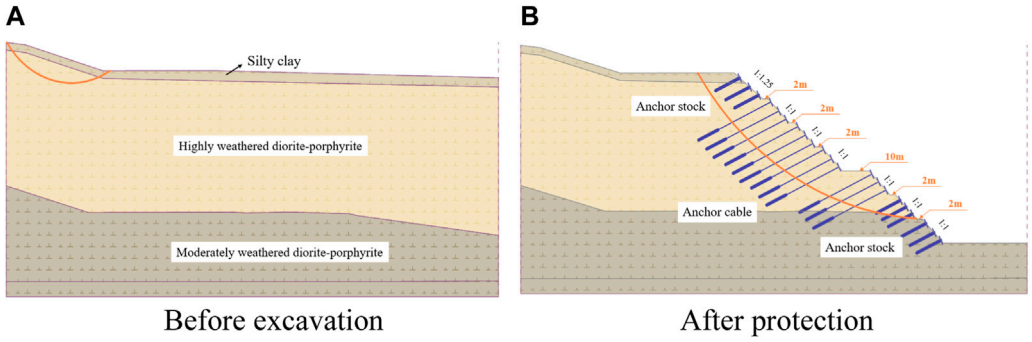

FIGURE 3
The calculation model of the slope before and after excavation and protection. **(A)** Before excavation. **(B)** After protection.

TABLE 1 The values of geotechnical parameters.

Type	The rainstorm conditions		
	Gravity G (kN/m^3)	C (kPa)	φ (°)
Land fills	20.0	13.0	15.0
Silty clay	20.5	12.0	13.0
Strongly weathered Tuff	21.5	36.0	20.0
Completely weathered diorite porphyrite	20.0	18.0	18.0
Strongly weathered diorite porphyrite	22.0	36.0	20.0
Moderately weathered diorite porphyrite	23.0	140.0	23.0

2 Project overview

The Huangmeishan double-arch tunnel belonged to the Ma'anshan-Wuhu Expressway, located in Ma'anshan City, Anhui Province, China. The design speed was 120 km/h, the tunnel length was 530 m, and the maximum burial depth was approximately 50 m. The width of the construction limit was 10.75 m, and the net height was 5 m. The design elevation of the tunnel pavement ranged from

TABLE 2 The safety coefficient of the slope after excavation and protection.

Slope	The safety coefficient	
	After excavation	After protection
Seventh-level side slope	1.98	2.1
Sixth-level side slope	1.41	1.71
Fifth-level side slope	1.28	1.43
Fourth-level side slope	1.18	1.27
Third-level side slope	1.19	1.25
Second-level side slope	1.15	1.15
First-level side slope	1.15	1.15

31.45 m to 33.63 m. The tunnel consisted of an entrance section that was 35 m long, an exit section that was 30 m long, and a rock-covered section. The entrance and exit sections were constructed as open-cut tunnels. The entrance mileage was K4+075, and the exit mileage was K4+605. The Huangmeishan Tunnel was a double-arch and one-way tunnel, the longitudinal slope of the line was 2.4% uphill and 1.52% downhill. Huangmeishan Tunnel location is shown in Figure 1.

The Huangmeishan Tunnel was located at the central part of the southern section of the Ningyan Volcanic Depression in Yangzihuai Terrace. The overlying soil comprised primarily of artificial fill and Quaternary Holocene alluvium. The basement strata mainly consisted of Upper Jurassic Tuff and Yanshanian epidote andesite. The surrounding rock was severely weathered and the rock quality was poor. The main lithology that the tunnel passed is shown in Figure 2. The tunnel area suffered from frequent flooding due to the heavy rainfall and cloudy weather from late June to early July each year.

According to the research, the horizontal and vertical alignment of the Huangmeishan Tunnel in the initial Nanjing-Wuhu Expressway failed to meet the current standard requirements. The inadequate distance between the tunnel exits and the

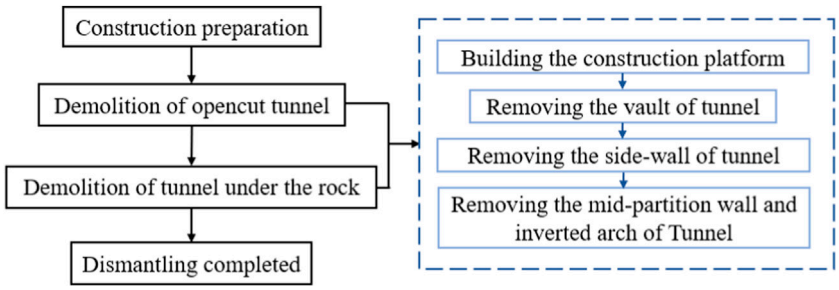

FIGURE 4
The demolition process for Huangmeishan Tunnel.

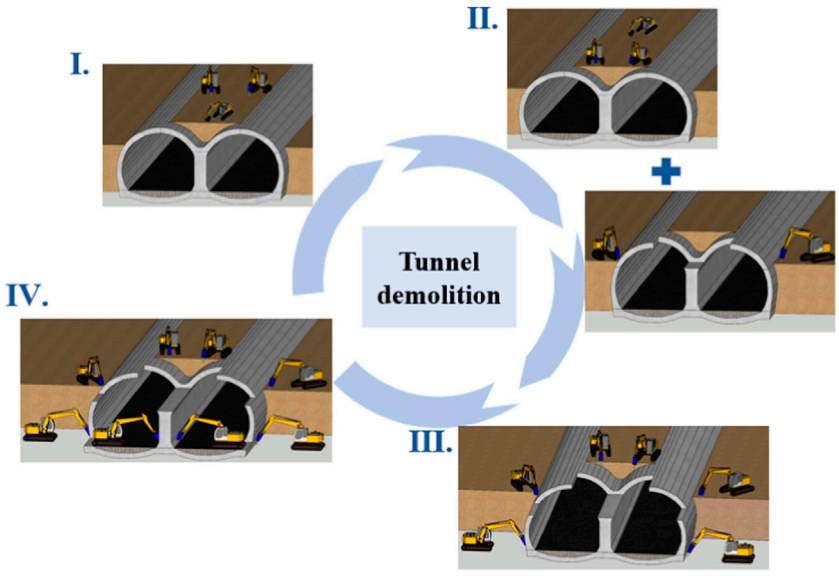

FIGURE 5
The demolition process of each section.

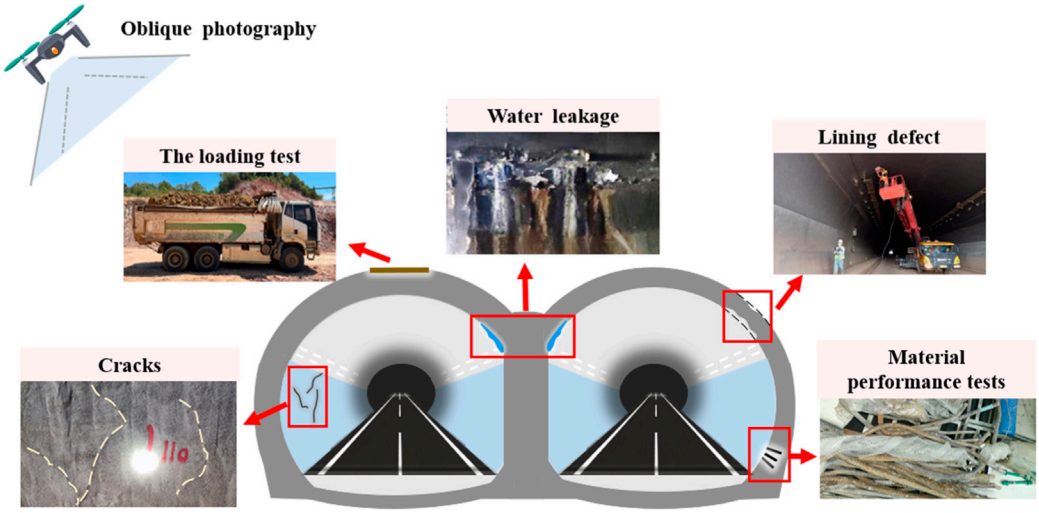

FIGURE 6
Research and testing during the tunnel demolition.



FIGURE 7
The 3D scene of Huangmeishan Tunnel.

interchange ramp exit resulted in frequent traffic accidents and heavy congestion within the tunnel. After evaluating various preliminary design options, the decision was made to repurpose the original tunnel into a graben. As a result, it became necessary to demolish the Huangmeishan Tunnel.

The common methods employed in the dismantling of existing tunnels are blasting demolition and mechanical demolition. The schedule for demolition by blasting is relatively short, but the risks are also higher. Meanwhile, the damage caused to tunnel structures by blasting demolition is uncontrollable. Conversely, mechanical demolition requires more time but is more secure. During the demolition process of the Huangmeishan Tunnel, materials such as steel reinforcement and concrete need to be sampled and tested. The rocks in the mountain are highly weathered and loose, which

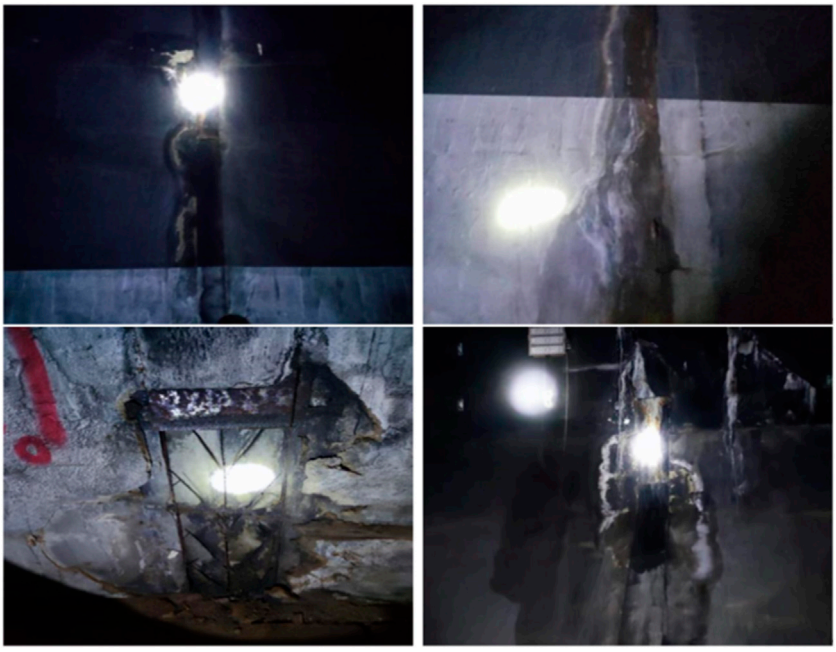

FIGURE 8
The image of water leakage disease in Huangmeishan Tunnel.

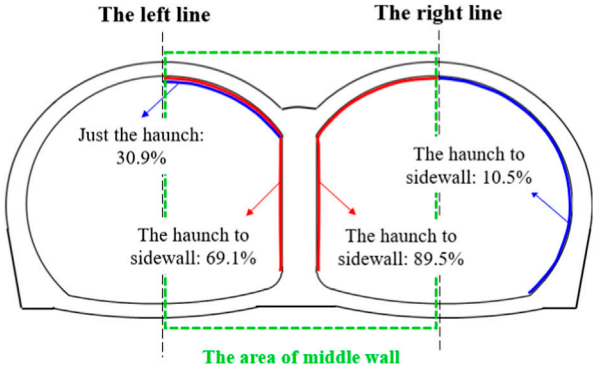

FIGURE 9
The distribution ratio of water leakage area in tunnel.

means a high risk of collapse after blasting. On the other hand, the time required for mechanical demolition construction meets the requirements of the overall project schedule. Therefore, the mechanical blasting method was adopted for the Huangmeishan double-arch Tunnel.

3 Demolishing scheme

The procedure for the mechanical demolition of the Huangmeishan Tunnel was divided into two steps, slope excavation and tunnel demolition. Both the entrance and exit sides were excavated and demolished simultaneously to enhance construction efficiency.

3.1 Slope excavation and reinforcement

The slope excavation of the Huangmeishan Tunnel was divided into seven levels, and each level was 8 m deep. The slope rate of 1:1 was applied to grades 1 to 6, while a slope rate of 1:1.25 was used for grade 7. A 10 m wide platform was established in the third level slope, while the remaining platforms were 2 m wide. The main lithology of the slope after excavation was diorite-porphyrite with joint and cracks developed, which shown poor rock integrity. These slopes were considered unstable and required enhanced support. The first, second, and seventh graded slopes were reinforced with anchor stock measuring 10 m in length. The other slopes were reinforced with anchor cable measuring 30 m in length (as shown in Figure 3B). The slopes were excavated in layers from top to bottom, and the excavated earth was transported to either the spoil ground or the roadbed area.

3.2 Assessment of slope stability

In consideration of the climatic conditions specific to the construction area, the rainstorm working condition parameters were employed for the analysis of slope stability. Table 1 presents the values of geotechnical parameters used in this study. The finite element software GEO and the Bishop method were used to investigate the stability of slope excavations and protection. The calculation model of the original slope is given in Figure 3A. The slope reinforcement scheme in the 3.1 section was adopted. The calculation model of the slope after excavation and subsequent protective measures is presented in Figure 3B.

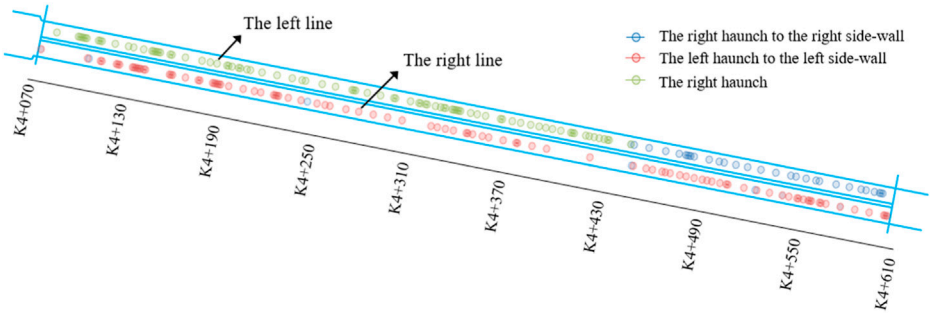

FIGURE 10
The distribution of water leakage along the tunnel axis.



FIGURE 11
The clogged drainpipe in the Huangmeishan Tunnel.

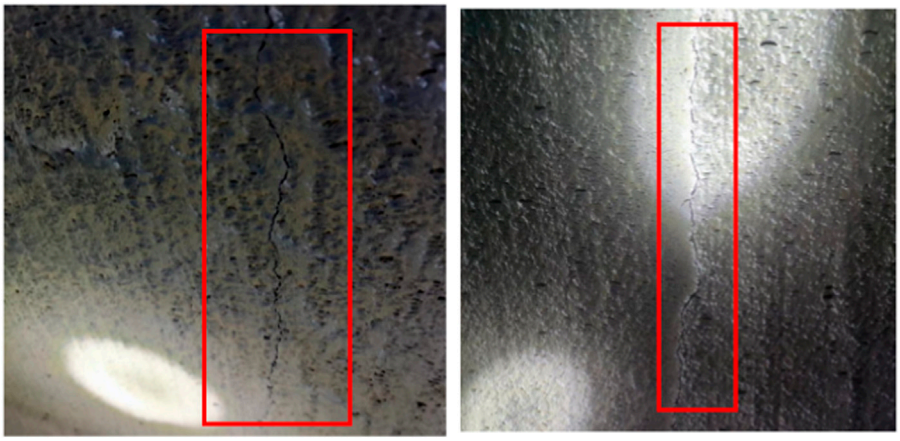

FIGURE 12
The image of crack disease in Huangmeishan Tunnel.

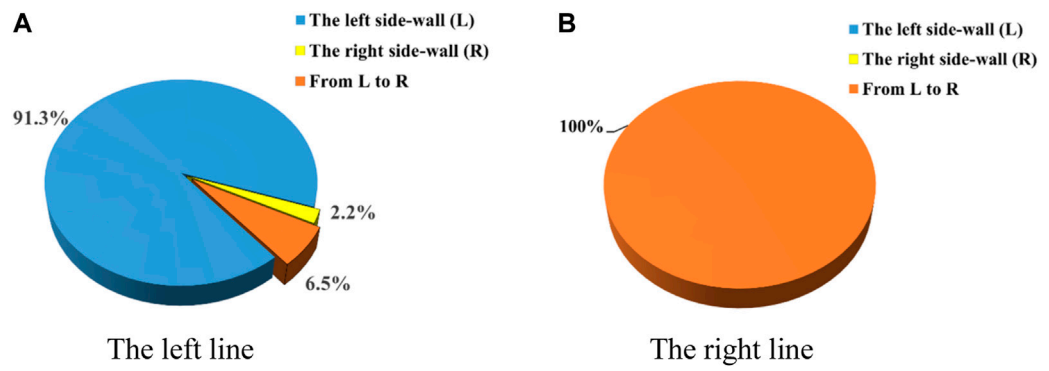

FIGURE 13
The distribution ratio of crack disease in tunnel. **(A)** The left line. **(B)** The right line.

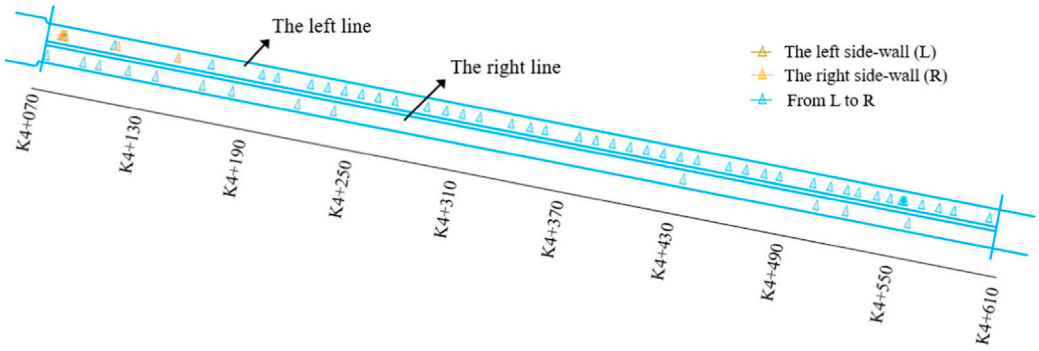

FIGURE 14
The distribution of crack disease along the tunnel axis.



FIGURE 15
Crack at section YK4+576.

The safety coefficient of the slope after excavation and protection is provided in Table 2. Under stormy conditions, all the slope stability factors exceed 1.05, which is the minimum value specified in the slope safety code. As a result, the slope can be generally stable. It can be concluded that the step-by-step excavation and protection measures comply with the code requirements for slope stability.

3.3 Tunnel demolition

The risks associated with demolishing the tunnel are different from those involved in constructing the tunnel. These risks primarily depend on the quality of the tunnel lining, the demolition scheme and method. In this project, the tunnel was dismantled in sections and the length of every section was 21 m. The mid-partition wall was used as the central axis for construction. The demolition process for the Huangmeishan Tunnel is shown in Figure 4. Initially, the open-cut section of the tunnel was demolished, followed by the section located under the rock. The demolition process for each section was divided into four steps (Figure 5), constructing the construction platform, demolishing the vault, the side-wall, and the remaining part of the tunnel.

3.3.1 Dismantling the open-cut section of the tunnel

First, the platform for the pickaxe machine was built from the side slope excavation to 5 m away from the tunnel. The excavator removed the soil from the side slope and placed it over the mid-

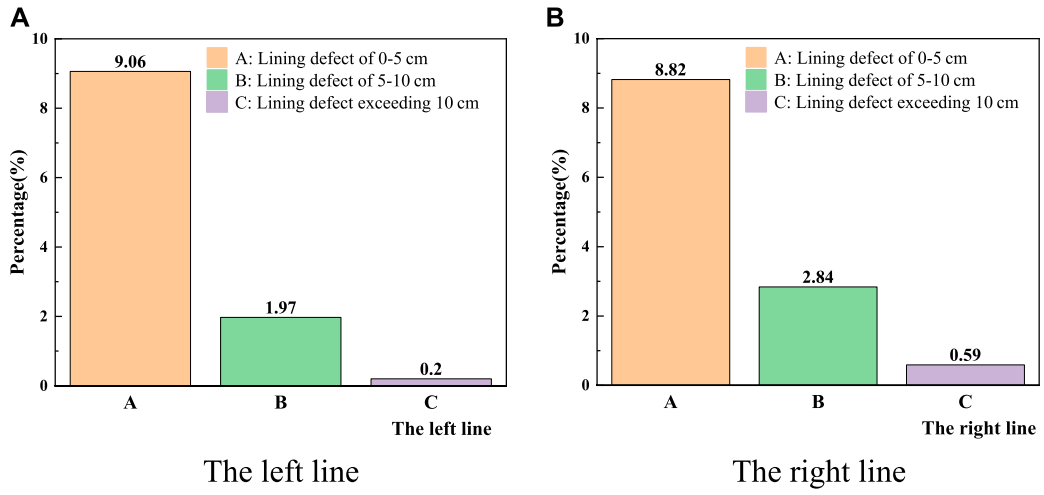

FIGURE 16
The percentage of insufficient lining thickness at the entrance of Huangmeishan Tunnel. **(A)** The left line. **(B)** The right line.

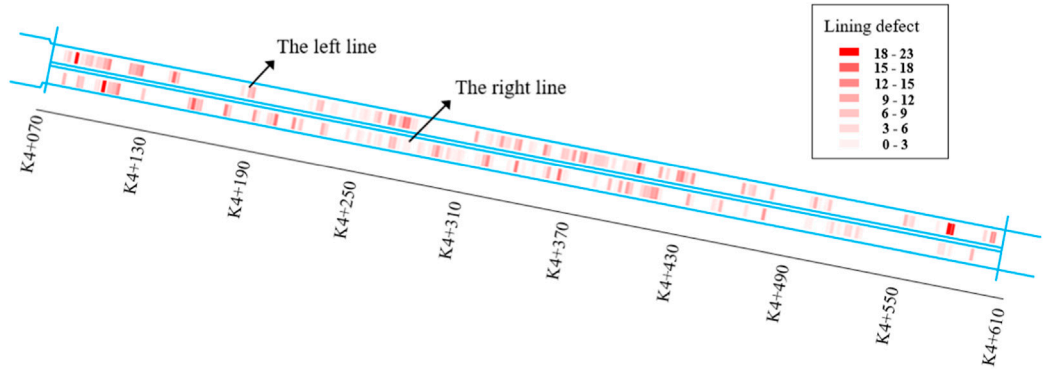

FIGURE 17
Distribution of insufficient thickness of the second lining along the axis of Huangmeishan Tunnel.

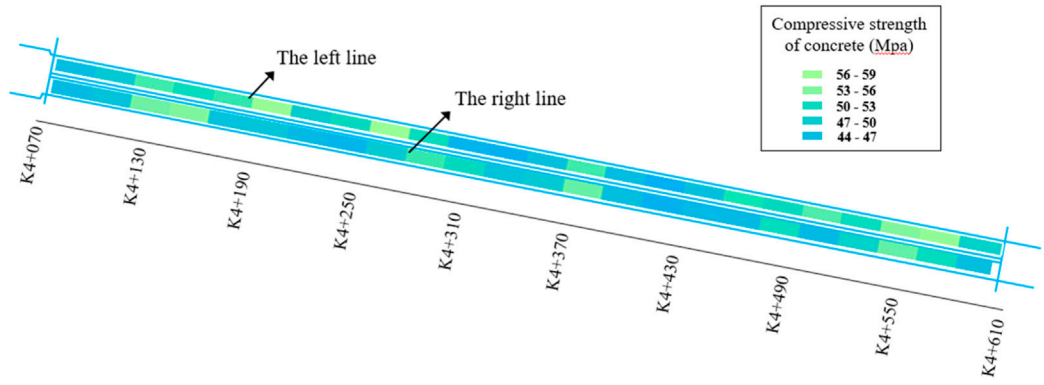

FIGURE 18
The distribution of concrete compressive strength along the tunnel axis.

TABLE 3 The average test results of rebar samples.

Type	Corrosion rates (%)	Tensile strength (MPa)
Steel	45.2	556.9

Next, the sidewall slope was excavated to create steps. The sidewall of the open-cut section of the tunnel was exposed, and promptly removing it.

Finally, the mid-partition wall and the inverted arch in the double-arched tunnel were demolished.

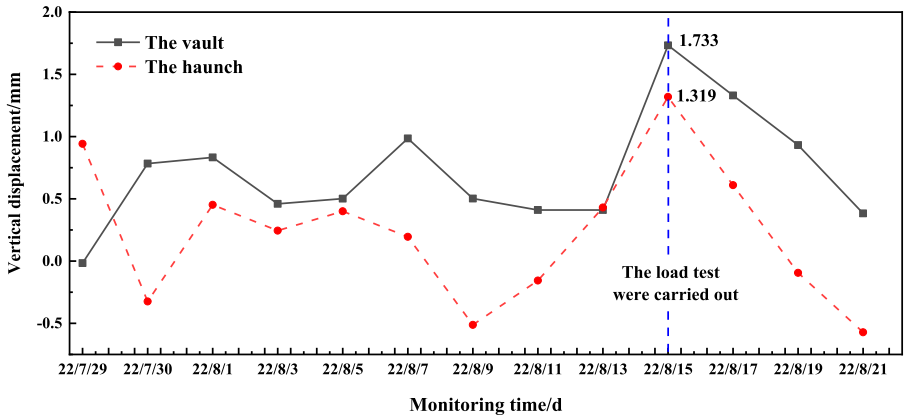

FIGURE 19
The time curves of the vertical displacement at the vault and the haunch at section ZK4+512.

TABLE 4 The treatment methods for cracks of different widths.

Crack width (mm)	Treatment
0.2–0.5	Surface coating
>0.5	Chiseling the crack and filling it with epoxy resin or epoxy mortar
<0.2	If stable, no treatment is needed

TABLE 5 The treatment methods for different locations of water leakage.

Location of water leakage	Treatment
Surface	Surface coating
Construction joints and ring seams	Chiseling and burying pipes combined with the active drainage
Longitudinal and diagonal joints	Chiseling and burying pipes

partition wall, creating the platform for the pickaxe machine to carry out the demolition. The width of the soil cover was wider than the combined width of two pickaxes and an excavator, while the thickness of the soil cover was less than the maximum height of the pickaxe construction. The digging machine was positioned at the centerline of the partition wall in the tunnel, with the pickaxe machine located behind it on both sides.

Then, after the platform was constructed, the pickaxe machine proceeded to remove the vault of the tunnel near the mid-partition wall. The slopes on both sides of the open-cut section of the tunnel were excavated by diggers to form steps, and the width of the steps meets the minimum width for safe construction for pickaxe machines. After that, the remaining vault of the open-cut section was demolished.

3.3.2 Dismantling the section under surrounding rock

The steps for dismantling the surrounded rock tunnel were identical to those of the open-cut section of the tunnel, but there are a few additional points to consider. When the construction platform was built, the side slopes were excavated vertically until 4.5 m from the tunnel arch, as the length of the tunnel anchors was 4.5 m.

Afterward, they were excavated horizontally. Rocks were left in place above the mid-partition wall to create a platform for the pickaxe machine. Furthermore, if the entire anchor became visible during excavation, a digger was used to level it in the direction of the tunnel axis. If only the anchor head was exposed, the exposed section was cut off.

4 Analysis of defects and deterioration of tunnel structures

Due to the specificity and scarcity of this project, research and testing were carried out at the same time as tunnel demolition, including oblique photography, analysis of tunnel defects, material performance tests, and loading tests (as shown in Figure 6). Then, based on the project of Huangmeishan Tunnel, the measures are proposed to prevent similar problems from occurring in other tunnels.

4.1 Tracking construction progress through oblique photography

Traditional low-altitude photogrammetry is widely used in many fields such as survey of large areas, security monitoring, disaster emergency response and environmental protection. However, traditional photography is limited to sensors and data processing algorithms. It is difficult to model the realistic construction site because of the lack of sufficient information. In contrast to low-altitude photography, oblique photography collects data from multiple angles. The modeling of oblique photography provides a realistic and comprehensive representation of the ground (Xu et al., 2022; Yang et al., 2022). Additionally, it can help construction managers comprehensively understand the real site information and reduce blind spots in site management (Zhao et al., 2021).

In this project, in order to obtain a detailed and accurate view of the construction scene and track the construction progress in real-time, UAV tilt photography was used to obtain multi-view high-resolution image data. The automatic data processing method was employed to accelerate the generation of detailed 3D models of large scenes. The real demolition process of the tunnel is accurately reconstructed by comparing different 3D models from various angles, as shown in Figure 7.

4.2 Disease analysis of Huangmeishan Tunnel

During the demolition work, manual recording, and Ground Penetrating Radar (GPR) were used to research the distribution and causes of structural and quality defects in the tunnel, including water leakage, cracks, and lining thickness. The distribution of defects in the tunnels after a long period of operation was revealed, which provided useful data for the development of treatment measures.

4.2.1 Diseases of water leakage

Preliminary studies indicated that the Huangmeishan Tunnel was leaking severely and extensively. Figure 8 shows the scene image of water leakage in the Huangmeishan Tunnel. Figure 9 gives the distribution ratio of water leakage area in the tunnel. Figure 10 presents the distribution of water leakage along the tunnel axis.

81 instances of water leakage were found in the left line of the Huangmeishan Tunnel, all of which were distributed in the haunch and side wall of the right tunnel. 76 instances of water leakage were found in the right line of the tunnel, with 89.5% of them occurring in the haunch and side wall of the left tunnel. This shows that the water leakage in the partition wall area of Huangmeishan Tunnel is significant. The waterproof design of the mid-partition wall is a key point during the construction of the double-arch tunnel (Shi et al., 2020).

The reasons for this phenomenon are various, such as design factors, construction factors, hydrological factor, and crack diseases. The mid-partition wall of the double-arch tunnel was in the shape of the letter Y. Water seepage within the mountain was collected above the mid-partition wall, resulting in frequent cracking and water leakage. Figure 11 presents the exposed tunnel drainage pipes after the lining structure is removed, which are severely clogged. Clogging of the drainage system was caused by various factors such as concrete leakage during construction, the deposition of crystals from chemical reactions and the degradation the degradation of drainage pipe performance (Zhang et al., 2022).

The extent of damage caused by blocked drains was extensive and harmful. The pressure on the support structure increased due to groundwater collecting above the tunnel, potentially leading to cracks in the support structure. A total of 47 cracks were found in the left line of the Huangmeishan Tunnel, with 68.09% of them simultaneously leaking water. Ensuring the quality of tunnel construction is essential to prevent concrete or cement from clogging the drainage system during construction.

Moreover, the geographical location of the Huangmeishan Tunnel inherently facilitates water seepage and leakage. This can be attributed to the tunnel situated in an area that serves as a natural drainage pathway for groundwater. The presence of blockages in the drainage control system within the Huangmeishan Tunnel further exacerbates water leakage.

Therefore, when constructing tunnels in areas with high groundwater levels, new types of drains can be employed to minimize water seepage and leakage issues, such as siphon drains and drains under electromagnetic fields (Zhou et al., 2018). Siphon drainage pipes prevent blockages caused by particle deposits through separating water and soil, and pipes under electromagnetic fields can prevent the formation of crystals.

4.2.2 Disease of cracks

Figure 12 presents the image of crack disease in Huangmeishan Tunnel. Figure 13 gives the distribution ratio of crack disease in tunnel. Figure 14 shows the distribution of crack disease along the tunnel axis. During the crack disease detection in the Huangmeishan Tunnel, a total of 46 cracks were monitored in the left line. Among these, 1 crack occurred in the left side-wall, 42 cracks occurred from the left side-wall to the right side-wall, and 3 cracks occurred in the right side-wall. In the right line, 13 cracks were monitored, and all of them occurred from the left side-wall to the right side-wall.

Most cracks have a length of less than 10 m and a width of less than 1 mm. The widest crack detected was found at section YK4+576, measuring 15 mm in width (as shown in Figure 15). It is worth noting that all the existing cracks in the Huangmeishan Tunnel were caused by construction joints.

Tunnel cracks may be caused by water leakage. Take the left line as an example, 32 cracks were found to be leaking water, accounting for 68.09% of the crack issues and 39.51% of the water leakage issues. The clogging of the tunnel drainage system accelerated the formation of sediments in the water. The lining was subjected to

prolonged periods of pressure from sediment and water, resulting in lining leakage and cracking disease.

Additionally, the external loads associated with the dismantling process were also a reason for cracking diseases. The stability of the rock beneath the Huangmeishan Tunnel was poor. Above the entrance to the tunnel is a road for heavy vehicles, and Figure 14 shows concentrated cracks on the left and right side-walls of the entrance lining. It can be inferred that the cracks at the portal are caused by external loads.

4.2.3 Monitoring the thickness of the lining

The results of the thickness detection for the lining concrete by GPR at the entrance of Huangmeishan Tunnel are presented in Figure 16. The distribution of insufficient thickness in the second lining along the axis of the Huangmeishan Tunnel is shown in Figure 17. A total of 1,012 records were collected from the left line, with 113 records (11.17%) falling below the design thickness of the lining. Among them, 92 data had a thickness lower than the design value within 5 cm, accounting for 9.09% of the total. Additionally, 20 data were lower than the design value of the second lining between 5 cm and 10 cm, accounting for 1.98%, and 1 data was lower than the design value by more than 10 cm, accounting for 0.10%.

Similarly, 1,020 records were collected from the right line, with 125 records (12.25%) falling below the design thickness of the lining. Among them, 90 data had a thickness lower than the design value within 5 cm, accounting for 8.82% of the total. 29 data were lower than the design value between 5 cm and 10 cm, accounting for 2.84%, and 6 data were lower than the design value by more than 10 cm, accounting for 0.59%.

These results indicate that the thickness of the secondary lining in the Huangmeishan Tunnel fails to meet the requirements. Several factors may have contributed to this issue, including poor construction methods, limited construction monitoring, and inexperienced workers (Lu et al., 2019). Insufficient excavation during tunnel construction and untimely construction of the secondary lining may result in lining defects. This untimely construction could lead to significant deformations in the lining, and the inner contour of the primary lining exceeding the expected contour (Lu et al., 2021; Jiang et al., 2023). Inadequate thickness of the lining can cause stress redistribution, reducing the stiffness of the lining and increasing the risk of collapse (Liu et al., 2020).

4.3 Material performance tests

The concrete rebound hammer was employed for assessing the compressive strength of the secondary lining concrete in the Huangmeishan Tunnel. The design strength for both the sprayed concrete and the secondary lining concrete of Huangmeishan Tunnel was 25 MPa. However, the average of the 48 test results was 50.27 MPa, and all test results exceeded the design value.

The distribution of concrete compressive strength along the tunnel axis is shown in Figure 18. The minimum values of concrete compressive strength often occur at the tunnel entrances or at the deepest part of the tunnel. This is primarily due to the susceptibility of the entrance section to environmental erosion, leading to degradation of the structural performance. Additionally, the tunnel structure at the deepest burial depth was subjected to significant loads, which resulted in the degeneration of the mechanical property of the concrete.

Besides, the rebars were sampled and tested during the demolition of the tunnel. The bars were sampled every 50 m, and the length of the samples was more than 50 cm. 11 bars were sampled from mileage K4+125~K4+575 on the right line, 7 bars were sampled from mileage ZK4+125~ZK4+575 on the left line, and 6 bars were sampled from mileage 190–550 on the mid-partition wall. The average test results of 23 rebar samples are shown in Table 3. The average corrosion rate of the rebar samples is 45.2%, and the average tensile strength is 556.9 MPa. There is no significant correlation between the yield strength and the sampling location or corrosion rate.

4.4 The loading test

The tunnel loading test is a method used to assess the strength and stability of a tunnel structure. It provides valuable information about the structural performance by monitoring the response of the structure under load. Conducting an on-site tunnel loading test before the demolition of an existing tunnel is necessary to identify the strength and stability of the tunnel structures under actual load conditions. The tunnel loading test is an important tool for ensuring the safety and reliability of underground infrastructure. It is widely used in tunnel engineering and construction projects around the world.

The demolition of the Huangmeishan Tunnel involved the complete excavation of the mountain above the tunnel, and the tunnel vault will be used as a traffic lane for heavy vehicles. The safety of traffic under shallow overburden conditions needs to be verified in advance. Therefore, a loading test of the tunnel was conducted.

During the tunnel demolition, a construction transport vehicle with a weight of 40 tons (when fully loaded) was used. A fully loaded truck is the maximum load for tunnel dismantling. Hence, a 40-ton load test was carried out at section ZK4+512 in the Huangmeishan Tunnel. The subsidence at the vault and the haunch was simultaneously monitored. Figure 19 presents the time curves of the vertical displacement at the vault and the haunch at section ZK4+512. The maximum vertical displacement of the tunnel arch and haunch after the loading test was determined to be 1.73 mm and 1.32mm, respectively. These findings indicate that the construction vehicles were able to safely move above the tunnel during the study, confirming the reasonableness of the demolition construction scheme.

5 Evaluation and suggestions

5.1 Evaluation of the status of the Huangmeishan Tunnel

According to the quality defects and deterioration detection of the Huangmeishan Tunnel, the main problems of the Huangmeishan Tunnel after a long period of service are water seepage, cracks, and insufficient thickness of the second lining.

Water leakage in the tunnel may cause damage to the concrete structure of the tunnel lining and reduce the performance of the lining in enclosing the tunnel rock. Localized thickness deficiencies of the tunnel lining may result in cracks defects. The bending moment at the tunnel lining with localized thickness deficiencies will be reduced, but the bending moment of the adjacent lining would be increased. Insufficient thickness of the tunnel lining will directly lead to the reduction of the bearing capacity of the tunnel lining structure. When the insufficient thickness of the tunnel lining is more serious, the tunnel lining may even fracture, collapse, and result in other catastrophic consequences that significantly impact the safety of the lining.

Therefore, during the dismantling process of the Huangmeishan Tunnel, heavy trucks were restricted from passing through sections where thickness defects and cracks were found. Concurrently, enhanced monitoring of convergence deformations around the tunnel entrance was implemented to mitigate safety risks, such as collapses and other potential accidents.

5.2 Suggestions for similar tunnels

Based on the case of the Huangmeishan Tunnel demolition project, this section aims to analyze the reasons and propose measures to prevent similar issues from appearing in the design, construction, and operation phases of other tunnels.

5.2.1 Design reasons and proposed measures

When designing a tunnel, there are limitations on the quantity and depth of investigation and design work. These limitations may prevent the acquisition of complete geological data. For example, factors such as inaccurate classifications of surrounding rock, insufficient understanding of the direction of rock layers, and unclear identifications of geological sections may lead to the lack of specificity during the design. Thus, it is imperative to implement the following measures.

Some advanced techniques and technologies such as ground penetrating radar and seismic surveys, could be employed to obtain a more comprehensive understanding of the subsurface conditions (Yun et al., 2018). The selection of an appropriate tunnel cross-section structure should be based on the specific geological conditions. Additionally, close attention must be paid to the construction site, enabling timely design modifications in response to the actual construction processes and geological conditions encountered.

To mitigate the risk of structural damage, it is recommended to employ a foundation structure for the tunnel arch foot featuring a straight outer side and a rounded inner side. This design configuration helps to distribute stress and prevent concentration, reducing the likelihood of cracking in both the arch foot and the sidewalls.

5.2.2 Construction reasons and proposed measures

In tunnel construction, common construction quality problems are often related to the initial support, the arch, drainage systems, and secondary lining construction processes. To address these issues, the following measures can be implemented.

To optimize the surface blasting effects, the drilling efficiency and precision are suggested to be improved. Specialized tools are employed to enhance the quality of the drainage system, such as an infrared scanning position system, ultrasonic welding, and longitudinal and circumferential water-stops. The flow and quality of concrete for the secondary lining are controlled by employing the window pouring technology. The arch mold grouting construction technique is utilized to minimize hollowing and insufficient thickness of the lining.

5.2.3 Treatment of diseases

Different widths of cracks require different treatment methods. The assessment of cracking is needed as it can be a serious structural issue and risk life. For cracks that do not jeopardize structural safety, Table 4 suggests the recommended treatment methods for cracks of different widths.

In the treatment of water seepage, instant sealants and high-performance waterproofing agents are used for direct sealing. A 1–2 mm thick cement-based penetrating crystalline waterproofing material is applied within a minimum range of 40 cm around the water seepage point. The treatment method for water leakage defects is correlated with the location of the leakage. Table 5 provides the treatment methods for different locations of water leakage.

6 Conclusion

Based on the demolition project of the Huangmeishan Tunnel, the current paper proposed a demolition scheme for the double-arch tunnel and presented various researches during the demolition. The safety of the Huangmeishan Tunnel structure can be guaranteed after a long period of operation. The conclusions were as follows:

(1) Mechanical excavation was used in this project to demolish the tunnel and the slope stability was analyzed. The demolition scheme of the double-arch tunnel was proposed, including building the construction platform, demolishing the vault, the side-wall, and the remaining part of the tunnel.
(2) Oblique photography combined with automated modeling provides a more comprehensive view of the construction site and surrounding environment. This was confirmed in the Huangmeishan demolition project.
(3) Tunnel dismantling found that most of the leakage damage was distributed by the mid-partition wall, and the drain pipes were clogged severely by cement. Most of the tunnel lining thickness defects were within 5 cm. In the material performance tests, the actual compressive strength of the concrete was 50.07Mpa and the average corrosion rate of the rebar was 45.2%.
(4) The largest displacements of the tunnel arch and haunch after the loading test were 1.73 mm and 1.32 mm respectively, which show that heavy vehicle traffic during tunnel dismantling is safe. The loading test is necessary in tunnel demolition project.
(5) Based on the results of the research, this paper presents recommendations for the lifecycle of similar tunnels. Besides, this study could provide a reference for similar demolition projects, and the results of the research could be applied in future work, such as the development of an evaluation model for the structural behavior of long-term service tunnels.

Data availability statement

The original contributions presented in the study are included in the article/Supplementary Material, further inquiries can be directed to the corresponding author.

Author contributions

XK: Writing–original draft. XL: Project administration, Writing–review and editing. JX: Funding acquisition, Project administration, Writing–review and editing. AR: Data curation, Writing–review and editing. TL: Data curation, Writing–review and editing. YR: Writing–review and editing.

Funding

The authors declare financial support was received for the research, authorship, and/or publication of this article. Anhui provincial communications Holding Group science and technology project (JKKJ-2021-22).

Conflict of interest

Author JX was employed by Anhui Transportation Holding Group Co., Ltd.

The remaining authors declare that the research was conducted in the absence of any commercial or financial relationships that could be construed as a potential conflict of interest.

The authors declare that this study received funding from Anhui provincial communications Holding Group science and technology project (JKKJ-2021-22). The funder had the following involvement in the study: provide data and participate in field trials.

Publisher's note

All claims expressed in this article are solely those of the authors and do not necessarily represent those of their affiliated organizations, or those of the publisher, the editors and the reviewers. Any product that may be evaluated in this article, or claim that may be made by its manufacturer, is not guaranteed or endorsed by the publisher.

References

Bai, Y., Li, X., Yang, W., Xu, Z., and Lv, M. (2022). Multiscale analysis of tunnel surrounding rock disturbance: a PFC3D-FLAC3D coupling algorithm with the overlapping domain method. *Comput. geotechnics* 147, 104752. doi:10.1016/j.compgeo.2022.104752

Bowers, K., and Moss, N. (2018). Investigation and reconstruction of a London Underground tunnel, UK. *Proc. Institution Civ. Eng. - Civ. Eng.* 171 (1), 43–48. doi:10.1680/jcien.17.00019

Chang, L., Zhang, D., and Zhang, S. (2021). Characteristics and treatment measures of lining damage: a case study on a mountain tunnel. *Eng. Fail. Anal.* 128, 105595. doi:10.1016/j.engfailanal.2021.105595

Chen, Z., Chen, J., Liu, H., and Zhang, Z. (2018). Present status and development trends of underground space in Chinese cities: evaluation and analysis. *Tunn. Undergr. Space Technol.* 71, 253–270. doi:10.1016/j.tust.2017.08.027

Ciro, C., and Isidoro, R. (2022). A 3D computational fluid dynamics model for assessing the concrete spalling of a tunnel lining in the event of a fire. *Comput. geotechnics* 152, 527–540. doi:10.1016/j.compgeo.2022.105041

Ding, L., Zhang, L., Wu, X., Skibniewski, M. J., and Qunzhou, Y. (2014). Safety management in tunnel construction: case study of Wuhan metro construction in China. *Saf. Sci.* 62, 8–15. doi:10.1016/j.ssci.2013.07.021

Ding, Y., Zhang, X., and Zhang, B. (2022). Preliminary study on double lining support design for water plugging of highway tunnel under high water pressure in mountain area based on limited drainage. *Appl. Sci.* 12 (15), 7905. doi:10.3390/app12157905

Eisch, J. E. (1983). Planning/design features and case studies in freeway reconstruction. PART I. *Inst. Transp. Eng. J.* 10 (53), 14–23.

Gianpiero, B. (2020). Astra-Tunnelerneuerungsmethode – erneuerung einer nicht armierten Innenschale in Nachtarbeit bei Gewährleistung des Betriebs aller Fahrstreifen in Spitzenzeiten. *Geomechanics Tunn.* 13, 547–556. doi:10.1002/geot.202000024

GongHe, C. X., Li, Y., He, S. Z., Cheng, X., Huang, L. Y., et al. (2017). Long-term field corrosion monitoring in supporting structures of China xiamen xiangan subsea tunnel. *Acta Metall. Sin. Lett.* 30 (004), 399–408. doi:10.1007/s40195-017-0552-0

Han, F., Liu, Z., Wang, Yi, et al. (2022). Influence of road tunnel transforming to cutting on safety of lining structure. *J. Chongqing Jiaot. Univ. Nat. Sci.* 41 (7), 104–112. doi:10.3969/1.155n1674-0696.2022.07.16

Hawley, C. J., and Gräbe, P. J. (2022). Water leakage mapping in concrete railway tunnels using LiDAR generated point clouds. *Constr. Build. Mater.* 361, 129644. doi:10.1016/j.conbuildmat.2022.129644

Höllrigl Michael, Josef, T., and Wanker, C. (2015). Tunneling under challenging conditions – general renovation, escape and safety passageways via the supply air duct at the. *Arlb. Road. Tunnel".* 10, 7–10.

Jia, Y., Xia, Y., Chen, X., Zhou, Y., Han, X., and Zhou, S. (2019). Force and deformation characteristics during the reconstruction and expansion of shallow single-tube tunnels into large-span multiarch tunnels. *Adv. Mater. Sci. Eng.* 2019, 1–13. doi:10.1155/2019/2783784

Jiang, Xi, Zhang, X., Wang, S., Yun, B., and Huang, B. (2022). Case study of the largest concrete earth pressure balance pipe-jacking project in the world. *Transp. Res. Rec.* 2676 (7), 92–105. doi:10.1177/03611981221076842

Jiang, Xi, Zhang, Y., Zhang, Z., and Bai, Y. (2021). Study on risks and countermeasures of shallow biogas during construction of metro tunnels by shield boring machine. *Transp. Res. Rec.* 2675 (7), 105–116. doi:10.1177/0361198121994594

Jiang, Xi, Zhu, H., Yan, Z., Zhang, F., Ye, F., Li, P., et al. (2023). A state-of-art review on development and progress of backfill grouting materials for shield tunneling. *Dev. Built Environ.* 16, 100250. doi:10.1016/j.dibe.2023.100250

Kiwamu, T., and Kiyoshi, K. (2020). Evaluation of spalling of concrete pieces from tunnel lining employing joint shear model. *Tunn. Undergr. Space Technol.* 103, 103456. doi:10.1016/j.tust.2020.103456

Lin, J. (2014). Existing operational railway tunnel water leakage causes and remediation technologies. *Adv. Mater. Res.* 1004-1005, 1444–1449. doi:10.4028/www.scientific.net/amr.1004-1005.1444

Liu, S., Yao, S., Sun, R., and Yang, J. (2020). Damage behavior and maintenance design of tunnel lining based on numerical evaluation. *Eng. Fail. Anal.* 109, 104209. doi:10.1016/j.engfailanal.2019.104209

Lu, P., Chen, C., Liao, C. C., et al. (2019). Model test on joint leakage in underwater shield tunnel. *Chin. J. Rock Mech. Eng.* 38 (5), 993–1004.

Lu, P., Qiao, D., Wu, C., Wang, S., He, X., Zhang, W., et al. (2021). Effect of defects and remediation measures on the internal forces caused by a local thickness reduction in the tunnel lining. *Undergr. Space* 1 (7), 94–105. doi:10.1016/j.undsp.2021.06.001

Lunardi, P. (2012). Widening the Nazzano motorway tunnel from two to three lanes + an emergency lane without interrupting traffic. *Avances Tecnol´ ogicos Einnovaci´*3, 894–905.

Mei, W., Zhou, Y., and Hou, J. (2010). Real-time georobot automatic monitoring during shield under-crossing existing tunnel[C]. *Int. Conf. Optoelectron. Image Process.* 11, 153–156. doi:10.1109/ICOIP.2010.237

Shi, J., Zhang, X., Liang, J., Hu, L., and Li, Z. (2020). Study on multi-arch tunnel leakage disease with influence of rainfall and groundwater change. *IOP Conf. Ser. Mater. Sci. Eng.* 741 (1), 012101. doi:10.1088/1757-899x/741/1/012101

Tang, L., Yu, Li, Luo, X., Zhou, J., Li, Z., Yang, H., et al. (2023). Shaking table test on the seismic response and reinforcement measures of double-arch tunnels in mountainous areas. *Tunn. Undergr. space Technol.* 2023 (139), 105232. doi:10.1016/j.tust.2023.105232

Wang, C., Zhang, M., and He, Y. (2015). Deformation calculation for the existing tunnel induced by undercrossing shield tunneling. *Int. J. Res. Eng. Sci.* 11 (3), 07–11.

Wang, S., Jiang, Xi, and Bai, Y. (2019). The influence of hand hole on the ultimate strength and crack pattern of shield tunnel segment joints by scaled model test. *Front. Struct. Civ. Eng.* 13 (13), 1200–1213. doi:10.1007/s11709-019-0546-2

Wang, Y., Li, J., Wang, Z. F., and Chang, H. (2022). Structural failures and geohazards caused by mountain tunnel construction in fault zone and its treatment measures: a case study in Shaanxi. *Eng. Fail. Anal.* 138 (4), 106386. doi:10.1016/j.engfailanal.2022.106386

Wu, B., Liu, W., Shi, P., Xu, X., and Liu, Y. (2022). A case study of newly tunnels over-crossing the existing subway tunnels. *Int. J. Distributed Sens. Netw.* 18 (3), 155013292210871–176. doi:10.1177/15501329221087183

Xu, N., Zhang, X., and Zhao, J. L. (2022). Study on construction technology of bridge structure based on oblique photography. *J. Phys. Conf. Ser.* 2158 (1), 012024. doi:10.1088/1742-6596/2158/1/012024

Yan, F., Qiu, W., Zheng, Y., Jiang, S., Hu, H., Gao, G. g., et al. (2021). Experimental investigation and numerical analysis of mechanical behaviour of railway station reconstruction over twin tunnels. *Tunn. Undergr. Space Technol.* 112, 103918. doi:10.1016/j.tust.2021.103918

Yang, B., Ali, F., Zhou, Bo, Li, S., Yu, Y., Yang, T., et al. (2022). A novel approach of efficient 3D reconstruction for real scene using unmanned aerial vehicle oblique photogrammetry with five cameras. *Comput. Electr. Eng.* 99, 107804. doi:10.1016/j.compeleceng.2022.107804

Yang, J., Chen, L., Chen, Q., and Xie, X. (2017). Performance of overlapped shield tunneling through an integrated physical model tests, numerical simulations and real-time field monitoring. *Undergr. Space* 2 (1), 45–59. doi:10.1016/j.undsp.2017.04.002

Yike, W., and Yu, L. (2021). Analysis of detection and treatment schemes of highway tunnel lining cracks. *J. Archit. Res. Dev.* 5 (1), 4–7. doi:10.26689/jard.v5i1.1820

Yun, B., Jiang, Xi, Diaz, D., et al. (2018). "TBMs: capabilities, limitations and challenges," in Proceedings of GeoShanghai 2018 International Conference: Tunnelling and Underground Construction, Shanghai, China, May, 2018, 528–535. doi:10.1007/978-981-13-0017-2_53

Zhang, S., Xu, Q., Yoo, C., Min, B., Liu, C., Guan, X., et al. (2022). Lining cracking mechanism of old highway tunnels caused by drainage system deterioration: a case study of Liwaiao Tunnel, Ningbo, China. *Eng. Fail. Anal.* 137, 106270. doi:10.1016/j.engfailanal.2022.106270

Zhang, X., Yu, J., et al. (2020). Mountain tunnel under earthquake force: a review of possible causes of damages and restoration methods. *J. Rock Mech. Geotechnical Eng.* 12 (02), 206–218. doi:10.1016/j.jrmge.2019.11.002

Zhao, S., Kang, F., Li, J., and Ma, C. (2021). Structural health monitoring and inspection of dams based on UAV photogrammetry with image 3D reconstruction. , *Automation Constr.* 130, 103832. doi:10.1016/j.autcon.2021.103832

Zheng, Y. (2023). Deep excavation technique for demolition and reconstruction of the existing jinji pass tunnel. *Subgr. Eng.* 2023 (01), 212–215. doi:10.13379/j.issn.1003-8825.202211040

Zhou, Y., Zhang, X., Wei, L., Liu, S., Zhang, B., and Zhou, C. (2018). Experimental study on prevention of calcium carbonate crystallizing in drainage pipe of tunnel engineering. *Adv. Civ. Eng.* 2018, 1–11. doi:10.1155/2018/9430517

Zhu, L., Wang, K., Wang, B., et al. (2018). Widening Montedomini tunnel in presence of traffic: evolution of Nazzano method. *Tunn. Constr.* 3 (38), 461–467. doi:10.3973/i.issn.2096-4498.2018.03.014

frontiers | Frontiers in Earth Science

TYPE Original Research
PUBLISHED 27 December 2023
DOI 10.3389/feart.2023.1298758

Check for updates

OPEN ACCESS

EDITED BY
Xiaoyu Bai,
Qingdao University of Technology, China

REVIEWED BY
Yaozhang Sai,
Ludong University, China
Bo Feng,
Huazhong University of Science and Technology, China

*CORRESPONDENCE
Lin Tang,
tanglin2024@163.com

RECEIVED 22 September 2023
ACCEPTED 06 November 2023
PUBLISHED 27 December 2023

CITATION
Su C, Zhang Y, Tang L and Zhang W (2023), Analysis and quantitative identification of guided wave propagation mechanism in concrete.
Front. Earth Sci. 11:1298758.
doi: 10.3389/feart.2023.1298758

COPYRIGHT
© 2023 Su, Zhang, Tang and Zhang. This is an open-access article distributed under the terms of the Creative Commons Attribution License (CC BY). The use, distribution or reproduction in other forums is permitted, provided the original author(s) and the copyright owner(s) are credited and that the original publication in this journal is cited, in accordance with accepted academic practice. No use, distribution or reproduction is permitted which does not comply with these terms.

Analysis and quantitative identification of guided wave propagation mechanism in concrete

Chenhui Su[1], Yuhang Zhang[1], Lin Tang[2]* and Wenchao Zhang[1]

[1]Shangdong Key Laboratory of Intelligent Buildings Technology, School of Information and Electrical Engineering, Shandong Jianzhu University, Jinan, China, [2]School of Materials Science and Engineering, Shandong Jianzhu University, Jinan, China

Concrete is widely used in bridges, tunnels, nuclear power plants and other buildings, the damage of concrete will bring significant safety hazards for the building, therefore, detecting concrete damage is of great significance. In this paper, the propagation characteristics of guided waves in concrete plates are investigated, and finite element simulation is used to analyze the sensitivity of guided waves to the damage of concrete materials under different excitation frequencies. Simulation experiments on guided wave propagation are performed on concrete materials containing damage in the excitation frequency range from 25 to 100 kHz. The signals received by the sensors are analyzed in the time domain, while the reflected wave signals resulting from the contact of the signals with the damage are analyzed in the frequency domain. The results show that the excitation frequencies of 25 and 60 kHz are more sensitive to damage, and the quantitative identification of damage without reference can be realized by using the peak signals in the frequency domain at different excitation frequencies.

KEYWORDS

concrete, guided wave, Abaqus, finite element analysis, quantitative recognition

1 Introduction

Concrete has excellent compression resistance (Liao et al., 2023) and durability, it is the main material for construction engineering, and has a wide range of applications in the field of railroad tunnels, bridge works (Zhang et al., 2022a), nuclear power plants (Nasir Ayaz Khan et al., 2022) and so on. China produces more than 3 billion cubic meters of commercial concrete annually, and China is the world's largest cement manufacturing country. The extensive use of concrete also brings with it a series of problems. Concrete is prone to structural damage under the influence of the external environment and load. The common damage defects include steel corrosion, cavity, crack, honeycomb and so on. Concrete is made by pouring method, which is easy to produce holes under the influence of internal gas and external environment. At the same time, due to the dense reinforcement inside, it is easy to have small diameter holes after a long time of use. These damages can affect material properties to different degrees. If defects can be discovered and maintained early, catastrophic incidents can be avoided, which is important for the protection of people's property safety and maintenance of social stability, so the damage detection of concrete is particularly important.

The development of modern architecture has put forward higher requirements for the performance of concrete materials, which has triggered people's research on concrete

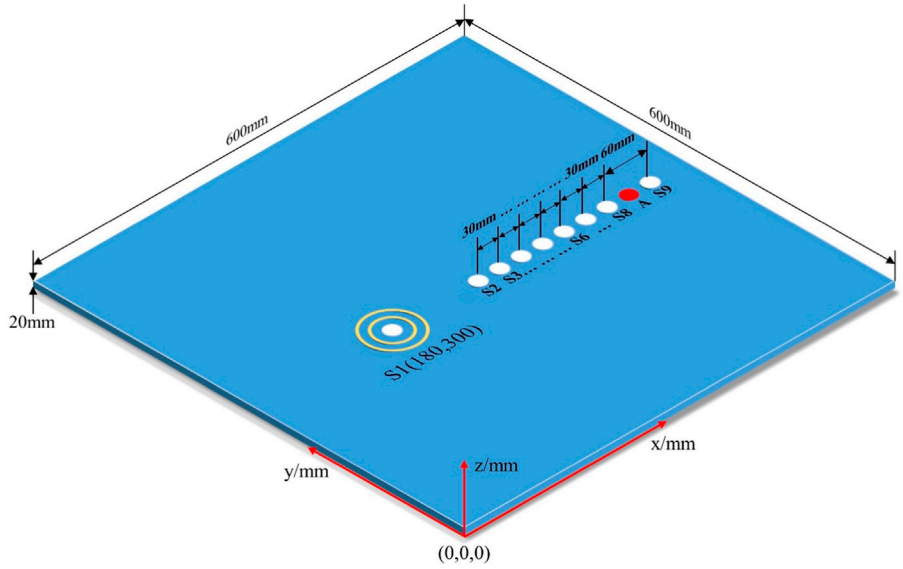

FIGURE 1
Simulation diagram.

TABLE 1 C60 concrete material parameters.

ρ(kg/m^3)	E (GPa)	ν
2,400	36	0.2

materials. For example, reinforcement fibers such as steel fiber (Cucuzza et al., 2023), basalt, and polyformaldehyde fiber (Yan et al., 2023) are added to improve the ability of concrete to resist cracking. Albidah et al. (2023) studied the effects of different coarse aggregate types on the properties of concrete materials. It is concluded that the increase of aggregate size reduces the number of cracks in the beam under four-point bending test and improves the shear strength of the beam. Xiao et al. (2023) analyzed the effect of pore structure on the performance of concrete.

Non-destructive testing (NDT) (Mićić et al., 2023) can detect the material without affecting the tested object. Common non-destructive testing methods include ultrasonic testing (Mousavi and Gandomi, 2021; Zhang et al., 2022b), acoustic emission method, infrared thermography, eddy current testing (Bao et al., 2021; Meng et al., 2021) and so on. Wang et al. (2023) used the acoustic emission method to observe the failure process of cemented asphalt filling mixes under different loads. Berthe et al. (2023) used high-speed infrared thermal imaging technology to observe materials under low-velocity impact and estimate the degree of damage. Every method has its advantages and limitations. Compared with these methods, ultrasonic guided wave method has the advantages of low cost, slow attenuation (Mei et al., 2020), sensitivity to small defects (Hu et al., 2022), and long propagation distance (Mitra et al., 2023). Over the years, a lot of achievements have been made in the directions of propagation mechanism, damage location (Feng et al., 2019), and healthy structure monitoring (Rautela et al., 2022; Mesnil et al., 2023). Therefore, the ultrasonic guided wave method can be used as an effective way to detect concrete damage detection.

Guided wave is a kind of elastic wave composed of transverse and longitudinal waves, and the propagation state is constrained by the geometry of the propagation medium. The interaction between guided wave and structural damage will produce phenomena such as reflection, scattering, and waveform conversion. The use of signal processing technology and damage discrimination methods to process the damage signal can be used to determine the type and location of the damage. Common materials include aluminum plates, composite plates, stiffened plates and so on. Lamb wave is a kind of guided wave transmitted in plate structure, which has the advantages of slow attenuation and long propagation distance and is suitable for damage monitoring of plate structures. Dr. Yongqing Yang used Lamb waves to analyze the dispersion curves of concrete plates under different conditions and the effect of the surrounding soil on the dispersion phenomenon. Hua et al. (2022) proposed an improved lamb-wave minimum variance imaging method to detect aluminum and composite laminates, which effectively identifies the damage location and reduces the imaging error. Some scholars have proposed a damage location algorithm (Pineda Allen and Ng, 2023) based on the contact non-linear combined frequency waves generated by the interaction between guided waves and damage, which can determine the layering damage location of composite laminates. Sikdar et al. (2023) proposed a structure monitoring method based on deep learning, it uses wavelet transform (Wu et al., 2021) to convert the high harmonics generated by the guided wave in contact with the damage into an image, and the damage of the stiffened plate can be obtained by analyzing and processing the image using deep learning. Feng et al. (2023) carried out low-speed impact experiments on carbon fiber composites, extracted time-frequency characteristics of signals, and used neural networks (Feng et al., 2022) to accurately detect impact locations.

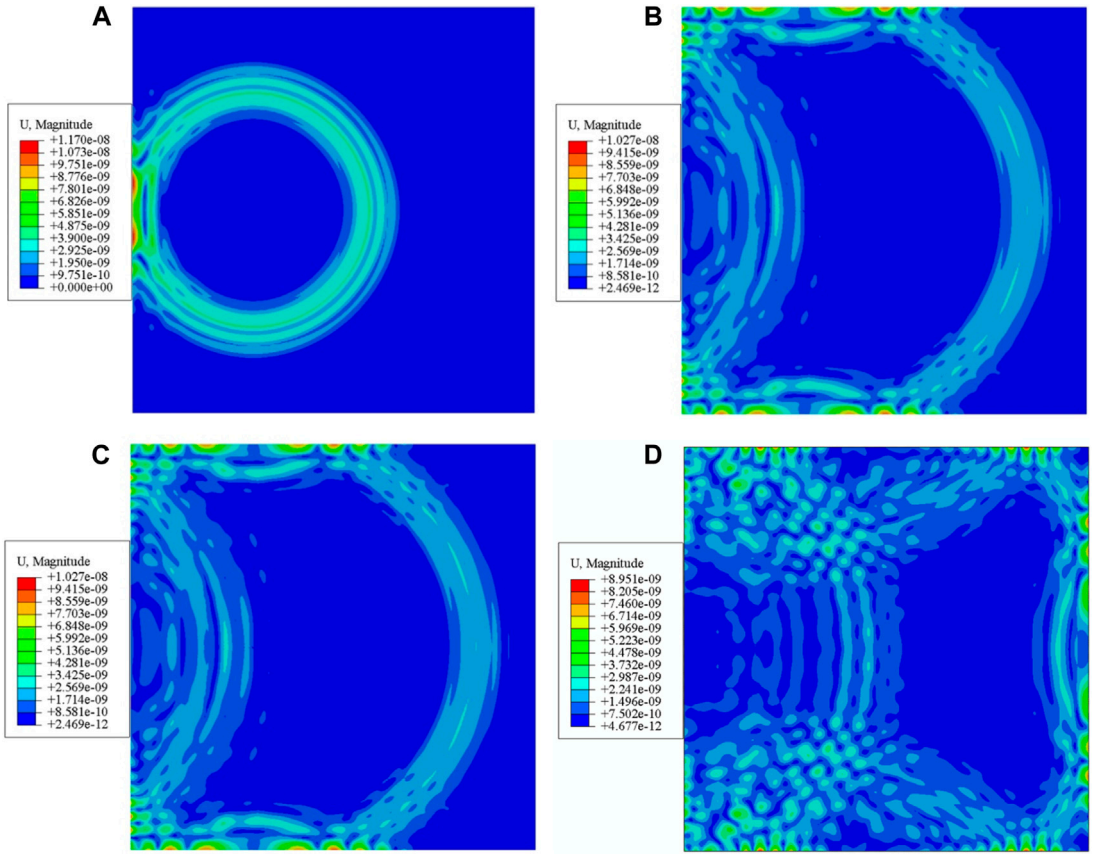

FIGURE 2
Cloud image of guided wave propagation under undamaged concrete at different time. **(A)** 0.103 ms; **(B)** 0.166 ms; **(C)** 0.195 ms; **(D)** 0.219 ms.

Based on the research of guided wave properties, NDT technology have also been used in the field of construction. Some scholars have used stress waves to test concrete covered with soft coatings for judging the material properties of modified concrete (Xu et al., 2022). Yu et al. proposed a theoretical method (Yu et al., 2021) for the location of concrete surface cracks based on the attenuation of Rayleigh wave propagation energy and conducted numerical verification. Liu et al. (2022) studied the effects of steel bar type, water-cement ratio, and concrete thickness on the corrosion process through ultrasonic guided wave amplitude. Aseem and Ng (2021) analyzed the de-bonding of reinforced concrete structures by using the nonlinear characteristics of ultrasonic guided wave in de-bonding detection. Lead zirconate titanate (PZT) sensor is one of the commonly used equipment when using guided wave to inspect concrete. Lim et al. (2016) monitored the material properties of concrete beams during the forming process by attaching PZT sensors to the surface. Yu et al. (2020) measured the material properties of concrete blocks using an embedded PZT sensor.

The above scholars have imaged and localized the damage and analyzed the material properties of concrete based on guided wave characteristics, which promotes the development of nondestructive testing technology. However, the selection of guided wave frequency was not described in detail, and the quantitative identification (Feng et al., 2020) of damage was not carried out. Selecting the excitation frequency sensitive to damage is helpful to improve the accuracy of damage identification and location. Therefore, based on the propagation characteristics of guided waves in concrete, this paper analyzes the concrete under damage conditions in the excitation frequency range of 25–100k Hz, and obtains the guided wave frequency sensitive to damage. Meanwhile, the concrete cavity type damage is quantitatively identified according to the amplitude value under different damage conditions.

2 Basic theory of lamb waves

Lamb wave is a kind of elastic stress wave propagating in a thin plate. Lamb waves (Lamb, 1917) were obtained by H. Lamb in England in 1917 when solving the fluctuation equations by the flat plate free boundary condition. Lamb waves have dispersion characteristics and multimodal characteristics (Li et al., 2022). The dispersion characteristic refers to the different propagation speed of the waves with different frequencies. The propagation speed of Lamb waves at different frequencies can be obtained by calculating the dispersion curve. The multimodal characteristic means that the mode of the wave will change after the wave is transferred to the upper and lower boundary. The wave modes in a thin plate can be divided into two kinds according to the different vibration directions of the particles in the plate: symmetric mode and antisymmetric mode. The two modes can be described by the Rayleigh-lamb equation:

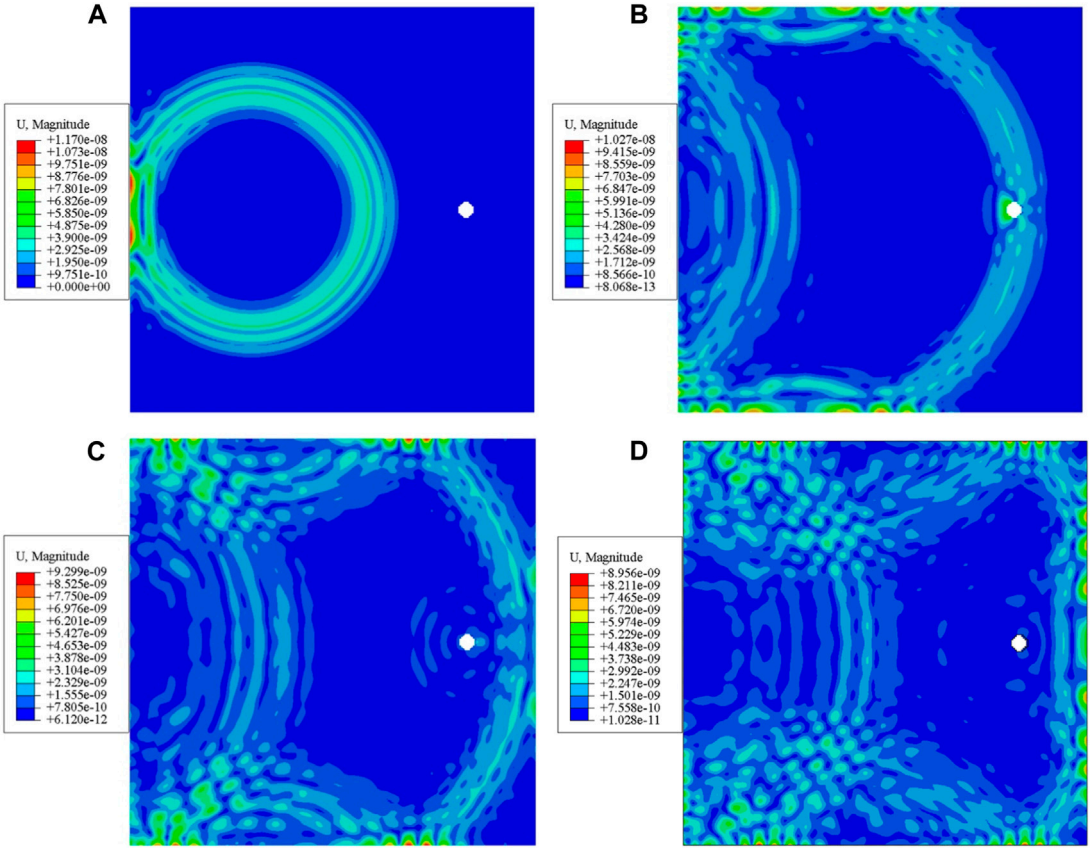

FIGURE 3
Cloud image of guided wave propagation under damaged concrete at different time. **(A)** 0.103 ms; **(B)** 0.166 ms; **(C)** 0.195 ms; **(D)** 0.219 ms.

Symmetry mode:

$$\frac{\tan(qh)}{\tan(ph)} = -\frac{4k^2pq}{(q^2-k^2)^2} \tag{1}$$

Antisymmetric model:

$$\frac{\tan(qh)}{\tan(ph)} = -\frac{(q^2-k^2)^2}{4k^2pq} \tag{2}$$

Where, $p^2 = \omega^2/{c_L}^2 - k^2$, $q^2 = \omega^2/{c_T}^2 - k^2$, c_L represents longitudinal wave velocity, c_T represents transverse wave speed, k is the wave number. Phase velocity and group velocity are two important parameters of Lamb waves, and due to the dispersive nature of Lamb waves, each individual wave has a specific propagation velocity. Phase velocity is used to express the rate of phase change of a certain frequency, which can be expressed as:

$$C_p = \frac{\omega}{k} \tag{3}$$

ω represents the excitation signal frequency, k represents the number of harmonic waves. In the transmission process of the signal in the plate, the waveform of different frequencies will be superimposed and then change the amplitude. Each wave packet in the Lamb wave is formed by the superposition of the amplitudes of several different waves. Assuming that two signals with the same amplitude and frequencies ω_1 , ω_2 are superimposed

$$f(x,t) = A\cos(k_1x - \omega_1t) + A\cos(k_2x - \omega_2t) \tag{4}$$

A represents the amplitude and k_1 and k_2 represent the wave numbers of the two harmonics, respectively. The following results can be obtained by transforming using the trigonometric formula.

$$f(x,t) = 2A\cos\left(\frac{k_1-k_2}{2}x - \frac{\omega_1-\omega_2}{2}t\right) \cdot \cos\left(\frac{k_1+k_2}{2}x - \frac{\omega_1+\omega_2}{2}t\right) \tag{5}$$

$$k_c = \frac{k_1+k_2}{2} \tag{6}$$

$$\Delta k = \frac{k_1-k_2}{2} \tag{7}$$

$$\omega_c = \frac{\omega_1+\omega_2}{2} \tag{8}$$

$$\Delta\omega = \frac{\omega_1-\omega_2}{2} \tag{9}$$

Substituting Eq. 3 gives the following result:

$$f(x,t) = 2A\cos(\Delta kx - \Delta\omega t)\cdot\cos(k_cx - \omega_ct) \tag{10}$$

The resulting waveform can be regarded as a combination of low frequency and high frequency terms. The phase velocity $C_p = \omega_c/k_c$ is in the high frequency term, and the group velocity $C_g = \Delta\omega/\Delta k = d\omega/dk$ is in the low frequency term. The formula for calculating group velocity can be written as

$$C_g = \frac{d\omega}{d\left(\frac{\omega}{C_p}\right)} = \frac{C_p^2}{C_p - \omega\frac{dC_p}{d\omega}} \tag{11}$$

3 Simulation analysis of guided wave propagation in concrete

3.1 Simulation model

In practical engineering, the damage of concrete is complicated. In order to find out the excitation frequency sensitive to structural damage, this experiment selects the hole-type damage as a common damage for simulation. ABAQUS finite element software was used for simulation, and the size of concrete slab was set as 600 mm*600 mm*20 mm. As shown in Figure 1, the model is equipped with a total of 9 sensors, ranging from S1 to S9. Which S1 (180, 300) as the exciter, S2~S9 as the sensors to receive the signal, the coordinates of sensor S2 are (300, 300), and A (510, 300) as the damage center, the schematic diagram is shown in Figure 1.

The concrete parameters of model C60 were used for simulation in the experiment, and the specific material parameters are shown in Table 1.

The parameters in Table 1 were used for calculation. In order to ensure the accuracy of numerical simulation, at least 10 grids should be included in a wavelength range. The shear modulus is as follows:

$$G = \frac{E}{2(1+2\nu)} = 1.5 \times 10^{10} Pa \tag{12}$$

The minimum phase velocity C_P is equal to the shear wave velocity C_T, and the shear wave velocity and longitudinal wave velocity C_L are calculated as follows:

$$C_T = \sqrt{\frac{G}{\rho}} = 2.5 \times 10^3 m/s \tag{13}$$

$$C_L = \sqrt{\frac{E(1-\nu)}{\rho(1+\nu)(1-2\nu)}} = 4083 m/s \tag{14}$$

The higher the frequency, the smaller the corresponding wavelength, and the higher the corresponding grid requirements. Select 100 kHz for calculation:

$$\lambda_{min} = \frac{C_P}{f_c} = \frac{C_T}{f_c} = 0.025 m \tag{15}$$

$$L_{max} \le \frac{\lambda_{min}}{10} = 0.0025 m \tag{16}$$

The raw materials of C60 concrete material are cement, mineral powder, fly ash, medium sand, 5–25 mm crushed stone and water. The wavelength of the 100 kHz excitation signal is about 25 mm, which is larger than the diameter of the coarse aggregate, so the scattering and diffraction attenuation of the coarse aggregate is ignored, and the concrete material is simplified to a uniform and isotropic medium (Lim et al., 2018). Lead zirconate titanate (PZT) sensor is often used to transmit and receive stress waves when testing concrete materials with guided waves. In the simulation process, the sensor is simplified as the excitation point, and the loading direction of the excitation signal is set as the vertical incidence excitation.

The signal propagates in the concrete plate, and is reflected and transmitted after contact with the hole type damage, and the reflected wave generated is received by the sensor. Because of the different excitation frequency and damage diameter, the amplitude and phase of the reflected wave will change.

The concrete plate model is established, and the material parameters are set according to Table 1. The center frequency is scanned from 25 to 100 kHz in steps of 10 and 15 kHz. The formula for the excitation frequency is as follows:

$$A = \frac{1}{2}\left[1 - \cos\left(\frac{2\pi f_c t}{n}\right)\sin\left(2\pi f_c t\right)\right] \tag{17}$$

Where A represents the amplitude, f_c represents the frequency, n represents the number of signal cycles (n = 5), and t represents the propagation duration of the waves. The sampling frequency is 1×10^7. The damage in the simulation is realized as through holes with a diameter range of 0–25 mm, and the step size of 5 mm. The concrete is constructed using a hexahedral reduced-integral three-dimensional solid cell (C3D8R). The mesh size of finite element simulation modeling is 2.5 mm and the number of cells is 460,800.

3.2 Simulation cloud map and time domain signal analysis

After contacting the damage, Lamb wave will produce more obvious reflected wave signal, which can be used to distinguish the damage of concrete. Taking the ex-citation frequency of 60 kHz as an example, the propagation cloud image of the simulation model before and after damage at the same time is shown in Figures 2, 3.

As can be seen from Figure 2, the guided wave propagates around from the excitation point and generates an obvious reflected wave after contacting the boundary. In Figure 3, in addition to the boundary reflected wave, the guided wave also produces obvious reflected wave signal after contact with the concrete damage. Next, excitation signals of different frequencies are used for simulation. Sensor S6 in Figure 1 is used to collect signals. The Lamb wave signals collected are shown in Figure 4. The boxed portion of Figure 4 contains the echo signal generated by the reflection of the signal after contact with the damage.

As can be seen from Figure 4, the first point is that as the frequency of the excitation signal increases, the obtained time-domain signal becomes intensive, and the amplitude gradually decreases. The second point is that with the change of the damage diameter, the peak size of the reflected signal wave packet fluctuates. At 25 and 40 kHz, it changes regularly: with the increase of the damage diameter, the amplitude of the reflected signal decreases. As the excitation frequency increases, the waveform becomes more complex. In order to obtain a more intuitive signal difference, the reflected signals in the boxed section are observed below by converting them from time-domain signals to frequency-domain signals.

3.3 Damage reflected wave frequency domain signal analysis

The reflected wave part of Lamb wave time domain signal collected by sensor S6 in Figure 1 is converted into frequency domain signal, as shown in Figure 5:

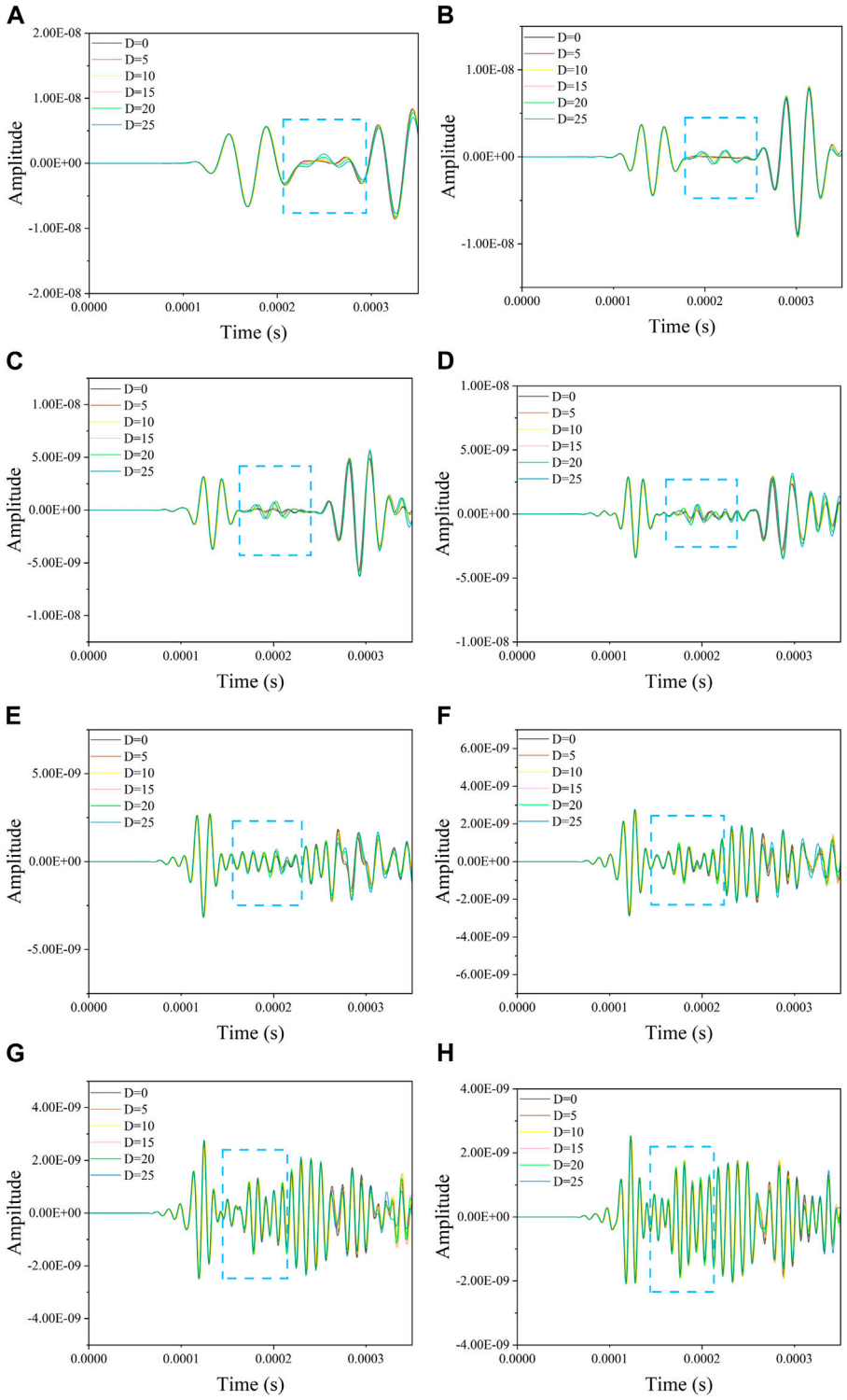

FIGURE 4
Time domain signal diagram of 25–100 kHz excitation frequency under different damage. **(A)** 25 kHz; **(B)** 40 kHz; **(C)** 50 kHz; **(D)** 60 kHz; **(E)** 70 kHz; **(F)** 80 kHz; **(G)** 90 kHz; **(H)** 100 kHz.

From the frequency domain signal plot in Figure 5, the first is that the frequency corresponding to the peak value of the frequency domain signal is close to the frequency of the excitation signal. The second is that the peak value of the frequency domain changes at different damage diameters. Among them, the peak signals in the frequency domain with excitation frequencies of 50, 70, 80, 90, and 100 kHz did not make regular changes with damage changes. They do not have an advantage when selecting the excitation signal

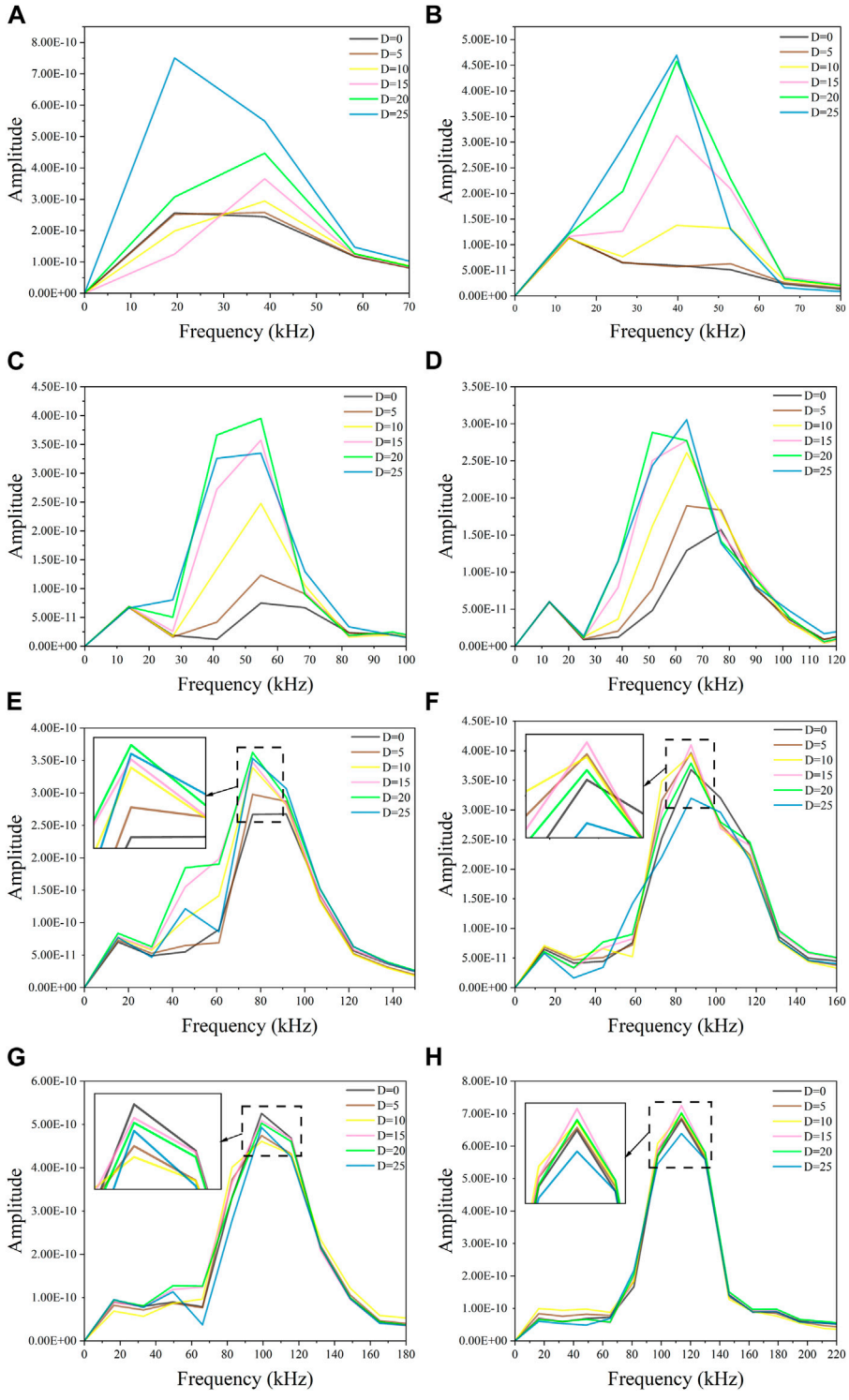

FIGURE 5
The frequency domain signal diagram of 25–100 kHz reflected wave signal under different damage. **(A)** 25 kHz; **(B)** 40 kHz; **(C)** 50 kHz; **(D)** 60 kHz; **(E)** 70 kHz; **(F)** 80 kHz; **(G)** 90 kHz; **(H)** 100 kHz.

sensitive to damage, while the frequency domain amplitude of excitation frequency of 25, 40, and 60 kHz increases with the increase of damage diameter, and the frequency domain peak value is consistent with the damage size arrangement.

From the perspective of amplitude and signal variation, 25, 40, and 60 kHz excitation signals are more conducive to signal acquisition and identification and are more sensitive to damage.

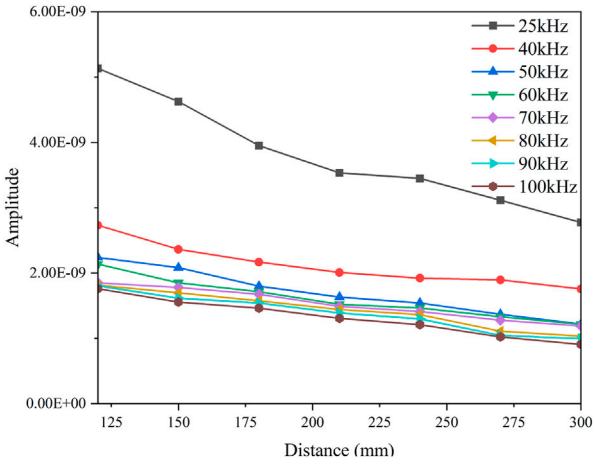

FIGURE 6
Frequency domain amplitude variation with propagation distance.

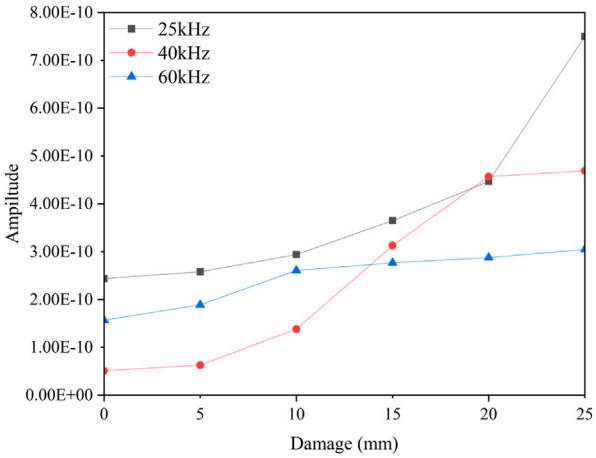

FIGURE 8
Reflection amplitude variation with damage diameter in frequency domain.

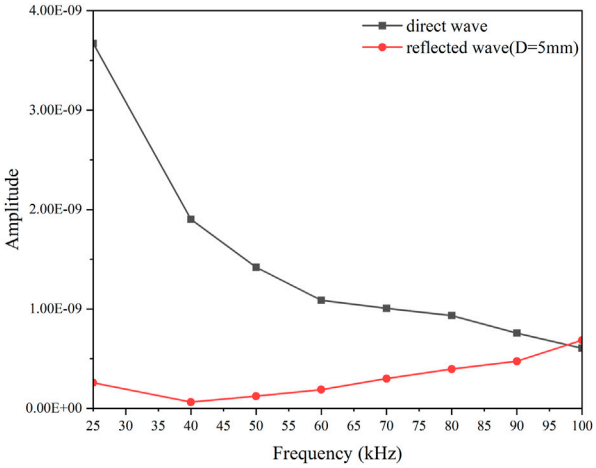

FIGURE 7
Direct wave and reflected wave comparison diagram.

4 Quantitative identification

4.1 Signal propagation distance and amplitude variation

In order to study the variation of the signal frequency domain amplitude with the propagation distance, seven sensors were set up on the model, and the sensor spacing is 30 mm, as shown in S2~S8 in Schematic Figure 1. The excitation signals sent by the sensor S1 pass through the sensors S2~S8, and the direct wave signals received by the sensor are selected for frequency domain analysis. As shown in Figure 6.

The direct wave signal received by the evenly spaced sensor s2~s8 is converted into the frequency domain signal, and the change of the peak signal and the propagation distance in the frequency domain is plotted. As can be seen from Figure 6, with the increase of the propagation distance, the peak value of the signal in the frequency domain decreases continuously, indicating that concrete is the attenuation medium of sound wave. Meanwhile, with the increase of frequency, the peak value of the signal in the frequency domain decreases continuously, proving that the amplitude of the low-frequency wave is large.

From Figure 6, the frequency domain amplitude decreases with increasing propagation distance and shows a clear linear variation. It can be concluded that the amplitude of the excitation signal decreases with the increase of the propagation distance. The transmissive wave at S9 was analysed, and the results show that the signal shows a regular arrangement only at 80–100 kHz: with the increase of the damage diameter, the amplitude of the transmissive wave frequency domain decreases.

4.2 Direct and reflected waves

To better analyze the amplitude changes before and after the damage, the direct and reflected waves at the sensor S6 in schematic Figure 1 were analyzed, and the diameter of the reflected wave damage was selected to be 5 mm, as shown in Figure 7.

From Figure 7, under the no damage condition, the amplitude in the frequency domain decreases with increasing frequency, and the overall reflected wave increases with increasing frequency, while a larger amplitude facilitates damage detection, so it is more appropriate to choose a lower excitation frequency. 25–70 kHz direct wave and reflected wave have obvious amplitude difference, but 40 kHz reflected wave frequency domain amplitude is small, so it is difficult to be used as a judgment condition.

4.3 Change of damage reflection amplitude

The variation of the frequency domain amplitude of the reflected wave with the size of the damage diameter at different frequencies is

plotted, and it is concluded that the frequency domain amplitude of the reflected wave changes regularly with the increase of the damage diameter at the excitation frequencies of 25, 40, and 60 kHz, as shown in Figure 8.

From Figure 8, the frequency domain amplitudes at all three frequencies become larger with the increase of damage diameter, and the regularly changing amplitudes are more favorable for damage discrimination. The three curves were linearly fitted using Origin software, and the corresponding fits for 25, 40, and 60 kHz were 0.79, 0.93, and 0.9, respectively. It can be concluded that the changes of reflected wave with damage diameter are more linear and regular under the excitation frequency of 40 and 60 kHz.

In Section 3 of the article, the frequency domain amplitude of the reflected wave increases with the increase of the damage diameter under the excitation frequency of 25, 40, and 60 kHz. Then, through the linear analysis of the reflected wave signal at 25, 40 and 60 kHz, and the comparison of the amplitude of the reflected wave and the direct wave, it is concluded that the excitation frequency of 60 kHz is the most suitable for damage detection. However, in Figure 8, the correlation coefficient R square of the peak signal in the frequency domain corresponding to 60 kHz after fitting is 0.9, which indicates that it has a good fitting effect, and further indicates that the relationship between the damage diameter and the peak value in the frequency domain is approximately linear. Therefore, based on this linear relationship, damage can be quantitatively identified without reference by measuring the peak value of a specific frequency in the frequency domain, and the magnitude of damage can be determined by comparing the detected data with the experimental data.

5 Conclusion

In this paper, the propagation characteristics of Lamb waves in concrete slabs are analyzed according to the relevant theories of ultrasound. Based on simulation, the damage detection of concrete plate is carried out, and the sensitivity of different excitation frequency to material damage is analyzed. Finally, quantitative identification without reference is carried out. The main conclusions are as follows:

(1) According to the simulation results, the increase of excitation frequency or propagation distance will reduce the signal amplitude, so the selection of lower frequency excitation signal is conducive to signal acquisition and damage discrimination.
(2) The Lamb wave produces a reflected wave signal upon contact with the damage. The peak value of the reflected wave signal generated by 25, 40, and 60 kHz is consistent with the damage size in the frequency domain and is more sensitive to the damage size. There is a suitable difference between the direct wave and the reflected wave amplitude of 25 and 60 kHz signals, and 60 kHz has better sensitivity, so it is more suitable as the excitation frequency for damage detection.
(3) The simulation results can be used for quantitative damage identification of signals at 25 and 60 kHz excitation frequencies without reference. The material is tested under the set excitation frequency, and the damage diameter can be obtained by comparing the detection result with the frequency domain peak value in the simulation result.

Data availability statement

The raw data supporting the conclusion of this article will be made available by the authors, without undue reservation.

Author contributions

CS: Writing–review and editing. YZ: Formal Analysis, Project administration, Supervision, Writing–review and editing. LT: Conceptualization, Data curation, Methodology, Writing–original draft. WZ: Funding acquisition, Resources, Validation, Visualization, Writing–review and editing.

Funding

The authors declare financial support was received for the research, authorship, and/or publication of this article. This research was funded by the Doctoral Research Fund Project of Shandong Jianzhu University under Grant X21037Z, Shandong Province Natural Science Foundation, China, ZR2021QF118.

Acknowledgments

The authors would like to thank the editors and reviewers for their valuable suggestions for this paper.

Conflict of interest

The authors declare that the research was conducted in the absence of any commercial or financial relationships that could be construed as a potential conflict of interest.

Publisher's note

All claims expressed in this article are solely those of the authors and do not necessarily represent those of their affiliated organizations, or those of the publisher, the editors and the reviewers. Any product that may be evaluated in this article, or claim that may be made by its manufacturer, is not guaranteed or endorsed by the publisher.

References

Albidah, A. S., Alqarni, A. S., Wasim, M., and Abadel, A. A. (2023). Influence of aggregate source and size on the shear behavior of high strength reinforced concrete deep beams. *Case Stud. Constr. Mater.* 19, e02260. doi:10.1016/j.cscm.2023.e02260

Aseem, A., and Ng, C. T. (2021). Debonding detection in rebar-reinforced concrete structures using second harmonic generation of longitudinal guided wave. *NDT E Int.* 122, 102496. doi:10.1016/j.ndteint.2021.102496

Bao, Y., Wan, T., Liu, Z., Bowler, J. R., and Song, J. (2021). Integral equation fast solver with truncated and degenerated kernel for computing flaw signals in eddy current non-destructive testing. *NDT E Int.* 124, 102544. doi:10.1016/j.ndteint.2021.102544

Berthe, J., Chaibi, S., Portemont, G., Paulmier, P., Laurin, F., and Bouvet, C. (2023). High-speed infrared thermography for in-situ damage monitoring during impact test. *Compos. Struct.* 314, 116934. doi:10.1016/j.compstruct.2023.116934

Cucuzza, R., Aloisio, A., Accornero, F., Marinelli, A., Bassoli, E., and Marano, G. C. (2023). Size-scale effects and modelling issues of fibre-reinforced concrete beams. *Constr. Build. Mater.* 392, 131727. doi:10.1016/j.conbuildmat.2023.131727

Feng, B., Pasadas, D. J., Ribeiro, A. L., and Ramos, H. G. (2019). Locating defects in anisotropic CFRP plates using ToF-based probability matrix and neural networks. *IEEE Trans. Instrum. Meas.* 68 (5), 1252–1260. doi:10.1109/tim.2019.2893701

Feng, B., Chen, W., Ito, S., Yusa, N., Hashizume, H., Ribeiro, A. L., et al. (2020). Quantitative evaluation of the delamination length in mechanical lap joints of high-temperature superconducting tapes using Lamb waves. *Measurement* 156, 107606. doi:10.1016/j.measurement.2020.107606

Feng, B., Ribeiro, A. L., Pasadas, D. J., and Ramos, H. G. (2022). Locating low velocity impacts on a composite plate using multi-frequency image fusion and artificial neural network. *J. Nondestruct. Eval.* 41 (2), 34. doi:10.1007/s10921-022-00865-2

Feng, B., Cheng, S., Deng, K., and Kang, Y. (2023). Localization of low-velocity impact in CFRP plate using time–frequency features of guided wave and convolutional neural network. *Wave Motion* 119, 103127. doi:10.1016/j.wavemoti.2023.103127

Hu, X., Ng, C.-T., and Kotousov, A. (2022). Early damage detection of metallic plates with one side exposed to water using the second harmonic generation of ultrasonic guided waves. *Thin-Walled Struct.* 176, 109284. doi:10.1016/j.tws.2022.109284

Hua, J., Zhang, H., Miao, Y., and Lin, J. (2022). Modified minimum variance imaging of Lamb waves for damage localization in aluminum plates and composite laminates. *NDT E Int.* 125, 102574. doi:10.1016/j.ndteint.2021.102574

Lamb, H. (1917). On waves in an elastic plate. *Proc. R. Soc. Lond. Ser. A, Contain. Pap. a Math. Phys. character* 93 (648), 114–128. doi:10.1098/rspa.1917.0008

Li, Y., Wang, K., Feng, W., Wu, H., Su, Z., and Guo, S. (2022). Insight into excitation and acquisition mechanism and mode control of Lamb waves with piezopolymer coating-based array transducers: analytical and experimental analysis. *Mech. Syst. Signal Process.* 178, 109330. doi:10.1016/j.ymssp.2022.109330

Liao, L., Wu, S., Hao, R., Zhou, Y., and Xie, P. (2023). The compressive strength and damage mechanisms of pervious concrete based on 2D mesoscale pore characteristics. *Constr. Build. Mater.* 386, 131561. doi:10.1016/j.conbuildmat.2023.131561

Lim, Y. Y., Kwong, K. Z., Liew, W. Y. H., and Soh, C. K. (2016). Non-destructive concrete strength evaluation using smart piezoelectric transducer—a comparative study. *Smart Mater. Struct.* 25 (8), 085021. doi:10.1088/0964-1726/25/8/085021

Lim, Y. Y., Kwong, K. Z., Liew, W. Y. H., Padilla, R. V., and Soh, C. K. (2018). Parametric study and modeling of PZT based wave propagation technique related to practical issues in monitoring of concrete curing. *Constr. Build. Mater.* 176, 519–530. doi:10.1016/j.conbuildmat.2018.05.074

Liu, Y., Ding, W., Zhao, P., Qin, L., and Shiotani, T. (2022). Research on in-situ corrosion process monitoring and evaluation of reinforced concrete via ultrasonic guided waves. *Constr. Build. Mater.* 321, 126317. doi:10.1016/j.conbuildmat.2022.126317

Mei, H., James, R., Haider, M. F., and Giurgiutiu, V. (2020). Multimode guided wave detection for various composite damage types. *Appl. Sci.* 10 (2), 484. doi:10.3390/app10020484

Meng, X., Feng, J., Pai, N., Zequan, H., Kaiyuan, L., Cheng, Z., et al. (2021). Effects of filler type and aging on self-sensing capacity of cement paste using eddy current-based nondestructive detection. *Measurement* 182, 109708. doi:10.1016/j.measurement.2021.109708

Mesnil, O., Recoquillay, A., Fisher, C., Serey, V., Sharma, S., and d'Almeida, O. (2023). Self-referenced robust guided wave based defect detection: application to woven composite parts of complex shape. *Mech. Syst. Signal Process.* 188, 109948. doi:10.1016/j.ymssp.2022.109948

Mićić, M., Brajović, L., Lazarević, L., and Popović, Z. (2023). Inspection of RCF rail defects – review of NDT methods. *Mech. Syst. Signal Process.* 182, 109568. doi:10.1016/j.ymssp.2022.109568

Mitra, A. K., Aradhye, A. A., and Joglekar, D. M. (2023). Low frequency ultrasonic guided wave propagation through honeycomb sandwich structures with non-uniform core thickness. *Mech. Syst. Signal Process.* 191, 110155. doi:10.1016/j.ymssp.2023.110155

Mousavi, M., and Gandomi, A. H. (2021). Wood hole-damage detection and classification via contact ultrasonic testing. *Constr. Build. Mater.* 307, 124999. doi:10.1016/j.conbuildmat.2021.124999

Nasir Ayaz Khan, M., Yaqub, M., and Malik, A. H. (2022). High density concrete incorporating grit scale aggregates for 4th generation nuclear power plants. *Constr. Build. Mater.* 337, 127578. doi:10.1016/j.conbuildmat.2022.127578

Pineda Allen, J. C., and Ng, C. T. (2023). Damage detection in composite laminates using nonlinear guided wave mixing. *Compos. Struct.* 311, 116805. doi:10.1016/j.compstruct.2023.116805

Rautela, M., Senthilnath, J., Monaco, E., and Gopalakrishnan, S. (2022). Delamination prediction in composite panels using unsupervised-feature learning methods with wavelet-enhanced guided wave representations. *Compos. Struct.* 291, 115579. doi:10.1016/j.compstruct.2022.115579

Sikdar, S., Ostachowicz, W., and Kundu, A. (2023). Deep learning for automatic assessment of breathing-debonds in stiffened composite panels using non-linear guided wave signals. *Compos. Struct.* 312, 116876. doi:10.1016/j.compstruct.2023.116876

Wang, S., Fu, L., Chen, X., Gong, M., Xiong, Z., and Hong, J. (2023). Characteristic analysis of cement grouted asphalt mixture cracking based on acoustic emission. *Constr. Build. Mater.* 375, 130927. doi:10.1016/j.conbuildmat.2023.130927

Wu, J., Xu, X., Liu, C., Deng, C., and Shao, X. (2021). Lamb wave-based damage detection of composite structures using deep convolutional neural network and continuous wavelet transform. *Compos. Struct.* 276, 114590. doi:10.1016/j.compstruct.2021.114590

Xiao, J., Lv, Z., Duan, Z., and Zhang, C. (2023). Pore structure characteristics, modulation and its effect on concrete properties: a review. *Constr. Build. Mater.* 397, 132430. doi:10.1016/j.conbuildmat.2023.132430

Xu, C., Chen, W., Hao, H., Pham, T. M., and Bi, K. (2022). Static mechanical properties and stress wave attenuation of metaconcrete subjected to impulsive loading. *Eng. Struct.* 263, 114382. doi:10.1016/j.engstruct.2022.114382

Yan, Y., Guo, R., Wei, Y., Pan, T., Li, X., and Tan, L. (2023). Strain-rate sensitivity analysis of the fracture behaviour of polyoxymethylene-fibre-reinforced airport-pavement concrete. *Constr. Build. Mater.* 402, 133048. doi:10.1016/j.conbuildmat.2023.133048

Yu, H., Lu, L., and Qiao, P. (2020). Assessment of wave modulus of elasticity of concrete with surface-bonded piezoelectric transducers. *Constr. Build. Mater.* 242, 118033. doi:10.1016/j.conbuildmat.2020.118033

Yu, H., Lu, L., and Qiao, P. (2021). Localization and size quantification of surface crack of concrete based on Rayleigh wave attenuation model. *Constr. Build. Mater.* 280, 122437. doi:10.1016/j.conbuildmat.2021.122437

Zhang, L., Cheng, X., Wu, G., and Wang, T. (2022a). Reference-free damage identification method for highway continuous girder bridges based on long-gauge fibre Bragg grating strain sensors. *Measurement* 195, 111064. doi:10.1016/j.measurement.2022.111064

Zhang, H., Liu, S., Rui, X., Zhu, X., and Sun, J. (2022b). A skin-core debonding quantitative algorithm based on hexagonal units reconstruction for air-coupled ultrasonic C-scan images of honeycomb sandwich structure. *Appl. Acoust.* 198, 108964. doi:10.1016/j.apacoust.2022.108964

frontiers | Frontiers in Earth Science

TYPE Original Research
PUBLISHED 27 December 2023
DOI 10.3389/feart.2023.1298025

Check for updates

OPEN ACCESS

EDITED BY
Jianyong Han,
Shandong Jianzhu University, China

REVIEWED BY
Zhenyu Zhang,
Chongqing University, China
Kai Liu,
University of Oxford, United Kingdom

*CORRESPONDENCE
Liyuan Liu,
liuliyuan@ustb.edu.cn

RECEIVED 21 September 2023
ACCEPTED 06 November 2023
PUBLISHED 27 December 2023

CITATION
Wang T, Ye W and Liu L (2023), Study on the mechanical properties and acoustic emission signal characteristics of freezing pipe.
Front. Earth Sci. 11:1298025.
doi: 10.3389/feart.2023.1298025

COPYRIGHT
© 2023 Wang, Ye and Liu. This is an open-access article distributed under the terms of the Creative Commons Attribution License (CC BY). The use, distribution or reproduction in other forums is permitted, provided the original author(s) and the copyright owner(s) are credited and that the original publication in this journal is cited, in accordance with accepted academic practice. No use, distribution or reproduction is permitted which does not comply with these terms.

Study on the mechanical properties and acoustic emission signal characteristics of freezing pipe

Tao Wang[1,2], Weiwei Ye[1] and Liyuan Liu[1,2]*

[1]School of Civil and Resources Engineering, University of Science and Technology Beijing, Beijing, China, [2]Beijing Key Laboratory of Urban Underground Space Engineering, University of Science and Technology Beijing, Beijing, China

The increase in freezing depth requires thicker, stronger, and colder freezing walls, and various complex factors in deep strata greatly increase the risk of freezing pipe fracture. To address the phenomenon of freezing pipe fracture, this paper designs freezing pipe and joint mechanical performance experiments based on acoustic emission (AE) technology, mainly testing the deformation of freezing steel pipes and composite joints at normal and low temperatures, changes in load bearing capacity, and corresponding AE characteristics of the process. Additionally, the associated AE characteristics throughout the process will be analyzed. The ultimate goal is to establish a discriminative pattern for identifying the critical fracture of freezing pipes based on the analysis of AE signal characteristics in conjunction with mechanical properties. The sensitivity of the AE system under low-temperature conditions and the reliability of the test were tested through pencil lead break experiments, and saltwater noise detection experiments were conducted to prevent noise interference from low-temperature saltwater flow and pipe wall friction in the identification of crucial signals for freezing pipe fracture. This study provides a basis for identifying the deformation mechanics and fracture warning of freezing pipes through dynamic analysis of AE monitoring information.

KEYWORDS

acoustic emission, fracture, freezing pipe, spectrum, mechanical deformation

1 Introduction

In freeze sinking, a method used for drilling in deep alluvial deposits, occurrences of wellbore wall fracturing and freezing pipe failures are not uncommon. Over the past 30 years, due to changes in energy structures, some developed countries have rarely initiated construction of large-scale freeze wellbores, and the development of freeze drilling technology has essentially stagnated (Li et al., 2011). In China, during the freeze sinking projects in the 1980s, particularly in the Lianghuai region, a large number of pipe failures and well flooding accidents were observed. While the continuous improvement of construction methods and the emergence of new technological solutions have facilitated the expansion of many domestic underground projects (Han et al., 2023), including artificial ground freezing techniques, the phenomenon of freezing pipe fractures in freeze well freezing has been temporarily brought under effective control. However, due to the lag in freeze technology theory, coupled with the increase in freeze circle diameter and the widespread adoption of multi-circle freeze schemes, a significant resurgence of freezing pipe fracture accidents has emerged once again (Sheng, 2009; Chen, 2012).

The safety of freezing pipes is one of the crucial factors determining the success or failure of freeze sinking projects. Scholars have conducted relevant research on the fracture mechanism and improvement measures of frozen pipes from various aspects, including frozen wall deformation, quality of frozen boreholes and frozen pipes, and blasting vibrations. Yang et al. (2013) established a relationship model between frozen wall displacement and the occurrence rate of pipe fractures based on statistical data, and used the maximum displacement of the frozen wall to predict the risk of frozen pipe fracture. Zheng et al. (2015) conducted numerical simulations, while Yang et al. (2016) performed engineering experiments to analyze the effects of blasting vibrations on frozen pipes. Wu and Lin (1992) designed flexible joints for frozen pipes by altering the stiffness and elongation rate of the joint location. Zhou (1996) calculated the stress and deformation characteristics of frozen pipes in the frozen wall deformation zone and during multi-loop freezing through stress analysis. Jing et al. (2004) established a more accurate mechanical model by analyzing the factors affecting the stress on frozen pipes during operation and studying the deformation characteristics. They conducted theoretical calculations to determine the critical locations of frozen pipe fracture. Zhang (2008) conducted tensile and bending tests on frozen pipes under both normal and low-temperature conditions, considering the presence or absence of joints. The results indicated the necessity of using inner lining steel pipes at the joint locations, as they demonstrated improved tensile and bending capacities. However, industry scholars' focus is primarily on freezing theory (Cui et al., 2011), frozen soil mechanics (Yang et al., 2009; Zhao et al., 2013), design methods (Wang et al., 2010; Deng et al., 2023), fracture mechanism (Li et al., 2023) and related aspects. There is relatively less emphasis on the safety monitoring and evaluation of freezing pipes.

The assessment of freezing pipe fractures in a freezing station relies on observing certain direct or indirect phenomena. These include the saltwater tank and the advancing face of the wellbore, which provide clues about the occurrence of freezing pipe fractures. After a freezing pipe fracture occurs, several indications can be observed. The bottom heave volume at the working face increases significantly, and there is a noticeable displacement of the wellbore. Additionally, the temperature of the incoming air decreases, and there may be the presence of saltwater seepage from the wellbore or well wall, characterized by a bitter and turbid taste. A decline in the saltwater level within the saltwater tank becomes apparent, and discrepancies in flow rate may occur in the saltwater circulation loop. Within the freezing trench, one can hear a distinct sound of flowing saltwater, often resembling a thumping noise. Furthermore, the rubber hose at the top of the fractured freezing pipe may undergo deformation due to atmospheric pressure. Indeed, the aforementioned phenomena are based on the premise that freezing pipe fractures have already occurred. It is evident that when these observations are made, a significant amount of saltwater has already leaked into the formation. In severe cases, this can lead to the formation of windows in the freezing wall, which subsequently gives rise to a series of safety issues. Moreover, it poses a potential risk for the treatment of the formation after pipe failure.

In the 1980s, a technology group was formed under the leadership of the China University of Mining and Technology to address the issue of frozen pipe fractures when using the freezing method to penetrate thick topsoil layers in the Huainan mining area of China. They conducted research on the development of a system to prevent frozen pipe fractures and saltwater leakage alarm, using an external pipe clamp and thread connection. The aim was to trigger an alarm by capturing the vibration signal at the moment of frozen pipe fracture. At that time, the traditional processing method for frozen pipes involved using an external pipe clamp and thread connection, which was prone to detachment and fracture at the joints, accompanied by significant noise. Based on this phenomenon, Zhang et al. (1989), Zhang et al. (1990) conducted research on frozen pipe fracture warning methods. They established a fracture warning system based on the principle of seismic measurement, with a focus on the dominant frequency characteristics of vibration signals at the connection point of the pipe clamp and tapered thread under room temperature conditions. However, the current methods of connecting frozen pipes have undergone fundamental changes. Currently, frozen pipes are typically connected using a composite joint, such as a polyurethane outer layer with internal grooved joint welding or a water-expanding rubber outer protective layer with internal grooved joint welding. The deformation characteristics, mechanical properties, and failure modes of these types of joints have not been thoroughly investigated.

Acoustic emission (AE) is the generation of instantaneous elastic waves within a material due to the rapid release of localized strain energy. Each AE signal contains rich information about the internal structure, defect properties, state changes, and damage evolution of the material. Research on the mechanisms of AE generation, signal propagation modes, detection methods, and analysis techniques for different materials under various conditions is thriving (Hase et al., 2023; Ma et al., 2023; Zhou et al., 2023). With the continuous improvement of detection equipment performance and the advancement of analysis techniques, AE technology, as a dynamic non-destructive testing method, has been applied in various fields, including petroleum, petrochemicals, power generation, aerospace, astronautics, metallurgy, railways, transportation, coal mining, construction, and mechanical manufacturing. It enables regular equipment inspections and online monitoring. AE technology is increasingly recognized as an irreplaceable research method and testing means in certain domains (Prokop'ev et al., 2023; Banerjee and Mukherjee, 2023; Barat et al., 2021; Sohaib et al., 2019).

An ideal freezing pipe monitoring system should be capable of real-time monitoring of its stress and operational status. It should promptly issue warnings when abnormal stress or deformation is detected in the freezing pipes, thereby alerting relevant parties to take remedial measures in advance. These measures may include ceasing excavation, increasing support to control wellbore deformation, and improving the stress on the freezing pipes. Alternatively, it should provide early notifications to close the valves of the freezing pipes to prevent excessive saltwater leakage. The effectiveness of various measures to prevent freezing pipe fractures faces numerous uncertainties when confronted with unique and complex geological

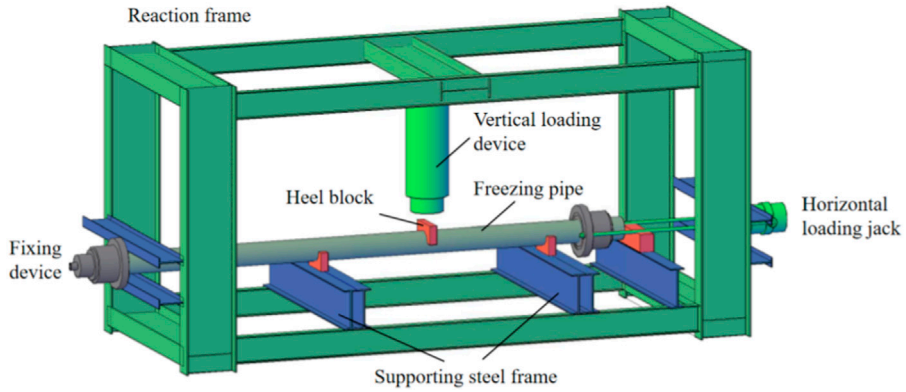

FIGURE 1
Experimental loading apparatus.

environments. Therefore, it is crucial to conduct real-time monitoring of the working status of freezing pipes. Analyzing the AE characteristics during the loading process of low-temperature freezing pipes and establishing the correlation between mechanical deformation and AE signals are particularly important and urgent for monitoring, analyzing, and early warning of freezing pipe fracture risks. This paper is based on AE testing techniques and aims to investigate the mechanical and AE performance of low-temperature freezing pipes and their joints. Through experimental analysis, the study captures and analyzes the spectral characteristics of AE signals at different stages of stress and deformation in freezing pipes and joints. It also examines the changing trends of different characteristic signals during the mechanical process. The paper establishes AE criteria for the deformation process and the critical state of fracture in freezing pipes. By dynamically analyzing the AE monitoring information, the study achieves the identification of the deformation mechanical process and enables fracture early warning in freezing pipes.

2 Materials and methods

2.1 Experimental apparatus

The mechanical performance experiments of the freezing pipes and joints were conducted on a loading reaction frame (Figure 1). The experimental freezing pipe section was subjected to loading using a bidirectional loading method. Axial tension was applied to the pipe section to provide preloading and control the axial stress state. Vertical loads were applied to induce radial displacement in the pipe section, simulating the deformation process of the freezing pipe.

2.2 Sample parameters and structure

Selection of samples with the same material and specifications as the on-site frozen engineering, as well as identical joint processing methods, was made to replicate the construction conditions as closely as possible. The base material of the freezing pipe is a high-quality low carbon seamless steel pipe (20#), with a diameter of Φ159 mm and a wall thickness of 9 mm. The basic mechanical properties of the pipe material are shown in Table 1.

The pipe sections were cut using mechanical cutting to minimize thermal damage and thermal stress. The experimental pipe sections, which included welded joints, were fabricated using an internal lining pipe and beveled butt welding (Figure 2). The length of the internal lining clamp was 80 mm. Compared to the external lining clamp joint configuration, this design reduced the number of joint seams by half, enhancing the reliability of the joints. The length of the experimental pipe section was determined as 4.2 m based on the dimensions of the experimental loading reaction frame. Both ends of the pipe section were welded with a variable diameter to facilitate the connection of the saline water circulation pipeline.

2.3 Experimental procedure

The freezing pipe has a length of 2.5 m and a span of 1.8 m. The supports of the loading apparatus act as the fixed points of a simply supported beam. The load is applied at the midpoint, specifically at the welded joint of the freezing pipe, in a concentrated loading manner. Twelve strain gauges and one displacement gauge are installed on the upper and lower sides of the test pipe section. A load cell is mounted directly above the joint weld to measure the load applied to the freezing pipe joint. The load cell is connected to a data acquisition system (DT80G-dataTaker) to record the load data. To ensure uniform loading on the joint, a U-shaped groove is placed directly above the joint, and a layer of insulation material is inserted inside the U-shaped groove to avoid noise interference during loading, thus maintaining experimental accuracy. A thermocouple sensor is positioned at the middle of the pipe to monitor the surface temperature of the freezing pipe in real-time. In order to achieve rapid cooling of the freezing pipe and better simulate the on-site construction conditions, a layer of insulation material is specifically applied to the surface of the freezing pipe. To facilitate the circulation of saline water, which simulates the on-site saltwater circulation system, small variable-diameter openings are left at both ends of the pipeline.

TABLE 1 Basic mechanical property indicators of pipe material.

Grade	Yield Strength/MPa	Tensile Strength/MPa	Elastic Modulus/(10^9 GPa)	Elongation/(%)
20# steel	≥210	≥420	210	≥25

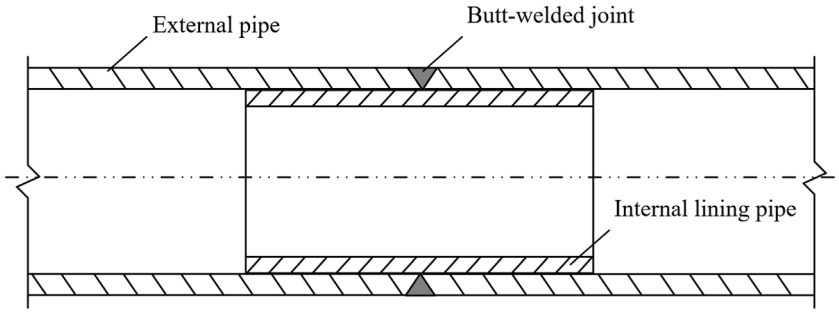

FIGURE 2
Structure of the internal lining pipe utilized with butt-welded joint.

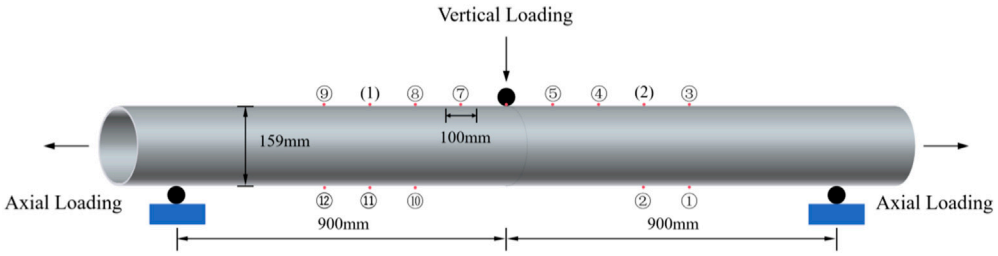

FIGURE 3
Schematic diagram of load measurement point layout for the freezing pipe.

The freezing pipe is loaded using a hydraulic oil pump as the power source. After each loading cycle, the instrument automatically records the data. Initially, the loading speed is relatively fast. As it approaches the yield deformation point, the loading rate gradually slows down. Yield deformation continues to develop at the point of concentrated force (the welding joint of the freezing pipe) until the joint fails or the pipe body becomes unstable, at which point the data collection stops. Additionally, an AE instrument is utilized to detect and record AE data during the experiment.

The measurement point layout of the freezing pipe is as shown in Figure 3. The strain gauges are labeled as ①–⑫, and (1)–(2) represent AE probes. The distance between each strain gauge and AE probe is 10 cm.

2.4 Data monitoring

The data collection for freezing pipe strain, displacement, and load cell data is performed using the DT85 data logger with a sampling interval of 2 s. For AE experiments, the PCI-2 AE Detection System is used for AE monitoring. The sampling rate is set to 1MSPS (Mega Samples Per Second), with a sampling length of 2 k. The preamplifier gain is set to 40 dB, and the threshold values are adjusted based on specific experimental conditions. The sensor type used in this experiment is a resonant sensor (narrowband sensor), and its parameters are shown in Table 2.

The strain gauge data on the freezing pipe is collected in real-time using DT80G-dataTaker. Real-time calculations are performed to obtain the axial stress of the freezing pipe. Once the axial stress reaches the design value, vertical loading is applied until the freezing pipe fractures or reaches the maximum deformation limit.

3 Results

3.1 Mechanical performance of the freezing pipe

The experimental procedure employed hydraulic pressure controlled by an oil pump to regulate the loading speed, with the hydraulic pressure set at 0.2 MPa. The loading duration was

TABLE 2 Parameters of the acoustic emission sensor.

Model	Operating temperature/°C	Center frequency/kHz	Frequency range/kHz
R15α	−65~175	30	20~180

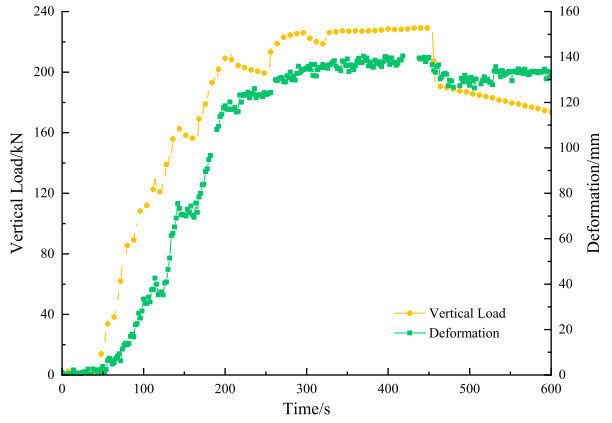

FIGURE 4
The loading and deformation process of the freezing pipe.

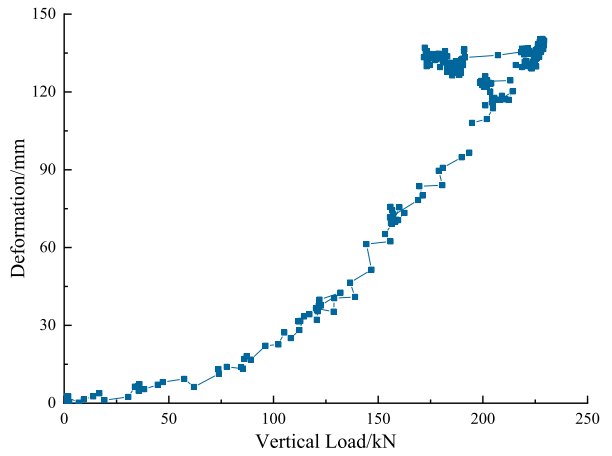

FIGURE 5
Load-deformation relationship of the freezing pipe.

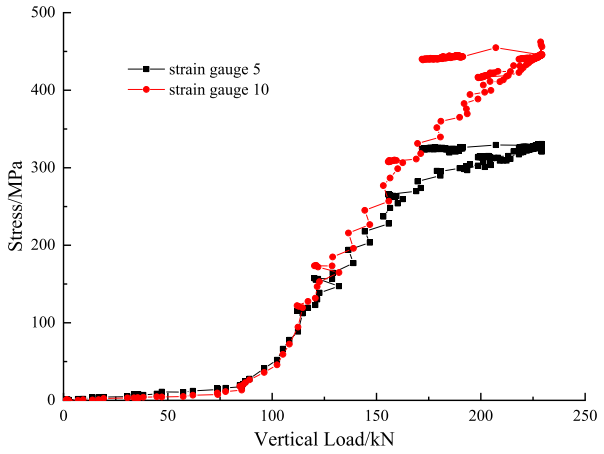

FIGURE 6
The stress curve of the freezing pipe under loading.

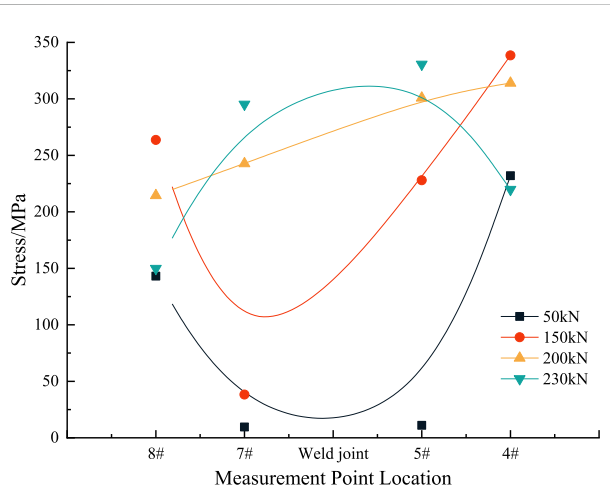

FIGURE 7
Spatial distribution patterns of stress in the freezing pipe under loading.

approximately 600 s, and the load cell recorded a maximum load of around 240 kN. During the vertical loading process, the bending deformation of the pipe body exhibited a consistent trend with the vertical load curve. At the loading limit, the maximum bending deformation of the pipe body was approximately 150 mm (Figure 4).

As the vertical load increases, the vertical displacement at the top surface of the freezing pipe steadily increases. However, the curve exhibits a parabolic shape (Figure 5), indicating that the deformation is a result of the combination of cross-sectional deformation (circular flattening into an elliptical shape) and bending deformation along the length of the pipe.

The strain data from strain gauges 5 and 10 on the pipe body were selected to examine the stress distribution during loading (Figure 6). The calculations revealed that both the upper and lower surfaces of the pipe body were primarily under tension. When the vertical load was below 90 kN, the stress in the pipe body showed minimal variation. At this stage, the deformation was mainly due to compaction from the loading device and deformation in the radial direction at the loading point. As the vertical load continued to increase, the stress in the pipe body exhibited a linearly increasing trend. When the vertical load

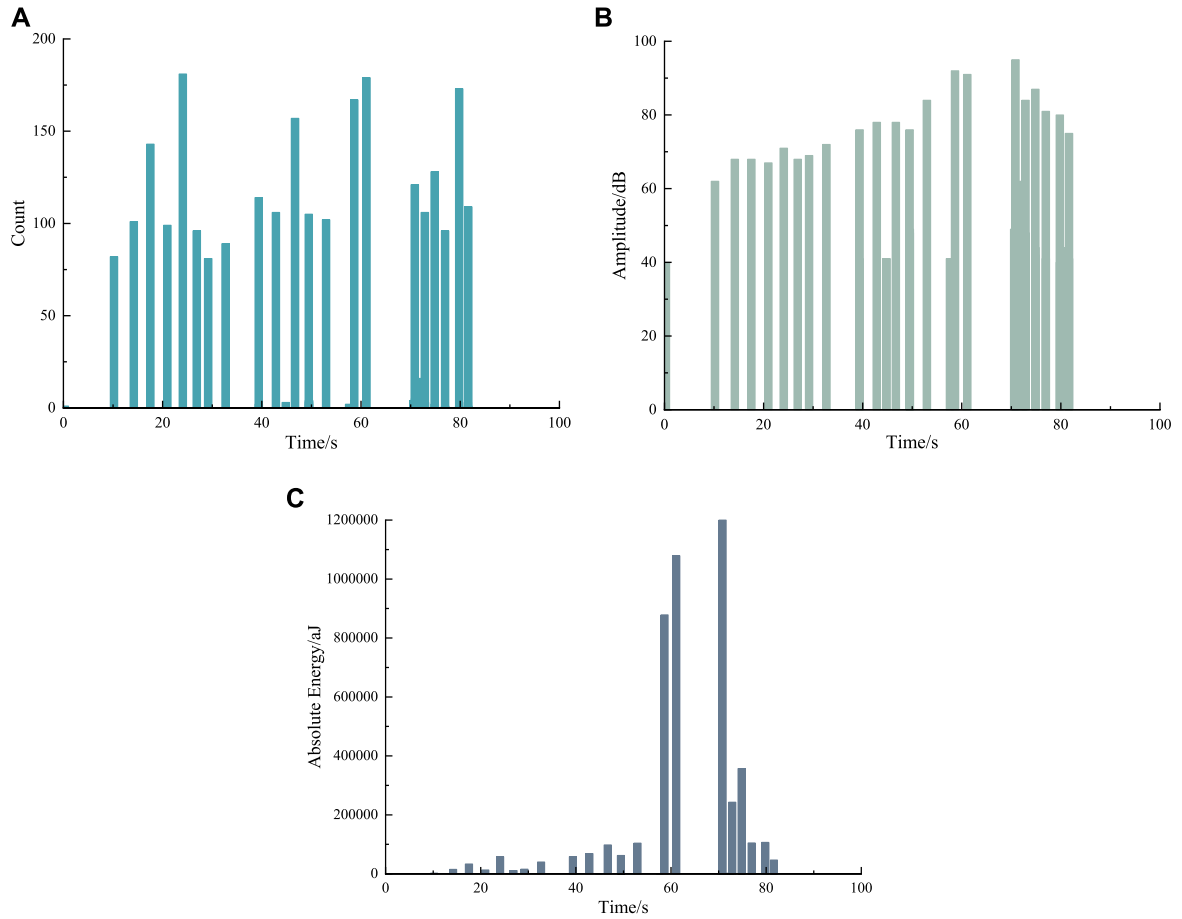

FIGURE 8
The characteristics of the pencil lead break signal under low-temperature conditions. **(A)** Acoustic emission count. **(B)** Amplitude of the acoustic emission signal. **(C)** Acoustic emission absolute energy.

reaches approximately 230 kN, the loading cylinder reaches its maximum stroke. At this point, the strain gauge 5 on the pipe body experiences a stress of approximately 315 MPa, while the strain gauge 10 experiences a stress of approximately 450 MPa at its location.

By examining the stress at the top surface of the pipe body at locations of strain gauges 8, 7, 5, and 4, the spatial stress distribution curve of the freezing pipe during the loading process is depicted (Figure 7). As the vertical load gradually increases, the curve transitions from a concave shape to a convex shape. Furthermore, during the initial stages of loading, the bending deformation and stress are relatively small near the loading point, primarily characterized by flattening and horizontal deformation. However, as the vertical load increases, the bending deformation of the pipe body becomes more significant, particularly at the loading point, where the deformation is greater compared to the distal end.

3.2 Pencil lead break signal testing

The freezing pipe was connected to a cold brine circulation system to test the sensitivity and reliability of the AE system under low-temperature conditions. The testing temperature was set at −28°C. From the characteristics of the AE amplitude, it can be observed that the AE testing system maintains good stability under low-temperature conditions (Figure 8). The amplitude of the AE signals ranges from 60 to 90 dB, which is comparable to the results obtained under room temperature conditions.

Waveform data from three segments of the AE signals were selected for spectral analysis (Figure 9). From the observation of the AE waveform signals, they exhibit distinct burst signal characteristics. The spectral curve shows energy distribution in the frequency range of 6–50 kHz, with a peak around 47 kHz.

3.3 Saltwater flow noise detection

In the operational state of a freezing pipe, low-temperature saltwater circulates within it, and the flow of saltwater creates interference noise through friction with the pipe wall. This noise mixes with the AE signals generated by the stress on the pipe material itself. It can be detected by the freezing pipe fracture monitoring system and interfere with the identification of critical signals related to pipe fracture. Therefore, it is necessary to identify the acoustic signal characteristics during saltwater flow. This will

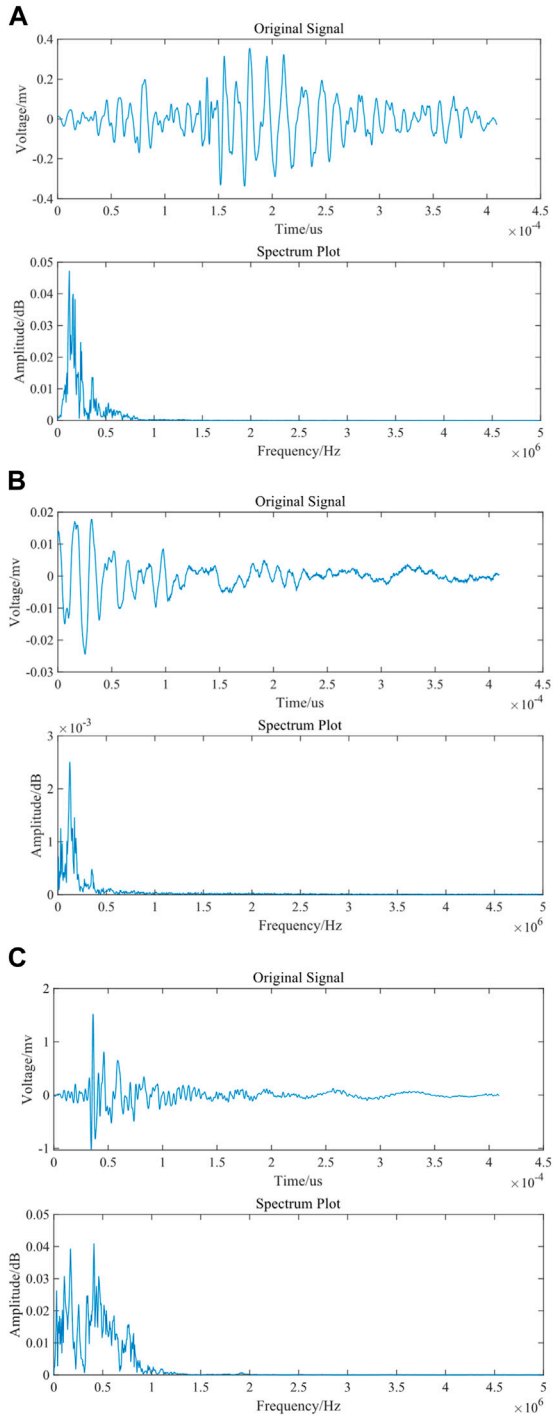

FIGURE 9
Waveform and spectral characteristics of the pencil lead break signal. **(A)** First segment. **(B)** Second segment. **(C)** Third segment.

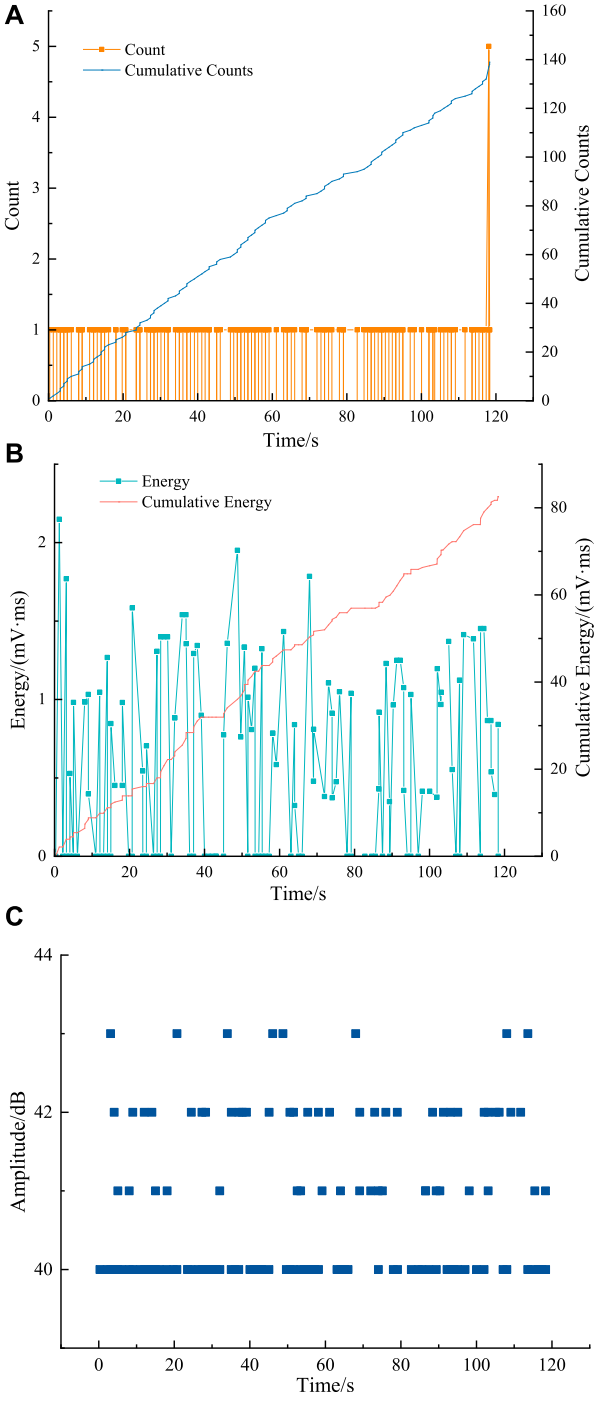

FIGURE 10
Saltwater flow noise test results. **(A)** Count-Time. **(B)** Energy-Time. **(C)** Amplitude-Time.

provide a basis for subsequent on-site AE signal detection, filtering, and signal processing.

In this saltwater noise detection experiment, an experimental section was designed to circulate low-temperature saltwater, simulating the operational state of a freezing pipe under field conditions. Subsequently, AE signals generated by the flow of saltwater in the freezing pipe were detected under unloaded conditions, obtaining AE characteristic parameters at different temperatures and saltwater pressures. Through pattern matching among multiple AE signal features and their mutual comparison, the detected AE signals were subjected to coupled extraction and comparative analysis of characteristic parameters. This process enables the identification of AE patterns corresponding to saltwater flow, leakage, and other states. The experimental section

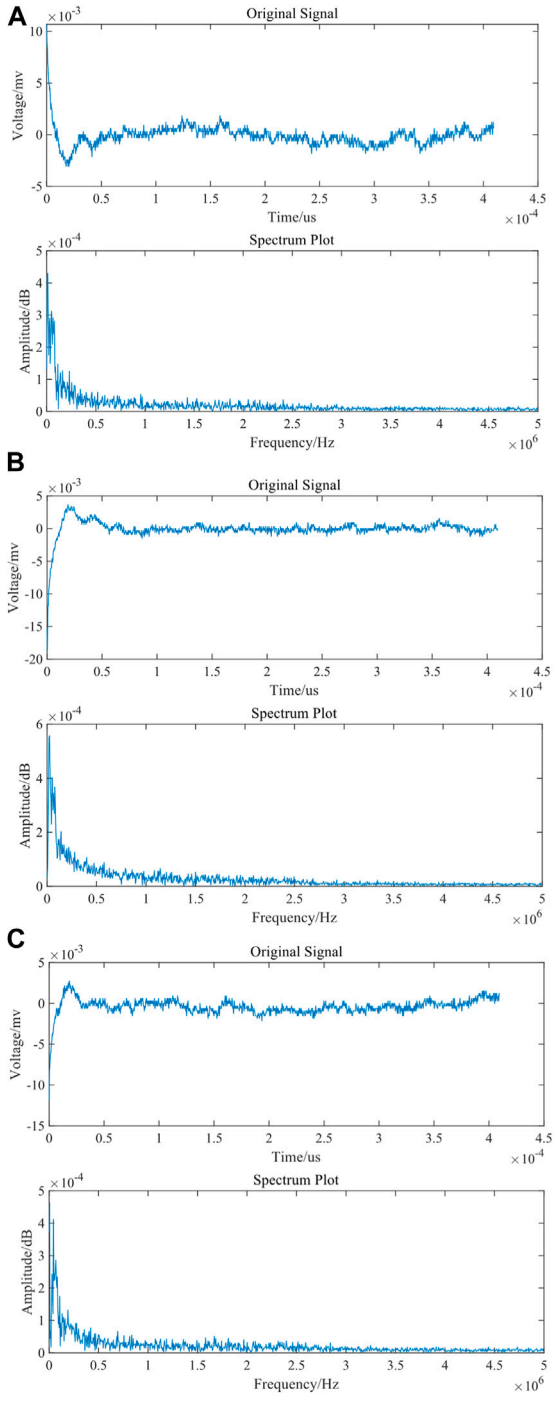

FIGURE 11
Spectral characteristics of saltwater flow noise. **(A)** First segment. **(B)** Second segment. **(C)** Third segment.

and connecting pipelines were insulated using polyurethane foam. Two AE measurement points were installed on the experimental section, and the pipe wall temperature was monitored using thermocouples.

Based on the experimental results, it was observed that normal saltwater flow within the freezing pipe generates continuous AE signals. The ringing count and energy remain stable within a certain range. The cumulative ringing count and energy exhibit linear growth, and the amplitude distribution is relatively uniform, consistently ranging between 40 and 43 dB (Figure 10). By detecting the normal flow of saltwater within the freezing pipe, it provides a basis for identifying signals related to saltwater leakage during pipe fracture.

Three segments of typical waveform data from the saltwater flow during the AE signal were selected for spectral analysis (Figure 11). It can be observed that the saltwater flow signal exhibits continuous AE characteristics, which can be clearly distinguished from burst signals in the raw waveform. After Fourier transformation, the frequency components are concentrated in the range of 19.53–48.83 kHz.

3.4 Acoustic emission signal characteristics of a loaded freezing pipe

The bending-tensile test of the freezing pipe had a duration of 650 s. At approximately 150 s into the test, a sharp and distinct sound was emitted. For this test, 11 strain gauges were used to measure the strain, and the maximum applied load was 227 kN. The AE threshold was set at 50 dB. Based on the results of the bending-tensile test on the freezing pipe (Figure 12), it is evident that the strain near the loaded section of the pipe is significantly higher than in other areas. The tensile strain on the loading side (Strain Gauge 10, approximately 60,000 με) is nearly twice the compressive strain on the opposite side (Strain Gauges 5 and 7, approximately 30,000 με). This indicates that tensile stress has a more pronounced effect on the deformation of the freezing pipe structure compared to compressive stress. These findings provide valuable insights for understanding the failure of welded joints in freezing pipes. As the pressure value increases, a significant number of AE signals are initially generated, mainly due to mechanical system noise. When the load reaches its maximum value and remains constant, there are no sudden bursts of AE signals. Instead, continuous signals are generated, indicating that the freezing pipe is in the plastic deformation stage. With the continuous increase in pressure, the deflection also increases. The maximum deflection reaches 138.9 mm, which is much larger than the deflection value of a regular freezing pipe. This demonstrates that the connection form of internal lining plus bevel groove welding greatly enhances the deformation capacity of the freezing pipe. The AE signals detected by the two channels show significant consistency and correlation. When the load increases linearly over time, the cumulative ringing count and cumulative energy exhibit linear consistency with the load growth. Furthermore, as the load increases, the magnitude of linear growth continues to increase.

3.5 Acoustic emission signal characteristics of a fractured freezing pipe

The loading duration of the pre-notched freezing pipe fracture test was approximately 400 s with a threshold of 50 dB for AE signals. During the experiment, four distinct sound events were observed at 49, 112, 205, and 352 s, coinciding with the fracture occurrence at the welding joint of the freezing pipe. From the experimental data

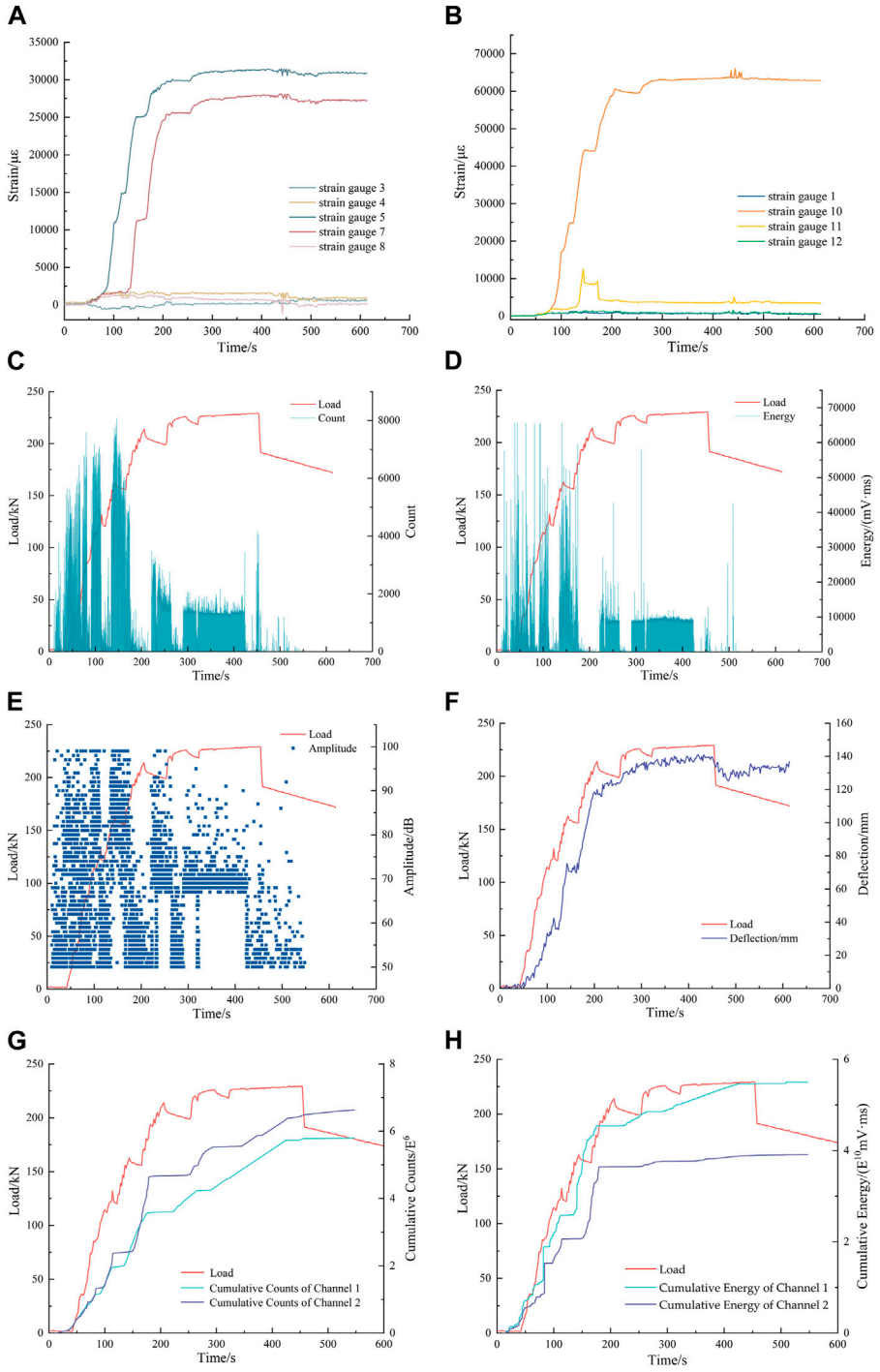

FIGURE 12
Results of the bending-tensile test on the freezing pipe. **(A)** Compressive strain. **(B)** Tensile strain. **(C)** Count. **(D)** Energy. **(E)** Amplitude. **(F)** Deflection. **(G)** Cumulative count. **(H)** Cumulative energy.

(Figure 13), it can be observed that the freezing pipe underwent significant plastic deformation, reaching a value of up to 160 mm. The compressive strain on the upper portion of the freezing pipe stabilized after reaching its peak pressure, while the tensile strain on the bottom side exhibited a certain correlation with pressure variations. This further supports the notion that the bottom portion of the freezing pipe under tension should be a critical focus area for research. Significant variations in pressure and tensile stress were observed at around 50, 115, 200, and 320 s. Concurrently, strong AE signals were detected around 50, 120, 200, and 340 s, indicating abrupt changes in the state of the freezing pipe at these instances. Furthermore, considering the substantial increase in cumulative count and cumulative energy around 100~120 s, it can be inferred that the freezing pipe experienced failure during this period.

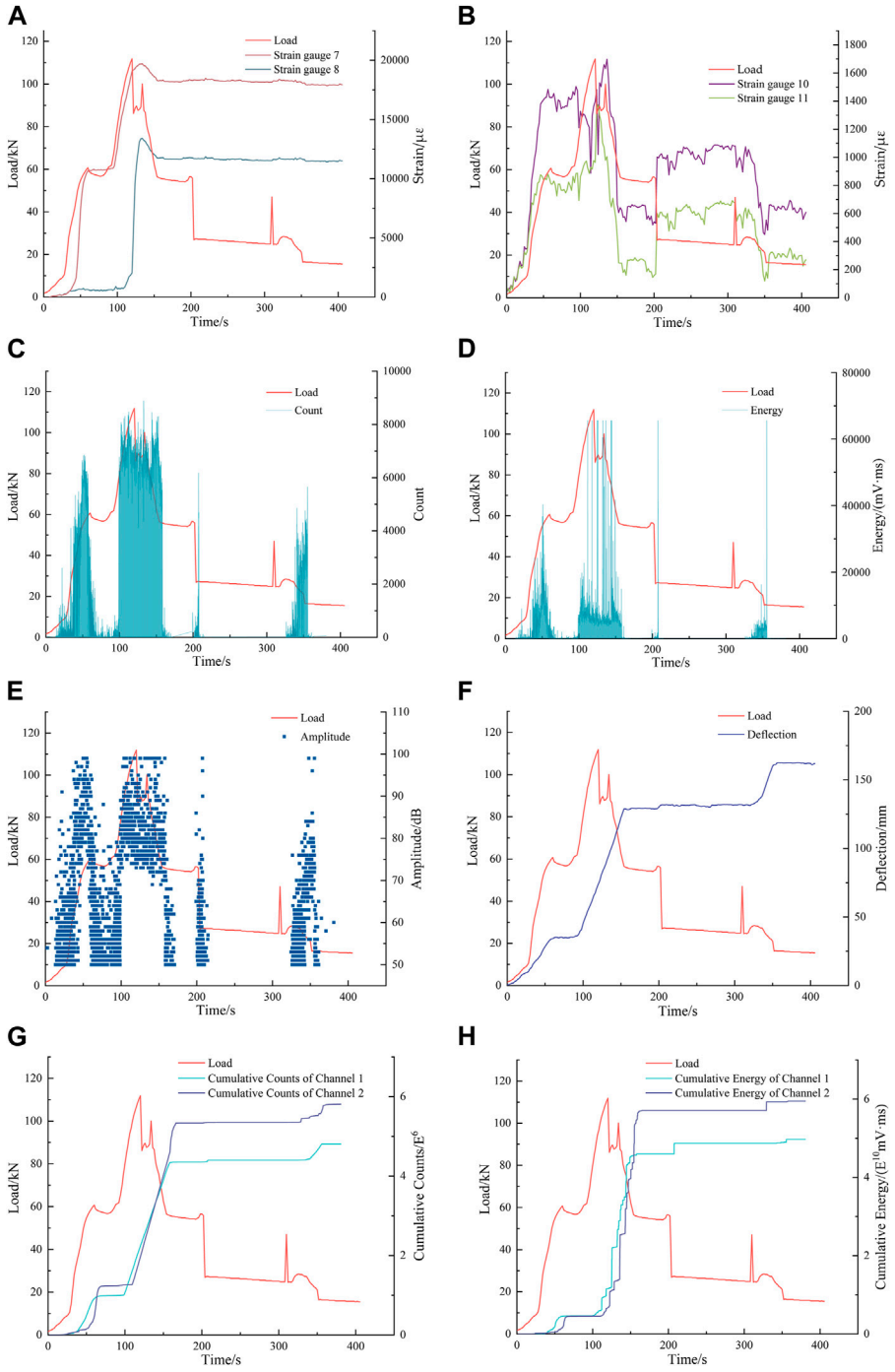

FIGURE 13
Results of the pre-notched freezing pipe fracture test. **(A)** Compressive strain. **(B)** Tensile strain. **(C)** Count. **(D)** Energy. **(E)** Amplitude. **(F)** Deflection. **(G)** Cumulative count. **(H)** Cumulative energy.

4 Conclusion

This study is based on AE technology and establishes an experimental system for the mechanical loading of freezing pipes and joints. We simulated the stress conditions of frozen pipes under different working conditions and investigated the AE signal characteristics of the mechanical performance and loading process of frozen pipes under low-temperature conditions.

With the presence of internal lining and clamps, freezing pipe joints can withstand higher loads and exhibit significant deformation capacity. The ultimate load-bearing capacity of the joints approaches the tensile limit of the pipe material, with a maximum deformation exceeding 120 mm. As the freezing pipe bears increasing loads, its deflection increases. However, the coordination of deformation between the joint and the freezing pipe becomes weaker. When the load eventually exceeds the strength of the joint, the joint fractures.

The flowing saltwater signal exhibits continuous AE signals, which can be distinctly differentiated from transient signals in the raw waveform. After performing Fourier transform for spectral analysis, the frequency components are concentrated within the range of 19.53–48.83 kHz.

During the elastic stage of the freezing pipe under tensile loading, the strain increases linearly with the increase in tensile stress. Significant AE signals are generated during this stage, accompanied by an increase in ringing count and energy. The cumulative ringing count also exhibits a linear growth characteristic with the increasing strain.

During the plastic deformation stage of the freezing pipe, there are no sudden bursts of AE signals. Most of the signals are continuous in nature. As the pressure continues to increase, the deflection of the pipe also increases, reaching a maximum deflection of 138.9 mm. The AE ringing count and energy remain relatively calm during this stage. The cumulative ringing count and cumulative energy curves exhibit a decreasing slope or even become flat, with amplitudes decreasing below 120 dB. The dominant frequency signal amplitudes of the AE during freezing pipe fracture are mainly concentrated around 50–90 dB and 160 dB. Prior to the fracture of the freezing pipe, the cumulative count and cumulative energy of the AE signals show a linear growth pattern. The maximum amplitude of the fracture signal can reach 220 dB.

By studying the changes in AE signals during the deformation and fracture of freezing pipes, it is possible to establish criteria based on AE for identifying the deformation process and the critical state of fracture in freezing pipes. These criteria provide a basis for the dynamic analysis of AE monitoring information, enabling the recognition of the mechanical deformation process and the early warning of fracture in freezing pipes.

Data availability statement

The original contributions presented in the study are included in the article/Supplementary Material, further inquiries can be directed to the corresponding author.

Author contributions

TW: Conceptualization, Formal Analysis, Funding acquisition, Methodology, Project administration, Resources, Supervision, Validation, Writing–original draft. WY: Conceptualization, Data curation, Formal Analysis, Methodology, Software, Validation, Writing–original draft. LL: Conceptualization, Funding acquisition, Methodology, Software, Supervision, Validation, Writing–review and editing.

Funding

The author(s) declare financial support was received for the research, authorship, and/or publication of this article. This research was funded by National Natural Science Foundation of China (Grant Nos 51874014, 52004015, and 52311530070), the fellowship of China National Postdoctoral Program for Innovative Talents (Grant No. BX2021033), the fellowship of China Postdoctoral Science Founda-tion (Grant No. 2021M700389), and the Fundamental Research Funds for the Central Universities of China (Grant Nos FRF-IDRY-20-003 and QNXM20210001).

Conflict of interest

The authors declare that the research was conducted in the absence of any commercial or financial relationships that could be construed as a potential conflict of interest.

Publisher's note

All claims expressed in this article are solely those of the authors and do not necessarily represent those of their affiliated organizations, or those of the publisher, the editors and the reviewers. Any product that may be evaluated in this article, or claim that may be made by its manufacturer, is not guaranteed or endorsed by the publisher.

References

Banerjee, A., and Mukherjee, A. (2023). A mathematical algorithm for predicting the crack in the junction of a steel truss bridge using acoustic emission testing. *Int. J. Steel Struct.* 23 (3), 747–757. doi:10.1007/s13296-023-00727-1

Barat, V., Marchenkov, A., Ivanov, V., Bardakov, V., Elizarov, S., and Machikhin, A. (2021). Empirical approach to defect detection probability by acoustic emission testing. *Appl. Sci.* 11 (20), 9429. doi:10.3390/app11209429

Chen, X. (2012). A space-time-dependant design method and the stability of ice wall for deep shafts. *Appl. Mech. Mater.* 1975, 3275–3281. doi:10.4028/www.scientific.net/AMM.204-208.3275

Cui, H., Li, W., and Wang, H. (2011). The mechanics experimental study of the artificially frozen soil in cretaceous strata. *Appl. Mech. Mater.* 1447, 1844–1847. doi:10.4028/www.scientific.net/amm.94-96.1844

Deng, S., He, Y., Yang, M., Zhou, F., Liu, H., Zhu, R., et al. (2023). Numerical analysis of shield tunnelling breakthrough working shaft by artificial ground freezing method under extreme conditions considering phase change latent heat. *Appl. Sci.* 13 (6), 3651. doi:10.3390/app13063651

Han, J., Wang, J., Cheng, C., Zhang, C., Liang, E., Wang, Z., et al. (2023). Mechanical response and parametric analysis of a deep excavation structure overlying an existing subway station: a case study of the Beijing subway station expansion. *Front. Earth Sci.* 10, 1079837. doi:10.3389/feart.2022.1079837

Hase, A., Morita, M., and Onodera, K. (2023). Analysis of seizure-resistance-improvement mechanism of polymer additives by acoustic emission sensing. *Tribol. Int.* 184, 108441. doi:10.1016/j.triboint.2023.108441

Jing, L., Gao, Q., and Yang, R. (2004). Fracture stress analysis and fracture position determination of freezing pipe. *Min. Metall. Eng.* 24 (4), 9–12.

Li, J., Wang, Y., Li, D., and Zhang, C. (2011). Model tests on stress and deformation of freezing-pipes during multi-circlefreezing before excavation. *Chin. J. Geotech. Eng.* 33 (7), 1072–1077.

Li, T., Zhao, W., Liu, R., Han, J., Jia, P., and Cheng, C. (2023). Visualized direct shear test of the interface between gravelly sand and concrete pipe. *Can. Geotech. J.* 2023. doi:10.1139/cgj-2022-0007

Ma, Y., Liu, M., Yang, L., Dai, P., and Fan, J. (2023). Damage analysis of concrete-filled square stainless steel columns based on acoustic emission and Markov chain methods. *Eng. Struct.* 281, 115730. doi:10.1016/j.engstruct.2023.115730

Prokop'ev, L. A., Andreev, Ya. M., and Lukin, E. S. (2023). Assessing hazard degree of crack-like defects based on acoustic emission testing under local low-temperature loading. *Russ. J. Nondestr. Test.* 58 (12), 1064–1070. doi:10.1134/S1061830922700103

Sheng, Y. (2009). On the reasons for brine intake fractured and ways to prevent brine intake fractured. *Coal Tech.* 28 (7), 176–177.

Sohaib, M., Islam, M., Kim, J., Jeon, D. C., and Kim, J. M. (2019). Leakage detection of a spherical water storage tank in a chemical industry using acoustic emissions. *Appl. Sci.* 9 (1), 196. doi:10.3390/app9010196

Wang, T., Yue, F., Jiang, Y., and Zheng, T. (2010). Research and practice on forced thaw technology applied to frozen wall of mine shaft. *J. China Coal Soc.* 35 (6), 918–922. doi:10.13225/j.cnki.jccs.2010.06.010

Wu, X., and Lin, S. (1992). Research on the flexible connectors for freezing pipes. *J. China Univ. Min. Technol.* 21 (1), 51–56.

Yang, R., Fu, X., Yang, L., Li, X., Chen, Q., Chen, C., et al. (2016). Research on the shaping control of frozen wall and blasting vibration mitigation of shaft wall effect in mine vertical shaft. *J. China Coal Soc.* 41 (12), 2975–2985. doi:10.13225/j.cnki.jccs.2016.1487

Yang, W., Du, Z., Yang, Z., and Bo, D. (2013). Plastic design theory of frozen soil wall based on interaction between frozen soil wall and surrounding rock. *Chin. J. Geotech. Eng.* 35 (10), 1857–1862.

Yang, Y., Lai, Y., and Li, J. (2009). Laboratory investigation on the strength characteristic of frozen sand considering effect of confining pressure. *Cold Reg. Sci. Technol.* 60 (3), 245–250. doi:10.1016/j.coldregions.2009.11.003

Zhang, J. (2008). Experimental study of mechanical characteristics of frozen steel pipe under normal temperature and low temperature. *Coal Tech.* 27 (12), 102–103.

Zhang, W., Hu, X., Wang, Y., and Yue, F. (1989). Microcomputerized alarm system for freezing pipe rupture. *J. China Univ. Min. Technol.* 18 (3), 46–53.

Zhang, W., Hu, X., Wang, Y., and Yue, F. (1990). Research on the experimentation for obtaining freezing pipe rupture signal. *J. China Univ. Min. Technol.* 19 (3), 76–80.

Zhao, X., Zhou, G., and Chen, G. (2013). Triaxial compression strength for artificial frozen clay with thermal gradient. *J. Cent. South Univ.* 20 (1), 218–225. doi:10.1007/s11771-013-1479-x

Zheng, Z., Xu, Y., Dong, J., Zong, Q., and Wang, L. (2015). Hard rock deep hole cutting blasting technology in vertical shaft freezing bedrock section construction. *J. Vibroeng.* 17 (3), 1105–1119.

Zhou, X. (1996). Stressing of freeze pipe in the deformed section of ice wall. *J. China Coal Soc.* 21 (1), 30–34.

Zhou, Y., Li, L., Liu, Y., Zhang, Z., and Matsui, T. (2023). Clustering analysis of acoustic emission signals in the monitoring of stone monuments: case of the freeze–thaw deterioration of tuffs. *Herit. Sci.* 11 (1), 119. doi:10.1186/S40494-023-00962-Z

frontiers | Frontiers in Earth Science

TYPE Original Research
PUBLISHED 28 December 2023
DOI 10.3389/feart.2023.1326597

Check for updates

OPEN ACCESS

EDITED BY
Jianyong Han,
Shandong Jianzhu University, China

REVIEWED BY
Hongzhan Cheng,
Hunan University, China
Wengang Dang,
National Sun Yat-sen University, Taiwan

*CORRESPONDENCE
Lu Bai,
lu.bai.a@chnenergy.com.cn

RECEIVED 23 October 2023
ACCEPTED 06 November 2023
PUBLISHED 28 December 2023

CITATION
Zou J, Wang M, Bai L and Yan C (2023), Numerical study on migration of overlying strata and propogation of cracks during multi-coal seams mining. *Front. Earth Sci.* 11:1326597. doi: 10.3389/feart.2023.1326597

COPYRIGHT
© 2023 Zou, Wang, Bai and Yan. This is an open-access article distributed under the terms of the Creative Commons Attribution License (CC BY). The use, distribution or reproduction in other forums is permitted, provided the original author(s) and the copyright owner(s) are credited and that the original publication in this journal is cited, in accordance with accepted academic practice. No use, distribution or reproduction is permitted which does not comply with these terms.

Numerical study on migration of overlying strata and propogation of cracks during multi-coal seams mining

Junpeng Zou[1], Man Wang[2], Lu Bai[1]* and Chongwei Yan[3]

[1]State Key Laboratory of Water Resource Protection and Utilization in Coal Mining, Beijing, China, [2]College of Information Engineering, Wuhan Business University, Wuhan, China, [3]Faculty of Engineering, China University of Geosciences, Wuhan, China

The surface subsidence caused by the coal seam mining seriously affects the ecology of the mining area. Compared with the single-coal seam mining, the mechanism of the overburden fracture and crack propagation caused by multi-coal seams mining is more complex, which has not been fully understood. Taking the 22,108 and 42,108 working faces of Buertai Coal Mine as a research object, the discrete element method is used to simulate the migration and failure characteristics of overlying strata, and the propogation of cracks in the process of multi-coal seams mining is also been investigated. So many cracks develop in the soft strata overlying the coal seam, and they cross each other and form a complex fracture system. The hard layer produces staggered cracks with a large size, mainly high-angle longitudinal cracks. The surface subsidence curve of the single coal seam mining shows a wide and slow "bowl" type, and the surface subsidence curve of the double coal seams mining show a "funnel" type with only one inflection point. The overburden structure disturbance caused by the previous coal seam and rock cracking—settlement have great influence on the mining of the latter coal seam. The research results are basically consistent with the field data comparison, which could provide a reference for the related research and engineering practice of shallow-buried double coal seam mining.

KEYWORDS

multi-coal seams mining, overlying strata migration, ground cracks, surface subsidence, particle flow code

1 Introduction

Repeated mining refers to a mining method in which rock strata and surface have been affected by one mining, resulting in movement, deformation, and destruction, and then affected by another mining, causing rock strata and surface to be destroyed again (Liu et al., 2022). In general, the initial mining will damage the overlying rock and cause the softening of rock masses resulting in a decrease in rock mass strength (Zhang et al., 2023a). During the secondary mining, the insufficient amount of damage in the upper coal seam mining will be "activated," therefore, the damage degree of repeated mining is greater than that of initial mining on rock and surface. To ensure safe production and better direct production, it is necessary to conduct in-depth research on repeated mining.

In recent years, aiming at the characteristics of overlying strata movement caused by single mining in shallow coal seams, scholars have accumulated a lot of practical experience and theoretical basis. However, for multi-seam mining, the overlying strata have been

disturbed to form gob area, the mechanical properties of rock have changed after damage, and the overburden stress is redistributed. The mechanical environment of the mine under the condition of multi-coal seam mining is greatly changed compared with that of shallow coal seam mining, the temporal-spatial evolution law of overlying rock mass and surface deformation is different from that of single coal seam mining. Therefore, the failure characteristics of multi-coal seam mining are quite different from single mining (Yu et al., 2016; Ghabraie et al., 2017a; Ghabraie et al., 2017b; Zhang et al., 2018; Ma and Hu, 2013). By assuming that the reduction of the expansion coefficient of the rock mass during the mining of multiple coal seams is proportional to the amount of expansion caused by the initial mining, combined with the field-measured data, the calculation formula for predicting the subsidence coefficient of the surface and rock mass under the mining conditions of multiple coal seams is given. The simulation study on the development law of overburden fracture under repeated mining conditions is carried out, and it is considered that repeated mining may cause the re-development of the water-conducting fractured zone of the upper coal seam (Yao et al., 2010). Zou et al. (2022a) studied the characteristics of mine tremor and stress distribution before and after deep hole blasting in the mining process of Dongtan Coal Mine in Shandong Province, and revealed the prevention and control effect of deep hole blasting on strong mine tremor. It is considered that deep hole blasting technology can effectively weaken and break the thick and hard rock strata overlying the coal seam, so as to achieve the purpose of releasing the strain energy of the overlying rock (Zou et al., 2022a). The surface and rock mass deformation characteristics under repeated mining conditions were analyzed by FLAC3D numerical simulation software. Based on the key strata theory of strata movement and mine earthquake monitoring technology, the collaborative migration and fracture characteristics of multi-key strata in deep coal mining and the energy propagation law of induced mine earthquakes were studied (Zhang et al., 2023b). Through on-the-spot observation and theoretical analysis of the working face of close distance thick coal seam group in 7 and 8 coal seams in the Datun mining area, it is concluded that the height of the lower coal falling zone increases when the failure range of the upper coal floor coincides with the development range of lower coal falling zone. Using numerical simulation, similar simulation, and engineering practice, the range of the shear fracture zone and stress concentration area near the working face is defined. Based on digital image correlation technology and traditional split Hopkinson pressure bar test, Zou et al. (2022b) conducted a series of repeated experiments on complete, rough and smooth joint surfaces, and described the process of stress wave propagation through joints in rock mass. The instability law of the damaged basic roof is studied based on the "S-R" theory of the "Voussoir beam structure." It is concluded that the damaged basic roof is more prone to sliding instability of the "Voussoir beam." and the greater the damage, the greater the probability of sliding instability (He et al., 2016). The hypothesis of "Voussoir beam" is proposed based on the characteristics of mining rock mass movement. With the advance of the working face, the hard rock above the goaf will be fractured into orderly rock blocks in the fracture zone, and the rock blocks will be hinged by horizontal thrust. Wei et al. (2022) analyzed the macroscopic and microscopic characteristics of overburden failure, fracture development, force chain evolution and rock mass damage law through UAV remote sensing technology, laboratory test and PFC2D numerical simulation, and compared them with field data. Based on the actual situation of 22,307 working face in Bulianta Coal Mine, Liu et al. studied the redevelopment of cracks and the change of permeability in the process of lower coal seam mining by using Particle Flow Code and corresponding physical experiments. The results show that after the lower coal seam mining, the upper and lower stopes are connected to form a new compound minefield; with the mining of the lower coal seam and the advancement of the working face, the permeability and the number of cracks in each area of the overlying strata show the law of ' stability-rapid increase-stability (Liu et al., 2019a; Liu et al., 2019b). Based on the BBR research system, Wang et al. (2020) used PFC numerical calculation and a top-coal caving experiment to study the top-coal caving mechanism of sublevel caving in steeply inclined coal seams under different sublevel heights and caving directions. The results show that the boundary curve of top coal can be fitted by a parabola. Like a flat coal seam, the drainage body of SLTCC is still a cutting variational ellipsoid. With the increase of the section height, the convex point of the top coal boundary moves to the goaf, which leads to the incomplete development of the top coal (Wang et al., 2020). Aiming at the problems of high gas concentration in overlying strata and uncertain roof height in the 7,435 working face of Kongzhuang Coal Mine, Wang et al. (2017) studied the caving characteristics of overlying strata by combining physical experiments of similar materials with numerical simulation of PFC (Particle Flow Code) software and verified each other. The relationship between fracture development and porosity variation characteristics is introduced to quantitatively determine the height of the local fracture zone. The quantitatively calculated wellbore height is compared with the wellbore height measured by the *in situ* drilling flow method (Wang et al., 2017). In order to study the strength behavior of coal pillars under different confining stresses, Zhang et al. carried out compressive tests under lateral constraints of 0~8.0 MPa, and the PFC model to study the strength enhancement mechanism of coal pillars at the particle scale. It is concluded that the strength and cumulative axial strain of coal increase with the increase of constraint, while Young's modulus is independent of constraint. Compared with the significant increase of peak compressive stress, the crack initiation stress increases slightly with the increase of constraint. In the early stage of loading, the high constraint inhibits the development of microcracks, while in the later stage of loading, the high constraint enhances the frictional resistance strength component. These two mechanisms together change the compressive strength of coal, which helps to mobilize the strength component (Zhang and Li, 2019). With the continuous development of measurement technology, a large number of scholars continue to apply new technologies to multi-seam mining surface deformation monitoring and achieved a series of results (Perski et al., 2009; Ge L. et al., 2007; Jung et al., 2007; Baek et al., 2008; Wu et al., 2008; Y et al., 2008).

The surface subsidence law and fracture propagation mechanism induced by multi-coal seam mining have been deeply studied by numerical simulation, field observation, laboratory test, and theoretical analysis. However, the research on the mechanism of repeated disturbance of lower coal seam mining to upper coal seam

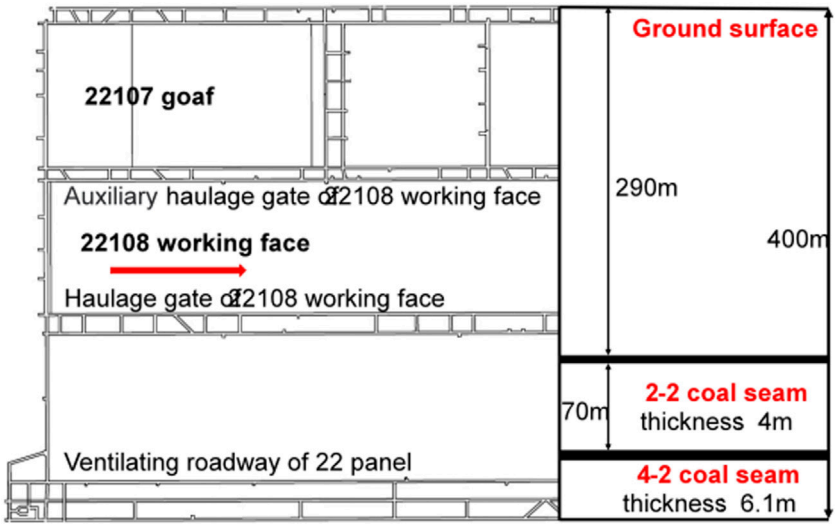

FIGURE 1
Roadway layout of 22,108 working face and the positional relationship between 2-2 and 4-2 coal seams.

goaf is still insufficient. This paper takes the 22,108 and 42,108 working face of the Buertai mining area as an example, PFC numerical simulation software is used to study the characteristics of surface subsidence and fracture propagation under the condition of double-layer downward mining, revealing the mutual feedback mechanism of strata movement law caused by upper and lower coal seam mining, to contribute to the study of overburden rock migration mechanism induced by multi-coal seam mining.

2 Engineering background

Buertai coal mine is located in Ordos city, inner Mongolia Autonomous Region. It is a super large production mine of Shenhua Coal Group Co., Ltd. The coal mine is designed in 2005, with a design production capacity of 20 million tons/year. Construction began in 2008, trial production in 2011, and production in 2014. The main mining 22 coal and 42 coal seam are extracted with the mechanized longwall retreat method, all falling method to deal with gob roof. This paper studies the 22,108 working face of the 2-2 coal seam and the 42,108 working face of the 4-2 coal seam. The compressive strength of the rock in the natural state of Buertai Coal Mine is relatively low, basically below 40 Mpa. The shear and tensile strength are relatively high, and the softening coefficient of the rock is mostly less than 0.75, all of which are softened rock. In general, the roof and floor rocks of coal seams in this area are mainly weak rocks, followed by semi-hard rocks.

Forty-two thousand one hundred and eight working face is the eighth working face of 42 coal seam, the width of 42,108 working face is 300.2 m and the mining length is 4,728.4 m, and the thickness of the overlying loose layer is 1~40 m. The average thickness of the coal seam is 6.1 m, the dip angle is 1°~3°, and the average buried depth is 360 m. The immediate roof of 42,108 working face is mostly sandy mudstone, partly mudstone and siltstone. The thickness of the immediate roof is 1~21 m, and the roof is easy to fall or separated strata. The 42,108 working face is north-south, and the east side is the 42,107 gob area. The width of the 22,108 working face is 300 m, and the stopping length is 4,724.7 m. The average thickness of the coal seam is 4 m, the dip angle is 1°~2°, and the average buried depth is 290 m. The direct roof of the 22,108 working face is also dominated by sandy mudstone, and the thickness of the immediate roof is large. The position relationship of the working face is shown in Figure 1, and the physical and mechanical properties of the coal measures strata are shown in Table 1. All parameters are obtained by field exploration and experimental tests.

3 Numerical simulation

PFC2D follows Newton's second law and force-displacement law to simulate the contact, motion, and interaction between particles. The contact force between particles is updated by the force-displacement law, and the position of particles and boundary is sought by Newton's law of motion to form a new contact. The linear parallel bond model is used in this paper, the particles form a whole through bonding contact and can withstand tension, pressure, and torsion within a certain range, contact between particles is broken beyond the range and degenerates into a linear model that only works under pressure. The model can realistically simulate the formation process of roof fracture and hinged structure in the mining process (Cho N. et al., 2007). The mechanical behavior of the linear parallel bond model is shown in Figure 2.

According to the actual distribution of overlying strata in 42,108 working faces, a 2D numerical model of double-layer mining is established. The length of the numerical model is 800 m and the height is 400 m. The minimum particle size is 0.4, the particle size ratio is 1.6, and a total of 321,569 particles are generated. The model's left and right and bottom boundaries are fixed, and the top is a free boundary, as shown in Figure 3. Displacement constraints are set on the left and right sides of the

TABLE 1 Physical and mechanical properties of coal and rock masses.

No.	Lithology	Density (kg/m^3)	Thickness (m)	Elasticity modulus (GPa)	Tensile strength (MPa)	Compressive strength (MPa)
1	Loess layer	1,600	12.72	0.12	0.03	0.33
2	Fine sandstone	2,280	20.97	0.6	0.89	11.2
3	Sandy mudstone	2,430	13.27	1.0	20	1.97
4	Medium sandstone	2,230	14.36	0.5	0.55	7.2
5	Coarse conglomerate	1800	20.64	1.5	0.92	12.3
6	Fine sandstone	2,280	15.5	0.6	0.89	11.2
7	Medium sandstone	2,230	20.03	0.5	0.55	7.2
8	Sandy mudstone	2,430	11.67	1.0	20	1.97
9	Medium sandstone	2,230	10.4	0.5	0.55	7.2
10	Fine sandstone	2,280	11.4	0.6	0.89	11.2
11	Sandy mudstone	2,430	20.1	1.0	20	1.97
12	Medium sandstone	2,230	13	0.5	0.55	7.2
13	Sandy mudstone	2,430	11.74	1.0	20	1.97
14	Medium sandstone	2,230	12.16	0.5	0.55	7.2
15	Sandy mudstone	2,430	11.18	1.0	20	1.97
16	Fine sandstone	2,280	16.43	0.6	0.89	11.2
17	Medium sandstone	2,230	15.49	0.5	0.55	7.2
18	Sandy mudstone	2,430	12	1.0	20	1.97
19	Fine sandstone	2,280	12.25	0.6	0.89	11.2
20	Sandy mudstone	2,430	9.93	1.0	20	1.97
21	2-2 coal seam	1,310	4	1.0	0.55	7.2
22	Mudstone	2,400	5.38	2.6	4.3	38
23	Fine sandstone	2,280	7.17	0.6	0.89	11.2
24	Sandy mudstone	2,430	6.63	1.0	20	1.97
25	Siltstone	2,380	11.24	2.0	1.97	16.5
26	Medium sandstone	2,230	5.1	0.5	0.55	7.2
27	Siltstone	2,380	14.57	2.0	1.97	16.5
28	Medium sandstone	2,230	8.39	0.5	0.55	7.2
29	Sandy mudstone	2,430	8.91	1.0	20	1.97
30	4-2 coal seam	1,310	6	1.0	0.55	7.2
31	Mudstone	2,400	20.07	2.6	4.3	38
32	Siltstone	2,380	17.3	2.0	1.97	16.5

model and the bottom boundary, and free boundary condition is set up on the top. The Mohr-Coulomb constitutive model is adopted.

The model considers 32 representative strata according to the drilling data, and the microscopic parameters of each rock layer are shown in Table 2. Before numerical calculation, we need to correct the microscopic parameters of the model according to the actual mechanical parameters of rock mass. Table 2 shows the corrected parameters. The mining height of the upper and lower coal seams is 4 and 6 m respectively, and the advancing distance of the working face is 300 m. Each working face is excavated 30 times, 10 m each time. To eliminate the influence of the boundary effect on the model,

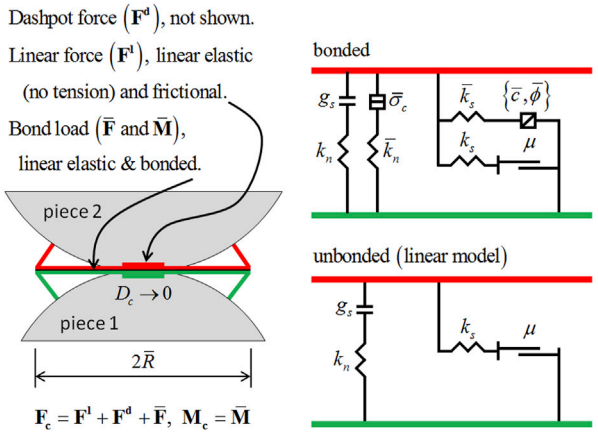

FIGURE 2
Linear parallel bond model diagram.

250 m boundaries are generated on both sides of the model. This research focuses on the characteristics and laws governing overburden and surface damage, omitting the temporary support effect of powered support in the working face.

4 Result in analysis

4.1 Analysis of mining overburden failure and fracture development law

As the first mining proceeds, the immediate roof gradually bends downward to produce separation, and the basic roof cracks develop. As shown in Figure 4, when advancing to 70 m, the immediate roof breaks for the first time, and the basic roof S1 forms a penetrating crack at the position of the cut-off and the working face. When advancing to 90 m, the basic roof S1 is broken, showing the form of a "Voussoir beam" structure, accompanied by separation, and the cracks in the upper middle sandstone soft rock layer of the basic roof S2 develop from both sides of the goaf to the middle. When advancing to 130 m, the basic roof S1 collapsed and the working face is first roof pressure, the central part of the falling zone gradually compacted, and the height of the falling zone is 21 m. The cracks in the S2 cut-off of the basic roof penetrated, and the cracks in the overlying weak medium sandstone layer gradually developed. The basic roof S1 repeats the failure process of "breaking-collapse-compaction." The falling zone only expands horizontally and no longer develops upward.

When the working face advances to 200 and 280 m respectively, the basic roof S2 forms penetrating cracks from the working face, resulting in a certain degree of damage. However, due to the small thickness of the first coal seam, and the large thickness of the basic roof, resulting in a high backfilling height of the gob area, the basic roof S2 does not collapse. When advancing to 300 m, the numerical simulation mining is completed, the gob area is compacted, the interlayer separation layer is basically closed, and the basic roof S2 exists in the form of a "Voussoir beam" structure with bearing capacity. Affected by the goaf, a large number of cracks are developed in the overlying weak rock layer. In the whole first mining process, there is no obvious bending separation phenomenon in the high overlying strata. The height of the water-conducting fractured zone is 65.1 m, the height of the falling zone is 21 m, and the ratio of mining to falling is 1:5, which is basically consistent with the conclusions of the empirical Eqs 1, 2 of "falling height" and "two-zone" height of medium hard rock strata studied by Liu Shiqi (Liu, 2016).

$$H_{\mathrm{m}} = 4.73M + 4.40 \tag{1}$$

$$H_{\mathrm{l}} = \frac{100M}{0.23M + 6.1} \pm 10.42 \tag{2}$$

In the formula: H_{m} is the height of the caving zone; M is the coal seam mining height; H_{l} is the height of the water-conducting fractured zone.

Similar to the first mining, as the working face advances, the hard roof R1 gradually bends. As shown in Figure 5, when the working face advances to 70 m, the bending, and sinking of the hard roof R1 are very obvious, and cracks are generated from the cut-off, accompanied by small separation layers, but not broken. When advancing to 100 m, as the subsidence space increases, the roof R1 breaks for the first time, the working face is first roof

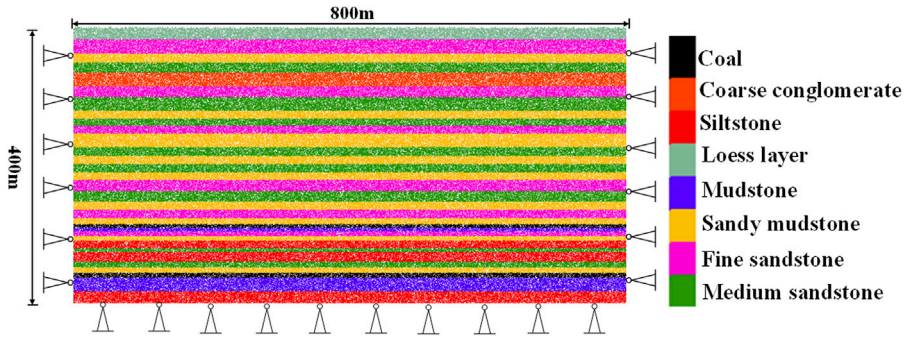

FIGURE 3
Numerical simulation model diagram.

TABLE 2 Microscopic parameters of overburdened rock.

Lithology	σ_c	σ_t	E*	fa	f	k
Loess layer	0.2	0.6	0.06	38	0.4	2
Fine sandstone	2.0	3.8	0.3	40	0.3	2
Sandy mudstone	5.0	9	0.5	43	0.3	2
Medium sandstone	1.0	2.7	0.25	43	0.3	2
Coarse conglomerate	1.9	3.7	0.75	42	0.4	2
Fine sandstone	2.0	3.8	0.3	40	0.3	2
Medium sandstone	1.0	2.7	0.25	43	0.3	2
Sandy mudstone	5.0	9	0.5	43	0.3	2
Medium sandstone	1.0	2.7	0.25	43	0.3	2
Fine sandstone	2.0	3.8	0.3	40	0.3	2
Sandy mudstone	5.0	9	0.5	43	0.3	2
Medium sandstone	1.0	2.7	0.25	43	0.3	2
Sandy mudstone	5.0	9	0.5	43	0.3	2
Medium sandstone	1.0	2.7	0.25	43	0.3	2
Sandy mudstone	5.0	9	0.5	43	0.3	2
Fine sandstone	2.0	3.8	0.3	40	0.3	2
Medium sandstone	1.0	2.7	0.25	43	0.3	2
Sandy mudstone (Basic roof S2)	5.0	9	0.5	43	0.3	2
Fine sandstone (Basic roof S1)	2.0	3.8	0.3	40	0.3	2
Sandy mudstone	5.0	9	0.5	43	0.3	2
2-2 coal seam	1.0	2.7	0.5	39	0.3	2
Mudstone	10	27	1.3	38	0.4	2
Fine sandstone	2.0	3.8	0.3	40	0.3	2
Sandy mudstone	5.0	9	0.5	43	0.3	2
Siltstone (Hard rock R3)	1.0	5	8.8	43	0.3	2
Medium sandstone	1.0	2.7	0.25	43	0.3	2
Siltstone (Hard rock R2)	1.0	5	8.8	43	0.3	2
Medium sandstone	1.0	2.7	0.25	43	0.3	2
Sandy mudstone (Hard rock R1)	5.0	9	0.5	43	0.3	2
4-2 coal seam	1.0	2.7	0.5	39	0.3	2
Mudstone	10	27	1.3	38	0.4	2
Siltstone	1.0	5	8.8	43	0.3	2

pressure, and longitudinal tensile cracks begin to appear in the hard rock R2. When advancing to 150 m, the hard rock R2 bends and breaks, forming a "Voussoir beam" structure. The separation occurs, and the hard rock R3 breaks from the middle of the suspension area, showing a "Cantilever beam" state. At this time, the mining-induced fracture extends to the floor of 22 coal seam and connects with the water-conducting fracture zone of 22,108 working face, forming an ultra-high water-conducting fracture zone.

When advancing to 300 m, the numerical simulation mining is completed. At this time, the hard rock R3 is also broken, forming a "Voussoir beam" structure, which is not unstable under the support of the filling rock in the goaf. The floor failure range of the upper coal is connected with the development range of the lower coal falling zone, the gob area is compacted and the separation layer is closed. The high-level hard rock breaks along the cut-off and the stop line, resulting in obvious bending and existing in the form of a "Voussoir beam." At this time, the height of the lower falling zone is 35.97 m, the ratio of mining to falling is 1:6 and the height of the water-conducting fractured zone is 184.57 m.

4.2 Analysis of development law of mining surface cracks

According to the theory and method of mining subsidence, coal mining ground cracks are mainly divided into boundary cracks and dynamic cracks. Boundary cracks are generally in the outer edge area of the stop line and cut-off. Dynamic cracks are located on the surface above the working face, parallel to the working face, and are continuously generated and closed as the working face advances (Hu et al., 2014). Based on elastic finite element theory, after coal mining, the stress distribution area of overlying strata can be divided into compressive stress area, tensile stress area, tensile stress area of positive curvature, compressive stress area of negative curvature, and supporting pressure area (Yang et al., 2019). Among them, the surface on both sides of the gob area belongs to the tensile stress area of positive curvature, and the surface above the goaf belongs to the compressive stress area of negative curvature.

With the first breaking of the main roof (working face advancing to 90 m), the longitudinal boundary cracks appeared on the surface for the first time. Since then, with the advancement of the working face, the mining boundary cracks appeared on the surface, and the boundary cracks are mainly vertical rock layer cracks, as shown in Figure 6, which is consistent with the research conclusion of Zhang Yujun (Zhang and Li, 2011). The first mining cracks are mainly boundary cracks. This is because the surface on both sides of the gob area is located in the tensile stress area, and the tensile strength of the surface loess overburden is almost negligible, which is easily damaged by tension under the influence of the goaf. The boundary crack of the cut-off behind the cut-off by 100 m and the average spacing of the cracks is 49 m. The boundary cracks of the stop line are 110 m ahead of the stop line, and the average spacing of the cracks is 34 m.

Compared with the first mining, surface damage is serious after repeated mining. As shown in Figure 7, after repeated mining, the boundary cracks develop to the position of the cut-off and stop line. The average spacing of boundary cracks of cut-off is 53.2 m, and that of the stop line is 38.7 m. The number of boundary cracks doubled, which is due to repeated mining caused by the extent of the roof bending damage, resulting in horizontal movement of surface soil to the gob area. Different from the first mining, after repeated mining, a "trapezoid" crack-intensive staggered area is formed at the surface position in the middle of the goaf. This is due to the increase of the longitudinal damage range of the overburden caused by repeated mining, resulting in the bending and sinking of the bedrock under

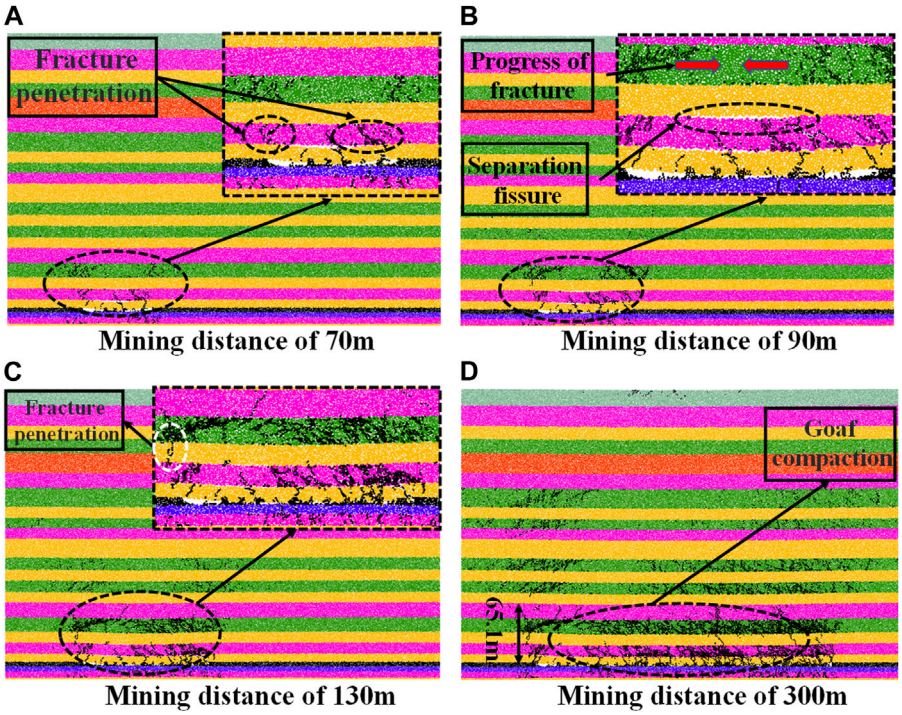

FIGURE 4
The first mining overburden structure evolution characteristic diagram. **(A-D)** show the mining distance of 70 m, 90 m, 130 m and 300 m, respectively.

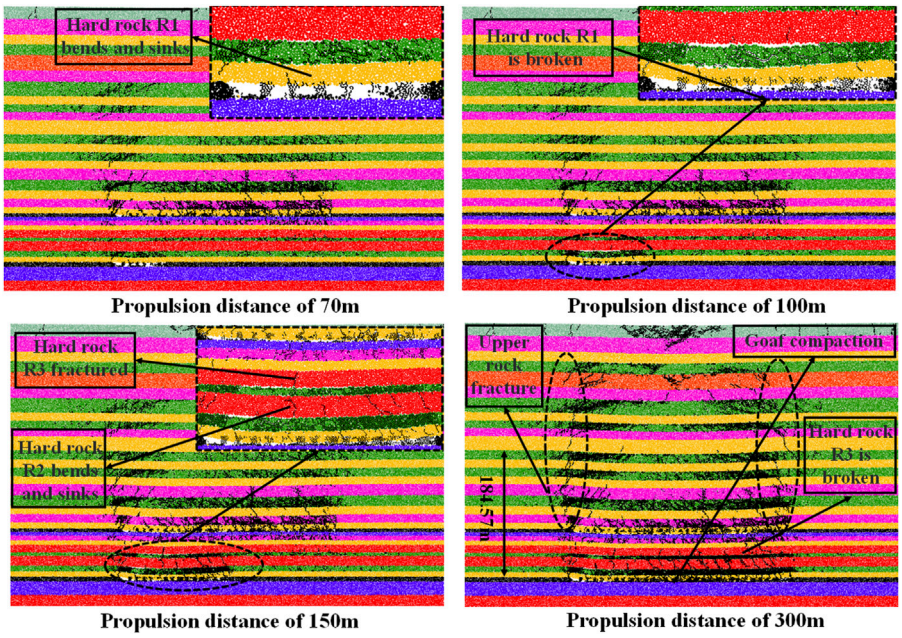

FIGURE 5
Overburden rock structure evolution characteristic diagram of repeated mining.

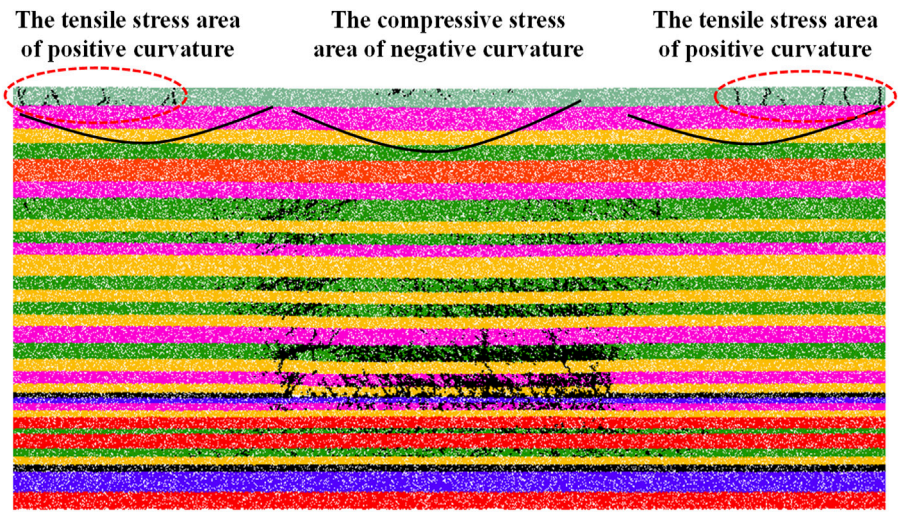

FIGURE 6
Development law diagram of surface cracks in the first mining.

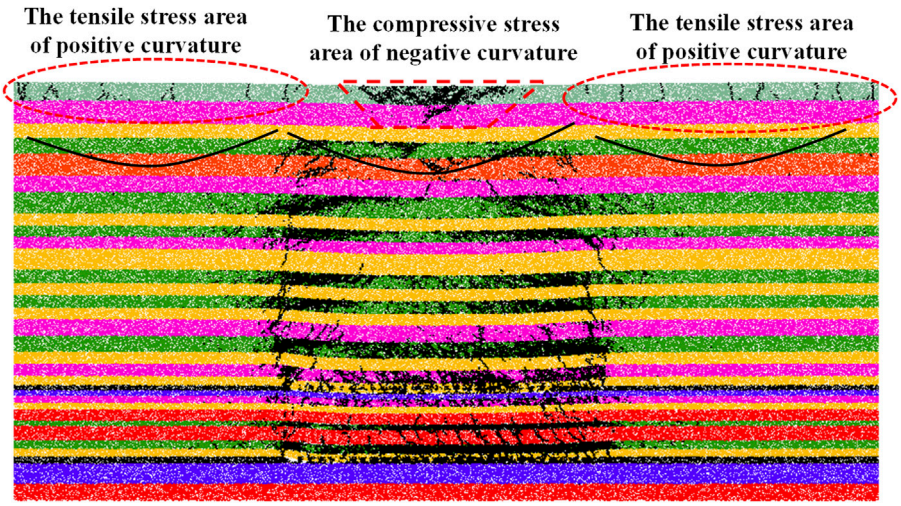

FIGURE 7
Surface crack development law diagram of repeated mining.

the loess overburden. The loess layer in the compressive stress area is destroyed by its own pressure, forming a dense compressive crack area.

4.3 Analysis of mining surface movement deformation

The planar position of the surface movement observation station is measured by GPS fast static method, and the level is measured by Leica DNA03s digital level. The layout of surface subsidence monitoring points in the 22,108 working face of Buertai Coal Mine is shown in Figure 8. There are 41 monitoring points in the trend direction of the 22,108 working face, with a spacing of 20 m and a number of L06~L46. A total of 5 plane observations and 32 leveling and elevation observations zre completed, and a large number of valuable observation data are obtained. The maximum surface subsidence is 2.209 m.

Numerical model after each step of excavation, compared with 22,108 working face surface subsidence monitoring point real point, every 20 m to set up a monitoring point, record the vertical displacement for statistical analysis, and draw a graph, as shown in Figure 9. Due to the influence of the adjacent goaf, the surface settlement curve monitored in the field is not symmetrical. The settlement value of the side adjacent to the goaf is relatively large. However, this is not the focus of this article, so it will not be described in detail.

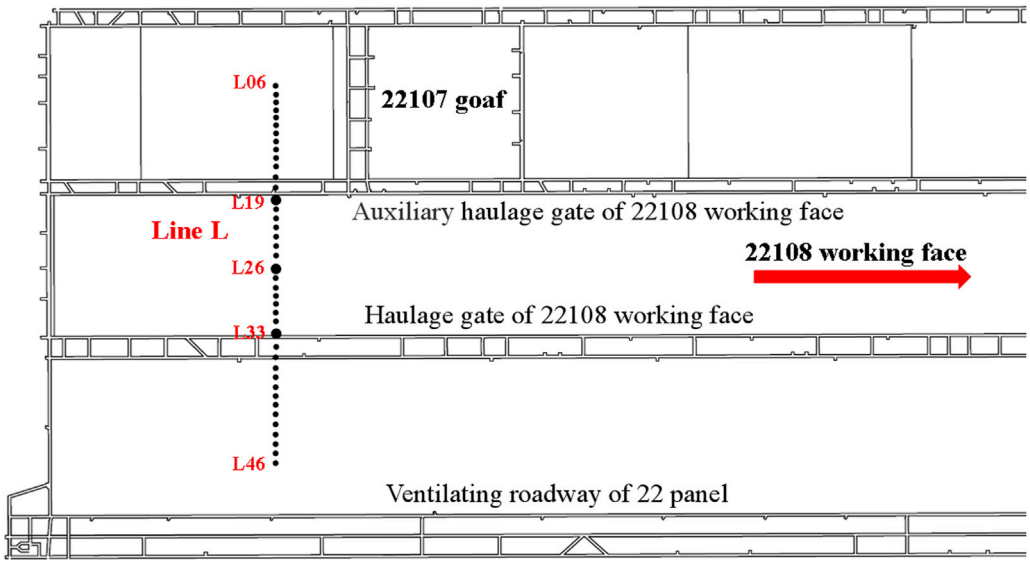

FIGURE 8
Twenty two thousand and one hundred and eight working face surface subsidence measuring point layout.

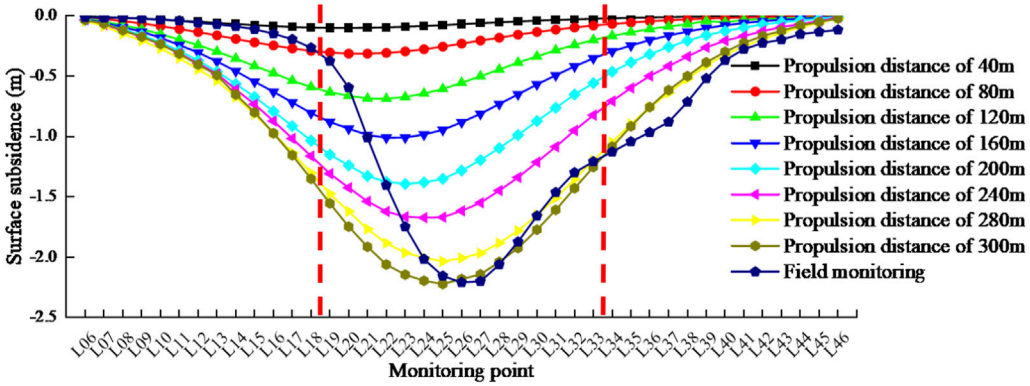

FIGURE 9
Vertical displacement characteristic diagram of first mining overburden.

During the mining process of the first mining face of 22,108, the surface settlement curve is a relatively gentle "bowl" shape. When the working face advances to 40, 80, 120, 160, 200, 240, 280, and 300 m, the maximum settlement is 0.099, 0.313, 0.687, 1.009, 1.393, 1.674, and 2.223 m respectively. With the continuous advancement of the working face, the range and amount of surface subsidence are increasing, the position of the maximum settlement is constantly moving to the right, and the settlement rate in the middle of the gob area is greater than that on both sides, finally, a relatively symmetrical subsidence basin is formed on the surface. The maximum subsidence of the surface is 2.22 m. The maximum subsidence position is located in the center of the goaf, which is slightly close to the direction of the cut-off, and the horizontal distance from the cut-off is 130 m. The surface subsidence trend of the 22,108 working face is the surface basin form of flat bottom, the overall trend is relatively flat, the distance between the boundary of gob area and the edge of the basin bottom is large, and the slope is small, which is a typical feature of shallow buried deep collapse basin (Li et al., 2010).

The settlement curve of the numerical simulation of the 300 m mining is compared with the settlement curve of the 300 m advancing measured in the 22,108 fields. The numerical simulation results are basically consistent with the maximum settlement in the field measurement results, and the position of the maximum settlement in the numerical simulation is slightly left. In general, the numerical simulation results are basically the same as the field measurement, and the settlement trend conforms to the general law, which indicates that the process research and result analysis of overburden failure and surface movement caused by coal seam mining are credible.

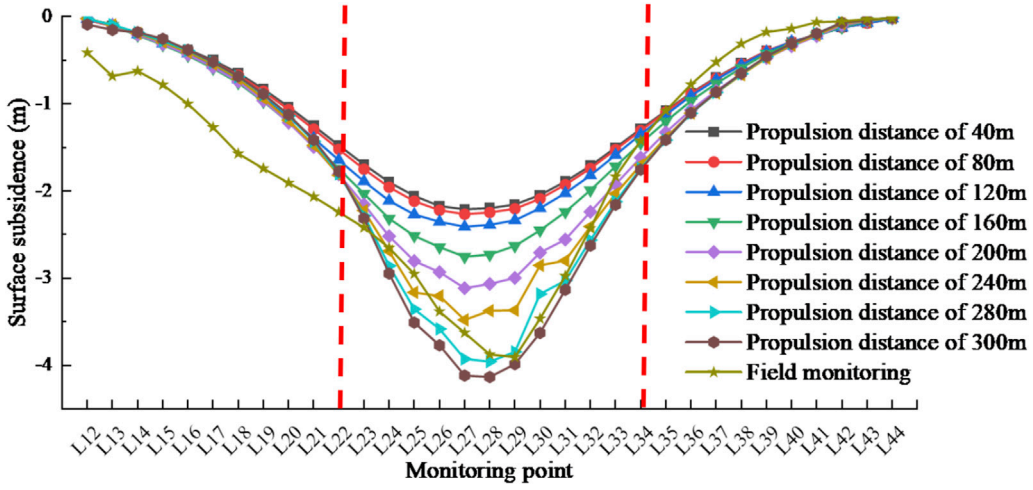

FIGURE 10
Vertical displacement characteristic diagram of repeated mining overburden rock.

During the mining process of the 42,108 repeated mining face, the surface subsidence curve is generally in a symmetrical "funnel" shape, with only one main inflection point. As shown in Figure 10, when the working face advances to 40, 80, 120, 160, 200, 240, 280, and 300 m, the maximum settlement is 2.209, 2.266, 2.410, 2.753, 3.112, 3.477, 3.955, and 4.132 m respectively. The position of the maximum settlement is stable in the direction of the central cutting hole of the 22,108 working face gob area. Compared with the first mining, the surface subsidence after repeated mining is significantly increased, and the maximum settlement is about 1.86 times the maximum settlement of the first mining. This shows that repeated mining changes the stable state of the broken roof of the upper coal seam, leading to the "activation" of the roof of the gob area, further aggravating the damage to the roof and even the surface.

The settlement curve of the numerical simulation of repeated mining 300 m is compared with the settlement curve of the 300 m measured in the 42,108 fields. The maximum settlement of the numerical simulation is 4.1 m, which is slightly larger than the 3.9 m measured in the field. The maximum settlement position of the numerical simulation is 20 m to the left.

4.4 Influence of panel incline width on overburden fracture

To study the influence of panel incline width on overlying rock strata failure law and surface fracture distribution, the mining overlying rock fracture and surface fracture distribution under the conditions of panel incline width of 340, 380, and 420 m are analyzed by using numerical simulation, respectively.

The selection of the panel incline width has a great influence on both the overlying rock strata and the surface, as shown in Figure 11. With the increase of the panel incline width, the influence range of the surface subsidence expands, especially when the panel incline width exceeds 380 m. The surface subsidence of the goaf also increases with the increase of the panel incline width, and the surface subsidence basin is approximately "flat bottom" shape.

As can be seen from Figure 12, the increase of the panel incline width will lead to the increase of the area of the direct overhead, the bending of the basic roof and the formation of longitudinal cracks. Comparing the caving morphology and fracture propagation characteristics of overlying rock strata under three kinds of panel incline widths, the caving zone height is 21 m and does not increase with the increase of panel incline widths. The basic roof S2 still exists in the form of stable "masonry beam" and does not collapse, which is related to the geological characteristics of large basic roof thickness and high backfill degree of gob in Buertai coal mine. At the same time, with the increase of the panel incline width, the surface cracks did not change very much, and the cracks expanded laterally. In the longitudinal direction, due to the existence of high thick hard bedrock, the cracks did not expand upward after expanding to a certain height, and the height of the water-conducting fracture zone is 65.1 m.

5 Discussion

With the expansion of the gob area, the movement range of overburden strata also expands, and the final movement range extends to the surface, causing surface movement and deformation. The surface subsidence is the result of the upward transmission of mining overburden strata. The lower coal seam mining activates the upper goaf, causing the "secondary damage" of the original damaged rock. The overlying strata of the upper gob area are broken again and deposited in the goaf in a loose state. Under the influence of secondary mining, the stress balance of overlying strata is also destroyed again, which leads to the instability and compaction of overlying strata in the previous gob area. Therefore, it will lead to

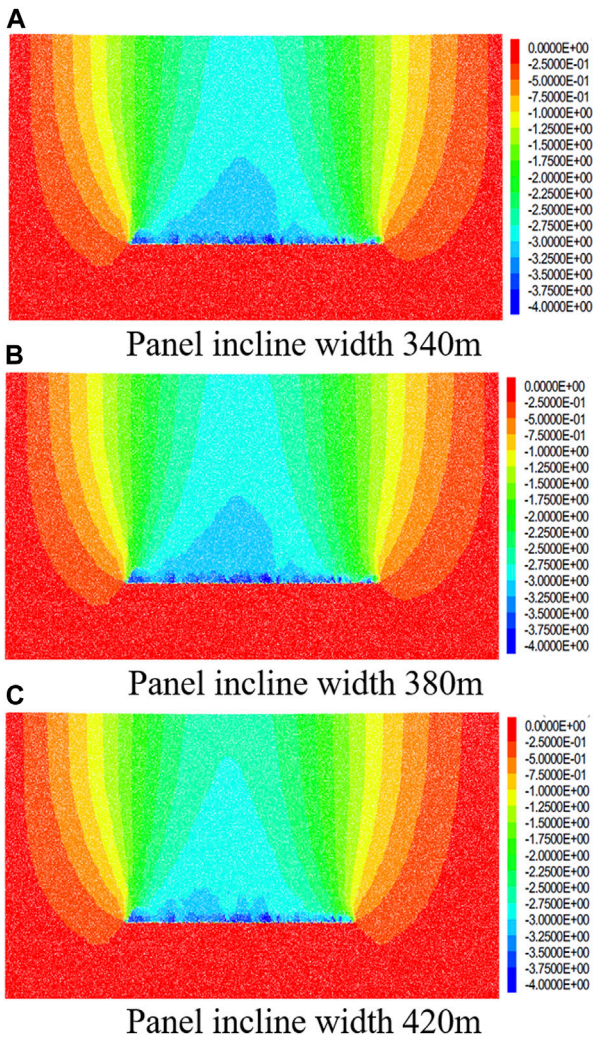

FIGURE 11
Vertical displacement cloud map of overlying rock strata under different panel incline widths. **(A-C)** show the panel incline width of 340 m, 380 m and 420 m, respectively.

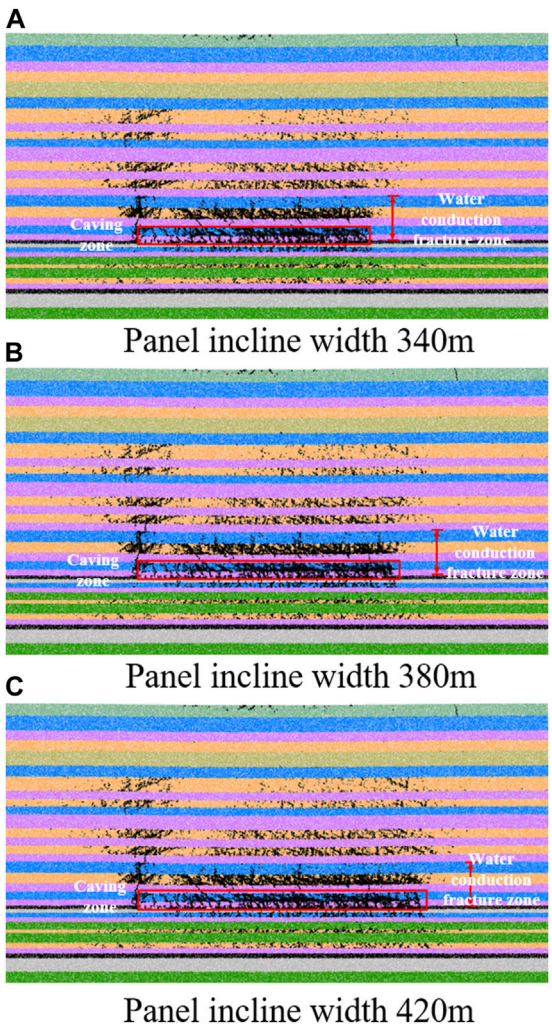

FIGURE 12
Overburden failure and fracture propagation under different panel incline widths. **(A-C)** show the panel incline width of 340 m, 380 m and 420 m, respectively.

the surface subsidence above the gob area again, and the degree of subsidence is much greater than the first mining. The working face is covered with 12~18 m loess. Compared with the bedrock, loess has the characteristics of low density, low strength, and no tensile strength, which makes it easy to deform when subjected to external forces, and cannot form a supporting structure similar to a "beam." Under its own pressure, it sinks with the sinking of bedrock.

Actually, the morphology of overburden fracture propagation caused by multi-seam mining is complex, and is related to many factors, including lithology, working face layout, mining speed, etc. The overburden migration prediction models for single coal seam mining are not applicable. However, From the illustration of a case study at Buertai Coal Mine, the overburden migration caused by mining multiple coal seams is not a simple superposition of the migration caused by each coal seam. The overburden structure disturbance caused by the previous coal seam and rock cracking—settlement have great influence on the mining of the latter coal seam.

6 Conclusion

In this paper, Taking the 22,108 and 42,108 working faces of Buertai Coal Mine as a research object, the surface subsidence monitoring technology and the discrete element method are used to simulate the migration and failure characteristics of overlying strata, and the propogation of cracks in the process of multi-coal seams mining is also been investigated. The conclusions are as follows:

(1) After the exploitation of the lower coal seam, the water-conducting fractured zone develops upward and is connected with the fracture zone of the upper coal seam. Due to the large thickness of the basic roof of the coal seam in Buertai Coal Mine, resulting in a high backfilling height of the goaf, and the overlying hard layer is easy to form a "Voussoir beam" structure with bearing capacity;
(2) So many cracks develop in the soft strata overlying the coal seam, and they cross each other and form a complex fracture

system. The hard layer is subjected to tensile action, resulting in crisscross cracks. The crack size is large, and they are mainly high-angle longitudinal cracks. In the process of single-layer mining, surface cracks are mainly longitudinal tensile cracks in the tensile stress area; after repeated mining, the compressive cracks in the surface compressive stress area are densely developed;

(3) In Buertai Coal Mine, the surface subsidence curve of single coal seam mining shows a wide and slow "bowl" type, and the surface subsidence curve of double coal seam mining shows a "funnel" type with only one inflection point. The maximum surface subsidence position is located on the left side of the center of the working face and is consistent with the maximum subsidence position when single-layer mining;

(4) The overburden migration caused by mining multiple coal seams is not a simple superposition of the migration caused by each coal seam. The overburden structure disturbance caused by the previous coal seam and rock cracking—settlement have great.

Data availability statement

The original contributions presented in the study are included in the article/Supplementary Material, further inquiries can be directed to the corresponding author.

Author contributions

JZ: Investigation, Writing–original draft, Funding acquisition. MW: Investigation, Writing–review and editing, Funding acquisition. LB: Methodology, Writing–review and editing. CY: Writing–review and editing, Software.

Funding

The authors declare financial support was received for the research, authorship, and/or publication of this article. This work was supported by Open Fund of the State Key Laboratory of Water Resource Production and Utilization in Coal Mining (No. WPUKFJJ 2019-18), and Education science and technology research plan guiding project of Hubei Provincial Department (No. B2021272), and Wuhan Knowledge innovation special project (No. 2022010801020429).

Conflict of interest

The authors declare that the research was conducted in the absence of any commercial or financial relationships that could be construed as a potential conflict of interest.

Publisher's note

All claims expressed in this article are solely those of the authors and do not necessarily represent those of their affiliated organizations, or those of the publisher, the editors and the reviewers. Any product that may be evaluated in this article, or claim that may be made by its manufacturer, is not guaranteed or endorsed by the publisher.

References

Adhikary, D., Khanal, M., Jayasundara, C., and Balusu, R. (2015). Deficiencies in 2d simulation: a comparative study of 2d versus 3d simulation of multi-seam longwall mining. *Rock Mech. Rock Eng.* 49, 2181–2185. doi:10.1007/s00603-015-0842-7

Baek, J., Kim, S. W., Park, H. J., and Jung, H. S. (2008). Analysis of ground subsidence in coal mining area using SAR interferometry. *Geosciences J.* 12 (3), 277–284. doi:10.1007/s12303-008-0028-3

Cho, N., Martin, C. D., and Sego, D. C. (2007). A clumped particle model for rock. *Int. J. Rock Mech. Min. Sci.* 44, 997–1010. doi:10.1016/j.ijrmms.2007.02.002

Ge, L., Chang, H. C., and Rizos, C. (2007). Mine subsidence monitoring using multi-source satellite SAR images. *Photogrammetric Eng. Remote Sens.* 73 (3), 259–266. doi:10.14358/pers.73.3.259

Ghabraie, B., Ren, G., James, B., and John, V. (2017b). A predictive methodology for multi-seam mining induced subsidence. *Int. J. Rock Mech. Min. Sci.* 93, 280–294. doi:10.1016/j.ijrmms.2017.02.003

Ghabraie, B., Ren, G., and Smith, J. V. (2017a). Characterising the multi-seam subsidence due to varying mining configuration, insights from physical modelling. *Int. J. Rock Mech. Min. Sci.* 93, 269–279. doi:10.1016/j.ijrmms.2017.02.001

Ghabraie, B., Ren, G., Zhang, X., and Smith, J. (2015). Physical modelling of subsidence from sequential extraction of partially overlapping longwall panels and study of substrata movement characteristics. *Int. J. Coal Geol.* 140, 71–83. doi:10.1016/j.coal.2015.01.004

Guoqing, Y., and Jingqin, M. (2008). D-InSAR technique for land subsidence monitoring. *Earth Sci. Front.* 15 (4), 239–243. doi:10.1016/s1872-5791(08)60059-7

He, S., Xie, S., Song, B., Zhou, D., Sun, Y., and Han, S. (2016). Breaking laws and stability analysis of damage main roof in close distance hypogynous seams. *J. China Coal Soc.* 41 (10), 2596–2605.

Hu, Z., Wang, X., and He, A. (2014). Distribution characteristic and development rules of ground fissures due to coal mining in windy and sandy region. *J. China Coal Soc.* 39 (01), 11–18.

Itasca Consulting Group (2005). *Inc.Manual of particle flow code in 2-dimension*. Minneapolis: Itasca Consulting Group Inc. Version 3.10.

Jung, H. C., Kim, S. W., Jung, H. S., Min, K. D., and Won, J. S. (2007). Satellite observation of coal mining subsidence by persistent scatterer analysis. *Eng. Geol.* 92 (1-2), 1–13. doi:10.1016/j.enggeo.2007.02.007

Li, L., Tang, C., and Liang, Z. (2010). Investigation on overburden strata collapse around coal face considering effect of broken expansion of rock. *Rock Soil Mech.* 31 (11), 3537–3541.

Liu, C., Li, H., and Mitri, H. (2019b). Effect of strata conditions on shield pressure and surface subsidence at a longwall top coal caving working face. *Rock Mech. Rock Eng.* 52, 1523–1537. doi:10.1007/s00603-018-1601-3

Liu, Z., Zhong, X., Botao, Q., et al. (2019a). Redevelopment of fractures and permeability changes after multi-seam mining of shallow closely spaced coal seams. *Archives Min. Sci.* 64 (4).

Liu, S. (2016). *The law of the overburden failure in thick coal seam m1n1ng and instability criterion of the clay aquiclude under the influence of mining[D]*. Beijing): China University of Mining and Technology.

Liu, Y., Yang, T., Ye, Q., Hou, X., Zhao, Y., Wei, L., et al. (2022). Characteristics of surface deformation under repeated mining in mountainous area. *J. Min. Saf. Eng.* 39 (03), 507–516.

Ma, W. J., and Hu, H. F. (2013). The strata movement regularity and parameter simulation analysis in multiple seams repeated mining, *Appl. Mech. Mater.* Trans Tech Publications Ltd 295, 2935–2939. doi:10.4028/www.scientific.net/amm.295-298.2935

Perski, Z., Hanssen, R., Wojcik, A., and Wojciechowski, T. (2009). InSAR analyses of terrain deformation near the Wieliczka Salt Mine, Poland. *Eng. Geol.* 106 (1-2), 58–67. doi:10.1016/j.enggeo.2009.02.014

Wang, G., Wu, M., Wang, R., Xu, H., and Song, X. (2017). Height of the mining-induced fractured zone above a coal face. *Eng. Geol.* 216, 140–152. doi:10.1016/j.enggeo.2016.11.024

Wang, J., Wei, W., Zhang, J., and Mishra, B. (2020). Numerical investigation on the caving mechanism with different standard deviations of top coal block size in LTCC. *Int. J. Min. Sci. Technol.* 30 (5), 583–591. doi:10.1016/j.ijmst.2020.06.001

Wei, J., Wang, S., Song, S., Sun, Q., and Yang, T. (2022). Experiment and numerical simulation of overburden and surface damage law in shallow coal seam mining under the gully. *Bull. Eng. Geol. Environ.* 81 (5), 207. doi:10.1007/s10064-022-02706-y

Wu, T., Zhang, H., Wang, C., Tang, Y., and Wu, H. (2008). Retrieval of urban slow deformation using the multi-baseline DInSAR technique. *Chin. Sci. Bull.* 53 (23), 3705–3714. doi:10.1007/s11434-008-0331-4

Yang, X., Wen, G., Dai, L., Sun, H., and Li, X. (2019). Ground subsidence and surface cracks evolution from shallow-buried close-distance multi-seam mining: a case study in Bulianta coal mine. *Rock Mech. rock Eng.* 52 (8), 2835–2852. doi:10.1007/s00603-018-1726-4

Yang, Y. U., Shen, W., and Gao, J. (2016). Deformation mechanism and controlof lower seam Roadway of contiguous seams. *J. Min. Saf. Eng.* 33 (01), 49–55.

Yao, B., Zhou, H., and Chen, L. (2010). Numerical simulation about fracture development in overlying rocks under repeated mining. *J. Min. Saf. Eng.* 27 (03), 443–446.

Zhang, J., and Li, Y. (2019). Coal strength development with the increase of lateral confinement. *Energies* 12 (3), 405. doi:10.3390/en12030405

Zhang, Q., Zou, J. P., Wang, J., Jiao, Y. Y., and Xu, H. (2023a). Mechanism of coal bump induced by joint slipping under static and dynamic stresses in graben structural area. *Acta Geotech.* doi:10.1007/s11440-023-01947-9

Zhang, Q., Zou, J. P., Wu, K. B., et al. (2023b). On the characteristics of mine earthquakes induced by key strata breaking during deep mining. *Chin. J. Rock Mech. Eng.* 42 (5), 1150–1161.

Zhang, X., Ghabraie, B., Ren, G., and Tu, M. (2018). Strata movement and fracture propagation characteristics due to sequential extraction of multiseam longwall panels. *Adv. Civ. Eng.* 2018, 1–17. doi:10.1155/2018/4802075

Zhang, Y., and Li, F. (2011). Monitoring analysis of fissure development evolution and height of overburden failure of high tension fully-mechanized caving mining. *Chin. J. Rock Mech. Eng.* 30 (1), 2994–3001.

Zhao, Y., Wang, X., Guo, Y., Danesh, N. N., and Jiang, Y. (2022). Mechanical properties and brittleness characteristics of sandstone from different burial depths. *Geomechanics Geophys. Geo-Energy Geo-Resources* 8 (5), 165. doi:10.1007/s40948-022-00470-7

Zou, J., Hu, X., Jiao, Y. Y., Chen, W., Wang, J., Shen, L. W., et al. (2022b). Dynamic mechanical behaviors of rock's joints quantified by repeated impact loading experiments with digital imagery. *Rock Mech. Rock Eng.* 55 (11), 7035–7048. doi:10.1007/s00603-022-03004-5

Zou, J., Wu, K., Zhang, X., Zhu, J., Zhou, Z., Zheng, F., et al. (2022a). Effective evaluation of deep-hole blasting for controlling strong tremors induced by deep coal mining-A case study. *Int. J. Rock Mech. Min. Sci.* 159, 105211. doi:10.1016/j.ijrmms.2022.105211

frontiers | Frontiers in Earth Science

TYPE Original Research
PUBLISHED 29 December 2023
DOI 10.3389/feart.2023.1320069

Check for updates

OPEN ACCESS

EDITED BY
Pengjiao Jia,
Soochow University, China

REVIEWED BY
Qian Bai,
Northeastern University, China
Antonio Munjiza,
University of London, United Kingdom

*CORRESPONDENCE
Hong Miao,
miaohong@ustc.edu.cn

RECEIVED 11 October 2023
ACCEPTED 08 December 2023
PUBLISHED 29 December 2023

CITATION
Zhou X, Ye Z, Miao H, Li W, Wang X and Li C (2023), Dynamic evolution and numerical analysis of rock deformation under impact failure based on corner correlation method.
Front. Earth Sci. 11:1320069.
doi: 10.3389/feart.2023.1320069

COPYRIGHT
© 2023 Zhou, Ye, Miao, Li, Wang and Li. This is an open-access article distributed under the terms of the Creative Commons Attribution License (CC BY). The use, distribution or reproduction in other forums is permitted, provided the original author(s) and the copyright owner(s) are credited and that the original publication in this journal is cited, in accordance with accepted academic practice. No use, distribution or reproduction is permitted which does not comply with these terms.

Dynamic evolution and numerical analysis of rock deformation under impact failure based on corner correlation method

Xingui Zhou[1,2], Zhongbao Ye[2], Hong Miao[1]*, Wei Li[1], Xueru Wang[2] and Chenfeng Li[2]

[1]CAS Key Laboratory of Mechanical Behavior and Design of Materials, University of Science and Technology of China, Hefei, China, [2]Anhui Province Key Laboratory of Building Structure and Underground Engineering, Anhui Jianzhu University, Hefei, China

To fulfill the requirement for deformation measurement within the failure area during rock failure, a newly developed digital image algorithm, known as the corner correlation method, was implemented. A corner correlation measurement system was established by utilizing a Split Hopkinson Pressure Bar (SHPB) and a high-speed camera. The study focused on monitoring the deformation and failure characteristics of sandstone samples under dynamic loading. The results show that the corner correlation method has its unique advantages in rock dynamic mechanics experiments, and can obtain the deformation of the failure region during the rock failure process. Specifically, the initiation, extension, and contraction processes of surface cracks on sandstone were examined. Parameters such as crack width, width propagation rate, and extension shrinkage rate were measured. The entire crack development process was analyzed, including crack width, crack initiation point, crack extension and contraction trajectory, elongation and contraction velocity, width expansion rate, and longitudinal crack penetration, which were obtained at any given time on the surface of the rock sample. Additionally, the attenuation law of stress, characterized by an exponential decay of the stress peak value, was obtained through numerical simulation using a similar model.

KEYWORDS

rock, optical measurement, corner correlation, dynamic impact, crack propagation

1 Introduction

As a natural brittle material, rock is interleaved with cracks, joints, faults and other structural planes of different scales, resulting in complex mechanical responses of rock mass. The deterioration and structural failure of rocks are closely related to the tiny cracks inside them, which will expand and extend when affected (Tian, 2021; Guo, 2022). Experimental research on rock fracture is crucial to the observation of rock force deformation. From a relatively limited perspective, we gain insight into the interaction among defects in rock masses. This understanding significantly aids in evaluating the mechanical behavior of engineering rock masses, ensuring slope stability, designing mining engineering projects, predicting water flow in fractured rock masses, and formulating tunnel support designs, among other engineering challenges (Zhang and Zhao, 2013; Dai et al., 2021; Oparin, 2022; Chen et al., 2023; Chu et al., 2023). On a broader scale, in order to better understand the

causes of earthquakes (Zhang Y. B. et al., 2021), it is particularly important for geologists to understand the compressive deformation of continental plates, and the surface deformation of brittle materials is of great help to this. Describing the entire process of crack initiation, propagation, and cessation is the central challenge in rock failure. Therefore, real-time monitoring of crack evolution during rock loading holds paramount importance.

At present, domestic and foreign scholars have conducted extensive research on surface crack propagation during rock failure and obtained many valuable research results (Wang et al., 2016; Zhao et al., 2018a; Liu et al., 2018; Xing et al., 2018; Wei et al., 2019; Liu et al., 2020; Xi et al., 2020; Li et al., 2021a; Zhang et al., 2021b; Jin et al., 2021; Sikka et al., 2021; Zhou et al., 2022a; Hu et al., 2022; Liu et al., 2022; Pan and Wang, 2022; Wu et al., 2022; Gong et al., 2023; Zhang et al., 2023). With the rapid advancement of computer technology, numerical simulation has emerged as a crucial tool for effectively addressing complex issues in rock engineering. Common numerical simulation methods for fracture treatment include Discontinuous Deformation Analysis (DDA), the Discrete Element Method (DEM), and the Finite Element Discrete Element Coupling Method (FDEM). Presently, FDEM stands as a relatively mature numerical simulation method that combines the advantages of both continuum and discontinuum methods, enabling the accurate simulation of block fracture and movement during rock failure. EarE. Knight and Esteban Rougier have utilized FDEM to simulate rock impact experiments with random cracks, investigating the influence of cracks on rock mechanical behavior and failure path (Rougier et al., 2014; Chau et al., 2020). Their innovations in FDEM theory and algorithm have led to its widespread application across various projects (Knight et al., 2020; Munjiza et al., 2020).

Zhang Ya-bin studied the crack propagation law of rocks with prefabricated cracks under cyclic impact by numerical simulation, and obtained the relationship between the peak failure strength of rocks and the angle and number of prefabricated cracks (Zhang et al., 2021c). Song Yi-min carried out a quantitative study on rock displacement field evolution and crack dynamic fracture parameters under impact load using a drop hammer impact testing machine and a digital speckle correlation method, and obtained the relationship between the stress intensity factor at the crack tip and crack propagation (Song et al., 2015). Pan Hong-yu studied the global strain field of rock mass under uniaxial compression by using the correlation method of digital images, and analyzed the law of crack propagation during the loading process of rock mass (Pan et al., 2018). Alneasan used HDDM to evaluate the validity of classical fracture criteria to predict the crack growth path of infinite internal cracks under I-II composite loading (Alneasan et al., 2020). Li conducted uniaxial compression experiments on prefabricated rock-like specimens with different types of defects, and obtained the crack initiation sequence, propagation phenomenon and failure mode of different defective rock-like specimens (Li et al., 2021b). Zhao Chen employed DIC technology to obtain the global strain field of the specimens. Through quantitative analysis at the mesoscopic level, the law of crack initiation and propagation, as well as the evolution characteristics of rock deformation and damage, were summarized (Zhao et al., 2015; Zhao et al., 2018b). Guo Wei-yao monitored the entire crack propagation process using acoustic emission (AE) and digital image correlation (DIC) techniques. The influence of loading rate on the mode-I crack propagation mechanism was investigated (Guo et al., 2023). The aforementioned research findings hold significant importance in comprehending the dynamic failure characteristics of rocks. Particularly, digital image correlation technology (DIC) has garnered increasing attention and experimentation by researchers. It is evident that DIC technology is primarily utilized for measuring strain and displacement fields in static rock tests. However, severe damage to the speckle field on the model's surface poses substantial challenges for DIC technology in matching relevant sub-regions. Previous studies have predominantly concentrated on the causes and influencing factors of crack initiation and propagation in rocks, with limited reporting on the specific crack propagation process and failure characteristics during dynamic failure. Hence, investigating the dynamic evolution characteristics of rock cracks in dynamic tests holds immense significance.

The study of stress wave attenuation law is of great significance to the application of seismic exploration, underground engineering, geotechnical engineering and so on. Feng Xiao-jun utilized COMSOL Multiphysics to establish six 3D models in order to investigate the impact of two preexisting faults with different orientations on the propagation process of explosion-induced stress waves and their reflection effect. The interactive effect between faults of varying sizes was also examined, taking into account the propagation process of stress waves (Feng et al., 2019). Li Di-yuan conducted dynamic impact tests on red sandstone specimens with a single bonded planar joint at various angles, using a split Hopkinson pressure bar (SHPB). The objective was to analyze the stress wave propagation and fracturing evolution of specimens consisting of two blocks. The findings indicate that the presence of a bonded joint leads to a reduction in dynamic strength ranging from 3.10% to 32.13% compared to intact specimens (Li et al., 2019). Therefore, understanding the attenuation law of stress waves in the medium holds significance in providing a theoretical basis for underground structure detection and geological disaster prediction in seismic exploration. Furthermore, it can offer guidance for addressing engineering concerns such as vibration control and seismic safety assessment in underground projects.

This paper presents the development of a novel measurement system that combines the SHPB test device, a high-speed camera, and a self-improved digital image algorithm called the corner correlation method. An impact compression experiment is conducted on a complete rock sample, and the images captured during the experiment are processed and analyzed using the developed algorithm. The algorithm is utilized to analyze the dynamic evolution of cracks on the rock surface, while numerical simulations are employed to study the propagation of stress waves in rock. This comprehensive approach provides an effective means for studying the mechanisms of rock deformation and failure on both macro and micro scales, offering valuable insights for underground engineering design and construction.

2 Corner correlation method

Our research group has developed a novel digital image algorithm-corner correlation method in the previous work. Combining the corner extraction and digital image correlation method, this method first detects the integral pixel displacement of corner through the Harris algorithm (Harris and Stephens, 1988), and then the Newton iteration method (Bruck et al., 1989) is used to obtain the subpixel displacement after the initial integral pixel corner deformation, finally obtaining the displacement field of the measured object surface. The full-field strain is calculated based on the local least squares fitting of displacement field proposed by Pan Bin (Pan, 2007). In the preliminary work,

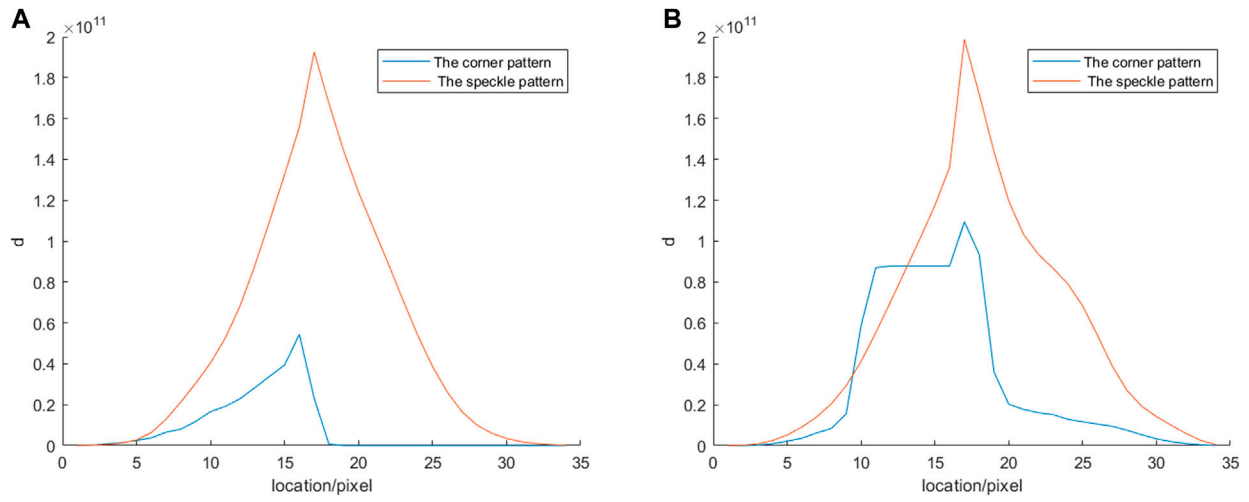

FIGURE 1
Curve of the relationship between crack position and error (Zhou et al., 2022b). **(A)** Longitudinal crack **(B)** Transverse crack.

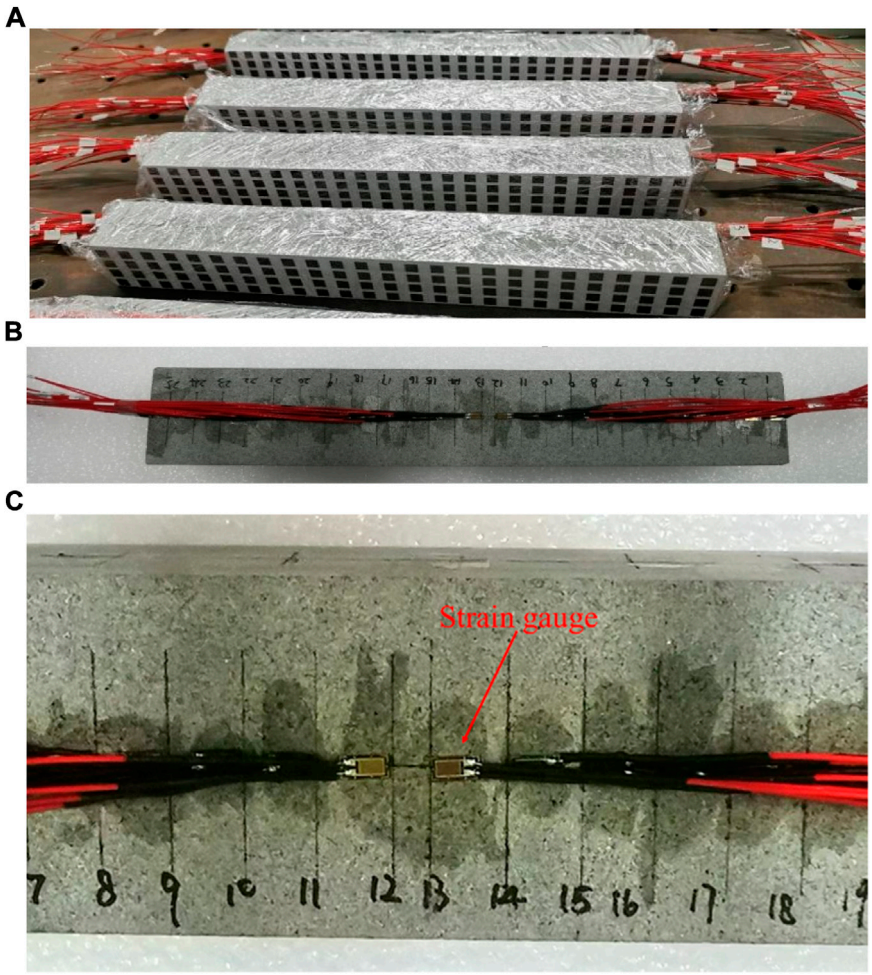

FIGURE 2
Rock sample. **(A)** Rock sample **(B)** Diagram of strain gauge adhesive position **(C)** Zoom of strain gauge.

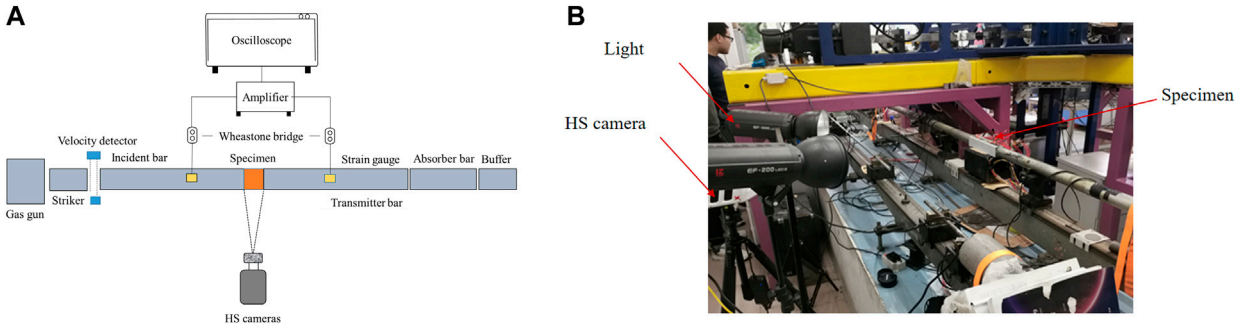

FIGURE 3
Experimental system. **(A)** Schematic diagram of the experimental system **(B)** Physical diagram of the experimental system.

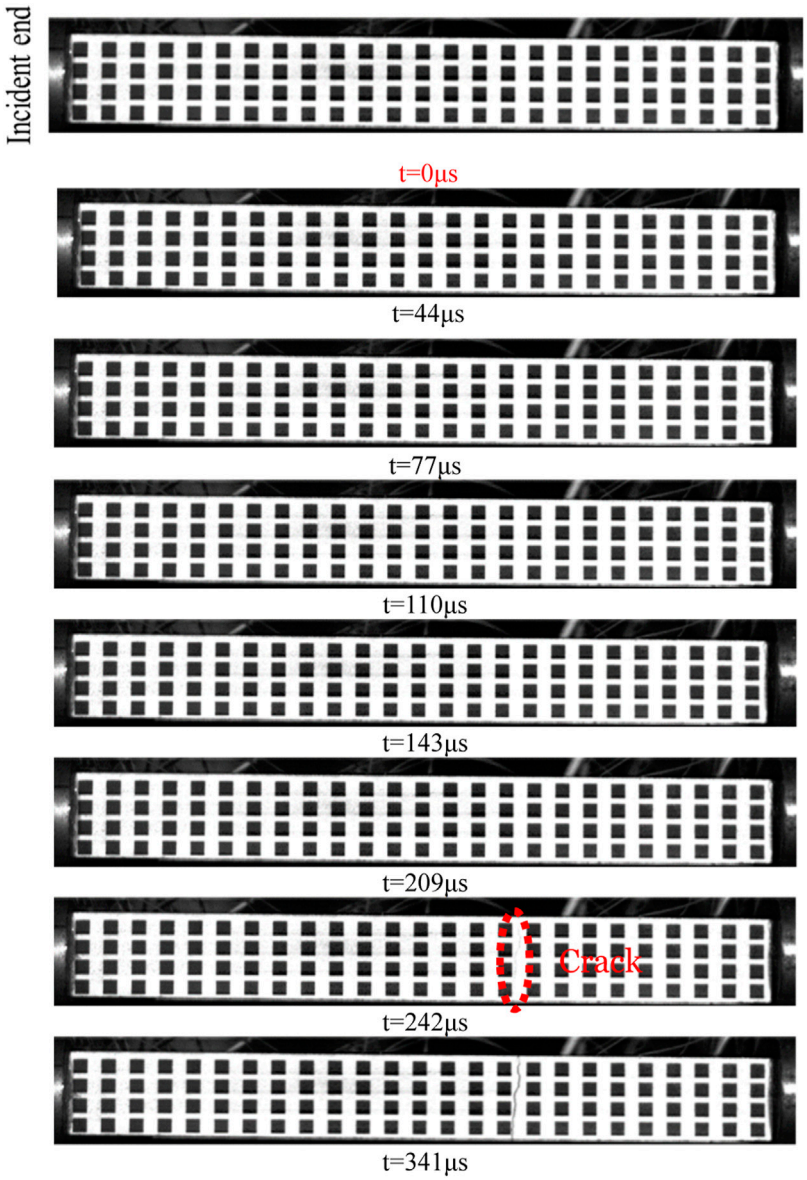

FIGURE 4
Experimental pictures.

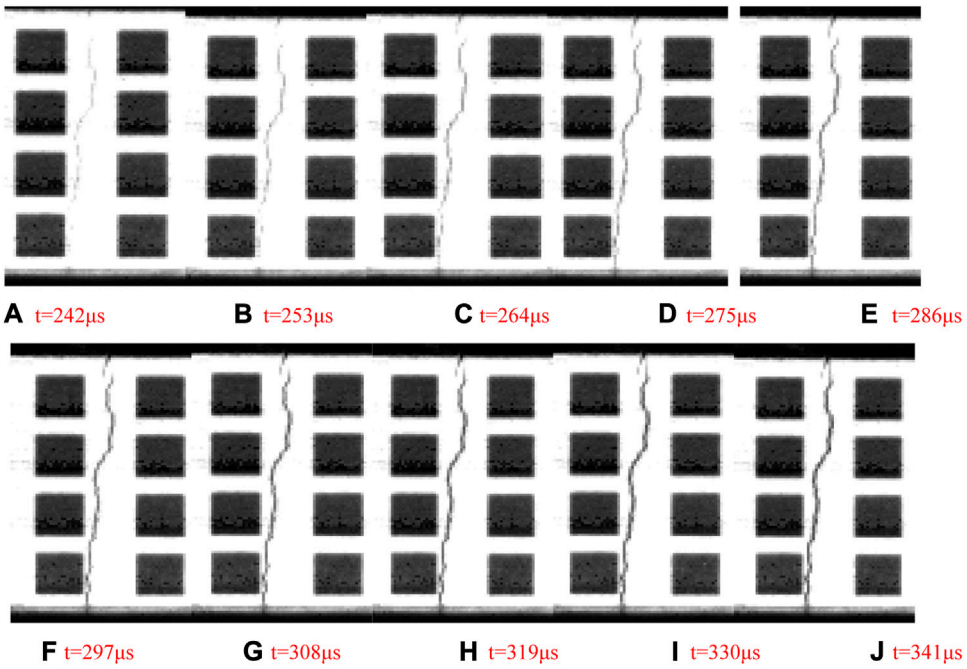

FIGURE 5
Zoom-ins of the crack localization zone. **(A)** t = 242 μs **(B)** t = 253 μs **(C)** t = 264 μs **(D)** t = 275 μs **(E)** t = 286 μs **(F)** t = 297 μs **(G)** t = 308 μs **(H)** t = 319 μs **(I)** t = 330 μs **(J)** t = 341 μs.

numerical simulation test, static tensile test and dynamic uniaxial compression test were used to evaluate and verify the calculation accuracy of diagonal corner correlation algorithm. It was concluded that the displacement field of Newton iteration method was smoother and the calculation accuracy was optimal, and its accuracy was controlled below 0.01 pixel in 0.1–0.9 pixel displacement mode. The strain field is measured with the displacement field obtained by Newton iteration method, and the maximum error of strain is controlled within 2×10^{-4}. By comparing the calculated values of the corner correlation method in static tensile test and dynamic uniaxial compression test with those measured by the strain gauge, the resolution of the strain measurement system is in the order of 10^{-4}. The deformation field of the failure region can still be calculated when complex failure occurs on the surface of the model. The calculation error of the cross-crack speckle plot and the corner plot is compared, and the calculation error of the corner plot of transverse and longitudinal cracks is smaller than that of the speckle plot. The result as shown in Figure 1. The detailed introduction and accuracy evaluation of the corner correlation method can be found author's article (Zhou et al., 2022b).

3 Sample preparation and experimental setup

3.1 Sample preparation

The sandstone samples were taken from a mine in Sichuan, China. Thin section identification and scanning electron microscope analysis were conducted on the sandstone samples. The sandstone was mainly composed of clay, orthoclase, gypsum, plagioclase, quartz, calcite, and dolomite. The particles consist primarily of minerals like quartz and feldspar, exhibiting distinct cleavage development on the surface of the feldspar particles and a high degree of self-filling of chlorite between the particles. To ensure the reliability of the constitutive model in numerical analysis, strain gauges were affixed to the specimen. Additionally, the development process of surface cracks in rock was monitored using the corner correlation method. Cuboid sandstone samples with dimensions of 50 mm × 50 mm × 250 mm were prepared, adhering strictly to the test standards of rock mechanics. The parallelism and flatness of the sample's cross section were carefully maintained, as depicted in Figure 2A. Grid marks in the form of spray paint points were arranged on the sample, with 4 rows and 25 columns of 5 mm × 5 mm grids placed on the shooting surface. Along the longitudinal symmetry axis, 25 strain gauges were applied to the rear surface of the rock, with each strain gauge corresponding to a specific grid. The strain gauge model employed was BE120-3AA, featuring dimensions of 6.4 mm × 3.5 mm and a resistance of 120 ± 0.1 Ω, as illustrated in Figure 2B.

3.2 Experimental system and scheme

The rock sample underwent a uniaxial impact compression test using the Split Hopkinson Pressure Bar (SHPB) test device with a rod diameter of 50 mm, located in the Impact Mechanics Laboratory of the University of Science and Technology of China. The incident and transmission bars of the experimental apparatus are both 100 cm in

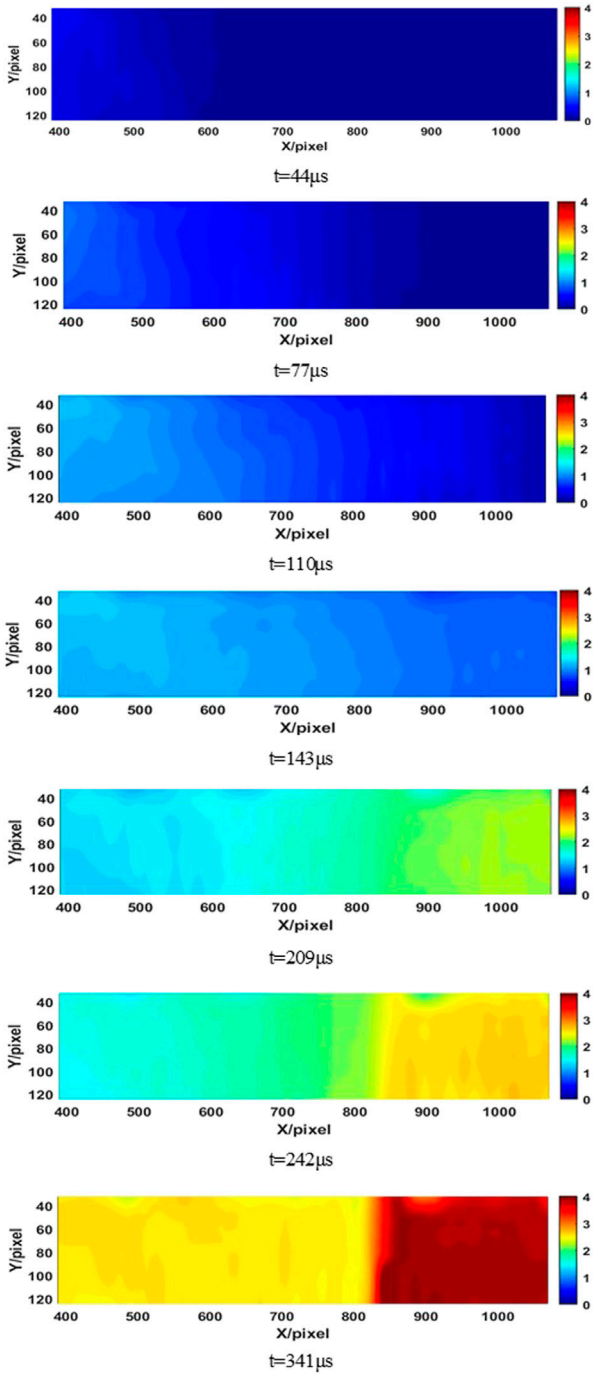

FIGURE 6
Axial displacement field.

length and are made of steel. The impact speed was set at 8.08 m/s, resulting in a strain rate of 98 s^{-1}. The sample experienced complete damage during the test. The entire dynamic impact process was captured using a high-speed camera known as the Thousand-eye Wolf X213. The frame rate of the camera was configured at 50,000 fps, capturing an image every 11 μs. The experimental system, as shown in Figure 3. To ensure uniform loading and prevent damage to the ends of the rock sample caused by uneven force, a steel plate was inserted between the rock sample and the incident and transmission rods. This steel plate

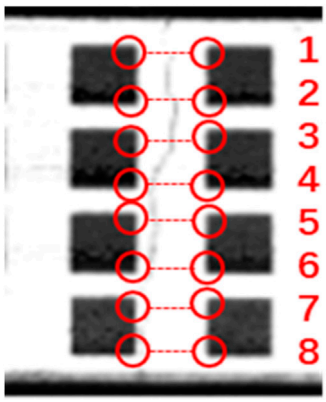

FIGURE 7
Schematic diagram of crack width calculation.

compensates for the difference in cross-sectional area between the rock sample and the rods. Importantly, the area of the steel plate exceeds that of the rock sample. To minimize interface friction, petroleum jelly was evenly applied to both sides of the steel plate, ensuring optimal contact between the rock sample, steel plate, and rods.

4 Analysis of experimental results

4.1 Specimen crack picture results

Throughout the experiment, a high-speed camera captured images of the sample every 11 μs. The experimental images selected depict several key times when the crack width changes, as illustrated in Figure 4. Furthermore, Figure 5 provides zoomed-ins of the crack localization zone.

Figure 4 illustrates that no significant changes occurred on the sample's surface between 77 and 143 μs. During this period, the internal micro-cracks of the sample were extruded and opened, resulting in small macroscopic cracks on the surface, a process imperceptible to the naked eye. From 143 to 231 μs, with the action of stress waves, the micro-cracks inside the sample gradually extend and reach the elastic limit. As depicted in Figure 5A, a micro-crack becomes visible to the naked eye when it reaches the surface of the specimen. At this stage, the crack expansion is minimal, and the sample's strength does not reach the limit value. Subsequently, from 242 to 341 μs, as shown in Figures 5B–J, the crack accelerated due to the repeated reflection of stress waves and the impact of the incident and transmission rods, leading to the imminent penetrate of the internal crack of the sample. Ultimately, when the stress value of the sample reached the compressive strength limit, the crack spread throughout the entire sample, resulting in its destruction.

4.2 Surface displacement field

The axial displacement field of the crack region was calculated by the corner correlation method, as shown in Figure 6.

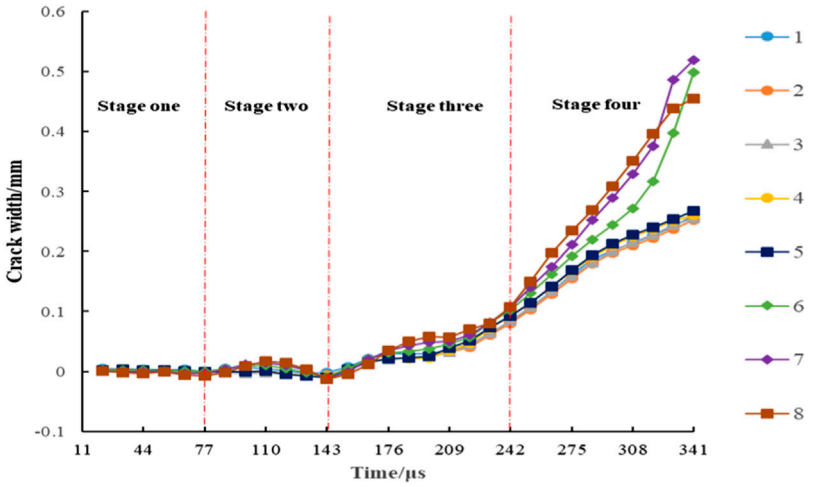

FIGURE 8
Crack width time curve.

When the crack initiates and starts to propagate, the axial displacement exhibits a consistently positive trend, indicating a continuous compression process within the sample. Figure 6 clearly illustrates the development of displacement from the incident end towards the transmitted end, with the displacement field continuously evolving. Eventually, a concentration phenomenon occurs at the crack site, as depicted in Figure 6. At 77 μs, the displacement on both sides of the initiation point begins to increase, reaching approximately 0.017 mm by 110 μs. Starting from 143 μs, the crack progressively expands and extends, leading to a gradual increase in displacement at the crack site. By 242 μs, the displacement on both sides of the crack reaches roughly 0.1 mm. At 341 μs, the displacement field becomes concentrated within the crack region, resulting in rapid crack width expansion and a displacement value of approximately 0.51 mm on both sides.

4.3 Crack development process

Corner points on both sides of the region where the crack is located are taken, and the distance between each two-corner points is 5 mm. The numbers 1–8 represent eight cross sections. The displacement difference between the left and right corner points of each section is represented by the crack width. The crack width calculation diagram, as shown in Figure 7, and the crack width time curve, as shown in Figure 8.

Figure 8 presents the crack width time curve, while Figure 9 illustrates the evolution process of the axial strain field. Throughout the loading process, the crack width variation curve with time was delineated into four stages. The first stage is the loading stage, during which no cracks manifest on the sample's surface, and it undergoes elastic deformation, as depicted in Figure 8. The sample experiences compression, compacting tiny cracks within, yet without significant expansion, signifying the gradual input of external energy and internal stress readjustment, as shown in Figure 9. In the second stage, at 77 μs, external input energy accumulates within the sample in the form of elastic strain energy. All curves exhibit a slight increase, indicating the onset of internal micro-crack expansion, with a small crack emerging on the surface, imperceptible to the naked eye, as evident in Figure 8. At this time, it can be seen from the strain diagram that stress concentration has occurred at the failure site, and the elastic strain energy has begun to be used for crack expansion. The internal micro-crack deformation reaches the elastic limit value, followed by a drop to approximately 0 at 143 μs, signifying the accumulation of elastic strain energy once again due to stress wave reflection within the sample. As mentioned above, "the stress wave propagates in the sample once is about 60 μs," indicating that cracks have appeared in the sample during the first propagation of stress waves. Subsequently, in the third stage, post-143 μs, all curves exhibit a steady upward trend, indicating the reappearance and development of surface cracks during stress wave reflection. At this juncture, internal micro-cracks once again reach the elastic limit value, commencing expansion and extension. The strain diagram reflects the elastic strain energy stored inside the sample is released. Stress concentration at the failure site becomes pronounced, with a portion of the stored elastic strain energy utilized for crack propagation and extension, while the remainder contributes to radiation energy and frictional heat generation. Finally, in the fourth stage, at 242 μs, all curves demonstrate a marked increase, signifying the commencement of rapid expansion of micro-cracks within the sample, culminating in the formation of through cracks. At this stage, the complete release of elastic strain occurs, leading to a rapid increase in dissipation energy, ultimately contributing to the sample's fracture failure.

The axial strain field's evolutionary process demonstrates that the strain in the failure zone exhibits compressive strain before 77 μs, as depicted in Figure 9, reflecting the entire compression stage. From 77 to 143 μs, the failure zone strain transforms into tensile strain, with a concentrated appearance towards the failure zone. By 242 μs, a concentrated zone has formed, and with the crack's expansion, the strain color in the crack region deepens and expands, signifying the rapid macroscopic crack expansion. Stages 2 and 3 of Figure 8 are respectively magnified in Figure 10 and Figure 11.

The crack widths of section 1 and sections 6-8 exhibit significant increases from 77 μs onwards, while the crack

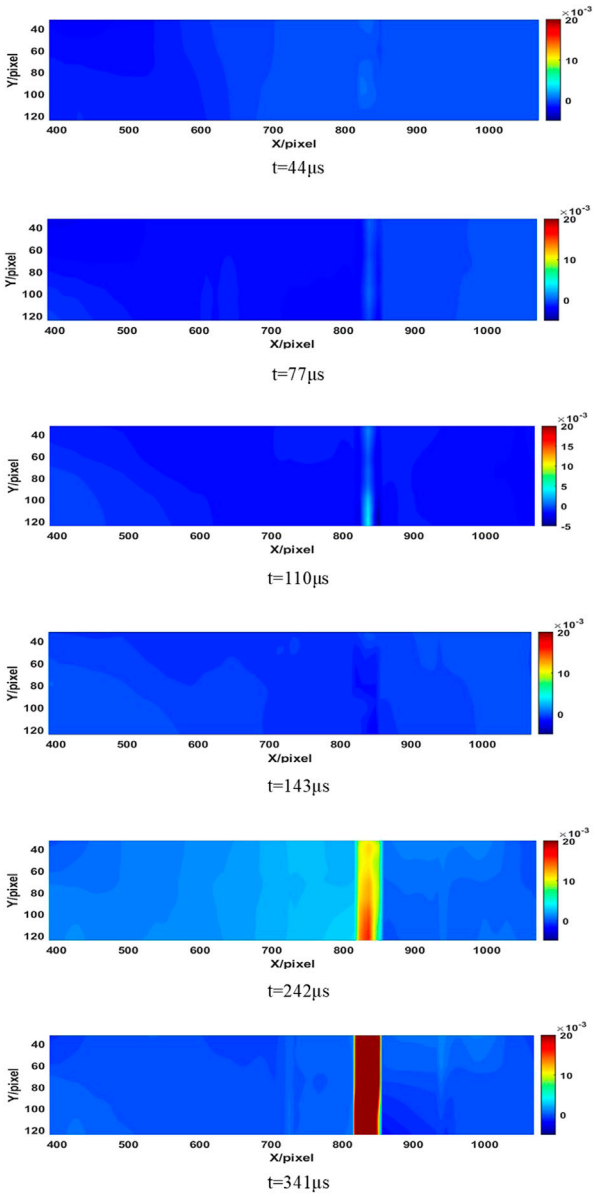

FIGURE 9
Axial strain field.

widths of other sections show minimal change. This suggests that the crack initiation point of the observation plane is at the upper and lower ends, and the crack progresses from these points towards the middle region, as illustrated in Figure 10. Following 110 μs, the crack widths of all sections decrease, attributed to the accumulation of strain energy resulting from stress wave reflection. In addition, at the initial stage, the specimen contains a small number of micro-cracks and has a large elastic modulus, leading to a gradual reduction in the original crack widths. By 143 μs, the crack width values of all sections are negative, representing the local deformation of the specimen under the compressive force of stress waves.

As depicted in Figure 11, between 143 and 154 μs, the crack widths of sections 1–8 are observed to increase, suggesting the extension of the crack to the entire observation area during this period. The distance of section 1–8 is measured at 35 mm. Consequently, the calculated average crack propagation velocity is approximately 3,182 m/s. The crack width exhibits a gradual decrease in the order of sections 8-1, indicating that more cracks penetrated from front to back at the lower end of the observation area during this stage.

The crack width growth rate presents a fluctuating property, which is a nonlinear change of the crack growth rate caused by the reflection and transmission of stress waves. It can be seen from Figure 12 that the crack width growth rate is negative at 110–143 μs, indicating that the crack width gradually decreases at this stage. The crack width growth rate of section 7 is the highest at 319 μs (10.04 m/s), and the crack width growth rate of section 6 is the highest at 330 μs (9.22 m/s), indicating that the damage of the two sections is more serious and the damage progress is the fastest at the above two times.

5 Numerical simulation of stress wave attenuation law

5.1 Calculation model

The rock density measures approximately 2.2 g/cm3, with a porosity ranging from 12% to 14%. The calculation model, as illustrated in Figure 13, is based on the ANSYS/LS-DYNA18.1 power display calculation method. A linear elastic constitutive model is employed for the bullet and the incident bar, with a density of 7.9 g/cm, an elastic modulus of 210GPa, and a Poisson's ratio of 0.3. The bullet is in contact with the incident rod, and the incident rod is in contact with the specimen. The bullet speed is 8.08 m/s, with the specimen section size measuring 5 cm × 5 cm and the unit surface size at 0.5 cm × 0.5 cm, as depicted in Figure 13.

5.2 Material parameter

This paper adopts the RHT constitutive model (Riedel-Hiermaier-Thoma), a mechanical model extensively utilized to characterize the dynamic response of rock and concrete materials under high strain rate and substantial deformation conditions, such as explosion impact and projectile penetration. The model incorporates the failure surface equation, elastic limit surface equation, and residual stress surface equation to define the failure surface. While the parameter determination of the model is more intricate, it offers better simulation adaptability. Consequently, it has found widespread application in numerical simulation, with relevant material parameters detailed in Table 1.

5.3 Reliability verification of numerical simulation results

The measured value and calculated value of the strain time history curve at the same position on the rock specimen at the impact velocity of 8.08 m/s are compared. The strain time

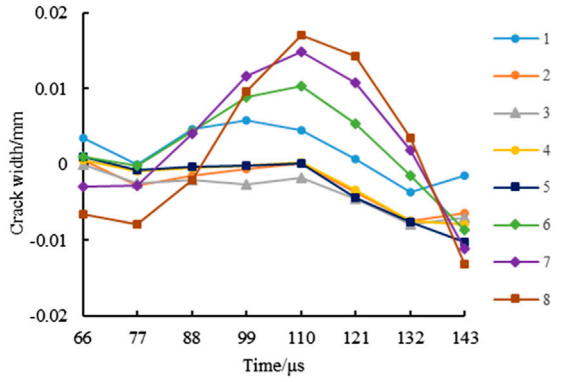

FIGURE 10
66–143 μs crack width time curve (Stage 2).

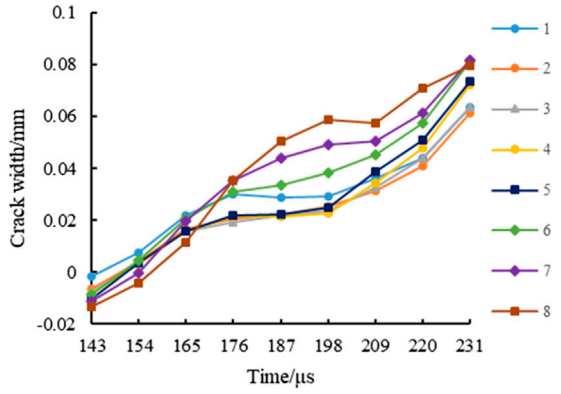

FIGURE 11
143–231 μs crack width time curve (Stage 3).

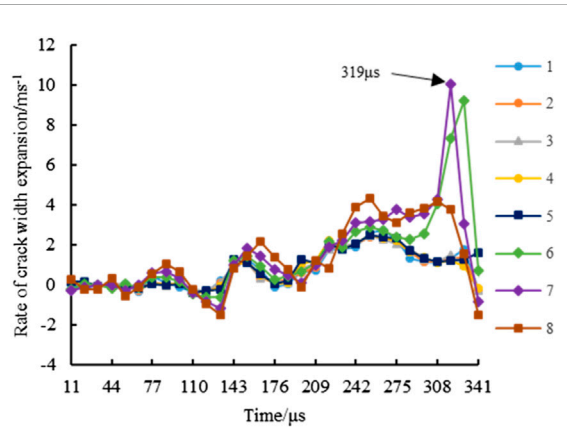

FIGURE 12
Time curve of crack width growth rate.

history curve is analyzed at the measuring points 5, 15, and 30 mm away from the impact end, as depicted in Figure 14. The

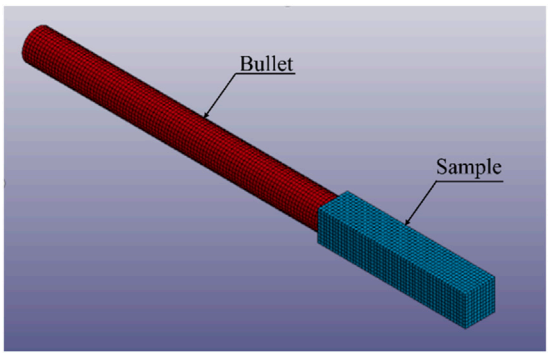

FIGURE 13
Calculation model.

numerical simulation results exhibit a strong agreement with the measured results in terms of stress wave peak value and pulse width, indicating the reliability of the numerical simulation outcomes. This also underscores the capability of the RHT constitutive model of rock and the selected material parameters to effectively characterize the pertinent properties of the rock materials used in the experiment. Consequently, this model and set of parameters can be confidently employed for further numerical simulations involving this type of rock.

5.4 Numerical simulation of one-dimensional stress wave propagation in rocks

To minimize the superposition of trans-reflective waves, we modified the experimental conditions by increasing the length of the specimen to 100 cm. We then selected points every 10 cm along a straight line beginning 1.5 cm away from the impact end face, as illustrated in Figure 15. All other experimental parameters remained unchanged.

5.4.1 Stress diagram

When the end of a rectangular section rod is subjected to left-lateral impact load, the peak stress in the rod presents an obvious decreasing trend with the increase of the distance from the rod end, as shown in Figure 16.

5.4.2 Typical position stress time history curve of *Z*-axis

The stress time-history curve at a typical position of the *Y*-axis, as shown in Figure 17. Under the impact load, the stress wave closer to the rod end presents a strong stress wave, and its steepness is larger, indicating that the duration of the rising edge is less and the pulse width is smaller. Due to the visco-plastic effect of the rock material, the steepness of the stress wave from the far end of the bar is small, which indicates that the rising duration is longer and the pulse width is increased.

TABLE 1 RHT Material parameter (Units: cm-g-μs).

Density *RO*	2.67	Failure surface parameter *N*	0.56
Shear modulus *SHEAR*	0.21	Failure surface parameter *A*	1.60
Compressive strength *FC*	0.0015	Against shear strength *FS**	0.38
Parameters of the equation of state B_0	1.68	Opposing tensile strength *FT**	0.10
Parameters of the equation of state B_1	1.68	Rhodes Angle correlation coefficient *B*	0.05
Parameters of the equation of state T_1	0.471	Tension meridian ratio Q_0	0.64
Reference compressive strain rate *EOC*	3.0e-11	Compressive strain rate at fracture *EC*	3.0e19
Reference tensile strain rate *EOT*	3.0e-12	Tensile strain rate at break *ET*	3.0e19
Tensile strain rate index *BETAT*	0.012	Compression yield surface parameters *GC**	0.4
Minimum damaged residual strain *EPM*	0.012	Tensile yield surface parameters *GT**	0.7
Damage parameter D_1	0.042	Shear modulus reduction factor *XI*	0.48
Damage parameter D_2	1.0	Hugoniot polynomial coefficients A_1	0.471
Residual surface parameter *AF*	1.6	Hugoniot polynomial coefficients A_2	0.7913
Residual surface parameter *NF*	0.6	Hugoniot polynomial coefficients A_3	0.4836
Extrusion pressure *PEL*	0.0005	Porosity index *NP*	4.0
Compaction pressure *PCO*	0.06	Initial voidage *ALPHA*	1.01
Gruneisen gamma	0.00	Compressive strain rate index *BETAC*	0.0085

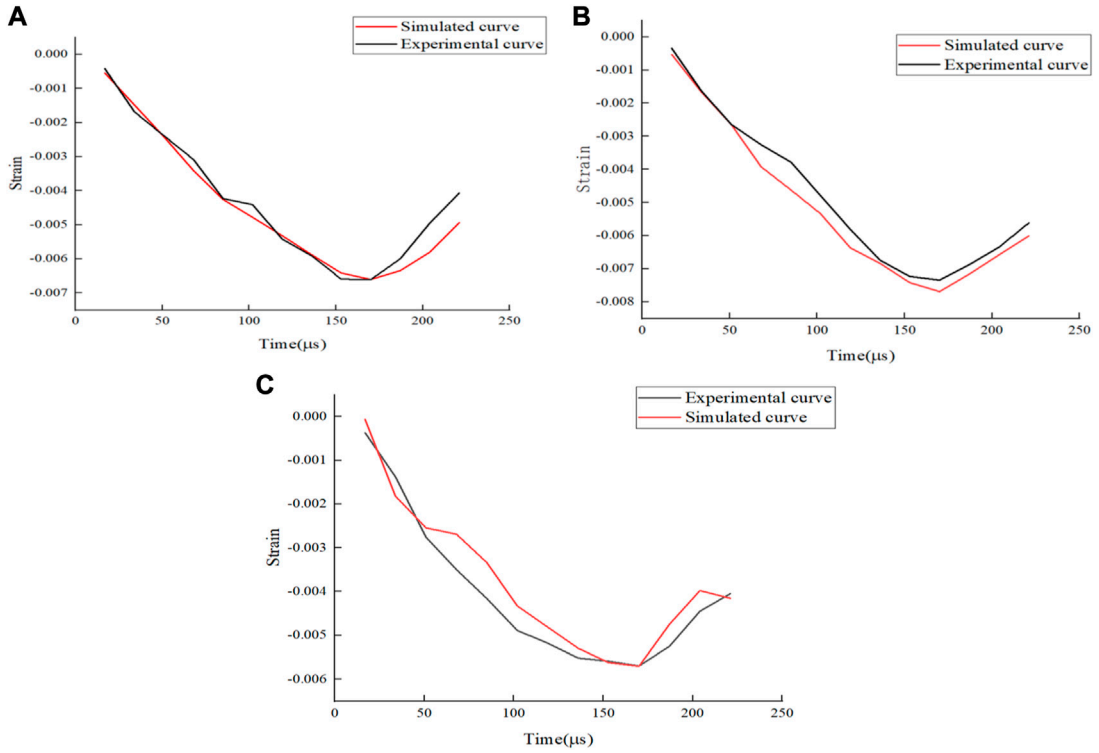

FIGURE 14
Comparison of experimental waveforms and numerical simulation waveforms at different positions. **(A)** d = 5 mm **(B)** d = 15 mm **(C)** d = 30 mm.

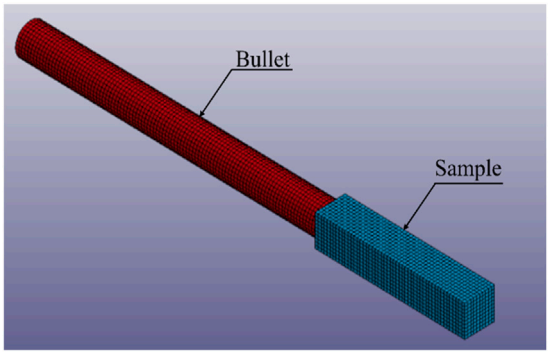

FIGURE 15
Sketch of numerical model.

5.4.3 Stress wave attenuation law

Based on the experimental data, it is found that the attenuation law of exponential form is satisfied by the basic equation and characteristic relation of one-dimensional strain bar and numerical simulation analysis. The peak stress in the rectangular cross-section bar shows an obvious attenuation trend during the propagation from the near to the far end of the load, which obviously satisfies the attenuation law in exponential form, as shown in Figure 17. Try to fit the peak stress at typical moments at different positions in the form of a function, as shown in Table 2. The fitting curve of stress wave attenuation law, as shown in Figure 18. According to the theory of least square method, the fitting curve is reasonable and meets the accuracy requirements.

6 Conclusion

To investigate the dynamic evolution characteristics of rock surface deformation under impact loading, dynamic failure tests were conducted on sandstone. The image was obtained through calculations using the self-developed corner correlation method. Additionally, a numerical simulation of a similar model was

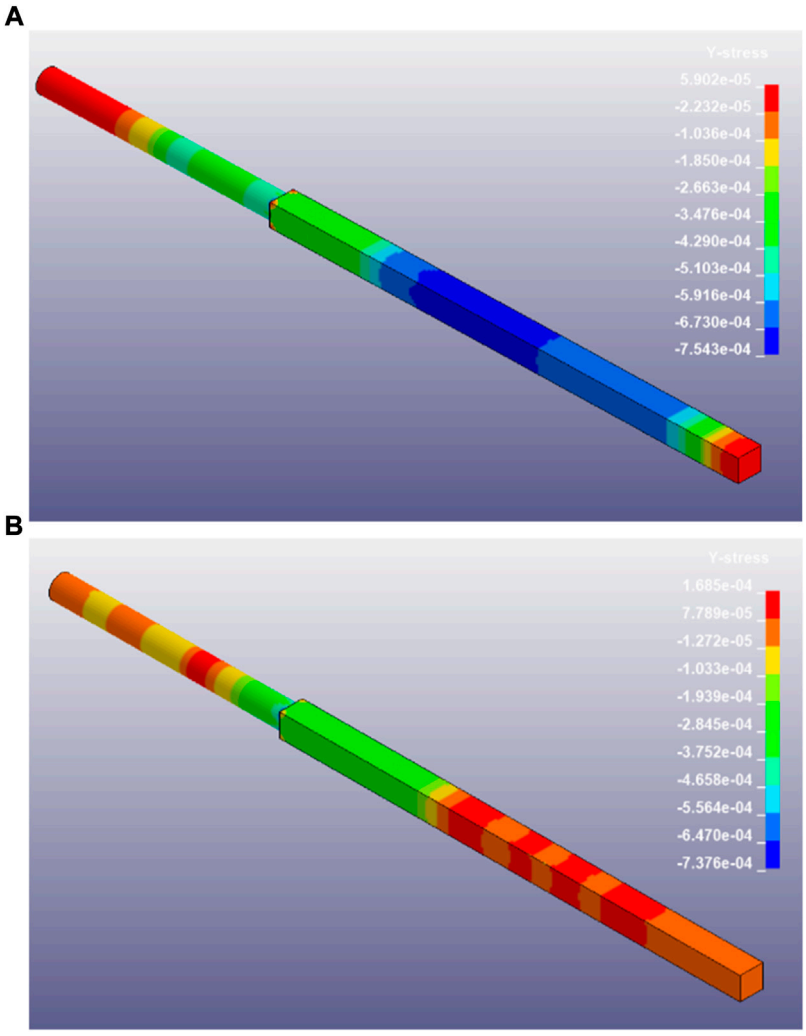

FIGURE 16
Typical temporal stress diagram. **(A)** T = 150 μs **(B)** T = 200 μs.

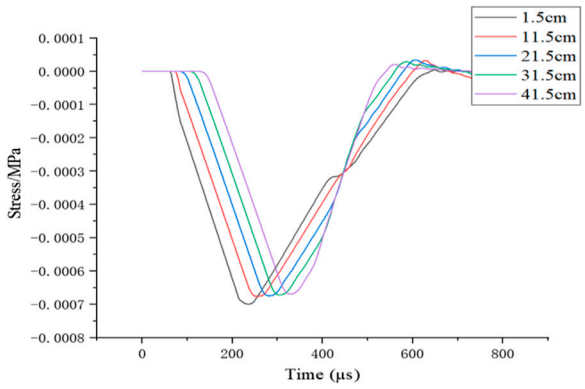

FIGURE 17
Y-axis typical time stress time history curve.

TABLE 2 Fitting parameter (Units: SI).

a	*b*	*c*
66.77996 ± 0.34959	−8898.7953 ± 24796	0.96629 ± 0.01187

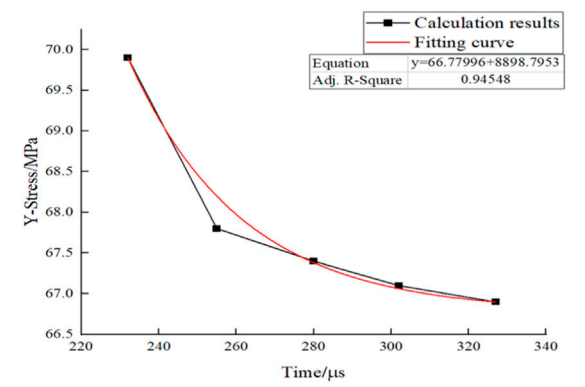

FIGURE 18
Attenuation law of stress wave.

conducted to investigate the attenuation law of stress waves in sandstone under impact loading, leading to the following conclusions:

1) The adjustment law governing the elastic strain energy during the process of crack propagation can be determined using the corner correlation method. Initially, during the loading stage, the presence of a minute crack within the sample results in compaction. This signifies the gradual input of external energy and the subsequent re-adjustment of internal stress within the sample. The second stage involves the accumulation of elastic strain energy within the sample. At this point, a small crack emerges on the surface of the sample, followed by a renewed accumulation of elastic strain energy within the sample due to the reflection of stress waves. In the third stage, the crack begins to expand and extend. During this stage, a portion of the energy is consumed by the expansion and extension of the crack, while the remaining energy is utilized for other forms of energy consumption. The fourth stage is characterized by the rapid expansion of micro-cracks within the sample, eventually leading to the gradual formation of through cracks. In this stage, the elastic strain is fully released, primarily contributing to the fracture failure of the sample.
2) The crack system is monitored by the corner correlation method, and the crack width, crack starting point, crack extension and contraction trajectory, extension and contraction speed, width expansion rate and longitudinal penetration of the crack are analyzed at any time and any position.
3) The law of stress wave evolution is obviously affected by the constitutive model of the material. It is reasonable to adopt the classical HJC constitutive in this paper, and a more reasonable equivalent constitutive of sandstone needs to be studied later. Visco-plastic materials have obvious dispersion and attenuation of stress waves, which is the root cause of exponential attenuation of stress peak value in rock materials.

Data availability statement

The original contributions presented in the study are included in the article/supplementary material, further inquiries can be directed to the corresponding author.

Author contributions

XZ: Writing–original draft, Formal Analysis, Methodology. ZY: Writing–review and editing. HM: Writing–review and editing. WL: Writing–original draft. XW: Writing–review and editing. CL: Software, Writing–review and editing.

Funding

The author(s) declare financial support was received for the research, authorship, and/or publication of this article. This research was funded by National Natural Science Foundation of China (Grant no. 11732009, 11890683).

Acknowledgments

The authors thank the reviewers for their insightful comments.

Conflict of interest

The authors declare that the research was conducted in the absence of any commercial or financial relationships that could be construed as a potential conflict of interest.

Publisher's note

All claims expressed in this article are solely those of the authors and do not necessarily represent those of their affiliated organizations, or those of the publisher, the editors and the reviewers. Any product that may be evaluated in this article, or claim that may be made by its manufacturer, is not guaranteed or endorsed by the publisher.

References

Alneasan, M., Behnia, M., and Bagherpour, R. (2020). Applicability of the classical fracture mechanics criteria to predict the crack propagation path in rock under compression. *Eur. J. Environ. Civ. Eng.* 24 (11), 1761–1784. doi:10.1080/19648189.2018.1485597

Bruck, H., Mcneill, S., Sutton, M., and Peters, W. (1989). Digital image correlation using Newton-raphson method of partial differential correction. *Exp. Mech.* 29 (3), 261–267. doi:10.1007/BF02321405

Chau, V., Rougier, E., Lei, Z., Knight, E. E., Gao, K., Hunter, A., et al. (2020). Numerical analysis of flyer plate experiments in granite via the combined finite–discrete element method. *Comput. Part. Mech.* 7, 1005–1016. doi:10.1007/s40571-019-00300-w

Chen, S. Y., Liu, Q. Y., Liu, P. X., and Zhuo, Y. Q. (2023). Prospect and research progress of detecting dynamic change in crustal stress by bedrock temperature. *Geohazard Mech.* 1 (2), 119–127. doi:10.1016/j.ghm.2023.04.002

Chu, Y. Y., Ren, G. F., Zhang, C. R., Zheng, Y., and Li, D. (2023). Acoustic emission parameters and energy dissipation law of cyclic load and unload damage of dihydrate gypsum under different loading rate. *Geohazard Mech.* 1 (2), 185–193. doi:10.1016/j.ghm.2023.06.001

Dai, L., Pan, Y., Li, Z., Wang, A., Xiao, Y., Liu, F., et al. (2021). Quantitative mechanism of roadway rock bursts in deep extra-thick coal seams: theory and case histories. *Tunn. Undergr. Space Technol.* 111, 103861–107798. doi:10.1016/j.tust.2021.103861

Feng, X., Zhang, Q., and Ali, M. (2019). Explosion-induced stress wave propagation in interacting fault system: numerical modeling and implications for chaoyang coal mine. *Shock Vib.* 1, 1–12. doi:10.1155/2019/5856080

Gong, F., Wang, Y., and Wang, Q. (2023). Peak-strength strain energy storage index for evaluating coal burst liability based on the linear energy storage law. *Geohazard Mech.* 1 (2), 153–161. doi:10.1016/j.ghm.2023.03.003

Guo, W., Chen, L., Yin, L., Zhang, L., Lu, D., Kong, B., et al. (2023). Experimental study on the influence of loading rate on the directional propagation law of rock mode-I cracks. *Theor. Appl. Fract. Mech.* 125, 103873. doi:10.1016/j.tafmec.2023.103873

Guo, Y. (2022). Failure mechanism and fracture development law of heterogeneous brittle rock. *Saf. Coal Mines* 53 (05), 67–72+80. doi:10.13347/j.cnki.mkaq.2022.05.011

Harris, C., and Stephens, M. (1988). *A combined corner and edge detector*. Manchester, UK: Proceedings of the 4th Alvey Vision Conference, University of Sheffield Printing Unit, 147–151.

Hu, Y., Yang, S., Zhong, Z., Wang, X., Zhang, T., and Zhou, R. (2022). Experimental study on unsaturated flow properties through a single limestone fracture under confining pressure. *J. Rock Mech. Eng.* 41 (S1), 2846–2856. doi:10.13722/j.cnki.jrme.2021.0823

Jin, Z., Peng, Y., Wen-Bo, L., Ming, C., and Gao-Hui, W. (2021). Propagation mechanism of fracture zones in single-hole rock mass under high *in-situ* stress. *IOP Conf. Ser. Earth Environ. Sci.* 861 (7), 072089. doi:10.1088/1755-1315/861/7/072089

Knight, E., Rougier, E., Lei, Z., Euser, B., Chau, V., Boyce, S. H., et al. (2020). HOSS: an implementation of the combined finite-discrete element method. *Comput. Part. Mech.* 7, 765–787. doi:10.1007/s40571-020-00349-y

Li, D., Han, Z., Zhu, Q., Zhang, Y., and Ranjith, P. (2019). Stress wave propagation and dynamic behavior of red sandstone with single bonded planar joint at various angles. *Int. J. Rock Mech. Min. Sci.* 117, 162–170. doi:10.1016/j.ijrmms.2019.03.011

Li, X., Bai, Y., Chen, X., Zhao, X., and Lv, M. (2021b). Experimental and numerical study on crack propagation and coalescence in rock-like materials under compression. *J. Strain Analysis Eng. Des.* 56 (8), 548–562. doi:10.1177/0309324720986913

Li, X., Zhu, Z., Wang, M., Wan, D., Zhou, L., and Liu, R. (2021a). Numerical study on the behavior of blasting in deep rock masses. *Tunn. Undergr. Space Technol.* 113, 103968. doi:10.1016/j.tust.2021.103968

Liu, J., Li, Z., Li, T., and Li, Z. (2020). Visualization study on seepage law considering the effects of multiple factors on sandstone fissures. *China Civ. Eng. J.* 53 (10), 106–119. doi:10.15951/j.tmgcxb.2020.10.011

Liu, X., Zhu, W., Liu, Y., and Guan, K. (2022). Reconstruction of rough rock joints: 2D profiles and 3D surfaces. *Int. J. Rock Mech. Min. Sci.* 156, 105113. doi:10.1016/j.ijrmms.2022.105113

Liu, Y., Pan, K., and Zhou, X. (2018). Study on impact failure properties of post-peak cracked standstone. *J. West Anhui Univ.* 34 (02), 123–127.

Munjiza, A., Rougier, E., Lei, Z., and Knight, E. E. (2020). FSIS: a novel fluid–solid interaction solver for fracturing and fragmenting solids. *Comput. Part. Mech.* 7, 789–805. doi:10.1007/s40571-020-00314-9

Oparin, V. N. (2022). Pendulum waves and basics of geomechanical thermodynamics. *Geohazard Mech.* 1 (1), 38–52. doi:10.1016/j.ghm.2022.12.001

Pan, B. (2007). *Digital image correlation method and its application in experimental mechanics*. Doctoral Dissertation. Tsinghua: Tsinghua University.

Pan, H. Y., Ge, D., Zhang, T., Dong, X., Zhang, L., and Zhou, A. (2018). Influence of strain rate on the rock fracture propagation law. *J. China Coal Soc.* 43 (03), 675–683. doi:10.13225/j.cnki.jccs.2017.1145

Pan, Y., and Wang, A. (2022). Disturbance response instability theory of rock bursts in coal mines and its application. *Geohazard Mech.* 1 (1), 1–17. doi:10.1016/j.ghm.2022.12.002

Rougier, E., Knight, S., Broome, A., Sussman, A. M., and Munjiza, A. (2014). Validation of a three-dimensional finite-discrete element method using experimental results of the split Hopkinson pressure bar test. *Int. J. Rock Mech. Min. Sci.* 70, 101–108. doi:10.1016/j.ijrmms.2014.03.011

Sikka, P., Asati, A., and Chandra, S. (2021). Real time FPGA implementation of a high speed and area optimized harris corner detection algorithm. *Microprocess. Microsystems* 80, 103514. doi:10.1016/j.micpro.2020.103514

Song, Y., He, A., Wang, Z., and Chen, H. (2015). Experiment study of the dynamic fractures of rock under impact loading. *Rock Soil Mech.* 36 (04), 965–970. doi:10.16285/j.rsm.2015.04.008

Tian, Y. (2021). Evolution characteristics of crack propagation under different confining pressure unloading rates. *Low. Temp. Archit. Technol.* 43 (10), 98–101. doi:10.13905/j.cnki.dwjz.2021.10.023

Wang, H., Xu, J., Liu, S., and Fang, X. (2016). Research on the dynamic strength criteria of rock with a single fissure based on numerical simulation. *Metal. Mine* (02), 7–12. doi:10.3969/j.issn.1001-1250.2016.02.002

Wei, L., Zhu, Z., Meng, Q., Jing, H., Su, H., and He, M. (2019). Dynamic characteristics of marble damaged by cyclic loading. *Explos. Shock Waves* 39 (08), 63–73. doi:10.11883/bzycj-2019-0164

Wu, X., Zheng, H., and Jiang, Y. (2022). Study on the evolution law of rock joint shear stiffness during shearing process through loading-unloading tests. *Tunn. Undergr. Space Technol.* 127, 104584. doi:10.1016/j.tust.2022.104584

Xi, X., Wu, X., Guo, Q., and Cai, M. (2020). Experimental investigation and numerical simulation on the crack initiation and propagation of rock with pre-existing cracks. *IEEE Access* 2020 (99), 129636–129644. doi:10.1109/ACCESS.2020.3009230

Xing, H., Zhang, Q., Ruan, D., Dehkhoda, S., Lu, G., and Zhao, J. (2018). Full-field measurement and fracture characterisations of rocks under dynamic loads using high-speed three-dimensional digital image correlation. *Int. J. Impact Eng.* 113, 61–72. doi:10.1016/j.ijimpeng.2017.11.011

Zhang, B., Liu, G., Li, Y., and Lin, Z. (2023). Experimental study on the seepage mutation of natural karst collapse pillar (KCP) fillings over mass outflow. *Environ. Sci. Pollut. Res.* 30, 110995–111007. doi:10.1007/s11356-023-30230-3

Zhang, Q., and Zhao, J. (2013). Determination of mechanical properties and full-field strain measurements of rock material under dynamic loads. *Int. J. Rock Mech. Min. Sci.* 60, 423–439. doi:10.1016/j.ijrmms.2013.01.005

Zhang, Y., Ai, R., and Tan, Z. (2021b). Study on crack propagation law of limestone under impact load. *Min. Res. Dev.* 41 (10), 79–83. doi:10.13827/j.cnki.kyyk.2021.10.014

Zhang, Y., Li, J., Yan, Y., and Li, H. (2021c). Experimental study on dynamic damage characteristics of roughness joint surface based on SHPB. *Rock Soil Mech.* 42 (02), 491–500. doi:10.16285/j.rsm.2020.0715

Zhang, Y. B., Yu, T., Zhang, T., Liu, S., and Zhou, J. (2021a). Experimental study of the permeability evolution of fractured mudstone under complex stress paths. *J. Univ. Sci. Technol.* 43 (07), 903–914. doi:10.13374/j.issn2095-9389.2020.05.27.005

Zhao, C., Tian, J., Song, T., Zhao, C., and Bao, C. (2015). Study on crack propagation and damage evolution characteristics of rock under uniaxial compression based on global strain field analysis. *J. Rock Mech. Eng.* 34 (04), 763–769. doi:10.13722/j.cnki.jrme.2015.04.013

Zhao, C., Zhou, Y., and Zhao, C. (2018a). Cracking processes and coalescence modes in rock-like specimens with two parallel pre-existing crack. *Rock Mech. Rock Eng.* 51 (11), 377–383 393. doi:10.1007/s00603-018-1525-y

Zhao, C., Zhou, Y., Zhao, C., and Bao, C. (2018b). Cracking processes and coalescence modes in rock-like specimens with two parallel pre-existing cracks. *Rock Mech. Rock Eng.* 51 (11), 3377–3383 393. doi:10.1007/s00603-018-1525-y

Zhou, X., Li, W., Liu, Y., Miao, H., Zhang, R., Xu, J., et al. (2022b). Establishment of the corner correlation method and its application in rock dynamic test. *KSCE J. Civ. Eng.* 26 (9), 4168–4177. doi:10.1007/s12205-022-0117-2

Zhou, X., Long, Y., and Ye, W. (2022a). Experimental investigations on the cracking and mechanical responses of PMMA samples with two 3D embedded elliptic flaws under uniaxial compression. *Geohazard Mech.* 1 (1), 77–85. doi:10.1016/j.ghm.2022.11.004

frontiers | Frontiers in Earth Science

TYPE Original Research
PUBLISHED 29 December 2023
DOI 10.3389/feart.2023.1289251

Check for updates

OPEN ACCESS

EDITED BY
Pengjiao Jia,
Soochow University, China

REVIEWED BY
Jianjun Ma,
Sun Yat-Sen University, China
Zude Ding,
Kunming University of Science and Technology, China
Haibing Cai,
Anhui University of Science and Technology, China

*CORRESPONDENCE
Chenghua Shi,
csusch@163.com

RECEIVED 05 September 2023
ACCEPTED 21 November 2023
PUBLISHED 29 December 2023

CITATION
Zheng K, Shi C, Zhao Q, Lei M, Jia C and Lou Y (2023), Failure mechanisms and dynamic process control measures of deep buried tunnels in tectonic fracture zones under high *in-situ* stresses—a case study in Southwestern China.
Front. Earth Sci. 11:1289251.
doi: 10.3389/feart.2023.1289251

COPYRIGHT
© 2023 Zheng, Shi, Zhao, Lei, Jia and Lou. This is an open-access article distributed under the terms of the Creative Commons Attribution License (CC BY). The use, distribution or reproduction in other forums is permitted, provided the original author(s) and the copyright owner(s) are credited and that the original publication in this journal is cited, in accordance with accepted academic practice. No use, distribution or reproduction is permitted which does not comply with these terms.

Failure mechanisms and dynamic process control measures of deep buried tunnels in tectonic fracture zones under high *in-situ* stresses—a case study in Southwestern China

Keyue Zheng[1,2,3], Chenghua Shi[1,2,3]*, Qianjin Zhao[3,4], Mingfeng Lei[3], Chaojun Jia[3] and Yili Lou[3]

[1]National Engineering Research Center of High-Speed Railway Construction Technology, Changsha, China, [2]China Railway Group Limited, Beijing, China, [3]School of Civil Engineering, Central South University, Changsha, China, [4]China Railway Kunming Group Co., Ltd., Kunming, China

Squeezing deformation in tectonic fracture zones under high *in-situ* stresses has created great difficulties to deep tunnel construction in Southwestern China. This study reports an investigation on large deformation and failure mechanisms of the Wanhe tunnel on the China-Laos Railway through several field tests including the *in-situ* stress, loosened zone, deformation monitoring, and internal stresses of steel arches. The dynamic process control method is proposed following the combination principle of stress releasing and support resistance. Further, the dynamic process control measures including the advanced and primary supports, the deep-shallow coupled delayed grouting method, and the double steel arches method were applied on site to resist the deformation development. The results of this study indicate that the rapid growth of the tunnel deformation in the early stage was caused by the squeezing effect, and later the loosening effect led to another growing trend of the vault settlement. The dynamic process control method allows to release the deformation of the surrounding rock in the rapid growth stage. Then, it requires to control the deformation within the reserved range by reinforcing the surrounding rock and increasing the stiffness of supports in the later stage. From the feedback of monitoring results, large deformation of Wanhe tunnel was well released and effectively controlled within the deformation allowance. Thus these countermeasures based on the dynamic process control method can guarantee the construction safety of deep buried tunnels in tectonic fracture zones under high *in-situ* stresses.

KEYWORDS

high *in-situ* stresses, tectonic fracture zone, squeezing effect, loosening effect, dynamic process control measures

1 Introduction

For soft rock with an uniaxial compressive strength below 25 MPa (Ulusay, 2015), squeezing will cause large deformation under high geostress, which has been a difficult challenge in the construction of deep soft-rock tunnels for a long time. Typical squeezing tunnels in the world mainly include the Enasan highway tunnel in Japan (Kimura et al.,

1987), the Tauern railway tunnel (Ayaydin and Leitner, 2009; Franz and Harald, 2009) and the Arlberg tunnel (John, 1980) in Austria, the Gotthard railway tunnel (Mezger et al., 2013) and the Simplon tunnel (Milnes, 1973) in Switzerland, the Lyon-Turin Base Tunnel (Bonini and Barla, 2012) connecting Italy and France, Y-Basque high-speed railway tunnels in northern Spain (Iasiello et al., 2021), etc. In China, most of the squeezing tunnels appear in the west, such as the Jiazhuqing tunnel (Zhang, 1997) on Nanning-Kunming Railway, the Wushaoling tunnel (Yang et al., 2006) on Lanzhou-Xinjiang Railway, the Guanjiao tunnel (Wan et al., 2014) on Qinghai-Tibet Railway, the Muzhailing tunnel (Zhang et al., 2010; Wu et al., 2015) on Lanzhou-Chongqing Railway, the Baozhen tunnel (Li et al., 2013) on Yichuan-Wanzhou Railway, etc. A large number of monitoring data from these projects showed that the squeezing deformation had the characteristics of large magnitude, large rate, and long duration, which led to the failure of the tunnel supports and even affected the operation stage.

Large squeezing deformation on site is difficult to control during tunnel construction. Generally, the controlling principles of large deformation include the stress releasing principle, the support resistance principle, and the combination principle of stress releasing and support resistance. The representative of stress releasing principle is the New Austrian tunneling method (NATM), which emphasizes the use of flexible support to release the rock deformation energy and make the most strength of rock mass itself so as to reduce the deformation load acting on the support structures (Jeong et al., 2014; Cao et al., 2018). Methods followed this principle mainly include increasing the reserved allowable deformation (Vrakas and Anagnostou, 2016; Guan et al., 2020; Zhang D. L. et al., 2022), driving the energy-absorbing rock bolts into the soft rock mass (VandeKraats and Watson, 1996; Li et al., 2014), arranging a compressible layer between rock and lining (Wang et al., 2012; Wu et al., 2018; Tian et al., 2021; Zhang Q. et al., 2022), using yielding supports such as steel arches with sliding connections (Cantieni and Anagnostou, 2009; Horyl et al., 2013; Rodríguez and Díaz-Aguado, 2013) or shotcrete lining with highly deformable elements (Radončić et al., 2009; Barla et al., 2011; Schubert et al., 2018; Tian et al., 2018). However, for soft rock tunnel under high *in situ* stress, using only the controlling principle of stress releasing will easily lead to the plastic yielding and failure of the surrounding rock (Tian et al., 2016; Tan et al., 2017; Cao et al., 2018). Conversely, the purpose of the support resistance principle is to restrain the squeezing deformation energy of the soft rock. Methods following this principle can be categorized as active control and passive control based on different supporting mechanisms (Wu et al., 2021). Active control refers to improving the bearing capacity of the surrounding rock, which can be implemented in two ways. One is arranging advanced supports such as small pipes and pipe roofs before tunnel excavation (Deng et al., 2022). The other is reinforcing the surrounding rock after excavation by grouting (Kang et al., 2021) or applying strengthened rock bolts (Wu et al., 2020; Sun et al., 2021). Passive control refers to strengthening the supporting structures to restrain rock deformation. Common methods following the passive format include thickening the shotcrete (Mezger et al., 2017), using heavy steel arches (Tan et al., 2022), reducing the arch spacing, supplementing additional layers of the initial lining (Chen et al., 2019), applying new types of supporting structures with high strength (Wang et al., 2017; Wang et al., 2018), etc. However, to resist the deformation load of the squeezing rock, common supports have limited bearing capacity. Many engineering cases following the resistance principle showed that heavy supports frequently failed to restrain large squeezing deformation and eventually needed a large amount of repairs during tunnel construction (Kimura et al., 1987; Ortlepp and Stacey, 1998; Aksoy et al., 2012). Using only the controlling principle of support resistance is considered uneconomical and impractical (Wu et al., 2021). Therefore, for soft-rock tunnels under high *in situ* stress, the control of the large squeezing deformation ought to be based on the combination principle of stress releasing and support resistance. This means that it is necessary to not only allow the rock mass deformation to exert its bearing capacity, but also to prevent the rock failure and control the deformation within the reserved range by reinforcing the surrounding rock or strengthening support structures. This can be defined as the principle of dynamic process control, which means that the development of squeezing deformation should be controlled in process. However, there are few tunneling cases following this principle in the existing research. Most squeezing tunnels were still finished through multiple removals of supports, re-profiling of tunnel sections and design changes, which greatly increased the engineering cost and delayed the construction period.

In recent years, as an important part of the Belt and Road Initiative, the Sichuan-Tibet Railway (Zhang C et al., 2022) and the Trans-Asian Railway (Rowedder, 2020) are under construction. There are more and more tunnelling projects in southwestern China. The tectonic movement of plates in the Southwest (especially the Yunnan-Guizhou Plateau) is complex, which causes strong tectonic stress accumulated in deep formation (Qiao et al., 2022; Wang et al., 2022). Joints and faults are formed when the rock formations are damaged by the squeezing of tectonic stresses (Zhang Q. et al., 2022; Lin et al., 2023; Ma et al., 2023). Deep rock masses in these geological structures are broken with developed fractures and poor integrity, which is called the tectonic fracture zone. Due to poor self-stabilization ability and high *in-situ* stresses field, severe squeezing deformation easily occurs during the tunnel construction. The China-Laos railway is an important part of the TAR (Trans-Asian Railway) plan, which connects Kunming in China and Vientiane in Laos. The Wanhe tunnel of the China-Laos railway from DK32+100 to DK32+725 passes through a tectonic fracture zone, which was the broken Yanshanian granite strata with well-developed fractures and in the shape of breccia. The maximum burial depth of the tunnel is more than 500 m. Serious deformation was encountered during construction. In this paper, the Wanhe railway tunnel was presented as a case study to discuss deformation characteristics and failure mechanisms of deep buried tunnels in tectonic fracture zones under high *in-situ* stresses. Further, this paper proposed the countermeasures of large deformation based on the dynamic control principle and process, which can provide a reference for similar tunnel construction in tectonic fracture zones under high *in-situ* stresses.

2 Project overview

2.1 Project background and engineering geology

The China-Laos railway connecting Kunming, China and Vientiane, Laos is an important part of the TAR (Trans-Asian

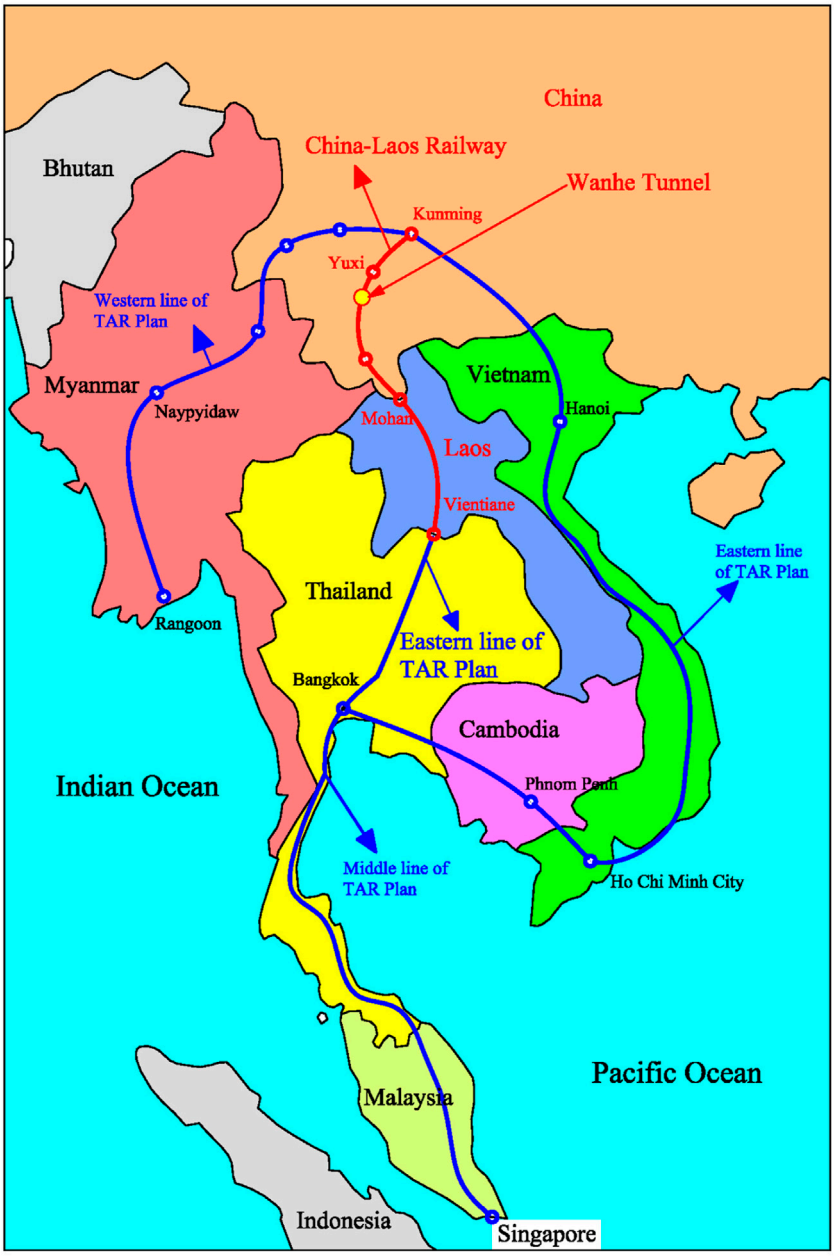

FIGURE 1
Locations of the China-Laos railway and the Wanhe tunnel.

Railway) plan, which is of great significance for China to implement the Belt and Road strategy and promote the development of the ASEAN Free Trade Area. The railway section in China starts from Kunming, Yunnan Province and ends at the Mohan on the China-Laos border, with a total length of 507 km. The Wanhe tunnel is located between the Eshan Station and Luoli Station, which is the second longest tunnel of the China-Laos railway with a length of 17.44 km. The starting and ending points of the tunnel are located at DK22+468 and DK39+909. Figure 1 shows the locations of the China-Laos railway and the Wanhe tunnel. The Wanhe tunnel is a double-track railway tunnel with a large section. The height and span of the tunnel are respectively 12.03 m and 12.96 m. The composite lining is used as the tunnel support system, which contains primary support, waterproofer, and secondary lining (shown in Figure 2). Figure 3 shows the geological conditions in the longitudinal sections of the Wanhe tunnel. The maximum buried depth of this tunnel is about 586 m. The Wanhe tunnel passes through two active fault zones, which are a reverse fault called Gongjipo and a normal faultnamed Lijiashan. The surrounding rock of the Wanhe tunnel is severely affected by the tectonic movement with developed faults and folds. The lithological characters of Wanhe tunnel consist of slate interbedded with sandstone, granite, sandstone interbedded with shale, mudstone interbedded with sandstone, and Quartz diorite. Laboratory experiments were conducted on core samples

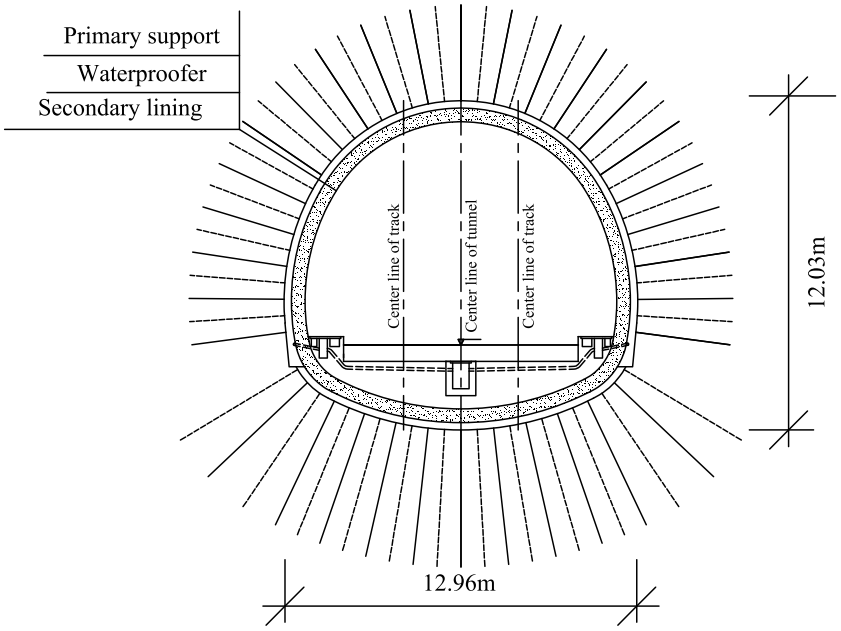

FIGURE 2
Cross section of the Wanhe tunnel.

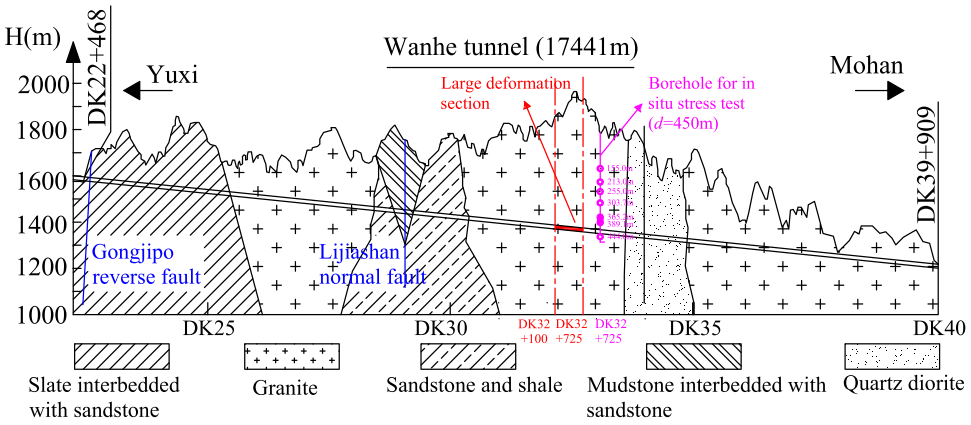

FIGURE 3
Geological conditions in the longitudinal sections of the Wanhe tunnel.

taken from core drilling. The mechanical properties of rock units, including density, uniaxial compressive strength, Young's modulus, and Poisson's ratio, are presented in Table 1.

2.2 Failure problems of large deformation

From July 2018 to March 2019, during the construction of the Wanhe tunnel from DK32+725 to DK32+100, large deformations frequently occurred at the vault and side wall. This section was excavated by the three-bench-step method and was supported with shotcrete, anchor bolts, steel arches, and lock-foot anchor pipes. According to the on-site monitoring of the railway section from DK32+475 to DK32+415, the maximum vault settlement reached 763.9 mm, and the maximum horizontal convergence reached 720.2 mm, which exceeded the deformation allowance and caused the cracking of shotcrete and the bending of steel arches. Failure problems of the primary supports on site are shown in Figure 4. The exposed stratum during the excavation of this heavily deformed section was the broken granite with well-developed joints, which is mostly in the shape of breccia as shown in Figure 5. Affected by complex tectonic movement, the originally hard granite in the deep (with the burial depth of nearly 500 m) was squeezed into broken rock mass with poor self-stabilization ability, which was easy to fail especially under high *in-situ* stresses during tunnel excavation.

TABLE 1 Physico-mechanical parameters of rock units.

Rock types	Density (kg/m^3)	Young's modulus	Poisson's ratio v	Uniaxial compressive strength
		E (GPa)		σ_c (MPa)
Slate	(2.20–2.50) × 10^3	3.60–7.30	0.23–0.32	3.20–8.35
Sandstone	(2.45–2.56) × 10^3	6.75–18.60	0.16–0.35	8.52–25.30
Shale	(2.38–2.45) × 10^3	5.20–15.30	0.18–0.39	2.10–5.50
Mudstone	(2.40–2.52) × 10^3	2.18–15.30	0.20–0.35	2.05–13.50
Granite	(2.60–2.80) × 10^3	0.50–6.35	0.36–0.48	1.80–8.00
Quartz diorite	(2.20–2.40) × 10^3	6.72–13.75	0.26–0.37	2.80–9.00

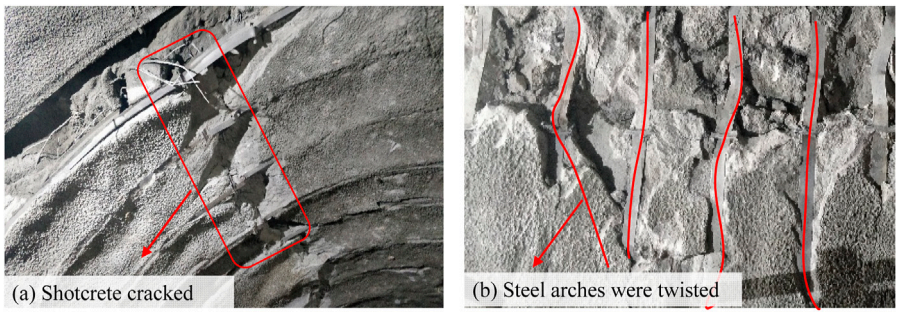

FIGURE 4
Typical diseases of large deformation. **(A)** Shotcrete cracked. **(B)** Steel arches were twisted.

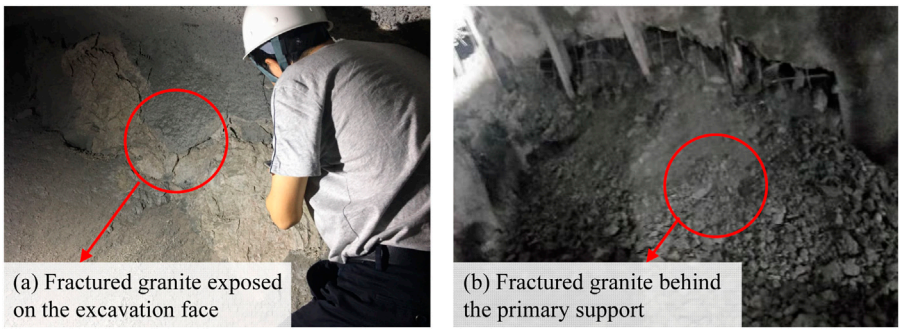

FIGURE 5
Rock mass of large deformation sections. **(A)** Fractured granite exposed on the excavation face. **(B)** Fractured granite behind the primary suppor.

3 Field investigations

3.1 Level of *in situ* stress

The level of *in situ* stress is an important factor causing large deformation of tunnels. To explore whether the failure of the Wanhe tunnel was induced by high geostress or not, *in situ* stress test using the hydraulic fracturing method was conducted before the tunnel construction. Figure 6 shows the test principle of the hydraulic fracturing method (International society for rock mechanics, 1987). σ_H represents the maximum horizontal principal stress around the borehole, and σ_h is the minimum horizontal principal stress. It can be deduced that the tangential stress (σ_θ) around the borehole in the direction of σ_H is $3\sigma_h$-σ_H. When the hydraulic pressure exceeds the sum of the tangential stress (σ_θ) and the rock tensile strength (R_t), the borehole wall will be fractured. Thereby, define the hydraulic pressure at this time as the initial fracturing pressure P_i with the formula as Eq. 1. Then, re-pressurize the borehole wall to make the fracture open again, and define the pressure at this time as the fracture reopening pressure P_r, which is equal to the tangential stress

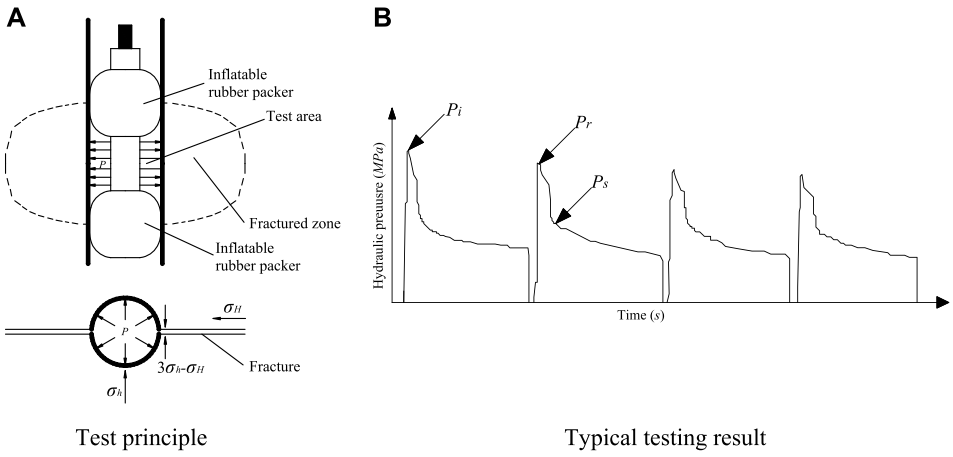

FIGURE 6
Test principle of the hydraulic fracturing method. **(A)** Test principle. **(B)** Typical testing result.

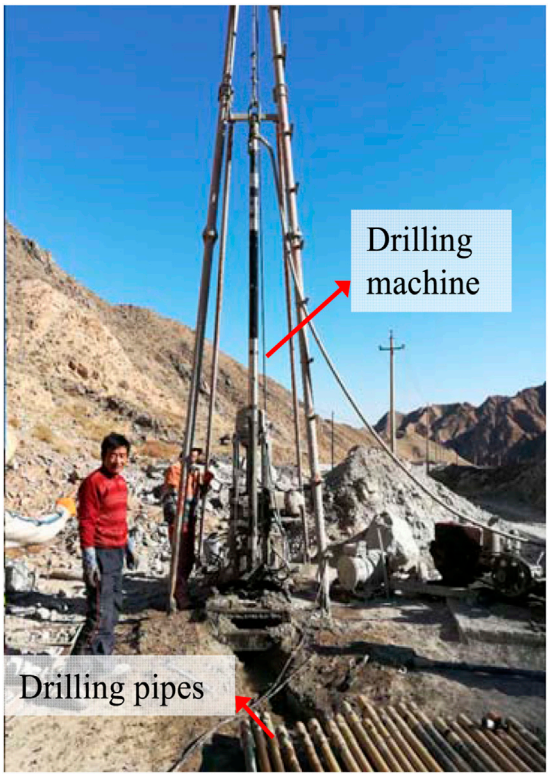

FIGURE 7
Borehole drilling on site.

σ_θ (Eq. 2). When the fracture depth exceeds 3 times the borehole diameter, the hydraulic pressure will remain steady. It can be defined as the steady pressure P_s, which is equal to the *in situ* stress σ_h as shown in Eq. 3. By combing the Eqs 1–3, the maximum horizontal principal stress (σ_H) and minimum horizontal principal stress (σ_h) can be solved. After fracturing, use a directional imprinting machine to record the length and direction of the fractures. Thus the direction of the maximum horizontal principal stress can be obtained.

$$P_i = 3\sigma_h - \sigma_H + R_t \quad (1)$$

$$P_r = 3\sigma_h - \sigma_H \quad (2)$$

$$P_s = \sigma_h \quad (3)$$

A borehole at DK33+58 with a depth of 450 m was drilled on site with the location shown in Figure 3, which is close to the tunnel section suffered large deformation. Figure 7 is the photo of the drilling on site. Seven measuring points at depths of 155.0 m, 213.0 m, 255.0 m, 303.7 m, 365.2 m, 389.1 m, and 444.0 m were selected for the test respectively. The directions of the maximum horizontal principal stress at depths of 303.7 m and 444.0 m were tested after fracturing. Table 2 shows the testing results of the borehole at DK33+58. In addition, the vertical stress (σ_v) is calculated according to the gravity of the rock mass. Figure 8 shows the distribution of stress with depth. The direction of the fractures at the depth of 444 m recorded by imprinting is shown in Figure 9. Thus, the distribution rules and characteristics of the *in situ* stress in the Wanhe tunnel can be summarized as follows:

(1) The horizontal principal stress increases almost linearly with depth, except for the test point at the depth of 300 m. For measuring points with a depth less than 400 m, the magnitudes of three principal stresses show the characteristics of "$\sigma_v > \sigma_H > \sigma_h$," which indicates that the *in-situ* stress field is dominated by the gravity of the rock mass. This is because the shallow soft rock mass can release the horizontal principal stress through rock deformation. The ratio of the maximum horizontal principal stress (σ_H) to the vertical stress (σ_v) is defined as the maximum lateral coefficient (K_v), which is mainly in the range of 0.6–0.8 for those testing points within the depth of 400 m. It can be noticed that the horizontal principal stress tested at the depth of 300 m is greater than the vertical stress with a maximum lateral coefficient of 1.6. The reason for this is that the shallow strata were affected by unloading, denudation, and weathering for a long time, which led to complex horizontal stress distributions. For measuring points with a depth greater than 400 m, the magnitudes of three principal stresses show the characteristics of "$\sigma_H > \sigma_v > \sigma_h$," and the maximum lateral

TABLE 2 Testing results of *in situ* stress by hydraulic fracturing method.

Depth of measuring point (m)	Hydraulic pressure (MPa)				Principal stress (MPa)			Direction of fractures
	P_i	P_r	P_s	R_t	σ_H	σ_h	σ_v	
155.0–155.6	8.14	7.07	3.69	1.07	3.36	3.69	4.11	
213.0–213.6	10.78	9.33	5.08	1.45	4.70	5.08	5.64	
255.0–255.6	11.00	9.20	5.00	1.80	4.18	5.00	6.76	
303.7–304.7	15.02	13.19	9.47	1.83	13.13	9.47	8.03	N33°W
365.2–365.8	12.18	10.67	7.18	1.51	8.17	7.18	9.67	
389.1–389.7	9.68	8.22	7.71	1.46	11.98	7.71	10.31	
444.0–444.6	14.85	13.98	10.92	0.87	15.31	10.92	11.77	N50°W

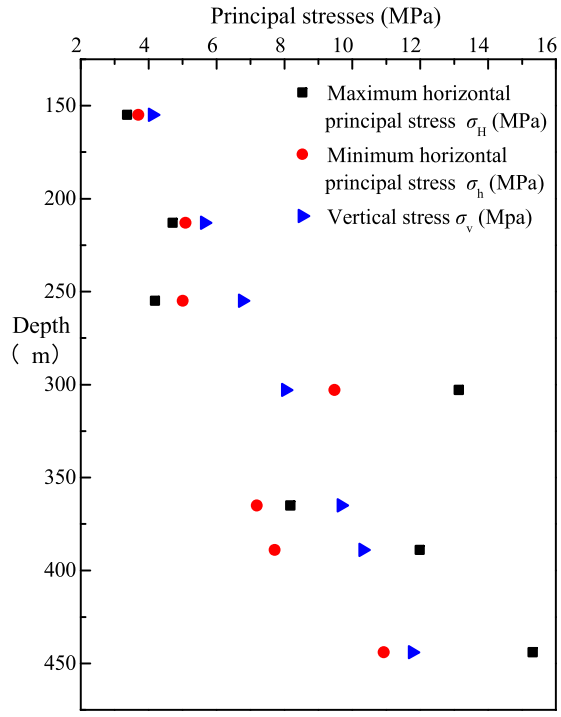

FIGURE 8
Distribution of principal stresses with depth.

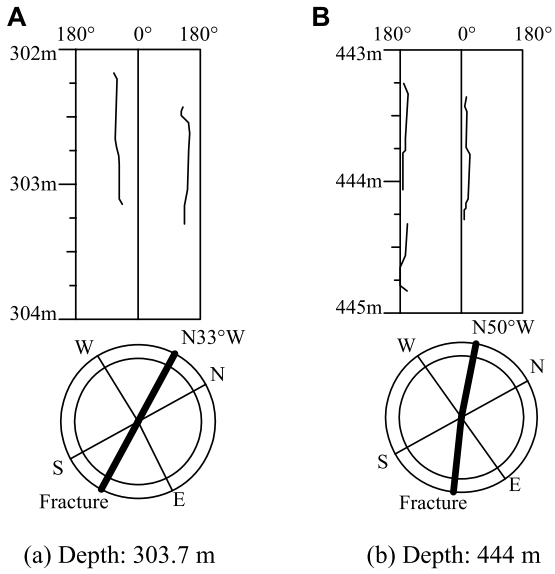

FIGURE 9
Direction of the fractures recorded by stamping. **(A)** Depth: 303.7 m. **(B)** Depth: 444 m.

coefficient ranges from 1.1 to 1.3. This indicates that the tectonic stress increases with depth and is dominant in the deep *in situ* stress field.

(2) The imprints of the fractures tested by the directional stamping machine are clear enough. It can be seen in Figure 9 that the fractures are vertical and symmetrical. The directions of the maximum horizontal principal stress at the depths of 303.7 m and 444.0 m are N33°W and N50°W, respectively, which is close to the trend of two active fault zones that the Wanhe tunnel passes through. This indicates that the directions of the maximum horizontal principal stress tested on site can represent the direction of the tectonic stress field. In addition, the direction of the maximum horizontal principal stress is nearly parallel to the direction of the tunnel axis with a small intersection angle, which indicates that the deformation of the tunnel section mainly depends on the minimum horizontal principal stress and vertical stress.

(3) The measuring point at the depth of 444 m is close to the large deformation section of the Wanhe tunnel. The maximum horizontal principal stress, minimum horizontal principal stress, and vertical stress at this point are 15.31 MPa, 10.92 MPa, and 11.77 MPa, respectively. *In situ* stress at this depth is dominated by horizontal tectonic stress. According to uniaxial compressive strength testing results of rock specimens, the uniaxial compressive strength (R_c) of soft granite at the large deformation section is 1.8 MPa. Thus the ratio of the uniaxial compressive strength (R_c) to the maximum principal stress (σ_{max}) is 0.12. In accordance with code for design on railway tunnels in China [TB10003—2016, (Code for design on railway tunnel, 2017)], the region with such a strength-stress ratio is

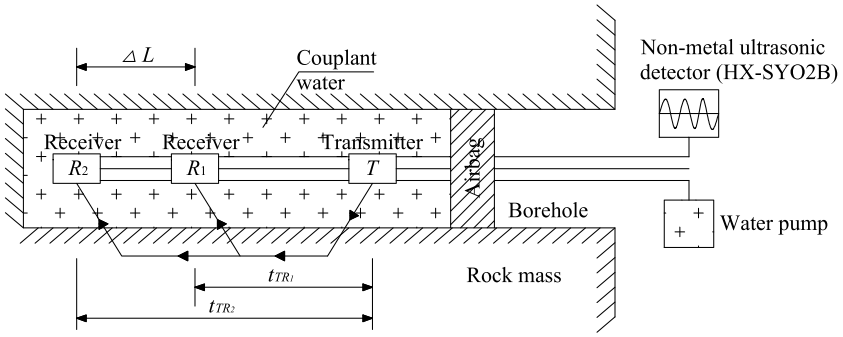

FIGURE 10
Test principle of loosened zone.

located in a high ground stress area, which can easily lead to large squeezing deformation of surrounding rock.

3.2 Loosened zone of surrounding rock

Tunnel excavation will induce stress redistribution, plastic deformation, and fracture propagation in the surrounding rock, thus resulting in a loosened zone around the tunnel. Especially for deep soft rock tunnels under high *in-situ* stress, expansion of the loosened zone will further worsen the development of tunnel deformation. Therefore, the extent of the loosened zone is an important factor affecting the squeezing deformation. To assess the loosened zone of the Wanhe tunnel, ultrasonic wave testing was conducted after tunnel excavation. Since the wave speed depends on the strength of the medium, the ultrasonic wave propagates more slowly in the loosened zone with soft and broken rock (Chen et al., 2015; Xu et al., 2018). The test principle and specific test process are shown in Figures 10, 11.

Firstly, drill several boreholes from the tunnel section to the deep by using the drilling machine of the pipe roof. Then, send the ultrasonic wave transmitter and receivers to the hole bottom, and inject water into this area as one kind of couplant. After that, the ultrasonic wave was emitted from the transmitter by operating the non-metal ultrasonic detector and received by two receivers after propagating in the rock mass. Thus the velocity of the ultrasonic wave (v_p) can be determined by Eq. 4, of which the $\triangle L$ is the distance between two receivers and the t_{TR} is the time when the receivers pick up the ultrasonic wave. By moving the transmitter and receivers 0.2 m each time from the bottom to the entrance and repeating the above steps, the wave velocity of surrounding rock at different borehole depths can be obtained. Ultrasonic waves propagate with lower velocity in soft media. Therefore, the wave speed in the loosened zone is lower than in other regions of the surrounding rock. According to Tan's research (Tan et al., 2022), the depth of the loosened zone at this borehole is the section with a lower average wave velocity.

$$v_p = \frac{\Delta L}{t_{TR_1} - t_{TR_2}} \tag{4}$$

The Wanhe tunnel was excavated by the three-step method. Six boreholes with a depth of 20 m and a diameter of 10 cm were drilled in each test section of the tunnel. These boreholes were respectively located at both sides of the steps, with a distance of 1.8 m from the hole center to the step boundary. Since the drilling machine of the pipe roof cannot drill the deep hole at the vault, the depth of the loosened zone at the vault was estimated as the average of the testing results at the upper bench. Due to the hole collapse at the bottom, the maximum depth that the transmitter can reach was about 16–18 m on site. The distribution curve of the wave velocity with the hole depth at the DK32+460 section is shown in Figure 12, which was tested 45 days after excavation. Thus, the distribution characteristics of the loosened zone can be summarized as follows:

(1) By taking the testing results of borehole A_2 as an example, the evaluation process of the loosened zone depth is introduced. The borehole A_2 is located on the right side of the upper step, and the maximum testing depth was 16.0 m. According to the testing results, the wave velocity at the depth of 14.4 m is the largest reaching 2.923 km/s. There was severe velocity fluctuation in the depth range of 0 m–12.6 m, which was mainly caused by weak rock mass or discontinuous fractures. However, when the testing depth exceeded 12.5 m, the wave velocity increased significantly. The average wave velocity in the depth range of 0 m–12.6 m was 0.476 km/s, which reached 1.887 km/s in the depth range of 12.6 m–16.0 m. Thus, based on the average wave velocity, it can be indicated that the depth of the loosened zone at the A_2 is 12.6 m. Based on this evaluation method, the depths of the loosened zone at other boreholes are respectively considered as 11.6 m (A_1), 9.0 m (B_1), 14.0 m (B_2), 4.0 m (C_1), and 6.8 m (C_2).

(2) According to the testing results of the wave velocity, the loosened zone boundary of the surrounding rock at the DK32+460 section can be obtained as shown in Figure 12. It can be seen that the maximum depth of the loosened zone is 14.0 m, which is located at the right side of the middle step. In contrast, the loosened zone depth at the left side wall is only 4.0 m. In addition, the loosened zone area on the right side of the surrounding rock is slightly larger than that on the left side. The gravity of the loosened rock mass will directly apply to the supporting structure, which will further worsen the development of tunnel deformation.

3.3 Deformation evolution characteristics

The monitoring plan was implemented immediately to measure the vault settlement and horizontal convergence when the Wanhe

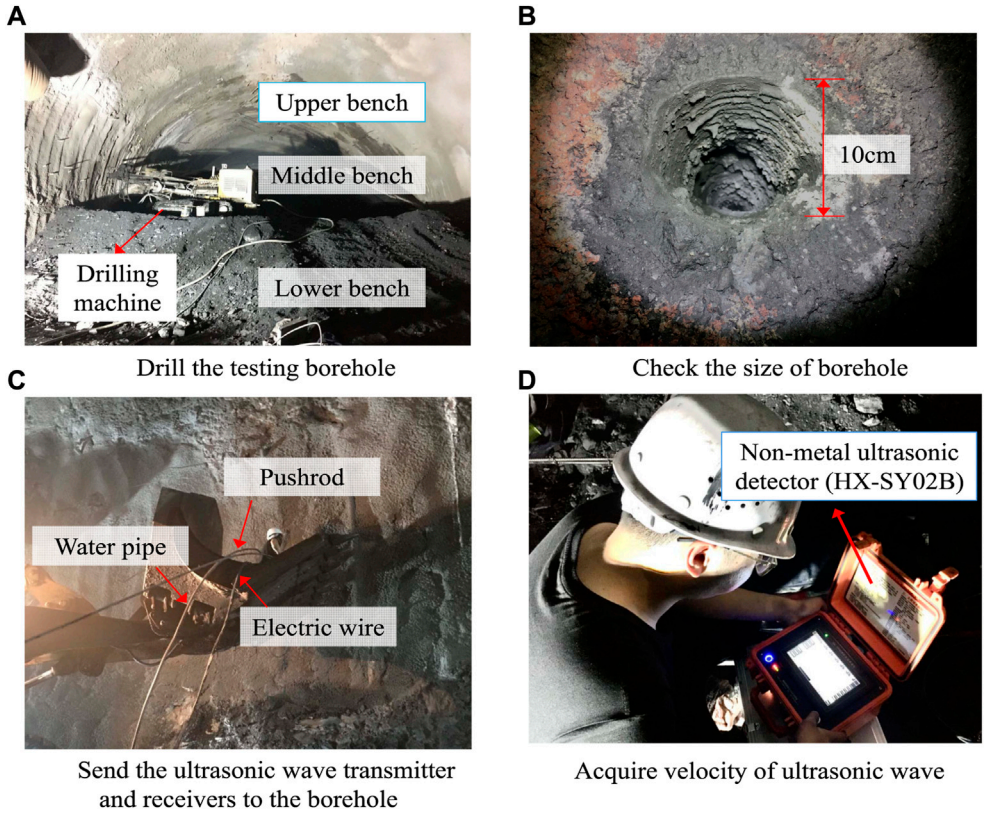

FIGURE 11
Test process of loosened zone on site. **(A)** Drill the testing borehole. **(B)** Check the size of borehole. **(C)** Send the ultrasonic wave transmitter and receivers to the borehole. **(D)** Acquire velocity of ultrasonic wave.

tunnel suffered large deformation. On-site monitoring was carried out at least once a day and lasted for nearly 3 months, so as to obtain the whole process of the deformation development. Figure 13 shows the evolution curves of deformation and deformation rate at section DK32+460 of the Wanhe tunnel. Point V_1 is the monitoring point for vault settlement. Line A_1-A_2, B_1-B_2, and C_1-C_2 are respectively used for monitoring the side wall convergence at the upper bench, middle bench, and lower bench. According to the monitoring results, the tunnel deformation characteristics are presented as follows:

(1) The evolution of vault settlement had gone through three stages, namely, the rapid growth stage, the slow growth stage, and the secondary growth stage. After the excavation of the upper bench, the vault settlement (Point V_1) increased rapidly within 20 days, while the maximum deformation rate of which reached 100.5 mm/d on the 17th day. After 20 days, the deformation rate decreased significantly and entered the slow growth stage with a maximum deformation rate of 11.1 mm/d. However, on the 33rd day, the deformation rate of the vault showed another growth trend, which reached 69.6 mm/d. Since 50 days after the excavation of the upper bench, the accumulative vault settlement at section DK32+460 reached 763.9 mm, which far exceeded the allowable deformation and caused cracking of the vault shotcrete.
(2) The horizontal convergence was most severe at the side wall of the middle bench, which increased significantly within 20 days after excavation. Then the horizontal convergence increased slowly with decreased deformation rate. After 30 days of middle bench excavation, the horizontal convergence remained constant with the accumulated value of 720.2 mm, which caused the side wall cracking and bending of steel arches. The accumulated horizontal convergences at the side wall of the upper bench and the lower bench respectively reached 498.3 mm and 399.6 mm.
(3) The entire deformation of the section at DK32+460 showed an obvious deformation characteristic of "vault settlement > middle bench convergence > upper bench convergence > lower bench convergence". The magnitude of the vault settlement is close to the middle bench convergence, which indicated that there is severe tectonic stress in the formation. In addition, the deformation development has the characteristics of the large growth rate and long duration in the early stage. In the later stage, the deformation development of vault settlement showed another growth trend with an increase of the deformation rate.

3.4 Internal stresses of steel arches

Strain gauges are arranged at DK32+460 section to monitor the internal stress of the steel arch. As shown in Figure 14, a total of nine monitoring points were placed on the tunnel profile. Among them, 5 points (G1~G5) are at the upper bench, G6 and G7 are at the

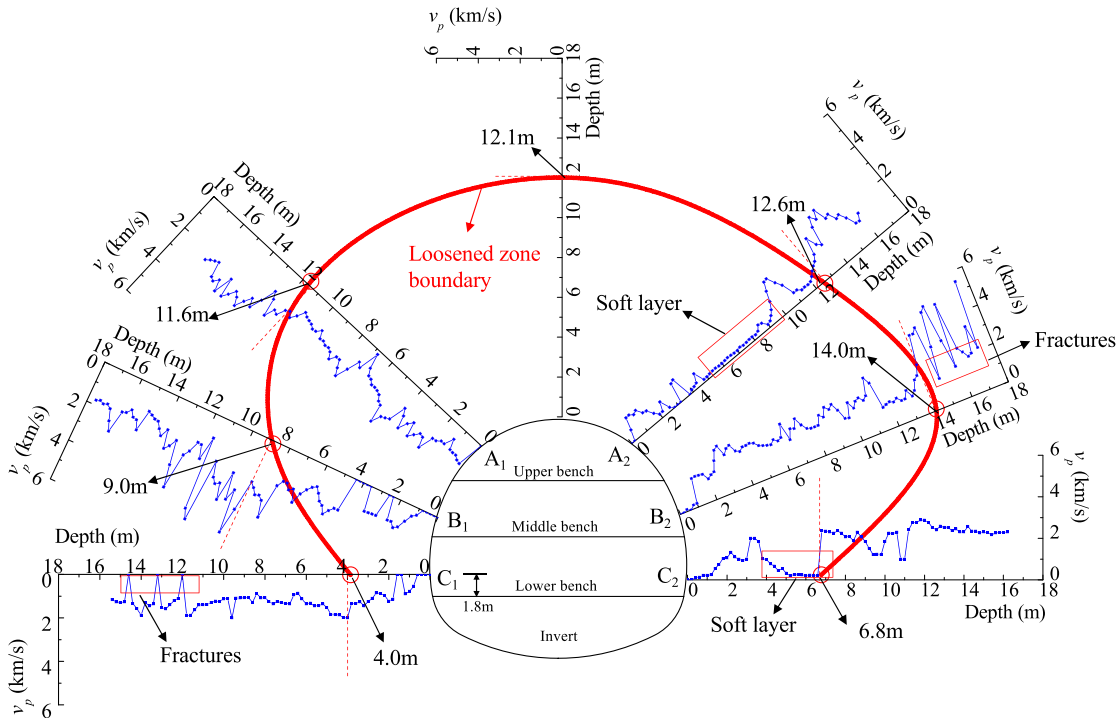

FIGURE 12
Loosened zone of the Wanhe tunnel tested on site.

middle bench, and G8 and G9 are at the lower bench. Strain gauges are arranged on the upper and lower flanges of the steel arch. Based on the testing results of internal stresses, the distribution of axial forces and bending moments can be obtained, as shown in Figure 15. It can be seen that the maximum axial force of the steel arch is located at the arch shoulder, which reaches 1747.6 kN. The maximum bending moment is located at the vault, which reaches 75.0 kNm. The stresses in both the vault and the shoulder exceeds the yield strength of the steel arch, which indicates that failure of support would happened at these two places. Field investigations on site showed that the steel arches at the vaults and shoulders were twisted and bended.

4 Failure mechanisms including squeezing and loosening effects

Through the analysis of on-site monitoring results, the failure mechanism of the Wanhe tunnel can be summarized as squeezing effect and loosening effect, which are explained as follows:

(1) The rapid growth of Wanhe tunnel deformation in the early first stage was caused by the squeezing effect. Due to tunnel excavation, the stress state of rock mass changes from a three-dimensional state to a two-dimensional state. Then the rock stress begins to redistribute with the release of deformation to reach a new equilibrium state. The field test results showed that the Wanhe tunnel was located in the broken granite stratum with low strength and high geostress. Thus tunnel excavation caused great disturbance to the surrounding rock, resulting in a sharp increase of the tangential stress around the tunnel section and a large amount of rock deformation squeezing the supporting structures. After 20 days, the tunnel deformation entered the slow growth stage, which means that most of the squeezing deformation had been released.

(2) The other growth trend of the vault settlement in the later stage was caused by the loosening effect. Figure 16 is the diagram of the convergence confinement method. GRC is the ground response curve, which represents the relationship between the rock pressure and the tunnel deformation. SCC is the support characteristic curve, which represents the relationship between the support force and the tunnel deformation. After tunnel excavation, the rock pressure gradually decreases with stress release and deformation development. The rock pressure at this stage is mainly the squeezing pressure. When the tangential stress around the tunnel section exceeds the yielding strength of the surrounding rock, plastic deformation and fracture propagation will develop in the rock mass, thus resulting in a loosened zone around the tunnel. The field test on site showed a significant loosened zone around the Wanhe tunnel, which created loosening pressure on the supporting structures and further worsened the tunnel deformation.

5 Dynamic process control measures and effectiveness assessment

5.1 Dynamic process control method

According to the on-site monitoring results, the deformation state of the tunnel in tectonic fracture zones under high *in-situ* stresses was

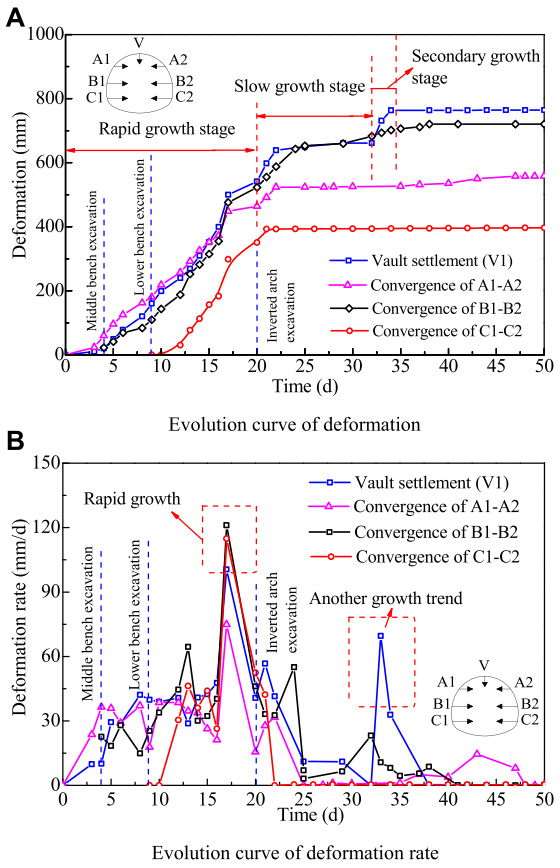

FIGURE 13
Deformation curve of DK32+460 section. **(A)** Evolution curve of deformation. **(B)** Evolution curve of deformation rate.

considered to be a dynamic process, which was not usually instantaneous and showed an obvious space-time effect. Deformation is the most direct indicator to reflect the state of the surrounding rock. It has the characteristics of large growth rate and long duration in the early stage caused by the squeezing effect and showed another growth trend in the later stage due to the loosening effect.

Based on these characteristics, this paper proposed the dynamic control process method. This method is based on the combination principle of stress releasing and support resistance. It first allows the rock mass deformation to exert its bearing capacity. Then, it requires the reinforcement of rock and the strengthening of supports to prevent rock failure and control the deformation within the reserved range. Figure 17 is the flowchart of the dynamic control process method. It requires the control measures to be taken in process by identifying the evolution stages of deformation through on-site monitoring. Details are described as follow: 1) Firstly, predict the deformation grade and determine the deformation allowance based on the ratio of the uniaxial compressive strength to the maximum principal stress through on-site measurement. 2) Before the tunnel excavation, advanced supports are installed to prevent the tunnel face instability. 3) After excavation, the flexible primary supports including the shotcrete and the steel arches should be conducted in time to form the ring closure of the tunnel, which is the premise of subsequent construction safety. 4) In the rapid growth stage, it allows to release the deformation of the surrounding rock based on the stress releasing principle to fully utilize the original bearing capacity of the surrounding rock. 5) When the deformation rate decreases significantly and enters the slow growth stage, active control methods are used to reinforce the surrounding rock in time to improve the resistance. 6) If the deformation rate shows another growing trend in the later stage, based on the support resistance principle, the passive control methods are used to strengthen the supporting structures and restrain the rock deformation within the reserved range.

5.2 Dynamic process control measures

5.2.1 Deformation grade and deformation allowance

Predicting the potential squeezing intensity and the deformation grade is the premise of the squeezing tunnel construction, which can improve the applicability of the control measures. In this paper, the deformation grade of the Wanhe tunnel was determined according to the Code for Tunneling in Squeezing Rock in China [Q/CR9812-2019, (Code for Tunnelling in Squeezing Rocks, 2019)], which divides the squeezing potential into three grades with the index of rock strength-stress ratio as shown in Table 3. According to the field testing results on site, the ratio of

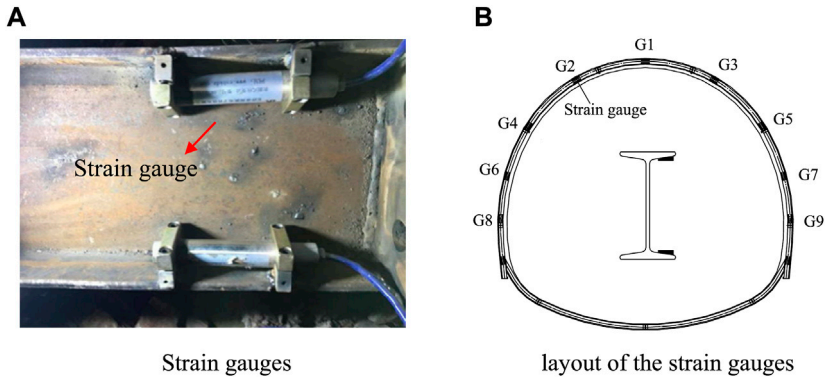

FIGURE 14
Test scheme of the internal stress of steel arches. **(A)** Strain gauges. **(B)** layout of the strain gauges.

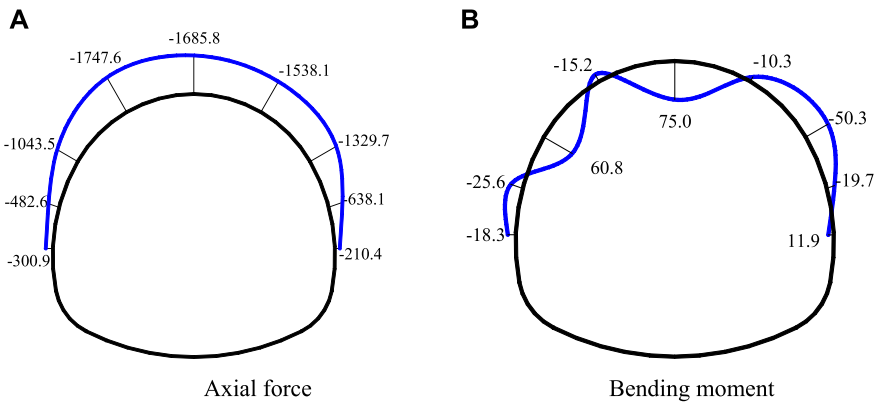

FIGURE 15
Testing results of the internal force. **(A)** Axial force. **(B)** Bending moment.

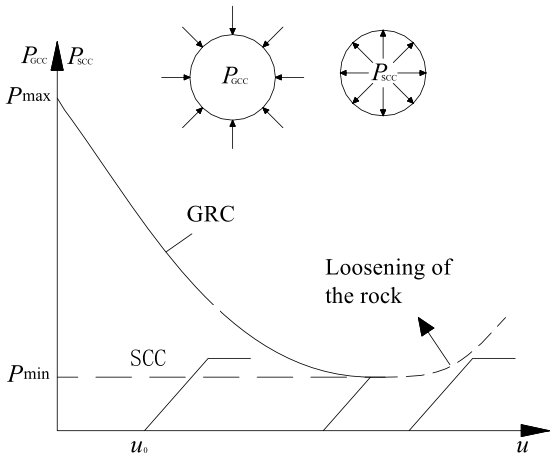

FIGURE 16
The convergence confinement method.

the uniaxial compressive strength (R_c) to the maximum *in-situ* stress (σ_{max}) is 0.12. Thus the deformation grade of the Wanhe tunnel can be determined as Grade III, which means that the tunnel has great squeezing potential. Further, the Code [Q/CR9812-2019, (Code for Tunnelling in Squeezing Rocks, 2019)] gives the recommended values of deformation allowance for different deformation grades in Table 3. Considering the previous maximum deformation monitored on site, the proposed deformation allowance of the Wanhe tunnel was 500 mm in this study.

5.2.2 Advanced support and primary support

Due to weak rock mass with developed joints, collapses at the top of the tunnel face often occurred during excavation. To prevent the tunnel face instability, an advanced support scheme was proposed during the Wanhe tunnel construction. Steel tubes of 6 m in length, and 76 mm in diameter were used as the advanced pipe roofs, which were arranged above steel arches with 40 cm circumferential spacing and 3.6 m longitudinal spacing. The angle between the steel pipe and the longitudinal direction is about 1°–2°. There are grouting holes at the ends of the steel pipes. The grout in the advanced pipe roof was the cement paste, which can bond the steel tubes and rock mass to improve the effect of advanced support. After installing the advanced supports, the Wanhe tunnel was excavated through the three-step method and supported with the primary support in time. The primary support consisted of steel arches, shotcrete, and anchor bolts. The steel arches are made of shaped steel of I20b with 0.6 m spacing. Shotcrete with the strength of C25 and the thickness of 27 cm was used on site. Anchor bolts of 3.5 m in length and 25 mm in diameter are installed at intervals of 1.0 m. This is a flexible support system with deformation release ability.

5.2.3 Active control measure-deep-shallow coupled delayed grouting

Grouting is one kind of active control method to improve the bearing capacity of surrounding rock by bonding the broken rock mass with slurry. However, for deep buried tunnels in tectonic fracture zones, the fissures in the surrounding rock are compacted by high *in-situ* stresses in the early stage, which makes it difficult to inject the grout. Therefore, the delayed grouting method following the dynamic control principle is proposed in this paper. It firstly allows to release the deformation of the surrounding rock in the rapid growth stage to develop the fissures in the surrounding rock, thus improving the injectability of grout. The time when the tunnel deformation begins to enter the slow growth stage is suggested as the best grouting timing. Based on the monitoring results of real-time deformation on site, grouting was carried out when the deformation rate decreased significantly during the construction of the Wanhe tunnel.

The thickness of the grouted reinforcement layer depends on the thickness of the loosened ring. The loosened zone is the area where the fissures in the surrounding rock are highly developed after excavation. The injectability of this area is relatively large under high *in situ* stress. The purpose of grouting is to repair and consolidate the surrounding rock in the loosened ring. In Figure 12, the field test on site showed a significant loosened zone with an average depth of 9.6 m. In order to ensure the range of reinforcement, steel tubes with a length of 6.0 m were selected for grouting. This paper proposed the deep-shallow coupled grouting scheme, the process of which is described as follows:

(1) Firstly, deep and shallow grouting holes were drilled in the surrounding rock with the layout shown in Figure 18. They were arranged in the shape of plum blossoms with distances of 3.0 m (for deep grouting holes) and 1.2 m (for shallow grouting

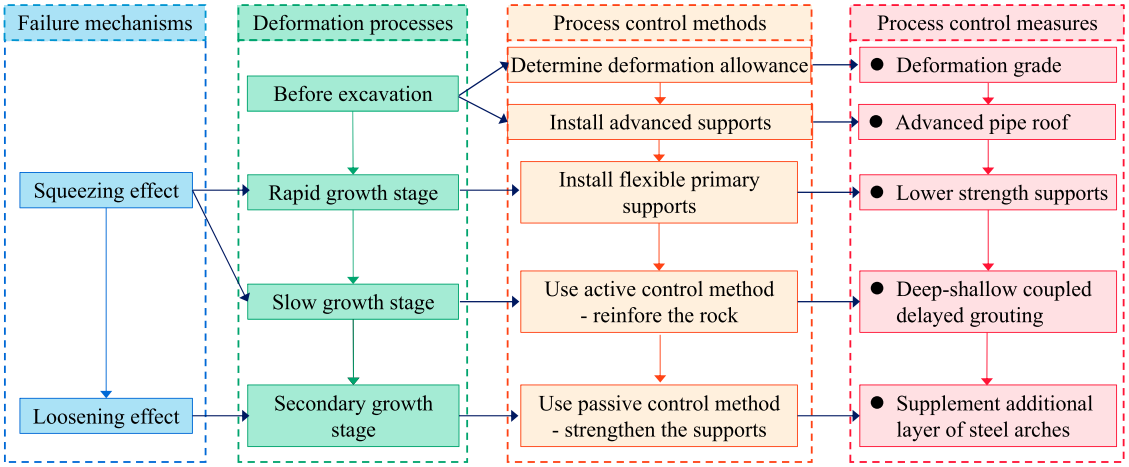

FIGURE 17
Dynamic process control method.

TABLE 3 Classification standard of deformation grade and suggested deformation allowance.

Deformation grade		I	II	III
Deformation potential		Slight	Large	Great
Rock strength-stress ratio		0.2–0.3	0.15–0.20	<0.15
Suggested deformation allowance (mm)	Tunnel span ≤12 m	100–200	200–300	300–400
	Tunnel span >12 m	150–250	250–350	350–450

holes) respectively. Steel tubes of 6.0 m in length and 42 mm in diameter were used for the grouting of deep holes, while the tubes with 2.0 m in length and 42 mm in diameter were used for the shallow holes.

(2) When the monitored deformation began to decrease, the loosened and broken rock mass in shallow was grouted first through the steel tubes in the shallow holes. Grouting started from the side wall of the middle bench, then to the spandrels of the upper bench, and finally to the tunnel vault. The grout was the mixture of the ordinary portland cement slurry (with a cement strength grade of 42.5 and a water-cement ratio of 0.8) and the water glass (with a mixing amount of 3%). The grouting pressure was controlled within a lower range from 0.5 to 1.0 MPa to ensure the safety of the primary supports.

(3) When the shallow grouting layer was solidified, the rock mass in deep was grouted through the steel tubes in the deep holes. By increasing the grouting pressure and using high-permeability materials, the slurry can be diffused to the deep, thereby improving the grouting range. During high-pressure grouting, the finished shallow grouting layer can stop the slurry and prevent slurry leakage. Otherwise, the high grouting pressure would damage the soft rock in shallow and further crush the primary supports. The grouting order was the same as that of the shallow holes. The grout material with high permeability and high strength contains the ordinary portland cement slurry (with a cement strength grade of 52.5 and a water-cement ratio of 0.6) and the water reducer (with the mixing amount of 0.7%). The grouting pressure was controlled within the range from 2.0 to 3.0 MPa.

5.2.4 Passive control measure-double steel arches

After grouting, some sections of the Wanhe tunnel continued to deform and even showed another growing trend in the later stage, which seemed difficult to converge within the deformation allowance. Thus, to restrain the tunnel deformation, the passive control method was carried out by supplementing another layer of steel arch. The second layer of steel arch is made of shaped steel of I22b with a spacing of 0.6 m, which were installed on the inverted arches reaching the required strength. Two adjacent arches were connected with the steel bars, which have a diameter of 22 mm and a circumferential spacing of 0.6 m. In addition, a total of six lock-feet anchor pipes with a diameter of 42 mm and a length of 4.5 m were installed at the arch foot of each ring. The end of the lock-feet anchor pipes has grout vent holes, which allows for consolidating the anchor pipes and the nearby rock by grouting so that the arch feet could not sink and slip. In order to transfer the deformation load from the first layer of the primary support to the second layer of steel arches, wooden blocks were used to wedge them.

5.3 Effectiveness evaluation

According to the dynamic process control method proposed in this paper, the large deformation of the Wanhe tunnel (from DK32+725 to DK32+100) was generally controlled by the basic comprehensive measures containing advanced supports, flexible primary supports, and delayed grouting. Further, the deformation of some special sections (sections at DK32+338~+171, DK32+400~ DK32+340, and

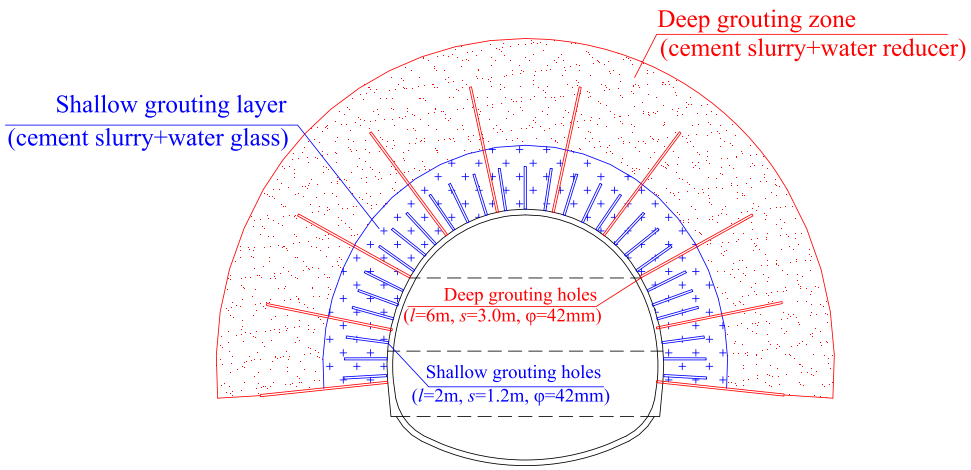

FIGURE 18
Deep-shallow coupled grouting scheme.

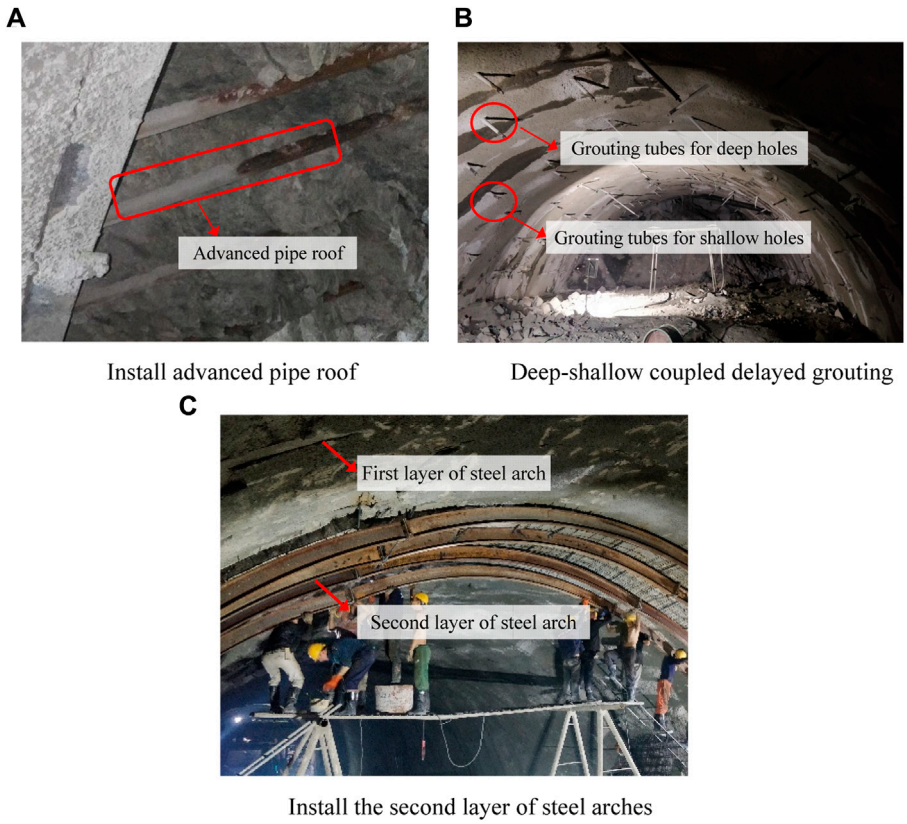

FIGURE 19
Dynamic process control measures on site. **(A)** Install advanced pipe roof. **(B)** Deep-shallow coupled delayed grouting. **(C)** Install the second layer of steel arches.

DK32+615~ DK32+415) still kept increasing without a stable trend after grouting reinforcement. Therefore, the control measure of the double steel arch was supplemented in these sections.

Figure 19 shows the dynamic process control measures carried out on site. As mentioned, monitoring is an efficient approach to evaluate the effect that countermeasures play on controlling tunnel deformation. By real-time measuring during the following construction, the evolution curves of vault settlement with time under the modified controlling measures are shown in Figure 20. The control effect can be evaluated as follows:

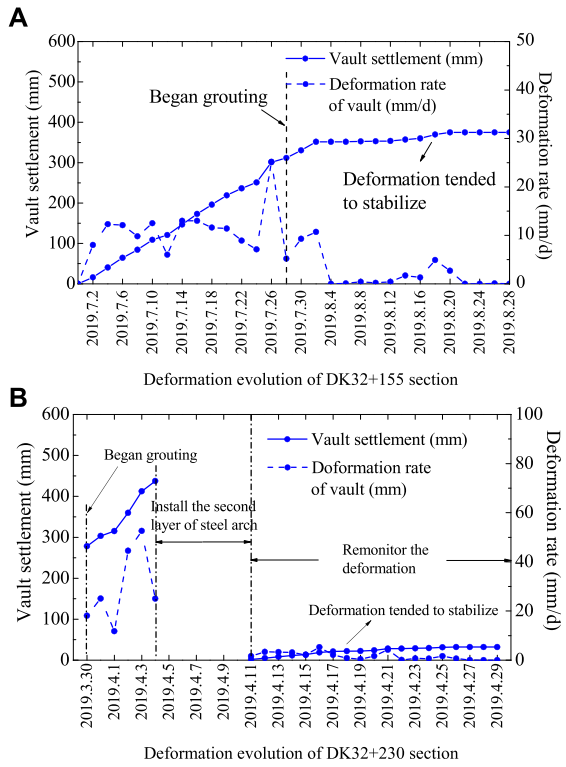

FIGURE 20
Deformation evolution after dynamic process control measures. **(A)** Deformation evolution of DK32+155 section. **(B)** Deformation evolution of DK32+230 section.

(1) Figure 20A shows that the vault settlement of the DK32+155 section had a rapid growth stage lasting 28 days, and then entered a slow growth stage. The rock grouting was carried out on the 29th day. After that, the vault settlement gradually converged and reached stability on the 50th day. The cumulative amount of vault settlement was 375.2 mm, which was less than the deformation allowance. This indicated that the delayed grouting method effectively reinforced the loosened rock mass and well controlled the tunnel deformation.

(2) Since the deformation of the DK32+230 section had no stable trend after grouting, the second layer of steel arch was implemented when the vault settlement reached 450 mm. Figure 20B shows that the deformation rate was greatly reduced after installing the second layer of steel arches. After 29 April 2019, the vault settlement became stable within the deformation allowance and did not increase again. This indicated that the second layer of steel arches had an obvious effect on restraining the development of the rock loosened zone and stabilizing the tunnel deformation.

(3) In addition, the tunnel cracking and steel twisting were greatly reduced in the Wanhe tunnel. These all indicated the rationality and applicability of the dynamic process control measures for large deformation tunnels in tectonic fracture zones under high *in-situ* stresses. Finally, the Wanhe tunnel completed in March 2020.

6 Conclusion

Based on the Wanhe tunnel of the China-Laos railway, this study discusses the failure mechanisms and proposed the dynamic process control measures for a deep buried tunnels in tectonic fracture zones under high *in-situ* stresses. The major conclusions of this study are as follows:

(1) *In situ* stress test through hydraulic fracturing method found out that the tunnel was located in a high geostress field and would be easily squeezed and deformed. The ultrasonic wave testing for the surrounding rock showed a significant loosened zone around the tunnel, which would further worsen the tunnel deformation. Deformation evolution had the characteristic of rapid growth in the early stage caused by the squeezing effect. In the later stage, the vault settlement had another growth trend due to the loosening effect of the surrounding rock. The squeezing and loosening effects lead to stresses in the vault and shoulder exceeding the yield strength of the steel arches.

(2) Aiming at the failure mechanism, this study proposed the dynamic process control method based on the combination principle of stress releasing and support resistance. It first allows to release the deformation of the surrounding rock in the rapid growth stage and then requires to control the deformation within the reserved range by reinforcing the surrounding rock and strengthening support structures in the later stage. Further, the dynamic process control measures were proposed in this paper including the advanced and primary supports, the deep-shallow coupled delayed grouting method, and the double steel arches method.

(3) Based on the *in situ* monitoring results, it was found that the vault settlement and horizontal convergence were well released and controlled with the dynamic process control measures and finally reached stability within the deformation allowance. In addition, tunnel cracking and steel twisting were greatly reduced. Finally, the construction of the Wanhe tunnel was well finished. This study suggests that the proposed measures can guarantee the construction safety of deep buried tunnels in tectonic fracture zones under high *in-situ* stresses.

Data availability statement

The original contributions presented in the study are included in the article/Supplementary material, further inquiries can be directed to the corresponding author.

Author contributions

KZ: Writing–original draft, Writing–review and editing. CS: Writing–original draft, Writing–review and editing. QZ: Data curation, Investigation, Writing–original draft. ML: Formal Analysis, Methodology, Writing–review and editing. CJ: Conceptualization, Writing–review and editing. YL: Data curation, Investigation, Methodology, Writing–review and editing.

Acknowledgments

The authors thank the Kunming Group Co., Ltd. and the 12th Bureau Group Co., Ltd. of China Railway for cooperation in the field tests and data collection for this study. The authors acknowledge the financial support provided by the Science and Technology Research and Development Program Project of China railway group limited (Key Project, No. 2021-Key-09).

Conflict of interest

Authors KZ and CS were employed by China Railway Group Limited. Author QZ was employed by China Railway Kunming Group Co., Ltd.

The authors declare that this study received funding from the Science and Technology Research and Development Program Project of China railway group limited (Key Project, No. 2021-Key-09). The funder was involved in the study design, cooperation for field investigation and evaluation of research results.

The remaining authors declare that the research was conducted in the absence of any commercial or financial relationships that could be construed as a potential conflict of interest.

Publisher's note

All claims expressed in this article are solely those of the authors and do not necessarily represent those of their affiliated organizations, or those of the publisher, the editors and the reviewers. Any product that may be evaluated in this article, or claim that may be made by its manufacturer, is not guaranteed or endorsed by the publisher.

References

Aksoy, C. O., Ogul, K., Topal, I., Ozer, S. C., Ozacar, V., and Posluk, E. (2012). Numerical modeling of non-deformable support in swelling and squeezing rock. *Int. J. Rock Mech. Min. Sci.* 52, 61–70. doi:10.1016/j.ijrmms.2012.02.008

Ayaydin, N., and Leitner, A. (2009). Tauern tunnel first and second tubes from the consultant's viewpoint. *Geomech. Tunn.* 2 (1), 14–23. doi:10.1002/geot.200900001

Barla, G., Bonini, M., and Semeraro, M. (2011). Analysis of the behaviour of a yield-control support system in squeezing rock. *Tunn. Undergr. Space Technol.* 26 (1), 146–154. doi:10.1016/j.tust.2010.08.001

Bonini, M., and Barla, G. (2012). The Saint Martin La porte access adit (Lyon–Turin Base tunnel) revisited. *Tunn. Undergr. Space Technol.* 30, 38–54. doi:10.1016/j.tust.2012.02.004

Cantieni, L., and Anagnostou, G. (2009). The interaction between yielding supports and squeezing ground. *Tunn. Undergr. Space Technol.* 24 (3), 309–322. doi:10.1016/j.tust.2008.10.001

Cao, C. Y., Shi, C. H., Lei, M. F., Yang, W. C., and Liu, J. W. (2018). Squeezing failure of tunnels: a case study. *Tunn. Undergr. Space Technol.* 77, 188–203. doi:10.1016/j.tust.2018.04.007

Chen, Y. F., Zheng, H. K., Wang, M., Hong, J. M., and Zhou, C. B. (2015). Excavation-induced relaxation effects and hydraulic conductivity variations in the surrounding rocks of a large-scale underground powerhouse cavern system. *Tunn. Undergr. Space Technol.* 49, 253–267. doi:10.1016/j.tust.2015.05.007

Chen, Z. Q., He, C., Xu, G. W., Ma, G. Y., and Yang, W. B. (2019). Supporting mechanism and mechanical behavior of a double primary support method for tunnels in broken phyllite under high geo-stress: a case study. *B. Eng. Geol. Environ.* 78 (7), 5253–5267. doi:10.1007/s10064-019-01479-1

Code for design on railway tunnel (TB10003—2016) (2017). *The professional standards compilation group of peoples Republic of China*. Beijing: China Railway Publishing House. (in Chinese).

Code for Tunnelling in Squeezing Rocks (Q/CR9812-2019) (2019). *Code for tunnelling in squeezing rocks (Q/CR9812-2019)*. Beijing: China Railway Publishing House. (in Chinese).

Deng, H. S., Fu, H. L., Shi, Y., Zhao, Y. Y., and Hou, W. Z. (2022). Countermeasures against large deformation of deep-buried soft rock tunnels in areas with high geostress: a case study. *Tunn. Undergr. Space Technol.* 119, 104238. doi:10.1016/j.tust.2021.104238

Franz, W., and Harald, L. (2009). The Tauern tunnel first and second tubes from the contractor's viewpoint. *Geomech. Tunn.* 2 (1), 24–32. doi:10.1002/geot.200900002

Guan, K., Zhu, W., Liu, X., Wei, J., and Niu, L. (2020). Re-profiling of a squeezing tunnel considering the post-peak behavior of rock mass. *Int. J. Rock. Mech. Min. Sci.* 125, 104153. doi:10.1016/j.ijrmms.2019.104153

Horyl, P., Snuparek, R., and Hlavackova, M. (2013). Loading capacity of yielding connections used in steel arch roadway supports. *Seventh Int. Symposium Ground Support in Min. Undergr. Constr.*, 461–470. doi:10.36487/ACG_rep/1304_31_Horyl

Iasiello, C., Guerra Torralbo, J. C., and Torrero Fernández, C. (2021). Large deformations in deep tunnels excavated in weak rocks: study on Y-Basque high-speed railway tunnels in northern Spain. *Undergr. Space* 6 (6), 636–649. doi:10.1016/j.undsp.2021.02.001

International society for rock mechanics (1987). Suggested methods for rock stress determination. *Int. J. Rock Mech. Min. Sci.* 24 (1), 55–73. doi:10.1016/0148-9062(87)91232-0

Jeong, S. S., Han, Y. C., Kim, Y. M., and Kim, D. H. (2014). Evaluation of the NATM tunnel load on concrete lining using the ground lining interaction model. *KSCE J. Civ. Eng.* 18 (2), 672–682. doi:10.1007/s12205-014-0597-9

John, M. (1980). Arleberg expressway tunnel - Part 4. Construction of the Arlberg expressway tunnel tube. *Int. J. Rock Mech. Min. Sci.* 17 (6), A114. doi:10.1016/0148-9062(80)90638-5

Kang, H., Jiang, P., Wu, Y., and Gao, F. (2021). A combined "ground support-rock modification-destressing" strategy for 1000-m deep roadways in extreme squeezing ground condition. *Int. J. Rock Mech. Min. Sci.* 142, 104746. doi:10.1016/j.ijrmms.2021.104746

Kimura, F., Okabayashi, N., and Kawamoto, T. (1987). Tunnelling through squeezing rock in two large fault zones of the Enasan Tunnel II. *Rock Mech. Rock Eng.* 20 (3), 151–166. doi:10.1007/BF01020366

Li, C. C., Stjern, G., and Myrvang, A. (2014). A review on the performance of conventional and energy-absorbing rockbolts. *J. Rock Mech. Geotech.* 6 (4), 315–327. doi:10.1016/j.jrmge.2013.12.008

Li, P. F., Tian, S. M., Zhao, Y., Zhu, Y., and Wang, S. (2013). *In-situ* monitoring study of mechanical characteristics of primary lining in weak rock tunnel with high grostress. *Chin. J. Rock Mech. Eng.* 32 (S2), 3509–3519. doi:10.3969/j.issn.1000-6915.2013.z2.066

Lin, Y. X., Lai, Z. S., Ma, J. J., Huang, L. C., and Lei, M. F. (2023). A FDEM approach to study mechanical and fracturing responses of geo-materials with high inclusion contents using a novel reconstruction strategy. *Eng. Fract. Mech.* 282, 109171. doi:10.1016/j.engfracmech.2023.109171

Ma, J. J., Zhao, J. X., Lin, Y. X., Liang, J. G., Chen, J. J., Chen, W. X., et al. (2023). Study on tamped spherical detonation-induced dynamic responses of rock and PMMA through mini-chemical explosion tests and a four-dimensional lattice spring model. *Rock Mech. Rock Eng.* 56 (10), 7357–7375. doi:10.1007/s00603-023-03426-9

Mezger, F., Anagnostou, G., and Ziegler, H. J. (2013). The excavation-induced convergences in the sedrun section of the gotthard Base tunnel. *Tunn. Undergr. Space Technol.* 38, 447–463. doi:10.1016/j.tust.2013.07.016

Mezger, F., Ramoni, M., Anagnostou, G., Dimitrakopoulos, A., and Meystre, N. (2017). Evaluation of higher capacity segmental lining systems when tunnelling in squeezing rock. *Tunn. Undergr. Space Technol.* 65, 200–214. doi:10.1016/j.tust.2017.02.012

Milnes, A. G. (1973). Structural reinterpretation of the classic Simplon tunnel section of the central alps. *GSA Bull.* 84 (1), 269–274. doi:10.1130/0016-7606(1973)84<269:SROTCS>2.0.CO;2

Ortlepp, W. D., and Stacey, T. R. (1998). Performance of tunnel support under large deformation static and dynamic loading. *Tunn. Undergr. Space Technol.* 13 (1), 15–21. doi:10.1016/S0886-7798(98)00022-4

Qiao, Y. F., Tang, J., Liu, G. Z., and He, M. C. (2022). Longitudinal mechanical response of tunnels under active normal faulting. *Undergr. Space* 7 (4), 662–679. doi:10.1016/j.undsp.2021.12.002

Radončić, N., Schubert, W., and Moritz, B. (2009). Ductile support design. *Geomech. Tunn.* 2 (5), 561–577. doi:10.1002/geot.200900054

Rodríguez, R., and Díaz-Aguado, M. B. (2013). Deduction and use of an analytical expression for the characteristic curve of a support based on yielding steel ribs. *Tunn. Undergr. Space Technol.* 33, 159–170. doi:10.1016/j.tust.2012.07.006

Rowedder, S. (2020). Railroading land-linked Laos: China's regional profits, Laos' domestic costs? *Eurasian Geogr. Econ.* 61 (2), 152–161. doi:10.1080/15387216.2019.1704813

Schubert, W., Brunnegger, S., Staudacher, R., and Wenger, J. (2018). Further development of yielding elements and connecting elements for shotcrete. *Geomech. Tunn.* 11 (5), 575–581. doi:10.1002/geot.201800038

Sun, X., Zhao, C., Tao, Z., Kang, H., and He, M. (2021). Failure mechanism and control technology of large deformation for Muzhailing Tunnel in stratified rock masses. *B. Eng. Geol. Environ.* 80 (6), 4731–4750. doi:10.1007/s10064-021-02222-5

Tan, X., Chen, W., Liu, H., Chan, A. H. C., Tian, H., Meng, X., et al. (2017). A combined supporting system based on foamed concrete and U-shaped steel for underground coal mine roadways undergoing large deformations. *Tunn. Undergr. Space Technol.* 68, 196–210. doi:10.1016/j.tust.2017.05.023

Tan, Z. S., Li, S. T., Yang, Y., and Wang, J. J. (2022). Large deformation characteristics and controlling measures of steeply inclined and layered soft rock of tunnels in plate suture zones. *Eng. Fail. Anal.* 131, 105831. doi:10.1016/j.engfailanal.2021.105831

Tian, H. M., Chen, W. Z., Tan, X. J., Yang, D. S., Wu, G. J., and Yu, J. X. (2018). Numerical investigation of the influence of the yield stress of the yielding element on the behaviour of the shotcrete liner for yielding support. *Tunn. Undergr. Space Technol.* 73, 179–186. doi:10.1016/j.tust.2017.12.019

Tian, H. M., Chen, W. Z., Yang, D. S., Wu, G. J., and Tan, X. J. (2016). Numerical analysis on the interaction of shotcrete liner with rock for yielding supports. *Tunn. Undergr. Space Technol.* 54, 20–28. doi:10.1016/j.tust.2016.01.025

Tian, Y., Chen, W. Z., Tian, H. M., Tan, X. J., Li, Z., and Lei, J. (2021). Parameter design of yielding layers for squeezing tunnels. *Tunn. Undergr. Space Technol.* 108, 103694. doi:10.1016/j.tust.2020.103694

Ulusay, R. (2015). *The ISRM suggested methods for rock characterization. Testing and monitoring 2007-2014.* Springer International Publishing. doi:10.1007/978-3-319-07713-0

VandeKraats, J. D., and Watson, S. (1996). *Direct laboratory tensile testing of select yielding rock bolt systems*. Carlsbad,NM (United States): Westinghouse Electric Corp. doi:10.2172/367133

Vrakas, A., and Anagnostou, G. (2016). Ground response to tunnel Re-profiling under heavily squeezing conditions. *Rock Mech. Rock Eng.* 49 (7), 2753–2762. doi:10.1007/s00603-016-0931-2

Wan, F., Tan, Z. S., and Ma, D. (2014). Optimizing design of support structure for Guanjiao Tunnel in fault-rupture zone F2-1. *Chin. J. Rock. Mech. Eng.* 33 (3), 531–538. doi:10.13722/j.cnki.jrme.2014.03.011

Wang, H., Chen, W. Z., Tan, X. J., Tian, H. M., and Cao, J. J. (2012). Development of a new type of foam concrete and its application on stability analysis of large-span soft rock tunnel. *J. Cent. South. Univ.* 19 (11), 3305–3310. doi:10.1007/s11771-012-1408-4

Wang, Q., Jiang, B., Pan, R., Li, S. C., He, M. C., Sun, H. B., et al. (2018). Failure mechanism of surrounding rock with high stress and confined concrete support system. *Int. J. Rock Mech. Min. Sci.* 102, 89–100. doi:10.1016/j.ijrmms.2018.01.020

Wang, Q., Pan, R., Jiang, B., Li, S. C., He, M. C., Sun, H. B., et al. (2017). Study on failure mechanism of roadway with soft rock in deep coal mine and confined concrete support system. *Eng. Fail Anal.* 81, 155–177. doi:10.1016/j.engfailanal.2017.08.003

Wang, Y. Q., Li, J. Q., Wang, Z. F., and Chang, H. T. (2022). Structural failures and geohazards caused by mountain tunnel construction in fault zone and its treatment measures: a case study in Shaanxi. *Eng. Fail. Anal.* 138, 106386. doi:10.1016/j.engfailanal.2022.106386

Wu, F. Q., Miao, J. L., Bao, H., and Wu, J. (2015). Large deformation of tunnel in slate-schistose rock: a case study on muzhailing tunnel, lan-yu railway, China. *China.* Eng. Geol. Soc. territ. 6, 17–23. doi:10.1007/978-3-319-09060-3_3

Wu, G., Chen, W., Jia, S., Tan, X., Zheng, P., Tian, H., et al. (2020). Deformation characteristics of a roadway in steeply inclined formations and its improved support. *Int. J. Rock. Mech. Min. Sci.* 130, 104324. doi:10.1016/j.ijrmms.2020.104324

Wu, G., Chen, W., Tian, H., Jia, S., Yang, J., and Tan, X. (2018). Numerical evaluation of a yielding tunnel lining support system used in limiting large deformation in squeezing rock. *Environ. Earth. Sci.* 77 (12), 439. doi:10.1007/s12665-018-7614-0

Wu, K., Shao, Z., Qin, S., Wei, W., and Chu, Z. (2021). A critical review on the performance of yielding supports in squeezing tunnels. *Tunn. Undergr. Space Technol.* 115, 103815. doi:10.1016/j.tust.2021.103815

Xu, D. P., Zhou, Y. Y., Qiu, S. L., Jiang, Q., and Wang, B. (2018). Elastic modulus deterioration index to identify the loosened zone around underground openings. *Tunn. Undergr. Space Technol.* 82, 20–29. doi:10.1016/j.tust.2018.07.032

Yang, J. S., Yan, L., Deng, S. J., and Li, G. L. (2006). Interactions of four tunnels driven in squeezing fault zone of Wushaoling Tunnel. *Tunn. Undergr. Space Technol.* 21 (3-4), 359. doi:10.1016/j.tust.2005.12.176

Zhang, C., Tan, X., Tian, H., and Chen, W. (2022). Lateral compression and energy absorption of foamed concrete-filled polyethylene circular pipe as yielding layer for high geo-stress soft rock tunnels. *Int. J. Min. Sci. Technol.* 32 (5), 1087–1096. doi:10.1016/j.ijmst.2022.08.011

Zhang, D. L., Sun, Z. Y., and Fang, Q. (2022). Scientific problems and research proposals for Sichuan–Tibet railway tunnel construction. *Undergr. Space.* 7 (3), 419–439. doi:10.1016/j.undsp.2021.10.002

Zhang, Q., Li, Y.-J., Wang, H.-Y., Yin, Q., and Wang, X.-F. (2022). Re-profiling response of heavily squeezed tunnels via ground reaction curves. *Tunn. Undergr. Space Technol.* 123, 104411. doi:10.1016/j.tust.2022.104411

Zhang, W. Q., Wang, Q. L., Li, J. W., and Gao, P. (2010). Case study on large deformation control technology of Muzhailing tunnel. *Tunn. Constr.* 30 (2), 157–161. CNKI:SUN:JSSD.0. 2010-02-013.

Zhang, Z. D. (1997). Main measures to control large deformation in Jiazhuqing Tunnel. *Mod. Tunn. Technol.* 1, 7–16. doi:10.13807/j.cnki.mtt.1998.01.012

frontiers | Frontiers in Earth Science

TYPE Original Research
PUBLISHED 08 January 2024
DOI 10.3389/feart.2023.1335756

Check for updates

OPEN ACCESS

EDITED BY
Jianyong Han,
Shandong Jianzhu University, China

REVIEWED BY
Bo Han,
Shandong University, China
Zhen Guo,
Zhejiang University, China

*CORRESPONDENCE
Junwei Liu,
liujunwei@qut.edu.cn

RECEIVED 09 November 2023
ACCEPTED 08 December 2023
PUBLISHED 08 January 2024

CITATION
Jia Y, Luan S, Asheghabadi MS, Xing D, Yuan H and Liu J (2024), Slope stability analysis of coastal geotechnical structures under combined effects of earthquake and rainfall.
Front. Earth Sci. 11:1335756.
doi: 10.3389/feart.2023.1335756

COPYRIGHT
© 2024 Jia, Luan, Asheghabadi, Xing, Yuan and Liu. This is an open-access article distributed under the terms of the Creative Commons Attribution License (CC BY). The use, distribution or reproduction in other forums is permitted, provided the original author(s) and the copyright owner(s) are credited and that the original publication in this journal is cited, in accordance with accepted academic practice. No use, distribution or reproduction is permitted which does not comply with these terms.

Slope stability analysis of coastal geotechnical structures under combined effects of earthquake and rainfall

Yuyue Jia[1], Shuyang Luan[1], Mohsen Saleh Asheghabadi[1], Dongliang Xing[2], Hang Yuan[3] and Junwei Liu[1]*

[1]School of Civil Engineering, Qingdao University of Technology, Qingdao, China, [2]Shandong Port Group Qingdao Port, Qingdao, China, [3]Qingdao Port International Co., Ltd., Construction Branch Office, Qingdao, China

The primary factors responsible for inducing landslide disasters are earthquakes and rainfall. Using the strength reduction method within the finite element analysis software Abaqus, a study was conducted to analyze the stability of coastal geotechnical slopes. This investigation considered the combined influence of rainfall and earthquakes, taking into account the geological conditions and characteristics specific to these coastal areas. The results indicate that, under the same seismic acceleration amplitude, the shear strength of the slope soil gradually decreases as the water content increases, resulting in a decrease in the stability coefficient. Similarly, with a constant water content in the slope, an increase in seismic acceleration amplitude leads to heightened soil shear stress, consequently decreasing the stability coefficient. Maintaining constant water content while increasing seismic acceleration results in elevated soil shear stress, reduced shear strength, and a subsequent decrease in the stability coefficient. The simultaneous occurrence of intense rainfall and a strong earthquake pushes the slope to its most precarious state, causing the most significant reduction in the stability coefficient. Incorporating anti-slip piles substantially enhances the slope's stability coefficient, and an optimal arrangement of anti-slip piles for the most unfavorable conditions is proposed.

KEYWORDS

slope stability, seismic effects, rainfall, anti-slide piles, coastal geotechnical structures

1 Introduction

Numerous studies (Chen and Meng, 1995; Lin, 2001; Chen et al., 2005) have provided substantial evidence indicating that rainfall, especially extreme rainfall events, is the primary factor responsible for inducing landslide disasters. Coastal geotechnical slopes, owing to their porous structure, loose composition, permeability, and susceptibility to deformation, are notably prone to erosion during rainfall conditions. This result in elevated soil water content, increased weight, and pore water pressure, subsequently reducing the shear strength of the soil. Furthermore, rainfall infiltration alters the slope's water table, inducing changes in the stress field environment. The impermeable structural surfaces of slopes experience hydrostatic pressure, leading to a reduction in the normal stress generated by the weight of the sliding mass. This decrease in normal stress diminishes the soil's resistance to sliding, heightening the slope's susceptibility to instability.

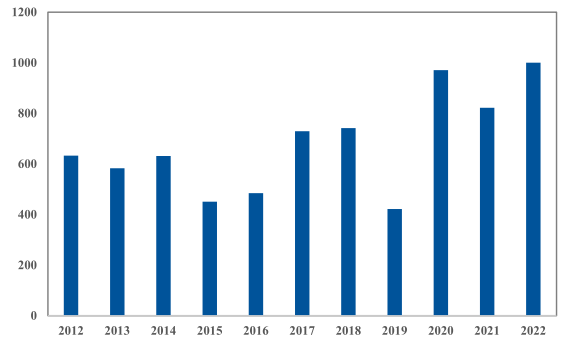

FIGURE 1
Historical precipitation histogram of Laoshan District (2012–2022).

Earthquakes, as indicated by Liangyu (2023), can profoundly affect slope stability. Unlike rainfall, which unfolds gradually, earthquakes exert a transient impact on slopes. In instances where slopes are already unstable and face an earthquake, the dynamic load from seismic waves intensifies shear stresses within the slope soil, thereby weakening its stability and reducing resistance to sliding forces.

When seismic loading is combined with the increased pore water pressure resulting from rainfall, it significantly reduces the slope's stability (Pu, 2017; Xu, 2019). Consequently, when a slope encounters dynamic loading from seismic waves alongside heavy rainfall, this compounded dynamic effect can exacerbate the instability of the slope.

Deploying anti-slip piles is an crucial method to mitigate slope slippage, through the anti-slip piles through the sliding surface of the slope body so that it acts on the layer, to provide better anchorage for the slope. Strategically positioning these piles can better balance the forces acting on the slope, significantly increasing its stability coefficient (JIA et al., 2023; Sang, 2023).

To investigate the stability of coastal geotechnical slopes, the strength reduction dynamic analysis method is employed to conduct dynamic stability analyses under various seismic and rainfall scenarios. The objective is to evaluate slope stability under the most severe conditions resulting from the combined impacts of earthquakes and rainfall, and to identify the optimal positioning of anti-slip piles.

2 Geological conditions and characteristics of geotechnical slopes in coastal areas

The Jiaodong Peninsula region features unique natural geography and engineering geological surroundings. In recent years, an escalation in extreme weather conditions has resulted in a noticeable rise in potential geological disasters, specifically an annual increase in coastal geotechnical slope instability events. This paper concentrates on the Fanlingqian slope in Laoshan District, Qingdao City, for its research. It conducts a comprehensive geological investigation of concealed coastal geotechnical slope disasters, intending to elucidate the regional geological conditions and fundamental characteristics of these disasters.

The landslide slope area in Laoshan District, Qingdao, covers approximately 1.5 km^2 in geographic coordinates. Laoshan District, Qingdao, experiences a warm-temperate monsoon climate, characterized by distinctive temperature and rainfall patterns year-round. It boasts an extensive coastline and can reach winter minimum temperatures of about minus six degrees, with limited hot weather during the summer. In terms of rainfall patterns, there is a higher concentration of precipitation during the summer and fall seasons, heightening the risk of landslide geological disasters. Figure 1 illustrates the recent rainfall data for Laoshan District.

The slopes in the landslide area are exposed in the following sequence, from oldest to newest: Mesozoic Cretaceous Lower Laiyang Group Zhifengzhuang Formation (KlZ) and Cenozoic Quaternary Holocene Shanqian Formation (QS). Bedrock outcrops are observable across the landslide area, characterized by Yanshan Late Granite (γ35) lithology. Site surveys indicate that the landslide area is covered with 3–6 m of slope residue, with well-established vegetation. Portions of the area feature terracing, with upper bedrock exposures. The distribution of rock stratigraphy is detailed in Table 1.

The Fanlingqian landslide comprises four distinct landslides: the main slipped landslide, along with landslides 1, 2, and 3, depicted in Figure 2. On the eastern side of the landslide area, the main slipped landslide has resulted in the formation of a gully, ranging in depth from 1 to 3 m, oriented approximately at 140°. As a consequence of erosive forces, the gully has accumulated numerous fragmented rocks, revealing localized bedrock exposures.

While the landslide area is a unified entity, continuous water flow over several years has divided it into two distinct sections. Consequently, during slope sliding, these two separate segments may slide independently, each having potentially distinct sliding characteristics. Landslide three is located on the southwest side of the main slipped landslide, exhibiting visible creeping deformation near the highway's vicinity, specifically along the trailing edge.

Landslide 1 spans an estimated area of 6.7×10^4 m^2 with a depth of approximately 15 m, categorized as a medium-sized landslide. Positioned 10–20 m from the sea surface, it maintains a trailing edge elevation ranging between 150 and 170 m. Along the highway, its length measures 200 m, and along the perpendicular highway, it extends from 220 to 410 m, gradually increasing from west to east. On the other hand, Landslide 2 covers an approximate area of 4.8×10^4 m^2 with a depth of about 4 m, also categorized as a medium-sized landslide. The shear exit is located between 5 and 20 m from the sea surface, with a trailing edge elevation ranging from 150 to 170 m. The highway spans a length of 255 m, while the perpendicular highway measures 170 m. As for the third landslide, it encompasses an estimated area of approximately 3.4×10^4 m^2, with a depth of about 16 m, categorizing it as a medium-sized landslide. Positioned 5–10 m from the sea surface, it maintains a trailing edge elevation between 55 and 85 m. The highway length within this region extends for 246 m.

In the study area, the predominant material composition of the slide indicates higher consistency in the covering layer, while the primary rock beneath the slide primarily consists of granite with some sandstone. The weathered section of the slide exhibits complexity and lacks uniformity due to the diverse composition of the original rock. As a whole, it can be inferred that the study area is susceptible to landslides, especially during periods of heavy rainfall.

TABLE 1 Composite stratigraphic column profiles.

Chronostratigraphic			Rock stratum						Histogram	thicknesses(m)	Petrographic description
Erathem	Sytem	Series	Group	Formation	Symbol						
Cenozoic	quaternary system	holocene system	—	Shanqian Formation	Q_S	Q_T	Q_Y	Q_{Xk}	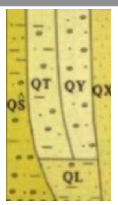	—	Q_YMiddle sedimentary phase Yellow, gray-yellow gravelly mixed-grained sand, 2.5 m thick Q_{Xk}Coastal phase Gray-yellow, light gray-white fine sand, medium fine sand, fine gravelly sand and a small amount of silt layer, 20 m thick Q_TFlood stage Clayey sandy gravel, 5 m thick. Q_LAlluvial phase Brownish-yellow, grayish-yellow clayey silt, gravelly medium-coarse-grained sand, clay, 16 m thick. Q_SResidual slope phase Grayish-yellow, brownish-yellow gravelly sandy clay, clayey sand, sandy clay, clay, 26 m thick
						Q_L					
Mesozoic Erathem	Cretaceous	Lower Cretaceous	Laiyang Group	Zhifengzhuang Formation	K_{LZ}				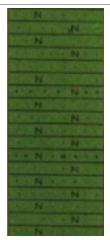	>1116.2	Greenish-gray angularly feldspathic fine-grained sandstone interbedded with greenish-gray angularly feldspathic fine-grained siltstone, coarse-grained feldspathic sandstone, conglomerate-bearing medium-coarse-grained feldspathic sandstone, medium-fine-grained feldspathic sandstone, and silty fine-grained feldspathic sandstone

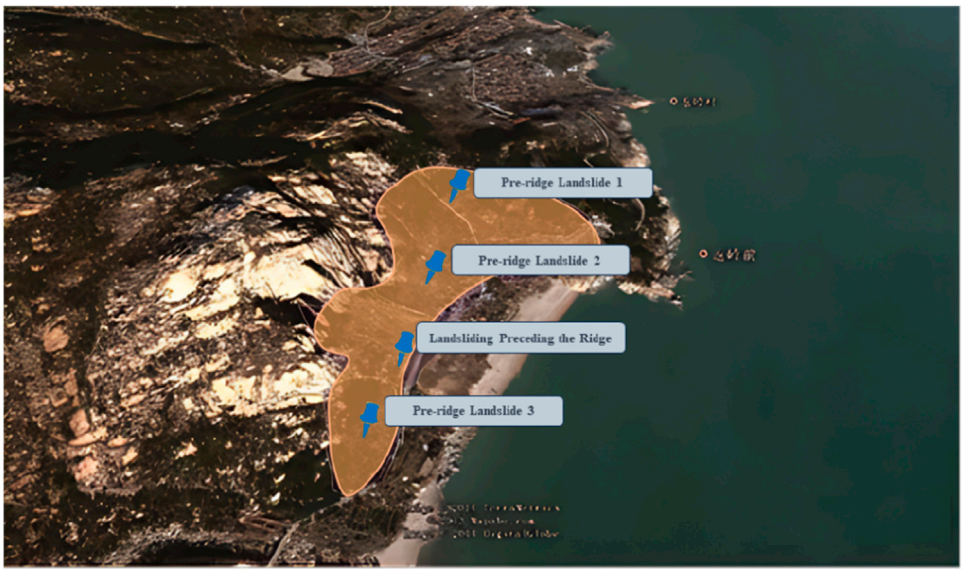

FIGURE 2
Location of landslides.

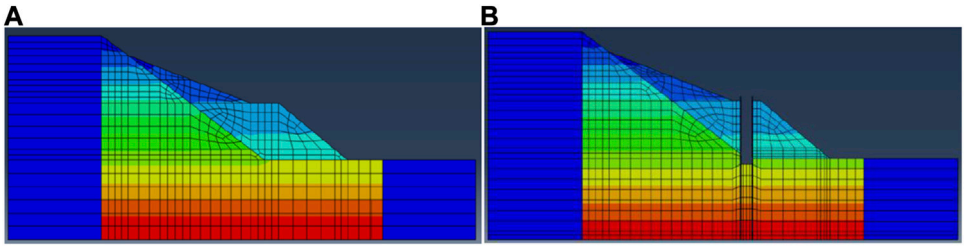

FIGURE 3
Numerical calculation model. **(A)** Free-field model. **(B)** Pile-soil model.

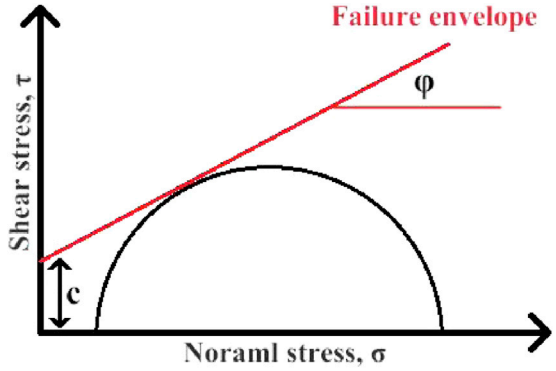

FIGURE 4
Mohr-Coulomb criterion diagram.

3 Using models and computational approaches for analysis

The implicit analysis module and the large deformation mode of the Abaqus finite element software have been chosen. A two-dimensional plane strain model is assumed for calculating and analyzing slope stability issues. The slope model is meshed using the CPE4R reduced integration unit (Asheghabadi et al., 2020a; Asheghabadi et al., 2020b) (Figure 3). The significance of boundary conditions in soil-structure seismic behavior cannot be overstated. Properly defined and implemented boundary conditions serve as a critical link between the modeled system and its real-world environment, influencing the accuracy and reliability of seismic simulations (Asheghabadi and Ali, 2019). In this study, for boundary conditions, infinite elements have been used to prevent the reflection of seismic waves into the model. This boundary condition effectively regulates seismic effects at the model boundaries, ensuring that they do not influence the results obtained from the analysis (Asheghabadi et al., 2019). These specialized elements, often employed in numerical simulations, possess unique characteristics that extend infinitely, facilitating a seamless transition between the modeled domain and its surroundings. Utilizing such elements enables the model to encapsulate seismic dynamics effectively, preventing undesired interactions and enhancing the accuracy of analytical outcomes.

TABLE 2 Soil properties.

Material type	γ(kg/m^3)	*E* (MPa)	*c* (kPa)	*φ*(°)	*μ*
the top of a building	1937	11.42	15.39	31.25	0.35
lowest rung (of society)	2,156	78.00	100.4	44.6	0.20

Slope modeling will use a model capable of accurately simulating the configuration of each geotechnical layer under diverse loading conditions. In this study, considering the model conditions and materials (soil and pile), we employ the elastic-plastic consiyutive model for the soil, the linear-elastic model for the piles, and choose the M-C criterion as the damage criterion. As depicted in Figure 4, the shear strength of the soil correlates with the normal stresses acting on the potential damage surface within the soil. This model is particularly suitable for cohesionless soils (e.g., sandy soils) and partially cohesive soils (e.g., silts) where the cohesion between soil particles is relatively low.

M- C Failure Criterion Eq:

$$\tau = c + \sigma * \tan \varphi$$

where τ is the shear stress on the damage surface; c is the cohesive force; and φ is the internal friction angle.

The calculation of the slope stability coefficient involves employing the strength reduction method to analyze the structure's stability. The analysis includes incrementally raising the reduction factor and iterating the process until reaching the limit state of damage. This state is identified when the slope displacement abruptly increases or when the maximum slope displacement undergoes a sudden change alongside variations in the reduction factor. At this point, the slope stability coefficient is determined.

For Mohr-Coulomb materials, the strength-based factor of safety can be expressed as follows:

$$\tau = \frac{c + \sigma * \tan \varphi}{\omega} = \frac{c}{\omega} + \sigma \frac{\tan \varphi}{\omega} = c' + \sigma \tan \varphi'$$

So there's

$$c' = \frac{c}{\omega}, \tan \varphi' = \frac{\tan \varphi}{\omega}$$

In the formula, c and φ represent the geotechnical cohesion and internal friction angle before reduction, while ω is the reduction

TABLE 3 List of parameters related to different water contents of the soil.

Moisture content (%)	Cohesive force (KPa)	Angle of internal friction (°)
19	44.72	25.42
21	27.41	22.38
26	18.34	19.45
31	14.43	15.17
33	12.80	11.12
39	10.14	8.64

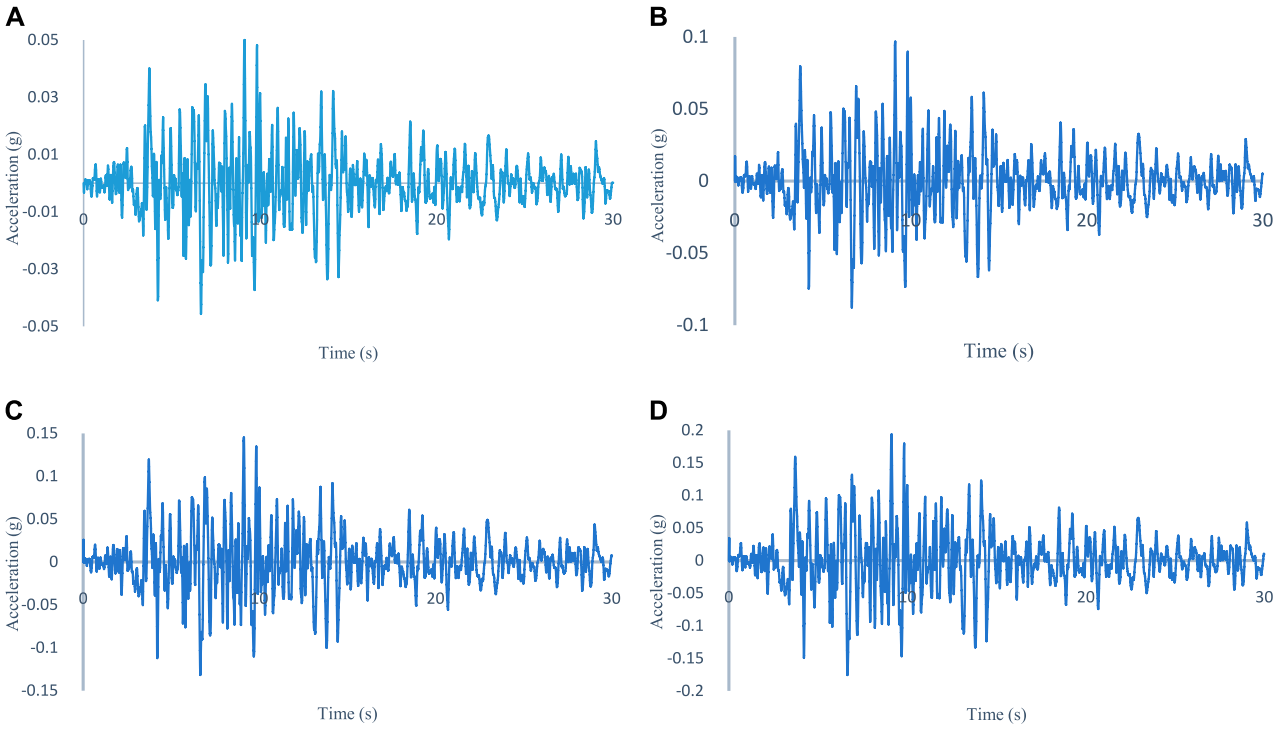

FIGURE 5
Input basement seismic acceleration-time curve **(A)** Free-field model **(B)** Pile-soil modeling. **(A)** PGA = 0.05 g. **(B)** PGA = 0.1 g. **(C)** PGA = 0.15 g. **(D)** PGA = 0.2 g.

coefficient. c' and φ' represent the geotechnical cohesion and internal friction angle after reduction.

4 Selection of physico-mechanical parameters and setting of loading conditions

The model in this study is a pile-soil model, consisting of two layers of soil with different geotechnical properties. Table 2 lists the physico-mechanical parameters for each layer of the geotechnical material.

Studies (Dang et al., 2007) have demonstrated that rainfall influences the geotechnical slope by infiltrating rainwater, consequently altering the water content, cohesion, and internal friction angle. As the water content increases, both cohesion and the internal friction angle non-linearly decrease. At a water content of 26%, the rate of cohesion reduction slows down while the internal friction angle experiences a noticeable decrease with further increases in water content.

To investigate the pattern of stability changes in slopes affected by the combined influence of earthquakes and rainfall, numerical simulations were conducted using soil with varying water content levels: 19%, 21%, 26%, 31%, 33%, and 39%. The relevant soil parameters for different water content levels were specified as detailed in Table 3. In accordance with the guidelines outlined in the 'People's Republic of China Industry Standard (JTGB02-2013, 2014) Seismic Design Code for Highway Engineering,' slope

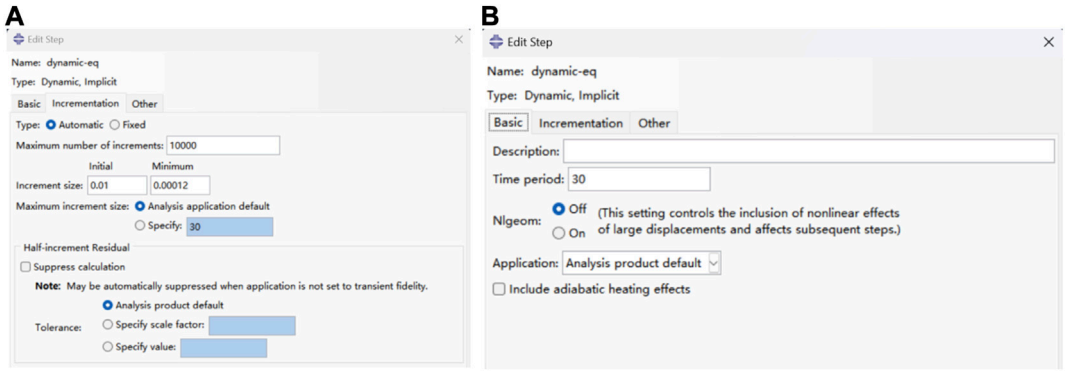

FIGURE 6
Time credit settings. **(A)** Free-field model. **(B)** Pile-soil modeling.

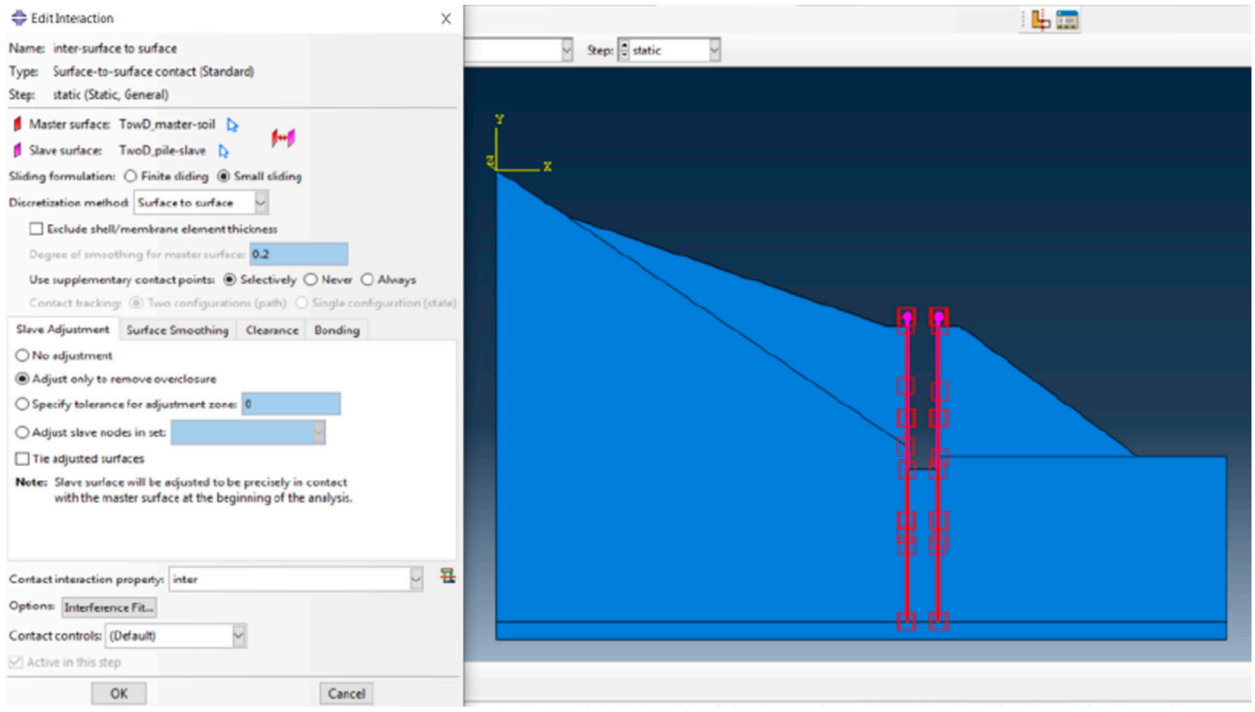

FIGURE 7
Interaction between soil and anti-slide pile through nodes and surface.

acceleration amplitudes of 0.05 g, 0.1 g, 0.15 g, and 0.20 g were applied to assess slope stability under diverse combinations of earthquake and rainfall conditions.

Seismic loading is applied by introducing seismic waves with acceleration amplitudes varying from 0.05 g to 0.20 g into the ABAQUS finite element analysis software. The seismic acceleration-time curves for the model's base inputs are illustrated in Figure 5.

Key features and considerations of the dynamic implicit approach in ABAQUS for seismic pile-soil modeling include:

Time Integration: the implicit time integration scheme used in ABAQUS ensures the attainment of accurate and stable solutions over a range of time steps, thereby enabling the simulation of earthquakes with various frequencies and magnitudes (as depicted in Figure 6).

Material Models: ABAQUS provides a variety of material models to represent the behavior of soils, piles, and interfaces under dynamic loading. These constitutive models capture effects such as plasticity, damping, and nonlinear behavior.

Contacts and Interactions: This method models the interactions between the soil and the pile, considering factors such as pile-soil interactions, as well as soil liquefaction. Figure 7 illustrates the definition of contact and interaction between the soil and the pile.

Boundary conditions: appropriate boundary conditions are defined to represent the constraints of the soil-anti-slide pile system in the actual project (Figure 8).

Damping: The dynamic implicit method allows the inclusion of damping effects, which are essential for accurately modeling the energy

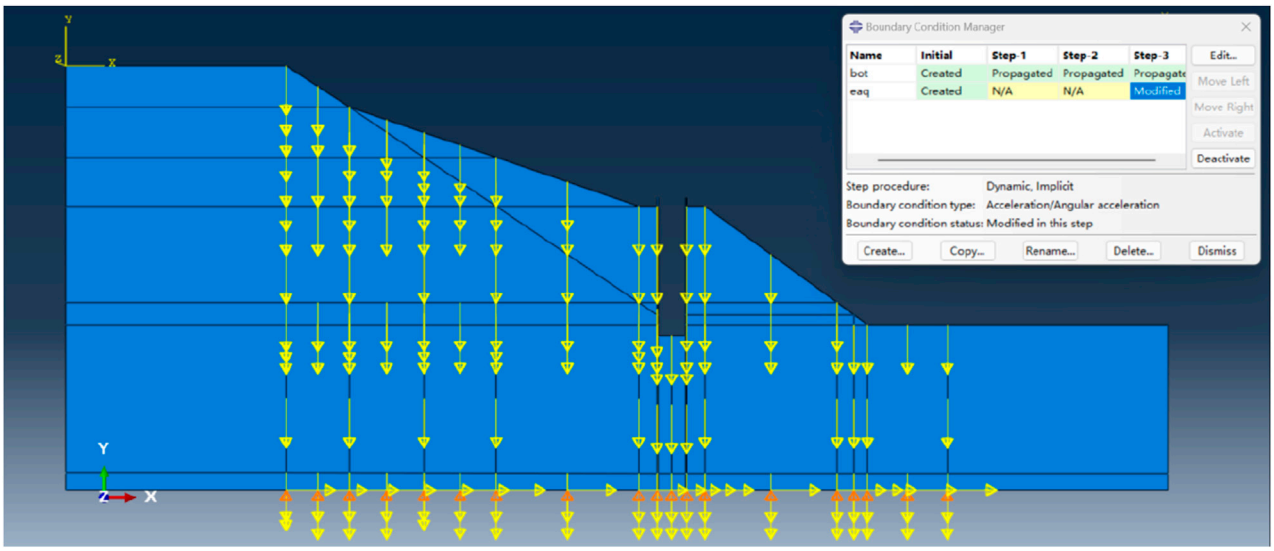

FIGURE 8
Boundary conditions of the model.

dissipation and damping mechanisms in pile-soil systems during earthquakes.

In ABAQUS, meshing is a crucial step in the Finite Element Analysis (FEA) process. Although ABAQUS lacks a dedicated 'meshing' module, meshing operations form the bedrock for generating precise and efficient simulations. Generally classified as part of the preprocessing phase, the meshing process is indispensable for converting intricate geometries and structures into discrete finite element sets. This representation allows for an approximation of the system's physical behavior during analysis. An appropriate mesh structure, element type, and density are crucial for achieving accurate simulation results. The mesh quality directly affects the precision of stresses, strains, displacements, and other simulation outcomes. Furthermore, the meshing process significantly influences the convergence of the analysis. A refined mesh promotes convergence in nonlinear and dynamic simulations, ensuring stable and accurate numerical solutions.

Meshing impacts model contacts and interactions, making properly meshed models easier to visualize and comprehend. ABAQUS visualization tools allow users to scrutinize meshes, detect potential issues, and make informed decisions regarding refinements.

5 Effects of earthquake and rainfall compounding on the plastic zone and displacement of slopes in coastal geotechnical bodies

5.1 Effect of water content on the plastic zone of slopes

By analyzing the graphs (Figure 9) depicting the change in the slope's plastic zone for different water contents (19%, 21%, 26%, 31%, 33%, and 39%), it is evident that water content has a highly significant effect on the development of the slope's plastic zone. As water content increases, there is a clear tendency for the slope's plastic zone to expand. When the water content is low, a small plastic zone forms from the base of the slope to the middle, and it is not widely connected. With the increase of water content, the plastic zone extends from the sliding area to the top of the slope. The equivalent plastic strain increases from 0.075 to 0.12, eventually forming a continuous plastic zone, with the equivalent plastic strain reaching 0.152. This closely aligns with the test results, and the location of fissures corresponds to the location of the plastic zone.

5.2 Effect of earthquake and rainfall compounding on slope displacement

This section analyzes the variations in displacement at specific representative points along the slope (points 9, 25, 28, 30, 36), as depicted in Figure 10. Figure 11 showcases the displacement changes observed at these five points. The descending order of displacement change among these points is as follows: point 28 > point 9 > point 30 > point 36 > point 25. This ranking suggests that the central area of the slope experiences the most significant displacement, followed by the trailing edge, while the leading edge shows the least displacement. Consequently, point 28, which exhibits the largest slope displacement, is selected for further analysis.

The displacement change curve at point 28 on the slope, with a water content of 39% and a seismic acceleration amplitude of 0.20 g, is plotted in Figure 12. It is apparent that the displacement at point 28 rises with increasing seismic acceleration magnitude, maintaining the same water content of 39%. The most significant increase occurs when the seismic acceleration magnitude varies from 0.05 g to 0.10 g. Figure 13 also illustrates the displacement at point 28. Under a consistent seismic acceleration magnitude of 0.20 g, the displacement at point 28 increases with higher water content. The most noticeable increase in displacement occurs when the slope water content varies from 31% to 39%.

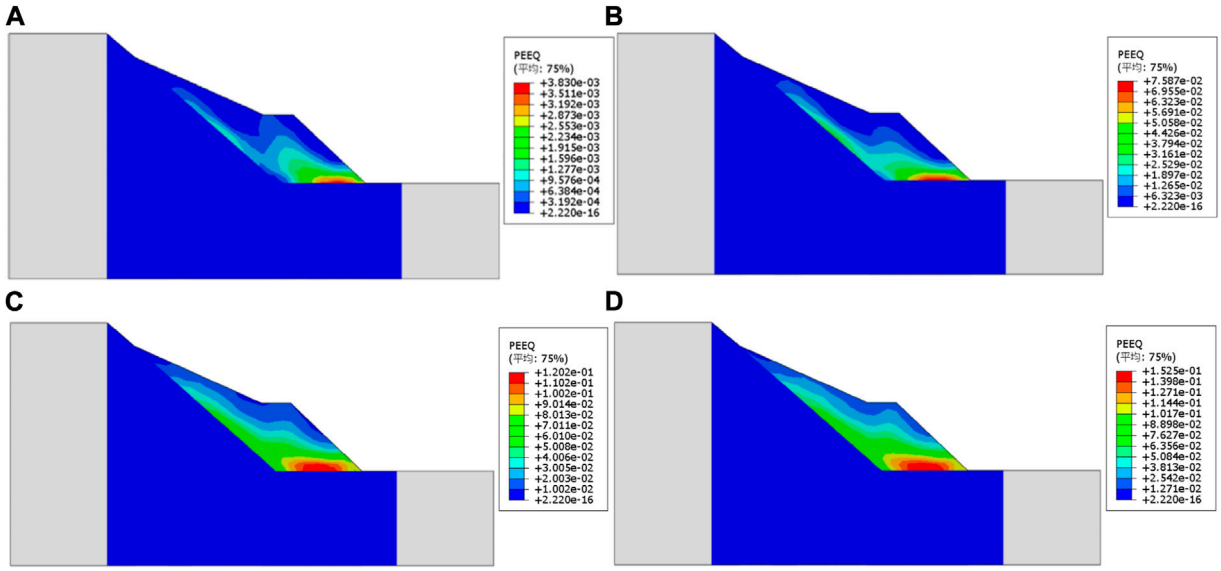

FIGURE 9
Variation of plastic zone of soil with difficult water content. **(A)** 19% water content **(B)** 26% water content **(C)** with 33% water content **(D)** 39% water content.

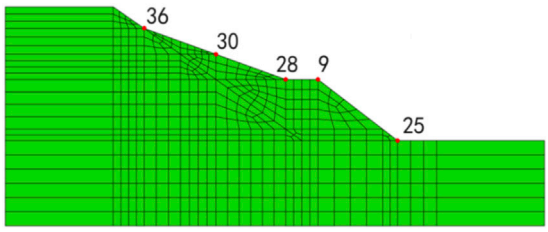

FIGURE 10
Map of observed point locations on the slope.

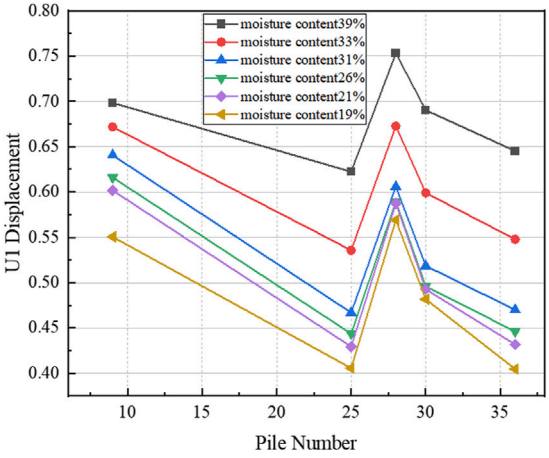

FIGURE 11
Curve of displacement with water content at different points on the slope.

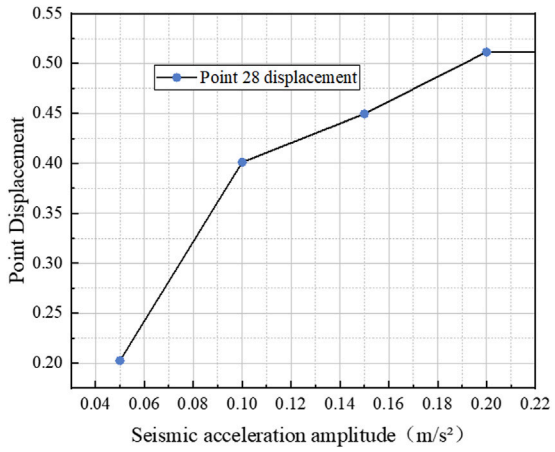

FIGURE 12
Curve of displacement as a function of seismic acceleration.

5.3 Slope stability analysis of coastal geotechnical bodies under composite conditions of earthquake and rainfall

5.3.1 Slope stability evolution laws under composite conditions of earthquake and rainfall

A total of 24 sets of loading conditions were established for various rainfall conditions (water content of 19%, 21%, 26%, 31%, 33%, 39%) and seismic conditions (seismic acceleration amplitude of 0.05 g, 0.1 g, 0.15 g, 0.20 g). These conditions enabled us to derive the stability coefficient change patterns of coastal geotechnical slopes under various combinations, as depicted in Table 4.

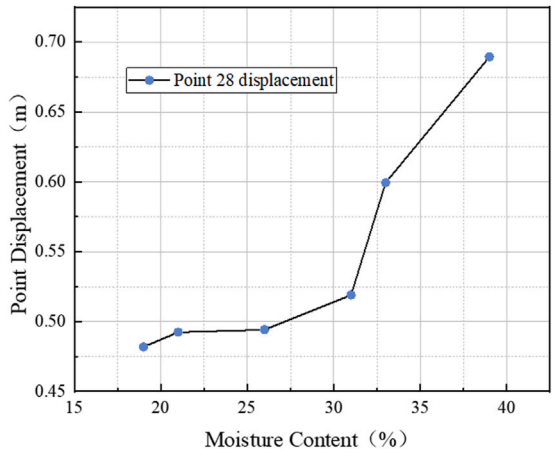

FIGURE 13
Curve of displacement as a function of moisture content.

TABLE 4 Slope stability coefficients under different combinations of working conditions.

Stability factor		Seismic acceleration amplitude (m/s)			
		0.05 g	0.1 g	0.15 g	0.2 g
moisture content (%)	19	1.31	1.27	1.23	1.18
	21	1.23	1.16	1.10	1.03
	26	1.13	1.04	0.98	0.93
	31	1.05	0.98	0.93	0.88
	33	0.97	0.92	0.87	0.82
	39	0.91	0.84	0.77	0.72

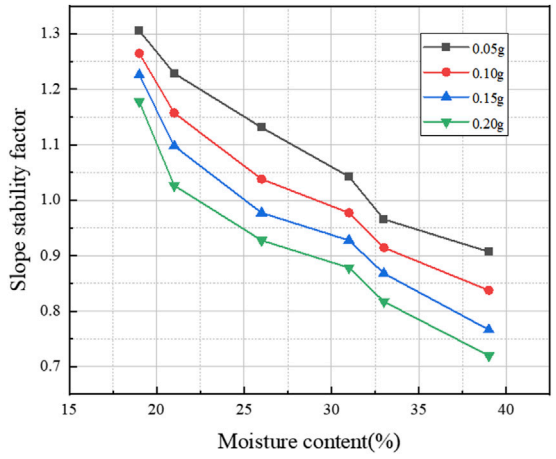

FIGURE 14
Variation curve of slope stability coefficient for different seismic acceleration amplitude conditions.

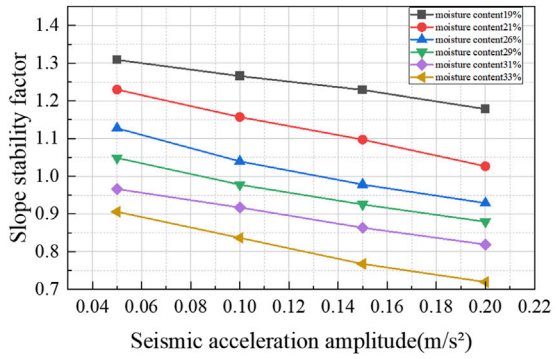

FIGURE 15
Variation curve of slope stability coefficient for different water content conditions.

As shown in Figure 14, under the same seismic acceleration amplitude (0.05 g, 0.10 g, 0.15 g, 0.20 g), the slope's shear strength decreases gradually as the water content increases, leading to a subsequent reduction in the stability coefficient. The stability coefficient decreases by 30.53%, 33.86%, 37.40%, and 38.98%, respectively, as the slope's water content increases from 19% to 39%. Similarly, as presented in Figure 15, under constant slope water content, the soil's shear stress on the slope rises with increasing seismic acceleration amplitude, causing a progressive decline in the stability coefficient. The stability coefficients decreased by 9.92%, 16.26%, 17.70%, 16.19%, 15.46%, and 20.88% sequentially as the acceleration amplitude increased from 0.05 g to 0.20 g for slope water contents of 19%, 21%, 26%, 31%, 33%, and 39%, respectively.

5.3.2 Plastic zone, displacement and stress analysis of slopes under the most unfavorable working conditions

Based on the analysis results presented in Figures 14, 15, it is observed that the slope stability coefficient is at its lowest when subjected to a seismic acceleration amplitude of 0.20 g and a water content of 39%. Hence, this condition can be designated as the most unfavorable working condition. The equivalent plastic strain, lateral displacement, minimum stress distribution, and maximum stress distribution of the slope under this most unfavorable condition are illustrated in Figure 16.

Under the most unfavourable condition combination, the plastic zone of the slope gradually expands from the top to the base of the slope, and the equivalent plastic strain at the base of the slope is the highest, reaching 0.152. In instances of slope instability, the plastic zone extends gradually from the base to the top of the slope. Lateral displacement predominantly occurs in the middle and lower sections of the slope, with the surface layer experiencing a maximum lateral displacement of 0.475 m. As the slope progresses towards its inner part, the lateral displacement steadily decreases. The maximum and minimum principal stresses along the longitudinal direction of the slope are 1206 N and 302.9 N, respectively. Additionally, the maximum lateral displacement of the slope surface is 0.475 m, which gradually reduces as it extends towards the interior of the slope.

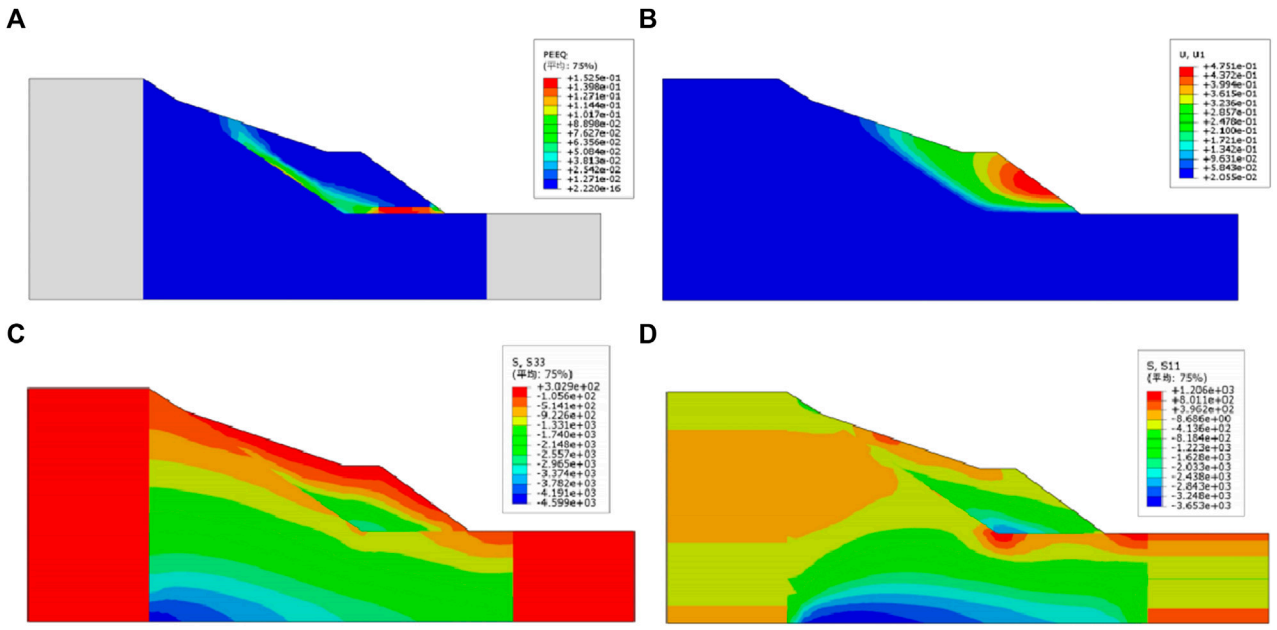

FIGURE 16
Characterization of stress field and strain field for the most unfavorable condition of the slope. **(A)** Equivalent plastic strain diagram **(B)** Lateral displacement map **(C)** Minimum stress distribution **(D)** Maximum stress distribution.

5.4 Optimized design of anti-slip pile location

In slope engineering management, anti-slip piles wield significant influence and are widely employed across various projects. In recent decades, they've been effectively used to stabilize numerous slopes. However, geological conditions in different landslide-prone areas can vary significantly. Particularly in the presence of sudden events such as earthquakes and heavy rainfall, the effectiveness of anti-slip piles and the overall stability coefficients of slopes can dynamically fluctuate. Moreover, traditional anti-slip pile design often involves a level of subjectivity and arbitrariness when determining design parameters. In specific slope lands, this design approach might pose potential risks to slope stability due to insufficient safety margins, while in other cases, it could result in unnecessary project costs due to excessive safety margins. Consequently, the theory and methodology of anti-slip pile design are not yet fully developed, especially lacking a unified standard for selecting principles and calculation methods for anti-slip pile design parameters. Moreover, the wide array of slope geotechnical parameters, slope types, and slope hydrogeology, among other factors, presents numerous variations that must be considered in the decision-making process to derive the most viable solutions. Thus, a comprehensive understanding of the mechanics of anti-slip piles becomes crucial for the specific slope environment. It involves elucidating the authentic pile-soil synergistic effects on internal displacement, plastic zone, and variations in the stability coefficient change patterns of the slope, thereby determining the optimal approach to anti-slip pile design. Of all the design aspects of anti-slip piles, the positioning of these piles stands out as the most crucial design parameter. This section delves into an analysis using the coastal geotechnical slope near Laoshan Railing in Qingdao as an example to explore the selection of different configurations for anti-slip piles. This investigation focuses on the most adverse conditions, encompassing the combined effects of rainfall and earthquakes. Specifically, the investigation involves a slope exposed to a seismic acceleration of 0.20 g and a soil water content of 39%. The study evaluates the impact of these factors on the plastic zone, displacement, and slope stability to determine the optimal design for anti-slip piles. To facilitate in the selection of the most suitable positioning for anti-slip piles under these extreme conditions and provide guidance for analogous designs of coastal geotechnical slopes, we have developed the following methodology for anti-slip pile design in such settings.

In this section, we consider the most extreme conditions involving the combined influence of earthquakes and rainfall, where the slope experiences a seismic acceleration amplitude of 0.20 g and maintains a soil water content of 39%. We investigate the optimal locations for anti-slip piles and propose three different pile positions, spanning from the foot to the lower part of the slope for the study (refer to Figure 17). Table 5 and Figures 18, 19 present the slope stability coefficients, maximum transverse displacements, and distribution regions of the plastic zone for the three types of pile positions, respectively.

As shown in Figure 18A and Figure 19A, when l/L is 0.321, the anti-slip pile is positioned very close to the slope. This positioning places the anti-slip pile too far forward, leaving a substantial area of unreinforced soil at the slope's rear vulnerable to potential sliding surfaces generated under external dynamic loads like earthquakes or rainfall. The slope's stability coefficient

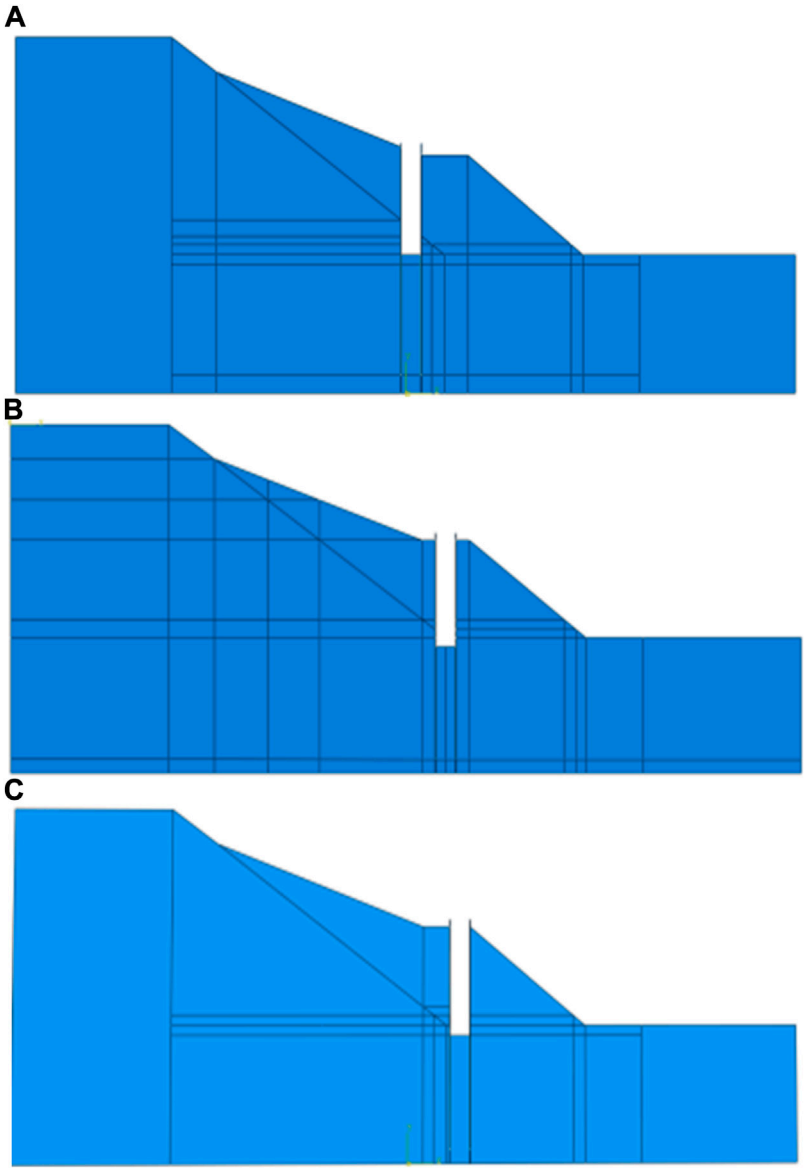

FIGURE 17
Schematic diagram of different pile designs. **(A)** Slip-resistant pile position occurs when *l*/*L* is 0.441. **(B)** Slip-resistant pile position occurs when *l*/*L* is 0.355. **(C)** Slip-resistant pile position occurs when *l*/*L* is 0.321.

TABLE 5 Table of simulation results for pile changes.

Pile position (*l*/*L*)	0.441	0.355	0.321	0
stability factor	1.41	1.22	1.16	0.72
transverse displacement(m)	0.017	0.018	0.019	0.475
equivalent plastic strain	0.005	0.125	0.169	0.152

stands at 1.16, marking a 61.11% increase over the value of 0.72 without piles. The maximum lateral displacement of the slope measures 0.019 m, accompanied by a maximum equivalent plastic strain of 0.169. Despite minimal slope displacement, the improper location design underutilizes the reinforcing capacity of the anti-slip piles, constraining their effectiveness.

At l/L = 0.355 (Figure 18B; Figure 19B), the slope's stability coefficient increases by 69.44% compared to the slope without piles, reaching a value of 1.22. The maximum lateral displacement measures 0.018 m, accompanied by a maximum equivalent plastic strain of 0.125. However, the slightly increased distance from the front leaves some unconsolidated soil similar to the scenario at l/L = 0.321. This unconsolidated soil may result in a new plastic zone in the rear of the slope, potentially forming a new sliding surface. Nonetheless, this solution represents an improvement over the previous one as it reinforces a larger area of the affected soil.

At l/L = 0.441 (Figure 18C; Figure 19C), with the anti-slip pile positioned at the back of the leading edge of the slope, the stability coefficient reaches 1.41. This marks a 95.83% increase in slope

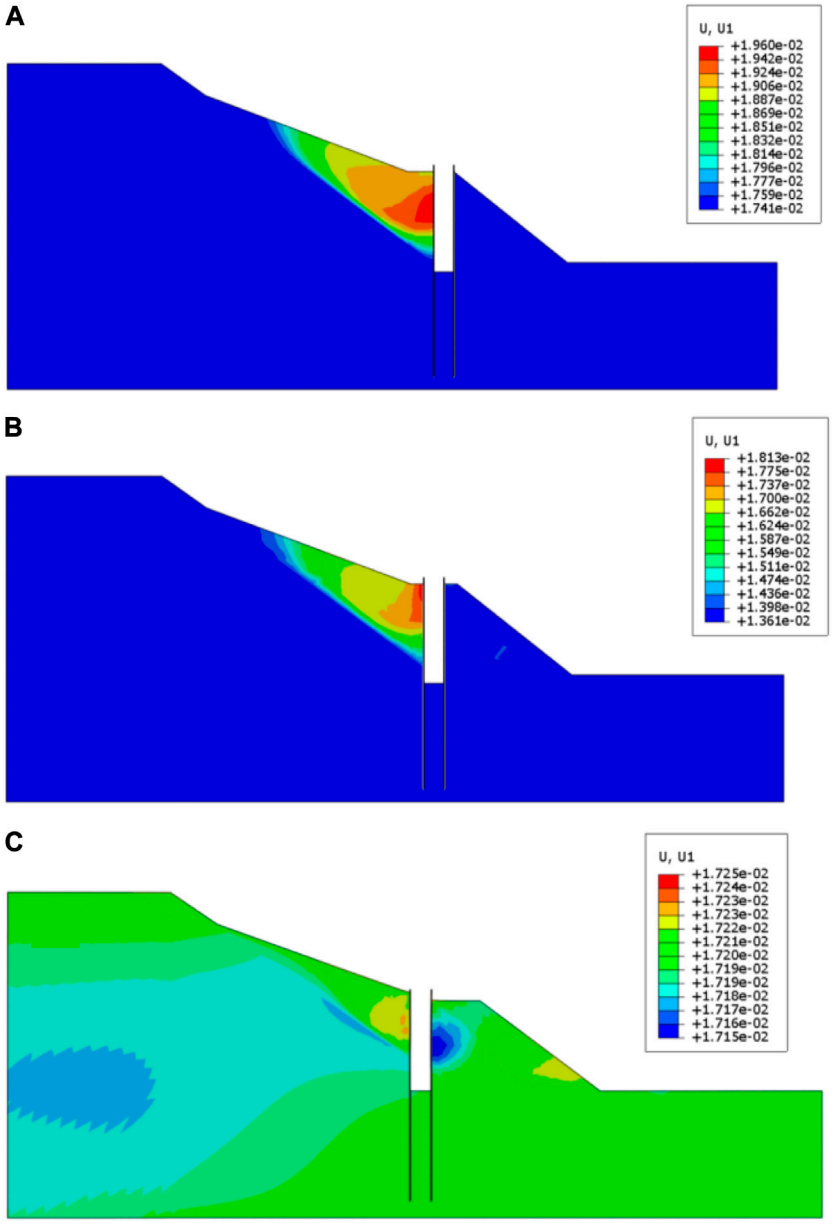

FIGURE 18
Lateral displacement of the slope for the most unfavorable condition when l/L change. **(A)** *l*/*L* = 0.321. **(B)** *l*/*L* = 0.355. **(C)** *l*/*L* = 0.441.

stability compared to the condition without piles. The maximum lateral displacement measures 0.017 m, with an equivalent plastic strain of only 0.005. This placement maximizes the strengthening effect of the anti-slip piles, resulting in the highest stability coefficient for the slope.

To summarize, it can be concluded that anti-slip piles enhance the stability coefficient of the slope. Overall slope stability improves with an increase in the distance between the anti-slip pile location and the leading edge of the slope. The optimal pile position is near the back of the leading edge with l/L equal to 0.441. At this point, the anti-slip pile's supporting effect is most effective, resulting in the highest slope stability.

5.5 Analysis of the mechanism of rainfall-earthquake composite action on landslides

After analyzing the calculation results, significant changes in the slope stability coefficient due to the combined effects of rainfall and earthquakes are evident. It is inferred that rainfall primarily impacts landslides in several ways. Firstly, rainfall exerts a load-boosting effect on landslide soils by increasing water infiltration, consequently raising the moisture content of rocks and soil, resulting in higher density. This, in turn, results in an increase in shear stress on the sliding surface. Secondly, rainfall infiltration affects the strength parameters of the landslide, as higher soil

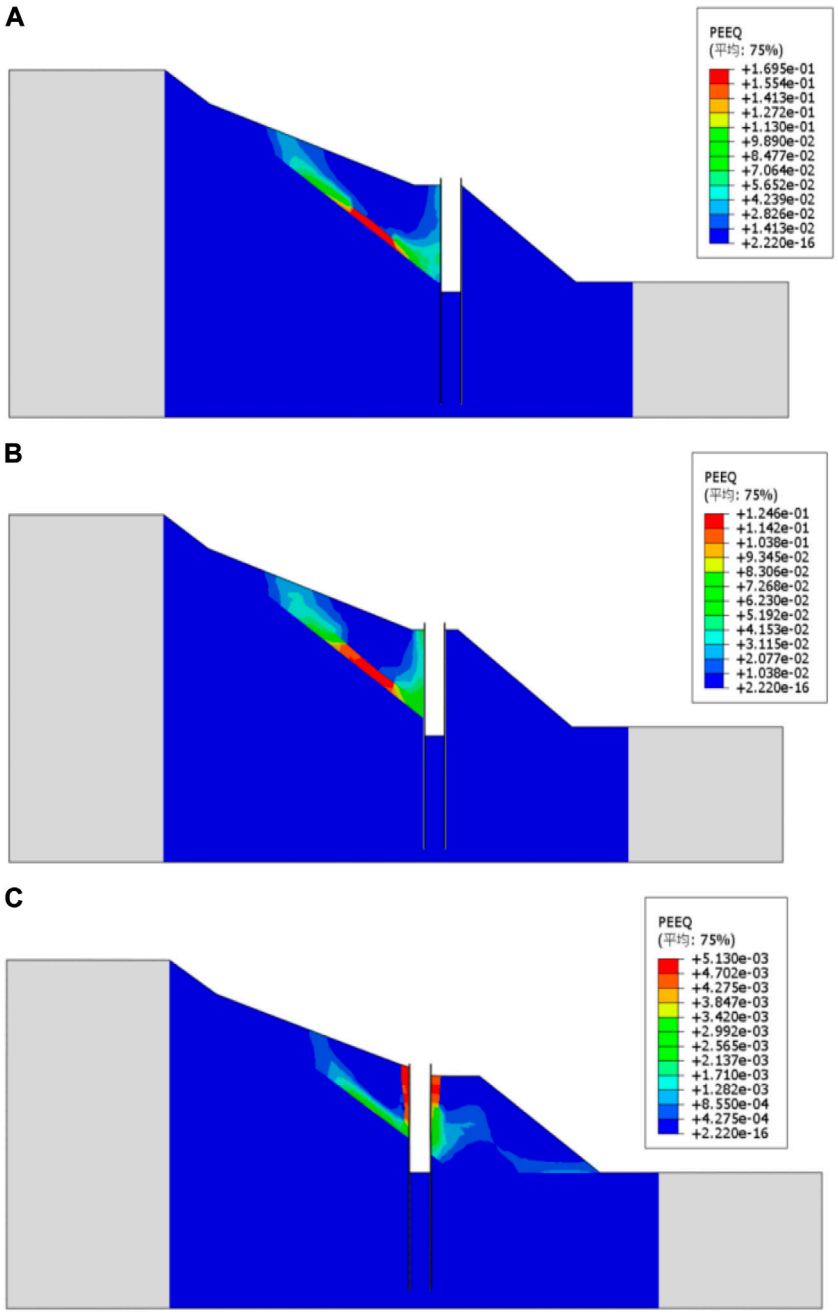

FIGURE 19
Distribution of slope plasticity zones for l/L is change. **(A)** *l*/*L*=0.321. **(B)** *l*/*L* = 0.355. **(C)** *l*/*L* = 0.441.

moisture content reduces matrix suction, consequently lowering the strength parameters.

The effects of seismic activity on landslides include the following phenomena: seismic loading induces significant disturbances within the landslide, leading to the enlargement of geotechnical cracks, increased permeability of the landslide, and subsequent plastic deformation. Additionally, seismic forces cause a sudden increase in pore water pressure within the geotechnical material, resulting in a decrease in effective stress. Both of these situations contribute to the reduction of geotechnical strength.

6 Conclusion

In this chapter, the stability of coastal geotechnical slopes under the combined effects of earthquakes and rainfall is analyzed based on actual conditions. Simultaneously, an optimal design study for anti-slip pile positioning is conducted by selecting the most unfavorable combination of conditions. The main conclusions are as follows.

(1) As the water content increases, the shear strength of the slope decreases, leading to an expansion of the plastic zone. When the

water content is low, a small and disjointed plastic zone forms from the base of the slope to the middle of the slide. However, with an increase in water content, the plastic zone extends from the sliding area to the top of the slope, gradually forming a continuous plastic zone.

(2) Analyzing the displacement patterns of representative key points on the slope while discounting the slope's shear strength parameters reveals that the central region of this coastal geotechnical slope experiences the greatest displacement, followed by the trailing edge, while the leading edge exhibits the least displacement. When focusing on the central point as the subject of analysis, it is observed that, at the same water content (39%), the displacement at the central point increases as the seismic acceleration amplitude rises. The most significant increase is noted when the seismic acceleration amplitude ranges from 0.05 g to 0.10 g. At the same seismic acceleration amplitude (0.20 g), the displacement at the central point increases with higher water content, particularly in the range from 31% to 39%, resulting in a notable rise in displacement. Similarly, for the equivalent seismic acceleration magnitude (0.20 g), an increase in water content leads to an increase in displacement at the central point. The most pronounced increase in displacement is observed when the water content varies from 31% to 39%.

(3) The combined influence of rainfall and earthquakes significantly impacts slope stability. With the same seismic acceleration amplitude, an increase in water content results in a decrease in slope shear strength and a subsequent gradual decline in its stability coefficient. Similarly, maintaining the same water content within the slope, an increase in seismic acceleration amplitude leads to heightened shear stress in the soil, consequently causing a gradual decrease in the slope's stability coefficient. Remarkably, the most substantial reduction in the slope stability coefficient happens when intense rainfall, marked by elevated water content within the slope, aligns with a high seismic acceleration amplitude, placing the slope in its most unfavourable working condition.

(4) The stability coefficient significantly increases with the installation of anti-slip piles on the slope. As the distance between the anti-slip pile and the leading edge of the slope increases, the stability coefficient of the slope gradually improves. Based on the project's conditions, the optimal location for the anti-slip pile is near the leading edge of the slope at the rear, with l/L equal to 0.441.

Data availability statement

The original contributions presented in the study are included in the article/Supplementary material, further inquiries can be directed to the corresponding author.

Author contributions

YJ: Methodology, Software, Writing–original draft, Writing–review and editing. SL: Writing–original draft, Writing–review and editing. MA: Software, Writing–original draft, Writing–review and editing. DX: Writing–review and editing. HY: Writing–review and editing. JL: Supervision, Writing–review and editing.

Funding

The authors declare financial support was received for the research, authorship, and/or publication of this article. Supported by the Shandong Provincial Natural Science Foundation (Grant No. ZR2021YQ31); Taishan Scholars Program (Grant No. tsqn202211176); National Nature Science Foundation of China (Grant No. 42277135); Joint Funds of the National Natural Science Foundation of China (Grant No. U2006225).

Conflict of interest

Author HY was employed by Qingdao Port International Co., Ltd.

The remaining authors declare that the research was conducted in the absence of any commercial or financial relationships that could be construed as a potential conflict of interest.

Publisher's note

All claims expressed in this article are solely those of the authors and do not necessarily represent those of their affiliated organizations, or those of the publisher, the editors and the reviewers. Any product that may be evaluated in this article, or claim that may be made by its manufacturer, is not guaranteed or endorsed by the publisher.

References

Asheghabadi, M. S., and Ali, Z. (2019). Infinite element boundary conditions for dynamic models under seismic loading. *Indian J. Phys.* 94 (6), 907–917. doi:10.1007/s12648-019-01533-4

Asheghabadi, M. S., and Cheng, X. (2020a). Analysis of undrained seismic behavior of shallow tunnels in soft clay using nonlinear kinematic hardening model. *Appl. Sci.* 10 (8), 2834. doi:10.3390/app10082834

Asheghabadi, M. S., and Cheng, X. (2020b). Investigation of seismic behavior of clay-pile using nonlinear kinematic hardening model. *Adv. Civ. Eng.* 2020, 1–15. doi:10.1155/2020/9617287

Asheghabadi, M. S., Sahafnia, M., Bahadori, A., and Bakhshayeshi, N. (2019). Seismic behavior of suction caisson for offshore wind turbine to generate more renewable energy. *Int. J. Environ. Sci. Technol.* 16 (16), 2961–2972. doi:10.1007/s13762-018-2150-8

Chen, J., Yang, Z., and Li, X. (2005). Relationship between landslide occurrence probability and precipitation conditions in the Three Gorges reservoir area. *J. Rock Mech. Eng.* 24 (17), 3052–3056.

Chen, Z., and Meng, B. (1995). Spatial and temporal distribution and correlation of rainfall-type landslide debris flows and their rainfall factors in Hubei Province. *Geotechnics* 16 (3), 62–69. doi:10.16285/j.rsm.1995.03.010

Dang, J., Hu, L., and Nan, S. (2007). Study on the effect of water content and natural density on shear strength parameters of soil. *West. China Sci. Technol.* 7 (5), 14–15.

Jia, Y., Lv, W., He, K., et al. (2023). Experimental study on slope stability of accumulation layer under traffic load. *J. Water Resour. Archit. Eng.* 21 (03), 65–73. doi:10.3969/j.lssn.1672-1144.2023.03.010

JTGB02-2013 (2014). *Seismic design Code for highway engineering [S]*. Beijing: People's Transportation Press.

Liangyu, C. (2023). *Stability analysis of slopes under the combined effect of rainfall and earthquake[D]*. Zhenjiang, Jiangsu, China: Jiangsu University.

Lin, X. (2001). Research on landslides and rainfall. *Geol. Hazards Environ. Prot.* 12 (3), 1–7.

Pu, X. (2017). *Study on the instability of loess slope under earthquake and rainfall coupling action based on large shaking table model test[D]*. Lanzhou, Gansu, China: Lanzhou Institute of Seismology.

Sang, G. (2023). *Study on the stability influencing factors and optimization analysis of slope reinforced by anti-slip pile[D]*. Hefei, Anhui, China: Anhui Jianzhu University.

Xu, J. (2019). *Numerical simulation analysis of the stability of ancient landslides in Longdongpo, Guizhou under rainfall and seismic conditions and study of damage mechanism[D]*. Xiamen, Fujian, China: Xiamen University.

frontiers | Frontiers in Earth Science

TYPE Original Research
PUBLISHED 09 January 2024
DOI 10.3389/feart.2023.1348366

Check for updates

OPEN ACCESS

EDITED BY
Jianyong Han,
Shandong Jianzhu University, China

REVIEWED BY
Shufeng Pei,
North China University of Water Conservancy and Electric Power, China
Xiaoqiang Zhang,
Taiyuan University of Technology, China

*CORRESPONDENCE
Bingrui Chen,
brchen@whrsm.ac.cn

RECEIVED 02 December 2023
ACCEPTED 28 December 2023
PUBLISHED 09 January 2024

CITATION
Li P, Wang Z, Chen B, Peng J, Zhang B, Zhao J and Xie H (2024), Rockburst hazard assessment and prevention and control strategies in the Ruihai gold mine.
Front. Earth Sci. 11:1348366.
doi: 10.3389/feart.2023.1348366

COPYRIGHT
© 2024 Li, Wang, Chen, Peng, Zhang, Zhao and Xie. This is an open-access article distributed under the terms of the Creative Commons Attribution License (CC BY). The use, distribution or reproduction in other forums is permitted, provided the original author(s) and the copyright owner(s) are credited and that the original publication in this journal is cited, in accordance with accepted academic practice. No use, distribution or reproduction is permitted which does not comply with these terms.

Rockburst hazard assessment and prevention and control strategies in the Ruihai gold mine

Pengxiang Li[1,2], Zongwen Wang[3], Bingrui Chen[1,2]*, Jianping Peng[3], Bochao Zhang[3], Jinshuai Zhao[4] and Houlin Xie[2]

[1]Institute of Underground Space for Stability and Support of Surrounding Rock, Heze University, Heze, China, [2]State Key Laboratory of Geomechanics and Geotechnical Engineering, Institute of Rock and Soil Mechanics, Chinese Academy of Sciences, Wuhan, China, [3]Zhaojin Mining Industry Co., Ltd., Laizhou, China, [4]Faculty of Civil Engineering and Mechanics, Jiangsu University, Zhenjiang, China

Ruihai gold mine is a super large underwater gold mine with an initial mining depth of more than 1,400 m. Deep mining may face rockburst disaster. In order to scientifically control the potential rockburst risk, ensure the safety of underground personnel and equipment, and realize the safe and efficient mining of the mine, it is necessary to evaluate the rockburst risk of the mine and formulate appropriate rockburst risk warning and mitigation strategies. XRD mineral composition analysis and conventional rock mechanical tests were carried out on the parent rock granite samples. The results show that there are differences in the lithologic composition and rock mechanics parameters of the three colors of granite, which are preliminarily determined as three kinds of granite; The rockburst tendency of three kinds of granites is evaluated by using three classical rockburst criteria, and the discrimination results of the three rockburst criteria are not completely consistent or even contradictory. The application limitations rockburst risk assessment based on index criteria are discussed and analyzed in detail. It is proposed to apply microseismic monitoring technology to warn and manage the rockburst risk of Ruihai gold mine in development and mining stages, and put forward microseismic monitoring layout schemes and targeted rockburst prevention and control measures in different stages. The research results can provide reference for similar projects.

KEYWORDS

deep buried mine, rockburst criterion, microseismic monitoring, warning and mitigation rockburst, rockburst risk

1 Introduction

With the depletion of shallow mineral resources, more and more mines are entering the deep or even ultra-deep mining areas (Cai and Brown, 2017; Liu et al., 2023). The frequent occurrence of rockburst disasters induced by high stress in deep mining areas has become a prominent issue. Rockburst is a complex dynamic geological disaster in which the elastic strain energy accumulated in the rock mass suddenly releases due to excavation or other external disturbances under high stress environment, leading to rock fracturing and ejection. It can cause serious casualties and equipment damage (Feng, 2017; Li et al., 2019a; Li et al., 2023a; He et al., 2023).

Extensive research has been conducted on rockburst mechanism, early warning and control since the first record of rockburst in the 19th century. However, rockburst is a global

challenge, and its mechanism remains not adequately understood, even reaching a consensus on its definition (Kaiser and Cai, 2012; Feng, 2017; Li et al., 2019b). In terms of rockburst warning, scholars have proposed various empirical criteria and assessment methods for evaluating rockburst risk based on the factors affecting rockburst occurrences (Zhou et al., 2018; Li et al., 2019a; Gong et al., 2020; He et al., 2023). These include criteria such as Russense criteria (Russenes, 1974), Barton criteria (Barton et al., 1974), Hoek criteria (Hoek and Brown, 1980), strain energy storage index (Kidybinski, 1981), potential energy of elastic strain (Wang and Park, 2001), residual elastic energy index (Gong et al., 2021), rock brittleness index (Xu and Wang, 1999), brittle deformation coefficient (Zhang et al., 2017), distance discrimination method (Gong and Li, 2007), artificial neural network method (Wang et al., 2024), etc. These criteria and assessment methods have greatly guided the prevention and control of rockburst risks and have achieved good economic and social benefits. They have played an important guiding role, particularly in formulating strategies for rockburst prevention and control, mine development design, selection of mining methods and mining processes, and design of support methods (Mazaira and Konicek, 2015; Leveille et al., 2017). With the continuous deepening of research on rockburst and the development of scientific technology, rockburst risk on-site monitoring technology is increasingly being applied to rockburst risk management of mines. On site monitoring mainly involves directly or indirectly monitoring a series of parameters such as stress, deformation, and damage of the surrounding rock mass, in order to evaluate and infer the risk of rockburst. Microseismic monitoring technology can detect the elastic waves generated by small fractures in rock masses. These elastic waves contain valuable information about the internal stress and fracture development trends of the rock mass (Li et al., 2019b; Zhao et al., 2022; Zhao et al., 2023). By monitoring and analyzing microseismic events (each elastic wave is considered a microseismic event) during the process of rock fracture damage, it is possible to infer the degree of damage and development trends of the rock mass, thereby achieving the prediction and early warning of rockburst disasters. Microseismic monitoring has the characteristic of 24-h continuous real-time monitoring. Microseismic technology has become an important means of early-warning and controlling rockburst disasters (Li et al., 2023b; Kan et al., 2023).

The Ruihai gold mine is characterized by "large mine reserves, large investment capital, long investment cycle, and long construction period". The designed mining capacity of the mine is 3.96 million tons per year, and the initial mining depth can reach over 1,400 m. It is a super-deep buried mine of a large scale. Deep mining may face the risk of rockburst disasters. To scientifically manage and control the potential rockburst risks, ensure the safety of underground personnel and equipment, and achieve safe and efficient mining of the mine, it is necessary to assess the rockburst risks of the mine and develop appropriate rockburst risk prevention and control strategies to realize the construction of a first-class modern mine.

In this paper, the samples of granite from Ruihai gold mine were separated into three sub-rock types based on XRD rock composition results, and uniaxial compression experiments were conducted on the three types of granite to obtain the basic mechanical parameters of the rocks. Then, rockburst tendency criteria such as rock brittleness criteria, deformation brittleness coefficient, Barton criteria were applied to determine the rockburst tendency of the three types of rocks. The results show that the three types of rocks have different degrees of rockburst risk, and it is necessary to warn and control rockburst risk based on rock type. The results also indicate that using different rockburst criteria for the same type of rock may yield different or even contradictory rockburst risk determination results, and the limitations of rockburs tendency criteria are discussed. Finally, considering the limitations of rockburst index criteria and the need for real-time warning in mines, the microseismic monitoring technique is then to be appliedto conduct comprehensive microseismic rockburst monitoring and early warning during the development and mining stages of the Ruihai gold mine. The layout plan for microseismic monitoring at different stages and specific rockburst prevention and control measures were determined. The research results have important guiding significance for the Ruihai gold mine and other similar projects, and can provide strong support for the construction of the first-class inherently safe mines.

2 Overview of the Ruihai gold mine project and geological conditions

The Ruihai gold mine is located in the northern part of Laizhou City and is currently the largest single rock gold deposit discovered in China. The total ore resource of the mine is about 114 million tons, with a gold resource reserve of more than 470 tons and an average grade of Au 4.12 g/t. The designed mining and selection capacity of the mine is 3.96 million tons per year, making it a super-large mine. Most of the ore bodies in the mine are buried at a depth of over 1,000 m, and the first mining area at the −1,480 section is over 1,400 m deep. During the production period, mining will continue to go deeper, and the mining depth will exceed 1,800 m. The mining of ultra-deep mines is very likely to induce rockburst and other problems, which pose a great threat to safety production, seriously endangering the lives and equipment safety of on-site personnel, and also causing a large amount of resources to be unrecoverable, becoming permanent losses.

The Ruihai gold deposit is completely located in the submarine rock formation, making it an underwater mining operation. The rock type of the mine is relatively uniform, with the roof and floor of the deposit consisting of schistose granite, schistose fractured rock, and pyrite schistose granite fractured rock. The rocks are relatively hard, and there is a risk of rockburst. The engineering geological conditions of the deposit depend on the degree of development of the rock structure. The fault structures in the area are well developed, and the local rocks within the fault zone are more fragmented, strongly altered, and have more developed fractures and broken cores, making them relatively unstable. Overall, the fault structures in the mining area are well developed, and the surrounding rocks near the deposit are relatively stable. However, there are some areas where engineering geological problems such as block falling and collapse are prone to occur, and the impact is severe. The complexity of the engineering geological conditions in the mining area is moderate.

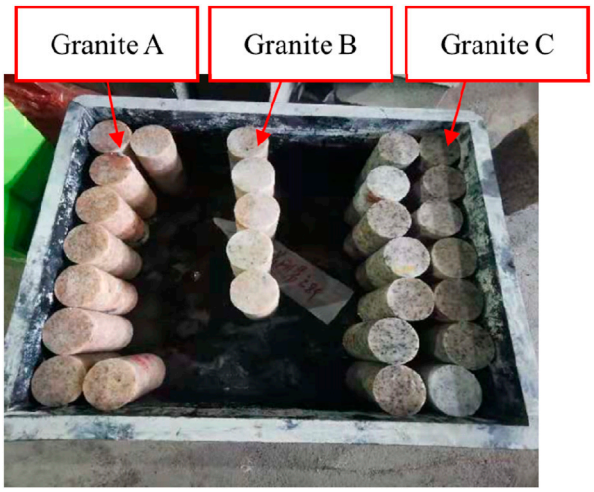

FIGURE 1
Rock specimens for tests.



FIGURE 2
Test equipment for the samples.

3 Rock mechanics test

3.1 Rock sample preparation

The surrounding rock of the ore body is mainly granite. We conducted conventional mechanical tests on the granite to assess its tendency for rockburst, in order to scientifically control the potential risk of rockburst. The granite samples were taken from the 1,300–1,480 level of the Ruihai gold mine, and more than 30 granite blocks were obtained. In the laboratory, diamond drill bits were used to drill rock cores, which were then processed into the following specimens using a cutting and grinding machine: the sample size for uniaxial compression strength (UCS) test was 50 mm × 100 mm, and the size of for Brazilian tensile strength (BTS) test was 50 mm × 25 mm. The ends and sides of the specimens were carefully ground, and the non-parallelism and non-perpendicularity were both less than 0.02 mm. The accuracy of the specimens met the experimental specifications recommended by the International Society for Rock Mechanics (ISRM). The rock specimens are shown in Figure 1.

During the processing, it was found that the granite specimens showed three different colors, which may be three different types of granite, as shown in Figure 1. For the time being, we named them Granite A, Granite B, and Granite C, in order to further analyze the differences in rock types, X-ray diffraction (XRD) analysis was performed on the three colors of granite, and the analysis results are shown in Table 1.

From the analysis results in Table 1, it can be seen that the rock composition of the three colors of granite differs significantly, and it can be determined that they are three different types of granite. Therefore, when conducting rock mechanics experiments, they need to be classified for testing. A total of 28 standard rock specimens for uniaxial compression strength test were processed, including 9 Granite A, 5 Granite B, and 14 Granite C specimens. There were also 5 Brazilian tensile strength test specimens for Granite A and Granite C, respectively.

3.2 Experimental equipment and methods

The equipment used in this experiment was the ZTRE-210 microcomputer-controlled rock triaxial testing system produced by Changchun Zhantuo Experimental Instrument Co., Ltd., as shown in Figure 2. Displacement control was used to apply loading to the rock samples for uniaxial compression test and Brazilian tensile test, with a loading speed of 0.0002 mm/s. The purpose of the uniaxial compression test was mainly to obtain the basic mechanical parameters of the rock and to determine its rockburst tendency, while the purpose of the Brazilian tensile test was mainly to obtain the tensile strength of the rock. Five standard specimens were selected for uniaxial compression strength tests for each type of granite, and five Brazilian disc specimens were selected for Granite A and Granite C for Brazilian tensile strength tests (there is no Brazilian tensile test samples for Granite B).

TABLE 1 Analysis results of X-ray diffraction composition of three types of granite.

Lithology	Quartz (%)	Feldspar (%)	Plagioclase (%)	Calcite (%)	Dolomite (%)	Clay mineral (%)	Biotite (%)
Granite A	33.7	12.1	46.5	1.9	2.4	1.1	2.3
Granite B	25.2	18	47.8	2.1	3.5	1.3	2.1
Granite C	32.7	15.4	42	0	3.1	2.1	4.7

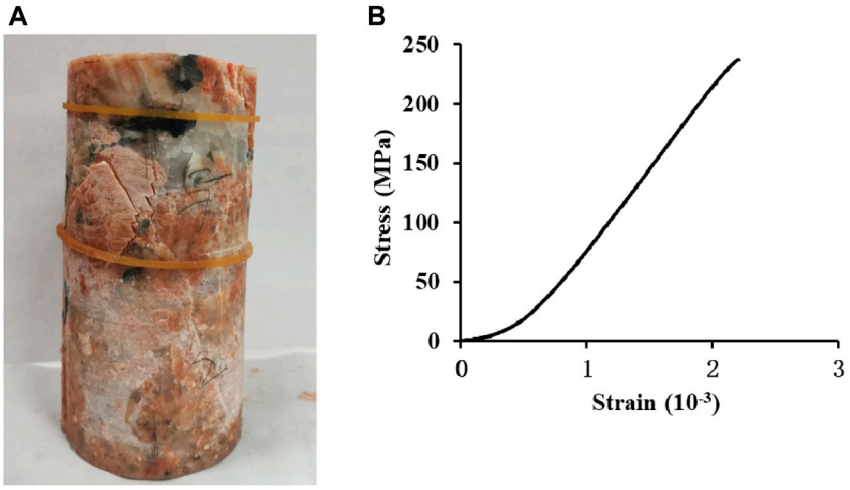

FIGURE 3
Results of uniaxial compression test on granite A. **(A)** Typical failure forms, **(B)** Stress-strain curve.

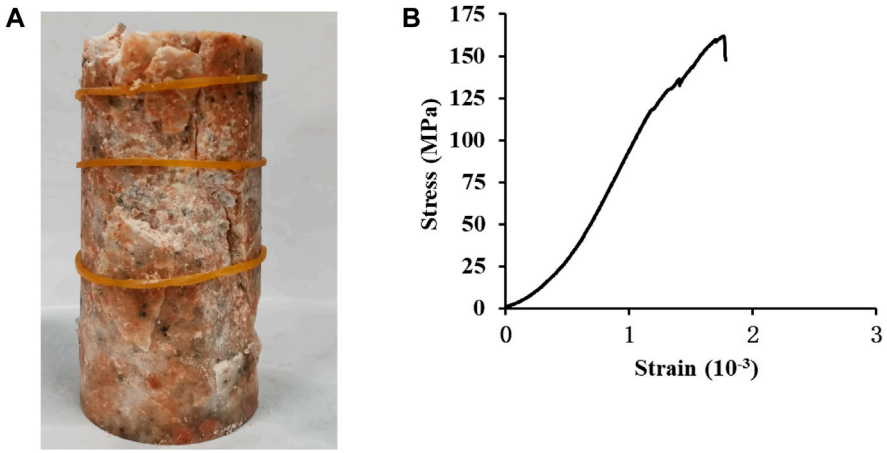

FIGURE 4
Results of uniaxial compression test on granite B. **(A)** Typical failure forms, **(B)** Stress-strain curve.

3.3 Experimental results

During the experimental process, varying degrees of rock powder and debris were observed to be ejected from all three types of granite, accompanied by sound and large rock fragments being ejected when sample failure approached. Overall, the above conditions were more pronounced in Granite C, followed by Granite A, and finally Granite B. The failure modes of the three types of granite are shown in Figures 3A, 4A, 5A.

Figures 3B, 4B, 5B show the typical full stress-strain curves of the three types of granite. It can be seen from the figures that the ultimate strain of the three types of granite is less than 3‰, with Granite B and C having an ultimate strain of less than 2‰, which is typical of brittle rocks. This can also be seen from the characteristics of rock failure in Figures 3A, 4A, 5A, where the rocks exhibit tensile and brittle failure. Due to the high strength and strong brittleness of the rocks, although the control of the loading speed at 0.0002 mm/s, only a small amount of post-peak deformation was observed in some of the rock samples. The basic mechanical parameters of Granite A, Granite B, and Granite C are shown in Table 2.

4 Assessment of rockburst tendency in the Ruihai gold mine

4.1 Rockburst tendency criterions used in the Ruihai gold mine

Using typical rockburst tendency criterions such as rock brittleness criteria (Xu and Wang, 1999), deformation brittleness coefficient (Zhang et al., 2017), and Barton criteria (Barton et al., 1974), a prediction of rockburst risk was made for the Ruihai gold mine. The expressions and discrimination intervals of the criterions are shown in Table 3.

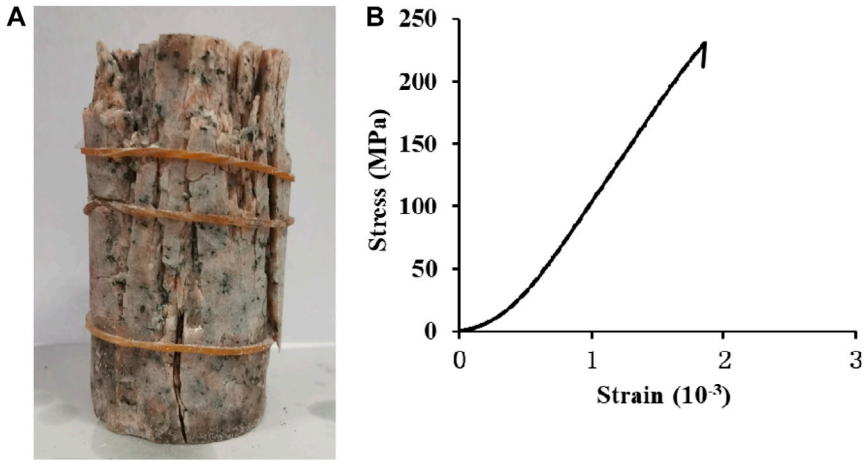

FIGURE 5
Results of uniaxial compression test on granite C. **(A)** Typical failure forms, **(B)** Stress-strain curve.

TABLE 2 Mechanical parameters of intact granite rocks.

Lithology	Uniaxial compression strength (MPa)	Tensile strength (MPa)	Elastic modulus (GPa)	Poisson's ratio
Granite A	116–237	9.5	135.2–140.0	0.21–0.32
Granite B	127–211	---	109.1–148.5	0.20–0.34
Granite C	202–244	7.8	140.1–167.0	0.22–0.31

TABLE 3 Typical criteria for evaluating rockburst risks.

Criteria name	Criteria expression	Prediction results of rockburst intensity			
		No rockburst	Slight rockburst	Moderate rockburst	Intense rockburst
Rock brittleness criteria	$B = \sigma_c/\sigma_t$	<10	10–14	14–18	≥18
Deformation brittleness coefficient	$K_U = U/U_I$	<2	2–6	6–9	≥9
Barton criteria	σ_c/σ_1	>10	5–10	2.5–5	≤2.5

Note: represents the uniaxial compressive strength of the rock; represents the tensile strength of the rock; represents the maximum principal stress of the original rock; U represents the total deformation before the peak strength of the rock, while U_I, represents the plastic deformation before the peak strength.

4.2 Rockburst tendency results determined by the brittle deformation coefficient and rock brittleness criterion

According to the experimental parameters of rock mechanics in section 3.3, the rock brittleness criterion B and the deformation brittleness coefficient K_U were applied to determine the rockburst tendency of three types of granite. The determination results of granite A, B, and C are shown in Tables 4–6. It can be seen from Tables 4–6 that the rockburst risk of granite C is moderate to intense, the rockburst risk of granite A is slight to intense, and the rockburst tendency of granite B is slight to moderate. The rockburst tendency of granite C is greater than that of granite A, and the rockburst tendency of granite A is greater than that of granite B.

4.3 Rockburst tendency results determined by the Barton criterion

According to the *in situ* stress test results of the 2# drill hole of the Ruihai gold mine, the stress field in the exploration area is mainly dominated by horizontal stress, and the ratio of maximum horizontal principal stress S_H to vertical principal stress S_v is 1.06–1.41, with an average of 1.24. The ratio of the two horizontal principal stresses is 1.19–1.54, with an average of 1.37 (Peng and Sun, 2016). The maximum value of the horizontal principal stress is 12.61–39.74 MPa, and the minimum value of the horizontal principal stress is 10.64–28.89 MPa.

From Figure 6, it can be observed that the two horizontal principal stresses and the vertical principal stress increase with the increase of the overlying rock layer thickness or burial depth,

TABLE 4 Prediction results of rockburst tendency of granite A.

Criteria name	Value of the criteria	Prediction results of rockburst intensity
Rock brittleness criteria	12.2–24.9	Slight to intense rockburst
Deformation brittleness coefficient K_U	4.6–6.2	Slight to moderate rockburst

TABLE 5 Prediction results of rockburst tendency of granite B.

Criteria name	Value of the criteria	Prediction results of rockburst intensity
Deformation brittleness coefficient K_U	4.3–6.1	Slight to moderate rockburst

TABLE 6 Prediction results of rockburst tendency of granite C.

Criteria name	Value of the criteria	Prediction results of rockburst intensity
Rock brittleness criteria	25.9–31.3	Intense rockburst
Deformation brittleness coefficient K_U	6.5–9.1	Moderate to intense rockburst

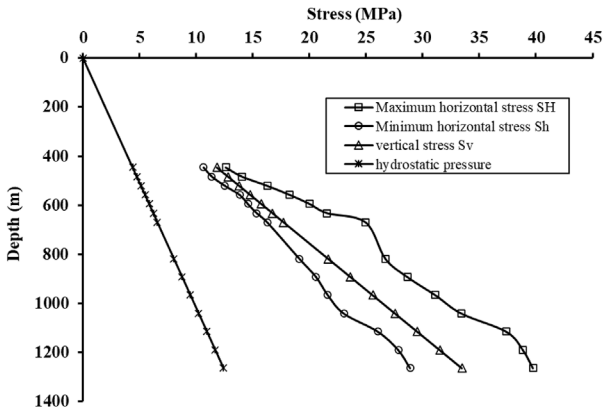

FIGURE 6
Diagram of the variation of principal stress values with depth (Results from number 2 borehole).

and they show a basically linear relationship. The linear regression equations for the maximum (S_H) and minimum (S_h) horizontal principal stresses of each measuring point in drill hole 2 of the gold mine in the northern waters of Sanshan Island are as follows:

$S_H = 0.74+0.033D$

$S_h = 1.08+0.022D$

$S_v = 0.00+0.027D$

Where D is the depth of the drill hole (positive downwards), m; S_H is the maximum horizontal principal stress, MPa; S_h is the minimum horizontal principal stress, MPa; S_v is vertical principal stress, MPa.

Based on the fitting relationship between the stress and depth, it can be inferred that the maximum principal stresses in the −1,480 and −1,300 levels are 49.6 and 43.6 MPa, respectively. By applying the rock mechanics parameters and stress conditions to the Barton criterion, the rockburst risks in the two sections can be predicted, as shown in Tables 7, 8. From the tables, it can be seen that in the −1,480 level, Granite A has a moderate to intense rockburst risk, Granite B and Granite C have a moderate rockburst risk; in the −1,300 section, Granite A and Granite B have a moderate rockburst risk, and Granite C has a slight to moderate rockburst risk.

4.4 Discussion about the rockburst tendency results determined by the different criterions

From the deformation brittleness coefficient, rock brittleness criterion, and Barton criterion for the rockburst tendency determined results of Granite A, Granite B, and Granite C, it can be seen that all three criterions indicate that there is a risk of rockburst occurrence in these three types of granite. However, it can also be observed that different criterions may lead to inconsistent or even different rockburst risk assessments for the same type of granite. For example, when using the deformation brittleness coefficient K_U criterion, granite C has the highest rockburst risk among the three types of granite, with a moderate to strong rockburst risk. However, when using the Barton criterion, granite C has the lowest rockburst risk among the three types of granite, with a slight to moderate rockburst risk at −1,300 level. Different criteria seem to lead to some contradictions in the rockburst risk levels assigned to the same rock. In fact, despite a series of explorations and studies by domestic and foreign scholars on rockburst, the understanding of the mechanism of rockburst and the warning of rockburst has been deepening. However, because rockbursts are an extremely complex dynamic phenomenon, there is still no unified understanding of the mechanism of rockburst.

Although there are many rockburst criterions at present, these criterions are mostly single factor criterion that are considered one-sided and do not consider the necessary and sufficient conditions for rockburst occurrence, namely, the external driving force of rockburst occurrence, i.e., stress conditions, and the internal conditions for rockburst occurrence, i.e., the inherent energy storage and

TABLE 7 Prediction results of rockburst intensity for 1,480 level using Barton Criterion.

Lithology	Uniaxial compression strength (MPa)	Maximum principal stress (MPa)	Calculated values of Barton criterion parameters	Prediction results of rockburst intensity
Granite A	116–237	49.6	2.3–4.8	Moderate to intense
Granite B	127–211	49.6	2.6–4.3	Moderate
Granite C	202–244	49.6	4.1–4.9	Moderate

TABLE 8 Prediction results of rockburst intensity for 1,300 level using Barton Criterion.

Lithology	Uniaxial compression strength (MPa)	Maximum principal stress (MPa)	Calculated values of Barton criterion parameters	Prediction results of rockburst intensity
Granite A	116–237	43.6	2.7–4.8	Moderate
Granite B	127–211	43.6	2.9–4.8	Moderate
Granite C	202–244	43.6	4.6–5.6	Slight to moderate

consumption characteristics of the rock. For example, criterions such as the Barton criterion, Russense criterion, and Hoek criterion criterion only consider stress conditions, without considering whether the rock itself has a tendency to rockburst. Energy and rock brittleness criteria, such as rock brittleness criteria, deformation brittleness coefficient, impact index K_E, and strain energy index W_{et}, only consider whether the rock mass itself has a tendency to rockburst, without considering whether the external driving force of stress conditions for rockburst occurrence has been reached. Both of the above criterions may lead to misjudgments of the occurrence level of rockburst. For example, in the first type of situation, the external driving force may reach the conditions for rockburst occurrence, but if the rock does not have a tendency to rockburst (such as soft rock), then the rockburst will not occur. In the second type of situation, although the rock itself is judged to be prone to rockburst, if the external driving force does not reach the rockburst threshold, then the rockburst will not occur, either. The above stress factors (external conditions) and the rock's own rockburst tendency (internal conditions) are both necessary conditions rather than sufficient conditions for rockburst. Rockburst can only occur if the above two conditions are met at the same time. Moreover, the above conclusion is only obtained at the experimental scale. Due to the complexity of engineering rock masses, such as local stress changes, variable rock structures, and geological conditions, the above indicators have certain limitations in predicting and warning rockburst. However, rockburst criterions still have important significance, as they can provide guidance for mine design, roughly delineate key areas of concern for rockburst, and develop rockburst prevention and control strategies.

5 Rockburst risk warning and prevention and control in the Ruihai gold mine

5.1 Microseismic monitoring system used in the Ruihai gold mine

Based on the above sections, it is evident that the Ruihai granite has a tendency for rockburst under all three criterions, and some even assess it as having a high level risk of rockburst. Therefore, it is necessary to carry out on-site monitoring to conduct daily risk management and control of rockburst.

Based on previous engineering experience and in combination with the microseismic monitoring methods recommended by the ISRM (Xiao et al., 2016), a new generation of high-precision intelligent microseismic monitoring system for rock fracture produced by Hubei Seaquake Technique Co., Ltd was selected. This system can continuously monitor rockburst disasters in rock engineering for 24 h, achieving real-time automatic data acquisition, analysis, and positioning of microseismic data. It can obtain micro-fracture information of the entire process of rockburst disaster incubation, providing a basis for the evaluation of rock mass stability and disaster warning and prediction, and providing technical support for engineering management and rockburst prevention and control. The hardware of the microseismic monitoring system mainly includes sensors, data acquisition devices, communication devices, time synchronization servers, and data servers. Some hardware is shown in Figure 7. The sensor converts the ground motion (ground velocity or acceleration) into a measurable electrical signal. The data acquisition device is responsible for converting the analog electrical signal from the sensor into a digital signal, and then transmitting the data to the data server for analysis and processing through the communication equipment.

The software of the microseismic monitoring system mainly consists of system configuration management software, microseismic waveform data processing software, microseismic event visualization and interpretation software, and real-time display software for microseismic events, as shown in Figure 8.

5.2 Microseismic monitoring and prevention and control of rockburst risk in development roadways of −1,300 and −1,480 levels

The design of the development roadway excavation adopts the drilling and blasting method. Considering the characteristics of

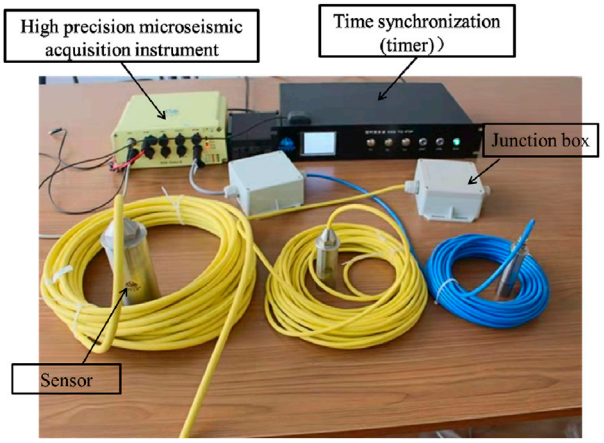

FIGURE 7
Hardware of microseismic monitoring system.

linear engineering of the development roadway and the optimized layout of the sensor array, combined with previous successful sensor layout schemes, the microseismic monitoring plan is as follows: one microseismic acquisition device and six microseismic sensors will be installed in the development roadway, including five uniaxial sensors and one triaxial sensor. Each sensor has a natural frequency of 10 Hz, a response ranging from 10 to 2,000 Hz, and a sensitivity of 100 V/m/s. They will be arranged in two cross-sections, with three sensors in each cross-section. The installation of the I-I monitoring section is selected at a distance of about 50–60 m from the working face (the specific distance depends on the on-site construction conditions), with the No. 1 sensor being a triaxial sensor and the other two being uniaxial sensors. The borehole depth for sensor installation is 2–3 m. The tunnel is excavated 40 m forward, which means that the I-I monitoring section is about 90–100 m away from the tunnel face. A second monitoring Section II-II is arranged at a distance of about 50–60 m from the tunnel face (the specific distance depends on the on-site

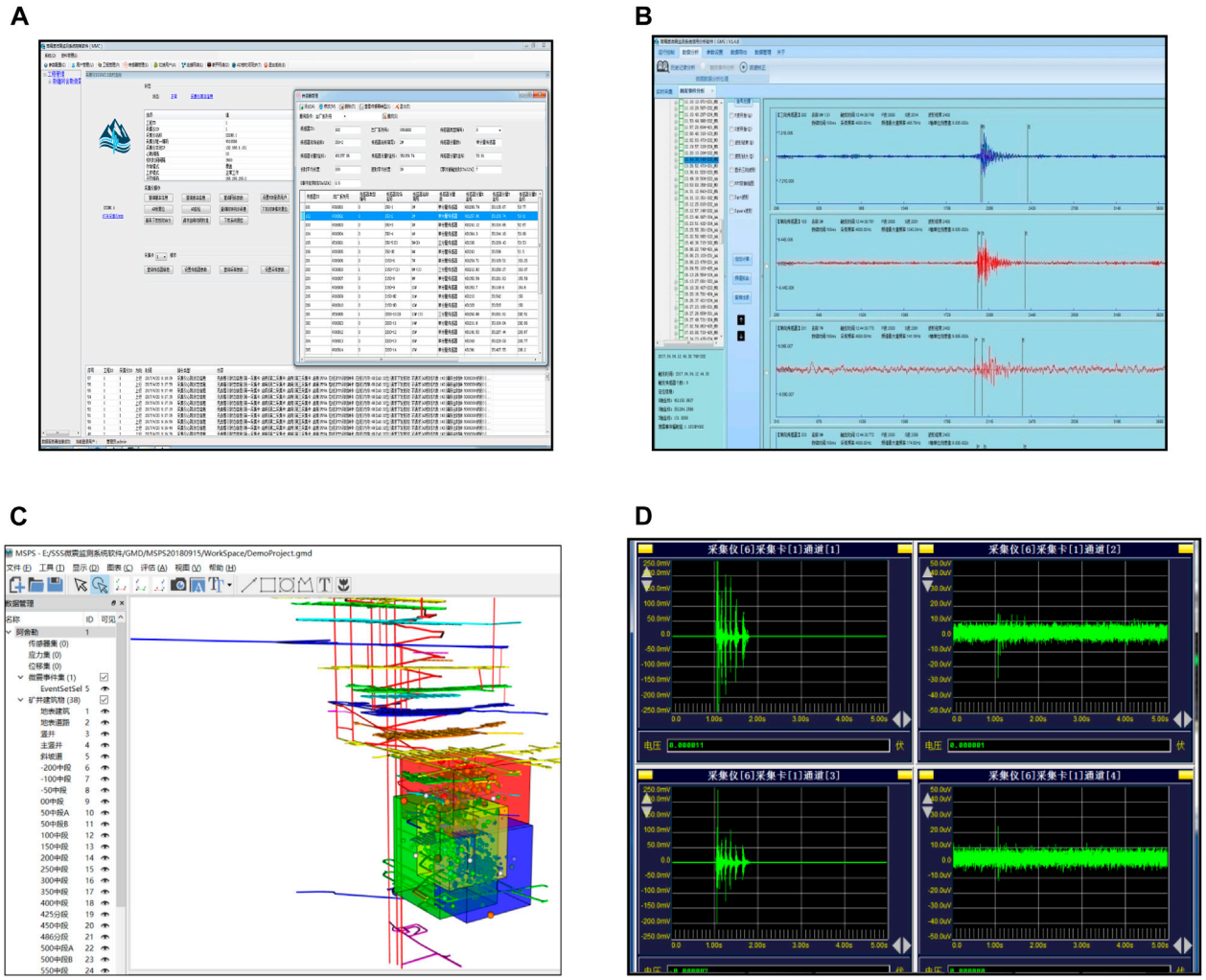

FIGURE 8
Software of microseismic monitoring system. **(A)** system configuration management software, **(B)** microseismic waveform data processing software, **(C)** microseismic event visualization and interpretation software, **(D)** microseismic waveform real-time display software.

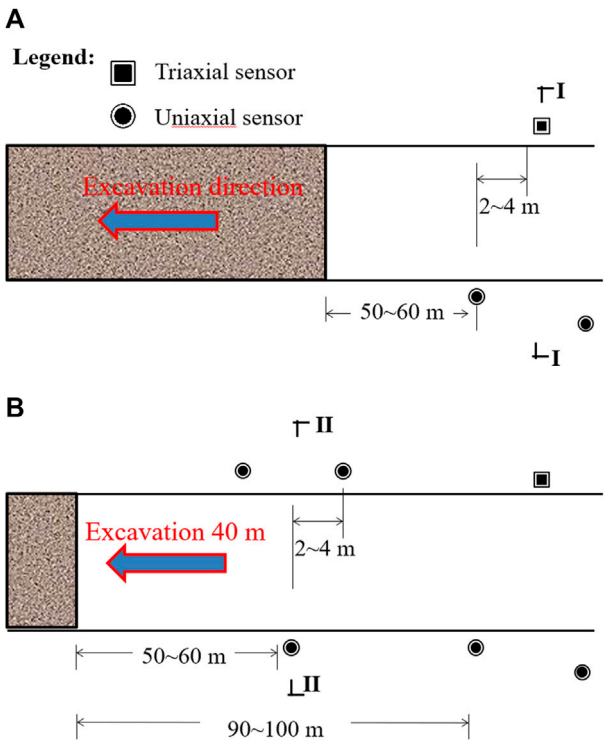

FIGURE 9
Plan layout of microseismic monitoring sensors. **(A)** Initial monitoring stage (single row sensor), **(B)** Normal monitoring stage (dual row sensors).

construction conditions). Sensor 3 is a triaxial sensor, and the other two are uniaxial sensors. As the tunnel continues to excavate another 40 m, the I-I section sensor is about 130–140 m away from the face. The I-I section sensor is recovered and arranged at a distance of about 50–60 m from the face. This cycle continues, and every 40 m of excavation, the last row of sensors is recovered and arranged at a distance of about 50–60 m from the face until the tunnel excavation is completed. To improve monitoring performance, it is planned to adopt an interlaced arrangement of sensors within the section, that is, the adjacent sensors within the section are spaced apart by 2–4 m. At the same time, when the sensors move, the two sensors on the left wall (or right wall) are replaced by the two sensors on the right wall (or left wall), so that the sensors are arranged in a spiral alternating pattern. The specific layout plan is shown in Figures 9, 10.

After the installation of the microseismic monitoring system, the rockburst risk of the roadway can be quantitatively predicted by rockburst warning formula based on the microseismic information recommended by the Technical Specification for Rock Burst Risk Assessment of Hydropower Engineering. This warning method can provide different levels of rockburst risk probability (Chen et al., 2015; Hydropower et al., 2019). When the potential rockburst risk is high, the basic excavation strategy of "short footage and weak blasting" should be followed. At the same time, measures such as destress boreholes and destress blasting can be taken, and strengthened support measures such as "Combining active and passive support, using rigid-flexible support together, and combining multiple support methods" can be used. When there is an extremely high level of rockburst risk, measures such as evacuation and suspension of construction should be taken.

5.3 Microseismic monitoring and prevention of rockburst risk during the mining stage

The first mining area is located in the −1,480 level, which is deeply buried. According to empirical rockburst criteria, the level of rockburst tendency is relatively high, and the volume of the mined

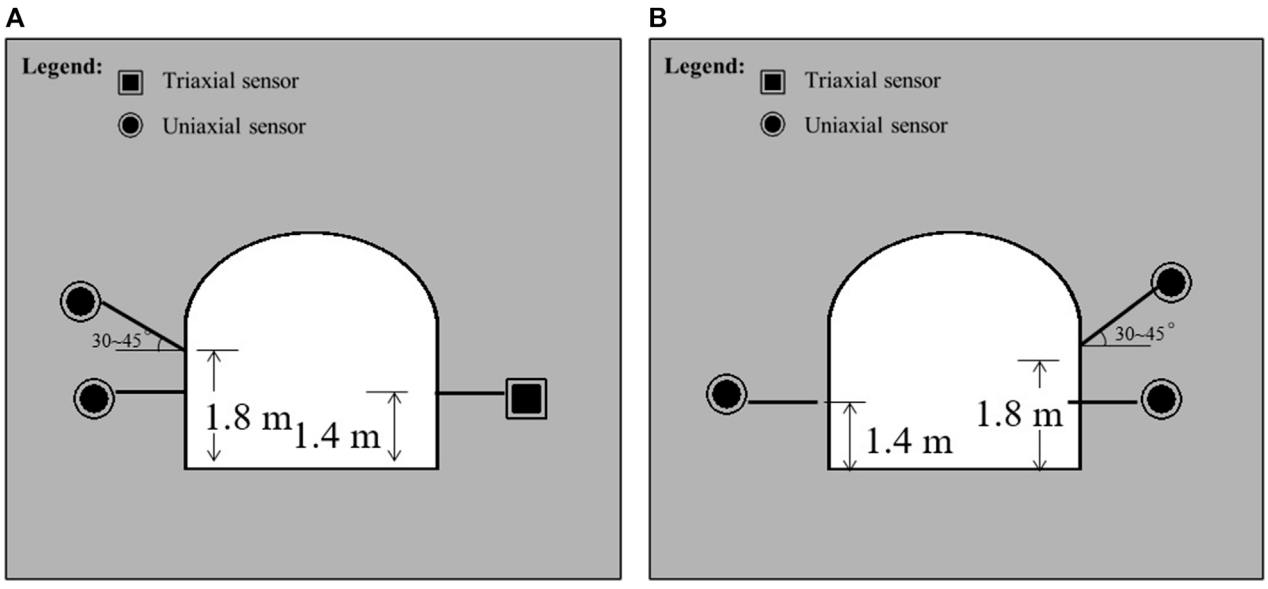

FIGURE 10
Sectional layout of microseismic sensors. **(A)** section I-I, **(B)** section II-II.

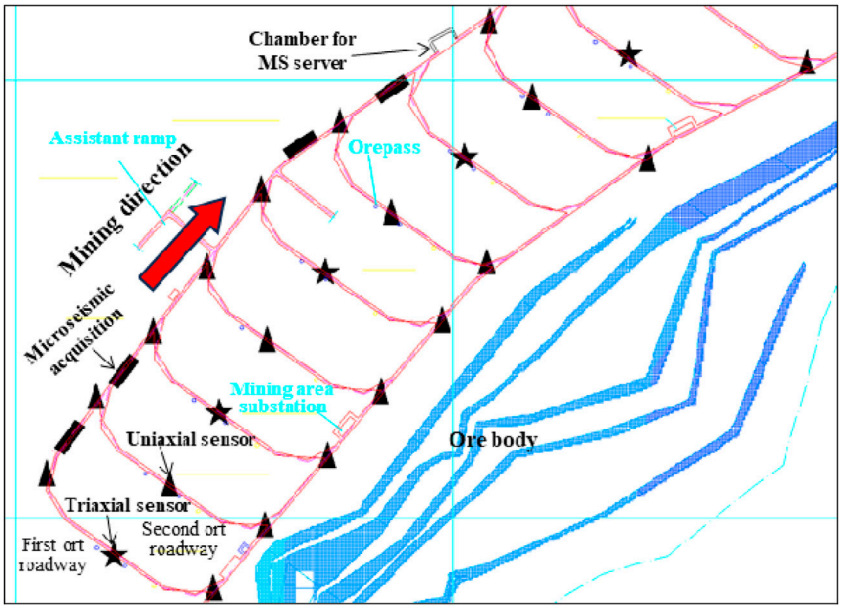

FIGURE 11
Microseismic sensor layout in the −1,480 level.

rock mass in the mining area is large. The stress adjustment of the surrounding rock is bound to be severe, and the maximum tangential stress can be several times higher than the original rock stress. Therefore, the occurrence probability of rockburst with high intensity is relatively high.

Taking into account factors such as the distribution of the ore body and key monitoring areas (ore body enrichment area), mining methods and processes, tunnel space layout, coverage of microseismic sensors, and distribution arrays of sensors, a sensor encryption and more triaxial sensor layout plan will be implemented in the key monitoring areas. The specific sensor layout plan is as follows: Firstly, a triaxial sensor is installed on the middle roof of the first ort roadway. Then, two uniaxial sensors are placed on the roof near the intersection area of first ort roadway and the two tramway transport entries, respectively, and another two sensors are placed on the roof near the intersection area of the second ort roadway and the two tramway transport entries and a microseismic monitoring network is preliminarily formed. As the mining progresses, a uniaxial sensor is installed on the middle roof of the second ort roadway, and two uniaxial sensors are placed on the roof near the intersection area of third ort roadway and the two tramway transport entries. As the mining continues, a triaxial sensor will be installed in the middle of the roof of the third ort roadway. This process will be repeated until the sixth ort roadway, covering the key monitoring area. The specific arrangement of microseismic sensors can be seen in Figure 11, and the monitoring layout plan for other areas can be seen in Figure 11. A total of 28 microseismic sensors are arranged in the middle section of 1,480, including 6 triaxial sensors and 22 uniaxial sensors. 40 microseismic channels are required, and 5 high-precision microseismic acquisition instruments produced by Hubei Seaquake Technique Co., Ltd are selected. Considering factors such as the layout of microseismic sensor cables and external construction disturbances, the microseismic acquisition instrument is arranged in one side of the transportation roadway, and the microseismic monitoring sever should be located in chambers in case been disturbed and damaged.

During microseismic monitoring in the mining process, close attention should be paid to the area where microseismic events are clustered in the surrounding rock of the mining area. The more clustered the microseismic events are, the more active the micro-fracturing of the rock mass in that area, the more intense the stress adjustment, and the higher the energy accumulated in the surrounding rock. The probability of micro-fractures penetrating each other to produce large fractures is higher, and the risk of rockburst is also higher. Therefore, when the number of microseismic events and the released energy suddenly increase in a certain area over a period of time, appropriate measures should be taken to prevent and control rockburst.

In the area where microseismic events are clustered, measures such as destress blasting or destress boreholes during mining, reducing the single charge amount of mining to reduce disturbance to the surrounding rock, and strengthening the support of the mining area should be taken to mitigate or even control the risk of rockburst. The mining rate of the mining area should be reduced to slow down the stress adjustment. The number of personnel working in the area should be reduced. When the risk of rockburst is extremely high, personnel should be evacuated from the working face.

6 Conclusion

Three rockburst criteria were employed to evaluate the rockburst risk of three kinds of granite in Ruihai ultra deep mine gold mine. The substantive reasons for the differences or even contradictions in the discrimination results of different criteria were analysed. Targeted rockburst microseismic monitoring methods and specific prevention

and mitigation measures were proposed for different mining stages for the Ruihai gold mine. The detailed analysis allows the conclusions listed below to be drawn.

1) XRD mineral composition analysis and basic rock mechanics tests were conducted on the three colors of granite in the Ruihai gold mine. The results showed that there were differences in the lithological composition and rock mechanics parameters of the three colors of granite, indicating that they were three different types of granite. Therefore, when conducting rockburst risk management and control, they should be classified separately.
2) Three rockburst criteria, namely, the deformation brittleness coefficient, rock brittleness criterion, and Barton criterion, were applied to evaluate the rockburst tendency of the three types of granite. All three criteria indicated that granite A, granite B, and granite C had the risk of rockburst. However, when different indicators were used to distinguish the same type of granite, the degree of rockburst tendency was inconsistent. After discussion and analysis, it was found that most of the existing rockburst criteria were based on a single condition, which was considered to be somewhat one-sided, as they did not consider the sufficient and necessary conditions for rockburst, namely, the inherent rockburst tendency of the rock itself and the external driving force, i.e., the stress condition.
3) It is proposed to use microseismic monitoring technology to manage rockburst risk during the development and mining stages of the Ruihai gold mine. Different microseismic monitoring layout schemes were proposed for different stages, and targeted rockburst prevention and control measures were proposed for different stages.

Data availability statement

The original contributions presented in the study are included in the article/Supplementary Material, further inquiries can be directed to the corresponding author.

Author contributions

PL: Conceptualization, Data curation, Validation, Writing–original draft. ZW: Investigation, Validation, Writing–review and editing. BC: Conceptualization, Funding acquisition, Methodology, Supervision, Validation, Writing–review and editing. JP: Supervision, Validation, Writing–original draft. BZ: Formal Analysis, Investigation, Writing–review and editing. JZ: Investigation, Validation, Writing–review and editing. HX: Formal Analysis, Validation, Writing–review and editing.

Funding

The author(s) declare financial support was received for the research, authorship, and/or publication of this article. This research was funded by the National Natural Science Foundation of China under Grants 42077263 and 52209132 and Natural Science Foundation of Shandong Provincial, China, under Grant No. ZR2020ME100.

Conflict of interest

Authors ZW, JP, and BZ were employed by Zhaojin Mining Industry Co., Ltd.

The remaining authors declare that the research was conducted in the absence of any commercial or financial relationships that could be construed as a potential conflict of interest.

Publisher's note

All claims expressed in this article are solely those of the authors and do not necessarily represent those of their affiliated organizations, or those of the publisher, the editors and the reviewers. Any product that may be evaluated in this article, or claim that may be made by its manufacturer, is not guaranteed or endorsed by the publisher.

References

Barton, N., Lien, R., and Lunde, J. (1974). Engineering classification of rock masses for the design of tunnel support. *Rock Mech.* 6 (4), 189–236. doi:10.1007/bf01239496

Cai, M. F., and Brown, E. T. (2017). Challenges in the mining and utilization of deep mineral resources. *Engineering* 3 (4), 432–433. doi:10.1016/J.ENG.2017.04.027

Chen, B. R., Feng, X. T., Li, Q. P., Luo, R. Z., and Li, S. J. (2015). Rock burst intensity classification based on the radiated energy with damage intensity at Jinping II Hydropower Station, China. *Rock Mech. Rock Eng.* 48, 289–303. doi:10.1007/s00603-013-0524-2

Feng, X. T. (2017). *Rockburst: mechanism, monitoring, warning and mitigation*. Amsterdam: Elsevier.

Gong, F. Q., and Li, X. B. (2007). A distance discriminant analysis method for prediction of possibility and classification of rockburst and its application. *J. Rock Mech. Eng.* 26 (5), 1012–1018. (in Chinese). doi:10.3321/j.issn:1000-6915.2007.05.021

Gong, F. Q., Wang, Y. l., and Luo, S. (2020). Rockburst proneness criteria for rock materials: review and new insights. *J. Central South Univ.* 27, 2793–2821. doi:10.1007/s11771-020-4511-y

Gong, F. Q., Wang, Y. l., Wang, Z. G., Pan, J. F., and Luo, S. (2021). A new criterion of coal burst proneness based on the residual elastic energy index. *Int. J. Min. Sci. Technol.* 31 (4), 553–563. doi:10.1016/j.ijmst.2021.04.001

He, M. C., Chen, T., Qiao, Y. F., and Li, H. R. (2023). A review of rockburst: experiments, theories, and simulations. *J. Rock Mech. Geotechnical Eng.* 15, 1312–1353. doi:10.1016/j.jrmge.2022.07.014

Hoek, E., and Brown, E. T. (1980). *Underground excavation in rock*. London: The Institute of Mining and Metallurgy.

Hydropower (2019). *NB/T 10143-2019 technical specification for rock Burst risk assessment of hydropower engineering*. Beijing: China Water Resources and Hydropower Publishing House.

Kaiser, P. K., and Cai, M. (2012). Design of rock support system under rockburst condition. *J. Rock Mech. Geotechnical Eng.* 4 (3), 215–227. doi:10.3724/sp.j.1235.2012.00215

Kan, J. L., Dou, L. M., Li, J. Z., Li, X. W., Bai, J. Z., and Wang, M. Q. (2023). Characteristics of microseismic waveforms induced by underground destress blasting: comparison with those induced by ground blasting and coal mining. *Front. Earth Sci.* 10, 797358. doi:10.3389/feart.2022.797358

Kidybinski, A. (1981). Bursting liability indices of coal. *Int. J. Rock Mech. Min. Sci.* 18 (4), 295–304. doi:10.1016/0148-9062(81)91194-3

Leveille, P., Sepehri, M., and Apel, D. B. (2017). Rockbursting potential of Kimberlite: a case study of Diavik diamond mine. *Rock Mech. Rock Eng.* 50, 3223–3231. doi:10.1007/s00603-017-1294-z

Li, P. X., Chen, B. R., Xiao, Y. X., Feng, G. L., Zhou, Y. Y., and Zhao, J. S. (2023a). Rockburst and microseismic activity in a lagging tunnel as the spacing between twin TBM excavated tunnels changes: a case from the Neelum-Jhelum hydropower project. *Tunn. Undergr. Space Technol.* 132, 104884. doi:10.1016/j.tust.2022.104884

Li, P. X., Chen, B. R., Zhou, Y. Y., Xiao, Y. X., Feng, G. L., and Zhu, G. Q. (2019a). Research progress of rockburst prediction and early warning in hard rock underground engineering. *J. China Coal Soc.* 44 (S2), 447–465. (in Chinese). doi:10.13225/j.cnki.jccs.2019.0665

Li, P. X., Feng, X. T., Feng, G. L., Xiao, Y. X., and Chen, B. R. (2019b). Rockburst and microseismic characteristics around lithological interfaces under different excavation directions in deep tunnels. *Eng. Geol.* 260, 105209. doi:10.1016/j.enggeo.2019.105209

Li, P. X., Zhao, J. S., Bu, W. K., Niu, W. J., Liu, P. P., and Sun, M. H. (2023b). Optimization of rockburst risk control measures for deeply buried tbm tunnels: a case study. *Buildings* 13, 1440. doi:10.3390/buildings13061440

Liu, G. F., Ran, G. H., Li, Z. Q., Duan, S. Q., Su, G. S., Yang, C. G., et al. (2023). An insight into the effect of primary hidden microfissures on mechanical behaviors and failure characteristics of brittle basalt *Theoretical and applied fracture mechanics*. 2023, 1. doi:10.1016/j.tafmec.2023.104138

Mazaira, A., and Konicek, P. (2015). Intense rockburst impacts in deep underground construction and their prevention. *Can. Geotechnical J.* 52, 1426–1439. doi:10.1139/cgj-2014-0359

Peng, H., and Sun, Y. (2016). *Report on* in-situ *stress measurement of hydraulic fracturing in borehole 2 of the gold mine in the northern sea area of Sanshan Island*. Beijing: Institute of Geomechanics, Chinese Academy of Geological Sciences.

Russenes, B. F. (1974). *Analysis of rock spalling for tunnels in steep valley sides*. USA: Norwegian Institute of Technology. [dissertation/master's thesis]. [Trondheim].

Wang, C., Liu, Y., Song, D., Xu, J., Wang, Q., and Zhang, S. (2024). Evaluation of bedding effect on the bursting liability of coal and coal-rock combination under different bedding dip angles. *Adv. Geo-Energy Res.* 11 (1), 29–40. doi:10.46690/ager.2024.01.04

Wang, J. A., and Park, H. D. (2001). Comprehensive prediction of rockburst based on analysis of strain energy in rocks. *Tunn. Undergr. Space Technol.* 16 (1), 49–57. doi:10.1016/s0886-7798(01)00030-x

Xiao, Y. X., Feng, X. T., Hudson, J. A., Chen, B. R., Feng, G. L., and Liu, J. P. (2016). ISRM suggested method for *in situ* microseismic monitoring of the fracturing process in rock masses. *Rock Mech. Rock Eng.* 49 (1), 343–369. doi:10.1007/s00603-015-0859-y

Xu, L. S., and Wang, L. S. (1999). Study on the laws of rockburst and its forecasting in the tunnel of Erlang Mountain road. *Chin. J. Geotechnical Eng.* 21 (5), 569–572. (in Chinese). doi:10.3321/j.issn:1000-4548.1999.05.009

Zhang, C. Q., Lu, J. J., Chen, J., Chen, J., Zhou, H., and Yang, F. J. (2017). Discussion on rock burst proneness indexes and their relation. *Rock Soil Mech.* 38 (5), 1397–1404. (in Chinese). doi:10.16285/j.rsm.2017.05.022

Zhao, J. S., Jiang, Q., Lu, J. F., Chen, B. R., and Wang, Z. L. (2022). Rock fracturing observation based on microseismic monitoring and borehole imaging: *in situ* investigation in a large underground cavern under high geostress. *Tunn. Undergr. Space Technol.* 126, 104549. doi:10.1016/j.tust.2022.104549

Zhao, J. S., Jiang, Q., Pei, S. F., Chen, B. R., Xu, D. P., and Song, L. B. (2023). Microseismicity and focal mechanism of blasting-induced block falling of intersecting chamber of large underground cavern under high geostress. *J. Central South Univ.* 30, 542–554. doi:10.1007/s11771-023-5259-y

Zhou, J., Li, X. B., and Mitrib, H. S. (2018). Evaluation method of rockburst: state-of-the-art literature review. *Tunn. Undergr. Space Technol.* 81, 632–659. doi:10.1016/j.tust.2018.08.029

frontiers | Frontiers in Earth Science

TYPE Original Research
PUBLISHED 11 January 2024
DOI 10.3389/feart.2023.1349933

Check for updates

OPEN ACCESS

EDITED BY
Pengjiao Jia,
Soochow University, China

REVIEWED BY
Wei Duan,
Southeast University, China
Weilong Song,
Hefei University of Technology, China

*CORRESPONDENCE
Zhicheng Ren,
2021155120@stu.sdjzu.edu.cn
Chao Li,
lichao21@sdjzu.edu.cn

RECEIVED 05 December 2023
ACCEPTED 27 December 2023
PUBLISHED 11 January 2024

CITATION
Zhang S, Ren Z, Zhang Y, Fan W, Li C, Liu C and Wang Y (2024), Study on bearing characteristics of super-long and super-large diameter pipe piles in silt foundation of alluvial plain of Yellow River.
Front. Earth Sci. 11:1349933.
doi: 10.3389/feart.2023.1349933

COPYRIGHT
© 2024 Zhang, Ren, Zhang, Fan, Li, Liu and Wang. This is an open-access article distributed under the terms of the Creative Commons Attribution License (CC BY). The use, distribution or reproduction in other forums is permitted, provided the original author(s) and the copyright owner(s) are credited and that the original publication in this journal is cited, in accordance with accepted academic practice. No use, distribution or reproduction is permitted which does not comply with these terms.

Study on bearing characteristics of super-long and super-large diameter pipe piles in silt foundation of alluvial plain of Yellow River

Sifeng Zhang[1], Zhicheng Ren[1]*, Yingguang Zhang[2], Wei Fan[2], Chao Li[1]*, Chao Liu[2] and Yushuai Wang[1]

[1]Department of Transportation Engineering, Shandongjianzhu University, Jinan, China, [2]Shandong Luqiao Group Co., Ltd., Jinan, China

In recent years, super-long and super-large diameter pipe piles have been gradually applied to the foundation in the Yellow River flood area. However, its bearing mechanism is not clear, especially the unclear bearing characteristics of the pile under the eccentric state, which limits its application and development. In this regard, this paper uses the method of combining field test and numerical simulation to analyze the bearing characteristics of super-long and super-large diameter pipe piles under different pile lengths, different pile diameters, different diameter-thickness ratios, and different offsets. Combined with the specific deviation form of the pipe pile, the calculation formula of the vertical ultimate bearing capacity of the super-long and super-long diameter pipe pile in the Yellow River flooding area under the influence of the construction effect is modified. The results show that when the length of the pipe pile changes, the vertical bearing capacity changes the most, and the vertical ultimate bearing capacity of the pipe pile increases linearly with the increase of the length of the pipe pile. When the wall thickness of the pipe pile increases, the vertical bearing capacity increases approximately linearly, but the reduction of the pile displacement decreases exponentially. The greater the deflection of the pipe pile, the smaller the vertical ultimate bearing capacity. When the deflection of the pipe pile is greater than 0.35°, the vertical ultimate bearing capacity decreases rapidly with the increase of the deflection. On the basis of the traditional formula, considering the deviation form of the pipe pile, the reduction coefficient of the bearing capacity correction formula of the super-long and super-large diameter pipe pile is proposed, and the correction formula is compared with the field example. It is proved that the formula can accurately calculate the bearing capacity of the super-long and super-large diameter pipe pile. The research results of this paper are of great significance to the application and promotion of super-long and super-large diameter pipe piles in the Yellow River flood area and the evaluation of vertical ultimate bearing capacity. At the same time, the research results of this paper can also provide a reference for the study of bearing characteristics of super-long and super-large diameter pipe piles in other foundations.

KEYWORDS

super-long and super-large diameter pipe piles, Yellow River flood area, numerical simulation, offset, bearing capacity correction formula

1 Introduction

Prestressed high strength concrete pipe pile (PHC) has the advantages of good performance, low price and convenient construction. It is widely used in wharf engineering (Coyle and Reese, 1966; Burland and Burland, 1973; Fleming, 1992). The bearing characteristics of pipe piles are an important part of pipe pile construction. Understanding the bearing characteristics of pipe piles is of great significance for engineering design, foundation improvement, structural design and construction control, which can ensure the safety, reliability and long-term stability of the project.

In theoretical analysis, Chin et al. (1990) combined the boundary element method with the elastic theory, and divided the foundation into upper and lower layers, and analyzed the bearing capacity of pile groups with high caps. Poulos and Davis (1974) used the Mindlin solution to analyze the three-dimensional stress at any point of the soil around the pile. At the same time, the soil around the pile is divided into small segments, and its distribution under pile side resistance and pile tip resistance is analyzed, which provides a theoretical basis for the layered summation method. Liu (2008) proposed a pile-sinking positive force prediction formula based on the side resistance degradation effect by using the h/D effect and the double-bridge static cone penetration data.M.H (El Naggar and Wei, 2000; Liu et al., 2010) have shown that the radial heterogeneity of the soil around the pile not only affects the bearing characteristics of the pile, but also has a significant effect on its dynamic characteristics (Tian et al., 2015; Li et al., 2017). In numerical simulation, Kee et al. (2006) used FLAC2D software to analyze the influence of pile-soil contact surface roughness on bearing capacity. Jae et al. (2012) analyzed the influence of different pile end contact surfaces on the bearing capacity of pile foundation by finite element method. Guo et al. (2004) predicted the eccentric bearing capacity of single PHC pipe pile by using successive linear probability method and residual error correction, and simulated it with finite element method. Matos et al. (2018) studied the cumulative settlement law of model pipe piles with different intervals under cyclic loading in sand, and proposed a method to calibrate the accuracy of finite element numerical simulation of model pipe piles. Lehane and Gavin (2001) found that there is no obvious difference between the load-settlement curves of the pile end of the closed pile and the open pile wall through the static pressure steel pipe pile load test in sand. Bekki et al. (2013) studied the change of ultimate bearing capacity of pile foundation model in sand under long-term cyclic loading, and found that the ultimate bearing capacity of pile foundation will increase first and then decrease under cyclic loading. Wang et al. (2019) studied the variation law of pile sinking resistance, pile axial force and unit side friction resistance of pile body in the process of static pressure sinking through FBG sensing technology. In the field test, Sivaraman and Muthukkumaran (2022) showed that the static load test of pile foundation on site showed that the use of fill for surcharge preloading could promote the consolidation of foundation soil and improve the shear strength. The depth could reach 5 m, and the bearing capacity of pile was significantly improved. The field test of pile foundation is also used to study the bearing capacity of a series of new pile foundations, such as large diameter belled concrete pile (Gao et al., 2019), cement stabilized gravel pile (Gao et al., 2022) and geothermal energy (Jiang et al., 2023). Hong and Chen (1985) carried out pile sinking test in composite foundation. The research shows that the exertion of pile side friction is not only affected by soil properties, but also related to pile diameter. Zhang et al. (2010) put forward the concept of side resistance degradation coefficient and time effect coefficient through two aspects of pile sinking process and time effect of bearing capacity. Randolph et al. (1991) studied and obtained the force balance equation of soil plug. Zang et al. (2009) carried out the timeliness test of pile foundation bearing capacity, and found that the increase of shear strength of pile side clay will significantly increase the bearing capacity of friction pile, and the ultimate bearing capacity is hyperbolic with time. Previous studies have summarized the influence of different lengths, different wall thicknesses and other factors on the bearing characteristics of pipe piles, and the formula for calculating the bearing capacity of pipe piles has been continuously improved. However, the research on the bearing characteristics of pipe piles in the Yellow River flood area with extremely complex engineering geology is extremely scarce. In the calculation of the bearing capacity of pipe piles, the influence of eccentricity on the bearing capacity of pipe piles is not considered. In the past research, the length of the pile is shorter. Compared with the short pile, the side resistance of the long pile plays a major role, while the end resistance of the short pile plays an important role in the whole bearing capacity. The length of the long pile is large, and the pile can also bear part of the load. The stiffness and strength of the pile also play a certain role in the load transfer.

In recent years, due to the continuous rise of large-scale projects, the demand for the diameter and length of pipe piles required in foundation reinforcement treatment has increased. Super-large diameter (pile diameter ≥800 mm) and super-long pipe piles have gradually been promoted. At present, there is no specific definition of super-long pile in the code and the engineering community. It is generally classified according to the length-diameter ratio or length of the pile. Sang and Tan (2014), Miao et al. (2018) and others think that PHC pipe piles with a length of more than 50 m are super-long piles. The super-long PHC pipe piles studied by Pan (2006) and Jiang (2012) are longer than 60 m and the length-diameter ratio is greater than 60. The super-long PHC pipe piles studied by Cai et al. (2006) are less than 50 m and the length-diameter ratio is greater than 40. This paper considers that the super-long PHC pipe pile is the pile length L is less than 50 m but the length-diameter ratio L/d is greater than or equal to 40. The Yellow River flood area is a swamp area formed after the diversion of the Yellow River. The soil is mainly composed of Quaternary new alluvial silt. It has the characteristics of poor adhesion between particles, high compressibility, low strength and poor particle gradation (Jin et al., 2020). Its engineering properties are poor. For the Yellow River flood area with complex engineering geology, it is not possible to accurately calculate and analyze the bearing capacity of the pile foundation in the later construction stage. The research on its bearing characteristics needs to be improved. In this paper, the influence of different factors on the bearing characteristics of super-long and super-large diameter pipe piles in the Yellow River flood area is studied by means of numerical simulation and field test. According to the offset form of pipe piles, the reduction coefficient of bearing capacity of pipe piles is proposed, and the traditional formula is modified.

TABLE 1 Engineering geological parameters of foundation soil.

Level number	Name of soil	Bottom buried depth (m)	Characteristic value of bearing capacity (kPa)	Standard value of ultimate shaft resistance of pile (kPa)	Standard value of ultimate end resistance of pile (kPa)			
					Prefabricated pile			
				Prefabricated pile	l≤9	9<l≤16	16<l≤30	30<l
1	Plain fill	0.5	—	—	—	—	—	—
2	Silt	7.1	100	0 (Liquefaction)	—	—	—	—
3	Silty clay	17.2	120	50	—	—	—	—
4	Silty sand	19.2	120	20 (Liquefaction)	—	—	1900	—
5	Silt	23.6	140	45	—	—	1900	—
6	Silty sand	26.1	160	50	—	—	3,000	—
7	Graining sand	42.1	200	55	—	—	4,500	5,000
8	Silt	50	180	50	—	—	—	3,600

2 Field test

2.1 Project profile

Jigao Expressway is connected to the east section of the second ring line of Jinan Ring Expressway under construction in the south, and to the Gaoqing to Guangrao section of Changshen Expressway under construction in the north. The total length of the road section is 94.340 km, and the design speed is 120 km/h. The starting and ending pile numbers of the fourth contract section of Jigao Expressway Road and Bridge Project are: K53 + 074 ~ K80 + 290, with a total length of 27.216 km. The test engineering pile is located in the K63 + 037 channel bridge of Haojia Village, Gaoqing County, Zibo City, the fourth section of Jigao Expressway.

The Φ800 mm PHC pipe pile is used in the field test, the pile length is 43.0 m, and the pile end is located in the fine sand layer. The ground elevation of the site is about 15.5 m. The foundation soil is divided into 8 layers from top to bottom. The composition and characteristics are shown in Table 1. Different types of soil have different mechanical properties. The cohesion and internal friction angle of soil determine the shear resistance of soil, which affects the lateral resistance of pipe pile, and then affects the bearing capacity of pipe pile. The foundation soil parameters include soil type, strength parameters, soil layer distribution and thickness, which have an important influence on the bearing characteristics of pipe piles. In the design and analysis of pipe piles, it is necessary to accurately evaluate and reasonably consider the parameters of foundation soil to ensure the safety and reliability of pipe piles.

In Table 1: Characteristic value of bearing capacity refers to the pressure value corresponding to the deformation specified in the linear deformation section of the foundation soil pressure deformation curve determined by the load test, and its maximum value is the proportional limit value. Standard value of ultimate shaft resistance of pile refers to the rock and soil resistance on the side surface of the pile when the ultimate load is applied to the pile top. Standard value of ultimate end resistance of pile refers to the rock and soil resistance at the end of the pile corresponding to the ultimate load of the pile top. Standard value of ultimate shaft resistance of pile and standard value of ultimate end resistance of pile are determined by the static load test by embedding the axial force test element of the pile body.



FIGURE 1
Static load test site.

2.2 Test scheme

The main equipment of the test is as follows: Reaction device: Using bagged sand and concrete, the concrete specification is 1 m × 1 m × 0.8 m, the specific gravity is 2.4t/m^3, and the specification of each bag of sand is 120 kg; three jacks with the specification of QF320; several displacement/pressure sensors; 3 oil pumps; one static load tester, model JSM-JC5 (G). The slow sustained load method was used in the test. The test site is shown in Figure 1.

The static load test should be carried out 14 days after the construction of the test pile. The vertical compressive static load test of single pile of large diameter pipe pile is carried out by slow

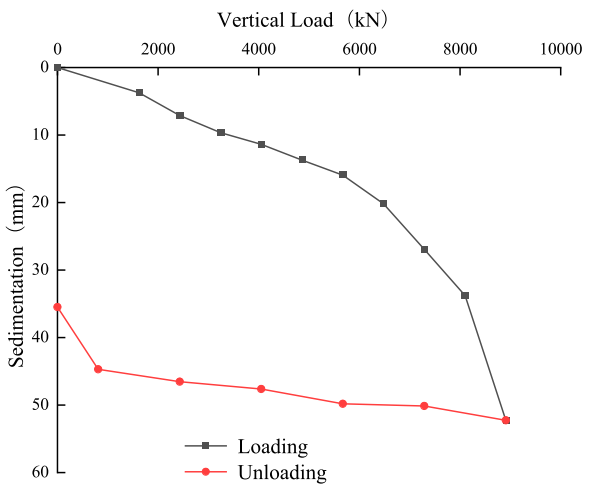

FIGURE 2
Q-S curve of test pile.

maintenance load method. The load of each stage is 810 kN. The initial loading value is 2 times of the loading value of each stage, that is, 1,620 kN. After that, the loading value of each stage is 810 kN, until the pile foundation reaches the limit state, and then the load is unloaded step by step.

The ultimate bearing capacity is determined according to the following principles: Steep drop type Q-S curve(Q stands for load, s stands for settlement), take the load value at the inflection point. According to the characteristics of the settlement time, the front load value of the tail of the S-lgt curve is obviously bent downward. The settlement caused by the applied load is more than 5 times of the settlement caused by the previous load, and the load value of the previous section is taken. The load value corresponding to the displacement S = 40 mm is taken from the gentle Q-S curve. For piles with a diameter of more than 800 mm, the load value corresponding to S = 0.05 times the pile diameter is taken.

After the loading is completed, the unloading should be graded, and 2 times of the value of each stage of loading should be taken as the first-level unloading amount. The rebound displacement of pile top should be monitored when each load is unloaded. After unloading each load, the rebound amount of the pile top is recorded. The monitoring, recording methods and standards are consistent with the monitoring when the load is applied and the settlement value of the pile top is recorded. Until the rebound value is stable, the first-stage load is unloaded in the same way. After the unloading is completed, the monitoring should be continued, and 4 times should be observed within 2 h.

2.3 Results and analysis

The Q-S curve of the static load test pile is shown in Figure 2. From the Q-S curve, it can be seen that the rebound amount of the pile top is 16.79 mm when the unloading is completed and stable after loading to the maximum load; the maximum test load Q and the corresponding pile top displacement S are 8,910 kN and 52.25 mm, respectively. The vertical ultimate bearing capacity of single pile Q and its corresponding pile top displacement S are 8,100 kN and 33.78 mm, respectively. The ultimate bearing capacity of the test pile is 8,100 kN measured by the static load test, and the characteristic value of the design bearing capacity is 3,500 kN. At the same time, the Q ~ S curve of the pile decreases obviously at 9,000 kN, indicating that the pile reaches the ultimate bearing capacity and has been damaged. It shows that the bearing capacity meets the requirements of the site.

3 Numerical simulation study

3.1 Modelling

Soil is a kind of loose medium, which is different from other materials. Under the continuous action of dynamic load, the connection force between soil particles will become smaller and smaller. Therefore, under the continuous dynamic load, the site soil will not only undergo elastic deformation but also produce great plastic deformation, so the inelastic characteristics of the soil should be fully considered. The commonly used elastic-plastic models of soil are Mohr-coulomb, Drucker-Prager, MCC, etc. Mohr-Coulomb can well simulate the mechanical parameters of soil under cyclic loading, which is widely used in the simulation of geotechnical materials. The Mohr-Coulomb constitutive model has exTaking the Mohr–Coulomb as the failure criterion, this model can consider both shear hardening and compression hardening, and can accurately reflect the nonlinear mechanical characteristics during soil loading and unloadingcellent analysis reliability in a certain range of lateral stress (Han et al., 2023). In addition, the Mohr-Coulomb constitutive model has excellent analysis reliability in a certain range of lateral stress. In addition, the model parameters are less and easy to obtain. Therefore, Mohr-Coulomb is used to simulate the mechanical parameters of soil in this paper.

Firstly, the soil mesh is established by layered grouping, and different groups are named, and the initial density of the soil is given. Then, the contact surface between pile and soil is established and given different parameters, and then the pile element is established. Next, different types of mechanical parameters are assigned to each soil layer and pile unit, including bulk modulus, shear modulus, cohesion, internal friction angle and structural density. Then, the pile is moved into the soil layer, and the boundary conditions are imposed on the soil around the pile. Finally, the system balances the model under the condition of self-weight stress, and applies vertical load in stages for calculation. The program uses the fast Lagrangian method in mathematics. Based on the explicit difference, the step-size solution of all the motion equations and constitutive equations of the model is obtained. The constitutive equation is derived from the fundamental stress-strain definition and Hooke's law. The motion balance equation directly applies the Cauchy motion equation, which is derived from Newton's law of motion.

A half-mode model is established in modeling, and the calculation model, in addition to the pipe pile, takes into account the influence of pipe pile construction on the soil around the pile, and also expands the model boundary of the soil to more than ten times of the pile diameter to ensure the accuracy of the simulation calculation.

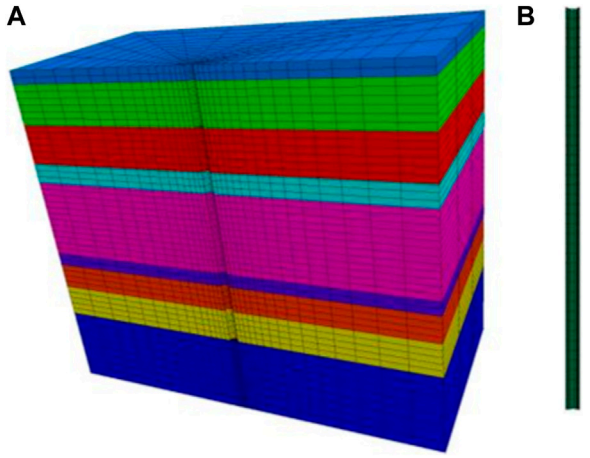

FIGURE 3
Model diagram. **(A)** Pipe pile. **(B)** Soil mass.

According to the relevant engineering experience, the influence range of the soil around the pile after the construction and construction of the pipe pile is about 10 times the diameter of the pile, and the boundary is more than 10 times the diameter of the pile when the model is established. The test model is 60 m long, 30 m wide and 60 m high. According to the deformation characteristics caused by the pipe pile, the grid of the soil around the pile is densely arranged. The grid far away from the pile can be sparsely arranged, which can reduce the amount of calculation and improve the accuracy of the data. Because FLAC3D can not realize the process of completely penetrating the pipe pile from the outside of the soil into the soil, the pipe pile is first penetrated into the soil through the built-in command, the fixed boundary conditions are used to constrain the normal direction of the model around and at the bottom, but the vertical load is not applied at the top of the pile, and the self-weight balance is carried out before the start of the bearing capacity characteristic test. The three-digit diagram of the model is shown in Figure 3.

To determine the frictional force of pipe strings, the contact characteristics between the pipe string and the surrounding medium and the mechanical law need to be understood (Li et al., 2023). The parameters of different soil layers are obtained from the geotechnical report of the construction site, as shown in Table 1 below. When establishing the contact surface, the "move-and-move" method is used to establish the contact surface between the pile and the soil. The soil depth corresponds to the depth of the contact surface, the interaction between pile and soil is realized by setting the contact surface between pile and soil and setting the parameters of the contact surface. The contact surface in FLAC3D adopts the non-thickness contact surface element, and the contact surface constitutive model adopts the Coulomb shear model. The contact surface parameters are shown in Table 2 and Table 3 below.

In the civil engineering simulation test, the original stress is also an important factor to control the calculation results, so it is necessary to consider the influence of the self-weight stress of the model on the stress and strain. In this experiment, there is no obstacle around the construction, so it is necessary to consider the influence of the initial stress of the model on the calculation results, and adopt the Mohr-Coulomb yield criterion. The stress cloud diagram of the established model after balance under self-weight balance is shown in the Figure 4.

The model is generated by flac3d built-in grids cshell and radcylinder. The grid is a reflective grid. The closer the grid is to the pipe pile, the denser the grid is. The number of grids in the model is 10,404 and the number of nodes is 12,619.

3.2 Model verification

In order to verify the correctness of the numerical model, after the model is established, the pile body and the pile side soil are filled on the basis of the semi-model test, and the vertical load is applied to record the displacement of the pile top under each load. Finally, the Q-S curve is obtained to verify the accuracy of the test. The default convergence of Flac3D is that the unbalanced force rate reaches the-5th power of 10 (1e-5), and the unbalanced force rate of each step reaches the-5th power of 10, so the model is convergent. The model is established and the results after the self-weight stress balance are shown in Figure 5.

When the model is balanced under self-weight stress, the vertical load is applied to the top of the model pile, and the displacement of the pile top node under each load is recorded. Finally, the Q-S curve of the pipe pile is made by using the load and displacement.

TABLE 2 Soil parameter table.

Soil group	The thickness of the layer (m)	Bulk($\times10^6$)	Shear($\times10^6$)	Coh($\times10^3$)	Fric(°)	ρ (g/cm^3)
Plain fill	0.5	6.094	3.101	14.7	21.7	1.85
Silt	6.6	8.472	5.984	12	24.5	2.05
Silty clay	10.1	6.944	3.968	14.3	20	1.87
Silty sand	2.0	6.818	3.516	0	25	2.05
Silt	4.4	8.472	5.984	12	24.5	2.05
Silty sand	2.5	6.918	3.712	0	25	2.00
Graining sand	16.0	20.556	6.175	0	18	1.95
Silt	7.9	17.510	5.398	20	21	1.80

TABLE 3 Contact surface parameter table.

Contact surface number	kn(x10^8)	ks(x10^8)	Coh(10^3)	Fric(°)
1	2.097	2.097	30	20
2	2.301	2.301	30	20
3	2.447	2.447	30	20
4	2.692	2.692	30	20
5	1.223	1.223	30	20
6	1.958	1.958	30	20
7	2.958	1.938	30	20
8	2.751	1.898	30	20
9 (pile bottom)	7.608	7.608	30	20

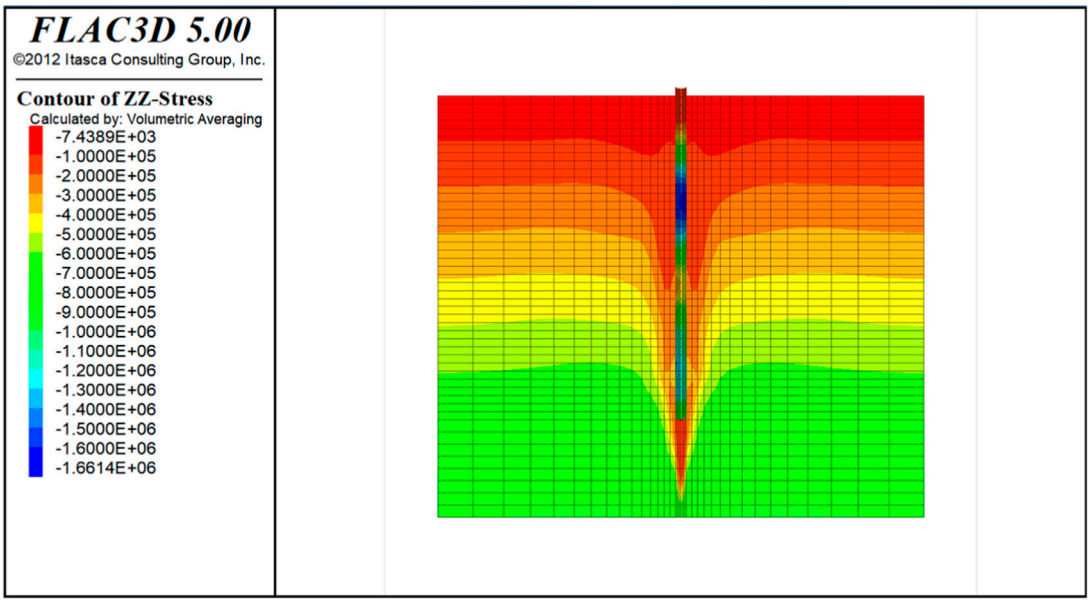

FIGURE 4
The stress cloud diagram of the established model after balance under self-weight balance.

The Q-S curve of the model test is obtained by the vertical displacement of the pipe pile measured when the vertical load is applied to the pile top. The vertical bearing Q-S curve of the pipe pile obtained by numerical simulation and field measurement is shown in Figure 6.

From Figure 6, it can be found that by establishing a numerical calculation model for the bearing capacity of pipe pile foundation, the measured vertical cumulative settlement deformation of pipe pile under the same vertical load is close to the actual measured cumulative settlement of pipe pile, which verifies the accuracy of the calculation results of this numerical model. Therefore, the numerical model can be used to study the vertical bearing capacity of pipe pile.

3.3 Study on influencing factors of vertical bearing characteristics of pipe pile

In this section, the vertical bearing characteristics of pipe piles under different pile lengths, pile diameters and diameter-thickness ratios are studied through the calculation model of pipe pile bearing capacity. After the completion of the model, the vertical load is applied to the pile top along the Z direction, and the Z-direction displacement of the pile top under the vertical load is monitored and recorded, so as to obtain the corresponding vertical displacement of the pile top under different vertical loads. Finally, the Q-S curve of the pipe pile is drawn. The length, diameter and diameter-thickness ratio of the pile are set as shown in Table 4.

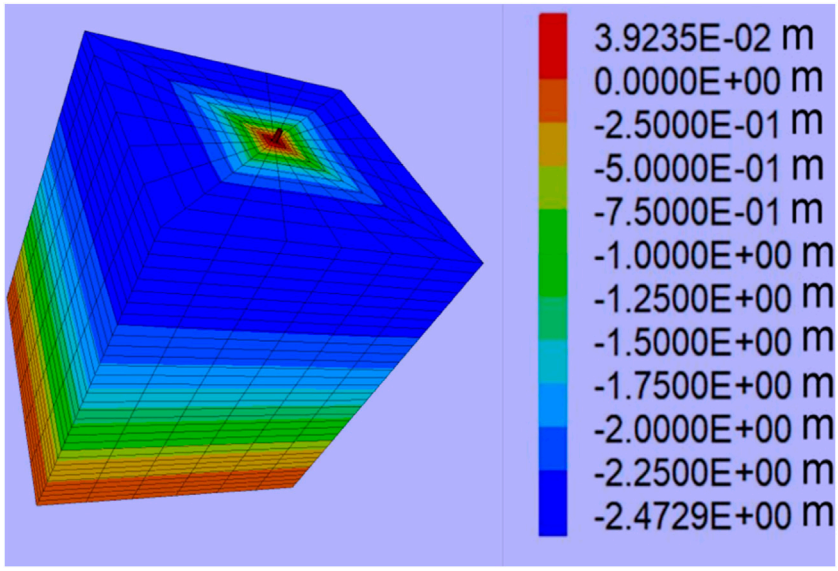

FIGURE 5
The Z-direction displacement cloud diagram of the model after self-weight balance.

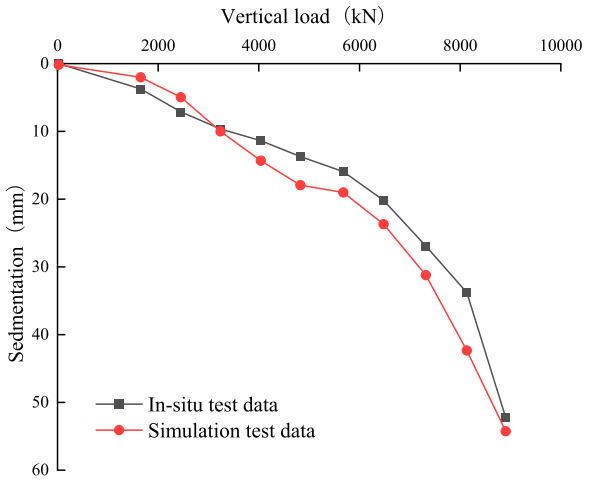

FIGURE 6
Q-S curve of pipe pile foundation measured by field and simulation.

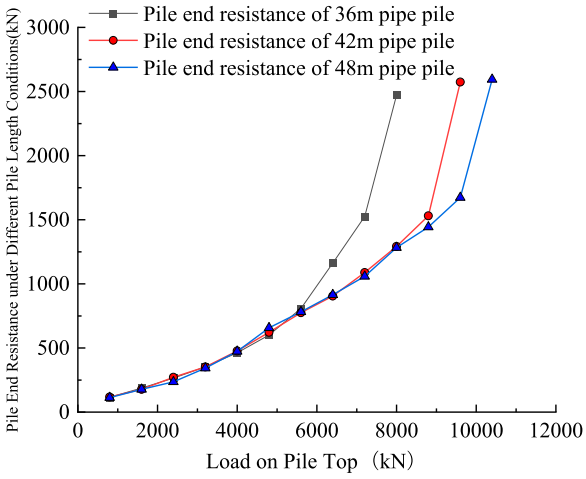

FIGURE 7
End resistance of pipe piles with different pile lengths.

TABLE 4 Pile length, pile diameter and diameter-thickness ratio.

Pile length (m)	9, 24, 30, 36, 42, 48
Pipe pile diameter and wall thickness (m)	outside diameter 0.4, 0.6, 0.7, 0.8
	wall thickness 0.06, 0.1, 0.15, 0.2, 0.25
Pile top offset (m)	0.1, 0.2, 0.3, 0.4, 0.5

3.3.1 The influenece of pile length

In this section, the vertical bearing capacity calculation model of single pipe pile is established, and the height of soil around the pile, pipe pile and layered soil in the simulation is modified to study the change of bearing characteristics of pipe pile under different pile lengths.

In the model test, the length of the model pile is set to 9 m, 24 m, 30 m, 36 m, 42 m, 48 m, the outer diameter of the pipe pile is 0.8 m, and the wall thickness is 0.06 m. Since the model is a half-mode model, the vertical load applied to the pile top is half of the full-mode model.

PHC prestressed concrete pipe piles are divided into friction piles and end-bearing piles. The friction piles mainly rely on the pile side resistance to improve the bearing performance of the bridge pile foundation, and the pile end resistance only plays a

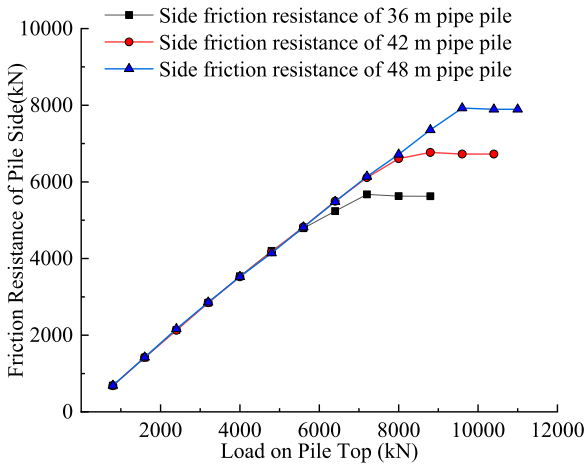

FIGURE 8
Pile side friction resistance of pipe piles with different pile lengths.

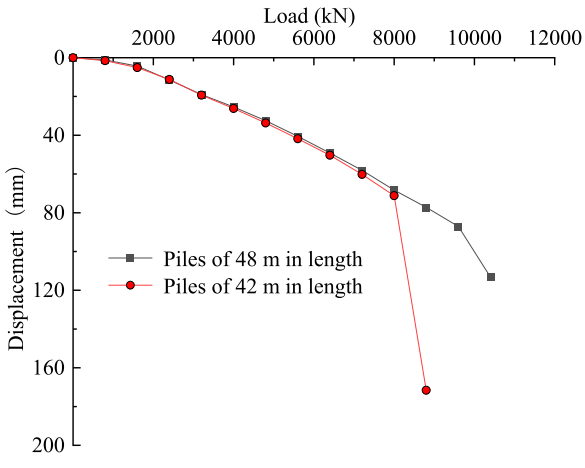

FIGURE 10
Load-displacement curves of 42m and 48 long pipe piles.

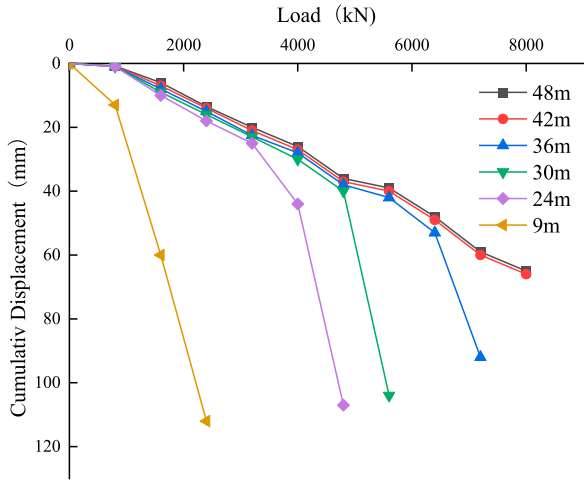

FIGURE 9
Load-displacement curves of pipe piles with different pile lengths.

secondary role in the bearing performance. For pipe piles with different pile lengths, the limit value of pile side friction resistance will also be different. The development of pile side resistance and pile end resistance of pipe piles under three different conditions of pile length of 36m, 42m and 48 m is shown in Figure 7 and Figure 8.

It can be seen from Figure 7 that the pile tip resistance of pipe piles with different pile lengths gradually increases with the increase of vertical load applied on the pile top, and the pile tip resistance increases slowly under the action of small vertical loads in the first few stages. When the vertical load on the pile top is large, the pile tip resistance increases faster. Comparing the changes of pile tip resistance under different pile lengths, it can be found that the pile length has little effect on the pile tip resistance, and regardless of the pile length, the ultimate resistance of the pile tip is close to each other.

It can be seen from Figure 8 that the pile side resistance of the pipe pile increases linearly with the increase of the pile top load. When the pile side resistance of the pipe pile reaches the maximum value that it can bear, the pile side resistance will be slightly reduced by continuing to apply the vertical load. When the pile top load continues to increase, the pile side resistance tends to be stable.

The vertical bearing capacity of pipe pile is closely related to the pile length. In order to study the influence of pile length on the bearing capacity of pipe pile, six kinds of pipe pile characteristics research models with pile length of 9 m, 24 m, 30 m, 36 m, 42 m and 48 m are established. The vertical load is applied to the top of the pile, and the bearing capacity displacement curve of the pipe pile under different pile length conditions is obtained. Figure 9 and Figure 10 are the bearing capacity displacement (Q-S) curves of pipe piles under different pile lengths.

From Figure 9 and Figure 10, it can be found that the bearing capacity of the pipe pile is positively correlated with the pile length. The 9 m long pipe pile produces large displacement deformation under the action of small vertical load, and its bearing capacity is weaker than that of the long pipe pile. When the vertical load on the pile top is small, the vertical displacement of the remaining pipe piles increases linearly with the increase of the load on the pile top. Continue to increase the load to reach the vertical ultimate bearing capacity of the 24 m long pipe pile. At this time, the pipe pile has a large vertical displacement, which indicates that the bearing capacity of the pipe pile reaches the limit value at this time. The restraint effect of the pile side friction on the pipe pile is weakened, and the pipe pile will penetrate the soil to cause its instability. The increase of pile length is mainly due to the increase of lateral resistance of pipe pile. At this time, the vertical ultimate bearing capacity of pipe pile is improved.

The ultimate bearing capacity of pipe pile under different pile length conditions is listed separately, and the variation diagram of ultimate bearing capacity of pipe pile under different pile length conditions is obtained, as shown in Figure 11. From the diagram, it can be found that the vertical ultimate bearing capacity of the pipe pile increases linearly with the increase of the length of the pipe pile. When the pile length of the pipe pile increases from 9 m to 48 m, the

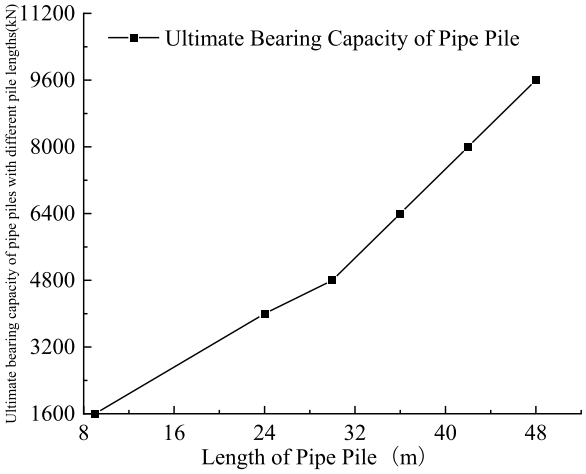

FIGURE 11
Ultimate bearing capacity of pipe piles with different pile lengths.

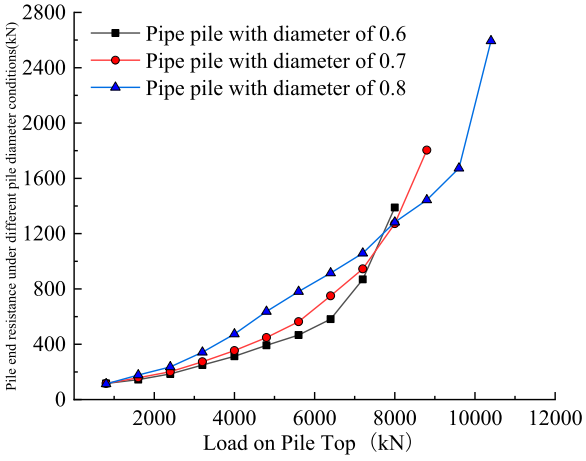

FIGURE 12
Pile end resistance of pipe piles with different pile diameters.

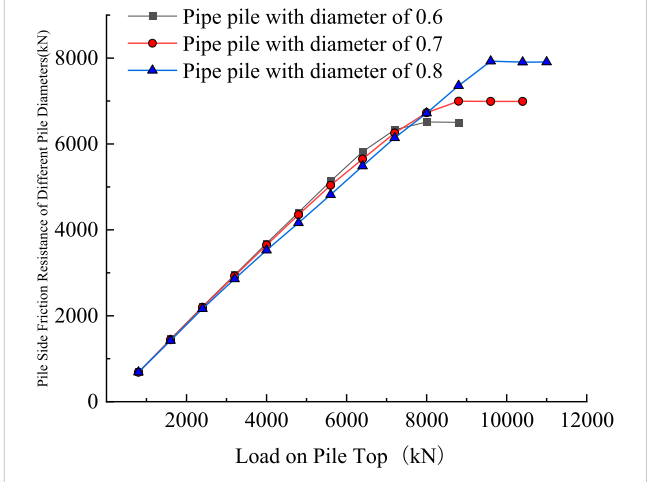

FIGURE 13
Pile side friction resistance of pipe piles with different pile diameters.

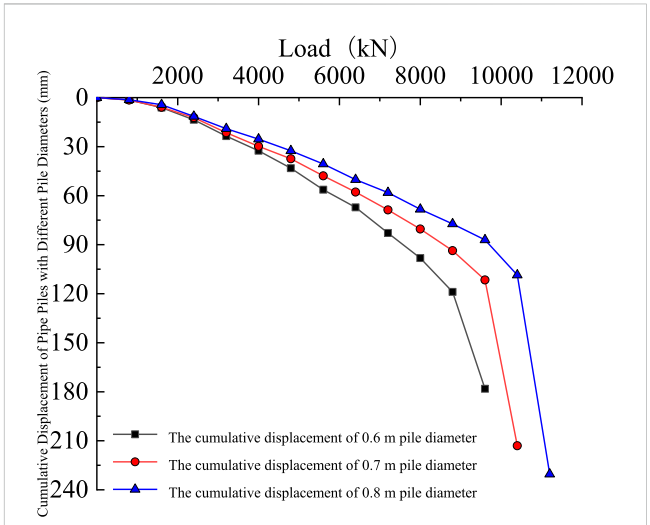

FIGURE 14
Q-S curve of pipe pile under different outer diameter conditions.

vertical ultimate bearing capacity of the pipe pile increases from 1,600 kN to about 9,600 kN. It can be seen that the pile length has a strong positive effect on the vertical bearing capacity of the pipe pile.

3.3.2 The influence of pile diameter

In this section, the outer diameter of the model pile is set to 0.6 m, 0.7~m, 0.8 m, and the length of the pipe pile is 48 m. The vertical load is applied to the pile top, and the gradient of each load is 800 kN. At the same time, the displacement of the pile top node, the pile end resistance and the pile side friction resistance are recorded when the vertical load is applied.

From Figure 12 and Figure 13, it can be found that the larger the diameter of the pipe pile is, the greater the bearing capacity of the pipe pile end is, and the more obvious the resistance of the pipe pile end is when it plays a bearing role. In the early stage of grading load loading, the growth rate of side resistance of pipe piles with different diameters is close to the same, and it shows a linear growth trend with the increase of pile top load. In the subsequent loading process, the displacement curve of the pipe pile with a diameter of 0.6 m has an inflection point when the pile top load is 8,000 kN. At this time, the pile top load exceeds the maximum value of the pile side resistance and the pile tip resistance, and the pipe pile produces a large displacement. Compared with the pipe pile with a diameter of 0.6 m, the pipe piles with a diameter of 0.7 m and 0.8 m have inflection points of the displacement curve at 8,800 kN and 9,600 kN, respectively. At this time, the lateral resistance no longer increases linearly with the increase of the pile top load, but decreases slightly and finally tends to be stable.

It can be found that the lateral resistance and the end resistance of the pipe pile are different in the stage of the bearing capacity of the pipe pile. The lateral resistance of the pipe pile mainly plays a role when the pipe pile does not produce a large displacement. At this

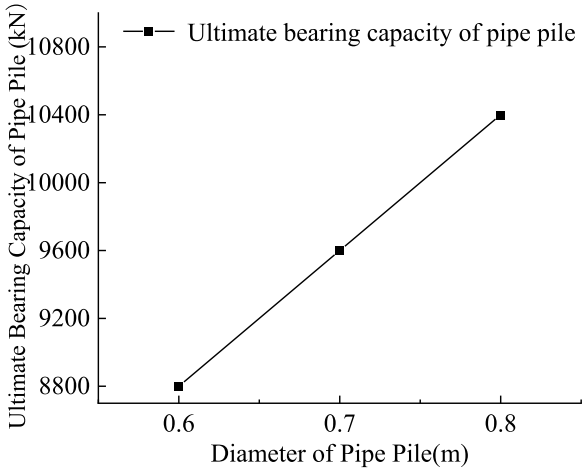

FIGURE 15
Ultimate bearing capacity of pipe pile under different outer diameter conditions.

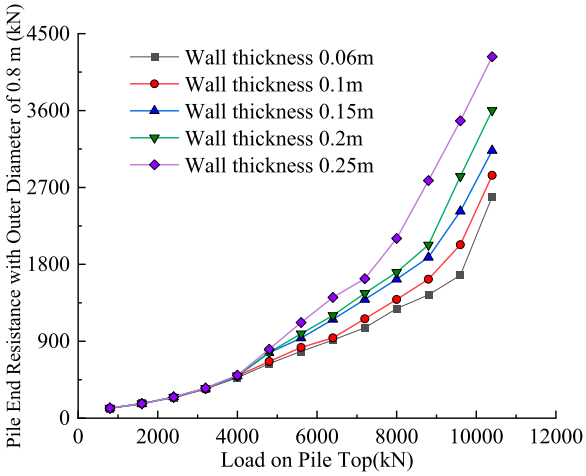

FIGURE 16
Curves of different bearing capacity of wall thickness with outer diameter of 0.7 m

time, the vertical displacement of the pipe pile is small, and the end bearing force plays a limited role. As the load on the top of the pile continues to increase, the pile end resistance gradually plays a bearing role together with the pile side resistance. In addition, the larger the diameter of the pipe pile, the larger the cross-sectional area of the pile side, the larger the contact area between the pipe pile and the soil around the pile, and the side resistance of the pipe pile will also increase.

The diameter of the pile is different, and its bearing characteristics under load are also different. The main difference is that the pile diameter is different, and the area of the contact surface between the pile side and the soil is different.

It can be seen from Figure 14 that the ultimate bearing capacity of the pipe pile will be improved when the diameter of the pipe pile increases. When the wall thickness of the pipe pile is constant and only the diameter of the pipe pile is increased, the slope of the load displacement curve of the pipe pile gradually becomes gentle with the increase of the pile diameter, which indicates that the larger the pile diameter, the smaller the vertical displacement of the pipe pile under the same vertical load.

As shown in Figure 15, by comparing the variation curves of the ultimate bearing capacity of the pipe pile under different pile diameters, it can be found that when the diameter of the pipe pile increases from 0.6 m to 0.7 m, its bearing capacity increases by 800 kN. When the pile diameter increases from 0.7 m to 0.8 m, its ultimate bearing capacity also increases by 800 kN. Comparing the change curve of bearing capacity when the pile length increases, it can be found that increasing the diameter of the pipe pile has a positive and almost linear effect on the ultimate bearing capacity of the pipe pile.

3.3.3 The influence of diameter-thickness ratio

In order to study the development law of pile end bearing capacity under different diameter-thickness ratio conditions, two kinds of pipe pile models with different pile wall thickness of 0.7 m and 0.8 m outer diameter were established in this simulation, and

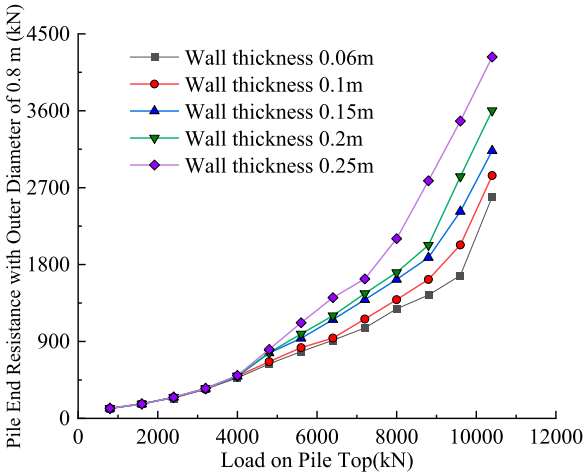

FIGURE 17
Curves of different bearing capacity of wall thickness with outer diameter of 0.8 m

the development and evolution law of pile end bearing capacity was studied. The variation of the bearing capacity of the pile end under different diameter-thickness ratios is shown in Figure 16 and Figure 17.

From the curve of bearing capacity change, it can be seen that in the early stage of load action, the pile end resistance increases gradually with the increase of pile top load, and the growth rate of pile end resistance is small. With the gradual increase of load, the tip resistance of pipe pile shows a quadratic curve growth trend. Comparing the bearing capacity curve of pipe pile end, it can be found that the sudden increase of pipe pile end resistance is related to the limit value of pile side resistance. At this time, the vertical load of pile top exceeds the limit value of pile side resistance, and the pipe pile produces large vertical deformation. In addition, compared with the same outer diameter, the pile end resistance curve of the pipe pile

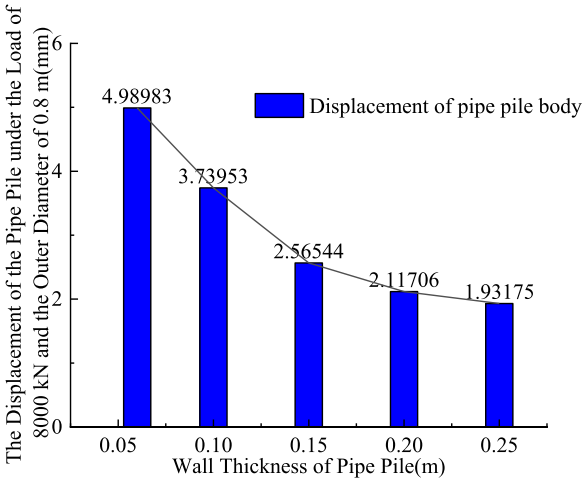

FIGURE 18
Vertical displacement of pipe pile under different wall thickness conditions.

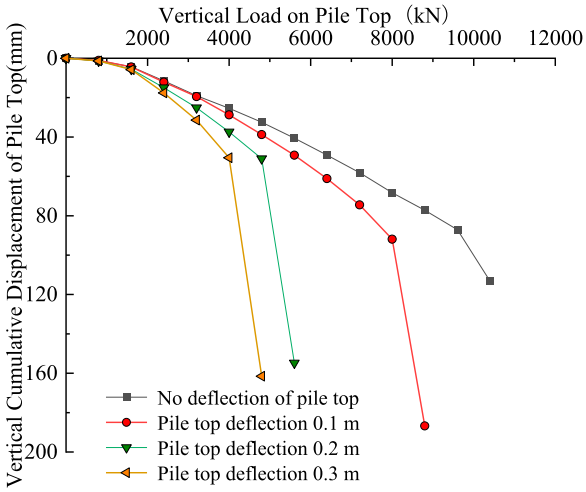

FIGURE 19
The bearing capacity-displacement curve of pipe pile under different deflections.

can be found when the pile wall thickness is different. The larger the wall thickness of the pipe pile, the greater the ultimate pile end resistance (end bearing force) that the pipe pile bottom can withstand.

When the vertical load is applied to the top of the pipe pile, the pipe pile body will also produce certain deformation, and the deformation of the pipe pile body is mainly related to the thickness of the pile wall and the material of the pile body.

It can be found from Figure 18 that the vertical displacement of the pile body is different under the same load when the wall thickness of the pipe pile is different. The thicker the pile wall is, the smaller the displacement deformation of the pile body under the load of the pile top is. The thinner the pile wall, the greater the displacement deformation of the pile under the load of the pile top. From the development of pile displacement under different wall thickness conditions, with the increase of pile wall thickness, the reduction of pile displacement decreases exponentially.

In this model test, the outer diameter of the model pile is 0.8 m, and the length of the pipe pile is 48 m. Under the condition that the diameter and length of the pipe pile do not change, the position of the pipe pile is changed, so that the bottom of the pipe pile is not moved, and the top of the pile is deflected to the side of the soil to study the bearing capacity of the pile foundation under different offset conditions. In the test, the deflection of the pipe pile is set to 0 m, 0.1 m, 0.3 m and 0.5 m respectively. The vertical load is applied to the pile top step by step, and the gradient of each load is 800 kN. At the same time, the displacement of the pile top node is recorded when the vertical load is applied. Finally, the vertical load-vertical displacement (Q-S) curve is output through the recorded node displacement, as shown in the following Figure 19.

Figure 19 is the bearing capacity-displacement curve of pipe pile under different deflection states. From the diagram, it can be found that when the pipe pile is deflected, its bearing capacity will also change greatly. The greater the deflection of the pile top, the smaller the ultimate bearing capacity of the pipe pile. When the pipe pile is vertical, its vertical ultimate bearing capacity is about 9,600 kN.

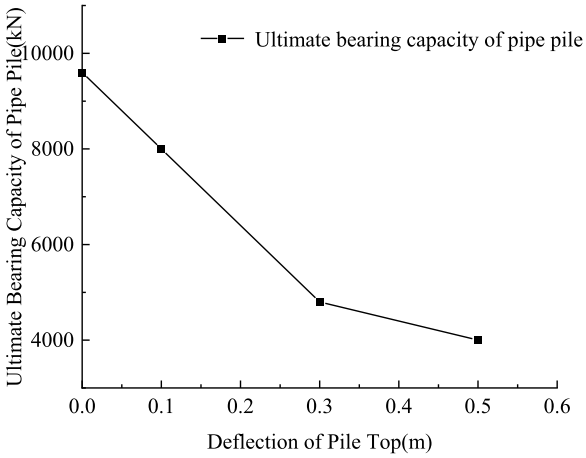

FIGURE 20
Curves of ultimate bearing capacity of pipe piles with different deflections.

When the deflection of the pile top reaches 0.5 m, the vertical ultimate bearing capacity of the pipe pile is only 4,000 kN.

Comparing the changes of the vertical ultimate bearing capacity of the pipe pile under different deflection states, as shown in Figure 20, it can be found that when the deflection of the pipe pile top is 0.1 m, 0.3 m, and 0.5 m, the ultimate bearing capacity is reduced by 1,600 kN, 3,200 kN, and 800 kN, respectively. This indicates that when the deflection state of the pipe pile gradually increases, the ultimate bearing capacity of the pipe pile shows a decreasing trend, that is, when the top of the pipe pile is just deflected, its ultimate bearing capacity is greatly reduced. When the deflection of the pile top exceeds 0.3 m, the trend of decreasing the ultimate bearing capacity is gradually weakened.

By comparing the bearing capacity curves of pipe piles under different deflection states, it can be found that the ultimate

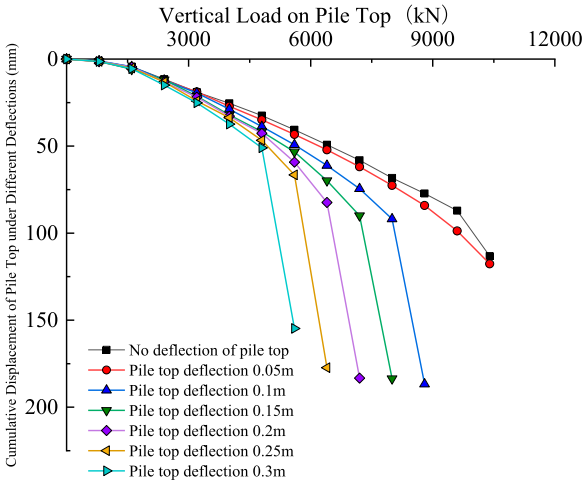

FIGURE 21
Load-displacement curves of pipe piles under different deflections.

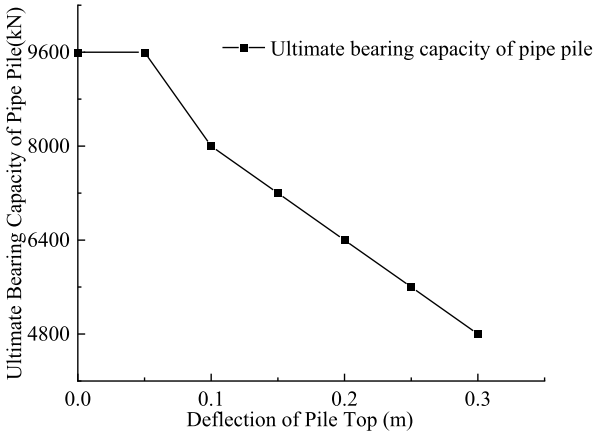

FIGURE 22
The change of ultimate bearing capacity of pipe pile under different deflection.

bearing capacity of pipe piles decreases rapidly when the pipe piles are just deflected. When the deflection is less than 0.3 m, the vertical ultimate bearing capacity decreases by 1,600 kN for every 0.1 m deflection of the pile top. When the deflection reaches 0.3 m, the decreasing trend of the vertical ultimate bearing capacity of the pipe pile is gradually weakened by increasing the deflection of the pile top. When the deflection of the pile top increases from 0.3 m to 0.5 m, the ultimate bearing capacity is only reduced by 800 kN.

In order to study the decreasing trend of vertical bearing characteristics of pipe pile when the deflection of pipe pile is 0.3 m, the deflection angle of pipe pile top is refined to determine the threshold value of horizontal deformation of pile. The horizontal deformation of the pile top is reduced from 0.1 m to 0.05 m. The vertical bearing capacity of the pipe pile is analyzed when the horizontal displacement of the pile top is 0.05 m, 0.1 m, 0.15 m and 0.2 m. The bearing capacity-displacement curve of the pipe pile is shown in Figure 21.

From Figure 21, it can be found that the change trend of each displacement curve under different deflection of pipe pile top is basically the same. When the deflection of the pile top is 0.05 m, the vertical ultimate bearing capacity of the pipe pile is close to the bearing capacity of the pipe pile without deflection, but the cumulative displacement of the pipe pile increases. When the deflection of the pile top increases from 0.05 m to 0.1 m, the ultimate bearing capacity decreases from 9,600 kN to 8,000 kN. After that, for every 0.05 m deflection of the pile top, the vertical ultimate bearing capacity of the pipe pile is reduced by 800 kN. It is found from Figure 22 that the vertical bearing capacity of the pipe pile decreases the most when the deflection increases from 0.05 m to 0.1 m. When the deflection of the pipe pile is greater than 0.05 m, the vertical ultimate bearing capacity decreases rapidly with the increase of the deflection. Therefore, under the test conditions simulated in this test, if the horizontal deflection of the pipe pile top exceeds 0.05 m, the vertical ultimate bearing capacity of the pipe pile is lower than the expected value.

4 Calculation correction formula of vertical bearing capacity of pipe pile

Through the change of the bearing capacity of the pipe pile under the above different influences, combined with the existing formula of the bearing capacity of the pipe pile, it is found that the existing formula of the bearing capacity of the pipe pile does not take into account the factors of the offset of the pipe pile. The calculation formula of the vertical ultimate bearing capacity of the pipe pile under the influence of the deflection factor is modified.

4.1 Calculation formula of vertical ultimate bearing capacity of pipe pile

According to JGJ94-2008 “Technical Code for Building Pile Foundations”, the existing calculation of the ultimate bearing capacity of prestressed concrete pipe piles includes two parts: pile side resistance and pile end resistance. The pile end resistance is also divided into the end resistance of the open part and the end resistance of the pipe wall. Therefore, the existing formula for calculating the vertical ultimate bearing capacity of pipe piles is:

$$Q_{uk} = Q_{sk} + Q_{pk} = \mu \sum q_{sik} l_i + q_{pk} A_p \quad (1)$$

Q_{sk} is the limit side resistance standard value (kN); Q_{pk} is the standard value of the ultimate end resistance (kN); the coefficient of side squeezing effect is 1; μ is the outer diameter of the pipe pile (m); q is the standard value of the ultimate lateral resistance of the pile (kpa); l is the thickness of each layer of soil (m^2); Q_{pk} is the standard value of the ultimate end resistance of the pile (kpa); A_p is the net area of the pile end of the hollow pile (m^2).

In addition, combined with the existing ’ Technical Code for Building Pile Foundations ’, a modified formula for calculating the vertical bearing capacity of pipe piles is established under the premise of considering the side friction resistance of the inner wall, which is:

TABLE 5 Design parameters of pile foundation in each soil layer in site survey depth.

Soil layer number	Name	Standard value of ultimate shaft resistance of pile (kPa)	Standard value of ultimate end resistance of pile (kPa)			
		Prefabricated pile	Prefabricated pile			
			l≤9	9<l≤16	16<l≤30	30≤l
1	Plain fill soil	—	—	—	—	—
2	Silt	0(Liquefaction)	—	—	—	—
3	Silty clay	50	—	—	—	—
4	Silty sand	20(Liquefaction)	—	—	1900	—
5	Silt	45	—	—	1900	—
6	Silty sand	50	—	—	3000	—
7	Fine sand	55	—	—	4500	5000
8	Silt	50	—	—	—	3600

$$Q_{uk} = (u_1 + au_2)\sum q_{sik}l_i + q_{pk}A_p \quad (2)$$

Here, u_1 and u_2 are the perimeter of the outer wall and inner wall of the pipe pile; a (Liu and Du, 2012) is the correction coefficient of soil plug effect, which is 0.15, 0.3 and 0.4 for cohesive soil, silt and sand, respectively. Other parameters are the same as those in Formula 1.

The Table 5 is the design parameters of pile foundation in each soil layer obtained after the completion of site exploration.

According to the above table and formula 1, the standard value of ultimate end bearing capacity Q_{pk} = 501.8976 kN and the standard value of ultimate pile side resistance Q_{sk} = 5,132.016 kN can be calculated, and then the standard value of vertical ultimate bearing capacity of single pile of pipe pile Q_{uk} = 5,633.9136kN, and the characteristic value of vertical bearing capacity is 2,816.9568kN; according to the above table and formula 2, the standard value of the ultimate vertical bearing capacity of the pipe pile is calculated to be 7,165.70608 kN;

Comparing the standard value of vertical ultimate bearing capacity of single pile calculated by Formula 1 with that obtained by field test, it can be found that the calculated standard value of vertical ultimate bearing capacity of pipe pile is 24.09% (8800 kN) lower than the measured value, and 46.54% lower than the simulated standard value of vertical ultimate bearing capacity of pipe pile. The vertical ultimate bearing capacity of single pile calculated by formula 2 is 18.57% lower than the measured value, and 25.36% lower than the simulated vertical ultimate bearing capacity of pipe pile.

It can be seen that the vertical ultimate bearing capacity of the pipe pile calculated according to the above formula is less than the measured and simulated values, but the calculation results of formula 2 are closer to the measured and simulated values, which is considering the influence of the soil plug effect of the pipe pile on the side resistance and the pile end resistance.

4.2 Correction of calculation formula for vertical bearing capacity of pipe pile

From the simulation results, it can be found that the side friction resistance and pile end resistance of the pipe pile will be affected by the shape of the pipe pile. In the construction of group piles and multiple pipe piles, the vertical state of the pipe pile in the soil will be affected by the post-penetration pile. Displacement or deflection will lead to changes in the vertical ultimate bearing capacity of the pipe pile.

The calculation formula of the bearing capacity of the open-end pipe pile foundation in the JGJ94-2008 "Technical Code for Building Pile Foundations" is the empirical formula for the calculation of the bearing capacity of the pipe pile. The vertical ultimate bearing capacity of the pipe pile calculated by this formula is obviously smaller than the measured value. This is because the standard value of the ultimate resistance of the pipe pile side is mostly selected according to the experience in the value range. In order to accurately calculate the standard value of the vertical ultimate bearing capacity of the pipe pile, the *in situ* test method can directly determine the side resistance and end resistance of the pile. *In-situ* test methods include static cone penetration test (CPT), standard penetration test (SPT) and pressuremeter test (PMT). Through these *in situ* test methods, the standard values of pile side and pile end resistance in different depths of soil can be accurately obtained. In addition, the standard value of pile side and pile end resistance can be calculated by static calculation method. The standard values of pile side and pile end resistance of silty soil, silty clay and silty fine sand in the Yellow River flood area can be calculated by the β method in the static calculation method. The expression is:

$$q_{su} = \sigma_v' k_0 tg\delta \quad (3)$$

For normally consolidated clayey soil, $k_0 \approx 1 - \sin\phi'$, $\delta \approx \phi'$, so:

$$q_{su} = \sigma_v'(1 - \sin\varphi')tg\varphi' = \beta\sigma_v' \quad (4)$$

In Formula 3: k_0—coefficient of Earth pressure at rest δ—External friction angle between pile and soil σ_v'—The average vertical effective stress of pile side soil layer.

In Formula 4: φ'—Effective internal friction angle of pile side soil layer.

Formula 2 is the revised calculation formula of vertical bearing capacity of pipe pile. In Formula 2, four parts of pile side resistance, soil plug resistance in pile and pile end resistance are considered. In

the calculation of soil plug resistance in pile, a certain reduction is carried out. Through reduction, the calculation results obtained accurately reflect the influence of soil plug in pile on bearing capacity. However, there is still a certain gap between the calculated vertical ultimate bearing capacity of pipe piles and the measured value due to the lack of full consideration of soil squeezing effect, soil layer difference, soil plugging depth and blocking effect. The influence of the soil plug in the pipe pile on the pile side resistance is added in Formula 2. After the construction of the longer pipe pile is completed, the soil plug formed at the pile end opening also has a certain influence on the pile end resistance.

Considering the blocking effect of the soil plug at the end of the pipe pile, another additional resistance will be formed at the end of the pipe pile after its formation. In order to calculate this resistance, it is necessary to assume that the static lateral pressure coefficient inside and outside the end of the pipe pile is similar to the gravity of the soil layer. At the same time, according to the calculation formula of the ultimate end resistance of the pile proposed by Vesic (1975) based on the theory of circular cavity expansion, the expression is:

$$q_{pu} = cN_c + \bar{p}N_q \tag{5}$$

In Formula 5: q_{pu}—ultimate pile end resistance c—internal cohesion of soil $\bar{p}$—The average vertical pressure on the side of the pile end plane N_c、 N_q—The dimensionless bearing capacity coefficient of strip foundation reflects the cohesion of soil and the influence of side load above the pile bottom plane.

Here:

$$\bar{p} = \frac{1 + 2K_0}{3}\gamma h \tag{6}$$

In Formula 6: K_0—Static lateral pressure coefficient of soil

Considering the blocking effect of the soil plug at the end of the pipe pile, it is assumed that the lateral pressure coefficient of the static inside and outside of the pipe pile end is similar to the gravity of the soil layer, so there is:

$$\bar{p} + \Delta p = \frac{1 + 2K_0}{3} = \gamma h(L + h_0) = \bar{p}\left(1 + \frac{h_0}{L}\right) \tag{7}$$

In Formula 7: h_0—The initial height of soil plug (m) L—Length of pipe pile body (m)

Through Eq. 7, the enhancement effect of the soil plug blocking effect on the bearing capacity of the pile end can be calculated. Therefore, the end resistance effect coefficient $1 + \frac{h_0}{L}$ can be considered. It can be recorded as u_3.Combined with Formula 2, the bearing capacity correction formula of pipe pile can be obtained as follows:

$$Q_{uk} = (u_1 + au_2)\sum q_{sik}l_i + q_{pk}(A_j + u_3A_{pl}) \tag{8}$$

In Formula 8: A_{pl}—Section area of pipe pile end opening

Among them, $u_3 = 1 + \frac{h_0}{L}$, the vertical ultimate bearing capacity of the pipe pile calculated by this formula is 8,211.1 kN, which is 6.69% different from the measured value of the vertical bearing capacity of the pipe pile, and 13.47% different from the simulation results. It can be seen that the vertical ultimate bearing capacity of the pipe pile obtained by the calculation results is in good agreement with the measured results. This is because the formula not only considers the influence of the soil plug effect on the side resistance of the inner wall of the open pipe pile, but also considers the influence of the soil plug effect on the bearing capacity of the pile end.

Formula 8 can accurately calculate the vertical bearing capacity of vertical pipe piles. In order to obtain the modified formula for calculating the bearing capacity of super-long and super-large diameter pipe piles in the Yellow River flood area, the formula for calculating the bearing capacity after deflection is modified based on the numerical simulation results. After the pipe pile is offset, its vertical bearing capacity decreases rapidly with the increase of offset. Combined with the numerical simulation results, there are:

$$Q'_{uk} = \eta\left[(u_1 + au_2)\sum q_{sik}l_i + q_{pk}(A_j + u_3A_{pl})\right] \tag{9}$$

In Formula 9: η—The values are shown in the following Table 6.

According to the value of the reduction factor in the above table, combined with the formula 9, the calculation method of the vertical ultimate bearing capacity of the super-large and super-long diameter displacement pile in the Yellow River flood area is obtained. The formula can be used to calculate the bearing characteristics of the super-large and super-long diameter pipe pile in the Yellow River flood area under the influence of the construction effect. The value of the reduction factor can be determined by comprehensive analysis according to the method described in this paper. In addition, the modified formula is only applicable to the calculation of the vertical ultimate bearing capacity of super-large and super-long diameter pipe piles under similar geological conditions. According to the value of the reduction factor in the above table, combined with the formula 9, the calculation method of the vertical ultimate bearing capacity of the super-large and super-long diameter displacement pile in the Yellow River flood area is obtained. The formula can be used to calculate the bearing characteristics of the super-large and super-long diameter pipe pile in the Yellow River flood area under the influence of the construction effect. The value of the reduction factor can be determined by comprehensive analysis according to the method described in this paper. In addition, the modified formula is only applicable to the calculation of the vertical ultimate bearing capacity of super-large and super-long diameter pipe piles under similar geological conditions. According to the modified formula for calculating the bearing capacity of the deflection pipe pile at the top of the pile, combined with the deviation value of the pile top, the vertical ultimate bearing capacity of the pipe pile under the deviation value can be quickly calculated, which can provide reference for engineering construction and design personnel. By accurately estimating the bearing capacity of pipe piles, over-design or insufficient design, insufficient bearing capacity or excessive loading can be avoided, thereby improving the economy and sustainability of the project. It helps to optimize design, improve resource efficiency, reduce environmental impacts, and ensure the safety and longevity of structures to achieve integrated sustainable development goals.

4.3 Verified by an engineering example

A residential building uses PHC pipe piles to reinforce the foundation. The physical and mechanical parameters of the soil obtained from the geological survey are shown in the following Table 7 (Zhou et al., 2007). The diameter of the pipe pile is 60 cm,

TABLE 6 The value of reduction coefficient of pipe pile bearing capacity calculation.

Deflection of pipe pile (m)	Deflection angle of pipe pile	η
0.05	0.059°	1
0.1	0.119°	0.83
0.15	0.179°	0.75
0.2	0.239°	0.67
0.25	0.299°	0.58
0.3	0.359°	0.5

TABLE 7 Physical mechanical parameters of soil.

Soil layer number	Average thickness(m)	Γ (kN/m^3)	E_s (MPa)	C (kPa)	Φ (°)
②	2.85	18.7	6.12	25	10
③	6.58	18.5	3.55	10	11.5
④	13.5	18.8	7.35	26	15
⑤	12.5	17.3	3.43	15	12
⑥	21.6	17.9	5.05	20	19
⑦	10.2	18.7	12.3	7	27
⑧	11.5	19.1	16.6	6	29
$⑨_1$	10.3	19.4	21	5	32
$⑨_2$	8.5	19.1	12.3	20	21

the length of the pipe pile is 50 m, and the vertical ultimate bearing capacity of the pipe pile is 3,550 kN. Under the action of the squeezing effect of the adjacent pipe pile construction, the deflection of the pipe pile top is caused, and the deflection amount is 16 cm and 32 cm respectively. After the accident, the bearing capacity of the deflected pipe pile is tested. The ultimate bearing capacity of the pipe pile with displacement of 16 cm and 32 cm is 2,335 kN and 1,760 kN respectively. The bearing capacity of the PHC pipe pile of the project is calculated by using the method in this paper. The ultimate bearing capacity of the pipe pile with deflection of 16 cm and 32 cm is 2,605 kN and 1,718 kN respectively. The error between the calculation results and the test results is between 2.38% and 11.56%, The comparison results are shown in Figure 23, and it is within the allowable range of engineering error. It shows that the calculation method is in good agreement with the field test results, which proves the accuracy of the correction formula.

The anothere project is located in the suburbs of Jiaxing City, Zhejiang Province, the total land area of the project is 40,251 m^2, the total construction area is about 94,385.5 m, the above-ground construction area is about 80,008.4 m^2, and the underground construction area is 14,377.1 m^2. The importance level of the project is grade two, the complexity level of the site is grade two, and the complexity level of the foundation is grade two. The project site belongs to the Yangtze River Delta marsh plain exploration depth of the Yangtze River Delta, which is composed of 9 engineering geological layers. The main physical and mechanical parameters of each soil layer are shown in the Table 8.

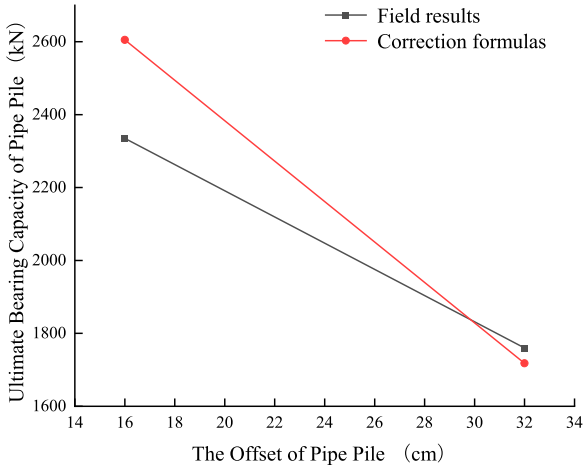

FIGURE 23
The comparison between the field results and the modified formula results.

The high-rise residential building (No. 1-9) of this project is a shear wall structure. The design adopts pile-raft foundation, the raft thickness is 700 mm, and the foundation beam adopts the dark beam under the wall. The pile type is PHC-A500 (100) −27a, the relative elevation of the pile top is-3.650 m, the pile end enters the seventh layer of sandy silt layer, the concrete strength of the pile body is C80, and the total number of piles is 81.

TABLE 8 The main physical and mechanical parameters.

Soil layer number	Soil name	Thickness (m)	Moisture content (%)	q_s (kPa)	q_p (kPa)	E_s (MPa)
①	Plain fill	0.3–1.5	—	—	—	—
②	Silty clay	0.4–1.1	34.8	7	—	3.7
③-1	Muddy clay	1.3–9.2	49.1	5	—	2.2
③-2	Silt clay	1.7–5.1	33.6	13	—	6.1
④-1	Silt clay	0.3–5.4	27.7	23	—	8.3
④-2	Silt clay	5.3–8.9	28.9	20	—	7.7
⑥-1	Silt clay	4.8–6.4	24.1	29	—	16.8
⑥-2	Silt clay	1.1–8.4	29.5	27	—	12.5
⑥-3	Sandy silt	1.1–4.3	33.3	27	500	15.6
⑦	Sandy silt	11.1–15.3	27.9	32	500	35.7
⑧	Silt	0.7–2.5	40.0	—	—	7.9
⑨-1	Silty clay	0.8–2.0	24.1	—	—	18.9
⑨-2	Clayey silt	Not drilled through	29.8	—	—	15.8

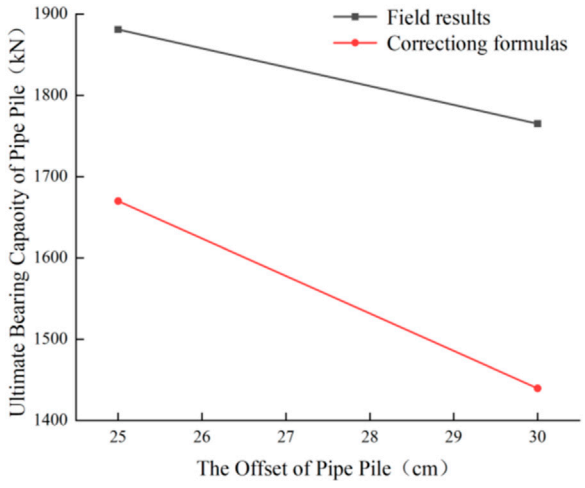

FIGURE 24
The comparison between the field results and the modified formula results.

After the construction of the engineering pile is completed, the foundation pit excavation of the "No.5 high-rise residential building" is first carried out. During the excavation process, 58 PHC pipe piles were found to be deviated, accounting for about 71.7% of the total number of piles, and each pile was deviated to the west. In order to detect the vertical compressive bearing capacity of the deviated pile, the designers put forward the requirement to carry out the high strain dynamic test of the pile foundation for the two most representative deviated piles. The test results are as follows: The vertical compressive ultimate bearing capacity of pile No. 58 (offset 300 mm) is 1765 kN, which is equivalent to 61.3% of that without offset. The vertical compressive ultimate bearing capacity of pile No. 74 (offset 250 mm) is 1,811 kN, which is equivalent to 62.9% of that without offset. This is no more than 11.3% different from the reduction factor proposed above, within the allowable error range. The comparison results are shown in Figure 24.

5 Conclusion

(1) In this paper, the vertical bearing capacity of pipe pile under different attribute conditions is studied by numerical simulation and theoretical derivation. The research shows that when the length of pipe pile changes, the vertical bearing capacity changes the most, and the vertical ultimate bearing capacity of pipe pile increases with the length of pipe pile. The growth trend is approximately linear; When the wall thickness of the pipe pile increases, the vertical bearing capacity increases positively and linearly, and the reduction of the displacement of the pile body decreases exponentially.

(2) The bearing capacity of the pile is mainly affected by the pile side resistance and the pile end resistance. When the pile top load is small, the pile side resistance plays a major bearing role. When the pile top load is large, the pile side resistance and the pile end resistance work together to exert the bearing capacity. After the pile side resistance reaches its limit value, the pile top load will continue to increase, and the pile side resistance will be slightly reduced. The limit value of the pile side resistance is related to the outer diameter of the pipe pile.

(3) The vertical bearing capacity of super-long and super-large diameter pipe pile will change when it is affected by the deflection deformation caused by the pile sinking. By studying the changes of the vertical bearing capacity of the pipe pile under different deflection states, it can be found that the larger the deflection angle of the pipe pile, the smaller the vertical ultimate bearing capacity. When the deviation angle of the pipe pile exceeds 0.35°, the vertical ultimate bearing capacity of the pipe pile is only 50% of the vertical pipe pile.

(4) According to the research results, the calculation formula of the vertical ultimate bearing capacity of the pipe pile in the "Technical Code for Building Pile Foundations" is derived and modified. The modified formula proposes a reduction factor for the calculation formula of the vertical ultimate bearing capacity of the super-large and super-long diameter pipe pile after deflection. The modified formula can accurately calculate the vertical ultimate bearing capacity of the offset pipe pile. Finally, the error between the calculation example and the field test results is within the allowable range of engineering error, which shows that the calculation method is in good agreement with the field test results, and proves the accuracy of the correction formula.

Data availability statement

The original contributions presented in the study are included in the article/supplementary material, further inquiries can be directed to the corresponding authors.

Author contributions

SZ: Conceptualization, Methodology, Project administration, Writing–review and editing. ZR: Conceptualization, Methodology, Writing–review and editing. YZ: Conceptualization, Methodology, Writing–review and editing. WF: Conceptualization, Methodology, Writing–original draft. CL: Conceptualization, Methodology, Project administration, Writing–review and editing. CLu: Conceptualization, Methodology, Writing–original draft. YW: Formal Analysis, Writing–review and editing.

Funding

The author(s) declare financial support was received for the research, authorship, and/or publication of this article. This research was funded by the Natural Science Foundation of Shandong Province of China (ZR2022QE082), and Shandong Provincial Transportation Science and Technology Plan (2021B89). The sponsorship and interest are gratefully acknowledged.

Acknowledgments

We deeply appreciate the warm and efficient work of the editors and reviewers.

Conflict of interest

Authors YZ, WF, and CLu were employed by Shandong Luqiao Group Co., Ltd.

The remaining authors declare that the research was conducted in the absence of any commercial or financial relationships that could be construed as a potential conflict of interest.

Publisher's note

All claims expressed in this article are solely those of the authors and do not necessarily represent those of their affiliated organizations, or those of the publisher, the editors and the reviewers. Any product that may be evaluated in this article, or claim that may be made by its manufacturer, is not guaranteed or endorsed by the publisher.

References

Bekki, H., Canou, J., Tali, B., Dupla, J. C., and Bouafia, A. (2013). Evolution of local friction along a model pile shaft in a calibration chamber for a large number of loading cycles. *Comptes Rendus Mec.* 341, 499–507. doi:10.1016/j.crme.2012.11.012

Burland, J. B., and Burland, J. B. (1973). Shaft friction of piles in clay - a simple fundamental approach. *Ground Eng.* 6 (3), 30–42.

Cai, J., Zhou, W. Q., Lin, Y. X., and Huang, L. Q. (2006). Experimental study on axial force behavior of super-long prestressed high-strength concrete pipe in deep soft soil. *China Civ. Eng. J.* 10, 102–106. doi:10.1016/S1872-1508(06)60035-1

Chin, J. T. C. Y. K. P., Chow, Y., and Poulos, H. (1990). Numerical analysis of axially loaded vertical piles and pile groups. *Comput. Geotechnics* 9, 273–290. doi:10.1016/0266-352x(90)90042-t

Coyle, H. M., and Reese, L. C. (1966). Load transfer for axiallyloaded piles in clay. *ASCE Soil Mech. Found. Div. J.* 92 (2), 1–26. doi:10.1061/jsfeaq.0000850

El Naggar, M. H., and Wei, J. Q. (2000). Uplift behaviour of tapered piles established from model tests. *Can. Geotechnical J.* 37 (1), 56–74. doi:10.1139/t99-090

Fleming, W. G. K. (1992). A new method for signle pile settlement prediction and analysis. *Geotechnique* 42, 411–425. doi:10.1680/geot.1992.42.3.411

Gao, F., Cheng, X. S., Chen, X. J., and Lv, Q. (2022). Bearing capacity characteristics of compacted cement StabilizedGravel pile composite foundation. *Int. J. Pavement Res. Technol.* 2022. doi:10.1007/s42947-022-00226-2

Gao, G. Y., Gao, M., Chen, Q. S., and Yang, J. (2019). Field load testing study of vertical bearing behavior of a large DiameterBelled cast-in-place pile. *KSCE J. Civ. Eng.* 23, 2009–2016. doi:10.1007/s12205-019-2065-z

Guo, H. L., He, W., Hu, Y. B., and Wang, Y. H. (2004). Predication of vertical ultimate bearing capacity of PHC piles. *Eng. Mech.* 12, 78–83.

Han, J. Y., Wang, J., Jia, D. F., Yan, F. S., Zhao, Y., Bai, X. Y., et al. (2023). Construction technologies and mechanical effects of the pipe-jacking crossing anchor-cable group in soft stratum. *Front. Earth Sci.* 10, 1019801. doi:10.3389/feart.2022.1019801

Hong, Y. K., and Chen, Q. H. (1985). Load transfer performance of bored pile. *Chin. J. geotechnical Eng.* 5, 22–35.

Jae, H. C., Jeongsoo, K., Harald, K., McVay, M. C., and Lai, P. (2012). A numerical and experimental study of bearing stiffness of drilled shafts socketed in heterogeneous rock. *Comput. Struct.* 90-91 (Jan), 145–152. doi:10.1016/j.compstruc.2011.09.004

Jiang, G., Shao, D., Zong, C. F., Chen, G., Huang, J., Lin, C., et al. (2023). Thermo-mechanical behavior of long-bored energy pile: a full-scale field investigation. *KSCE J. Civ. Eng.* 27, 145–155. doi:10.1007/s12205-022-0588-1

Jiang, Z. C. (2012). Experimental study on vertical bearing characteristics of super-long prestressed high-strength concrete pipe pile in soft clay. *Rock Soil Mech.* 33, 2639–2644.

Jin, Q., Zheng, Y. J., Cui, X. Z., Cui, S. Q., Qi, H., Zhang, X. N., et al. (2020). Evaluation of dynamic characteristics of silt in Yellow river flood fieldafter freeze-thaw cycles. *J. Central South Univ.* 27, 2113–2122. doi:10.1007/s11771-020-4434-7

Kee, K., Jayantha, K., and Asadul, H. (2006). Numerical modelling of the side resistance development of piles in mudstone with direct use of sidewall roughness. *Int. J. Rock Mech. Min. Sci.* 43, 987–995. doi:10.1016/j.ijrmms.2006.01.002

Lehane, B. M., and Gavin, K. G. (2001). Base resistance of jacked pipe piles in sand. *J. Geotechnical Geoenvironmental Eng.* 127, 473–480. doi:10.1061/(ASCE)1090-0241(2001)127:6(473)

Li, T. L., Zhao, W., Liu, R., Han, J. Y., Jia, P. J., and Cheng, C. (2023). Visualized direct shear test of the interface between gravelly sand and concrete pipe. *Can. Geotechnical J.* doi:10.1139/cgj-2022-0007

Li, Z. Y., Wang, K. H., and Wu, W. B. (2017). Vertical dynamic impedance oflarge-diameter pile considering its transverse inertia effect and constructiondisturbance effect. *Mar. Georesources Geotechnol.* 35, 256–265. doi:10.1080/1064119X.2016.1149259

Liu, F. T., Zhao, C. F., and Wu, J. (2010). Experimentalresearch on bearing behavior and size effect of large diameter boredcast-in-situ piles Changzhou area. *Chin. J. RockMechanics Eng.* 29, 858–864.

Liu, J. W. (2008). *Study on installationand bearing capacity character of jacked pile*. Qingdao: Qingdao Technological University.

Liu, Z. R., and Du, L. H. (2012). Ultimate bearing capacity analysis of prestressed concrete open pipe piles. *Concrete* 02, 120–123. doi:10.3969/j.issn.1002-3550.2012.03.037

Matos, R., Pinto, P., Rebelo, C., Veljkovic, M., and Simões da Silva, L. (2018). Axial monotonic andcyclic testing of micropiles in loose sand. *Geotechnical Test. J.* 41, 526–542. doi:10.1520/GTJ20160284

Miao, C. J., Shi, B., and Zheng, X. (2018). BOFDA internal force test of offshore super-long PHC pipe. *J. Nanjing Univ.* 54, 1057–1063. doi:10.13232/j.cnki.jnju.2018.06.001

Pan, Z. H. (2006). The application of super-long PHC pipe pile in high-precision engineering static pressure method construction. *Build. Oper.* 09, 674–675. doi:10.3969/j.issn.1004-1001.2006.09.006

Poulos, H., and Davis, E. (1974). Elastic solutions for soil and rock mechanics. *Int. J. Rock Mech. Min. Sciences&Geomechanics Abstr.* 11, 311–411.

Randolph, M. F., Leong, E. C., and Houlsby, G. T. (1991). One-dimensional analysis of soil plugs in pipe piles. *Geotechnique* 41, 587–598. doi:10.1680/geot.1991.41.4.587

Sang, D. F., and Tan, D. Y. (2014). Numerical simulation study on vertical bearing characteristics of large diameter PHC pile. *Mar. Traffic Eng.* 01, 168–172. doi:10.3969/j.issn.1002-4972.2014.01.031

Sivaraman, S., and Muthukkumaran, K. (2022). Consolidation effect on pile capacity assessment based on instrumented field pile load test. *Arabian J. Sci. Eng.* 47, 4913–4927. doi:10.1007/s13369-021-06305-z

Tian, X. J., Hu, W. T., and Gong, X. N. (2015). Longitudinal dynamic response ofpile foun dation in anonuniform initial strain field. *KSCE J. Civ. Eng.* 19, 1656–1666. doi:10.1007/s12205-014-0049-6

Wang, Y. H., Zhang, M. Y., and Bai, X. Y. (2019). Study of penetrationcharacteristics and influence factor of jacked pile based on fiber bragg grating sensing technology. *Rock Soil Mech.* 40, 4801–4812.

Zang, M. Y., Liu, J. W., and Yu, X. X. (2009). Field test study of time effect on ultimate bearing capacity of jacked pipe pile in soft clay. *Rock Soil Mech.* 30, 3005–3008. doi:10.3969/j.issn.1000-7598.2009.10.020

Zhang, Z. M., Liu, J. W., and Yu, F. (2010). Relationship between terminativejacking force and ultimate bearing capacity of jacked pipe piles. *Chin. J. Geotechnical Eng.* 32, 1207–1213.

Zhou, J., Zhang, Z., and Wang, L. (2007). Study on the influence of super-long PHC pipe offset on its vertical bearing capacity. *Build. Struct.* 11, 378–386. JournalArticle/5aeb1a23c095d70944fe98e6. doi:10.19701/j.jzjg.2007.11.018

frontiers | Frontiers in Earth Science

TYPE Original Research
PUBLISHED 02 February 2024
DOI 10.3389/feart.2023.1314034

Check for updates

OPEN ACCESS

EDITED BY
Pengjiao Jia,
Soochow University, China

REVIEWED BY
Ang Li,
Chang'an University, China
Jinjin Ge,
Anhui University of Science and Technology, China

*CORRESPONDENCE
Peng-Xiang Li,
lipengxiangsd@163.com
Xin-Hao Zhu,
zhuxinhao01@163.com

RECEIVED 10 October 2023
ACCEPTED 20 November 2023
PUBLISHED 02 February 2024

CITATION
Zhao J-S, Yang J-H, Li P-X, Zhu X-H, Chen C-F and Zhang J-C (2024), Mechanical performance and failure mechanism of U-steel support structure under blast loading. *Front. Earth Sci.* 11:1314034. doi: 10.3389/feart.2023.1314034

COPYRIGHT
© 2024 Zhao, Yang, Li, Zhu, Chen and Zhang. This is an open-access article distributed under the terms of the Creative Commons Attribution License (CC BY). The use, distribution or reproduction in other forums is permitted, provided the original author(s) and the copyright owner(s) are credited and that the original publication in this journal is cited, in accordance with accepted academic practice. No use, distribution or reproduction is permitted which does not comply with these terms.

Mechanical performance and failure mechanism of U-steel support structure under blast loading

Jin-Shuai Zhao[1,2], Jia-Hao Yang[1], Peng-Xiang Li[3]*, Xin-Hao Zhu[4]*, Chong-Feng Chen[5] and Jian-Cong Zhang[6]

[1]Faculty of Civil Engineering and Mechanics, Jiangsu University, Zhenjiang, China, [2]Key Laboratory of Geotechnical Mechanics and Engineering of Ministry of Water Resources, Yangtze River Scientific Research Institute, Wuhan, China, [3]College of Urban Construction, Heze University, Heze, China, [4]State Key Laboratory of Geomechanics and Geotechnical Engineering, Institute of Rock and Soil Mechanics, Chinese Academy of Sciences, Wuhan, China, [5]Xi'an Research Institute, China Coal Technology and Engineering Group Corporation, Xi'an, China, [6]PowerChina Huadong Engineering Corporation Limited, Hangzhou, China

The U-steel support structures of underground caverns are prone to instability and failure under blast loads. The purpose of the underground cavern reinforcement is to mobilise the self-supporting capacity of the surrounding rock to resist the blast. To better understand the mechanical performance and failure mechanism of the U-steel support, the fracture process and vibration behaviour of the support structure under blast loading are investigated by the microseismic monitoring experiment. The dynamic responses of the cavern support structures under blast loading are investigated, and the potentially hazardous sections of the U-steel support structure are revealed by the theoretical analysis. The microseismic monitoring results show that the blast induced microseismic events are concentrated in the arch shoulder of the small chainage, correspondingly the U-steel structures in this region have been partially extruded and deformed. The failure mechanism of the supporting structure is presented. In order to effectively inhibit the internal fracture evolution or macroscopic failure of the rock mass, the synergetic reinforcement scheme of the structures is proposed. The results of the research can be used as a reference for the design and control method of the U-steel support in similar projects.

KEYWORDS

underground cavern, u-steel support, blast load, microseismic monitoring, structural performance

1 Introduction

As geotechnical engineering progresses to depth, excavation-induced seismicity and rockburst disasters increase (Feng et al., 2017; Gong et al., 2018; Zhao et al., 2024; Li et al., 2023c; Li et al., 2023d; Cui et al., 2023). The underground caverns are usually excavated by the traditional drilling and blasting (D&B) technique. The shock wave released by the blast will inevitably damage the bearing capacity of the rock mass structure (Dong et al., 2016; Dong et al., 2020; Zhao et al., 2022a; Zhao et al., 2022b; Zheng et al., 2023a; Zheng et al., 2023b). Blast excavation of underground caverns can cause varying degrees of damage

or failure of the rock mass, seriously threatening the safety of workers and delaying the progress of the project (Yang et al., 2021; Yang et al., 2023; Zhao et al., 2023). Blast technology in cavern excavation is a double-edged sword, i.e., a reasonable and useful blast design can effectively fracture the rock within the desired limits of excavation (Ma et al., 2018; Chen et al., 2020; Feng et al., 2021; Feng et al., 2023; Guo et al., 2023). However, inappropriate blasting excavation will damage the rock mass of the cavern (Brady and Brown, 2005; Liu et al., 2023; Mei et al., 2023).

As an important line of defence, rock support measures are used to prevent or minimize damage to excavations, thereby improving workplace safety (Kaiser and Cai, 2012; Xu et al., 2023a; Xu et al., 2023b). Rock reinforcement refers to the method of using artificial components to strengthen and stabilize the rock mass (Li and Doucet, 2012). Rock reinforcement measurements can effectively control the inner fracture of the surrounding rock (Jiang et al., 2015; Xu et al., 2022). U-steel is a kind of support structure that commonly used in mines and underground caverns. In recent years, the U-steel support structure of rock engineering has attracted much attention from scholars due to its high strength, high rigidity and good mechanical properties (Barla et al., 2011; Wong et al., 2013; Zhao et al., 2015; Cheng et al., 2023a; Cheng et al., 2023b; Lu et al., 2023). Wang et al. (2018) studied the deformation and damage zone of soft rock by *in-situ* acoustic wave testing technology, and proposed a combined support technology with U-steel support and anchor grouting. Wu et al. (2019) assessed the response of rock bolts and U-steel under coal-burst conditions, with the aim of improving the knowledge of the application of support systems in coal-burst-prone mines. Wang et al. (2021) used numerical simulation to study the interaction between the U-steel reinforcement element and the surrounding rock under dynamic loading. In a word, the point or surface mechanical properties of U-steel were effectively revealed.

Actually, the high precision three-dimensional monitoring method can directly reflect the mechanical properties of support structure (Ma et al., 2019). The microseismic monitoring is a timely and regional monitoring method, which can monitor the failure process of rock mas or support structure of whole underground cavern in 3D perspective (Ma et al., 2013; Dai et al., 2016; Laura and Martin, 2017; Xu et al., 2018). Chen et al. (2015) used microseismic monitoring technology to deeply study the rock mass damage and rockburst in the deep-buried tunnel of Jinping II Hydropower Station. Based on the experimental study of rock failure acoustic emission, Liu et al. (2021) established a prediction method of rock burst disasters of mine. Microseismic monitoring technology has been widely used in rock engineering under high stress, and has become a common means of deep engineering disaster research (Li et al., 2022; Li et al., 2023a.; Li et al., 2023b; Xia et al., 2023a; Xia et al., 2023b; Chen et al., 2023).

The above-mentioned literature are concerned with the local damage or failure of U-steel structure. However, there are few researches on the vibration response characteristics and failure mechanism of support structure under blast loading. In order to investigate the evolution mechanism of the U-steel support, a three-dimensional microseismic monitoring test of the support structure of the underground cavern was carried out. The vibration response and failure mechanism of the support structure under blast load were investigated. The research results also provide reference for further study on the synergetic reinforcement mechanism of rockbolt and U-steel support structure.

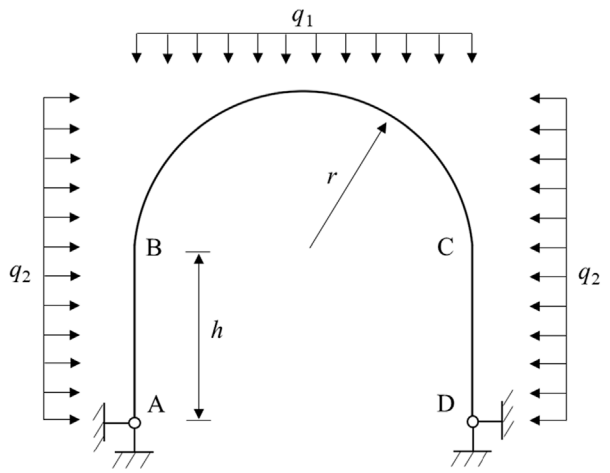

FIGURE 1
Mechanical model of the U-steel.

2 Dangerous section of U-steel

2.1 Mechanical model

The mechanical model of the U-steel support is established as a rigid frame structure with a straight wall and a semi-circular arch (Figure 1). In the figure, h is the height of the shed leg of the U-steel, and r is the radius of the semi-circle arch. In order to simplify the calculation, these conditions are supposed as follows: 1) the connection between arch beam and shed leg is rigid junction; 2) the U-steel support is closely attached to surrounding rock, and there is no air gap between the U-steel and rock mass; 3) regardless of the elastic resistance of surrounding rock to the support. Assuming that the U-steel is subjected to vertical load q_1 and horizontal load q_2, and the calculation formula is:

$$q_1 = \gamma H \tag{1}$$

$$q_2 = \lambda q_1 = \lambda \gamma H \tag{2}$$

In the Eqs. 1, 2, γ is the average bulk density of the overlying surrounding rock, H is buried depth, and λ is the lateral pressure coefficient.

2.2 Solution of constraint reaction force

The mechanical model of the plane rigid frame is a statically indeterminate structure. In Figure 1, both ends A and D are fixed hinges. The principle of force method is adopted to solve the problem. Supposing the horizontal constraint of point D is released, and the force F is used instead, thus the basic statically system with hinged end A and rolling support end D is obtained. The basic

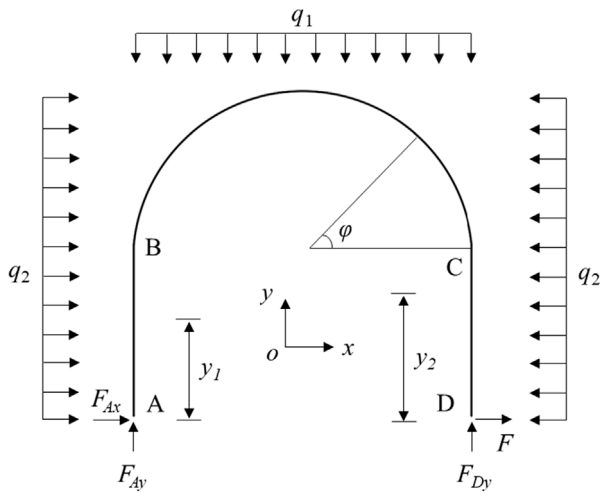

FIGURE 2
Calculation model of internal force equation under external load.

structural system after removing redundant constraints is shown in Figure 2. The displacement of the point D is calculated by the principle of force method. Assuming that a right horizontal unit force is applied to the point D, then the equation of axial force and the bending moment of rigid frame can be calculated. Actually, the end D is a fixed hinge support, the horizontal displacement of point D is zero, and the calculation formula is:

$$\Delta D_x = 0 \tag{3}$$

From the static equilibrium equation of Eq. 3, the force F can be resolved:

$$F = \frac{b}{a}q_1 + \frac{c}{a}q_2 \tag{4}$$

$$a = \frac{\pi}{2S} + \frac{2h^3}{3I} + \frac{1}{I}\left(\pi h^2 + 4r + \frac{\pi}{2}r^2\right) \tag{5}$$

$$b = \frac{2r}{3S} - \frac{r^2}{I}\left(\frac{\pi h}{4} + \frac{2r}{3}\right) \tag{6}$$

$$c = \frac{1}{S}\left(\frac{\pi h}{2} + \frac{4}{3}r\right) + \frac{h^4}{4I} + \frac{1}{2I}\left(\pi h^3 + 6h^2 r + \frac{3}{2}\pi h r^2 + \frac{4}{3}r^3\right) \tag{7}$$

The bending moment equation of AB, CD and BC sections of plane rigid frame are listed in Eqs. 8–10:

$$M_1(y_1) = Fy_1 - \frac{1}{2}q_2 y_1^2 \tag{8}$$

$$M_2(y_2) = -Fy_2 + \frac{1}{2}q_2 y_2^2 \tag{9}$$

$$M(\varphi) = \frac{1}{2}q_2(h + r\sin\varphi)^2 + \frac{1}{2}q_1 r^2(1 - \cos\varphi)^2 - F(h + r\sin\varphi) - q_1 r^2(1 - \cos\varphi) \tag{10}$$

Where φ is the angle between the arbitrary section of BC segment and the section of point C.

TABLE 1 The basic mechanical parameters of U-steel support.

Sectional area (cm^2)	Inertia moment (cm^4)	Design height of shed leg m)	Design arch radius m)
45.69	928.65	5	6

2.3 Determination of dangerous section position

The sections AB and CD of plane rigid frame are symmetrical structures, and the positions of dangerous sections are also symmetrically distributed. Therefore, the AB section is used as the analysis object to determine the dangerous section of the U-steel support. Taking the uniform load ($q_1 = q_2 \neq 0$) of the support as an example. The basic mechanical parameters of U-steel support that used in the tunnel cavern are listed in Table 1. The above mechanical parameters are substituted into Eqs. 4–7, then the force F can be solved in Eq. 11:

$$F = -1.18q_1 + 5.65q_2 \tag{11}$$

According to the bending moment equation of the plane rigid frame AB section, the bending moment curve is a quadratic parabola. Differentiating the bending moment equation of the plane rigid frame AB section, as shown in Eq. 12:

$$M_1'(y_1) = 0 \tag{12}$$

The location of the dangerous section of the AB section of the U-steel support is calculated in Eq. 13:

$$y_1 = \frac{F}{q_2} = -\frac{1.18q_1}{q_2} + 5.65 \tag{13}$$

According to the condition of $q_1 = q_2 \neq 0$, the potential dangerous section of AB section is 4.47 m away from the foot of shed leg. It can be judged from Eq. 10 that the dangerous section of the BC section is the middle of the arch. In practical engineering, the sectional area, inertia moment and cavern size are relatively constant. The change of dangerous section position of support is related to the lateral pressure coefficient, that is, the force transferred between support and surrounding rock, which is manifested in the difference of contact force between support and surrounding rock.

3 Case study

3.1 Engineering background

The excavation size of left and right bank underground cavern groups of the Baihetan Hydropower Station are huge, among them the layout of designed right caverns is indicated in Figure 3. The powerhouse is divided into ten layers along the elevation, and the cavern is excavated by the traditional D&B method. The designed excavation and blasting scheme of the powerhouse is demonstrated in Figure 4.

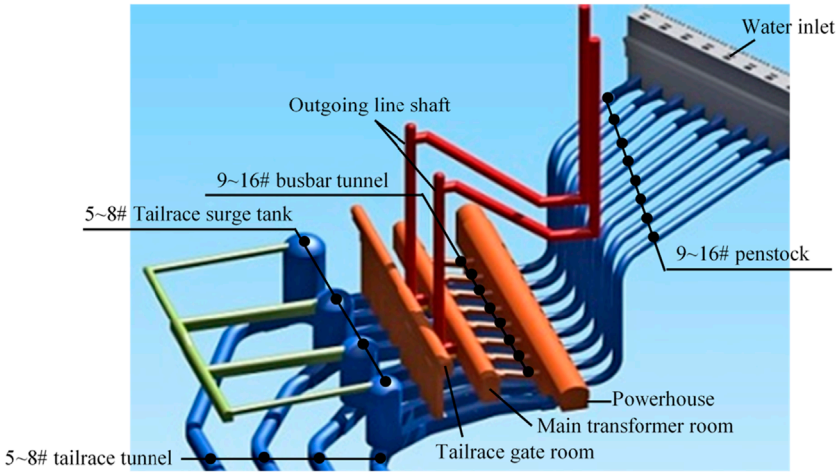

FIGURE 3
The layout of designed right underground cavern groups.

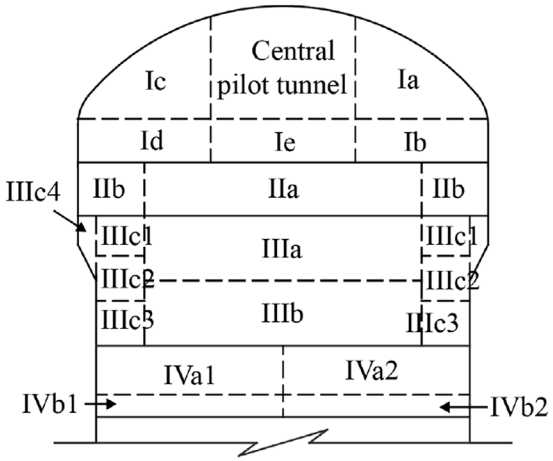

FIGURE 4
Blasting excavation scheme of the underground powerhouse.

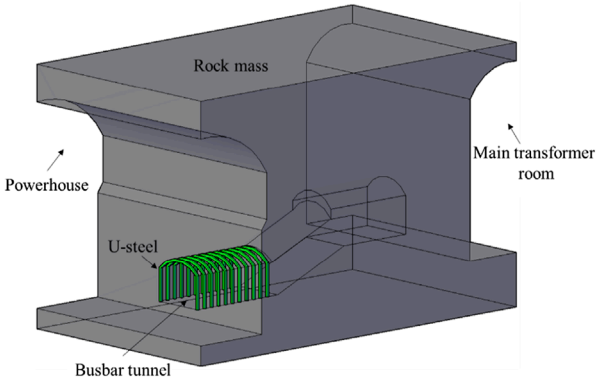

FIGURE 5
Schematic diagram of the U-steel support of the busbar tunnel.

3.2 *In-situ* seismic monitoring experiment

The excavation size of underground cavern group is large, and the cavern group is in high stress environment, which means it is easy to induce the failure of the surrounding rock. Due to the unfavourable multi-face empty environment of the busbar tunnel, the disturbance degree of blast excavation unloading on surrounding rock near the intersecting cavern is obviously greater than that of single cavern. In order to effectively inhibit the internal fracture evolution or macroscopic deformation of surrounding rock of busbar tunnel, the reinforcement measures such as rockbolt and U-steel support scheme are often used. The schematic diagram of the U-steel support of the busbar tunnel is shown in Figure 5.

The busbar tunnel intersects with the powerhouse, and the U-steel supports of the busbar tunnel are inevitably be impacted by the blasting excavation of the powerhouse. In order to study the dynamic response characteristics of the U-steel support under blast excavation load, a microseismic monitoring test was carried out during the excavation of the cavern. The 11# intersecting cavern area is selected as the research object. Three-dimensional layout of microseismic sensor network of underground cavern is described in Figure 6. There are three monitoring sections surrounding the research area. Two microseismic sensors are installed on each section, and the distance between adjacent monitoring section is 30 m. The adopted microseismic sensor in underground cavern is the uniaxial geophone. The bandwidth and sensitivity of the geophones used are 7–2000 Hz and 100 V/m/s, respectively.

3.3 Vibration response of the support structure

3.3.1 Blast signal characteristic

The forced vibration of U-steel support structure is excited by blast load. Studying the vibration signal excited by blast load is

10.3389/feart.2023.1314034

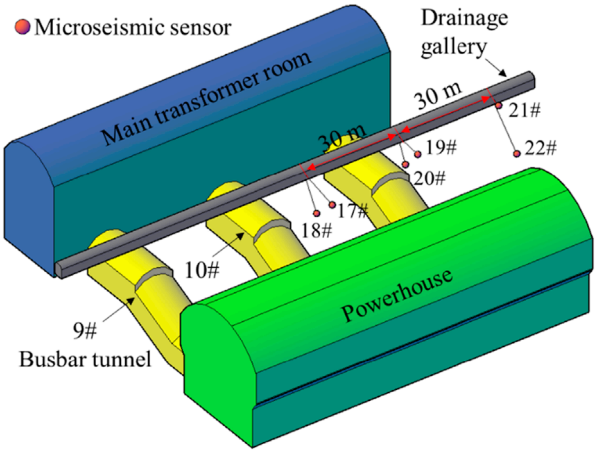

FIGURE 6
Three-dimensional layout of microseismic sensor network of underground cavern.

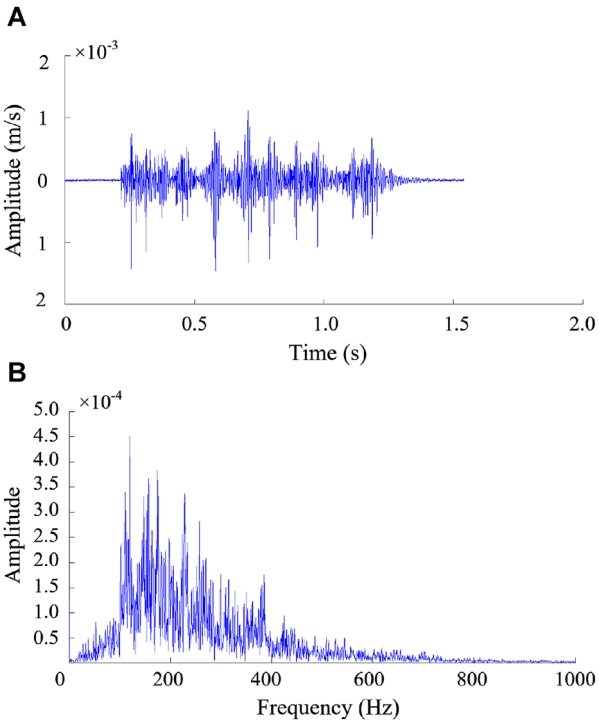

FIGURE 7
Waveform characteristics of blast signal: **(A)** amplitude-time curve, **(B)** amplitude-frequency curve.

helpful to understand the dynamic characteristics and mechanical mechanism of support structure. The representative waveform of the blast signal received by the MS sensor is shown in Figure 7. Millisecond blast technology is used in the field construction of underground cavern, resulting in multiple persistence of the excited blast spectrum, that is, a single blast spectrum contains multiple similar subwaveforms.

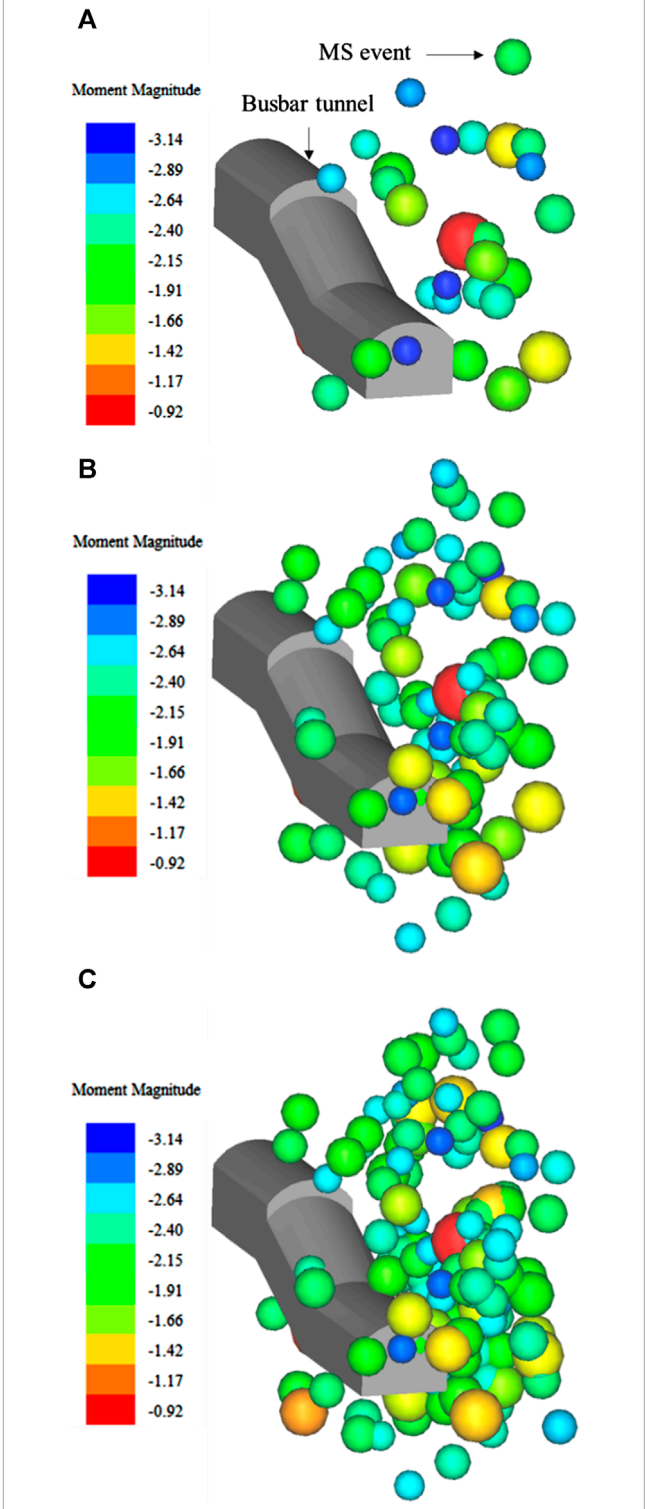

FIGURE 8
Spatial evolution of microseismic events in rock mass induced by blast load. **(A)** Crack initiation period, **(B)** crack propagation period, and **(C)** crack cluster period.

3.3.2 Evolution mechanism of MS events

In the process of blast excavation of underground cavern, the blast shock wave is not directly applied to the support structure, but is transmitted to the support structure through the rock mass

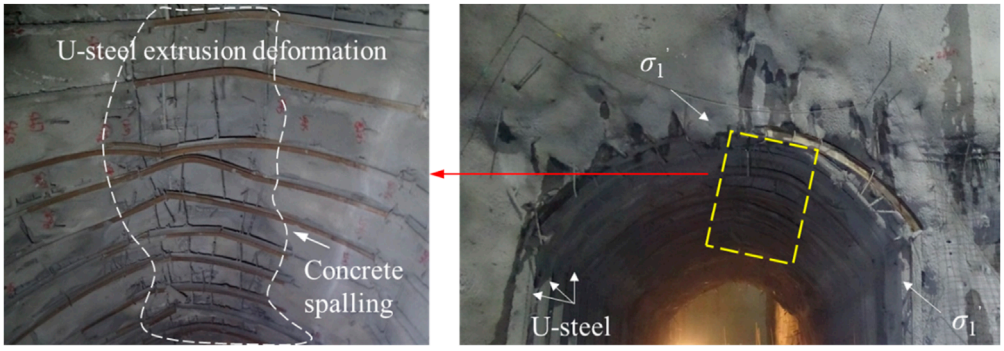

FIGURE 9
Blast-induced local failure of U-steel support structure.

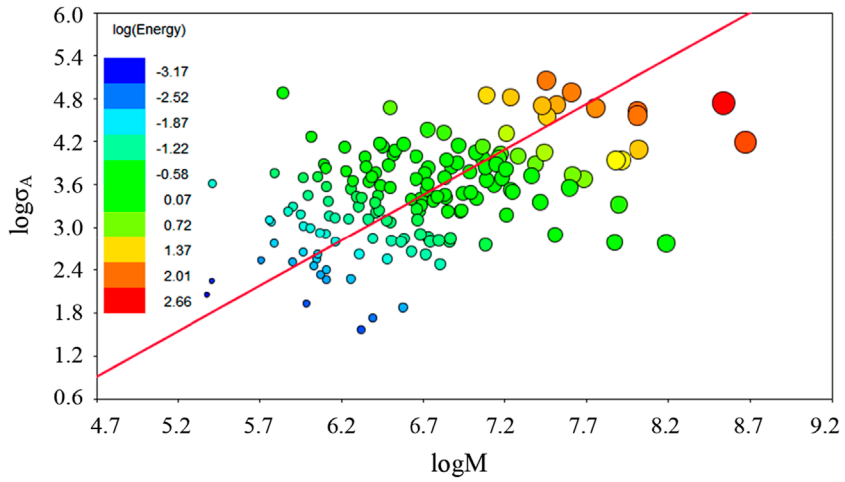

FIGURE 10
Relationship between apparent stress and seismic moment.

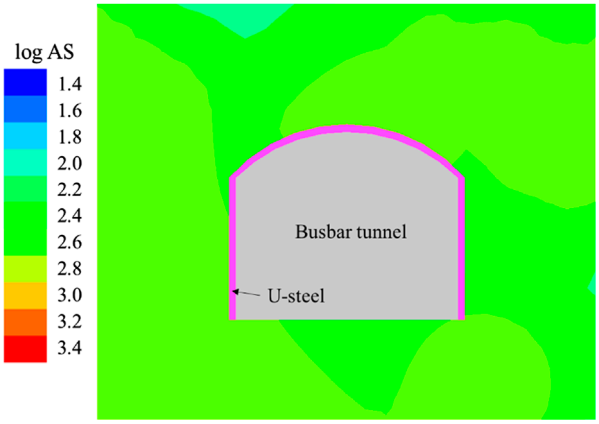

FIGURE 11
Apparent stress (AS) cloud of microseismic events induced by blast load.

medium. Therefore, the fracture process of rock mass around the support structure can also reflect the vibration characteristics of the support structure. When rock breaks, energy is released in the form of an elastic wave. Theoretically, any fracture will produce an elastic wave accompanied by a slight vibration. If the vibration signal generated by the rock fracture triggers the sensor, then the rock fracture is recorded as a microseismic event. The spatial evolution of microseismic events induced by blast excavation is displayed in Figure 8. In the diagram, the color of the ball represents the moment magnitude. The brighter the color, the larger the magnitude. Moment magnitude is a source parameter that uses the seismic moment to describe the magnitude of an earthquake rupture. The size of the ball represents the radiated microseismic energy, and the larger the radius of the ball, the greater the released microseismic energy. According to the vibration response degree of support structure to on-site blast excavation, the spatial evolution of microseismic events can be divided into three stages: 1) Crack initiation period (Figure 8A). There are a few microseismic events induced by blast excavation. The spatial evolution shows that the micro-fracture initiates at the arch shoulder of the small chainage side of busbar tunnel. 2) Crack propagation period (Figure 8B). A small number of large magnitude events are induced by blast excavation, accompanied by a large number of small magnitude events, which indicates that primary fracture propagation or new fracture initiation occurs in rock mass under the action of tangential

concentrated stress. 3) Crack cluster period (Figure 8C). The rock mass enters the active period of deformation and fracture influenced by the strong blast load. At this stage, the microseismic events occur frequently, and the cumulative microseismic energy increases.

In addition, blast load is the important factor causing the damage and deterioration of surrounding rock of the busbar tunnel. It is found that the microseismic events of large magnitude near the working face often occur within a few hours after blast. Blast load is equivalent to the transient convergence of rock mass after excavation, providing favorable conditions for deformation and failure of U-steel support structure. Therefore, the excavation method of short footage and discontinuous blasting should be adopted when the working face advances to the vicinity of the intersecting cavern.

The on-site survey found that the concrete spray layer of busbar tunnel peeled off and the U-steel structure was partially extruded and deformed. The failure of U-steel is the extrusion deformation under compressive stress. The damage location of U-steel support structure is consistent with the cluster area of microseismic events, as shown in Figure 9. The cluster nucleation of microseismic events indicates that the internal fracture of surrounding rock in this area is serious, and the deformation and failure of hard brittle surrounding rock first occurs in the stress concentration area. The failure of the U-steel support is also closely related to the redistribution stress after blast excavation.

3.3.3 Apparent stress of microseismic events

Apparent stress can effectively measure the magnitude of dynamic stress release in the seismic source, which is a microseismic parameter independent of the source model. The calculation formula of apparent stress is:

$$\sigma_A = \frac{\mu E}{M} \tag{14}$$

In the formula, μ is the shear modulus, E is the radiated microseismic energy, and M is the seismic moment.

The relationship between apparent stress and seismic moment of microseismic events is illustrated in Figure 10. The color of the ball in the figure represents the microseismic energy of the microseismic event. The lighter the color, the smaller the energy released. The size of the ball represents the moment magnitude of the microseismic event. The larger the radius of the ball, the larger the magnitude

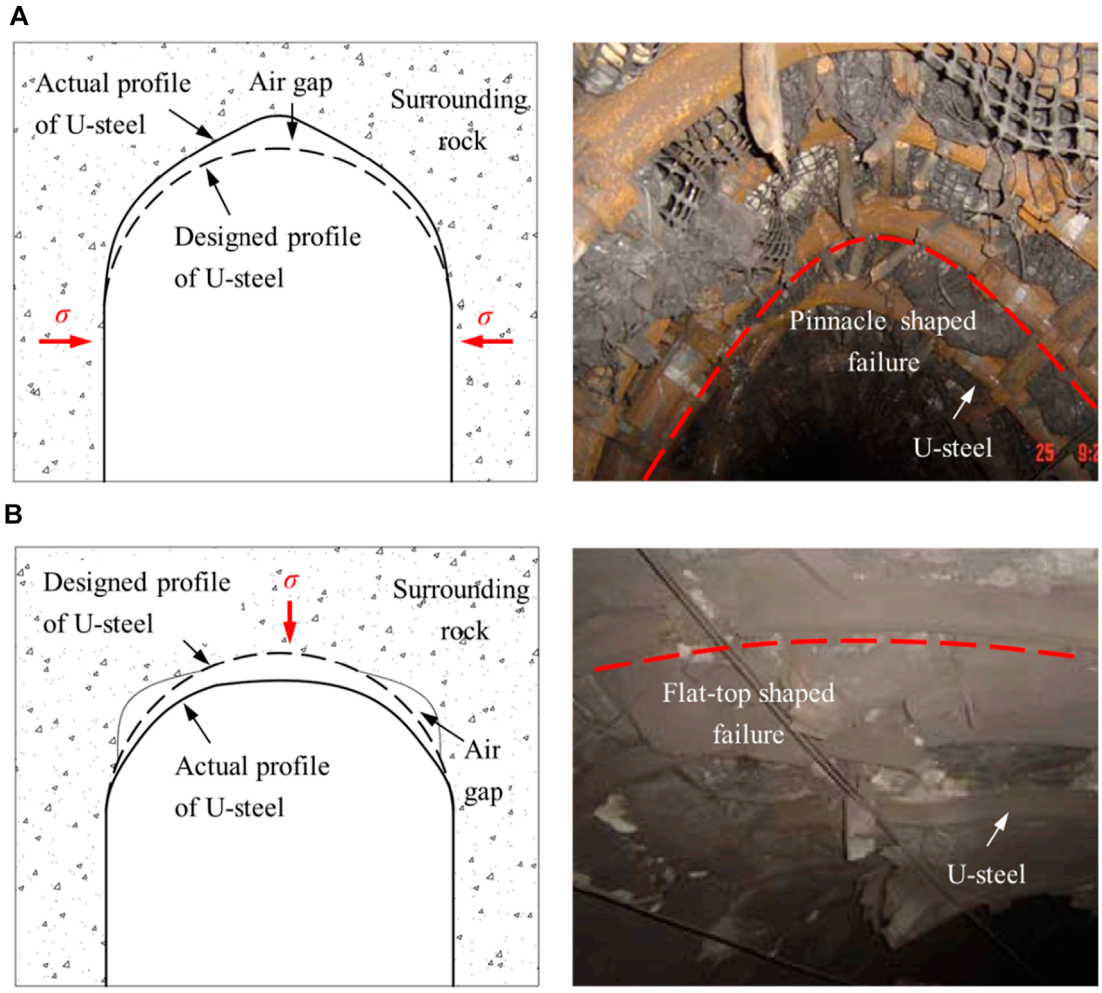

FIGURE 12
Schematic diagram of structural instability failure of U-steel support: **(A)** pinnacle shaped failure, **(B)** flat-top shaped failure.

of the event. The apparent stress and seismic moment relation is approximately power-law, and so a linear fit is used in the log-log plot. The instability dynamic process of the structure can be expressed by Eq. 14, which depends on the stiffness ratio of the unstable rock to the surrounding rock mass.

In general, the greater the degree of stress concentration, the greater the elastic strain energy released when the rock mass breaks. The magnitude of energy release can be reflected by the source parameter of apparent stress. The blast-induced cloud diagram of apparent stress of microseismic events is shown in Figure 11. As shown in the figure, the apparent stress is concentrated in the contour of busbar tunnel, especially in the arch shoulder of the small chainage and the arch foot of the large chainage. The apparent stress concentration indicates that the stress level and the risk of fracture of the support structure are high. In addition, the busbar tunnel is in an unfavorable multi-face empty and multi-faceted unloading stress environment, which further aggravates the risk of failure to the U-steel support structure.

4 Discussion

The instability of U-steel structure induced by blast loading is the main cause of extrusion deformation of the support. To ensure the safety and stability of the supporting load-bearing structure, the impact stress can be decreased by reducing the excavation footage and blasting charge. The structural stability of the support structure is also an important factor affecting the deformation and instability of U-steel support. In reality, the area between the U-steel and the surrounding rock is usually unevenly distributed, influenced by the

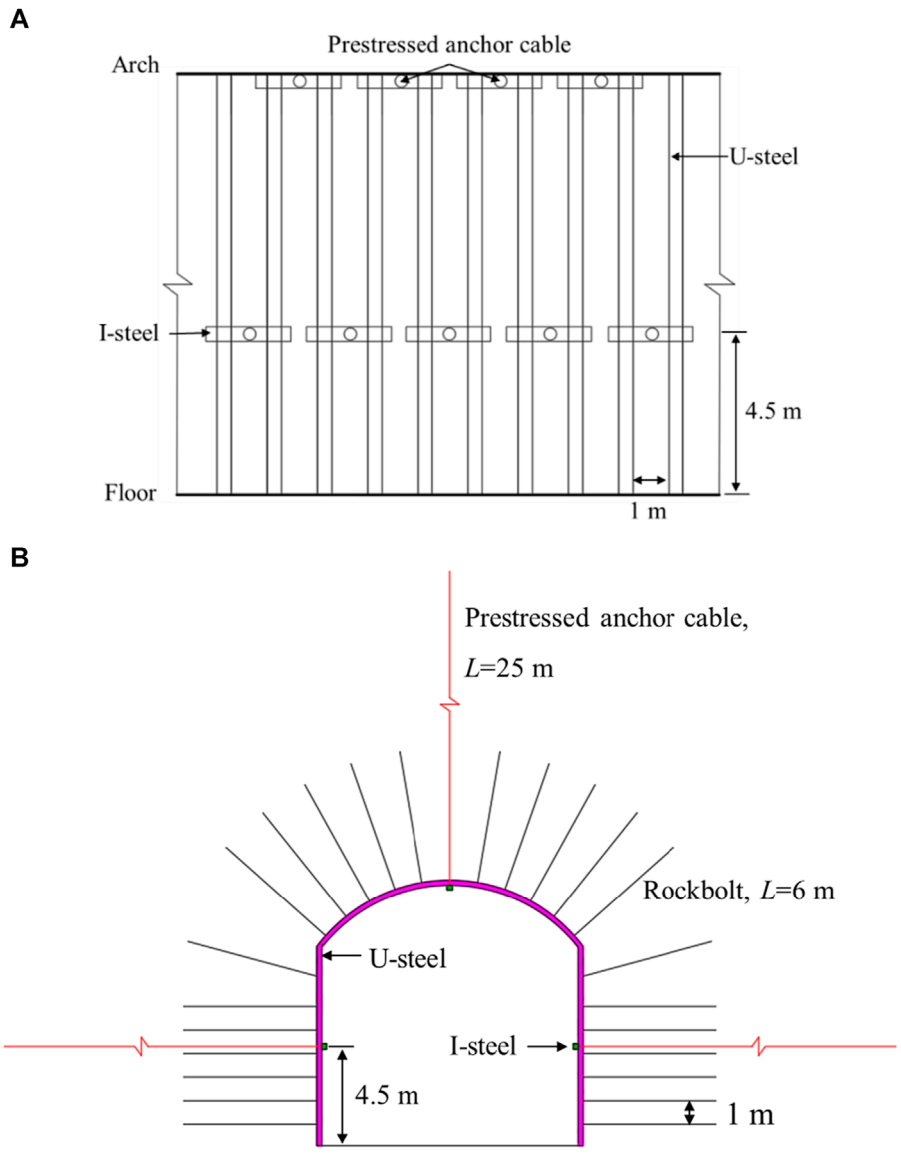

FIGURE 13
Synergetic reinforcement scheme of U-steel and prestressed cable: **(A)** lateral view, **(B)** front view of support structure.

blasting technique, lithology and structural plane, resulting in poor mechanical interaction between the rock and the support structure. In addition, the unfavourable interaction relationship significantly reduces the overall load-bearing capacity of the U-steel structure, resulting in structural instability of the support. The specific form of structural instability failure is closely related to the region of uneven air gaps distribution behind the U-steel. For example, the pinnacle shaped failure of U-steel when the air gap is distributed in the top arch (Figure 12A), and the flat-top shaped failure of U-steel when the air gaps are distributed in the spandrel of cavern (Figure 12B).

Based on the above-mentioned typical unstable section and the failure characteristics of U-steel support, a synergetic reinforcement scheme is proposed. The designed synergetic reinforcement scheme of structure with support and surrounding rock is shown in Figure 13. The synergetic reinforcement is a method in which the U-steel, the back wall filling and the pre-stressed anchor cable are coupled together. The synergetic reinforcement compensates the bearing capacity and structural stability of the support by the anchor cable at a reasonable position, which can improve the overall bearing capacity and structural stability of the U-steel support. At the same time, the U-steel support provides a good surface protection component for the anchor cable, and improves the anchoring performance of the anchor cable. In essence, the main purpose of reinforcement is the mobilisation of the self-supporting capacity of the surrounding rock to the greatest extent possible. After the installation of U-steel and the filling behind the wall, the I-steel coupling joist is used to install the prestressed anchor cable at the dangerous section. On the one hand, the scheme can effectively realize the efficient transmission of the prestress, and provide certain structural compensation force to the unstable section position. The stress of the potential failure section of the support structure is greatly reduced after adopted the synergetic reinforcement scheme. On the other hand, the synergetic reinforcement measure can promote the uniform distribution of the external load of the support, thereby improving the overall bearing performance of the support structure.

5 Conclusion

An *in-situ* microseismic monitoring system is established in the cavern of the Baihetan Hydropower Station, and the impact of blasting on the U-steel support structure is investigated. The dynamic response and failure process of the U-steel support under blast loading are obtained by microseismic monitoring experiment and theoretical analysis. The monitoring results show that the forced vibration of the U-steel support structure is excited by the blast load. The concrete spray layer of the busbar tunnel is delaminated and the U-steel structure is partially extruded and deformed under the blast load. Furthermore, the location of the damage to the U-steel support structure is consistent with the area of the cluster of microseismic events. The apparent stress is concentrated in the contour of the busbar tunnel, particularly in the arch shoulder of the small chainage and the arch foot of the large chainage.

In addition to the effects of blast loading, the structural stability of the support is an important factor in the deformation and instability of the U-steel support. Therefore, the synergetic reinforcement scheme is proposed to inhibit the deterioration of the surrounding rock. The results showed that the designed synergetic reinforcement scheme could provide a certain structural compensating force to the unstable section position, and improve the overall bearing performance of the U-steel support structure.

Data availability statement

The original contributions presented in the study are included in the article/Supplementary material, further inquiries can be directed to the corresponding authors.

Author contributions

J-SZ: Funding acquisition, Methodology, Writing–original draft, Data curation, Resources, Supervision. J-HY: Formal Analysis, Supervision, Writing–review and editing. P-XL: Formal Analysis, Investigation, Methodology, Writing–review and editing. X-HZ: Validation, Writing–review and editing. C-FC: Methodology, Writing–review and editing. J-CZ: Methodology, Writing–review and editing.

Funding

The author(s) declare financial support was received for the research, authorship, and/or publication of this article. This research is supported by the National Natural Science Foundation of China (52209132, 52209120), the CRSRI Open Research Program (Program SN: CKWV20231173/KY), and China Postdoctoral Science Foundation (2023M733317).

Acknowledgments

The authors would like to thank Bing-Rui Chen and Quan Jiang for their help with the MS monitoring experiment.

Conflict of interest

J-CZ is employed by the PowerChina Huadong Engineering Corporation Limited.

The remaining authors declare that the research was conducted in the absence of any commercial or financial relationships that could be construed as a potential conflict of interest.

Publisher's note

All claims expressed in this article are solely those of the authors and do not necessarily represent those of their affiliated organizations, or those of the publisher, the editors and the reviewers. Any product that may be evaluated in this article, or claim that may be made by its manufacturer, is not guaranteed or endorsed by the publisher.

References

Barla, G., Bonini, M., and Semeraro, M. (2011). Analysis of the behaviour of a yield-control support system in squeezing rock. *Tunn. Undergr. Sp. Tech.* 26 (1), 146–154. doi:10.1016/j.tust.2010.08.001

Brady, B. H. G., and Brown, E. T. (2005). *Rock mechanics for underground mining*. New York, NY, USA: Kluwer Academic Publishers.

Chen, B.-R., Feng, X.-T., Li, Q.-P., Luo, R.-Z., and Li, S. (2015). Rock burst intensity classification based on the radiated energy with damage intensity at jinping II hydropower station, China. *Rock Mech. Rock. Eng.* 48 (1), 289–303. doi:10.1007/s00603-013-0524-2

Chen, B.-R., Wang, X., Zhu, X., Wang, Q., and Xie, H. (2023). Real-time arrival picking of rock microfracture signals based on convolutional-recurrent neural network and its engineering application. *J. Rock Mech. Geotech. online*. doi:10.1016/j.jrmge.2023.07.003

Chen, S.-j., Feng, F., Wang, Y.-j., Li, D.-y., Huang, W.-p., Zhao, X.-d., et al. (2020). Tunnel failure in hard rock with multiple weak planes due to excavation unloading of *in-situ* stress. *J. Cent. South. Univ.* 27 (10), 2864–2882. doi:10.1007/s11771-020-4515-7

Cheng, C., Jia, P., Ni, P., Wang, Y., Zhao, W., Guan, Y., et al. (2023a). Upper bound analysis of longitudinally inclined EPB shield tunnel face stability in dense sand strata. *Transp. Geotech.* 41, 101031. doi:10.1016/j.trgeo.2023.101031

Cheng, C., Yang, H., Jia, P., Ni, P., Shi, P., Ma, P., et al. (2023b). Face stability of shallowly buried large-section EPB box jacking crossing the beijing-hangzhou grand canal. *Tunn. Undergr. Sp. Tech.* 138, 105200. doi:10.1016/j.tust.2023.105200

Cui, X. Z., Li, J., Yang, G. D., Fei, W., Ding, S., and Fan, Y. (2023). Spatial migration and distribution of suspended particles in saturated sand layer under the impact of temperature. *Hydrol. Process.* 37 (2), e14833. doi:10.1002/hyp.14833

Dai, F., Li, B., Xu, N. W., Fan, Y. L., and Zhang, C. Q. (2016). Deformation forecasting and stability analysis of large-scale underground powerhouse caverns from microseismic monitoring. *Int. J. Rock. Mech. Min.* 86, 269–281. doi:10.1016/j.ijrmms.2016.05.001

Dong, L.-j., Tang, Z., Li, X.-b., Chen, Y.-c., and Xue, J.-c. (2020). Discrimination of mining microseismic events and blasts using convolutional neural networks and original waveform. *J. Cent. South. Univ.* 27, 3078–3089. doi:10.1007/s11771-020-4530-8

Dong, L.-J., Wesseloo, J., Potvin, Y., and Li, X.-B. (2016). Discriminant models of blasts and seismic events in mine seismology. *Int. J. Rock. Mech. Min.* 86, 282–291. doi:10.1016/j.ijrmms.2016.04.021

Feng, F., Chen, S., Han, Z., Golsanami, N., Liang, P., and Xie, Z. (2023). Influence of moisture content and intermediate principal stress on cracking behavior of sandstone subjected to true triaxial unloading conditions. *Eng. Fract. Mech.* 284, 109265. doi:10.1016/j.engfracmech.2023.109265

Feng, F., Chen, S., Wang, Y., Huang, W., and Han, Z. (2021). Cracking mechanism and strength criteria evaluation of granite affected by intermediate principal stresses subjected to unloading stress state. *Int. J. Rock. Mech. Min.* 143, 104783. doi:10.1016/j.ijrmms.2021.104783

Feng, X. T., Pei, S. F., Jiang, Q., Zhou, Y. Y., Li, S. J., and Yao, Z. B. (2017). Deep fracturing of the hard rock surrounding a large underground cavern subjected to high geostress: *in situ* observation and mechanism analysis. *Rock Mech. Rock. Eng.* 50 (8), 2155–2175. doi:10.1007/s00603-017-1220-4

Gong, F.-q., Luo, Y., Li, X.-b., Si, X.-f., and Tao, M. (2018). Experimental simulation investigation on rockburst induced by spalling failure in deep circular tunnels. *Tunn. Undergr. Sp. Tech.* 81, 413–427. doi:10.1016/j.tust.2018.07.035

Guo, H., Sun, Q., Feng, G., Li, S., and Xiao, Y. (2023). *In-situ* observations of damage-fracture evolution in surrounding rock upon unloading in 2400-m-deep tunnels. *Int. J. Min. Sci. Techno.* 33 (4), 437–446. doi:10.1016/j.ijmst.2022.11.008

Jiang, Q., Feng, X.-T., Cui, J., and Li, S.-J. (2015). Failure mechanism of unbonded prestressed thru-anchor cables: *in situ* investigation in large underground caverns. *Rock Mech. Rock. Eng.* 48 (2), 873–878. doi:10.1007/s00603-014-0574-0

Kaiser, P. K., and Cai, M. (2012). Design of rock support system under rockburst condition. *J. Rock Mech. Geotech.* 4, 215–227. doi:10.3724/SP.J.1235.2012.00215

Laura, B., and Martin, H. (2017). Identification of stress change within a rock mass through apparent stress of local seismic events. *Rock Mech. Rock. Eng.* 50, 81–88. doi:10.1007/s00603-016-1092-z

Li, A., Dai, F., Wu, W., Liu, Y., Liu, K., and Wang, K. (2022). Deformation characteristics of sidewall and anchorage mechanisms of prestressed cables in layered rock strata dipping steeply into the inner space of underground powerhouse cavern. *Int. J. Rock. Mech. Min. Sci.* 159, 105234. doi:10.1016/j.ijrmms.2022.105234

Li, B., Xu, N., Xiao, P., Xia, Y., Zhou, X., Gu, G., et al. (2023a). Microseismic monitoring and forecasting of dynamic disasters in underground hydropower projects in southwest China: a review. *J. Rock Mech. Geotech.* 15, 2158–2177. doi:10.1016/j.jrmge.2022.10.017

Li, C.-C., and Doucet, C. (2012). Performance of D-bolts under dynamic loading. *Rock Mech. Rock. Eng.* 45, 193–204. doi:10.1007/s00603-011-0202-1

Li, P. X., Chen, B. R., Xiao, Y. X., Feng, G. L., Zhou, Y. Y., and Zhao, J. S. (2023b). Rockburst and microseismic activity in a lagging tunnel as the spacing between twin tbm excavated tunnels changes: a case from the neelum-jhelum hydropower project. *Tunn. Undergr. Sp. Tech.* 132, 104884. doi:10.1016/j.tust.2022.104884

Li, Z.-W., Huang, C.-Y., Wang, H.-X., Xing, S.-C., Long, M.-C., and Liu, Y. (2023c). Determination of heat transfer representative element volume and three-dimensional thermal conductivity tensor of fractured rock masses. *Int. J. Rock. Mech. Min. Sci.* 170, 105528. doi:10.1016/j.ijrmms.2023.105528

Li, Z.-W., Long, M.-C., Xu, P., Huang, C.-Y., and Wang, Y.-S. (2023d). Thermal contact resistance of granite joints under normal stress. *Rock Mech. Rock. Eng. online* 56, 8317–8338. doi:10.1007/s00603-023-03450-9

Liu, G. F., Ran, G., Li, Z., Duan, S., Su, G., Yan, C., et al. (2023). An insight into the effect of primary hidden microfissures on mechanical behaviors and failure characteristics of brittle basalt. *Theor. Appl. Fract. Mec. online* 128, 104138. doi:10.1016/j.tafmec.2023.104138

Liu, J.-p., Si, Y.-t., Wei, D.-c., Shi, H.-x., and Wang, R. (2021). Developments and prospects of microseismic monitoring technology in underground metal mines in China. *J. Cent. South. Univ.* 28, 3074–3098. doi:10.1007/s11771-021-4839-y

Lu, B., Jia, P., Zhao, W., Zheng, Q., Du, X., and Tang, X. (2023). Longitudinal mechanical force mechanism and structural design of steel tube slab structures. *Tunn. Undergr. Sp. Tech.* 132, 104883. doi:10.1016/j.tust.2022.104883

Ma, C., Jiang, Y., and Li, T. (2019). Gravitational search algorithm for microseismic source location in tunneling: performance analysis and engineering case study. *Rock Mech. Rock. Eng.* 52, 3999–4016. doi:10.1007/s00603-019-01809-5

Ma, K., Tang, C.-a., Xu, N.-w., Liu, F., and Xu, J.-w. (2013). Failure precursor of surrounding rock mass around cross tunnel in high-steep rock slope. *J. Cent. South. Univ.* 20, 207–217. doi:10.1007/s11771-013-1478-y

Ma, T.-H., Tang, C.-A., Tang, S.-B., Kuang, L., Yu, Q., Kong, D.-Q., et al. (2018). Rockburst mechanism and prediction based on microseismic monitoring. *Int. J. Rock. Mech. Min. Sci.* 110, 177–188. doi:10.1016/j.ijrmms.2018.07.016

Mei, S., Feng, X.-T., Li, Z., Yang, C., and Gao, J. (2023). Experimental study on the failure process of fault rock bursts in tunnels based on a 3D-printed large-scale physical model. *Int. J. Geomech.* 23, 04023139. doi:10.1061/IJGNAI.GMENG-8510

Wang, H., Zheng, P.-q., Zhao, W.-j., and Tian, H.-m. (2018). Application of a combined supporting technology with U-shaped steel support and anchor-grouting to surrounding soft rock reinforcement in roadway. *J. Cent. South. Univ.* 25, 1240–1250. doi:10.1007/s11771-018-3821-9

Wang, Q., Ye, H., Li, N., Chi, X., Xie, W., Chen, D., et al. (2021). A study of support characteristics of collaborative reinforce system of U-steel support and anchored cable for roadway under high dynamic stress. *Geofluids* 2021, 1–12. doi:10.1155/2021/9881280

Wong, L. N. Y., Fang, Q., and Zhang, D. (2013). Mechanical analysis of circular tunnels supported by steel sets embedded in primary linings. *Tunn. Undergr. Sp. Tech.* 37, 80–88. doi:10.1016/j.tust.2013.03.011

Wu, Y., Gao, F., Chen, J., and He, J. (2019). Experimental study on the performance of rock bolts in coal burst-prone mines. *Rock Mech. Rock. Eng.* 52, 3959–3970. doi:10.1007/s00603-019-01794-9

Xia, K. Z., Chen, C., Liu, X., Liu, X., Yuan, J., and Dang, S. (2023a). Assessing the stability of high-level pillars in deeply-buried metal mines stabilized using cemented backfill. *Int. J. Rock. Mech. Min. Sci.* 170, 105489. doi:10.1016/j.ijrmms.2023.105489

Xia, Y. L., Xu, D. P., Qiu, S. L., Liu, X. Y., Huang, X., and Li, Z. G. (2023b). Experimental study on mechanical properties of deeply buried granite during layered excavation of large underground caverns. *Rock Mech. Rock. Eng.* 56 (7), 4757–4778. doi:10.1007/s00603-023-03304-4

Xu, D., Liu, X., Jiang, Q., Li, S., Zhou, Y., Qiu, S., et al. (2022). A local homogenization approach for simulating the reinforcement effect of the fully grouted bolt in deep underground openings. *Int. J. Min. Sci. Techno.* 32, 247–259. doi:10.1016/j.ijmst.2022.01.003

Xu, H. S., Li, S. J., Xu, D. P., Huang, X., Zheng, M., He, J., et al. (2023a). Numerical back analysis method of three-dimensional *in situ* stress fields considering complex surface topography and variable collinearity. *Int. J. Rock Mech. Min. Sci.* 170, 105474. doi:10.1016/j.ijrmms.2023.105474

Xu, H. S., Xu, D. P., Li, S. J., Zheng, M., Huang, X., Chen, B., et al. (2023b). Stress tensor similarity index based on euclidean distance for numerical back analysis of *in situ* stress fields. *Comput. Geotech.* 159, 105457. doi:10.1016/j.compgeo.2023.105457

Xu, N., Wu, J., Dai, F., Fan, Y., Li, T., and Li, B. (2018). Comprehensive evaluation of the stability of the left-bank slope at the baihetan hydropower station in southwest China. *B. Eng. Geol. Environ.* 77, 1567–1588. doi:10.1007/s10064-017-1018-3

Yang, G., Fan, Y., Wang, G., Cui, X., Li, Q., and Leng, Z. (2023). Experimental and numerical investigation on dynamic behavior of RC orifice targets subjected to underwater explosions. *Eng. Struct.* 279, 115541. doi:10.1016/j.engstruct.2022.115541

Yang, G., Wang, G., Fan, Y., Deng, K., Lu, W., and Zhao, J. (2021). Dynamic response and performance of submarine tunnel subjected to surface explosions. *Mar. Struct.* 80, 103091. doi:10.1016/j.marstruc.2021.103091

Zhao, J.-S., Chen, B.-R., Jiang, Q., Lu, J.-F., Hao, X.-J., Pei, S.-F., et al. (2022a). Microseismic monitoring of rock mass fracture response to blasting excavation of large underground caverns under high geostress. *Rock Mech. Rock. Eng.* 55, 733–750. doi:10.1007/s00603-021-02709-3

Zhao, J.-S., Duan, S.-Q., Chen, B.-R., Li, L., He, B.-G., Li, P.-X., et al. (2024). Failure mechanism of rock masses with complex geological conditions in a large underground cavern: a case study. *Soil. Dyn. Earthq. Eng.* 177, 108439. doi:10.1016/j.soildyn.2023.108439

Zhao, J.-S., Jiang, Q., Lu, J.-F., Chen, B.-R., Pei, S.-F., and Wang, Z.-L. (2022b). Rock fracturing observation based on microseismic monitoring and borehole imaging: *in situ* investigation in a large underground cavern under high geostress. *Tunn. Undergr. Sp. Tech.* 126, 104549. doi:10.1016/j.tust.2022.104549

Zhao, J.-s., Jiang, Q., Pei, S.-f., Chen, B.-r., Xu, D.-p., and Song, L.-b. (2023). Microseismicity and focal mechanism of blasting-induced block falling of intersecting chamber of large underground cavern under high geostress. *J. Cent. South. Univ.* 30, 542–554. doi:10.1007/s11771-023-5259-y

Zhao, Y., Liu, N., Zheng, X., and Zhang, N. (2015). Mechanical model for controlling floor heave in deep roadways with U-shaped steel closed support. *Int. J. Min. Sci. Techno.* 25, 713–720. doi:10.1016/j.ijmst.2015.07.003

Zheng, Z., Li, R., and Zhang, Q. (2023a). A novel anisotropic deterioration mechanical model for rock ductile-brittle failure under 3D high-stress and its application. *Comput. Geotech.* 162, 105665. doi:10.1016/j.compgeo.2023.105665

Zheng, Z., Tang, H., Zhang, Q., Pan, P., Zhang, X., Mei, G., et al. (2023b). True triaxial test and PFC3D-GBM simulation study on mechanical properties and fracture evolution mechanisms of rock under high stresses. *Comput. Geotech.* 154, 105136. doi:10.1016/j.compgeo.2022.105136

frontiers | Frontiers in Earth Science

TYPE Original Research
PUBLISHED 06 February 2024
DOI 10.3389/feart.2024.1333117

Check for updates

OPEN ACCESS

EDITED BY
Jianyong Han,
Shandong Jianzhu University, China

REVIEWED BY
Xia Bian,
Hohai University, China
Jun Wu,
Shanghai Normal University, China

*CORRESPONDENCE
Jiaxin Ling,
lingjiaxin@tongji.edu.cn
Yi Rui,
ruiyi@tongji.edu.cn

RECEIVED 04 November 2023
ACCEPTED 12 January 2024
PUBLISHED 06 February 2024

CITATION
Li X, Chen Z, Tang L, Chen C, Li T, Ling J, Lu Y and Rui Y (2024), Predicting rock mass rating ahead of the tunnel face with Bayesian estimation.
Front. Earth Sci. 12:1333117.
doi: 10.3389/feart.2024.1333117

COPYRIGHT
© 2024 Li, Chen, Tang, Chen, Li, Ling, Lu and Rui. This is an open-access article distributed under the terms of the Creative Commons Attribution License (CC BY). The use, distribution or reproduction in other forums is permitted, provided the original author(s) and the copyright owner(s) are credited and that the original publication in this journal is cited, in accordance with accepted academic practice. No use, distribution or reproduction is permitted which does not comply with these terms.

Predicting rock mass rating ahead of the tunnel face with Bayesian estimation

Xiaojun Li, Ziyang Chen, Li Tang, Chao Chen, Tao Li, Jiaxin Ling*, Yanyun Lu and Yi Rui*

Department of Geotechnical Engineering, Tongji University, Shanghai, China

The rock mass rating (RMR) system plays a crucial role in geomechanics assessments for tunnel projects. However, conventional methods combining empirical and geostatistical approaches often yield inaccuracies, particularly in areas with weak strata such as faults and karst caves. To address these uncertainties and errors inherent in empirical techniques, we propose a progressive RMR prediction strategy based on the Bayesian framework. This strategy incorporates three key components: 1) Variogram modeling: utilizing observational data from the excavation face, we construct and update a variogram model to capture the spatial variability of RMR. 2) TSP-RMR statistic model: we integrate a TSP-RMR statistical model into the Bayesian sequential update process. 3) Bayesian maximum entropy (BME) integration: the BME method combines geological information obtained from tunnel surface excavation with tunnel seismic prediction (TSP) data, ultimately enhancing the RMR prediction accuracy. Our methodology is applied to the Laoying rock tunneling project in Yunnan Province, China. Our findings demonstrate that the fusion of soft data and geological interpretation significantly improves the accuracy of RMR predictions. At selected prediction points, the relative error of our method is less than 15% when compared to the traditional Kriging method. This approach holds substantial potential for advancing RMR estimation ahead of tunnel excavation, particularly when advanced geological forecast data are available.

KEYWORDS

rock mass rate prediction, tunnel seismic prediction, dynamic Bayesian framework, multisource data fusion, geostatistical method

1 Introduction

The surrounding rock plays a vital role in tunnel engineering as it concerns both safety and efficiency in the design and construction phases. During construction, the variety of geological conditions might lead to serious hazards or collapses, resulting in casualties and financial losses. Hence, an accurate rock quality assessment ahead of the tunnel surface to dynamically revise the support schemes could decrease the hazards during construction.

To accurately reflect the quality of the surrounding rock, conventional rock mass classification systems are still employed in current tunnel construction practice, and a variety of rock mass classification systems have come forward to evaluate the quality of the geological conditions. Standard rock classification methods include the Q-system classification, rock mass rating (RMR) classification (Bieniawski, 1973), geological strength

index (GSI) classification (Hoek et al., 1997), and the basic quality (BQ) approach. Among them, RMR is one of the most extensively used rock mass classification systems because of its comprehensiveness of the indicators and convenient application. The RMR system consists of six main indicators: the uniaxial compressive strength (UCS) of rock material, rock quality designation (RQD), joint and bedding spacing, joint condition, groundwater conditions, and orientation of discontinuities for the opening axis.

The current practice in predicting RMR involves a comprehensive evaluation of the rock mass based on several parameters, which typically include the uniaxial compressive strength of the rock material, RQD, spacing of discontinuities, condition of discontinuities (such as persistence, aperture, roughness, infilling, and weathering), groundwater conditions, and the orientation of discontinuities. For instance, Niedbalski et al. (2018) calculated RMR based on the engineering properties and quality of rock mass. In addition to various rock classification systems, different techniques predicting lithological and structural heterogeneities ahead of the tunnel face have also been developed to lay a solid foundation for the revision and majorization of the initial design scheme, one representative of which is the tunnel seismic prediction (TSP). TSP is a non-destructive tool using the elastic differences in the physical properties to characterize different rock types. TSP is a seismic method specifically tailored for use in tunneling and mining. It involves generating seismic waves at the tunnel face, which then travel through the rock mass and are recorded by sensors placed along the tunnel. By analyzing the travel times and characteristics of the seismic waves, geophysicists can construct a profile of the rock mass ahead of the tunnel face. Figure 1 displays the equipment layout of TSP. The seismic waves are formed by installed burst points (normally 12 points per side) and received by two or four receivers fixed on the side walls. Through subsequent analysis of the direct and reflected waves, it is found that the compression wave velocities (V_P) and shear wave velocities (V_S) reveal the rock properties as the propagation of

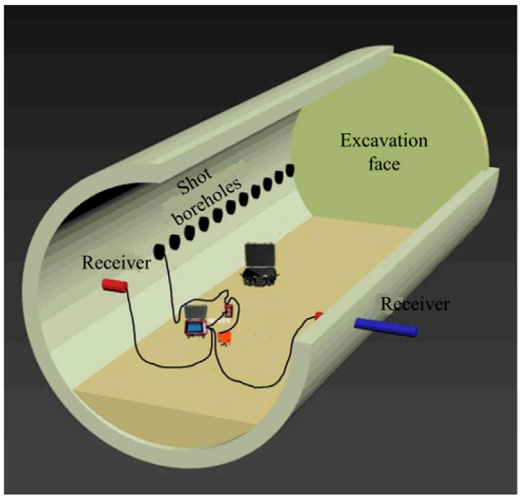

FIGURE 1
Equipment layout of TSP.

TABLE 1 Formulas denoting the relation between RMR and wave velocity in the literature.

No.	Empirical formula	Reference
1	$S = (s_1, s_2, s_3 \ldots s_m)$	Nourani et al. (2017)
2	$S = (s_1, s_2, s_3 \ldots s_m)$	Nourani et al. (2017)
3	$S = (s_1, s_2, s_3 \ldots s_m)$	Esmailzadeh et al. (2018)
4	$S = (s_1, s_2, s_3 \ldots s_m)$	Esmailzadeh et al. (2018)

seismic velocity depends on various parameters, including density, rock strength, water conditions, weathering, and the type of filler material for discontinuities (Montalvo et al., 2015; Bu et al., 2018; Li et al., 2019a). Accordingly, the relationship between rock mass rating and seismic wave velocity can be quantified, as demonstrated in Table 1 by previous studies.

Many research studies (Von and Ismail, 2017; Zhou et al., 2017; Li et al., 2019a; Hou et al., 2019; Lu et al., 2020) have proven that the seismic wave velocity information acquired by TSP can reflect the geological conditions in front of the tunnel face. To be specific, a portion of studies (Montalvo et al., 2015; Von and Ismail, 2017; Zhou et al., 2017; Bu et al., 2018; Li et al., 2019b; Hou et al., 2019; Shan et al., 2019; Lu et al., 2020) have revealed the link between the rock quality index and seismic wave, in particular engineering cases. For instance, Esmailzadeh et al. (2018) proposed a statistical model for RMR and TSP data. Bu et al., 2018 introduced an optimization method for classifying the advanced surrounding rock based on TSP data. Chen et al. (2017) proposed a geostatistical method for inferring RMR ahead of tunnel face excavation using dynamically exposed geological information. However, such an interpretation of refined geological data depends on the engineer's experience, and the interpretation results are usually qualitative (Santos et al., 2015; Esmailzadeh et al., 2018). A handful of research studies have focused on the mutual link between the rock mass rating and the seismic wave velocity (Nourani et al., 2017). Moreover, considering the site characteristics, most of the models fitting the relationship between the surrounding rock quality and wave velocity have been hypothesized and optimized, which means that the estimation error of these fitting models will increase when the engineering environment changes.

Due to the ability to consider uncertainty, geostatistical approaches have been gradually adopted to estimate the RMR in different engineering projects. At present, extensive studies (Chen et al., 2018; Zhang and Zhu, 2018; Li et al., 2019b; He et al., 2020) are using the Kriging method to directly interpolate the RMR value of the whole area based on the surface exploration data and borehole data. However, these studies use limited data in the early survey stage without adopting the geological information obtained during construction. Such a phenomenon is worse in mountain tunnels as boreholes are scattered for economic reasons (Chen et al., 2017). As a result, there is a significant error in the estimation of the quality of the surrounding rock utilizing typical empirical methods. It is well-known that tunnel excavation is a dynamic process, and with the advance of the tunnel, new tunnel faces are exposed, which creates an opportunity to gather more

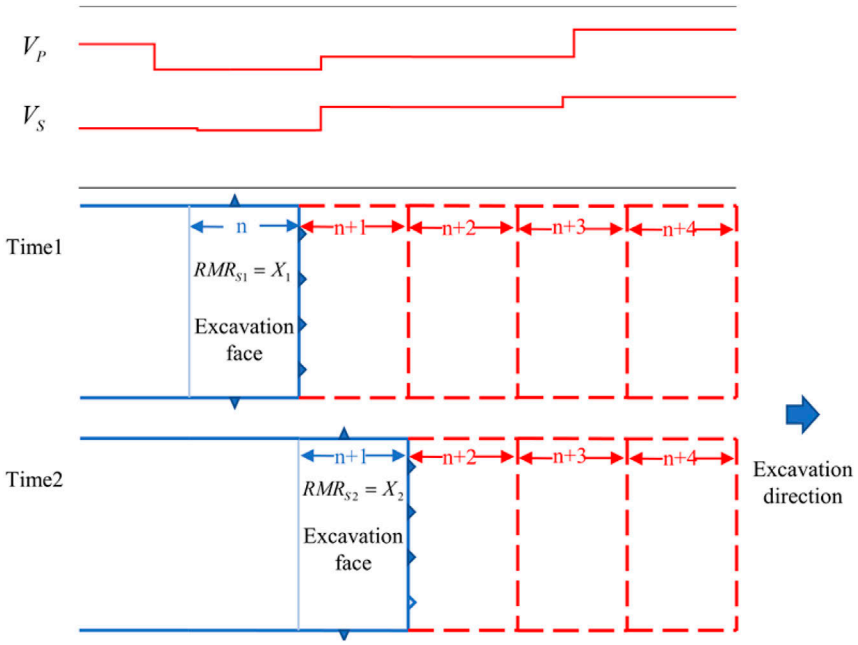

FIGURE 2
Progressive exposure characteristics of the tunnel's surrounding rock.

detailed and accurate geological information. However, previous studies fail to take newly exposed geological information into account. Therefore, the main research gap this study aims to fill is how to integrate on-site data, which includes advanced geological prediction data and tunnel face data, during tunnel construction to reduce the prediction error and uncertainty of the surrounding rock.

The spatiotemporal Bayesian maximum entropy method has been successfully applied in data fusion problems in civil engineering (Li et al., 2013; Hayunga and Kolovos, 2016; Jat and Serre, 2016; Zhang et al., 2016; Gelman et al., 2017; Hu et al., 2021). However, the relation of seismic wave velocity in surrounding rock is not clear, and the BME method cannot be used to fuse the wave velocity data directly. To enhance the forecasting accuracy of rock mass quality in front of the tunnel face, it is necessary to study the prediction method that can integrate TSP wave velocity data.

Hence, in this study, the BME method integrating the TSP method is proposed to describe the relationship between newly exposed geological information and TSP data. Moreover, the observed and predicted values of RMR are compared and verified to estimate the effects of various physical parameters. Then, the performances of ordinary Kriging (OK) and BME approaches are also compared in uniform formation and the fault fracture zone to highlight the influence of the data used in RMR prediction. This study focuses on employing a dynamic Bayesian framework to quantitatively estimate RMR values in advance of the excavation face throughout tunnel construction. The main contributions of the study are summarized as follows: (1) A progressive prediction strategy for a tunnel's surrounding rock quality was proposed. (2) The TSP-RMR statistic model was established by the Bayesian sequential update framework. (3) The uncertainty of the RMR prediction results was quantified and compared with traditional geostatistical methods. Results show that the prediction results can be improved by 15% by integrating soft data from geological interpretation.

2 Methodology

This section begins by introducing the characteristics of TSP data and explaining how to utilize TSP data for predicting the RMR value (Subsection 2.1). It then analyzes the spatial structural variability of RMR data (Subsection 2.2). Subsequently, based on the actual measurement data from the excavation face and the TSP forecast data, soft data on seismic wave velocity are obtained through Bayesian sequential updating (Subsection 2.3). Finally, the data undergo dynamic Bayesian maximum entropy fusion to yield the RMR classification results (Subsection 2.4).

2.1 RMR prediction by integrating TSP

As the tunnel excavation progresses, the geological body is exposed round by round. More accurate geological information can be obtained by a series of advanced technologies, as shown in Figure 2. The assumptions of the approach to predict RMR ahead of the excavation face include the following: (i) the geological conditions change only along the excavation direction; (ii) the RMR values obtained from the tunnel face are accurate. The design of the tunnel support structure is mainly based on the

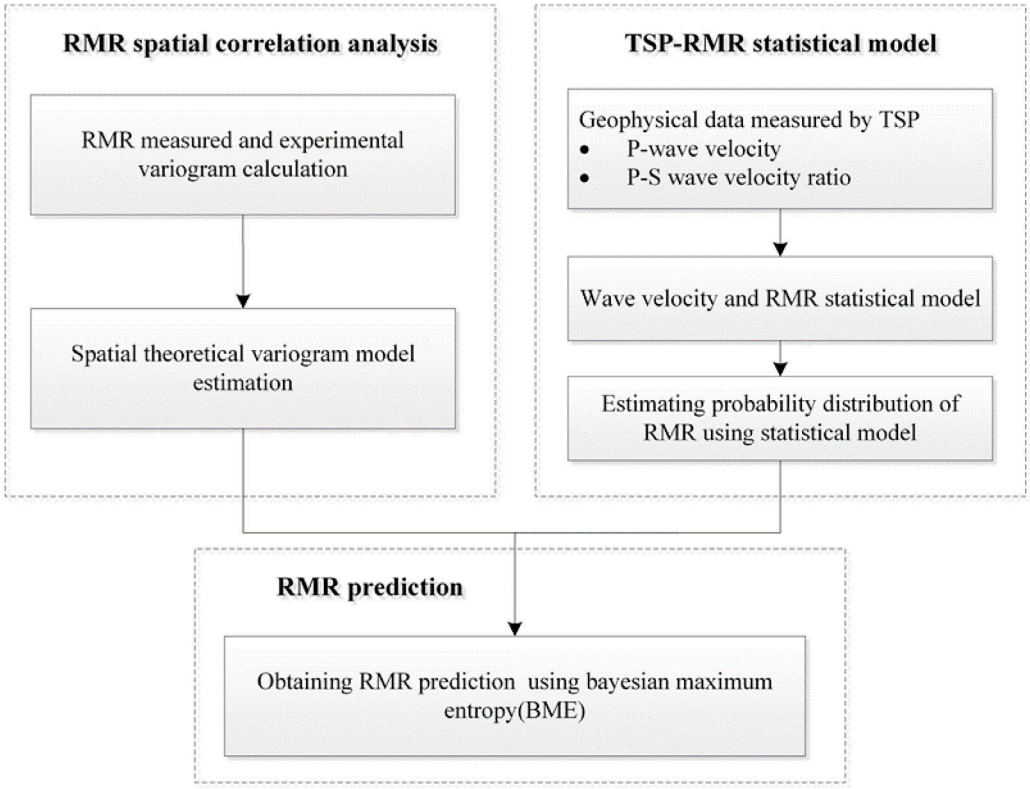

FIGURE 3
Framework of the progressive prediction strategy for the surrounding rock quality of the tunnel.

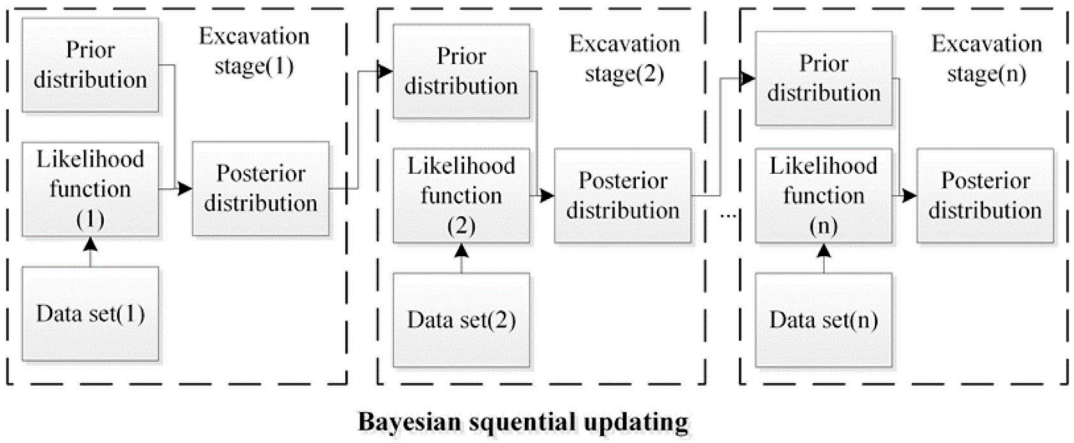

FIGURE 4
Processing of soft data based on Bayesian sequential updating.

grade of the tunnel's surrounding rock during the excavation, and it is easy to collect rock information on the tunnel face. Therefore, the above two assumptions can be accepted in the actual construction procedure of the tunnel. Assuming that $S = (s_1, s_2, s_3 \ldots s_m)$ represents the excavation position, the RMR of the surrounding rock parameters at the *xth* position can be denoted as $RMR(s_x)$.

For the position of S_q, $RMR_{\text{measured}} = RMR(s_1, s_2, \ldots, s_x | x < q)$ represents the measured RMR value. The forecast for the geophysical parameters can be denoted as $(s_1, s_2, \ldots, s_{q-1}, s_q, s_{q+1}, \ldots, s_{q-n})$, where n is the advanced prediction detection range. Such data can be divided into two parts: $V_{measured} = V(s_1, s_2, \ldots, s_{q-1})$ represents the values of the measured seismic wave velocity at the given location, and $V_{prediction} = V(s_q, s_{q+1}, \ldots, s_{q+n})$ portrays

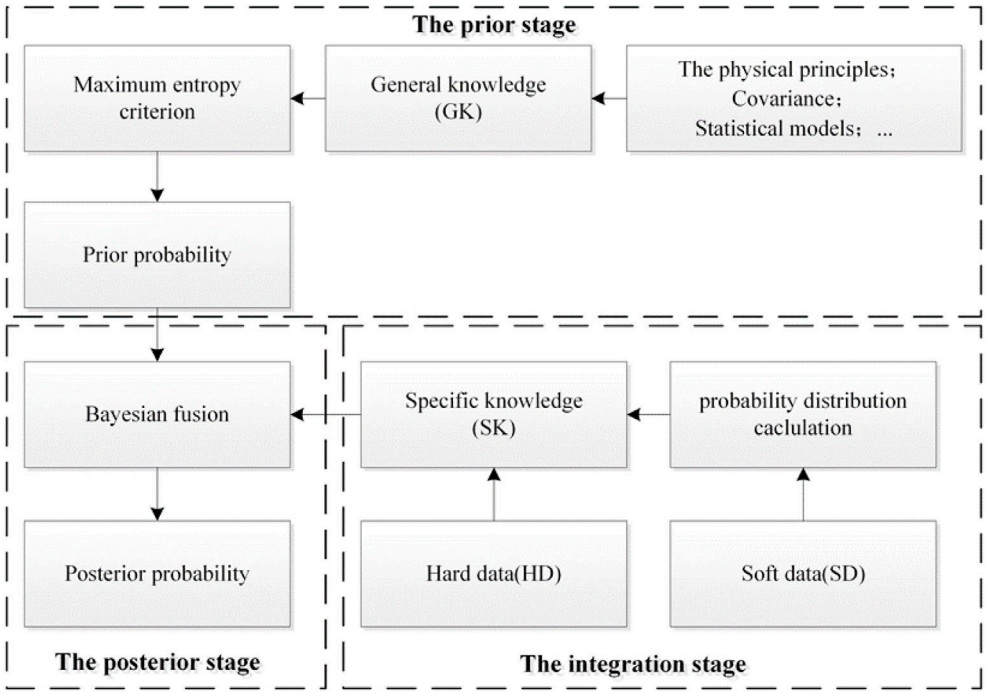

FIGURE 5
Framework of the Bayesian maximum entropy approach.

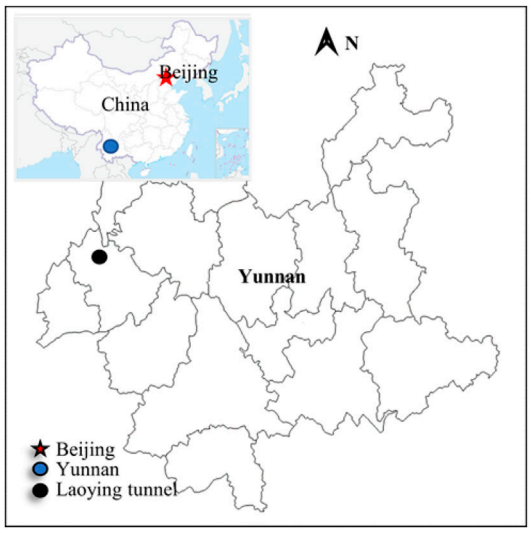

FIGURE 6
Location of the Laoying tunnel in China.

the geophysical parameters in front of the tunnel face. At this point, there is no measured RMR value in the process. The predicted value of RMR before tunnel excavation can be expressed as follows:

$$RMR_{\text{prediction}} = RMR\left(s_q, s_{q+1}, \ldots, s_{q+n}\right). \quad (2.1)$$

Accordingly, a Bayesian stochastic analysis framework is proposed for inference RMR values in front of the tunnel face. Two types of information are used in the following prediction process: (1) RMR values measured and calculated from excavation sketches and (2) geophysical data obtained from the tunnel seismic prediction (TSP), including V_P and V_P/V_S. Depending on the uncertainty of the data, these two types of data can also be divided into hard data (measured value such as RQD) and soft data (seismic interpretation result). The conceptual workflow of the RMR prediction procedure is outlined in Figure 3.

The progressive prediction strategy of RMR can be separated into the following three steps:

1) RMR spatial correlation analysis and construction of a variogram.
2) TSP-RMR statistical model based on the Bayesian updating framework.
3) RMR prediction based on the BME approach.

The RMR values were calculated, and the corresponding theoretical variogram model was fitted accordingly. The range of the variogram can be used to determine the locations of the data points used in the prediction. All steps are described in the following sections in detail.

2.2 RMR spatial correlation analysis and the built of the variogram

In the hypothesis of the geostatistical theory, adjacent geological data show similar properties (Chen et al., 2017); therefore, RMR



FIGURE 7
Data measured from the tunnel face.

data from similar areas can be used to forecast the quality of the surrounding rock at unknown points. This spatial correlation of the geological condition of the excavation face at different positions can be expressed by a variogram. The variogram is defined as the expectation of the variance of regional variables as follows:

$$2\gamma(x,h) = \mathrm{var}[Z(x) - Z(x+h)] = \{E[Z(x) - Z(x+h)]\}^2, \quad (2.2)$$

where Z represents a stationary random function, including the known mean m and variance σ^2, which is independent of location; therefore, $m(x) = m$ and $\sigma^2(x) = \sigma^2$ for all places x in the research region. The RMR of the tunnel excavation surface can be treated as a one-dimensional variable along the tunnel axis. The spatial correlation is obtained by calculating the experiment variogram and fitted using theoretical variogram models (i.e., spherical model, exponential model, and Gaussian model).

Due to that, the peculiarities of the geological data are gradually revealed during tunnel excavation, and a series of observation data are utilized to build a variogram model for each prediction point. The range and sill are two essential components in the variogram function. The hard data beyond the range will not be included in the prediction.

2.3 TSP-RMR statistical model based on the Bayesian updating framework

2.3.1 Dynamic Bayesian framework

Assume that the relationship between RMR and wave velocity can be shown by.

$$f(x) = \mathbf{x}^{\mathrm{T}}\mathbf{w}, \mathbf{y} = a\mathbf{x} + b + \boldsymbol{\varepsilon}, \quad (2.3)$$

$$a \sim N(\mu_a, \sigma_a^2), b \sim N\left(\mu_b, \sigma_b^2\right), \boldsymbol{\varepsilon} \sim N(0, \sigma_t^2), \quad (2.4)$$

where x is the wave velocity data (V_{P} or $V_{\mathrm{P}}/V_{\mathrm{S}}$), y shows the observed performance, $w = \{a, b\}$ are the regression parameters, and ε represents the uncertainty variable, describing the observation error. The model parameter w is assumed to be a normal or lognormal distribution. The Gaussian error with zero mean and variance σ_t^2 is used to represent the observation error ε.

The Bayesian method can use observation samples to update model parameters. The posterior distribution of model parameter $\theta = \{\mathbf{w}, \varepsilon\}$ can be obtained by integrating prior information and the likelihood function from the observation values, which is expressed in Eq. 2.5.

$$P(\theta|\mathbf{x}, \mathbf{y}) = \frac{P(\mathbf{y}|\mathbf{x}, \theta)P(\theta)}{\int P(\mathbf{y}|\mathbf{x}, \theta)P(\theta)\mathrm{d}\theta} = kP(\mathbf{y}|\mathbf{x}, \theta)P(\theta), \quad (2.5)$$

where k is a normalization constant to ensure that the posterior probability density function (PDF) $P(\theta|x, y)$ is valid. $P(\theta)$ is the prior PDF of parameters, which can be obtained through previous engineering information and expert experience. $P(y|x, \theta)$ is the likelihood function, reflecting the observation conditional probability of y. $P(\theta|x, y)$ represents the posterior PDF.

Figure 4 demonstrates the basic principle of the Bayesian updating framework, and $P(\theta)$ is updated in each step of the prediction. Its implementation can be summarized as considering the posterior distribution of the parameters predicted in the previous step as the prior distribution of the parameters updated in the next step. According to the Bayesian theorem, the posterior distribution of the stage is expressed as follows:

$$P(\theta|\mathrm{DATA}_1) = K_I P(\mathrm{DATA}_I|\theta)P(\theta). \quad (2.6)$$

Due to the complexity of the likelihood function and integral term, an analytic representation of posterior distribution is difficult to obtain directly. Thus, it is gained through the numerical integration method or sampling method. In this paper, the sampling method based on the Markov chain Monte Carlo (MCMC) simulation is suitable for deriving the posterior PDF. MCMC is a numerical method to generate random sample data to obtain distribution parameters. The Gibbs sampling algorithm is used in MCMC to generate the equivalent sample.

Tunnel excavation is a process in which the measured data gradually increase. The measured RMR data and wave velocity information gradually revealed can be used as a dataset to calculate the likelihood function of the new stage. Therefore, in the Bayesian sequence updating framework, each excavation process of the tunnel can be regarded as a new updating stage.

TABLE 2 Measured RMR values on the tunnel faces.

Number	Position	Measured RMR value	V_P	V_P/V_S
1 *	K12 + 320	45	3,051	1.79
2 *	K12 + 300	52	3,209	2.13
3 *	K12 + 280	51	3,533	1.92
4	K12 + 260		3,600	2.14
5 *	K12 + 240	32	2,872	1.62
6 *	K12 + 220	38	2,979	1.63
…	…	…	…	…
50 *	K11 + 340	39	3,056	1.57
51 *	K11 + 320	38	2,875	1.55

Note:*represents the position number with the measured RMR values.

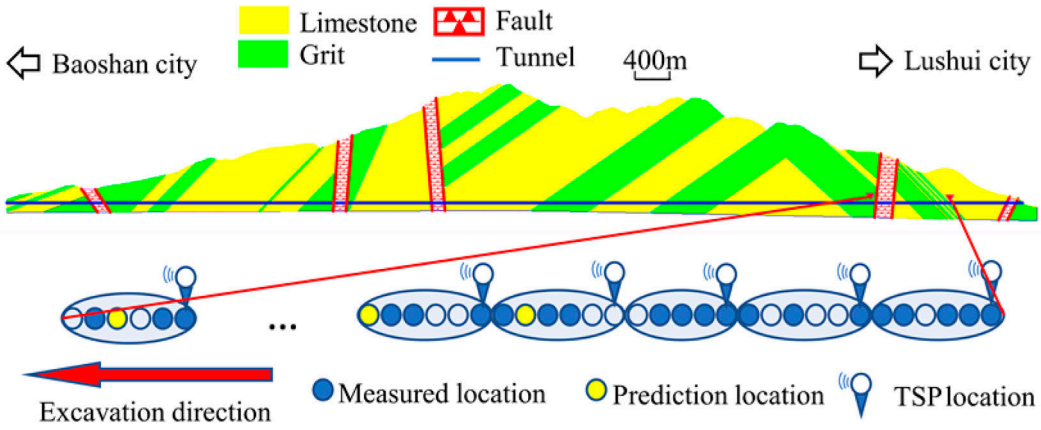

FIGURE 8
Excavation profile of the Laoying tunnel.

2.3.2 Prior PDF parameter setting

The prior distribution of the parameters is determined by the posterior distribution of the previous prediction results. The model parameter w is assumed to be a normal distribution with a mean of u_w and a variance of σ_w^2.

$$\mathbf{w} \sim N(\mathbf{u}_\mathbf{w}, \boldsymbol{\sigma}_\mathbf{w}^2). \tag{2.7}$$

In the first step of prediction, the prior information about the model can be determined according to the engineering experience. Assuming that the prior information is $\mu_a = \mu_b = 0$, $\sigma_a^2 = \sigma_b^2 = 10^4$ represents that model parameters can be specified in a certain range before the observation data are obtained.

It should also be noted that the observation error is very important in the estimate of the likelihood function. The observation error (ε) is assumed to be a normal distribution with zero mean and a standard deviation of 1.0, based on the experience in Yunnan and the reports in the literature about measured RMR based on photography.

2.3.3 Soft data probability distribution calculation

After the posterior distribution of the model parameters is obtained, the RMR probability distribution from wave velocity inversion can be calculated by Eq. 2.8:

$$P(\mathbf{y}|\mathbf{x}, \mathrm{DATA}) = \int \theta P(\mathbf{y}, \theta|\mathbf{x}, \mathrm{DATA}) \mathrm{d}\theta. \tag{2.8}$$

In this study, the model parameters $\mathbf{w}$ and observation errors ε follow the assumption of normal distribution and are independent of each other. Therefore, the RMR soft data obtained by wave velocity fitting also conform to normal distribution.

2.4 Bayesian maximum entropy (BME) approach

The overall framework of the Bayesian maximum entropy approach is shown in Figure 5. The Bayesian maximum entropy

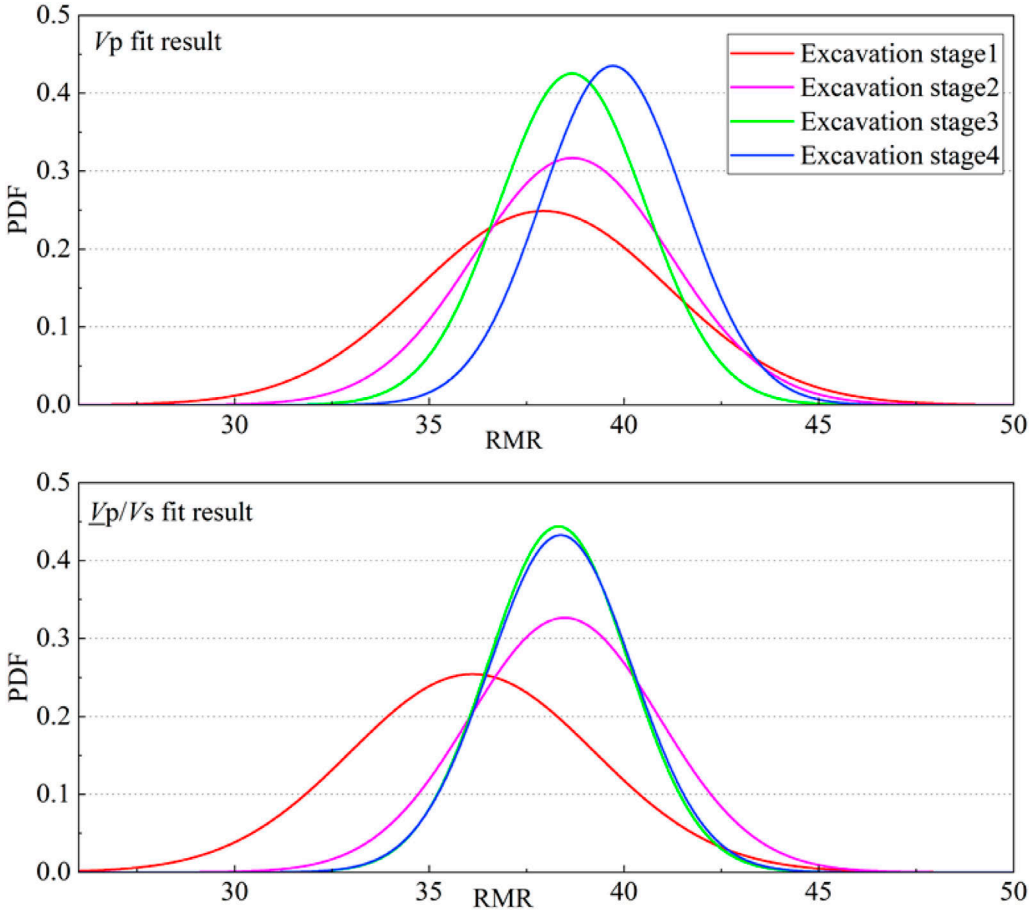

FIGURE 9
RMR interpretation values in different excavation stages at K11 + 360.

approach can integrate physical knowledge from different sources, uncertainty information, and statistical moments into a spatiotemporal random field (Christakos, 1990). The interpretation results of RMR with TSP based on Bayesian dynamic updating are substituted into the Bayesian maximum entropy framework as soft data, and finally, the predicted RMR value at the unexcavated position beyond the tunnel excavation face can be obtained.

Suppose that there are a total of m data points in the sampling space, which contain h hard data and $m-h$ soft data. Accordingly, the hard data are represented as $x_{\text{hard}} = (x_1,...,x_h)$, and the soft data are represented as $x_{\text{soft}} = (x_{h+1},...,x_{h+m})$. The BME method is used to predict the point values and calculate posterior PDF based on the estimated values from the expected value. The posterior probability of the prediction is calculated as follows:

$$f(x_k|x_1,x_2,...,x_m) = \frac{f(x_k|x_1,x_2,...,x_m,x_k)}{f(x_1,x_2,...,x_m)}, \tag{2.9}$$

$$\overline{x_{km}} = \int x_k f(x_k) dx_k. \tag{2.10}$$

The basic flow of BME (Figure 5) includes three basic steps:

1) The prior stage: at this stage, the basic knowledge (BK) is integrated with the prior distribution, which is given using the maximum entropy criterion. Generally, the prior PDF of maximum entropy can be calculated by the Lagrange optimization operator, which can be calculated as follows:

$$f_G(x) = K^{-1} \exp\left[\sum_{\alpha=1}^{N} \mu_\alpha g_\alpha(x)\right], \tag{2.11}$$

where $f_G(x)$ is the prior probability distribution under the maximum-entropy condition. g_α is a known function between the random variables. μ_α is the Lagrange multiplier. N represents the number of constraints, and K represents the regularization parameter.

2) The integration stage: this phase combines the hard and soft data to form a specific knowledge base (SK). In this paper, the hard data come from the measured RMR on the tunnel face, while the soft data come from the **wave** velocity data obtained by TSP advance prediction and from the fitting model of the surrounding rock parameters.
3) The posterior stage: at this stage, GK and SK are integrated. The prior PDF obtained in the first step and the specific knowledge base in the second step are processed by the Bayes rule to solve the posterior PDF. Finally, the mathematical expectation is obtained as the predicted value of the point to be estimated.

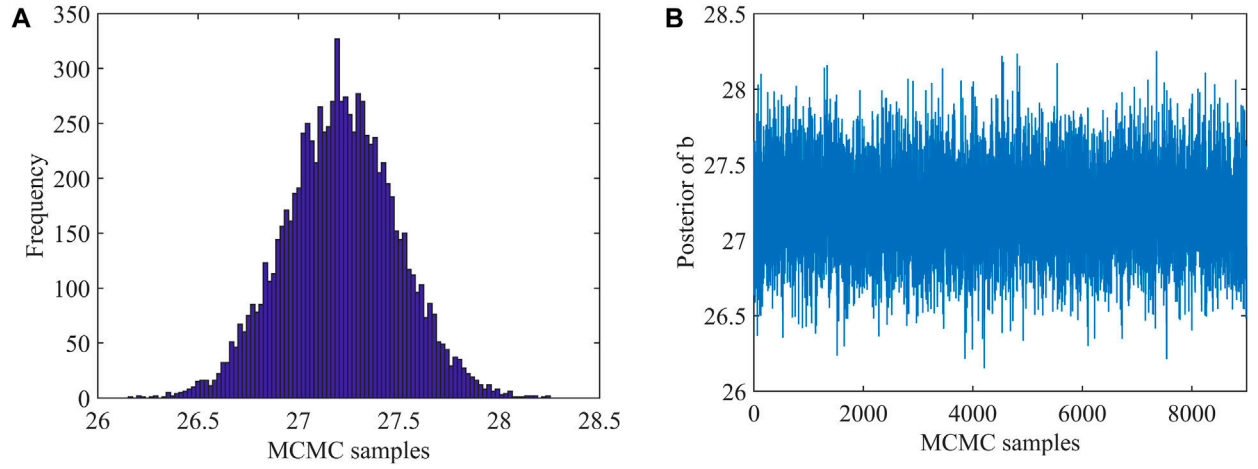

FIGURE 10
TSP and RMR statistical parameters in excavation stage 1; **(A)** equivalent sample frequency distribution; **(B)** equivalent samples based on MCMC.

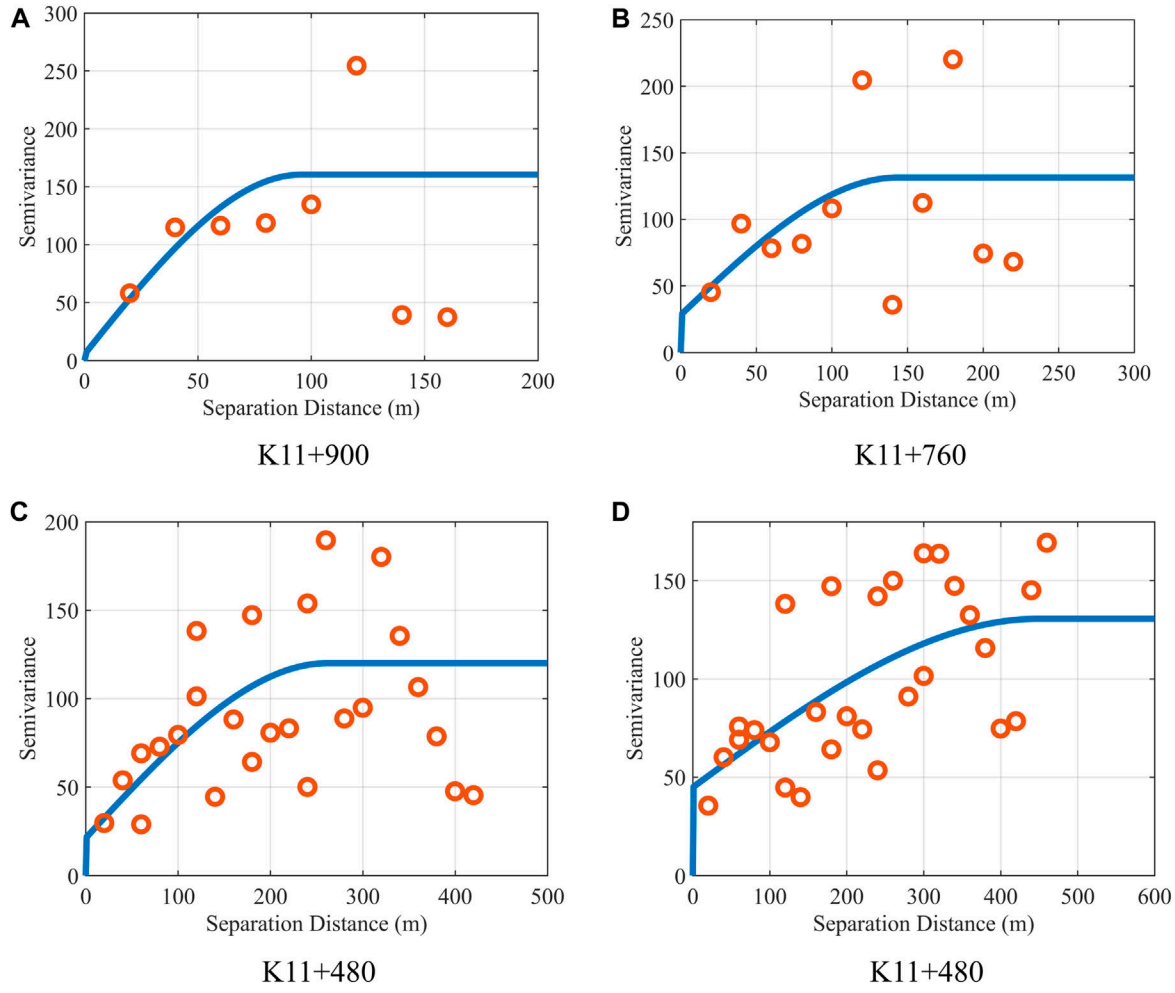

FIGURE 11
Variogram function fitting: **(A)** K11 + 900 variogram model, **(B)** K11 + 760 variogram model, **(C)** K11 + 480 variogram model, and **(D)** K11 + 360 variogram model.

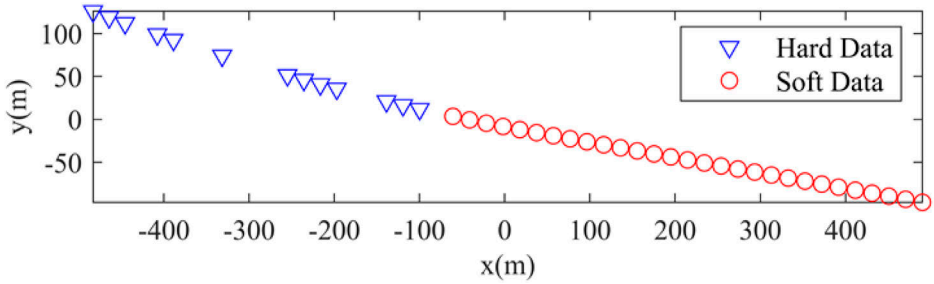

FIGURE 12
K11 + 900 soft data and hard data location distribution.

TABLE 3 Cross-validation criteria for different excavation stages (V_P as soft data).

Prediction location	Nugget	Range(m)	Sill
K11 + 900	5.27	95.54	155.17
K11 + 760	28.19	124.44	103.25
K11 + 480	21.17	261.93	98.88
K11 + 360	44.87	448.83	85.76

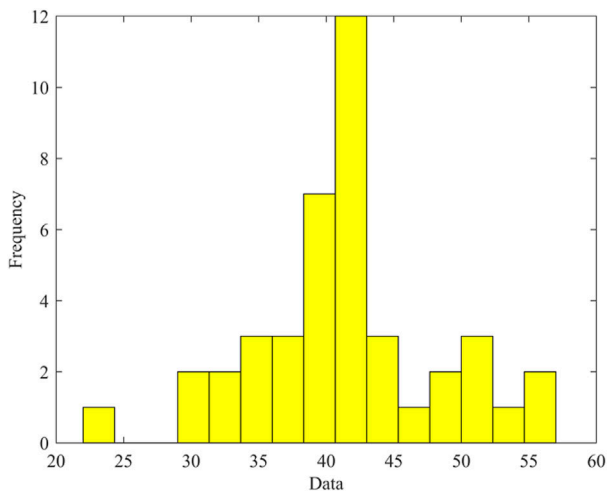

FIGURE 13
Frequency distribution histogram of measured RMR.

3 Case study of the Laoying tunnel

3.1 Project overview

A case study was performed to validate the RMR prediction method proposed in this study. The Laoying rock tunnel is a separate rock tunnel constructed by the drilling and blasting method in Baoshan, Yunnan, China (see Figure 6). The study area is located between the mileages K12 + 320 and K11 + 320, with a total length of 1,115 m. The maximum buried depth of the Laoying tunnel is approximately 1,264 m. The underground space traversed by the project mainly contains rock layers such as sandstone and limestone, and the preliminary survey reveals five large faults along the tunnel axis.

3.2 Data collection

A series of photogrammetry and field tests were performed to obtain the value of RMR on the tunnel face as hard data. The new tunnel face, which was exposed by tunnel drilling and blasting, created opportunities for engineers to inspect the rock masses. In this study, the surrounding rock evaluation parameters in RMR are collected herein. As shown in Figure7, the integrity index (RQD value, joint spacing, and joint condition) of the tunnel face was obtained by the photogrammetry-based mapping technique (Li et al., 2016), and the UCS of the rock mass can be obtained through the rebound tests of the rock mass. Ground water (GW) data are obtained by field observation. A part of the measured RMR values of the tunnel faces is given in Table 2.

During tunnel construction, a total of nine TSP tests were conducted in the designated location from K11 + 320 to K12 + 320 (see Figure 8). Each TSP seismic wave forecast can observe the seismic p-wave and s-wave velocities in the rock mass within 100–120 m in front of the tunnel face. By analyzing the wave velocity inversion results of the nine TSP predictions, V_P and V_S of the rock mass were collected every 20 m from the position of K12 + 320. In the selected study area, the tunnel passes through a fault zone, which is approximately located between K11 + 470 and K11 + 320, according to the preliminary geological survey.

4 Results and discussion

4.1 Probabilistic characteristics of RMR with wave velocity fitting

Figure 9 displays the RMR values of K11 + 360, as interpreted by V_P and V_S/V_S, respectively. A total of 10,000 equivalent samples of the statistic parameters were generated using the proposed Bayesian sequential updating approach to ensure that the MCMC method achieves a stable convergence state. The RMR value at K11 + 360

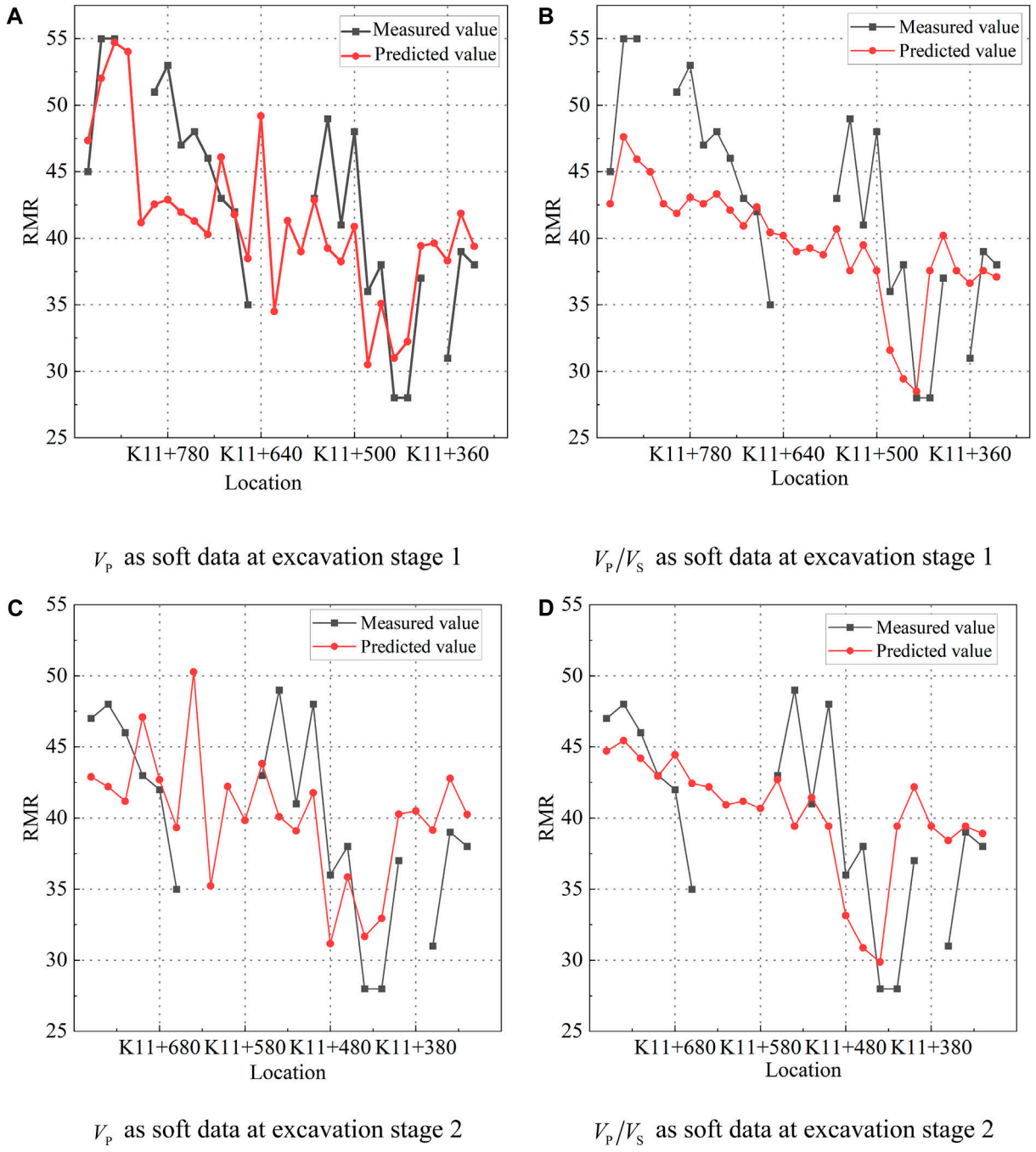

FIGURE 14
(Continued).

was interpreted when the tunnel was excavated to K11 + 880, K11 + 740, K11 + 480, and K11 + 340, referring to excavation stages 1, 2, 3, and 4, respectively. Figure 10 displays the MCMC equivalent sample and statistical diagram of the parameter at K11 + 360 under the conditions of the first excavation stage. Therefore, as the excavation continues, the available measured data gradually increase, and the predicted variance decreases. For each prediction point, soft data select the interpretation results of the stage in which the excavation position is closest to the prediction point. In excavation stage 4, where the excavation faces reach K11 + 340, when V_P and V_P/V_S are used to interpret RMR, the mean and variance of K11 + 360 interpretation data are (39.7032, 3.509) and (38.5254, 3.387), respectively. These two values are used as soft data at K11 + 360, when the excavation position is closest to the prediction point as many measured data can be employed. The soft data forecasting the rest of K11 + 360 also employed MCMC statistics from this construction phase. Correspondingly, when predicting K11 + 900, K11 + 760, and K11 + 480, the parameters of the excavation stage

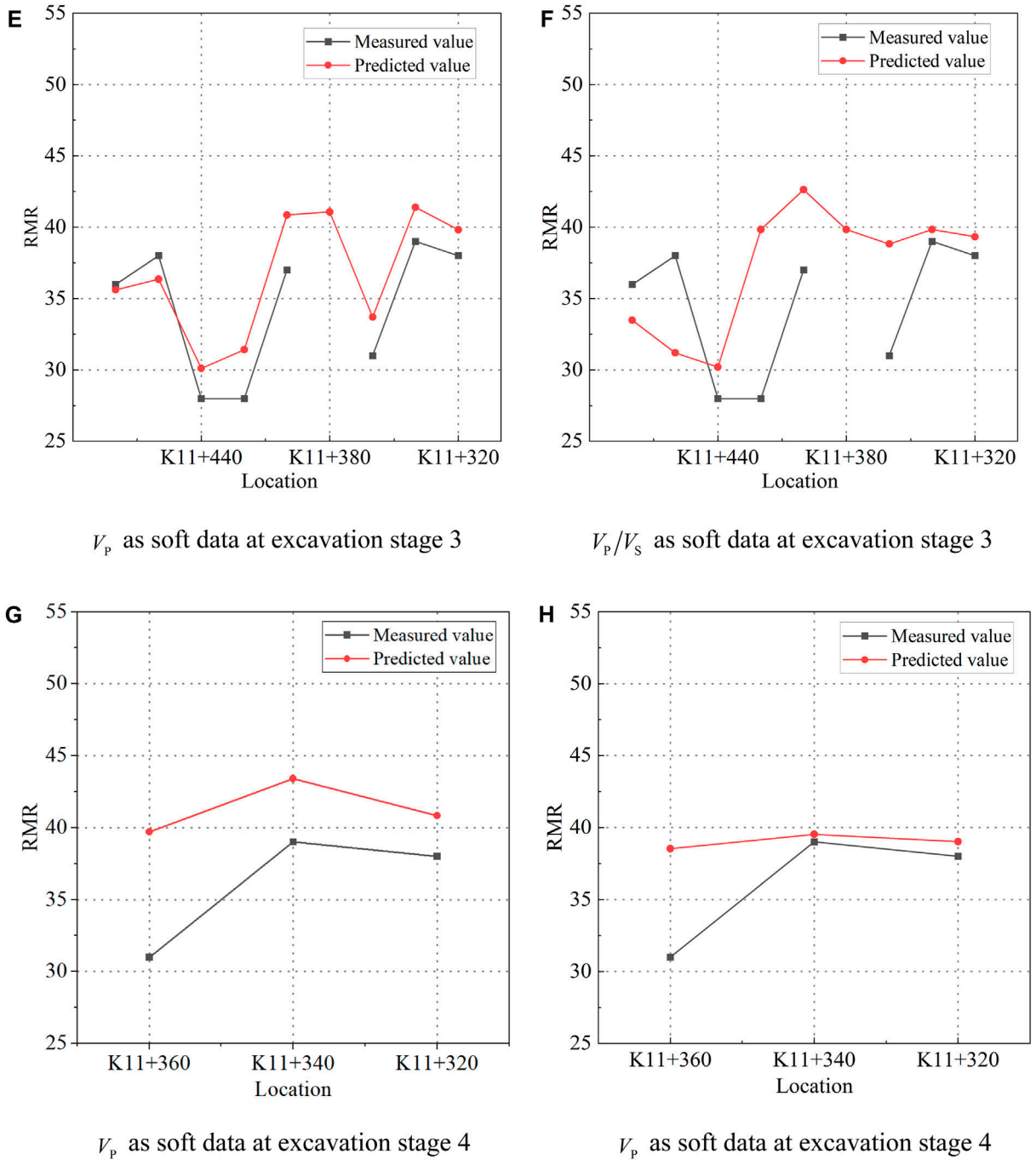

FIGURE 14
(Continued). BME prediction result at different excavation stages (**(A, B)**: excavation stage 1; **(C, D)**: excavation stage 2; **(E, F)**: excavation stage 3; **(G, H)**: excavation stage 4).

1, stage 2, and stage 3 are used, respectively. In order to increase the prediction accuracy, all available hard data are used in this process.

4.2 Hard data spatial variability

Figure 11 shows the results of the variogram calculation by fitting the positions of the four predicted points to the spherical theoretical variogram. The variogram function reflects the spatial variability of the surrounding rock parameters. The data range and sill are listed in Table 3, and the data points outside the range will no longer participate in the prediction.

The variogram function changes as the measurement data increase, which can be seen from the fitting results. The range grows with more measured data, indicating that more hard data need to be included to yield more accurate results in the limited area.

TABLE 4 Cross-validation criteria for different excavation stages (V_P as soft data).

Criterion	Excavation to K11 + 900	Excavation to K11 + 760	Excavation to K11 + 480	Excavation to K11 + 360
MD	10.11	8.14	3.85	1.82
ME	−1.78	1.63	0.156	1.64
RMSE	5.11	4.68	2.50	1.65

TABLE 5 Cross-validation criteria for different excavation stages (V_P/V_S as soft data).

Criterion	Excavation to K11 + 900	Excavation to K11 + 760	Excavation to K11 + 480	Excavation to K11 + 360
MD	10.10	11.42	5.63	1.52
ME	−1.63	0.133	1.64	0.69
RMSE	5.11	5.36	3.13	0.93

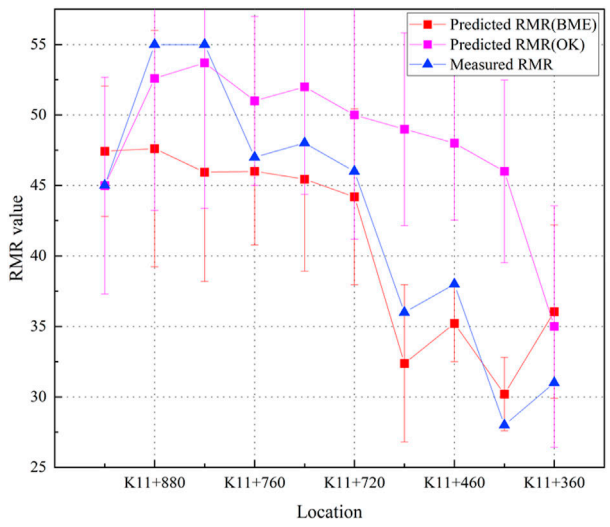

FIGURE 15
Result comparison of Kriging and BME methods.

TABLE 6 Relative errors of different prediction methods.

Criterion	Method	
	BME (V_P)	BME (V_P/V_S)
ME	1.05	0.344
RMSE	2.91	2.35

However, the nugget increases with a larger sample size, proving that the influence of the aggregate error of the sampling measurement increases accordingly. The prediction deviation caused by the internal randomness of the surrounding rock mass parameters will be more evident in the regions that do not conform to the hypothesis of second-moment stability, such as the fault fracture zone. Therefore, it is necessary to perform advanced geological prediction to improve the prediction accuracy.

4.3 Exploratory spatial data analysis

Figure 12 shows the data location for the prediction of mileage K11 + 760. A total of 17 hard data and 22 soft data were collected for advanced geological prediction. The prediction point lies between the measurement position of the hard data and soft data. The measured values of RMR ranged from 22 to 57, the mean is 40.8, and the standard deviation is 9.69. Figure 13 also illustrates the frequency distribution histogram of RMR. The Shapiro–Wilk method was used to test the normality of the RMR data distribution. The results show that the measured values of RMR do not reject the normal distribution at the significance level of 5%. The BME method requires the hard data used to follow the normal distribution, so the hard data used for the other predicted positions are also tested for the normal distribution.

4.4 Comparison and analysis of the prediction results

4.4.1 Comparison and verification with the measure values

The prediction results of different excavation stages are summarized in Figure 14, where a prediction that considers V_P as

TABLE 7 Validation criteria for two BME prediction strategies.

Geological conditions		Homogeneous formation		Fault fracture zone	
Prediction location		K11 + 900	K11 + 760	K11 + 480	K11 + 360
Relative error (%)	Kriging method	8.89	8.51	27.78	41.94
	BME (V_P)	8.21	4.07	4.82	9.14
	BME (V_P/V_S)	5.82	2.13	7.28	3.37

soft data and a prediction that considers V_P/V_S as soft data are presented separately. The performance metrics, maximum deviation (MD), mean error (ME), and root mean squared error (RMSE) are used for evaluating the prediction accuracy. As shown in Table 4 and Table 5, these evaluation parameters should be as small as possible. The predicted accuracy increases with the amount of hard data. At excavation stage 1 (from excavation to K11 + 900), when the number of the measured data is 12, the RMSE of the predicted result is 5.11. At excavation stage 4, when the number of the measured data increased to 30, the RMSE of predicted result is 1.65, which causes a smaller RMR prediction uncertainty compared with that of excavation stage 1.

Moreover, as illustrated in Table 4 and Table 5, the RMR prediction results using V_P and V_P/V_S have almost similar estimation accuracies in terms of MD, ME, and RMSE values. However, from the perspective of the discretization and volatility of the prediction results, the volatility of the prediction results is smaller when V_P/V_S is used as soft data. For example, when the construction reaches K11 + 900, the sample variances of the two prediction methods are 5.94 and 3.32, respectively.

4.4.2 Comparison and verification with the measure values

For the Kriging method (Hayunga and Kolovos, 2016; Zhang et al., 2016; Gelman et al., 2017; He and Kolovos, 2018), the measured value of RMR for each excavated surface is taken as sample points, and the variogram function in Figure 11 is used for the fitting prediction. In the Kriging prediction framework, only hard data from the excavation face are included in the prediction. The RMR prediction uncertainty can be quantified by considering the model uncertainty and spatial variability. The estimation with the 68% confidence interval of RMR can be represented as follows: $\left[\mu_{\text{lower}} - \sigma, \mu_{upper} - \sigma\right]$. As illustrated in Figure 15, the blue line represents the actual measured RMR at the excavated positions, and the purple and red lines represent the predicted RMR value using the OK and BME methods, respectively.

As is shown in Figure 15, the BME-based approach shows a smaller prediction error than the OK-based method, and such a phenomenon is more obvious in the fault area. According to the tunnel preliminary geological survey, the area between K11 + 470 and K11 + 320 is located in a fault. It is tough to forecast the accuracy of drastic changes in geological conditions in bad geological sections such as faults. Therefore, it is necessary to apply an advanced geological prediction to assist in predicting the geological conditions. Table 6 indicates the relative errors of the three prediction approaches in the formation of relatively uniform sections, such as the K11 + 900 and K11 + 760 forecast points. The relative errors of the three methods are reasonably minor, and the relative errors of the predicted results are less than 15%. However, the relative error predicted by the Kriging method is up to 30% when the local layer varies significantly in fault fracture zones, such as at K11 + 480 and K11 + 360. At this time, the prediction results have a larger deviation, which proves the previous hypothesis. It is difficult to capture large strata changes using traditional Kriging methods. In comparison, the two BME prediction results, which combine the wave velocity of the surrounding rock in advance, have better prediction results at the fault layer. Two performance metrics, ME and RMSE, are used to assess the overall predictive accuracy. The ME should approach zero. The RMSE shows the difference between the predicted and the measured values, which needs to be as small as possible. As shown in Table 7, RMSE for BME (V_P) and BME (V_P/V_S) are 2.91 and 2.35, respectively. Therefore, V_P/V_S information as soft data in the research area has a relatively higher accuracy.

5 Conclusion

This paper proposes a statistical method based on the Bayesian maximum entropy framework, which uses geological information on the tunnel face and TSP geological prediction to quantitatively infer the RMR value of the unexcavated rock mass. The proposed method is applied in the Laoying rock tunnel in Yunnan, China. The RMR values at each excavation position of the tunnel are obtained by photogrammetry and other complementary methods. Additionally, the variances of different measured data are calculated.

Second, two parameters, the s-wave velocity and p-wave velocity ratio of surrounding rock, were selected to fit the RMR of the surrounding rock, and the least square fitting interval of the 95% confidence level was selected as the wave velocity measurement point to participate in the Bayesian maximum entropy prediction.

Finally, the Bayesian maximum entropy and traditional Kriging methods are used to analyze the prediction results of the normal uniform formation and the fault fracture zone in the study area. Meanwhile, the prediction results using p-wave velocity and p-wave velocity ratio as soft data are compared. The results show that the

Bayesian maximum entropy can integrate the advanced geological prediction data, and the prediction accuracy is higher in the sections where the geological conditions change significantly, such as the fault fracture zone. In comparison, V_P/V_S information as soft data has a relatively higher accuracy.

The results indicate that the fusion of soft data and geological interpretation can make the prediction of RMR more accurate. The relative error of the method is less than 15% at the selected prediction points compared with that of the traditional Kriging method. This method shows significant potential for estimating RMR values ahead of tunnel excavation with advanced geological forecast data.

Data availability statement

The raw data supporting the conclusion of this article will be made available by the authors, without undue reservation.

Author contributions

XL: data curation, funding acquisition, resources, supervision, writing–original draft, and writing–review and editing. ZC: methodology and writing–original draft. LT: formal analysis, methodology, and writing–review and editing. CC: writing–review and editing. TL: methodology and writing–review and editing. JL: writing–review and editing. YL: data curation and writing–review and editing. YR: funding acquisition, supervision, validation, and writing–review and editing.

Funding

The author(s) declare financial support was received for the research, authorship, and/or publication of this article. This work was financially supported by the National Natural Science Foundation of China (grant number: U1934212). The authors would like to thank the financial support.

Conflict of interest

The authors declare that the research was conducted in the absence of any commercial or financial relationships that could be construed as a potential conflict of interest.

Publisher's note

All claims expressed in this article are solely those of the authors and do not necessarily represent those of their affiliated organizations, or those of the publisher, the editors, and the reviewers. Any product that may be evaluated in this article, or claim that may be made by its manufacturer, is not guaranteed or endorsed by the publisher.

References

Bieniawski, Z. (1973). Engineering classification of jointed rock masses. *Civ. Eng.* 15, 334–345.

Bu, L., Li, S. C., Shi, S. S., Xie, X. K., Li, L. P., Zhou, Z. Q., et al. (2018). A new advance classification method for surrounding rock in tunnels based on the set-pair analysis and tunnel seismic prediction system. *Geotechnical Geol. Eng.* 36, 2403–2413. doi:10.1007/s10706-018-0471-5

Chen, G. X., Zhu, J., Qiang, M., and Gong, W. (2018). Three-dimensional site characterization with borehole data - a case study of Suzhou area. *Eng. Geol.* 234, 65–82. doi:10.1016/j.enggeo.2017.12.019

Chen, J., Li, X., Zhu, H., and Rubin, Y. (2017). Geostatistical method for inferring RMR ahead of tunnel face excavation using dynamically exposed geological information. *Eng. Geol.* 228, 214–223. doi:10.1016/j.enggeo.2017.08.004

Christakos, G. (1990). A Bayesian maximum-entropy view to the spatial estimation problem. *Eng. Geol.* 22, 763–777. doi:10.1007/bf00890661

Esmailzadeh, A., Mikaeil, R., Shafei, E., and Sadegheslam, G. (2018). Prediction of rock mass rating using TSP method and statistical analysis in Semnan Rooziyeh spring conveyance tunnel. *Tunneling Undergr. Space Technol.* 79, 224–230. doi:10.1016/j.tust.2018.05.001

Gelman, A., Simpson, D., and Betancourt, M. (2017). The prior can often only Be understood in the context of the likelihood. *Entropy* 19, 555–625. doi:10.3390/e19100555

Hayunga, D. K., and Kolovos, A. (2016). Geostatistical space-time mapping of house prices using Bayesian maximum entropy. *Int. J. Geogr. Inf. Sci.* 30, 2339–2354. doi:10.1080/13658816.2016.1165820

He, H. H., He, J., Xiao, J. Z., Zhou, Y., and Liu, Y. (2020). 3D geological modeling and engineering properties of shallow superficial deposits: a case study in Beijing, China. *Tunn. Undergr. Space Technol.* 100, 103390–103418. doi:10.1016/j.tust.2020.103390

He, J., and Kolovos, A. (2018). Bayesian maximum entropy approach and its applications: a review. *Stoch. Environ. Res. Risk Assess.* 32, 859–877. doi:10.1007/s00477-017-1419-7

Hoek, E., and Brown, E. T. (1997). Practical estimates of rock mass strength. *International Journal of Rock Mechanics and Mining Sciences* 34 (8), 1165–1186.

Hou, F., Xie, X., Shi, S., Song, S., Bu, L., Li, L., et al. (2019). Dynamic optimization classification model for submarine tunnel surrounding rocks and its application in engineering. *J. Coast. Res.* 15, 311–315. doi:10.2112/si94-064.1

Hu, B., Ning, P., Li, Y., Xu, C., Christakos, G., and Wang, J. (2021). Space-time disease mapping by combining Bayesian maximum entropy and Kalman filter: the BME-Kalman approach. *Int. J. Geogr. Inf. Sci.* 35, 466–489. doi:10.1080/13658816.2020.1795177

Jat, P., and Serre, M. (2016). Bayesian Maximum Entropy space/time estimation of surface water chloride in Maryland using river distances. *Environ. Pollut.* 219, 1148–1155. doi:10.1016/j.envpol.2016.09.020

Li, J., Zhang, H., and He, J. (2019a). Application of integrated geophysical methods to advanced prediction of a tunnel in a limestone area. *Geol. Explor.* 55, 1452–1462.

Li, N., Song, X. L., Li, C., Xiao, K., Li, S., and Chen, H. (2019b). 3D geological modeling for mineral system approach to GIS-based prospectivity analysis: case study of an MVT Pb–Zn deposit. *Nat. Resour. Res.* 28, 995–1019. doi:10.1007/s11053-018-9429-9

Li, X., Chen, J., and Zhu, H. (2016). A new method for automated discontinuity trace mapping on rock mass 3D surface model. *Comput. Geosciences* 89, 118–131. doi:10.1016/j.cageo.2015.12.010

Li, X., Li, P., and Zhu, H. (2013). Coal seam surface modeling and updating with multi-source data integration using Bayesian Geostatistics. *Eng. Geol.* 164, 208–221. doi:10.1016/j.enggeo.2013.07.009

Lu, Q., Zhao, B., and Pan, S. (2020). Classification of tunnel surrounding rock based on TSP system and PCA-bayes discriminant method. *Chin. J. Undergr. Space Eng.* 16, 80–86.

Montalvo, D., Mclaughlin, M., and Degryse, F. (2015). Efficacy of hydroxyapatite nanoparticles as phosphorus fertilizer in andisols and oxisols. *Soil Sci. Soc. Am. J.* 79, 551–558. doi:10.2136/sssaj2014.09.0373

Niedbalski, Z., Małkowski, P., and Majcherczyk, T. (2018). Application of the NATM method in the road tunneling works in difficult geological conditions–The Carpathian flysch. *Tunn. Undergr. Space Technol.* 74, 41–59. doi:10.1016/j.tust.2018.01.003

Nourani, M., Moghadder, M. T., and Safari, M. (2017). Classification and assessment of rock mass parameters in Choghart iron mine using P-wave velocity. *J. Rock Mech. Geotechnical Eng.* 9, 318–328. doi:10.1016/j.jrmge.2016.11.006

Santos, V., Da, S., and Graca, M. B. (2015). Prediction of RMR ahead excavation front in D&B tunnelling. *Eng. Geol. Soc. Territ.* 6, 415–419.

Shan, S. W., Lam, T. C., and Stamer, W. D. (2019). The effects of a Rho-associated protein kinase (ROCK) inhibitor (Y39983) on human trabecular meshwork cells - a morphological and proteomic study. *Investigative Ophthalmol. Vis. Sci.* 60, 9–12.

Von, W., and Ismail, M. (2017). "Evaluation of tunnel seismic prediction (TSP) result using the Japanese highway rock mass classification system for pahang-selangor raw water transfer tunnel," in Proceedings of the International Conference of Global Network for Innovative Technology and Awam International Conference in Civil Engineering, Penang, Malaysia, August 8–9, 2017.

Zhang, F., Zhong, S., Yang, Z., Sun, C., Wang, C. L., and Huang, Q. Y. (2016). Spatial estimation of losses attributable to meteorological disasters in a specific area (105.0°e–115.0°E, 25°N–35°N) using bayesian maximum entropy and partial least squares regression. *Adv. Meteorology* 2016, 1–16. doi:10.1155/2016/1547526

Zhang, Q., and Zhu, H. (2018). Collaborative 3D geological modeling analysis based on multi-source data standard. *Eng. Geol.* 246, 233–244. doi:10.1016/j.enggeo.2018.10.001

Zhou, Z., Li, S., and Li, L. (2017). Classification method of rock mass quality and its engineering application. *J. Central South Univ. Sci. Technol.* 48, 1049–1056.

frontiers | Frontiers in Earth Science

TYPE Original Research
PUBLISHED 21 February 2024
DOI 10.3389/feart.2024.1369814

Check for updates

OPEN ACCESS

EDITED BY
Pengjiao Jia,
Soochow University, China

REVIEWED BY
Bangxiang Li,
Shandong University of Technology, China
Yaxun Xiao,
Chinese Academy of Sciences (CAS), China

*CORRESPONDENCE
Jiarui Su,
2418559382@qq.com

RECEIVED 13 January 2024
ACCEPTED 07 February 2024
PUBLISHED 21 February 2024

CITATION
Chen Y, Su J, Gao T, Jing Y, Zhang H, Duan H and Zhao W (2024), Research and application of macro-micro fracture correlation of heterogeneous granite.
Front. Earth Sci. 12:1369814.
doi: 10.3389/feart.2024.1369814

COPYRIGHT
© 2024 Chen, Su, Gao, Jing, Zhang, Duan and Zhao. This is an open-access article distributed under the terms of the Creative Commons Attribution License (CC BY). The use, distribution or reproduction in other forums is permitted, provided the original author(s) and the copyright owner(s) are credited and that the original publication in this journal is cited, in accordance with accepted academic practice. No use, distribution or reproduction is permitted which does not comply with these terms.

Research and application of macro-micro fracture correlation of heterogeneous granite

Yunjuan Chen[1,2], Jiarui Su[2]*, Tao Gao[3], Yi Jing[4], Huifu Zhang[2], Hongjie Duan[2] and Wenbin Zhao[2]

[1]Key Laboratory of Building Structural Retrofitting and Underground Space Engineering, Ministry of Education, Shandong Jianzhu University, Jinan, China, [2]Civil Engineering College, Shandong Jianzhu University, Jinan, China, [3]Shandong Earthquake Agency, Jinan, China, [4]School of Qilu Transportation, Shandong University, Jinan, Shandong, China

Granite structure has the characteristics of discrete distribution and random distribution of minerals, which is particularly critical to the stability of surrounding rock of underground caverns, and the research process is extremely complicated. In this paper, the granite of Dagangshan tunnel in rock sections of class III was taken as the research object, and the mineral composition and proportion, the macro and micro characteristics of granite was analyzed by XRD analysis, SEM and laboratory compressive test; Dagangshan tunnel's section model with surrounding rock of class III was established using the particle flow program PFC and the numerical simulation was done, thus the influence of micro composition and proportion on surrounding rock masses' stability with the tunnel excavation was analyzed. Results show that: The content of illite and albite is the most, and illite is the weak mineral of the granite. For the granite of Dagangshan tunnel with rock masses of class III, the rock failure is mainly caused by shear force and secondary by tensile force. Fracture is mainly concentrated in the enrichment area of "weakened minerals," where as the breakthrough point and expands to other parts, and further connects. The "enhanced minerals" are basically stable because of their high hardness and strong link between each other. After tunnel excavation, cracks of tunnel's side walls and the arch foots are more serious, so the supporting measures of these parts should be strengthened.

KEYWORDS

heterogeneous, granite, test, numerical simulation, macro-micro scopic correlation

1 Introduction

Heterogeneous granite has multi-scale characteristics, and its mechanical properties have spatial variation. The rupture correlation is affected by many factors (Shi et al., 2020; Xu et al., 2020; Huang et al., 2021a; Vahid and Abbas, 2021; Li et al., 2023; Chen et al., 2022a), which not only affects the stability of surrounding rock of underground caverns, but also increases the difficulty of stability evaluation. By studying the macroscopic and microscopic fracture of granite and establishing the correlation between the microscopic structure of rock mass and macroscopic fracture, we can deeply understand the mechanism and process of rock fracture, which is of great significance for the safe construction and green operation of engineering construction. At the same time, it can also provide important support for predicting and controlling the fracture behavior of rock (Xia et al., 2021; Chen et al., 2022b; Chen et al., 2022c; Sun et al., 2019; Han et al., 2023).

In recent years, both domestic and international scholars have conducted experimental and simulation studies on the macro-micro failure characteristics of rock mass and rock heterogeneity (Peng and Chen, 2021; Liu et al., 2020; Zhang et al., 2022). Based on the macro-micro structure of layered rock mass, Liu et al. (2021) derived an anisotropic multi-scale damage model and permeability evolution equation for saturated layered rock mass under hydraulic coupling load within the framework of thermodynamics. Zheng et al. (2005) carried out meso-CT scanning test on fractured rock, and found that the damage evolution and crack propagation of rock were affected by different minerals in the rock. Cracking and failure generally began from the surface with weak mineral strength. Through uniaxial compression simulation, Ni et al. (2015) found that particle size is an important factor affecting rock mass fracture. Voronoi diagram is introduced to analyze elastic modulus and flexibility. It is found that elastic modulus is inversely proportional to size, and flexibility does not change significantly with rock mass size. Zhang et al. (2017) investigated the micro-level damage process of rock mass using PFC3D particle flow program and obtained its evolutionary law. Yang (2018), based on experimental research and numerical simulation, compared contact force chains and velocity fields in the micro structure of rock mass, suggesting that changes in the micro field are essentially consistent with macro state evolution. Li, (2017) established a three-dimensional inhomogeneity rock model by RFPA numerical simulation software, and believed that the damage evolution of rock and the internal meso-inhomogeneity have a direct impact, and pointed out that the meso-mineral composition of rock materials is the essential reason that affects the macro-strength and fracture mode. Yang et al. (2016) concluded based on discontinuous deformation (DDA) simulation platform that macro strength of rock masses is closely related to their micro non-uniformity. Huang et al. (2021b) established a 3D DFN numerical model to investigate seepage characteristics of fractured rocks, and found out mineral composition, distribution as well as fracture grid had significant impacts.

Li (2017) found that the uneven mineral composition of rock samples has a direct effect on the degree of fragmentation of rock failure by using PFC particle flow method and random analysis method simulation. At the same time, it also proves the accuracy of using discrete element method to simulate the non-uniform characteristics of rock. Liu et al. (2019) carried out the Brazilian disc acoustic emission test of granite and marble, and combined with scanning electron microscopy to analyze the microscopic morphology of the fracture surface. It was found that the macroscopic and mesoscopic crack propagation and failure of rock were mainly affected by the properties of weak mineral particles.

Most of the existing studies have primarily focused on analyzing the macro and micro fracture characteristics of granite, without exploring the macro-micro correlation. To address this gap, this study investigates the macro-micro failure characteristics of rock, as well as the type and composition ratio of mineral particles in III-level surrounding rock section of Dagangshan Tunnel. This is achieved through XRD testing, SEM analysis, and uniaxial compression tests conducted on granite specimens collected from the site. Subsequently, a numerical calculation model for non-uniform granite with particle flow is established to compare the influence of different types of mineral particles on surrounding rock stability.

2 Project overview

The Dagangshan Tunnel of Luding-Asbestos Expressway is situated in the southeastern periphery of the Tibetan Plateau, with its planned route extending from the Sichuan Basin to the central region of southwest high mountains in Sichuan. This area is characterized by towering mountains, frequent geological movements, extensive and deep valleys, as well as numerous glacial activities within the Dadu River basin water system. Groundwater primarily occurs in shallow weathering fissures, tectonic fissures, and deep tectonic fissures on slopes. The water content within these fissures is abundant, resulting in generally favorable hydrological conditions throughout this region. The overall topography exhibits a ladder-like pattern with elevated peaks towards the west gradually descending towards lower elevations in the east. Spanning a total length of 7,254 m, this tunnel represents an exceptional engineering feat due to its considerable length. The slope of the tunnel entrance and exit ranges from 25° to 30°, and the tunnel is extensively distributed within the granite geological layer. Due to the influence of engineering geological characteristics, the initial support in the study section consists of C25 concrete sprayed with a thickness of 22 cm, allowing for an anticipated deformation of up to 8 cm. The secondary lining comprises a waterproof C30 concrete with a thickness of 35 cm. This study focuses on Section K57+960~K58+060, which represents a III-level surrounding rock condition. Figure 1 illustrates the geological profile and sampling point locations within the tunnel. The granite in this section consists mainly of weathered granite, a relatively hard rock with a massive structure. The overall rock mass is relatively intact, with localized joints and fractures present. Groundwater primarily occurs through dripping, rainfall, and small streams. The elevation at the tunnel is situated at 1,214°m, while reaching an elevation peak at 2,114 m above sea level for mountain topography; consequently resulting in a burial depth of approximately 900 m.

3 Fracture laws analysis for granite of laboratory-scale

In order to investigate the macroscopic mechanical properties of granite samples, sampling was conducted from the III-level surrounding rock section of Lushi Dagangshan Tunnel. Considering the discrete nature of granite mineral composition, a set of rock samples was collected every 20 m along the longitudinal axis of the tunnel, resulting in a total of three sets. These samples were then processed into cylindrical standard specimens measuring 50 mm × 100 mm. The granite samples met the requirements specified in "Standard for Test Methods of Engineering Rock Mass" (GB/T 50266-2013), with end surface unevenness less than 0.05 mm and height error controlled within 0.3 mm, the finished specimen is shown in Figure 2A.

The mechanical properties of granite were evaluated using the TAW-1000D multi-function testing machine for rheological

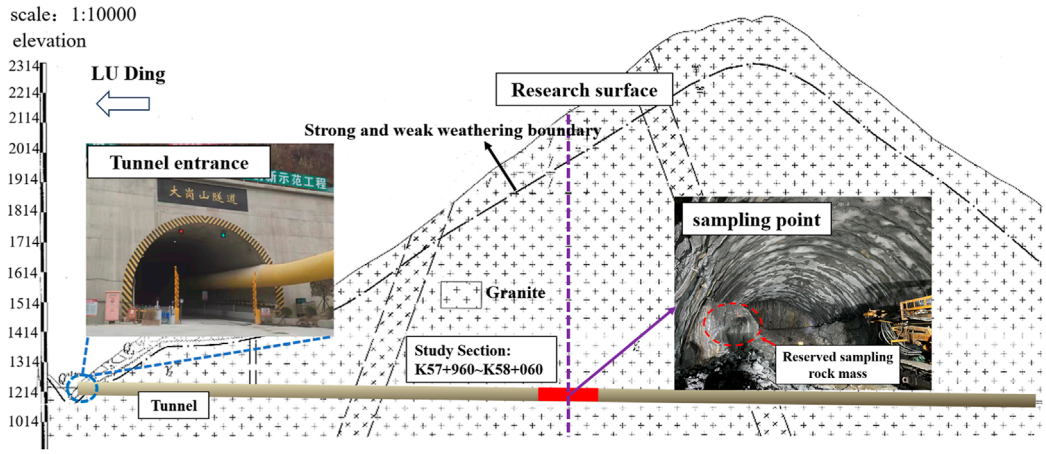

FIGURE 1
Geological profile and sampling position.

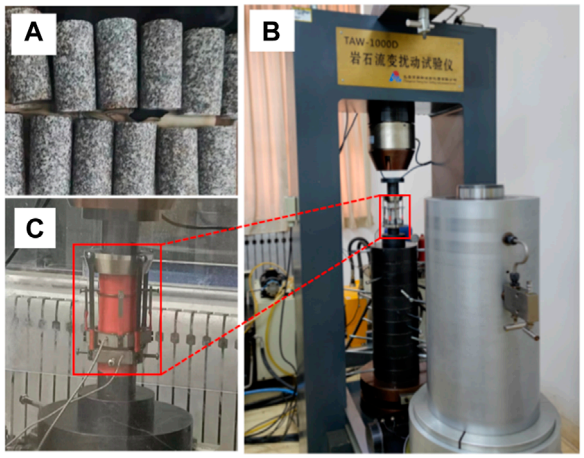

FIGURE 2
Uniaxial compression test of granite.

analysis of rock in the laboratory of rock mechanics at Shandong Jianzhu University. The maximum axial pressure capacity of the testing machine was 1,000 kN. At the onset of the test, the contact distance between the loading end and the top position of the specimen was initially increased at a rate of 20 mm/s. Once this contact distance reached approximately 1–2 mm, force control was implemented with a speed of 10 N/s. Subsequently, after complete contact between the testing machine and specimen was established, displacement control was switched to a loading rate of 0.1 mm/min. The experimental setup for conducting these tests is illustrated in Figure 2B, the placement of rock specimens is shown in Figure 2C, while Figure 3A presents the failure modes observed in each specimen tested. The entire test process data were recorded using axial strain gauges and a loading system, with stress-strain monitoring curves depicted in Figure 3B (Chen et al., 2023).

The fracture morphologies of the three groups of rock samples are observed to be similar, as depicted in Figure 3. In the III-level surrounding rock section, compression predominantly damages the granite, while shear cracks originate from tensile stress during penetration. The angle between the tensile cracks and the main fracture surface is less than 90°, indicating that shear failure is primary with supplementary tensile failure. Macroscopic fracture analysis reveals a relatively smooth main fracture surface with adhering flocculent crystal particles. Additionally, micro-rock bursts occur during axial compression damage due to continuous loading, where released tensile stress leads to local rock caving and audible sounds.

According to the complete stress-strain curve, during the initial compaction stage (OA), the stress-strain relationship exhibits an uneven quadratic growth pattern. In the stage of elastic deformation (AB), the growth of the curve follows a linear function. The overall stability of the specimen in the initial two stages is excellent, with no occurrence of cracks within the area and no visible cracks on the rock surface. In the unstable fracture stage (BC), microcracks are initiated on the surface of the specimen, which subsequently propagate under increasing axial load. Localized detachment of rock fragments occurs, accompanied by acoustic emissions, indicating progressive development and expansion of internal cracks within the rock sample. The rate of stress growth gradually diminishes. Finally, in the overall failure stage (CD), peak stress is reached accompanied by a distinct “excessive noise,” resulting in a rapid decline of the stress curve and formation of macro fractures as internal and external cracks connect. These findings indicate that granite within this III-level surrounding rock section possesses hard brittleness and high compressive strength. The process of crack initiation, propagation, and ultimate fracture within the rock mass involves energy migration with large-scale release upon loss of bearing capacity.

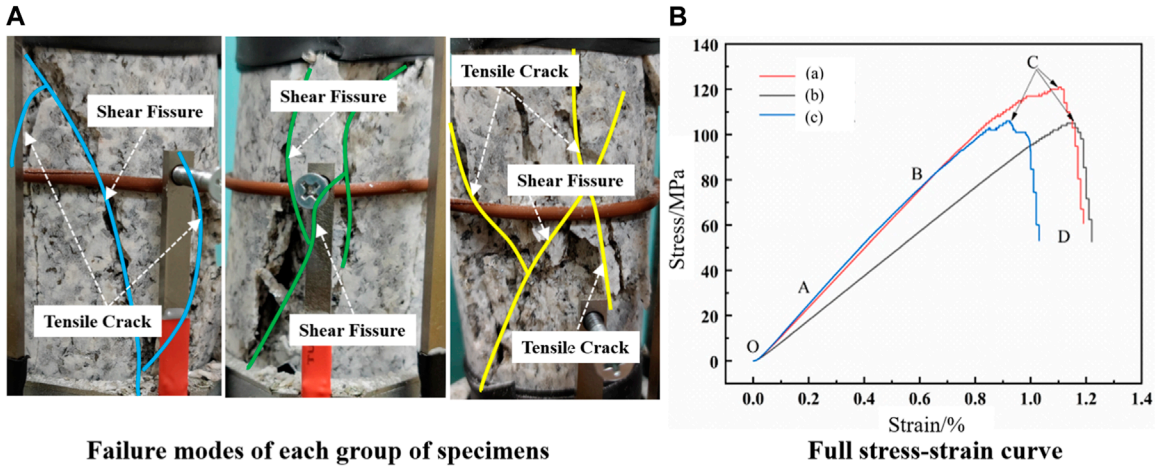

FIGURE 3
Rock failure mode and stress-strain curve.

4 Revealing the mineral composition and fracture behavior of granite via XRD analysis

4.1 XRD analysis of Granite's mineral composition

In order to investigate the influence of granite mineral composition on the fracture morphology and strength of rock mass, samples were randomly collected from three groups of indoor test specimens. The sampling location is illustrated in Figure 5, with a sampling size of 5 mm × 5 mm × 5 mm. After sampling, the granite samples should be ground uniformly in a dry environment free from any impurities. Once each group of granite powder has been ground to meet the standard specifications, all powders from these three groups should be combined and thoroughly mixed and ground together. The negative pressure test screen size should be Ø150 × 25. Finally, powder particles with a diameter less than 0.08 mm were extracted for mineral composition analysis using an X-ray diffraction instrument (XRD testing machine). Considering that the granite test blocks were obtained from the same batch of rock mass, it was assumed that their mineral composition content represented that of the engineering section and aligned with the microscopic properties of granite. The experimental procedure is depicted in Figure 4.

The XRD testing machine of Shandong Jianzhu University was utilized for the experiment, with an X-ray scanning range from 0° to 90°. Due to the unique crystal structure possessed by each mineral component, which acts as a three-dimensional grating for X-ray diffraction, when passing through this crystal structure, X-rays generate diffraction patterns with varying intensities. By analyzing the position and intensity of these diffraction lines in the patterns, it is possible to determine both the mineral composition and structure accurately. This principle of diffraction adheres to the Bragg formula, as shown in Formula 1.

$$2d \sin \theta = n\lambda \quad (1)$$

where d represents the interatomic spacing in the crystal, θ represents the half-diffractive angle, n represents the diffraction series, and λ represents the wavelength of X-ray radiation.

Following X-ray diffraction analysis on three groups of specimens, minerals corresponding to each peak value were identified and labeled in Figure 5. The respective RIR values for each mineral were obtained. The ratio of each mineral's RIR value to its modified diffraction intensity represented the adjusted intensity of that mineral, while the ratio of each mineral's adjusted intensity to the total diffraction intensity indicated its relative content. The X-ray diffraction patterns for each group and quantitative analysis results regarding granite mineral composition are presented in Figure 6.

The mineral composition of granite in the III-level surrounding rock section of Dagangshan is predominantly composed of illite [$Al_4Si_2O_9(OH)_3$], albite ($NaAlSi_3O_8$), K-feldspar ($KAlSi_3O_8$), quartz (SiO_2), and kaolinite [$Al_4(OH)_8Si_4O_{10}$], as depicted in Figure 5. Illite and albite exhibit the highest abundance with respective proportions of 39.3% and 30% among all minerals present. Conversely, kaolinite exhibits the lowest content. From the perspective of mineral hardness, quartz and feldspar minerals have significantly higher mineral strength than the other three, which are 7 and 6, respectively, while the hardness of illite is about 1–2, and the hardness of kaolinite is 2–2.5. According to Liu et al. (2019) study of granite and marble, it is found that mineral particles with weak hardness are more prone to fracture mechanical behavior under external load. Based on the strength and mineral content of these five minerals, the micro-fracture morphology and rock strength changes of mineral particles in inhomogeneous granite will be studied below.

4.2 SEM analysis of granite micro-fractures

The damaged rock mass after uniaxial compression is analyzed using scanning electron microscopy (SEM) technology. SEM can magnify the rock mass up to 100,000 times with a resolution reaching the nanometer level. By utilizing a focused electron

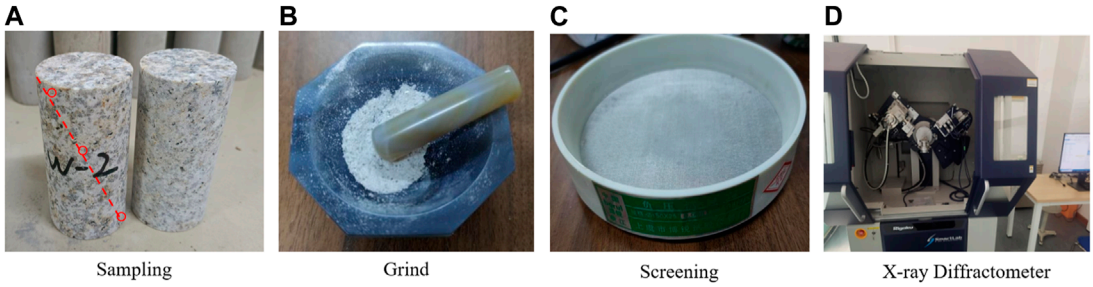

FIGURE 4
Test steps of granite mineral composition.

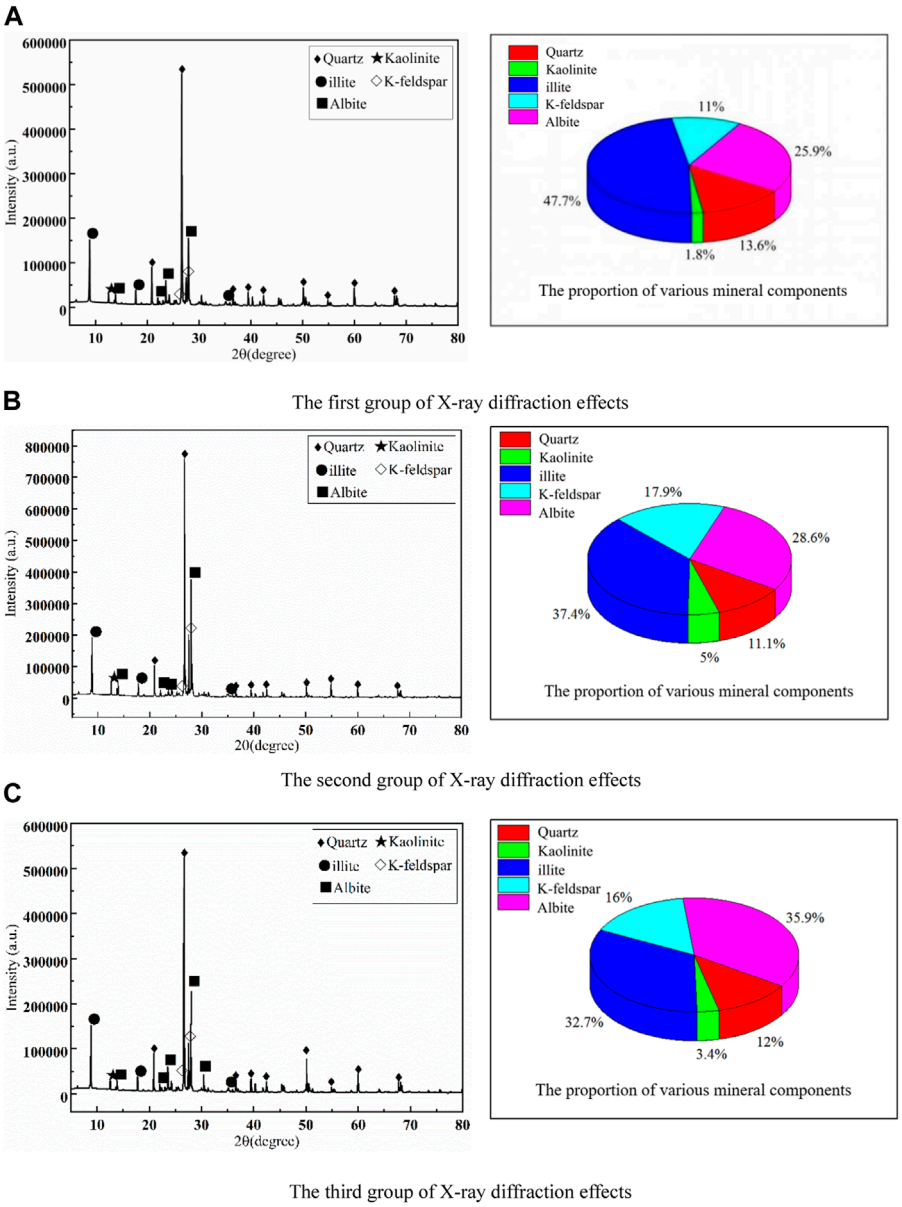

FIGURE 5
X-ray diffraction pattern and composition proportion of granite.

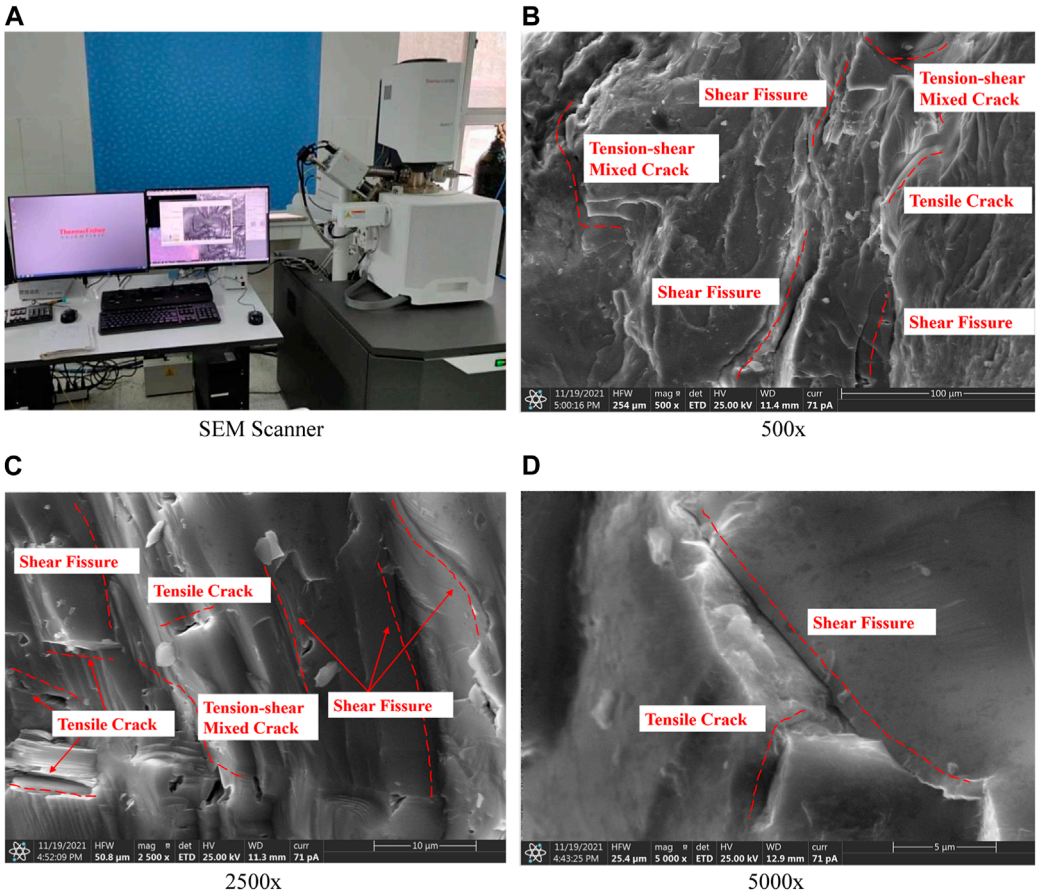

FIGURE 6
SEM scanner and some test results of granite.

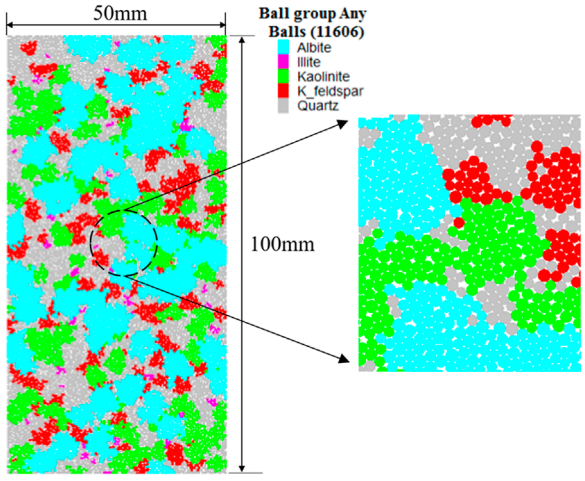

FIGURE 7
Granite non-uniform particle mineral model.

beam, SEM bombards the sample surface to generate secondary electrons, backscattered electrons, absorbed electrons, characteristic X-rays, and other physical signals. These signals are then captured, magnified, processed using various types of detectors and scanned point by point on the sample surface through a scanning coil for imaging purposes. Narrow focus high-energy electron beam scanning of specimens allows for interaction between the emitted beam and the sample material to represent its physical information behavior accurately. This process involves collecting, amplifying and re-imagining information in order to obtain microscopic morphological images of the samples.

The representative fracture section of granite was selected for laboratory testing, and subsequent SEM scanning analysis was conducted to examine its microscopic failure characteristics. The Thermo Scientific Quattro SEM system at Shandong University was employed for the SEM scanning. Prior to the experiment, ultrasonic cleaning was conducted on the samples to eliminate surface impurities. Subsequently, the granite fracture sections were scanned and analyzed under seven conditions: ×500, ×1,000, ×1,500, ×2,000, ×2,500, ×3,500, and ×5,000 magnifications. Figure 6 presents both the testing instrument used and some test results.

As depicted in Figure 6, the failure modes among particles exhibit three primary forms: shear fracture, tensile fracture, and tensile-shear composite fracture. Shear fracture plays a dominant role while tensile fracture and tensile-shear composite fractures act as auxiliary factors, which is consistent with the macroscopic characteristics of rock mass fracturing. Shear fractures are darker in

TABLE 1 Physical and mechanical parameters of granite particle model.

Mineral names	Minerals proportion /%	Density ρ/(kg·m^{-3})	Effective Shot Sex modulus E_c/GPa	Stiffness ratio k_n/k_s	Rub coefficient *mu*	Porosity *Lambda.*	Tensile intensity σ_c/MPa	Cohesive force *c*/MPa	Friction angle Phi/(°)
Quartz	12.3	2,900	60	2.5	0.5	3e-5	265	280	35
Potash Feldspar	15.0	2,700	45	2.5	0.5	3e-5	130	135	30
Albite	30.1	2,650	42	2.5	0.5	3e-5	110	120	30
Illite	39.2	2,800	11	2.5	0.5	3e-5	30	50	27
Kaolin	3.40	2,850	18	2.5	0.5	3e-5	25	40	27

color, closer together and denser in closure, with longer elongation lengths that mainly occur along mineral particle slips. The meso-shear fractures of granite present a layered structure formed primarily by axial external force compression and natural joints along the granite crystal. Furthermore, based on our analysis of mineral particle hardness above, illite is identified as the weak mineral within the granite sample; thus generating obvious layered structural cracks on its surface during fracturing processes. These cracks develop over long distances with joint step surfaces parallel to them; this type of failure mode is more sensitive to external loads but requires less energy for internal fracturing.

The fracture with lighter color, larger width and shorter extension length is tensile fracture, which is mainly formed under tension. Tensile fracture mostly occurs between relatively complete quartz mineral particles. Due to the high strength and hardness of quartz minerals and the smooth jointless surface, the particles around the tensile fracture are irregularly concave and convex. The reason is that the crystal particles are brittle due to the action of tensile stress, and the crisp loud noise in the process of uniaxial compression test is mainly the fracture of quartz brittle mineral materials. There is also a local tensile-shear composite fracture between the two failures, and the fracture is mostly manifested as a twisted shape in the direction of tensile stress.

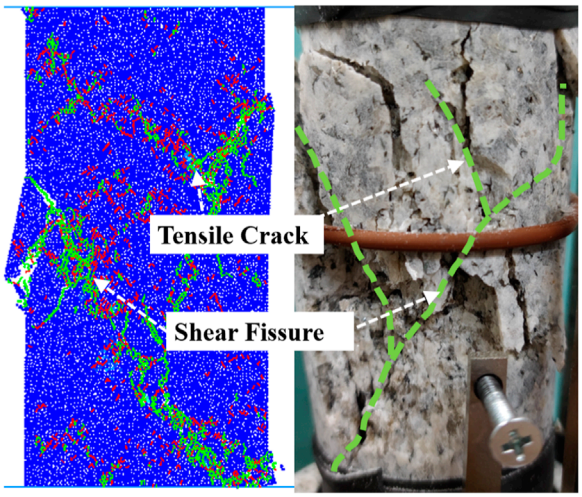

FIGURE 8
Comparison of PFC particle flow simulation and laboratory test (Chen, et al., 2023)

5 The correlation between macro-micro of granite and stability analysis of tunnel surrounding rock

Considering the analysis of tunnel surrounding rock stability, the utilization of finite element or finite difference analysis methods enables the simulation of macroscopic information such as surrounding rock stress and strain, thereby offering guidance for engineering construction. However, there is a lack of microscopic-scale research and an inability to establish a correlation between microscopic and macroscopic scales. Therefore, by employing XRD component analysis and SEM electron microscope scanning analysis in conjunction with laboratory test results, we utilize PFC software to construct a particle flow tunnel model and investigate the influence of microscopic components on the macroscopic failure of surrounding rock mass.

5.1 Construction and calibration of non-uniformity discrete element model

According to the requirements specified in the Standard for Test Methods of Engineering Rock Mass (GB/T50266-2013), a granite particle model is constructed with a diameter of 50 mm and a height ranging from 2.0 to 2.5 times the diameter (i.e., a height of 100 mm) using a linear parallel bonding model. The weak mineral illite is used as the reference point of PFC micro-adjustment parameters. According to the field survey report, the coefficients of particle porosity and particle radius range are assigned, and the equilibrium state is achieved by eliminating the "overlap cloud" between particles. Corresponding to the mineral composition of the XRD test, the ball group command was used to group the particles,

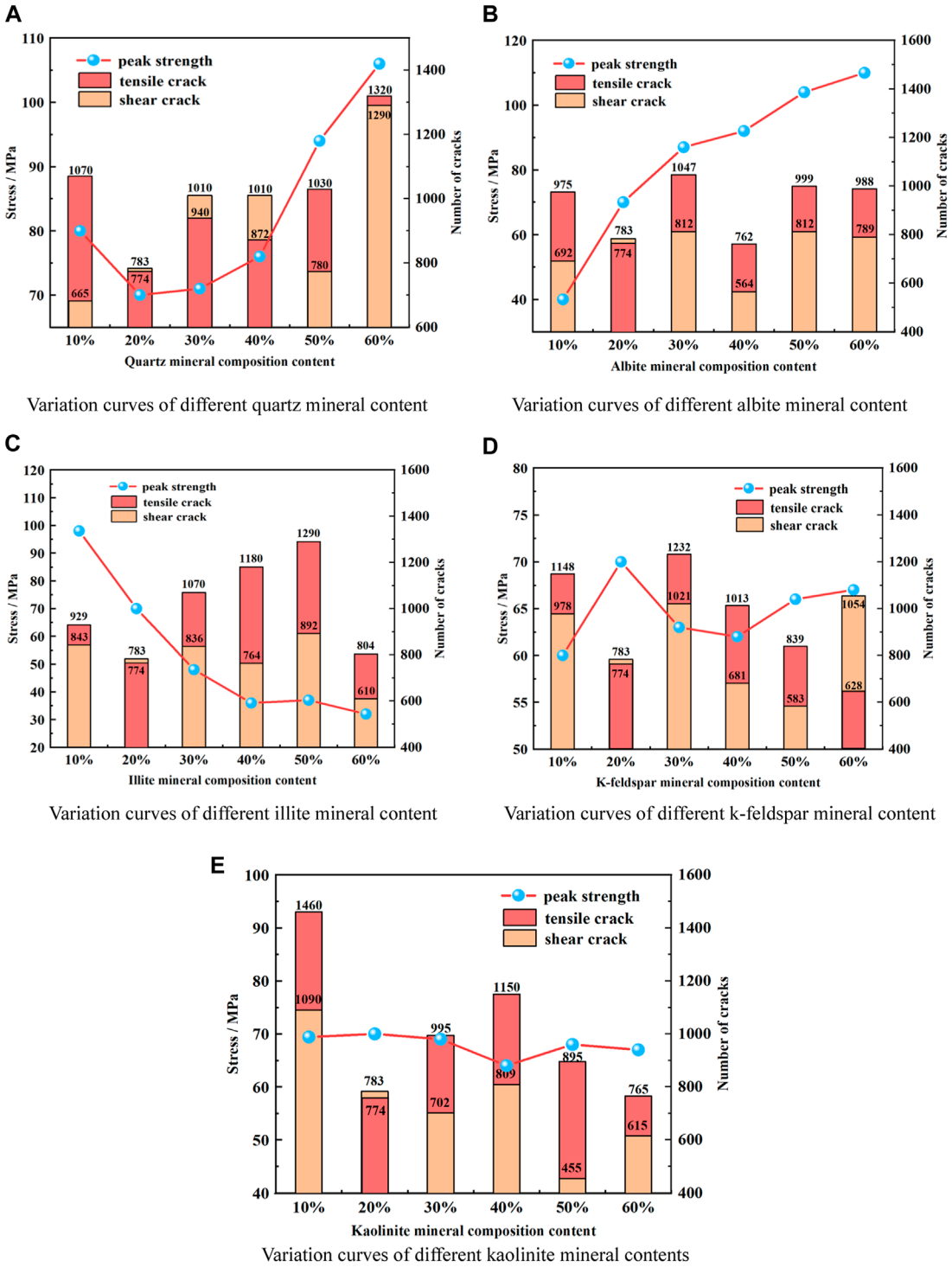

FIGURE 9
The curve of peak strength and failure crack of each mineral.

and the area ratio was used to control the random distribution of the mineral particles. The cluster particle family property of FISH language is developed to generate discrete element particles, and the distribution morphology of the grouped mineral particles is controlled according to the Weibull random distribution function. The distribution morphology, composition content and mineral category conditions of specific minerals are controlled, and the generated non-uniform model particles are shown in Figure 7.

In this study, the parameters of the parallel bonding model were calibrated. Firstly, the elastic modulus was calibrated using direct tensile testing. Subsequently, the stiffness ratio coefficient (kratio) was determined through hypothesis analysis and mechanical testing.

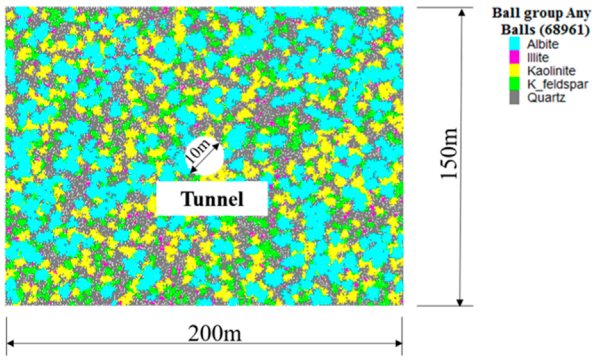

FIGURE 10
Tunnel excavation model of granular flow.

The range of bonding ratio was approximated based on failure mode and post-peak stress curve obtained from uniaxial compression tests on granite specimens, which ranged between 1.0 and 2.0 in our simulation. Finally, the peak strength served as a reference point for comparison with laboratory test results, ensuring that differences in peak strength remained within 5%.

By iteratively fine-tuning microscopic parameters based on calibration and mechanical properties derived from laboratory compression tests on granite particles, we established a set of parameters presented in Table 1. Using these parameters as a basis, we conducted simulations to compare against laboratory test results discussed earlier in this paper; Figure 8 illustrates the comparison outcomes.

The numerical simulation in Figure 8 reveals that, the numerical simulation results exhibit a high level of agreement with laboratory tests, displaying distinct "Y" type shear cracks along with some accompanying tensile cracks. Shear failure remains dominant in the final failure mechanism of the rock mass, albeit accompanied by tension. These calibrated parameters are believed to accurately reflect the mechanical behavior of grade III granite surrounding rock segment discussed in this paper. Consequently, based on this model, an analysis is conducted below to investigate how changes in microscopic parameters influence surrounding rock stability.

5.2 Relevance of microscopic composition alteration to macroscopic fracture

Based on the aforementioned non-uniform granite model, the influence of microscopic composition changes on macroscopic fracture in granite was further investigated by adjusting the proportion of each mineral content using the control variable method. Each mineral content was quantitatively increased or decreased by 10% individually, with a maximum mineral content of 60%. The remaining mineral content was equally distributed, accounting for approximately 10%, to avoid limitations imposed by insufficient mineral content on the non-uniformity granite model. The curve of crack number, stress change and peak strength changing with content under each working condition is shown in Figure 9.

As can be seen from Figure 9A, when the quartz content is within the range of 10%~20%, the failure of granite is mainly tensile cracks, which is consistent with the SEM test results. When the quartz content increases, the cracks turn to be mainly shear cracks. When the quartz content is high, tensile cracks play a dominant role. The increase in quartz content simultaneously enhances the overall strength of the rock, referred to as "enhanced minerals." As depicted in Figure 9B, the peak strength of albite also exhibits a linear increase with a significant magnitude, indicating that albite is also an "enhanced mineral" and effectively improves the rock's strength. The number of tensile cracks during overall failure is substantial, while the disparity between shear crack numbers remains relatively stable. As depicted in Figure 9C, the overall strength of rocks decreases with an increase in illite content, which is classified as a "weakened mineral." This suggests that illite is a weak mineral particle with poor bonding performance, and its internal particles are prone to breakage and damage due to slip, which is a contributing factor to weakened rock strength. This phenomenon also confirms the accuracy of SEM scanning tests in identifying illite as a weak mineral. Furthermore, Figures 9D, E demonstrate that an increase in K-feldspar and kaolinite mineral content does not significantly affect the peak strength or number of cracks in rocks; instead, it results in balanced mineral particles where tension cracks outnumber shear cracks.

5.3 Stability analysis of surrounding rock of Dagangshan tunnel

The composition of grade III surrounding rock in the section of K57+960~K58+060 of Dagangshan Tunnel has been determined through XRD testing, and the proportion represents the average value obtained from three sets of tests as shown in Figure 5. The physical and mechanical parameters are presented in Table 1. Considering the characteristics of PFC, this study adopts an equivalent cross-section area method to represent the tricentric tunnel section as a circular one with a diameter of 10 m. After accounting for boundary effects, the overall size of the model is set to be 200 m × 150 m, ensuring that there is a distance equal to five times the tunnel diameter between one side of the tunnel and the model boundary. A total number of 68,961 particles are generated within this calculation model, as illustrated in Figure 10. The fracture patterns exhibited by mineral particles within surrounding rock after tunnel excavation and collapse disasters occurring in field sections are depicted in Figure 11.

According to the numerical simulation analysis in Figure 11A, the tunnel displacement field distribution of the non-uniform granite numerical model is basically consistent with the conventional modeling law, indicating that the application of non-uniformity modeling method is accurate. Blue represents albite, and gray represents quartz. Albite is mainly destroyed by shearing through mineral particles, and a small amount of rock burst particles are scattered on the edge of the tunnel, which are mainly sheared minerals of albite. It can be seen from the surrounding rock near the tunnel entrance that the quartz mineral structure basically has no cracks, and a small part of surrounding rock particles are destroyed by quartz sliding along mineral particles, indicating that the expansion and penetration of cracks around the "enhanced

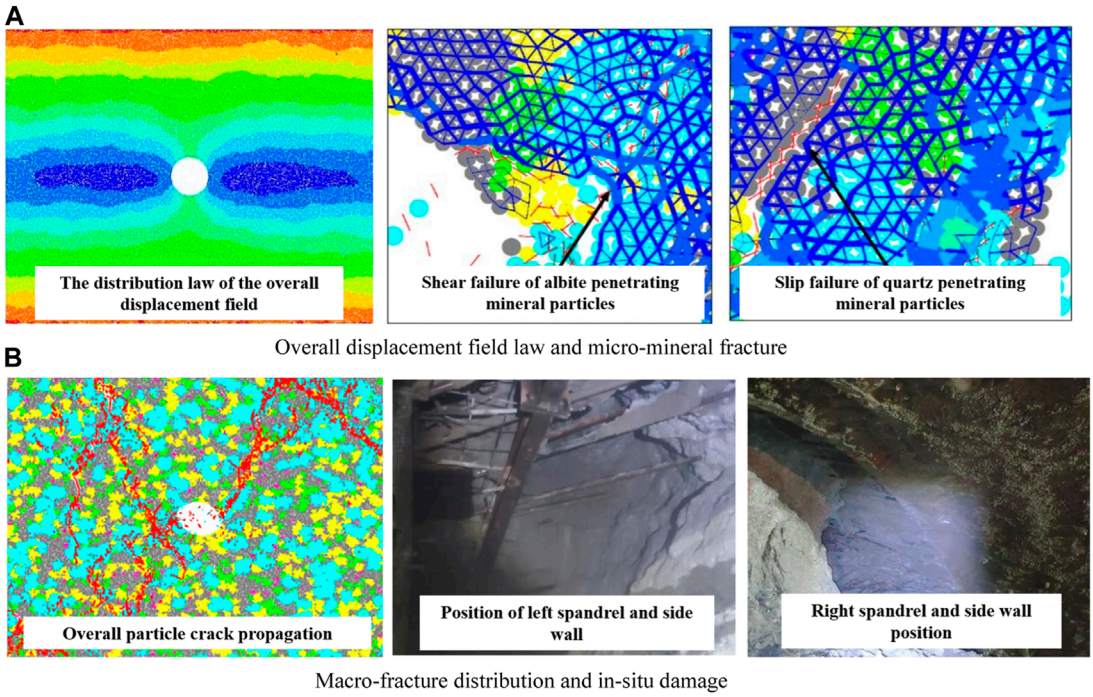

FIGURE 11
Fracture pattern of surrounding rock in tunnel excavation.

minerals" are not obvious. As can be seen from Figure 11B, three obvious shear fracture zones appear in the surrounding rock of the tunnel excavation, mainly caused by the expansion and penetration of cracks in the purple mineral, namely, illite area, indicating that the strength of the "weakened mineral" itself and the force chain strength between minerals are far lower than that of the "enhanced mineral." Therefore, the content and distribution of the "weakened mineral" have a greater impact on the stability of the surrounding rock. The left and right arch shoulders and side walls are damaged seriously during tunnel excavation, and the main damage is shear fracture. Figure 11B shows the rock mass collapses of the left and right arch shoulders and the upper side walls after the chain disaster occurs in the tunnel, which are in good agreement with the numerical simulation results. Therefore, it is suggested to strengthen the support measures of the left and right arch shoulders and side walls under similar working conditions.

6 Conclusion

(1) Shear fracture is the predominant mode of failure in grade III granite under compression. The primary fracture surface exhibits a smooth texture, with flocculent crystal particles adhering to it. Additionally, tension cracks are observed surrounding the main fracture surface. The rock mass demonstrates evident hardness and brittleness, resulting in a pronounced release of instantaneous energy upon loss of bearing capacity, producing a crisp sound.

(2) XRD analysis can better determine the composition and proportion of rock minerals. Combined with SEM electron microscope scanning, the microscopic angle shows that the fracture of rock fracture plays a controlling role, supplemented by tensile fracture and tensile-shear composite fracture, and the fracture mainly occurs in the enrichment area of weak minerals such as illite.

(3) Among the minerals in the granite, quartz and albite are "enhanced minerals," which are mainly characterized by the increase of rock strength with the increase of content, while illite is "weakened minerals." The stability of the surrounding rock in tunnels is primarily influenced by the presence of "weakened minerals," whereas "enhanced minerals" tend to exhibit inherent stability due to their hardness and strong inter-mineral bonding. Following tunnel excavation, the most severe issues arise from cracking observed in both left and right arch shoulders as well as side walls; therefore, it is imperative to reinforce the supporting function of this particular section.

Data availability statement

The original contributions presented in the study are included in the article/supplementary material, further inquiries can be directed to the corresponding author.

Author contributions

YC: Data curation, Funding acquisition, Methodology, Writing–review and editing, Writing–original draft. JS: Data curation, Writing–original draft. TG: Methodology, Software,

Writing–original draft. YJ: Writing–review and editing, Resources, Software. HZ: Writing–review and editing. HD: Writing–review and editing. WZ: Writing–review and editing.

Funding

The authors declare financial support was received for the research, authorship, and/or publication of this article. This study is financially supported by the National Natural Science Foundation of China (Nos 42172310 and 51609130).

Acknowledgments

The authors gratefully acknowledge Shandong Jianzhu University and Shandong University that have contributed to the research results reported within this paper.

Conflict of interest

The authors declare that the research was conducted in the absence of any commercial or financial relationships that could be construed as a potential conflict of interest.

Publisher's note

All claims expressed in this article are solely those of the authors and do not necessarily represent those of their affiliated organizations, or those of the publisher, the editors and the reviewers. Any product that may be evaluated in this article, or claim that may be made by its manufacturer, is not guaranteed or endorsed by the publisher.

References

Chen, X., Zhou, X., Xu, B., et al. (2022b). Investigation on the macro-micro shear damage mechanical behaviors of fractured rocks. *Chin. J. Rock Mech. Eng.* 41, 0–10. doi:10.13722/j.cnki.jrme.2022.0152

Chen, Y., Gao, T., Gao, C., et al. (2022a). Fracture propagation and acoustic emission energy damage law of fractured rock mass under hydraulic coupling action. *J. Central South Univ. Sci. Technol.* 53 (6), 2325–2335. doi:10.11817/j.issn.1672-7207.2022.06.032

Chen, Y., Gao, T., Yin, F., Liu, X., and Wang, J. (2022c). Study on influence of joint locations and hydraulic coupling actions on rock masses' failure process. *Energies* 15 (11), 4024. doi:10.3390/en15114024

Chen, Y., Liu, M., Gao, T., and Jing, Y. (2023). Macro–micro failure and energy evolution in heterogeneous fault rock masses. *Geotechnical Geol. Eng.*, 1–15. doi:10.1007/s10706-023-02705-0

Gao, T. (2022). *Study on macroscopic and microscopic failure and energy evolution of inhomogeneous granites*. Jinan: Shandong Jianzhu University. doi:10.27273/d.cnki.gsajc.2022.000589

Han, J., Wang, J., Yang, W., Wang, X., Ma, R., Wang, W., et al. (2023). Experimental study on the properties of a polymer-modified superfine cementitious composite material for waterproofing and plugging. *Case Stud. Constr. Mater.* 19, e02552. doi:10.1016/j.cscm.2023.e02552

Huang, N., Jiang, Y., Cheng, Y., et al. (2021a). Experimental and numerical study of hydraulic properties of three-dimensional rough fracture networks based on 3D printing technology. *Rock Soil Mech.* 42 (6), 1659–1680. doi:10.16285/j.rsm.2020.1448

Huang, X., Xiao, P., Dong, L., et al. (2021b). Mechanical response and failure mechanism of rock mass during excavation of underground caverns under high geostress. *Hazard Control Tunn. Undergr. Eng.* 3 (3), 85–93. doi:10.19952/j.cnki.2096-5052.2021.03.09

Li, H. (2017). *Aging rupture mechanism and microscopic evolution mechanism of deep heterogeneous rock mass*. Wuhan: Changjiang River Scientific Research Institute.

Li, T., Zhao, W., Liu, R., Han, J., Jia, P., and Cheng, C. (2023). Visualized direct shear test of the interface between gravelly sand and concrete pipe. *Can. Geotechnical J.* 61, 361–374. doi:10.1139/cgj-2022-0007

Liu, W., Lu, Q., Guo, S., et al. (2021). Study on the hydro-mechanical coupling numerical model for layered rocks based on macro-micro structures. *Chin. J. Rock Mech. Eng.* 40 (Suppl. 1), 2851–2860. doi:10.13722/j.cnki.jrme.2020.0789

Liu, X., Liu, Z., Li, X., et al. (2019). Acoustic emission and micro-fracture characteristics of rock under splitting load. *J. Eng. Sci.* 41 (11), 1422–1432. doi:10.13374/j.issn2095-9389.2018.11.29.005

Liu, Z., Zhang, L., Liu, G., Li, W., Li, S., Wang, F., et al. (2020). Material constituents and mechanical properties and macro-micro-failure modes of tight gas reservoirs. *Energy Explor. Exploitation* 38 (6), 2631–2648. doi:10.1177/0144598720913069

Ni, H., Xu, W., Shi, A., et al. (2015). Scale effect on equivalent continuum elastic modulus of columnar jointed rock masses by distinct element method. *Eng. Mech.* 32 (3), 90–96. doi:10.6052/j.issn.1000-4750.2013.09.0849

Peng, Z., Zeng, Y., Chen, X., and Cheng, S. (2021). A macro-micro damage model for rock under compression loading. *Appl. Sciences-Basel* 11 (24), 12154. doi:10.3390/app112412154

Shi, X., Guan, Q., Wang, W., et al. (2020). Numerical simulation of rock fragmentation process by TBM cutter in double-joint rock mass. *J. Shandong Univ. Eng. Sci.* 50 (4), 70–79. doi:10.6040/j.issn.1672-3961.0.2019.744

Sun, H., Belhaj, H., Tao, G., Vega, S., and Liu, L. (2019). Rock properties evaluation for carbonate reservoir characterization with multi-scale digital rock images. *J. Petrloeum Sci. Eng.* 175, 654–664. doi:10.1016/j.petrol.2018.12.075

Tang, C., Liang, Z., Yang, T., et al. (2005). Three-dimensional damage soften model for failure process of heterogeneous rocks and associated numerical simulation. *Chin. J. Geotechnical Eng.* 27 (12), 1447–1452. doi:10.3321/j.issn:1000-4548.2005.12.015

Vahid, M., and Abbas, M. (2021). Directional rock mass rating (DRMR) for anisotropic rock mass characterization. *Bull. Eng. Geol. Environ.* 80 (6), 4471–4499. doi:10.1007/s10064-021-02143-3

Xia, Y., Meng, Q., Tang, C., et al. (2021). Applications of realistic failure process analysis in tunnel engineering disaster simulation. *Hazard Control Tunn. Undergr. Eng.* 3 (3), 36–49. doi:10.19952/j.cnki.2096-5052.2021.03.05

Xu, Z., Yu, S., and Fu, Q. (2020). Numerical simulation of mechanical properties of layered jointed rock mass. *J. Shandong Univ. Eng. Sci.* 50 (3), 66–72. doi:10.6040/j.issn.1672-3961.0.2019.393

Yang, Y. (2018). *Study on macroscopic and micro mechanical characteristics of coarse-grained Soil fillers based on triaxial and CT test*. Changsha: Changsha University of Science and Technology. doi:10.26985/d.cnki.gcsjc.2018.000327

Yang, Z., Ning, Y., Luo, M., et al. (2016). Characterization of rock heterogeneity modeled by discontinuous deformation analysis method. *J. Chongqing Univ.* 39 (5), 97–102. doi:10.11835/j.issn.1000-582X.2016.05.013

Zhang, K., Wang, L., Lu, Y., et al. (2017). Study on numerical simulation of rock under true triaxial stress. *Coal Technol.* 37 (4), 68–71. doi:10.13301/j.cnki.ct.2018.04.026

Zheng, L., He, H., Zou, Y., Liu, H., Liu, X., and Qiu, Q. (2022). Research on macro-micro failure mechanism of interbedded sandstone in the deep of lannigou gold mine. *Lithosphere* 2022, 2998830. special 10). doi:10.2113/2022/2998830

Zheng, X., Hu, Z., Liu, C., et al. (2005). Deformation characteristic of crack rock fatigure failure by using CT testing. *J. Xi'an Univ. Sci. Technol.* 25 (4), 469–472. doi:10.3969/j.issn.1672-9315.2005.04.015

frontiers | Frontiers in Earth Science

TYPE Original Research
PUBLISHED 22 February 2024
DOI 10.3389/feart.2024.1322495

Check for updates

OPEN ACCESS

EDITED BY
Jianyong Han,
Shandong Jianzhu University, China

REVIEWED BY
Qing Ma,
Tsinghua University, China
Yubing Gao,
China University of Mining and Technology, Beijing, China
Tianran Ma,
China University of Mining and Technology, China
Hamdi Omar,
Ghent University, Belgium

*CORRESPONDENCE
Juan Jin,
jinjuan022@petrochina.com.cn
Weixi Chen,
chenwxqh@petrochina.com.cn

RECEIVED 16 October 2023
ACCEPTED 05 February 2024
PUBLISHED 22 February 2024

CITATION
Jin J, Liu J, Chen W, Li G, Cheng W, Zhang X and Luo Y (2024), The impact of high temperature on mechanical properties and behaviors of sandstone.
Front. Earth Sci. 12:1322495.
doi: 10.3389/feart.2024.1322495

COPYRIGHT
© 2024 Jin, Liu, Chen, Li, Cheng, Zhang and Luo. This is an open-access article distributed under the terms of the Creative Commons Attribution License (CC BY). The use, distribution or reproduction in other forums is permitted, provided the original author(s) and the copyright owner(s) are credited and that the original publication in this journal is cited, in accordance with accepted academic practice. No use, distribution or reproduction is permitted which does not comply with these terms.

The impact of high temperature on mechanical properties and behaviors of sandstone

Juan Jin[1,2]*, Jiandong Liu[1,2], Weixi Chen[3]*, Guoping Li[4], Wei Cheng[1,2], Xiaowen Zhang[1,2] and Yifan Luo[5]

[1]Key Laboratory of Oil & Gas Production, CNPC, Beijing, China, [2]Research Institute of Petroleum Exploration & Development, PetroChina, Beijing, China, [3]Engineering and Technology Department, PetroChina Qinghai Oilfield Company, Dunhuang, China, [4]Drilling & Production Technology Research Institute, PetroChina Qinghai Oilfield Company, Dunhuang, China, [5]School of Civil and Resources Engineering, University of Science and Technology Beijing, Beijing, China

The impact of high temperature environments on the physical and mechanical properties of rocks is a significant factor to consider. The investigation into the impact of elevated temperatures on the physical and mechanical characteristics of rocks holds great importance in the advancement and exploitation of deep-seated mineral reserves, as well as in ensuring the safety and stability of subterranean engineering projects. This study utilizes the state-of-the-art GCTS Mechanical Loading Test System to conduct uniaxial and triaxial compression tests on sandstone after thermal treatment from 25°C to 650°C. In addition, XRD, SEM and nuclear magnetic resonance experiments were carried out on the sandstone after thermal treatment. The aim of the experiments is to provide a quantitative characterization of mechanical properties and behaviors of the rock samples. The results show that the mass, density, and wave velocity of sandstone decrease with increasing temperature, while volume and porosity increase. The mass, volume, and rate of density change of sandstone exhibit a significant increase when subjected to temperatures above 500°C. The uniaxial compressive strength and elastic modulus exhibit an initial increase followed by a subsequent decrease as the temperature rises, with 300°C serving as the critical turning point. The axial peak strain and Poisson's ratio increase with increasing temperature. The cohesion decreases with increasing temperature, while the internal friction angle increases. Additionally, it is observed that the rate of change for both properties exhibits an increase beyond the temperature threshold of 400°C.

KEYWORDS

rock mechanics, high temperature, sandstone, GCTS mechanical loading test system, mechanical property

1 Introduction

The demand for underground mining and construction are increasing with the continuing development of society and economy (Liu et al., 2021; Liu et al., 2022). The continuous exploitation of shallow resources has led to their depletion. Therefore, the development and utilization of deep mineral resources are the most effective and rapid ways to solve the shortage of mineral resources (Xie, 2019; Cai et al., 2021; Cai et al., 2022). In engineering projects such as deep geothermal resource development and utilization, high-temperature radioactive waste disposal, shale gas reservoir thermal fracturing, *in-situ*



FIGURE 1
Rock specimens.



FIGURE 2
KSL-1700X muffle furnace.

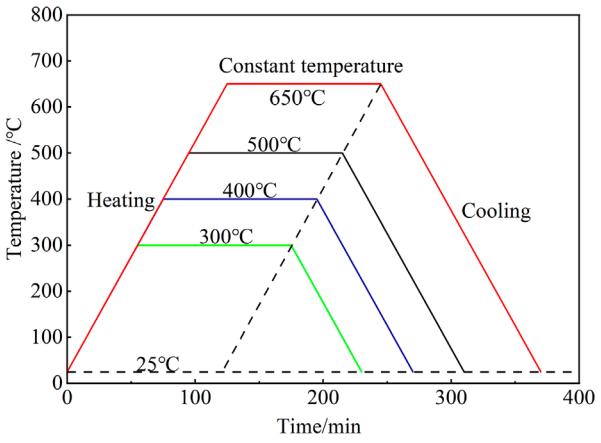

FIGURE 3
Programmed heating path of sandstone.

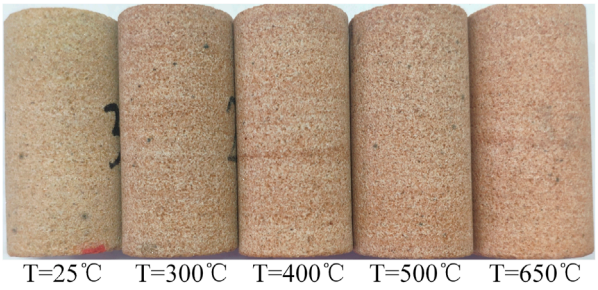

FIGURE 4
Sandstone after different temperature treatments.

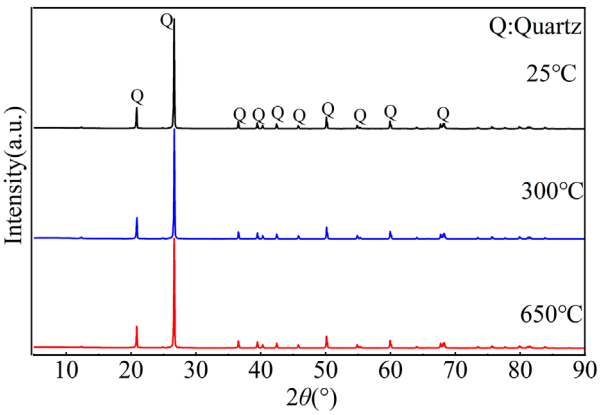

FIGURE 5
XRD spectra of sandstone powder at different temperatures.

gasification and thermal energy transfer of coal and oil shale, ultra-deep well drilling, oil and gas field development, and post-disaster reconstruction of rock underground engineering, rocks may undergo high-temperature heating and cooling. High temperatures can cause changes in the microstructure and mineral composition of rocks, which can affect the strength and deformation characteristics of rocks (Liu et al., 2018; Liu et al., 2020). As a result, the productivity as well as safety stability of the engineering projects may be affected (Luo and Wang, 2011; Sygała et al., 2013; Kong et al., 2016). Therefore, studying the influence of thermal damage on the mechanical properties of rocks is of utmost importance for rock engineering design and the long-term safety evaluation of rock engineering (Ozguven and Ozcelik, 2013; Xu et al., 2022).

Rocks are natural geological materials that are typically considered dual-porosity media, consisting of a mineral matrix and voids (pores and fractures). The physical and mechanical properties of rocks are influenced by the structure and density of pores and fractures (Ma et al., 2021; Ma et al., 2023). The pore and fracture structure of rocks are closely linked to the temperature conditions they experience (Chaki et al., 2008; Yavuz et al., 2010). The impact of high temperatures on the physical and mechanical properties of

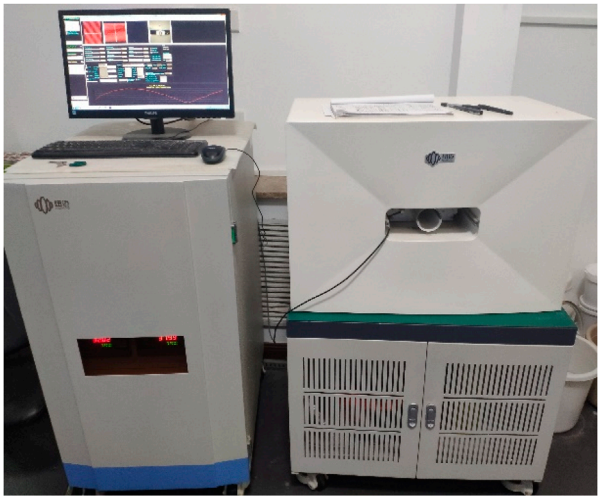

FIGURE 6
MesoMR magnetic resonance imaging analyzer.

rocks has become a significant issue in the fields of rock mechanics and deep earth resource extraction. Many researchers have conducted numerous experimental studies on the impact of high temperatures on the physical and mechanical properties of rocks (Ranjith et al., 2012; Sun et al., 2015; Chen et al., 2017; Xi et al., 2020; Chen et al., 2023; Zhao et al., 2023). Many mechanical properties of rocks, such as strength, elastic modulus, longitudinal wave velocity, cohesion, and internal friction angle, can either increase or decrease with rising temperature (Liang et al., 2006; Chen et al., 2012; Faoro et al., 2016; Sun et al., 2016). Zhang et al. (2022) conducted an experimental study on the mechanical properties of rocks under different cooling methods. The study demonstrates that the sample's deterioration increases gradually as the temperature rises. The peak strength follows a trend of initially increasing and then decreasing with rising temperature. Li et al. (2023) conducted physical and uniaxial compression tests on granite after high-temperature treatment ranging from 25°C to 350°C. The results showed that as the temperature increased, the rate of change in volume, mass, density, longitudinal wave velocity, and porosity of granite also increased. Li and Liu. (2022) studied the physical and mechanical properties of sandstone heat treated from 25° to 800°C. The experimental results showed that when the temperature is lower than 400°C, the physical and mechanical properties of sandstone are not affected, and the failure behavior of sandstone changes from brittleness to ductility with the increase of temperature. Zhao et al. (2017) utilized a polarizing microscope to observe the microstructural alterations in sandstone, granite, and marble following heat treatment at various temperatures. The analysis compared the changes in physical and mechanical properties (such as longitudinal wave velocity, porosity, Young's modulus, peak stress, and corresponding strain) of the three types of rocks during the heat treatment process from room temperature to 800°C, and correlated them with the microstructural change. Yang et al. (2017) conducted uniaxial compression tests on granite to evaluate the effects of high-temperature treatments (200, 300, 400, 500, 600, 700, and 800°C) on crack damage, strength, and deformation failure behavior of the granite. Zhao et al. (2020) conducted research on the changes in the microscopic structure and mechanical properties of a sandstone sample at different temperatures (25°C ~ 900°C) using experimental methods such as nuclear magnetic resonance (NMR), electron microscopy (EM), X-ray diffraction (XRD), and uniaxial compression. It was found that when the temperature exceeds 600 °C, the number of medium and large pores increases rapidly, resulting in a significant increase in permeability and a decrease in the strength of the sandstone. Huang et al. (2023) conducted a study on the effects of real-time high temperature on the mechanical properties of granite. They conducted impact compression tests on granite specimens at temperatures ranging from 20° to 800°C. The results showed that the peak stress of the specimens increased and then decreased with the increase of temperature. It reached a strength threshold at 200°C and then continued to decrease. Chen et al. (2023) conducted triaxial compression experiments on sandstone samples that were subjected to acid corrosion at temperatures of 25, 300, 600, and 900°C. The experimental results showed that the combined effects of chemical damage and thermal damage significantly affected



FIGURE 7
GCTS mechanical loading test system.

various properties of the rock, including mass, density, wave velocity, porosity, uniaxial compressive strength, elastic modulus, and compressive failure characteristics. Kang et al. (2023) utilized the RTX-3000 high-temperature and high-pressure triaxial rock testing machine to perform conventional triaxial compression tests and triaxial unloading confining pressure tests on granite that was heated to 800°C. The objective was to investigate the mechanical properties of thermally treated granite under various rates of unloading confining pressure. Pan et al. (2023) conducted a study on the strength and deformation properties of granite that had been subjected to high temperatures and treated with a chemical solution. This was done through uniaxial compression tests. Based on this, a statistical damage constitutive model was established that considers both the initial thermal-chemical damage and loading damage. The study also discusses the impact of thermal-chemical treatment on the evolution of damage in granite under uniaxial compression.

This research primarily focuses on the impact of high temperatures on different properties of granite. Few studies have been conducted on the evolution of mechanical properties of sandstone after high temperature exposure, and even less research on dense, homogeneous sandstone with fewer mineral impurities.

This article focuses on studying the impact of temperature on sandstone that exhibits good compactness and homogeneity. Heat the sandstone to temperatures of 300°C, 400°C, 500°C, and 650°C, and compare it with specimens at room temperature (25°C). Analyze the influence of high temperature heating on basic physical parameters such as mass, volume, density, and longitudinal wave velocity of sandstone. XRD, SEM and nuclear magnetic resonance experiments were carried out on the sand after thermal treatment. The heat-treated sandstone was subjected to uniaxial and triaxial compression tests using the GCTS-RTR rock triaxial apparatus to obtain the evolution of parameters such as compressive strength, elastic modulus, Poisson's ratio, cohesion, and friction angle with temperature. The study on the evolution of mechanical properties of sandstone with temperature provides a theoretical basis for the extraction of mineral resources in deep sandstone formations and post-disaster engineering construction.

2 Materials and methods

2.1 Sample preparation

To ensure the accuracy of the experimental results, samples were taken from rocks with good appearance structure, compactness, and homogeneity. The rock specimens were all taken from the same rock block to enhance the comparability of the test results. The rock blocks were cored, cut, and polished to obtain standard cylindrical sandstone specimens with a diameter of 25 mm and a height of 50 mm. The specimens meet the requirements of the parallelism of the upper and lower end faces not exceeding 0.05 mm, the diameter deviation of the upper and lower ends not more than 0.1 mm, and the axial deviation less than 0.25°, as shown in Figure 1. We measured the mass, diameter, height, and wave velocity of sandstone at room temperature using an electronic balance, a vernier caliper, and a non-metallic ultrasonic testing analyzer JY-80B. We determined the density and volume from measurement data. In its natural state, the rock sample has an average density of 2.195 g/cm^3, a P-wave velocity of 4188 m/s, and a porosity of 7.65%.

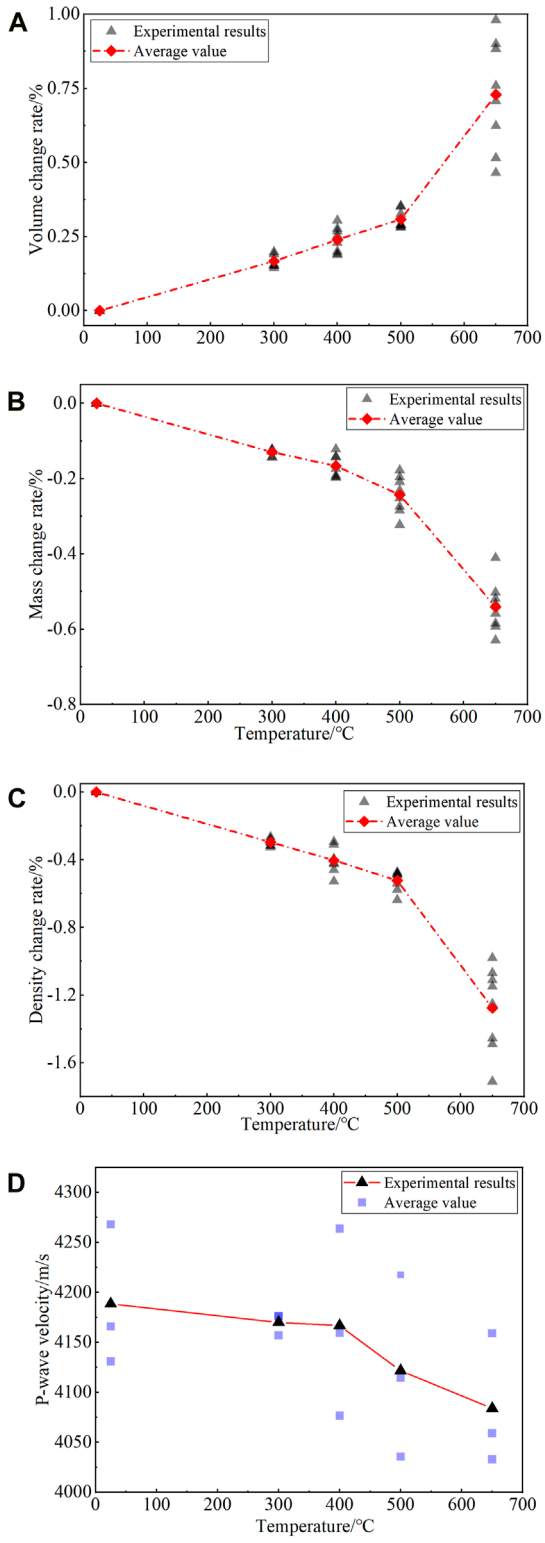

FIGURE 8
The variation of physical parameters of sandstone with temperature. **(A)** Volume. **(B)** Mass. **(C)** Density. **(D)** P-wave velocity.

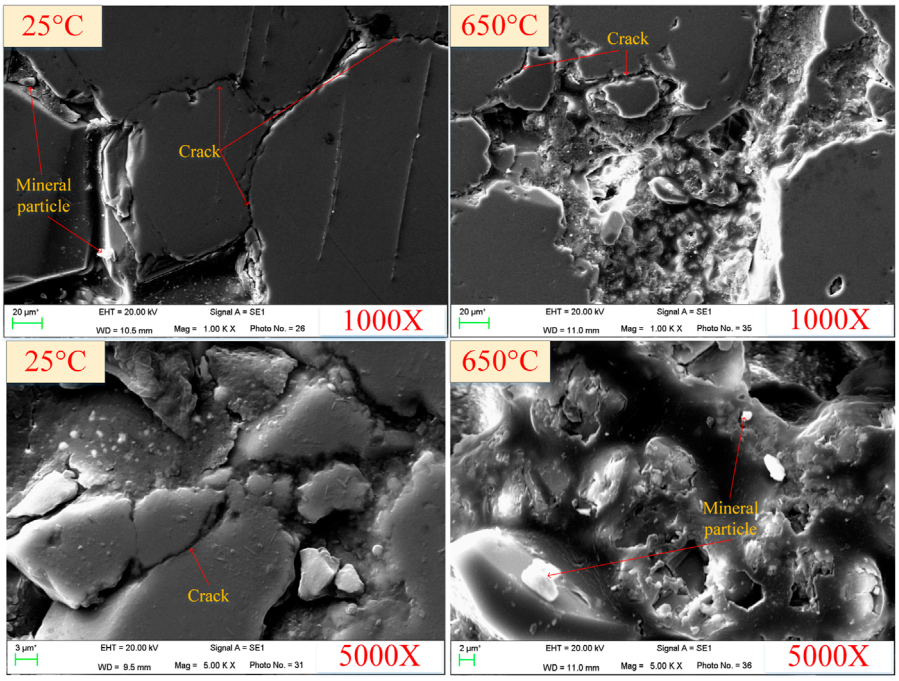

FIGURE 9
SEM images of sandstone microstructure under different heat treatment.

2.2 Thermal treatment

The rock samples were subjected to thermal treatment using a muffle furnace model KSL-1700X (Figure 2). The muffle furnace has a maximum power of 2.5 kW, a maximum working temperature of 1700°C, and a temperature control accuracy of 1°C. The sandstone samples were divided into five groups, and the muffle furnace was used to heat four groups of standard sandstone samples at temperatures of 300°C, 400°C, 500°C, and 650°C, respectively. Before heating, we evenly placed the specimens in the furnace. The heating rate was 5°C/min, with a constant temperature holding time of 2 hours, followed by a cooling rate of 5°C/min (Figure 3). After cooling to room temperature, removed the samples and we measured the mass, dimensions, and P-wave velocity of the specimens. The apparent morphology of rock samples changed at room temperature and after heat treatment (Figure 4). We can be observed that the color of the sandstone gradually deepens from light yellow to orange-yellow with increasing temperature. The surface of the specimens shows an obvious increase in powdery particles and signs of detachment, while the collision sound between the rocks becomes increasingly crisp.

2.3 X-ray diffraction experiment (XRD)

The physical and mechanical properties of rocks at high temperatures are closely related to their mineral composition. By analyzing the mineral composition, we can gain a deeper understanding of the chemical reaction process and the micro-corrosion mechanism. We grinded and sieved three sandstone samples treated at 25°C (room temperature), 300°C, and 650°C. The powder should meet the requirement of 320 mesh. We take 1–2 g of the sample for the XRD experiment. The resulted XRD diffractograms indicate that the sandstone contains almost no other mineral impurities and is predominantly composed of quartz (Figure 5). In addition, we analyzed the XRD pattern and found no change in the intensity of the diffraction peaks.

2.4 Nuclear magnetic resonance experiment

For the rock specimens subjected to high temperatures, a vacuum pressure saturation device was used to perform vacuum pressure saturation for 24 h prior to conducting NMR experiments. The NMR experimental equipment used in this study was the MesoMR magnetic resonance imaging analyzer (Figure 6) with a magnetic field strength of 0.5 ± 0.08T and a main frequency of 21.3 MHz. The diameter of the probe coil was 60 mm. NMR experiments can determine the quantity and distribution of water or other fluids in porous media by measuring the relaxation characteristics of protons in the media. This allows for the analysis of changes in the pore structure of rock samples. NMR analysis enable to were carried out on the four groups of sandstones before heating. Afterwards the four groups of sandstones were heat-treated at high temperatures of 300, 400, 500, and 650°C, respectively, and then,

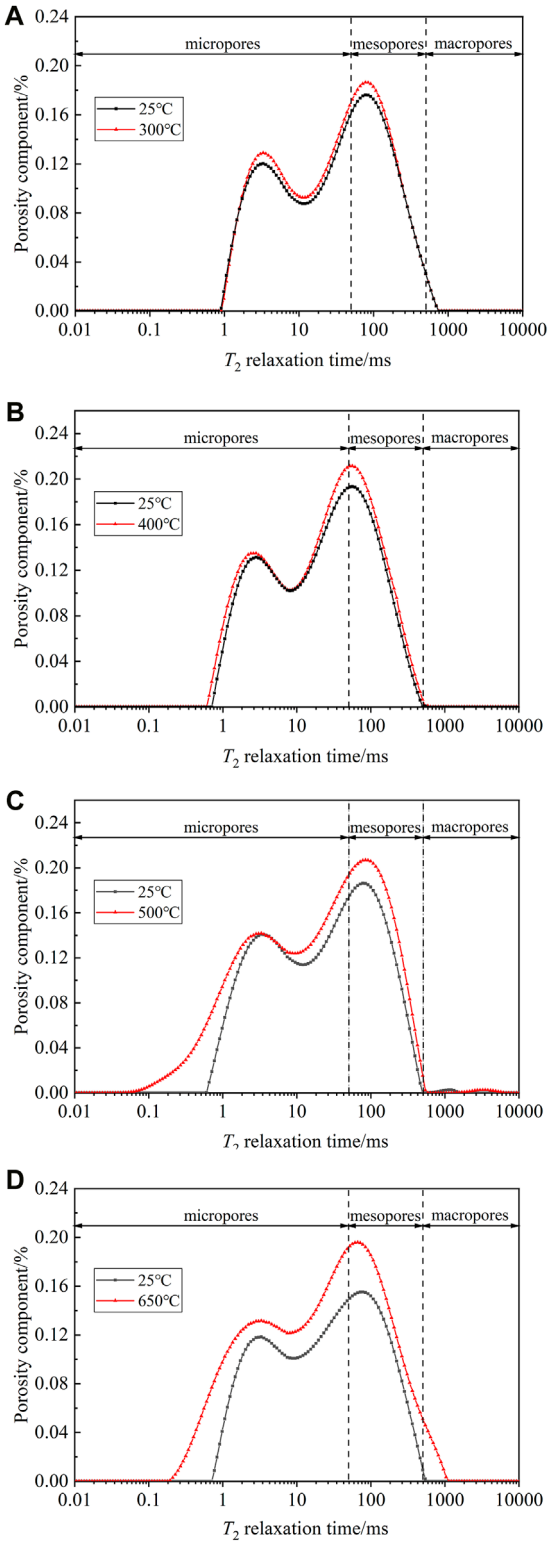

FIGURE 10
Evolution of T_2 relaxation curve after room temperature and heat treatment. **(A)** 300°C. **(B)** 400°C. **(C)** 500°C. **(D)** 650°C.

another set of NMR experiments were carried out to compare the changes in the pore parameters of the sandstones before and after the experiments.

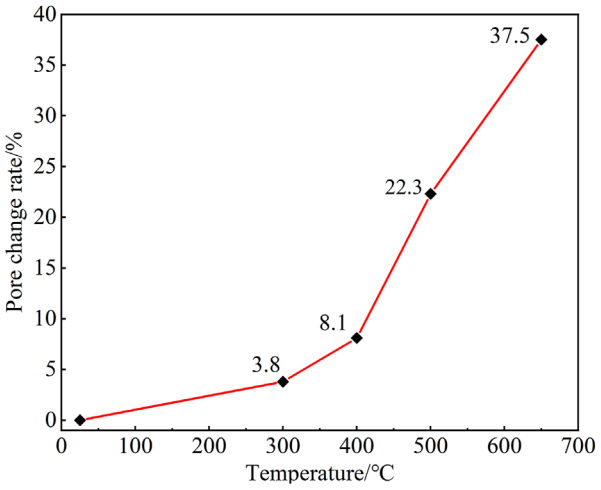

FIGURE 11
The change rate of porosity of sandstone before and after heat treatment.

2.5 Mechanical test

All mechanical tests were conducted on the GCTS Mechanical Loading Test System (GCTS-RTR) (Figure 7). This instrument can perform various tests under different environmental and condition settings, including uniaxial compression tests, uniaxial creep tests, triaxial compression tests under varying confining pressures, permeability tests, dynamic triaxial tests, high-temperature triaxial tests, and ultrasonic velocity measurements. The maximum axial load is 1,500 kN, the maximum confining pressure is 140 MPa, the maximum pore pressure can reach 140 MPa, and the highest operating temperature is 150°C. Sandstone samples at temperatures of 25°C, 300°C, 400°C, 500°C, and 650°C were selected for uniaxial and triaxial compression tests. In the uniaxial compression tests, the axial loading rate was controlled by the percent deformation of the height of the sandstone, which was set at 0.02%/min. The stress-strain curves of sandstone with different heat treatments were obtained during the loading process. In the triaxial compression tests, the confining pressures were set at 10 MPa and 20 MPa, respectively. Before axial compression, the confining pressure was first applied, then, axial compression was performed at a deformation-controlled axial loading rate of 0.025%/min.

3 Results and discussion

3.1 Variation of basic physical parameters

To better represent the variation of volume, mass, and density of rock specimens before and after heating treatment, the volume change rate, mass change rate, density change rate, porosity change rate and P-wave velocity change rate are defined as follows:

$$\eta = \frac{n_a}{n_0} - 1$$

Where η represents the change rate of the parameters; n_0 and n_a represents the value of parameters before and after heating.

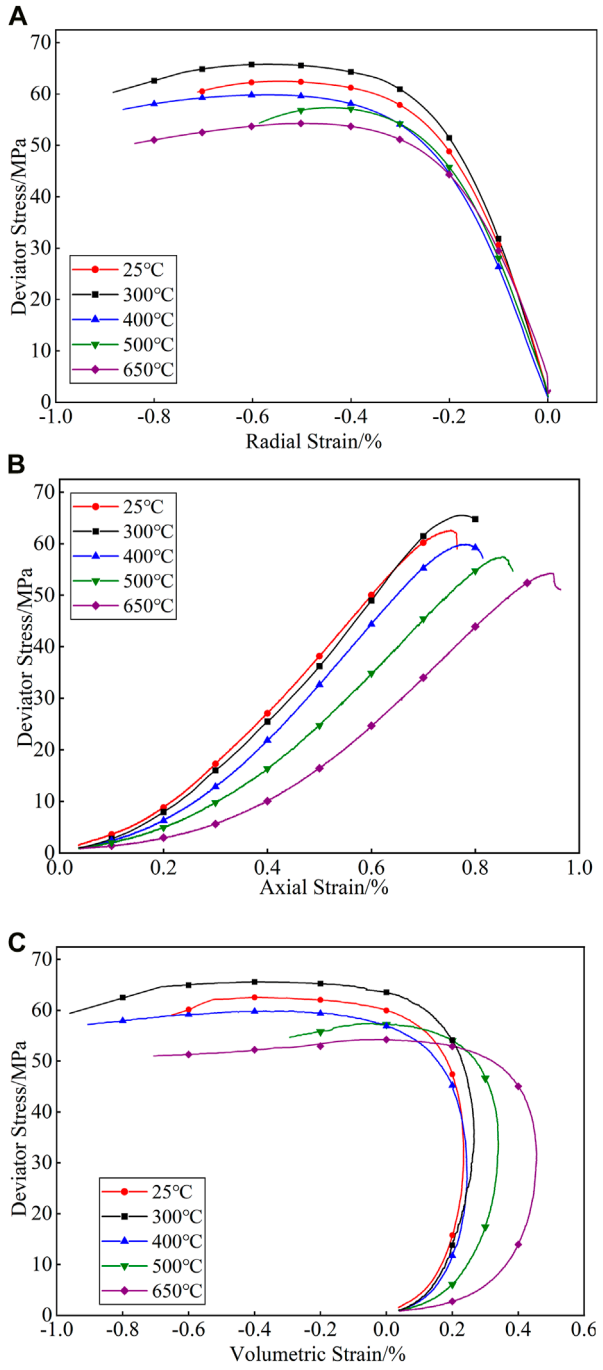

FIGURE 12
Stress–strain curve of sandstone exposed to different temperatures. **(A)** Radial strain. **(B)** Axial strain. **(C)** Volumetric strain.

The changes in the mass, volume, density, and velocity change rate of sandstone specimens after different high-temperature treatments with temperature are shown in Figure 8. By observing the figure, it is evident that the volume of the sandstone specimens increases following high-temperature treatment and further escalates with rising temperatures. At 500°C, the average volume of the sandstone increases by 0.31%. After exceeding 500°C, the growth rate increases significantly, and at 650°C, the volume growth rate is 0.73%. The reason for this phenomenon may be that the high temperature causes thermal expansion of the mineral particles in the sandstone, resulting in irreversible deformation (Dong et al., 2022). After exceeding 500°C, some mineral crystals undergo a phase transformation, and quartz grains transform from the α phase to the β phase at 573°C, as shown by the observation result of SEM (Figure 9). Microfracture expansion or new cracks are generated, resulting in a rapid increase in the volume of the sandstone specimens (Su et al., 2022). The mass decreases with the increase in temperature, as shown in Figure 8B. As the heating process progresses, the weakly bound water inside the rock continuously evaporates. At 500°C, the mass decreases by 0.24%, and there is a slight acceleration in mass loss after exceeding 500°C, with a mass reduction of 0.54% at 650°C. This may be due to the decomposition of a small amount of internal minerals in the rock and the evaporation of strongly bound water (Lei et al., 2019). Due to the increase in volume and decrease in mass, the density decreases with the increase in temperature, with a decrease of 1.28% at 650°C. The P-wave velocity of the specimen decreases as the temperature rises, albeit the change is relatively minor overall. From 25°C to 650°C, the P-wave velocity of the sandstone specimen decreased from 4,188 m/s to 4,084 m/s, resulting in a decrease of 2.5%.

3.2 Porosity of sandstone after heat treatment

The nuclear magnetic resonance analysis of porous media such as rocks involves using the CPMG pulse sequence under fully saturated conditions to measure the transverse relaxation time T_2. By analyzing the changes in T_2 spectrum, the number and size distribution of pores in the rock sample can be determined. This device is used to measure the porosity, transverse relaxation time T_2 spectrum, and changes in pore size distribution of rock specimens before and after heat treatment. The alteration in rock porosity, both pre- and post-heating, exhibits a positive correlation with the peak value of the T_2 spectrum. A higher peak value corresponds to a greater number of pores of the corresponding size. The position of the T_2 spectrum peak on the relaxation time axis is directly proportional to the pore radius. In other words, a higher T_2 value indicates a larger pore radius. Typically, the rock pores are categorized into micropores (<1 μm), mesopores (1–10 μm), and macropores (>10 μm) based on their respective sizes. Based on the relationship between relaxation time calculated by the NMR analyzer and pore size distribution, micropores are identified as those with relaxation times less than 50 ms, mesopores fall within the range of 50 ms–500 ms, and macropores are characterized by relaxation times exceeding 500 ms. The experimental results before and after heating are shown in Figure 10, revealing that the development of pores occurs gradually as the temperature increases. Below 500°C, there is a gradual formation of micropores and mesopores, accompanied by a slow increase in porosity. Post 500°C, there is rapid formation of micropores and mesopores, and at 650°C, macropores increase in the rock, resulting in a rapid increase in total porosity. The variation rate of sandstone porosity before and after heat treatment is depicted in Figure 11. Overall, porosity increases with temperature, with the rate of change significantly accelerating after reaching 400°C. At 650°C,

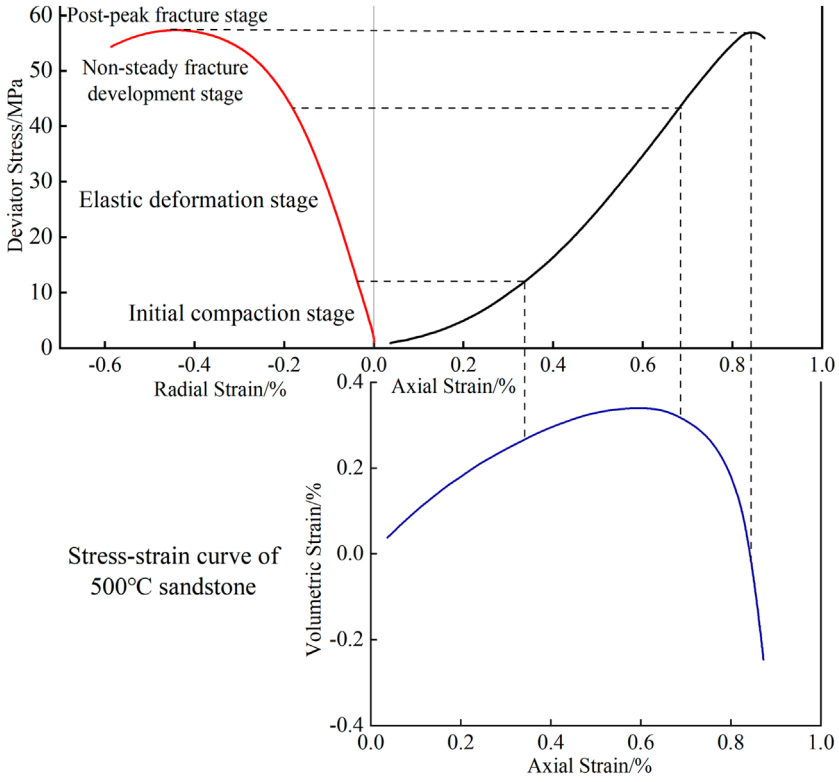

FIGURE 13
The fracture process of heat-treated sandstone specimens.

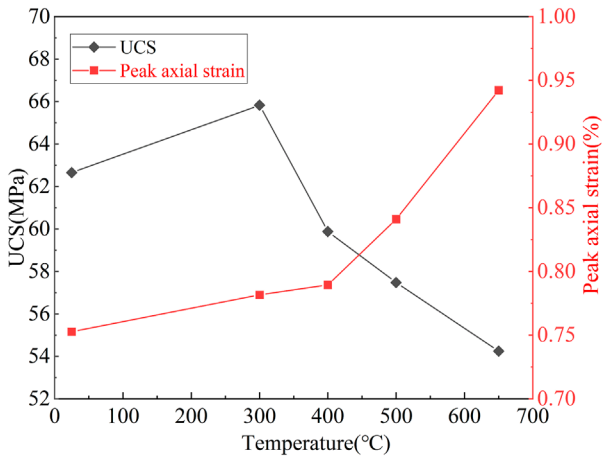

FIGURE 14
Axial peak strain and UCS of sandstone after heat treatment.

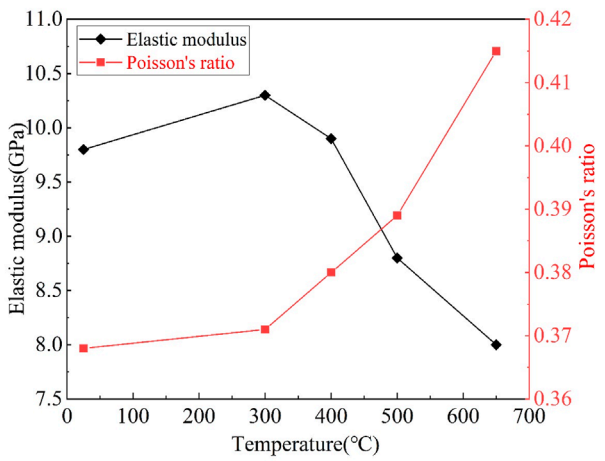

FIGURE 15
Elastic modulus and Poisson's ratio of sandstone after heat treatment.

porosity increases by 37.5%. Before reaching a temperature of 400°C, the main changes in sandstone include the volatilization of water components and the initiation of microcracks. When the temperature exceeds 400°C, there is an increase in macropores pores and interconnected pores, as well as a significant increase in total porosity.

3.3 Mechanical properties of sandstone after high-temperature heating

We conducted uniaxial and triaxial compression tests on the sandstone specimens after heat treatment. Figure 12 shows the stress-strain curves of sandstone samples under uniaxial

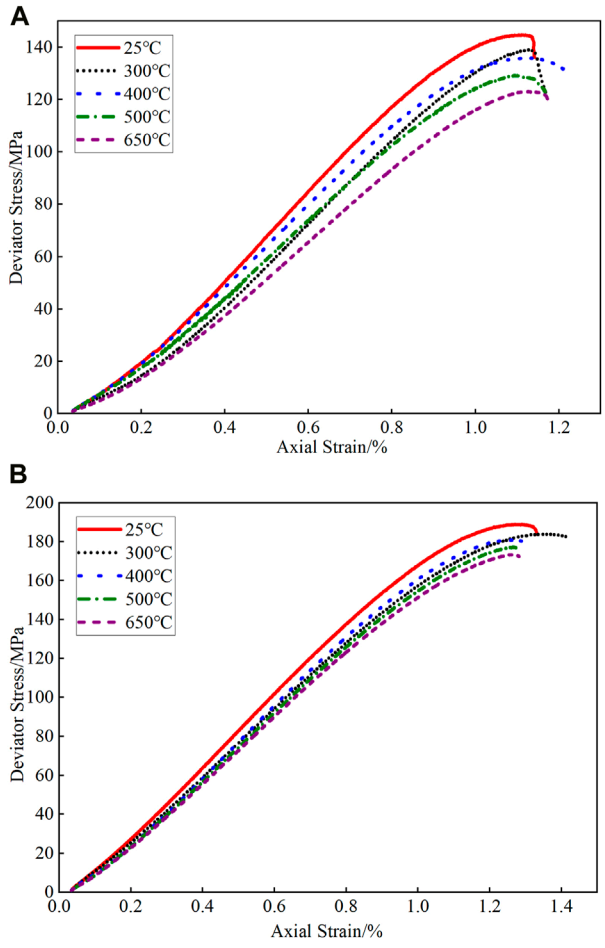

FIGURE 16
Stress-strain curves of rock after heat treatment under different confining pressures. **(A)** 10 MPa. **(B)** 20 MPa.

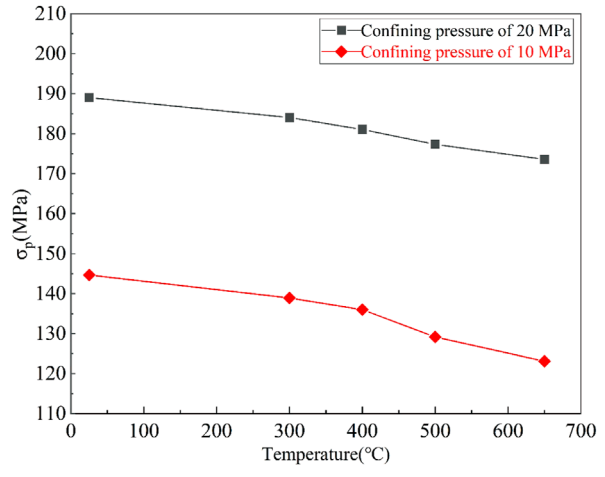

FIGURE 17
Peak stress in triaxial compression test of sandstone after heat treatment.

compression at different temperatures. The peak stress, axial peak strain, elastic modulus and Poisson's ratio of sandstone are obtained from the peak and slope of the curve.

The deformation stage of heat-treated sandstone specimens can be divided into four stages: the initial compaction stage, the elastic deformation stage, the non-steady fracture development stage, and the post-peak fracture stage, as shown in Figure 13. At the initial compaction stage, the original cracks inside the rock specimen are compacted under the action of external load, to produce crack closure, and the slope of the curve gradually increases as the external load continues to increase. During the elastic deformation stage, the stress-strain curve of the rock is approximately linear, and the deformation of the rock follow similar trends as the applied stress. During the non-steady fracture development stage, the continuous increase of external load leads to the formation of new cracks appear the rock specimen that extend in different directions until the specimen loses its bearing capacity and fails. The post-peak fracture stage is characterized by the damaging of the internal structure of the rock specimens after the bearing capacity of the rock reaches the peak strength. Moreover, the bearing capacity of the specimen rapidly decreases with the increase of deformation.

The variation of uniaxial compressive strength (UCS) and axial peak strain of sandstone at different temperatures is shown in Figure 14. The UCS of sandstone increases from 62.66 MPa to 65.83 MPa, with a growth rate of 4.8%, as the temperature rises from 25°C to 300°C. However, the UCS of sandstone decreases rapidly with the increase in temperature from 300°C to 650°C, and at 650°C, it decreases to 54.25 MPa, which is a 13.4% reduction compared to the sandstone at room temperature. This may be due to the expansion of rock particles caused by high temperatures below 300°C, leading to the closure of micropores and microcracks, resulting in an increase in the strength of the sandstone specimens. However, after 300°C, the development of micropores and microcracks within the rock rapidly reduces its strength (Sirdesai et al., 2019). The peak strain gradually increases with the increase in temperature, from 0.75% to 0.94%. The increase in peak strain is slow from 25°C to 400°C, but it increases rapidly from 400°C to 650°C.

The elastic modulus and Poisson's ratio can be used to measure the ability of granite to deform under stress. The elastic modulus and Poisson's ratio of rock samples can be determined during the elastic deformation stage. The elastic modulus is the ratio of the change in axial stress to the change in axial strain, while Poisson's ratio is defined as the ratio of the change in radial strain to the change in axial strain. The variation of the elastic modulus and Poisson's ratio of sandstone at different temperatures is shown in Figure 15. The elastic modulus of sandstone increases from 9.8 GPa to 10.3 GPa with a growth rate of 5.1% as the temperature rises from 25°C to 300°C. Beyond 300°C, the elastic modulus gradually decreases as the temperature increases. At 650°C, the elastic modulus is 8.0 GPa with a reduction rate of 18.4%, which exhibits a similar trend as the uniaxial compressive strength. Generally, Poisson's ratio increases with increasing temperature. At room temperature, the Poisson's ratio is initially 0.368. The rate of change of Poisson's ratio gradually increases with temperature, reaching 0.415 at 650°C, increasing by 12.8%.

The cohesion and internal friction angle are two important mechanical parameters of rocks, which can be obtained through the

TABLE 1 Parameters of the principal stress.

Temperature (°C)	σ_1 (MPa)	σ_3 (MPa)	σ_1' (MPa)	σ_3' (MPa)
25	10	144	20	189
300	10	138	20	184
400	10	135	20	181
500	10	129	20	177
650	10	123	20	173

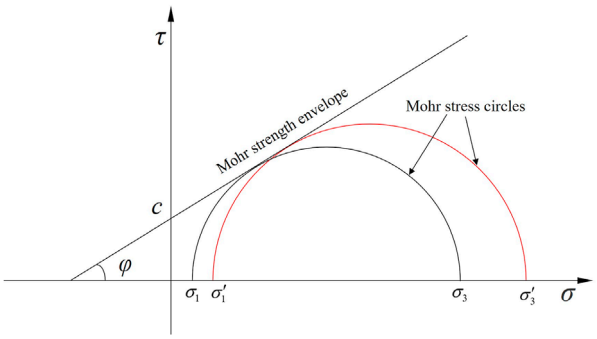

FIGURE 18
Mohr stress circles and Mohr Strength Envelope.

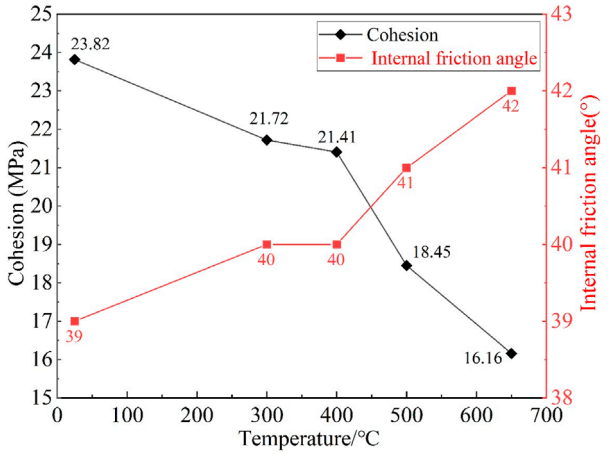

FIGURE 19
Cohesion and internal friction angle of sandstone after heat treatment.

equation of Mohr-Coulomb criterion as follows:

$$\frac{1}{2}(\sigma_1 - \sigma_3) = c\cos\varphi + \frac{1}{2}(\sigma_1 + \sigma_3)\sin\varphi$$

Where σ_1 and σ_3 represent the minimum and maximum principal stresses respectively; c represents the cohesive strength of the rock; φ represents the internal friction angle of the rock.

The results of the triaxial compression test are shown in Figure 16. Base on the experimental results, peak stress in triaxial compression test of sandstone after heat treatment were calculated and reported in Figure 17. In addition, we sorted out the principal stress related parameters as shown in Table 1. The difference between the maximum principal stress and the minimum principal stress at each level of confining pressure is taken as the diameter, and the average value of the maximum principal stress and the minimum principal stress is taken as the center to draw the Mohr stress circles. The tangent line of the Mohr stress circles is the Mohr strength envelope. The intercept of the tangent line on the y-axis is cohesion, and the angle between the tangent line and the positive direction of the x-axis represents the internal friction angle, as shown in Figure 18.

Figure 19 shows the variation of cohesion and internal friction angle with temperature. Overall, the cohesion decreases with increasing temperature. Between 25°C and 400°C, cohesion slowly decreases from 23.82 MPa to 21.41 MPa. The rate of decrease in cohesion accelerates between 400°C and 650°C, and at 650°C, cohesion is only 16.16 MPa, a decrease of 32.2%. On the other hand, the internal friction angle increases with increasing temperature. At room temperature, the internal friction angle is 39°, while at 650°C, it is 42°, increasing by 7.7%. Compared to cohesion, the change in internal friction angle is relatively slow.

4 Conclusion

The sandstone samples are light yellow at room temperature, and as the heat treatment temperature increases, the color gradually deepens and becomes orange-yellow. The sound of the rocks colliding becomes crisper. Additionally, the surface particles increase and there is phenomenon of powder shedding.

Through XRD experiments, it was discovered that the main component of sandstone is quartz (SiO2). Other mineral contents are extremely low, and after being heated to 650°C, there is no change in the mineral composition.

The mass and density of sandstone decrease with increasing temperature, while the volume increases. The rate of change of these three parameters experiences a significant increase when the temperature surpasses 500°C. The P-wave velocity decreases with increasing temperature, but the magnitude of change is relatively small. The porosity of sandstone increases with increasing temperature, and when the temperature exceeds 400°C, the porosity increases sharply.

Through the GCTS mechanical testing system, the uniaxial compressive strength, axial peak strain, deformation modulus, Poisson's ratio, cohesion, and internal friction angle of sandstone were obtained. The uniaxial compressive strength and elastic modulus of sandstone first increase and then decrease when increasing from 25°C to 650°C, and an inflection point occurs at 300°C. The axial peak strain and Poisson's ratio increase with increasing temperature. Cohesion decreases with increasing temperature, while the internal friction angle increases. When the temperature surpasses 400°C, there is an escalation in the rate of alteration for both cohesion and internal friction angle.

Data availability statement

The original contributions presented in the study are included in the article/supplementary material, further inquiries can be directed to the corresponding authors.

Author contributions

JJ: Conceptualization, Formal Analysis, Funding acquisition, Methodology, Project administration, Resources, Supervision, Visualization, Writing–original draft. JL: Conceptualization, Methodology, Writing–original draft. WxC: Data curation, Formal Analysis, Writing–original draft. GL: Software, Validation, Writing–original draft. WCg: Software, Supervision, Validation, Writing–original draft. XZ: Conceptualization, Funding acquisition, Methodology, Writing–original draft. Yifan Luo: Writing–review and editing.

Funding

The author(s) declare financial support was received for the research, authorship, and/or publication of this article.

Conflict of interest

Authors JJ, JL, WCg, and WZ were employed by CNPC. Authors JJ, JL, WCg, and XZ were employed by PetroChina. Author WxC was employed by PetroChina Qinghai Oilfield Company. Author GL was employed by PetroChina Qinghai Oilfield Company.

The remaining author declares that the research was conducted in the absence of any commercial or financial relationships that could be construed as a potential conflict of interest.

The author(s) declare financial support was received for the research, authorship, and/or publication of this article. This research was funded by Study on the evolution law of mineral structure and rock mechanical properties under ultra-high temperature conditions (Project Number: 2022-KFKT-02, PetroChina RIPED). The funder had the following involvement in the study: study design, data collection, provision of experimental equipment, decision to submit it for publication.

Publisher's note

All claims expressed in this article are solely those of the authors and do not necessarily represent those of their affiliated organizations, or those of the publisher, the editors and the reviewers. Any product that may be evaluated in this article, or claim that may be made by its manufacturer, is not guaranteed or endorsed by the publisher.

References

Cai, M., Dor, J., Chen, X., Mao, J., Tang, C., Liu, Z., et al. (2021). Development strategy for Co-mining of the deep mineral and geothermal resources. *Stud. CAE.* 23 (6), 43–45. doi:10.15302/J-SSCAE-2021.06.006

Cai, M., Ma, M., Pan, J., Xi, X., and Guo, Q. (2022). Co-mining of mineral and geothermal resources: a state-of-the-art review and future perspectives. *Chin. J. Eng.* 44 (10), 1669–1681. doi:10.13374/j.issn2095-9389.2022.08.24.001

Chaki, S., Takarli, M., and Agbodjan, W. (2008). Influence of thermal damage on physical properties of a granite rock: porosity, permeability and ultrasonic wave evolutions. *Constr. Build. Mat.* 22 (7), 1456–1461. doi:10.1016/j.conbuildmat.2007.04.002

Chen, G., Li, Y., Li, T., and Zhang, G. (2023a). Experimental study on the mechanical properties of intermittent jointed sand-stone considering water-rock interaction and confining pressure effect. *Bull. Eng. Geol. Environ.* 82 (4), 113. doi:10.1007/s10064-023-03156-w

Chen, Q., Chen, Y., Xiao, P., Du, X., Pan, Y., and Azzam, R. (2023b). Mechanical properties and damage constitutive model of sandstone after acid corrosion and high temperature treatments. *Int. J. Min. Sci. Technol.* 33 (06), 747–760. doi:10.1016/j.ijmst.2022.11.011

Chen, S., Yang, C., and Wang, G. (2017). Evolution of thermal damage and permeability of Beishan granite. *Appl. Therm. Eng.* 110, 1533–1542. doi:10.1016/j.applthermaleng.2016.09.075

Chen, Y., Ni, J., Shao, W., and Azzam, R. (2012). Experimental study on the influence of temperature on the mechanical properties of granite under uniaxial compression and fatigue loading. *Int. J. Rock Mech. Min. Sci.* 56, 62–66. doi:10.1016/j.ijrmms.2012.07.026

Dong, Z., Chen, Y., Wang, X., Kong, L., Wang, L., Li, X., et al. (2022). Evaluation of thermophysical and mechanical properties of sandstone due to high-temperature. *Materials* 15 (23), 8692. doi:10.3390/ma15238692

Faoro, I., Elsworth, D., and Candela, T. (2016). Evolution of the transport properties of fractures subject to thermally and mechanically activated mineral alteration and redistribution. *Geofluids* 16 (3), 396–407. doi:10.1111/gfl.12157

Huang, Y., Qu, L., Li, Y., Zhai, Y., and Xie, Y. (2023). Mechanical properties of granite under impact compression after re-al-time high temperature. *Explos. Shock Waves* 43 (02), 62–75. doi:10.11883/bzycj-2022-0196

Kang, P., Jing, Z., Hao, L., Gao, X., and Zheng, C. (2023). Mechanical properties of thermally treated granite subjected to different multi-stage unloading paths. *Environ. Earth Sci.* 82 (1), 53. doi:10.1007/s12665-022-10656-7

Kong, B., Wang, E., Li, Z., Wang, X., Liu, J., and Li, N. (2016). Fracture mechanical behavior of sandstone subjected to high-temperature treatment and its acoustic emission characteristics under uniaxial compression conditions. *Rock Mech. Rock Eng.* 49 (12), 4911–4918. doi:10.1007/s00603-016-1011-3

Lei, R., Wang, Y., Zhang, L., Liu, B., Long, K., Luo, P., et al. (2019). The evolution of sandstone microstructure and mechanical properties with thermal damage. *Energy Sci. Eng.* 7 (6), 3058–3075. doi:10.1002/ese3.480

Li, F., Li, C., He, H., Yang, B., and Lu, J. (2023). Research on physical-mechanical properties and energy evolution characteristics of granite after high temperature treatment. *Therm. Sci.* 27 (1B), 497–504. doi:10.2298/TSCI220827009L

Li, M., and Liu, X. (2022). Effect of thermal treatment on the physical and mechanical properties of sandstone: insights from experimentsand

simulations. *Rock Mech. Rock Eng.* 55, 3171–3194. doi:10.1007/s00603-022-02791-1

Liang, W., Xu, S., and Zhao, Y. (2006). Experimental study of temperature effects on physical and mechanical characteristics of salt rock. *Rock Mech. Rock Eng.* 39 (5), 469–482. doi:10.1007/s00603-005-0067-2

Liu, L., Ji, H., Elsworth, D., Zhi, S., Lv, X., and Wang, T. (2020). Dual-damage constitutive model to define thermal damage in rock. *Int. J. Rock Mech. Min. Sci.* 126, 104185. doi:10.1016/j.ijrmms.2019.104185

Liu, L., Ji, H., Lü, X., Wang, T., Zhi, S., Pei, F., et al. (2021). Mitigation of greenhouse gases released from mining activities: a review. *Int. J. Min. Metall. Mater* 28, 513–521. doi:10.1007/s12613-020-2155-4

Liu, L., Zhang, L., and Ji, H. (2022). Mechanism analysis of rock damage and failure based on the relation between deep chamber axial variation and *in situ* stress fields. *Chin. J. Eng.* 44 (4), 516–525. doi:10.13374/j.issn2095-9389.2021.04.09.003

Liu, L., Zhu, W., Wei, C., Elsworth, D., and Wang, J. (2018). Microcrack-based geomechanical modeling of rock-gas interaction during supercritical CO2 fracturing. *J. Pet. Sci. Eng.* 164, 91–102. doi:10.1016/j.petrol.2018.01.049

Luo, J., and Wang, L. (2011). High-temperature mechanical properties of mudstone in the process of underground coal gasification. *Rock Mech. Rock Eng.* 44 (6), 749–754. doi:10.1007/s00603-011-0168-z

Ma, T., Jiang, L., Shen, W., Cao, W., Guo, C., and Nick, H. (2023). Fully coupled hydro-mechanical modeling of two-phase flow in deformable fractured porous media with discontinuous and continuous Galerkin method. *Comput. Geotech.* 164, 105823. doi:10.1016/j.compgeo.2023.105823

Ma, T., Zhang, K., Shen, W., Guo, C., and Xu, H. (2021). Discontinuous and continuous Galerkin methods for compressible single-phase and two-phase flow in fractured porous media. *Adv. Water Resour.* 156, 104039. doi:10.1016/j.advwatres.2021.104039

Ozguven, A., and Ozcelik, Y. (2013). Investigation of some property changes of natural building stones exposed to fire and high heat. *Constr. Build. Mat.* 38 (2), 813–821. doi:10.1016/j.conbuildmat.2012.09.072

Pan, J., Zhang, Y., Li, P., Wu, X., and Xi, X. (2023). Mechanical properties and thermo-chemical damage constitutive model of granite subjected to thermal and chemical treatments under uniaxial compression. *Constr. Build. Mat.* 390, 131755. doi:10.1016/j.conbuildmat.2023.131755

Ranjith, P., Viete, D., Chen, B., Samintha, M., and Perera, A. (2012). Transformation plasticity and the effect of temperature on the mechanical behaviour of Hawkesbury sandstone at atmospheric pressure. *Eng. Geol.* 151, 120–127. doi:10.1016/j.enggeo.2012.09.007

Sirdesai, N., Mahanta, B., Ranjith, P., and Singh, T. (2019). Effects of thermal treatment on physico-morphological properties of Indian fine-grained sandstone. *Bull. Eng. Geol. Environ.* 78, 883–897. doi:10.1007/s10064-017-1149-6

Su, H., Nie, Y., Feng, Y., Yu, L., Chen, G., and Wang, W. (2022). Experimental investigation on microstructure characteristics and deformation failure behaviors of sandstone after high temperature under Brazilian splitting. *Geomech. Geophys. Geo-Energy Geo-Resour.* 8 (4), 121. doi:10.1007/s40948-022-00429-8

Sun, Q., Lu, C., Cao, L., Li, W., Geng, J., and Zhang, W. (2016). Thermal properties of sandstone after treatment at high temperature. *Int. J. Rock Mech. Min. Sci.* 85, 60–66. doi:10.1016/j.ijrmms.2016.03.006

Sun, Q., Zhang, W., Xue, L., Zhang, Z., and Su, T. (2015). Thermal damage pattern and thresholds of granite. *Environ. Earth Sci.* 74, 2341–2349. doi:10.1007/s12665-015-4234-9

Sygała, A., Bukowska, M., and Janoszek, T. (2013). High temperature versus geomechanical parameters of selected rocks-the present state of research. *J. Sustain. Min.* 12 (4), 45–51. doi:10.7424/jsm130407

Xi, B., Wu, Y., and Wang, S. (2020). Experimental study on mechanical properties of granite taken from Gonghe basin, Qinghai province after high temperature thermal damage. *Chin. J. Rock Mech. Eng.* 39 (1), 69–83. doi:10.13722/j.cnki.jrme.2019.0182

Xie, H. (2019). Research review of the state key research development program of China: deep rock mechanics and mining theory. *J. China Coal Soc.* 44 (5), 1283–1305. doi:10.13225/j.cnki.jccs.2019.6038

Xu, X., Yue, C., and Xu, L. (2022). Thermal damage constitutive model and brittleness *index Based on energy Dissipation for deep rock. Math. Math. (Basel).* 10 (3), 410. doi:10.3390/math10030410

Yang, S., Ranjith, P., Jing, H., Tian, L., and Ju, Y. (2017). An experimental investigation on thermal damage and failure mechanical behavior of granite after exposure to different high temperature treatments. *Geothermics* 65, 180–197. doi:10.1016/j.geothermics.2016.09.008

Yavuz, H., Demirdag, S., and Caran, S. (2010). Thermal effect on the physical properties of carbonate rocks. *Int. J. Rock Mech. Min. Sci.* 47 (1), 94–103. doi:10.1016/j.ijrmms.2009.09.014

Zhang, J., Lu, Y., Pang, J., and Bu, Y. (2022). Experimental study on mechanical properties of high temperature granite with different cooling methods. *Appl. Sci.* 12, 5968. doi:10.3390/app12125968

Zhao, C., Ma, Q., Sun, X., and Su, H. (2023). Research progress of thermal damage mechanical properties of high-temperature rocks. *Water Sci. Technol. Econ.* 29 (01), 8–13. doi:10.3969/j.issn.1006-7175.2023.01.002

Zhao, Y., Wei, K., Zhou, J., Li, X., and Chen, Y. (2017). Laboratory study and micromechanical analysis of mechanical behaviors of three thermally damaged rock. *Chin. J. Rock Mech. Eng.* 36 (01), 142–151. doi:10.13722/j.cnki.jrme.2015.1750

Zhao, Y., Wu, C., Jin, A., and Sun, H. (2020). Experimental study of sandstone microstructure and mechanical properties under high temperature. *Soils Rocks* 41 (07), 2233–2240. doi:10.16285/j.rsm.2019.1436

frontiers | Frontiers in Earth Science

TYPE Original Research
PUBLISHED 28 February 2024
DOI 10.3389/feart.2024.1373627

Check for updates

OPEN ACCESS

EDITED BY
Xiaoyu Bai,
Qingdao University of Technology, China

REVIEWED BY
Lu Chen,
Changsha University of Science and Technology, China
Peng Li,
Ocean University of China, China

*CORRESPONDENCE
Mengyue Liu,
liuyuximeng@163.com
Mengzhen Su,
smz15615480738@163.com

RECEIVED 20 January 2024
ACCEPTED 05 February 2024
PUBLISHED 28 February 2024

CITATION
Chen Y, Liu M, Su M, Ding M, Li H and Jing Y (2024), Prediction of water inflow and analysis of surrounding rock stability in unfavorable geological mountain tunnel.
Front. Earth Sci. 12:1373627.
doi: 10.3389/feart.2024.1373627

COPYRIGHT
© 2024 Chen, Liu, Su, Ding, Li and Jing. This is an open-access article distributed under the terms of the Creative Commons Attribution License (CC BY). The use, distribution or reproduction in other forums is permitted, provided the original author(s) and the copyright owner(s) are credited and that the original publication in this journal is cited, in accordance with accepted academic practice. No use, distribution or reproduction is permitted which does not comply with these terms.

Prediction of water inflow and analysis of surrounding rock stability in unfavorable geological mountain tunnel

Yunjuan Chen[1,2], Mengyue Liu[1]*, Mengzhen Su[1]*, Mingxu Ding[1], Haolin Li[1] and Yi Jing[3]

[1]School of Civil Engineering, Shandong Jianzhu University, Jinan, Shandong, China, [2]Key Laboratory of Building Structural Retrofitting and Underground Space Engineering, Ministry of Education, Shandong Jianzhu University, Jinan, Shandong, China, [3]School of Qilu Transportation, Shandong University, Jinan, Shandong, China

During the construction of a mountain tunnel, water inflow and rock instability are common occurrences due to unfavorable geological conditions, posing serious threats to construction safety. This study focuses on a proposed mountain tunnel and employs multiple formulas to predict potential water inflow during excavation. Based on the amount of water inflow and deformation of surrounding rocks, comprehensive determinations are made for the thickness of grouting rings and permeability coefficients. The results demonstrate that: 1) Different formulas yield slightly varied outcomes but overall trends remain consistent; considering various calculations, the normal water inflow for this tunnel is approximately 115.5908×10^3 m^3/d with a maximum at 210.9100×10^3 m^3/d 2) Increasing grouting ring thickness or decreasing permeability coefficient can effectively reduce water inflow, but the reduction range is gradually narrowed. 3) Pre-grouting curtains have an evident effect in enhancing stability; however, their effectiveness decreases with increased thickness. 4) Taking into account both safety and economic factors, it is recommended that the grouting ring thickness be set at 8 m with a permeability coefficient equaling one 100th that of surrounding rocks for this tunnel project.

KEYWORDS

mountain tunnel, adverse geology, water inflow, rock stability, grouting ring, numerical simulation

1 Introduction

During the construction process of tunnel engineering, two primary concerns have always been tunnel water inrush and surrounding rock stability. Particularly when tunnels traverse unfavorable geological conditions, excavation can trigger the initiation and propagation of rock fractures around the tunnel, leading to a disruption in seepage equilibrium and alterations in surrounding seepage dynamics. These changes in the seepage field will inevitably weaken the physical and mechanical properties of the surrounding rock, while modifications in the surrounding rock may continue to impact the underground water environment around the tunnel. The interaction between these two adverse factors ultimately gives rise to issues related to tunnel instability.

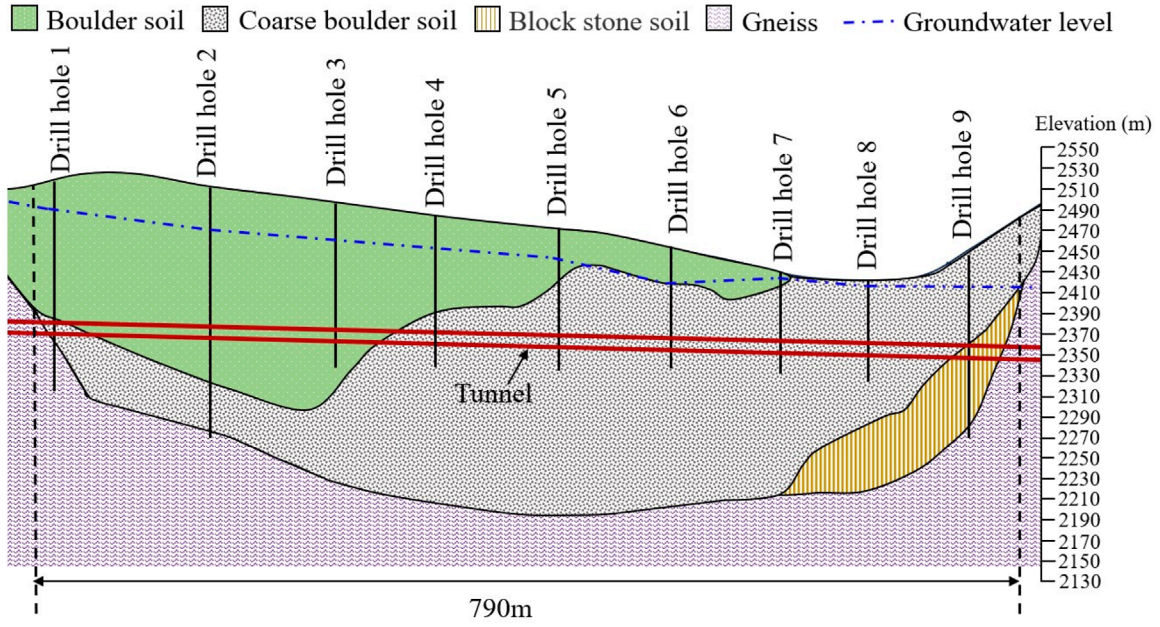

FIGURE 1
Schematic diagram of the strata.

Therefore, prior prediction of tunnel water inflow and analysis of surrounding rock stability hold significant theoretical and practical implications for successful tunnel excavation.

In recent years, a multitude of scholars have proposed diverse prediction formulas for water inflow and substantiated their feasibility through numerical simulation or engineering field practice (Liu et al., 2022; Li et al., 2021; Li et al., 2023; Xu et al., 2022). These research findings can serve as valuable references for future warning, monitoring, and prevention of similar tunnel construction projects to ensure safe execution. Wu et al. (2019) comprehensively summarized the commonly employed methods for predicting water inflow, encompassing empirical formula method, analytical formula method, numerical calculation method, and physical simulation method. They elucidated the underlying principles of these methods while analyzing their applicability conditions as well as advantages and disadvantages. Lin et al. (2021) proposed an analytical formula that accounts for soil anisotropic permeability to predict water inflow volume effectively. Chen et al. (2017), demonstrated the reliability of multiple empirical formulas in theoretically predicting water inflow through numerical simulation calculations. Furthermore, Fu et al. (2022) established a seepage differential balance equation and solved it using boundary conditions alongside steady-state drop funnel curve equation with drainage parameters to further determine water inflow volume. When confronted with substantial amounts of tunnel water inflows during construction processes grouting is often utilized for waterproofing treatment thus making determination of grouting parameters crucially important. Chen et al. (2023) proposed an analytical solution for the stable seepage field of deep-buried grouting tunnels, considering anisotropic infiltration. Ye (2023) predicted the maximum inflow during tunnel construction using empirical formulas and numerical simulations, proposing a construction scheme to control inflow through radial grouting. Lan et al. (2021) and Yuan et al. (2019) have put forward effective grouting schemes to address tunnel water inrush problems. Jianyong Han et al. (2023) studied a high-performance and effective polymer modified composite material, the research results provide guidance for improving the impermeability of grouting material. Hua Tao et al. (2023) conducted a study on the range of grouting reinforcement for karst water-rich tunnels under V-grade surrounding rock using numerical simulation, combined with seepage and stability analysis. Zheng et al. (2022) analyzed the influence of grouting and support parameters on seepage through model tests and theoretical analysis methods respectively. Xue et al. (2015) based on the concept of groundwater environment balance, established relevant functions to evaluate the effectiveness of grouting by utilizing empirical formulas and underground runoff modulus to obtain permeability coefficient under practical tunnel engineering conditions. Excavation-induced disturbances pose significant threats to the stability of surrounding rocks near excavations. Chen and Zhang (2019) established an analytical solution of soil's plastic zone around circular digging holes based on Superposition Principle and Rubin's Answer. Moreover, Chen et al. (2022) studied the influence of joint crack distribution on the stability of surrounding rock under hydraulic coupling conditions in underground engineering construction. Grouting is considered as an effective method for controlling tunnel deformation (Wang et al., 2022; Wang, 2023; Cheng et al., 2024). Filling cracks around tunnels can not only prevent water ingress but also improve rock stability. Peng et al. (2022) established numerical models for different distribution profiles of karst caves and tunnels, studying respectively the deformation and mechanical response of lining rocks with or without grouting. Jiang et al. (2023) proposed a coupled deformation analysis method between grout construction

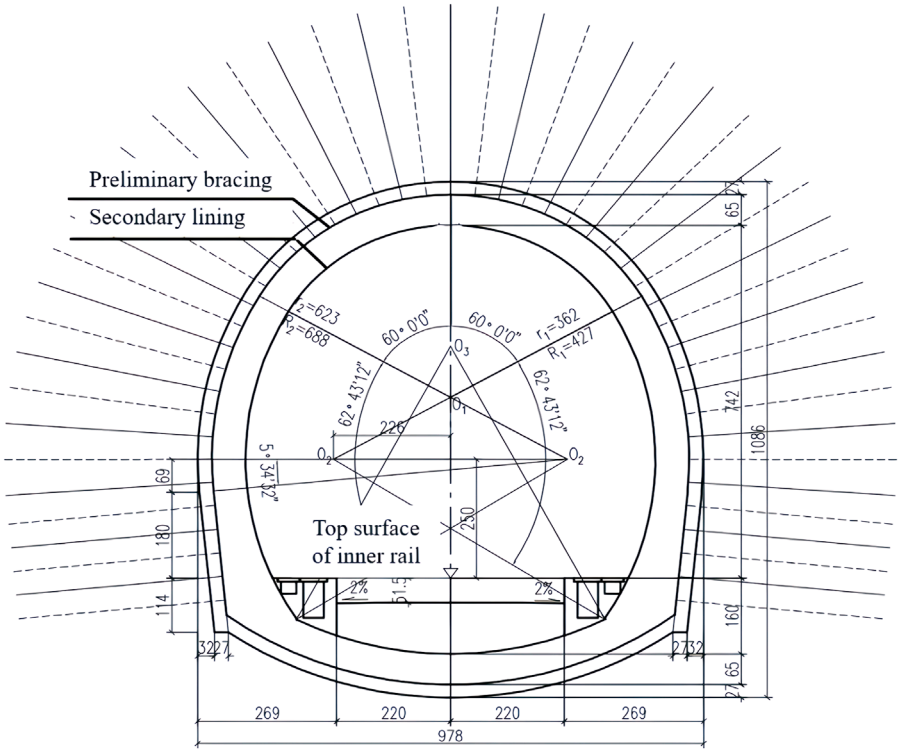

FIGURE 2
Cross-section of the tunnel.

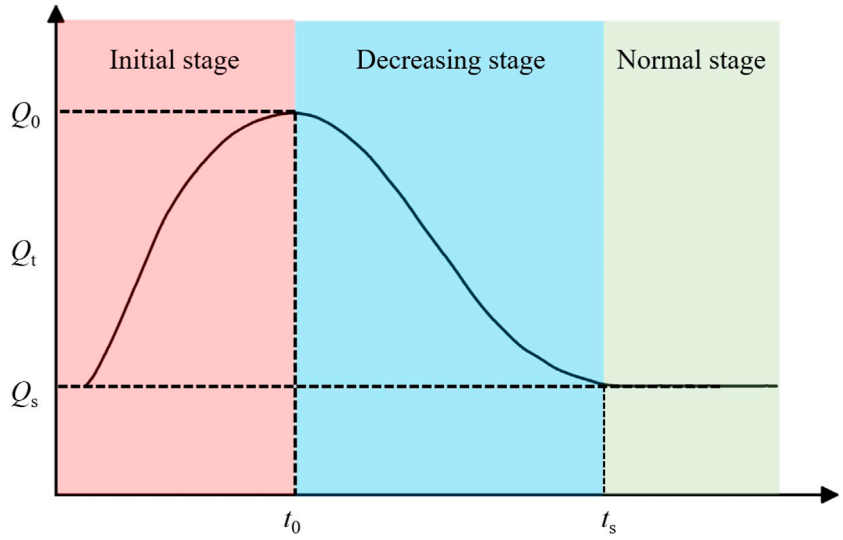

FIGURE 3
Temporal variation curve of tunnel water inflow.

and adjacent existing tunnels that holds important theoretical significance in formulating grouting schemes.

The present study investigates the water inflow and surrounding rock stability in a specific mountain tunnel through a combination of theoretical analysis and numerical simulation. Firstly, four empirical formulas, namely, Oshima Yoshi formula, Railway experience formula, Kuniaki Sato formula, and Koskyakov formula are employed to theoretically predict the water inflow in different sections. The results obtained from these calculations are comprehensively analyzed. Secondly, FLAC3D is utilized to numerically simulate the stability of surrounding rocks in nine drilling sections under fluid-solid coupling conditions. Finally,

TABLE 1 Experimental results of drilling water extraction test.

Drill hole number	Drilling depth (m)	Static water level (m)	Drop depth of the water level (m)	Water yield (m^3/d)	Permeability coefficient (m/d)
Drill hole 3	156	43.05	49.73	212.198	1.25
Drill hole 4	146	44	15.33	205.546	2
Drill hole 5	140	30.46	15.31	180.144	2.07
Drill hole 7	103	10.6	13.69	218.9376	2.9
Drill hole 8	101.2	4	11.7	218.93	3.9

TABLE 2 Calculation parameters for different sections.

Section	Section length (m)	Distance between the water level and the center of the cave body (m)	Permeability coefficient (m/d)	Equivalent circular radius of tunnel (m)
Section 1	100	114.4514	1.25	6.53
Section 2	100	103.2969	1.25	6.53
Section 3	100	95.8801	1.25	6.53
Section 4	100	88.1050	2.00	6.53
Section 5	100	59.0999	2.07	6.53
Section 6	100	63.5136	2.90	6.53
Section 7	100	63.9698	3.15	6.53
Section 8	90	64.0791	3.90	6.53

TABLE 3 Water inflow throughout the tunnel.

Length (m)	Maximum water inflow (10^3 m^3/d)			Normal water inflow (10^3 m^3/d)		
	Oshima Yoshi formula	Railway empirical formula	Kuniaki Sato formula	Koskyakov formula	Railway empirical formula	Kuniaki Sato formula
790	210.0357	249.9690	211.7843	103.9135	70.1305	172.7283

considering factors such as water inflow, rock stability, and economic considerations; reasonable parameters for grouting permeation and thickness range are determined to provide a theoretical basis for tunnel design and construction.

2 Project background

A section of the planned mountain tunnel traverses a deep and steep valley with challenging geological conditions. The maximum burial depth in this section is 145 m, while the minimum burial depth is 63 m. The strata within the tunnel primarily comprise Quaternary gravelly soils, including coarse boulder gravel soil, boulder soil, and block stone soil. Locally, there are also sandy soils such as fine sand and medium sand. The groundwater is fully saturated, and the surrounding rock has a grade VI classification. The sediment in this area is loose and contains abundant silt and sand particles. Figure 1 illustrates the schematic diagram of the strata, while Figure 2 depicts the cross-section of the tunnel.

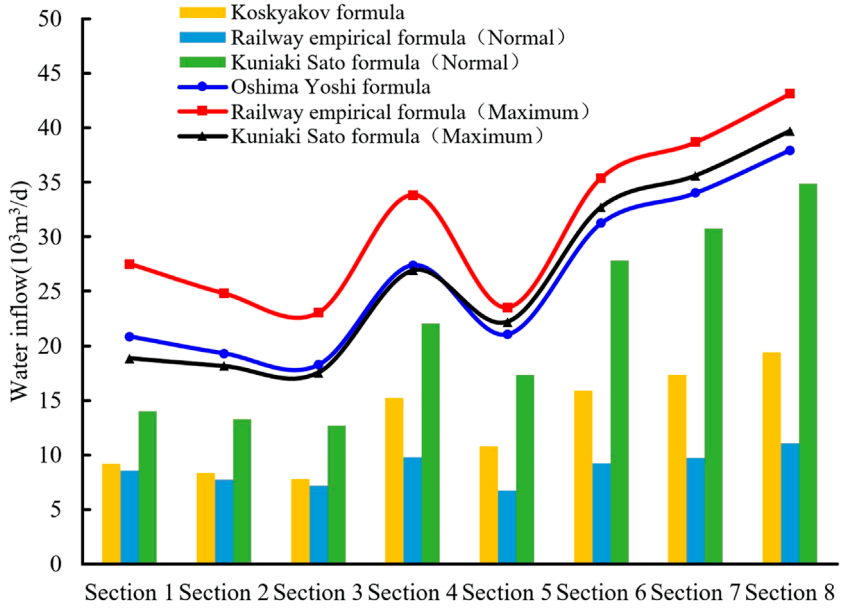

FIGURE 4
Water inflow in each section of the tunnel.

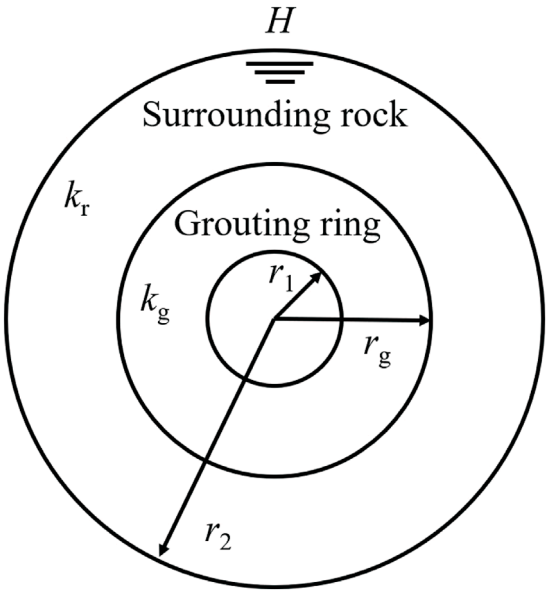

FIGURE 5
Schematic diagram of calculation model.

3 Prediction of water inflow in proposed tunnel

The calculation of tunnel water inflow refers to the estimation of water influx under the assumption of conventional excavation, without considering support and lining throughout the entire tunnel. This represents an idealized scenario for water inflow, and the temporal variation curve of tunnel water inflow is depicted in Figure 3.

The variation of tunnel water inflow can be classified into three stages: initial, decreasing, and normal stages. Therefore, the prediction of tunnel water inflow often involves calculating the maximum and normal inflows. During the initial stage of tunnel excavation, groundwater balance is disrupted due to excavation activities, resulting in a continuous influx of groundwater into the tunnel. Consequently, this stage is generally considered as having the highest water inflow rate. As groundwater is discharged and a drawdown funnel forms, the seepage field gradually reaches a new equilibrium stage which represents the normal phase of water inflow. For construction safety purposes, it is recommended to use maximum water inflow for safety protection design; whereas for drainage during tunnel construction and environmental protection measures, estimating normal water inflow is suggested. Different calculation methods used to predict tunnel water inflows may yield varying results in practical engineering projects; each prediction method has specific application conditions and limitations. Relying on a single formula for predicting large-scale tunnel water inflows leads to poor accuracy and can result in inadequate design leading to accidents or excessive conservatism causing wastage of manpower, resources, and finances. Therefore, it is advisable to employ multiple methods to comprehensively assess the situation regarding tunnel water infiltration.

3.1 Tunnel water inflow calculation formula

3.1.1 Oshima Yoshi formula

The Oshima Yoshi formula is a widely employed rough estimation method during the preliminary survey

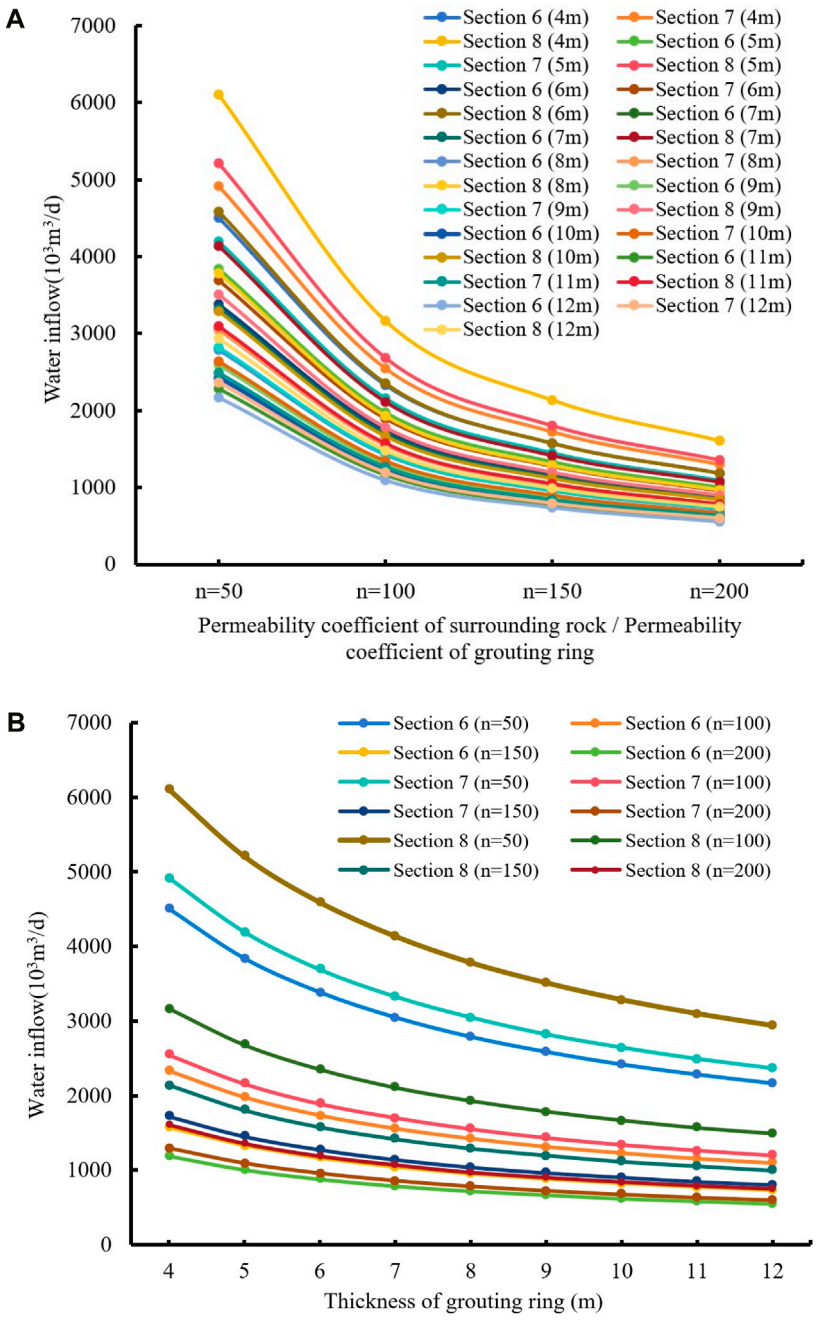

FIGURE 6
Variation curve of water inflow in the section with different parameters of grouting ring. **(A)**, Change curve of water inflow with different grouting ring permeability coefficient; **(B)**, Change curve of water inflow with different grouting ring thickness.

phase of tunnel construction for assessing the volume of water inflow from subterranean cavities. Consequently, it is currently utilized to forecast potential water inflow during tunnel excavation. Its empirical formula is shown as Eq 1.

$$Q_0 = L\frac{2\pi K(H\text{-}r)m}{\ln\frac{2(H\text{-}r)}{r}} \quad (1)$$

Where, Q_0 represents the maximum water inflow rate through the tunnel, m^3/d; K is the permeability coefficient of the aquifer, m/d; H is the distance from static water level to the center of an equivalent circular section in the tunnel, m; d is the diameter of an equivalent circular section derived from actual cross-section of the tunnel, m; r is its corresponding radius, m; L denotes length of aquifer traversed by tunnel; m is a conversion factor with a typical value 0.86.

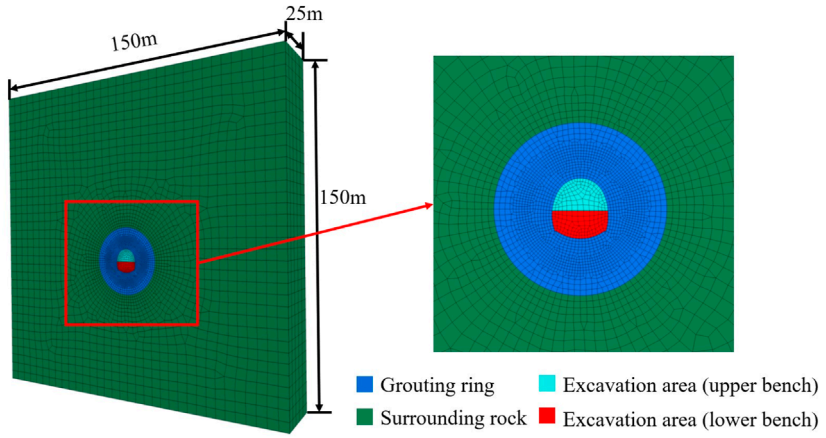

FIGURE 7
Full 3D numerical calculation model.

The actual cross-sectional shape can be simplified into an equivalence circle with its radius expressed as follows:

$$r = \frac{\sqrt{4h^2 + d^2}}{4\cos\left[\arctan\left(\frac{d}{2h}\right)\right]} \tag{2}$$

Where, r denotes the equivalent circular radius derived from the cross-sectional area of the borehole, m; d represents the span of the original tunnel section, m; and h signifies the height of the original tunnel section, m.

3.1.2 Railway empirical formula

Railway empirical analytical formulas can calculate the initial maximum water inflow, denoted as Q_0, and the normal water inflow, denoted as Q_s:

$$Q_0 = L(0.0255 + 1.9224KH) \tag{3}$$

$$Q_s = LKH(0.676\text{-}0.06K) \tag{4}$$

Where, Q_s refers to the normal water inflow of the tunnel through the water body, m^3/d; the other parameters are the same as (1).

3.1.3 Kuniaki Sato formula

$$Q_0 = L\frac{2\pi KHm}{\ln\left[\tan\frac{\pi(2H\text{-}r)}{4h_c}\cot\frac{\pi r}{4h_c}\right]} \tag{5}$$

$$Q_s = Q_0\text{-}0.584\overline{\varepsilon_0}Kr \tag{6}$$

Where, h_c is the thickness of aquifer; $\overline{\varepsilon_0}$ is the test coefficient, generally 12.8; the other parameters are the same as (1).

3.1.4 Koskyakov formula

When the water body contained in the bedrock mountain crossing tunnel is unconfined and has a substantial thickness, Koskyakov gives the formula of the stable water inflow of the tunnel as follows:

$$Q_s = \frac{2K\left(\frac{\pi}{2} + \frac{H}{R}\right)HL}{\ln\left(\frac{R}{r}\right)} \tag{7}$$

Where, R is the quoted recharge radius of the water gushing section of the tunnel which can be obtained by the permeability coefficient, m; the other parameters are the same as (1).

Among them, the influence radius is calculated using the Kusakin formula, which can be expressed as follows:

$$R = 2S\sqrt{KH} \tag{8}$$

Where, S is the drop depth of the tunnel water level.

3.2 Water inflow calculation parameters

Based on hydrogeological parameters obtained from drilling and pumping tests, combined with geophysical and engineering geological investigations, the hydrogeological parameters and tunnel dimensions for different sections are determined using 100 m as the unit length. Among the nine boreholes in this section, five underwent pumping tests, with the results presented in Table 1. The groundwater level at the tunnel site ranges approximately between 2418m and 2502 m above sea level, situated about 39.328m–118.995 m higher than the proposed tunnel elevation. The permeability coefficient of surrounding rock varies from 1.25 to 3.90 m/d. Specific calculation parameters for each section are provided in Table 2.

TABLE 4 The parameters of different strata and grouting rings.

Stratum	Density/(g·cm^{-3})	Young modulus/MPa	Poisson's ratio	Friction angle/°	Cohesion/MPa
Gneiss	2,650	20,000	0.2	43	20
Coarse boulder soil	1880	400	0.41	29.4	0.082
Boulder soil	1,650	140	0.32	20.8	0.017
Block stone soil	1940	600	0.43	32.2	0.116
Grouting ring	2,100	1,300	0.3	35	0.23

3.3 Analysis of water inflow prediction results

Using the water inflow calculation formula, the total water inflow of the tunnel can be calculated as shown in Table 3, and the water inflow of each section is shown in Figure 4.

According to Table 2; Figure 4, it can be observed that there are certain discrepancies in the calculation results obtained from different formulas; however, the overall trend of water inflow remains consistent. Comparing the maximum water inflow for the tunnel, it is evident that Oshima Yoshi formula and Kuniaki Sato formula yield relatively similar values of 210.0357×10^3 m^3/d and 211.7843×10^3 m^3/d respectively. The railway empirical formula produces the highest calculated maximum water inflow (249.9690×10^3 m^3/d), which is approximately 19% higher than the other two formulas. Regarding normal water inflow, significant variations exist among the three formulas. Among them, the calculation result of Kuniaki Sato formula of normal water inflow is the largest, which is 172.7283×10^3 m^3/d. The calculation result of Koskyakov formula is relatively close to that of railway empirical formula, which is 103.9135×10^3 m^3/d and 70.1305×10^3 m^3/d. By conducting a comprehensive analysis of these calculation results obtained from different formulas, it can be concluded that Section 6, Section 7, and Section 8 exhibit relatively high levels of water inflow while Section 4 experiences a comparatively significant amount of water inflow.

Due to oversimplification of the aquifer as a homogeneous and isotropic ideal state in simulating and calculating water inflow, the predicted results may be distorted in actual tunnel engineering where surrounding rocks exhibit heterogeneity and anisotropy. Additionally, considering the deep burial depth of the tunnel, complex topography and geomorphology, as well as challenges in accurately defining rock parameters, uncertainties arise in predicting water inflow. To account for these unpredictability, the average value (115.5908×10^3 m^3/d) of Koskyakov formula, railway experience, and Kuniaki Sato formula is used to represent the normal water inflow of the tunnel.

Furthermore, reflecting maximum water inflow during tunnel excavation process can be represented by an average value (210.9100×10^3 m^3/d) obtained from Oshima Yoshi formula and Kuniaki Sato formula maximum water inflow formula. These calculations consider unfavorable conditions such as intense changes in permeability due to reverse groundwater infiltration leading to drastic increase in permeability coefficient within certain rock formations.

4 Tunnel water inflow prevention and treatment

For situations involving significant water inflow, a remedial measure can be implemented by employing the technique of full-section advanced curtain grouting to mitigate the volume of water ingress. The diffusion of grout can effectively seal cracks in the surrounding rock ahead of the tunnel face, obstruct seepage pathways, and establish a watertight barrier, thereby substantially enhancing the impermeability of the surrounding rock mass. Additionally, it has the potential to enhance both physical and mechanical properties of the rock mass, preventing water infiltration during construction activities and ensuring construction safety.

4.1 Prediction formula for water inflow estimation after grouting

When the tunnel is situated in a confined aquifer with ample water supply, and the drainage of the tunnel has negligible impact on hydraulic head in distant regions, the model can be simplified as a steady flow model of vertical wells in an infinite aquifer, as depicted in Figure 5. The inner radius of the tunnel is denoted by r_1, corresponding to a hydraulic head value of h_1 at that specific location; r_g represents the outer radius of the grouting ring, corresponding to a hydraulic head value of h_g at that specific location; H signifies the hydraulic head in far field, while r_2 denotes the distance from far-field water level to the center of the tunnel; k_g refers to permeability coefficient for grouting ring and k_r indicates permeability coefficient for surrounding rock.

To simplify the calculations, the following assumptions are made: 1) The grouting ring and surrounding rock of the tunnel are assumed to be homogeneous, isotropic, and extend infinitely in the axial direction. 2) Groundwater is instantaneously released and seepage follows Darcy's law with steady flow. 3)The permeability coefficients of both the surrounding rock and grouting ring are

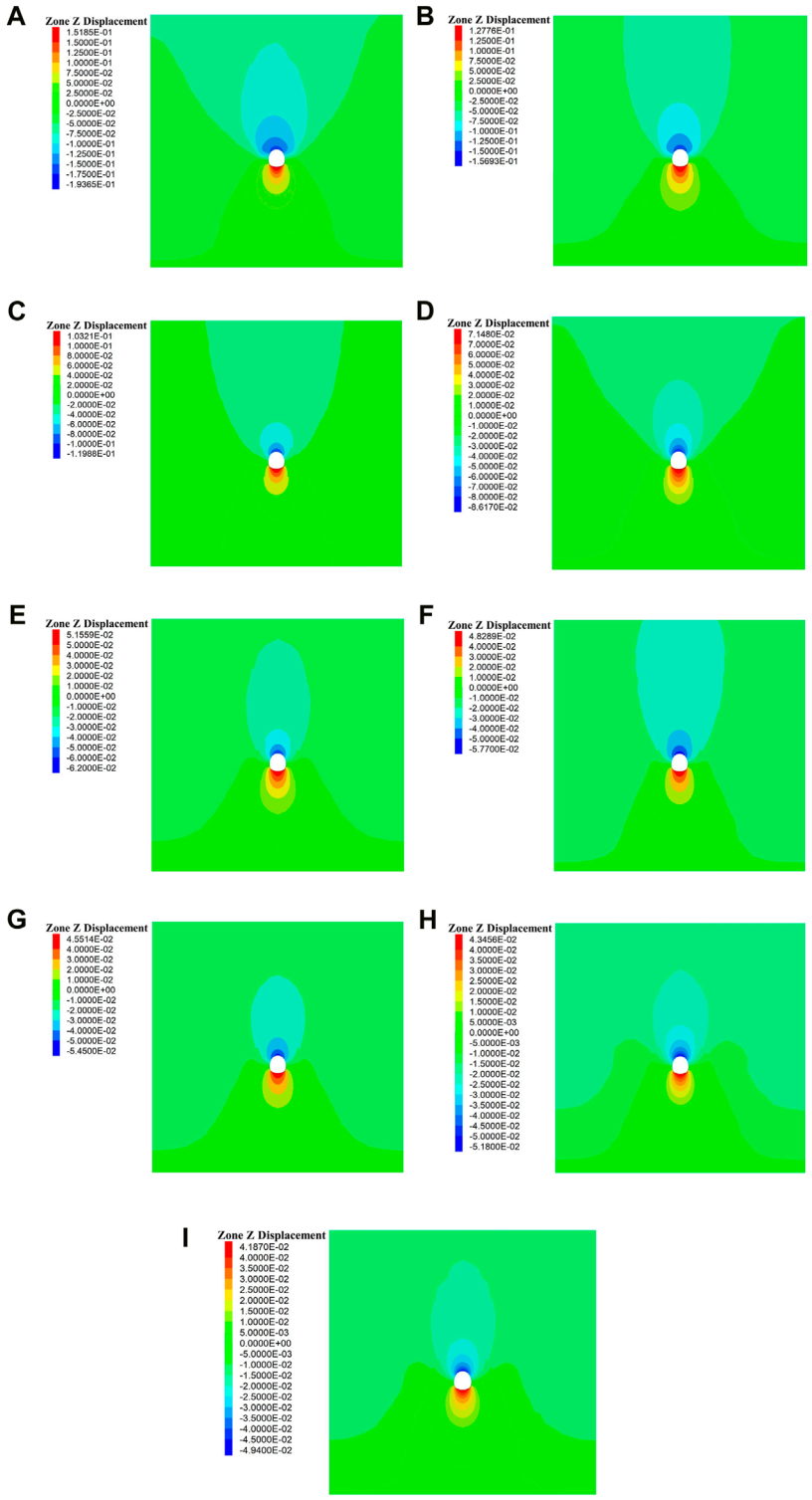

FIGURE 8
Vertical displacement image for various grouting thickness of drill hole 1. **(A)**, The thickness of grouting ring is 4 m; **(B)**, The thickness of grouting ring is 5 m; **(C)**, The thickness of grouting ring is 6 m; **(D)**, The thickness of grouting ring is 7 m; **(E)**, The thickness of grouting ring is 8 m; **(F)**, The thickness of grouting ring is 9 m; **(G)**, The thickness of grouting ring is 10 m; **(H)**, The thickness of grouting ring is 11 m; **(I)**, The thickness of grouting ring is 12 m.

assumed to be equal in all directions. 4) The fluid is considered incompressible. The hydraulic head distribution of radial water flow in tunnels satisfies Laplace's equation for seepage continuity. This equation describes the relationship between pressure difference on either side of a curved liquid surface and factors such as surface tension coefficient and radius of curvature.

By considering the shape of confined wells, we transform planar Laplace's equation into its corresponding cylindrical coordinate form:

$$\nabla^2 = \frac{1}{r}\frac{\partial}{\partial r}\left(r\frac{\partial h}{\partial r}\right) + \frac{1}{r^2}\frac{\partial^2 h}{\partial \varphi^2} + \frac{\partial^2 h}{\partial z^2} = 0 \tag{9}$$

Flow is perpendicular to the Z-axis, so $\frac{\partial h}{\partial r} = 0$, hydraulic head h about Z axial symmetry, so $\frac{\partial h}{\partial \varphi} = 0$. Therefore, it can be simplified as

$$\frac{1}{r}\frac{\partial}{\partial r}\left(r\frac{\partial h}{\partial r}\right) = 0 \tag{10}$$

Where the tunnel and grouting ring sizes r_1 and r_g are always nonzero, the above formula is simplified as follows:

$$\frac{\partial}{\partial r}\left(r\frac{\partial h}{\partial r}\right) = 0 \tag{11}$$

By integrating Eq 11:

$$r\frac{\partial h}{\partial r} = C\,(C\,\text{is constant}) \tag{12}$$

Since the radius of tunnel and grouting ring is not zero, the general solution of this equation can be obtained as:

$$h(r) = C_1 \ln r + C_2\,(C_1、\ C_2\,\text{is constant}) \tag{13}$$

According to the boundary conditions, the definite solutions are discussed in the lining and surrounding rock regions respectively.

1 Grouting ring area ($r_1 \le r \le r_g$):

$$\begin{cases} h_1 = C_1 \ln r_1 + C_2 \\ h_g = C_1 \ln r_g + C_2 \end{cases} \qquad C_1 = \frac{h_g - h_1}{\ln\left(r_g/r_1\right)}, C_2 = \frac{h_1 \ln r_g - h_g \ln r_1}{\ln\left(r_g/r_1\right)} \tag{14}$$

Then the hydraulic head value at any point in the grouting ring is:

$$h(r) = \frac{h_g - h_1}{\ln\left(r_g/r_1\right)}\ln r + \frac{h_1 \ln r_g - h_g \ln r_1}{\ln\left(r_g/r_1\right)} = \frac{h_g \ln\left(r/r_1\right) + h_1 \ln\left(r_g/r\right)}{\ln\left(r_g/r_1\right)} \tag{15}$$

2 Surrounding rock area ($r_g \le r \le r_2$):

$$\begin{cases} h_g = C_3 \ln r_g + C_4 \\ h_2 = C_3 \ln r_2 + C_4 \end{cases} \qquad C_3 = \frac{h_2 - h_g}{\ln\left(r_2/r_g\right)}, C_4 = \frac{h_g \ln r_2 - h_2 \ln r_g}{\ln\left(r_2/r_g\right)} \tag{16}$$

Then the hydraulic head value at any point in the surrounding rock area is:

$$h(r) = \frac{h_2 - h_g}{\ln\left(r_2/r_g\right)}\ln r + \frac{h_g \ln r_2 - h_2 \ln r_g}{\ln\left(r_2/r_g\right)} = \frac{h_2 \ln\left(r/r_g\right) + h_g \ln\left(r_2/r\right)}{\ln\left(r_2/r_g\right)} \tag{17}$$

The formula for calculating the water head value at any position of the tunnel is:

$$h(r)\begin{cases} \dfrac{h_g \ln\left(r/r_1\right) + h_1 \ln\left(r_g/r\right)}{\ln\left(r_g/r_1\right)}, r_1 \le r \le r_g \\ \dfrac{h_2 \ln\left(r/r_g\right) + h_g \ln\left(r_2/r\right)}{\ln\left(r_2/r_g\right)}, r_g \le r \le r_2 \end{cases} \tag{18}$$

According to Darcy's law, the formula for steady flow through a section is as follows:

$$Q = 2\pi r v = 2\pi r k\frac{dh}{dr} \tag{19}$$

The deformation of darcy's law left and right sides of the separation variable integral can be obtained after grouting flow Q_1 of the circle area:

$$\int_{h_1}^{h_g}\frac{2\pi k_g}{Q_1}dh = \int_{r_1}^{r_g}\frac{1}{r}dr \tag{20}$$

$$Q_1 = \frac{2\pi k_g\left(h_g - h_1\right)}{\ln\left(r_g/r_1\right)} \tag{21}$$

Similarly available flow Q_2 of the surrounding area:

$$Q_2 = \frac{2\pi k_r\left(h_2 - h_g\right)}{\ln\left(r_2/r_g\right)} \tag{22}$$

Since the flow rate of the tunnel through different sections is the same, that is, $Q_1 = Q_2$, and the hydraulic potential of the lining wall after tunnel excavation is 0, that is, $h_1 = 0$, the calculation formula of the water inflow of the tunnel can be obtained by combining the above formulas (21) and (22), and adding $h_1 = 0$:

$$Q = \frac{2\pi k_r k_g h_2}{k_r \ln\left(r_g/r_1\right) + k_g \ln\left(r_2/r_g\right)} \tag{23}$$

4.2 Parameter determination of grouting ring

Taking Section 6, Section 7, and Section 8 as representative examples of sections with relatively high water inflow, this study investigates the impact of grouting ring thickness and permeability coefficient on water inflow. The objective is to provide valuable insights for determining optimal parameters for grouting rings. Considering various grouting thicknesses ranging from 4.0m to 12.0 m (in increments of 1.0 m) and a range of ratios (n) between rock mass and grouting ring permeability coefficients (50, 100, 150, and 200), under different working conditions, Figure 6 illustrates the variation in water inflow concerning the parameters of the grouting ring across different sections.

From Figure 6, it can be observed that the water inflow exhibits a non-linear decrease as the permeability coefficient of the grouting ring decreases and its thickness increases. Notably, an increase in the permeabilitycoefficient of the grouting ring leads to a significant reduction in water inflow. Specifically, when reducing the permeability coefficient of the groutingring from 1/50 to 1/100 of

that of surrounding rock, there is an approximate 49% reduction in water inflow. Similarly, further decreasing it from 1/100 to1/150 results in about a 33% reduction with diminishing magnitude. However, once reaching a certain threshold (when the permeability coefficientequals that of surrounding rock divided by 100), no significant decrease in water inflow is observed. Moreover, while increasing the thickness of thegrouting ring gradually reduces tunnel water inflow, beyond a certain threshold (e.g., 8-m thickness), no further significant reduction occurs.Considering both economic costs and construction capabilities, employing a permeability coefficient ratio (n) between surrounding rock and groutingring at n=100 along with an 8 m thick grouting ring effectively controls water inflow.

5 Stability analysis of tunnel surrounding rock

Due to unfavorable geological conditions and the low quality of surrounding rocks, FLAC3D three-dimensional simulation software was employed to analyze the stability of surrounding rocks in a 25 m section at 9 drilling locations during tunnel construction. The objective of this study was to investigate the impact of different grouting ring thicknesses on rock stability, determine the optimal grouting reinforcement thickness, ensure safe tunnel construction, and optimize costs. A total of 153 scenarios were considered by setting seventeen grouting scenarios for each drilling area with varying grouting thicknesses ranging from 4.0m to 12.0 m. Through numerical forward simulations, we obtained spatiotemporal evolution patterns of tunnel rock displacement under different scenarios and analyzed the stability of surrounding rocks under fluid-solid coupling conditions using various scenarios.

5.1 Model establishment

An external software was utilized to model and import FLAC3D, establishing a numerical calculation model with dimensions of 150m×150m×25m, as illustrated in Figure 7. The front, back, left, right, and bottom boundaries of the model were fixed while the top surface remained free. Following Darcy's law, it is assumed that the surrounding rock of the tunnel constitutes a homogeneous, continuous, isotropic medium with constant flow permeability. The groundwater level remains unchanged during tunnel excavation drainage.

The parameters of different strata and grouting rings in numerical simulation are shown in Table 4.

5.2 Numerical simulation result

Using the tunnel cross-section in the initial drilling area as a case study, this investigation examines the deformation image of vertical displacement under varying grouting thicknesses. By conducting a comprehensive analysis of arch settlement curves at different sections with diverse grouting thicknesses, an informed conclusion regarding the optimal grouting thickness is derived. The vertical displacement image for various grouting ring thickness of drill hole 1 are presented in Figure 8.

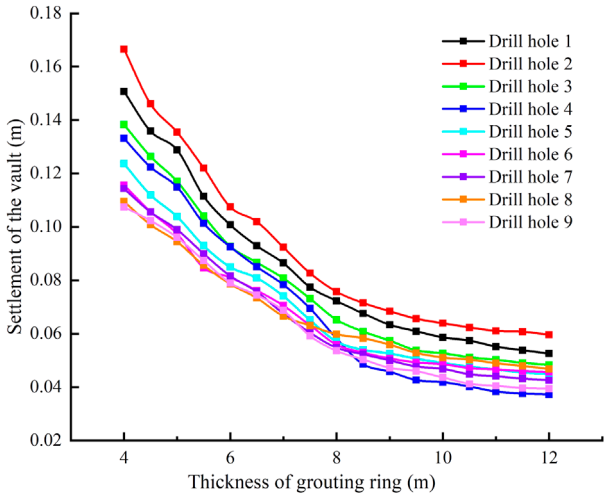

FIGURE 9
Variation curve of vault settlement with different grouting thickness at each drill hole.

By analyzing the vertical displacement field in Figure 8, it can be inferred that the deformation pattern of surrounding rock after tunnel excavation remains consistent across different grouting thicknesses, with the maximum deformation occurring at the crown. As the grouting thickness increases, there is a gradual reduction in maximum settlement at the crown. When increasing the grouting thickness from 4 m to 8 m, successive maximum settlements at the crown are observed as 19.4 cm, 15.7 cm, 12 cm, 8.6 cm, and finally reaching a decrease of more than 2 cm each time; further increasing grouting thickness up to 12 m only slightly reduces successive maximum settlements at the crown to values of 5.77 cm, 5.45 cm, 5.18 cm and eventually reaching a minimum reduction of merely 0.53 cm. Variation curve of vault settlement with different grouting thickness at each drill hole is showed in Figure 9.

By analyzing the settlement variation curve in Figure 9, it can be observed that for each drilling section, the effect of arching settlement control becomes quite evident as the grouting thickness increases from 4 m to 8 m, resulting in a reduction of settlement values by 45%–56%. The curve stabilizes after reaching a grouting thickness of 8 m and continues to increase up to 12 m only leads to a marginal decrease in settlement values by 18%–36%. This indicates that further increasing the grouting thickness does not have a significantly stronger control effect on vertical displacement. Considering safety and cost-effectiveness factors, it is recommended to choose a grouting thickness of 8 m.

6 Conclusion

(1) The predicted results of different formulas for calculating water inflow may exhibit slight variations; however, the overall trend of water inflow remains consistent. Considering the inherent unpredictability of tunnel water inflow, and taking into account various calculation results, the estimated normal water inflow in this tunnel is approximately 115.5908×10^3 m^3/d; with a

maximum potential water inflow around 210.9100×10^3 m^3/d, particularly in Sections 6, 7, and 8 where the water inflow is relatively large.

(2) Pre-grouting curtain serves as an effective measure to prevent and control water inflow. Increasing the thickness of grouting rings while reducing their permeability coefficient can effectively mitigate the amount of infiltrating water entering the tunnel. However, further adjustments to these parameters yield diminishing returns in terms of reducing water inflow. In this particular tunnel project, employing a permeability coefficient n) value of 100 for surrounding rock along with an optimal grouting thickness set at 8 m would sufficiently control the volume of incoming groundwater.

(3) Pre-grouting curtain exhibits a noticeable effect on enhancing stability in tunnel surrounding rock; however, its strengthening effect diminishes as its thickness increases beyond a threshold. Increasing the grouting thickness from 4m to 8 m effectively controls arch settlement effects. However, further increasing the grouting thickness does not significantly enhance control over vertical displacement. Taking safety and economic factors into consideration, it is suggested that an optimal grouting thickness should be at least set at 8 m.

Data availability statement

The original contributions presented in the study are included in the article/Supplementary material, further inquiries can be directed to the corresponding authors.

Author contributions

YC: Funding acquisition, Project administration, Writing–review and editing. ML: Data curation, Formal Analysis, Writing–original draft. MS: Data curation, Investigation, Writing–original draft. MD: Data curation, Software, Writing–original draft. HL: Investigation, Writing–original draft. YJ: Software, Writing–original draft.

Funding

The author(s) declare financial support was received for the research, authorship, and/or publication of this article. This study is financially supported by the National Natural Science Foundation of China (Nos 42172310 and 51609130).

Acknowledgments

The authors gratefully acknowledge Shandong Jianzhu University and Shandong University that have contributed to the research results reported within this paper.

Conflict of interest

The authors declare that the research was conducted in the absence of any commercial or financial relationships that could be construed as a potential conflict of interest.

Publisher's note

All claims expressed in this article are solely those of the authors and do not necessarily represent those of their affiliated organizations, or those of the publisher, the editors and the reviewers. Any product that may be evaluated in this article, or claim that may be made by its manufacturer, is not guaranteed or endorsed by the publisher.

References

Chen, D., Chen, Y., Hong, J., et al. (2017). Prediction of water inflow in the long diversion tunnel of Danba Hydropower Station. *J. Wuhan Univ. Eng. Ed.* 50 (02), 193–199+206. doi:10.14188/j.1671-8844.2017-02-006

Chen, Q., Liang, L., Zou, B., Xu, C., Kong, B., and Ma, J. (2023). Analytical solutions of steady a seepage field for deep-buried tunnel with grouting ring considering anisotropic flow. *J. Mar. Sci. Eng.* 10 (12), 1861. doi:10.3390/jmse10121861

Chen, Y., Gao, T., Yin, F., Liu, X., and Wang, J. (2022). Study on influence of joint locations and hydraulic coupling actions on rock masses' failure process. *Energies* 15 (11), 4024. doi:10.3390/en15114024

Chen, Y. J., and Zhang, X. (2019). Analytical plastic solution around soil-digging holes for inclined building and its application. *Int. J. Civ. Eng.* 17, 245–252. doi:10.1007/s40999-017-0230-7

Cheng, X., Sheng, L., Xia, Z., Liu, Y., Ma, X., Pan, J., et al. (2024). Grouting theory and strategy of simultaneous control of the horizontal and vertical deformations of tunnels. *Int. J. GEOMECHANICS* 24 (2), 04023267. doi:10.1061/IJGNAI.GMENG-8839

Fu, H. L., An, P. T., Cheng, G. W., Wen, S., and Li, J. (2022). Calculation of the allowable drainage of parallel tunnels based on ecological environment protection. *KSCE J. Civ. Eng.* 26 (5), 2420–2427. doi:10.1007/s12205-022-0401-1

Han, J., Wang, J., Yang, W., Wang, X., Ma, R., et al. (2023). Experimental study on the properties of a polymer-modified superfine cementitious composite material for waterproofing and plugging. *Case Stud. Constr. Mater.* 19, e02552. doi:10.1016/j.cscm.2023.e02552

Jiang, P., Zhang, Z., Zheng, H., and Huang, J. k. (2023). Coupling analysis method of grouting construction with deformation response of adjacent existing tunnel. *Undergr. SPACE* 15, 312–330. doi:10.1016/j.undsp.2023.07.005

Lan, X., Zhang, X., Yin, Z., Li, X., and Yang, T. (2021). Mitigation of karst tunnel water inrush during operation in seasonal variation zone: case study in nanshibi tunnel. *J. Perform. Constr. Facil.* 35 (3), 04021010. doi:10.1061/(ASCE)CF.1943-5509.0001573

Li, L., Chen, H. H., Li, J. P., and Sun, D. (2021). A semi-analytical solution to steady-state groundwater inflow into a circular tunnel considering anisotropic permeability. *Tunn. And Undergr. Space Technol.* 116, 104115. doi:10.1016/j.tust.2021.104115

Li, T. L., Zhao, W., Liu, R., Han, J., Jia, P., and Cheng, C. (2023). Visualized direct shear test of the interface between gravelly sand and concrete pipe. *Can. Geotechnical J.* 61, 361–374. doi:10.1139/cgj-2022-0007

Lin, L., Chen, H., Li, J., and Sun, D. (2021). A semi-analytical solution to steady-state groundwater inflow into a circular tunnel considering anisotropic permeability. *Tunn. Undergr. space Technol.* 116, 104115. doi:10.1016/j.tust.2021.104115

Liu, J. Q., Sun, Y. K., Li, C. J., Yuan, H. l., Chen, W. Z., Liu, X. Y., et al. (2022). Field monitoring and numerical analysis of tunnel water inrush and the environmental changes. *Tunn. And Undergr. Space Technol.* 122, 104360. doi:10.1016/j.tust.2021.104360

Peng, P., Peng, F., Sun, Z., and Zhang, D. (2022). Grouting for tunnel stability control and inadequate grouting section recognition: a case study of countermeasure of giant karst cave. *Appl. SCIENCES-BASEL* 12 (23), 11895. doi:10.3390/app122311895

Tao, H., Liu, S., Zhang, X., Meng, L., and Wang, P. (2023). Numerical analysis of grouting of water-enriched karst highway tunnel based on critical water-enriched height. *Processes* 11 (1), 149. doi:10.3390/pr11010149

Wang, L. (2023). Prediction of water inflow in submarine tunnels and optimization of waterproof and drainage systems. *Jinan, Shandong Jianzhu University*. doi:10.27273/d.cnki.gsajc.2023.000525

Wang, T., Zhou, Q., Guo, C., Yang, S., Dan, L., et al. (2022). "Application analysis on convergence deformation of soft soil shield tunnel controlled by grouting," in 2022 8TH INTERNATIONAL CONFERENCE ON HYDRAULIC AND CIVIL ENGINEERING: DEEP SPACE INTELLIGENT DEVELOPMENT AND UTILIZATION FORUM ICHCE, Xi'an, China, 25-27 November 2022, 324–332. doi:10.1109/ICHCE57331.2022.10042634

Wu, J., Zhou, Z., Li, M., et al. (2019). Research progress on calculation methods for predicting tunnel water inflow. *J. Eng. Geol.* 27 (04), 890–902. doi:10.13544/j.cnki.jeg.2018-245

Xu, L. L., Cai, M. F., Dong, S. N., Yin, S., Xiao, T., Dai, Z., et al. (2022). An upscaling approach to predict mine water inflow from roof sandstone aquifers. *J. Hydrology* 612 (C), 128314. doi:10.1016/j.jhydrol.2022.128314

Xue, X., Zhang, J., Su, Z., et al. (2015). Study on the grouting pre-reinforcement mechanism and effect evaluation in water-rich loess tunnel. *Proc. Int. Conf. Adv. Des. Manuf. Eng.* 39, 1084–1088.

Ye, W. (2023). Water inrush prediction and plugging technology scheme for shallow buried tunnels on the Binggou Fushui fault. *China Railw.* (06), 25–31. doi:10.19549/j.issn.1001-683x.2022.12.01.002

Yuan, J., Chen, W., Tan, X., Yang, D., and Wang, S. (2019). Countermeasures of water and mud inrush disaster in completely weathered granite tunnels: a case study. *Environ. Earth Sci.* 78 (18), 576. doi:10.1007/s12665-019-8590-8

Zheng, L., Quan, C.Z., He, C., Ma, C. C., and Duan, C. R. (2022). Seepage field distribution and water inflow laws of tunnels in water-rich regions. *J. Mt. Sci.* 19 (2), 591–605. doi:10.1007/s11629-020-6634-x

frontiers | Frontiers in Earth Science

TYPE Original Research
PUBLISHED 29 February 2024
DOI 10.3389/feart.2024.1372537

Check for updates

OPEN ACCESS

EDITED BY
Pengjiao Jia,
Soochow University, China

REVIEWED BY
Jidong Teng,
Central South University, China
Zhen Wang,
Yangzhou University, China
Changshuo Wang,
Ningbo University, China
Ren Weizhong,
Chinese Academy of Sciences (CAS), China

*CORRESPONDENCE
Guangli Xu,
xu1963@cug.edu.cn

RECEIVED 18 January 2024
ACCEPTED 15 February 2024
PUBLISHED 29 February 2024

CITATION
Xue M, Xu G, Yao F and Ma Z (2024), Research on characteristics and geological genesis of large-scale deep-seated landslide in tuff formation.
Front. Earth Sci. 12:1372537.
doi: 10.3389/feart.2024.1372537

COPYRIGHT
© 2024 Xue, Xu, Yao and Ma. This is an open-access article distributed under the terms of the Creative Commons Attribution License (CC BY). The use, distribution or reproduction in other forums is permitted, provided the original author(s) and the copyright owner(s) are credited and that the original publication in this journal is cited, in accordance with accepted academic practice. No use, distribution or reproduction is permitted which does not comply with these terms.

Research on characteristics and geological genesis of large-scale deep-seated landslide in tuff formation

Mengqi Xue[1], Guangli Xu[1,2]*, Feixiang Yao[3] and Zhuo Ma[4]

[1]Institute of Geological Survey, China University of Geosciences, Wuhan, China, [2]Faculty of Engineering, China University of Geosciences, Wuhan, China, [3]China United Engineering Corporation Limited, Hangzhou, China, [4]China Energy Engineering Group Yunnan Electric Power Design Institute, Kunming, China

In engineering practice, engineers generally treated tuff as a lumpy material with a poorly defined laminated structure and a rock group that was not susceptible to slide failure. Most studies of tuff landslides had focused on small clastic landslides in shallow strata with weathering boundaries and lithologic interfaces as slip surfaces. This paper takes a large-scale, deep-seated tuff landslide on the southeast coast of China as the research project. We used borehole TV imaging and exploration tunnels to confirm the material composition and structural characteristics of the tuff stratum and used exploration tunnels to expose the slip soil directly. Microscopic identification, mineralogical composition analysis, zircon U-Pb isotope dating, and Hf isotope analysis of slip soils collected from the exploration tunnels elucidated the geologic background and genesis of the large-scale deep-seated landslides in the tuff stratum. It was found that the formation of a tuff stratum in the landslide area was caused by multi-volcanic orogeny and multi-phase tectonics. The timing of the melting of the original magma from these volcanic events also differs. During these intervals between eruptions, deposition occurred, and this sedimentary material formed the slip soil.

KEYWORDS

large-scale landslide, deep-seated landslide, tuff, intermittent eruption, slip soil

1 Introduction

Volcanic activity is a potential geological force leading to global climate change and the extinction of biological populations (Rampino and Stothers, 1988; Olsen, 1999; Wignall, 2001). Tuff, one of the direct products of volcanic activity, is also a research hotspot at present (Benito et al., 1998; Xu et al., 2004; Hints R. et al., 2006; He et al., 2007). Tuff, which belongs to pyroclastic rock, is a transitional type between igneous rock and ordinary sedimentary rock and is thought to be formed after the fall of volcanic ash (Haaland et al., 2000; Grevenitz et al., 2003). The tuff stratum, in which landslides are generally developed, is widely distributed in the southeast coastal area of China. In Zhejiang Province, on the southeast coast of China, the Lidong landslide, Shanzao village landslide, and Xiabanling landslide caused more than 70 deaths, and the Xiageliao landslide caused potential economic losses of $62,640,000. The series of heavy and massive landslides and geological disasters have brought enormous damage and threats to people's lives, health, and property safety. Tuff normally, the igneous rock widely used as a natural building material, is considered hard rock without apparent stratum rationality. Therefore, tuff does not have the primary

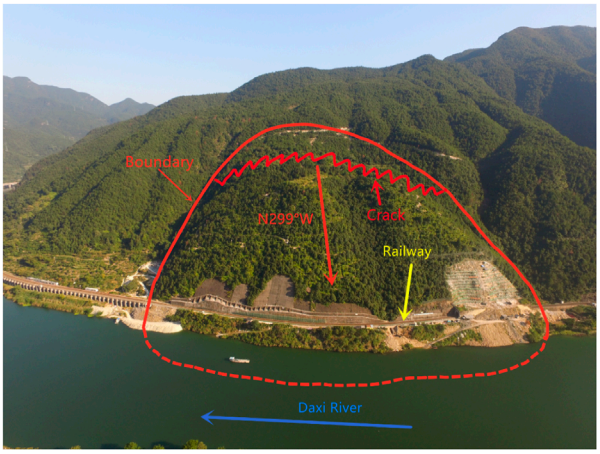

FIGURE 1
The basic situation of the Xiageliao landslide by aerial photograph.

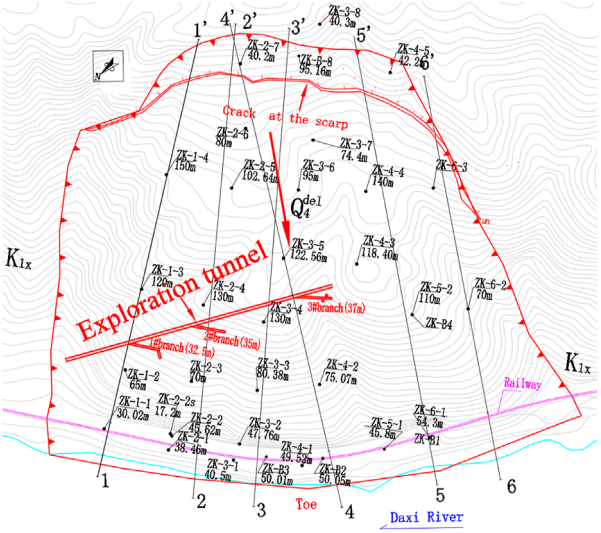

FIGURE 2
The plan for Xiageliao landslide.

conditions for many landslides. However, multiple tuff landslides above have occurred or are developing evidence that the tuff stratum is very suitable to breed large and even super large-scale deep-seated landslides.

There are few research studies on large-scale, deep-seated tuff landslides, which are still in the preliminary exploration stage. Used the X-ray diffraction method to determine the clay minerals composition of tuff from the Kunimi landslide and concluded that the content of clay minerals was higher in the groundwater enrichment zone of the landslide (Shuzui and Shimoda, 1987; Shuzui, 2001). When a landslide occurred in the tuff formation accompanied by continuous deformation, the content of clay minerals in the slip-surface continued to increase under the action of groundwater. In contrast, the content of detrital minerals decreased. It was the most critical factor in the decline of anti-sliding ability in slip-surface. Lu compared three landslides in the Cayley volcanic area in the United Kingdom and analyzed the similarities and differences between the tuff and dacite tuff landslides, including the slip-surface geotechnical properties and landslide motion forms (Lu, 1993). Trandafir et al. analyzed the formation mechanism of the Norwood Tuff landslide. They concluded that the landslide was a gradual destruction process due to the rise of groundwater level and human activities (Trandafir and Amini, 2009). Beisner et al. analyzed and studied the dynamic displacement characteristics of the Norwood Tuff landslide underwater level and seismic acceleration (Beisner, 2011). Hiroyuki et al. researched the Oshinkoshin landslide in Shiretoko Peninsula, eastern Hokkaido, Japan. They proposed that landslides were mainly controlled by the thick-hard shale with multiple thin strata of soft tuff (Maeda et al., 2014). Masahiro conducted a systematic study on the characteristics of deep-seated tuff landslides, considering the two influencing factors of rainfall and earthquakes (Masahiro, 2016).

We researched the Xiageliao landslide in Zhejiang Province, China. We used drilling, borehole photography, and tunnel exploration as the primary survey methods to study the large-scale, deep-seated tuff landslide characteristics. Some experiments were done to explain the relationship between landslides and tuff formation. Finally, a development model of the large-scale deep-seated tuff landslide was summarized.

2 Investigation and research on xiageliao landslide

As shown in Figure 1, Xiageliao landslide is located on the right bank of the Daxi River in Qingtian County, Zhejiang Province, on the southeast coast of China, with the foot of the slope submerging into the 38 m deep river water and a freight railway in the foot of the slope about 15 m above the river. The landslide was first discovered in 2012 when the retaining wall of the railway was cracked due to the deformation of the landslide, and the trains could only run at a speed of 26 km/h to ensure safety. In April 2016, a crack with a length of about 500 m and a width of about 0.5 m was discovered on the rear edge of the landslide, which caused the railway's suspension and residents' relocation.

Figure 2 and Figure 3 show that the main sliding direction of the landslide is about 299°, the length of the landslide is about 510 m, the width is about 580 m, the elevation is between 20 and 275 m above sea level, and the total area is about 200,000 m^2. The thickness of the landslide is 20–105 m, and the total volume of the landslide body is about 1100×10^4 m^3, so the landslide was defined as a large-scale, deep-seated landslide. To better study the Xiageliao landslide, we drilled 42 boreholes within the landslide area; these boreholes totaled 2976.17 m in length; the boreholes exposed the structural characteristics of the tuff and also provided good sampling conditions, see Figure 4A. Similarly, an exploration tunnel was constructed from the gully at the right boundary of the landslide, see Figure 4B. This tunnel consists of a 270 m-long main tunnel and three branch tunnels that cross the slip surface. The dimensions of the main tunnel were 3 m × 3 m, and the branch tunnels were 2.25 m × 2 m. The main tunnel provided more intuitive information about the structural changes of the slip body, and all three branch tunnels

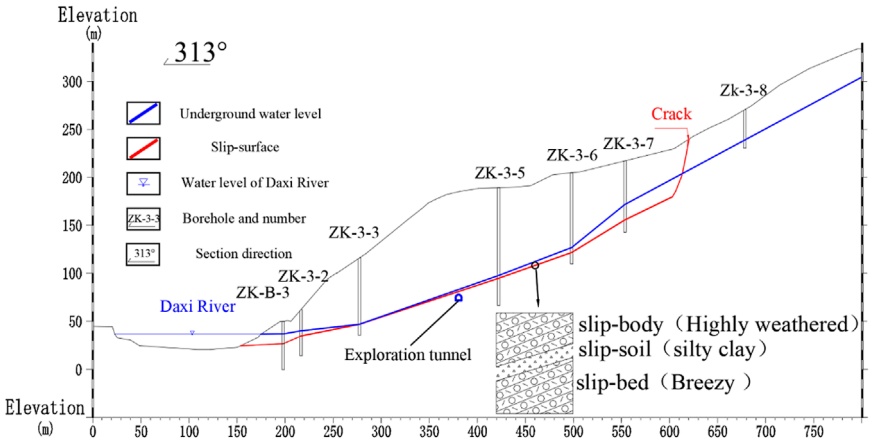

FIGURE 3
The profile of Xiageliao landslide (Section 3-3′).



FIGURE 4
Photographs of the core and exploration tunnel for the Xiageliao landslide. **(A)** Photographs of the core from the borehole. **(B)** Photographs of the exploration tunnel.

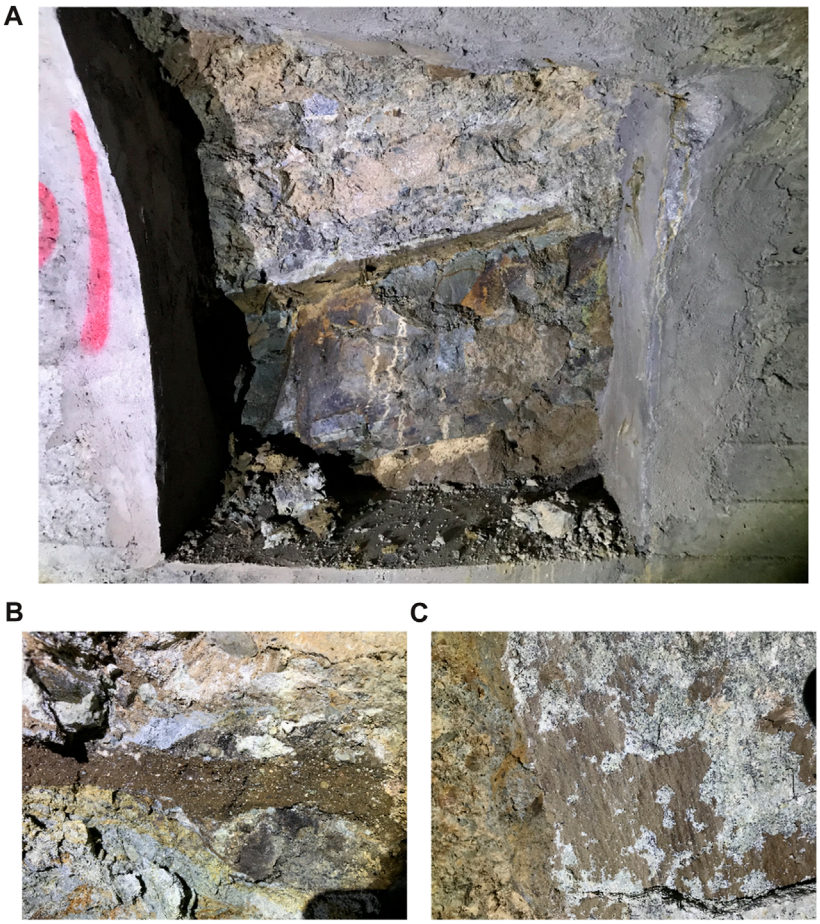

FIGURE 5
Slip soil revealed by exploration tunnels. **(A)** Distant view of slip soil. **(B)** Close-up of slip soil. **(C)** Scratch marks.

accurately revealed the location of the slip surface and provided good observation conditions and sampling conditions for the undisturbed slip soil.

Figure 5A presents the slip-surface observation window in 3# branch tunnel located about 100 m below the ground surface, and the slip-soil is a stratum of clay with a thickness of about 5–12 cm between the strongly weathered slip-body and the slightly weathered slip-bed. Figure 5B shows a close-up of slip-soil with occurrence 295°∠21°which, which is yellow-brown clay with a thickness of 3–15 cm. The slip-soil is relatively dense with a slippery feel, hard plastic-soft plastic, and easy to soften in contact with water, leading to the local seepage area. Figure 5C shows a close-up of slip-soil scratches. The width of the groove is about 2 mm, and the scratch direction is 300°, which is consistent with the sliding direction of the landslide, so this clay stratum is the slip-soil.

The Xiageliao landslide is developed in the Cretaceous (K_1x) tuff stratum. In this paper, the exploration results of borehole zk3-5, located in the middle of the landslide, were selected to be presented and studied. Figure 5 presents the basic situation of the landslide tuff formation. Figure 6A is a schematic diagram for the stratum structure of borehole ZK3-5 and shows that the tuff formation above the slip-bed has alternated between broken and intact many times. This situation was also found in other boreholes, and according to data collection, this phenomenon also occurred in areas outside the landslide range. Figure 6B shows the partial results by borehole TV imaging in borehole ZK3-5, and in the 64–76 m section of ZK3-5, the complete fragmentation (strong-medium weathered) of the tuff changes many times. While macroscopic observations of the stratigraphic structure of the tuff stratum were made through boreholes, core samples were also sampled and numbered according to s1 to s8. The specific sampling location can be seen in the dotted line position in Figure 6A.

To explore the performance of the landslide tuff on the micro level, eight sets of core samples from the borehole ZK3-5 were selected for microscopic identification. The sampling locations are shown in Figure 6A. The microscopic identification instrument was a microscope (OLYMPUS BX51, China University of Geosciences (Wuhan)); the results are shown in Figure 7. S-1 sampling depth of 8.5 m was identified as light metamorphic dacite lithic-crystal tuff, mainly composed of crystal fragments, detritus, and volcanic ash. The crystal fragment was locally altered by weathering and is mainly composed of quartz and feldspar. S-2 sampling depth of 24.4 m was identified as light metamorphic dacite lithic-crystal tuff, similar to s-1. The plagioclase in the sample was weathered and altered under the action of late stress. The late extensional fissure interspersed the fractional crystal fragment, and along both sides of

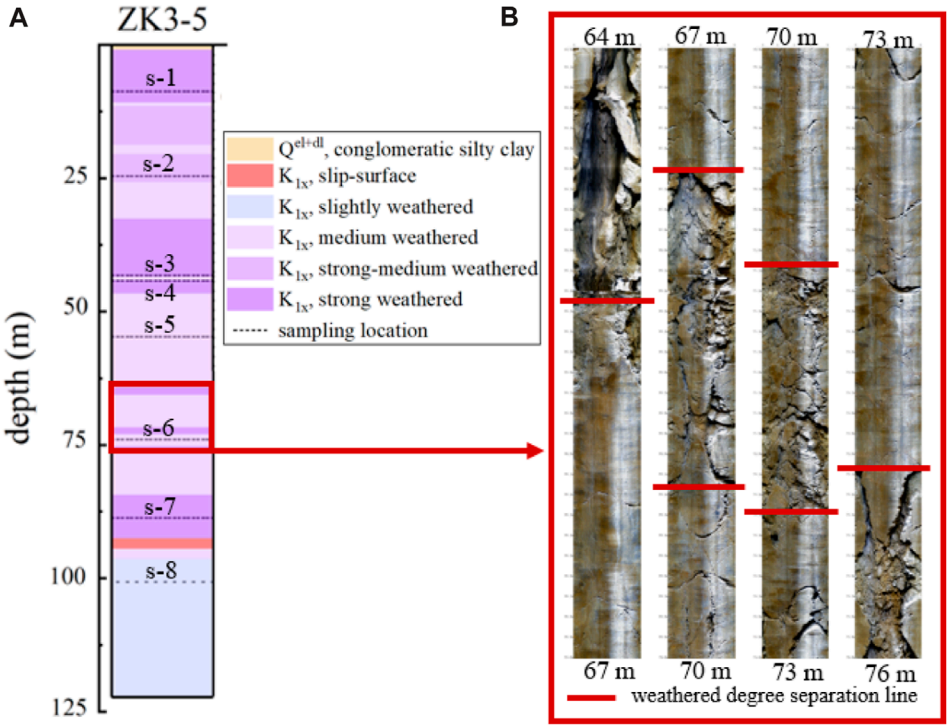

FIGURE 6
Stratum structure characteristics of Xiageliao landslide. **(A)** Schematic diagram of the core structure of the borehole. **(B)** Borehole TV images.

the fissure, the weathering and erosion became intense. Part of the feldspars were eroded into sericite and clay minerals. The detritus are mainly quartzite debris in mid-late rock. S-3 sampling depth 43 m was identified as lithic crystal tuff, mainly composed of crystal fragments, detritus, and volcanic ash; the rock crystal fragment was strongly weathered and altered. Quartz veins were squeezed to relax, wave-like are developed in the rock, and partial quartz veins were compressed to form a stone sausage structure. It shown a soft-hard inter-stratum structure in this area. S-4, with a sampling depth of 43.8 m, was identified as lithic crystal tuff, similar to s-3, and the crystal fragment was mainly feldspar and quartz. Quartz veins with compression and torsion characteristic are developed. Figure S-5, sampling depth 54.5 m, identified as rhyolitic lithic-crystal tuff with malleable rhyolite structure mainly composed of crystal fragments, detritus, and volcanic ash. Quartz sericite had an obvious intermittent orientation. S-6 sampling depth of 73.8 m was identified as silicified crystal lithic tuff. The robust, weathered rock presented a silicified state with small, interspersed, compressed quartz veins. Figure S-7 sampling depth 88.5 m was strong weathered tuff in slip-surface, and the basic was lithic crystal tuff. The crystal fragment is mainly quartz (15%), followed by feldspar (7%), and sericite is well-developed. S-8 sampling depth 99.5 m was medium weathered tuff in slip-bed identified as lithic crystal tuff with mainly larger particle size plagioclase crystal fragment with a reasonable degree of self-shape with glassy tuff vein partially interspersed.

The tuff in the landslide area is mainly composed of lithic crystal tuff, of which the shallow part is composed chiefly of dacite tuff, and the deep stratum is mostly basic rhyolitic tuff. The degree of weathering is quite different at different depths, and the crystal fragments and veins also show that some stratum from different depths are subject to more significant compression stress. It indicates that the later geological forces suffered by tuff strata are of different periods. Similarly, the different types of tuff in each stratum also reveal that the volcanic structures that formed these tuff stratum were different.

With the identification of the Xiageliao landslide's characteristics, the research's core issue is: Why did the volcanic tuff formation without apparent stratification give birth to large-scale deep-seated landslides like the Xiageliao landslide? This problem can be divided into two aspects. The first is to determine how such a complex tuff formation is formed, and the second is to determine the formation of a continuous clay slip surface about 100 m below the surface. For this purpose, three experiments were designed in this study: age dating, isotope analysis, and compositional determination of tuff.

3 Materials and methods

3.1 *In-situ* U-pb dating of zircon by LA-ICP-MS

Zircon is a relatively common by-mineral, commonly found in magmatic rocks, with a stable crystal structure and high stability of closure, which has the property of persistently maintaining the physical and chemical characteristics of the mineral at the time of its

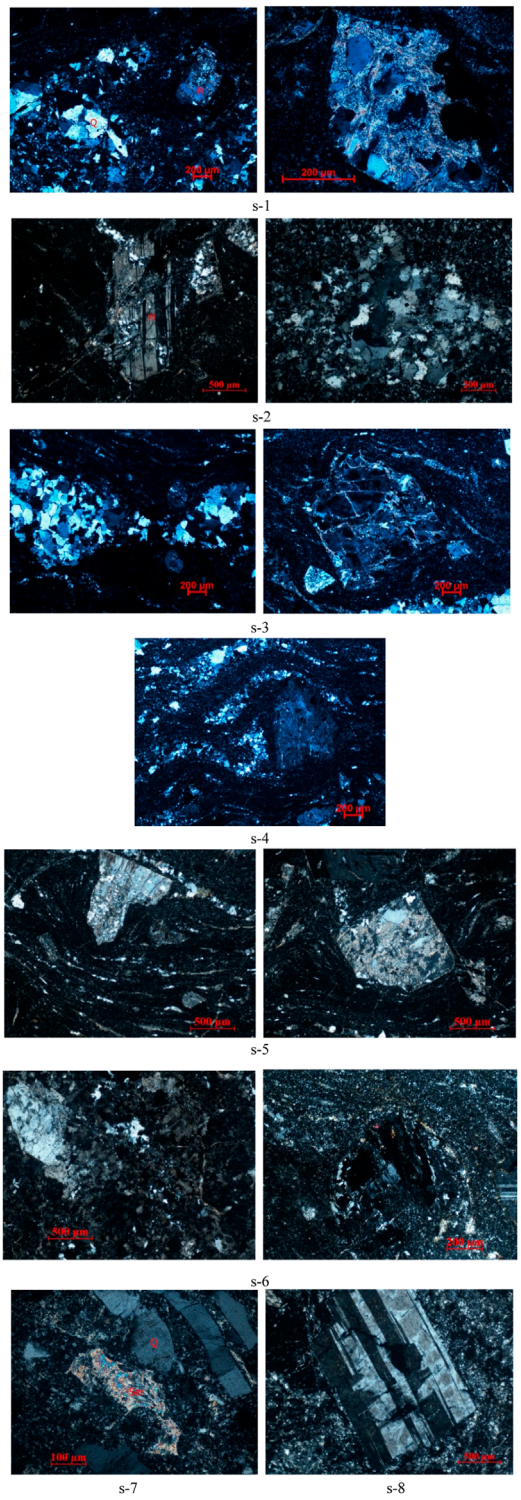

FIGURE 7
Micrographs of tuff at different depths of the Xiageliao landslide.

formation and its structure and composition reflect the geological processes experienced by the rock. The high U and Th content of zircon makes it the most frequently studied object in U-Pb isotope geochronology, and zircon dating utilizes the decay of U and Th isotopes into Pb isotopes. To analyze the evolutionary history and characteristics of the geotechnical bodies in the landslide area, more than 20 sets of rock samples were taken from 6 boreholes at different depths in the 3–3′ section of the landslide and from the rock layers above and below the landslide zone and analyzed for zircon U-Pb dating. The zircon U-Pb isotope dating and trace element content were analyzed using the LA-ICP-MS method, which is commonly used nowadays.

Zircon U-Pb isotopic dating, Hf isotope determination, and X-ray diffraction analysis were designed to explain the complex stratification of the tuff in the landslide area and to validate the hypothesis about the formation of the tuff. The samples were taken from the cores in boreholes of different depths, and the undisturbed slip-soil samples were taken directly from the exploration tunnel.

Figure 8 shows the photos of zircon U-Pb dating samples and selected points of zircon CL images of zircon tuffs in the landslide area; the red circles in the picture show laser test chosen points. Zircons were selected from core samples from different locations in different boreholes. Then, the tuff samples were crushed, and single-grained zircons were randomly chosen by gravity and magnetic sorting to avoid artificial selectivity as much as possible. These zircons were then spaced so that they were independent of each other, arranged in an orderly manner, and finally made into targets. Transmitted light, reflected light, and cathodoluminescence (CL) images were taken of the zircon targets, and zircons with good crystal shape and transparency were selected as the basis for the zircon dating analysis. Finally, the pointing and data processing were carried out.

U-Pb dating of zircon was conducted by LA-ICP-MS. Laser sampling was performed using a GeolasPro laser ablation system that consists of a COMPexPro 102 ArF excimer laser (wavelength of 193 nm and maximum energy of 200 MJ) and a MicroLas optical system. An Agilent 7700e ICP-MS instrument was used to acquire ion-signal intensities. The spot size and frequency of the laser were set to 32 μm and 5 Hz, respectively, in this study. Detailed operating conditions for the laser ablation system and the ICP-MS instrument and data reduction are the same as description by (Liu et al., 2008; Liu et al., 2010; Hu et al., 2015; Zong et al., 2017). Zircon 91,500 and glass NIST610 were used as external standards for U-Pb dating and trace element calibration, respectively. Each analysis incorporated a background acquisition of approximately 20–30 s, followed by 50 s data acquisition from the sample. An Excel-based software, ICPMSDataCal, was used to perform off-line selection and integration of background and analyzed signals, time-drift correction, and quantitative calibration for trace element analysis and U-Pb dating (Liu et al., 2008; Liu et al., 2010)17,18. Concordia diagrams and weighted mean calculations were made using Isoplot/Ex_ver3 (Ludwig, 2003).

3.2 Hf isotope ratio analyses by LA-ICP-MS

The zircon samples used in this experiment were also derived from the age-determined zircon in the previous section. These zircons were pre-treated and analyzed for Hf isotopes. All chemical preparations were performed on class 100 work benches within a class 1000 over-pressured clean laboratory. Sample digestion: (1) Sample powder (200 mesh) was placed in an oven at 105°C

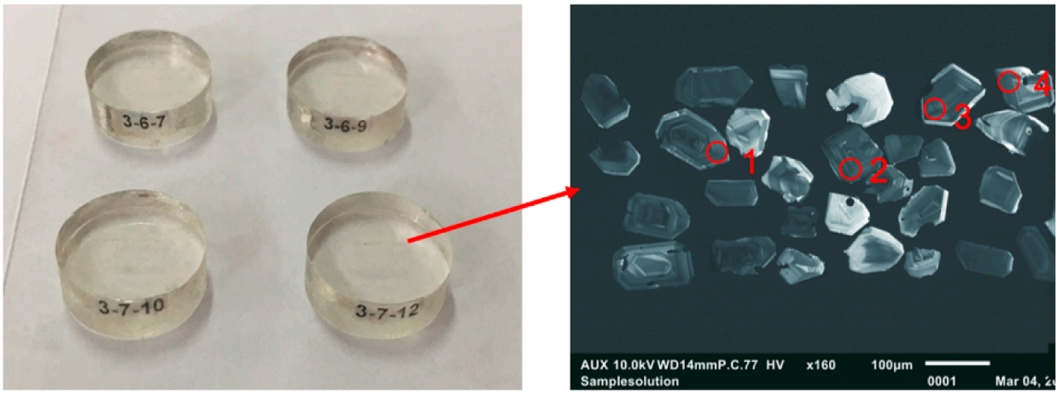

FIGURE 8
Zircon target and CL camera view.

for drying of 12 h; (2) 50–200 mg sample powder was accurately weighed and placed in a Teflon bomb; (3) 1–3 mL HNO_3 and 1–3 mL HF were added into the Teflon bomb; (4) Teflon bomb was put in a stainless steel pressure jacket and heated to 190°C in an oven for >24 h; (5) After cooling, the Teflon bomb was opened and placed on a hotplate at 140°C and evaporated to incipient dryness, and then 1 mL HNO_3 was added and evaporated to dryness again; (6) The sample was dissolved in 3.0 M HF. Column chemistry: After centrifugation, the supernatant solution was loaded into an ion exchange column packed with LN-Spec resin. After complete draining of the sample solution, columns were rinsed with 3 M HCl, 6 M HCl, and 4 M HCl+H_2O_2 (0.5%) to remove undesirable matrix elements. Finally, the Hf fraction was eluted using 2.0 M HF and gently evaporated to dryness before mass-spectrometric measurement.

Experiments of *in situ* Hf isotope ratio analysis were conducted using a Neptune Plus MC-ICP-MS (Thermo et al.) in combination with a Geolas HD excimer ArF laser ablation system (Coherent, Göttingen, Germany). The laser energy is 8 mJ/cm^2, the frequency is 8 Hz, and the laser beam spot diameter is 44 μm. Detailed instrument operating conditions and analysis methods can be referred to (Hu et al., 2012). This laser ablation system includes a "wire" signal smoothing device, producing smooth signals even at meager laser repetition rates down to 1 Hz. Helium was used as the carrier gas within the ablation cell and was merged with argon (makeup gas) after the ablation cell. Small amounts of nitrogen were added to the argon makeup gas flow to improve the sensitivity of Hf isotopes (Hu et al., 2012). Off-line selection, analysis of analyte signals, and mass bias calibrations were performed using ICPMSDataCal (Liu et al., 2010).

3.3 X-ray diffraction test

The XRD test was commissioned by the State Key Laboratory of Geological Processes and Mineral Resources (China University of Geosciences), and the instrument model is X'Pert PRO DY2198. The test samples were slip soils and tuffs above and below them, taken from the exploration tunnels.

Samples for XRD analysis were crushed coarsely and moderately; after grinding, the samples were ground to 200 mesh with a mortar and pestle. After grinding, the samples were dried at 105 °C, and 5 g were weighed accurately. After drying at 105°C, 5 g of the sample was weighed accurately and placed in a crucible. After the sample was dried at 105°C, 5 g was weighed accurately and placed in a crucible. A mixture of lithium tetraborate-lithium metaborate-lithium nitrate was added to the crucible. After confirming that the sample and the melt were thoroughly mixed, the sample was melted in a high-precision melting furnace at 1050°C. The molten slurry was poured into a platinum model, cooled to form a fused sheet, and then analyzed by X-ray diffraction.

Then X-ray diffraction analysis was performed. The experimental conditions were as follows: voltage 40kV, current 40 mA, 2θ angle from 5° to 60°, step size of 0.04°/step, and scanning speed of 5 s/step. The scanning speed was 5 s/step. The accuracy of the goniometer was less than 0.01° (2θ angle), and the detection limit of mineral content was about 1%. The accuracy of the goniometer is less than 0.01° (2θ angle), and the detection limit of the mineral content is about 1%. Mineral species were analyzed using JADE6.5 software with standard curves of various minerals. The mineral species were determined by comparing them with the standard curves of various minerals using JADE6.5 software. In the XRD test, high-purity silica powder was chosen as the calibration standard, and the 2θ angle of the sample to be tested was calibrated by the external standard method. In the XRD test, high-purity silica powder was chosen as the calibration standard, and the 2θ angle of the sample to be tested was corrected by the external standard method. The standard sample and the sample to be tested were analyzed with the same instrument and under the same experimental conditions. The standard sample and the sample to be tested were diffracted with the same instrument and under the same experimental conditions, and the data of the standard sample were compared with the standard values. The data of the standard sample was compared with the standard value to find out the correction value of each 2θ angle. Then the 2θ angle of the measured sample was corrected by the external traditional method. Then, the 2θ angle of the measured sample is fixed.

10.3389/feart.2024.1372537

TABLE 1 Laboratory test results on samples from the Xiageliao landslide.

Sample number	Sample position	Depth of slip-surface(m)	Sample identification	U-Pb isotopic data of zircons from tuff				Hf isotopic data of zircons from tuff	
				Concordia age (Ma)	MSWD	Weighted mean age (Ma)	Concordance (%)	T_{dm1} (Ma)	T_{dm2} (Ma)
3-6–5	borehole ZK3-6 (50.8 m)	78.9	Rhyolitic Crystal Tuff	124.55 ±0.85	4.63	124.5 ± 1.1	95	1124.81–1293.73	1854.72–1947.32
3-6–7	borehole ZK3-6 (61.4 m)		Lithic Crystal Tuff	127.86 ±0.32	2.7	127.85 ± 0.85	95	1202.87–1463.35	1837.98–2164.73
3-6–9	borehole ZK3-6 (89.8 m)		Tuff	128.9 ± 1.0	0.99	130.5 ± 1.3	95	1191.05–1495.59	1805.75–2259.83
3-7–3	borehole ZK3-7 (10.9 m)	59.7	Dacitic Tuff	128.28 ±1.1	2.2	128.3 ± 1.5	95	1241.90–1338.94	1906.68–2025.25
3-7–4	borehole ZK3-7 (18.8 m)		Biotite Dacitic Crystal Fragment Tuff	130.8 ±0.50	1.11	130.76 ± 0.98	95	1223.50–1285.44	1866.24–1925.32
3-7–10	borehole ZK3-7 (49.6 m)		Rhyolitic Crystal Tuff	130.33 ±1.1	7.2	130.3 ± 1.4	95	1276.05–1511.88	1946.68–2193.58
3-7–12	borehole ZK3-7 (64.5 m)		Lithic Crystal Tuff	132.52 ±0.40	1.4	132.52 ± 0.97	95	1179.22–1467.35	1798.98–2200.27

TABLE 2 U-Pb isotopic data of zircons from the Xiageliao landslide.

Sample number	Th232 ppm	U238 ppm	207Pb/206 Pb	207 Pb/235U	206 Pb/238U	208Pb/232Th	238U/232Th
			Ratio	Ratio	Ratio	Ratio	Ratio
3-6–5	450.52 ± 149.14	484.63 ± 171.78	0.05 ± 0.013	0.13 ± 0.004	0.02 ± 0.001	0.006 ± 0.001	0.19 ± 0.134
3-6–7	560.54 ± 495.140	337.80 ± 256.632	0.05 ± 0.002	0.13 ± 0.007	0.02 ± 0.001	0.006 ± 0.001	0.79 ± 0.229
3-6–9	308.32 ± 145.76	308.55 ± 171.82	0.07 ± 0.017	0.19 ± 0.060	0.02 ± 0.001	0.006 ± 0.001	1.07 ± 0.511
3-7–3	584.76 ± 470.915	358.95 ± 234.855	0.05 ± 0.003	0.14 ± 0.008	0.02 ± 0.001	0.006 ± 0.001	0.88 ± 0.446
3-7–4	578.90 ± 427.72	477.84 ± 427.721	0.05 ± 0.003	0.14 ± 0.008	0.02 ± 0.001	0.006 ± 0.001	0.87 ± 0.429
3-7–10	634.57 ± 289.973	467.84 ± 156.502	0.05 ± 0.003	0.14 ± 0.009	0.02 ± 0.001	0.006 ± 0.001	0.91 ± 0.376
3-7–12	291.63 ± 213.878	317.59 ± 221.683	0.05 ± 0.003	0.14 ± 0.009	0.2 ± 0.001	0.007 ± 0.001	1.02 ± 0.373

4 Results

According to Table 2, the Th/U values of zircons in the Xiageliao landslide range from 0.58 to 2.19, with an average value of 1.28, which is significantly greater than 0.1, indicating an apparent magmatic origin (Koschek, 1993). Tables 1 and 2 show the U-Pb zircon date results of the tuff at different depths. The Xiageliao landslide's tuff belongs to the lower Cretaceous stratum, and the test results show that the adjacent tuff stratum (15–20 m interval) has an age difference of about 1–2 Ma. This proves the multi-period eruption theory of the landslide formation mentioned above. The volcanic activity that formed the landslide tuff stratum was frequent with short intervals. According to the top and bottom stratum of the slip surface (e.g., samples 3-7-3 and 3-7–5), the age difference between the two strata is about 1 Ma, more significant than that of the tuff stratum under the same conditions in the slip-body. It is evidenced that the intervals of volcanic activity after the tuff formation as slip-bed was more prolonged than other periods. Because of the long quiet period (3.5 Ma), this tuff area received sedimentation and weathering to form the original slip-soil material.

Table 1 and Table 3 show that the 176Lu/177Hf value of zircon from the landslide tuff is 0.000669–0.003317, which is smaller than the 176Lu/177Hf (0.0093) value of the upper crust (Vervoort et al., 1996). The 176Hf/177Hf value is 0.282210–0.282417. The average value is 0.282333, and fLu/Hf = −0.98~-0.90, which is less than the value of mafic crust value (−0.34) and silica-aluminum crust value (−0.72) (Vervoort et al., 1996; Amelin et al., 2000). The εHf(t) ranges from −17.13 to −9.71, indicating that the zircon originated from the re-melting of the ancient crust. The samples' two-stage model age (T_{dm2}) can better reflect when tuff was extracted from the depleted mantle or the mean age of source rock in the crust. The two-stage model age is between 1798.98 Ma and 2193.58 Ma, which belongs to the Paleoproterozoic and extends from the early Paleoproterozoic to the middle and late Paleoproterozoic. Although the εHf(t) of each sample is negative, the variation interval of the εHf(t) is eight ε units, which exceeds the error caused by the analysis method (Wu et al., 2006). The magma heterogeneity should cause it (Bolhar et al., 2008; Mo et al., 2009). Combined with the calculation results of the two-stage model age, it can be concluded that the magma formed tuff is from the continental crust material, but the specific material source, melting time, and volcanic edifice are different.

For the analysis of the mineralogical composition of the landslide material, we took two samples of tuff from the slip body above the slip soil, one sample of yellowish-brown slip soil, one sample of greenish-gray tuff that had been clayed under the slip soil, and two samples of tuff from the slip bed from the exploration tunnels. The test results of these samples can be seen in Figure 9, numbered A to F in that order.

Figures 9A,B presents slip-body tuff, and Figures 9E,F shows slip-bed tuff. The tuff has low clay mineral content (14.2%–30.8%) and very high clastic mineral content, especially quartz (50.8%–58.6%), typical volcanic clastic rock. Figures 9C,D shows the result as clay, among which Figure 9C is slip-soil with the highest clay mineral content (41.2%) and the lowest quartz content (16.01%). Although Figure 9D shows the result as clay-like, the overall mineral composition, especially the quartz content, differs significantly from the surrounding tuff and has prominent inheritance characteristics. It can be judged as the weathering

TABLE 3 Hf isotopic data of zircons from the Xiageliao landslide.

Sample number	Hf176/Hf177	Lu176/Hf177	εHf(t)	fLu/Hf
3-6–5	0.28238 ± 0.00002	0.00138 ± 0.00059	−11.38512 ± 0.78866	−0.95558 ± 0.00442
3-6–7	0.28233 ± 0.00007	0.00177 ± 0.00110	−12.98760 ± 2.60296	−0.94675 ± 0.03309
3-6–9	0.28231 ± 0.0010	0.00134 ± 0.00043	−13.45365 ± 3.68028	−0.95914 ± 0.01283
3-7–3	0.28235 ± 0.0003	0.00120 ± 0.00040	−12.40956 ± 0.94716	−0.96382 ± 0.01200
3-7–4	0.28238 ± 0.00001	0.00165 ± 0.00053	−11.25333 ± 0.46768	−0.95029 ± 0.01604
3-7–10	0.28230 ± 0.00005	0.00215 ± 0.00117	−14.05297 ± 1.96205	−0.93517 ± 0.03509
3-7–12	0.28233 ± 0.0009	0.00140 ± 0.00058	−12.89645 ± 3.18181	−0.95770 ± 0.01742

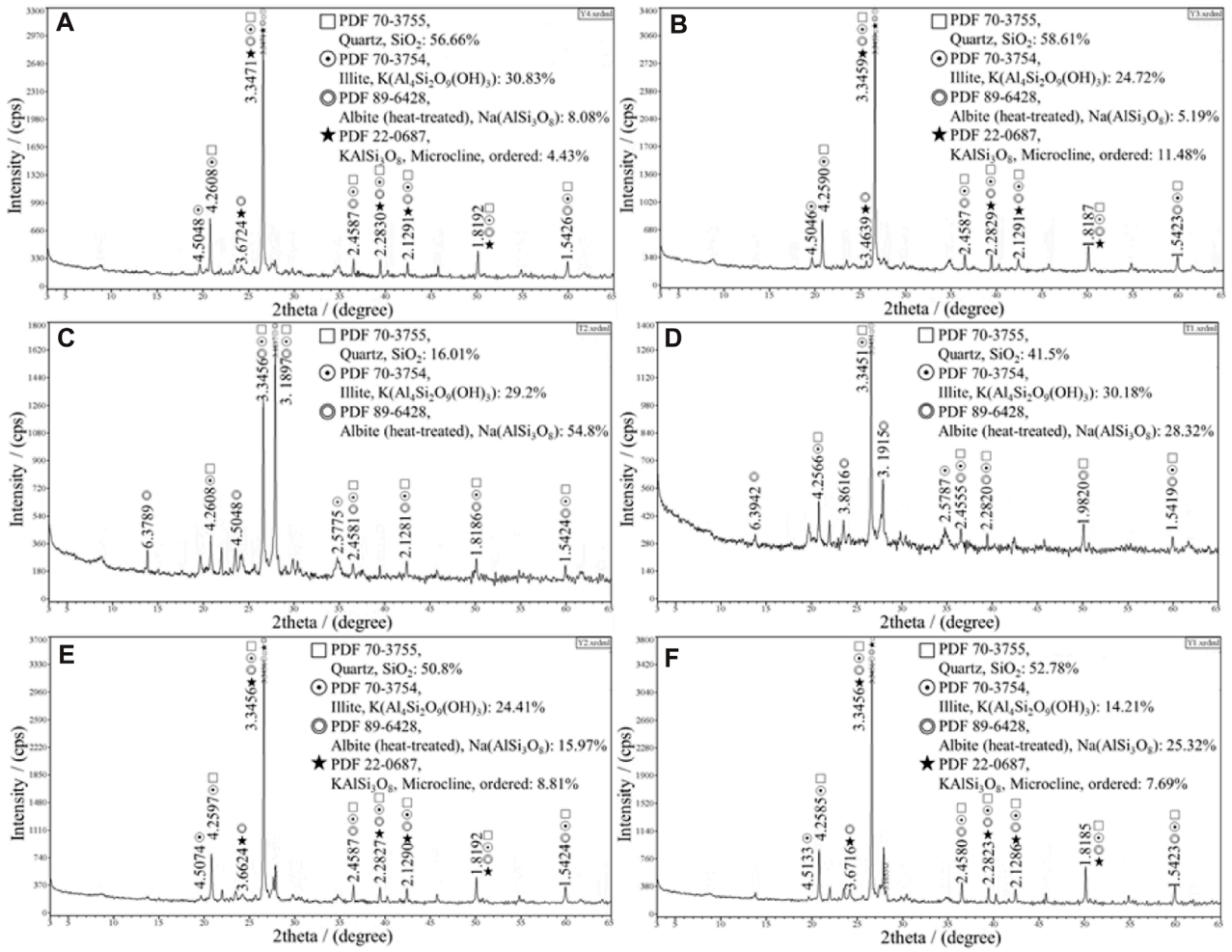

FIGURE 9
Mineral composition analysis of landslide material. **(A)** Tuff of the slip- body. **(B)** Tuff above slip soil. **(C)** Yellow-brown slip soil. **(D)** Greenish gray clay below slip soil. **(E)** Slip-bed tuff. **(F)** Slip-bed tuff.

disintegration production of tuff. After field identification and laboratory observation, no significant diagenetic signs and no rock skeleton were found in the slip-soil (Figure 9C). The content of quartz (Figure 9C) is much lower than that of tuff or its hydrolyzed clay (Figure 9 (d)). As a very stable mineral, quartz is unlikely to disappear due to weathering and hydrolysis. Similarly, quartz cannot be migrated out in such an occurrence environment. In other words, this yellow-brown clay did not develop from tuff, and these two are not homologous. It is not possible that the tuff formation was followed by the formation of a continuous

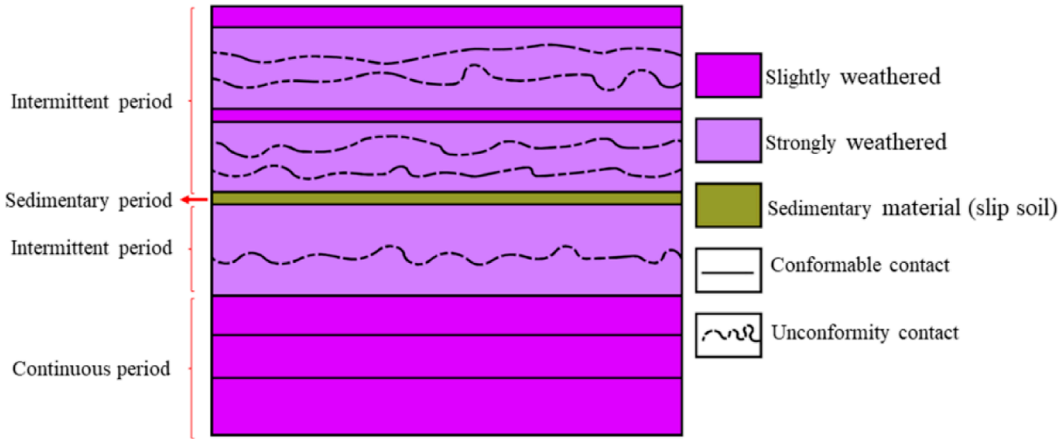

FIGURE 10
Model diagrams of tuff and slip soil formation.

clay stratum 90 m deep from the external material. It can only be formed in the early Cretaceous with tuff, and it is inferred that it is the production of sedimentary material during the eruption interval.

5 Conclusion

After the investigation and test results of the Xiageliao landslide, the following conclusions are drawn:

(1) The Xiageliao landslide was developed in a complex set of tuff strata. The tuff in the landslide area consisted of many different types with different levels of weathering. Through microscopic identification, it is found that these tuffs at different depths have different tectonic traces. This indicates that the formation of the tuff strata in the landslide area results from multiple volcanic activities and phases of tectonic action.

(2) The slip surface of the Xiageliao landslide is a continuous layer of yellowish-brown clay with a maximum depth of 90 m. By comparing the mineral composition of the slip soil and the tuff above and below it, it can be seen that it is not a product of tuff disintegration and weathering but was formed by the deposition of external materials. Combined with the location of the slip soils and the zircon dating results, the slip soils should be the products of sediments deposited during the intervals of volcanic activities.

(3) According to zircon dating, the tuffs at different depths are close in age of formation, but there is still a particular age gap. Combined with the microscopic identification and other auxiliary results, it can be concluded that several volcanic activities with short intervals formed this group of stratum. These volcanic activities were partially subjected to sedimentation during quiet periods. Similarly, during the quiet periods, the tuff strata that had been formed at that time were subjected to weathering and tectonic activities, resulting in the recurrence of strongly weathered and weakly weathered tuffs.

(4) According to Hf isotope analysis, more than one volcanic activity formed the tuff, and the melting time of the original magmatic material from these volcanic activities varied at different times. This explains the complex variations in tuff types and compositions in the landslide area.

Based on the above conclusions about the Xiageliao landslide, we can summarize the mechanism by which the tuff formed a large-scale deep-seated landslide, as shown in Figure 10. The multiple volcanic activities that formed the tuff stratum occurred discontinuously, with partially longer quiet periods long enough to receive enough sedimentary material. The repeated occurrence of this continuous eruption-interrupted process creates a complex stratum assemblage. When external conditions such as tectonic movements, river incision, and artificial slope cutting are appropriate, landslides can occur along the weak interlayers of sedimentary or weathered strata formed during the eruption-pause process as rainfall or groundwater changes.

Data availability statement

The original contributions presented in the study are included in the article/Supplementary Material, further inquiries can be directed to the corresponding author.

Author contributions

MX: Conceptualization, Data curation, Formal Analysis, Funding acquisition, Investigation, Methodology, Project administration, Resources, Software, Supervision, Validation, Visualization, Writing–original draft, Writing–review and editing. GX: Data curation, Investigation, Methodology, Project administration, Writing–review and editing. FY: Investigation, Data curation, Methodology, Writing–review and editing. ZM: Data curation, Investigation, Writing–review and editing.

Funding

The author(s) declare financial support was received for the research, authorship, and/or publication of this article. This study was supported by the project "Research on Characteristics and Prevention Technology of Large-scale Deep-seated Tuff Landslide (2017K03)" from China Railway Siyuan Survey and Design Institute Group Corporation Limited. We are very grateful for this.

Conflict of interest

Author FY was employed by China United Engineering Corporation Limited. Author ZM was employed by China Energy Engineering Group Yunnan Electric Power Design Institute.

The remaining authors declare that the research was conducted in the absence of any commercial or financial relationships that could be construed as a potential conflict of interest.

Publisher's note

All claims expressed in this article are solely those of the authors and do not necessarily represent those of their affiliated organizations, or those of the publisher, the editors and the reviewers. Any product that may be evaluated in this article, or claim that may be made by its manufacturer, is not guaranteed or endorsed by the publisher.

References

Amelin, Y., Lee, D. C., and Halliday, A. N. (2000). Early-middle Archaean crustal evolution deduced from Lu-Hf and U-Pb isotopic studies of single zircon grains. *Geochim. Cosmochim. Acta* 64, 4205–4225. doi:10.1016/S0016-7037(00)00493-2

Beisner, K. E. (2011). "Dynamic displacement analysis of a shallow landslide in Norwood tuff," in *First international symposium on uncertainty modeling and analysis and management (ICVRAM 2011) and fifth international symposium on uncertainty modeling and anaylsis (ISUMA)* (The University of Utah ProQuest Dissertations Publishing). Available at: https://ascelibrary.org/doi/epdf/10.1061/41170%28400%2980.

Benito, R., Garcia-Guinea, J., Walle-Fuentes, F. J., and Recio, P. (1998). Mineralogy, geochemistry and uses of the mordenite–bentonite ash-tuff beds of Los Escullos, Almeria, Spain. *J. Geochem. Explor.* 62, 229–240. doi:10.1016/S0375-6742(97)00075-7

Bolhar, R., Weaver, S. D., Whitehouse, M. J., Palin, J. M., Woodhead, J. D., and Cole, J. W. (2008). Sources and evolution of arc magmas inferred from coupled O and Hf isotope systematics of plutonic zircons from the Cretaceous Separation Point Suite (New Zealand). *Earth Planet. Sci. Lett.* 268, 312–324. doi:10.1016/j.epsl.2008.01.022

Grevenitz, P., Carr, P., and Hutton, A. (2003). Origin, alteration and geochemical correlation of late permian airfall tuffs in coal measures, Sydney basin, Australia. *Int. J. Coal Geol.* 55, 27–46. doi:10.1016/S0166-5162(03)00064-8

Haaland, H. J., Furnes, H., and Martinsen, O. J. (2000). Paleogene tuffaceous intervals, Grane field (block 25/11), Norwegian north sea: their depositional, petrographical, geochemical character and regional implications. *Mar. Pet. Geol.* 17, 101–118. doi:10.1016/S0264-8172(99)00009-4

He, B., Xu, Y., Huang, X., Luo, Z., Shi, Y., Yang, Q., et al. (2007). Age and duration of the Emeishan flood volcanism, SW China: geochemistry and SHRIMP zircon U–Pb dating of silicic ignimbrites, post-volcanic Xuanwei Formation and clay tuff at the Chaotian section. *Earth Planet. Sci. Lett.* 255, 306–323. doi:10.1016/j.epsl.2006.12.021

Hints, R., Kirsimäe, K., Somelar, P., Kallaste, T., and Kiipli, T. (2006). Chloritization of late ordovician k-bentonites from the northern baltic palaeobasin–influence from source material or diagenetic environment? *Sediment. Geol.* 191, 55–66. doi:10.1016/j.sedgeo.2006.01.004

Hu, Z., Liu, Y., Gao, S., Liu, W., Zhang, W., Tong, X., et al. (2012). Improved *in situ* Hf isotope ratio analysis of zircon using newly designed x skimmer cone and jet sample cone in combination with the addition of nitrogen by laser ablation multiple collector ICP-MS. *J. Anal. At. Spectrom.* 27, 1391–1399. doi:10.1039/c2ja30078h

Hu, Z., Zhang, W., Liu, Y., Gao, S., Li, M., Zong, K., et al. (2015). Wave" signal-smoothing and mercury-removing device for laser ablation quadrupole and multiple collector ICP MS analysis: application to lead isotope analysis. *Anal. Chem.* 87, 1152–1157. doi:10.1021/ac503749k

Koschek, G. (1993). Origin and significance of the SEM cathodoluminescence from zircon. *J. Microsc.* 171, 223–232. doi:10.1111/j.1365-2818.1993.tb03379.x

Liu, Y., Gao, S., Hu, Z., Gao, C., Zong, K., and Wang, D. (2010). Continental and oceanic crust recycling-induced melt-peridotite interactions in the trans-north China orogen: U-Pb dating, Hf isotopes and trace elements in zircons from mantle xenoliths. *J. Petrol.* 51, 537–571. doi:10.1093/petrology/egp082

Liu, Y., Hu, Z., Gao, S., Günther, D., Xu, J., Gao, C. G., et al. (2008). *In situ* analysis of major and trace elements of anhydrous minerals by LA-ICP-MS without applying an internal standard. *Chem. Geol.* 257, 34–43. doi:10.1016/j.chemgeo.2008.08.004

Lu, Z. (1993). Landslides and geotechnical properties of volcanic tuff on Mount Cayley, British Columbia. Thesis. Canada: University of Alberta (Canada) ProQuest Dissertations Publishing.

Ludwig, K. R. (2003). *Isoplot 3.00: a geochronological toolkit for microsoft excel*. California, Berkeley: Berkeley Geochronology Center, 39.

Maeda, H., Kohno, M., Shigenori, H., Sawano, H., and Higaki, S. (2014). Geological characteristics of dip slope type landslides occurred on hard shale dominant formation in the green tuff region: an example of the Oshinkoshin landslide area in the Shiretoko peninsula, east Hokkaido, Japan. *J. Jpn. Landslide Soc.* 51, 1–9. doi:10.3313/JLS.51.81

Masahiro, C. (2016). Disasters caused by deep-seated catastrophic landslides and prediction of their potential sites. *J. Southwest Jiaot. Univ.* 51, 981–986. doi:10.3969/j.issn.0258-2724.2016.05.022

Mo, X., Dong, G., Zhao, Z., Zhu, D., Zhou, S., and Niu, Y. (2009). Mantle input to the crust in southern gangdese, tibet, during the cenozoic: zircon Hf isotopic evidence. *J. Earth Sci.* 20, 241–249. doi:10.1007/s12583-009-0023-2

Olsen, P. E. (1999). Giant lava flows, mass extinctions, and mantle plumes. *Science* 284, 604–605. doi:10.1126/science.284.5414.604

Rampino, M. R., and Stothers, R. B. (1988). Flood basalt volcanism during the past 250 million years. *Science* 241, 663–668. doi:10.1126/science.241.4866.663

Shuzui, H. (2001). Process of slip-surface development and formation of slip-surface clay in landslides in tertiary volcanic rocks, Japan. *Eng. Geol.* 61, 199–220. doi:10.1016/S0013-7952(01)00025-4

Shuzui, H., and Shimoda, S. (1987). Clay minerals of landslide clays in the Kunimi area, Toyama prefecture. *Nendo Kagaku* 27, 211–220. doi:10.11362/jcssjnendokagaku1961.27.211

Trandafir, A. C., and Amini, Z. A. (2009). Yielding mechanism of shallow mass movements in completely decomposed Norwood tuff: the zigzag sign landslide, Utah. *Environ. Geol.* 57, 1443–1451. doi:10.1007/s00254-008-1422-x

Vervoort, J. D., Patchett, P. J., Gehrels, G. E., and Nutman, A. P. (1996). Constraints on early earth differentiation from hafnium and neodymium isotopes. *Nature* 379, 624–627. doi:10.1038/379624a0

Wignall, P. B. (2001). Large igneous provinces and mass extinctions. *Earth-Sci. Rev.* 53, 1–33. doi:10.1016/S0012-8252(00)00037-4

Wu, F., Yang, Y., Xie, L., Yang, J., and Xu, P. (2006). Hf isotopic compositions of the standard zircons and baddeleyites used in U-Pb geochronology. *Chem. Geol.* 234, 105–126. doi:10.1016/j.chemgeo.2006.05.003

Xu, Y. G., He, B., Chung, S. L., Menzies, M. A., and Frey, F. A. (2004). Geologic, geochemical, and geophysical consequences of plume involvement in the Emeishan flood-basalt province. *Geology* 32, 917–920. doi:10.1130/G20602.1

Zong, K., Klemd, R., Yuan, Y., He, Z., Cuo, J., Shi, X., et al. (2017). The assembly of Rodinia: the correlation of early Neoproterozoic (ca. 900 ma) high-grade metamorphism and continental arc formation in the southern Beishan orogen, southern central Asian orogenic belt (Caob). *Precambrian Res.* 290, 32–48. doi:10.1016/j.precamres.2016.12.010

frontiers | Frontiers in Earth Science

TYPE Original Research
PUBLISHED 06 March 2024
DOI 10.3389/feart.2024.1375979

Check for updates

OPEN ACCESS

EDITED BY
Pengjiao Jia,
Soochow University, China

REVIEWED BY
Chaoxuan Zhang,
Taizhou University, China
Cheng Lyu,
Sichuan University, China

*CORRESPONDENCE
Li Wang,
21203077017@stu.xust.edu.cn

RECEIVED 24 January 2024
ACCEPTED 20 February 2024
PUBLISHED 06 March 2024

CITATION
Zhang J, Wang L, Yang T, Gao S, He Y and Wu J (2024), Study on overburden failure characteristics and ground pressure behavior in shallow coal seam mining underneath the gully.
Front. Earth Sci. 12:1375979.
doi: 10.3389/feart.2024.1375979

COPYRIGHT
© 2024 Zhang, Wang, Yang, Gao, He and Wu. This is an open-access article distributed under the terms of the Creative Commons Attribution License (CC BY). The use, distribution or reproduction in other forums is permitted, provided the original author(s) and the copyright owner(s) are credited and that the original publication in this journal is cited, in accordance with accepted academic practice. No use, distribution or reproduction is permitted which does not comply with these terms.

Study on overburden failure characteristics and ground pressure behavior in shallow coal seam mining underneath the gully

Jie Zhang[1,2], Li Wang[1]*, Tao Yang[1,2], Shoushi Gao[1], Yifeng He[1] and Jianjun Wu[1]

[1]School of Energy, Xi'an University of Science and Technology, Xi'an, China, [2]Key Laboratory of Mine Mining and Disaster Prevention in West China, Ministry of Education, Xi'an University of Science and Technology, Xi'an, China

Introduction: This study focuses on investigating the characteristics of overburden failure and ground pressure behavior in shallow coal seam mining beneath a gully. The research is conducted at the 135201 working face of Shaliang Coal Mine in the Shenfu Mining Area.

Methods: The study employs physical similarity simulation tests, theoretical analysis, and field measurements to analyze the ground pressure and overburden failure characteristics at the working face.

Results: The research findings indicate that the ground pressure is stronger in the uphill section compared to the gully bottom and downhill sections. The weighting interval in the uphill section is the smallest. A mechanical analysis model for the failure structure of the key stratum in the uphill section is established based on monitored ground pressure data and physical simulation test results. A calculation formula for the weighting interval in the uphill section is derived. The relationship between the caving interval, the thickness of the key stratum in the uphill section, and the gully slope is also analyzed. The on-site measurements align well with the theoretical results.

Discussion: The study proposes a prediction method for ground pressure and suggests hazard prevention and control measures for shallow coal seam mining beneath a gully based on the research findings.

KEYWORDS

shallow coal seams, gully terrain, failure characteristic, key stratum, ground pressure law

1 Introduction

In the mining area of western China, there exists a significant number of shallow buried coal seams with large surface fluctuations, particularly in gully development areas. These areas exhibit more complex geological conditions compared to general terrains. The mining of shallow buried coal seams in gully terrains is susceptible to geological hazards, including landslides, surface subsidence, and dynamic load pressure, with the latter being particularly prominent (Yang et al., 2021; Feng et al., 2022; Miao et al., 2022).

The diversified occurrence of gully slopes contributes to more severe mine pressure behavior for shallow buried coal seams in comparison to general terrains, as observed in production practice and related research. Specifically, the working face experiences shorter pressure durations, accompanied by greater and more destructive pressure levels. Consequently, serious geological disasters, such as frame crushing, roof fall, and rib spalling, occur within the working face, significantly endangering mine safety and production (Huang, 2002; Xu et al., 2009; Zhang et al., 2017; Dai et al., 2018; Dai et al., 2020; Dai et al., 2022; Wang Q. et al., 2023; Zhang B. et al., 2023; Dai et al., 2023; Liu et al., 2023; Pan and Wang, 2023). Hence, urgent research efforts are required to mitigate the occurrence of sudden disasters.

To address the intricate geological issue of abnormal pressure on the working face resulting from mining shallow buried coal seams in gully terrains, scholars in the field have conducted the following research studies. Zhang et al. (Zhang et al., 2011) and Ma and Kang (Ma and Kang, 2022) studied the ground pressure law at the working face for shallow coal seam mining underneath the gully through the on-site measurement and the theoretical analysis, and they concluded that the support resistance at the working face increased significantly in the uphill section. Wang et al. (Wang et al., 2010) studied the structural evolution law of the mining slope underneath the gully with the physical simulation and theoretical analysis, and then established a mechanical analysis model for initial failure of the main roof of shallow coal seam underneath the gully. The research results indicated that the failed rock blocks in the overburden occurred rotary sinking with the advancement of the working face, and that the larger the slope angle, the more obvious the ground pressure behavior. Li et al. (Li J. et al., 2016; Li et al., 2019) conducted an in-depth study on the factors affecting the ground pressure behavior in shallow coal seams, and concluded that the thickness of key stratum was the most important factor affecting the weighting interval. Zhao et al. (Zhao et al., 2018) investigated the ground pressure law during the shallow and thick coal seam mining underneath the gully through the numerical simulation, and discovered that the influence zone of original rock stress field on the mining pressure law at the working face underneath the gully could be divided into significant, attenuated, and unaffected zones according to the depth of the coal seam. Li et al. (Li et al., 2020), through theoretical analysis and physical simulation, explored the influence of slope angle, height, and direction on the stability of masonry beam structures. Wang et al. (Wang X. et al., 2023) argued that gully topography modifies the original stress field of the rock mass and leads to significant stress concentration during coal seam mining.

Yang et al. (Yang et al., 2020) investigated the overburden structure and mining pressure law in the shallow fully-mechanized top-coal caving face. The findings revealed that the high-level key stratum masonry beam structure and the low-level key stratum cantilever beam structure were destabilized by the influence of mining, resulting in strong ground pressure at the working face. Based on the variations of the support resistance at the mining working face underneath the gully, Xiao et al. (Xiao and Yao, 2021) concluded that the main and secondary factors affecting the working resistance of the support at the working face were the gully cutting coefficient and the slope foot, respectively. Zhang et al. (Zhang et al., 2019; Zhang et al., 2021) studied the dynamic loading problem of the working face underneath the gully through physical simulation, and they constructed the "non-uniformly loaded beam structure", and revealed the mechanism of the dynamic ground pressure generated by the non-uniform loads. Through numerical analysis and physical simulation, Huang et al. (Huang and Du, 2018) studied the relationship between the stress concentration of coal pillars in multi-coal seam mining and the staggered distance of section coal pillars and the development of overburden fractures. The research shows that the mechanism of slowing down the concentrated stress of coal pillar group and realizing the uniform settlement of ground surface. Yu et al. (Yu et al., 2020) conducted a study using PFC2D to investigate the impact of coal mining on the deformation and failure characteristics of high and steep slopes. Xu et al. (Xu et al., 2016) examined the influence of underground mining on the rock strata and surface of open-pit slopes through discrete element numerical simulation. Zhao et al. (Zhao et al., 2023) focused on the effect of coal mining on the stability of loess slopes using physical simulation, identifying the slope angle and height as crucial factors for slope stability. Tang et al. (Tang et al., 2019) developed a fracture model for bedding rock slopes and verified its reliability through physical simulation. Zhang et al. (Zhang D. et al., 2023) investigated the impact of different gully topographies on working face pressure using optical fiber and digital image technology. Dai et al. (Dai et al., 2021) obtained through physical simulation that the failure mode of the bedding rock slope under mining disturbance is the landslide form of the initial traction later stage. The breaking characteristics and movement law of rock strata are of great significance for revealing the law of mine pressure in working face. Researchers have put forward many hypotheses of rock fracture structure (Li Z. et al., 2016; Yiouta-Mitra and Sofianos, 2018). Among them, the key stratum hypothesis proposed by Chinese academician Qian has been widely used to reveal the relationship between the fracture structure of overburden rock and the law of mine pressure in working face. However, this hypothesis simplifies the load of key stratum to uniform load. For coal seams with large buried depth and small surface fluctuation, this hypothesis is very suitable. However, for shallow coal seams with gully surface, if the surface load is simplified to uniform load, it will produce large errors. Therefore, in this study, the load of key stratum of shallow coal seam under gully terrain is simplified to linear load.

The existing research mainly focuses on the factors affecting the stability of the slope and the analysis of the stability of the slope (He et al., 2015a), and the control method of the stability of the slope (He et al., 2015b; Lai et al., 2024; Lu et al., 2024). The research methods mainly include field measurement, theoretical analysis, physical simulation and numerical simulation. The above research results and research methods are very important, but due to the diversity of geological occurrence conditions, it is difficult to achieve individual cases to guide the safe and efficient mining of the mine in this paper. Therefore, with reference to the terrain and ground pressure features of the research area as well as the on-site operating conditions, this paper took the 135,201 working face of Shaliang Coal Mine in Shenfu Mining Area as the research object to analyze the overburden failure characteristics and ground pressure law of the working face underneath the gully. A mechanical calculation model of the key stratum for mining underneath the gully was established,

and the key stratum caving and its influencing factors were analyzed. The results of the study can provide meaningful guidance for the prevention and control of ground pressure-related hazards in the working face for shallow coal seam mining underneath the gully.

2 Engineering background and ground pressure behavior

2.1 Overview of the project

Shaliang Coal Mine is located in Shenfu mining area, Shaanxi Province, China, with a length of 8.4 km from east to west and a width of 5.9 km from north to south, and the depth of the coal seams ranges from 40 to 150 m. There are 5 layers of recoverable coal seams, where the 5-2 coal seam featured by a relatively stable thickness and an uncomplicated structure is mainly mined at present.

The terrain of the mine field is a typical gully and valley landform, with numerous gullies and ridges forming natural watersheds along the north-east to south-west direction. There are Daxi Gully, Maimai Gully, and Luancai Gully developed from west to east in the mine field. The depth of the gully in the Shaliang Coal Mine area is generally 10–60 m, with an average depth of 35 m. The width of the gully is 34–780 m, with an average width of 407 m. The gully slope is 8°–38°, with an average slope of 23°.

There is only one working face (i.e., 135,201 working face) in Shaliang Coal Mine, whose coal seam thickness ranges from 2.90 to 3.34 m, with an average of 3.12 m, and the dip angle of the coal seam ranges from 0° to 2°. Its immediate roof is siltstone with a thickness of 4.75 m, and its main roof is medium-grained sandstone with an average thickness of 9.1 m. Its immediate floor is sandy mudstone with an average thickness of 3.4 m, and its main floor is fine-grained sandstone with an average thickness of 10 m.

The ground surface above 135,201 working face is undulating, which is low in the middle and high on both sides. The maximum elevation is 1,248 m, which is 1,320 m away from the open-off cut of the working face. The minimum elevation is 1,168 m, which is located in the 795 m section of the return airway of the 135,201 working face, i.e., it is in the gully at the northwestern part of Yangye village. The location of the working face and the development of surface fractures are illustrated in Figure 1.

2.2 Distribution characteristics of ground pressure at the working face underneath the gully

When the 135,201 working face passed through the gully, the ground pressure monitoring was conducted on the upper, middle, and lower regions of a total of 21 supports at the working face by means of the KJ440 Coal Mine Roof Pressure Monitoring System. The pressure distribution characteristic of each support during working face advancement was drawn according to the monitoring data. The difference between the ground pressures in the downhill and uphill sections of the gully was analyzed to understand the pressure pattern when the working face passed through the gully terrain.

2.2.1 Ground pressure behavior in the downhill section

Figure 2 presents the distribution characteristic of the support resistances at the working face. It was observed that the average periodic weighting interval in the downhill section of the gully terrain was 16.95 m. The support resistance during the weighting was 20–22 kN, with an average of 20.5 kN. The ground pressure behavior at the working face in the downhill section was more moderate. The ground pressure was characterized by the fact that the weighting firstly occurred in the head or tail region of the working face, and then shifted to the middle part as the working face advanced. The resistance of the supports accounted for about 78% of the rated working resistance. During the weighting, the coal wall of the working face experienced flaking, which was mainly concentrated in the region of 60#-110# supports in the middle, and the depth of flaking was generally 500 mm.

2.2.2 Ground pressure behavior in the uphill section

The average periodic weighting interval in the uphill section of the gully terrain was 16.95 m, which indicated that the overburden transport at the working face in the uphill section was stronger than that in the downhill section. During the weighting, the support resistances were 20–22 kN, with an average of 21 kN. The flaking was observed in 40–126# supports when the weighting occurred in the working face, with the depth of flaking being 300–800 mm, and there were occasional roof leakage in front of the individual supports.

2.2.3 Characterization of ground pressure behavior

When the 135,201 working face in Shaliang Coal Mine crossed the gully terrain, the weighting in the uphill section was stronger than that in the downhill section. The weighting was occasionally accompanied by flaking and roof leakage, but the overall depth of flaking was not large, and the safety valve of the support had not been opened. No dynamic loading ground pressure occurred in the section of the working face crossing the gully, which was obviously different from the existing dynamic loading ground pressures at the working face crossing the gully. The main reason for this was that the main key stratum was covered by loess when the 135,201 working face passed through the gully terrain. The working face that was not affected by weathering and stripping did not experience dynamic loading during the passage through the gully terrain, which ensured the recovery safety of the working face.

3 Physical similarity simulation test on the working face crossing the gully

3.1 Design of the similarity simulation test

A similarity simulation test was conducted to study overburden caving and failure characteristics when the working face passed through the gully, and to analyze the influence of fracture development on the recovery safety of the working face. The design

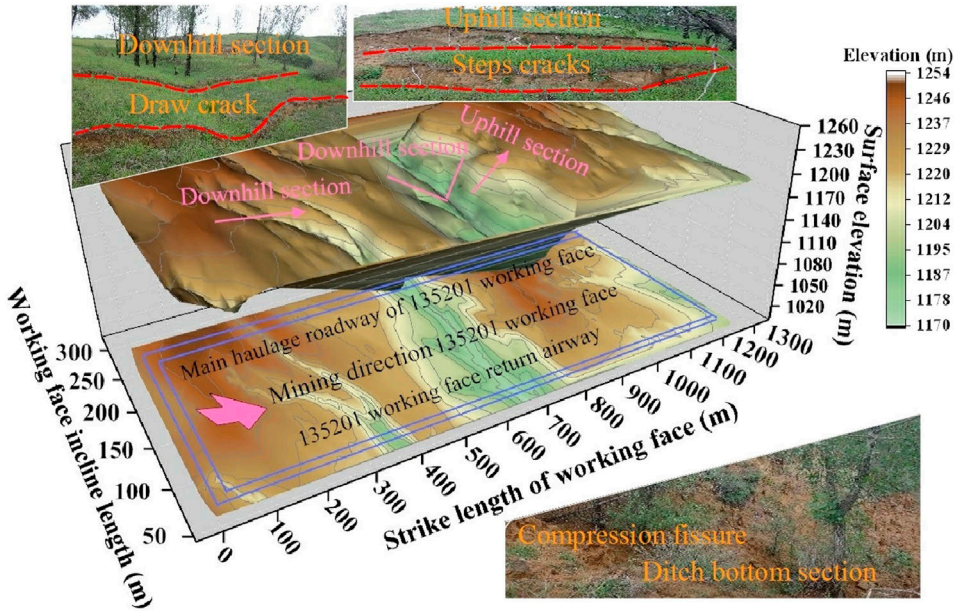

FIGURE 1
Surface terrain and damage characteristics above the working face.

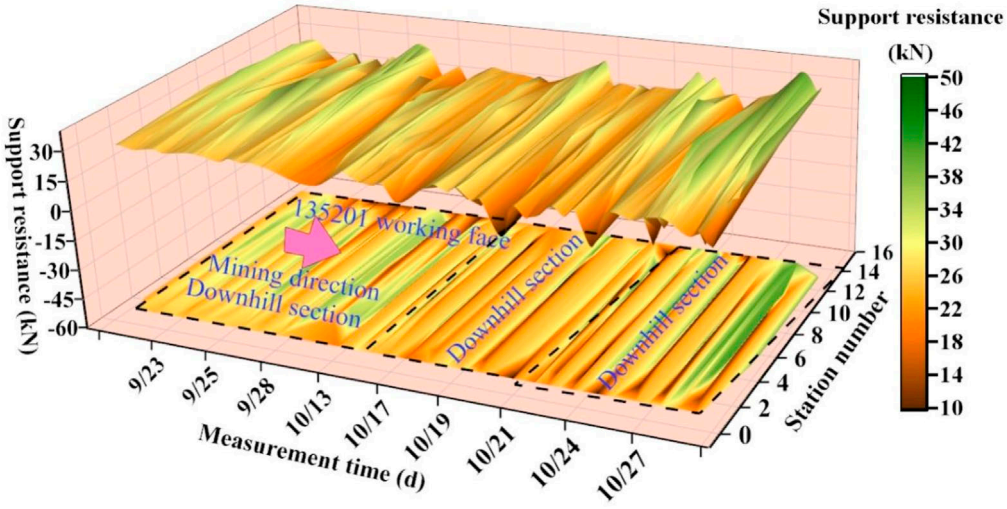

FIGURE 2
Support resistance distribution at the 135,201 working face.

diagram of the similarity simulation test is presented in Figure 3. According to the geological conditions of the 135,201 working face, a 3 m × 1.3 m planar simulation experiment platform was designed to study the terrain conditions such as downhill scenario, gully scenario, and uphill scenario, respectively. Based on the physical similarity constants, the similarity ratios of geometry, stress, and time of the model were taken as 1:100, 1:80 and 1:4, respectively, and the similarity ratios of dimensionless physical parameters (e.g., internal friction angle, strain, Poisson's ratio, coefficient of friction, *etc.*) were all set to be 1.

The LY-350 pressure sensor was used to monitor the floor pressure during the advancement of the working face, and the AD-36 pressure computer data collector was used to collect the pressure data. The 128-channel data analysis system was adopted to process the data. These data were used to investigate the ground pressure behavior in the uphill, gully bottom, and downhill sections. The displacement monitoring system mainly consists of PENTAXR-322NX optical total station and GOM ARAMIS system. A total of three roof displacement observation lines were embedded in the model, which were labeled as R1-R3.

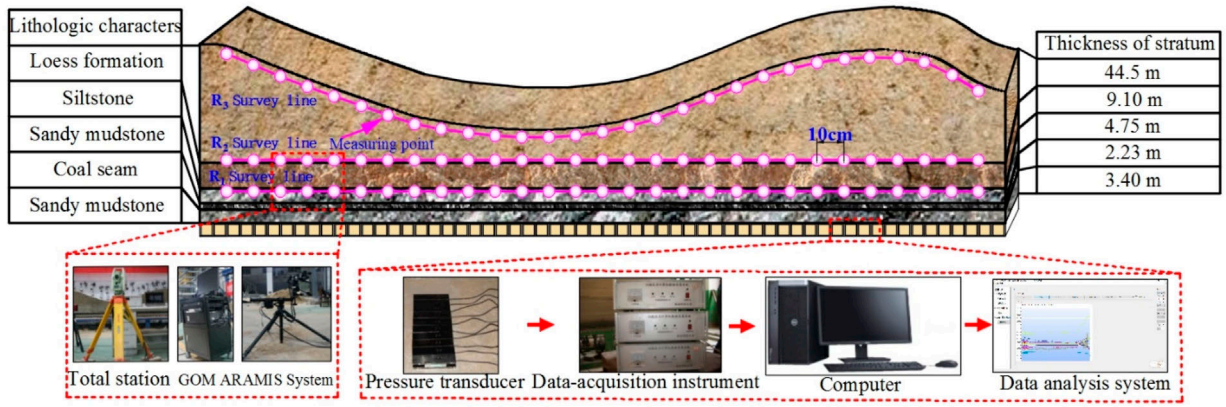

FIGURE 3
The design diagram of the similarity simulation test.

TABLE 1 The mixing ratios of similar materials.

Number of rock layer	Name of rock layer	Thickness of rock layer (m)	Thickness of the model (cm)	Ratio (sand: gypsum: calcium carbonate)	Compressive strength (MPa)	Elastic modulus (GPa)	Cumulative height (cm)
1	Loess	44.5	44	919 20 1			66.5
2	Siltstone	9.10	9.5	837 8.53:0.32:0.75	25	20	22.5
3	Sandy mudstone	4.75	5.5	837 8.53:0.32:0.75	19	17	13.0
4	5–2 coal	2.23	2.5	2.1 0.10:0.52:2.10	13	15	7.5
5	Sandy mudstone	3.40	5.0	837 8.53:0.32:0.75	19	17	50.0

With consideration of the lithology of the roof and floor of Shaliang Coal Mine as well as the experimental demand, the parameters of the roof and floor of the 135,201 working face were simplified, and the physical and mechanical parameters of each stratum were determined according to the similarity theory. The similar material used river sand as aggregate, gypsum and calcium carbonate as cement, and a layer of mica as the lamination was laid at the interface of rock layers. The mixing ratios of similar materials are summarized in Table 1.

3.2 Analysis of overburden failure characteristics

The first weighting occurred in the downhill section when the working face advanced to 42 m, and the failure length of the main roof was 32 m. When the working face advanced to 80 m, the caving occurred in the lower part of the main roof, forming a hinge structure with the coal wall ahead of the working face. The second periodic weighting happened in the working face, with a weighting interval of 19 m, as depicted in Figure 4A. When the working face advanced to 115 m, 140 m, and 170 m respectively, three times of periodic weighting occurred in the gully bottom mining section, with the weighting intervals of 35.2 m, 25.0 m, and 29.8 m, and the average weighting interval of 30.0 m. The surface at the gully experienced stepwise subsidence, as displayed in Figure 4B. When the working face advanced from the gully bottom mining section to the uphill mining section, the working face in the uphill section underwent four times of periodic weighting at 185 m, 200 m, 215 m, and 230 m, with the weighting intervals of 15.3 m, 15.2 m, 14.9 m, and 15.4 m, respectively, and the average weighting interval of 15.2 m. The overburden fractures were mainly tensile fractures when the working face advanced to the uphill section, and the width of surface fractures was 1.5 m, with a vertical stagger of 1 m, as illustrated in Figure 4C. When the working face advanced to the convex terrain mining section, two times of periodic weighting occurred when the working face advanced to 245 m and 260 m. The weighting intervals were 17.5 m and 19.8 m, with an average weighting interval of 18.7 m. With the advancement of the working face, the fractures in the uphill section were closed, and new fractures were formed on the right side of the convex terrain, and the loess layer at the slope top was

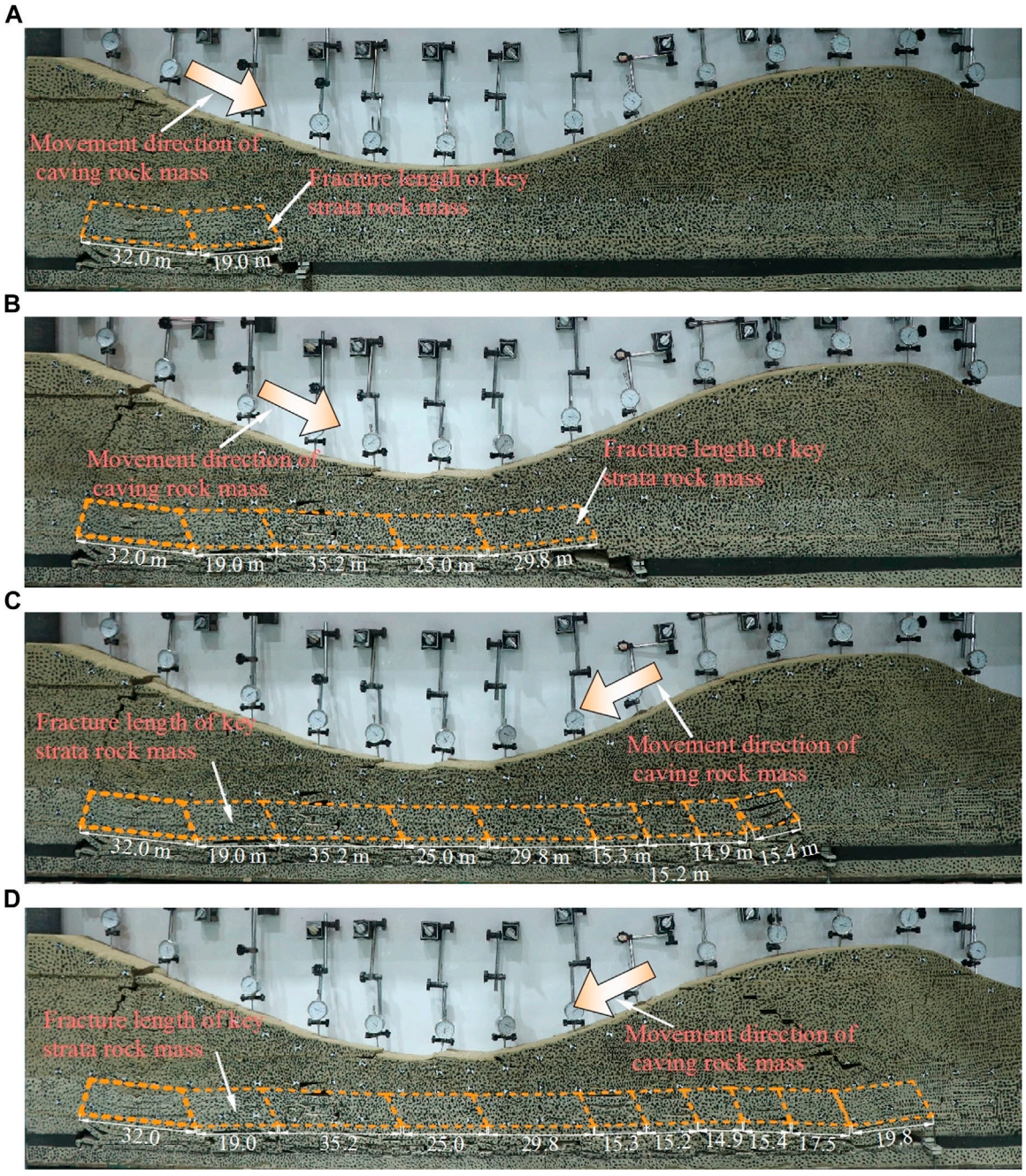

FIGURE 4
Characteristics of overburden caving during the advancement of working face. The number marked in the diagram is the key layer collapse distance.

formed into a V-shape structure, as illustrated in Figure 4D. Due to the different thicknesses of the loose layer in each section, the average periodic weighting was also different, where the order of the weighting interval was the gully bottom section > downhill section > uphill section. The damage to the slope surface was more severe.

3.3 Distribution characteristics of overburden displacement

It was observed from the overburden displacement nephogram in Figure 5 that the vertical displacement of the bedrock was larger than that of the surface. When the working face advanced to the

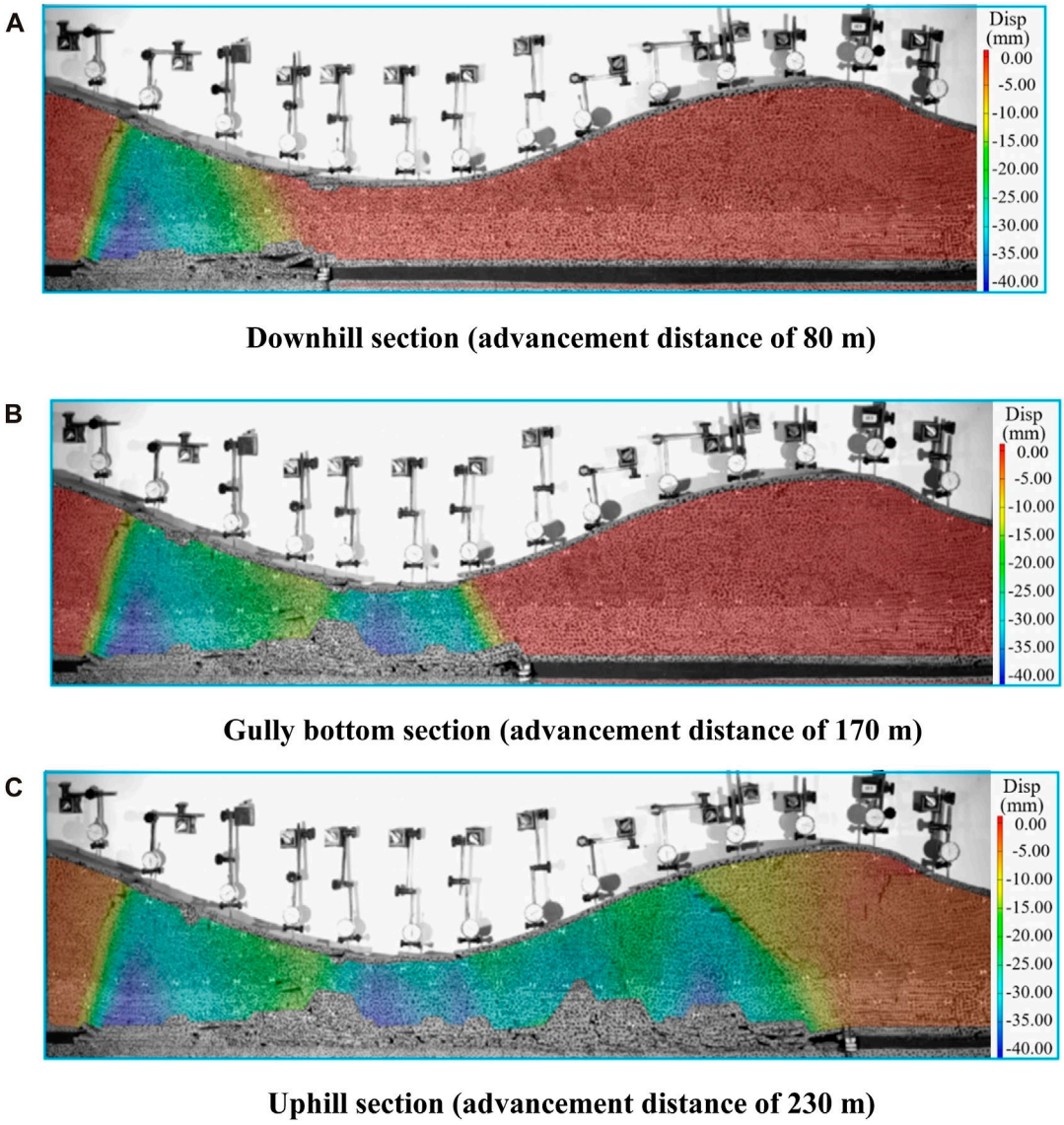

FIGURE 5
Displacement nephogram of the overburden.

downhill section, the maximum subsidence of the bedrock and the surface was 2.36 m and 1.54 m, respectively, and the surface subsidence coefficient was 0.62 m.

Bedrock and surface subsidence gradually increased as the working face advanced from the downhill mining section to the gully bottom mining section. The subsidence at the gully bottom was larger at 40 m and 110 m, with the maximum bedrock and surface subsidence at 110 m. The maximum bedrock and surface subsidence was 2.37 m and 2.13 m, respectively, and the surface subsidence coefficient was 0.75.

When the working face advanced from the gully bottom mining section to the uphill mining section, the maximum bedrock and surface subsidence was at 110 m. The maximum bedrock and surface subsidence was 2.37 m and 2.14 m, respectively, and the surface subsidence coefficient was 0.86.

Figure 6 presents the distribution characteristics of the displacements obtained from observation lines embedded in the overburden. When the 135201working face of Shaliang Coal Mine advanced underneath the gully terrain, the bedrock load changed obviously due to the different thicknesses of the loose layer in each section. The maximum subsidence coefficients of bedrock and surface were also different, in which the maximum subsidence coefficients were in the order of gully bottom section > uphill section > downhill section.

3.4 Evolutionary characteristics of floor pressure

The change rule of the floor pressure during the advancement of the working face is illustrated in Figure 7. Due to the different bedrock loads, the floor pressure varied significantly when recovering underneath the gully terrain. The advanced abutment pressure of the working face in the downhill section

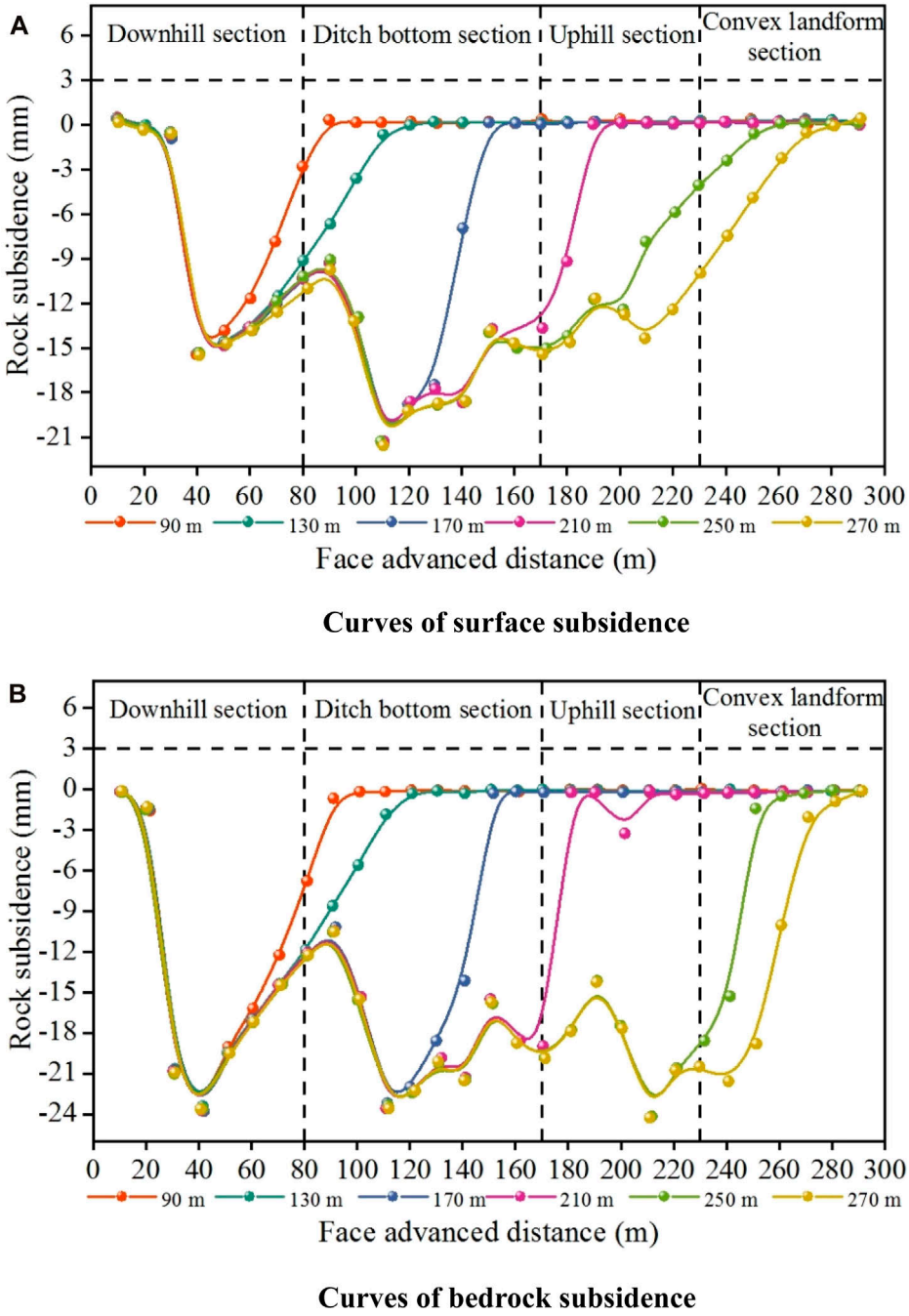

FIGURE 6
Distribution characteristics of the displacements obtained from observation lines embedded in the overburden. Among them, 90, 13, 170, 210, 250 and 270 m are the advancing distance of the working face.

was 750–870 kN, with an average of 810 kN. The ground pressure behavior of the working face was relatively moderate throughout the mining in the downhill section. As the working face continued to advance from the downhill mining section to the gully bottom mining section, the advanced abutment pressure during the advancement of the working face ranged from 421 to 1,140 kN, with an average of 780 kN. As the working face continued to advance from the gully bottom mining section to the uphill mining section, the advanced abutment pressure during the advancement of the working face ranged from 1,370 to 1,990 kN, with an average of 1,680 kN. When the working face was mined in the gully bottom section and the uphill section, the rotational deformation of the overburden easily led to the stress concentration at the slope foot. The distribution patterns of the floor pressure during the advancement of the working face was: uphill section > downhill section > gully bottom section.

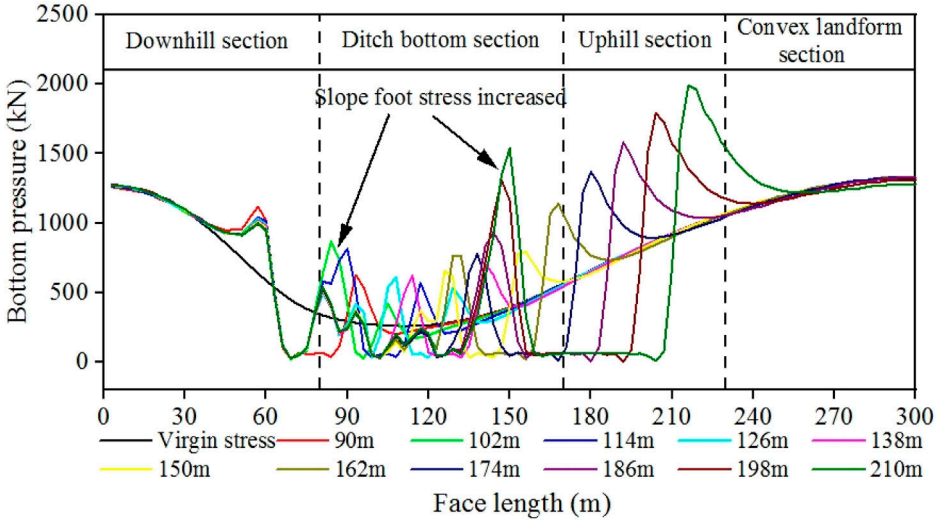

FIGURE 7
Change rule of floor pressure.

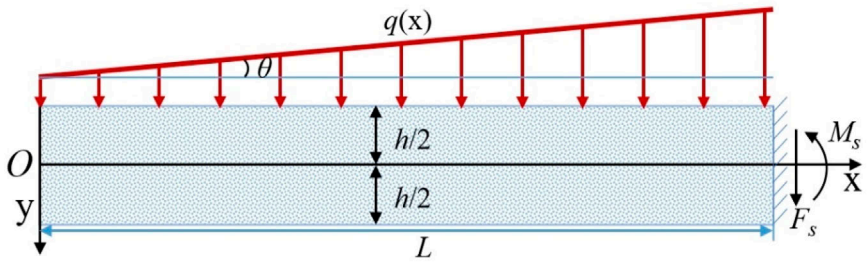

FIGURE 8
Mechanical model of key stratum of the overburden.

4 Analysis of overburden failure structure of the working face underneath the gully

4.1 Mechanical analysis of overburden failure structure

Since the ground pressure behavior was intense when the working face advanced to the uphill section, the mechanical mechanism of the key stratum failure of the overburden in the uphill section was analyzed. According to the failure characteristics of the key stratum of the overburden in the uphill section revealed by the physical similarity simulation test, the force characteristics of the key stratum in the uphill mining section underneath the gully terrain were simplified to a problem of a cantilever beam subjected to the linear loads, as illustrated in Figure 8.

In Figure 8, θ is the gully slope in the uphill section, with a unit of °; $q(x)$ is the load applied to the key stratum of the overburden, with a unit of MPa; $q(x)=x\rho g\tan\theta$; h is the thickness of the key stratum, with a unit of m; L is the length of the rock block of the key stratum, with a unit of m; F_s is the shear force at the fixed-end, with a unit of MPa; and M_s is the bending moment at the fixed-end, with a unit of kN·m.

According to the plane stress equation, the stress boundary condition of the cantilever beam in this mechanical model can be derived as shown in Eq. 1:

$$\begin{cases} \left(\sigma_y\right)_{y=-\frac{h}{2}} = -x\rho g\tan\theta \\ \left(\sigma_y\right)_{y=\frac{h}{2}} = 0 \\ \left(\tau_{xy}\right)_{y=\pm\frac{h}{2}} = 0 \\ \left(\sigma_x\right)_{x=0} = 0 \end{cases} \tag{1}$$

where σ_x and σ_y are the positive stresses of the rock block of the key stratum in the x and y directions, respectively, with a unit of MPa; τ_{xy} is the stress of the rock block of the key stratum in the xy direction, with a unit of MPa; ρg is the volumetric force of rock mass, with a unit of MN/m^3.

Setting $\sigma_y=f(y)x$, According to Saint-Venant's theorem, the stress distribution expression in the key strata can be solved as shown

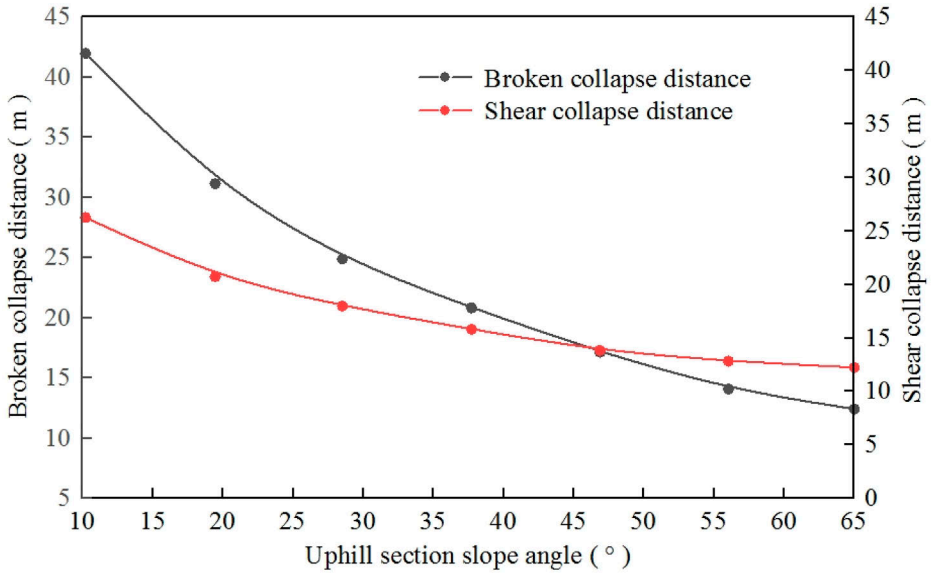

FIGURE 9
Relationship between limit collapse distance of key strata and slope change.

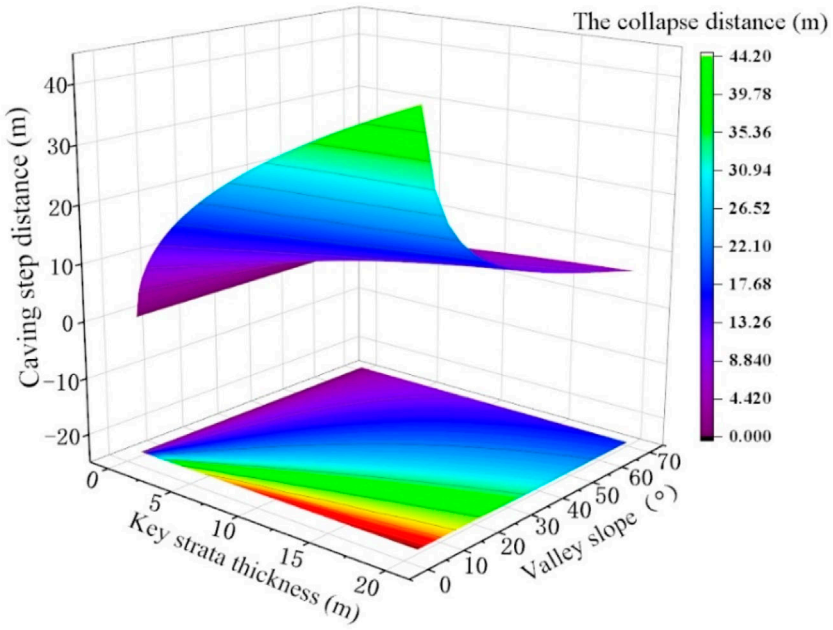

FIGURE 10
Relationship among the overburden failure span, the thickness of key stratum, and the gully slope.

in Eq. 2:

$$\begin{cases} \sigma_x = \dfrac{\rho g \tan\theta}{5h^3}\left(-10x^3y + 20xy^3 - 3h^2xy\right) \\ \sigma_y = \rho g \tan\theta\left(\dfrac{-2y^3}{h^3} + \dfrac{3y}{2h} - \dfrac{1}{2}\right)x \\ \tau_{xy} = \rho g \tan\theta\left(-\dfrac{y^4}{h^3} + \dfrac{3}{10h}y^2 - \dfrac{3y^2}{h^3}x^2 - \dfrac{3}{4h}x^2 - \dfrac{h}{80}\right) \end{cases} \quad (2)$$

where x and y are the amounts of change in the thickness and length of the rock block of the key stratum, with a unit of m.

The shear force F_s and the bending moment M_s at the fixed end of the cantilever beam subjected to linear loads could be solved from the mechanics of materials as Eqs 3, 4:

$$(F_s)_{x=L} = \int_{-\frac{h}{2}}^{\frac{h}{2}} (\tau_{xy})_{x=L}\, dy = -\frac{\rho g L \tan\theta}{2} \quad (3)$$

$$(M_s)_{x=L} = \int_{-\frac{h}{2}}^{\frac{h}{2}} (\sigma_x)_{x=L}\, y\, \mathrm{d}y = -\frac{\rho g L^2 \tan\theta}{6} \tag{4}$$

The analysis of the mechanical model of the key stratum indicated that the danger point of the cantilever beam was at the fixed end, and its failure modes were tensile failure and shear failure. Firstly, the ultimate span of cantilever beam in tension failure was analyzed. The analysis of the stress distribution and bending moment of the cantilever beam determined that the danger point of tensile failure was at (L,-h/2), and the maximum tensile stress at this point was Eq. 5:

$$(\sigma_x)_{\max} = \rho g L_T \left(\frac{L_T^2}{h^2} - \frac{1}{5}\right)\tan\theta \tag{5}$$

where $(\sigma_x)_{man}$ is the maximum tensile stress at the fixed end of the rock block of the key stratum, with a unit of m; L_T is the caving interval of the key stratum in tension failure, with a unit of m.

When $(\sigma_x)_{man}$=R_t, i.e., the positive stress in the rock mass at this point reached the ultimate tensile strength of the rock mass, the rock mass would be fractured at this point. The ultimate span of the beam when it broke is Eq. 6:

$$L_t = -\frac{\sqrt[3]{Y_1} + \sqrt[3]{Y_2}}{3} \tag{6}$$

where Y_1 and Y_2 are shown in Eq. 7

$$Y_{1,2} = -\frac{27}{2}\frac{h^2\sigma_t}{\rho g \tan\theta} \pm \sqrt{\left(\frac{9h^2\sigma_t}{\rho g \tan\theta}\right)^2 - \frac{12}{125}h^6} \tag{7}$$

where σ_t is the ultimate tensile strength of the rock block of the key stratum, with a unit of MPa.

When $(\tau_{xy})_{max}$=R_s, the ultimate caving interval formed when the beam was sheared is Eq. 8:

$$L_S = \sqrt{\frac{2hR_S}{3\rho g \tan\theta}} \tag{8}$$

where $(\tau_{xy})_{max}$ is the maximum tensile stress at the fixed end of the rock block of the key stratum, with a unit of MPa; Ls is the caving interval of the key stratum in tension damage, with a unit of m; R_s is the shear strength of the rock block of the key stratum, with a unit of MPa.

In summary, the expression of the limit collapse step of the key stratum is Eq. 9

$$L = \min(L_T, L_S) \tag{9}$$

According to the theoretical analysis and physical simulation experiment, the relationship between the limit caving distance of the key stratum and the slope toe in the uphill stage of the 135,201 working face of Shaliang Coal Mine is shown in Figure 9. When the gully slope angle is greater than 46°, the key stratum rock mass shows shear fracture, and the broken rock block slides and loses stability. When the gully slope angle is less than 46°, the key stratum rock mass shows tensile fracture, and the broken rock block rotates and loses stability.

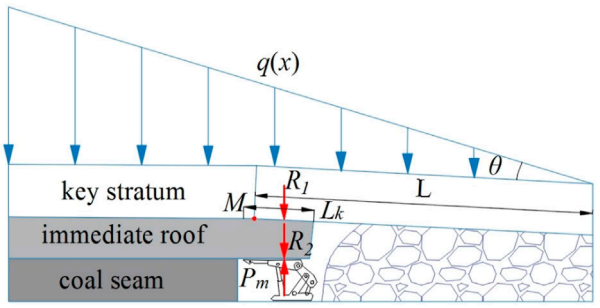

FIGURE 11
Working face rock pressure calculation model of uphill section.

4.2 Analysis of factors influencing the overburden failure

The main roof of the 135201working face in Shaliang Coal Mine was 9.1 m thick medium-grained sandstone. The physical and mechanical test results of the key stratum confirmed that the ultimate tensile strength R_t and the shear strength R_s, of the rock block of the key stratum were 2.5 MPa, 3.7 MPa, respectively, and the volume force ρg of the key stratum was 0.024 MN/m^3. On this basis, the relationship among the caving interval L, the thickness of the key stratum h, and the gully slope θ could be obtained, as displayed in Figure 10.

In case of mining under the gully, the ultimate caving interval of the overburden was closely related to both the thickness of the key stratum and the gully slope. The ultimate span increased as the thickness of the key layer increased in the uphill section. When the thickness of the key stratum remained unchanged, the ultimate span decreased with the increase of the gully slope.

4.3 Analysis of mine pressure in working face

The calculation model for mine pressure in the working face of the uphill section under valley terrain is illustrated in Figure 11. The linear load applied by the overlying strata of the key stratum is represented by q(x), while the hinge point of the key stratum rock block is denoted by point M The mine pressure, P_m, at the working face is mainly comprised of two components.

The first component is the pressure, R_2, exerted by the immediate roof rock mass. The second component is the pressure, R_1, applied once the key stratum rock mass has become broken and unstable. By conducting a mechanical analysis of Figure 11, we can derive the expression for the support pressure at the working face, as follows Eq. 10:

$$P_m = \gamma_0 L_k b h_0 + \frac{\gamma L^3 b \tan\theta}{3L_k} \tag{10}$$

In the formula: γ_0 is the average bulk density of the immediate roof strata above the support. b and L_k are the width of the hydraulic support and the length of the control roof, respectively. h_0 is the thickness of immediate roof strata.

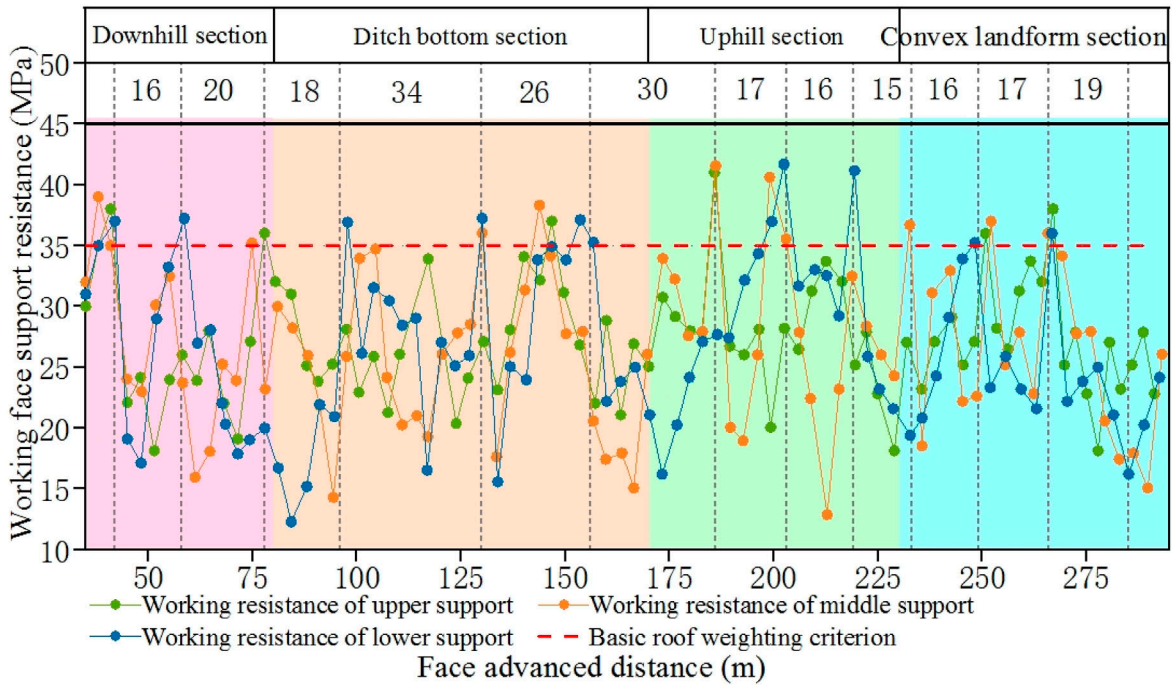

FIGURE 12
Change curves of support resistances at the working face.

According to the above analysis, it can be concluded that the working face pressure is proportional to the cubic and slope angle of the limit collapse distance of the key strata in the uphill mining stage. Obviously, the mine pressure of the working face is more affected by the change of slope angle.

5 Hazard prevention and ground pressure prediction for the working face underneath the gully

(1) Prediction of ground pressure pattern for gully-crossing mining

To verify the reliability and accuracy of the research results, the monitoring of the ground pressure was carried out on the gully-crossing section of the 135,202 working face of Shaliang Coal Mine. A total of 118 sets of ZY9200/15/29 type powered supports were used at the 135,202 working face. Three powered supports were respectively selected from the upper, middle, and lower parts of the working face, and the average values of their monitoring data were taken as the final support resistances. The monitoring section was from 35 m of the open-off cut to the departure of gully, with a length of 290 m. The change curves of the support resistances at the 135,202 working face in the gully-crossing section are displayed in Figure 12.

The monitored support resistances indicated that three times of weighting occurred at the working face in the downhill section. The interval of the first weighting was about 32 m, the periodic weighting intervals were about 16 m and 20 m, respectively, with an average periodic weighting interval of 18 m and a maximum pressure of 41 MPa. Four times of periodic weighting occurred in the gully bottom section, and the weighting intervals were about 18 m, 34 m, 26 m, and 30 m, respectively, with an average weighting interval of 27 m and a maximum pressure of 37 MPa. Three times of the weighting occurred in the uphill section, and the weighting intervals were 17 m, 16 m, and 15 m, respectively, with an average weighting interval of 16 m and a maximum pressure of 41 MPa. There were three times of weighting occurred in the convex terrain section, and the weighting intervals were 16 m, 17 m, and 19 m, respectively, with an average weighting interval of 17.3 m and a maximum pressure of 38 MPa. The location of the maximum weighting was in the uphill section. The weighting intervals were ordered from largest to smallest as: gully bottom section, downhill section, convex terrain section, and uphill section. The monitoring results were in good agreement with the experimental and theoretical results, which indicated that the current study provided valuable theoretical support for shallow coal seam mining underneath the gully.

(2) Hazard prevention measures for shallow coal seam mining underneath the gully

According to this study, the preliminary idea of prediction and prevention of mining pressure law in shallow coal seam is put forward. When the working face is mined through the ditch, the dynamic pressure dangerous area and the mine pressure law of the working face should be pre-dicted first, so as to put forward targeted preventive measures to prevent and control the mine pressure disaster. The previous research shows that the thickness of the key stratum and the slope of the valley are the key factors affecting the pressure law, and the dangerous area of the later section can be identified accordingly. For the area where the key layer is missing,

the support resistance should be increased, the advance speed should be accelerated appropriately, the mining height should be reduced locally, the support should be moved with pressure and supported in time; in the case of large gully slope angle of thick loose layer, the loose layer can be stripped in advance to reduce the load of the key layer, so as to effectively ensure the safe mining of the working face when crossing the gully.

6 Conclusion

(1) The weighting in the uphill section was stronger than that in the downhill section during the 135,201 working face of Shaliang Coal Mine passed though the gully terrain. The weighting was occasionally accompanied by flaking and roof leakage, but the overall depth of flaking was not large, and the safety valve of the support had not been opened. No dynamic loading ground pressure occurred in the section of the working face crossing the gully, which was obviously different from the existing dynamic loading ground pressures at the working face crossing the gully.

(2) The model test results confirmed that the average periodic weighting varied due to the different thickness of the loose layer in each section. The weighting intervals were in the order of gully bottom section > downhill section > uphill section. The bedrock loads varied significantly, and the maximum subsidence coefficients of bedrock and surface were also different. The order of the maximum bedrock subsidence coefficients was: gully bottom section > uphill section > downhill section. When the working face was mined in the gully bottom section and the uphill section, the rotational deformation of the overburden easily led to the stress concentration at the slope foot. The distribution pattern of the floor pressure during the advancement of the working face was: uphill section > downhill section > gully bottom section.

(3) Based on the monitored ground pressure law in the field and the overburden failure characteristics of shallow coal seam underneath the gully obtained by physical similarity simulation test, a mechanical analysis model for failure structure of key stratum in the uphill section was established, and the calculation formula for weighting interval in the uphill section was deduced. The ultimate span increased as the thickness of the key stratum increased and the gully slope decreased.

(4) The ground pressure monitoring on the gully-crossing section of the 135,202 working face of Shaliang Coal Mine revealed that the weighting intervals in the uphill section were 17 m, 16 m, and 15 m, respectively, with an average weighting interval of 16 m. The location of the maximum weighting was in the uphill section. The weighting intervals were ordered from largest to smallest as: gully bottom section, downhill section, convex terrain section, and uphill section. The monitoring results were in good agreement with the experimental and theoretical results, which could provide valuable theoretical support for shallow coal seam mining underneath the gully.

Data availability statement

The original contributions presented in the study are included in the article/Supplementary material, further inquiries can be directed to the corresponding author.

Author contributions

JZ: Writing–review and editing, Conceptualization, Project administration. LW: Data curation, Methodology, Writing–original draft. TY: Methodology, Supervision, Writing–review and editing. SG: Data curation, Investigation, Writing–review and editing. YH: Validation, Writing–review and editing. JW: Validation, Writing–review and editing.

Funding

The author(s) declare that no financial support was received for the research, authorship, and/or publication of this article.

Conflict of interest

The authors declare that the research was conducted in the absence of any commercial or financial relationships that could be construed as a potential conflict of interest.

Publisher's note

All claims expressed in this article are solely those of the authors and do not necessarily represent those of their affiliated organizations, or those of the publisher, the editors and the reviewers. Any product that may be evaluated in this article, or claim that may be made by its manufacturer, is not guaranteed or endorsed by the publisher.

References

Dai, L., Pan, Y., Li, Z., Wang, A., Xiao, Y., Liu, F., et al. (2023). Quantitative mechanism of roadway rockbursts in deep extra-thick coal seams: theory and case histories. *Tunn. Undergr. Space Technol.* 111, 103861–107798. doi:10.1016/j.tust.2021.103861

Dai, L., Pan, Y., and Wang, A. (2018). Study of the energy absorption performance of an axial splitting component for anchor bolts under static loading. *Tunn. Undergr. Space Technol.* 81, 176–186. doi:10.1016/j.tust.2018.07.009

Dai, L., Pan, Y., Zhang, C., Wang, A., Canbulat, I., Shi, T., et al. (2022). New criterion of critical mining stress index for risk evaluation of roadway rockburst. *Rock Mech. Rock Eng.* 55, 4783–4799. doi:10.1007/s00603-022-02888-7

Dai, L., Xiao, Y., Pan, Y., Wang, A., Fan, C., and Guo, J. (2020). Mechanical behavior and factors influencing axial splitting energy absorbers and optimized application for rock bolts. *Tunn. Undergr. Space Technol.* 102, 103427–107798. doi:10.1016/j.tust.2020.103427

Dai, Z., Zhang, L., Wang, Y., Jiang, Z., and Xu, S. (2021). Deformation and failure response characteristics and stability analysis of bedding rock slope after underground adverse slope mining. *Bull. Eng. Geol. Environ.* 80, 4405–4422. doi:10.1007/s10064-021-02258-7

Feng, D., Hou, E., Xie, X., Che, X., Hou, P., and Long, T. (2022). Prediction and treatment of water leakage risk caused by the dynamic evolution of ground fissures in gully terrain. *Front. Earth Sci.* 9, 803721. doi:10.3389/feart.2021.803721

He, Y., Hazarika, H., Yasufuku, N., and Han, Z. (2015a). Evaluating the effect of slope angle on the distribution of the soil-pile pressure acting on stabilizing piles in sandy slopes. *Comput. Geotechnics* 69, 153–165. doi:10.1016/j.compgeo.2015.05.006

He, Y., Hazarika, H., Yasufuku, N., Teng, J., Jiang, Z., and Han, Z. (2015b). Estimation of lateral force acting on piles to stabilize landslides. *Nat. Hazards* 79, 1981–2003. doi:10.1007/s11069-015-1942-0

Huang, Q. (2002). Ground pressure characteristics of shallow coal seam and definition of shallow coal seam. *J. Rock Mech. Eng.* 21, 1174–1177. doi:10.3321/j.issn:1000-6915.2002.08.014

Huang, Q., and Du, J. (2018). Study on coupling control of section coal pillar stress and surface crack in shallow coal seam group mining. *J. Coal* 03, 591–598. doi:10.13225/j.cnki.jccs.2017.0462

Lai, X., Xu, H., Shan, P., Hu, Q., Ding, W., Yang, S., et al. (2024). Research on mechanism of rockburst induced by mined coal-rock linkage of sharply inclined coal seams. *Int. J. Miner. Metall. Mater.* doi:10.1007/s12613-024-2833-8

Li, J., Liu, C., Wang, W., and Wang, C. (2019). Linkage-induced mechanism and control technology of pressure bump and surface geological damage in shallow coal seam mining of gully area. *Arabian J. Geosciences* 12, 349. doi:10.1007/s12517-019-4511-0

Li, J., Liu, C., and Zhao, J. (2016a). Sensitivity analysis of influencing factors of mining pressure behavior in shallow coal seam mining. *J. Min. Saf. Eng.* 05, 853–859. doi:10.13545/j.cnki.jmse.2016.05.014

Li, Z., Dou, L., Cai, W., Wang, G., Ding, Y., and Kong, Y. (2016b). Mechanical analysis of static stress within fault-pillars based on a voussoir beam structure. *Rock Mech. Rock Eng.* 49, 1097–1105. doi:10.1007/s00603-015-0754-6

Li, Z., Yu, S., Zhu, W., Feng, G., Xu, J., Guo, Y., et al. (2020). Dynamic loading induced by the instability of voussoir beam structure during mining below the slope. *Int. J. Rock Mech. Min. Sci.* 132, 104343. doi:10.1016/j.ijrmms.2020.104343

Liu, C., Li, J., Zhao, J., Chen, Y., Zhang, H., and Yu, X. (2023). Mechanism of dynamic mine pressure and distribution characteristics of gas-conducting fractures in overlying strata of shallow-buried thick coal seam mining in gully area. *J. Min. Saf. Eng.* 40, 965–971. doi:10.13545/j.cnki.jmse.2023.0256

Lu, B., Sheil, B., Zhao, W., Jia, P., Bai, Q., and Wang, W. (2024). Laboratory testing of settlement propagation induced by pipe-roof pre-support deformation in sandy soils. *Tunn. Undergr. Space Technol.* 146, 105645. doi:10.1016/j.tust.2024.105645

Ma, S., and Kang, Y. (2022). Characteristics of mining-induced slope movement and ground behavior under gully landforms. *Sustainability* 14, 13941. doi:10.3390/su142113941

Miao, K., Tu, S., Tu, H., Liu, X., Li, W., Zhao, H., et al. (2022). Research on fractal evolution characteristics and safe mining technology of overburden fissures under gully water body. *Fractal Fract.* 6, 486. doi:10.3390/fractalfract6090486

Pan, Y., and Wang, A. (2023). Disturbance response instability theory of rock bursts in coal mines and its application. *Geohazard Mech.* 1, 1–17. doi:10.1016/j.ghm.2022.12.002

Tang, J., Dai, Z., Wang, Y., and Zhang, L. (2019). Fracture failure of consequent bedding rock slopes after underground mining in mountainous area. *Rock Mech. Rock Eng.* 52, 2853–2870. doi:10.1007/s00603-019-01876-8

Wang, Q., Wang, Y., Jiang, B., Jiang, Z., and Xue, H. (2023a). Geomechanics model test research on large deformation control mechanism of roadway disturbed by strong dynamic pressure. *Geohazard Mech.* 1, 140–152. doi:10.1016/j.ghm.2023.06.002

Wang, X., Cai, L., Zhang, B., Wu, J., Zhu, Q., and Cui, Z. (2023b). Simulation study on surface deformation of shallow buried coal seam mining in a gully area. *Front. Earth Sci.* 11, 1287981. doi:10.3389/feart.2023.1287981

Wang, X., Zhang, D., Lu, X., Xu, M., and Qiu, X. (2010). Mining pressure behavior characteristics of shallow buried coal seam under sandy gully slope. *Coal Sci. Technol.* 06, 18–22. doi:10.13199/j.cst.2010.06.24.wangxf.008

Xiao, G., and Yao, W. (2021). Mine pressure behavior law of shallow buried coal seam in valley terrain of Madiliang Coal Mine. *J. Min. Strata Control Eng.* 04, 96–103. doi:10.13532/j.jmsce.cn10-1638/td.20210610.001

Xu, J., Zhu, W., Wang, X., and Yi, M. (2009). Classification of key strata structure of overlying strata in shallow coal seam. *Coal J.* 34 (7), 865–870. doi:10.13225/j.cnki.jccs.2009.07.00

Xu, N., Zhang, J., Tian, H., Mei, G., and Ge, Q. (2016). Discrete element modeling of strata and surface movement induced by mining under open-pit final slope. *Int. J. Rock Mech. Min. Sci.* 88, 61–76. doi:10.1016/j.ijrmms.2016.07.006

Yang, T., Yang, Y., Zhang, J., Gao, S., and Li, T. (2021). Study on development law of mining-induced slope fracture in gully mining area. *Adv. Civ. Eng.* 2021, 1–9. doi:10.1155/2021/9990465

Yang, Z., Guo, R., and Yang, Y. (2020). Study on mine pressure behavior law and control of shallow buried deep fully mechanized caving face. *Industrial Min. automation* 09, 44–50. doi:10.13272/j.issn.1671-251x.2020060003

Yiouta-Mitra, P., and Sofianos, A. I. (2018). Multi-jointed stratified hard rock roof analysis and design. *Int. J. Rock Mech. Min. Sci.* 106, 96–108. doi:10.1016/j.ijrmms.2018.03.021

Yu, J., Zhao, J., Yan, H., Lai, Q., Huang, R., Liu, X., et al. (2020). Deformation and failure of a high-steep slope induced by multi-layer coal mining. *J. Mt. Sci.* 17, 2942–2960. doi:10.1007/s11629-019-5941-6

Zhang, B., Liu, G., Li, Y., and Lin, Z. (2023a). Experimental study on the seepage mutation of natural karst collapse pillar (KCP) fillings over mass outflow. *Environ. Sci. Pollut. Res.* 30, 110995–111007. doi:10.1007/s11356-023-30230-3

Zhang, D., Huang, Z., Ma, Z., Yang, J., and Chai, J. (2023b). Research on similarity simulation experiment of mine pressure appearance in surface gully working face based on BOTDA. *Sensors* 23, 9063. doi:10.3390/s23229063

Zhang, D., Li, W., Lai, X., Fan, G., and Liu, W. (2017). Research progress on basic theory of water resources protection in coal mining in northwest China. *Coal J.* 42, 36–43. doi:10.13225/j.cnki.jccs.2016.5045

Zhang, J., Li, H., Yang, S., Wang, X., Bai, W., He, Y., et al. (2021). Study on mine pressure law and support adaptability of working face under very close gully terrain. *Min. Res. Dev.* 12, 48–51. doi:10.13827/j.cnki.kyyk.2021.12.025

Zhang, J., Long, J., Yang, T., Wang, B., and Zhou, F. (2019). Study on dynamic load mechanism of mining under gully in shallow coal seam. *J. Min. Saf. Eng.* 06, 1222–1227. doi:10.13545/j.cnki.jmse.2019.06.019

Zhang, Z., Xu, J., Wang, L., and Zhu, W. (2011). Study on the influence of gully slope angle on ground pressure of shallow coal seam working face. *J. Min. Saf. Eng.* 28, 560–565. doi:10.3969/j.issn.1673-3363.2011.04.011

Zhao, B., Guo, Y., Wang, W., and He, S. (2023). Impact of underground coal seam mining on stability and slippage of the loess slope. *Sustainability* 15, 6485. doi:10.3390/su15086485

Zhao, J., Liu, C., and Li, J. (2018). Stress field distribution and mine pressure behavior characteristics of shallow buried thick coal seam mining in gully area. *J. Min. Saf. Eng.* 04, 742–750. doi:10.13545/j.cnki.jmse.2018.04.011

frontiers | Frontiers in Earth Science

TYPE Original Research
PUBLISHED 07 March 2024
DOI 10.3389/feart.2024.1361283

Check for updates

OPEN ACCESS

EDITED BY
Jianyong Han,
Shandong Jianzhu University, China

REVIEWED BY
Wentong Wang,
Shandong University of Science and Technology, China
Junhui Peng,
Changsha University of Science and Technology, China

*CORRESPONDENCE
Xiangyang Li,
1134236098@qq.com
Jianwen Hao,
hjwww1717@163.com

RECEIVED 25 December 2023
ACCEPTED 05 February 2024
PUBLISHED 07 March 2024

CITATION
Wang S, Li X, Ti Y, Zhang X, Yin T, Wang R, Jiang X, Su Z and Hao J (2024), Investigation on shakedown response-behavior of thawed subgrade soils under long-term traffic loading.
Front. Earth Sci. 12:1361283.
doi: 10.3389/feart.2024.1361283

COPYRIGHT
© 2024 Wang, Li, Ti, Zhang, Yin, Wang, Jiang, Su and Hao. This is an open-access article distributed under the terms of the Creative Commons Attribution License (CC BY). The use, distribution or reproduction in other forums is permitted, provided the original author(s) and the copyright owner(s) are credited and that the original publication in this journal is cited, in accordance with accepted academic practice. No use, distribution or reproduction is permitted which does not comply with these terms.

Investigation on shakedown response-behavior of thawed subgrade soils under long-term traffic loading

Shujian Wang[1], Xiangyang Li[2]*, Yanzheng Ti[1], Xiaoning Zhang[3], Tao Yin[1], Ruibing Wang[1], Xiufeng Jiang[1], Zhikai Su[1] and Jianwen Hao[2]*

[1]Shandong High-speed Construction Management Group Co., Ltd., Jinan, China, [2]School of Civil Engineering, Shandong University, Jinan, China, [3]School of Civil Engineering, Chongqing University, Chongqing, China

The shakedown state of the subgrade is crucial for the sustainable design and long-term stability evaluation of pavement structures. In order to characterize the plastic deformation and shakedown behavior of subgrade soil in seasonal frozen regions, cyclic triaxial tests were conducted on the thawed subgrade soil after seven cycles of freeze-thaw. The influences of the numbers of cycle loading, the amplitude of cyclic deviator stress, and the confining stress were considered variables. The evolution features of accumulative plastic strain, accumulative plastic strain rate, and critical dynamic stress were experimentally analyzed. Based on the shakedown theory, the ensuing discoveries were that the accumulative plastic strain response-behavior of thawed subgrade soil was typically divided into plastic shakedown, plastic creep, and incremental collapse under the long-term cyclic loading. Furthermore, the shakedown standard for thawed subgrade soil was also proposed based on the evolution of the accumulative plastic strain rate. The critical dynamic stresses can be obtained by the proposal formula to determine the different plastic deformation ranges.

KEYWORDS

shakedown theory, accumulative plastic strain, subgrade soil, freeze-thaw cycles, critical dynamic stress

1 Introduction

The subgrade is regarded as the support layer for the pavement or railway structures and undertakes the dynamic stress induced by the moving traffic loadings (Beskou and Theodorakopoulos, 2011; Krechowiecki-Shaw et al., 2016; Bian et al., 2018; Cui et al., 2022; Cui et al., 2023a; Cui et al., 2023b; Cui et al., 2024). Under long-term cyclic loadings, the accumulative plastic deformation of subgrade soils gradually increases, where the accumulative plastic deformation induced by long-term traffic loading accounts for the majority (75%–90%) of the total permanent deformation of the subgrade (Li and Selig, 1996; Chai and Miura, 2002; Puppala et al., 2009; Cui et al., 2014; Cai et al., 2018; Lu et al., 2018; Zhang et al., 2020a; Zhao et al., 2024). The overlarge permanent deformation in the subgrade layer will lead to pavement failures, such as uneven settlement, rutting, or cracking disasters in the asphalt layer (Brown, 1996). It is worth noting that when the pavement infrastructures are constructed in the seasonal frozen regions, the development

trends of permanent deformation of subgrade soils will accelerate dramatically subject to the coupled effect of cyclic loading and freeze-thaw cycle (Lin et al., 2017; Wang et al., 2018; Lu et al., 2019; Hao et al., 2022; Hao et al., 2023; Pei et al., 2024). Meanwhile, the shakedown behavior of subgrade soils can be considered a reliable evaluation of the long-term performance of subgrade structures in the service period (Werkmeister et al., 2011). Thus, the credible understanding of accumulative plastic strain and the shakedown response of thawed subgrade soil can be considered an urgent demand for pavement and subgrade engineering in seasonal frozen regions.

The permanent deformation under traffic loading and critical dynamic stress are the essential parameters for pavement structure designs and performance maintenance that meet the allowable deformation limit based on the shakedown theory. The shakedown theory was first applied to reveal the dynamic behavior-response of the ideal elastic-plastic materials subjected to cyclic loadings. In the field of pavement engineering, the shakedown theory was introduced into the design of pavement structure and assessment of in-service life by Sharp and Booker (1984) and has been used widely to explore the plastic permanent deformation behavior of pavement materials (Boulbibane et al., 2005; Chazallon et al., 2009; Xiao et al., 2017; Qian et al., 2019; Wang and Yu, 2021; Liu et al., 2022; Lei et al., 2023). Then, S. Werkmeister et al. (Werkmeister et al., 2011) developed the primary concept of shakedown theory for application in subgrade engineering, which illustrated that the plastic deformation characteristics of subgrade materials can be classified into three types based on the shakedown theory (Figure 1).

1. Plastic shakedown (range A) means that when the cyclic load level is low, the granular material first appears as small plastic deformation, and then the overall deformation behavior changes to resilient deformation with the increase of loading cycles. This deformation type indicates that the plastic permanent deformation behavior of the subgrade structure is safe, which is considered the ideal state of the subgrade material in the design.
2. Plastic creep (range B) means that when the cyclic load level is higher, the granular material first appears as a certain plastic deformation, and then with the increase in loading cycles, the plastic deformation gradually increases but the accumulative deformation rate basically remains stable. This deformation type indicates that the permanent deformation behavior of the subgrade structure is controllable and safe within a certain service life, which is considered the controllable allowable state of the subgrade material in the design.
3. Incremental collapse (range C) means that when the cyclic load level is high, the development of plastic deformation of granular materials increases sharply with the increase in loading cycles, and the accumulative deformation rate keeps increasing, which finally leads to structure failure due to the excessive permanent deformation. This deformation type indicates that the permanent deformation behavior of the subgrade structure is uncontrollable and unsafe, and this state should be avoided for the subgrade materials in the design.

For the subgrade materials, many researchers proposed different standards to judge the permanent deformation behaviors and calculated the different deformation areas boundaries and critical

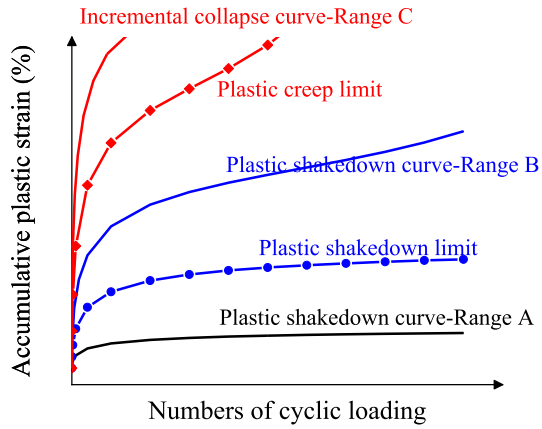

FIGURE 1
Schematic drawing of shakedown theory for subgrade materials.

dynamic stress, such as for unbound granular material (Gu et al., 2017; Xiao et al., 2018a; Xiao et al., 2018b; Zhao et al., 2022), coarse-grained soil (Leng et al., 2017; Zhai et al., 2020; Wang and Zhuang, 2021), fine-grained soil (Zhang et al., 2020b; Li et al., 2021; Cui et al., 2023c), and frozen soil (Wang et al., 2018; Zhou et al., 2020; Zhou et al., 2022). For the highway engineering practice, the sustainable design and hazard prevention of pavement structures demand an in-depth understanding of the plastic deformation and shakedown behavior of the thawed subgrade soils to further meet the requirement of long-term serviceability. However, according to the above literature review, there is a lack of comprehensive understanding for analyzing the shakedown response-behavior of thawed subgrade soils.

Thus, this paper aims to experimentally reveal the evolution of the accumulative plastic strain behavior of thawed subgrade soils by freeze-thaw and cyclic triaxial tests conducted on the subgrade soils. Furthermore, the classification standards for different limits of plastic deformation ranges and calculations for critical dynamic stress are established based on the shakedown theory.

2 Experimental investigation

2.1 Tested soil and specimen

The subgrade soils used for plastic deformation tests were selected from the low liquid silt (ML) that had a strong freeze-thaw sensitivity and poor water stability, whereas these typical silt soils have been widely constructed in seasonally frozen subgrade engineering (Xiao et al., 2014; Zhang et al., 2020b; Li et al., 2021; Hao et al., 2022; Cui et al., 2023a; Hao et al., 2023; Zhang et al., 2023). Meanwhile, the silt soils in this paper were taken from the highway construction site of the Rizhao-Lankao highway in Shandong Province, China (Hao et al., 2023). The gradation curve and basic physical properties are presented in Figure 2 and Table 1. Besides, the cylinder specimens were prepared and remodeled with a diameter of 39.1 mm and height of 80 mm, where the compaction degree and initial moisture content were set as 96% and optimal moisture content, respectively.

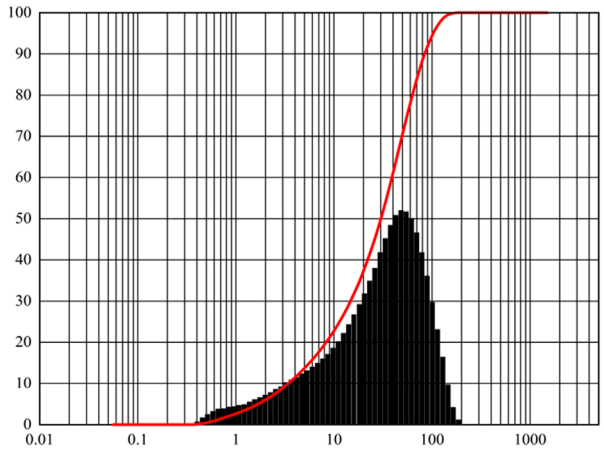

FIGURE 2
Gradation curve of tested soil.

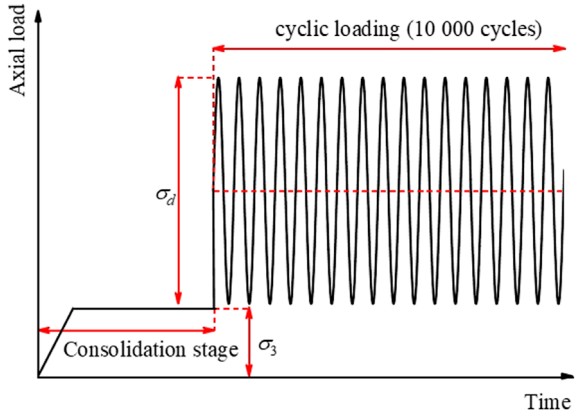

FIGURE 3
Loading curve for cyclic triaxial test in this study.

TABLE 1 Basic physical properties of tested soil.

Liquid limit/%	Plastic limit/%	Plastic index/%	Maximum dry density/g·cm^{-3}	Optimal moisture content/%
25.2	17.6	7.6	1.81	12.1

TABLE 2 Test conditions.

Deviator stress amplitude/kPa	Confining stress/kPa	Number of freeze-thaw cycles	Loading frequency/Hz
30, 60, 90, 120, 150	15, 30, 45, 90	7	1

2.2 Test procedure

2.2.1 Freeze-thaw setting

According to existing literature, the mechanical properties of fine-grained soils would be a stable state after 7–10 times of freeze-thaw cycles in the seasonal frozen environment (Qi et al., 2006; Qi et al., 2008; Wang et al., 2015; Liu et al., 2016; Lin et al., 2017; Zhang et al., 2021), and combining the previous studies of silt by our group, the tested subgrade soils were chosen as thawed silt subjected to the 7 times of freeze-thaw cycles (Hao et al., 2022; Hao et al., 2023; Zhang et al., 2023). Moreover, the freezing temperature and thawing temperature were set as −10°C and 15°C, respectively.

2.2.2 Cyclic loading setting

The cyclic loading mode takes the single-stage loading used by the triaxial repeated loading device, and the half-sine wave was adopted to simulate the dynamic stress of subgrade soil induced by traffic loading (Ramos et al., 2020). The stress levels were set as 30, 60, 90, 120, and 150 kPa for amplitude of cyclic deviator stress and 15, 30, 45, and 60 kPa for confining stress, which is considered the stress state of subgrade under traffic loading and the further development of load level of heavy-haul traffic loading, and the determination of stress levels were based on the subgrade dynamic response of the theoretical model and *in situ* test by our research group (Cui et al., 2022; Cui et al., 2023a; Cui et al., 2023b). The loading progress is divided into the consolidation stage and cyclic loading stage, where the consolidation stress is equal to the confining stress of the soil specimen, and the number of loading cycles is 10000, as shown in Table 2 and Figure 3, where the loading frequency is set as 1 Hz considering the moving speed of highway (Cui et al., 2023a). Meanwhile, due to freeze-thaw cycles occurring mostly on the surface of the subgrade and the persistence and instantaneity of traffic loads, the fine-grained soil subgrade generally has no time for drainage during the melting stage. Therefore, the cyclic triaxial test in this manuscript is selected as the undrained test. Besides, the failure standard of the soil specimen was taken as 10% axial strain that stops loading, or else the loading stage continues to the 10000 numbers of loading cycles.

3 Results and discussions

3.1 Analysis of plastic deformation behavior

Figure 4 shows the development of an accumulative plastic strain of thawed silts under different stress states. It can be concluded obviously that the accumulative plastic strain increases with the increase of deviator stress amplitude. Taking Figure 4B as an example, it can be known that when the amplitude of cyclic deviator stress is smaller (σ_d = 30 and 60 kPa), the accumulative plastic strain of soil specimens increases rapidly only at the initial stage of the cyclic loading, then the development of accumulative plastic strain remains in a stable state, where the value of accumulative plastic strain is 0.23% and 1.58% at the 10000 numbers of loading cycles, corresponding to σ_d = 30 and 60 kPa, respectively. With the increase of amplitude of cyclic deviator stress to 90 kPa, the development of accumulative plastic strain not only increases rapidly at the

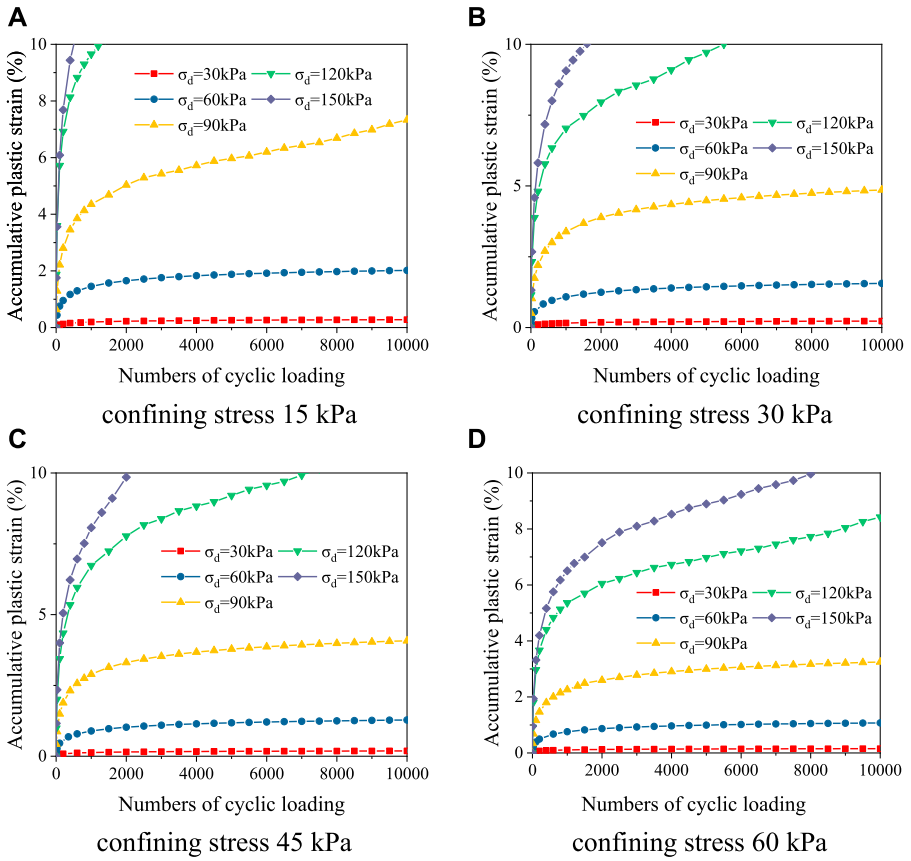

FIGURE 4
Development of accumulative plastic strains under different stress states.

initial stage of cyclic loading but also maintains a certain increased trend at the subsequent loading stage. Although the soil specimen remains in a stable state at the end of the loading (N = 10000), the accumulative plastic strain and accumulative strain rate of the soil specimen are large at this state. If the soil specimen continues to be cyclically loaded, the specimen may fail due to excessive accumulative plastic strain. Thereafter, when the amplitude of cyclic deviator stress is further increased to 120 and 150 kPa, the accumulative plastic strain increases dramatically until it reaches the experimental termination standard at the initial stage of the cyclic loading.

Furthermore, Figure 4 shows that with the increase in confining pressure, the accumulative plastic strain of soil specimen decreases obviously under the same amplitude of cyclic deviator stress. When the confining stress is at a high level, the accumulative plastic strain increases sharply at the initial stage of cyclic loading, and with the increase in the number of loading cycles, the accumulative plastic strain gradually slows down and remains in a stable state. However, when the confining stress is at a low level, the accumulative plastic strain under the same amplitude of cyclic deviator stress does not tend to be stable at the subsequent loading stage but still increases at a certain accumulative deformation rate, and the soil structures present eventually become incremental plastic failure. The reason is that the radial constraints on the soil skeleton are produced by increasing confining stress, which means that a more compact soil skeleton structure can resist greater cyclic load manifested as a process of accumulative plastic strain reduction from a macro perspective.

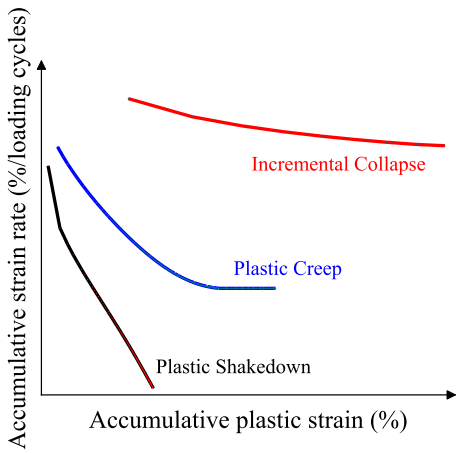

FIGURE 5
Criteria for classifying plastic deformation behaviors based on the shakedown theory.

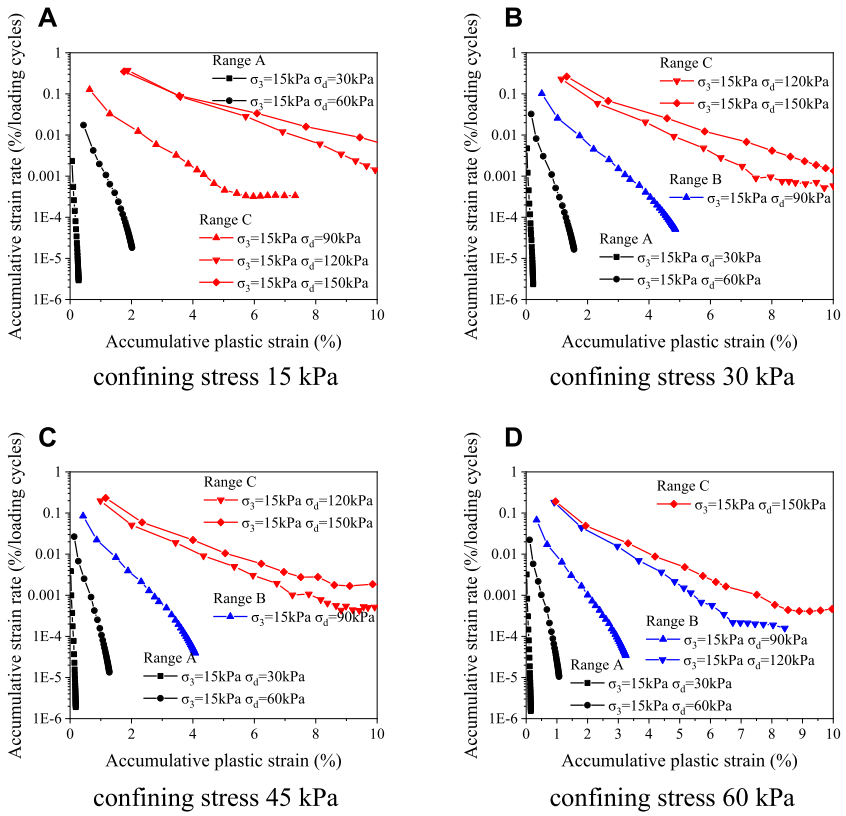

FIGURE 6
Accumulative plastic strains versus accumulative strain rates.

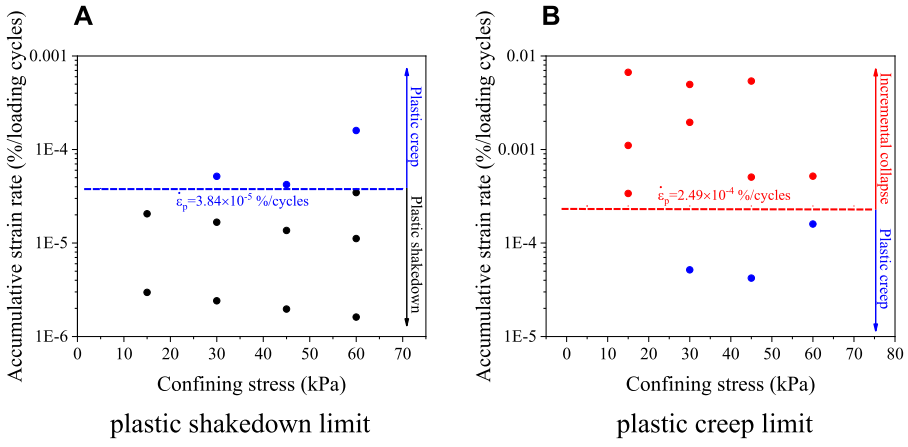

FIGURE 7
Accumulative strain rates at different plastic deformation behaviors.

3.2 Shakedown standard for typical deformation range

In order to determine the deformation range that belongs to which dynamic state of thawed subgrade soil, it is indispensable to propose a classification standard for different accumulative plastic strain behaviors of thawed soils under long-term cyclic loading. Based on the shakedown theory, S. Werkmeister et al. (Werkmeister et al., 2011) proposed two methods for analyzing the plastic deformation behavior of subgrade soils. One method is that the difference of accumulative plastic strain corresponding to fixed loading times (3,000 and 5,000) is used as the standard of plastic

deformation behavior. The other method is the relationship between the accumulative plastic strain and the accumulative strain rate. S. Werkmeister et al. (Werkmeister et al., 2011) observed that there were significant differences in the variation rules of accumulative plastic strain rate corresponding to different types of deformation behaviors as shown in Figure 5, and the accumulative plastic strain rate changes under different types of plastic deformation properties were statistically analyzed to establish a classification criterion based on the accumulative plastic strain rate for three plastic deformation behaviors of coarse-grained soil. However, the first method was not suitable for thawed subgrade silt under long-term traffic loading because, for the incremental collapse specimen, the loading numbers were approximately 3,000 times lower, corresponding to the failure state. Thus, the second method was selected for this paper. Meanwhile, the accumulative plastic strain rate is defined and calculated as Eq. 1.

Then, by using this method mentioned above, Li et al. (2021) and Wang et al. (Wang and Zhuang, 2021) were the proposed shakedown standard for silty soil and coarse-grained soil under cyclic loading, respectively. Thus, this paper established a shakedown standard for thawed subgrade soils by analyzing the accumulative plastic strain rate.

$$\dot{\varepsilon}_p = \mathrm{d}\varepsilon_p/\mathrm{d}N \tag{1}$$

where $\mathrm{d}\varepsilon_p$ is the increment of accumulative plastic strain in each loading cycle, and N is the number of loading cycles.

Figure 6 shows the accumulative plastic strain rates of thawed subgrade soils by processing the experimental data. It can be concluded clearly that the accumulative plastic strain rates of thawed subgrade soils can be classified into three categories: first, with the increase in loading cycles, the accumulative plastic strain rate of the specimen continues to decrease to a lower level, and the accumulative plastic strain is basically stable, which is determined to be plastic shakedown state, namely, range A; second, although the accumulative plastic strain rate decreases with the increase in loading cycles, it still maintains a certain level, and the accumulative plastic strain is still in a continuous development state, which is determined to be plastic creep state, namely, range B; third, the accumulative plastic strain rate decreases with the increase in loading cycles, but it still remains at a high level, and the accumulative plastic strain still increases rapidly, which is determined to be incremental collapse state, namely, range C. According to the above analysis, the classification results of thawed subgrade soils under various stress states have been noted in Figure 6.

The distributions of accumulative plastic strain rates of different plastic deformation behaviors are plotted, using counting minimum values of accumulative plastic strain rates of different ranges, as shown in Figure 7. Then, it can be indicated that the accumulative plastic strain rates under different plastic deformation behaviors show obvious differences and limits. The limit between plastic shakedown and plastic creep is defined as the plastic shakedown limit. The limit between plastic creep and incremental collapse is defined as the plastic creep limit. Furthermore, the intermediate values of the upper and lower boundary values are used as the critical rates for different plastic deformation behaviors, and the results are calculated by Eqs 2–4, which is the shakedown standard for determining the plastic deformation behavior of the thawed subgrade soils.

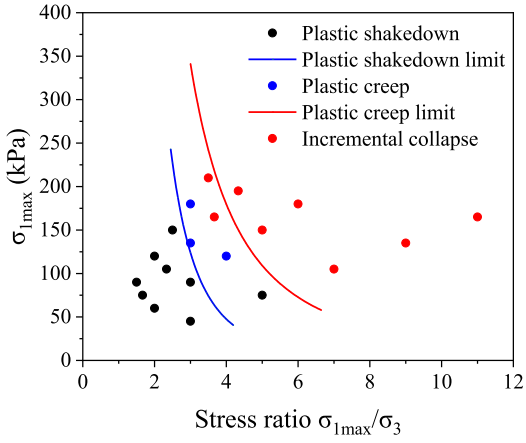

FIGURE 8
Critical dynamic stress for plastic shakedown and plastic creep.

Plastic shakedown range:

$$\dot{\varepsilon}_p < 3.84 \times 10^{-5}\%/\text{cycles} \tag{2}$$

Plastic creep range:

$$3.84 \times 10^{-5}\%/\text{cycles} \le \dot{\varepsilon}_p < 2.49 \times 10^{-4}\%/\text{cycles} \tag{3}$$

Incremental collapse range:

$$\dot{\varepsilon}_p \ge 2.49 \times 10^{-4}\%/\text{cycles} \tag{4}$$

3.3 Critical dynamic stress formula

In the shakedown theory, the critical dynamic stress for plastic shakedown and plastic creep limits can be expressed by the following equation (Werkmeister et al., 2011):

$$\sigma_{1\,\max} = \alpha\left(\frac{\sigma_{1\,\max}}{\sigma_3}\right)^{\beta} \tag{5}$$

where the σ_{1max} is the maximum of axial stress, σ_3 is the confining stress, α and β are the material parameters.

According to the above method, it can be seen from Figure 8 that the different plastic deformations have obvious boundaries, and the plastic shakedown, plastic creep, and incremental collapse are located in the left, middle, and right regions, respectively. Based on the distribution as shown in Figure 8, the calculation formulas can be fitted by Eq. 5. The fitted results and the calculations for critical dynamic stress are obtained and listed as Eqs 6 and 7 for plastic shakedown limit and plastic creep limit, respectively. It should be noted that due to the limited experimental conditions and data in

this paper, the empirical formula for the critical dynamic stress still needs more experimental data for improvement.

Plastic shakedown limit:

$$\sigma_{1\,\max} = 4802.1\left(\frac{\sigma_{1\,\max}}{\sigma_3}\right)^{-3.32} \quad (6)$$

Plastic creep limit:

$$\sigma_{1\,\max} = 3957.4\left(\frac{\sigma_{1\,\max}}{\sigma_3}\right)^{-2.23} \quad (7)$$

4 Conclusion

In this paper, a series of cyclic triaxial tests were conducted on the thawed subgrade soil to explore the accumulative plastic strain behavior under long-term traffic loading where the low liquid silt was selected as the typical subgrade material. The shakedown theory was adopted to analyze the evolution of the accumulative plastic deformation of the thawed subgrade soil, the shakedown standards for classifying different deformation ranges were investigated, and the calculations for critical dynamic stress were proposed based on the experimental results. The conclusions are summarized as follows:

(1) The development of an accumulative plastic strain of thawed subgrade soils was classified into three categories: plastic shakedown, plastic creep, and incremental collapse under different stress states. The dominant influences on the plastic deformation were caused by the amplitude of cyclic deviator and confining stress levels.

(2) By using the concept of accumulative plastic strain rate, the plastic deformation ranges were analyzed in detail, and the criteria of range classification were also defined, that is, the accumulative rate was greater than 2.49×10^{-4}%/cycles for incremental collapse range, less than 3.84×10^{-5}%/cycles for plastic shakedown range, and the other range for plastic creep state.

(3) The boundary functions for three different ranges were established through the confining stress (σ_3) and axial stress maximum (σ_{1max}), which is defined as the calculations for critical dynamic stress of plastic shakedown limit and plastic creep limit. This can provide a theoretical guideline for the evaluation of subgrade stability in the design and dynamic control in the service period.

Data availability statement

The original contributions presented in the study are included in the article/Supplementary material, further inquiries can be directed to the corresponding authors.

Author contributions

SW: Investigation, Writing–original draft. XL: Formal Analysis, Methodology, Writing–original draft. YT: Conceptualization, Writing–original draft. XZ: Writing–original draft. TY: Writing–original draft. RW: Writing–review and editing. XJ: Writing–review and editing. ZS: Writing–original draft. JH: Supervision, Validation, Writing–original draft, Writing–review and editing.

Funding

The author(s) declare that no financial support was received for the research, authorship, and/or publication of this article.

Conflict of interest

Authors SW, YT, TY, RW, XJ, and ZS were employed by Shandong High-speed Construction Management Group Co., Ltd.

The remaining authors declare that the research was conducted in the absence of any commercial or financial relationships that could be construed as a potential conflict of interest.

Publisher's note

All claims expressed in this article are solely those of the authors and do not necessarily represent those of their affiliated organizations, or those of the publisher, the editors and the reviewers. Any product that may be evaluated in this article, or claim that may be made by its manufacturer, is not guaranteed or endorsed by the publisher.

References

Beskou, N. D., and Theodorakopoulos, D. D. (2011). Dynamic effects of moving loads on road pavements: a review. *Soil Dyn. Earthq. Eng.* 31 (4), 547–567. doi:10.1016/j.soildyn.2010.11.002

Bian, X., Li, W., Hu, J., Liu, H., Duan, X., and Chen, Y. (2018). Geodynamics of high-speed railway. *Transp. Geotech.* 17, 69–76. doi:10.1016/j.trgeo.2018.09.007

Boulbibane, M., Collins, I. F., Ponter, A. R. S., and Weichert, D. (2005). Shakedown of unbound pavements. *Road Mater. Pavement Des.* 6 (1), 81–96. doi:10.1080/14680629.2005.9690000

Brown, S. F. (1996). Soil mechanics in pavement engineering. *Geotechnique* 46 (3), 383–426. doi:10.1680/geot.1996.46.3.383

Cai, Y., Chen, Y., Cao, Z., and Ren, C. (2018). A combined method to predict the long-term settlements of roads on soft soil under cyclic traffic loadings. *Acta Geotech.* 13 (5), 1215–1226. doi:10.1007/s11440-017-0616-3

Chai, J. C., and Miura, N. (2002). Traffic-load-induced permanent deformation of road on soft subsoil. *J. Geotechnical Geoenvironmental Eng.* 128 (11), 907–916. doi:10.1061/(asce)1090-0241(2002)128:11(907)

Chazallon, C., Koval, G., Hornych, P., Allou, F., and Mouhoubi, S. (2009). Modelling of rutting of two flexible pavements with the shakedown theory and the finite element method. *Comput. Geotechnics* 36 (5), 798–809. doi:10.1016/j.compgeo.2009.01.007

Cui, K., Qing, Y., Li, Q., Zhang, D., Li, P., and Liu, J. (2023c). Plastic shakedown limit of compacted clay: experiments and predicted model. *Eng. Geol.* 320, 107057. doi:10.1016/j.enggeo.2023.107057

Cui, X., Du, Y., Bao, Z., Xiao, Y., Hao, J., Li, X., et al. (2023b). Field evaluation of the three-dimensional dynamic stress state of the subgrade induced by the heavy-haul train load. *Transp. Geotech.* 38, 100903. doi:10.1016/j.trgeo.2022.100903

Cui, X., Du, Y., Hao, J., Bao, Z., Jin, Q., Li, X., et al. (2023a). Three-dimensional spatial stress state of highway subgrade under vehicle load: experimental evidence and evaluation model. *Int. J. Pavement Eng.* 24 (1). doi:10.1080/10298436.2023.2268795

Cui, X., Li, X., Du, Y., Bao, Z., Zhang, X., Hao, J., et al. (2024). Macro-micro numerical analysis of granular materials considering principal stress rotation based on DEM simulation of dynamic hollow cylinder test. *Constr. Build. Mater.* 412, 134818. doi:10.1016/j.conbuildmat.2023.134818

Cui, X., Li, X., Hao, J., Wang, Y., Bao, Z., Du, Y., et al. (2022). Dynamic response of unsaturated poroelastic ground underlying uneven pavement subjected to vehicle load. *Soil Dyn. Earthq. Eng.* 156, 107164. doi:10.1016/j.soildyn.2022.107164

Cui, X., Zhang, N., Zhang, J., and Gao, Z. (2014). *In situ* tests simulating traffic-load-induced settlement of alluvial silt subsoil. *Soil Dyn. Earthq. Eng.* 58, 10–20. doi:10.1016/j.soildyn.2013.11.010

Gu, F., Zhang, Y., Luo, X., Sahin, H., and Lytton, R. L. (2017). Characterization and prediction of permanent deformation properties of unbound granular materials for Pavement ME Design. *Constr. Build. Mater.* 155, 584–592. doi:10.1016/j.conbuildmat.2017.08.116

Hao, J., Cui, X., Bao, Z., Jin, Q., Li, X., Du, Y., et al. (2023). Dynamic resilient modulus of heavy-haul subgrade silt subjected to freeze-thaw cycles: experimental investigation and evolution analysis. *Soil Dyn. Earthq. Eng.* 173, 108092. doi:10.1016/j.soildyn.2023.108092

Hao, J., Cui, X., Qi, H., Zheng, Y., and Bao, Z. (2022). Dynamic behavior of thawed saturated saline silt subjected to freeze-thaw cycles. *Cold Regions Sci. Technol.* 194, 103464. doi:10.1016/j.coldregions.2021.103464

Krechowiecki-Shaw, C. J., Jefferson, I., Royal, A., Ghataora, G. S., and Alobaidi, I. M. (2016). Degradation of soft subgrade soil from slow, large, cyclic heavy-haul road loads: a review. *Can. Geotechnical J.* 53 (9), 1435–1449. doi:10.1139/cgj-2015-0234

Lei, H., Zhang, J.-F., Qian, J.-G., Dai, Y.-C., and Shen, J. (2023). Dynamic shakedown limits of the pavement on saturated subgrade subjected to traffic rolling-sliding loading. *Comput. Geotechnics* 163, 105743. doi:10.1016/j.compgeo.2023.105743

Leng, W., Xiao, Y., Nie, R., Zhou, W., and Liu, W. (2017). Investigating strength and deformation characteristics of heavy-haul railway embankment materials using large-scale undrained cyclic triaxial tests. *Int. J. Geomechanics* 17 (9). doi:10.1061/(asce)gm.1943-5622.0000956

Li, D., and Selig, E. T. (1996). Cumulative plastic deformation for fine-grained subgrade soils. *J. Geotechnical Eng.* 122 (12), 1006–1013. doi:10.1061/(asce)0733-9410(1996)122:12(1006)

Li, Y., Nie, R., Leng, W., Guo, Y., Dong, J., and Sun, B. (2021). Cumulative permanent strain and critical dynamic stress of silty filler for subgrade subjected to intermittent cyclic loading of trains. *Bull. Eng. Geol. Environ.* 80 (4), 3079–3096. doi:10.1007/s10064-021-02125-5

Lin, B., Zhang, F., Feng, D., Tang, K., and Feng, X. (2017). Accumulative plastic strain of thawed saturated clay under long-term cyclic loading. *Eng. Geol.* 231, 230–237. doi:10.1016/j.enggeo.2017.09.028

Liu, H., Wang, C., Liu, X., Wu, D., Yang, H., Zhang, Z., et al. (2022). Deformation characteristics and prediction of unbound volcanic ash pavement based on the mechanistic-empirical design guide. *Constr. Build. Mater.* 327, 126975. doi:10.1016/j.conbuildmat.2022.126975

Liu, J., Chang, D., and Yu, Q. (2016). Influence of freeze-thaw cycles on mechanical properties of a silty sand. *Eng. Geol.* 210, 23–32. doi:10.1016/j.enggeo.2016.05.019

Lu, Z., Fang, R., Yao, H., Hu, Z., and Liu, J. (2018). Evaluation and analysis of the traffic load–induced settlement of roads on soft subsoils with low embankments. *Int. J. Geomechanics* 18 (6). doi:10.1061/(asce)gm.1943-5622.0001123

Lu, Z., She, J., Wu, X., and Yao, H. (2019). Cumulative strain characteristics of compacted soil under effect of freeze-thaw cycles with water supply. *Transp. Geotech.* 21, 100291. doi:10.1016/j.trgeo.2019.100291

Pei, Q. Y., Zou, W. L., Han, Z., Wang, X. Q., and Xia, X. L. (2024). Compression behaviors of a freeze–thaw impacted clay under saturated and unsaturated conditions. *Acta Geotech.* doi:10.1007/s11440-023-02188-6

Puppala, A. J., Saride, S., and Chomtid, S. (2009). Experimental and modeling studies of permanent strains of subgrade soils. *J. Geotechnical Geoenvironmental Eng.* 135 (10), 1379–1389. doi:10.1061/(asce)gt.1943-5606.0000163

Qi, J., Ma, W., and Song, C. (2008). Influence of freeze–thaw on engineering properties of a silty soil. *Cold Regions Sci. Technol.* 53 (3), 397–404. doi:10.1016/j.coldregions.2007.05.010

Qi, J., Vermeer, P. A., and Cheng, G. (2006). A review of the influence of freeze-thaw cycles on soil geotechnical properties. *Permafr. Periglac. Process.* 17 (3), 245–252. doi:10.1002/ppp.559

Qian, J., Wang, Y., Wang, J., and Huang, M. (2019). The influence of traffic moving speed on shakedown limits of flexible pavements. *Int. J. Pavement Eng.* 20 (2), 233–244. doi:10.1080/10298436.2017.1293259

Ramos, A., Gomes Correia, A., Indraratna, B., Ngo, T., Calçada, R., and Costa, P. A. (2020). Mechanistic-empirical permanent deformation models: laboratory testing, modelling and ranking. *Transp. Geotech.* 23, 100326. doi:10.1016/j.trgeo.2020.100326

Sharp, R. W., and Booker, J. R. (1984). Shakedown of pavements under moving surface loads. *J. Transp. Eng.* 110 (1), 1–14. doi:10.1061/(asce)0733-947x(1984)110:1(1)

Wang, J., Ling, X., Li, Q., Zhang, F., and Li, Y. (2018). Accumulated permanent strain and critical dynamic stress of frozen silty clay under cyclic loading. *Cold Regions Sci. Technol.* 153, 130–143. doi:10.1016/j.coldregions.2018.05.007

Wang, J., and Yu, H. S. (2021). Shakedown analysis and its application in pavement and railway engineering. *Comput. Geotechnics* 138, 104281. doi:10.1016/j.compgeo.2021.104281

Wang, K., and Zhuang, Y. (2021). Characterizing the permanent deformation Response-Behavior of subgrade material under cyclic loading based on the shakedown theory. *Constr. Build. Mater.* 311, 125325. doi:10.1016/j.conbuildmat.2021.125325

Wang, T.-l., Liu, Y.-j., Yan, H., and Xu, L. (2015). An experimental study on the mechanical properties of silty soils under repeated freeze–thaw cycles. *Cold Regions Sci. Technol.* 112, 51–65. doi:10.1016/j.coldregions.2015.01.004

Werkmeister, S., Dawson, A. R., and Wellner, F. (2011). Permanent deformation behaviour of granular materials. *Road Mater. Pavement Des.* 6 (1), 31–51. doi:10.3166/rmpd.6.31-51

Xiao, J., Juang, C. H., Xu, C., Li, X., and Wang, L. (2014). Strength and deformation characteristics of compacted silt from the lower reaches of the Yellow River of China under monotonic and repeated loading. *Eng. Geol.* 178, 49–57. doi:10.1016/j.enggeo.2014.06.008

Xiao, J., Zhang, D., Wei, K., and Luo, Z. (2017). Shakedown behaviors of railway ballast under cyclic loading. *Constr. Build. Mater.* 155, 1206–1214. doi:10.1016/j.conbuildmat.2017.07.225

Xiao, Y., Zhang, Z., Chen, L., and Zheng, K. (2018a). Modeling stress path dependency of cyclic plastic strain accumulation of unbound granular materials under moving wheel loads. *Mater. Des.* 137, 9–21. doi:10.1016/j.matdes.2017.10.024

Xiao, Y., Zheng, K., Chen, L., and Mao, J. (2018b). Shakedown analysis of cyclic plastic deformation characteristics of unbound granular materials under moving wheel loads. *Constr. Build. Mater.* 167, 457–472. doi:10.1016/j.conbuildmat.2018.02.064

Zhai, B., Leng, W., Xu, F., Zhang, S., Ye, X., and Leng, H. (2020). Critical dynamic stress and shakedown limit criterion of coarse-grained subgrade soil. *Transp. Geotech.* 23, 100354. doi:10.1016/j.trgeo.2020.100354

Zhang, J., Peng, J., Zhang, A., and Li, J. (2020a). Prediction of permanent deformation for subgrade soils under traffic loading in Southern China. *Int. J. Pavement Eng.* 23, 673–682. doi:10.1080/10298436.2020.1765244

Zhang, L., Ren, F., Li, H., Cheng, D., and Sun, B. (2021). The influence mechanism of freeze-thaw on soil erosion: a review. *Water* 13 (8), 1010. doi:10.3390/w13081010

Zhang, X., Zhang, Y., Liu, X., Liu, J., and Liu, J. (2020b). Shakedown behavior of yellow river alluvial silt stabilized with lignin–lime combined additive. *J. Mater. Civ. Eng.* 32 (1). doi:10.1061/(asce)mt.1943-5533.0002954

Zhang, X.-n., Cui, X.-z., Ding, L.-q., Luan, J.-y., Wang, Y.-l., Jiang, P., et al. (2023). Effects of a novel hybrid polymer material on the hydro-mechanical behavior of subgrade silts considering freeze-thaw cycles. *Cold Regions Sci. Technol.* 205, 103698. doi:10.1016/j.coldregions.2022.103698

Zhao, J. S., Duan, S. Q., Chen, B. R., Li, L., He, B. G., Li, P. X., et al. (2024). Failure mechanism of rock masses with complex geological conditions in a large underground cavern: a case study. *Soil Dyn. Earthq. Eng.* 177, 108439. doi:10.1016/j.soildyn.2023.108439

Zhao, J. S., Jiang, Q., Lu, J. F., Chen, B. R., Pei, S. F., and Wang, Z. L. (2022). Rock fracturing observation based on microseismic monitoring and borehole imaging: *in situ* investigation in a large underground cavern under high geostress. *Tunn. Undergr. Space Technol.* 126, 104549. doi:10.1016/j.tust.2022.104549

Zhou, Z., Ma, W., Li, G., and Shen, M. (2020). A novel evaluation method for accumulative plastic deformation of granular materials subjected to cyclic loading: taking frozen subgrade soil as an example. *Cold Regions Sci. Technol.* 179, 103152. doi:10.1016/j.coldregions.2020.103152

Zhou, Z., Shen, M., and Wang, Q. (2022). Critical dynamic stress for the frozen subgrade soil. *Road Mater. Pavement Des.* 24 (4), 935–959. doi:10.1080/14680629.2022.2052940

frontiers | Frontiers in Earth Science

TYPE Original Research
PUBLISHED 14 March 2024
DOI 10.3389/feart.2024.1378264

Check for updates

OPEN ACCESS

EDITED BY
Jianyong Han,
Shandong Jianzhu University, China

REVIEWED BY
Yong Niu,
Shaoxing University, China
Chao Wang,
Kunming University of Science and Technology, China

*CORRESPONDENCE
Jian-Cong Zhang,
zhang_jc4@hdec.com
Shu-Feng Pei,
peishufeng@ncwu.edu.cn

RECEIVED 29 January 2024
ACCEPTED 28 February 2024
PUBLISHED 14 March 2024

CITATION
Zhao J-S, Zhang J-C, Pei S-F, Xing L, Chen C-F and Zhang G-D (2024), Investigation on the failure mechanism of the collapse of the columnar jointed basalt in underground cavern.
Front. Earth Sci. 12:1378264.
doi: 10.3389/feart.2024.1378264

COPYRIGHT
© 2024 Zhao, Zhang, Pei, Xing, Chen and Zhang. This is an open-access article distributed under the terms of the Creative Commons Attribution License (CC BY). The use, distribution or reproduction in other forums is permitted, provided the original author(s) and the copyright owner(s) are credited and that the original publication in this journal is cited, in accordance with accepted academic practice. No use, distribution or reproduction is permitted which does not comply with these terms.

Investigation on the failure mechanism of the collapse of the columnar jointed basalt in underground cavern

Jin-Shuai Zhao[1,2,3], Jian-Cong Zhang[1]*, Shu-Feng Pei[4]*, Liang Xing[5], Chong-Feng Chen[6] and Guang-Duan Zhang[7]

[1]PowerChina Huadong Engineering Corporation Limited, Hangzhou, China, [2]Faculty of Civil Engineering and Mechanics, Jiangsu University, Zhenjiang, China, [3]Key Laboratory of Geotechnical Mechanics and Engineering of Ministry of Water Resources, Yangtze River Scientific Research Institute, Wuhan, China, [4]North China University of Water Resources and Electric Power, Zhengzhou, China, [5]Guangdong Provincial Academy of Building Research Group Corporation Limited, Guangzhou, China, [6]Xi'an Research Institute, China Coal Technology and Engineering Group Corporation, Xi'an, China, [7]Heze Mudan District Natural Resources Bureau, Heze, China

Columnar jointed basalt (CJB) is a kind of jointed rock with a polygonal cylinder mosaic structure that has complex mechanical properties such as discontinuity and heterogeneity. The typical geological structure of the CJB is the intercolumnar joint plane and the implicit joint plane, which obviously affect the mechanical properties of the rock mass. Controlling the unloading relaxation of the CJB is a key problem during the construction of underground engineering. In this paper, *in-situ* acoustic wave and panoramic borehole camera measurements were carried out in the cavern of the Baihetan project to understand the failure mechanism of the collapse of the CJB. It was quite clear that the evolution of the excavation damage zone (EDZ) of the CJB depends on the time and spatial effects. The closer to the collapse zone, the greater the degree of relaxation failure of the columnar joint rock mass; the further away from the cavern perimeter, the more stable the surrounding rock. The correction between wave velocity and cracks in the rock mass was also discussed. This field test and theoretical analysis can provide a reference for studying the failure mechanism and control measures of CJB in underground caverns under high geostress.

KEYWORDS

columnar jointed basalt, underground cavern, collapse mechanism, mechanical properties, rock fracture

1 Introduction

The columnar joint is a common primary fracture structure in basalt (Hoek and Brown, 1980; Jiang et al., 2014; Shi et al., 2020; Zhao et al., 2022a; b). Columnar joints are formed by cooling shrinkage during diagenesis and are more common in thick lavas (Schultz, 1995; Almqvist et al., 2012; Jiang et al., 2019; Liu et al., 2023). Columnar joints divide the rock mass into regular polygonal long columns, essentially perpendicular to the lava plane. As a type of dense jointed rock with a regular planar network structure, columnar jointed rock has complex mechanical response processes under high

geostress, such as joint surface opening, rock block fracture and relaxation failure (Brady and Brown, 2005; Xia et al., 2020; 2023; 2024; Hu et al., 2023; Zheng et al., 2023a; b; Si et al., 2024a; b; Wang et al., 2024). Given the weak and complex mechanical properties of columnar joints, it is easy to induce failures during the excavation of the CJB in underground caverns (Hao et al., 2016; 2021; 2022; Li et al., 2020; 2023; Zhao et al., 2023).

Structural planes such as joints, fissures and faults are common in rock materials (Saliba and Jagla, 2003; Li et al., 2021; 2022; 2024; Zhang et al., 2022). The structural plane is the most important factor in controlling the deformation, strength and permeability of the surrounding rock of the tunnel (Smith and Holden, 2021; Cai et al., 2022a; b, 2023; Guo et al., 2023a; b; Xu et al., 2024; Lu et al., 2024). The structural plane derives the complex properties such as anisotropy and heterogeneity of the surrounding rock, which makes the mechanical behavior of the rock mass much more complex than that of general homogeneous, continuous and isotropic materials (Jin et al., 2014; Xia et al., 2020; Lei et al., 2023; Chen et al., 2024; Zhao et al., 2024a; Zhao et al., 2024b). In essence, the fracture of the CJB is a three-dimensional evolutionary process (Feng et al., 2021; Yang et al., 2021; Deng et al., 2023). To fully understand the mechanical property of rock fracture, high-precision microseismic (MS) monitoring technology is introduced into underground caverns to monitor the fracture process of the CJB (Chen et al., 2014; Han et al., 2023). The 3D fracture process of the CJB under strong excavation unloading, in particular the time-dependent relaxation and spatial heterogeneity, has been successfully revealed by MS monitoring (Feng et al., 2015). In short, the MS monitoring technology can effectively resolve the basic spatiotemporal characteristics of the microseismicity of the CJB in caverns.

To investigate the relaxation characteristics and failure mechanism of the collapse of the CJB, acoustic velocity measurements and a panoramic borehole camera were carried out in the underground cavern. The results presented in this paper provide an indication of the excavation induced mechanical response of the CJB.



FIGURE 1
Aerial view of the Baihetan project in the Jinsha River, China.

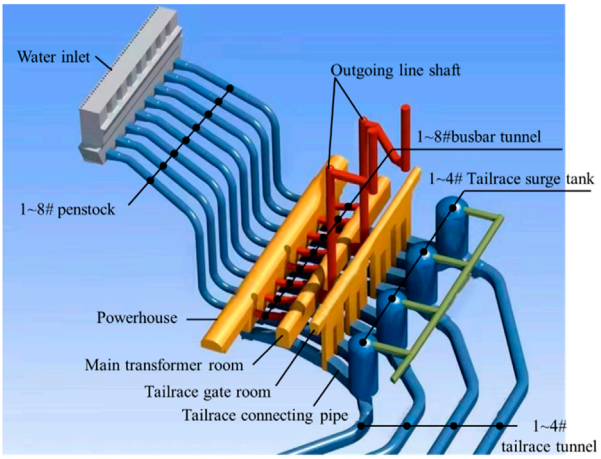

FIGURE 2
Spatial layout of the left caverns in the Baihetan project.

2 Project background

2.1 Project introduction

The aerial view of the Baihetan project is shown in Figure 1. The hydropower project is equipped with eight sets of hydropower generating units on both the left and right banks. The capacity of each hydropower generator of the project is 1000 MW. The total excavation length and volume of the underground cavern groups are 217 km and 25 million m^3, respectively. The concrete dam of the project is designed as a double curved dam, which is located in an asymmetrical valley in the V shape.

The spatial layout of the left cavern groups of the Baihetan project is exhibited in Figure 2. The four large caverns, namely, the powerhouse, the tailrace surge tank, the main transformer room and the tailrace gate room, are arranged parallel to each other. The busbar tunnels and the tailrace connection pipes are arranged perpendicular to the axis of the powerhouse.

2.2 Geological information

The columnar jointed basalts of the Baihetan project are developed in several rock flow layers, and the columnar jointed basalts of the $P_2\beta_2^3$ layer are exposed in the tailrace connection pipes. Depending on the diameter and length of the column, the Baihetan columnar jointed basalts can be divided into three categories: small, medium and large columnar jointed basalts. The small columnar jointed basalt is 13–25 cm in diameter, and 2–3 m in length. The micro-cracks are developed, and the length of the cut block is about 5 cm. The diameter of the medium columnar jointed basalt is 25–50 cm, and the length of the column is generally 0.5–2.0 m. The internal micro-cracks are developed, but the mutual occlusion is not completely cut off, and the block size is about 10 cm. The large columnar jointed basalt has a diameter of 0.5–2.5 m and a length of 1.5–5 m.

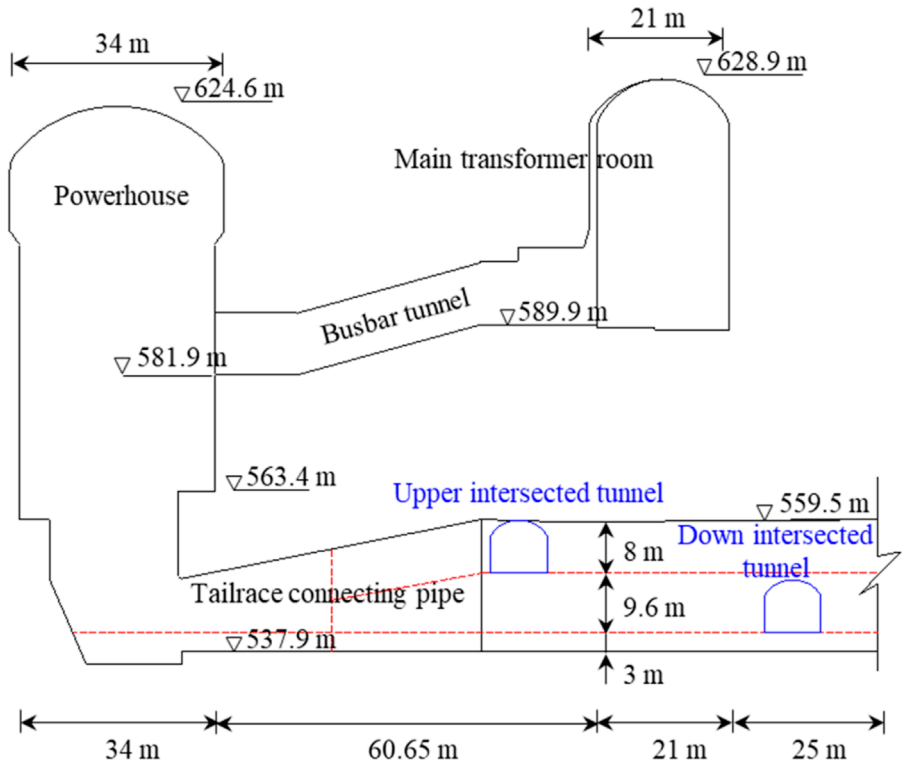

FIGURE 3
Excavation scheme of the tailrace connection pipe in the caverns.

2.3 Excavation scheme

The tailrace connection pipes are located between the powerhouse and the tailrace surge tank. The axis of the tailrace connection pipe is perpendicular to the axis of the powerhouse. There are a total of eight tailrace connection pipes, which are arranged approximately in parallel with equal spacing of 38 m. The sectional shape of the tailrace connection pipe is a straight wall and semi-circular arch. The width and the height of the tailrace connection pipe are 16.0 and 20.6 m, respectively. Therefore, the tailrace connection pipes adopt a layered excavation scheme along the elevation direction. The specific excavation scheme of the tailrace connection pipe is shown in Figure 3. The tailrace connection pipe is divided into three layers along the elevation direction, and the excavation heights of each layer are 8, 9.6 and 3.0 m, respectively. The layer excavation boundary of the tailrace connection pipe is indicated by the red dashed line in Figure 3.

3 Collapse mechanism of the CJB

3.1 Characteristics of collapse

During the excavation of the cavern, a large scale collapse of the rock mass occurred in the sidewalls of the No. 5 tailrace connection pipe. The depth of the collapsed area is approximately 1.5 m, and the extent of the collapse failure is very severe (Figure 4). The site investigation shows that the CJB was developed in this region. The collapse area is close to the working face and the vibration damage to the CJB in this area is severe under the influence of the blast disturbance. In addition, only steel mesh and shotcrete support is used after excavation and no effective reinforcement measures, such as systematic bolting and anchoring cables, are adopted to control the relaxation failure of the CJB. This is another important reason for the collapse of the surrounding rock in this area.

3.2 Geological analysis

The geological survey reveals that the typical CJB exposed in the tailrace connection pipes is shown in Figure 5. The cross section of the CJB is irregular polygon, mainly pentagon and hexagon. The edge length of the irregular polygon is in the range of 10–25 cm, and the axis inclination of the CJB is about 75° ~ 85° (Figure 5A). The intercolumnar joint plane, formed by condensation shrinkage of the basalt, is the main structural plane of the CJB. The intercolumnar joint plane is covered with a chlorite film and has an oily sheen. In addition to the intercolumnar joint plane, there are a large number of implicit joint planes in the CJB (Figure 5B). Note that, depending on the occurrence of joints, the implicit joints developed in the column are mainly steeply inclined implicit joints and gently inclined implicit joints.

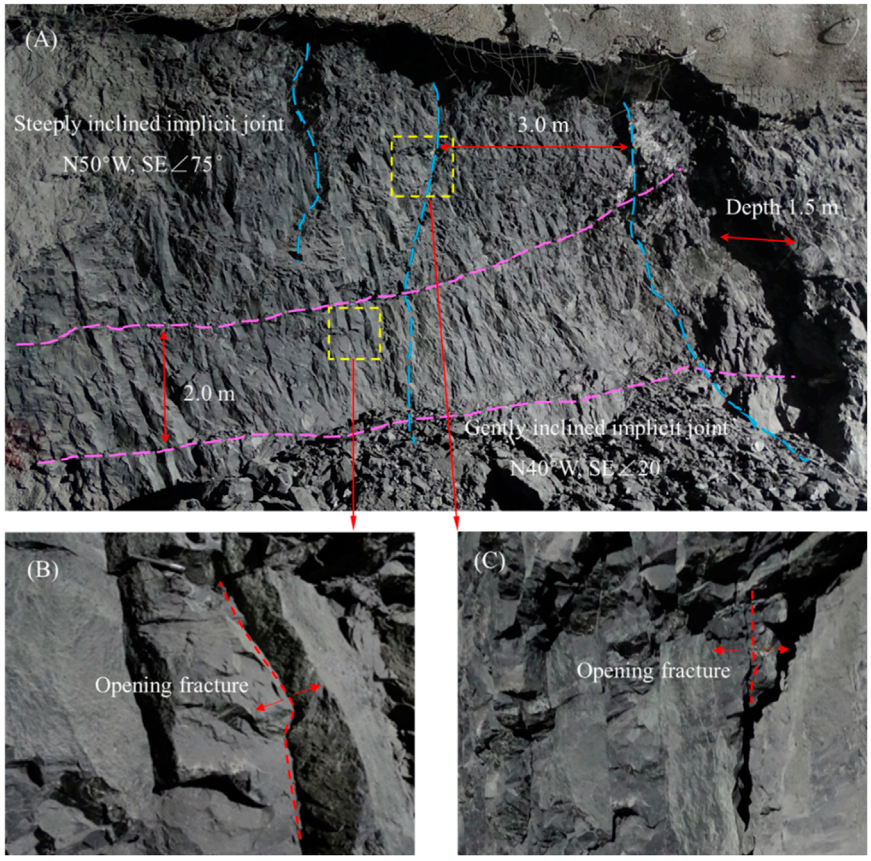

FIGURE 4
Collapse of the columnar jointed basalt. **(A)** geological of the collapse zone, **(B)** opening failure of the intercolumnar joint plane, **(C)** fracture of the implicit joint plane.

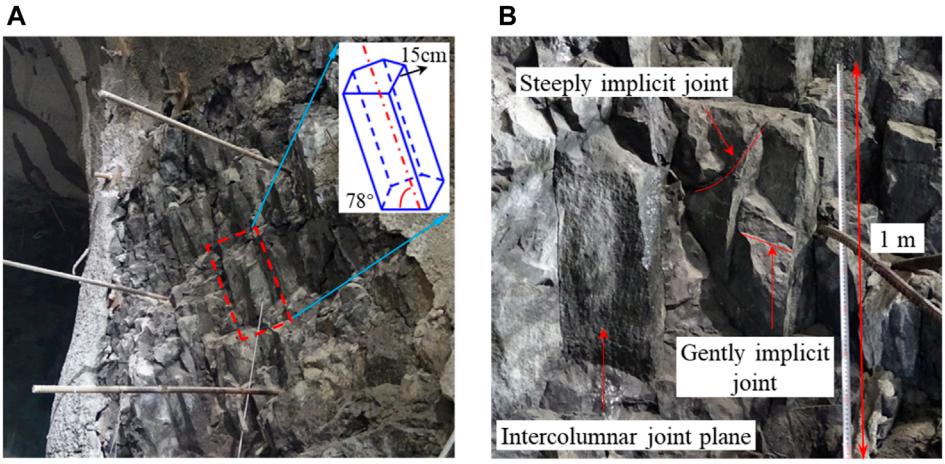

FIGURE 5
Typical characteristic of the columnar jointed basalt exposed in the cavern. **(A)** irregular polygon, **(B)** intercolumnar and implicit joint planes.

In the stress compression state, the internal joints of the rock are tightly closed and embedded, and the mechanical performance of the rock mass is good. However, the stress is adjusted and redistributed after excavation and unloading. It has been found that the material discontinuity of the structural plane has a significant influence on the failure mode of the rock mass during cavern

excavation. The joint surface between the columns slowly opens after the confining pressure is released (Figure 4B). The implicit joints in the column then rupture (Figure 4C). Failure of the joint plane, such as opening and sliding during excavation unloading, results in a significant reduction in the mechanical strength of the CJB. Under the action of unfavorable geological conditions and excavation unloading, the CJB relaxes, resulting in deformation and collapse to the air face.

3.3 Acoustic measurement

3.3.1 Layout of boreholes

An *in-situ* acoustic wave measurement was carried out in the No. 5 tailrace connection pipe to deeply detect and reveal the failure mechanism of the collapse of the columnar jointed basalt under blast disturbance. Four acoustic boreholes were drilled in the sidewalls near the collapse area of the No. 5 tailrace connection pipe. The specific layout of the acoustic boreholes is shown in Figure 6. From the left to the right sidewall of the No. 5 tailrace connection pipe, the acoustic boreholes are labelled D1, D2, D3, and D4, respectively. These boreholes are arranged parallel to each other, and the distance between the adjacent boreholes is 1 m. The length of these boreholes is 8 m.

3.3.2 Relaxation characteristics

Excavation-induced unloading relaxation characteristics of the rock mass can be reflected by the acoustic wave testing. In order to study the temporal evolution of the relaxation characteristics of the CJB, multiple acoustic tests were carried out in the collapse area of the No. 5 tailrace connection pipe. The criterion for assessing the relaxation depth of the rock mass is the apparent inflection point of the acoustic velocity (Feng et al., 2016). It is clearly shown that the acoustic velocity of the relaxation zone is less than 3,500 m/s, displaying that the relaxation fracture of the surrounding rock is severe in this part of the area (Figure 7). The acoustic velocity is related to the lithology, rigidity and integrity of the rock mass. It is therefore concluded that the micro-cracks and fractures in the relaxation zone are open. The acoustic velocity of the surrounding rock in the deeper zone away from the free face is approximately 5,500 m/s, indicating that the surrounding rock in this area is relatively intact. Notably, there is a localised zone of acoustic velocity decrease in the surrounding rock, which drops to approximately 4,200 m/s (Figures 7C, D). In fact, the surrounding rock in the deeper part of the borehole is in a three-dimensional compressional state and the rapid decrease in acoustic velocity indicates that there is a micro-crack zone in this area. The results of multiple acoustic wave measurements show that the relaxation depth of the CJB gradually increases with time. The acoustic velocity of the rock mass also decreases with time. It is quite clear that the evolution of the unloading relaxation of the CJB is dependent on the effect of time. Therefore, timely and effective placement of support reinforcement after excavation is of great importance to control the growth of the relaxation depth of the CJB.

The temporal evolution of the excavation damage zone of the CJB in the No.5 tailrace connection pipe is shown in Figure 8. The EDZs of the No.5 tailrace connection pipe are in the range of 1.8–2.4 m. Obviously, the measured excavation damage zone of the borehole near the collapse area (D1 and D3) is greater than that of the borehole away from the collapse area (D2 and D4). The maximum excavation damage zone of the boreholes near and far from the collapse area is 2.4 and 2.1 m, respectively. And the

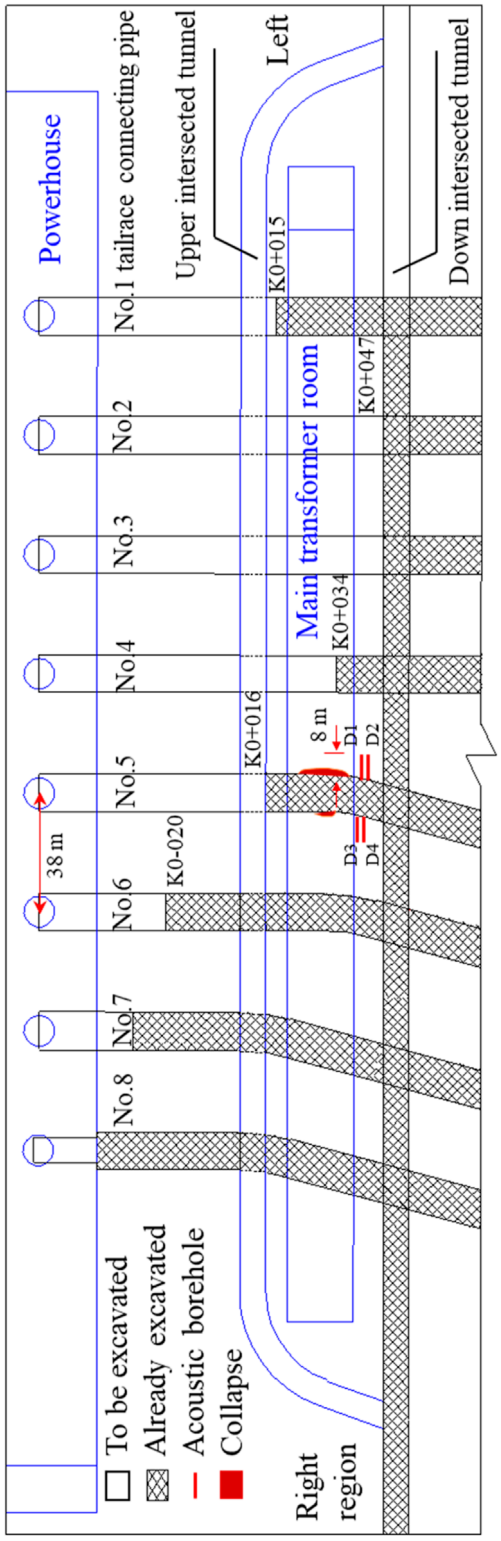

FIGURE 6
Layout of the acoustic boreholes of the No.5 tailrace connection pipe.

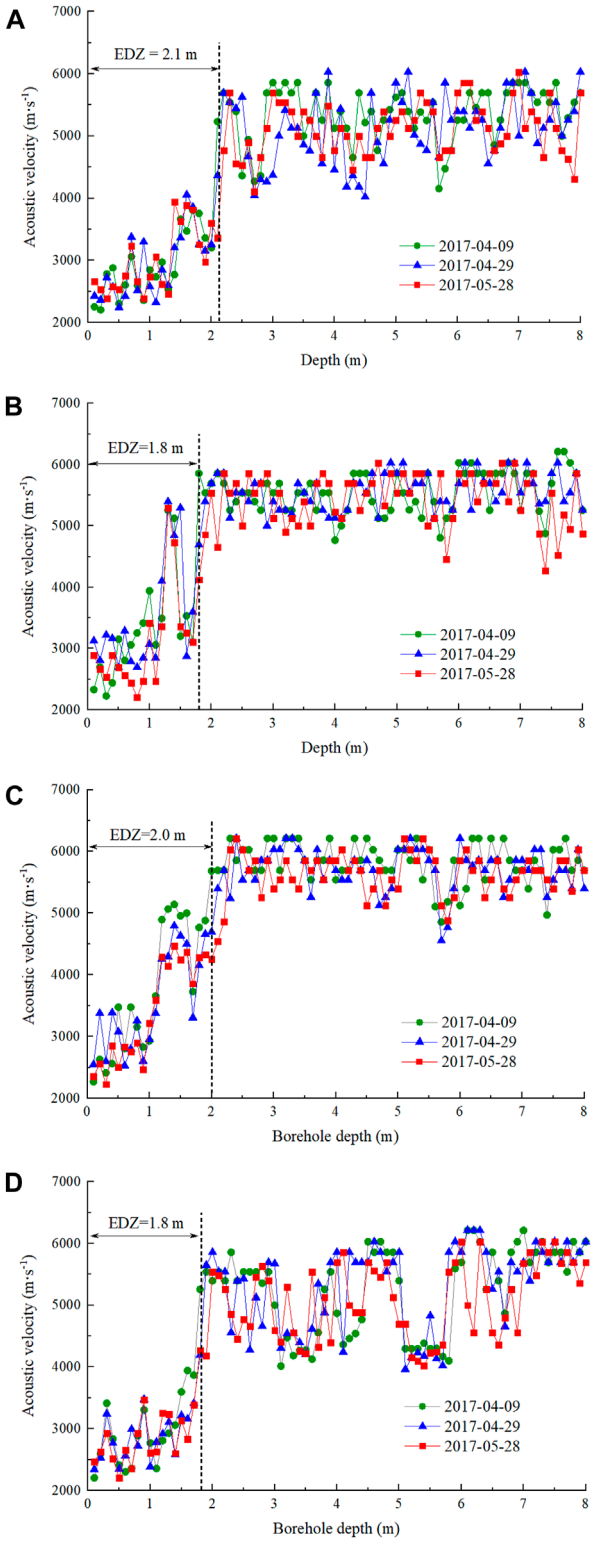

FIGURE 7
Observed acoustic velocity of the rock mass in boreholes **(A)** D1, **(B)** D2, **(C)** D3, **(D)** D4.

minimum excavation damage zone of the boreholes near and far from the collapse area is 2.0 and 1.8 m, respectively. Therefore, the development of the excavation damage zone of the CJB also depends on the spatial effect. In other words, the closer to the collapse zone, the greater the degree of relaxation failure of the CJB; the further away from the cavern perimeter, the more stable the rock mass.

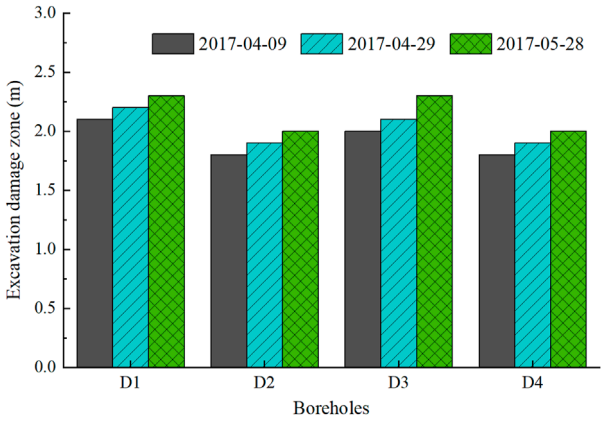

FIGURE 8
Temporal evolution of the excavation damage zone of the columnar jointed basalt.

3.4 Panoramic borehole camera

In order to study the internal joints in the EDZ of the surrounding rock more intuitively, the crack characteristics of the CJB were observed using the panoramic borehole camera. Typical test results from a borehole camera are shown in Figure 9. The observation results display that there are a large number of joints or macroscopic fractures in the region of 0–1 m from the cavern perimeter, illustrating that the integrity of the CJB is very poor. The widths of these macroscopic fractures are 1–3 cm, with a maximum of 5 cm. The fracture planes extend to a depth of 2 m from the cavern perimeter, indicating that stress relaxation and fracturing of the rock mass is severe. Macroscopic cracks with a width of 2–8 cm are also distributed in the deeper part of the surrounding rock. In addition, a large number of implicit joints are developed in the region of 4–8 m from the cavern perimeter, declaring that the lithology of the CJB as a whole is poor.

In the absence of excavation disturbance, the implicit joints are in a closed state and the rock mass shows no obvious damage. However, the typical geological structure such as the intercolumnar joint plane and the implicit joint plane are developed in the CJB. These discontinuous geological structure not only reduces the integrity of the rock mass, but also affect the mechanical properties of the rock mass. Therefore, under the action of excavation unloading or external force disturbance, the CJB has a potential risk of large-scale unloading relaxation damage. Under the disturbance of excavation unloading, the joint surface between the columns tends to relax and open, forming macroscopic cracks and increasing the risk of collapse failure of the rock mass. In addition, the borehole camera results show that the internal joint surface and cracks are more developed and the cracks cut through the rock mass, resulting in poor overall integrity of the surrounding rock of the CJB (Muller, 1998; Antonellini and Mollema, 2019). This is also the reason why the shallow surrounding rock of the cavern is prone to collapse after mining of the CJB.

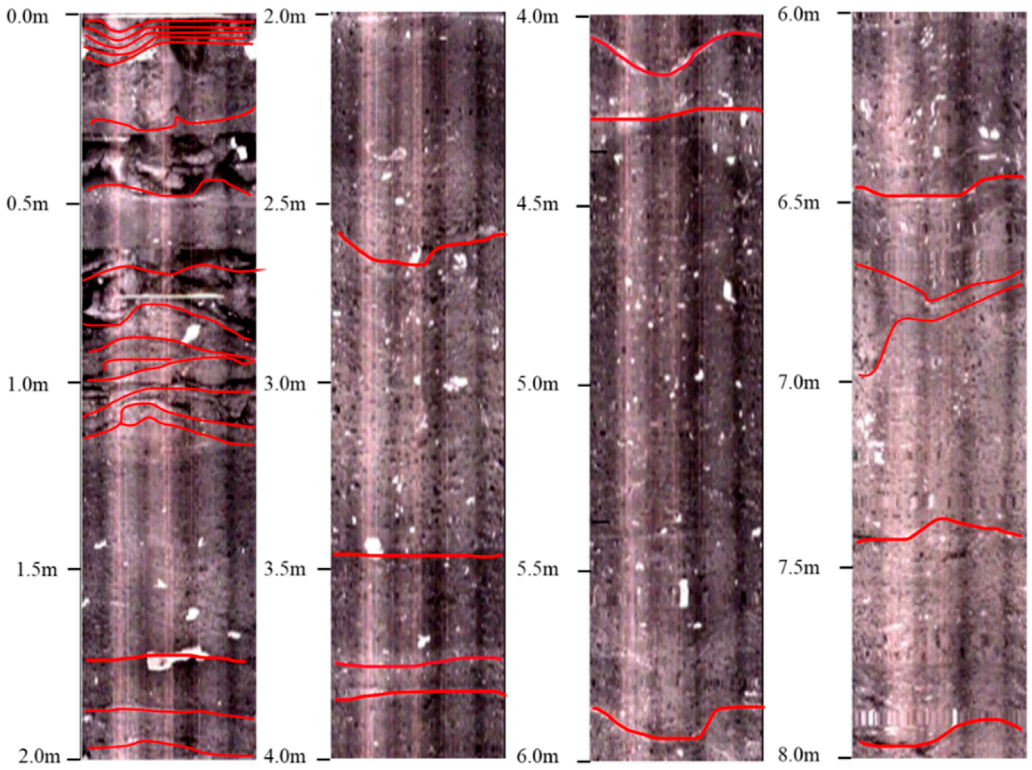

FIGURE 9
Results of borehole camera observations of the columnar jointed basalt.

4 Discussion

4.1 Correlation between acoustic velocity and cracks

A comparison between the acoustic velocity results and the cracks in the CJB is indicated in Figure 10. The acoustic test shows that the velocity of the CJB in the shallow range of 0–1 m from the cavern perimeter is significantly reduced by excavation unloading, and the average wave velocity is reduced to 2,500 m/s. The average velocity of the rock in the 1–2 m range increases to 4,200 m/s and it is speculated that the quality or integrity of the rock in this area is slightly better than that in the 0–1 m range. The panoramic borehole camera shows that many cracks are developed in the range of 0–1 m from the cavern perimeter, and breakouts are also observed in the borehole. With respect to the range of 0–1 m, the number and size of cracks in the range of 1–2 m are significantly reduced. It is worth noting that the wave velocity of the rock mass drops sharply at a depth of approximately 4.4 m, corresponding to a distinct fracture observed by the borehole camera (see star in Figure 10). The same feature is found at a depth of approximately 5.8 m from the cavern perimeter. Therefore, comparative analysis of the borehole camera and acoustic test shows that the variation in wave velocity is consistent with the distribution of cracks. In other words, the velocity of the surrounding rock is significantly reduced in the area where the cracks are densely developed.

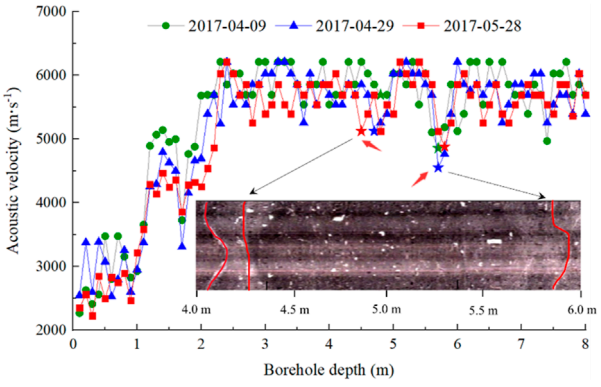

FIGURE 10
Comparison between the results of acoustic velocity and cracks in the borehole.

4.2 Strength of the CJB

The strength of the rock mass is closely related to the quality of the rock. The main basis for assessing rock quality is the structural characteristics and the structure plane state of the rock mass. The physical and mechanical properties of jointed rock can be quantitatively characterised by the Hoek-Brown criterion. And the computational formula of the criterion is as shown in Eqs. 1–4

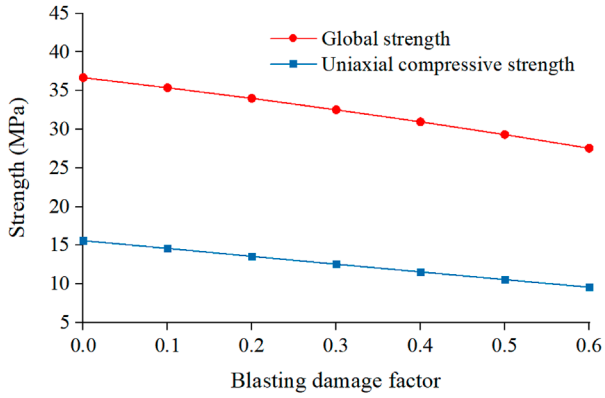

FIGURE 11
Evolution of rock mass strength with variation of the blasting damage factor.

(Martin et al., 1999):

$$\sigma_1 = \sigma_3 + \sigma_c\left(m_b\frac{\sigma_3}{\sigma_c} + s\right)^a \quad (1)$$

$$m_b = m_i \exp\left(\frac{GSI - 100}{28 - 14D}\right) \quad (2)$$

$$s = \exp\left(\frac{GSI - 100}{9 - 3D}\right) \quad (3)$$

$$a = \frac{1}{2} + \frac{1}{6}\left(\exp\left(-\frac{GSI}{15}\right) - \exp\left(-\frac{20}{3}\right)\right) \quad (4)$$

Where σ_c is the uniaxial compressive strength of the intact rock; m_i is the rock material constant; m_b, s, and a are the empirical parameters of the Hoek-Brown criteria; GSI is the geological strength index; D is the blasting damage factor.

The Geological Strength Index (GSI) is a quantitative index for assessing the strength of the rock mass (Hoek et al., 1998). As an important parameter of the Hoek-Brown criterion, GSI realises the quantitative calculation of the rock mass strength. The rock mass parameters of the CJB under blasting excavation can be calculated using the RocLab software (Hoek and Brown, 1988), as shown in Figure 11. It is evident that the global strength and the uniaxial compressive strength of the field rock mass have an approximately negative linear correlation with the blast damage factor. As the blast damage factor increases, the global strength and uniaxial compressive strength of the field rock mass progressively decrease. For every 0.1 increase in the blast damage factor, the strength of the rock mass is reduced by approximately 4%–7%.

The rock structure of the CJB is a mosaic structure. Prior to excavation, the structure of the rock is tightly compacted and the mechanical properties are good, whereas after excavation the mechanical properties decrease sharply. Therefore, on the one hand, short footages and small charges should be used in blasting excavation to reduce the degree of deterioration and damage to the CJB. On the other hand, rock bolts and anchor cables should be used to strengthen the rock and prevent secondary damage.

5 Conclusion

In this paper, *in-situ* acoustic wave velocity and borehole camera tests were carried out to investigate the collapse of the CJB in the tailrace connection pipe of the Baihetan hydropower station, China. The failure mechanism of the collapse of the CJB was systematically investigated, and the main conclusions are listed as below.

The panoramic borehole camera results show that the joints in the CJB of the tailrace connection pipes are densely developed, and the relaxation and joint surface opening behaviour after excavation unloading is evident. And the mechanical properties of the CJB show a clear spatiotemporal effect under the influence of the unloading of the excavation. The results of the continuous field observations show that the excavation damage zones of the CJB increase slowly, i.e., the unloading relaxation of the CJB is a time-dependent failure process. The development of the excavation damage zone of the CJB also depends on the spatial effect. That is, the closer to the collapse zone, the greater the degree of relaxation failure of the CJB; the further away from the cavern perimeter, the more stable the rock mass.

As the cavern is excavated and unloaded, the intercolumnar joint plane and the implicit joint planes of the CJB gradually open. CJB is prone to collapse under the action of external forces, posing a serious threat to the safety of mechanical equipment and construction personnel. The research results in this paper can provide a reference for studying the failure mechanism and control measures of CJB. In other words, how to effectively prevent the opening and fracturing of the joint plane is the key to preventing the failure of the CJB of the cavern.

Data availability statement

The original contributions presented in the study are included in the article/Supplementary material, further inquiries can be directed to the corresponding authors.

Author contributions

J-SZ: Writing–review and editing, Writing–original draft, Resources, Methodology, Funding acquisition, Data curation. J-CZ: Writing–review and editing, Formal Analysis. S-FP: Writing–review and editing, Methodology. LX: Writing–original draft, Validation, Supervision. C-FC: Writing–original draft, Methodology, Investigation. G-DZ: Writing–original draft, Methodology, Investigation.

Funding

The author(s) declare financial support was received for the research, authorship, and/or publication of this article. This research is supported by the National Natural Science Foundation of China (52209132), China Postdoctoral Science Foundation (2023M733317) and the CRSRI Open Research Program (Program SN: CKWV20231173/KY).

Acknowledgments

The authors would like to thank Prof. Xia-Ting Feng for his help with the *in-situ* measurements using acoustic waves and the panoramic borehole camera.

Conflict of interest

Authors J-SZ and J-CZ were employed by PowerChina Huadong Engineering Corporation Limited. Author LX was employed by Guangdong Provincial Academy of Building Research Group Corporation Limited. Author C-FC was employed by China Coal Technology and Engineering Group Corporation.

The remaining authors declare that the research was conducted in the absence of any commercial or financial relationships that could be construed as a potential conflict of interest.

Publisher's note

All claims expressed in this article are solely those of the authors and do not necessarily represent those of their affiliated organizations, or those of the publisher, the editors and the reviewers. Any product that may be evaluated in this article, or claim that may be made by its manufacturer, is not guaranteed or endorsed by the publisher.

References

Almqvist, B. S. G., Bosshard, S. A., Hirt, A. M., Mattsson, H. B., and Hetényi, G. (2012). Internal flow structures in columnar jointed basalt from Hrepphólar, Iceland: II. Magnetic anisotropy and rock magnetic properties. *B. Volcanol.* 74, 1667–1681. doi:10.1007/s00445-012-0622-0

Antonellini, M., and Mollema, P. N. (2019). Outcrop fracture network characterization for unraveling deformation sequence, geomechanical properties distribution, and slope stability in a flysch sequence (Monte Venere Formation, Northern Apennines, Italy). *Int. J. Earth Sci.* 108, 735–751. doi:10.1007/s00531-019-01685-y

Brady, B.-H.-G., and Brown, E.-T. (2005). *Rock mechanics for underground mining*. New York: Kluwer Academic Publishers.

Cai, W., Zhu, H., and Liang, W. (2022a). Three-dimensional stress rotation and control mechanism of deep tunneling incorporating generalized Zhang–Zhu strength-based forward analysis. *Eng. Geol.* 308, 106806. doi:10.1016/j.enggeo.2022.106806

Cai, W., Zhu, H., and Liang, W. (2022b). Three-dimensional tunnel face extrusion and reinforcement effects of underground excavations in deep rock masses. *Int. J. Rock Mech. Min. Sci.* 150, 104999. doi:10.1016/j.ijrmms.2021.104999

Cai, W., Zhu, H., Liang, W., Vu, B., and Wu, W. (2023). Physical and numerical investigation on nonlinear mechanical properties of deep-buried rock tunnel excavation unloading under complicated ground stresses. *Tunn. Undergr. Sp. Tech.* 138, 105197. doi:10.1016/j.tust.2023.105197

Chen, B.-R., Li, Q.-P., Feng, X.-T., Xiao, Y.-X., Feng, G.-L., and Hu, L.-X. (2014). Microseismic monitoring of columnar jointed basalt fracture activity: a trial at the Baihetan Hydropower Station, China. *J. Seismol.* 18, 773–793. doi:10.1007/s10950-014-9445-0

Chen, J., Hu, T., Hu, X., and Jia, K. (2024). Study on the influence of crack depth on the safety of tunnel lining structure. *Tunn. Undergr. Sp. Technol.* 143, 105470. doi:10.1016/j.tust.2023.105470

Deng, Z., Pan, M., Niu, J., Jiang, S., Wu, B., and Li, S. (2023). Spatial prediction of rockhead profile using the Gaussian process regression method. *Can. Geotech. J.* 60, 1849–1860. doi:10.1139/cgj-2022-0372

Feng, G., Feng, X., and Chen, B. (2015). Temperal-spatial characteristics of microseismic activity in columnar jointed basalt in tunnelling at Baihetan hydropower station. *Chin. J. Rock Mech. Eng.* 34, 1967–1975. (in Chinese). doi:10.13722/j.cnki.jrme.2013.1860

Feng, G., Zhang, J., Jiang, Q., Li, S., Xiao, Y., and Yao, Z. (2021). Synergistic observation and mechanism analysis of time-dependent fracture process of columnar jointed rockmass under strong unloading during excavation. *Chin. J. Rock Mech. Eng.* 40, 3041–3051. (in Chinese). doi:10.13722/j.cnki.jrme.2021.0200

Feng, X. T., Hao, X., Jiang, Q., Li, S., and Hudson, J. A. (2016). Rock cracking indices for improved tunnel support design: a case study for columnar jointed rock masses. *Rock Mech. Rock. Eng.* 49, 2115–2130. doi:10.1007/s00603-015-0903-y

Guo, H., Sun, Q., Feng, G., Li, S., and Xiao, Y. (2023a). *In-situ* observations of damage-fracture evolution in surrounding rock upon unloading in 2400-m-deep tunnels. *Int. J. Min. Sci. Techno.* 33, 437–446. doi:10.1016/j.ijmst.2022.11.008

Guo, Y., Luo, L., Ma, R., Li, S., Zhang, W., and Wang, C. (2023b). Study on surface deformation and movement caused by deep continuous mining of steeply inclined ore bodies. *Sustainability* 15, 11815. doi:10.3390/su151511815

Han, J., Wang, J., Jia, D., Yan, F., Zhao, Y., Bai, X., et al. (2023). Construction technologies and mechanical effects of the pipe-jacking crossing anchor-cable group in soft stratum. *Front. Earth Sci.* 10, 1019801. doi:10.3389/feart.2022.1019801

Hao, X., Feng, X., Yang, C., Jiang, Q., and Li, S. J. (2016). Analysis of EDZ development of columnar jointed rock mass in the Baihetan diversion tunnel. *Rock Mech. Rock. Eng.* 49, 1289–1312. doi:10.1007/s00603-015-0829-4

Hao, X., Yuan, L., Sun, Z., Zhao, Y., Ren, B., Zhao, D., et al. (2022). An integrated study of physical and numerical modelling on the stability of underground tunnel influenced by unloading rate. *Tunn. Undergr. Sp. Tech.* 129, 104602. doi:10.1016/j.tust.2022.104602

Hao, X., Zhang, Q., Sun, Z., Wang, S., Yang, K., Ren, B., et al. (2021). Effects of the major principal stress direction respect to the long axis of a tunnel on the tunnel stability: physical model tests and numerical simulation. *Tunn. Undergr. Sp. Tech.* 114, 103993. doi:10.1016/j.tust.2021.103993

Hoek, E., and Brown, E. T. (1988). "The Hoek-Brown failure criterion - a 1988 update," in *Proc. 15th Canadian rock mech. Symp*. Editor J. C. Curran (University of Toronto), 31–38.

Hoek, E., and Brown, T. (1980). *Underground excavation in rock*. London, Britain: The Institute of Mining and Metallurgy.

Hoek, E., Marinos, P., and Benissi, M. (1998). Applicability of the geological strength index (GSI) classification for very weak and sheared rock masses: the case of Athens Schist Formation. *Bull. Eng. Geol. Env.* 57, 151–160. doi:10.1007/s100640050031

Hu, T., He, S., Kang, Z., Tu, P., and Wang, D. (2023). Establishment and engineering application of viscoelastic-plastic constitutive laws for creep modeling in interbedded rock masses. *Sci. Rep.* 13, 20668. doi:10.1038/s41598-023-48003-w

Jiang, Q., Feng, X.-t., Hatzor, Y. H., Hao, X.-j., and Li, S.-j. (2014). Mechanical anisotropy of columnar jointed basalts: an example from the Baihetan hydropower station, China. *Eng. Geol.* 175, 35–45. doi:10.1016/j.enggeo.2014.03.019

Jiang, Q., Wang, B., Feng, X.-T., Fan, Q.-X., Wang, Z., Pei, S., et al. (2019). *In situ* failure investigation and time-dependent damage test for columnar jointed basalt at the Baihetan left dam foundation. *B. Eng. Geol. Environ.* 78, 3875–3890. doi:10.1007/s10064-018-1399-y

Jin, C., Yang, C., Fang, D., and Xu, S. (2014). Study on the failure mechanism of basalts with columnar joints in the unloading process on the basis of an experimental cavity. *Rock Mech. Rock. Eng.* 48, 1275–1288. doi:10.1007/s00603-014-0625-6

Lei, Y., Liu, Q., Liu, H., Chu, Z., Liu, P., and Wen, J. T. (2023). An updated Lagrangian framework with quadratic element formulations for FDEM. *Comput. Geotech.* 164, 105837. doi:10.1016/j.compgeo.2023.105837

Li, A., Dai, F., Liu, Y., Du, H., and Jiang, R. (2021). Dynamic stability evaluation of underground cavern sidewalls against flexural toppling considering excavation-induced damage. *Tunn. Undergr. Sp. Tech.* 112, 103903. doi:10.1016/j.tust.2021.103903

Li, A., Dai, F., Wu, W., Liu, Y., Liu, K., and Wang, K. (2022). Deformation characteristics of sidewall and anchorage mechanisms of prestressed cables in layered rock strata dipping steeply into the inner space of underground powerhouse cavern. *Int. J. Rock. Mech. Min.* 159, 105234. doi:10.1016/j.ijrmms.2022.105234

Li, A., Liu, Y., Dai, F., Liu, K., and Wei, M. (2020). Continuum analysis of the structurally controlled displacements for large-scale underground caverns in bedded rock masses. *Tunn. Undergr. Sp. Tech.* 97, 103288. doi:10.1016/j.tust.2020.103288

Li, P. X., Chen, B. R., Xiao, Y. X., Feng, G. L., Zhou, Y. Y., and Zhao, J. S. (2023). Rockburst and microseismic activity in a lagging tunnel as the spacing between twin TBM excavated tunnels changes: a case from the Neelum-Jhelum hydropower project. *Tunn. Undergr. Sp. Tech.* 132, 104884. doi:10.1016/j.tust.2022.104884

Li, T., Zhao, W., Liu, R., Han, J., Jia, P., and Cheng, C. (2024). Visualized direct shear test of the interface between gravelly sand and concrete pipe. *Can. Geotech. J.* 61 (2), 361–374. doi:10.1139/cgj-2022-0007

Liu, G. F., Ran, G., Li, Z., Duan, S., Su, G., Yan, C., et al. (2023). An insight into the effect of primary hidden microfissures on mechanical behaviors and failure characteristics of brittle basalt. *Theor. Appl. Fract. Mec.* 128, 104138. doi:10.1016/j.tafmec.2023.104138

Lu, B., Sheil, B. B., Zhao, W., Jia, P., Bai, Q., and Wang, W. (2024). Laboratory testing of settlement propagation induced by pipe-roof pre-support deformation in sandy soils. *Tunn. Undergr. Sp. Tech.* 146, 105645. doi:10.1016/j.tust.2024.105645

Martin, C. D., Kaiser, P. K., and McCreath, D. R. (1999). Hoek–Brown parameters for predicting the depth of brittle failure around tunnels. *Can. Geotech. J.* 36, 136–151. doi:10.1139/t98-072

Muller, G. (1998). Experimental simulation of basalt columns. *J. Volcanol. Geoth. Res.* 86, 93–96. doi:10.1016/S0377-0273(98)00045-6

Saliba, R., and Jagla, E. A. (2003). Analysis of columnar joint patterns from three-dimensional stress modeling. *J. Geophys. Res.* 108, 1–7. doi:10.1029/2003JB002513

Schultz, R. A. (1995). Limits on strength and deformation properties of jointed basaltic rock masses. *Rock Mech. Rock. Eng.* 28, 1–15. doi:10.1007/BF01024770

Shi, A., Wei, Y., Zhang, Y., and Tang, M. (2020). Study on the strength characteristics of columnar jointed basalt with a true triaxial apparatus at the Baihetan Hydropower Station. *Rock Mech. Rock. Eng.* 53, 4947–4965. doi:10.1007/s00603-020-02195-z

Si, X., Luo, Y., Gong, F., Huang, J., and Han, K. (2024a). Temperature effect of rockburst in granite caverns: insights from reduced-scale model true-triaxial test. *Geomech. Geophys. Geo-energ. Geo-resour.* 10, 26. doi:10.1007/s40948-024-00736-2

Si, X., Luo, Y., and Luo, S. (2024b). Influence of lithology and bedding orientation on failure behavior of "D" shaped tunnel. *Theor. Appl. Fract. Mec.* 129, 104219. doi:10.1016/j.tafmec.2023.104219

Smith, J. V., and Holden, L. (2021). Rock slope kinematic instability controlled by large-scale variation of basalt column orientation. *B. Eng. Geol. Environ.* 80, 239–250. doi:10.1007/s10064-020-01917-5

Wang, C., Liu, Y., Song, D., Xu, J., Wang, Q., and Zhang, S. (2024). Evaluation of bedding effect on the bursting liability of coal and coal-rock combination under different bedding dip angles. *Adv. Geo-Energy Res.* 11, 29–40. doi:10.46690/ager.2024.01.04

Xia, K., Chen, C., Liu, X., Liu, X., Yuan, J., and Dang, S. (2023). Assessing the stability of high-level pillars in deeply-buried metal mines stabilized using cemented backfill. *Int. J. Rock Mech. Min. Sci.* 170, 105489. doi:10.1016/j.ijrmms.2023.105489

Xia, K., Chen, C., Liu, X., Zheng, X., Zhou, Y., Song, X., et al. (2024). Ground collapse and caving mechanisms in strata overlying sublevel caving mines: a case study. *B. Eng. Geol. Environ.* 83, 21. doi:10.1007/s10064-023-03529-1

Xia, Y., Zhang, C., Zhou, H., Chen, J., Gao, Y., Liu, N., et al. (2020). Structural characteristics of columnar jointed basalt in drainage tunnel of Baihetan hydropower station and its influence on the behavior of P-wave anisotropy. *Eng. Geol.* 264, 105304. doi:10.1016/j.enggeo.2019.105304

Xu, H., Zhang, Z., Zhang, Y., Jiang, Q., Qiu, S., Zhou, Y., et al. (2024). Effects of natural stiff discontinuities on the deformation and failure mechanisms of deep hard rock under true triaxial conditions. *Eng. Fail. Anal.* 158, 108034. doi:10.1016/j.engfailanal.2024.108034

Yang, G.-D., Wang, G.-H., Fan, Y., Deng, K., Lu, W.-B., and Zhao, J.-S. (2021). Dynamic response and performance of submarine tunnel subjected to surface explosions. *Mar. Struct.* 80, 103091. doi:10.1016/j.marstruc.2021.103091

Zhang, J., Jiang, Q., Feng, G., Li, S., Pei, S., and He, B. (2022). Geometrical characteristic investigation of the Baihetan irregular columnar jointed basalt and corresponding numerical reconstruction method. *J. Cent. South Univ.* 29, 455–469. doi:10.1007/s11771-022-4940-x

Zhao, J.-S., Chen, B.-R., Jiang, Q., Lu, J.-F., Hao, X.-J., Pei, S.-F., et al. (2022a). Microseismic monitoring of rock mass fracture response to blasting excavation of large underground caverns under high geostress. *Rock Mech. Rock. Eng.* 55, 733–750. doi:10.1007/s00603-021-02709-3

Zhao, J.-S., Chen, B.-R., Jiang, Q., Xu, D.-P., He, B.-G., and Duan, S.-Q. (2024a). *In-situ* comprehensive investigation of deformation mechanism of the rock mass with weak interlayer zone in the Baihetan Hydropower Station. *Tunn. Undergr. Sp. Tech.*

Zhao, J.-S., Duan, S.-Q., Chen, B.-R., Li, L., He, B.-G., Li, P.-X., et al. (2024b). Failure mechanism of rock masses with complex geological conditions in a large underground cavern: a case study. *Soil. Dyn. Earthq. Eng.* 177, 108439. doi:10.1016/j.soildyn.2023.108439

Zhao, J.-S., Jiang, Q., Lu, J.-F., Chen, B.-R., Pei, S.-F., and Wang, Z.-L. (2022b). Rock fracturing observation based on microseismic monitoring and borehole imaging: *in situ* investigation in a large underground cavern under high geostress. *Tunn. Undergr. Sp. Tech.* 126, 104549. doi:10.1016/j.tust.2022.104549

Zhao, J.-s., Jiang, Q., Pei, S.-f., Chen, B.-r., Xu, D.-p., and Song, L.-b. (2023). Microseismicity and focal mechanism of blasting-induced block falling of intersecting chamber of large underground cavern under high geostress. *J. Cent. South. Univ.* 30, 542–554. doi:10.1007/s11771-023-5259-y

Zheng, Z., Li, R., and Zhang, Q. (2023a). A novel anisotropic deterioration mechanical model for rock ductile-brittle failure under 3D high-stress and its application. *Comput. Geotech.* 162, 105665. doi:10.1016/j.compgeo.2023.105665

Zheng, Z., Tang, H., Zhang, Q., Pan, P., Zhang, X., Mei, G., et al. (2023b). True triaxial test and PFC3D-GBM simulation study on mechanical properties and fracture evolution mechanisms of rock under high stresses. *Comput. Geotech.* 154, 105136. doi:10.1016/j.compgeo.2022.105136

frontiers | Frontiers in Earth Science

TYPE Original Research
PUBLISHED 19 March 2024
DOI 10.3389/feart.2024.1371212

Check for updates

OPEN ACCESS

EDITED BY
Jianyong Han,
Shandong Jianzhu University, China

REVIEWED BY
Jingqiang Yuan,
Chinese Academy of Sciences (CAS), China
Yongfeng Deng,
Southeast University, China

*CORRESPONDENCE
Pengfei Liu,
pfliu0229@foxmail.com

RECEIVED 16 January 2024
ACCEPTED 05 March 2024
PUBLISHED 19 March 2024

CITATION
Ji F, Liu P, Yang Z, Wen B and Hu Q (2024), Experimental study and mechanism analysis of high-pressure water jet for mud cake cutting during shield tunneling.
Front. Earth Sci. 12:1371212.
doi: 10.3389/feart.2024.1371212

COPYRIGHT
© 2024 Ji, Liu, Yang, Wen and Hu. This is an open-access article distributed under the terms of the Creative Commons Attribution License (CC BY). The use, distribution or reproduction in other forums is permitted, provided the original author(s) and the copyright owner(s) are credited and that the original publication in this journal is cited, in accordance with accepted academic practice. No use, distribution or reproduction is permitted which does not comply with these terms.

Experimental study and mechanism analysis of high-pressure water jet for mud cake cutting during shield tunneling

Fuquan Ji[1], Pengfei Liu[1,2]*, Zhao Yang[1], Bowei Wen[1] and Qinxin Hu[3]

[1]CCCC Second Harbor Engineering Company Ltd., Wuhan, Hubei, China, [2]Key Laboratory of Safe Construction and Intelligent Maintenance for Urban Shield Tunnels of Zhejiang Province, Hangzhou, Zhejiang, China, [3]Department of Civil and Environmental Engineering, University of Strathclyde, Glasgow, United Kingdom

When the opening rate of the cutter head of tunnel boring machines is insufficient for the removal of excavated soil in a timely manner, the soil tends to accumulate in front of the cutter head and inside the earth or slurry chamber, leading to mud caking. High-pressure water jetting is an effective method for removing mud cakes. This study explored the influence of high-pressure water jet parameters on the efficiency of mud cake cleaning by using highly weathered argillaceous siltstone as experimental materials. Mud cake compaction equipment and high-pressure water jetting devices were developed. In addition, the impact of jetting parameters such as jet pressure and flow rate on the mud cake cutting performance was investigated. The results indicated that with an increase in the erosion distance, the cutting width of the mud cake first increased and then gradually decreased to zero, while the cutting depth progressively diminished. Under the same jet pressure, when the flow rate increased from 49.1 L/min to 110 L/min, the cutting width of the high-pressure water jet increased. With further increase in the flow rate from 110 L/min to 202.8 L/min, the cutting width decreased and the cutting depth increased. Under the same jet flow, the increase in water pressure resulted in greater cutting width and depth.

KEYWORDS

cohesive strata, shield tunneling, mud cake treatment, high-pressure water jet, mud cake cutting

1 Introduction

Rapid urbanization has led to the construction of a large number of urban tunnels in China (Han et al., 2023; Li et al., 2023). The shield tunneling method has become a preferred approach in urban tunneling projects because of its high efficiency and minimal risk (Liu et al., 2018; Wang er al., 2019; Wang er al., 2022). However, the operation of a shield machine in cohesive geological formations is challenging. When the opening rate of the cutter head fails to meet requirements for the removal of excavated soil in a timely manner, the soil tends to accumulate in front of the cutter head and inside the earth or slurry chamber. This can lead to inefficient mud discharge from the cutter head, increased friction between

the cutting tools and soil, and higher temperatures of the excavated materials (Hollmann and Thewes, 2013; Oliveria, 2018; Yang et al., 2023). Under such conditions, the excavated soil often consolidates into a mass, which then adheres to the cutter head as "mud cakes" and significantly hampers the construction efficiency (Langmaack and Lee, 2016; Li et al., 2022; Ding et al., 2023). Shield tunneling for the treatment of mud cakes is often performed using three contemporary methods. In the first method, dispersants are injected into the shield chamber to break down mud cakes (Du et al., 2022; Fang et al., 2022). However, dispersants may also decompose the clay on the tunnel face, potentially causing its collapse. In the second method, mud cakes are manually removed after opening the shield chamber. However, this approach is risky in soft soil strata and exhibits low efficiency in mud cake removal (Min et al., 2015; Wang et al., 2021). The third method involves equipping the shield machine with high-pressure water jetting systems in advance, which are then used to remove mud cakes whenever they are formed. This method is safe and efficient, and it is often used when constructing tunnels with very large diameters (Wang and Feng, 2017; Zhao and Yao, 2017).

Contemporary research on ultra-high-pressure water jets primarily focuses on rock cutting. Hagan (1992) investigated the cutting capabilities on rocks under the combination of rolling cutter tools and high-pressure water jets. The author extended the research to factors such as nozzle diameter, water pressure, jet velocity, and the number of jet cutting passes in the same cut path, among which water pressure was identified as the most significant factor affecting the disruption of rock surface as well as the cutting process. Ciccu and Grosso (2014) discovered that using a 150 MPa water jet on one side of the roller cutter to assist in cutting rock can considerably enhance the efficiency of rock cutting with rolling cutters. Luo et al. (2023) employed numerical simulations and laboratory experiments to examine the effects of cutting depth and spacing between rolling cutters on the capability of high-pressure jets in rock cutting. With the increase in the cutting depth of the high-pressure jet, the vertical force and the rolling force exerted by the rolling cutter decreased considerably. Liu et al. (2023) utilized the Eulerian-Lagrangian Coupling (CEL) method and the finite discrete element method to simulate the rock fracturing process induced by high-pressure water jets. They addressed the challenges of high nonlinearity, fluid solid coupling, and large deformations, and through laboratory experiments, they verified the reliability of the proposed computational approach. Cheng et al. (2022) investigated the impact of high-pressure water jet slotting depth and slotting spacing on the normal indentation force of the rolling cutter, the volume of rock debris, and specific energy. The average peak force noticeably decreased with the increasing slotting depth, and the maximum volume of rock debris and the minimum specific energy were achieved at a slotting depth of 18.14 mm. Zhang et al. (2020) investigated the influence of the depths of slots created by varying high-pressure water jets on the load and efficiency of shield tunneling rolling cutters for rock fragmentation. Regular slots produced by high-pressure water jets enhanced the efficiency of rock breaking by the rolling cutter. This decreased the specific energy required for cutting; the normal force on the cutter head decreased by nearly 40%. Ge et al. (2023) examined the fragmentation characteristics of high-temperature granite and shale under the influence of high-pressure water jets. Their research indicated that rock fragmentation under high-temperature conditions is significantly greater than that under heating-cooling and room temperature conditions. Research on high-pressure water jets has mainly focused on aiding rock breakage, while a few studies have considered their use in removing mud cakes from cutter heads. Xiao et al. (2020) found that when the convergence angle of the nozzle reached 13°, the jet velocity reached the peak at the same pressure. However, the effects of parameters such as nozzle diameter, jet flow rate, and jet pressure on the mud cake cutting efficiency remain unclear. Therefore, it is necessary to conduct in-depth research on the impact of high-pressure water jet parameters on the cutting efficiency of shield tunneling mud cakes.

In this study, initially, an erosion cutting device and a mud cake compaction device were developed. Then, the influence of parameters, such as erosion distance, water jet pressure, and flow rate on the mud cake cutting efficiency was explored. The findings of this study provide a scientific basis for the systematic arrangement of high-pressure water jets in shield tunneling.

2 Experimental introduction

2.1 Experimental materials

The shield tunneling machine encountered a situation where "mud cakes" formed around its cutterhead during its excavation through highly weathered argillaceous siltstone strata in a particular section of the Guangzhou Metro, China. Analysis of the extracted mud cake revealed a water content of 17%–22% and a density of 2.10–2.13 g/cm^3. The degree of saturation ranged from 0.824 to 0.992. Under direct fast shearing conditions, the cohesive strength of reshaped soil samples ranged from 44.6 to 47.4 kPa, with an internal friction angle between 23.5° and 25.6°. To explore the effectiveness of high-pressure water jets in eroding these mud cakes, this study used similar highly weathered argillaceous siltstone sourced from the excavation sites in Guangzhou as the test material. As depicted in Figure 1, the largest particle size of the soil sample was 0.13 mm, and >90% of the particles had a size of <0.075 mm. Based on the Chinese Standard Code for the Design of Building Foundation (2019), this soil sample was classified as silty clay. According to the "Geotechnical Testing Standards" (2019), the maximum particle size of soil samples for determining the liquid limit should not exceed 0.5 mm. After removing particles larger than 0.5 mm and highly weathered argillaceous siltstone from the mud cake, the liquid limits were determined as shown in Table 1. The liquid limits of the mud cake were 30.7% and 20.1%, while those of highly weathered argillaceous siltstone were 29.8% and 19.7%, indicating a slight difference. The specific gravities of the two soil samples were 2.85 and 2.83, respectively. Considering the Atterberg limits and particle specific gravity test results, the physical properties of the shield tunnel mud cake and the highly weathered argillaceous siltstone were similar, indicating that the excavated soil within the foundation pit can be used as a substitute for mud cake as a test soil sample. The water content of the mud cake specimens compressed in the laboratory was 20%, with a density of 2.12 g/cm^{3}and a saturation degree of 0.939. Under consolidated fast shearing conditions, the cohesive strength of the soil samples was 44.9 kPa, with an internal

TABLE 1 Physical and mechanical parameters of soil.

Soil name		Mud cake	Highly weathered argillaceous siltstone
Specific gravity		2.85	2.84
Atterberg limits (<0.5 mm) (%)	Liquid limit	30.7	29.8
	Plastic limit	20.1	19.7
Water content (%)		17–22	20
Density (g/cm^3)		2.10–2.13	2.12
Saturation degree		0.824–0.992	0.939
Consolidation fast direct test	Cohesive strength (kPa)	34.6–37.4	36.5
	Internal friction angle (°)	23.5–25.6	24.7

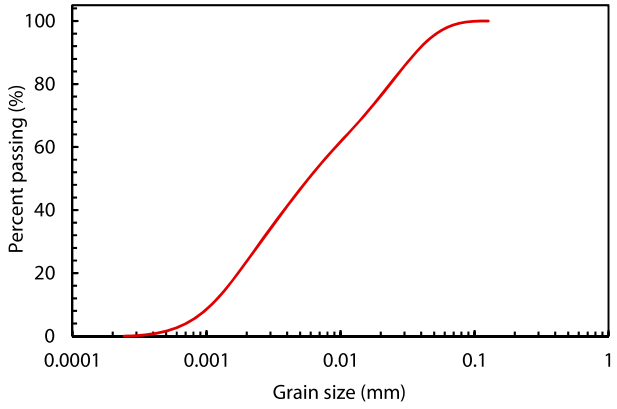

FIGURE 1
Soil gradation curve.

friction angle of 24.4°, which was essentially the same as the physical and mechanical parameters of the shield tunnel mud cake.

2.2 Experimental equipment

2.2.1 Mud cake compaction device

To replicate the state of mud cakes on the cutterhead of a shield tunneling machine, a mud cake compaction device was developed (Figure 2). The device, including its top oil cylinder expansion pipeline, had a height of 2.2 m. The reaction frame had a height and width of 1.7 m and 1.8 m, respectively, and the overall structure resembled a double isosceles trapezoid from front to back. The pressure telescopic rod could be extended up to a maximum length of 1.2 m, and the connected hydro-cylinder could provide a maximum thrust of 2 MPa. The container designed for storing mud cakes was precision-engineered with uniform dimensions to ensure a seamless fit beneath the compaction apparatus. A small hole was strategically located at the bottom center of the mud cake compaction box. This hole assisted in venting during the compaction process to prevent gas pressure from obstructing the normal compaction of mud cakes. The compressed mud cakes produced using this method measured 50 × 50 × 30 cm^3.

2.2.2 High-pressure water jet device

The experimental setup of high-pressure water jet is depicted in Figure 3. It comprised a supercharger, hydraulic unit, water supply device, high-pressure pump, accumulator, control valve, and jet nozzle. Water entered through a pipeline to the water supply device, where it was stored, and it was then extracted and pushed out by the high-pressure pump, providing the basic static pressure for its flow. The supercharger, driven by the low pressure of the hydraulic device, moved the piston reciprocally to further increase the pressure, generating the pulse pressure. This pressure was stabilized by the accumulator before it entered the jet control valve, ensuring stable pressure in the jet pipeline. Finally, the high-pressure water jet was controlled and ejected through the control valve.

2.2.3 Nozzle structure of the high-pressure water jet device

The cutting capacity of the high-pressure water jet was closely related to its flow rate and water pressure, which were controlled mainly by two factors, nozzle diameter and internal structure. The high-pressure water jet nozzle, as illustrated in Figure 4, employed a flared structure for the internal jet. When the length-to-diameter ratio of the internal transition section was increased, the dynamic pressure and flow velocity at the nozzle outlet also increased, which resulted in an increase in the overall flow rate and pressure of the device.

3 High-pressure water jet erosion test on mud cakes

Nozzle diameters of 2.0 mm, 3.0 mm, 3.5 mm, and 4.0 mm were selected. Depending on the nozzle size, the pressure capability of the erosion equipment varied, ranging between 37 and 45 MPa. During the experiments, the nozzles of different diameters were

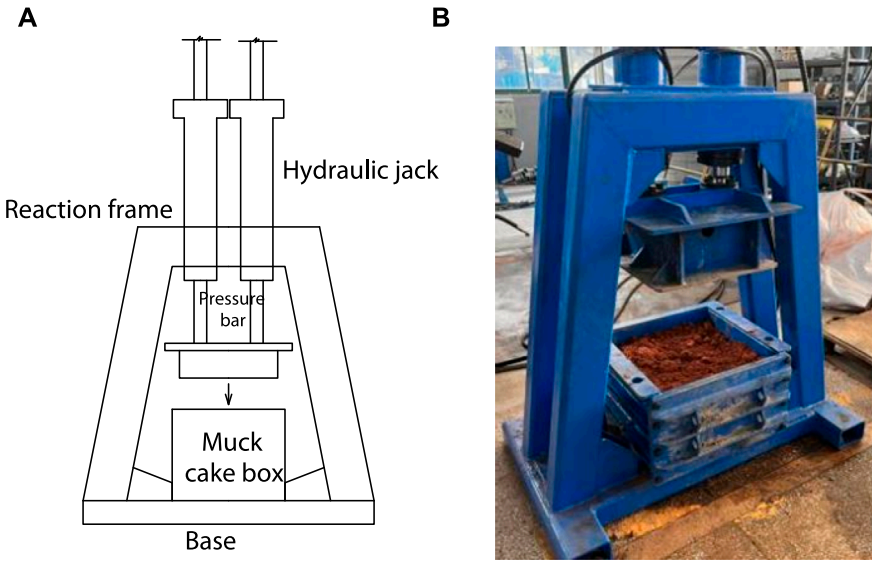

FIGURE 2
Mud cake compaction device. **(A)** Schematic of the device. **(B)** Photo of the device.

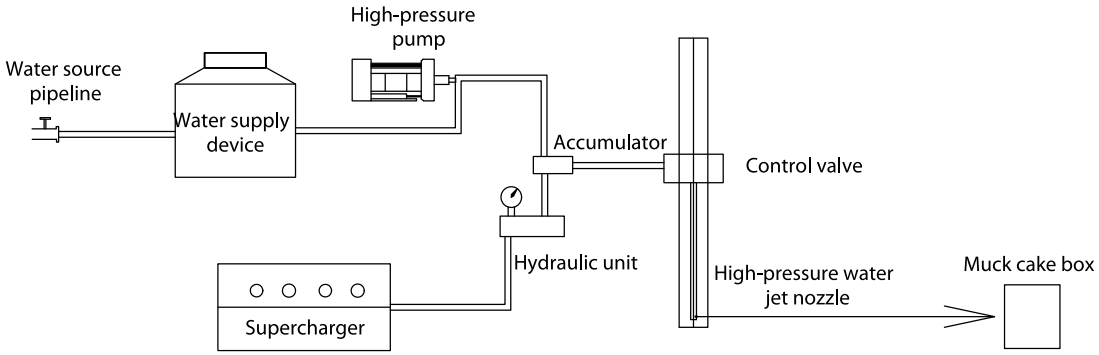

FIGURE 3
Schematic of the working principle of the high-pressure water jet experimental device.

switched to adjust the water flow rate while keeping the water pressure constant. Similarly, the nozzles of various diameters were interchanged to alter the water pressure while maintaining a steady flow rate. In the constant pressure tests, water pressure was regulated at 35 MPa, whereas in the constant flow rate tests, the jet flow was set to 110 L/min. Significant erosion effects were evident within 30 s after the water jet impacted the mud cake. If the mud cake was breached within this timeframe, the high-pressure water jet would directly pass through the created hole. Consequently, we set the erosion duration to 30 s. All test conditions are listed in Table 2. The experimental procedure involved the following steps:

(1) The soil sample was dried in an oven and then crumbled. A certain amount of water was added to attain a water content of 20% in the sample. After thorough mixing, the sample was sealed with cling film and left undisturbed for at least 24 h to ensure it was fully moistened.
(2) After the soil sample was uniformly moistened, it was poured into the mud cake box in four installments, each with a mass of 42.75 kg. The soil sample was then subjected to loading (Figure 5A), with each layer of soil compressed to a height of 7.5 cm. After the completion of one layer of compaction (Figure 5B), the surface of the soil sample was roughened to strengthen interlayer connections.
(3) After the final layer of soil sample was completely compacted, soil samples were taken from three positions on the specimen surface by using a cutting ring to determine water content (Figure 5C). If the measured water content differed from the target water content by <1%, the sample had to be prepared again.
(4) The compressed mud cake, along with the box used to secure it, was placed at the target position for high-pressure water jet cutting. To stabilize the mud cake and resist the impact force exerted by the water jet, supplementary weights were strategically placed behind the mud cake box.
(5) The direction of the high-pressure water jet nozzle was adjusted downward to tune the water pressure or flow rate. Once the water pressure or flow rate reached the experimental

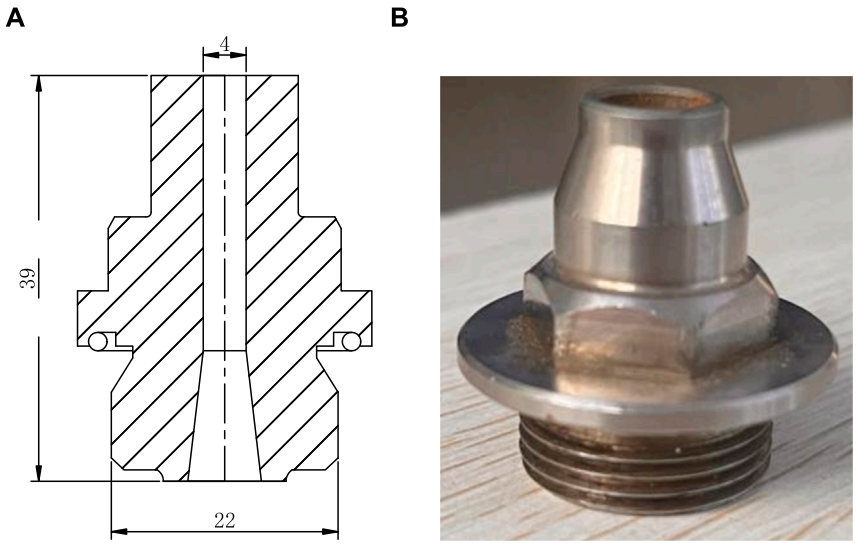

FIGURE 4
High-pressure water jet nozzle. **(A)** Schematic diagram (mm). **(B)** Photograph of the device.

TABLE 2 Overview of the testing conditions.

Water pressure (MPa)	Water flow rate (L/min)	Erosion distance (m)
35	49.1	0.67, 1.25, 1.81, 2.22, 2.69, 3.15, 3.57
	110.0	0.5, 1.5, 2.1, 2.45, 2.99, 3.36, 3.61, 3.84, 4.49
	202.8	0.72, 1.71, 2.23, 2.78, 3.14, 3.43, 3.84, 4.16
35	110	0.5, 1.5, 2.1, 2.45, 2.99, 3.36, 3.61, 3.94, 4.49
18.2		0.69, 1.22, 1.70, 2.22, 2.48, 2.80, 3.06, 3.60, 4.10
10.75		0.69, 1.33, 1.71, 2.21, 2.64, 3.06, 3.60, 4.10

requirements, the position of the high-pressure water jet nozzle was switched back to the mud cake cutting position for a 30 s wash (Figure 5D).

(6) After the erosion process was completed, the direction of the nozzle's jet was altered to prevent the erosion of the mud cake, and the high-pressure water jet erosion system was then shut down. Subsequently, the maximum width and depth of the diameter at the eroded location were measured using a caliper.

4 Experimental results

4.1 Variation in high-pressure water jet cutting capability at different erosion distances

Figure 6 illustrates the variations in both cutting width and cutting depth of mud cake in relation to the erosion distance when a nozzle of 3-mm diameter and 18.2-MPa water pressure was used. At shorter erosion distances, when the distance increased, the cutting width of the mud cake first increased and then gradually decreased to 0, while the cutting depth progressively decreased. At an erosion distance of 2–3 m, the cutting width reached its maximum value of 20 cm. As the cutting width decreased, the depth of cutting also gradually decreased. The reduced cutting effectiveness of the high-pressure water jet made its penetration into the mud cake insufficient.

4.2 Variation in high-pressure water jet cutting capability under constant water pressure

When the water pressure was set to 35 MPa, the flow rates for nozzles with the diameters of 2.0 mm, 3.0 mm, and 4.0 mm were 49.1 L/min, 110 .0L/min, and 202.8 L/min, respectively. The variations in cutting width and cutting depth with erosion distance under these working conditions are illustrated in Figure 7. Under constant water pressure and a flow rate of 49.1 L/min, as the erosion distance increased, the cutting width first reached the upper limit and then gradually decreased. At an erosion distance of approximately 3.5 m, the cutting width essentially decreased to

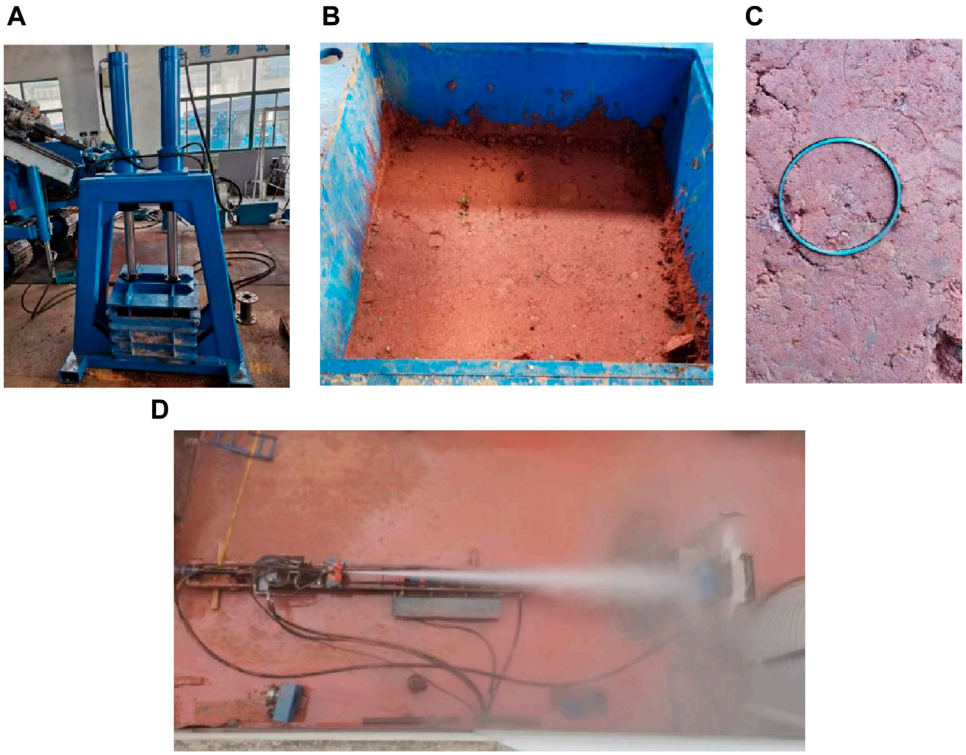

FIGURE 5
Main experimental steps of high-pressure water jetting: **(A)** compressing soil, **(B)** completion of one layer of compaction, **(C)** cutting ring sampling, and **(D)** cutting mud cake.

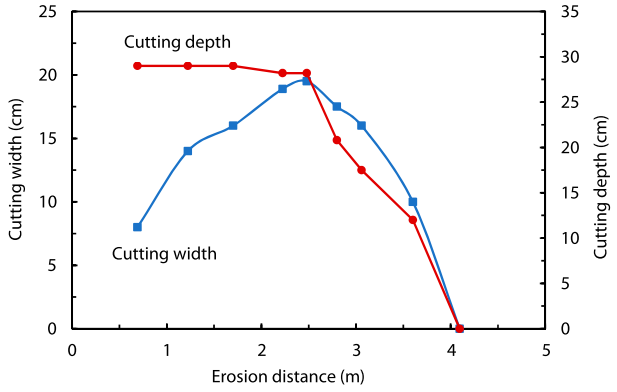

FIGURE 6
Variation in cutting width and depth with distance.

zero. At a flow rate of 110 L/min, the maximum cutting width of 23 cm was attained around an erosion distance of approximately 2.5 m, gradually decreasing thereafter. At a flow rate of 202.8 L/min, the maximum cutting width was achieved at an erosion distance of 2.5–3 m. Although the maximum cutting width for this diameter was not the largest among the three nozzles with different sizes, the cutting width for this diameter decreased relatively slowly and was maintained at a certain erosion distance. When the erosion distance d was ≤3 m, at the same erosion distance, the cutting width was the maximum at a flow rate of 110 L/min. When the erosion distance was in the range of 3–4 m, the cutting width achieved with the 4.0-mm nozzle at a flow rate of 202.8 L/min was greater than that achieved with the 3.0-mm nozzle.

In terms of cutting depth, as the cutting aperture width gradually decreased, the cutting depth still remained relatively large, almost penetrating through the mud cake, at a flow rate of 49.1 L/min and an erosion distance of 2 m. Moreover, the cutting depth at a flow rate of 202.8 L/min exceeded by those at the flow rates of 49.1 L/min and 110 L/min. Thus, an increase in the flow rate can cause an enhancement in the cutting depth of the mud cake.

4.3 Variation in high-pressure water jet cutting capacity at the same water flow rate

In the constant water flow rate experiments, the jet flow rate was maintained at 110 L/min. However, the 2.0-mm nozzle, even under maximum pressure, could not attain a flow rate of 110 L/min. As a result, nozzles with diameters of 3.0 mm, 3.5 mm, and 4.0 mm were employed, which exhibited the jet pressures of 35 MPa, 18.2 MPa, and 10.75 MPa, respectively, at the flow rate of 110 L/min. Variations in mud cake cutting width and depth with erosion distance under a constant jet flow rate and diverse jet pressures are shown in Figure 8. As shown in the graph depicting changes in cutting width with erosion distance (Figure 7A), nozzles

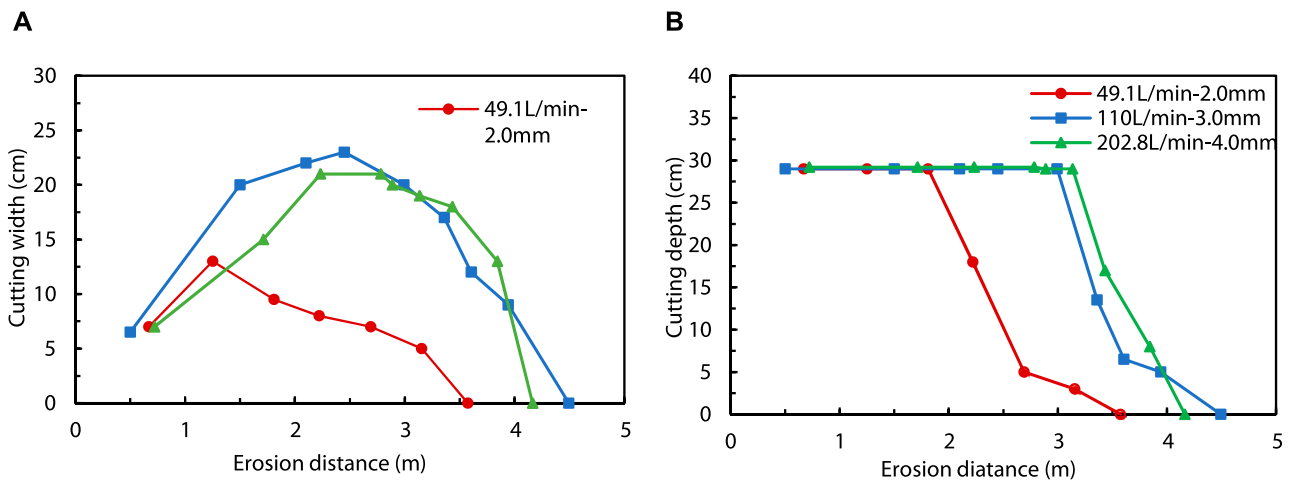

FIGURE 7
Variations in **(A)** width and **(B)** depth of high-pressure water jet cutting with erosion distance at constant water pressure.

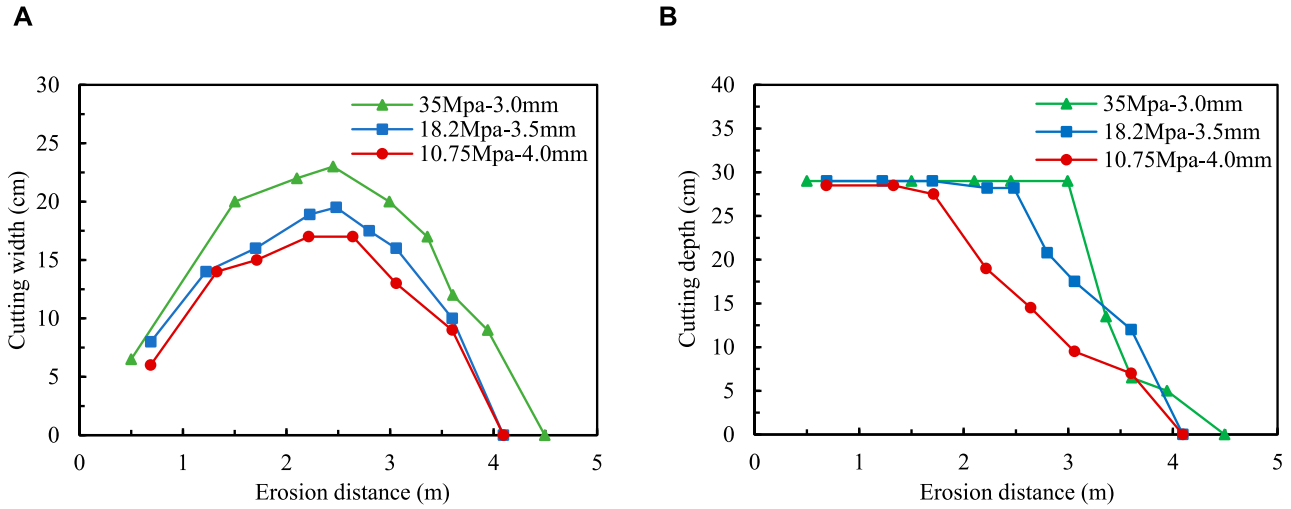

FIGURE 8
Variations in **(A)** cutting width and **(B)** cutting depth of high-pressure water jet with erosion distance under the same water flow rate.

of varying apertures exhibited similar patterns of cutting width variations. Cutting width initially increased to reach the peak and subsequently decreased with increasing distance from the nozzle, which signifies the decrease in the cutting efficiency. At the same flow rate, the smaller the cutting nozzle aperture of the three types of nozzles, the greater was the corresponding pressure, and the higher was their cutting efficiency. Simultaneously, under the same flow rate, jets with higher pressure also achieved a greater maximum cutting distance.

Comparison of cutting depths (Figure 7B) showed that the ultimate breakthrough distances for pressures of 10.75 MPa, 18.2 MPa, and 10.75 MPa were 1.7 m, 2.6 m, and 3.2 m, respectively. These results indicated that under the same flow rate conditions, nozzles with higher pressure values attained greater ultimate breakthrough distances when penetrating the mud cake.

5 Discussion on the mechanism of high-pressure water jet cutting of mud cakes

The high-pressure water jet was divided into four segments after it exited the nozzle: the initial segment, transition segment, basic segment, and dissipation segment (Figure 9). In the initial stage, despite intense turbulence and diffusion with the release of water jet into the ambient medium, the velocity of the water jet remained essentially unchanged. The density and dynamic pressure along the axis of the jet also remained constant despite the vigorous energy exchange that occurred because of its interaction with the surrounding environment. After the initial segment, in a brief section, referred to as the transition segment, the outermost water flow expanded outward because of the diffusion of water jet

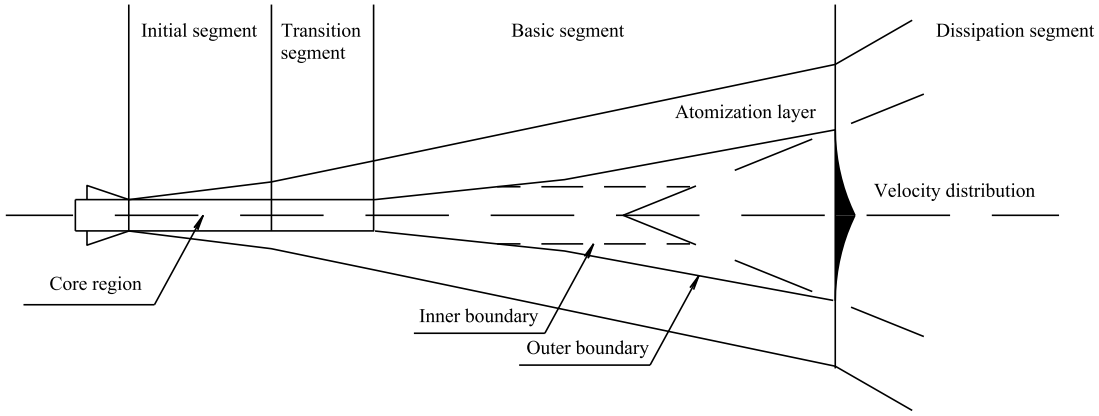

FIGURE 9
Structure schematic diagram of high-pressure water jet.

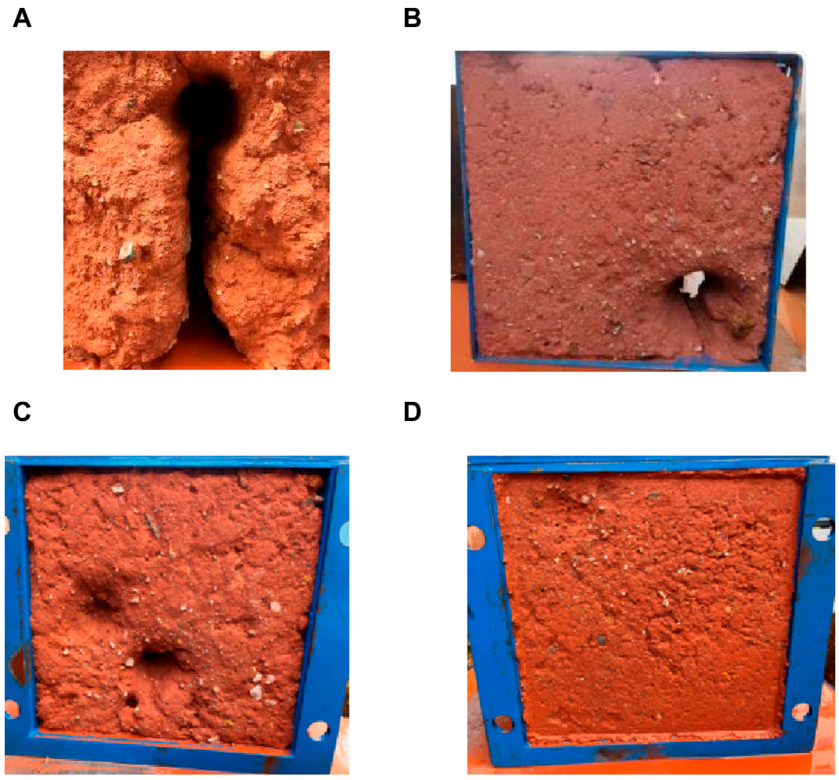

FIGURE 10
Cutting effect at different water jet segments. **(A)** Uniformly wide strip-like cutting pattern. **(B)** Truncated-cone form. **(C)** Absence of penetrability erosion holes. **(D)** Erosion action on the mud cake.

pressure. After the transition segment, there was still a relatively long jet segment in the middle of the water column. Because of natural velocity attenuation and under the influence of friction, both the dynamic pressure and axial velocity of the jet gradually decreased. However, in the cross-section perpendicular to the axis, the dynamic pressure and axial velocity of the jet exhibited a Gaussian distribution. The final section of the high-pressure water jet was the dissipation segment, in which the jet was completely merged with the surrounding environment, and both the jet pressure and axial velocity were very low. The initial, transition, and basic segments exhibit fairly high energy and are commonly used for cutting metals or rock and soil. In contrast, the dissipation segment has relatively low energy and is often used for cleaning purposes.

As depicted in Figure 10, with an increase in the erosion distance, the high-pressure water jet exhibited different forms after cutting through the mud cake. When the cutting distance was small, the jet was in the initial segment, where the velocity and pressure of the inner and outer layers of the jet were nearly equal.

Consequently, after the water jet cut through the mud cake, the overall shape of the erosion hole appeared cylindrical. During the up-and-down movement of the water flow, it presented a uniformly wide strip-like cutting pattern (Figure 10A). At this stage, the cutting width was comparatively narrow. As the erosion distance increased, the jet, which was situated at either the transition or the front-end of basic section, exhibited higher water velocity and pressure in its inner layer than those in its outer layer. This differential pattern allowed the inner layer of the jet to effectively penetrate the mud cake, while hindering the penetration of the outer layer. Consequently, the erosion hole, which was aligned with the erosion axis, assumed a truncated-cone form. The width of the hole was larger near the surface of the mud cake and decreased toward its interior (Figure 10B); thus, the cutting width surpassed that of the initial segment. With further increase in the erosion distance, the jet was positioned at the terminal part of the basic segment. The inability of both the inner and outer layers of the water flow to penetrate through the mud cake resulted in the absence of penetrability erosion holes (Figure 10C), which caused a reduction in the cutting width. Additional increment in the erosion distance led to the jet transitioning to the dissipation segment. Consequently, the water flow failed to generate an effective cutting impact, but it manifested an erosion action on the mud cake (Figure 10D), and the cutting width decreased to zero.

6 Conclusion

This study developed a self-designed mud cake compaction apparatus and a high-pressure water jet device. The effect of parameters such as jet pressure and flow rate on the cutting width and depth of mud cakes was investigated. The main findings are as follows:

(1) With the increase in erosion distance, the cutting width of the mud cake first increased and then gradually diminished to zero, while the cutting depth decreased from 30 cm to eventually zero.
(2) Under identical jet pressure conditions, an increase in the flow rate from 49.1 L/min to 110 L/min increased the cutting width by the high-pressure water jet. However, as the flow rate continued to increase from 110 L/min to 202.8 L/min, the cutting width decreased. Simultaneously, the cutting depth increased with the increasing flow rate.
(3) At a constant jet flow rate, high water pressure corresponded to the increased cutting width and depth. Essentially, under identical flow rates, a smaller nozzle diameter enhanced the cutting efficiency.
(4) When the mud cake was in the initial segment of the water jet, the erosion hole formed after cutting through the cake assumed a cylindrical shape. Furthermore, when the mud cake was in the transition segment of the jet and the front section of the basic segment, the erosion hole along the erosion axis was in a truncated-cone form. The width of hole was greater near the surface of the mud cake and exhibited a gradual decrease toward the interior. However, when the mud cake was in the latter segment of the basic segment, non-penetrative erosion holes emerged. In the dissipation segment, the water flow primarily manifested erosive effects on the mud cake. These results indicated that the cutting capabilities of the high-pressure water jet were primarily concentrated in the initial and basic segments.

Data availability statement

The original contributions presented in the study are included in the article/Supplementary material, further inquiries can be directed to the corresponding author.

Author contributions

FJ: Investigation, Conceptualization, Writing–review and editing. PL: Supervision, Investigation, Funding acquisition, Data curation, Writing–original draft. ZY: Software, Formal Analysis, Data curation, Writing–review and editing. BW: Validation, Supervision, Software, Resources, Writing–review and editing. QH: Visualization, Validation, Formal Analysis, Writing–review and editing.

Funding

The author(s) declare financial support was received for the research, authorship, and/or publication of this article. The financial supports from the China Postdoctoral Science Foundation (Grant No. 2022M723536) and open fund project of Key Laboratory of Safe Construction and Intelligent Maintenance for Urban Shield Tunnels of Zhejiang Province (Grant No. HZCU-UST-23-03) are acknowledged and appreciated.

Acknowledgments

The authors are also grateful to the help from Shihong Zhai, Xiaofeng Tan, Guanjun You, Haijiang Xu, Gang Li, Qing Yang, Heng Sun, Chao Xu, Zhiyong Yang, and Jun Yu in CCCC Second Harbor Engineering Company Ltd.

Conflict of interest

Authors FJ, PL, ZY, and BW were employed by CCCC Second Harbor Engineering Company Ltd.

The remaining author declares that the research was conducted in the absence of any commercial or financial relationships that could be construed as a potential conflict of interest.

Publisher's note

All claims expressed in this article are solely those of the authors and do not necessarily represent those of their affiliated

organizations, or those of the publisher, the editors and the reviewers. Any product that may be evaluated in this article, or claim that may be made by its manufacturer, is not guaranteed or endorsed by the publisher.

References

Cheng, J., Yang, S., Han, W., Zhang, Z., Jiang, Z., and Lu, J. (2022). Experimental and numerical study on the indentation behavior of tbm disc cutter on hard-rock precutting kerfs by high-pressure abrasive water jet. *Arch. Civ. Mech. Eng.* 22 (1), 37. doi:10.1007/s43452-021-00360-x

Ciccu, R., and Grosso, B. (2014). Improvement of disc cutter performance by water jet assistance. *Rock Mech. rock Eng.* 47, 733–744. doi:10.1007/s00603-013-0433-4

Ding, X., Xie, A. Y., Yang, H., and Li, S. (2023). Quantifying multifactor effects on mud cake formation risk for a tunnel boring machine with the analytical hierarchy process. *Buildings* 13, 355. doi:10.3390/buildings13020355

Du, C., Zhu, H., Wang, S., and Zhang, J. (2022). Test and application study on dispersion and disintegration of mud cake on slurry shield. *Tunn. Constr.* 42 (5), 847–853. (In Chinese). doi:10.3973/j.issn.2096-4498.2022.05.011

Fang, Y., Yao, Y., Song, T., Wei, L., Liu, P., and Zhuo, B. (2022). Study on disintegrating characteristics and mechanism of cutterhead mud-caking in cohesive strata. *Bull. Eng. Geol. Environ.* 81, 510. doi:10.1007/s10064-022-03018-x

Ge, Z., Zhang, H., Zhou, Z., Cao, S., Zhang, D., Liu, X., et al. (2023). Experimental study on the characteristics and mechanism of high-pressure water jet fracturing in high-temperature hard rocks. *Energy* 270, 126848. doi:10.1016/j.energy.2023.126848

Hagan, P. C. (1992). "The cuttability of rock using a high pressure water jet. Western Australia conference on mining geomechanics," in Proceedings of the Western Australian conference on mining geomechanics, Australia, 8-10 June 1992 (IEEE), 8–10.

Han, J., Wang, J., Yang, W., Wang, X., Ma, R., Wang, W., et al. (2023). Experimental study on the properties of a polymer-modified superfine cementitious composite material for waterproofing and plugging. *Case Stud. Constr. Mater.* 19, e02552. doi:10.1016/j.cscm.2023.e02552

Hollmann, F. S., and Thewes, M. (2013). Assessment method for clay clogging and disintegration of fines in mechanised tunnelling. *Tunelling Undergr. Space Technol.* 37, 96–106. doi:10.1016/j.tust.2013.03.010

Langmaack, L., and Lee, K. F. (2016). Difficult ground conditions? Use the right chemicals! Chances–limits–requirements. *Tunn. Undergr. Space Technol.* 57, 112–121. doi:10.1016/j.tust.2016.01.011

Li, T., Zhao, W., Liu, R., Han, J., Jia, P., and Cheng, C. (2023). Visualized direct shear test of the interface between gravelly sand and concrete pipe. *Can. Geotechnical J.* 61, 361–374. doi:10.1139/cgj-2022-0007

Li, X., Yang, Y., Li, X., and Liu, H. (2022). Criteria for cutting head clogging occurrence during slurry shield tunneling. *Appl. Sci.* 12, 1001. doi:10.3390/app12031001

Liu, P., Wang, S., Ge, L., Thewes, M., Yang, J., and Xia, Y. (2018). Changes of Atterberg limits and electrochemical behaviors of clays with dispersants as conditioning agents for EPB shield tunnelling. *Tunn. Undergr. Space Technol.* 73, 244–251. doi:10.1016/j.tust.2017.12.026

Liu, Z., Ma, Z., Liu, K., Zhao, S., and Wang, Y. (2023). Coupled CEL-FDEM modeling of rock failure induced by high-pressure water jet. *Eng. Fract. Mech.* 277, 108958. doi:10.1016/j.engfracmech.2022.108958

Luo, X., Zhang, J., Yang, F., He, F., and Xia, Y. (2023). Research on the hard rock cutting characteristics of disc cutter under front-mounted water jet precutting kerf conditions. *Eng. Fract. Mech.* 287, 109330. doi:10.1016/j.engfracmech.2023.109330

Min, F., Zhu, W., Lin, C., and Guo, X. (2015). Opening the excavation chamber of the large-diameter size slurry shield: a case study in Nanjing Yangtze River Tunnel in China. *Tunn. Undergr. Space Technol.* 46, 18–27. doi:10.1016/j.tust.2014.10.002

Oliveira, D. (2018). *EPB excavation and conditioning of cohesive mixed soils: clogging and flow evaluation*. Kingston: Queen's University.

Wang, B., Zhang, H., Li, D., and Li, F. (2021). "Chamber opening under pressure technology of shield," in *Shield tunneling technology in hard-soft uneven stratum and extremely-soft stratum. Key technologies for tunnel construction under complex geological and environmental conditions*. Editor K. Hong (Singapore: Springer).

Wang, S., Liu, P., Gong, Z., and Yang, P. (2022). Auxiliary air pressure balance mode for EPB shield tunneling in water-rich gravelly sand strata: feasibility and soil conditioning. *Case Stud. Constr. Mater.* 6, e00799. doi:10.1016/j.cscm.2021.e00799

Wang, S., Qu, T., Fang, Y., Fu, J., and Yang, J. (2019). Stress responses associated with earth pressure balance shield tunneling in dry granular ground using the discrete-element method. *Int. J. Geomechanics* 19 (7), 04019060. doi:10.1061/(asce)gm.1943-5622.0001434

Wang, Z., and Feng, H. (2017). Clay cake prevention for a slurry shield cutterhead in argillaceous siltstone stratum. *Mod. Tunn. Technol.* 54, 217–222. (In Chinese). doi:10.13807/j.cnki.mtt.2017.06.029

Xiao, X., Xia, Y., Mao, X., Wang, Y., Fang, Z., Wang, F., et al. (2020). Effect of the nozzle structure of the large-diameter slurry shield cutterhead on the scouring characteristics. *J. Braz. Soc. Mech. Sci. Eng.* 42, 157. doi:10.1007/s40430-020-2255-0

Yang, Z., Liu, P., Chen, P., Li, S., and Ji, F. (2023). Clogging prevention of slurry–earth pressure balance dual-mode shield in composed strata with medium–coarse sand and argillaceous siltstone. *Appl. Sci.* 13, 2023. doi:10.3390/app13032023

Zhang, J., Li, Y., Zhang, Y., Yang, F., Liang, C., and Tan, S. (2020). Using a high-pressure water jet-assisted tunnel boring machine to break rock. *Adv. Mech. Engng* 12 (10), 168781402096229–16. doi:10.1177/1687814020962290

Zhao, G., and Yao, Y. (2017). Reason and solution for mud cake developing of cutting wheel center. *Railw. Constr. Technol.* 03, 69–72. (In Chinese). doi:10.3969/j.issn.1009-4539.2017.03.017

frontiers | Frontiers in Earth Science

TYPE Methods
PUBLISHED 21 March 2024
DOI 10.3389/feart.2024.1364752

Check for updates

OPEN ACCESS

EDITED BY
Pengjiao Jia,
Soochow University, China

REVIEWED BY
Qian Bai,
Northeastern University, China
Cheng Cheng,
Soochow University, China

*CORRESPONDENCE
Guangbiao Shao,
shaogb@sdjzu.edu.cn

RECEIVED 03 January 2024
ACCEPTED 05 March 2024
PUBLISHED 21 March 2024

CITATION
Liu G, Jia P, Sun J, Jiang Z, Yang F, Yang G and Shao G (2024), Research and application of new anti-floating anchor in anti-floating reinforcement of existing underground structures.
Front. Earth Sci. 12:1364752.
doi: 10.3389/feart.2024.1364752

COPYRIGHT
© 2024 Liu, Jia, Sun, Jiang, Yang, Yang and Shao. This is an open-access article distributed under the terms of the Creative Commons Attribution License (CC BY). The use, distribution or reproduction in other forums is permitted, provided the original author(s) and the copyright owner(s) are credited and that the original publication in this journal is cited, in accordance with accepted academic practice. No use, distribution or reproduction is permitted which does not comply with these terms.

Research and application of new anti-floating anchor in anti-floating reinforcement of existing underground structures

Guohui Liu[1], Pingsheng Jia[2], Jianping Sun[3], Zongbao Jiang[1], Fan Yang[1], Guorui Yang[3] and Guangbiao Shao[3]*

[1]Design Institute of Appraisal and Strengthening of Shandong Jianzhu University Co Ltd, Jinan, China, [2]The Second Construction Co Ltd of China Construction Seventh Bureau, Suzhou, China, [3]School of Civil Engineering, Shandong Jianzhu University, Jinan, China

In recent years, due to the changing climate conditions and the continuous deepening of water resource conservation measures, the groundwater level in northern China has gradually risen, leading to the increasingly prominent issue of anti-floating in existing buildings and structures. The development and adoption of reliable anti-floating reinforcement techniques for existing structures are crucial for ensuring the quality of such reinforcements. Therefore, focusing on the limitations of the anchor method for anti-floating reinforcement, this paper proposes a new type of anti-floating prestressed compression anchor that features a full-length anti-compressive steel pipe with a bearing body at the end and uses non-bonding tendons throughout its length. Firstly, the structural form of this pressure-type anchor is introduced; subsequently, combined with the results of on-site pull-out tests of the anchor, an analysis is conducted on the working principle, lateral resistance distribution, and internal force transfer mechanism of the new anti-floating anchor, and its load-bearing characteristics are elucidated. Finally, relying on actual anti-floating reinforcement projects and through numerical calculations, the changes in internal forces under different anti-floating conditions of existing structures reinforced with the new anchor compared to conventional anchors are contrasted. Research findings and engineering practice indicate that this new anti-floating anchor improves the mechanical performance of the grout body of the anchor, solves the water seepage problem at the anchor location of the waterproof slab, effectively suppresses cracking of the foundation waterproof slab after reinforcement, and enhances the anti-floating and durability of existing structures.

KEYWORDS

existing underground structures anti-floating reinforcement, design of anti-floating reinforcement, prestressed anti-floating compression anchor, anchor field test, FBG sensor

1 Introduction

Since the early 1990s, a large number of underground structures have been constructed in northern China. Due to factors such as lower precipitation and excessive groundwater exploitation at that time, the groundwater level in cities of northern China was generally low. Many designs of underground structures at this time were

inadequately considered or not considered for anti-floating stability. But in recent years, the groundwater level in northern China has been rising year by year. There are two reasons for this phenomenon. Firstly, the increment of rainfall recharges the underground water. Secondly, the protection policy of groundwater has been gradually tightened. Especially during the rainy season in years of abundant rainfall, the groundwater level in many areas has increased significantly compared to previous years (e.g., in 2021, the groundwater level in certain areas of Jinan has risen by more than 20 m compared to previous years). As a result, many underground structures were floated up or cracking of waterproof slabs. The above forms of damage have frequently occurred in recent years.

Compared with newly constructed structures, the choice of anti-floating methods for existing structures may be constrained due to limitations related to the current usage status of the structure, engineering geological and hydrogeological conditions, as well as on-site construction conditions. There are primarily three methods used for anti-floating reinforcement of such foundation types: weighting for anti-floating, water interception and pressure reduction methods, and the method of anti-floating piles and anti-floating anchors (Zheng et al., 2004; Yuan, 2007). The weighting method is simple in technique, but when adding weight to the top of an underground structure, one must consider the outdoor site elevation and the load-bearing capacity of the roof slab; whereas adding weight to the slab bottom may affect the useable space of basements. Water interception and pressure reduction methods (Cao et al., 2016) require long-term maintenance, and their reliability and durability over extended service life are difficult to ensure. Although anti-floating piles have high pullout resistance, their construction may cause damage to the existing foundation slab, and the equipment required for construction is not easily adaptable for indoor reinforcement project, hence these methods only used for outdoor underground structures like swimming pools and large water tanks (Han et al., 2009). Anti-floating anchor methods offer flexible arrangements, higher pullout resistance, strong adaptability to different strata, and compared to anti-floating piles, anchors need smaller opening of slab than piles that reduce damage to the foundation slab and disturbance to the subgrade, making them widely used in anti-floating reinforcement projects.

Currently, conventional anti-floating anchors are divided into tension-type and pressure-type. Tension-type anchors transmit loads through the bond between the anchor body (steel bar or steel strand) and the grout in the anchorage section, but tension on the anchor may cause cracking of grout bodies (Chen, 2024), leading to reduced durability. Pressure-type anchors transfer the tension directly from the anchor to the end of bearing body, which under traction, compresses the front-end grout body. During the hole life of the anchor, the grout body remains in a state of compression, avoiding tensile cracking, and thus their load-bearing capacity and durability performance are superior to tension-type anchors (Li et al., 2007). However, it should be noted that when reinforcing independent foundations with waterproof slabs using additional pressure-type anchors, the prestressed load directly act on the existing waterproof slab, changing its stress state and potentially causing insufficient bottom reinforcement, downward deflection, and cracking failure, leading to slab water leakage and reduced durability. Moreover, waterproofing around the holes made in the waterproof slab is also an urgent engineering issue that needs addressing. Therefore, the development and application of new anti-floating anchor technologies for existing underground structures is an important task for engineering technicians.

To address these engineering problems, this paper proposes and introduces a new type of anti-floating anchor. Combining the results of on-site pullout tests of the anchor, analyses are conducted on the working principle, lateral resistance distribution, and internal force transfer mechanism of the new anti-floating anchor, and its load-bearing characteristics are described. Relying on actual anti-floating reinforcement projects and engineering applications, modelling analysis is performed to compare the changes in internal forces under different buoyancy conditions of existing structures reinforced with the new anchor *versus* conventional anchors. The reinforcement characteristics of the new anti-floating anchor are summarized, providing a reference for design advices of the new anchor.

2 Novel prestressed steel pipe anchors

2.1 Structure and construction of the new anchor

To address the problem of insufficient bending capacity at the bottom of the original waterproof slab under low water levels when conventional anchors are prestressed on existing waterproof slabs, this novel type of prestressed steel pipe anti-floating anchor was invented.

As depicted in Figure 1A, the structure of this anti-floating anchor comprises the anchor body, a bottom bearing plate with dedicated anchorage fittings, and a top bearing plate with dedicated anchorage fittings. The anchor body is constructed from a finished steel pipe and unbonded stranded wires located inside the steel pipe. At the bottom of the stranded wires, a bearing plate and dedicated anchorage fittings are used to secure them to the bottom end of the steel pipe. The bottom bearing plate is welded to the bottom end of the steel pipe, and dedicated anchorage fittings are used to anchor one end of the stranded wire bundle to the bearing plate. To ensure the durability of the bottom anchorage fittings and the ends of the stranded wires, a short steel pipe is welded over the anchorage fittings. A circular steel plate is welded at the bottom of the short steel pipe to seal it, and the short steel pipe is treated for corrosion resistance. This creates a closed space at the bottom of the bearing plate, serving to protect the lower bearing body.

The annular space between the steel pipe and the borehole wall, as well as the gap between the steel pipe and the unbonded strands, are thoroughly filled with cement mortar, as illustrated in Figure 1B. Upon the grout attaining the designated strength, a top compression plate and anchorage system are installed. Thereafter, prestressing force is applied to the strand bundles in accordance with the design specifications, and the strands are locked in place with the prestressing force equivalent to the characteristic load-bearing capacity of the anti-floating anchors. Above the existing waterproof slab, a cast-in-place reinforced concrete composite layer of a certain thickness, determined by calculation, is constructed. This layer is made to spread loads to the original waterproof slab through structural integration techniques such as concrete surface preparation and dowel bar insertion.

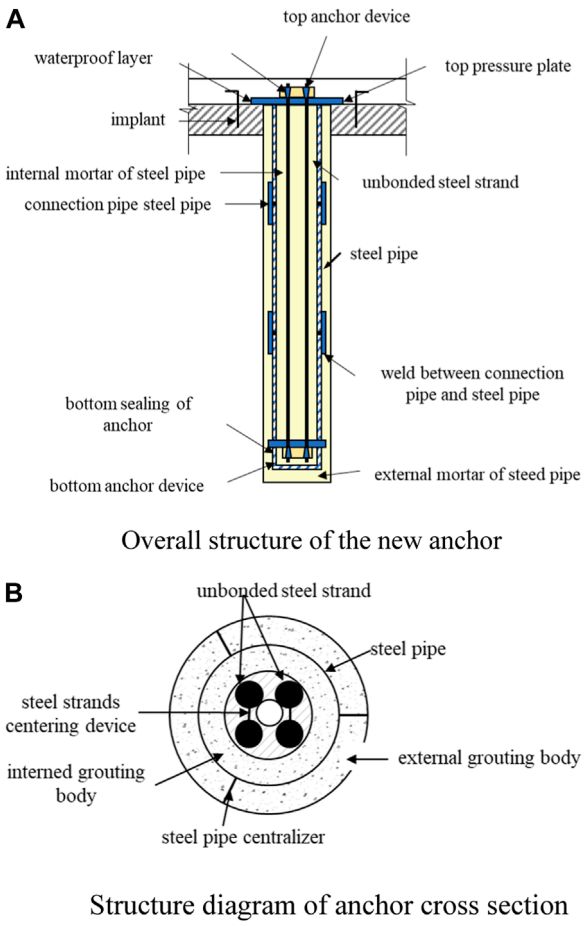

FIGURE 1
Anti-floating anchor structure. **(A)** Overall structure of the new anchor. **(B)** Structure diagram of anchor cross section.

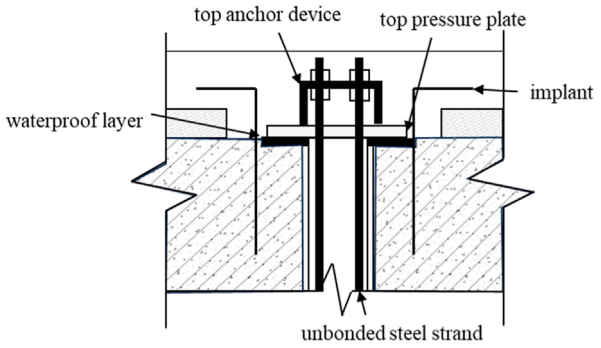

FIGURE 2
Design of anchor waterproof.

Additionally, when installing anchors in existing underground structures, the height of the basement space often restricts the construction of anchors. The steel pipe must be lowered into the hole in sections and then connected. In this new type of anchor, the stranded wires can be inserted into the hole in one go, ensuring their integrity and not affecting the stress transfer. The steel pipe is constructed in segments according to the on-site clearance height, with adjacent sections welded together using steel sleeves.

2.2 Waterproofing measures for waterproof slabs and anchors

When adding anti-floating anchors to existing underground structures, the junction between the waterproof slab and the anchor, as well as the anchor itself, are weak points prone to leakage, which can affect the use of the underground structure and the durability of the anti-floating structure. Therefore, appropriate waterproofing measures must be taken for the weak parts of the waterproof slab and the anchor.

Waterproofing measures include those for the anchor itself and for the joint between the waterproof slab and the anchor. The waterproofing of the anchor itself in this project is robust, mainly due to the application of an anti-corrosion lubricant on the exterior of the stranded wires inside the anchor and wrapping them with extruded high-density polyethylene resin sheathing. Additionally, the stranded wires are located within the grouting body inside the steel pipe, ensuring that groundwater cannot penetrate along the stranded wires. The bond between the grout body of the anchor and the original waterproof slab is relatively weak; hence, a micro-expansive agent is added to the cement mortar to prevent cracking at the interface due to shrinkage of the grout body. Furthermore, a cement-based penetrating crystalline waterproof coating is applied at the top of the anchor, and the anchor head is enclosed within the new concrete composite layer (as seen in Figure 2). During the construction of the new waterproof slab, integral casting is performed to avoid water leakage at the openings in the original waterproof slab, thereby enhancing the waterproof performance of the reinforcement project.

2.3 Interaction mechanism of the new anchor and waterproof slab

Under low water level conditions, the pre-stress is borne by the anchor itself. The downward force exerted by the bearing plate acts on the steel pipe and the grout inside and outside the steel pipe. The anchor body behaves like a miniature steel pipe pile, possessing significant vertical compressive load-bearing capacity, relieving the waterproof slab from the applied pre-load; this avoids the additional internal forces generated in the original waterproof slab when conventional pressure-type anchors are pre-stressed.

When the groundwater level rises, the bottom of the waterproof slab experiences an increase in buoyancy due to the water level. At this point, the stress distribution in the waterproof slab is consistent with that under conventional prestressed anchors. Throughout the process, the grout body of the anchor remains in compression without cracking, ensuring the durability of the anchor.

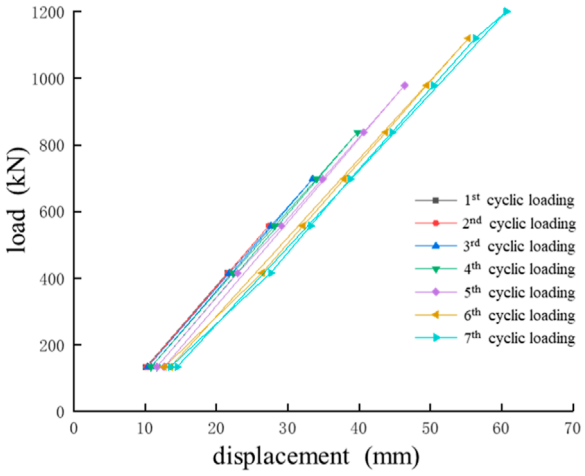

FIGURE 3
Basic test load-displacement curve of anchor.

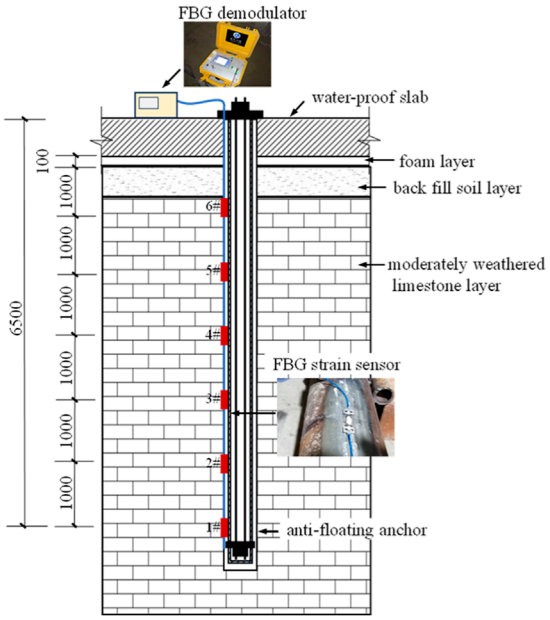

FIGURE 4
Sensor layout diagram.

3 Field testing

3.1 Basic test of anchors

Based on the practical project mentioned in Chapter 4 of this paper, the basic test of the new anti-floating anchor is carried out. Field testing was conducted on three test anchors to determine their tensile load-bearing capacity and basic performance. The test sites were chosen in areas with relatively uniform rock layers, with the total length of the anchor body is 6.5 m, which 6 m below the waterproof slab. The diameter of the anchor is 220 mm, the design pull-out capacity of the anchor is 600 kN.Test anchors were constructed using the same techniques as the actual anti-floating anchors on site, and loading tests were performed 28 days after the completion of anchor construction. The methods of loading and unloading, displacement measurement, and determination of ultimate load-bearing capacity for the test anchors were in accordance with the relevant provisions of the "Technical Specifications for Geotechnical Anchors and Shotcrete Support Engineering" (GB 50086-2015) (China Construction Industry Publishing House, 2013). Due to the considerable anchorage length of the anchors in this project, and provided that the strength of the anchor materials permitted, loading was carried out in 9 stages, with the maximum load set at 1200 kN. The tensile load-bearing capacities of all three tested anchors met the requirements. The typical test results of anchor 1 are shown in Figure 3. Under the maximum test load of 1200 kN, the displacement of the steel strand at the end of the three anchor contains elastic displacement and a small amount of plastic displacement. There is no relative displacement between the anchor grout body and the original waterproof slab in the test.

3.2 Anchor lateral resistance test

To investigate the mechanical behaviour, pull-out resistance, and the distribution pattern of lateral resistance of the pressure-type prestressed anchor, an additional anchor was subjected to a tensile test. Fiber Bragg grating (FBG) strain sensors were affixed to the lateral surface of the steel pipe to measure the strain along the rod body, with the sensor arrangement depicted in Figure 4.

By analysing the wavelength changes of the fibre optic sensors attached to the anchor body, as measured on-site, and utilizing Equations (1) and (2), the axial forces along different sections of the anchor under varying tensile loads can be calculated. This, in turn, allows for the computation of the corresponding lateral frictional resistances for each segment.

$$\varepsilon = \frac{\lambda_i - \lambda_0}{k} \tag{1}$$

$$N_i = \varepsilon \sum E_{si} A_i \tag{2}$$

Where λ_i is the grating monitoring wavelength, λ_0 is the initial wavelength of the grating, k is the strain primary term coefficient, ε is the axial strain at the monitoring position, N_i is Axial force of anchor, E_{si} is elastic modulus, which the steel pipe is E_s=2.06×10^{5}N/mm^2, the mortar is E_s=3×10^{4}N/mm^2, A_i is the respective cross-sectional area of steel pipe and mortar.

The variation curve of the axial force of the anchor along the depth under different loads is shown in Figure 5. The variation curve of the lateral resistance between the anchor and the rock under different loads is shown in Figure 6 (due to the damage of optical fibre No.④, no effective data has been obtained).

From Figure 6, it can be observed that under the application of tensile loads, the side resistance of the rock along the depth of the anchor varies unevenly. Initially, during the early stages of loading, the lower to middle sections of the anchor exhibit greater rock side resistance. As the applied load increases, the side resistance in these sections continues to rise; however, its relative

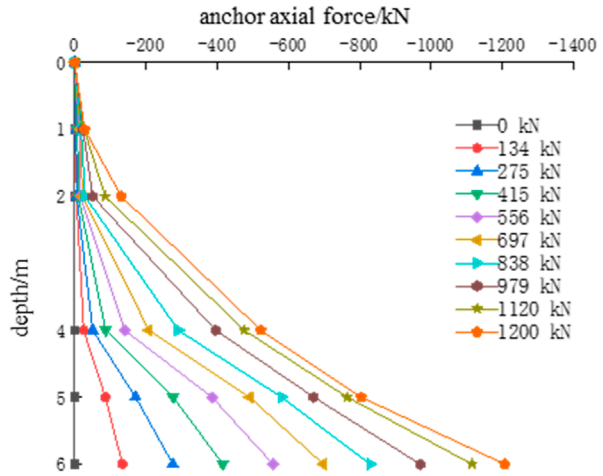

FIGURE 5
Anchor axial force.

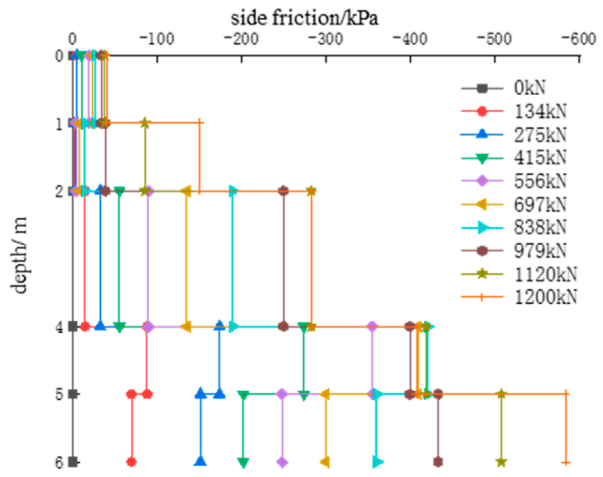

FIGURE 6
Anchor lateral resistance from side friction.

proportion diminishes. For instance, when the tensile load is 275 kN, the combined rock side resistance between the 4 m–6 m depth is 224 kN, accounting for 81% of the total side resistance. When the tensile load reaches 697 kN, the combined rock side resistance in the same depth range is 490 kN, representing 70% of the total side resistance. At a maximum load of 1200 kN, the combined side resistance of the anchor between 4 m and 6 m depth is 684 kN, making up 57% of the total side resistance. This indicates that initially, the lower rock side resistance plays a significant role, but as the tensile load increases, the side resistance progressively engages from bottom to top.

When the maximum load value of 1200 kN is reached, the rock side resistance is 584 kPa, which is significantly below the recommended values suggested by standards. This discrepancy primarily arises because the project's determination of anchor length considered overall failure factors, leading to a conservatively longer design length. For this individual anchor, under the application of the designed ultimate load, the rock side resistance has not yet been fully realized.

4 Engineering applications

4.1 Overview of engineering geology and hydrogeology

The strata beneath the structure base consist of moderately weathered limestone. The groundwater is primarily karst fissure water distributed within the bedrock fissures, recharged by vertical infiltration of atmospheric precipitation and lateral supply from the same aquifer. Groundwater levels are sensitive to meteorological factors and can change rapidly; the originally designed anti-floating water level was 4.5 m.

4.2 Description of the existing structure

The existing structure is a commercial complex comprising two main towers and a podium, with the above-ground portion of the main towers reaching 40 stories and the podium having 5 (locally 6) stories. There are three underground levels, with the north side and the east-west sides housing a three-story underground garage. The layout is illustrated in Figure 7. The main tower use a raft foundation, while the podium and the underground garage employ independent foundation with a waterproof slab. The concrete strength grade of independent foundations and waterproof slab is C35. The slab thickness of waterproof slab is 500 mm, using double-layer bidirectional reinforcement, with a bottom layer of φ14@200 and a top layer of φ16@200. Beneath the waterproof slab lies 500 mm of fill soil, with the slab aligned in elevation with the top of the independent foundation. Both the raft and independent foundations bear on moderately weathered limestone.

Construction of the project commenced in October 2012, and the main structure was completed at the beginning of 2015 before the project was halted. The project resumed at the beginning of 2019. During the hiatus, it was discovered that water levels during the high-water season were substantially higher than the original anti-floating level. Since the post-pouring strip of basements had not yet been cast, groundwater could drain through it, preventing any uplift damage to the subterranean structure. Based on the observed water level changes during the hiatus and upon re-evaluation, the total anti-floating design head was raised to 10.3 m. The original design did not meet the anti-floating requirements and necessitated reinforcement anti-floating forces.

4.3 Anti-floating reinforcement design scheme

Due to the deep burial of the underground structure in this project, the adjusted anti-floating design water level is high. Furthermore, the site is underlain by limestone with well-developed karst features, and water levels rise rapidly after rainfall. Therefore, it is impractical to employ anti-floating reinforcement measures such

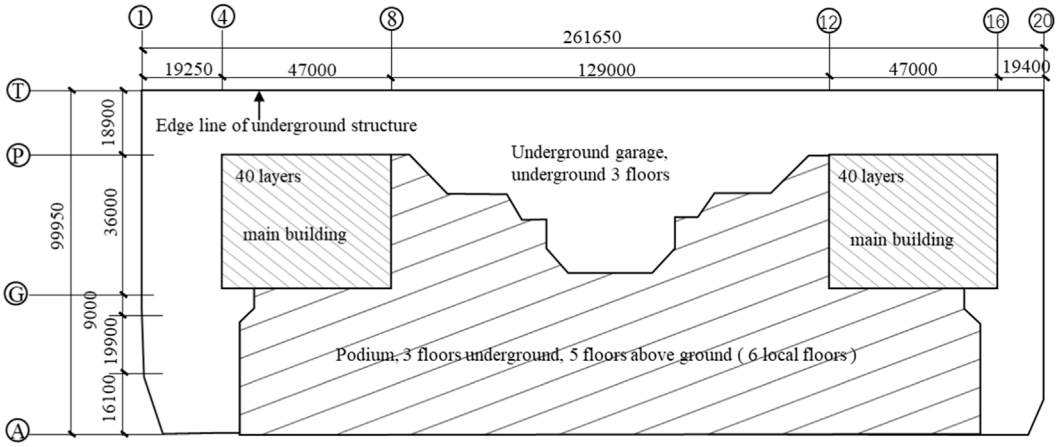

FIGURE 7
Basement arrangement of this project.

as interception and drainage decompression. Additionally, the top of the basement is constrained by outdoor elevation limits, and the indoor clear height is restricted by usage conditions, which also precludes the use of ballast for anti-floating reinforcement. Consequently, it has been determined that anti-floating anchors will be used for reinforcement.

Since neither the overall anti-floating capacity of the underground structure nor the stress on the waterproof slab meets the requirements, and considering the restriction of a 150 mm increase in the thickness of the waterproof slab due to the clear height of the third basement level, it has been determined, after comprehensive consideration of the above conditions, that the anchors should be installed within the waterproof slab area.

A standard column grid of 9 m×9 m is adopted for the overall anti-floating calculation. Within the standard column grid range of the pure underground garage area, the anti-floating shortfall is 5046.3 kN, while for the podium section, it is 2292.3 kN. In the pure garage area, nine anchors are arranged, with each anchor bearing an uplift resistance of 5046.3/9=560.7 kN; in the podium area, four anchors are arranged, with each rod bearing an uplift resistance of 2292.3/4=573.1 kN. The characteristic value of the uplift resistance of a single anchor is determined to be 600 kN. The arrangement of the anti-floating anchors in the underground garage area is shown in Figure 8A; the arrangement in the podium area is shown in Figure 8B.

The average uniaxial saturated compressive strength of the limestone beneath the foundation is 46 MPa, and the diameter of the prestressed anchor hole is taken as 220 mm. Due to the well-developed karst in the site, the rock failure surface is considered as a hard structural plane with poor cohesion, and the tensile strength is taken as 70 kPa based on the cohesion of the structural plane (China Construction Industry Publishing House, 2013). Considering there is a 500 mm thick soil layer beneath the waterproof slab, when the length of the anchor is 5.1 m, the minimum uplift resistance capacity is 600 kN. The actual length of the anchor selected is 6.0 m, which satisfies the capacity requirements.

The anti-floating reinforcement construction was completed in July 2021, and the whole project was put into use on 30 September 2022. In the case of more rainfall in the rainy season of the year and the higher water head of the basement waterproofing board, the deformation of the basement waterproofing board of the underground garage and the podium is normal.

4.4 Variation in waterproof slab stress after reinforcement with different anchors

In order to study the stress changes of the waterproof slab after reinforcement with different types of anti-floating anchors, the anchor arrangement of the underground garage shown in Figure 8A is used as the prototype for modelling and analysis. MIDAS GTS NX finite element analysis software is used for numerical calculation to analyse the influence of conventional anti-floating anchors and new pressure-type anti-floating anchors on the waterproof slab at low water level (i.e., without considering water buoyancy) and different water levels.

The independent foundation, surrounding rock and soil in the established model adopt 3D solid element, and the waterproof slab adopts 2D plate element. The thickness of the existing waterproof slab is 0.65 m after reinforcement construction, and the anti-floating anchor adopts 1D implantable truss element. The concrete strength of foundation and waterproof board is C35, in which the foundation size is 1.8 m×1.8 m×1.2 m, and the linear elastic model is used to simulate the elastic modulus is E=3×10^4 MPa, Poisson's ratio is μ=0.2, and the material weight is γ=25.2 MPa. The anti-floating anchor is 6 m long, the diameter of the ordinary anchor is d=100 mm, the diameter of the new anti-floating anchor is d=108 mm, and the rod body is steel. The linear elastic model is used to simulate the elastic modulus E=2.1×10^5 MPa, Poisson's ratio μ= 0.2, material weight γ=78.5 MPa, pre-loading is N=260 kN, and the ordinary anchor does not set pre-axial force. The depth of the stratum is 8 m below the floor, of which the thickness of the surface miscellaneous fill is 1 m, and the moderately weathered limestone

TABLE 1 Soil and rock parameters.

Soil horizon	Gravity γ(kN/m^3)	Force of cohesion c (kPa)	Angle of internal friction φ(°)	Modulus of compression E_s (MPa)
miscellaneous fill	17.8	7	10	2.00
medium weathered limestone	22	85	40	200.00

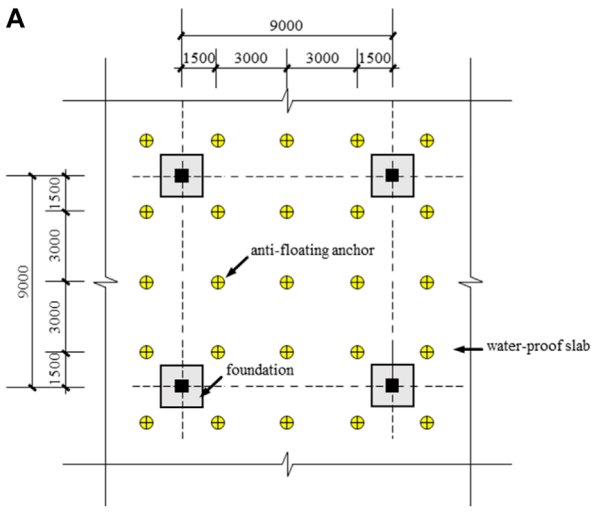

FIGURE 8
Standard layout of anchors. **(A)** Anchor layout plan for underground garage. **(B)** Anchor layout plan for podium.

is 2 m. The rock and soil mass is simulated by Mohr-Coulomb constitutive model, and the parameters are shown in Table 1.

This study focuses on the stress of the waterproof slab under the action of anchor restraint and buoyancy. The displacement

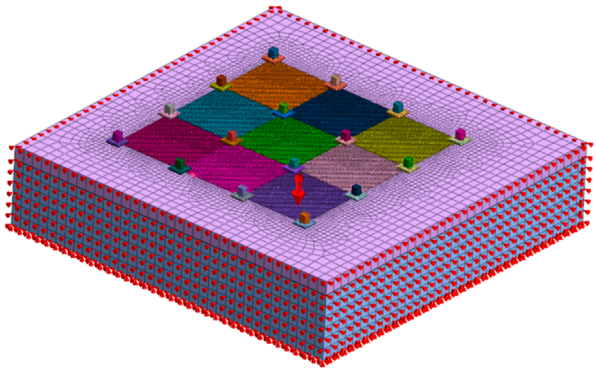

FIGURE 9
Calculation model of anchors.

boundary conditions are appropriately simplified, and the displacement and vertical displacement on both sides are constrained at the bottom of the model and the bottom of the independent foundation. By applying a uniform load on the waterproof board to simulate the floating effect under different anti-floating water levels, the construction step function in MIDAS GTS NX is used to load each time the anti-floating water level rises by 2 m (i.e., the uniform load increases by 20 kPa), and the design floating water level is 0 m, 2 m, 4 m, 6 m, 8 m, 10 m respectively. The overall calculation model is shown in Figure 9.

The bending moment calculation results of the middle span of the central waterproof slab of the waterproof slab calculation model reinforced by ordinary anti-floating anchor and new anti-floating anchor are extracted, and Figure 10 and Figure 11 are drawn respectively. From the diagram, it can be seen that the bending moment distribution trend of ordinary anti-floating anchor reinforcement and new anti-floating anchor reinforcement is basically the same. With the increase of the design anti-floating water level, the bending moment distribution of each span of the new anti-floating anchor is more uniform. Under the same design anti-floating water level, the peak value of the negative bending moment of the waterproof slab reinforced by the new anti-floating anchor is smaller than that of the ordinary anti-floating anchor. The positive bending moment of the middle anchor position of the new anchor scheme is greater than that of the ordinary anchor scheme, while the positive bending moment of the anchor position on both sides shows the opposite trend. In addition, the

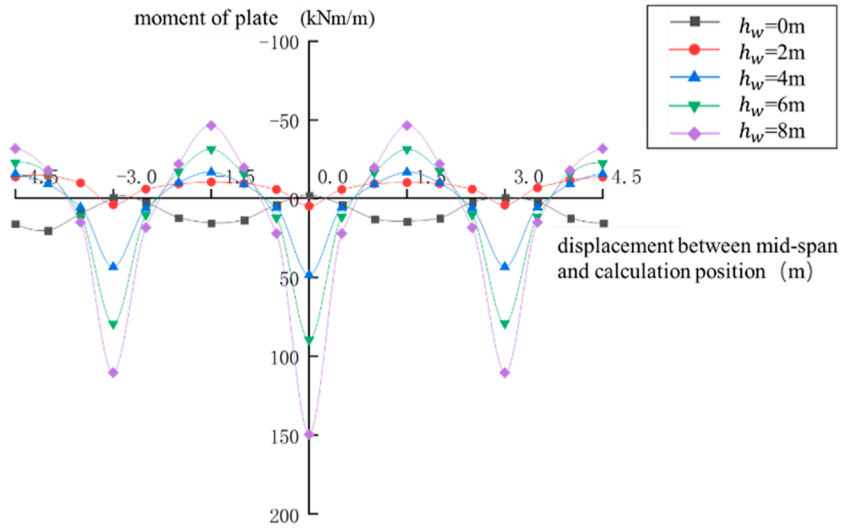

FIGURE 10
Moment distribution of waterproof slab reinforced by conventional anchor (kNm).

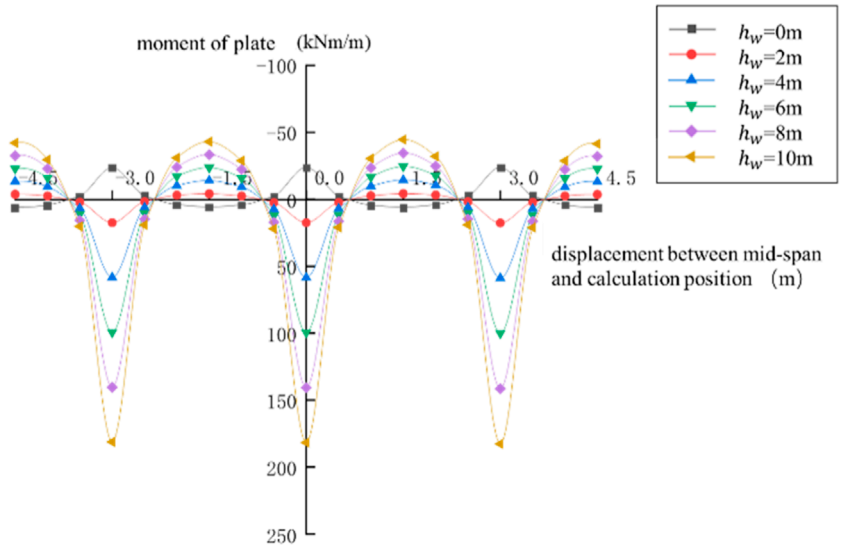

FIGURE 11
Moment distribution of waterproof slab reinforced by new anti-floating anchor (kNm).

model calculation of the conventional anchor scheme does not converge when the design anti-floating water level is 10 m. It can be considered that the anti-floating anchor and the waterproof slab have been destroyed and failed under the design anti-floating water level, while the new anchor reinforcement scheme could still bear the load without damage, and the bending moment value continues to increase, but the bending moment distribution of the waterproof slab has no significant change compared with the previous loading (h_w is design anti-floating water level.)

5 Conclusion

With a focus on the limitations of existing anchor methods for anti-floating reinforcement, this paper proposes a new type of prestressed compression anti-floating anchor. Combining the results of on-site anchor pull-out tests, the paper analyses the load-bearing characteristics of the new anti-floating anchor. Relying on an actual anti-floating reinforcement project and based on numerical calculation results, this study compares the changes in internal forces of the existing structure under different anti-floating

conditions after being reinforced with new and conventional anchors. The conclusions of this study are as follows:

(1) The new pressure-type steel pipe prestressed anti-floating anchor has a high uplift resistance capacity. Under the maximum test load of 1200 kN, it can still function normally. The steel pipe and grout form a structure similar to steel pipe concrete, which has superior compressive performance compared to conventional anchors. It will solve the anti-floating problems of insufficient reinforcement at the bottom of the existing underground structures.
(2) The new pressure-type steel pipe prestressed anti-floating anchor has good durability, simple construction operations, and is suitable for construction in narrow spaces.
(3) Engineering practice shows that the new anti-floating anchor improves the stress performance of the anchor body, this characteristic may solves the water seepage problem at the anchor location on the waterproof slab, effectively suppresses cracking of the foundation waterproof slab after reinforcement, and enhances the existing structure's anti-floating performance and durability.

Data availability statement

The original contributions presented in the study are included in the article/Supplementary material, further inquiries can be directed to the corresponding author.

Author contributions

GL: Data curation, Formal Analysis, Funding acquisition, Resources, Writing–original draft, Writing–review and editing. PJ: Supervision, Validation, Funding acquisition, Project administration, Resources, Writing–review and editing. JS: Data curation, Formal Analysis, Funding acquisition, Project administration, Resources, Visualization, Writing–review and editing. ZJ: Investigation, Methodology, Software, Supervision, Visualization, Writing–original draft. FY: Investigation, Software, Supervision, Writing–review and editing. GY: Methodology, Supervision, Validation, Writing–original draft. GS: Software, Supervision, Resources, Writing–review and editing.

Funding

The author(s) declare financial support was received for the research, authorship, and/or publication of this article. This work was supported by the State Key Program of the National Natural Science Foundation of China [Grant No. 52038006].

Conflict of interest

Authors GL, ZJ, and FY were employed by Design institute of Appraisal and Strengthening of Shandong Jianzhu University Co Ltd.

Author PJ was employed by The Second Construction Co Ltd of China Construction Seventh Bureau.

The remaining authors declare that the research was conducted in the absence of any commercial or financial relationships that could be construed as a potential conflict of interest.

Publisher's note

All claims expressed in this article are solely those of the authors and do not necessarily represent those of their affiliated organizations, or those of the publisher, the editors and the reviewers. Any product that may be evaluated in this article, or claim that may be made by its manufacturer, is not guaranteed or endorsed by the publisher.

References

Cao, H., Pan, H., and Luo, G. (2016). A new anti-floatation method by drainage: concept and application. *Chin. J. Rock Mech. Eng.* 35 (12), 2542–2548. doi:10.13722/j.cnki.jrme.2016.0343

Chen, M. (2024). *Seismic response analysis of sand-rubber isolation cushion*. Hefei, China: AnHui University of Science and Technology.

China Construction Industry Publishing House (2012). *Code for design of building foundation*. GB 50007-2011. Beijing: China Construction Industry Publishing House.

China Construction Industry Publishing House (2013). *Technical code for building slope engineering*; GB 50330-2013. Beijing: China Construction Industry Publishing House.

China Construction Industry Publishing House (2015). *Technical code for engineering of ground anchorages and shotcrete support*. GB 50086-2015. Beijing: China Plan Publishing House.

China Construction Industry Publishing House (2019). *Technical standard for building engineering against uplift*. JGJ 476-2019. Beijing: China Construction Industry Publishing House.

Development of the People's Republic of China (2011). *Code for design of building foundation*. GB 50007-2011. Beijing: Ministry of Housing and Urban-Rural Development of the People's Republic of China.

Han, L., Wang, D., Qu, T., and Zheng, T. (2009). Design and application of anti-floating anchored structure by blast-expanding bore in large-scale underground sewage pool. *Chin. J. Rock Mech. Eng.* 28 (z1), 2960–2965.

Li, Z., Zhou, X., Liu, J., Tian, T., Sun, Y., and Yin, H. (2007). Study and application of anchor rod to against floatation of high-rise building. *Build. Struct.* 37 (4), 55–57.

Qian, L. I. (2008). Discussion on design of the raft foundation consisting of individual footing combining with water-proof slab in Beijing. *Ind. Archit.* (z1), 718–720.

Wu, L. I. U., Li, N., Tan, G., and Xiong, J. (2016). Design of the independent foundation with water-proof slab. *Build. Struct.* (s2), 520–523. doi:10.19701/j.jzjg.2016.s2.110

Yuan, Z. (2007). Problems in design of anti-up lift in underground engineering. *Chin. Jou mal Undergr. Space Eng.* 3 (3), 519–521.

Zheng, G., Wang, X., and Hu, D. (2004). Application status analysis of anti-floating technical measures. *Undergr. Space* (1).

frontiers | Frontiers in Earth Science

TYPE Original Research
PUBLISHED 28 March 2024
DOI 10.3389/feart.2024.1373140

Check for updates

OPEN ACCESS

EDITED BY
Jiayong Han,
Shandong Jianzhu University, China

REVIEWED BY
Wei-Hai Yuan,
Hohai University, China
Zhixiong Zeng,
Hong Kong University of Science and Technology, Hong Kong, SAR China

*CORRESPONDENCE
Maolong Xiang,
xiangmaolong@csu.edu.cn

RECEIVED 19 January 2024
ACCEPTED 15 March 2024
PUBLISHED 28 March 2024

CITATION
Liu F, Zhang X, Xiang M, Lyu J, Feng R and LIU S (2024), Experimental study on stress and deformation characteristics of foundation pit considering excavation width using 3D printing technology.
Front. Earth Sci. 12:1373140.
doi: 10.3389/feart.2024.1373140

COPYRIGHT
© 2024 Liu, Zhang, Xiang, Lyu, Feng and LIU. This is an open-access article distributed under the terms of the Creative Commons Attribution License (CC BY). The use, distribution or reproduction in other forums is permitted, provided the original author(s) and the copyright owner(s) are credited and that the original publication in this journal is cited, in accordance with accepted academic practice. No use, distribution or reproduction is permitted which does not comply with these terms.

Experimental study on stress and deformation characteristics of foundation pit considering excavation width using 3D printing technology

Fengzhou Liu[1,2], Xu Zhang[3], Maolong Xiang[4]*, Jingkang Lyu[4], Rui Feng[2] and Shouhua LIU[5]

[1]Shandong University, Jinan, China, [2]Jinan Rail Transit Group Co., Ltd, Jinan, China, [3]China Railway 14th Bureau Group Co., Ltd, Jinan, China, [4]School of Civil Engineering, Central South University, Changsha, China, [5]Architectural Engineering Institute, Huaiyin Institute of Technology, Huaian, China

A sophisticated model of the foundation pit support structure was developed via a model test that incorporated 3D printing technology. A meticulously scaled-down simulation of foundation pit excavation was conducted, utilizing the excavation width of the foundation pit as the sole variable, to evaluate and compare the impact of various foundation pit widths on the force and deformation characteristics of the foundation pit following layer-by-layer excavation. The findings indicate that the stress and deformation characteristics of the retaining structure shift from the "cantilever" mode to a composite mode of "internally convex" or "concave-convex" as the pit is excavated and internal support is installed. The change in pit width has minimal influence on the mechanical response law of the support structure during excavation. Nonetheless, the alteration in the pit width had a direct effect on both the internal force and deformation of the support structure, as well as the change in surface settlement value. In the experiment, wider pits had monitoring values that increased multiple times compared to narrower pits. The width of the foundation pit has a considerable impact on the mechanical response and stability of the pit, which is evident in the relatively lower lateral earth pressure on the outside of the retaining structure in narrower pits. This results in less stress and deformation of the pit structure. Moreover, the decrease in the passive zone of the pit contributes to better stability, indicating that the lower lateral earth pressure on the outside of the retaining structure is an innate reason for the excellent stability of narrower pits.

KEYWORDS

foundation pit width, 3D printing technology, model test, deformation characteristics, mechanical response, stability

1 Introduction

Numerous engineering practices have demonstrated significant differences in the stability and failure modes of foundation pits of varying widths. Narrow foundation pits exhibit relatively small deformations and less frequent

kicking phenomena. The existing calculation methods for different foundation pit widths, especially narrow foundation pit, cannot match the engineering practice (Li L. et al., 2022). This leads to overly conservative design of the foundation pit. With the emergence of foundation pit projects of different width types will inevitably cause a lot of unnecessary waste. Exploring the influence of foundation pit width effect on the deformation characteristics and stability of foundation pit has become the focus of engineering researchers.

At present, many scholars have carried out research related to the effect of pit width on the mechanical response and stability of pits using numerical simulation, theoretical calculation analysis and physical model test. There have been a lot of research results about numerical simulation (Faheem et al., 2004; Orazalin et al., 2015; Ying et al., 2018; Zhang et al., 2018; Zeng et al., 2019; He et al., 2020; He et al., 2022; Zhao et al., 2022; Huang et al., 2023), for example, Ying et al. (2018) conducted a numerical simulation of deep pits with different widths to obtain the distribution law of potential uplift slip crack surface at the bottom of pits. Zeng et al. (2019) conducted numerical simulations to study the impact of different pit widths on the mechanical behavior of retaining walls and surrounding soil. There are also some relevant results in the theoretical analysis (Wang and Sun, 2012; Liu et al., 2020; Xu et al., 2016; Xu et al., 2023), for example, Wang and Sun (2012) derived a method for calculating of the earth pressure reduction factor on the enclosure structure that can consider the influence of pit width. Liu et al. (2020) used an analytical method to compare the force and deformation characteristics of the enclosure wall under different excavation width conditions.

In the field of physical model experimental research, there are fewer relevant studies using pit width or width-to-depth ratio as a single variable, but there are still a large number of relevant 1 g normal gravity pit model tests (Chen et al., 2021; Zhang et al., 2023; Wang et al., 2018; Cheng et al., 2017; Zeng et al., 2021; Wang et al., 2017; Li et al., 2024) and centrifugal model tests (Hu et al., 2018; Chen et al., 2022) available. For example, Chen et al. (2021) studied the coordinated deformation characteristics among the internal support, retaining wall and soil behind the wall by designing a 1 g normal gravity model test with a scalable internal support system. Hu et al. (2018) conducted centrifugal model experiments using a deep excavation pit as a background to explore the impact of factors such as pit length and excavation depth on the mechanical response law of the pit.

For the numerical simulation research, there are problems in selecting appropriate models and parameters due to the unclear damage pattern of the pit when the pit width changes. Theoretical analysis is often constrained by the assumptions set. Compared with other research methods, physical model testing is better at reflecting the fundamental influence law when considering only the pit width variable. Among the physical model tests, the 1 g normal gravity model test has clear advantages over the centrifugal test regarding operability, such as the stepwise excavation and filling of the pit. In this paper, the 1 g normal gravity physical modeling test is used to investigate the influence of pit width on the mechanical behavior and stability of the pit after excavation layer by layer at the same pit excavation depth, in order to provide theoretical guidance and reference for relevant engineering applications.

2 Model test program

2.1 The application feasibility of 3D printing technology

3D printing is a rapid prototyping technology that constructs objects by printing layer by layer with adhesive materials, based on 3D digital models. This technique offers several advantages in the field of civil engineering testing, particularly in the production of structural models (Jiang and Song, 2018; Zuo et al., 2019; Li et al., 2020; Li Z.et al., 2022; Liu, 2022; Han et al., 2023):

(1) With a processing accuracy of up to 0.1 mm–0.2 mm, 3D printing offers high molding accuracy, and even considering the deformation caused by uneven heat dissipation during printing, the resulting model can meet the accuracy requirements of model testing;
(2) The forming process is highly controllable and only needs to build the digital structure model, which needs to be printed, can easily realize the complex model making, which is difficult to realize by traditional methods;
(3) 3D printing materials are diverse, the mechanical parameters of different materials have large differences, and the physical and mechanical properties of printed products cover a wide range of parameters, which makes the mechanical properties of 3D printed products can basically meet the needs of civil engineering model testing.

3D printed material products can be broadly classified into "rock-like products" and "elastomeric material-like products" according to their mechanical properties (Li et al., 2020). In the design of foundation pits, the support structure should be in the elastic-plastic stage. Existing 3D printing materials exhibit elastic-plastic characteristics in their initial deformation, with a maximum strain in the elastic stage greater than 0.2% (Jiang and Song, 2018), which can meet the demand of the deformation characteristics of the foundation pit support structure in the model test simulation.

2.2 Test model and material parameters

The test model box size is 1.6 m × 1.2 m × 0.56 m (length × height × width), the test box shape is rectangular, the model box frame is made of square steel welding, the internal is acrylic plate box without top cover, the test system is shown in Figure 1. The geometric similarity ratio between the test model and the actual project is 1: 50, the excavation depth of the pit is 40 cm, and the burial depth of the ground-connection wall is 56 cm. 3D printing technology is introduced to produce the pit support structure, and the pit support structure, including the underground diaphragm wall, internal support and waist beam, are all load-bearing components in the test. According to the stress-strain characteristics of commonly used printing materials (Li et al., 2020), and considering the geometric similarity ratio of the model test, the pit support structure is selected as ABS material, the relevant material parameters are shown in Table 1. The size of the retaining wall is 56 cm × 56 cm, the thickness is 20 mm. As shown in Figures 2A,B, the retaining wall and beam are bonded using AB

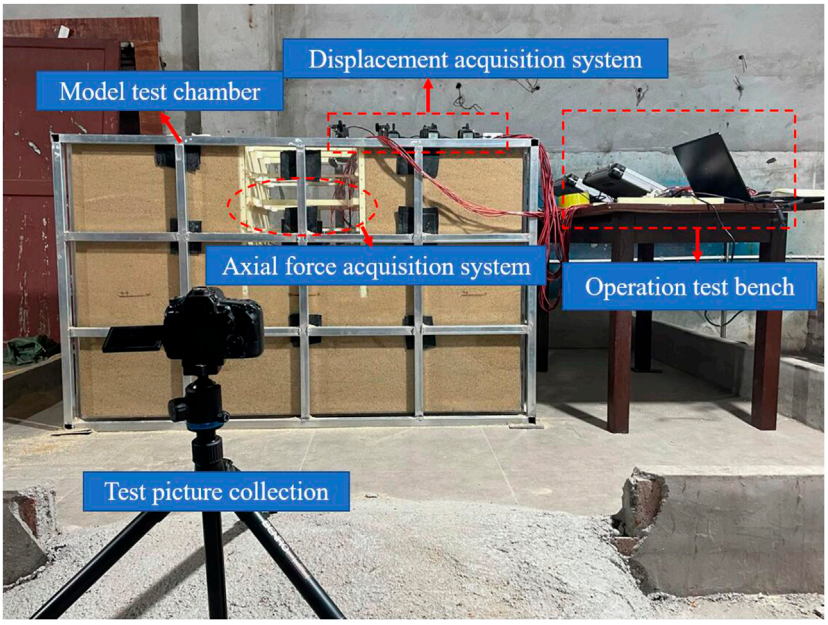

FIGURE 1
Foundation pit model experiment system.

TABLE 1 Physical and mechanical parameters of ABS printing materials used in the experiment.

Material	Elastic modulus (MPa)	Tensile strength (MPa)	Flexural strength (MPa)	Printing deviation (%)
Simulated material	2,178–2,222	47	67	0.3

glue, and buckles are set between the inner support of each layer and the retaining wall, then the inner support can be applied directly on the buckles after the excavation of the foundation pit. It is worth pointing out that some of the displacement gauges in existing studies are directly erected on the model box without considering the influence of the deformation and vibration of the model box on the displacement gauges. To avoid this influence, as shown in Figures 2A,C special displacement gauges bracket is designed and welded in this test, which is independent of the model box system to accurately monitor the surface displacement.

To accurately simulate the excavation process of an actual foundation pit, a layer of internal support is immediately installed for every layer of soil excavated from the pit. There are a total of four layers of internal support, with a vertical spacing of 10 cm between each layer, the first layer and the third layer of internal support for concrete support, each layer of concrete support set three. The second layer and the fourth layer of internal support for steel support, each layer of steel support set five, steel support cross-sectional size of 10 mm × 10 mm, concrete support cross-sectional size of 20 mm × 20 mm, the solid model of the foundation pit after excavation as shown in Figure 2D.

This experiment was conducted under 1 g normal gravity conditions and aimed to investigate the influence and mechanism of the pit width on the mechanical response and stability of the pit. The experiment is not intended to provide reference for the design, construction, or deformation prediction of any specific project. Therefore, the geological conditions were simplified. Homogeneous sand soil was used as the soil in the experiment, and its physical and mechanical parameters are detailed in Table 2.

2.3 Arrangement of testing points

During the experiment, real-time monitoring was carried out on the stress and deformation of the pit support structure, surface settlement behind the wall, and soil pressure behind the wall. The layout of the monitoring points can be seen in Figure 3. Six pairs of strain gauges (01–06) were installed on the right side of the retaining structure, and three pairs of strain gauges (07–18) were installed on each layer of internal support, located in the middle and outermost support positions. Ten CJLY-350 strain-type miniature soil pressure boxes (501–510) were installed on the inner and outer sides of the left retaining structure. Capacitance grid displacement transducers (with an accuracy of 0.001 mm) were installed 10 cm, 25 cm, and 40 cm away from the outer edge of the retaining structure to monitor ground displacement (101–103), as shown in Figure 2D, the displacement measuring point is arranged 25 mm × 25 mm rigid PVC sheet, with the micrometer probe in contact with the sheet.

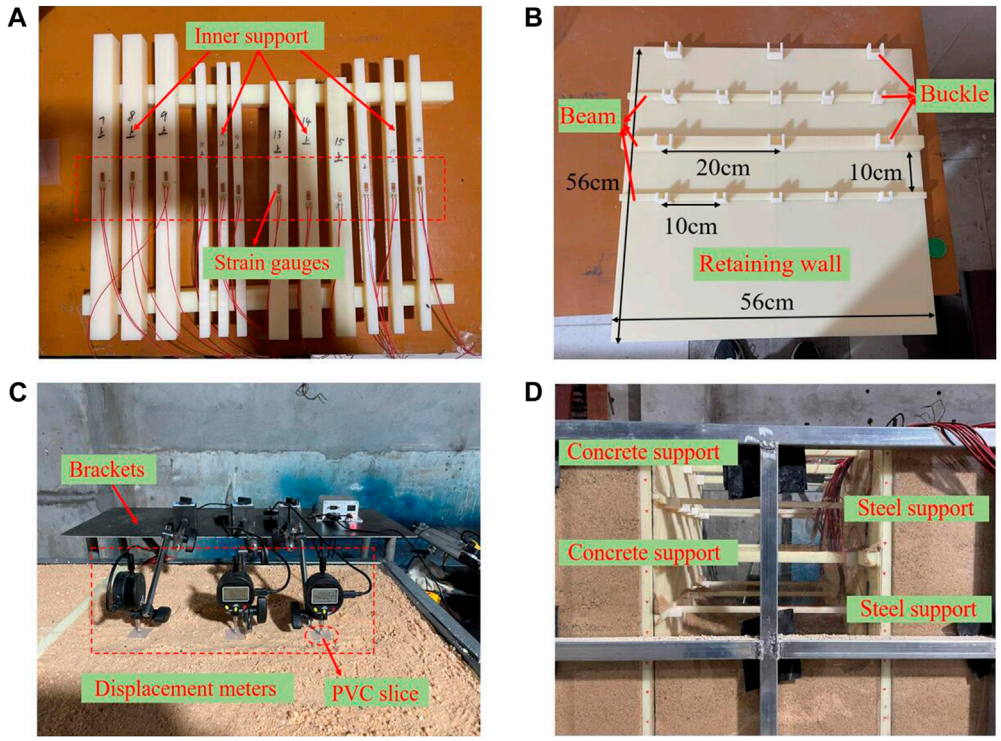

FIGURE 2
Solid drawing and displacement meter layout of each component of foundation pit: **(A)** Internal support. **(B)** Retaining wall and buckle arrangement. **(C)** Layout of displacement meter. **(D)** Model diagram after foundation pit excavation.

TABLE 2 Physical and mechanical parameters of sand used in the experiment.

Parameter	Specific gravity	Mean diameter	Coefficient of uniformity	Maximum void ratio	Minimum void ratio	Peak friction angle (°)
Simulated material	2.67	0.23	2.25	0.85	0.43	33.5

2.4 Test process and test conditions

During the experiment, the pit enclosure was assembled using AB glue bonding, and strain gauges and soil pressure boxes were installed. The assembled pit enclosure was placed in the model box, and the testing system was activated. The soil was then filled and compacted layer by layer, and the displacement meter was installed after the soil backfill was completed. Once the testing system data stabilized, the strain gauges and displacement meter were zeroed for the corresponding testing channel. The stable strain value of the soil pressure box testing channel was recorded as the initial value of the soil pressure box reading. The excavation of the foundation pit and erection of the internal support consisted of nine construction steps, as shown in Table 3 and Figure 4 from Step 1 to Step 9.

In the case of ensuring the depth of the foundation pit unchanged, as shown in Figure 5, a total of three sets of scale model tests with different foundation pit widths were set up. The geometric similarity ratio of the test is 1: 50. The widths of the foundation pit of Group A, Group B and Group C were 16 cm, 30 cm and 40 cm, respectively; that is, the corresponding actual foundation pit widths were 8 m, 15 m and 20 m, and the corresponding width-depth ratios were 0.40, 0.75 and 1.00, respectively. The support structure and stratum parameters were the same in the three groups of tests except for the width of the pit. The buried depth of the center of the four internal support sections is 3 cm, 13 cm, 23 cm and 33 cm, respectively. The specific test group and working conditions are shown in Table 3.

3 Test results

3.1 Characteristics of deep horizontal displacement of enclosure structure

The curvature radius and curvature arc angle of the measuring point are calculated according to the strain difference between the inner and outer sides of the measuring point of the retaining

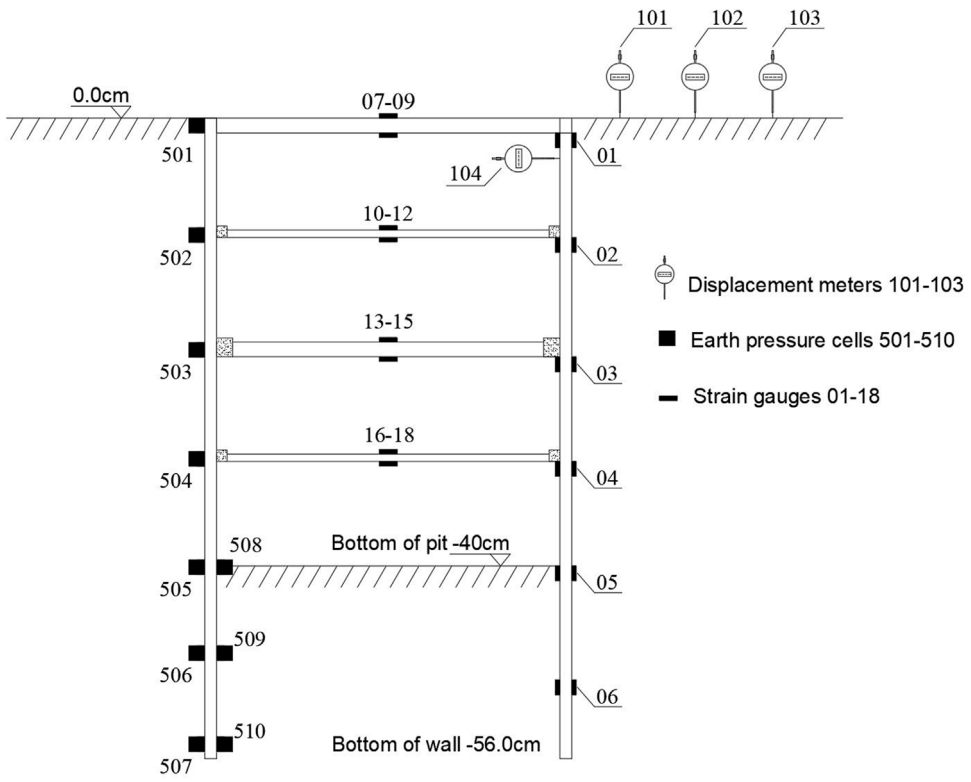

FIGURE 3
Layout of measuring points.

structure. The curvature radius ρ_r and curvature arc angle θ are given as Eq. 1 and Eq. (2),

$$\rho_r = h/(\varepsilon_1 - \varepsilon_2) \tag{1}$$

$$\theta = l/\rho_r \tag{2}$$

$$dx = -\rho_r(1 - \cos\theta) \tag{3}$$

Where h is the thickness of the retaining structure, $(\varepsilon_1 - \varepsilon_2)$ is the strain difference between the inner and outer strain gauges, and l is the arc length corresponding to the curvature arc angle θ.

Assuming the displacement of the bottom of the retaining structure is 0, the horizontal displacement dx of the measuring point of the retaining structure is calculated as Eq. 3. The top of the retaining structure is taken as the origin of the longitudinal axis, and the deformation of the retaining structure to the inside of the foundation pit is positive. As shown in Figure 6, the spline curve is used to draw the deep horizontal displacement curve of the retaining structure. It should be noted that the purpose of this experiment is to explore the influence of the width of the foundation pit on the deformation characteristics and stability of the foundation pit. It does not rely on a practical project, so the follow-up test results are analyzed by the actual monitoring results in the model test.

Figures 6A–C show the deep horizontal displacement curve of the retaining structure under different foundation pit widths, and the step in Figure 6 is the construction step. It can be seen from Figure 6 that the deformation mode of the retaining structure under different foundation pit widths is similar. The retaining structure presents a "cantilever" deformation mode when the inner support is not erected. With the erection of the inner support and the soil excavation in the pit, the deformation mode changes from the "cantilever" when the inner support is not erected after excavation to the "internally convex" composite deformation mode. At the same time, with the excavation of the soil in the pit and the erection of the internal support, the horizontal displacement of the enclosure structure in different test groups increases continuously, and the position of the maximum horizontal displacement continues to move downward. After the final excavation, the maximum horizontal displacement is located at the excavation depth of about 33 cm.

Figure 6D shows a comparison of the deep horizontal displacement of the retaining structures for the different test groups after excavation was completed. With the excavation of the soil and the erection of the internal support, the horizontal displacement of the retaining structures in the different test groups continued to increase, and the location of the maximum horizontal displacement gradually moved downward. After the excavation was completed and stabilized, the maximum horizontal displacements of the retaining structures in groups A, B, and C were 0.82 mm, 1.24 mm, and 1.50 mm, respectively. Compared to Group C, the maximum horizontal displacement of the retaining structure in Group B decreased by 17.3%, while the maximum horizontal

TABLE 3 Experimental groups and condition setting.

Test group (width of foundation pit)	Working condition (Construction step)	Excavation depth (cm)	Specific conditions
Test Group A (16 cm)	Step 1	3	Excavate to the first support
	Step 2	3	Install the first inner support
	Step 3	13	Excavate the first layer of soil
	Step 4	13	Install the second inner support
	Step 5	23	Excavate the second layer of soil
	Step 6	23	Install the third inner support
	Step 7	33	Excavate the third layer of soil
	Step 8	33	Install the fourth inner support
	Step 9	40	Excavate the fourth layer of soil
Test Group B (30 cm)	Step 1~Step 9	Same as test group A	Same as test group A
Test Group C (40 cm)	Step 1~Step 9	Same as test group A	Same as test group A

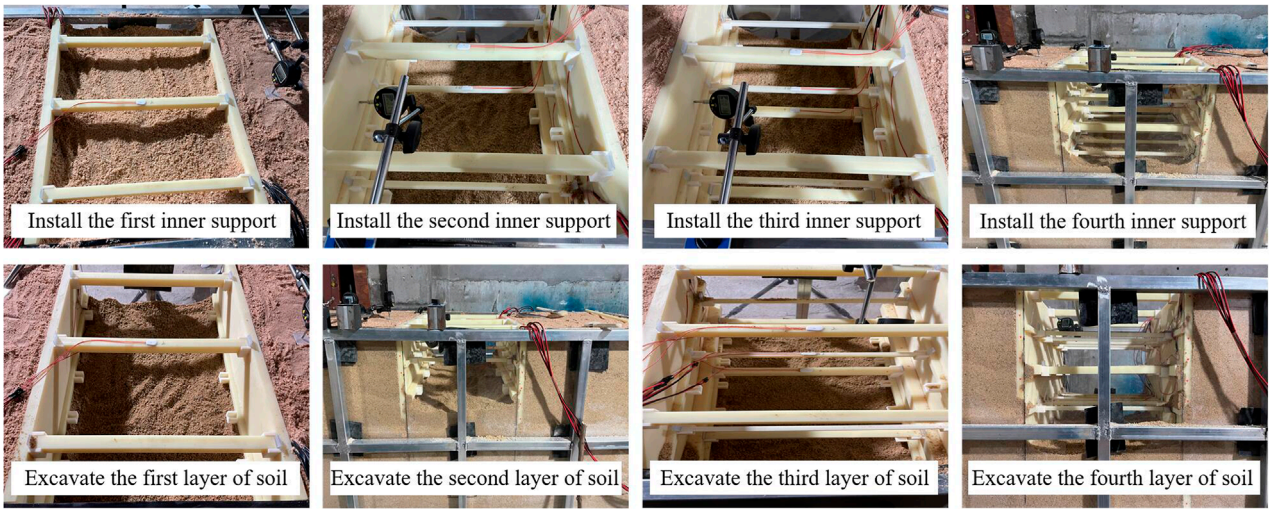

FIGURE 4
Construction step diagram.

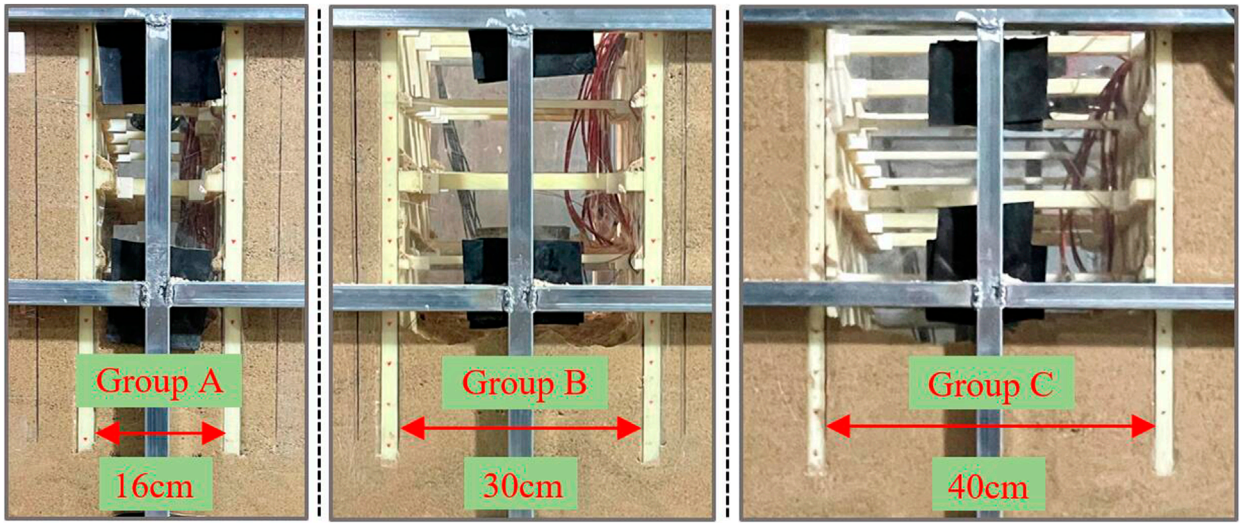

FIGURE 5
Test groups with different foundation pit widths.

displacement in Group A decreased by 45.3%. The narrower the pit width, the smaller the horizontal displacement of the retaining structure, and the impact of the narrower pit width was more significant.

3.2 Bending moment distribution characteristics of the enclosure structure

The curvature radius of the measuring point is calculated according to the strain difference between the inner and outer sides of the measuring point of the retaining structure, and then the bending moment value of the envelope structure under different construction conditions under different experimental groups is calculated. The top of the retaining structure is used as the origin of the ordinate, as shown in Figure 7, and the outer tension of the retaining structure is used as the positive value. The spline curve is used to draw the bending moment distribution curve of the retaining structure.

From Figures 7A–C, it can be observed that as soil is excavated from the pit and internal support is installed, a negative bending moment appears in the retaining structure, and both positive and negative bending moments gradually increase. The retaining structure is subjected to the constraint of both the soil in the pit and the internal support. The force mode of the retaining structure changes from the "cantilevered" mode before installing internal support after excavation to the "concave-convex" composite force mode. This corresponds to the deep horizontal displacement characteristics of the retaining structure discussed in Section 3.1. After the excavation of the third layer of soil (Step 7), the positive bending moment of the enclosure structure reaches the maximum value. The maximum negative bending moment of the enclosure structure appears after the end of the excavation of the pit (Step 9), which is different from the location of the maximum horizontal displacement of the enclosure structure. The maximum negative bending moment all appear near the location of the pit bottom, which is mainly caused by the small deformation of the enclosure structure at the pit bottom under the effect of soil restraint.

Figure 7D shows a comparison of the bending moments of the retaining structures for the different test groups after excavation was completed. As can be seen from the figure, the internal force pattern of the retaining structure was the same for different pit widths. However, after excavation was completed and stabilized, the maximum bending moments of the retaining structures in groups A, B, and C were −6.03 N·m, −7.22 N·m, and −7.96 N·m, respectively. Compared to Group C, the maximum bending moment of the retaining structure in Group B decreased by 9.2%, while the maximum bending moment in Group A decreased by 24.2%. Consistent with the horizontal displacement trend of the retaining structure, the narrower the pit width, the smaller the maximum bending moment of the retaining structure.

3.3 Distribution characteristics of axial force of internal support

Based on the assumptions of linear elasticity and plane section, the strain values (ε_1, ε_2) of the upper and lower measurement points of the internal support are calculated, then the values of the axial force F of the internal support under different construction conditions in different experimental groups can be written as Eq. 4,

$$F = \left(\frac{\varepsilon_1 + \varepsilon_2}{2}\right) EA \tag{4}$$

Where E is the elastic modulus, A is the sectional area of the internal support.

Taking internal support under pressure as positive, the axial force variation curves of the internal support with construction

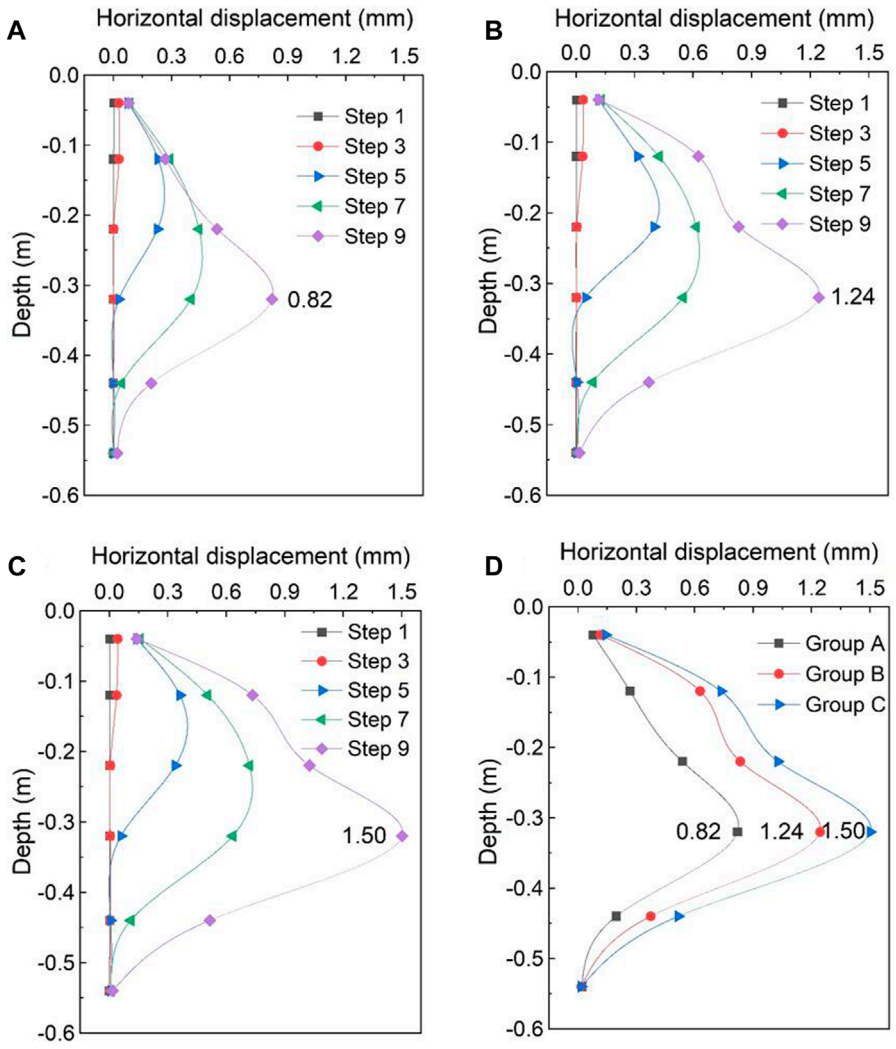

FIGURE 6
Deep horizontal displacement curve of retaining structure: **(A)** Group A. **(B)** Group B. **(C)** Group C. **(D)** Deep horizontal displacement of each group in Step 9.

steps for different experimental groups are drawn in Figures 7A–C. From Figure 8, it can be seen that the inner support axial force change pattern is similar under different pit width conditions. With the construction step, there are certain fluctuations of the first layer of internal support axial force, but the magnitude is generally small. The second layer and the fourth layer of internal support axial force increase slightly with the construction step, and the increment is basically within the range of 5 N. It is worth noting that the third layer of internal support axial force grows more obviously with the construction step, and the increment is up to 44 N. Combined with the deformation of the enclosure structure (section 3.1), the internal support axial force change and the horizontal displacement of the enclosure structure have obvious correlation. The development of the internal support axial force is synchronized with the development of the horizontal displacement of the structure.

Figure 8D shows a comparison of the axial forces in the internal support for the different test groups after excavation was completed. It can be seen from the figure that after excavation was completed and stabilized, the maximum axial forces in the internal support for groups A, B, and C were 61.0 N, 76.7 N, and 84.5 N, respectively, with the maximum axial force occurring in the third layer of support. This corresponds to the location of the maximum horizontal displacement in Section 3.1. Compared to Group C, the maximum axial force in the internal support in Group B decreased by 9.2%, while the maximum axial force in Group A decreased by 27.8%. The narrower the pit width, the smaller the maximum axial force in the internal support, and the impact of the narrower pit width was more significant.

3.4 Surface settlement characteristics around the foundation pit

The displacement readings for each construction step were recorded for the different test groups, and a spline curve was used to plot the ground settlement with the top of the retaining structure as the origin of the horizontal axis and negative values

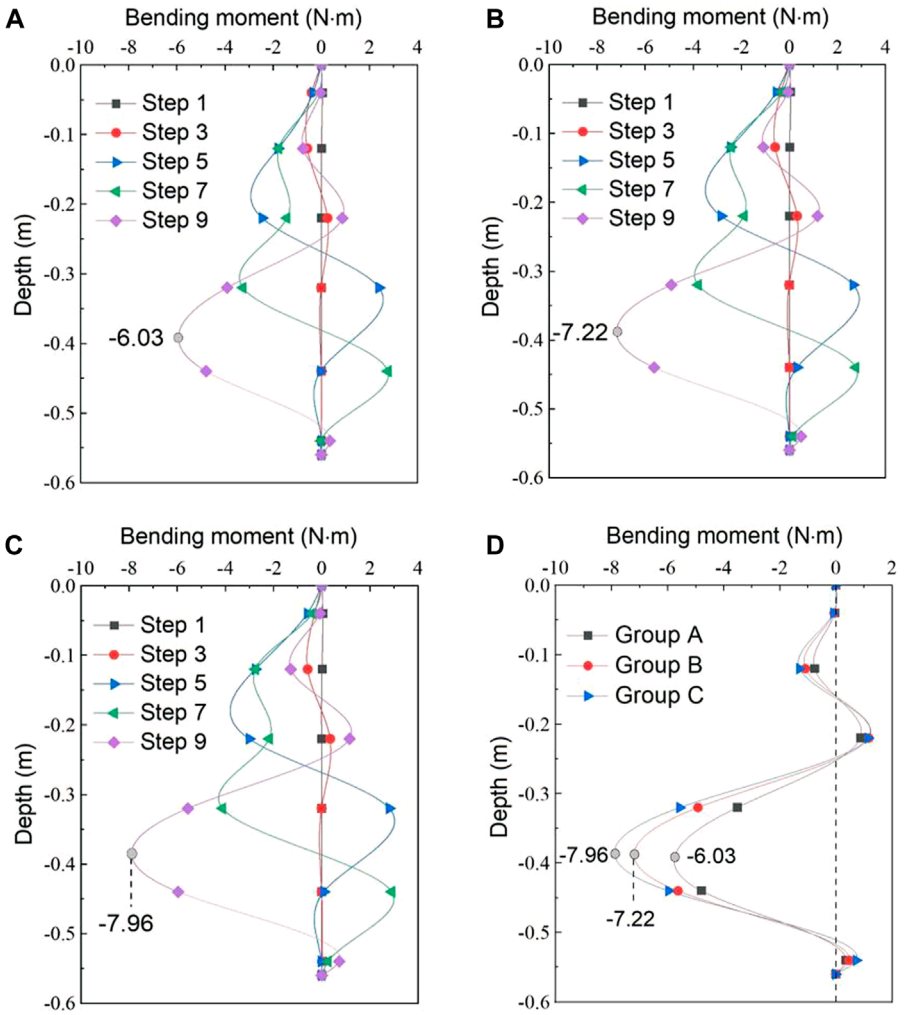

FIGURE 7
Moment curve of retaining structure: **(A)** Group A. **(B)** Group B. **(C)** Group C. **(D)** Bending moment of each retaining structure in Step 9.

indicating settlement. Figures 9A–C show the settlement curves of the ground surface at the back of the retaining structure for different test groups under different construction conditions. For different test groups, the soil behind the enclosure structure showed a "groove-type" settlement pattern, and the maximum settlement point appeared at 14 cm from the outer edge of the enclosure structure. The surface settlement at 40 cm from the edge of the enclosure structure is no longer obvious. In addition, with the soil excavation in the pit, the surface settlement gradually increased. The soil after the enclosure structure in different test groups showed the most significant increase in the settlement after the excavation of the fourth layer of soil.

The maximum surface settlement after the foundation pit excavation in different test groups was counted and plotted as a curve, as shown in Figure 9D. It can be seen from the figure that the smaller the width of the foundation pit, the smaller the surface settlement value at the same measuring point. When the foundation pit is excavated to the bottom of the pit, the maximum surface settlement after the retaining structure of Group A, Group B and Group C is −0.69 mm, −1.09 mm and −1.34 mm, respectively. Compared to Group C, the maximum ground settlement behind the retaining structure in Group B decreased by 18.7%, while in Group A, it decreased by 48.5%. The narrower the pit width, the smaller the maximum ground settlement behind the retaining structure, and the weaker the impact on the surrounding environment, with a more significant impact as the pit width decreased. It is worth noting that the maximum settlement point of each test group occurred near 14 cm away from the outer edge of the retaining structure, and according to the geometric similarity ratio of 1:50, the maximum ground settlement was estimated to occur approximately 7 m away from the pit edge.

3.5 Soil pressure distribution characteristics of the enclosure structure

According to the strain value of the strain-type miniature earth pressure box arranged on the envelope structure, multiplied by the calibration coefficient of each earth pressure box, the earth pressure of the envelope structure under different construction conditions

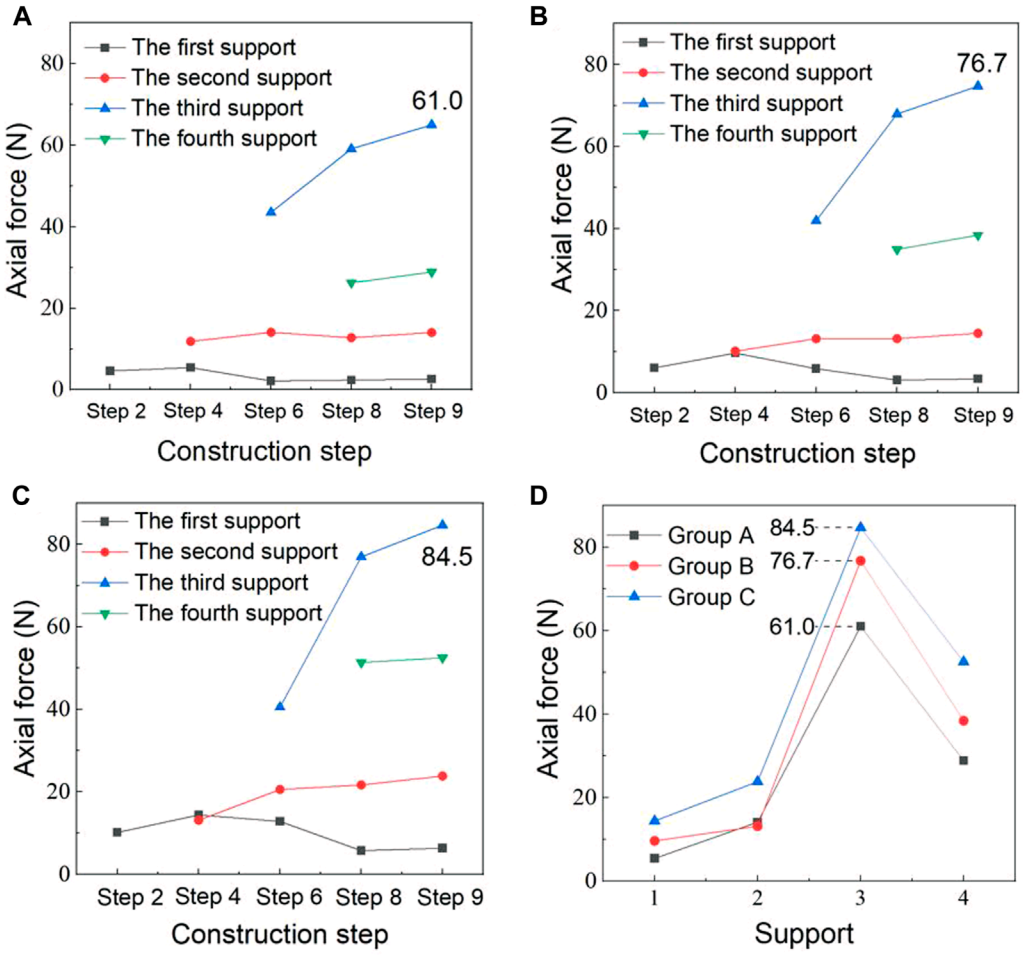

FIGURE 8
Curve of support axial force: **(A)** Group A. **(B)** Group B. **(C)** Group C. **(D)** Supporting axial force in each group in Step 9.

under different test groups is obtained. As shown in Figure 10, the top of the envelope structure is used as the origin of the longitudinal axis spline curve to draw the earth pressure distribution curve outside the envelope structure.

From Figures 10A–C, it can be seen that for the foundation pit with different widths, the change rule of the earth pressure outside the retaining structure with the construction step is the same. When the earth pressure outside the retaining structure is distributed at Step 1, it is basically static earth pressure, which is close to the stable earth pressure after filling. With the excavation, the earth pressure on the outside of the retaining structure decreases. The earth pressure near the top and bottom of the retaining structure (No. 501, 502, 506, and 507 earth pressure boxes) is not significantly reduced, while the earth pressure in the middle of the retaining structure (No. 503, 504, and 505 earth pressure boxes) is significantly reduced. The earth pressure on the outside of the retaining structure at different parts shows a differential growth feature. This is also the same as the characteristics of horizontal displacement and internal support axial force of the retaining structure. The earth pressure boxes from No. 508 to No. 510 do not change regularly due to the influence of manual excavation.

The external earth pressure of the retaining structure outside the completion of foundation pit excavation in different test groups was summarized and plotted as a curve, as shown in Figure 10D. It can be seen from the figure that the soil pressure on the outside of the enclosure structure has the same vertical distribution rule under different foundation pit widths, and the narrower the foundation pit at different depths, the smaller the soil pressure on the outside of the enclosure structure. The maximum values of soil pressure on the outer side of the retaining structure for Groups A, B, and C were 4.14 kPa, 5.17 kPa, and 5.81 kPa, respectively. Compared to Group C, the maximum soil pressure on the outer side of the retaining structure in Group B decreased by 11.0%, while that in Group A decreased by 28.7%. The narrower the pit, the smaller the maximum soil pressure on the outer side of the retaining structure. The soil pressure on the outer side of the retaining structure is the direct cause of the stress on the pit, and the smaller the soil pressure on the outer side of the retaining structure, the smaller the stress and deformation of the pit, the better the stability of the pit, and the smaller the impact on the surrounding environment. Therefore, the smaller soil pressure on the outer side of the retaining structure in narrow pits is the

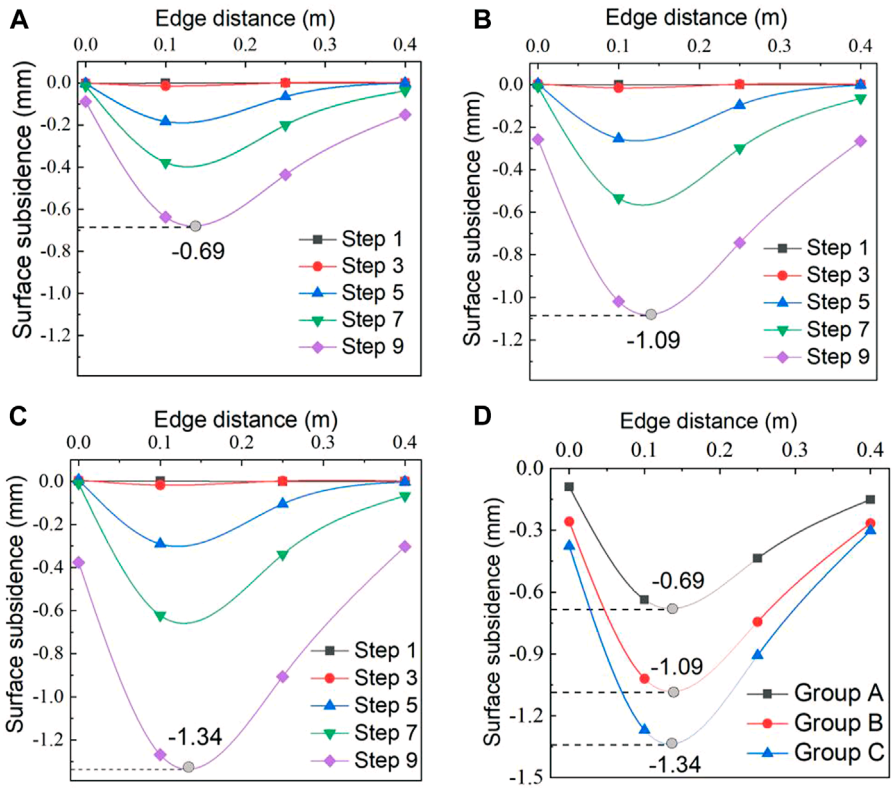

FIGURE 9
Surface settlement curve behind the retaining structure: **(A)** Group A. **(B)** Group B. **(C)** Group C. **(D)** Surface subsidence curves of each group in Step 9.

inherent reason for the better stability of narrow pits compared to wide pits.

4 Discussions

In this paper, through the design of a 1 g constant gravity physical model test, the mechanical response and stability influence law of foundation pit after layer-by-layer excavation under different foundation pit widths are explored. 3D printing technology is used to construct the foundation pit support structure. The setting of fine components, such as internal support buckles, makes excavating the foundation pit layer by layer more feasible. The physical and mechanical properties of printed components can meet this test's needs, proving that 3D printing technology has good application value in the field of foundation pit model tests. It is worth noting that 3D printing is rich in raw materials. In this experiment, ABS materials are uniformly selected as raw materials. Different components, such as concrete support and steel support, can be distinguished in subsequent experiments. Powder metal materials can also be used to print some components to simulate the physical and mechanical properties of different types of components.

The test results further verify that the narrow foundation pit has better stability, and the narrower the foundation pit, the more significant the influence on the stability. The test reveals that the change in the width of the foundation pit has little effect on the mechanical response characteristics of the supporting structure, and the position of the maximum deformation and the maximum internal force has not changed. The influence of the width effect of the foundation pit is directly reflected in the internal force and deformation of the supporting structure and the change in the value of the surface settlement. Taking the test results of Group C as the benchmark, the percentage reduction of the test results of Group A is about three times the percentage reduction of the test results of Group B, and its stability has improved substantially. It should be noted that due to the limited number of test groups, more detailed regularity conclusions and theoretical analysis need to be further explored. Subsequent tests can appropriately increase the test group for support, such as setting different working conditions of equal gradient foundation pit width or width-depth ratio.

5 Conclusion

In this study, an elaborated foundation pit supporting structure is constructed by 3D printing technology, and the scaled model test of foundation pit excavation is carried out. The deformation and stress laws of foundation pit are analyzed with the foundation pit's width as single variable. The main conclusions are as follows:

(1) The width of foundation pit significantly affects the stress, deformation and surface settlement of the supporting

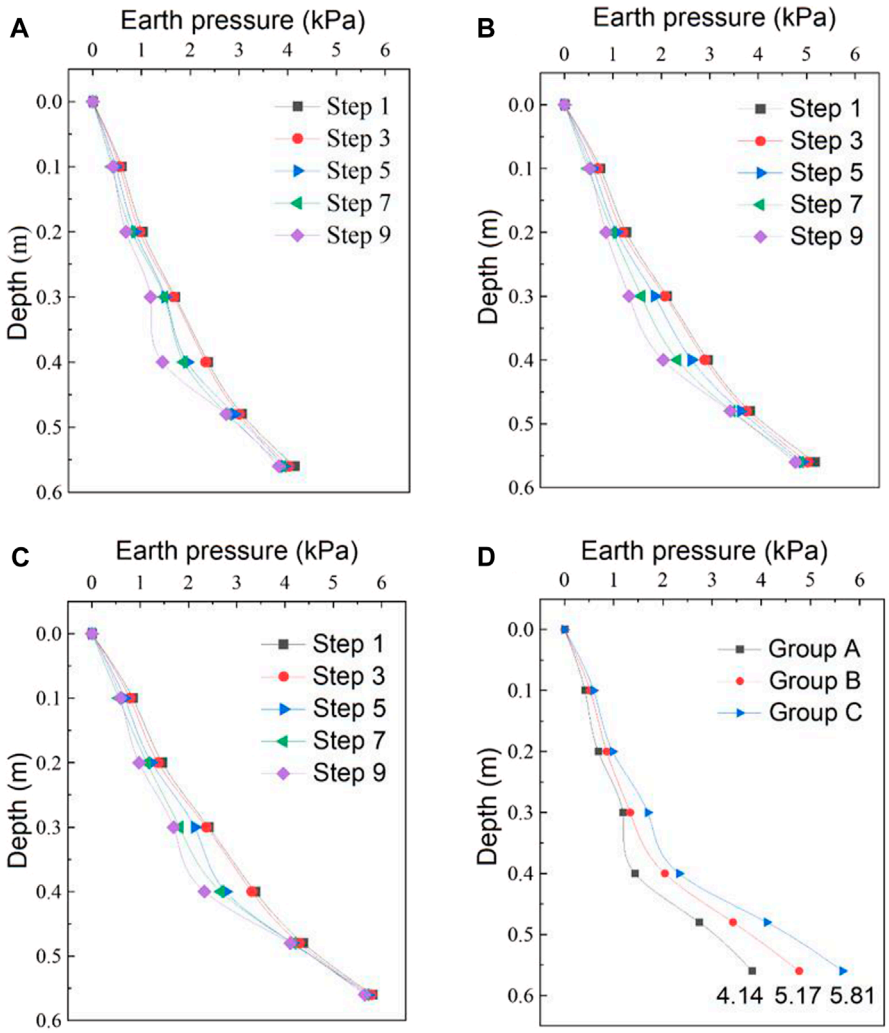

FIGURE 10
Earth pressure curve outside retaining structure: **(A)** Group A. **(B)** Group B. **(C)** Group C. **(D)** Deep soil pressure of each group in Step 9.

structure. Compared with the 40 cm foundation pit width, the maximum horizontal displacement of the retaining structure of the 16 cm and 30 cm foundation pit width is reduced by 17.3% and 45.3% respectively. At the sanme time, the maximum surface settlement is reduced by 18.7% and 48.5% respectively, and the maximum earth pressure outside the retaining structure is reduced by 11.0% and 28.7% respectively.

(2) With the excavation of foundation pit and the erection of internal support, the retaining structure is subjected to the constraint of the soil and the internal support in the pit. The deformation and stress characteristics are gradually converted from the "cantilever" pattern to the "internally convex" or "concave-convex" composite deformation and stress pattern. In addition, the maximum displacement of the retaining structure appears between the third support and the bottom of the pit. And the maximum bending moment appears near the bottom of the pit.

(3) Taking the foundation pit's width as the single variable, the narrower the width of the foundation pit, the lower the earth pressure on the outer side of the retaining structure, which leads to the smaller deformation and stress of the foundation pit. Additionally, the reduction in the passive zone of the pit makes the stability of the foundation pit better, resulting in less surface settlement and impact on surrounding buildings. The inherent reason for the good stability of narrow pits is the small lateral earth pressure on the outside of the support structure.

Data availability statement

The original contributions presented in the study are included in the article/supplementary material, further inquiries can be directed to the corresponding author.

Author contributions

FL: Writing–original draft. XZ: Writing–review and editing. MX: Writing–review and editing. JL: Writing–review and editing. RF: Writing–review and editing. SL: Writing–review and editing.

Funding

The author(s) declare that financial support was received for the research, authorship, and/or publication of this article. This study was supported by the National Natural Science Foundation of China (No. U1934211), the Huaian Science and Technology Plan Project Natural Science Research (Grant No. HAB202365), and Basic Research (Natural Science) Research Project of Jiangsu Province Higher Education Institutions (Grant No. 23KJB560003). The corresponding author gratefully acknowledges their financial support.

Conflict of interest

Authors FL and RF were employed by Jinan Rail Transit Group Co., Ltd.

Author XZ was employed by China Railway 14th Bureau Group Co., Ltd.

The remaining authors declare that the research was conducted in the absence of any commercial or financial relationships that could be construed as a potential conflict of interest.

Publisher's note

All claims expressed in this article are solely those of the authors and do not necessarily represent those of their affiliated organizations, or those of the publisher, the editors and the reviewers. Any product that may be evaluated in this article, or claim that may be made by its manufacturer, is not guaranteed or endorsed by the publisher.

References

Chen, B., Yan, T., Song, D., Luo, R., and Zhang, G. (2021). Experimental investigations on a deep excavation support system with adjustable strut length. *Tunn. Undergr. Space Technol.* 115, 104046. doi:10.1016/j.tust.2021.104046

Chen, S., Cui, J., and Liang, F. (2022). Centrifuge model investigation of interaction between successively constructed foundation pits. *Appl. Sciences-Basel.* 12, 7975. doi:10.3390/app12167975

Cheng, X., Zheng, G., Diao, Y., Huang, T., Deng, C., Nie, D., et al. (2017). Experimental study of the progressive collapse mechanism of excavations retained by cantilever piles. *Can. Geotechnical J.* 54 (4), 574–587. doi:10.1139/cgj-2016-0284

Faheem, H., Cai, F., and Ugai, K. (2004). Three-dimensional base stability of rectangular excavations in soft soils using FEM. *Comput. Geotechnics* 31 (2), 67–74. doi:10.1016/j.compgeo.2004.02.005

Han, J., Wang, J., Yang, W., Wang, X., Ma, R., Wang, W., et al. (2023). Experimental study on the properties of a polymer-modified superfine cementitious composite material for waterproofing and plugging. *Case Stud. Constr. Mater.* 19, e02552. doi:10.1016/j.cscm.2023.e02552

He, C., Lu, Y., and Yang, Y. (2022). Effect of size on the stability of narrow foundation pits. *Adv. Civ. Eng.* 2022, 1–9. doi:10.1155/2022/7391622

He, L., Liu, Y., Bi, S., Wang, L., Broggi, M., and Beer, M. (2020). Estimation of failure probability in braced excavation using Bayesian networks with integrated model updating. *Undergr. Space* 5 (4), 315–323. doi:10.1016/j.undsp.2019.07.001

Hu, Y., Li, Y., Li, B., Li, C., and Xiao, J. (2018). Centrifugal model tests and numerical simulation of three-dimensional space effect of deep and large foundation pit under the confined water level fluctuation. *Rock Soil Mech.* 39 (06), 1999–2007.

Huang, M., Li, H., Yu, J., Zhang, C., and Ni, Y. (2023). On the simplified method for evaluating tunnel response due to overlying foundation pit excavation. *Transp. Geotech.* 42, 101048. doi:10.1016/j.trgeo.2023.101048

Jiang, Q., and Song, L. (2018). Application and prospect of 3D printing technology to physical modeling in rock mechanics. *Chin. J. Rock Mech. Eng.* 37 (01), 23–37.

Li, L., Yang, J., Fu, J., Wang, S., Zhang, C., and Xiang, M. (2022). Experimental investigation on the invert stability of operating railway tunnels with different drainage systems using 3D printing technology. *J. Rock Mech. Geotechnical Eng.* 14 (5), 1470–1485. doi:10.1016/j.jrmge.2021.12.013

Li, L., Yang, J., Wang, L., Gao, C., Jiang, M., and Wang, Z. (2020). Application and research of 3D printing technology in simulation test of invert heaving disease of high-speed railway tunnel. *Chin. J. Rock Mech. Eng.* 39 (07), 1369–1384.

Li, T., Zhao, W., Liu, R., Han, J., Jia, P., and Cheng, C. (2024). Visualized direct shear test of the interface between gravelly sand and concrete pipe. *Can. Geotechnical J.* 61 (2), 361–374. doi:10.1139/cgj-2022-0007

Li, Z., Zhao, G., Deng, X., Zhu, J., and Zhang, Q. (2022). Further development of distinct lattice spring model for stability and collapse analysis of deep foundation pit excavation. *Comput. Geotechnics* 144, 104619. doi:10.1016/j.compgeo.2021.104619

Liu, S. (2022). Study on deformation mechanism of supporting structure and stability for long and narrow deep excavations. Central South University.

Liu, Y., Xia, C., Xu, C., and Chen, X. (2020). Analytical solution and centrifugal test for the optimization of retaining wall insertion depth in narrow foundation pits. *Chin. J. Rock Mech. Eng.* 39 (03), 593–607.

Orazalin, Z., Whittle, A., and Olsen, M. (2015). Three-Dimensional analyses of excavation support system for the stata center basement on the MIT campus. *J. Geotechnical Geoenvironmental Eng.* 141 (7). doi:10.1061/(asce)gt.1943-5606.0001326

Wang, H., and Sun, Y. (2012). Test study and bar system FEM for foundation pits considering excavation width. *Rock Soil Mech.* 33 (09), 2781–2787+2795.

Wang, J., Deng, Y., Ma, R., Liu, X., Guo, Q., Liu, S., et al. (2018). Model test on partial expansion in stratified subsidence during foundation pit dewatering. *J. Hydrology* 557, 489–508. doi:10.1016/j.jhydrol.2017.12.046

Wang, J., Liu, X., Wu, Y., Liu, S., Wu, L., Lou, R., et al. (2017). Field experiment and numerical simulation of coupling non-Darcy flow caused by curtain and pumping well in foundation pit dewatering. *J. Hydrology* 549, 277–293. doi:10.1016/j.jhydrol.2017.03.070

Xu, C., Chen, Q., Wang, Y., Hu, W., and Fang, T. (2016). Dynamic deformation control of retaining structures of a deep excavation. *J. Perform. Constr. Facil.* 30 (4), 04015071. doi:10.1061/(asce)cf.1943-5509.0000819

Xu, Q., Xie, J., Lu, L., Wang, Y., Wu, C., and Meng, Q. (2023). Numerical and theoretical analysis on soil arching effect of prefabricated piles as deep foundation pit supports. *Undergr. Space* 16, 314–330. doi:10.1016/j.undsp.2023.09.011

Ying, H., Wang, X., and Zhang, J. (2018). Analysis on heave-resistant stability considering the effect of excavation width. *Eng. Mech.* 35 (5), 118–124.

Zeng, C., Song, W., Xue, X., Bai, N., and Mei, G. X. (2021). Construction dewatering in a metro station incorporating buttress retaining wall to limit ground settlement: insights from experimental modelling. *Tunn. Undergr. Space Technol.* 116, 104124. doi:10.1016/j.tust.2021.104124

Zeng, C., Zheng, G., Zhou, X., Xue, X. L., and Zhou, H. Z. (2019). Behaviours of wall and soil during pre-excavation dewatering under different foundation pit widths. *Comput. Geotechnics* 115, 103169. doi:10.1016/j.compgeo.2019.103169

Zhang, J., Xie, R., and Zhang, H. (2018). Mechanical response analysis of the buried pipeline due to adjacent foundation pit excavation. *Tunn. Undergr. Space Technol.* 78, 135–145. doi:10.1016/j.tust.2018.04.026

Zhang, S., Yue, Z., Lu, X., Zhang, Q., Sun, T., and Qi, Y. (2023). Model test and numerical simulation of foundation pit constructions using the combined artificial ground freezing method. *Cold Regions Sci. Technol.* 205, 103700. doi:10.1016/j.coldregions.2022.103700

Zhao, J., Tan, Z., Yu, R., Li, Z., Zhang, X., and Zhu, P. (2022). Deformation responses of the foundation pit construction of the urban metro station: a case study in Xiamen. *Tunn. Undergr. Space Technol.* 128, 104662. doi:10.1016/j.tust.2022.104662

Zuo, Z., Gong, J., Huang, Y., Zhan, Y., Gong, M., and Zhang, L. (2019). Experimental research on transition from scale 3D printing to full-size printing in construction. *Constr. Build. Mater.* 208, 350–360. doi:10.1016/j.conbuildmat.2019.02.171

frontiers | Frontiers in Earth Science

TYPE Original Research
PUBLISHED 09 April 2024
DOI 10.3389/feart.2024.1387028

Check for updates

OPEN ACCESS

EDITED BY
Pengjiao Jia,
Soochow University, China

REVIEWED BY
Gong Weiming,
Southeast University, China
Wei Qin,
Wenzhou University, China

*CORRESPONDENCE
Lingjun Huang,
120565165@qq.com

RECEIVED 16 February 2024
ACCEPTED 25 March 2024
PUBLISHED 09 April 2024

CITATION
Huang L, Gao R, Chi J and Yan X (2024), Study on load-bearing behaviors of prestressed post-grouting tubular piles in the karst region of northern Fujian Province, China.
Front. Earth Sci. 12:1387028.
doi: 10.3389/feart.2024.1387028

COPYRIGHT
© 2024 Huang, Gao, Chi and Yan. This is an open-access article distributed under the terms of the Creative Commons Attribution License (CC BY). The use, distribution or reproduction in other forums is permitted, provided the original author(s) and the copyright owner(s) are credited and that the original publication in this journal is cited, in accordance with accepted academic practice. No use, distribution or reproduction is permitted which does not comply with these terms.

Study on load-bearing behaviors of prestressed post-grouting tubular piles in the karst region of northern Fujian Province, China

Lingjun Huang[1]*, Rui Gao[2], Jingou Chi[3] and Xiaocai Yan[4]

[1]Architectural Engineering Institute, Sanming University, Sanming, China, [2]School of Civil Engineering, Wuhan University, Wuhan, China, [3]Fujian Southeast Design Group Co., Ltd., Sanming, China, [4]Fujian Jinding Construction Development Co., Ltd., Sanming, China

The karst that is dominated by medium-weathered limestone and caves with various spatial features is widely distributed in the northern Fujian Province. This paper discusses the load-bearing behaviors of post-grouting tubular piles in karst region of north Fujian Province with reference to the prestressed tubular piles adopted in the residential buildings of Haixi Comprehensive Trade City Phase II Project in Sanming City. The load-settlement curve, pile side friction resistance, and pile end resistance of tubular piles are analyzed by finite element numerical simulations and field static load tests. The load-bearing behaviors of prestressed tubular piles under karst geological conditions with two different spatial features are comparatively investigated, and the effectiveness of tubular pile reinforcement is verified by field settlement observation. The results reveal that the finite element numerical model can effectively simulate the tubular pile-soil interaction. The use of pile end post-grouting of prestressed tubular piles in the karst region can significantly increase their load-bearing capacities. The top settlements of grouted tubular piles under the maximum test load can be reduced by 16.8%–22.3% compared with these of ungrouted test piles, and the theoretical simulated ultimate load-bearing capacity can be increased by 27.3%. The adoption of pile end post-grouting technique can reduce the pile end displacement of tubular piles and improve the proportion of pile end resistance. Plastic-hard plastic breccia silty clay can be used as a bearing stratum for post-grouting to achieve excellent grouting performance. The bead-shaped karst caves are more unfavorable to the exertion of load-bearing capacity of the tubular piles than the karst caves filled with plastic-hard plastic breccia silty clay to which the piles have direct access. The field monitored average settlements of the 19# and 17# buildings under karst geological conditions with two different spatial features are −12.88 mm and −8.98 mm, respectively, both of which do not exceed the warning value, indicating that it is feasible for the project to adopt the pile end post-grouting technique of the tubular piles. The achievements of this study help to further reveal the load-bearing mechanism of this type of pile, which can provide a basis for its engineering design and construction optimization.

KEYWORDS

karst region of northern Fujian Province, prestressed tubular pile, post-grouting, load-bearing behaviors, breccia silty clay

1 Introduction

Tubular piles are widely used in soft ground (containing rockburst stratum (Lianpeng et al., 2018; Lianpeng et al., 2021; Dai et al., 2022; Yishan and Aiwen, 2023)) reinforcement due to their good quality and convenient construction (Jinjin et al., 2023). However, the pile side friction resistances are often under-exerted due to the smooth surface of the pile body. Together with the influence of adverse geological conditions, it is often necessary to reinforce the ground at the pile end by post-grouting to achieve the improvement of load-bearing capacity.

Currently, scholars mainly adopt the combination of theoretical calculations and model tests (Qi et al., 2023) or the field static load tests to study the load-bearing behaviors of tubular piles. Kou et al. (Paik and Salgado, 2004; Li et al., 2019; Xiucheng et al., 2019; Wang et al., 2020; Kou et al., 2020; Shimeng and Xinsheng, 2020; Sheng-Hua et al., 2022; Yan et al., 2022; Bo et al., 2024) studied the load-bearing behaviors of tubular piles under different geological

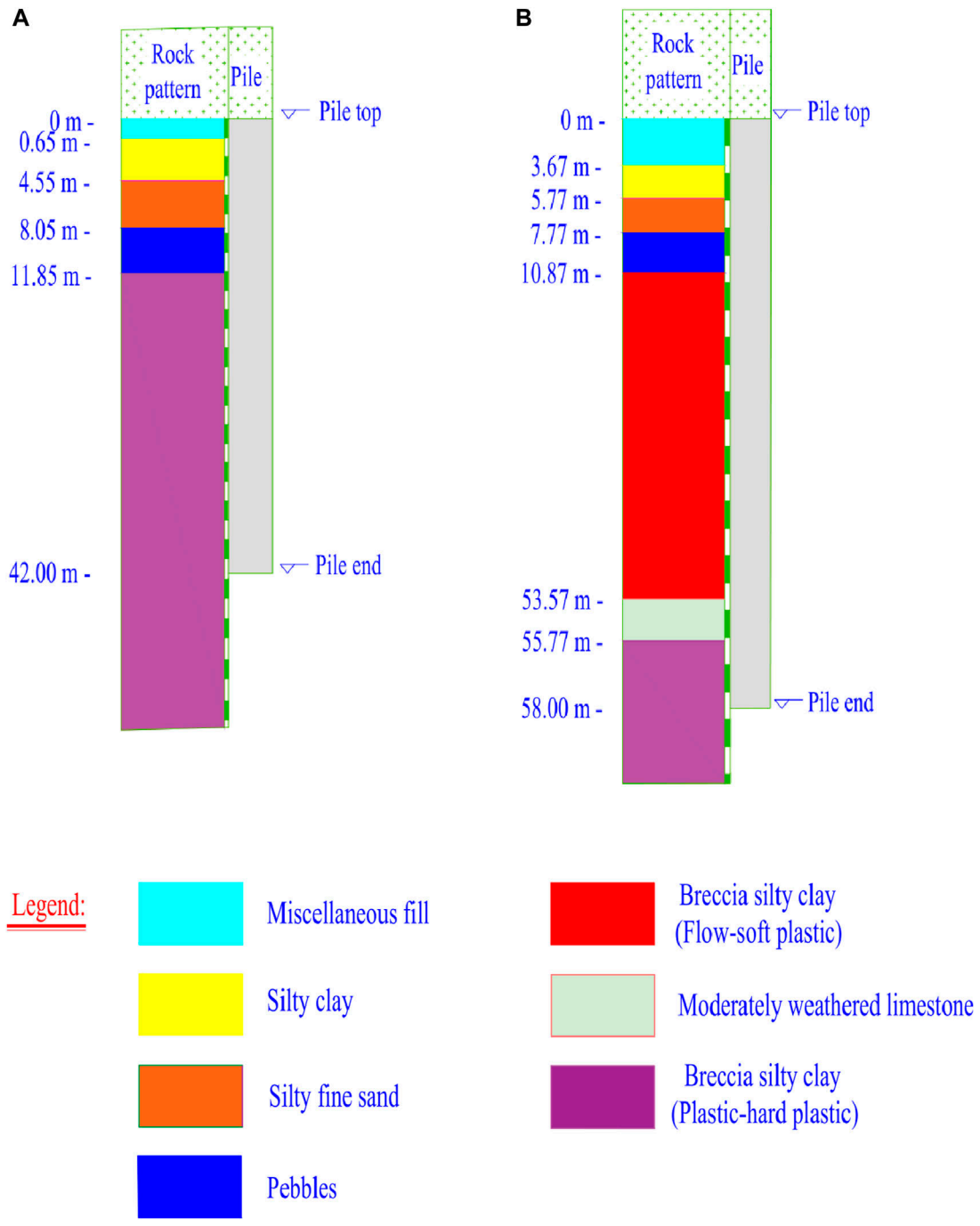

FIGURE 1
Spatial features of typical karst caves at the site. **(A)** Feature 1 **(B)** Feature 2.



FIGURE 2
Picture of displacement gauge installation.

conditions and construction methods, optimized the load-bearing capacity detection means, and proposed the methods for improving the load-bearing capacity of pile foundation. Gong et al. (Wen et al., 2020; Hou et al., 2021; Dai et al., 2023; Gong et al., 2023) carried out a study on the improvement of load-bearing capacity of tubular piles by post-grouting technique, and they analyzed the pile friction resistance and pile-soil relative displacement by changing the post-grouting position and grouting material. Gong et al. (Gong et al., 2023) used end-side joint post-grouting technique to improve the load-bearing capacity of the pile foundation. They pointed out that the post-grouting significantly increased the load-bearing capacity of the pile foundation and reduced the relative displacement required to mobilize the vertical resistance of the test pile. For the floating pile phenomenon caused by rapid pile sinking of precast tubular piles in deep saturated cohesive soil layer, Qiang (Dai et al., 2023) implemented a post-grouting reinforcement programme for prestressed concrete precast tubular piles in the field. The results showed that the post-grouting technique can effectively eliminate the unfavorable effects of floating piles, and the load-bearing capacity of a single pile was greatly improved. Hou et al. (Hou et al., 2021) optimized the proportion of cement mixture with four-factor five-level orthogonal test by using the silicate cement as raw material and water reducer as well as the expansion agent and early strength agent as additives. Accordingly, the effect of physical and mechanical properties of grouting materials on the molecular resistance and load-bearing performance of PHC piles without extruded soil was investigated. Wen et al. (Wen et al., 2020) discussed the relationship between the side friction resistance of grouted steel piles and the pile-soil relative displacement of each soil layer in marine soft clay, and the load-bearing capacity of miniature piles was improved by the post-grouting technique. The above studies on the load-bearing behaviors of different types of tubular piles with and without post-grouting technique have achieved considerable outcomes. However, the pile side friction resistance, pile end resistance, and pile-soil interaction of the widely used prestressed piles under their own characteristics still need to be further analyzed.

Tubular piles are also applicable to the soft ground reinforcement in karst region (Boyang et al., 2023). Wang et al. (Wei et al., 2017; Dong et al., 2018; Huang et al., 2019; Wang et al., 2020) analyzed the influence of different parameters such as span, thickness, pile diameter, and inclination on the load-bearing behaviors of the pile foundation. They revealed the damage mechanism of the karst cave roof and obtained the optimal calculation method of the embedded depth of the pile foundation. Tao et al. (Tao et al., 2017; Ding-Wei et al., 2018; Xiang et al., 2019; Xuefeng, 2019) investigated the effect of pile side or pile end post-grouting technique on the load-bearing capacity of pile foundation in karst region, and made comparative analyses of pile top displacement, pile side friction resistance, and pile end resistance under different loading conditions. They also made specific statements on post-grouting technique to improve the pile load-bearing capacity and to control the settlement. However, the above studies mainly focus on composite foundations reinforced by bored piles and rigid piles, but less on tubular piles. It is worthwhile to explore the similarities and differences in load-bearing behaviors between tubular piles and other types of piles in reinforcing the soft ground in karst regions.

The karst regions in northern Fujian Province are mostly dominated by moderately weathered limestone, and the spatial features of the karst caves are diverse, which can be locally bead-shaped. In this paper, the prestressed tubular piles adopted in the residential buildings of Haixi Comprehensive Trade City Phase II Project in Sanming City are taken as a reference to carry out the research. The tubular piles are located in the karst region, where karst funnels and caves are well-developed, most of the karst caves or soil caves are filled with breccia silty clay, and a few of them are empty caves. The load-settlement curves, pile side friction resistance, and pile end resistance of tubular piles are analyzed by finite element numerical simulations and field static load tests. The load-bearing behaviors of prestressed tubular piles under karst geological conditions with two different spatial features are comparatively investigated, and the effectiveness of tubular pile reinforcement is verified by field settlement observation. Numerical modelling focuses on the tubular pile-soil interaction, pile top settlement, pile end displacements, pile side friction resistance, and pile end resistance, while field static load test emphasizes on the monitoring of pile top settlement. The results demonstrate the effectiveness of the post-grouting technique. The study clarifies the unique load-bearing mechanism of these piles in the karst region of northern Fujian Province, which can provide a basis for their engineering design and construction optimization.

2 Overview of the project

The Haixi Comprehensive Trade City Phase II Project consists of 13 residential buildings and is located to the west of Shaxi River in Sanming City. The original geomorphological unit of the site is alluvial terrace. The original topography is relatively flat, open, and slightly inclined to Shaxi, which is then transformed into the current situation by artificial backfilling due to the construction of the Sanming South Station. The adverse geology of the site is

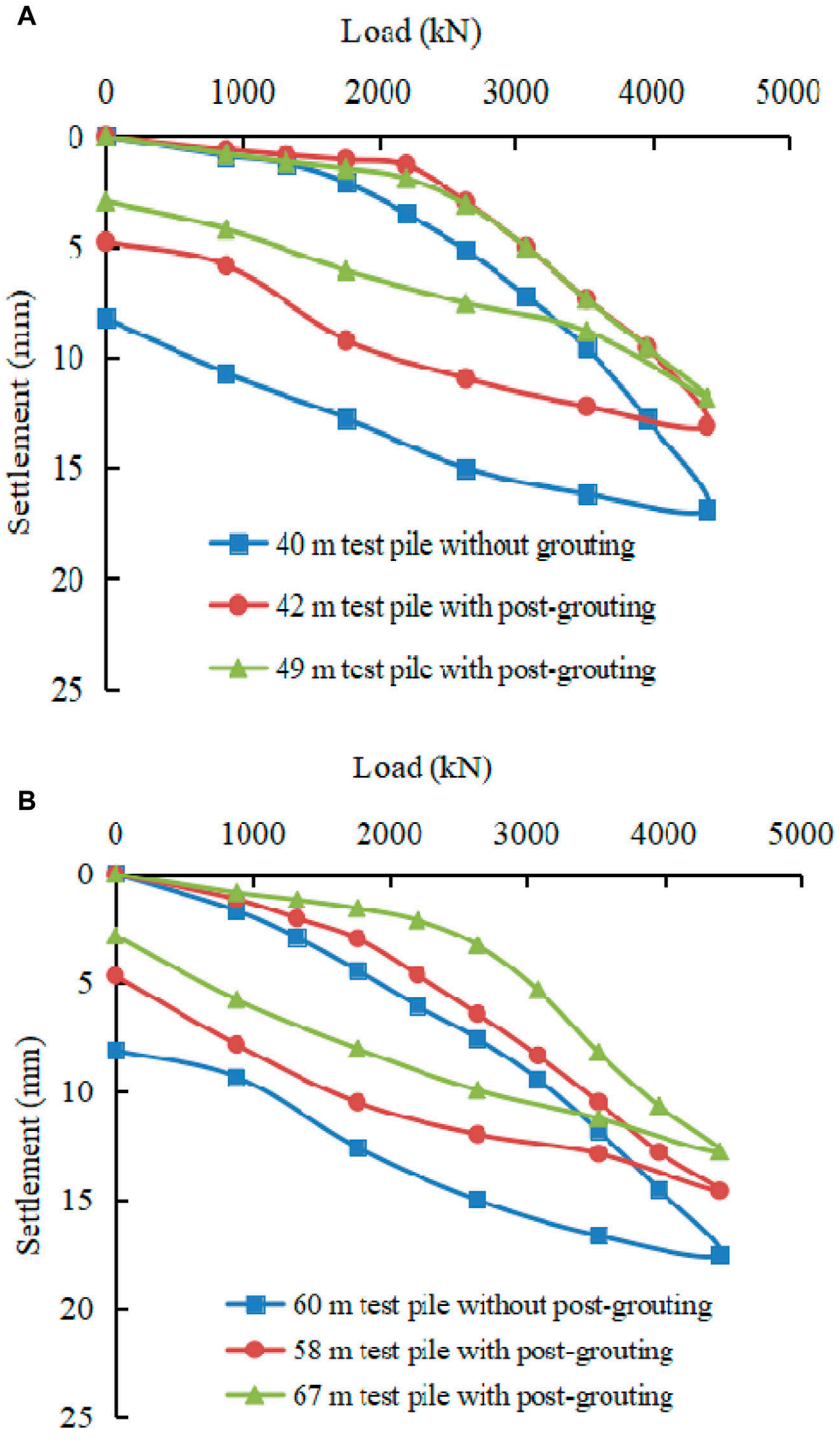

FIGURE 3
Load-settlement curves of the test piles. **(A)** Test pile of #19 building **(B)** Test pile of #17 building.

mainly the basically stable soil holes and karst caves. The borehole drillings reveal that the karst action at the site is relatively strong. The development of soil holes and caves is uneven and irregular, which can be locally bead-shaped, and a few of them are empty caves. The height of the karst or soil caves is 0.90–73.40 m, and the thickness of the karst cave roof is 1.20–8.10 m. The rock mass surface of the roof varies greatly. Karst or soil caves are mainly filled with breccia silty clay (fluid-soft plastic or plastic-hard plastic), and a few of them are empty caves.

The top-to-bottom stratigraphy of the site mainly includes: miscellaneous fill with a layer thickness of 0.40–10.40 m, silty clay with a layer thickness of 0.90–8.20 m, silty fine sand with a layer thickness of 1.60–8.10 m, pebbles with a layer thickness of 0.60–10.90 m, strongly weathered siltstone with a layer thickness

TABLE 1 Results of the static load tests on test piles.

Test pile of #19 building	Maximum settlement (mm)	Unloading rebound (mm)	Test pile of #17 building	Maximum settlement (mm)	Unloading rebound (mm)
19-1# (40 m)	16.87	8.63	17-1# (60 m)	17.49	9.39
19-2# (42 m)	13.10	8.32	17-2# (58 m)	14.56	9.89
19-3# (49 m)	11.82	8.87	17-3# (67 m)	12.76	9.94

of 6.70–39.51 m, a few boreholes exposing cavities, breccia silty clay (flow-soft plastic), breccia silty clay (plastic-hard plastic), and moderately weathered limestone. Prestressed tubular piles are adopted for the reinforcement of the residential buildings. Given the different geological conditions of the site, the pile length ranges from 30 to 75 m, and the pile diameter is 500 mm. The pile bearing stratum is mainly plastic-hard plastic breccia silty clay. A few piles enter directly into moderately weathered limestone, which requires a post-grouting technique to reinforce the strata at the pile end.

Two typical geological features of the project site that require post-grouting reinforcement of pile foundations are as follows. (1) The pile foundations enter directly into the karst caves filled with plastic-hard plastic breccia silty clay. (2) The pile foundations directly enter the karst caves filled with plastic-hard plastic breccia silty clay after passing through the karst caves filled with flow-soft plastic breccia silty clay. The two types of karst caves within the pile length are vertically beads-shaped. The two geological profiles represented by 42-m long pile (19-2#) and 58-m long pile (17-2#) are illustrated in Figure 1.

3 Field static load test of prestressed tubular pile

3.1 Static load test programme

For the two more typical geological features at the project site that require post-grouting to reinforce the pile foundation, the foundation sites of 19# and 17# buildings are typical representatives of the geological Features (1) and (2), respectively. Three prestressed tubular piles are selected as test piles for each building. The lengths of the test piles of #19 building are 40 m (19-1#), 42 m (19-2#), and 49 m (19-3#), respectively, while those of #17 building are 60 m (17-1#), 58 m (17-2#), and 67 m (17-3#), respectively. The design diameters of all test piles are 500 mm, and the pile body is made of C80 concrete. The design load-bearing capacity of the test piles is 2,200 kN, and the maximum test load is 4,400 kN. The staged load is 1/10 of the maximum test load, i.e. 440 kN. The first-stage load is 2 times the staged load, i.e. 880 kN. Each subsequent stage load is increased by 440 kN. The unloading of each stage is taken as two times the staged load, i.e. 880 kN. The test piles are loaded by slow loading method, and the settlement is measured at 5, 15, 30, 45, 60, 90, and 120 min after each stage of load application, and the data at 120 min is taken as the stable measurement of the test. Four displacement gauges are installed symmetrically at the test pile top to measure the pile top settlement under various stages of loading (see Figure 2).

3.2 Post-grouting design

Post-grouting pile reinforcement is carried out at the pile end to improve the load-bearing behaviors of the pile bearing stratum (plastic-hard plastic breccia silty clay).

High-pressure jet grouting is utilized to inject the grout into the end of the PHC pile. The radius and height of jet grouting pile are 1.2 m and 3 m, respectively. High-pressure jet grouting is performed after the piling. Jet grouting reinforcement is performed within 3 m of the pile base by extending a high-pressure jet grouting drill rod in the center of the prestressed tubular pile to the pile base. High-pressure jet grouting adopts double-pipe technique, and the diameter of jet grouting pile is 1,200 mm. Grouting pressure is 20–30 MPa, with a water-to-cement ratio of 1.2. The grade 42.5 Ordinary silicate cement is used, with a dosage of 500 kg/m^3, and the total amount of a single pile is 3t. The 40-m long pile of #19 building (19-1#) and the 60-m long pile of #17 building (17-1#) are set as the reference piles, which are not post-grouted, all pile load tests are completed, post-grouting treatments applied to 17-1# and 19-1# at a later stage.

3.3 Field test results

All the test piles are loaded to 4,400 kN. The load-settlement curves of the test piles are displayed in Figure 3. The results of the static load tests are summarized in Table 1.

Table 1; Figure 3 demonstrate that none of the test piles reach the ultimate state under the 4,400 kN. The difference between the top settlements of the grouted and ungrouted piles is not significant when the load is small, which indicates that the soil in the grouted zone has not yet exerted its load-bearing capacity. The displacement difference gradually increases with the gradual increase of load. Due to large stiffness of the C80 concrete pile body, the ultimate state is not reached under the test load condition. The tubular piles are mainly in a compression-elastic state, and the residual settlement is the sum of the pile end settlement and the plastic deformation of the pile body. The maximum settlement and unloading rebound of test piles from 1# to three# of 17# building are slightly larger than those of test piles with shorter pile lengths of 19# building, indicating that the Feature 2 with bead-shaped karst caves is more unfavorable to the exertion of load-bearing capacity of tubular piles.

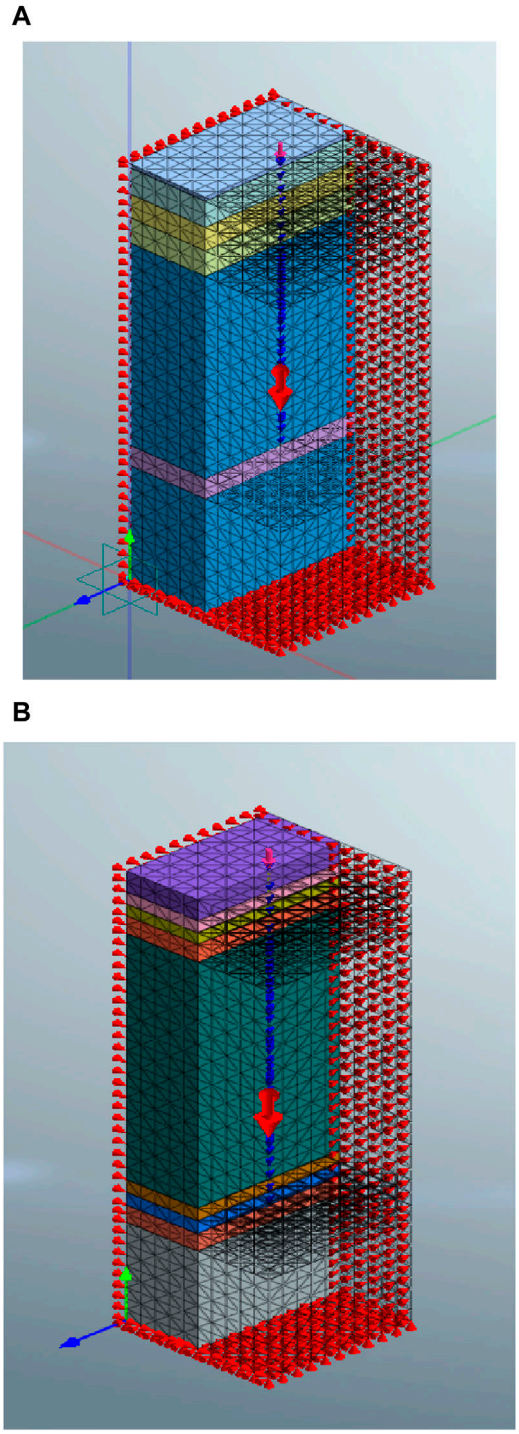

FIGURE 4
Finite element model of the pile foundation. **(A)** Test pile of 19# building **(B)** Test pile of 17# building.

For the three test piles of 19# building, the difference in length between the 19-2# (42 m) test pile with post-grouting and the 19-1# (40 m) test pile without post-grouting is relatively small, while there is a more obvious improvement in the load-bearing performance of the 19-2#, and its maximum pile top settlement is reduced by 22.3% under the 4,400 kN. The load-bearing capacity of the 19-3# test pile (49 m) under the same post-grouting condition is improved to a certain extent due to a 7-m increase in pile length compared with that of the 19-2# test pile (42 m). The maximum pile top settlement under 4,400 kN is reduced by 9.77% compared with that of the 19-2# test pile.

For the three test piles of 17# building, the difference in length between the 17-2# (58 m) test pile with post-grouting and the 17-1# (60 m) test pile without post-grouting is relatively small, while there is also a more obvious improvement in the load-bearing performance of the 17-2#, and its maximum pile top settlement is reduced by 16.8% under the 4,400 kN. The load-bearing capacity of the 17-3# test pile (67 m) under the same post-grouting condition is improved to a certain extent due to a 9-m increase in pile length compared with that of the 17-2# test pile (58 m), and the maximum pile top settlement under the 4,400 kN is reduced by 12.36% compared with that of the 17-2# test pile.

TABLE 2 Parameters of the piles.

Material model	Weight/(kN/m^3)	Elastic modulus (MPa)	Poisson's ratio
Linear elasticity	24	38,000	0.2

4 Numerical simulation

4.1 Model establishment

Figure 4 presents the finite element model of the pile foundation. The soil and grouted reinforcement bodies are simulated with an elasto-plastic constitutive model that obeys the Mohr-Coulomb yield criterion. Considering the influence of the soil layer around the pile and at the pile end, the horizontal range of the soil layer is taken to be not less than 10 times the diameter of the pile (taken as 20 m) in *X* and *Y* directions and about 1.5 times the length of the pile in the vertical direction. The pile body is modelled by a beam unit linear elastic model to capture the actual force characteristics. The pile-soil interface is modelled by a friction contact unit that is unique in the finite element software. The pile end is modelled by a spring unit to simulate the support. The soil body, grouted reinforcement body, and piles are automatically meshed, the size of the soil body and grouted reinforcement body does not exceed 1.7 m, while the pile beam unit is achieved through the connection of corresponding nodes in the soil body. *Rz* constraints are set at the boundaries of the pile elements, while normal boundaries are set around the soil elements, with fixed boundaries at the bottom and free boundaries at the surface.

4.2 Determination of numerical parameters

The diameters of the numerical test piles are all 500 mm, and the pile lengths are the same as the actual lengths of the test piles of the 19# and 17# buildings. The pile parameters are listed in Table 2.

TABLE 3 Calculation parameters of soil and grouting reinforcement bodies.

Soil layer	Weight (kN/m^3)	Elastic modulus (MPa)	Cohesion (kPa)	International friction angle (°)	Poisson's ratio
Miscellaneous fill	18	20	8	15	0.18
Silty clay	18.2	50	30	15	0.30
Silty fine sand	17.5	40	4	30	0.31
Pebbles	21	150	3	42	0.32
Flow-soft plastic breccia silty clay	18	40	18	10	0.22
Moderately weathered limestone	22.5	300	—	—	0.22
Plastic-hard plastic breccia silty clay	18.5	60	25	16	0.35
Grouting reinforcement body	20.5	150	90	39	0.28

The grouting process at the base of high-pressure jet grouting piles involves reinforcing the pile end area with a radius of 1.2 m and a height of 3 m. Grout is injected into the surrounding soil under high pressure, solidifying the sediment at the bottom of the pile and altering soil parameters to enhance the ultimate load-bearing capacity. Both soil and grouting reinforcement adhere to Mohr-Coulomb yield criterion, with calculation parameters derived from geological prospecting data and laboratory tests (Table 3). Due to close proximity between pile foundations on-site (average center distance approximately 1.6 m), a numerical simulation model considers soil layers within 3 m depth as part of the grouting reinforcement model. The bearing characteristics of the test pile are analyzed through numerical simulation, disregarding any variations in pile bearing capacity during the grouting process.

The shear and normal stiffness moduli of the pile-soil contact surface at the pile side in the numerical simulation are 100 MPa and 300 GkN/m^3, respectively. Considering the insufficient exertion of side friction resistance of the prestressed tubular piles, and combining with the standard value of side friction resistance in each soil layer provided by the geological investigation data (about 30% less than the standard value of pile side friction resistance in the same condition of grouted piles), the final shear stress is taken as 35 kPa for miscellaneous fill, silty clay, and silty fine sand, 80 kPa for pebbles, 30 kPa for flow-soft plastic breccia silty clay, 50 kPa for plastic-hard plastic breccia silty clay, and 180 kPa for moderately weathered limestone in the numerical simulation. The stiffness of the spring element at the pile bottom can be determined using the estimated pile tip reaction and the pile tip settlement ratio. The estimated pile tip reaction for ungrouted piles is 1500kN, while for grouted piles it is 2200 kN. The pile tip settlement value can be calculated by subtracting the unloading rebound from the maximum settlement of the pile in Table 1.

4.3 Analysis of numerical simulation results

Concentrated forces are applied to the piles in the numerical simulations. Non-linear control is employed in the analyses, and the loads are accumulated according to the actual load increments. Theoretical numerical calculations are performed for six test piles of 19# and 17# buildings, and the results are as follows.

4.3.1 Analysis of load-settlement curves

The numerical and monitored load-settlement curves at the pile top and at the pile end of the test piles are illustrated in Figure 5, where the test pile in the numerical model are loaded to the ultimate load. The load at which a sudden steep drop in the settlement occurs for the same load increment is considered the ultimate load point. Taking the ungrouted 19-1# and grouted 19-2# test piles as an example, the settlement nephograms of the tubular piles under 4,400 kN are displayed in Figure 6.

Figure 5 demonstrates that the load-settlement curves at the pile top obtained from the numerical simulation are in good agreement with those measured in the field, indicating that the calculation parameters of the pile body, soil body, and grouting reinforcement body adopted in the numerical simulation are reliable. However, the numerical values are slightly larger than the measured values (expect for the measured value of 17–2# test pile), which is mainly due to the simulation deviation of the software and the disagreement between the actual geology and the geological investigation data. As indicated in Figure 7, the pile top settlements of 19–1# and 19-2# test piles under the 4,400 kN are 18.9 mm and 13.2 mm, respectively, which are slightly larger than the measured values of 16.87 mm and 13.1 mm of the corresponding test piles in Table 1.

The actual loads applied to the test piles of 19# and 17# buildings are not up to the ultimate value, so there is not an obvious inflection point in the load-settlement curve at the pile top. The load-settlement curves at the pile top in the numerical simulation are subjected to the ultimate load, and the ungrouted

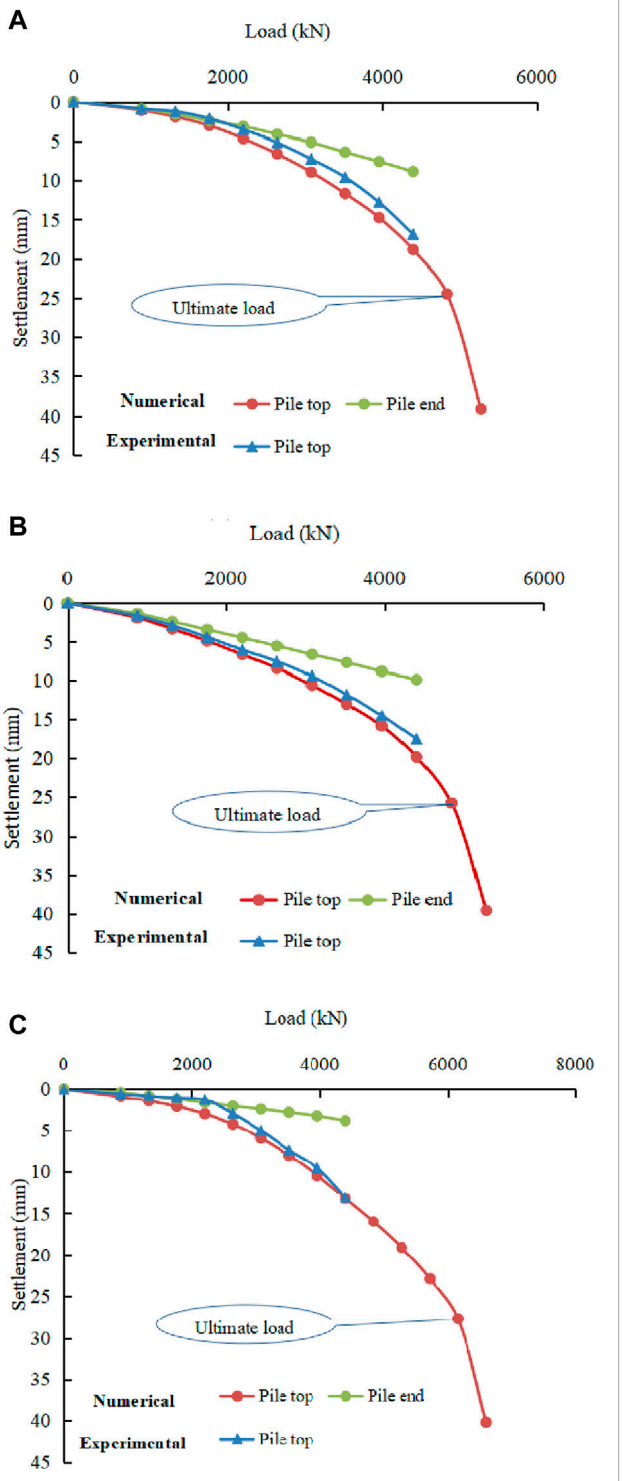

FIGURE 5
(Continued).

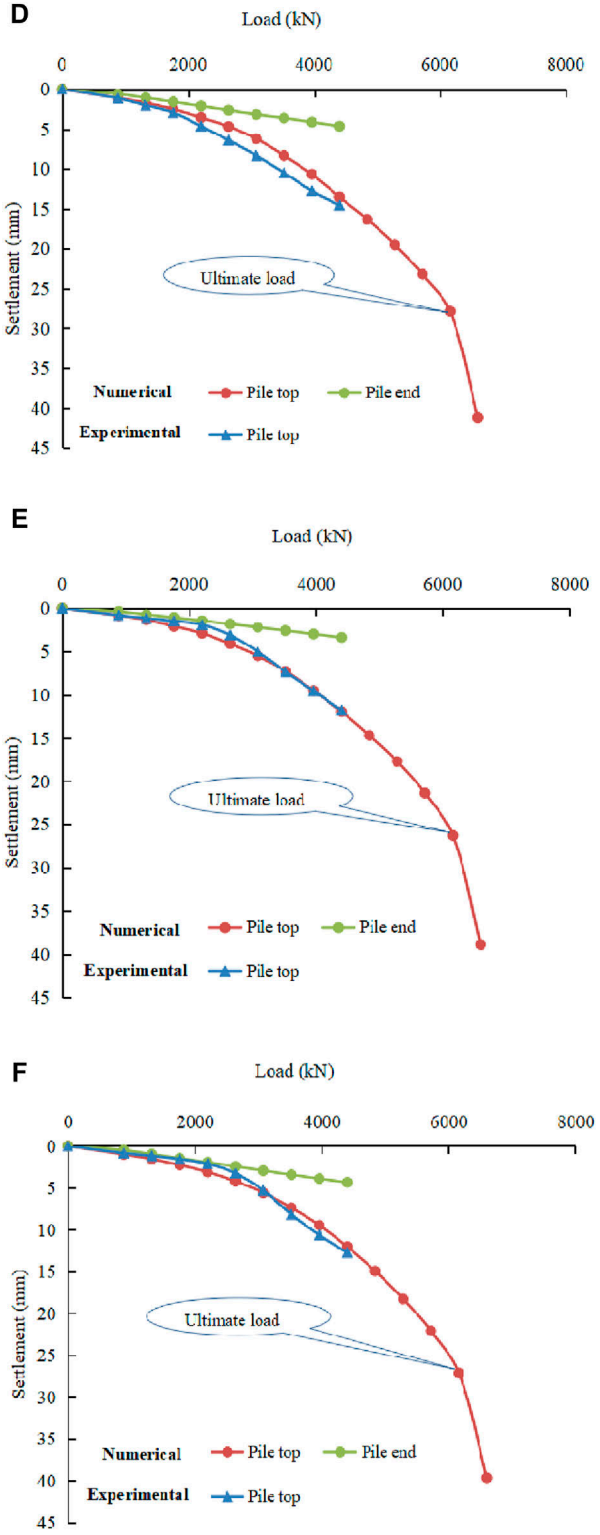

FIGURE 5
(Continued). Load-settlement curves of the test piles at the pile top and end. **(A)** 19-1# test pile **(B)** 17-1# test pile **(C)** 19-2# test pile **(D)** 17-2# test pile **(E)** 19-3# test pile **(F)** 17-3# test pile.

19-1# and 17-1# test piles yield an inflection point under the 4,840 kN, which can be taken as the theoretical ultimate load. The inflection points of 19–2#, 19-3#, 17-2# and 17-3# test piles with post-grouting appear only under the 6,160 kN, and their theoretical ultimate load-bearing capacities increases by 27.3% compared with those of the ungrouted test piles, which indicates that post-grouting at the pile end yield an obvious improvement of the load-bearing capacity of tubular piles. The increase in pile length of the 19-3# and 17-3# test piles compared with

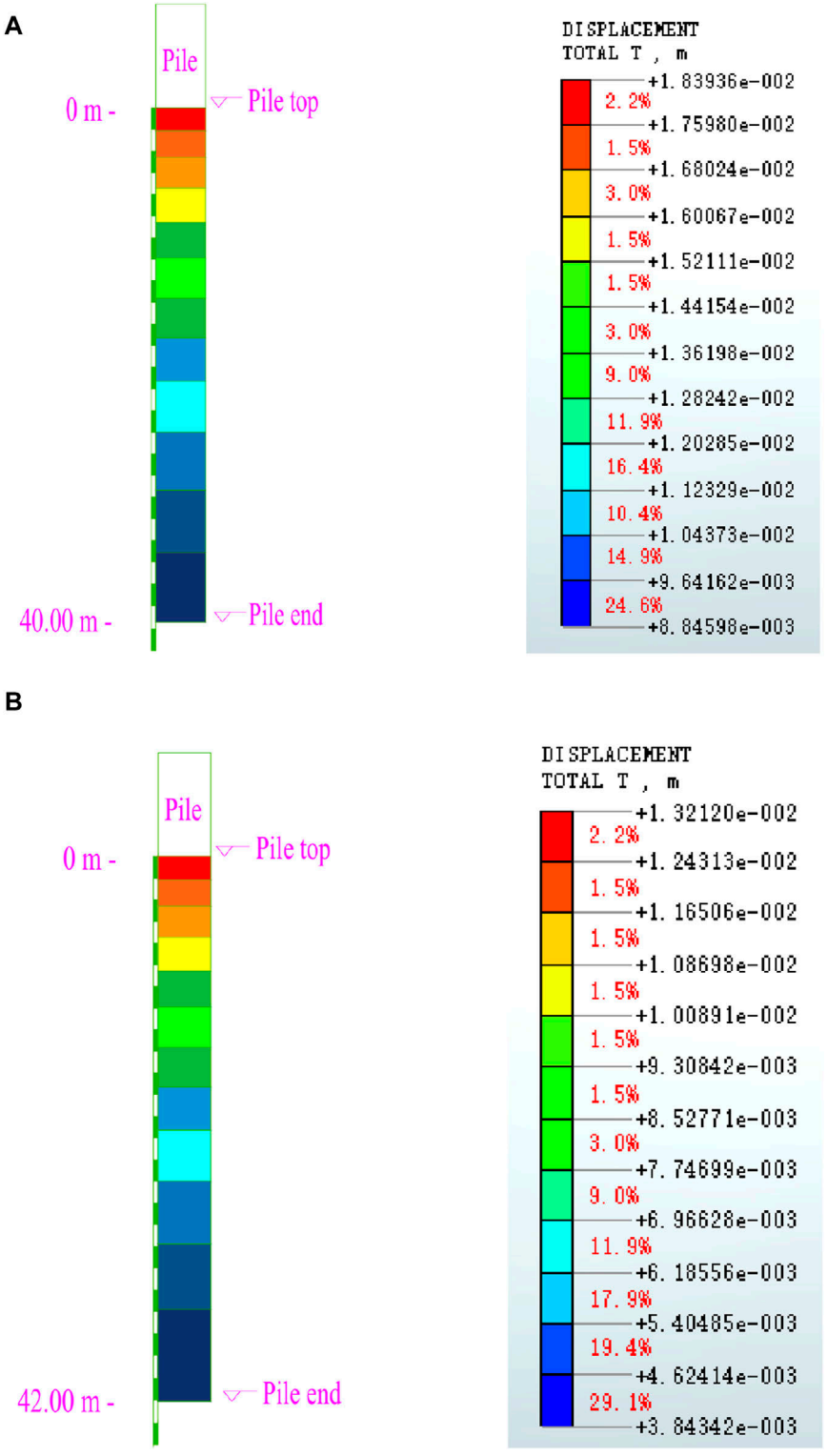

FIGURE 6
Settlement nephograms of the test pile under the 4,400 kN. **(A)** 19-1# test pile **(B)** 19-2# test pile.

the 19-2# and 17-2# test piles has improved their load-bearing capacities to some extent, and the calculated displacements at the pile top under the theoretical ultimate load of the 6,160 kN are slightly smaller.

When the load is small, the calculated pile end displacement and pile top settlement are close to each other, which indicates that the compression of the tubular piles is small due to their large stiffness, and that it is mainly manifested as the

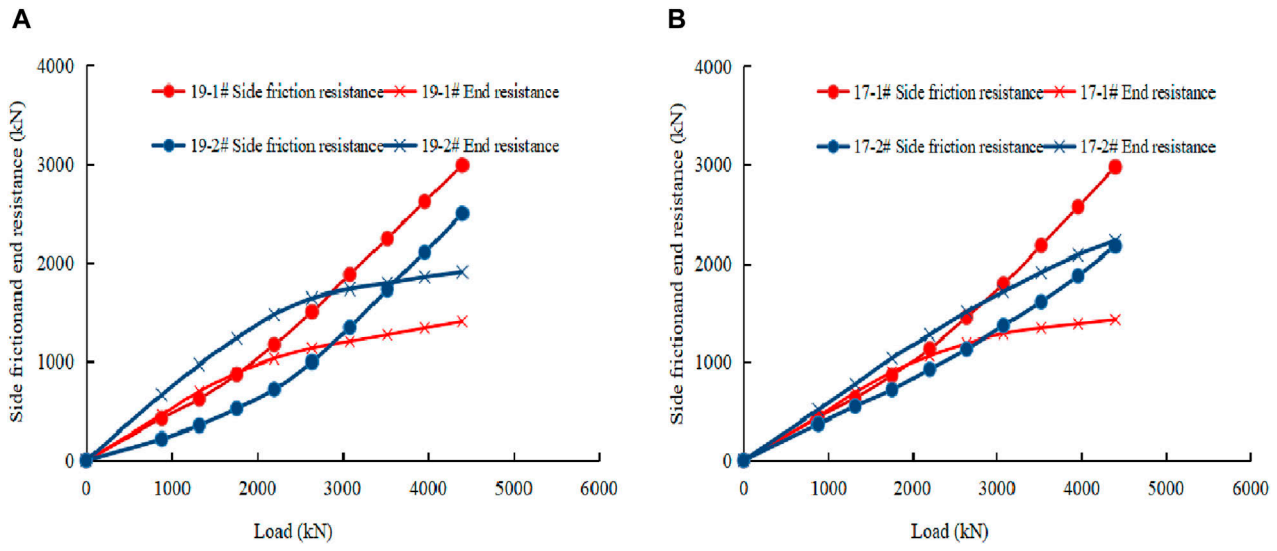

FIGURE 7
Curves of the calculated pile side friction resistance and the pile end resistance. **(A)** Test pile of 19# building **(B)** Test pile of 17# building.

TABLE 4 Test results of the pile end resistance.

Test piles	Test load (kN)	Pile end resistance (kN)	Pile side friction resistance (kN)	Proportion of pile end resistance (%)	Proportion of pile side friction resistance (%)
19-1#(40 m)	4,400	1,408.5	2,991.5	32.01	67.99
19-2#(42 m)	4,400	1904.2	2,495.8	43.28	56.72
19-3#(49 m)	4,400	1811.5	2,588.5	41.17	58.83
17-1#(60 m)	4,400	1,426.3	2,973.7	32.42	67.58
17-2#(58 m)	4,400	2,227.8	2,172.2	50.63	49.37
17-3#(67 m)	4,400	2056.1	2,343.9	46.73	53.27

overall sinking of the pile. With the increase of load, the difference of the calculated pile end displacement and pile top settlement is also accelerated, indicating that the pile side friction resistance works.

The calculated pile end displacements of grouted 19-2# and 17-2# test piles under the 4,400 kN (3.84 mm and 4.64 mm) are reduced by 56.6% and 53.4% compared with those of ungrouted 19-1# and 17-1# test piles (8.85 mm and 9.87 mm), respectively. The calculated pile end displacements of 19–3# and 17-3# test piles (3.37 mm and 4.36 mm) are reduced by 61.9% and 55.8% compared with those of 19–1# and 17-1# test piles, respectively. This confirms that the application of post-grouting technique to the plastic-hard plastic breccia silty clay can significantly reduce the pile end displacement and thus improve the load-bearing capacity of the tubular piles. The calculated pile end displacements of 19–1# and 19-2# test piles are presented Figure 6.

4.3.2 Analysis of pile end resistance and stress distribution at the pile end

The calculated pile end resistances of the test piles under the loaded conditions are illustrated in Table 4; Figure 7, where the side friction resistance is obtained by subtracting the calculated pile end resistance from the pile top load. When the load is small, the pile end resistance is larger than the pile side friction resistance. Due to the larger stiffness, the compression of the pile itself is small and the pile end resistance accounts for a larger proportion. With the increase of load, the pile side friction resistance gradually works. Due to the accelerated growth rate, a concave growth curve is observed in the figure, while the corresponding increase in pile tip resistance gradually decelerates, so a concave growth curve is observed in the figure. Compared with the ungrouted 19-1# and 17-1# test piles, the proportions of pile end resistance of grouted 19-2# and 17-2# test piles are always larger. As revealed in Table 4, the use of post-grouting technique at pile end for test piles can increase the pile

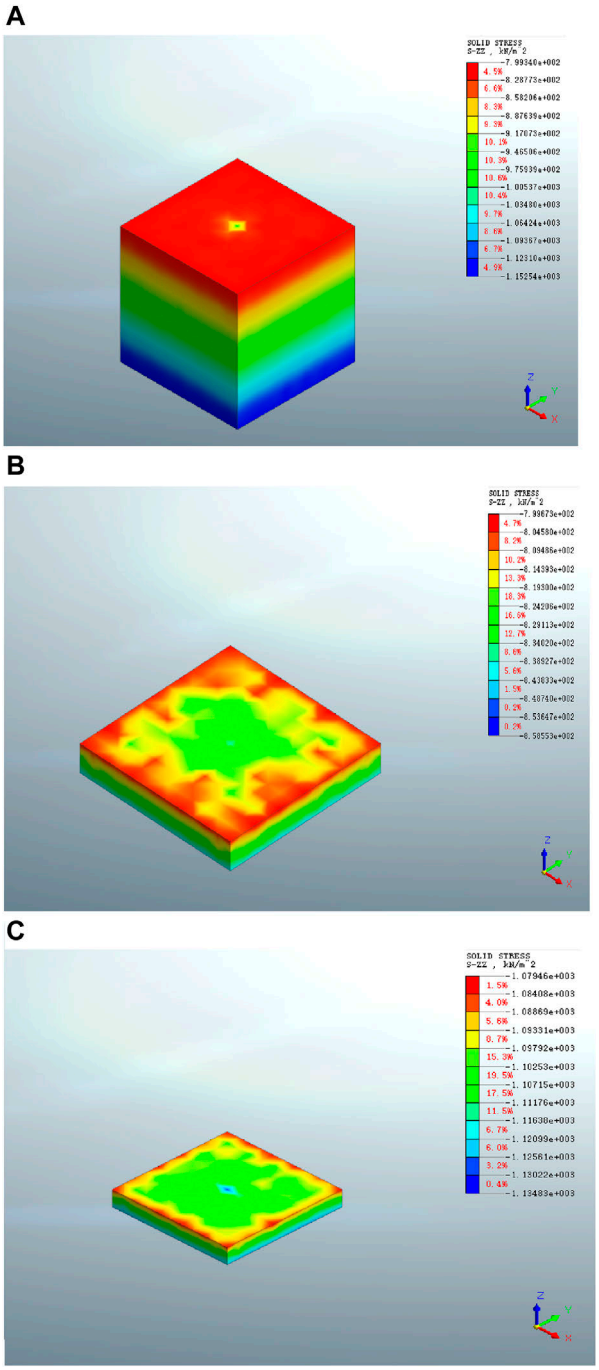

FIGURE 8
The vertical stress nephograms of the soil in the bearing stratum under the 4,400 kN. **(A)** 19-1# test pile **(B)** 19-2# test pile **(C)** 17-2# test pile.

end load-bearing capacity more significantly. Compared with the ungrouted 19-1# and 17-1# test piles, the proportions of pile end resistance of grouted 19-2# and 17-2# test piles are increased by 11.27% and 18.21%, respectively. Post-grouting with plastic-hard plastic breccia silty clay as the bearing stratum can yield excellent grouting effect.

Taking the ungrouted 19-1# and grouted 19-2# test piles and 17-2# test pile as an example, the vertical stress nephograms of the soil in the pile end bearing stratum under the 4,400 kN is presented in Figure 8. It is observed that compared with the ungrouted 19-1# test pile, the vertical stress within the 3-m high grouting bearing stratum zone at the end of grouted 19-2# test pile is larger, and the area with the vertical stress varying from −809 to −834 kn/m^2 accounts for a larger proportion. The vertical stresses within the 3-m high grouting zone at the end of 19–1# test pile are mainly concentrated in the range varying from −799 to −828 kN/m^2 (red color). The vertical stresses within the 3-m high grouting zone at the end of 17–2# test pile with grouting are mainly distributed in the range varying −1,070 from −1,100 kN/m^2. The vertical stress in the bearing stratum of 17–2# test pile is larger than that of 19–2# test pile, which is compatible with the calculation results in Table 4. This is mainly due to the fact that the bead-shaped karst caves are more unfavorable for the side friction resistance of the tubular piles to be exerted, so the pile end resistance is larger.

4.3.3 Analysis of pile side friction resistance

Calculated pile side friction resistance with depth of test piles under the 4,400 kN is illustrated in Figure 9 (load is calculated in three levels in each figure), where the depth of 0–8 m is mainly miscellaneous fill, silty clay, and silty fine sand. For 19-1# and 2# test piles, the depth below 12 m is mainly the bearing stratum of plastic-hard plastic breccia silty clay. For 17-1# and 2# test piles, the depth of 12–54 m is flow-soft plastic breccia silty clay, the depth of 54–57 m is moderately weathered limestone, and the depth below 57 m is the bearing stratum of plastic-hard plastic breccia silty clay.

It is observed that as the load applied to the pile top increases, the side friction resistance of the upper soil layer around the pile body is more fully utilized and gradually approaches the final shear stress set at the contact surface. However, the increase in the side friction resistance gradually decreases, while the lower soil layer has a lower exertion rate of side friction resistance than the upper layer. With the increase of load, the side friction resistance can approach the final shear stress set at the contact surface. However, the greater the depth, the greater the deviation of the side friction resistance from the final shear stress. As depicted in the figure, the curve exhibits a sudden change at the location of pebble layer and weathered limestone due to a significant increase in their final shear value compared to that of adjacent soil layers. The upper soil layers around the pile body fail to reach the final specified shear stresses (30 kPa for miscellaneous fill, silty clay, and silty fine sand while 80 kPa for pebbles), indicating that the use of post-grouting at the pile end does not improve the pile side friction resistance. Under the same loading, the side friction resistances of grouted 19-2# and 17-2# test piles decrease significantly compared with those of ungrouted 19-1# and 17-1# test piles, which indicates that the load-bearing capacity at the pile end in the bearing stratum after grouting works progressively during the loading process. The presence of a long segment of flow-soft plastic breccia silty clay (final shear stress is only 30 kPa) in the strata crossed by the 17-1# and 17-2# test piles is the cause for the bead-shaped karst caves restricting the exertion of side friction resistance of the tubular piles.

5 Effectiveness and verification

Pile settlement monitoring is conducted using a precision digital level to investigate the effectiveness of pile end post-grouting

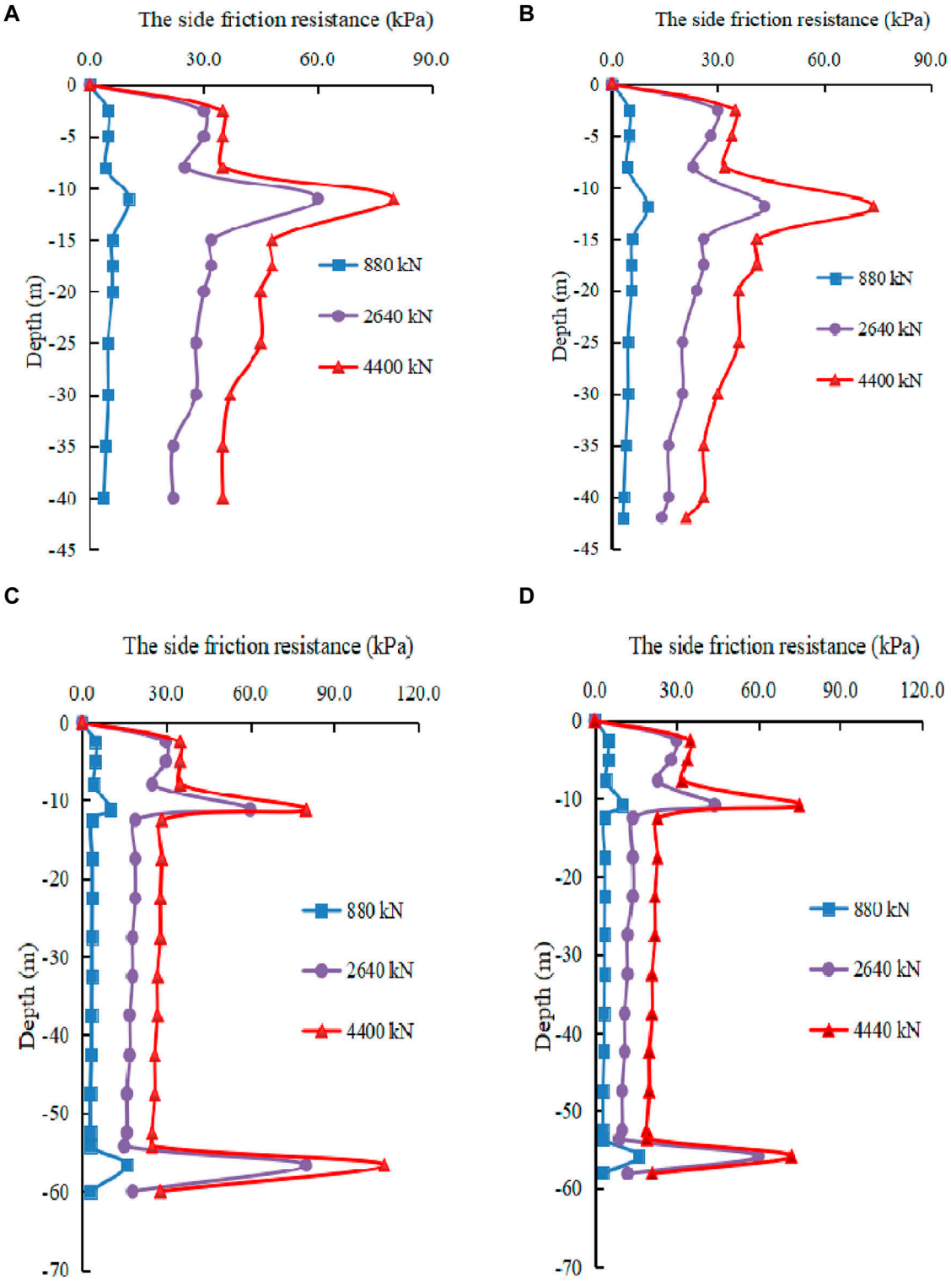

FIGURE 9
Variation of pile side friction resistance with the depth. **(A)** 19-1# test pile **(B)** 19-2# test pile **(C)** 17-1# test pile **(D)** 17-2# test pile.

technique for the tubular piles. The measurement frequency is one observation every 15 days (adjusted according to the construction progress) during the construction period, one observation every 1 month to 3 months after the completion of the overall structural construction, and one observation every 3 months to 6 months after the building is completed and stabilized. The final observation duration is 2 years. Combined with the actual situation of the site, six observation points are equipped in both 19# and 17# buildings.

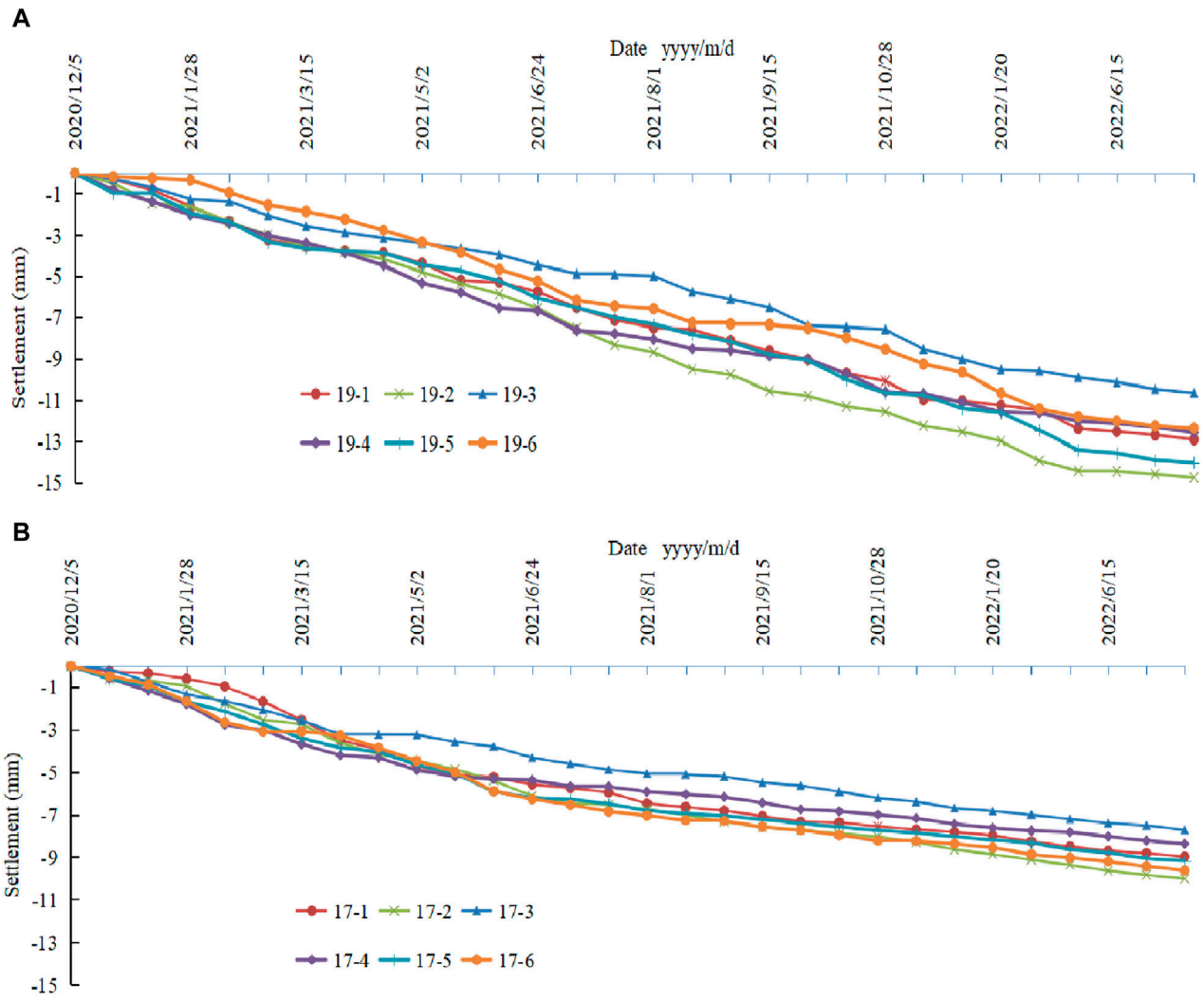

FIGURE 10
Measured settlement curves. **(A)** 19# building **(B)** 17# building.

Settlement observation points are installed by on-site drilling and embedding special settlement nails, which are labelled as 17-1-17–6 and 19-1-19–6, respectively.

The monitored settlement curves of the 19# and 17# buildings are illustrated in Figure 10. It is demonstrated that the buildings do not experience obvious deformation throughout the construction stage and after the completion of construction, and the displacement gradually tends to stabilize. The maximum cumulative settlement of the 19# building is −14.75 mm, with an average settlement of −12.88 mm. The maximum cumulative settlement of the 17# building is −10.01 mm, with an average settlement of −8.98 mm. The cumulative settlement warning value is −20 mm, and there is no abnormality in the settlement observation. The incremental settlement value of each measurement is less than 1 mm, the settlement rate continues to decrease and gradually tends to zero. The settlement of the buildings is within the safe limits.

The above findings indicate that the post-grouting technique adopted in the project significantly reduces the pile end displacement and suppresses the pile top settlement. The post-grouting technique at the end of tubular piles can control the settlement of the building for a long time, thus avoiding abnormal settlement of the building. The settlement observation results indicate that the post-grouting technique adopted in the project is feasible.

6 Conclusion

(1) The pile end load-bearing capacity of prestressed tubular piles in karst region can be significantly increased by adopting post-grouting technique at the pile end. Under the maximum test load, the pile top settlement of grouted test piles can be reduced by 16.8%–22.3% compared with that of ungrouted test piles, and the theoretically simulated ultimate load-bearing capacity can be increased by 27.3%.

(2) Under the maximum test load, the use of post-grouting at the pile end reduces the pile end displacements of tubular piles

by 53.4%–56.6% and increases the proportions of pile end resistance by 11.27% and 18.21%, respectively, which indicates the post-grouting with plastic-hard plastic breccia silty clay as the bearing stratum can yield excellent grouting effect.

(3) The bead-shaped karst caves are more unfavorable to the load-bearing capacity of the tubular piles than these filled with plastic-hard plastic breccia silty clay to which the piles have direct access. The presence of a long segment of flow-soft plastic breccia silty clay with a low final shear stress in the strata crossed by the test pile is the cause for the insufficient exertion of side friction resistance of the tubular piles.

(4) The finite element model can effectively simulate the tubular pile-soil interaction. The theoretical analysis of load-bearing behavior of tubular piles in karst region of northern Fujian Province is performed by considering the insufficient exertion of side friction resistance of the prestressed tubular piles and determining the calculation parameters of the pile body, soil body, and grouting reinforcement body.

(5) The average settlements of the test piles of 19# and 17# buildings under karst geological conditions with two different spatial features are −12.88 mm and −8.98 mm, respectively, both of which do not exceed the warning value, indicating that the pile end post-grouting technique adopted in the project is feasible.

(6) The side friction resistance of the upper soil layer around the tubular pile body works earlier than that of the lower soil layer during the loading process. The larger the depth, the greater the deviation of the friction force from the final shear stress. Pile end post-grouting does not increase the side friction resistance. The side friction resistance of grouted test piles is significantly reduced compared with that of ungrouted test piles under the same loading as the pile end load-bearing capacity of the grouted test piles works gradually.

Data availability statement

The original contributions presented in the study are included in the article/Supplementary material, further inquiries can be directed to the corresponding author.

Author contributions

LH: Conceptualization, Data curation, Formal Analysis, Funding acquisition, Investigation, Methodology, Project administration, Resources, Software, Supervision, Validation, Visualization, Writing–original draft. RG: Methodology, Writing–review and editing. JC: Data curation, Writing–review and editing. XY: Formal Analysis, Writing–review and editing.

Funding

The author(s) declare that no financial support was received for the research, authorship, and/or publication of this article. This project is supported by the "Fujian Natural Science Foundation General Project (2021J011122)" and the "Research on the Bearing Characteristics of Bridge Pile Foundations and the Failure Mode of Underlying Karst Cave Roof in North Fujian" funded by the fund.

Conflict of interest

Author JC was employed by Fujian Southeast Design Group Co., Ltd. Author XY was employed by Fujian Jinding Construction Development Co., Ltd.

The remaining authors declare that the research was conducted in the absence of any commercial or financial relationships that could be construed as a potential conflict of interest.

Publisher's note

All claims expressed in this article are solely those of the authors and do not necessarily represent those of their affiliated organizations, or those of the publisher, the editors and the reviewers. Any product that may be evaluated in this article, or claim that may be made by its manufacturer, is not guaranteed or endorsed by the publisher.

References

Bo, L., Brian, B., Sheil, W., Zhao, P., Qian, B., and Wang, W. (2024). Laboratory testing of settlement propagation induced by pipe-roof pre-support deformation in sandy soils. *Tunn. Undergr. Space Technol.* 146, 105645. doi:10.1016/j.tust.2024.105645

Boyang, Z., Gang, L., Yingchun, L., and Lin, Z. (2023). Experimental study on the seepage mutation of natural karst collapse pillar (KCP) fillings over mass outflow. *Environ. Sci. Pollut. Res.* 30 (51), 110995–111007. doi:10.1007/s11356-023-30230-3

Dai, G., Ouyang, H., Gao, L., Guo, Q., and Gong, W. (2023). Experimental study on monotonic and cyclic lateral behavior enhancing mechanism of semi-rigid pile under different foundation reinforced methods in clay. *Ocean. Eng.* 273 (1), 113955–113961.12. doi:10.1016/j.oceaneng.2023.113955

Dai, L., Pan, Y., Zhang, C., Wang, A., Canbulat, I., Shi, T., et al. (2022). New criterion of critical mining stress index for risk evaluation of roadway rockburst. *ROCK Mech. ROCK Eng.* 55 (8), 4783–4799. doi:10.1007/s00603-022-02888-7

Ding-Wei, B., Jian-Lin, M. A., and Xing-Guo, L. I. (2018). Experimental study on post grouting of pile foundation of high-speed railway in karst area. *Railw. Stand. Des.* 62 (06), 83–88. doi:10.13238/j.issn.1004-2954.201706200003

Dong, Y. X., Feng, Z. J., and Hao, Y. M. (2018). Experiment on bearing capacity of bridge pile foundations in karst areas and reasonable rock-socketed depth. *J. Traffic Transp. Eng.* 18 (6), 27–36. doi:10.19818/j.cnki.1671-1637.2018.06.004

Gong, W., Zhang, Z., Lin, Y., Dai, G., and Huang, H. (2023). Full-scale field test study of bearing characteristics of post-grouting pile for offshore wind turbines. *Ocean. Eng.* 268 (15), 113451. doi:10.1016/j.oceaneng.2022.113451

Hou, Z., Tang, M., Liang, S., and Zhu, Y. (2021). Optimization of the physical and mechanical properties of grouting material for non-soil-squeezing PHC pipe pile. *Crystals* 12 (1), 10. doi:10.3390/cryst12010010

Huang, M., Fu, J., and Chen, F. (2019). Shaking table test of seismic dynamic characteristics of karst roof under pile load. *Harbin Gongye Daxue Xuebao/Journal Harbin Inst. Technol.* 51 (2), 126–135. doi:10.11918/j.issn.0367-6234.201712163

Jinjin, D., Qipeng, C., and Shizhuo, S. (2023). Numerical simulation of vertical bearing capacity of short core PHC pipe piles with cement soil roots. *J. Overseas Chin. Univ. Nat. Sci. Ed.* 42 (06), 740–747. doi:10.11830/issn.1000-5013.202101034

Kou, H., Li, W., Chu, J., and Yang, D. L. (2020). Model tests on open-ended concrete pipe piles jacked in sand. *Mar. Georesources Geotechnol.* 38 (7), 939–946. doi:10.1080/1064119x.2019.1642972

Li, X., Dai, G., Zhu, M., and Gong, W. (2019). Application of static loading tests to steel pipe piles with large diameters in Chinese offshore wind farms. *Ocean. Eng.* 186 (15), 106041. doi:10.1016/j.oceaneng.2019.05.023

Lianpeng, D., Yishan, P., and Aiwen, W. (2018). Study of the energy absorption performance of an axial splitting component for anchor bolts under static loading. *Tunn. Undergr. Space Technol.* 81, 176–186. doi:10.1016/j.tust.2018.07.009

Lianpeng, D., Yishan, P., Zhonghua, L., Aiwen, W., Yonghui, X., Feiyu, L., et al. (2021). Quantitative mechanism of roadway rockbursts in deep extra-thick coal seams: theory and case histories. *Tunn. Undergr. Space Technol.* 111 (May), 103861.1–103861.14. doi:10.1016/j.tust.2021.103861

Paik, K., and Salgado, R. (2004). Effect of pile installation method on pipe pile behavior in sands. *Geotechnical Test. J.* 27 (1), 1–11. doi:10.1520/gtj11391

Qi, W., Yuncai, W., Bei, J., Zhenhua, J., and Haojie, X. (2023). Geomechanics model test research on large deformation control mechanism of roadway disturbed by strong dynamic pressure. *Geohazard Mech.* 1 (2), 140–152. doi:10.1016/j.ghm.2023.06.002

Sheng-Hua, X., Zheng-Wu, L., Yong-Feng, D., Bian, X., Zhu, H. H., Zhou, F., et al. (2022). Bearing performance of steel pipe pile in multilayered marine soil using fiber optic technique: a case study. *Mar. Georesources Geotechnol.* 40 (11), 1453–1469. doi:10.1080/1064119x.2021.2005192

Shimeng, W., and Xinsheng, Y. (2020). Study on seismic performance of C105 prestressed high strength concrete hollow pipe pile. *Mater. Sci. Forum* 980, 282–290. doi:10.4028/www.scientific.net/msf.980.282

Tao, J., Jin, R., and Lu, F. (2017). Field testing of rigid pile composite foundation for high-rise buildings in karst area. *Jianzhu Jiegou Xuebao/Journal Build. Struct.* 38 (6), 163–174. doi:10.14006/j.jzjgxb.2017.06.018

Wang, P., Ding, H., and Zhang, P. (2020b). Influence of karst caves at pile side on the bearing capacity of super-long pile foundation. *Math. Problems Eng.* 2020 (2), 1–13. doi:10.1155/2020/4895735

Wang, Z. M. G., Ni, P., Chen, Z., and Mei, G. (2020a). Consolidation solution of soil around a permeable pipe pile. *Mar. Georesources Geotechnol.* 38 (9a10), 1097–1105. doi:10.1080/1064119x.2019.1655119

Wei, W., Qingke, N., and Wei, Y. (2017). Research on the effect of roof failure to the load-bearing characteristics of single pile penetrating karst cave. *Tumu Gongcheng Xuebao/China Civ. Eng. J.* 50 (S1), 88–93. doi:10.15951/j.tmgcxb.2017.s1.016

Wen, L., Kong, G., Li, Q., and Zhang, Z. (2020). Field tests on axial behavior of grouted steel pipe micropiles in marine soft clay. *Int. J. Geomechanics* 20 (6), 06020006. doi:10.1061/(asce)gm.1943-5622.0001656

Xiang, L., Ji, Y., and Jiaqi, W. (2019). Optimization practice of pile foundation for high-rise buildings in deep karst areas. *Karst China* 38 (04), 591–599. doi:10.11932/karst20190418

Xiucheng, L., Jie, X. U., and Xinpeng, Y. (2019). Study on bearing behavior of large diameter driven steel pipe pile in coral reef geology. *Ocean Eng.* 37 (06), 157–163. doi:10.16483/j.issn.1005-9865.2019.06.017

Xuefeng, C. (2019). Application of high pressure grouting in reinforcement treatment of pile end bearing layer. *Constr. Technol.* 48 (S1), 216–218.

Yan, Z., Deng, L. F., and Zhang, H. Q. (2022). Vertical field behavior of a deep large-diameter driven pipe pile in multilayered soils. *Ocean. Eng.* 247 (Mar.1), 110782–110782.13. doi:10.1016/j.oceaneng.2022.110782

Yishan, P., and Aiwen, W. (2023). Disturbance response instability theory of rock bursts in coal mines and its application. *Geohazard Mech.* 1 (1), 1–17. doi:10.1016/j.ghm.2022.12.002

frontiers | Frontiers in Earth Science

TYPE Original Research
PUBLISHED 30 April 2024
DOI 10.3389/feart.2024.1388612

Check for updates

OPEN ACCESS

EDITED BY
Jianyong Han,
Shandong Jianzhu University, China

REVIEWED BY
Fanfei Meng,
China University of Mining and Technology, China
Jia Liu,
Xi'an University of Technology, China

*CORRESPONDENCE
Zheng-Zheng Cao,
caozz@hpu.edu.cn

RECEIVED 20 February 2024
ACCEPTED 28 March 2024
PUBLISHED 30 April 2024

CITATION
Zhang P-D, Wu Y-J, Cao Z-Z, Li Z-H, Du F, Wang W-Q and Zhai M-L (2024), Study on overburden failure characteristics and displacement rule under the influence of deep faults.
Front. Earth Sci. 12:1388612.
doi: 10.3389/feart.2024.1388612

COPYRIGHT
© 2024 Zhang, Wu, Cao, Li, Du, Wang and Zhai. This is an open-access article distributed under the terms of the Creative Commons Attribution License (CC BY). The use, distribution or reproduction in other forums is permitted, provided the original author(s) and the copyright owner(s) are credited and that the original publication in this journal is cited, in accordance with accepted academic practice. No use, distribution or reproduction is permitted which does not comply with these terms.

Study on overburden failure characteristics and displacement rule under the influence of deep faults

Pei-Ding Zhang[1], Yong-Jiang Wu[2], Zheng-Zheng Cao[2,3,4]*, Zhen-Hua Li[3,4,5], Feng Du[3,4,5], Wen-Qiang Wang[5] and Ming-Lei Zhai[5]

[1]Shanghai Datun Energy Resources Co., Ltd., Xuzhou, Jiangsu, China, [2]International Joint Research Laboratory of Henan Province for Underground Space Development and Disaster Prevention, School of Civil Engineering, Henan Polytechnic University, Jiaozuo, Henan, China, [3]Henan Mine Water Disaster Prevention and Control and Water Resources Utilization Engineering Technology Research Center, Henan Polytechnic University, Jiaozuo, Henan, China, [4]Collaborative Innovation Center of Coal Work Safety and Clean High Efficiency Utilization, Jiaozuo, Henan, China, [5]School of Energy Science and Engineering, Henan Polytechnic University, Jiaozuo, Henan, China

Deep faults significantly impact the structural stabilities and deformation behaviors of their overburden rocks, which are key factors in underground engineering and geological hazard research. Considering the problem of deep-fault-overburdened breaking during mining of super-thick coal seams and taking the Yaoqiao Coal Mine as the research object, the mining fracture evolution characteristics and overburden displacement law of the non-structured and fault-bearing overburden corresponding to fully mechanized caving mining are compared and analyzed using numerical simulations and physical similarity simulations. The results of this study show the following: 1) The fracture height of the overlying rock presents a specific change law with advancement of the working face; the initial rapid increase to a maximum height of 74 m is achieved when the working face advances to 90 m; with the development of the plastic zone indicating past yield, the fracture height decreases to 54 m and becomes stable, and the final caving angle of the fracture stabilizes at 70°. 2) In coal mining under normal fault conditions, when the working face advances from the upper to lower walls, the roof forms a masonry beam structure that slows down fault activation and crack development. When moving away from the fault, the overburden movements and water-conducting cracks are fewer, and the crack height is lower than that without faults. When approaching the fault, the influence of the faults in the fracture zone increases, and the height of fracture development reaches the maximum value after crossing the fault, highlighting the significant influence of the fault on fracture development. 3) Through a similarity simulation test, it is shown that the overburden caving zone is further compacted by the overburden rock and that the roof collapses in a large range, resulting in rapid upward development of the overburden rock cracks and separation of the central overburden rock cracks that are gradually compacted and closed. These

findings are expected to have important theoretical and practical significance for deep underground engineering design, geological disaster prevention, and fault activity monitoring.

KEYWORDS

deep fault, overburden failure, numerical simulation, mining-induced fissure, similarity simulation

1 Introduction

With the exploitation of large quantities of coal resources, shallow coal resources seem to have been exhausted gradually, such that the current coal mining situation in China has shifted from shallow to deep mining (Wang et al., 2023a; Zheng et al., 2024a; Yongjiang et al., 2024). During actual coal mining, the balance of the space material environment of the underground system is destroyed, which may lead to various geological disasters (Wei et al., 2023; Zheng et al., 2024b; Pengshuai et al., 2024). The overall safety of coal mine production is also greatly threatened by water damage (Wang et al., 2023b; Wang et al., 2023c; Xue et al., 2024). In modern coal mine engineering, the stability of the working face is key to ensuring safe and efficient mining (Li et al., 2023; Zheng et al., 2023; Jun et al., 2024). The Yaoqiao Coal Mine is located in a complex geological environment, and its unique water-rich faults pose significant challenges to mine safety. In particular, under the influence of faults, the evolution law of the water-conducting fissures in the overlying rock of the working face has become an urgent problem to be solved.

Water conductivity is one of the most concerning features of overburden fractures. Zhang et al. (2022) considered the boundary faults of the mining area and concluded through comprehensive analyses that fault spacing and positive sectional pressure are the main factors affecting the sealing property. Wang and Wang (2021) studied crack development in the protected layer using field measurements, analyzed the crack evolution and permeability characteristics of the protected layer during mining, and concluded that the pressure relief amplitude and expansion rate of the protected layer would increase after mining. The height and shape of the water-conducting fracture zone, various factors affecting its development, and various models for predicting such factors have also been the focus of research for many scholars. Some scholars (Cai et al., 2024; Zheng et al., 2024c; Teng et al., 2024) have determined through research that the final shape of the water-conducting fissure belt is "saddle shaped." Guobiao et al. (2021) used numerical simulation, theoretical analysis, and engineering analogy to study the water-guiding fracture zone of the rock overlying the working face of large mining height and proposed that the shape of the water-guiding fracture zone was of the "ladder" type, with the mining height and advancing speed being the main factors affecting the height of the water-guiding fracture zone. Shao and Yu (2018), Chen et al. (2021), and Zhang et al., 2013 established a prediction model for the height of the water-conduction fracture zone to provide a research reference for other water-conduction fracture zones under similar conditions. Compared to theoretical analyses and numerical simulations, actual measurements may be the most direct and accurate method of studying overburden fractures.

In recent years, scholars have mainly used theoretical analyses, numerical simulations, and similarity simulation tests to analyze the evolution law of mining overlay fractures and reported many phased achievements (Cheng et al., 2016; Kong et al., 2018; Zhang et al., 2020). Xingliang and Qingxiang (2022) studied the development characteristics of water-conducting fractures in underwater coal mining bodies by combining deformation analysis with numerical simulations; they reported that soft rock in the overlying rock layer with a certain thickness could inhibit the upward development of water-conducting fracture zones. Jialin and Minggao (2004) revealed the two-stage development law of mining fracture development in overburden rock and the distribution characteristics of the "O" ring. Zhiliang et al. (2017) discussed the roles of the key layers in the distribution of the fracture network and reported that open fractures and separation fractures will eventually penetrate each other in the mining process, forming an elliptical scattering zone distribution in the overlying rock. Zhao et al. (2021) established the relationship between the fractal dimension of the overburden fractures and energy dissipated using experimental and numerical simulations. Based on the complexity and disorder of the cracks, Heping et al. (1999) used geometric fractal theory to study mining-induced fractures in the overlying rocks, and their results show that mining-induced fractures have self-similarity and fractal characteristics. Zhang et al. (2001) used discrete element software and noted that the fractal dimension is an important parameter for describing the fractal law of mining-induced rock fracture network. Wang et al. (2012) studied the fracture evolution process of a mining-induced rock mass with initial fractures and found that the larger the initial damage, the larger are the fractal dimensions of the fracture distribution in the mining-induced rock mass. Zhao (2022) analyzed the influences of fault sizes, numbers, and different distributions on overburden fracture development using similarity simulations and rock failure process analysis (RFPA) numerical simulations; they found that the faults located near the incision holes had greater impacts on overburden fracture failures, and for larger faults, the water-conducting fracture zone extent is deeper along the fault face with the higher degree of development.

At present, many scholars have conducted studies on the overlying rock failure characteristics under the influence of the fault activation mechanism, which has very important significance for this study; however, there is a lack of research on the overlying rock failure characteristics and fracture-zone development characteristics under the influence of deep faults in the Yaoqiao Coal Mine. Therefore, based on the hydrogeological conditions of the Yaoqiao Coal Mine, the

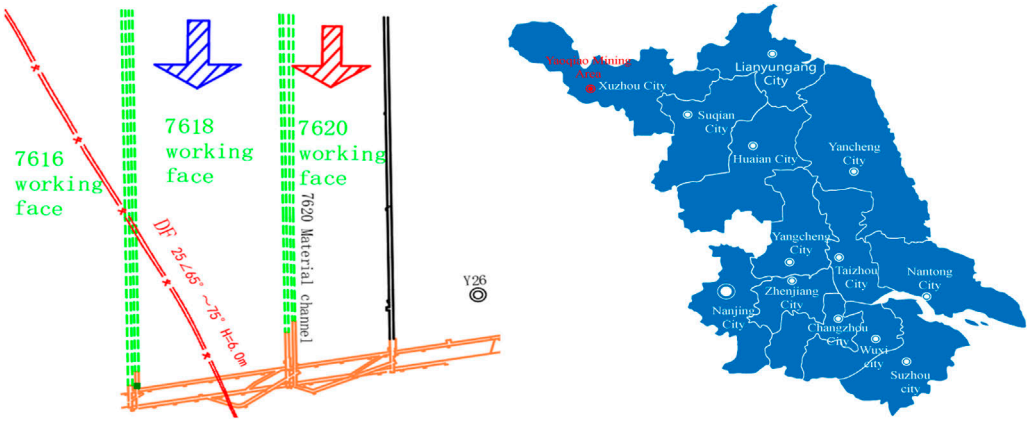

FIGURE 1
Schematic diagram showing the position of the working face.

exploitation fissure evolution characteristics and overburden displacement laws of the non-tectonic overburden and fault-bearing overburden corresponding to fully mechanized caving mining are compared and analyzed through numerical simulation and physical similarity simulation. These research results are expected to have important theoretical and practical significance for deep underground engineering design, geological disaster prevention, and fault activity monitoring.

2 Project overview

The Yaoqiao Coal Mine is one of the large mines in the Datun Mining area that is located approximately 82 km northwest of Xuzhou City, Jiangsu Province, and approximately 17 km south of Peixian County. At present, the Yaoqiao Coal Mine is being mined at the deep working face of the XiVI mining area, and the 7,620 working face has already been mined. It is expected that the next step would involve mining the 7,618 working face, which is adjacent to the 7,620 working face in the north and 7,616 working face in the south; the position of the 7,618 working face is shown in Figure 1. The DF25 normal fault having a fault drop of 6 m is shown in Figure 1 for the positions of the working face, fault, and its column.

3 Numerical simulation

3.1 Analysis of the mining fracture evolution law of unstructured overburden rock

3.1.1 Numerical model

The numerical model is based on the 7,618 working face of the west wing of the Yaoqiao Coal Mine. The geometric size of the model is 300 m × 100 m, thickness of the coal seam is 4.71 m, and mining depth is 650 m. Considering the boundary effects caused by mining, 50-m boundary protection coal pillars are set on both sides of the model, and 10 m is excavated each time for a total of 200 m of excavation. The overlying strata are placed at the top of the model with equivalent uniform loads. The vertical displacement constraint is applied to the bottom of the model, and the horizontal displacement constraint is applied to the left and right sides of the model. The numerical model is thus established according to the stress and structural characteristics of the overlying strata of the coal seam.

3.1.2 Development law of the overburden water channel in fully mechanized caving mining

Figure 2 shows the plastic zone diagram, mining-induced fracture development law diagram, and caving form diagram corresponding to fully mechanized caving mining. The mining-induced fracture development law diagram is considered in accordance with the principle that the rock mass opening is a medium opening between 1 and 5 mm; Table 1 and Figure 3 show the development law of the fracture zone height with advancement of the working face. To facilitate comparative analyses, the model selects the calculated results for every 40 m of advancement.

As seen from the plastic zone diagram in Figure 2, when the working face advances, the composite rock is in the past yield state in the plastic zone diagram, indicating that the fracture is healed gradually. From the fracture development diagram, it is seen that small cracks develop in the mudstone, but these have lost the ability to conduct water, and the height of the fracture zone decreases gradually to become stable at approximately 54 m. As seen from the fracture development diagram in Figure 2 and Table 1, with the advancement of the working face, the development height of the overlying rock fracture increases. When the working face advances by 30 m, the old roof fractures, and the overlying mudstone collapses. The initial pressing step of the working face is approximately 30 m. When the working face advances to approximately 90 m, the height of the fracture zone is highest at approximately 74 m. With continuous advancement of the working face, the caving angle of the rock stratum movement

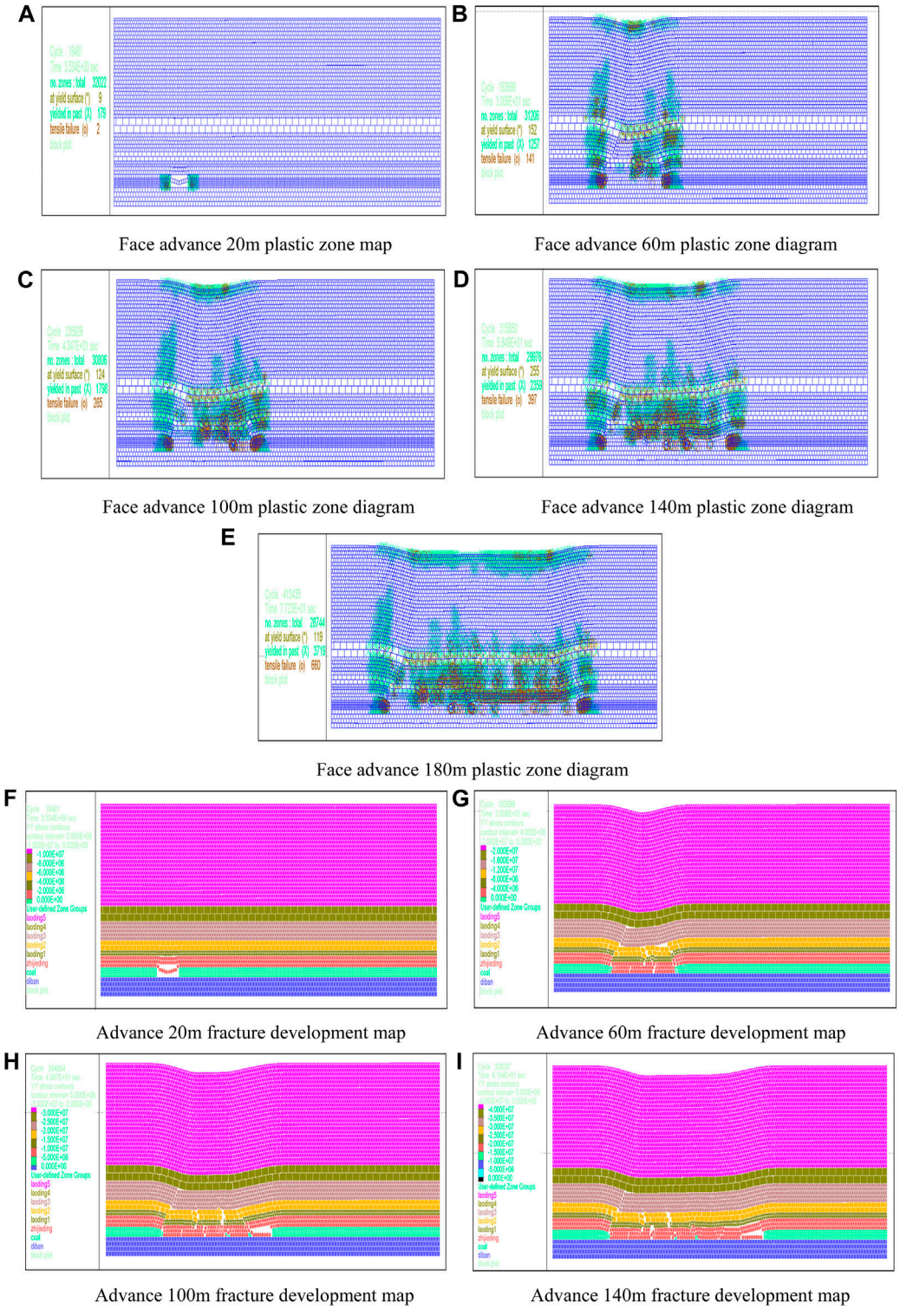

FIGURE 2
(Continued).

changes constantly and finally stabilizes at about 70°, and the caving angle at the cutting hole is more obvious than that at the stop-mining line. The cracks near the cutting eye and stop-mining line change minimally with the advancement of the working face and form permanent cracks with the largest final height value.

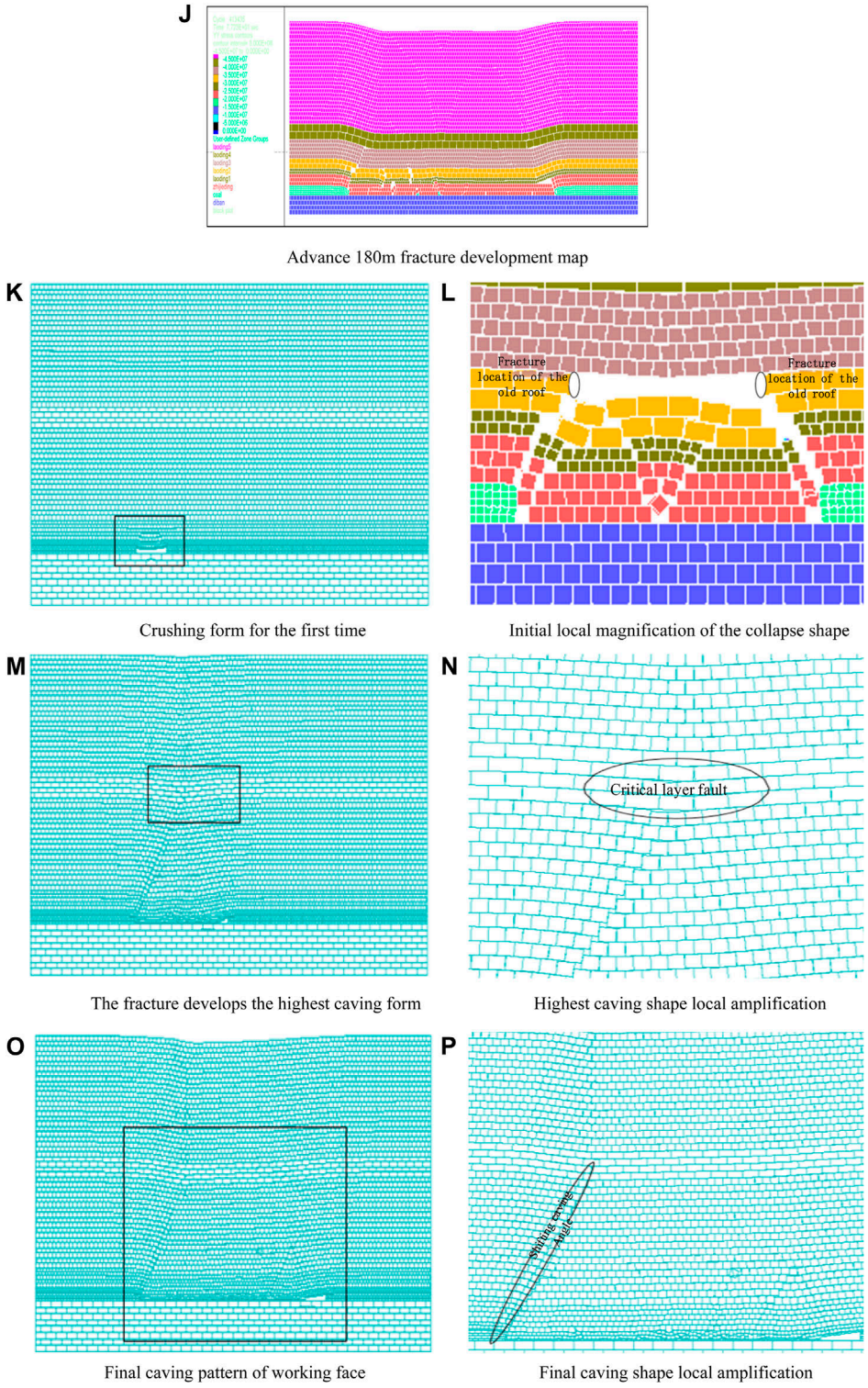

FIGURE 2
(Continued). Plastic zone diagram, mining-induced fracture development law diagram, and caving form diagram corresponding to fully mechanized caving mining. **(A)** Face advance 20 m plastic zone map. **(B)** Face advance 60 m plastic zone diagram. **(C)** Face advance 100 m plastic zone diagram. **(D)** Face advance 140 m plastic zone diagram. **(E)** Face advance 180 m plastic zone diagram. **(F)** Advance 20 m fracture development map. **(G)** Advance 60 m fracture development map. **(H)** Advance 100 m fracture development map. **(I)** Advance 140 m fracture development map. **(J)** Advance 180 m fracture development map. **(K)** Crushing form for the first time. **(L)** Initial local magnification of the collapse shape. **(M)** The fracture develops the highest caving form. **(N)** Highest caving shape local amplification. **(O)** Final caving pattern of working face. **(P)** Final caving shape local amplification.

TABLE 1 Changes in the fracture development height with advancement of the working face.

L/m	30	60	90	120	150	180
H/m	24	45	74	68	54	53

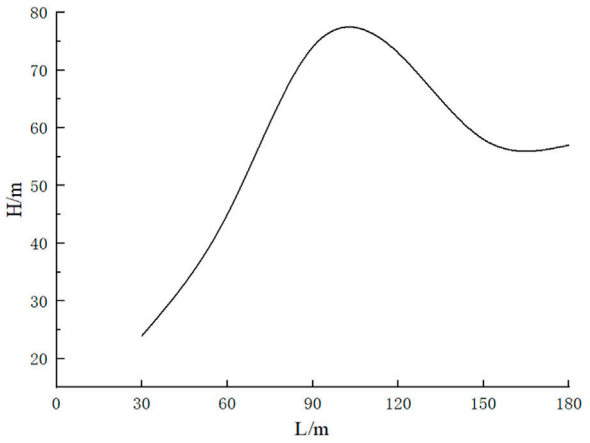

FIGURE 3
Variation in the fracture development height with advancement of the working face.

3.2 Analysis of the mining fracture evolution law of fault-bearing overburden

3.2.1 Numerical model

When mining coal under water, it is of great theoretical and practical significance to study the development law of water conduction under the influence of faults because the maximum height and failure characteristics of the mining fracture zone in the area with faults and other geological structures will change greatly compared with the area without geological structures, which often leads to water inrush or flooding accidents. Therefore, a numerical model of the fault-bearing overburden is established to analyze the evolution law of the water channel. To facilitate comparative analyses, the numerical model used is the prototype of the 7,618 working face as mentioned above, and the model size, loading mode, constraint conditions, and rock physical and mechanical parameters remain unchanged. The physical and mechanical parameters of the fractured rock mass in the fault zone are as shown in Table 2.

3.2.2 Developmental regularity of the mining water channel in fault-bearing overburden rock

Figure 4 shows the caving plastic zone and fracture development diagrams of the mining overburden fracture process under fully mechanized caving with fault overburden. Table 3 and Figure 5 show the development law of the fracture zone height with advancement of the working face, and Figure 6 shows the fracture zone development morphology diagram under the influence of faults. To facilitate comparative analyses, the model selects the calculated results for every 30 m of advancement.

Here, L is the relative position from the fault, the negative sign indicates that the working face is located in the upper wall of the fault, and the positive sign indicates that the working face is located in the lower wall of the fault; HIII is the height of fracture development.

(1) When the working face advances from the upper to lower walls of the normal fault, the roof is easily formed by a balanced structure of masonry beams, and the fault is not easily activated. When the distance from the fault is greater, the overburden movement is slower than that when mining without faults, the development of water-conducting cracks is smaller, and the development height of the cracks is slightly lower than that when mining without faults.
(2) As the working face advances to the vicinity of the fault plane, the fault begins impacting the development of the fracture zone, and the working face has the greatest impact on the height of fracture development when it pushes past the fault for a certain distance.
(3) From the distribution of the plastic zone in Table 3, it is seen that when a large-dip normal fault enters the fault from the upper wall, it greatly influences the development height of the mining-induced fissure, which may be up to 91 m.
(4) Owing to the role of the faults, the mining fracture has a "double-saddle shape" development pattern, whose boundary region C is near the fault and the peak value of zone B is near the fault under the condition of large fault inclination.
(5) The highest position of fracture development is when the working face enters the footer and is farther away from the fault. At a distance of 70 m from the fault, the crack development is highest.

4 Study on similarity simulation of overburden failure characteristics in deep mining

Taking the 7,620 working face of the Yaoqiao Coal Mine as the prototype, a physical similarity simulation was established to study the deformation and failure characteristics of the overlying rock in the goaf and evolution of the water-conducting fracture zone.

4.1 Similarity simulation parameter determination

4.1.1 Similarity conditions

Based on the purpose of the similarity simulation, considering the operability and reliability of the test as well as the similarity criterion, the similarity simulation parameters are as follows:

1) Geometric similarity ratio

$$C_L = \frac{L_m}{L_p} = 1{:}150 \tag{1}$$

2) Poisson's ratio similarity ratio

$$C_\mu = \frac{\mu_m}{\mu_p} = 1{:}1.5 \tag{2}$$

10.3389/feart.2024.1388612

TABLE 2 Physical and mechanical parameters of the fractured rock mass.

Lithology	Capacity/kg/m^3	Elastic modulus/GPa	*V*	Tensile strength/MPa	Cohesion/MPa	*C*/°
Geologic fault	2,500	10	0.30	0.5	0.8	18

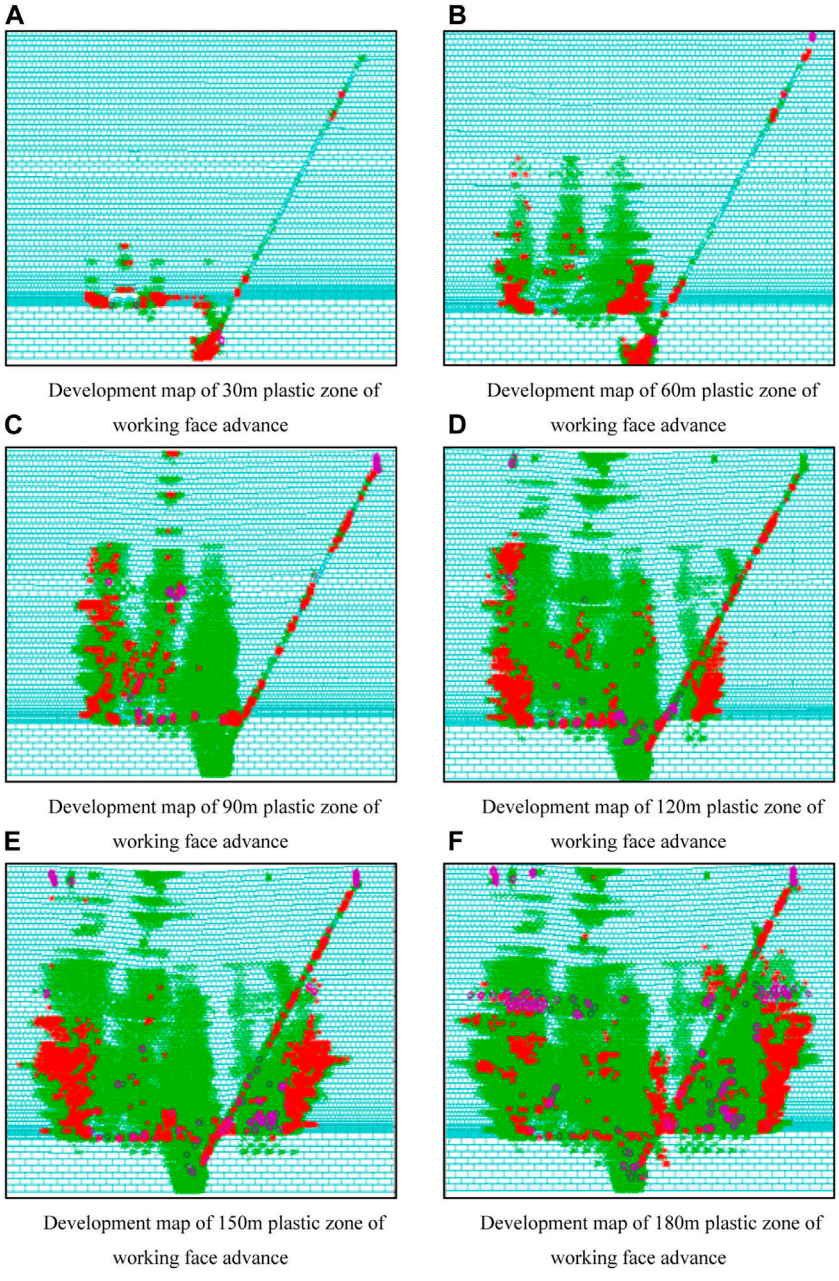

FIGURE 4
(Continued).

3) Density similarity ratio

$$C_\rho = \frac{\rho_m}{\rho_p} = 1{:}1.5 \tag{3}$$

4) Stiffness similarity ratio

$$C_E = \frac{\sigma_E}{\sigma_\rho} = C_L \times C_\rho = 1/225 \tag{4}$$

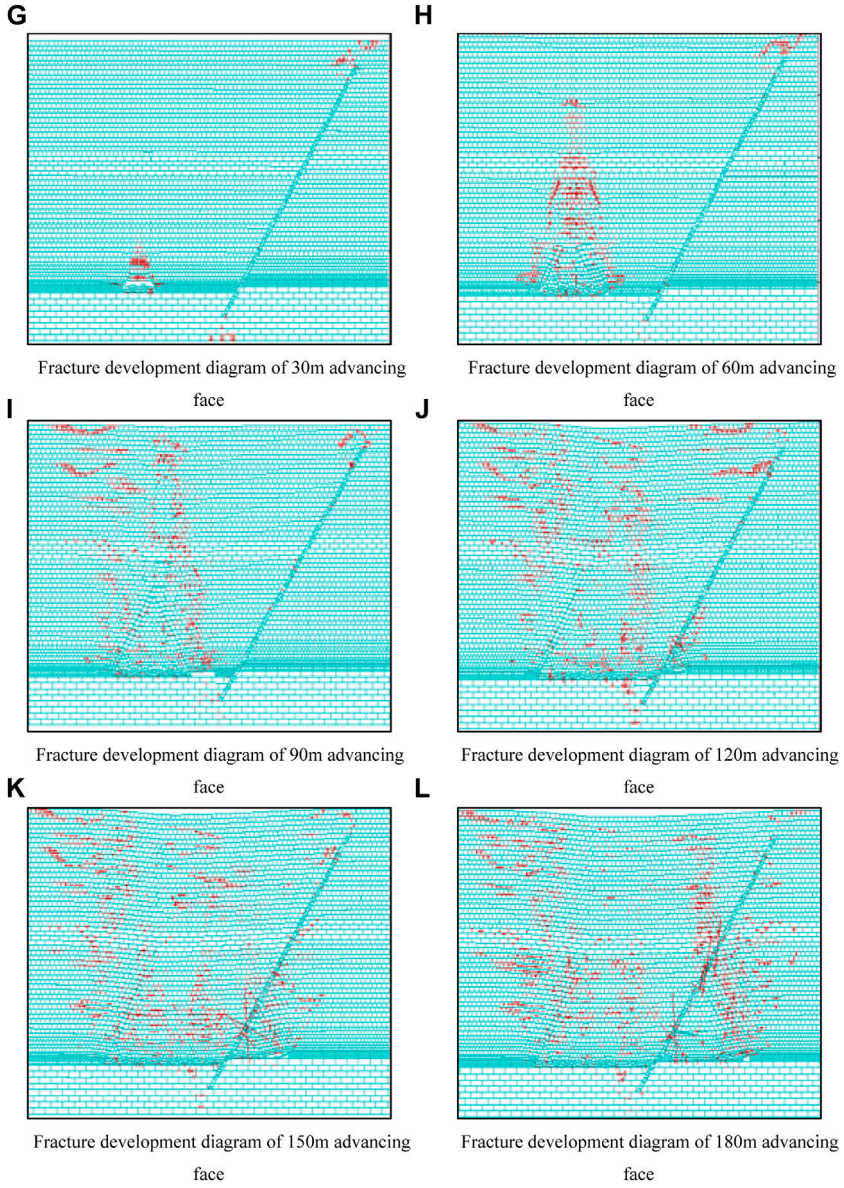

FIGURE 4
(Continued). Plastic zone and fracture development diagram. **(A)** Development map of 30 m plastic zone of working face advance. **(B)** Development map of 60 m plastic zone of working face advance. **(C)** Development map of 90 m plastic zone of working face advance. **(D)** Development map of 120 m plastic zone of working face advance. **(E)** Development map of 150 m plastic zone of working face advance. **(F)** Development map of 180 m plastic zone of working face advance. **(G)** Fracture development diagram of 30 m advancing face. **(H)** Fracture development diagram of 60 m advancing face. **(I)** Fracture development diagram of 90 m advancing face. **(J)** Fracture development diagram of 120 m advancing face. **(K)** Fracture development diagram of 150 m advancing face. **(L)** Fracture development diagram of 180 m advancing face.

TABLE 3 Variation in the height of fissure development for different relative distances from the fault.

L/m	−70	−40	−10	10	40	70
H_m/m	20	80	91	15	35	85

5) Time similarity ratio

$$C_t = \frac{t_m}{t_p} = \sqrt{C_L} = 1/12 \tag{5}$$

6) Stress similarity ratio

Because of the large depth of the coal seam, the model cannot be built directly up to the surface, so the stress similarity ratio is considered. According to the principle of similarity simulation, the pressure at the top of the model should be the weight of the rock layer that cannot be simulated. Then, as per the original model, this should be a loaded value:

$$q_p = \frac{P}{F} = \gamma_p(H - H_l), \tag{6}$$

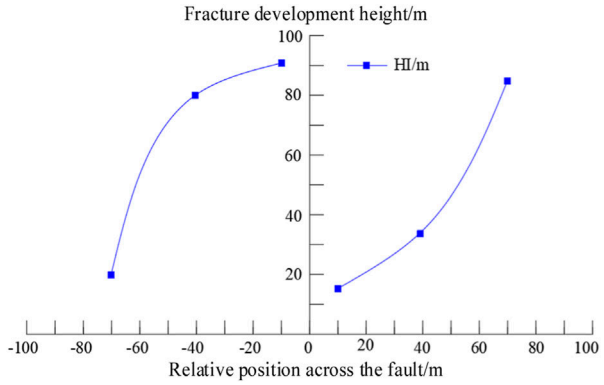

FIGURE 5
Variation in the fracture development height for different relative positions away from the fault.

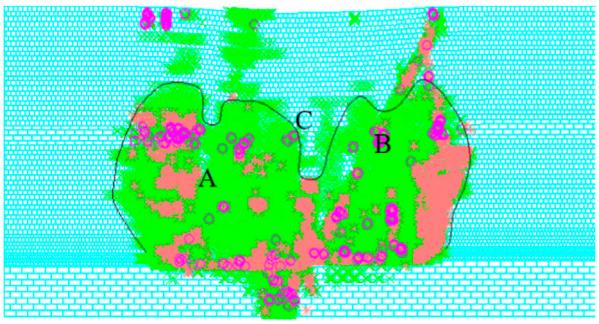

FIGURE 6
Developmental morphology of the fracture zone under the influence of faults.

where q_p is the prototype that does not simulate rock pressure, kPa; H is the mining depth, m; H_1 is the simulated height of the roof strata, m.

The value q_m loaded on the model is given by

$$q_m = \frac{q_p}{C_L \cdot C_\gamma} = \frac{\gamma_p(H - H_1)}{C_L \cdot C_\gamma}. \quad (7)$$

The thickness of the unsimulated overlying rock stratum is 700 m, and the average volume reweighting of the overlying rock stratum is 2560 kN/m^3. From the above formula, it is noted that the load q_m that should be applied to the model is 1,075.2 kPa and that this load is compensated by the pressurization of the hydraulic column on the test bench.

4.1.2 Calculation of the ratio of similar materials

Based on the actual coal seam condition of the working face, sand was used as the aggregate, calcium carbonate and gypsum were used as the cementing materials, and borax was used as the retarding agent. From calculations of the simulated strength values of similar materials and references to relevant literature, the reasonable ratio of each layer of similar material is obtained by repeated adjustments. According to the cross-sectional area, rock (coal) thickness, and geometric similarity ratio of the model frame, the volume of similar materials required can be calculated; then, the weights of similar materials in each of the rock (coal) layers can be calculated from the bulk density and ratio number of similar materials (considering the affluence coefficient of 1.2). The total weight of the materials in each layer can be calculated using the following formula:

$$M_i = L \times b \times H_i \times \gamma_i \times 1.2, \quad (8)$$

where M_i is the total weight of the layered material, kg; L is the frame length, m; b is the frame width, m; H_i is the model layer thickness, m; and γ_i is the bulk weight of the material, kg/m^3.

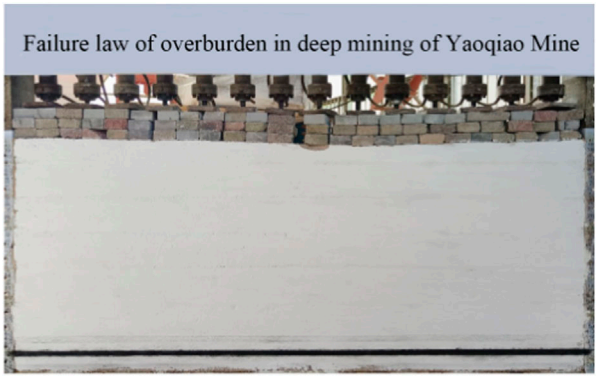

FIGURE 7
Physical model.

4.2 Model creation

4.2.1 Model design

According to the test conditions, evaluations were carried out on a test bench of 2500 mm × 1300 mm × 200 mm (length × height × width), where the design model height is 1300 mm, coal thickness is 56 mm, and floor thickness is 130 mm.

4.2.2 Model loading

First, according to the ratio number and rock layer distribution, the mixture is modulated layerwise. Then, the mold is loaded, ingredients are loaded in the mold, flat surface is spread to the corresponding height, and a mica sheet is spread on it so that the rock layer can be relatively distinct for the simulation; the above steps are then repeated until the simulated height. During molding, the thickness of the rock layer is generally 1.0–3.5 cm each time, and a layer that is too thick cannot be easily rammed, which results in the layer becoming dense and loose, with unevenly laid material. When the rock layer is less than 1.0 cm, rock formation difficulties are caused. Before loading the model, the total volume and total mass of each layer must be calculated according to the ratio number of strength, and the filling must be applied within 5–10 min after mixing evenly to prevent the gypsum from solidifying before loading and affecting the properties of similar materials. Finally the mold is removed one week after production completion; if the template is difficult to remove, it is properly relaxed and maintained at an appropriate distance from the coal rock until dry. The physical model of the loading is shown in Figure 7.

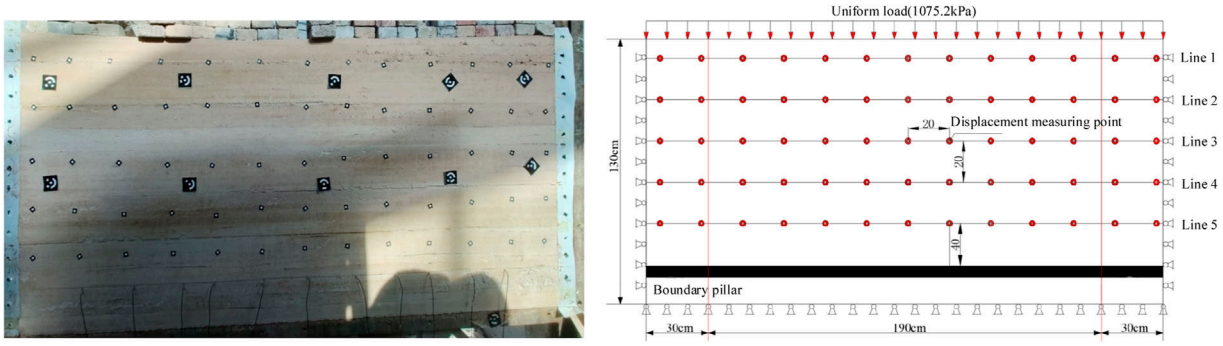

FIGURE 8
Layouts of the model survey lines and displacement measurement points.

4.3 Excavation and survey-line layout of the model

4.3.1 Model excavation scheme

To fully study the overburden fracture migration characteristics and development height of the water-conducting fracture zone during the excavation of the Yaoqiao 7# coal seam, a model is established for excavation along the coal seam, which is equivalent to advancing the simulated working face. The model is excavated stepwise, with a 30-cm protective coal pillar left on both sides and 190 cm of total excavation that is equivalent to advancing the working face by 190 m.

4.3.2 Line arrangement

To observe the changes in the overlying rock displacement during advancement of the working face, five survey lines were laid in the rock layer along the coal seam roof from bottom to top. Survey line 5 is 40 cm away from the coal-seam roof, survey line 4 is 60 cm away from the coal-seam roof, survey line 3 is 80 cm away from the coal-seam roof, survey line 2 is 100 cm away from the coal-seam roof, and survey line 1 is 120 cm away from the coal-seam roof. Each survey line is arranged along the mining direction of the coal seam with 13 measurement points, and the spacing between adjacent measurement points is 20 cm. A total of 65 displacement measurement points are thus arranged in the entire model. The arrangement of the displacement measurement points and working faces is shown in Figure 8.

During the process from opening the hole to mining 190 cm, the model was excavated in steps of 4 cm each time, which is equal to advancing the working face by 4 m; the total excavation of 190 cm was mined directly in a single attempt, which is equal to 190 m along the actual working face. During excavation, the fracture characteristics and fracture development of the overlying rock were observed and recorded. At the same time, a digital camera was used to monitor the movements of the overlying strata. Then, the digital images were processed via computer image processing technology to analyze the changes to the overlying rock displacements with the mining face. A final measurement was obtained after the strata movement stabilized at the end of the simulated mining.

4.4 Overburden fracture characteristics and evolution law of the water-conducting fracture zone

When the working face advances from the cutting hole to 20 m, the overburden fracture characteristics are as shown in Figure 9A. Owing to the influence of mining, the immediate top starts to develop separation fractures. When the working face advances to 25 m (see Figure 9B), the as separation fractures of the direct roof become more obvious, and the initial overall collapse of the direct roof occurs along the coal wall, and the fractures do not appear obviously in the overburden of the direct roof.

When the working face advances from 25 to 40 m, the first pressure occurs at the working face, and the overburden fracture characteristics are as shown in Figure 9C. The stratification cracks and longitudinal cracks develop rapidly upward, and the old roof caves successively. The caving of the old top rock strata in the coal wall overhangs by approximately 2 m, and the goaf is not sufficiently compacted. When the working face advances from 40 to 56 m, the first cycle of pressure occurs with the step distance of 16 m, and the fracture characteristics of the overlying rock are as shown in Figure 9D. At this time, the caving block of the overlying rock is relatively broken, while a new obvious separation layer appears in the overlying rock 26 m above the coal seam and longitudinal cracks develop upward slowly at the cutting hole and working face.

When advancing from 56 to 70 m, the second pressure cycle occurs with the step distance of 14 m, and the fracture characteristics of the overlying rock are shown in Figure 9E. At this time, the original goaf is filled with caving blocks and begins to be compressed by the subsidence of the overlying rock. At the same time, a new obvious separation of the overlying rock appears 38.5 m above the coal seam, and the development height of the water-conducting fracture zone is approximately 42.2 m. When the working face advances from 70 to 86 m, a third cycle of pressure occurs with the step distance of 16 m, and the fracture characteristics of the overlying rock are as shown in Figure 9F. The overlying rock separation is more obvious 38.5 m above the coal seam, and the roof separation of the overlying rock is more obvious. Moreover, there are obvious longitudinal cracks at the cutting hole and working face, and the development height of the water-conducting fracture zone is approximately 46 m.

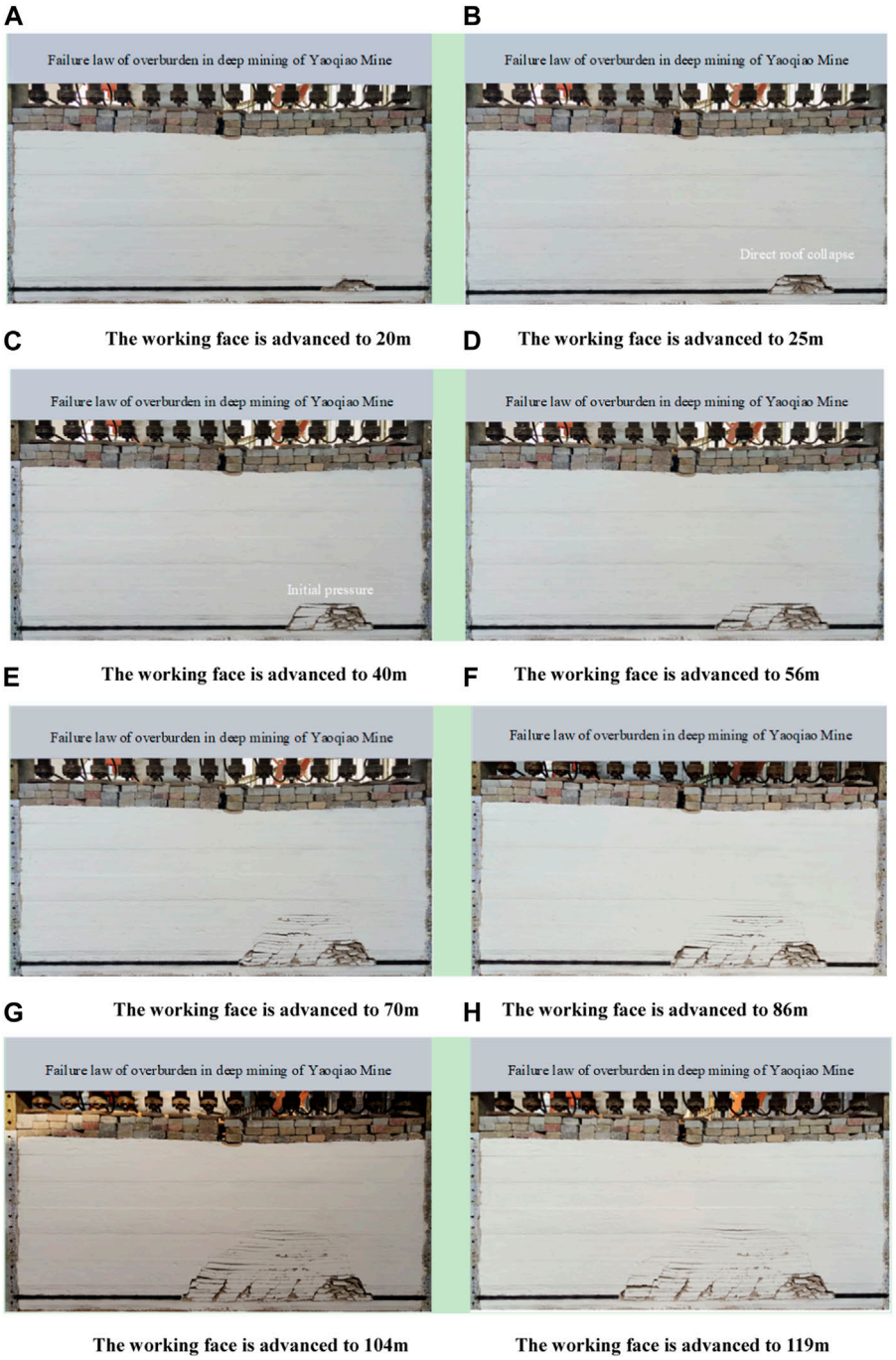

FIGURE 9
(Continued).

When advancing from 86 to 104 m, the fourth pressure cycle occurs with the step distance of 18 m, and the fracture characteristics of the overlying rock are as shown in Figure 9G. At this time, the goaf is further compacted by the sinking of the overlying rock, and the development height of the water-conducting fracture zone is approximately 52.4 m. When the working face advances from 104 to 119 m, the fifth cycle of pressure occurs with the step distance of 15 m, and the overburden fracture characteristics are as shown in Figure 9H. At this time, the caving zone gradually stabilizes, the caving zone of the overlying rock is compacted, and the roof collapses in a large area, resulting in rapid upward development of cracks in the overlying rock such that the split layer cracks in the central overlying rock are gradually compacted and closed. There are obvious longitudinal cracks above the working face, and the longitudinal cracks at the cutting hole develop upward rapidly; at this time, the development height of the water-conducting fracture zone is approximately 54.5 m.

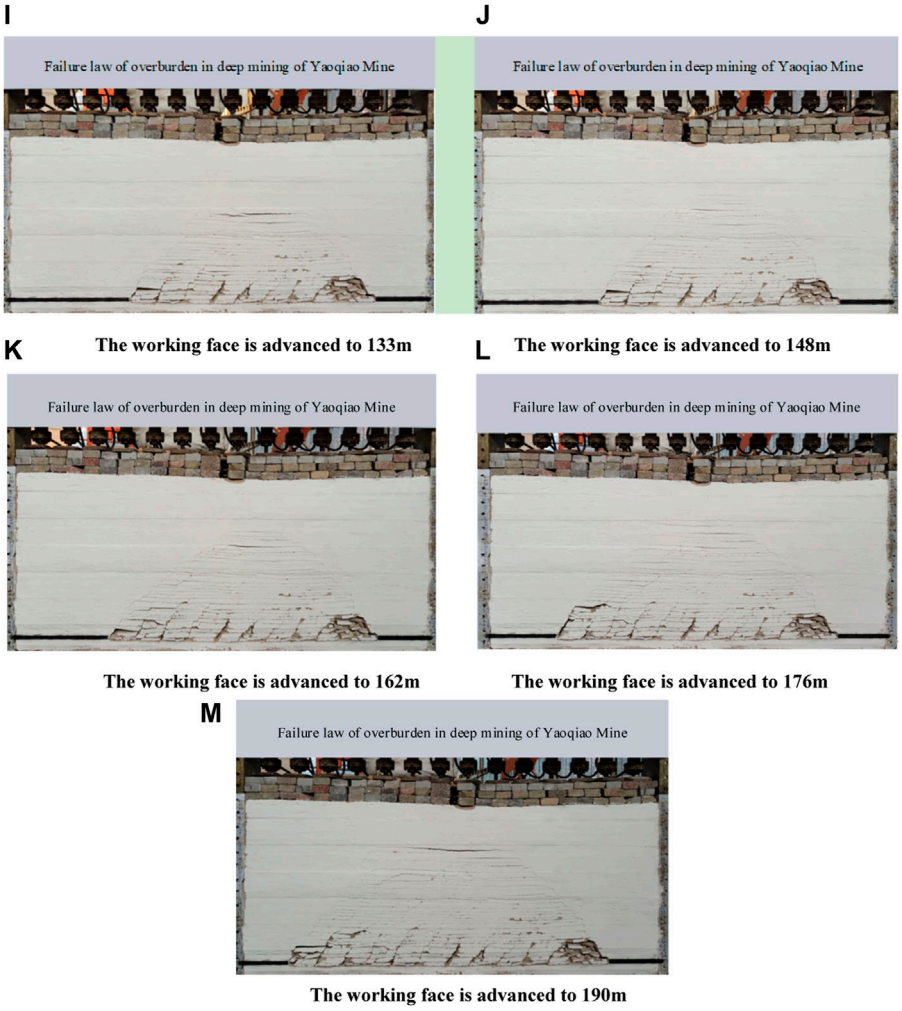

FIGURE 9
(Continued). Overburden fracture characteristics at different advancements. **(A)** The working face is advanced to 20 m. **(B)** The working face is advanced to 25 m. **(C)** The working face is advanced to 40 m. **(D)** The working face is advanced to 56 m. **(E)** The working face is advanced to 70 m. **(F)** The working face is advanced to 86 m. **(G)** The working face is advanced to 104 m. **(H)** The working face is advanced to 119 m. **(I)** The working face is advanced to 133 m. **(J)** The working face is advanced to 148 m. **(K)** The working face is advanced to 162 m. **(L)** The working face is advanced to 176 m. **(M)** The working face is advanced to 190 m.

When advancing from 119 to 133 m, the sixth pressure cycle occurs with the step distance of 14 m, and the fracture characteristics of the overlying rock are as shown in Figure 9I. In the middle of the overlying rock, the separation fractures expand, and the longitudinal fractures above the cutting hole and working face continue to develop upward. At this time, the development height of the water-conducting fracture zone is approximately 62.3 m. When the working face advances from 133 to 148 m, the seventh cycle of pressure occurs with the step distance of 15 m, and the fracture characteristics of the overlying rock are as shown in Figure 9J. At this time, the goaf is further compacted by the subsidence of the overlying rock, and the separation fissures of the central overlying rock start closing. The longitudinal cracks above the cutting eye and working face continue to develop upward, and the development height of the water-conducting fracture zone is approximately 70.8 m.

When advancing from 148 to 162 m, the eighth pressure cycle occurs with the step distance of 14 m, and the fracture characteristics of the overlying rock are as shown in Figure 9K. The overlying rock bends and subsides as a whole, the existing underlying fissures are closed, and the development rate of the longitudinal fissure at the cutting hole and above the working face slows to become stable. At this time, the height of the water-conducting fracture zone is 72.3 m. When the working face advances from 162 to 176 m, the ninth pressure cycle occurs with the step distance of 14 m, and the fracture characteristics of the overlying rock are as shown in Figure 9L. At this time, the overlying rock bends and sinks, and the height of the water-conducting fracture zone is 74.6 m.

When the working face advances from 176 to 190 m, the tenth cycle pressure occurs with the step distance of 14 m, and the overburden fracture characteristics are as shown in Figure 9M. The uppermost stratum develops fractures in the middle of the overburden rock, and the gaps in the stratum expand. The existing fractures in the lower overburden layers are closed, and the fractures stop developing. The longitudinal fissures also stop developing at the cutting hole of the working face. At this time, the excavation

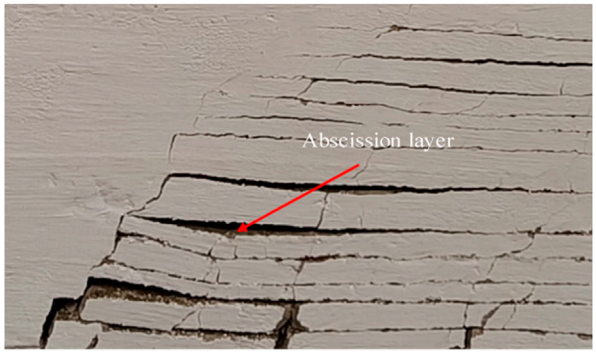

FIGURE 10
Caving zone characteristics.

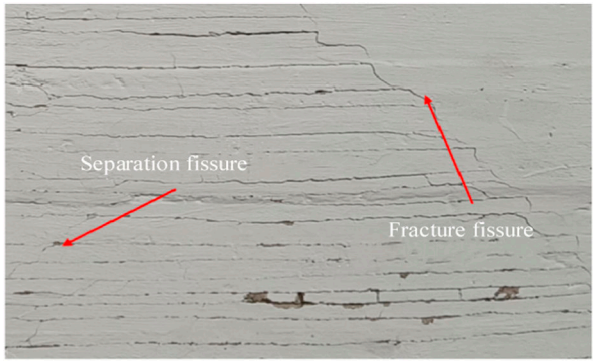

FIGURE 11
Characteristics of the fracture zone.

is complete, and the development height of the water-conducting fissure zone is finally determined as 74.6 m.

From the above statistical analysis of the overburden caving morphology for different advancement distances, it can be seen that there are ten pressure cycles in this experiment, with an average step distance of 14.9 m. In the process of coal-seam excavation, pressure is exerted by the period, and the roof of the working face undergoes separation as well as formation of cracks and fractures during testing, which finally generate the caving zone. The caving zone is roughly shaped as a trapezoidal platform, and its characteristics can be seen in Figure 10. With continuous advancement of the working face, many longitudinal and stratified fractures appear in the old overburdened rock, the formation of the water-conducting fracture zone develops rapidly, and the stratified fractures present a dynamic process of formation, expansion, contraction, and closure, as shown in Figure 11. Thus, the water gusher channel is mainly dominated by the fracture of the rock layer. As the dynamic process of the separation fracture shrinks and closes with advancement of the working face, thereby compacting gradually, the water gusher channels of the overlying water-bearing rock layer have difficulty passing through the separation fractures, as shown in Figure 12.

With the advancement of the working face, the water-guiding fracture zone continues to develop upward. To reflect the relationship between the water-guiding fracture zone and advancement of the working face more intuitively, Origin mapping software is used to draw the distribution curves according to the test data, as shown in Figure 13. As can be seen from Figure 13, with the advancement of the working face, the development height of the water-conducting fracture zone increases rapidly at first and then increases slowly to a stable level. The development height of the water-conducting fracture zone then stabilizes at approximately 74.6 m and does not develop further. This shows that the maximum development height of the water-conducting fracture zone is approximately 74.6 m, which is 15.87 times the thickness of the coal layer.

4.5 Analysis of the displacement law of the overlying rock model

In the physical similarity simulation experiments, the coal seam was excavated stepwise, and the displacement measurement points on the back of the test platform were moved by different degrees after each excavation. The movement of each displacement measurement point can be obtained by comparison with the initial position. The lateral and longitudinal displacements of the measuring points can be recorded and calculated using the XTDP 3D optical photogrammetry system. The longitudinal subsidence of each measurement point is obtained using XTDP 3D optical photogrammetry because the lateral displacements of the rock strata are very small and can be ignored. A total of three measurement lines are arranged on the back of the model, and the subsidence displacements of the measurement lines are shown in Figures 14–16.

Figure 14 shows the changes in the vertical displacements of survey line 3 during coal-seam excavation. The vertical distance of survey line 6 from the coal-seam roof is 80 m. Before the working face advances to 133 m, survey line 3 only has slight deformation, indicating that the mining dynamic disturbance has not affected the place 50 m before the working face advances to 133 m. When the working face advances to 148 m, the vertical displacement of survey line 6 changes greatly. At this time, the maximum subsidence displacement is 0.51 m, indicating that the caving zone of the overlying rock is further compacted and that the roof collapses in a large area, resulting in rapid upward development of cracks in the overlying rock such that the breakaway cracks in the middle of the overlying rock are gradually compacted and closed. In the process of gradually advancing to 190 m, given the periodic breaking of the overlying rock, the vertical displacement measurement lines change in stages, and the final maximum subsidence value was 0.58 m.

Figure 15 shows the changes in the vertical displacements of survey line 2 in the process of coal-seam excavation. The vertical distance of survey line 2 from the coal-seam roof is 100 m. In the process of advancement of the working face, survey line 2 only deforms slightly, indicating that survey line 2 is in the bending subsidence zone. When the working face advances to 190 m, the vertical displacement of survey line

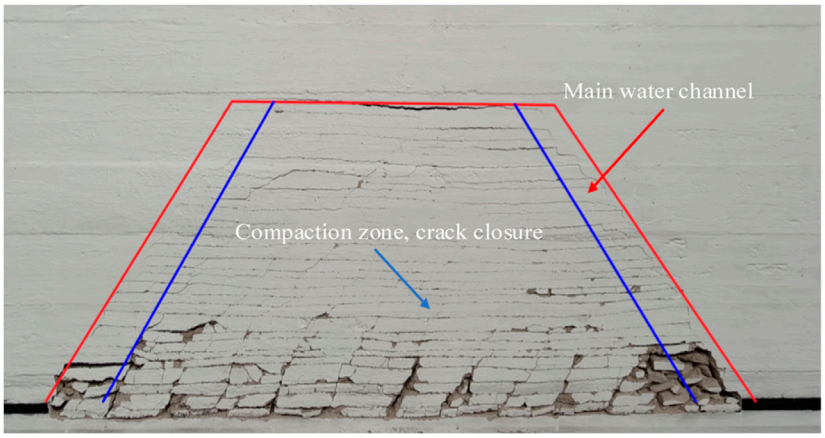

FIGURE 12
Main water channel in the fracture zone.

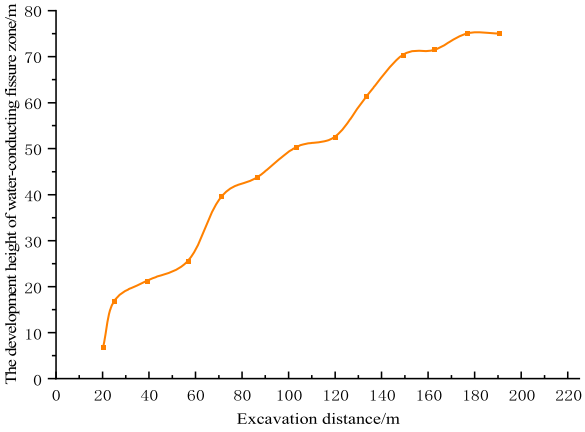

FIGURE 13
Distribution of the development height of the fracture zone with advancement of the working face.

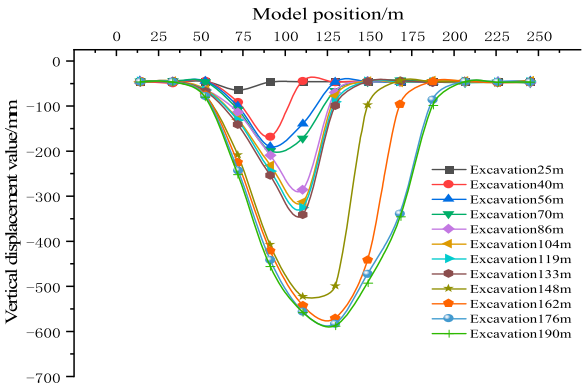

FIGURE 14
Vertical displacement curve at survey line 3.

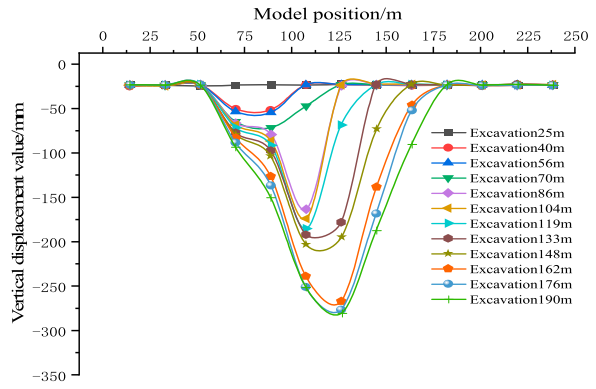

FIGURE 15
Vertical displacement curve at survey line 2.

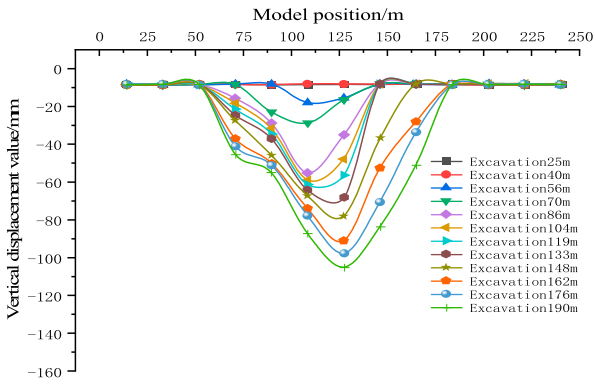

FIGURE 16
Vertical displacement curve at survey line 1.

2 reaches the maximum value, and the maximum subsidence displacement is 0.28 m.

Figure 16 shows the changes in the vertical displacements of measurement line 1 during coal-seam excavation. The vertical distance of survey line 1 from the coal-seam roof is 120 m, and its overall subsidence changes minimally. Survey line 1 is located in the curved subsidence zone; when the coal seam is excavated to 190 m, the subsidence does not change greatly, and the final maximum subsidence is 0.12 m.

5 Conclusion

To address the problem of deep-fault overlying rock breakage during the mining of ultra-thick coal seams, this study adopted numerical simulation and physical similarity simulation to compare and analyze the mining fracture evolution characteristics and overlying rock displacement laws of non-tectonic and fault-bearing overlying rock corresponding to fully mechanized caving mining based on the engineering background of the Yaoqiao Coal Mine; the failure characteristics and displacement laws of the overlying rock are thus systematically explained under the influence of deep faults. The main conclusions of this study are as follows:

(1) The fracture height of the overlying rock presents a specific change law with advancement of the working face: it rapidly increases to a maximum of 74 m at the initial stage (when the working face advances to 90 m), then decreases to 54 m and becomes stable with the development of the plastic zone indicating past yield, such that the final caving angle of the fracture is stable at 70°.

(2) In coal mining under normal fault conditions, when the working face advances from the upper to lower walls, the roof forms a masonry beam structure to slow down fault activation and crack development. When moving away from the fault, the overburden movements and water-conducting cracks are fewer, and the crack height is lower than that without faults. When approaching the fault, the influence of the faults on the fracture zone increases, and the height of fracture development reaches the maximum value after crossing the fault, highlighting the significant influence of the fault on fracture development.

(3) Through similarity simulation tests, it is seen that the caving zone of the overlying rock is compacted further and that a large area of roof caving occurs, resulting in rapid upward development of the cracks in the overlying rock along with gradual compaction and closure of the separation cracks in the central overlying rock. In the process of gradual advancement of the working face to 190 m, given the periodic breaking of the overlying rock, the vertical displacement measurement line changed in stages, and the final maximum subsidence value was 0.58 m.

Data availability statement

The raw data supporting the conclusions of this article will be made available by the authors, without undue reservation.

Author contributions

P-DZ: writing–original draft and writing–review and editing. Y-ZW: writing–original draft and writing–review and editing. Z-ZC: writing–review and editing. Z-HL: writing–review and editing. FD: writing–review and editing. W-QW: writing–review and editing. M-LZ: writing–review and editing.

Funding

The author(s) declare that financial support was received for the research, authorship, and/or publication of this article. This research was supported by the Natural Science Foundation of Henan Province (Grant Nos 222300420007 and 242300421246), the National Natural Science Foundation of China (Grant Nos 52004082, 52174073, and 52274079), the Key Supported Project of the National Natural Science Foundation of China Regional Innovation and Development Joint Fund (Grant No. U23A20600), the Science and Technology Project of Henan Province (Grant No. 232102321098), the Program for the Scientific and Technological Innovation Team in Universities of Henan Province (Grant No. 23IRTSTHN005), the Program for Science & Technology Innovation Talents in Universities of Henan Province (Grant No. 24HASTIT021), the Cultivation Project of "Double First-Class" Creation of Safety Discipline (Grant No. AQ20240724), and the Young Teacher Foundation of Henan Polytechnic University (Grant Nos 2023XQG-01 and 2019XQG-08).

Conflict of interest

Author P-DZ was employed by Shanghai Datun Energy Resources Co., Ltd.

The remaining authors declare that the research was conducted in the absence of any commercial or financial relationships that could be construed as a potential conflict of interest.

Publisher's note

All claims expressed in this article are solely those of the authors and do not necessarily represent those of their affiliated organizations, or those of the publisher, the editors, and the reviewers. Any product that may be evaluated in this article, or claim that may be made by its manufacturer, is not guaranteed or endorsed by the publisher.

References

Cai, Y., Ma, Y., Teng, T., Xue, Y., Wang, L., Cao, Z., et al. (2024). Risk assessment and analysis of rock burst under high-temperature liquid nitrogen cooling. *Water* 16 (4), 516–615. doi:10.3390/w16040516

Cheng, W., Sun, L., Wang, G., Du, W., and Qu, H. (2016). Experimental research on coal seam similar material proportion and its application. *Int. J. Min. Sci. Technol.* 26 (5), 913–918. doi:10.1016/j.ijmst.2016.05.034

Chen, L., Wang, Y., Qinghua, O. U., et al. (2021). Prediction model for development height of water-conducting fractured zone during mining near loose stratum considering influence of overburden structure: a case study of Huaibei coalfield. *J. Eng. Geol.* 29 (4), 1048–1056.

Guobiao, KANG, Bian, T., and Pingwu, P. U. (2021). Study on development height and influencing factors of overburden water conducting fracture zone in large mining height face. *Coal Sci. Technol.* 49 (S2), 19–24.

Heping, X. I. E., GuangmingYANG, Y. U. L., et al. (1999). Research on the fractal effects of crack network in overburden rock stratum. *Chin. J. Rock Mech. Eng.* 18 (2), 147–151.

Jialin, X. U., and Minggao, QIAN (2004). Study and Application of mining-induced fracture distribution in green mining. *J. China Univ. Min. Technol.* 33 (2), 17–20.

Jun, W., Han, J., Zhu, C., Lu, W., Zhang, Y., He, X., et al. (2024). Structural optimization and engineering application of concrete-filled steel tubular composite supports. *Eng. Fail. Anal.* 159, 108082. doi:10.1016/j.engfailanal.2024.108082

Kong, H., Wang, L., Gu, G., and Xu, B. (2018). Application of DICM on similar material simulation experiment for rock-like materials. *Adv. Civ. Eng.* 12 (1), 1–15. doi:10.1155/2018/5634109

Li, T. L., Zhao, W., Liu, R., Han, J., Jia, P., and Cheng, C. (2023). Visualized direct shear test of the interface between gravelly sand and concrete pipe. *Can. Geotechnical J.* 61, 361–374. doi:10.1139/cgj-2022-0007

Pengshuai, W., Zhengzheng, C., Zhenhua, L., Feng, D., Wenqiang, W., Minglei, Z., et al. (2024). Experimental research on mechanical performance of grouting plugging material with large amount of fly ash. *Sci. Rep.* 14, 6308. doi:10.1038/s41598-024-53623-x

Shao, L., and Yu, Z. (2018). Application of QGA-RFR model in prediction of height of water flowing fractured zone. *China Saf. Sci. J.* 28 (3), 19–24.

Teng, T., Li, Z., Wang, Y., Liu, K., and Jia, W. (2024). Experimental and numerical validation of an effective stress-sensitive permeability model under hydromechanical interactions. *Transp. Porous Media* 151, 449–467. doi:10.1007/s11242-023-02043-y

Wang, L. C., Xue, Y., Cao, Z., Kong, H., Han, J., and Zhang, Z. (2023c). Experimental study on mode I fracture characteristics of granite after low temperature cooling with liquid nitrogen. *Water* 15, 3442. doi:10.3390/w15193442

Wang, L. C., Zhang, W., Cao, Z., Xue, Y., Liu, J., Zhou, Y., et al. (2023b). Effect of weakening characteristics of mechanical properties of granite under the action of liquid nitrogen. *Front. Ecol. Evol.* 11. doi:10.3389/fevo.2023.1249617

Wang, W., Li, Z., Du, F., Cao, Z., and Li, G. (2023a). Untersuchung von Technologien zur Kontrolle von Wassereinbrüchen sowie der Nutzung von Wasserressourcen beim Kohleabbau in einem Karstgebiet. *Mine Water Environ.* 42, 546–559. doi:10.1007/s10230-023-00953-3

Wang, G., Guangming, Y. U., Yongjiang, Y. U., et al. (2012). Study on cracks fractal evolution laws of mining rock mass. *J. Mining&Safety Eng.* 29 (6), 859–863.

Wang, J., and Wang, X. (2021). Seepage characteristic and fracture development of protected seam caused by mining protecting strata. *J. Min. Strata Control Eng.* 3 (3), 033511.

Wei, L., Dang, F., Ding, J., Wu, X., Li, J., and Cao, Z. (2023). An analysis of thixotropic micropore variation and its mechanism in loess. *Front. Ecol. Evol.* 11. doi:10.3389/fevo.2023.1242462

Xingliang, L. I., and Qingxiang, HUANG (2022). High development characteristics of water flowing fractured zone in fully-mechanized top-caving mining of extremely thick coal seam under water. *J. Min. Saf. Eng.* 39 (01), 54–61.

Xue, Y., Wang, L., Liu, J., Ranjith, P. G., Gao, F., Cai, C., et al. (2024). Experimental study on the effect of heating and liquid nitrogen-cooling cyclic treatment on mechanical properties and fracturing characteristics of granite. *Int. J. Rock Mech. Min. Sci.* 176, 105691. doi:10.1016/j.ijrmms.2024.105691

Yongjiang, W., Zhengzheng, C., Zhenhua, L., Feng, D., Wenqiang, W., Minglei, Z., et al. (2024). Seepage evolution characteristics and water inrush mechanism in collapse column under mining influence. *Sci. Rep.* 14, 5862. doi:10.1038/s41598-024-54180-z

Zhang, H., Zhu, Z., Huo, B., et al. (2013). Water flowing fracture zone height prediction based on improved FOA-SVM. *China Saf. Sci. J.* 23 (10), 9–14.

Zhang, J., Wang, Z., and Song, Z. (2020). Numerical study on movement of dynamic strata in combined open-pit and underground mining based on similar material simulation experiment. *Arabian J. Geosciences* 13 (16), 785–800. doi:10.1007/s12517-020-05766-0

Zhang, P., Daqiang, X. U., Xiang, F. U., et al. (2022). Evaluation of hydraulic conductivity based on fault confinement studies. *J. Min. Strata Control Eng.* 4 (2), 023033.

Zhang, X., Zhengrong, X. U., Su, Z., et al. (2001). Study on computer simulation of fracture network in mined rock masses. *Chin. J. Rock Mech. Eng.* 20 (6), 809–812.

Zhao, L. (2022). Study on water inrush mechanism of overlying rock in mining face under fault action. *Coal Sci. Technol.* 50 (S1), 207–211.

Zhao, Y., Chunwei, L., Liu, B., et al. (2021). Fracture evolution and energy dissipation of overlying strata in shallow-buried underground mining with ultra-high working face. *J. Min. Saf. Eng.* 38 (1), 9–18.

Zheng, C., Pengshuai, W., Zhenhua, L., and Feng, D. (2024c). Migration mechanism of grouting slurry and permeability reduction in mining fractured rock mass. *Sci. Rep.* 14, 3446. doi:10.1038/s41598-024-51557-y

Zheng, C., Qiang, S., Zhenhua, L., and Feng, D. (2024b). Abnormal ore pressure mechanism of working face under the influence of overlying concentrated coal pillar. *Sci. Rep.* 14, 626. doi:10.1038/s41598-024-51148-x

Zheng, C., Xiangqian, Y., Zhenhua, L., and Feng, D. (2024a). Evolution mechanism of water-conducting fractures in overburden under the influence of water-rich fault in underground coal mining. *Sci. Rep.* 14, 5081. doi:10.1038/s41598-024-54803-5

Zheng, C., Yunlong, J., Zhenhua, L., and Feng, D. (2023). Research on slurry diffusion and seepage law in mining overburden fractures based on CFD numerical method. *Sci. Rep.* 13, 21302. doi:10.1038/s41598-023-48828-5

Zhiliang, L. I., Shugang, Ll, Lin, H., et al. (2017). Study of the dynamic evolution rules of mining fracture based on acoustic emission technique. *J. Xi'an Univ. Sci. Technol.* 37 (2), 159–163.

frontiers | Frontiers in Earth Science

TYPE Original Research
PUBLISHED 17 May 2024
DOI 10.3389/feart.2024.1388311

Check for updates

OPEN ACCESS

EDITED BY
Pengjiao Jia,
Soochow University, China

REVIEWED BY
Cheng Lyu,
Sichuan University, China
Lei Shi,
China University of Mining and Technology, Beijing, China
Shun Yi,
Changjiang River Scientific Research Institute (CRSRI), China

*CORRESPONDENCE
Chenxi Miao,
miaochenxi@tyut.edu.cn

†PRESENT ADDRESS
Wei Zhang,
China Railway 15th Bureau Group Urban Construction Design and Research Institute, Wuhan, China

RECEIVED 19 February 2024
ACCEPTED 09 April 2024
PUBLISHED 17 May 2024

CITATION
Pang D, Chen X, Gao M, Miao C and Zhang W (2024), Experimental study on the load bearing behavior of shored mechanically stabilized earth wall.
Front. Earth Sci. 12:1388311.
doi: 10.3389/feart.2024.1388311

COPYRIGHT
© 2024 Pang, Chen, Gao, Miao and Zhang. This is an open-access article distributed under the terms of the Creative Commons Attribution License (CC BY). The use, distribution or reproduction in other forums is permitted, provided the original author(s) and the copyright owner(s) are credited and that the original publication in this journal is cited, in accordance with accepted academic practice. No use, distribution or reproduction is permitted which does not comply with these terms.

Experimental study on the load bearing behavior of shored mechanically stabilized earth wall

Dongdong Pang[1], Xiaoyi Chen[2], Mengliang Gao[3], Chenxi Miao[1,3,4]* and Wei Zhang[5†]

[1]College of Civil Engineering, Taiyuan University of Technology, Taiyuan, China, [2]Shangqiu Institute of Technology, Shangqiu, China, [3]Shanxi Transportation Technology Research and Development Co., Ltd., Taiyuan, China, [4]Shanxi Key Laboratory of Civil Engineering Disaster Prevention and Control, Taiyuan, China, [5]Beijing Urban Construction Design and Development Group Co., Ltd., Beijing, China

Shored mechanically stabilized earth (SMSE) walls have been increasingly applied in the projects of widening existing roads or new construction of roads on slopes because of their good carbon emission reduction and mechanical performance. In this paper, a scaled-down model test of SMSE wall with shoring wall batter of 1H:2V was conducted to study the load-bearing behavior of SMSE wall under this terrain condition, and the results including wall deformations, earth pressures, reinforcement strains, and potential failure surface were analyzed. The results show that although the backfill near the shoring wall was not directly compressed by the load, it still slipped along the backfill-shoring wall interface. The loading created a tensile pressure zone in the upper part of the backfill-shoring wall interface, which may lead to tensile cracking. The uppermost layer of geogrid was more prone to sliding, while the tensile deformation was smaller, and its strain value was overall smaller than the strain value of the geogrid below it. As the load increases, the potential failure surface changed from a Rankine failure surface to a bilinear potential failure surface. The potential failure surface did not pass through the heel of the SMSE wall under large loads.

KEYWORDS

shored mechanically stabilized earth wall, model test, load bearing behavior, potential failure surface, failure mechanism

1 Introduction

With the development of the economy, the engineering control requirements for transportation infrastructure continue to increase (Lianpeng et al., 2021; Anvar, 2023; Boyang et al., 2023; Jia et al., 2024; Lu et al., 2024). As a flexible support structure with excellent force and deformation properties, low carbon emissions, simple construction and superior seismic performance, reinforced earth retaining wall have been extensively adopted in road embankment support (Miao et al., 2014; Yang et al., 2014; Costa et al., 2016; Fei ZHANG et al., 2021; Ren et al., 2022a; Chengzhi et al., 2023; Saalim and Samsunnahar, 2023). However, in the project of widening existing roads or new construction of roads on slopes in mountainous areas, due to space constraints, it is difficult for traditional reinforced soil retaining walls to meet the requirements of reinforcement length stipulated by the relevant specifications (0.7H, where H is the height of the wall) (Berg et al., 2009; BSI. BS

8006-1:, 2010, 2010). Therefore, shored mechanically stabilized earth (SMSE) walls have been developed for use in such projects (Lee et al., 2010; Yang et al., 2011; Xu et al., 2016a; Ren et al., 2022b). More information on the construction of SMES walls can be found in the design guidelines of the Federal Highway Administration (FHWA) (Morrison et al., 2006).

Due to the existence of existing slopes/structures (hereafter referred to as shoring wall) and a smaller width-to-height ratio (the ratio of the length of reinforcement to the height of the wall) than that of a conventional reinforced earth retaining wall, the SMES wall exhibits different mechanical behaviors. Lawson and Yee (2005) concluded from theoretical analysis that due to the limited space in the backfill zone, the horizontal earth pressure coefficient in the backfill zone is larger than that of a conventional horizontal earth pressure coefficient. And he found that the failure surface of SMSE walls were the "single-line" type, but the failure surface inclination was greater than that of the Rankine failure surface. Woodruff (2003); Lee et al. (2010) observed through centrifuge model tests that the failure surfaces of the SMSE walls were the "double-line" type. However, Yang et al. (2011) found that the failure surface of the SMSE walls are related to the width-to-height ratio. With the increase of the width-to-height ratio, the failure surface of the SMSE walls were transformed from "double-line" type to the "single-line" type. And at low width-to-height ratios, the failure surface formed partially through the reinforced soil and partially along the interface between the reinforced soil and the shoring wall. In addition, Yang et al. (2008) used the finite element program Plaxis to simulate the centrifuge test of the SMSE wall, and found that there was a zero pressure zone at the upper part of the interface between the backfill zone and the shoring wall, and that with the narrowing of the backfill zone, the zero pressure zone was extended to the lower part of the retaining wall. Xu et al. (2016b) found through centrifugal model tests of SMSE wall that there was only contact stress between reinforced soil and shoring wall. As the wall height or top load increased, the SMSE wall deformed significantly and was prone to collapse.

To enhance the stability of SMSE walls, it is common to connect the reinforcement to the shoring walls or to extend the length of the upper reinforcement of the retaining walls. Xu et al. (2016c) concluded that connecting the reinforcement to the shoring walls can compensate for the lack of reinforcement length, reduce the deformation, and improve the overall stability. Ren et al. (2022b) investigated the load-bearing response of SMSE walls with different types of connections and relative densities of fillers, and demonstrated that increasing the relative density and adopting sandwich-type reinforcement arrangement can reduce the deformation of the retaining walls. However, Morrison et al. (2006) concluded that the benefits of connecting the reinforcement to the shoring walls are minimal and have little effect on retaining wall deformation and stability. And he suggested extending the two layers of geogrids at the top of the SMSE wall to 0.6H to enhance the stability of the SMSE wall.

In the current studies of SMSE walls, the shoring walls are often vertical or minimally sloped, so the reinforcement length of the SMSE wall bottom and top is basically the same, both of which are relatively shorter. However, in actual projects, a large number of shoring walls are gently sloping, and the length of the two layers of reinforcement at the top of the SMSE walls constructed in this terrain is longer than 0.6 H. The stability and mechanical behavior of the SMSE walls in this terrain condition (The slope of the shoring wall is relatively gentle) are still not clear. Therefore, in this paper, a scaled-down model test of SMSE wall with shoring wall batter of 1H:2V (horizontal: vertical) was performed to investigate the load bearing behaviors of the SMSE wall under this terrain condition. At this batter (1H:2V), the length of the two layers of reinforcement at the top of the SMSE wall is greater than 0.6 H even though the base width of the SMSE wall reinforcement section is 0.3 H (the minimum base width value recommended by the code) (Morrison et al., 2006). The test results including the wall deformation, soil pressure, reinforcement strain, and potential fracture surfaces are analyzed. The results of this study can provide insights into the application of SMSE walls in this terrain condition and the need for re-strengthening.

2 Experimental program

2.1 Model configuration

The SMSE wall model has a height of H = 1.4 m and are designed for 1/5-scale (scaling factor λ = 5) model. The SMSE wall height corresponds to a height of 7 m for the prototype structure, which is a typical height for field SMSE wall (Morrison et al., 2006; Ren et al., 2022b). Based on the identified length scaling factor λ=5 and the similarity theory (Yuan, 1998), the similarity relationships for other physical quantities are derived as shown in Table 1, which has been adopted in many previous 1-g reduced-scale model tests of reinforced earth structure (Xiao et al., 2016; Yoo et al., 2022; Deng et al., 2023).

The SMSE wall model structure and dimensions is shown in Figure 1. The panel was placed above the concrete footing at an angle of 4° to the plumb plane, which is within the typical range of field SMSE wall panel inclination (Morrison et al., 2006; Lee et al., 2010; Ren et al., 2022b). The vertical spacing of the reinforcements is 0.1 m, which corresponds to a typical vertical spacing of 0.5 m for the prototype SMSE wall. This vertical spacing (0.5 m) complies with the maximum recommended vertical reinforcements spacing of 0.6 m for SMSE walls (Morrison et al., 2006). And their length is determined by the distance between the panel and the shoring wall at a given level. A base width of 0.4 m for the reinforced section is selected, which is closed to the minimum required reinforcement length of 0.3 H (Morrison et al., 2006). The shoring wall is constructed at a batter of 1H:2V (horizontal: vertical) behind the reinforced section. The reinforcement is not connected to the shoring wall.

The SMSE wall model is constructed in a steel model box with inner dimensions of 1.6 m × 1.0 m × 1.6 m (length × width × height). Loading of the model is accomplished by a loading system that precisely controls the magnitude of the applied load. During the test, the load is transferred to the SMSE wall through a loading plate, which is made of 10 mm thick steel plate welded together. The model box and loading system are shown in Figure 2. Tempered glass was assembled on one side of the model box to dynamically monitor the deformation and damage behavior of the model. The sidewalls of the model box and the outside of the bottom plate were set with channel steel skeleton, and no significant deformation of

TABLE 1 Similitude relationships for 1-g reduced-scale model test.

Physical quantity	Unit	Scaling factor (Prototype/Model)	Scale factor used in this study (Prototype/Model)
Length	m	λ	5
Density	kg/m^3	1	1
Stress	kPa	λ	5
Strain	1	1	1
Reinforcement strength	kN/m	λ^2	25
Reinforcement stiffness	kN/m	λ^2	25
Modulus	kPa	λ	5
friction angle	—	1	1

[a]λ: symbolized the scale of prototype to physical model (in present study its equals 5).

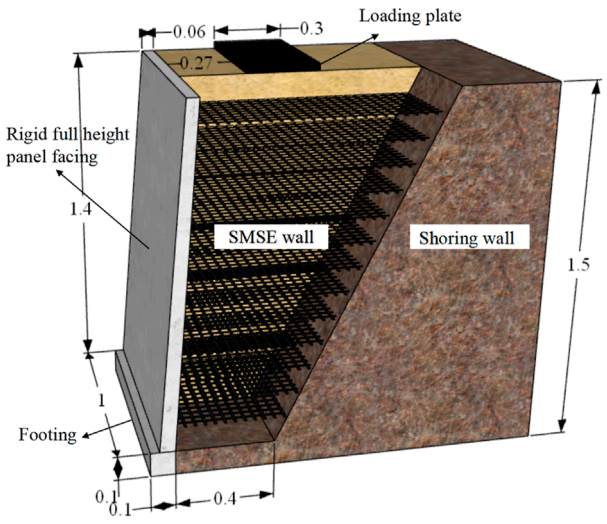

FIGURE 1
SMSE wall model and dimensions (unit: m).

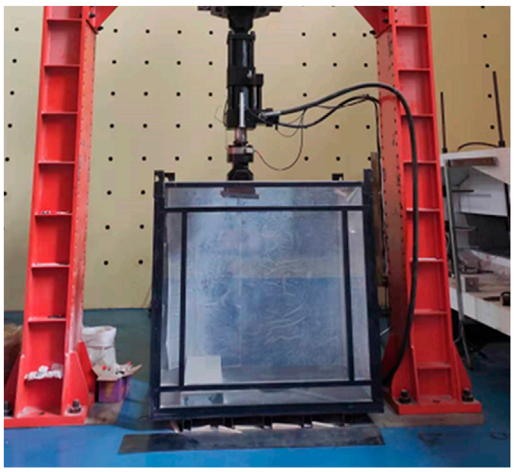

FIGURE 2
Model box and loading system.

the model box was observed in the range of loading amplitude in this test. To reduce the friction between the sidewalls of the model box and the filling material and to fulfill the requirement of plane strain, the internal sidewalls of the model box were coated with PTFE film.

2.2 Model materials

2.2.1 Shoring wall

In this test, the shoring wall is primarily a topographical construct and there is no requirement for its material to be similar to that of the prototype structure. The shoring wall model in this test was made of river sand, gypsum powder, and water mixed uniformly by the mass ratio of 8.5:1.5:1.3, and the density of the mixed material is 2.06 g/cm^3. The gypsum retarder of 6‰ mass of water was incorporated into the mixture, which ensured that the mixture would not undergo incipient coagulation during the shoring wall shaping process. The measured uniaxial compressive strength of the mixture after hardening is 919.8 kPa.

2.2.2 Backfill material

In this test, river sand with water content of 0.3% was used as backfill soil. The maximum particle size of sandy soil in this experiment is 5 mm, and the grain size distribution of river sand is shown in Figure 3. Its uniformity coefficient (Cu) and coefficient of curvature (Cc) are 4.78 and 0.80, respectively. The maximum and minimum dry densities of sandy soil are 1.96 g/cm^3 and 1.44 g/cm^3, respectively. And the dry density was controlled at 1.764 g/cm^3 (70% relative density) during filling, which has been widely used in current reinforced soil structure model tests (Jun et al., 2022; Deng et al., 2023). Based on the

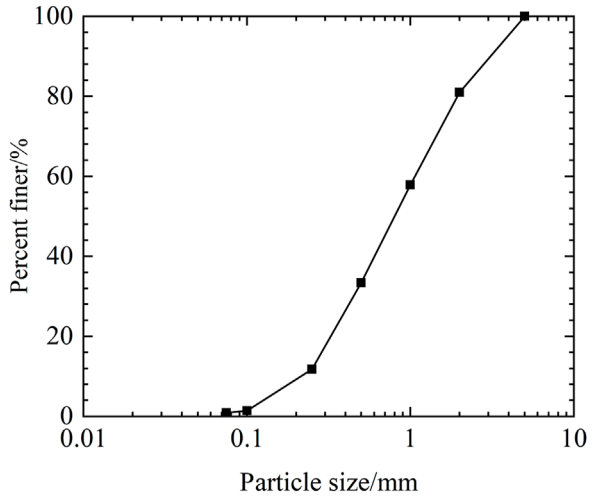

FIGURE 3
Grain size distribution of the backfill soil.

triaxial consolidated drained shear test and interpretation of the linear Mohr-Coulomb failure envelope, the internal friction angle of the sandy soil at this density is 45.3° assuming zero cohesion (Figure 4).

2.2.3 Reinforcement

Reinforcement adopted glass fiber bi-directional geogrid with thickness of 0.9 mm and mesh size of 40 mm×40 mm. The ultimate tensile strength is 6 kN/m and the ultimate tensile strain is 9.5% as measured by the single-rib tensile test (Figure 5). The tensile stiffness corresponding to 2% and 5% elongations of the geogrids are 100 kN/m and 79.4 kN/m, respectively, which correspond to 2,500 kN/m and 1985 kN/m for the prototype geogrids according to the scaling factor in this study (see Table 1), which are in the typical range of geogrid used for MSE walls in the field (Liu et al., 2017; Xu et al., 2021).

2.2.4 Footing and panel

The footing and panel both were cast from C30 concrete. The footing is a solid strip rectangle with dimensions of 100 mm × 100 mm × 1,000 mm.

The dimensions of the panel and the finished model are presented in Figure 6. The interior of the panels was equipped with a reinforcing mesh made of 8 mm diameter steel bars. A row of L-shaped hooks for the mechanical connection of the panels to the geogrid was arranged at intervals of 100 mm in the height direction. There are five hooks in each row, with a lateral distance of 200 mm, and the distance of the hooks on both the left and right sides from the edge of the corresponding side panel is 90 mm.

2.3 Test instrumentation

In this test, linear variable differential transformers (LVDT), pressure cells, and strain gauges were adopted to monitor the wall top settlement, the facing displacement, the earth pressure, and the tensile strain of the geogrid, respectively. The data monitored by each component was collected via the XL2101GE40 static data collector. Figure 7 shows the actual picture of each monitoring component and the data collector. Figure 7A shows the LVDT with a measuring range of −50 mm–50 mm and a test accuracy of 0.01 mm; Figure 7B shows the pressure cells with a diameter of 16 mm, a measuring range of 0 kPa–1,000 kPa, and an accuracy of 0.5% FS; Figure 7C shows the strain gauges patch with a sensitivity coefficient of 2.22% ± 1% and a resistance value of 120.1 ± 0.1Ω; Figure 7D shows the XL2101GE40 static data collector, which has a total of 40 channels and can simultaneously collect multiple types of data such as earth pressure, strain, displacement, etc. In this experiment, two identical data collector of this type were used.

The layout of instrumentation of the model are shown in Figure 8. All sensors were installed on the centerline section in the out-of-plane direction of the model. The earth pressure cell P1 is 20 mm away from the panel, and the lateral spacing of P1-P4 is 130 mm. The earth pressure cells (P5-P9) at the backfill-shoring wall interface were placed close to the shoring wall, with the same inclination as the shoring wall. Thel earth pressure cells (P10-P14) behind the panels are 20 mm away from the panels. Thel earth pressure cells (P15-P18) underneath the loading plate are 420 mm away from the panel. Strain gauges were attached to the 1st, 4th, 7th, 10th and 13th layers of geogrids (Geogrid layers are numbered from bottom to top). The spacing between the first strain gauge and the panel in each layer of the geogrid is 60 mm, and the horizontal spacing of each strain gauge is 120 mm.

2.4 Model preparation

The main procedures for model preparation are as follows.

(1) Placement of footing and panel, the footing was fixed by wooden cubes, and the outer side of the panel was limited by wires and wooden cubes.
(2) Fill the shoring wall in layers, the thickness of each layer is 50 mm. And the slope of the shoring wall was precisely controlled by the method of overfilling first and then cutting the slope.
(3) Fill the sandy soil of backfill area in layers according to the determined density, and the thickness of each layer is 50 mm. Geogrids and panel were mechanically connected: The cross ribs of the mesh at the end of the geogrids were linked to the steel bars through ties, and the steel bars were placed on the panel hooks, which can ensure the reliability of the mechanical connection and at the same time make the tension of the reinforcement being transferred uniformly to the wall, as shown in Figure 9.
(4) Remove the wire and wooden cubes holding the panel. The finished test model is presented in Figure 10.

2.5 Loading scheme

In this test, a hydraulic servo actuator was used to apply a graded loading to the top bar loading plate of the wall. the load increment Δp is 20 kPa for each level from 0 to 200 kPa, and Δp

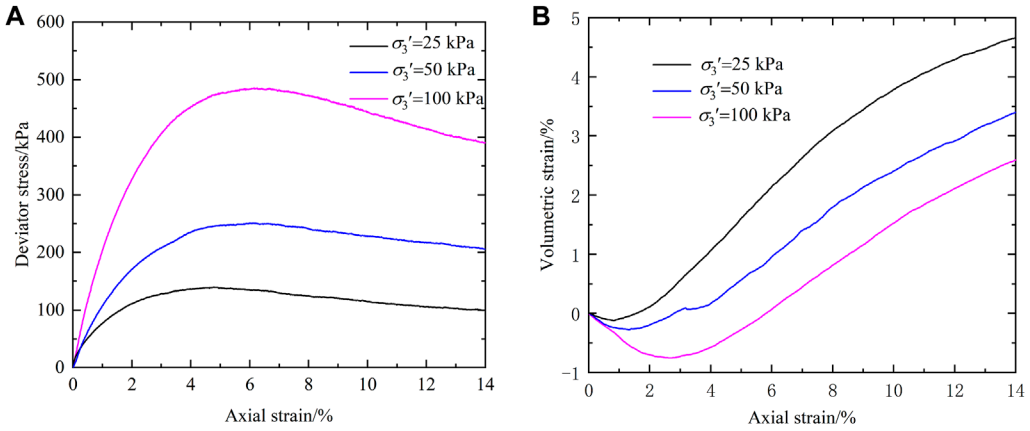

FIGURE 4
Triaxial compression test results: **(A)** deviator stress versus axial strain; **(B)** volumetric strain versus axial strain.

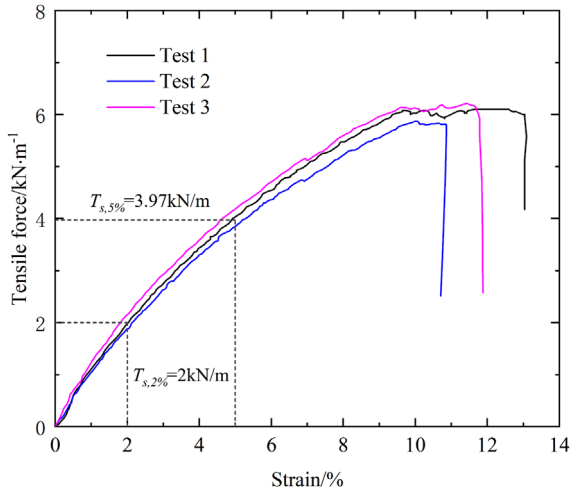

FIGURE 5
Single rib tensile tests for geogrid.

is 50 kPa for each level after 200 kPa. The time interval between each level of loading during the test is 30 min to ensure the model to reach the static equilibrium state. When there is a sudden increase in the displacement of the SMSE wall panel or the wall top settlement under a certain level of loading, it is considered that the SMSE walls reach the load-bearing limit and the loading is stopped.

3 Results and discussion

Experimental results including the wall top settlement, facing displacements, vertical and lateral earth pressures, and reinforcement tensile strains for the SMSE wall under different applied vertical stresses are discussed and analyzed. Test results are incremental values with respect to the values after construction.

3.1 Facing displacements

The distribution of horizontal displacements of the facing along the wall height under various levels of loading is illustrated in Figure 11. The horizontal displacement of the facing is linearly distributed along the wall height. The facing displacement is dominated by the rotation around the heel of the wall accompanied by a smaller translational movement. Therefore, the horizontal displacement at the top of the panel is the largest under all levels of loading. Specifically, the top displacement under a 400 kPa load reaches 30.7 mm (2.19% of the wall height), of which the translational displacement is 3.5 mm. Figure 12 shows the curve of horizontal displacement of the top of the facing with load. It can be seen that when the load is less than 350 kPa, the rate of increase of horizontal displacement at the top of the facing with increasing load remains constant, and the rate of increase of displacement increases significantly when the load is in 350–400 kPa.

3.2 Settlement at the top of the SMSE wall

Figure 13 presents the settlement distribution of the top of the wall under various levels of loading. It can be seen that the top of the wall under the load produces different degrees of settlement at various locations, which increases with the increase of the additional load. Among them, the settlement below the loading plate is larger, and the settlement on both sides of the loading plate is not uniform. The settlement difference increases with increasing load. The backfill near the panel and the shoring wall is not directly extruded by the load, so the settlement is small compared with that under the loading plate. At the end of the test, the backfill near the panel produces a localized collapse with a width of about 60 mm, as indicated in Figure 14A. From the relationship between localized collapse and the position of L6, it can be seen that L6 can not fully reflect the settlement at that location. Compared with the data measured by L6 (settlement value of 3.6 mm under 400 kPa load), the backfill

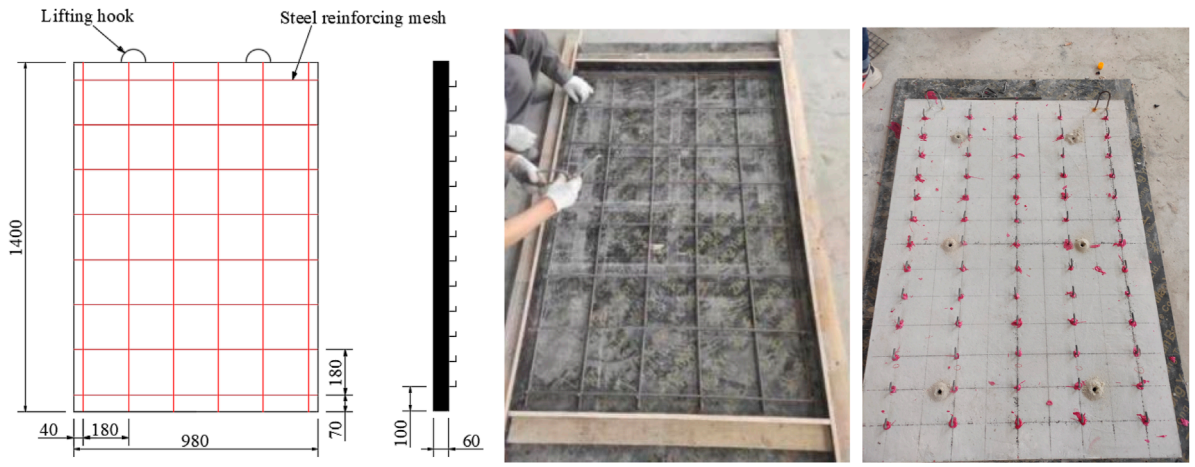

FIGURE 6
Panel size and panel actual picture (unit: mm).

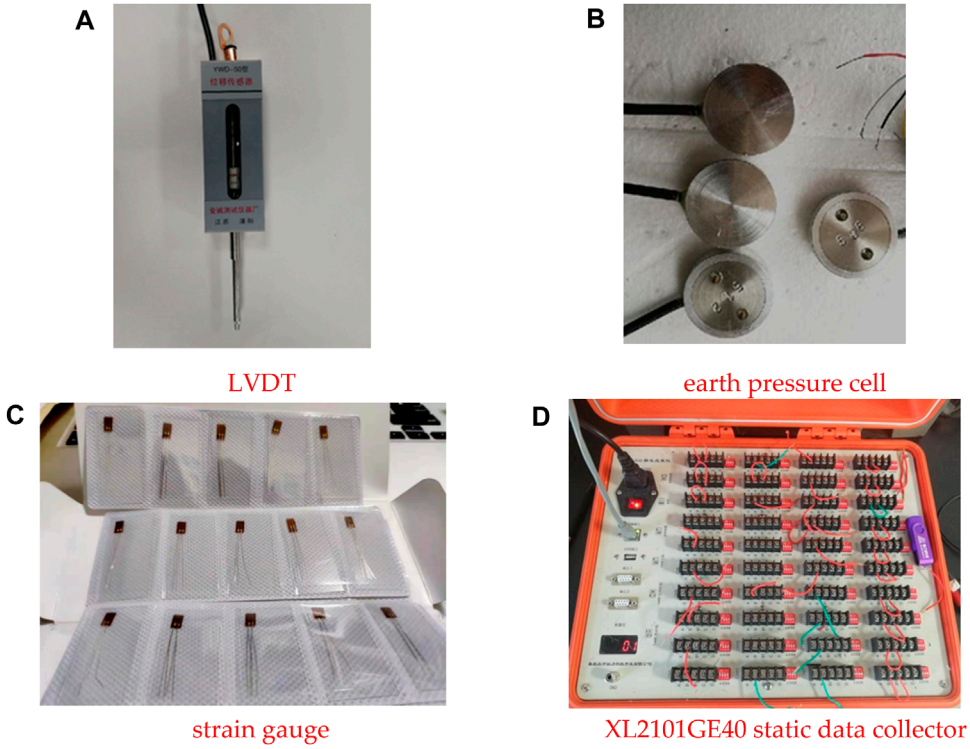

FIGURE 7
Physical pictures of LTVD, earth pressure cell, strain gauge and XL2101GE40 static data collector.

soil settlement value at this location is larger. The settlement at this location is due to the large horizontal displacement of the panel. The indentations caused by settlement of backfill soil can be observed near the support wall, as shown in Figure 14B. L9 has effectively monitored the settlement value of the backfill soil at this location. Under a load of 400 kPa, the settlement value at this location is 4.9 mm, indicating a slight sliding of backfill soil l along the backfill soil support wall interface.

Figure 15 presents the load-settlement curves of the loaded plate, where the settlement is calculated as the mean value of the displacements (L7 and L8) measured at the two edges of the loaded plate. When the load is less than 350 kPa, the settlement increases linearly with the increase of load. However, the settlement increases sharply when the load is increased to 400 kPa, at which time the settlement value is 35 mm, and the corresponding vertical strains are 2.5% for the 1.4 m-high retaining wall. It can be seen from

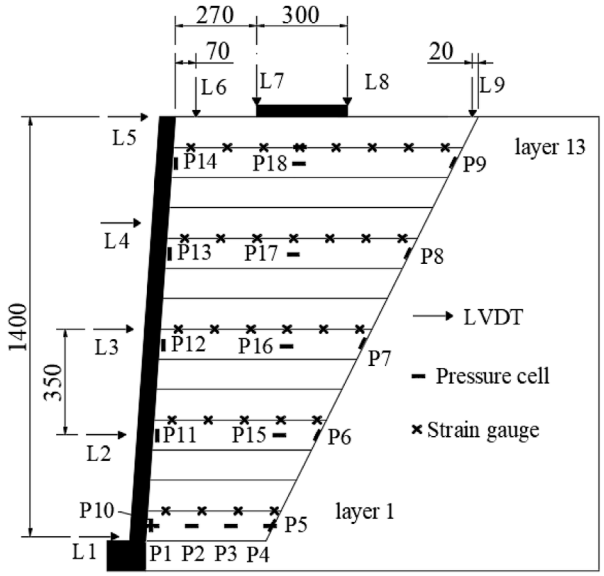

FIGURE 8
Instrumentation layout (unit: mm).

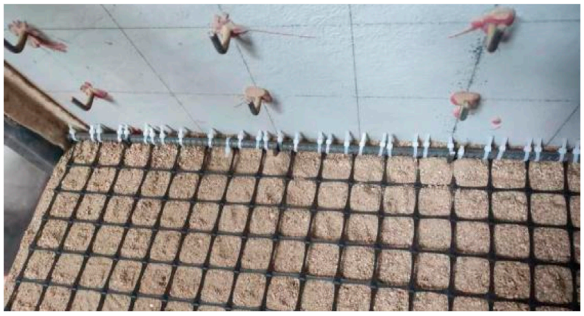

FIGURE 9
Mechanical connection between geogrids and panel.

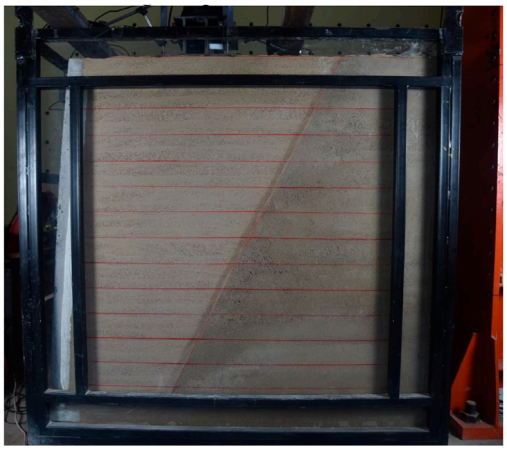

FIGURE 10
SMSE wall model.

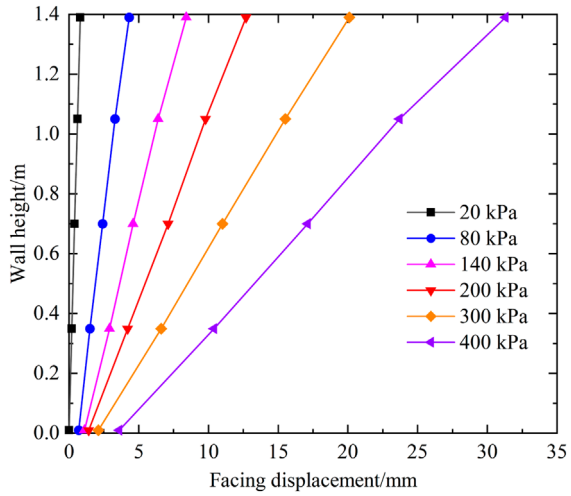

FIGURE 11
Distribution curve of panel displacement along wall height.

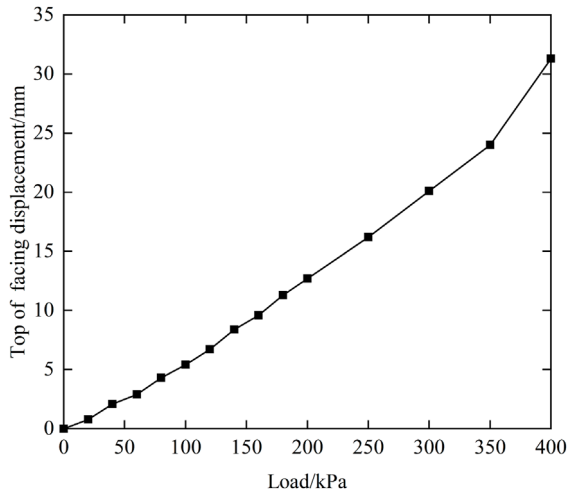

FIGURE 12
Variation curve of horizontal displacement with loading at the top of the facing.

the displacement curve of the facing (Figure 12) and the settlement curve of the top of the wall (Figure 15) that the model reaches its bearing limit when 400 kPa load is applied.

3.3 Earth pressure

3.3.1 Earth pressure at backfill-shoring wall interface

Figure 16 shows the distribution curve of earth pressure along the wall height at the backfill-shoring wall interface under additional load. It can be seen that the earth pressure generated by the additional load at the interface is prominent at P8 (location see Figure 8), and the earth pressures in the rest locations are relatively small. The earth pressure at P8 is as high as 110 kPa under the

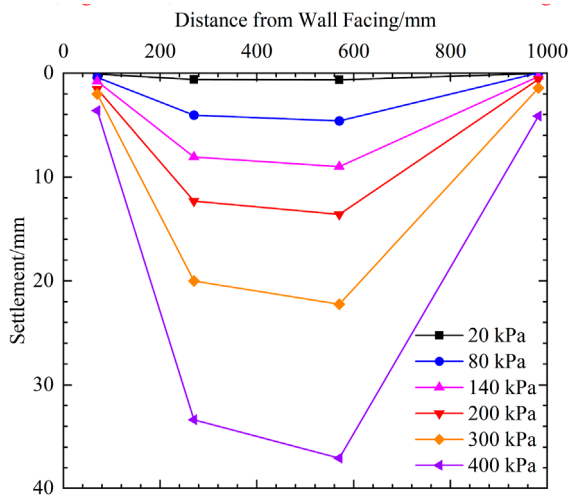

FIGURE 13
Top settlement distribution of the SMSE wall.

load of 400 kPa, which may result in the extruded damage of the shoring wall. The earth pressure at P7 increases dramatically after applying a 400 kPa load, which is due to the large deformation of the SMSE wall and the redistribution of earth pressure within the backfill.

Overall, the earth pressure at this interface tends to increase with the increase of additional loads for both condition sets. However, it is worth noting that an anomaly in the earth pressure occurs at P9. After the load was applied, the earth pressure at this point continues to decrease, with a negative value,i.e., the earth pressure there under surcharge load is less than the soil pressure generated by the soil's self-weight there. A similar phenomenon was also observed in the numerical simulation of the SMSE wall by Yang et al. (Yang et al., 2008). The results demonstrate that there is a tensile pressure zone at the upper part of the backfill-shoring wall interface, which may produce tensile cracks. On the one hand, the tensile pressure zone is generated because the geogrid at this location produce a large pullout displacements under the additional load, and the backfill soil on both sides of the geogrid moves toward the panel under friction. On the other hand, since the lateral displacement of the upper part of the panel is large, the backfill soil of the upper layer slides along the direction of the panel. The test indicates that even if the slope of the shoring wall is small enough to make the upper reinforcement of SMSE wall larger than 0.6 H, it is still difficult to avoid the generation of tensile pressure zone. Therefore, it is still necessary to connect the geogrid with the support cantilever or extend the length of the reinforcement further.

3.3.2 Vertical earth pressure under loading plate

The distribution curve of vertical earth pressure along the depth below the loading plate under additional load is shown in Figure 17. The earth pressure at the depth of 1.35 m presented in the figure is the measured value at P3. It is observed that the earth pressure decreases with the increase of depth, and the earth pressure decreases faster in a certain depth range in the upper part of the retaining wall, and decreases less in the middle and lower parts. In the process of load application, the distribution pattern of earth pressure along the depth of the retaining wall generally remains unchanged.

Figure 17 also shows the calculated incremental vertical earth pressure using both the 2:1 distribution recommended by the FHWA for SMSE wall (Morrison et al., 2006) and the Boussinesq solution recommended by the FHWA for the GRS-IBS (Page, 2018). Comparison of the theoretical calculated and measured earth pressures indicates that the Boussinesq solution is able to accurately predict the earth pressures over the entire depth range for loads no more than 40 kPa. As the load increases, the Boussinesq solution is small compared to the test values except for the uppermost part. This is because the effect of shoring wall on the transfer of vertical earth pressure increases with the increase of load, while the Boussinesq solution does not take into account the effect of shoring wall on earth pressure transfer. The Boussinesq solution correctly predicts the value of additional earth pressure in the upper part of the SMSE wall for the full range of loads. This is because the upper part of the retaining wall is wider and the effect of the shoring wall is smaller. The 2:1 distribution takes into account the effect of the shoring wall on the spread of earth pressure, so it is more accurate in the upper and middle parts of the retaining wall. However, the reduction of the width of the reinforced area in the lower part of the retaining wall fails to increase the measured earth pressure as the theoretically calculated value. Comparison of the measured earth pressures with the Boussinesq solution and the 2:1 distribution shows that the diffusion of additional earth pressures in the deeper part of the retaining wall increases to some extent due to the effect of the shoring wall, but the current 2:1 distribution for the SMSE wall clearly overestimates this effect.

3.3.3 Vertical earth pressure at the bottom of the wall

The variation curve of vertical earth pressure at the bottom of SMSE wall with additional load is illustrated in Figure 18. It is observed that the vertical earth pressure at the bottom of the wall all increases with the increase of additional load. The vertical earth pressures at the bottom of the wall are all nonlinearly distributed along the length of the geogrid, with larger values in the center and decreasing toward the panel and shoring wall. The small value of earth pressure at P4 suggests that an arch may exist near the shoring wall at the bottom of the wall.

In examining the foundation load-bearing capacity of the SMSE wall, the FHWA design guidelines (Morrison et al., 2006) assumes that the additional earth pressures generated by the load are uniformly distributed at the bottom of the wall, and that the uniformly distributed additional earth pressures are calculated using a 2:1 distribution. Figure 19 illustrates the comparison between the tested and theoretical values of earth pressure in the middle of the wall bottom. Comparison of the theoretically calculated values with the measured values reveals that the use of 2:1 distribution calculated values is too conservative in examining the load-bearing capacity of the foundation.

3.3.4 Horizontal earth pressure behind the panel

Figure 20 presents the distribution curve of horizontal earth pressure along the depth of the SMSE wall behind the panel wall. The horizontal earth pressure increases with the increase of

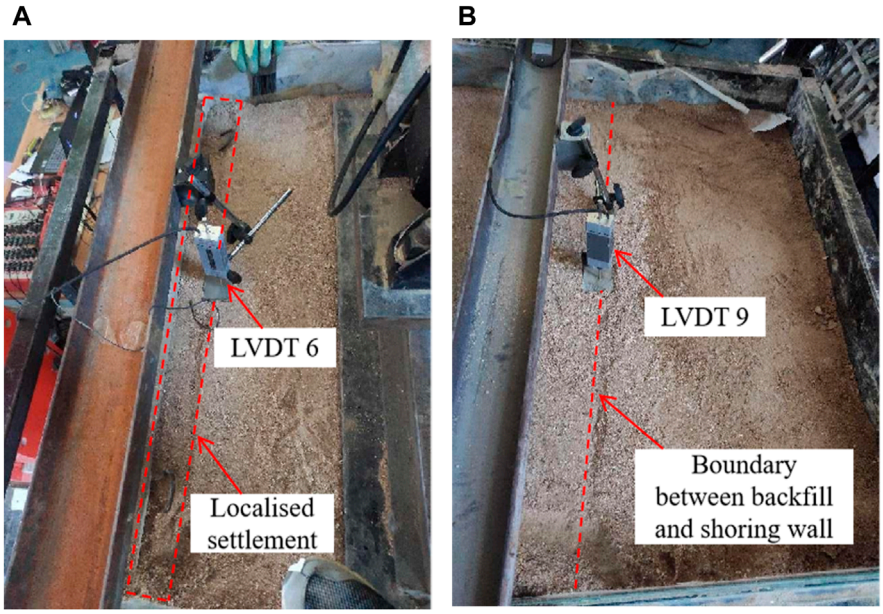

FIGURE 14
Localized settlement at the top of the wall. **(A)** Settlement near panel **(B)** Settlement near shoring wall.

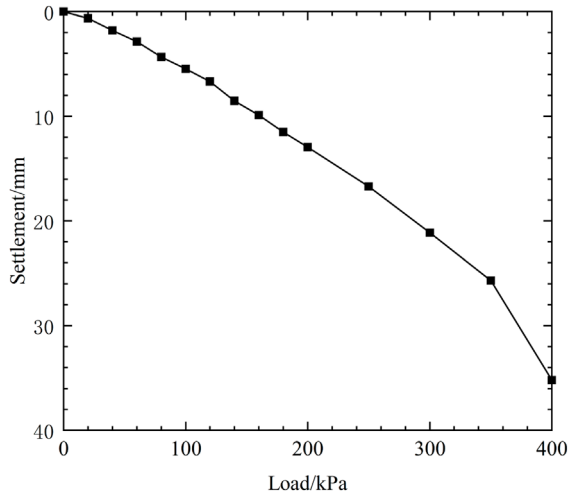

FIGURE 15
Load-settlement curves for loaded plate.

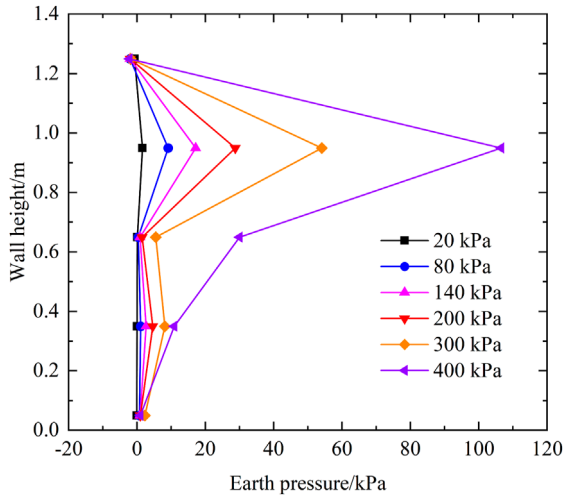

FIGURE 16
Distribution curve of earth pressure along the wall height at the backfill-shoring wall interface.

load, and it increases first and then decreases along the depth of the SMSE wall. When the load of 400 kPa was applied, the peak point of horizontal earth pressure shifts downward, which may be related to the inclination of the loading plate. The pattern of horizontal earth pressure distribution wall is generally similar to that measured in Ahmadi's (Ahmadi and Bezuijen, 2018) full-scall test of conventional rigid-faced reinforced earth retaining wall, but there is a difference at the toe of the wall. Ahmadi et al. measured an increasing trend of horizontal earth pressure at the toe of the wall compared to the upper part of the wall, whereas the present test continues to be smaller along the depth. This is due to the weak restraint at the bottom of the panel. The lateral displacement of the bottom of the panel under load released some of the earth pressure.

3.4 Geogrid strains and potential failure surface

Figure 21 illustrates the distribution of geogrid strains along the length of the geogrid. When 300 kPa load was applied, the strain gauges in the upper geogrid failed more, so Figure 21 only shows the strain distribution of geogrids below 300 kPa load. However, at

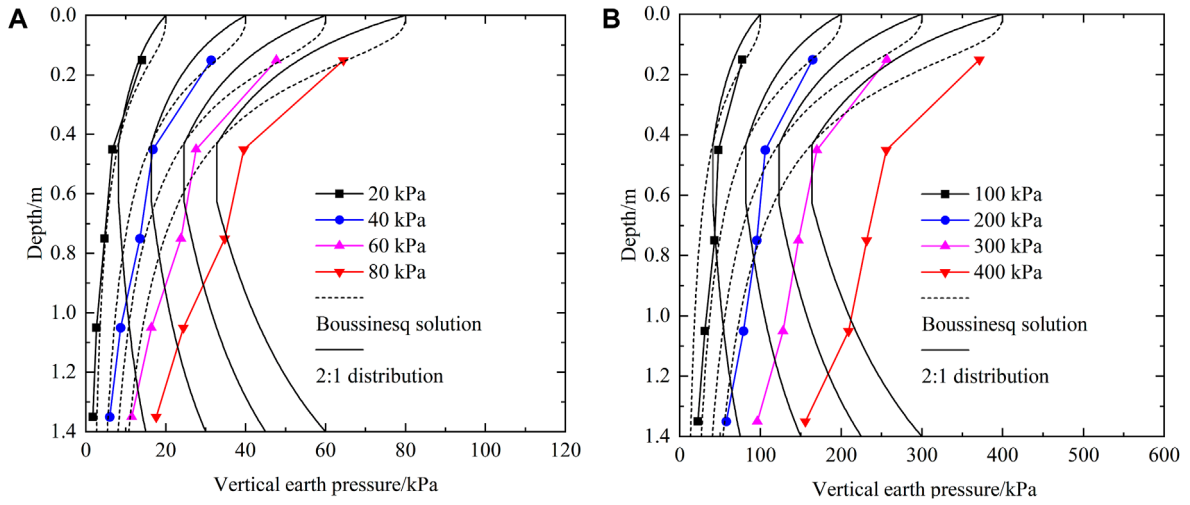

FIGURE 17
Vertical earth pressure distribution curve along the depth under loading plate. **(A)** Applied vertical stresses ranging from 20 kPa to 80 kPa; **(B)** Applied vertical stresses ranging from 100 kPa to 400 kPa.

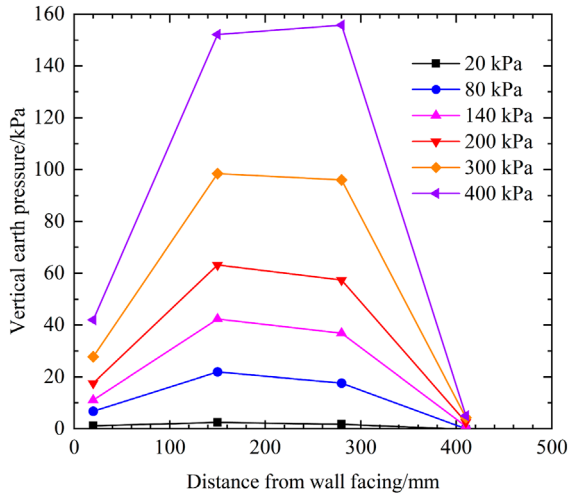

FIGURE 18
Earth pressure distribution curve at the bottom of the SMSE wall.

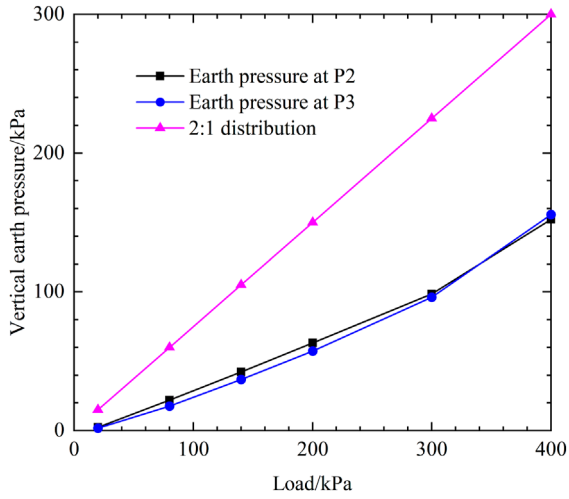

FIGURE 19
Comparison between the tested and theoretical values of vertical earth pressure.

the end of the test, no fracture was observed in all layers of geogrids. The geogrid strain increases with the increase of the additional load. Despite the fact that the displacement is greatest in the upper part of the panel and the additional stress decreases with depth, the maximum geogrid strain does not occur in the uppermost layer of geogrids. The strains in the 10th layer of geogrids under all levels of loading in this test are generally larger than those in the 13th layer. This may be due to the shallower overburden on the upper part of the retaining wall and the insufficient friction between the geogrids and the fill, which makes the geogrids more prone to sliding and less to tensile deformation.

When the 160 kPa load was applied, the strain distribution pattern of geogrid changed: with the increase of load, the strain peak of geogrid became more obvious, and the peak shifted to the direction of *in situ* slope. A reasonable prediction of the potential failure surface of the retaining wall based on the peak geogrid strain is illustrated by the red connecting line in Figure 21. When the load does not exceed 140 kPa, the potential failure surface of the retaining wall is consistent with the shape of the Rankine failure surface, which coincides with the potential failure surface of the SMSE wall as recommended by the FHWA design guidelines (Morrison et al., 2006). When the load exceeds 140 kPa, the potential failure surface changes to a bilinear potential failure surface. And the potential failure surface is closer to the shoring wall, which means that the "Resistant Zone" decreases, and the grating resistance to pullout is weakened. In addition, from the peak strain of the lowermost layer of geogrids, it is determined that the potential failure surface does not pass through the heel of the wall under large loads.

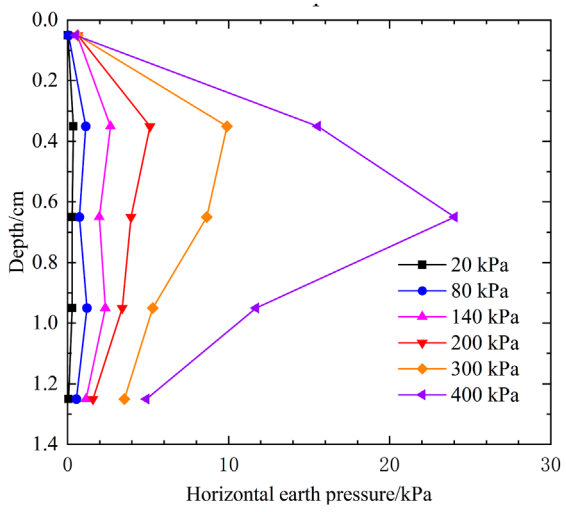

FIGURE 20
Horizontal earth pressure distribution curve behind the panel.

3.5 Failure mechanism of the model

For SMSE wall with rigid full height panel facing, internal stability failure is mainly manifested by geogrid rupture or pullout (i.e., geogrid sliding in the backfill) (Morrison et al., 2006). At the end of the test (when the model reached its load-bearing limit), no rupture of the geogrid was observed in any of the layers, indicating that the sudden change in panel displacement was due to the insufficient pullout resistance provided by the geogrid. And the pullout resistance of the geogrid is provided by the friction between the geogrid and its surrounding soil beyond the failure surface of the model.

When the load is small (not more than 140 kPa in this test condition), the potential failure surface is consistent with the Rankine failure surface (Figure 21A), which indicates that potential shear failure occurring throughout the entire depth range. With the increase of the load, the failure mechanism is a combination of punching shear failure of the loading plate and internal shear failure of the lower soil body. Therefore, the potential failure surface is characterised by a vertical downward progression (punching shear failure), followed by a failure surface consistent with the Rankine failure surface, which develops downward from the location of the punching shear failure within the soil (Figure 21B). It should be noted that the potential failure surface of the model is closer to the shoring wall for large loads (>140 kPa) (Figure 21), which means that the geogrid beyond the failure surface that can provide pullout resistance becomes shorter. This indicates that as the additional load increases, not only does the tensile force of the panel on the geogrid increase, but the pullout resistance of the geogrid also deteriorates.

In addition, there is a risk that the model slides along the backfill-shoring wall interface. For the SMSE wall studied in this experiment (the slope of the shoring wall is relatively gentle), although the backfill slipped a little along the backfill-shoring wall interface, its sliding displacement is small, and the model dose not collapse before a sudden change in panel displacement. The failure of the model is mainly due to the pullout failure caused by the insufficient length of the geogrid. For the SMSE wall studied in this paper, the geogrid should be connected to the shoring wall to enhance the pullout resistance of the geogrid.

4 Conclusion

In this paper, a scaled-down model test of SMSE wall with shoring wall batter of 1H:2V is performed to study the load-bearing behavior of SMSE walls under this terrain condition, and the results including wall deformations, earth pressures, reinforcement strains, and potential failure surface are analyzed. The following conclusions are drawn:

(1) When the SMSE wall reached its load-bearing limit (400 kPa), the maximum horizontal displacement of the facing and the settlement of the top of the wall are 2.19% and 2.5% of the wall height, respectively. The backfill near the shoring wall, although not directly compressed by the load, also settled to some extent, which indicated that the backfill slip along the interface of the backfill - shoring wall.

(2) A tensile pressure zone exists at the upper part of the backfill-shoring wall interface under surcharge load, i.e., the earth pressure there under surcharge load is less than the earth pressure generated by the soil's self-weight there, which may lead to tensile cracks.

(3) The vertical earth pressure generated by the additional load below it decays faster in the upper part of the SMSE wall and less in the middle and lower parts of it. The Boussinesq solution accurately predicts the vertical earth pressure generated by the additional load below it when the load is small, and as the load increases, the Boussinesq solution without considering the effect of the shoring wall on earth pressure transfer is small compared to the measured value. The 2:1 distribution considering the effect of shoring wall accurately predicted the vertical earth pressure generated by the additional load in the upper and middle parts of the SMSE wall, but overestimated this effect at the bottom of the retaining wall, and the theoretical value was much larger than the measured value.

(4) Vertical earth pressures at the bottom of the SMSE wall are all nonlinearly distributed along the length of the geogrid, with larger values in the middle part and decreasing toward the panel and the shoring wall. The earth pressure values at the bottom of the shoring wall are extremely low, which suggests that arching may be present at this location. The current 2:1 distribution adopted by FHWA to examine the load-bearing capacity of foundations is overly conservative.

(5) The maximum geogrid strain does not appear in the uppermost layer of the geogrid, which may be because the upper part of the retaining wall is covered with shallow soil, and the friction between the geogrid and the filling is insufficient, so the geogrids are more prone to sliding, and the tensile deformation is less. As the load increases, the potential failure surface changes from a Rankine failure surface to a bilinear potential failure surface. At the same time the potential rupture

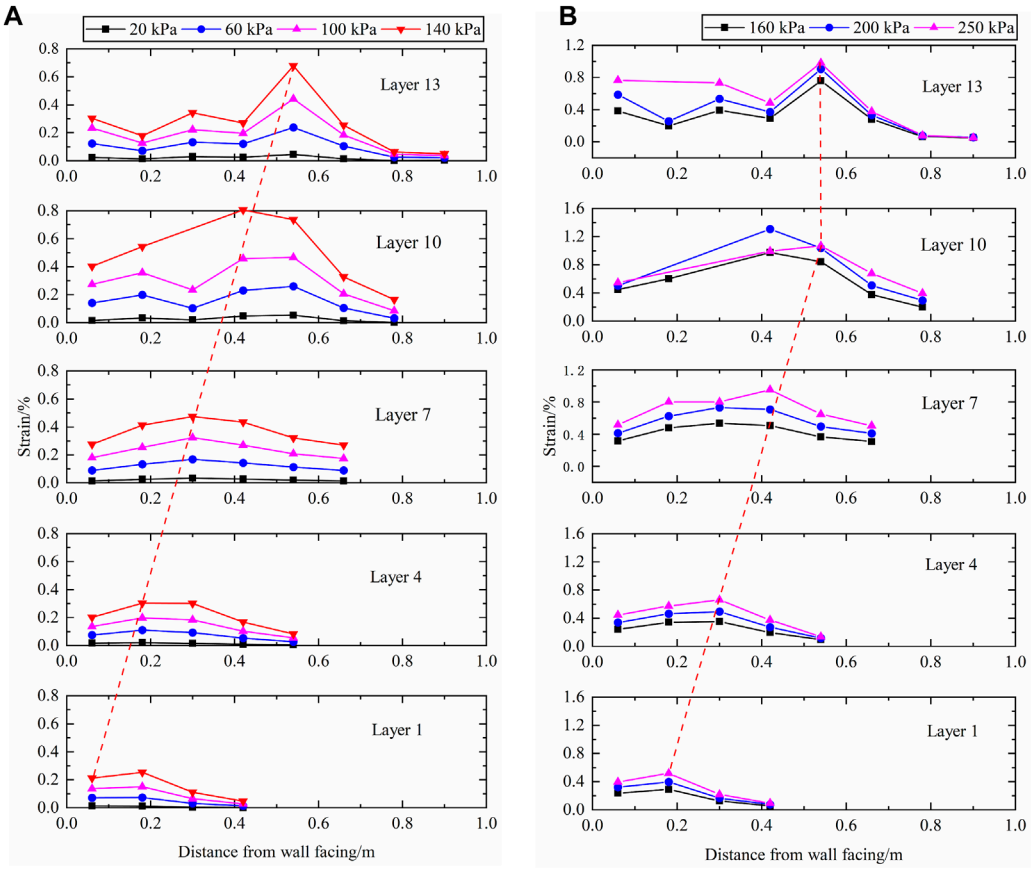

FIGURE 21
Geogrid strain distribution curve. **(A)** applied vertical stresses ranging from 20 kPa to 140 kPa; **(B)** applied vertical stresses ranging from 160 kPa to 250 kPa.

surface is close to the shoring wall, which implies a weakening of the geogrid's resistance to pullout. The potential failure surface did not pass through the heel of the wall under large loads.

Data availability statement

The raw data supporting the conclusion of this article will be made available by the authors, without undue reservation.

Author contributions

DP: Project administration, Writing–original draft. XC: Validation, Writing–original draft. MG: Formal Analysis, Writing–original draft. CM: Funding acquisition, Writing–review and editing. WZ: Writing–review and editing.

Funding

The author(s) declare that financial support was received for the research, authorship, and/or publication of this article. This research was supported by the National Natural Science Foundation of China (Nos 52178341; 52278360; 51809191) and Shanxi Province Basic Research Program Project (202303021224001).

Acknowledgments

The authors are appreciative to the external reviewers for their insightful and constructive comments.

Conflict of interest

Authors MG and CM were employed by Shanxi Transportation Technology Research and Development Co., Ltd. Author WZ was employed by Beijing Urban Construction Design and Development Group Co., Ltd.

The remaining authors declare that the research was conducted in the absence of any commercial or financial relationships that could be construed as a potential conflict of interest.

Publisher's note

All claims expressed in this article are solely those of the authors and do not necessarily represent those of their affiliated organizations, or those of the publisher, the editors and the reviewers. Any product that may be evaluated in this article, or claim that may be made by its manufacturer, is not guaranteed or endorsed by the publisher.

References

Ahmadi, H., and Bezuijen, A. (2018). Full-scale mechanically stabilized earth (MSE) walls under strip footing load. *Geotext. Geomembranes* 46, 297–311. doi:10.1016/j.geotexmem.2017.12.002

Anvar, C. (2023). A way to determine the positive direction of the shear force on the elemental area. *Geohazard Mech.* 1, 179–184. doi:10.1016/j.ghm.2023.04.004

Berg, R. R., Christopher, B. R., and Samtani, N. C. (2009). *Design and construction of mechanically stabilized earth walls and reinforced soil slopes*. Washington, DC, USA: Federal Highway Administration Publication US Department of Transportation.

Boyang, Z., Gang, L., Yingchun, L., and Zhibin, L. (2023). Experimental study on the seepage mutation of natural karst collapse pillar (KCP) fillings over mass outflow. *Environ. Sci. Pollut. Res.* 30, 110995–111007. doi:10.1007/s11356-023-30230-3

BSI. BS 8006-1: 2010 (2010). *Code of practice for strengthened/reinforced soils and other fills*. London, UK: British Standards Institution BSI.

Chengzhi, Q., Chunsheng, L. A. I. C., Xiaozhao, L., Xiaolei, Q., and Qu, X. (2023). Preliminary study on the determination of the Weibull modulus of strength distribution in quasi-brittle materials. *Geohazard Mech.* 1, 103–109. doi:10.1016/j.ghm.2023.05.002

Costa, C. M. L., Zornberg, J. G., de Souza Bueno, B., and Costa, Y. D. J. (2016). Centrifuge evaluation of the time-dependent behavior of geotextile-reinforced soil walls. *Geotext. Geomembranes* 44, 188–200. doi:10.1016/j.geotexmem.2015.09.001

Deng, J., Zhang, J., Qi, Z., Zheng, Y., and Zheng, J.-j. (2023). Experimental study on the load bearing behavior of geosynthetic reinforced soil bridge abutments on yielding foundation. *Geotext. Geomembranes* 51, 165–178. doi:10.1016/j.geotexmem.2023.06.003

Fei Zhang, Y.-m.Z., Yang, S.-chuan, and Wang, S.-mao (2021). Emission mitigation analysis of geosynthetic▪reinforced walls. *J. Jilin Univ. Technol. Ed.* 51, 631–637. doi:10.13229/j.cnki.jdxbgxb20191141

Jia, Y., Zhang, J., Tong, L., Zheng, J.-J., and Zheng, Y. (2024). Human vulnerability assessment based on bullet motion and cavity expansion model with tissue identification. *Geosynth. Int.*, 1–15. doi:10.1080/10255842.2023.2294263

Jun, Z., Yafei, J., Wenhao, G., Jianbin, Z., Jianming, L., and Yewei, Z. (2022). Experimental study on the load bearing behavior of geosynthetic reinforced soil bridge abutments with different facing conditions. *Geotext. Geomembranes* 50, 632–643. doi:10.1016/j.geotexmem.2022.03.004

Lawson, C., and Yee, T. (2005). "Reinforced soil retaining walls with constrained reinforced fill zones," in *Proceedings of the slopes and retaining structures under seismic and static conditions* (China: Slopes and Retaining Structures Under Seismic and Static Conditions), 1–14.

Lee, Y.-B., Ko, H.-Y., and McCartney, J. (2010). Deformation response of shored MSE walls under surcharge loading in the centrifuge. *Geosynth. Int.* 17, 389–402. doi:10.1680/gein.2010.17.6.389

Lianpeng, D., Yishan, P., Zhonghua, L., Aiwen, W., Yonghui, X., Feiyu, L., et al. (2021). Quantitative mechanism of roadway rockbursts in deep extra-thick coal seams: theory and case histories. *Tunn. Undergr. Space Technol. incorporating Trenchless Technol. Res.* 111, 103861. doi:10.1016/j.tust.2021.103861

Liu, Z., Shi, K.-y., and Huang, T.-q. (2017). Field test of static and dynamic response of reinforced earth retaining wall under vehicle load. *Hydrogeology Eng. Geol.* 44, 91–97. (in chinese). doi:10.16030/j.cnki.issn.1000-3665.2017.04.14

Lu, B., Sheil, B. B., Zhao, W., Jia, P., Bai, Q., and Wang, W. (2024). Laboratory testing of settlement propagation induced by pipe-roof pre-support deformation in sandy soils. *Tunn. Undergr. Space Technol. incorporating Trenchless Technol. Res.* 146, 105645. doi:10.1016/j.tust.2024.105645

Miao, L., Wang, F., Han, J., and Lv, W. (2014). Benefits of geosynthetic reinforcement in widening of embankments subjected to foundation differential settlement. *Geosynth. Int.* 21, 321–332. doi:10.1680/gein.14.00019

Morrison, K. F., Harrison, F. E., Collin, J. G., Dodds, A. M., and Arndt, B. (2006). *Shored mechanically stabilized earth (SMSE) wall systems design guidelines*. Lakewood, CO, USA: US Department of Transportation, Federal Highway Administration. Publication No. FHWA-CFL/TD-06-001.

Page, T. R. D. (2018). *Design and construction guidelines for geosynthetic reinforced soil abutments and integrated bridge systems*.

Ren, F., Huang, Q., and Chen, J. (2022a). Centrifuge modeling of geosynthetic-reinforced soil retaining walls subjected to the combined effect of earthquakes and rainfall. *Geotext. Geomembranes* 50, 470–479. doi:10.1016/j.geotexmem.2022.01.005

Ren, F.-f., Xu, H., Ji, Y.-j., Huang, Q.-q., and Tian, X. (2022b). Experimental study on the mechanical behavior of shored mechanically stabilized earth walls for widening existing reinforced embankments. *Geotext. Geomembranes* 50, 737–750. doi:10.1016/j.geotexmem.2022.03.013

Saalim, S. M., and Samsunnahar, P. (2023). An assessment of earthquake vulnerability by multi-criteria decision-making method. *Geohazard Mech.* 1, 94–102. doi:10.1016/j.ghm.2022.11.002

Woodruff, R. (2003). *Centrifuge modeling for MSE-shoring composite walls* (Boulder, CO, USA: Univ. of Colorado). MS Thesis.

Xiao, C., Han, J., and Zhang, Z. (2016). Experimental study on performance of geosynthetic-reinforced soil model walls on rigid foundations subjected to static footing loading. *Geotext. Geomembranes* 44, 81–94. doi:10.1016/j.geotexmem.2015.06.001

Xu, C., Luo, Y.-s., Chen, H.-s., and Jia, B. (2016a). Effects of interface connections on narrowed mechanically stabilized earth walls. *Environ. Earth. Sci.* 75, 1411. doi:10.1007/s12665-016-6226-9

Xu, C., Luo, Y.-s., Chen, H.-s., and Jia, B. (2016c). Effects of interface connections on narrowed mechanically stabilized earth walls. *Environ. Earth Sci.* 75, 1411. doi:10.1007/s12665-016-6226-9

Xu, C., Luo, Y.-s., and Jia, B. (2016b). Effects of connection forms on shored mechanically stabilized earth walls by centrifugal model tests. *Chin. J. Geotechnical Eng.* 38, 180–186. doi:10.11779/CJGE201601020

Xu, H., Xia, L., and Ren, X. (2021). Experimental study on reinforced retaining wall with wrapped face on high embankmen. *J. Highw. Transp. Res. Dev.* 38, 70–77. (in chinese). doi:10.3969/j.issn.1002-0268.2021.06.010

Yang, G.-Q., Liu, H., Zhou, Y.-T., and Xiong, B.-L. (2014). Post-construction performance of a two-tiered geogrid reinforced soil wall backfilled with soil-rock mixture. *Geotext. Geomembranes* 42, 91–97. doi:10.1016/j.geotexmem.2014.01.007

Yang, K., Kniss, K., Zornberg, J., and Wright, S. (2008). "Finite element analyses for centrifuge modeling of narrow MSE walls," in Proceedings of the Proceedings of First Pan American Geosynthetics Conference, GEOAMERICAS, USA, February 5-8, 2023 (IEEE).

Yang, K.-H., Zornberg, J. G., Hung, W.-Y., and Lawson, C. R. (2011). Location of failure plane and design considerations for narrow geosynthetic reinforced soil wall systems. *J. Geoeng.* 6, 27–40.

Yoo, C., Tabish, A., Yang, J., Abbas, Q., and Song, J. (2022). Effect of internal drainage on deformation behavior of GRS wall during rainfall. *Geosynth. Int.* 29, 137–150. doi:10.1680/jgein.21.00015

Yuan, W.-z. (1998).*Similarity theory and hydrostatic modeling tests*. USA: Southwest Jiao tong University Press. in chinese.

frontiers | Frontiers in Earth Science

TYPE Hypothesis and Theory
PUBLISHED 21 May 2024
DOI 10.3389/feart.2024.1403663

Check for updates

OPEN ACCESS

EDITED BY
Xiaoyu Bai,
Qingdao University of Technology, China

REVIEWED BY
Hong Zheng,
Chinese Academy of Sciences (CAS), China
Arif Ali Baig Moghal,
National Institute of Technology
Warangal, India

*CORRESPONDENCE
Li Shi,
lishi@zjut.edu.cn

RECEIVED 19 March 2024
ACCEPTED 29 April 2024
PUBLISHED 21 May 2024

CITATION
Liang X, Xu J, Huang Y, Shi L, Zeng Z, Miao B, Huang L and Wu J (2024), Consolidation effects on pipe-soil interaction due to tunneling.
Front. Earth Sci. 12:1403663.
doi: 10.3389/feart.2024.1403663

COPYRIGHT
© 2024 Liang, Xu, Huang, Shi, Zeng, Miao, Huang and Wu. This is an open-access article distributed under the terms of the Creative Commons Attribution License (CC BY). The use, distribution or reproduction in other forums is permitted, provided the original author(s) and the copyright owner(s) are credited and that the original publication in this journal is cited, in accordance with accepted academic practice. No use, distribution or reproduction is permitted which does not comply with these terms.

Consolidation effects on pipe-soil interaction due to tunneling

Xu Liang[1], Jian Xu[1], Yong Huang[2,3], Li Shi[4]*, Zhiquan Zeng[2,3], Baozhu Miao[4], Lei Huang[2,5] and Jian Wu[2,5]

[1]Hangzhou Urban Infrastructure Construction Management Center, Hangzhou, Zhejiang, China, [2]Power China Huadong Engineering Corporation Limited, Hangzhou, Zhejiang, China, [3]Zhejiang Huadong Engineering Construction and Management Corporation Limited, Hangzhou, Zhejiang, China, [4]College of Civil Engineering, Zhejiang University of Technology, Hangzhou, Zhejiang, China, [5]Zhejiang Engineering Research Center of Green Mine Technology and Intelligent Equipment, Hangzhou, Zhejiang, China

Existing studies on soil-pipe interaction due to tunneling mainly focus on short-term responses. However, in areas with high water tables and low permeability soil, long-term ground movement and associated pipe responses may occur due to dissipation of excess pore pressure generated during tunnel construction. In this paper, a Winkler solution with time-varying subgrade modulus and the corresponding greenfield soil displacement formula are developed to investigate the tunneling effects on existing pipelines. The pipe is considered as an infinite Euler beam of finite width resting on a poroelastic half-space, and adhesion and drainage effects between the pipe and soil are considered using bounding techniques. The greenfield consolidation settlement is evaluated using a modified Gaussian curve. The findings indicate that the subgrade modulus decreases while greenfield soil displacement increases during the consolidation process. The time-dependent behavior of the subgrade modulus is governed by the drainage condition at the pipe-soil interface, whereas the greenfield soil displacement is primarily influenced by the drainage condition at the tunnel-soil interface. The study reveals that the bonded contact condition, hydraulic boundary condition, and displacement constraint conditions all influence the bending moment of the pipe.

KEYWORDS

seepage consolidation, winkler solution, tunneling effects, existing pipelines, bending moment

1 Introduction

The tunnel construction causes volume loss of soil, and the surrounding soil deforms into the gap between the tunnel wall and lining. Ground deformation causes soil settlement around nearby underground facilities, e.g., the existing pipelines. The pipe suffers deformation and bending moment when it is subjected to the soil settlement. To guide the design of protective measures on the pipelines, it is of vital importance to develop predictive methods to evaluate the tunneling effects on the existing pipelines.

The core of the problem at hand is the pipe-soil-tunnel interaction, of which a complete description generally requires a continuum-theory based model including the three objects at the same time. The most widely adopted approach should be the finite element method (FEM). By discretizing the pipeline and soil in to shell and solid elements, respectively,

Klar and Marshall (2008) investigated the deformation of the pipeline when subjected to a nearby tunneling construction. Based on a similar modeling technique, Marshall et al. (2010) simulated the pipeline deformation caused by tunnel underpass and compared to the observed mechanical behavior from a centrifugal model test. Wang et al. (2011) conducted parameter analysis using finite element software and obtained the relationship between the normalized bending moment of the pipeline and the relative stiffness coefficient between the pipe and soil. However, the preparing of FEM model and mesh could be cumbersome especially at the design stage, which involves a lot of parametric studies. Meanwhile, the finite element method is less effective in identifying nondimensional parameters governing the pipe-soil-tunnel system. Alternatively, the existing studies on this problem generally decouple the pipe from tunnel by adopting relaxing assumptions, e.g., the pipe does not affect the tunnel when the tunneling-induced ground displacement happens (Mair et al., 2005); and the soil response to pipe loading at the pipe level is not aware of the tunnel (Vorster et al., 2005).

With the above assumptions, the problem was solved using a two-step method in the literature: i) obtain the ground displacement profile at the pipeline level (i.e., the so-called greenfield soil displacement); ii) solve the pipe soil interactions using the greenfield displacement as input.

At step i), only the tunnel and the ground are involved. The tunneling induced ground displacement was evaluated using either field observation method (Mair et al., 1993), Peck (1969) and Schmidt (1969), after processing a large amount of surface settlement data, believe that the cross-sectional surface settlement curve caused by tunnel excavation can also be represented by a Gaussian curve, analytical method (Loganathan and Poulos, 1998) or numerical method (Wongsaroj et al., 2013). Based on field observations, the tunneling-induced ground settlement is commonly fitted into empirical formulas, e.g., a Gaussian curve (Peck, 1969). However, in some cases the Gaussian curve is not satisfactory to accurately describe the soil settlement (Celestino et al., 2000). Later, the Gaussian curve was modified by Voster et al. (2005) and by Wei (2013) to admit more flexibility in adjusting the shape of the ground settlement profile. It is noted that the existing studies on the tunneling induced ground displacement are generally focused on the short-term response, which is caused by undrained shear deformation of soil happen immediately after the tunnel construction. In comparison, the long-term ground displacement would happen with the dissipation of excess pore water pressure induced by tunneling. Actually, when the pore water flows to the new drainage boundary imposed by the tunnel, the soil consolidates, and the consolidation of the soil leads to certain changes in the parameters of the soil, which in turn leads to continued settlement of the soil (Venkata Vydehi et al., 2022). Moreover, changes in the nature of the soil can have an effect on the consolidation of the soil (Moghal et al., 2020). It is demonstrated by Stallebrass et al. (2000) that the long-term settlement (i.e., by the seepage consolidation) can be 30% larger than the short term for soils of low permeability. In this paper, we will consider the soil settlement due to the seepage consolidation effect of the soil after shield excavation.

At step ii), the interaction problem between the pipe and soil is solved using the tunneling-induced soil displacement as inputs. The conventional approach for this problem is the Winkler-based models (Attewell et al., 1986), i.e., the pipe is governed by the Euler beam theory; and the soil is represented by a series of individual springs connected to the beam. If the soil is modeled as a continuum, this problem can be solved in a more rigorous manner, which leads to the elastic continuum solution developed by Vorster et al. (2005). Later, the continuum-based solution has been extended to include the effects of pipe joints (Klar et al., 2008) and elastoplastic behaviors (Klar et al., 2007) on the pipeline responses.

When the Winkler-based model is adopted, the appropriate spring coefficient (i.e., the subgrade stiffness) is of vital importance for the accurate prediction of pipeline responses. Attewell et al. (1986) suggested the use of Vesic (1961) equation for the subgrade modulus. After comparing to the elastic continuum solution, Klar et al. (2007) suggested a new equation for the subgrade modulus. By considering the embedding depth of pipes, Yu et al. (2013) proposed different equations for the subgrade modulus. It is noted that the existing equations for the subgrade modulus are obtained for the pipe (modeled as Euler beam) interacting with an elastic continuum (representing the soil). As a result, the subgrade modulus does not change with time (i.e., the pore water and seepage are not considered). However, as mentioned in the above, the soil would experience seepage consolidation, and thus the subgrade modulus is subjected to change with the consolidation process.

To sum up, the two-step method is commonly adopted to evaluate the tunneling effects on existing pipelines, in which both the greenfield soil displacement and the subgrade modulus are important intermediate results; however, they are generally evaluated for the short-term responses. Once the soil layer that the tunnel and pipelines are buried is of relatively low permeability, the seepage consolidation of soil after the tunnel construction would become important, and thus the time-dependent greenfield displacement and subgrade modulus should be considered.

In this paper, a Winkler solution with time-varying subgrade modulus and the greenfield soil displacement is developed to investigate the tunneling effects on existing pipelines. In evaluating the subgrade modulus, the pipe is treated as an infinite Euler beam of finite width resting on a poroelastic halfspace. The influence of adhesion and drainage effects between the pipe and soil is considered by bounding techniques for prescribing the boundary conditions on the interface. As for the tunneling-induced consolidation settlement, the evaluation method proposed by Laver et al. (2017) is followed. Based on the developed Winkler solution, the time-dependent bending moment responses of the existing pipeline induced by the tunneling can be evaluated.

2 Analysis model and assumptions

The tunneling induced deformation of the ground and pipeline is schematically shown in Figure 1. A new tunnel of diameter D is excavated under an existing pipeline of diameter d. The tunnel excavation generates soil displacement around the pipeline, which causes the pipe to deform and suffer bending moment. The burying depth of the pipe and tunnel (measured to the centerline) are denoted as z_0 and h $(h \geq z_0)$, respectively. The centerlines of tunnel and pipe are considered vertical to each other, which represents the most unfavorable case of the tunneling effect on pipelines (Attewell, 1981).

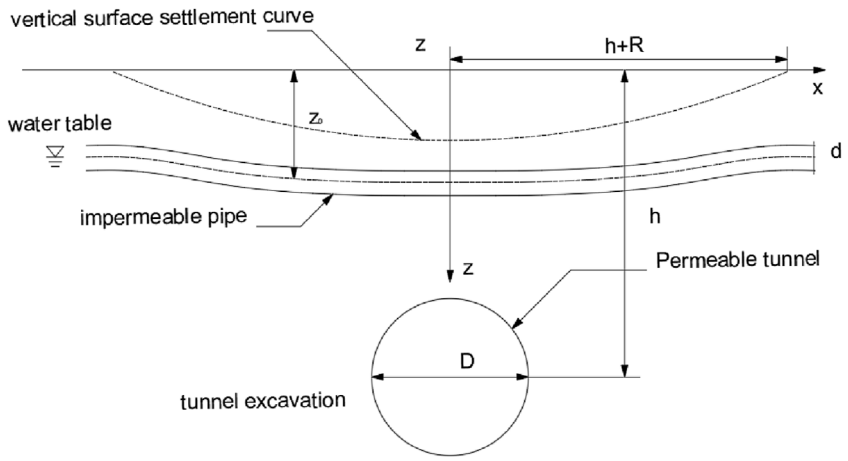

FIGURE 1
Schematic representation of tunneling effects on existing pipeline.

According to the two-step approach, the assumptions widely adopted in the literature are followed: a) the pipeline is continuous, and it is buried in a homogenous ground; b) the pipe is always in contact with the soil; c) the pipe does not affect the tunnel when the tunneling-induced ground displacement happens; d) the soil response to pipe loading at the pipe level is not aware of the tunnel.

Since the long-term responses of the tunnel-soil-pipe system are considered herein, additional assumptions are needed for the seepage consolidation analysis: e) the pipe does not affect the seepage-deformation coupled process of ground when the pore water flows to the new drainage boundary imposed by the tunnel; f) the seepage consolidation of soil to the pipe loading at the pipe level is not aware of the tunnel; g) the groundwater table is at the pipeline level, and thus the soil is fully saturated; h) the pipe is impermeable, and the tunnel is permeable. Essentially, assumptions e) and f) have the same physics with assumptions c) and d), respectively. In other words, if assumptions c) and d) are acceptable, assumptions e) and f) become valid automatically.

Based on assumptions c) and e), the consolidation displacement of ground can be evaluated without considering the pipe. While assumptions d) and f) allow the interaction analysis between the pipe and saturated soil without the tunnel. Thus, the tunneling effects on the existing pipe considering the seepage consolidation of ground can be analyzed by the classic two-step approach, which is elaborated in the following sections.

3 Winkler model of pipe-soil interaction analysis

The essentials of a Winkler model are an Euler beam of infinite length representing the pipe and a series of independent springs representing the soil. The governing equation of the Winkler model reads:

$$EI\frac{\partial^4 w_b(x,t)}{\partial x^4} + K(t)w_b(x,t) = K(t)U_z(x,t) \tag{1}$$

where EI is the bending stiffness of pipe; w_b denotes the deflection of pipe; K represents the subgrade modulus; U_z is the greenfield soil displacement (i.e., the soil settlement at the pipe level if the pipe did not exist); x axle is along the pipe centerline, and measures the distance from the tunnel centerline; and t denotes time. K and U_z become time dependent when the seepage consolidation of soil is considered.

By introducing $\beta = \sqrt[4]{\frac{K}{4EI}}$, Eq. 1 can be re-written as

$$\frac{\partial^4 w_b}{\partial x^4} + 4\beta^4 w_b = 4\beta^4 U_z \tag{2}$$

For an infinite Winkler beam, a concentrated load P induces a bending moment M_b of the following magnitude at a distance x from the location of the load (Klar et al., 2007)

$$M_b = \frac{P}{4\beta}\exp(-\beta x)(\cos(\beta x) - \sin(\beta x)) \tag{3}$$

The infinitesimal concentrated loads $\mathbf{d}P(x)$ can be related to the soil settlement by the subgrade modulus, i.e.,

$$\mathbf{d}P(x) = KU_z dx \tag{4}$$

The maximum bending moment in the pipe occurs above the tunnel centerline, referred to as the maximum sagging moment. According to Eqs 2–4 and by integrating the distribution of the infinitesimal concentrated loads, we can obtain the maximum bending moment:

$$M_b|_{\max} = \int_{-\infty}^{\infty} \mathbf{d}M_b(x) = \int_{-\infty}^{\infty} \frac{KU_z}{4\beta}\exp(-\beta x)(\cos(\beta x) - \sin(\beta x))\mathbf{d}x \tag{5}$$

4 Subgrade modulus

The knowledge of subgrade modulus K plays important in evaluating the pipeline responses. The Vesic equation (1961) is commonly adopted for the subgrade modulus, i.e.,

$$K = \frac{0.65E_0}{1-\nu^2}\left(\frac{E_0 d^4}{EI}\right)^{\frac{1}{12}} \tag{6}$$

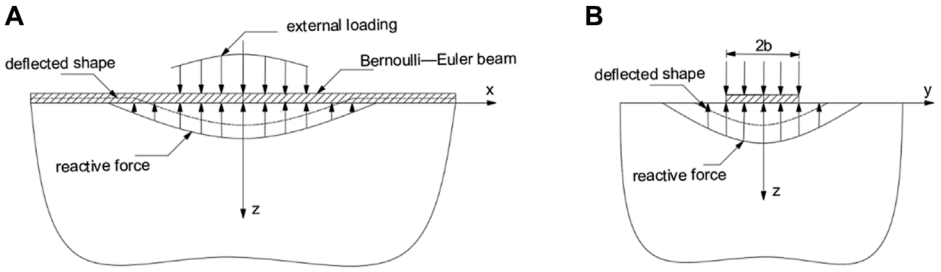

FIGURE 2
Analysis model of a beam resting on a saturated poroelastic half-space (after Selvadurai and Shi, 2015): **(A)** longitudinal view; **(B)** cross section view.

in which, E_0 and v are the drained elastic modulus and Poisson's ratio of soil, respectively. As indicated by Klar et al. (2007), the physical meaning of Eq. 6 is allowing a beam on Winkler foundation to exhibit similar displacements and moments to those of a beam on an elastic foundation when loaded with concentrated loads. In other words, the subgrade modulus is evaluated by referring to a beam resting on the surface of a halfspace.

In the literature the short-term settlement is routinely considered, and thus Eq. 6 is obtained for a beam on an elastic halfspace. The short-term settlement is caused by undrained shear deformation of the soil, which happens immediately in the tunnel construction process. However, when the seepage consolidation of soil is involved, the subgrade modulus becomes time-dependent (typically in soil layers of low permeability). Under this condition, the subgrade modulus should be evaluated by referring to a beam resting on a saturated poroelastic halfspace.

The analysis model of an infinite beam resting on the surface of a saturated poroelastic halfspace is shown in Figure 2. A rectangular section of width $2b$ ($2b$=d, d is the pipe diameter) is assigned to the beam. The beam experiences flexure only in the longitudinal direction (i.e., x axle), i.e., the beam section is infinitely rigid in the transverse direction (no flexure in the y-z plane).

For convenience of presentation, the region of the surface of the halfspace in contact with the beam is denoted by: Γ_c (i.e., $x \in (-\infty,\infty); y \in (-b,b); z=0$) and the combined region of the half-space exterior to Γ_c is denoted by Γ_e (i.e., $\Gamma_e = \Gamma_{e1} \cup \Gamma_{e2}$ and in $\Gamma_{e1}(x \in (-\infty,\infty); y \in (b,\infty); z=0)$ and in $\Gamma_{e2}(x \in (-\infty,\infty); y \in (-\infty,b); z=0)$.

4.1 Governing equations

The constitutive equations governing the seepage consolidation response of a poroelastic halfspace, which consists of an isotropic soil skeleton saturated with a compressible pore fluid, are expressed as

$$\sigma_{ij} = \frac{2v\mu}{1-2v}\varepsilon_{kk}\delta_{ij} + 2\mu\varepsilon_{ij} - \frac{3(v_u - v)}{B(1-2v)(1+v_u)}p\delta_{ij} \tag{7}$$

$$p = \frac{2\mu B^2(1-2v)(1+v_u)^2}{9(v_u - v)(1-2v_u)}\zeta_v - \frac{2\mu B(1+v_u)}{3(1-2v_u)}\varepsilon_{kk} \tag{8}$$

where p is the pore fluid pressure; ζ_v is the volumetric strain in the pore fluid; σ_{ij} is the total stress tensor. Also, ε_{ij} represents the soil skeleton strain defined by

$$\varepsilon_{ij} = \left(u_{i,j} + u_{j,i}\right)/2 \tag{9}$$

where u_i $(i = x, y, z)$ corresponds to displacement components and the comma denotes a partial derivative with respect to a spatial variable. In the absence of body forces, the quasi-static equations of equilibrium take the forms

$$\sigma_{ij,j} = 0 \tag{10}$$

The equations governing the quasi-static fluid flow are defined by Darcy's law, which takes the form

$$v_i = -kp_{,i} \tag{11}$$

where v_i denotes the specific discharge vector in the pore fluid; k is the hydraulic conductivity and γ_w is the unit weight of the pore fluid. The continuity equation associated with the quasi-static fluid flow is

$$\frac{\partial \zeta_v}{\partial t} + v_{i,i} = 0 \tag{12}$$

The basic Equations 7–12 are characterized by five independent material parameters which are the drained Poisson's ratio, the undrained Poisson's ratio v_u, the shear modulus μ, Skempton's pore pressure coefficient B and the permeability coefficient k.

According to assumption h), boundary Γ_c is impermeable; while boundary Γ_e is permeable. For bonded contact between an impermeable elastic beam and a poroelastic halfspace where the exterior region is allowed to drain freely, the following boundary conditions are applicable (Biot, 1941):

$$u_z(x,y,0,t) = w_b(x,t);\ (x,y) \in \Gamma_c \tag{13a}$$

$$u_x(x,y,0,t) = u_y(x,y,0,t) = 0;\ (x,y) \in \Gamma_c \tag{13b}$$

$$\sigma_{zx}(x,y,0,t) = \sigma_{zy}(x,y,0,t) = \sigma_{zz}(x,y,0,t);\ (x,y) \in \Gamma_e \tag{13c}$$

$$v_z(x,y,0,t) = 0;\ \ (x,y) \in \Gamma_c \tag{13d}$$

$$p(x,y,0,t) = 0;\ \ (x,y) \in \Gamma;\ \forall t \geq 0 \tag{13e}$$

As is evident, the poroelastic adhesive contact problem for the infinite beam on a poroelastic halfspace defined by Eq. 13 has to consider not only the mixed boundary conditions applicable to $u(x,t)$ and $\sigma(x,t)$ but also a set of mixed boundary conditions applicable to the pore fluid pressure $p(x,t)$, which makes the analysis extremely complex. Alternatively, we develop bounds to the poroelasticity by prescribing free draining-frictionless (Case A), impervious-frictionless (Case B), free draining-inextensible (Case C) and impervious-inextensible (Case D) boundary conditions on Γ (Selvadurai and Shi, 2015).

Case A: considering the shear traction free and pervious boundary conditions prescribed over Γ, the resulting boundary value problem is given by

$$u_z(x,y,0,t) = w_b(x,t);\quad (x,y) \in \Gamma_c \tag{14a}$$

$$\sigma_{zx}(x,y,0,t) = \sigma_{zy}(x,y,0,t) = 0;\ (x,y) \in \Gamma \tag{14b}$$

$$\sigma_{zz}(x,y,0,t) = 0;\quad (x,y) \in \Gamma_e \tag{14c}$$

$$p(x,y,0,t) = 0;\quad (x,y) \in \Gamma \tag{14d}$$

Case B: considering the shear traction free and impervious boundary conditions prescribed over Γ, the initial boundary value problem is given by

$$u_z(x,y,0,t) = w_b(x,t);\ (x,y) \in \Gamma_c \tag{15a}$$

$$\sigma_{zx}(x,y,0,t) = \sigma_{zy}(x,y,0,t) = 0;\quad (x,y) \in \Gamma \tag{15b}$$

$$\sigma_{zz}(x,y,0,t) = 0;\quad (x,y) \in \Gamma_e \tag{15c}$$

$$v_z(x,y,0,t) = 0;\quad (x,y) \in \Gamma \tag{15d}$$

Case C: considering the inextensibility and pervious boundary conditions prescribed over Γ, the initial boundary value problem is given by

$$u_z(x,y,0,t) = w_b(x,t);\quad (x,y) \in \Gamma_c \tag{16a}$$

$$u_x(x,y,0,t) = u_y(x,y,0,t) = 0;\quad (x,y) \in \Gamma \tag{16b}$$

$$\sigma_{zz}(x,y,0,t) = 0;\quad (x,y) \in \Gamma_e \tag{16c}$$

$$p(x,y,0,t) = 0;\quad (x,y) \in \Gamma \tag{16d}$$

Case D: considering the inextensibility and impervious boundary conditions prescribed over Γ , the resulting initial boundary value problem is given by

$$u_z(x,y,0,t) = w_b(x,t);\ (x,y) \in \Gamma_c \tag{17a}$$

$$u_x(x,y,0,t) = u_y(x,y,0,t) = 0;\quad (x,y) \in \Gamma \tag{17b}$$

$$\sigma_{zz}(x,y,0,t) = 0;\ (x,y) \in \Gamma_e \tag{17c}$$

$$v_z(x,y,0,t) = 0;\ (x,y) \in \Gamma \tag{17d}$$

4.2 Fundamental solutions of the poroelastic halfspace

For convenience, the beam half-width b, the shear modulus μ and the consolidation coefficient c governing the soil-pipeline interaction, where c is given in Eq. 18

$$c = \frac{2\mu B^2(1-\nu)(1+\nu_u)^2 k}{9\gamma_w(\nu_u-\nu)(1-\nu_u)} \tag{18}$$

are introduced to render all physical quantities non-dimensional as

$$x^* = \frac{x}{b}, t^* = \frac{ct}{b^2}, w_b^* = \frac{w_b}{b}, u^* = \frac{u}{b}, \sigma_{ij}^* = \frac{\sigma_{ij}}{\mu}, p^* = \frac{p}{\mu}, k^* = \frac{\mu k}{c\gamma_w}$$
$$\nu^* = \frac{b\nu}{c}, EI^* = \frac{EI}{\mu b^4}, M_b^* = \frac{M_b}{\mu b^3}, q_c^* = \frac{q_c}{\mu b}, K^* = \frac{K}{\mu} \tag{19}$$

In Eq. 19, $q_c^* = K^* w_b^*$ is the dimensionless contact force between the beam and soil; and the other variables have been defined previously.

We adopt a method that involves the use of Fourier and Laplace transforms to obtain the fundamental solutions of the poroelastic halfspace. Adopting the relaxed boundary conditions (Eqs 14a–17d), the pipe-soil interaction analysis will become relatively easy. At the same time, the pipe-soil interaction solution under the strict boundary condition (Eq. 13a) should be within the range limited by the above four post-relaxation solutions. Details of the derivation can be found in the paper by Selvadurai and Shi (2015). The fundamental solutions of pore pressure, soil displacement and traction stresses are expressed in the transform domain, as shown in Supplementary Appendix SA1. The solutions are expressed as functions of ξ, η, z and s along with undetermined constants A_1, A_2, A_3 and A_4. It is noted that the counterparts of ξ, η and s in the spatial-temporal domain are x^*, y^* and t^*, respectively.

4.3 Evaluating subgrade modulus

The subgrade modulus in the transform domain can be expressed as

$$\overline{K}^*(\xi,s) = \frac{\overline{\tilde{q}}_c^*(\xi,s)}{\overline{\tilde{w}}_b^*(\xi,s)} \tag{20}$$

where the tidal and bar above the symbol denote variable in the transform domain. For the formulation of the subgrade modulus, the contact force q_c^* over Γ_c is assumed to be composed of a number of strip loads of equal width and finite amplitude across the beam section, and the contact stress distribution within each strip is considered to be uniform, as shown in Figure 3A. The number and amplitude of the strip loads are determined to yield an approximately constant displacement w_b^* of the beam at any cross section by satisfying the displacement compatibility condition at discrete middle points of the strips (see Figure 3B).

As can be seen from Figure 3, the beam-halfspace interface is discretized into N strips with equal width Δy^* and the continuous variable y^* across the interface is changed into a discrete variable y_n^*, which is expressed as

$$y_n^* = -1 + \frac{2n-1}{2}\Delta y^* \tag{21}$$

In Eq. 21, $1 \le n \le N$; $-1 \le y_n^* \le 1$ and $N = 2/\Delta y^*$. The contact

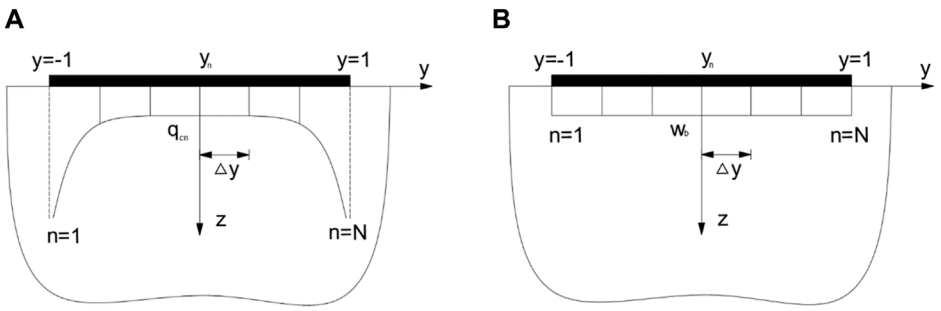

FIGURE 3
Discretization of contact boundary conditions over the beam-half space interface Γ_c: **(A)** contact normal stress; **(B)** beam section displacement.

normal stress and the displacement compatibility condition over the interface Γ_c can then be readily obtained:

$$\sigma_{zz}{}^{*}(x^{*},y^{*},0,t^{*}) = -\sum_{n=1}^{N}\frac{q_{cn}{}^{*}(x^{*},y_n{}^{*},t^{*})}{\Delta y^{*}}\mathrm{H}(\Delta y^{*}-|y^{*}-y_n{}^{*}|);\quad (x^{*},y^{*},y_n{}^{*})\in\Gamma_c \tag{22}$$

$$u_z{}^{*}(x^{*},y_n{}^{*},0,t^{*}) = w_b{}^{*}(x^{*},t^{*});\quad (x^{*},y_n{}^{*})\in\Gamma_c \tag{23}$$

where q_{cn}^{*} is the unknown contact force acting along the center line of the nth strip.

After replacing the displacement compatibility condition in Cases A to D by Eq. 23 and combining the left boundary conditions in each case with Eq. 22, a set of algebraic equations can be formed in Fourier-Laplace transform domain to evaluate the subgrade modulus defined in Eq. 20. The details of derivation can be found in the paper by Shi and Selvadurai (2015). Take Case A as an example, the subgrade modulus can be obtained by solving

$$\sum_{n=1}^{N}\int_{-\infty}^{-\infty}\chi_{\mathrm{A}}\times\frac{\sin(\eta\Delta y^{*}/2)}{\gamma_2(\eta\Delta y^{*}/2)}\times e^{i\eta(y_m{}^{*}-y_n{}^{*})}d\eta\times\frac{\bar{\bar{q}}_{cn}{}^{*}(\xi,y_n{}^{*},s)}{\bar{\bar{w}}_{\mathrm{b}}{}^{*}(\xi,s)} = 4\pi \tag{24}$$

where $1\le m\le N$. For Cases B to D, Eq. 24 still applies; however, χ_{A} should be replaced by χ_{B} to χ_D, respectively, whose expressions are given in Supplementary Appendix SA1. After solving Eq. 24, the subgrade modulus in the transform domain can be obtained as

$$\bar{\bar{K}}^{*}(\xi,s) = \sum_{n=1}^{N}\frac{\bar{\bar{q}}_{cn}{}^{*}(\xi,s)}{\bar{\bar{w}}_{\mathrm{b}}{}^{*}(\xi,s)} \tag{25}$$

and its value (Eq. 25) in the spatial-temporal domain can be obtained by performing inverse Fourier-Laplace transformations.

5 Greenfield soil settlement

It is a common practice to describe the short-term greenfield soil settlement due to tunneling using a Gaussian curve. However, as reported by Vorster et al. (2005) the Gaussian curve is not satisfactory to accurately describe the soil settlement in many cases. Instead, they proposed a modified Gaussian curve of the following form

$$S_{\mathrm{c}}(x) = \frac{\omega S_{\mathrm{cmax}}}{(\omega-1)+\exp\left[\alpha\left(\frac{x}{i}\right)^2\right]} \tag{26}$$

in which, S_{cmax} denotes the maximum settlement along the settlement profile; i is the distance to the inflection point of the greenfield settlement trough profile; ω is the shape function parameter controlling the width of the profile, i.e.,

$$\omega = e^{\alpha}\frac{2\alpha-1}{2\alpha+1}+1 \tag{27}$$

In Eq. 27, α is a parameter to ensure i remains the distance to the inflection point.

Following the same profile function, Wongsaroj et al. (2013) investigated the long-term settlement induced by the dissipation of the tunneling-generated excess pore water pressure towards the drainage boundaries. Later, Laver et al. (2017) extended the work of Wongsaroj et al. (2013), and proposed an empirical formula-based chart for evaluating the consolidation settlement for both transient and steady-state long-term conditions. Here, we follow the chart by Laver et al. (2017), and list the main steps as follows

Step (1), evaluate the dimensionless settlement DS, i.e.,

$$DS = \frac{1}{1+1.4RP^{-1}} \tag{28}$$

In Eq. 28, RP is a dimensionless parameter measuring the relative soil-lining permeability,

$$RP = \frac{DK_t\gamma_{\mathrm{w}}}{2k}\ln\left(\frac{2C_{\mathrm{s}}}{D}+1\right) \tag{29}$$

In Eq. 29, $K_t = \frac{k_t}{\gamma_w t_t}$ is the seepage coefficient of lining, k_t and t_t denotes the permeability and thickness of the lining, respectively; $C_s = h - z_0 - D/2$ measures the thickness of soil between the tunnel crown level and the water table.

Step (2), evaluate the steady state nondimensional settlement $NS_{c\,\max(\mathrm{ssi})}$ and $NS_{c\,\max(\mathrm{ssp})}$ for the fully impermeable and permeable lining cases, respectively, i.e.,

$$\begin{cases} NS_{c\,\max(\mathrm{ssi})} = 4.4V_L \\ NS_{c\,\max(\mathrm{ssp})} = -0.25 - 0.046\dfrac{h}{D} \end{cases} \tag{30}$$

In Eq. 30, V_L denotes volume loss of tunneling construction. It is reported by Attewell et al. (1986) that the volume loss of tunneling in clay soil is generally 0.5%–2.5%. Here, we take an average value, i.e., $V_L = 1.5\%$.

Step (3), evaluate the steady state nondimensional settlement $NS_{c\,\max(\mathrm{ss})}$ at permeability of lining,

$$NS_{c\,\max(\mathrm{ss})} = NS_{c\,\max(\mathrm{ssi})} + DS\left(NS_{c\,\max(\mathrm{ssp})} - NS_{c\,\max(\mathrm{ssi})}\right) \tag{31}$$

Step (4), according to Eq. 31, convert the nondimensional settlement to actual settlement, i.e.,

$$S_{c\,\max(ss)} = \frac{5\mathrm{DL_c}\gamma_w}{E_0}\mathrm{NS}_{c\,\max(ss)} \tag{32}$$

In Eq. 32, $L_c = h\text{-}z_0$ is the tunnel axis depth below the water table.

Step (5), according to the actual steady-state settlement, find the transient settlement at required time,

$$S_{c\,\max} = \left[1 - \frac{2}{3}\exp\left[\ln\left(\frac{3}{2}\right) - 3A_{RS}T_v^{B_{RS}}\right]\right]S_{c\,\max(\mathrm{ss})} \tag{33}$$

In Eq. 33, T_v is the dimensionless consolidation time depending on the permeability of the soil covering the tunnel and the drainage distance from the soil to the tunnel; A_{RS} and B_{RS} are empirical functions of $\frac{h}{D}$ and RP. Expressions of the above parameters are given as

$$T_v = \frac{c_t t}{C_s^2} \tag{34}$$

$$A_{RS} = \begin{cases} 0.5 \\ 0.12 + 0.055\dfrac{h}{D} \end{cases};\ B_{RS} = \begin{cases} 0.8 \\ 1 \end{cases};\ \text{for} \begin{cases} \text{settlement}, S_{c\,\max(ss)} < 0 \\ \text{heave}, S_{c\,\max(ss)} \geq 0 \end{cases} \tag{35}$$

In Eq. 34, $c_t = \frac{E_0 k}{\gamma_w}$ denotes the consolidation coefficient governing the soil-tunnel interaction.

Step (6), evaluate the transverse distribution of the transient settlement at required time (i.e., the ground settlement profile at particular time) according to the modified Gaussian curve. By replacing i in Eq. 26 by $K_L h$, we have

$$S_c(x) = \frac{\omega S_{c\,\max}}{(\omega - 1) + \exp\left[\alpha\left(\frac{x}{K_L h}\right)^2\right]} \tag{36}$$

In Eq. 36, K_L and α can be empirically related to V_L and RP, respectively, i.e.,

$$K_L = 0.8 - 6V_L;\ \alpha = \begin{cases} -0.004 & \text{for } RP < 0.1 \\ 0.1 & \text{for } RP \geq 0.1 \end{cases} \tag{37}$$

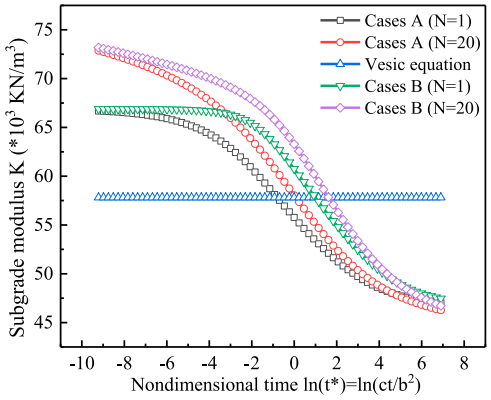

FIGURE 4
Verification on subgrade modulus K.

Step (7), evaluate the transient settlement profile at the pipeline level (i.e., $U_z(x,t)$), which is achieved by Eqs 33–37 and scaling the maximum settlement $S_{c\,\max}$ and trough width $K_L h$, i.e.,

$$U_z = \frac{\omega\chi S_{c\,\max}}{(\omega - 1) + \exp\left[\alpha\left(\frac{x}{K_L h/\chi}\right)^2\right]} \tag{38}$$

In Eq. 38, $\chi = \frac{0.5h}{0.5h - 0.325z_0}$ (Klar et al., 2008).

6 Verification

Since no results have been published on the consolidation effects on the pipe-soil interaction problem due to tunneling, the solution developed in this study will be simplified and then verified at elementary levels: (1) the subgrade modulus; and (2) the bending moment of pipeline subjected to short-term settlement caused by tunneling.

(1) Verification on subgrade modulus K. The analysis consider an infinite pipeline resting on a saturated homogeneous half-space is considered. The pipeline is of diameter d=$2b$=0.8 m, wall thickness d_t=20 mm, and bending rigidity EI=1.3×10^4 kN m^2. The material parameters of the saturated soil are as follows: E_0=40 MPa, ν=0.3, ν_u=0.5, k=5×10^{-8} m/s, μ=15.4 MPa, B=1, and γ_w=10 kN/m^3.

As indicated in Figure 3, to establish a bonded contact condition between the pipeline and the soil, the contact area is discretized into multiple strips, ensuring a constant displacement of the pipeline across all sections. This contact condition can be simplified to the "average contact" condition when N=1, where the contact force q_c^* over Γ_c is uniformly distributed, and the displacement compatibility condition is satisfied only at the midpoint of the beam section. It should be noted that the commonly used Vesic equation (Eq. 6) was derived for the "average contact" condition (i.e., N=1).

Using the aforementioned parameters, computational results for the subgrade modulus K are presented in Figure 4 for Cases A and B. The figure also includes the prediction from Vesic equation (Eq. 6).

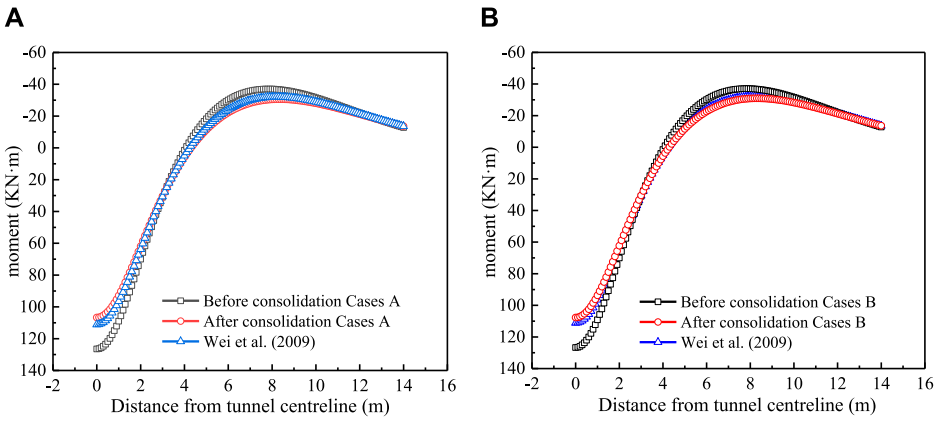

FIGURE 5
Verification on bending moment of pipeline subjected to transient short-term settlement: **(A)** Cases A; **(B)** Cases B.

Initially, the soil exhibits fully undrained behavior governed by the undrained Poisson's ratio v_u. As consolidation occurs, the soil behavior gradually transitions to a fully drained state governed by the drained Poisson's ratio v. As $v_u>v$, the magnitude of the subgrade modulus decreases with the consolidation of the soil. The Vesic equation, based on the fully drained condition, within the scope of "average contact" (N=1) and "bonded contact" condition (N=20) calculations. The range calculated by "bonded contact" condition (N=20) is greater than "average contact" (N=1).

(2) Verification of bending moment of pipeline subjected to short-term settlement. Wei et al. (2009) studied the bending moment response of a pipeline, considering only the transient soil settlement induced by tunneling. The tunnel and pipeline axes have burying depth of h=5 m and z_0=1.5 m, respectively. The pipeline is of diameter d=0.8 m, wall thickness d_t=0.12 m, and bending rigidity EI=4.58×10^5 kN m^2. The tunnel, constructed in a homogenous elastic ground with elastic modulus E_0=3.08 MPa and Poisson's ratio v =0.35, is of diameter D=1.5 m. Wei et al. (2009) employed a Gaussian curve to describe the short-term greenfield soil settlement induced by tunneling. The maximum greenfield settlement occurs right above the tunnel is related to the volume loss V_L by the equation $S_{\max}=\frac{V_L}{i\sqrt{2\pi}}\left(1-\frac{z_0}{h}\right)^{-0.3}$. By using the short-term greenfield soil settlement as input in the developed solution, the distribution of bending moment along the pipeline can be evaluated and compared to the results obtained by Wei et al. (2009), as depicted in Figure 5. In our solution, the bonded contact condition is established between the pipeline and soil (N=20). It is seen that the results of Wei et al. (2009) are encompassed within the computational results at both small and large consolidation times from the developed solution presented herein.

By conducting thorough verification on the subgrade modulus and the bending moment of the pipeline subjected to short-term settlement, it is established a strong foundation for further investigation into the consolidation effects on the pipe-soil interaction problem due to tunneling.

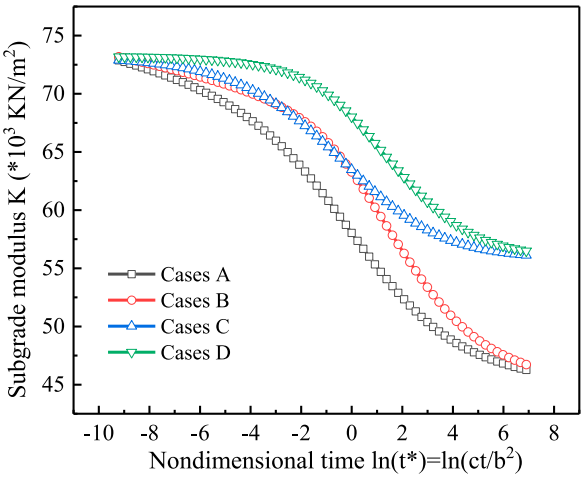

FIGURE 6
The variation of subgrade modulus with the seepage consolidation of soil.

7 Numerical results

By using the two-step method, the tunneling effects on an existing pipeline striking perpendicularly to an underpassing tunnel are investigated in this section. The burying depths of the tunnel and pipeline axes are h=10 m and z_0=1 m, respectively. The tunnel of radius D=6 m is constructed in a homogenous saturated poroelastic ground. The tunnel lining is of thickness t_t=0.2 m and permeability k_t=1×10^{-9} m/s. The pipeline is of diameter d=2b=0.8 m, wall thickness d_t=20 mm and bending rigidity EI=1.3×10^4 kN m^2. Material parameters of the saturated soil are E_0=40 MPa, v=0.3, v_u=0.5, k=5×10^{-8} m/s, μ=15.4 MPa, B=1 and γ_w=10 kN/m^3. As stated in Section 5, the volume loss of soil induced by tunneling is V_L=1.5%.

With the above parameters, the following intermediate parameters can be evaluated: the thickness of soil between the tunnel crown level and the water table C_S=6 m; the relative soil-lining

TABLE 1 Comparisons on subgrade modulus K between Cases A~D.

Boundary condition	Case A	Case B	Case C	Case D	Vesic equation (Eq. 6)
At the beginning of consolidation	72.88	73.18	72.89	73.18	57.81
At the end of consolidation	46.26	46.71	56.12	56.49	

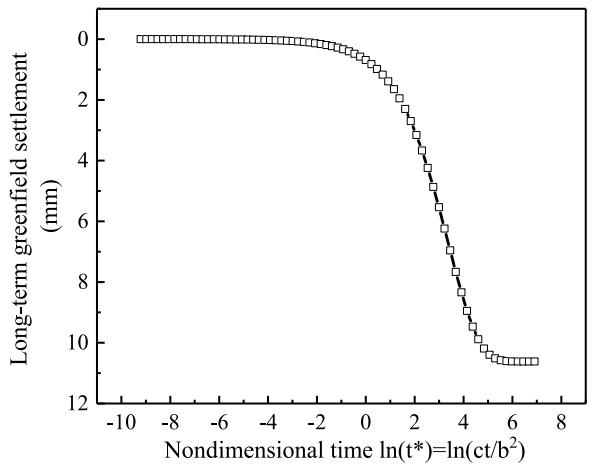

FIGURE 7
Long-term greenfield settlement for the point of pipeline (x = 0) that is right above the tunnel.

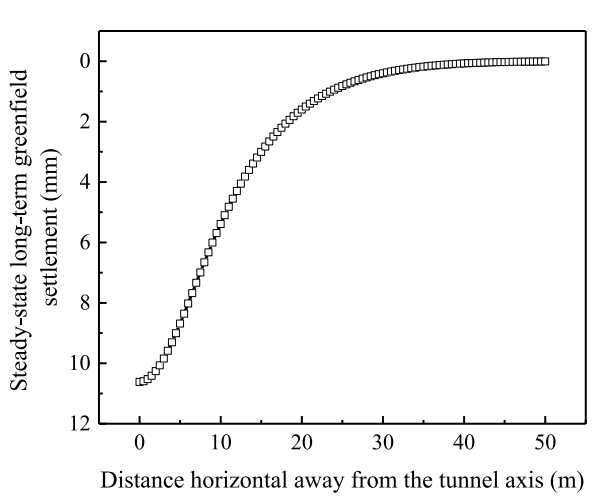

FIGURE 8
Distribution of steady-state long-term settlement along the pipeline.

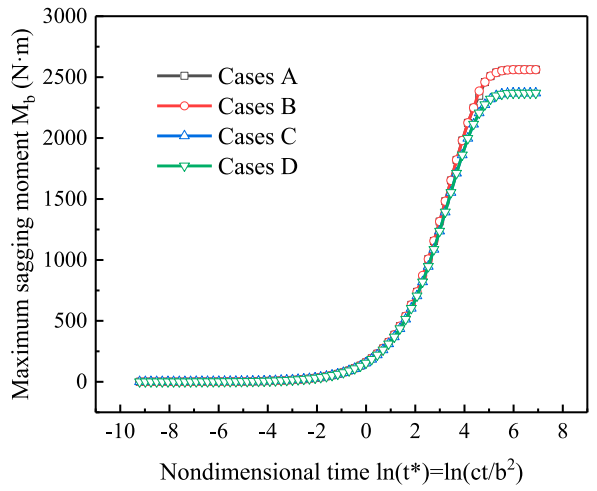

FIGURE 9
The development of maximum sagging moment of pipe with seepage consolidation.

permeability RP=23.1; the dimensionless settlement DS=0.54; the distance to the inflection point of the greenfield settlement trough profile i=10.65; the consolidation coefficients governing the tunnel-soil and pipeline-soil interactions are c_t=2×10^{-4} and c= 2.15×10^{-6}, respectively.

7.1 Subgrade modulus

With the above-listed parameters, the subgrade modulus K resulting from the pipeline-soil interaction can be evaluated by using the method provided in Section 4. Figure 6 presents the time-dependent subgrade modulus under the four boundary conditions (i.e., Cases A~D). A decrease in the subgrade modulus can be observed for all the four boundary conditions (i.e., Cases A~D) with the elapsing consolidation time. Initially ($t* \to 0$), the soil behaviors fully undrained, and the soil is volumetrically incompressible due to ν_u =0.5. Thus, the subgrade modulus K is of the same magnitude between Cases A~D. With the seepage consolidation of soil, it is seen that the subgrade modulus associated with Cases B and D is higher than that associated with Cases A and C. The difference is due to the hydraulic boundary condition at the ground surface. In Cases B and D, the surface is impervious, which implies that the excess pore water pressure can only be dissipated into the infinity of ground. In comparison, the surface is pervious in Cases A and C, and the water can flow freely out of the surface. Then, it is understood that K of Cases B and D is large since the water flow (of nearly zero compressibility) is constrained. When the time approaches the end of consolidation, the subgrade moduli of Cases A and B (and similarly Cases C and D) converge to a same limiting value. It is seen that the limiting K ($t* \to \infty$) of Cases C and D is higher

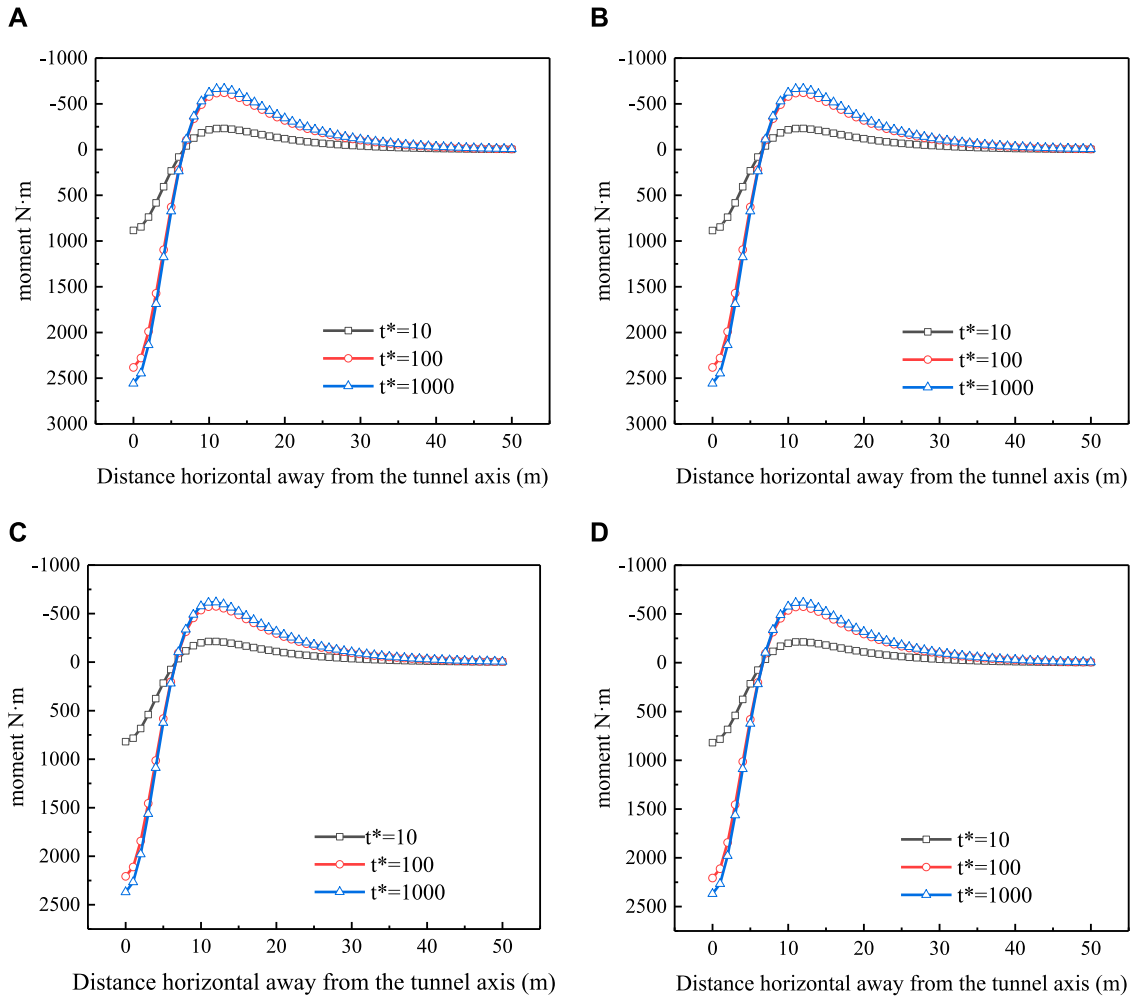

FIGURE 10
Distribution of bending moment along the pipeline at time instants t^* =10, 100 and 1,000: **(A)** Case A; **(B)** Case B; **(C)** Case C; **(D)** Case D.

than that of Cases A and B. The explanation is that an inextensible ground surface (Cases C and D) would render a stiffer support to the pipeline when compared to the ground of frictionless surface (Cases A and B).

To facilitate the comparison, the magnitude of subgrade modulus K is summarized in Table 1 for the beginning and end of the seepage consolidation, respectively. Also included in Table 1 is the prediction by Vesic equation, which is well bounded by the subgrade modulus associated with the four boundary conditions (Cases A~D).

7.2 Greenfield soil settlement

According to the steps listed in Section 5, the long-term settlement induced by the dissipation of the tunneling-induced excess pore water pressure can be obtained. It is noted that the short-term settlement caused by undrained shear deformation of soil during the tunnel construction is not considered. For the point of pipeline that is right above the tunnel, its greenfield settlement gradually increases with the seepage consolidation

TABLE 2 The maximum sagging moment of the pipeline associated with the four boundary conditions.

Time	Case A	Case B	Case C	Case D
t ∗ =10	884.9	885.2	819.6	819.8
t ∗ =100	2,383.1	2,383.4	2,207.4	2,207.7
t ∗ =1,000	2,558.9	2,559.1	2,370.5	2,370.6

TABLE 3 The maximum hogging moment of the pipeline associated with the four boundary conditions.

Time	Case A	Case B	Case C	Case D
t ∗ =10	230.2	230.2	213.2	213.1
t ∗ =100	620.3	620.3	574.3	574.3
t ∗ =1,000	666.2	666.2	616.8	616.8

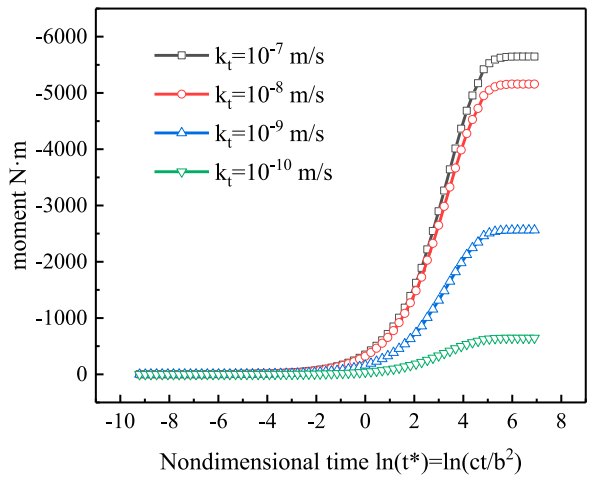

FIGURE 11
Development of maximum sagging moment with seepage consolidation under four permeabilities of tunnel lining.

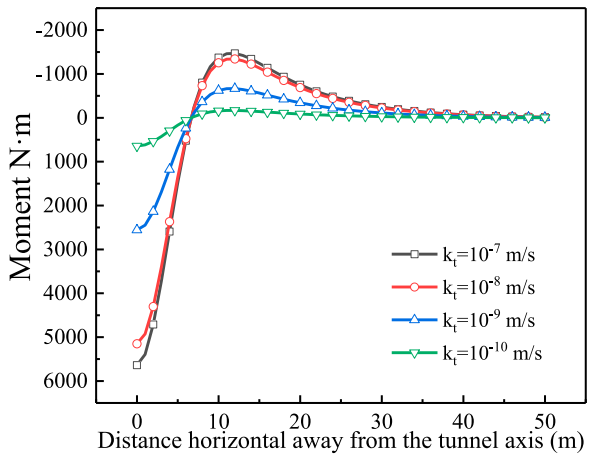

FIGURE 12
Distribution of bending moment along the pipeline under four permeabilities of tunnel lining.

process, as shown in Figure 7. At initial stage of the seepage consolidation, the gain in settlement is marginal, which is due to the relatively large drainage distance C_s. Then, the consolidation settlement develops quickly before it reaches a stable value at the end of the consolidation (i.e., ln $(t*)$ =6). The steady-state long-term settlement reads 11 mm.

When the seepage consolidation is completed, the distribution of the steady-state settlement along the pipeline is shown in Figure 8. It is seen that the largest steady-state settlement happens right above the tunnel (i.e., x=0). With the horizontal distance away from the tunnel, the settlement decreases, which forms a typical trough profile covering a range x=0–50 m. From the figure, the distance to the inflection point of the settlement trough profile is 25 m.

7.3 Bending moment of pipeline

With the subgrade modulus K and greenfield soil settlement at the pipeline level U_z being determined in Sections 7.2, 7.3, respectively, the bending moment response of the pipeline can be evaluated by using the equations detailed in Section 3. The development of the maximum sagging moment (i.e., the bending moment in the pipe right above the tunnel centerline) (Eq. 5) with the nondimensional time ln $(t*)$ is shown in Figure 9. The develop pattern of the maximum sagging moment resembles that of the greenfield settlement (see Figure 8), i.e., the increasing of bending moment is extremely slow before ln $(t*)$ =0, after which the bending moment gains until the time ln $(t*)$ =5. The curves associated with the four boundary conditions (Cases A~D) basically overlap before the time ln $(t*)$ =2, even though obvious difference between the subgrade moduli of the four cases exist (see Figure 7). This observation implies that the bending moment response of the pipeline is governed by the greenfield settlement input, especially during the initial and middle stages of the seepage consolidation. Towards the end of the consolidation, the maximum sagging moment associated with Cases A and B is about 10% larger than that with Cases C and D, which agrees with the finding that the pipe with stiffer subgrade would suffer smaller bending moment (Zhang and Huang, 2012).

As consolidation proceeds, the subgrade modulus decreases and the soil settlement increases. The pipe bending moment is affected by the soil settlement input and gradually increase, and its law of change with time is consistent with the law of change of soil settlement with time.

Since the bending moment develops quickly when the nondimensional time ln $(t*)$>2, the distributions of bending moment along the pipeline are presented in Figure 10 for three selected time instants, i.e., $t*$=10, $t*$=100, and $t*$=1,000. It is seen that the maximum sagging moment (of positive value) happens right above the tunnel (i.e., x=0 m), and the maximum hogging moment (of negative value) occurs near the edge of the settlement trough (i.e., x≈12 m). The maximum sagging and hogging moments of the pipeline associated with the four boundary conditions are summarized in Tables 2, 3, respectively. The exact value of maximum bending moment of the pipeline subjected to tunneling should fall within the bounds provided by Cases A~D. Take the sagging moment as an example, its exact value at the steady state (i.e., $t*$=1,000) should be within the range (2370 N m, 2559 N m), whose upper and lower bounds are provided by Cases C and Case A, respectively. It is noted that this range is narrow enough for an engineering judge on the failure of pipeline.

7.4 Influence of permeability of tunnel lining

As indicated by Wongsaroj et al. (2013), the consolidation settlement by tunneling can be significantly influenced by the permeability of tunnel lining. Here, we consider four permeability of lining, i.e., k_t=10^{-7} m/s, 10^{-8} m/s, 10^{-9} m/s and 10^{-10} m/s, respectively. The other parameters of the soil, pipe and tunnel are the same as those depicted at the beginning of Section 7. Take Case

A as an example, the comparison on the maximum sagging moment is presented in Figure 11. It is seen that the increase of bending moment with time follows the same pattern between the four permeabilities, i.e., the bending moment increases slowly initially ($\ln(t*)<0$), and then it grows quickly with time before it reaches a stable value around $\ln(t*)=5$. The steady-state value of sagging moment increases with the increasing permeability. For example, the steady-state sagging moment associated with $k_t=10^{-7}$ m/s is about 8 times that with $k_t=10^{-10}$ m/s.

When the seepage consolidation is completed, the distribution of bending moment along the pipeline is presented in Figure 12. Similar to the sagging moment, it is observed that the maximum hogging moment also increase with the increasing permeability of lining. For example, the hogging moment associated with $k_t=10^{-7}$ m/s is about 6 times that with $k_t=10^{-10}$ m/s.

8 Conclusion

To overcome the deficiency that only transient response can be considered in the analysis of the pipeline force caused by shield excavation, the pipe-soil contact stiffness is first derived taking into account the seepage consolidation effect of soft soil. Using the "two-step method", the deformation field resulting from seepage consolidation in the adjacent layer due to shield excavation is input to develop an analytical prediction method for the force exerted on the adjacent pipeline. This approach takes full account of the effects of seepage consolidation in soft ground. The following conclusions are drawn:

(1) The subgrade modulus K decreases gradually with seepage consolidation. Initially, the subgrade modulus K is the same for the four boundary conditions. As the soil consolidates, the subgrade modulus associated with Case B and Case D are higher than that associated with Case A and Case C. This is because the surface is impervious in Cases B and D and pervious in Cases A and C. When the time approaches the end of consolidation, the subgrade moduli of Cases A and B (and similarly Cases C and D) converge to a same limiting value. It is seen that the limiting K ($t*\to\infty$) of Cases C and D is higher than that of Cases A and B. The explanation is that an inextensible ground surface (Cases C and D) would render a stiffer support to the pipeline when compared to the ground of frictionless surface (Cases A and B).

(2) The greenfield settlement increases gradually during the consolidation process, with slow development in the early stage, and accelerated growth in the middle stage.

(3) The development pattern of the maximum sagging moment mirrors that of the greenfield settlement. The increase in bending moment is initially slow, accelerates during the middle stage, and eventually stabilizes. Under four boundary conditions investigated, the difference between the final stable maximum and minimum bending moment is 10%.

(4) The steady-state value of sagging moment increases with increasing permeability. Specifically, the steady-state sagging moment associated with a larger permeability of lining k_t would be higher than that associated with a lower k_t.

Data availability statement

The original contributions presented in the study are included in the article/Supplementary Material, further inquiries can be directed to the corresponding author.

Author contributions

XL: Conceptualization, validation, formal analysis, writing–original draft. JX: Conceptualization, formal analysis, data curation. YH: methodology, validation, writing–original draft. LS: writing–original draft, data curation, writing–review and editing. ZZ: methodology, writing–original draft, data curation. BM: writing–original draft, data curation, writing–review and editing. LH: Conceptualization, formal analysis. JW: methodology, data curation, writing–review and editing.

Funding

The author(s) declare that financial support was received for the research, authorship, and/or publication of this article. This research was supported by Zhejiang Province Construction Research Projects (2023K155).

Conflict of interest

Authors YH, ZZ, LH, and JW were employed by Power China Huadong Engineering Corporation Limited. Authors YH and ZZ were employed by Zhejiang Huadong Engineering Construction and Management Corporation Limited.

The remaining authors declare that the research was conducted in the absence of any commercial or financial relationships that could be construed as a potential conflict of interest.

Publisher's note

All claims expressed in this article are solely those of the authors and do not necessarily represent those of their affiliated organizations, or those of the publisher, the editors and the reviewers. Any product that may be evaluated in this article, or claim that may be made by its manufacturer, is not guaranteed or endorsed by the publisher.

Supplementary material

The Supplementary Material for this article can be found online at: https://www.frontiersin.org/articles/10.3389/feart.2024.1403663/full#supplementary-material

References

Attewell, P. B. (1981). Engineering contract, site investigation and surface movements in tunnelling works.

Attewell, P. B., Yeates, J., and Selby, A. R. (1986). *Soil movements induced by tunnelling and their effects on pipelines and structures*. new york ny: methuen inc.

Biot, M. A. (1941). General theory of three-dimensional consolidation. *J. Appl. Phys.* 12, 155–164. doi:10.1063/1.1712886

Celestino, T. B., Gomes, R. A. M., and Bortolucci, A. A. (2000). Errors in ground distortions due to settlement trough adjustment. *Tunneling Undergr. Space Technol.* 15 (1), 97–100. doi:10.1016/s0886-7798(99)00054-1

Klar, A., and Marshall, A. M. (2008). Shell versus beam representation of pipes in the evaluation of tunneling effects on pipelines. *Tunn. Undergr. Space Technol. Incorporating Trenchless Technol. Res.* 23 (4), 431–437. doi:10.1016/j.tust.2007.07.003

Klar, A., Marshall, A. M., Soga, K., and Mair, R. J. (2008). Tunneling effects on jointed pipelines. *Can. Geotechnical J.* 45, 131–139. doi:10.1139/t07-068

Klar, A., Voster, T. E. B., Soga, K., and Mair, R. J. (2007). Elastoplastic solution for soil-pipe-tunnel interaction. *J. Geotechnical Geoenvironmental Eng.* 133 (7), 782–792. doi:10.1061/(asce)1090-0241(2007)133:7(782)

Laver, R. G., Li, Z. L., and Soga, K. (2017). Method to evaluate the long-term surface movements by Tunneling in London clay. *J. Geotechnical Geoenvironmental Eng.* 143 (3), 06016023. doi:10.1061/(asce)gt.1943-5606.0001611

Loganathan, N., and Poulos, H. G. (1998). Analytical prediction for tunneling-induced ground movements in clays. *J. Geotechnical Geoenvironmental Eng.* 124 (9), 846–856. doi:10.1061/(asce)1090-0241(1998)124:9(846)

Mair, R. J., Soga, K., Klar, A., and Vorster, T. E. B. (2005). Soil-pipe interaction due to tunnelling: comparison between winkler and elastic continuum solutions. *Geotechnique* 55 (6), 461–466. doi:10.1680/geot.2005.55.6.461

Mair, R. J., Taylor, R. N., and Bracegirdle, A. (1993). Subsurface settlement profiles above tunnels in clays. *Geotechnique* 43 (2), 315–320. doi:10.1680/geot.1993.43.2.315

Marshall, A. M., Elkayam, I., and Klar, A. (2010). *Centrifuge and discrete element modelling of tunnelling effects on pipelines*.

Moghal, A. A. B., Vydehi, V., Moghal, M. B., Almatrudi, R., AlMajed, A., and Al-Shamrani, M. A. (2020). Effect of calcium-based derivatives on consolidation, strength, and lime-leachability behavior of expansive soil. *J. Mater. Civ. Eng.* 32 (4), 04020048. doi:10.1061/(asce)mt.1943-5533.0003088

Peck, R. B. (1969). Deep excavation and tunneling in soft ground. *7th Int. Cof. Soil Mech. Found. Eng. State Arts Volume*.

Schmidt, B. (1969). Settlements and ground movements associated with tunnelling in soil.

Selvadurai, A. P. S., and Shi, L. (2015). Biot's problem for a Biot material. *Int. J. Eng. Sci.* 97, 133–147. doi:10.1016/j.ijengsci.2015.09.004

Stallebrass, S. E., Jovicic, V., and Taylor, R. N. (2000). "Short term and long-term settlements around a tunnel in stiff clay," in *Numerical methods in geotechnical engineering*.

Venkata Vydehi, K., Moghal, A. A. B., and Basha, B. M. (2022). Reliability-based design optimization of biopolymer-amended soil as an alternative landfill liner material. *J. Hazard. Toxic, Radioact. Waste* 26 (3), 04022011. doi:10.1061/(asce)hz.2153-5515.0000697

Vesic, A. B. (1961). Bending of beams resting on isotropic elastic solid. *J. Eng. Mech. Div.* 87, 35–53. ASCE. doi:10.1061/jmcea3.0000212

Vorster, T. E., Klar, A., Soga, K., and Mair, R. J. (2005). Estimating the effects of tunneling on existing pipelines. *J. Geotechnical Geoenvironmental Eng.* 131 (11), 1399–1410. doi:10.1061/(asce)1090-0241(2005)131:11(1399)

Wang, Y., Shi, J. W., and Ng, C. W. W. (2011). Numerical modeling of tunneling effect on buried pipelines. *Can. Geotechnical J.* 48 (7), 1125–1137. doi:10.1139/t11-024

Wei, G. (2013). Prediction of ground deformation induced by double parallel shield tunneling. *Disaster Adv.* 6 (13), 91–98.

Wongsaroj, J., Soga, K., and Mair, R. J. (2013). Tunnelling-induced consolidation settlements in London Clay. *Geotechnique* 63 (13), 1103–1115. doi:10.1680/geot.12.p.126

Yu, J., Zhang, C. R., and Huang, M. S. (2013). Soil-pipe interaction due to tunnelling: assessment of Winkler modulus for underground pipelines. *Comput. Geotechnics* 50, 17–28. doi:10.1016/j.compgeo.2012.12.005

Zhang, Z., and Huang, M. (2012). Boundary element model for analysis of the mechanical behavior of existing pipelines subjected to tunneling-induced deformations. *Comput. Geotechnics* 46 (Nov), 93–103. doi:10.1016/j.compgeo.2012.06.001

Glossary

b	Beam half-width
B	Skempton's pore pressure coefficient
c	consolidation coefficient
c_t	consolidation coefficient governing the soil-tunnel interaction
d	diameter of pipeline
d_t	wall thickness
D	diameter of tunnel
EI	bending stiffness of pipe
E_0	drained elastic modulus
h	burying depth of the tunnel
i	distance to the inflection point of the greenfield settlement trough profile
k	hydraulic conductivity
k_t	permeability of the lining
K	subgrade modulus
L_c	tunnel axis depth below the water table
M_b	bending moment
p	pore fluid pressure
q_c^*	contact force
RP	dimensionless parameter measuring the relative soil-lining permeability
S_{max}	maximum settlement along the settlement profile
t_t	thickness of the lining
T_v	dimensionless consolidation time
U_Z	greenfield soil displacement
V_L	volume loss of tunneling construction
z_0	burying depth of the pipe
α	a parameter to ensure i remains the distance to the inflection point
μ	shear modulus
ω	shape function parameter controlling the width of the profile
w_b	deflection of pipe
ν	Poisson's ratio of soil
v_i	specific discharge vector in the pore fluid
ν_u	undrained Poisson's ratio
ζ_v	volumetric strain in the pore fluid
σ_{ij}	total stress tensor
ε_{ij}	soil skeleton strain
γ_w	unit weight of the pore fluid
Γ_c	region of the surface of the halfspace in contact with the beam
Γ_e	combined region of the half-space exterior to Γ_c
$NS_{c\,max(ssi)}$	steady state nondimensional settlement for the fully impermeable lining
$NS_{c\,max(ssp)}$	steady state nondimensional settlement for the permeable lining

frontiers | Frontiers in Earth Science

TYPE Original Research
PUBLISHED 14 June 2024
DOI 10.3389/feart.2024.1381689

Check for updates

OPEN ACCESS

EDITED BY
Jianyong Han,
Shandong Jianzhu University, China

REVIEWED BY
Pengju An,
Ningbo University, China
Xuefeng Ou,
Changsha University of Science and Technology, China

*CORRESPONDENCE
Jiacheng Li,
13278883522@163.com

RECEIVED 04 February 2024
ACCEPTED 13 May 2024
PUBLISHED 14 June 2024

CITATION
Tian W, Chen P, Li J and Ji F (2024), Design and application of a monitoring device for embedded foundation side friction resistance. *Front. Earth Sci.* 12:1381689. doi: 10.3389/feart.2024.1381689

COPYRIGHT
© 2024 Tian, Chen, Li and Ji. This is an open-access article distributed under the terms of the Creative Commons Attribution License (CC BY). The use, distribution or reproduction in other forums is permitted, provided the original author(s) and the copyright owner(s) are credited and that the original publication in this journal is cited, in accordance with accepted academic practice. No use, distribution or reproduction is permitted which does not comply with these terms.

Design and application of a monitoring device for embedded foundation side friction resistance

Wei Tian[1,2], Peishuai Chen[2], Jiacheng Li[2]* and Fuquan Ji[2]

[1]School of Civil Engineering, Southeast University, Nanjing, China, [2]CCCC Second Harbor Engineering Company, Ltd., Wuhan, China

In geotechnical engineering, side friction resistance (SFR) is difficult to be measured directly. To further understand distribution law of the SFR, this paper developed a monitoring device that can directly measure the SFR. Further, a theoretical conversion formula for the elastic deformation and the SFR that considers the end effect of sensor sealing was proposed to guide the selection of sensor size and sealing material. Moreover, the monitoring device for the SFR was then calibrated using a large-scale direct shear apparatus and analyzed the stability of the sensor. The calibration results revealed that under cyclic loading and unloading conditions, the linear correlation coefficient of the sensor was greater than 0.996, and the sensitivity after sealing could reach 4.836 με/kPa, which met requirements of the engineering application. The developed monitoring device characterized by simple testing principle, low cost, and high precision were successfully applied to an open caisson project in Harbin City, which contributes to address the difficult problem of efficiently collecting the SFR in highways, bridges, water conservancy, and other projects.

KEYWORDS

embedded foundation, SFR sensor, large-scale direct shear apparatus, open caisson, field monitoring

1 Introduction

In geotechnical engineering, soil pressure and side friction resistance are important mechanical parameters, which have significant impacts on the study of soil mechanics and engineering practice. For example, the design and construction of embedded foundation, such as open caisson, caisson, and driven piles, all need to be based on accurate side friction resistance values (Tanimoto and Takahashi, 1994; Mitkina, 1996; Chakrabarti et al., 2006; Allenby et al., 2009; Ali and Madhav, 2013). However, it is difficult to directly monitor the SFR of submerged foundation, which makes it impossible to accurately capture the subsidence resistance during the construction process, which in turn prevents the controllable and efficient subsidence of embedded foundations from being realized. Compared with soil pressure sensors, attempts to directly test side friction resistance are limited. Stroud (Stroud, 1971) developed a device that can simultaneously monitor soil pressure and shear load. Although the device has a novel structure, there is a significant

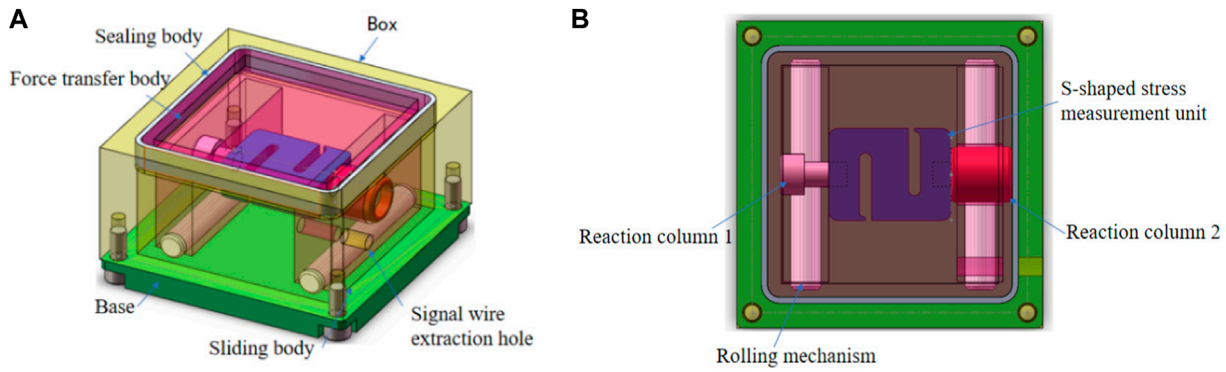

FIGURE 1
Three-dimensional structure diagram of the SFR sensor: **(A)** Three dimensional axonometry; **(B)** Cross-sectional view of the SFR sensor.

cross-effect between the monitored parameters, and it has rarely been used in engineering projects so far. More recently, Gan (Gan et al., 2018) has developed a shear stress sensor to monitor the shear strain at the interface between soil and structure, but the device remains in the laboratory stage due to unresolved waterproof sealing issues.

At present, scholars worldwide mainly adopt *in-situ* monitoring, laboratory test, numerical calculation, and theoretical analysis to study the SFR. In the field tests, New and Bowers (1994), Zhu et al. (2019), Yan et al. (2021) and Houlsby et al. (2006) obtained the SFR by multiplying the earth pressure on the side wall of a caisson by a certain friction coefficient through field monitoring. In addition, Pelecanos (Wang et al., 2019) and Wang et al. (Plecanos et al., 2017)used BOTDR and FBG respectively to measure the change value of axial stress of pile body to determine the average shear stress. Due to the indirect test method, there are certain errors in the actual SFR values, and the monitoring data are relatively discrete and poorly repeatable. This brings difficulties to theoretical analysis, and therefore many scholars have carried out laboratory experiments and numerical calculations.

In terms of laboratory tests, Tehrani (Tehrani et al., 2016) and Abidemi et al. (Olujide Ilori et al., 2017) concluded from laboratory model tests that normal pressure, concrete surface roughness, and soil compactness restricted the exertion of the SFR. Wang (Wang et al., 2013) and Mu (Mu et al., 2014) carried out sinking model tests of open caisson to investigate the change characteristics of side wall friction resistance, settlement range of soil surface outside the wall, and flow trend of soil particles when sinking the open caisson to different depths. Zhou et al. (2018) performed a series of laboratory centrifugal tests to study the distribution of the SFR under different caisson wall forms. Also, many scholars investigated the SFR of the embedded foundations through theoretical analysis. Yang et al. (2023) and Lai et al. (2022) proposed a calculation method for the SFR of the caisson during sinking, in which soil arch effect and stress relaxation effect of soil surrounding the caisson were considered. Based on the actual monitoring data of engineering projects, Li et al. (2023) and Dong et al. (2023) adopted the trained artificial neural network to predict soil parameters under different working conditions.

In summary, the studies on the SFR of embedded foundation have yielded remarkable achievements. Since the indirect test methods used in the field tests, laboratory tests, and theoretical analyses focus on a single soil layer or are simplified, and there are certain differences between test and actual SFR values (Sejia et al., 2014; Cao-Jiong et al., 2022). In order to solve the difficult problem of obtaining SFR directly, a new type of direct monitoring device for side friction resistance is proposed in this paper and applied in a caisson project in Harbin to verify the reliability of the device.

2 Structure design of the SFR sensor

For geotechnical tests such as triaxial test, ring shear test and direct shear test, the average shear stress of a characteristic shear surface represents the approximate shear stress at a point (Thermann et al., 2006). A shear stress sensor was developed based on the concept of the surface with points, which consisted of six parts: box, base, force transfer body, inverse column, S-shaped stress measurement unit, and sealing body (as illustrated in Figure 1). The S-shaped stress measurement unit was made of high elastic alloy, one end of which was fixed to the force transfer body through the reaction column 1, and the other end of which was fixed to the box through the reaction column 2. The two reaction columns could provide constraints for the S-shaped stress measurement unit. The box, base, and force transfer body were made of the stainless steel metal, while the sealing body adopted flexible waterproof sealing material. In addition, considering that the medium in contact with the soil affected the results of the SFR monitoring, a groove was set on the top of the force transfer body, which was filled with the same material as the measured medium.

Since the SFR sensor was only sensitive to friction, it was not sensitive to positive pressure. Therefore, the key problem to be solved was the decoupling of the positive pressure and the SFR. To reduce the friction between the carrier and the base under the normal force, two decoupling methods, i.e., roller type and ball type, were designed in this study. Meanwhile, a gap was reserved between the carrier and the top of the box to prevent the contact between the force carrier and the box when the maximum shear force was applied.

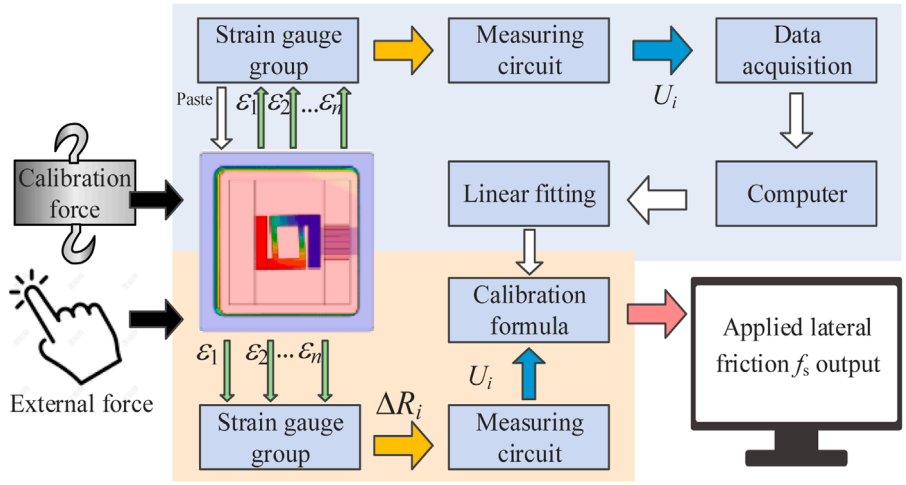

FIGURE 2
Schematic diagram of sensor working principle.

3 Theory and simulation of the SFR sensor

3.1 Working principle

It was observed from Figure 2 that when the sensing surface was subjected to the SFR, the normal load was filtered by the sliding decoupling mechanism, and the force transfer body only transferred the SFR to the S-shaped stress measurement unit. Due to the constraint of the reaction pillar on the S-shaped stress measurement unit, the tension-and-compression stress sensor underwent a slight elastic deformation, causing strain recorded by the strain gauge. This in turn led to a change in the resistance of the strain gauge. The demodulation device detected the changes in the electrical signals and demodulated the corresponding side slip resistance value signals, thus achieving the measurement of the side slip resistance. However, there was an end effect at the contact point between the force transfer body and the sealing material under the influence of side slip resistance, which certainly affected the measured shear stress values. To elucidate the working mechanism of the sensor, it is necessary to study the structural mechanical characteristics of the S-shaped tension-and-compression sensor after taking into account the end effect generated by the sensor sealing.

3.2 Analysis of elastic element forces

The elastic element in the side slip resistance sensor was a S-shaped load cell, with the upper strain gauges located in the same position as the cantilever beam structure (Figure 3A). For ease of calculation and analysis, the S-shaped load cell could be simplified to a closed framework structure with one end fixed and the other end acting as a cantilever (Geonea et al., 2020). In this simplified analysis, a concentrated force F and a counterclockwise bending moment of 0.5 FL were applied to the end of the upper balance beam. The structural mechanical model could be simplified to a single-span, three-degree-of-freedom statically indeterminated rigid framework, as indicated in Figure 3B.

To solve the three unknown forces, the following equations could be established (Hjelmstad, 2007):

$$\begin{bmatrix} \delta_{11} & \delta_{12} & \delta_{13} \\ \delta_{21} & \delta_{22} & \delta_{23} \\ \delta_{31} & \delta_{32} & \delta_{33} \end{bmatrix} \begin{bmatrix} X_1 \\ X_2 \\ X_3 \end{bmatrix} = - \begin{bmatrix} \Delta_{1P} \\ \Delta_{2P} \\ \Delta_{3P} \end{bmatrix} \tag{1}$$

That was:

$$\overline{\delta}\{X_i\} = -\{\Delta_{iP}\}$$

where δ_{ij} is the generalized displacement corresponding to X_i when X_i is the unit value; Δ_{ip} is the generalized displacement corresponding to X_i due to the load.

The displacement coefficients could be obtained using the method of graph multiplication:

$$\overline{\delta} = \begin{bmatrix} \frac{H^2 L}{2EI_H} + \frac{H^3}{12EI_V} & 0 & 0 \\ 0 & \frac{2L^3}{3EI_H} & -\frac{L^2}{EI_H} \\ 0 & -\frac{L^2}{EI_H} & \frac{H}{EI_V} + \frac{2L}{EI_H} \end{bmatrix} \tag{2}$$

where I_H is the moment of inertia of the horizontal beam section; I_V is the moment of inertia of the vertical beam section, and E is the elastic modulus of the sensor material; L is the length of the horizontal balance beam; H is the length of the vertical beam.

$$\{\Delta_{iP}\} = \left[0, -\frac{FL^3}{12EI_H}, 0\right]^T \tag{3}$$

By substituting Eqs 2, 3 into Eq. 1, the following equation could be obtained:

$$\{X_i\} = \left[0, -\frac{F}{2} + \frac{3}{8+4K}F, -\frac{FL}{4} + \frac{2L}{8+4K}F\right]^T \tag{4}$$

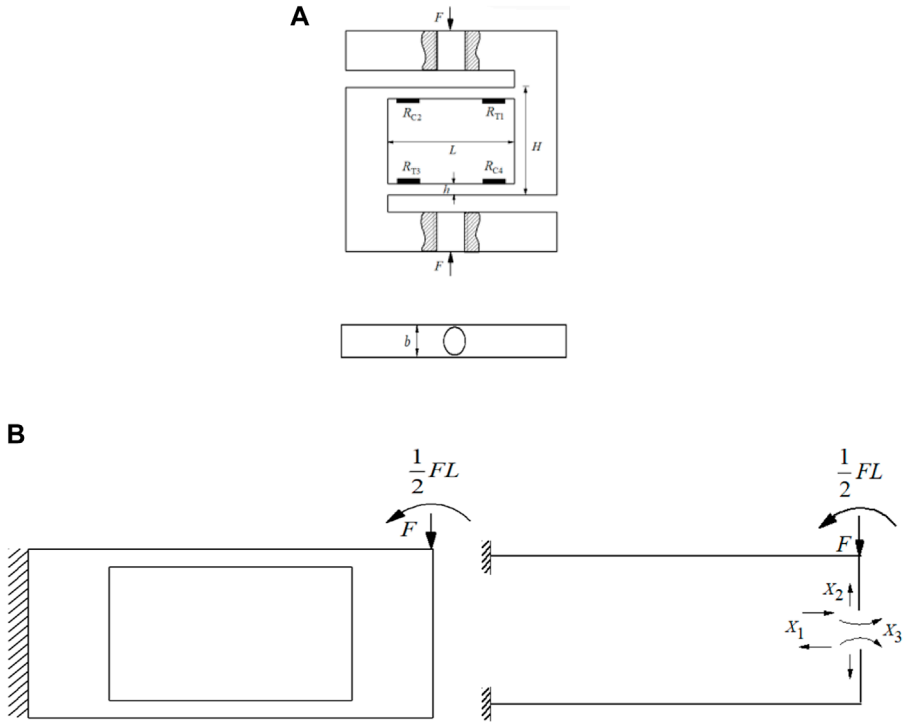

FIGURE 3
S-shaped load cell and mechanical model: **(A)** S-shaped load cell and the placement of strain gauges; **(B)** Equivalent mechanical model.

where $K = LI_V/HI_H$.

By substituting the Eq. 4, the bending moment diagram of the S-shaped load cell could be solved. The bending moment at the ends of the parallel beam was given by:

$$M_1 = M_3 = \frac{FL}{4} + \frac{2FL}{8+4K}$$
$$M_2 = M_4 = -\frac{FL}{4} - \frac{FL}{8+4K} \tag{5}$$

According to Eq. 5, the maximum bending stress and strain at the ends of the parallel beam were:

$$\varepsilon_1 = \varepsilon_3 = -\frac{3FL}{2Ebh^2} - \frac{3FL}{(4+2K)Ebh^2}$$
$$\varepsilon_2 = \varepsilon_4 = \frac{3FL}{2Ebh^2} + \frac{3FL}{(2+K)Ebh^2} \tag{6}$$

The vertical beam I_V was much larger than the horizontal beam I_H, i.e., K was large. Eq. 6 was arranged as:

$$\varepsilon_1 = \varepsilon_3 = -\varepsilon_2 = -\varepsilon_4 = -\frac{3FL}{2Ebh^2} \tag{7}$$

where b and h are the width and thickness of the horizontal balance beam, respectively.

The strain of the elastic element was converted into a change in the resistance to monitor the strain generated in the S-shaped load cell subjected to force. Also, to improve the sensitivity of the sensor and to eliminate the influence of temperature, four strain gauges were connected to form a resistance-strain full bridge (Arshak et al., 1997). The conversion principle of this sensor is displayed in Figure 4.

The output voltage of the full bridge was given by:

$$U_0 = \frac{(R_1+\Delta R_1)(R_3+\Delta R_3) - (R_2-\Delta R_2)(R_4-\Delta R_4)}{(R_1+R_2+\Delta R_1-\Delta R_2)(R_3+R_4+\Delta R_3-\Delta R_4)} U_S \tag{8}$$

where the U_s is the supply voltage; U_0 is the output voltage, R_1=R_2=R_3=R_4. By substituting the relation between resistance and strain into Eq. 8, U_0 can be rewritten as:

$$U_0 = \frac{1}{4} G \frac{\varepsilon_1 + \varepsilon_3 - \varepsilon_2 - \varepsilon_4}{\left[1 + \frac{1}{2}(\varepsilon_1 + \varepsilon_2 + \varepsilon_3 + \varepsilon_4)\right]} U_S \tag{9}$$

where ε_j is the micro-strain of the strain gauge.

By rearranging the Eq. 9 the relationship between the SFR and the output voltage can be obtained:

$$f_s = \alpha \frac{2Ebh^2}{3L} \frac{U_0}{AGU_S} \tag{10}$$

where the f_s is the SFR; A is the sensing area of the SFR sensor; and α is the end effect coefficient. The Eq. 10 reflects that the sensor sensitivity is related to the elastic beam size and material.

To verify the rationality of the derived formula for S-shaped load cell, this study utilized ABAQUE software to calculate and analyze the maximum strain at the end of the balanced beam with beam lengths of 12 mm, 14 mm, and 16 mm as well as different beam thicknesses h. The sensor chosen for analysis had a Young's modulus of 200 GPa and a Poisson's ratio of 0.3. A load of 1000 N was applied to the sensor. It was observed from Figure 5 that the theoretical calculation results of the maximum strain at the beam end matched well with the finite element simulation results, which verified the reasonableness of the derived theoretical formula.

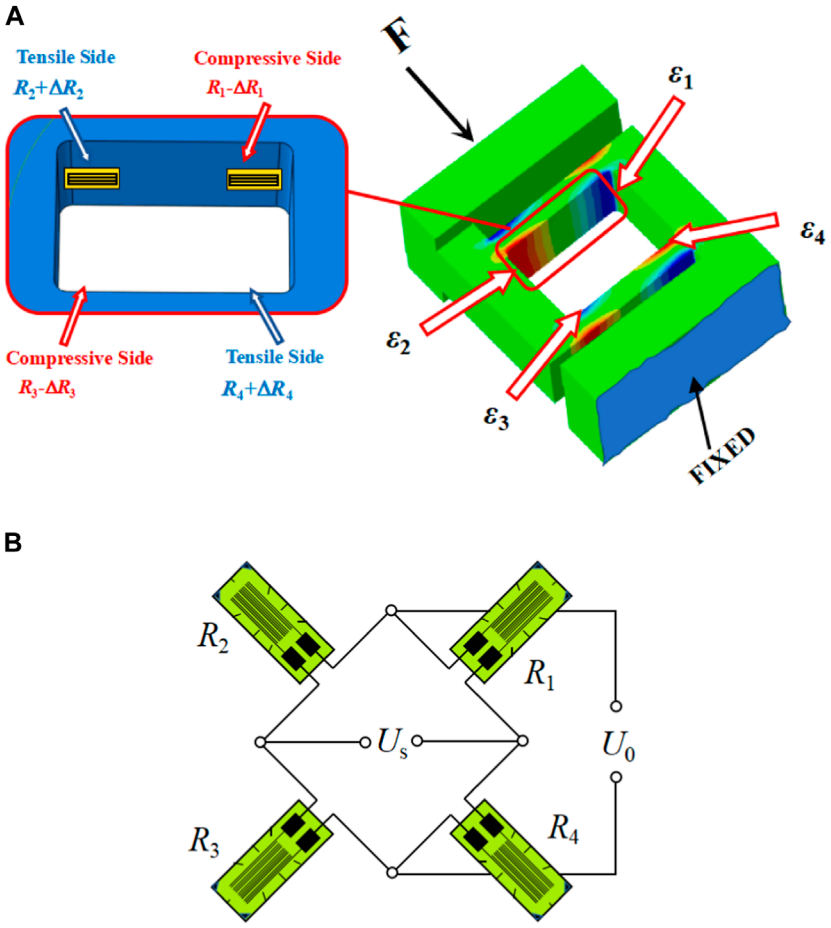

FIGURE 4
Schematic diagram of the SRF sensor strain gauge adhesive and circuit: **(A)** Sensor strain gauge adhesive; **(B)** Wheatstone bridge circuit.

4 Determination of sensor size and sealing material

4.1 Selection of sensor size

The sizes of sensor were selected with the main consideration of facilitating the convenient layout, so that it could be installed between the longitudinal main ribs. The spacing between the steel bars in the field typically ranged from 12 cm to 20 cm. Therefore, the sizes of the sensor were determined to be 10 cm (length)×10 cm (width) ×6 cm (height). The sensing area on the SFR surface were determined to be 7.0 cm long and 7.0 cm wide (Figure 6).

To satisfy the range requirements for monitoring the SFR in large-scale sinking foundations, the maximum measurement range of the SFR device was set to 200 kPa. Based on the sensing area (49 cm^2), the maximum tension and compression force on the strain gauge was calculated to be 980 N. According to Eq. 7, the relationships between the balanced beam length, thickness, and the strain as well as maximum stress at the end of beam under a SFR of 200 kPa are illustrated in Figure 7. It was observed that as the thickness of the parallel beam decreased and the length increased, the strain of the elastic element under the load increased, indicating a more sensitive sensor. However, the maximum tension and compression stress σ_{max} also increased, which might cause the sensor to reach the yielding state. To meet the high-precision requirements for the sensor with a large measurement range, the parameters of the elastic element were determined, as summarized in Table 1. The S-shaped stress measurement unit and the SFR sensor were made of stainless steel, and their physical appearances are displayed in Figure 8.

4.2 Selection of sealing material

The SFR sensor in geotechnical engineering is always exposed to the environment of high water and soil pressures that require sealing. However, the sealing will produce end effect on the force transfer body and affect the test results. In order to reduce the strain loss of the S-shaped stress measurement unit after the sealing of SFR sensor, it is necessary to analyze the force of the sensor to provide guidance for the selection of sealing material. Although the strain loss caused by the end effect can be compensated by the laboratory calibration test, the sensitivity of the sensor will

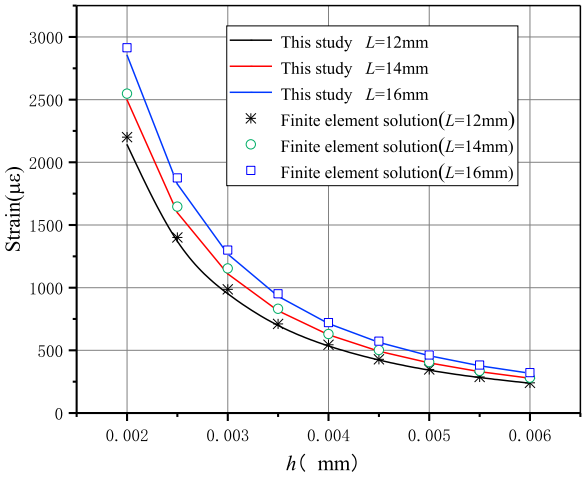

FIGURE 5
Comparison between theoretical solution and numerical simulation results.

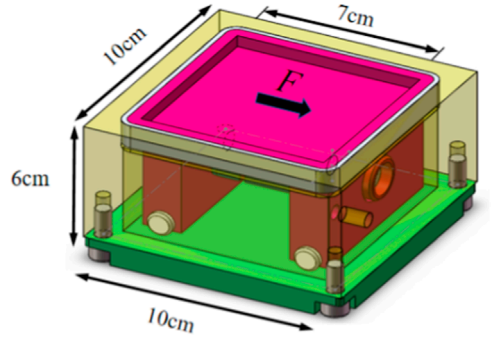

FIGURE 6
The SFR Sensor external profile dimensions.

be reduced if the strain loss is too large. Due to the constraint effect of the sealing body on the force transfer body after the sensor is sealed, the force of the sensor is relatively complicated and the traditional analytical algorithm cannot capture the mechanical characteristics of the elastomer well. Therefore, the finite element method was utilized to simulate the working condition of the sensor to make up for the shortage of theoretical analytical calculation.

In this section, the ABAQUS finite element software was employed to establish a finite element analysis model of the SFR sensor in Figure 9. The S-shaped load cell in the sensor was fixed inside the housing by a reaction column. Therefore, both the elastic body and the reaction column were constrained. In addition, the bottom of the force transfer body was a sliding mechanism that allows tangential displacement. Therefore, the bottom of the force transfer body was only constrained for normal displacement. Since the lateral force transfer was influenced by both the elastic body and the sealing material, the stress characteristics of the sensor were related to the ratio of the elastic modulus of the sealing material to the elastic modulus of the elastic body (E_g/E_s). In this case, the elastic body of the sensor was an elastic structure. Based on the principle of virtual work (Craig and Taleff, 2020), the formula for calculating the equivalent modulus, E_g of the sensor can be solved in Eqs 11a, b:

$$\Delta_g = \int \frac{\overline{M}^2 ds}{EI_H} = \frac{L^3}{24EI_H} \tag{11a}$$

$$E_g = \frac{1}{\Delta_g} = \frac{2Ebh^3}{L^3} \tag{11b}$$

where Δ_g is the horizontal displacement of the SFR sensor under the action of unit force; $\overline{M}$ is the sectional bending moment of the S-shaped force measurement unit under a unit force. Six working conditions were numerically calculated to analyze the influence of the strain transfer coefficient of the sensor under different modulus ratios, as listed in Table 2.

Figure 10 displays the relationship between the modulus ratio of the elastic body and the sealing material as well as the strain ratio. It was observed that the strain at the beam end of the parallel beam of the S-shaped load cell without any sealing material was 1,216 uε. As the elastic modulus of the sealing material (E_s), i.e., the ratio E_s/E_g increased, the maximum strain at the beam end of the parallel beam gradually decreased. In case of E_s/E_g=0.0125 (i.e., E_s=0.5 MPa), the strain of the parallel beam was 0.9 times that without sealing material, demonstrating a 10% strain loss after sealing. In case of E_s/E_g=0.025 (i.e., E_s=1.0 MPa), the strain loss after sealing was 19%. This loss increased until E_s/E_g=0.25 (i.e., E_s=10 MPa), where the strain loss after sealing reached 65%. Therefore, it is crucial to select an appropriate sealing material to minimize the loss of sensitivity of the sensor.

The commonly used sealing materials and their parameters are illustrated in Table 3. It was observed from the numerical calculation results that the strain loss after sealing with a rubber ring (E_s=7.8 MPa) varied from 50% to 65%. However, the strain loss was only 10% when a silicone structural adhesive (E_s=0.5 MPa) was used for sealing. Hence, the selection of a silicone structural adhesive with a lower elastic modulus had the least impact on sensor sensitivity.

5 Sensor calibration and stability analysis

5.1 Testing equipment and scheme

The calibration system was designed and modified on the basis of a large-scale direct shear apparatus to realize the graded loading calibration of the SFR sensor. As displayed in Figure 11A, the SFR sensor calibration system consisted of the large-scale direct shear apparatus, the SFR sensor, the sensor transmitter, the signal transmission line, the straight shear apparatus control system, and the signal acquisition system.

Considering that the calibration of the SFR sensor needed to verify the validity of the decoupling of the positive pressure and the SFR of the sensor, the normal and horizontal force transfer mechanisms were designed on the basis of the large-scale direct shear instrument, and the force transfer ends were embedded in the sensor groove to realize the

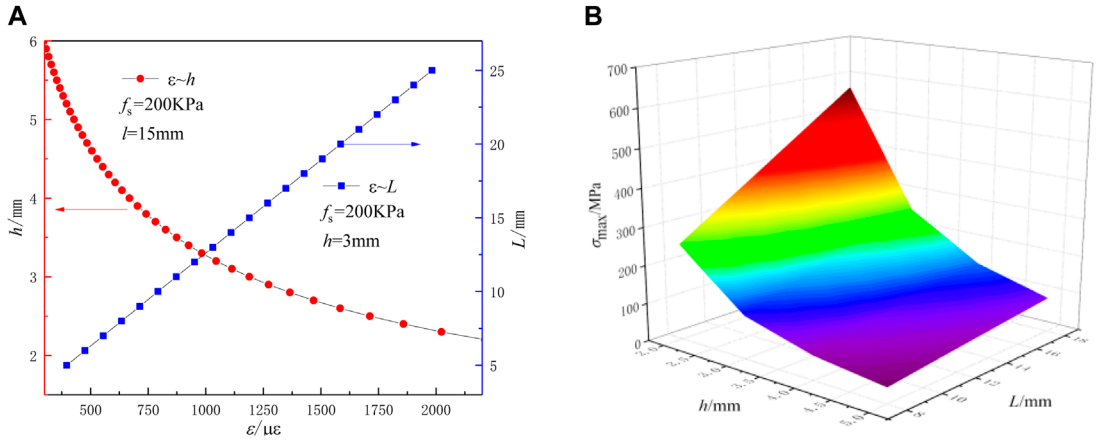

FIGURE 7
The relationship between strain and maximum stress of balance beam and h and L: **(A)** The relationship between ε and h, L; **(B)** The relationship between σ_{max} and h, L.

TABLE 1 Dimension parameters of tension and pressure sensors.

Size parameter	*L* (mm)	*h* (mm)	*b* (mm)	*H* (mm)
Value	15	3	10	19

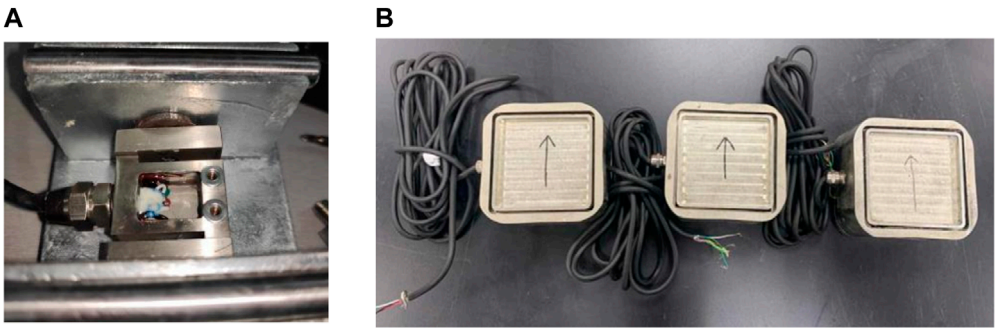

FIGURE 8
The S-shaped load cell and the SRF sensor: **(A)** S-shaped stress measurement unit; **(B)** The SRF sensor.

quantitative loading of normal and horizontal forces (Figure 11B). The loading was controlled by servo motor with constant shear force.

5.2 Analysis of test results

5.2.1 Comparison of decoupling methods

The sensors were calibrated using two methods to compare the effect and stability of the two decoupling methods. Three normal pressures of 50 kPa, 100 kPa, and 200 kPa were applied to each set of tests to obtain the corresponding sensitivity coefficients C_1, C_2, and C_3 for the SFR sensor.

As revealed in Figure 12, the calibration curves of both decoupling methods exhibited obvious linear characteristics, and the loading curves under different normal stresses were in good agreement. In addition, the sensitivity coefficient decreased with the increase of the normal force, indicating that the balls or rollers inside the sensor generated friction under the normal force.

The test results showed that the correlation coefficient of the sensor calibration curve obtained by the roller decoupling method was 0.995, and the average sensitivity coefficient of the sensor was 5.059 με/kPa. The correlation coefficient obtained by the ball decoupling method was 0.998, and the sensitivity coefficient was 5.267 με/kPa. Therefore, the calibration curve of the SFR

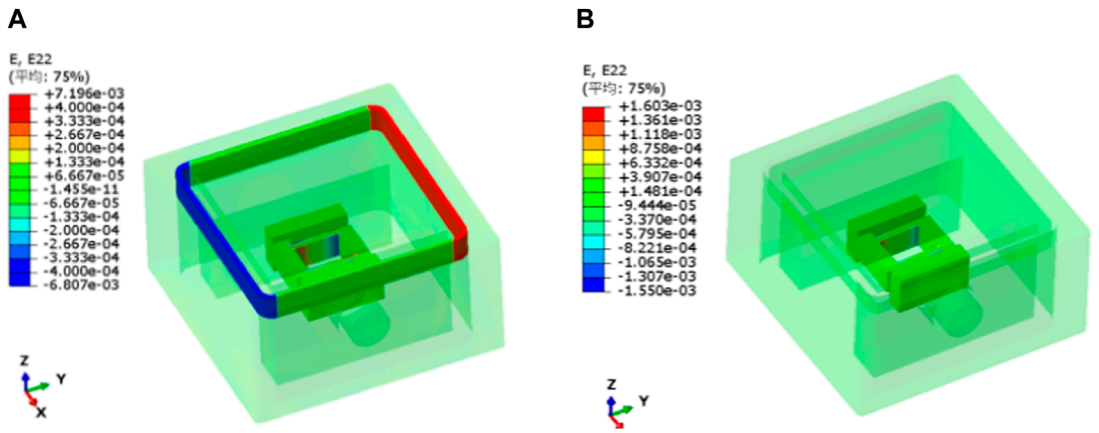

FIGURE 9
Finite element analysis results of SRF sensor with different modulus ratios at side friction resistance of 200 kPa: **(A)** *Es*/*Eg* = 0.25; **(B)** *Es*/*Eg* = 0.

TABLE 2 Numerical calculation conditions.

Working conditions	E_s(Mpa)	E_g(Mpa)	*Es*/*Eg*
1	10	40	0.25
2	5	40	0.125
3	2	40	0.05
4	1	40	0.025
5	0.5	40	0.0125
6	0	40	0

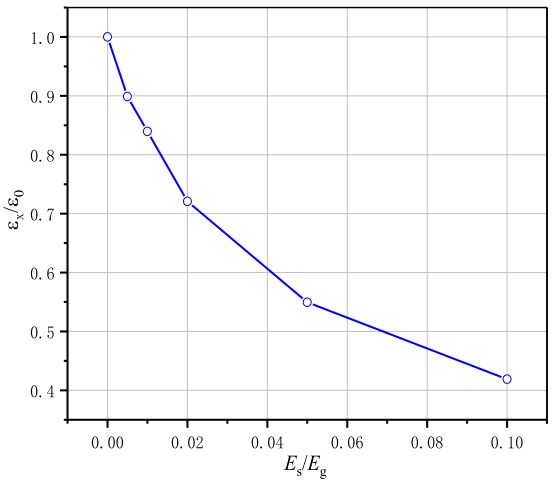

FIGURE 10
Relation curves of different stiffness ratios and strains.

sensor obtained using the ball decoupling method had better linear correlation and higher sensor sensitivity. The ball decoupling method would be used for the follow-up study.

In addition, to examine the filtering effectiveness of the SFR sensor against the normal load of the panel, the SFR of the sensor subjected only to vertical pressure was observed. As demonstrated in Figure 13, the normal force-SFR curves of the two SFR sensors were essentially parallel to the horizontal axis. The roller sensor was slightly more affected by the normal force compared with the ball sensor, but in general the SFR was close to 0 kPa for different vertical pressures. This indicated that both decoupling methods were effective in filtering the interference of the normal force perpendicular to the sensor panel.

5.2.2 Comparison of performance before and after sealing

Figure 14 displays the sensor calibration curves before and after sealing. The cyclic loading and unloading process basically overlapped and exhibited obvious linear characteristics. The fitting sensitivity coefficients before and after sealing were 5.194 με/kPa (R^2 =0.997) and 4.836 με/kPa (R^2 =0.996), respectively. Comparison of the sensitivity coefficients before and after sealing revealed that some of the SFR would be lost when the sealing material was filled between the force transfer body of the SFR sensor and the box, resulting in a certain decrease in the sensitivity of the sensor.

The loss rate of sensitivity after sealing was calculated to be 8.5% (numerically calculated to be 10%). Therefore, the SRF sensor response considering the sealing effect could be expressed as follows:

$$f_s = \frac{\varepsilon}{C} \tag{12}$$

where C is calibration factor after sealing, with a value of 4.836 με/kPa. According to Eq. 12, the sensor strain can be converted into the side friction resistance.

5.2.3 Sealing performance test

To test the sealing effect of the SFR sensor, the sensor was immersed in a sealed container filled with water (Figure 15A), then

TABLE 3 Commonly used sealing materials and parameters.

Materials	Elastic modulus (MPa)	Poisson's ratio
Epoxy resin	1,000	0.38
Silica gel	1,200	0.48
Silicone structural adhesive	0.5	0.48
Rubber	7.8	0.47

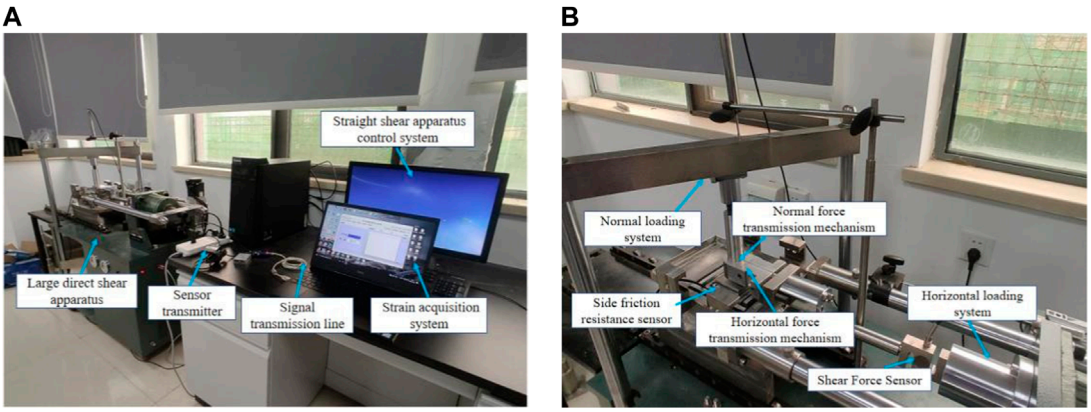

FIGURE 11
Calibration system of the SFR sensor: **(A)** Calibration system composition; **(B)** Calibration system force transmission mechanism.

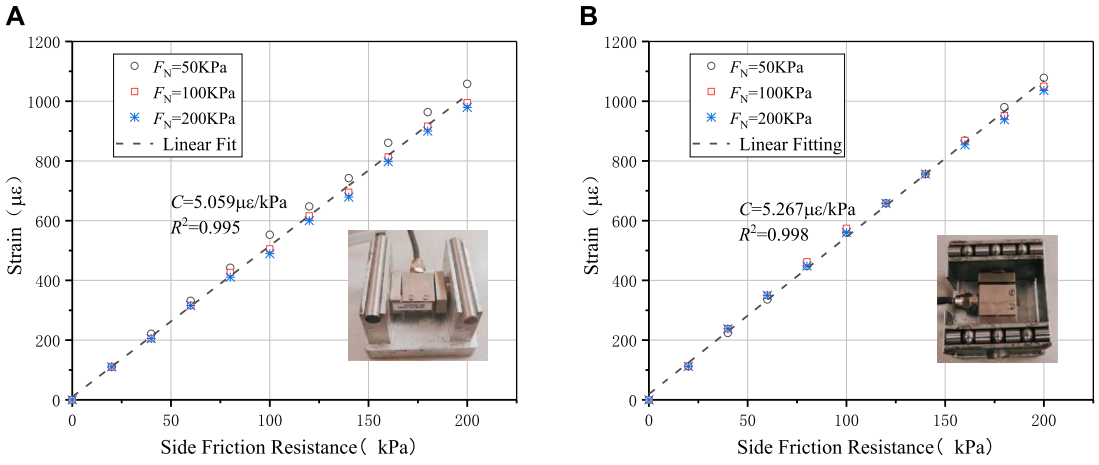

FIGURE 12
Calibration curves of the SFR sensor under different normal forces: **(A)** Roller decoupling method; **(B)** Ball decoupling method.

the pressure inside the container was increased to 0.7 MPa by an air compressor, and the sensor was continuously tested for 1 month at this pressure. Figure 15B displays the strain curve of the sensor during the 30-day sealing test. The test results confirmed that the sensor could work normally under high water pressure condition and had good sealing and waterproof performance.

6 Project application

6.1 Test condition and sensor position

To evaluate performance of the SFR sensor, a field test was conducted on the pipe-jacking receiving well of the No. 1 open

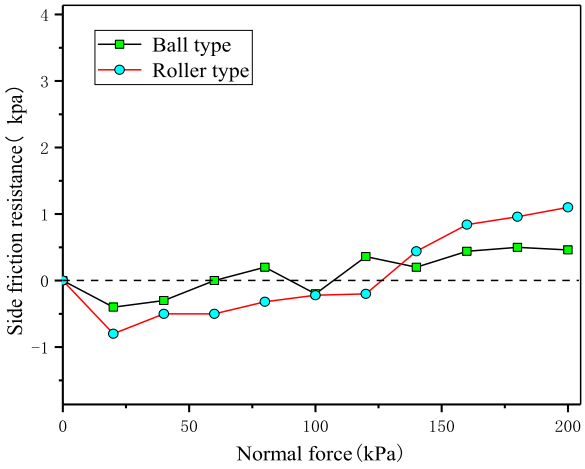

FIGURE 13
Curve of the SFR versus normal force under horizontal load of 0 kPa.

caisson of a wastewater treatment plant in Harbin City. The open caisson had a diameter of 17 m, a height of 32.35 m, and a wall thickness of 1.5–1.8 m. A top-to-bottom distribution of soil layers is displayed in Table 4. The groundwater in the open caisson site was pore diving. The depths of the initial groundwater level and the static water level were 0.00–0.96 m and 0.00–0.69 m, respectively.

In the field test, two monitoring sections were selected from the side wall of the open caisson. Three earth pressure boxes (ET) and three SFR monitoring devices (FT) were installed in each monitoring section, and their distances from the edge of the open caisson were 1 m, 6 m, and 11 m, respectively, as displayed in Figure 16A. The earth pressure boxes and the SFR monitoring devices were installed at the same elevation of the shaft wall, with a transverse distance of 40 cm. The data from the two sensors were transmitted to the ground signal transmitting module via the acquisition module, and then they were uploaded to the cloud platform through the signal transmitting module to enable data monitoring and storage. In addition, the sinking depth and plane deviation of the caisson were regularly monitored by the total station. Abidemi Olujide Ilori et al. (Olujide Ilori et al., 2017) stated that the surface material and roughness of the structure were crucial factors affecting the friction coefficient of soil-structure interface. Therefore, the SFR sensors were embedded in the outer wall of the open caisson, and their sensing surface should be flush with the sunken wall. The groove of the sensing surface should be filled with cement mortar to ensure that the roughness of the contact interface of the sensors were consistent with that of the sunk wall. The field installation is presented in Figures 16B, C.

6.2 Monitoring results

6.2.1 Overall sinking

As shown in Figure 17A, the sinking of the open caisson began on 28 April 2022 and reached the design elevation on 26 August 2022, with a cumulative sinking depth of 32.5 m. The average sinking speed was about 0.33 m/d, with the fastest sinking speed of 2 m/d.

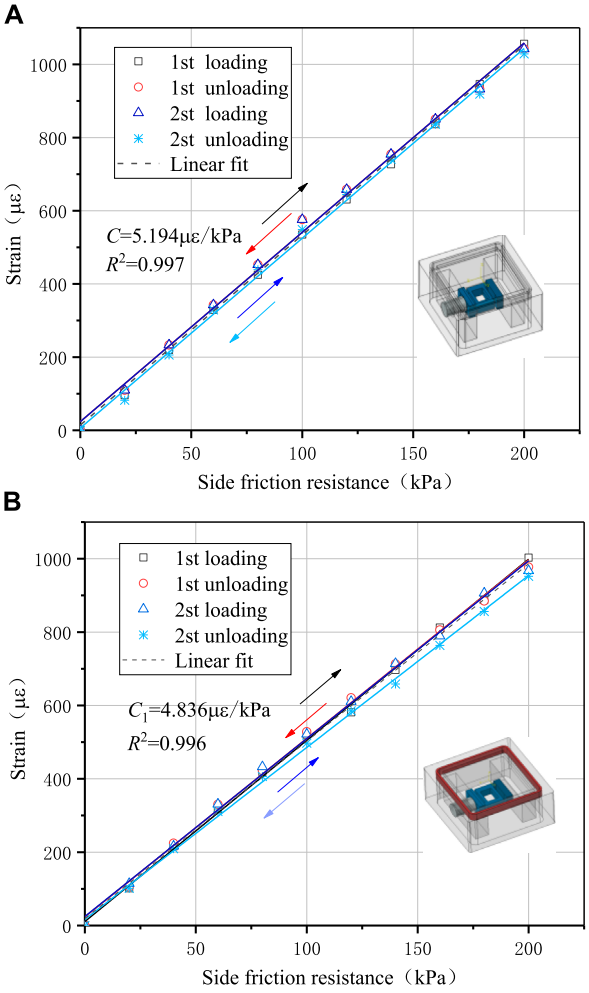

FIGURE 14
Calibration curves before and after sealing of the SFR sensor: **(A)** Sensor calibration curve before sealing; **(B)** Sensor calibration curve after sealing.

The sinking speed was faster in sandy soil layers and relatively slower in cohesive soil layers. As shown in Figure 17B, *x*-*x* and *y*-*y* were two mutually orthogonal coordinate axes. It was observed that the deviation of the open caisson during the initial sinking stage was quite drastic. However, as the depth of the open caisson increased, the surrounding soil provided a stronger constraint on the open caisson, and the inclination of the open caisson only changed slightly. This highlighted the importance of ensuring that the open caisson was in excellent condition during the initial sinking stage.

6.2.2 Sensor monitoring results

The lateral pure earth pressure σ'_n on the side wall of open caisson is obtained by subtracting water pressure from the earth pressure sensors, which can be calculated from Eq. 13a.

$$\sigma'_n = \sigma_n - p \tag{13a}$$

where σ_n is the total normal stresses measured by individual ETs; and p is the fluid pressure.

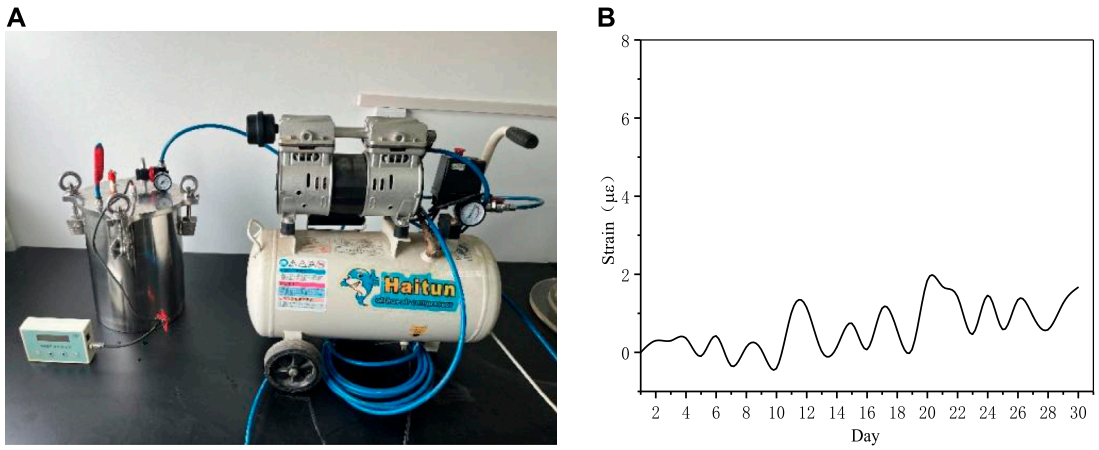

FIGURE 15
Sealing performance test of the SFR sensor: **(A)** Sensor sealing performance test; **(B)** Strain curve of the sensor during the sealing test.

TABLE 4 Distribution of engineering geological layer.

ID	Soil layer	*C* (kPa)	ϕ (°)	*N*	Standard value of side friction resistance(kPa)
1	①Miscellaneous fill	10	16.7	6.0	15
2	③Medium sand	5.6	31.4	16.5	18
3	④Coarse sand	4.5	33.2	19.1	18
4	⑦Clay	23.3	16.4	17.2	18
5	$⑦_1$Medium sand	4.1	34	27.7	18
6	$⑦_3$Clay	26.3	20.8	21.6	37
7	$⑦_1$Medium sand	4.1	34	27.7	18

The variation of lateral pure earth pressure with depth is shown in Figure 18, which indicated that the lateral earth pressure increased with the increase of depth. When the open caisson attitude changed greatly, the lateral earth pressure on the measured wall varied between the passive earth pressure and the active earth pressure, which led to drastic change of the lateral earth pressure. In the late sinking stage, the open caisson attitude tended to be stable, and the lateral earth pressure values from the earth pressure sensors at the same depth were close to each other.

The SFR of the open caisson could be acquired by the monitoring device buried at the site. The monitoring results of the SFR in Figure 19 revealed that the SFR of the side wall of the open caisson varied between 0 and 60 kPa, which was the same as the fact that the earth pressure increases with the increasing soil depth. It was also observed that the fluctuation of the SFR test results was basically consistent with that of the soil pressure test results, which verified the reliability of the monitoring results of the SFR device.

The friction resistance between caisson and soil mainly depends on the friction coefficient δ at the soil-concrete interface, which can be calculated from Eq. 13b:

$$\delta = \tan^{-1}\left(\frac{f_s}{\sigma_n'}\right) \tag{13b}$$

where f_s is the shear stresses measured by individual FCs.

The variation of interface friction coefficient with depth is shown in Figure 20, where the tanδ at the concrete interface is also plotted for comparison (Potyondy, 1961). It was observed that the interface friction coefficient δ for sand-concrete and clay-concrete were 0.6 φ'-0.7 φ' and 0.8 φ'-0.9 φ', respectively. However, Potyondy conducted a large number of direct shear tests to study the shear tests between various soils and structural interfaces, and found that the interface friction coefficients for sand-concrete and clay-concrete were 0.9 φ' and φ', respectively. The reason for this is that the sinking of caisson causes the surrounding soil to become looser,

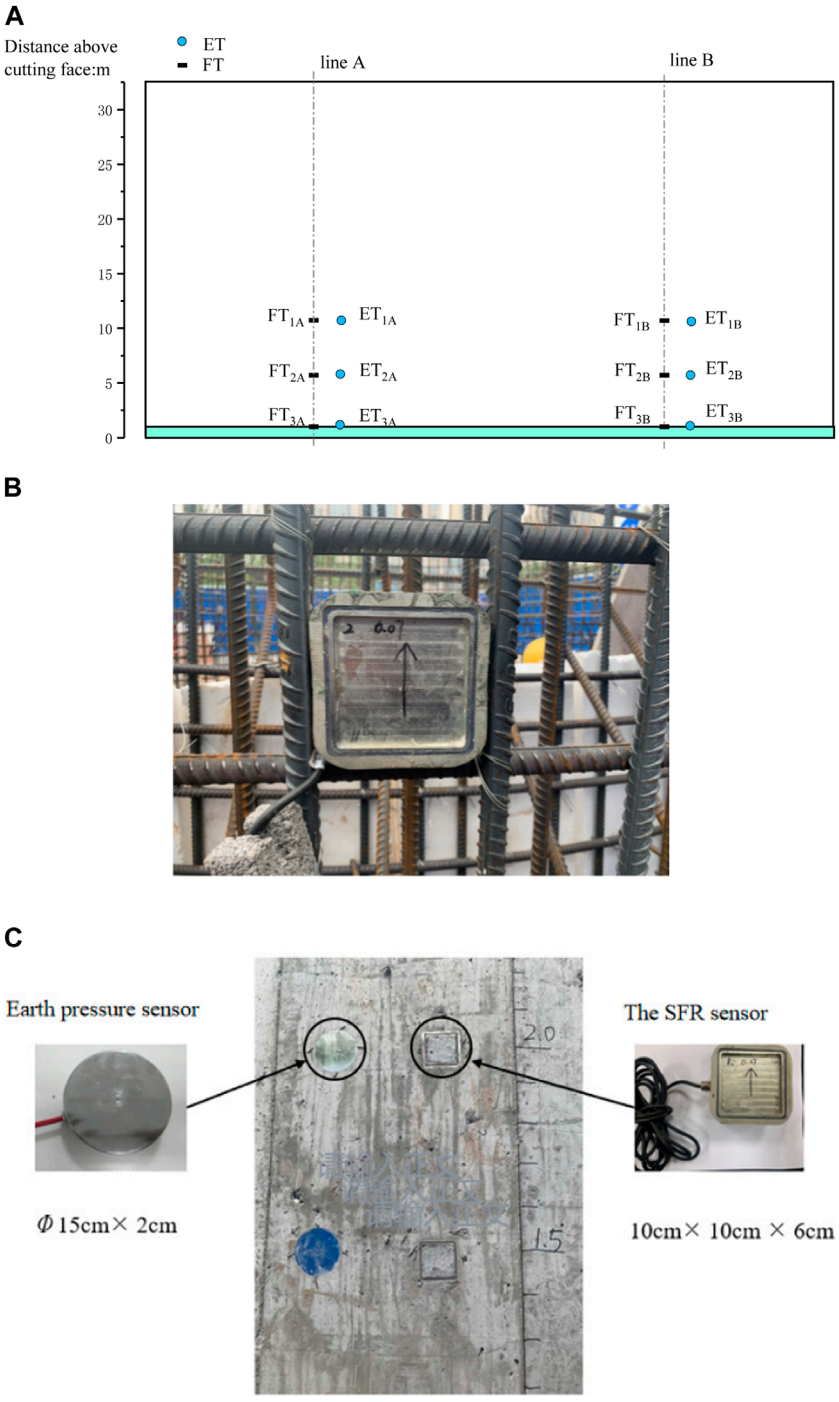

FIGURE 16
The SRF sensor deployed in the field: **(A)** Monitoring instrument layout diagram; **(B)** Sensor fixed to steel rebar prior to casting of the concrete walls; **(C)** Sensor exposed surface after casting.

and the friction interface of groundwater infiltration also leads to a decrease in the interface friction coefficient. Therefore, the friction coefficient from direct shear test for the construction of caisson will overestimate the side friction resistance. It is necessary to use direct test method to obtain the SFR for the design and construction of embedded foundation.

7 Conclusion

A monitoring device that can directly collect the SFR was developed to address the problem of difficulty and low accuracy in capturing the SFR during the construction of sinking foundations. Sensitivity analysis was carried out on

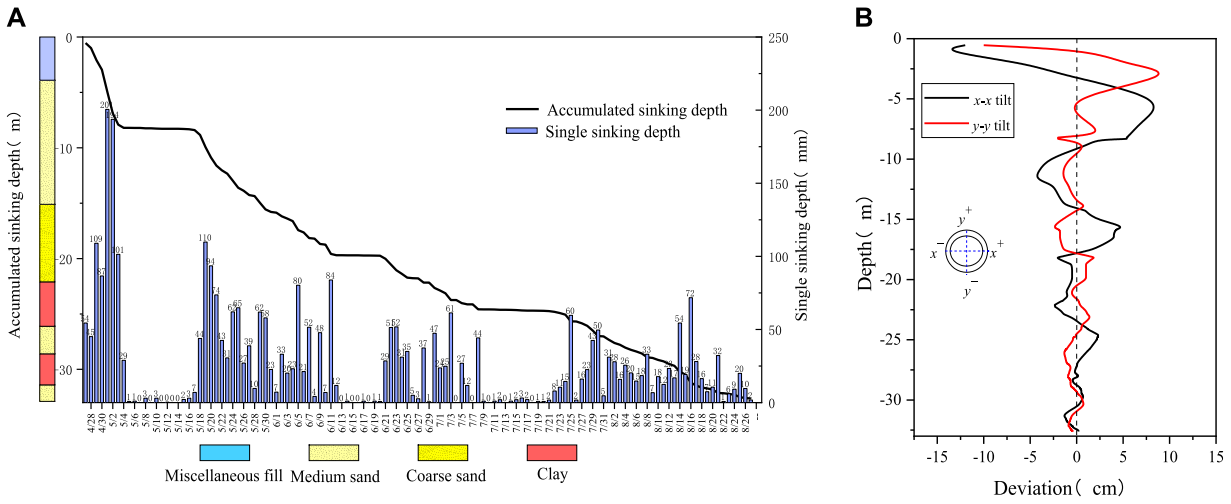

FIGURE 17
Overall sinking of the open caisson: **(A)** Sinking curve; **(B)** Deviation curve.

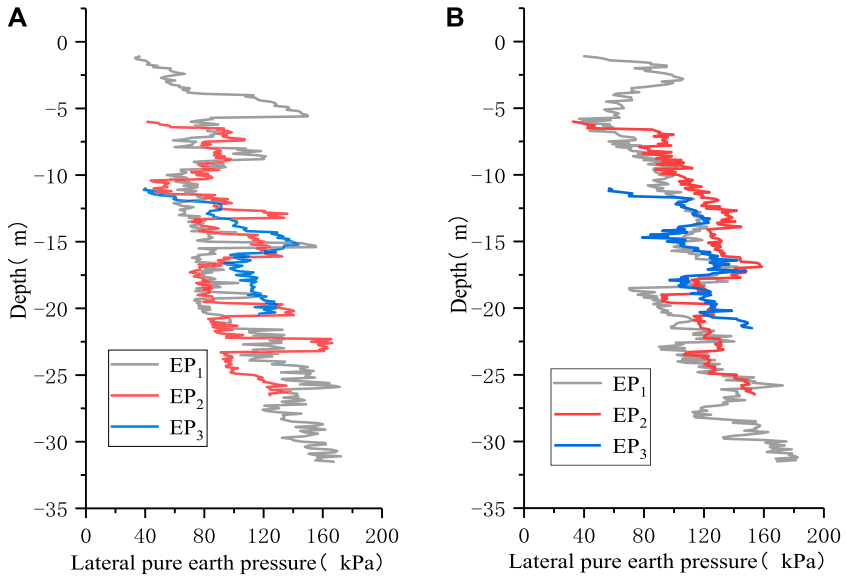

FIGURE 18
Lateral pure earth pressure vs. soil depth: **(A)** Results of monitoring line A; **(B)** Results of monitoring line B.

parameters such as sensor structure size and sealing material properties through sensing theory and numerical simulation analysis methods. A SFR test method was established through the sensing theory analysis and the laboratory calibration experiment, and field tests were carried out in caisson projects. The main work and research results carried out in this paper were as follows:

(1) A monitoring device for directly acquiring the SFR was proposed. The S-shaped force measurement unit was simplified into a closed frame structure, and the theoretical conversion formula for the strain and the SFR of the sensor was derived. The rationality of the theoretical derivation formula was verified by comparing with the numerical simulation results. Based on the sensitivity analysis of the sensor structure size parameters, the sizes of S-shaped stress measurement unit of L = 15 mm, b = 10 mm, h = 3 mm were determined.

(2) The ratio of the equivalent modulus of the S-shaped force measurement unit to the modulus of the sealing material affected the sensitivity of the SFR sensor. As the modulus ratio increased, the strain at the end of the balance beam

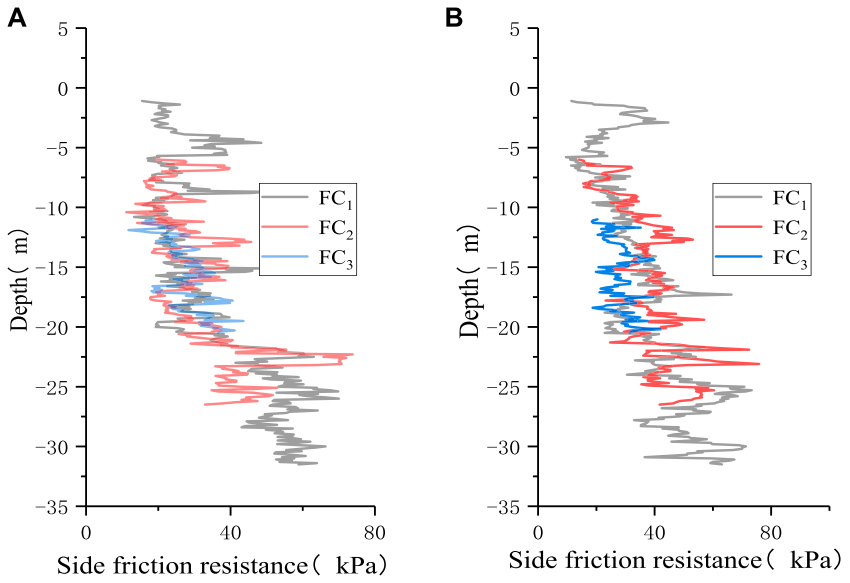

FIGURE 19
Curves of side friction vs. soil depth: **(A)** Results of monitoring line A; **(B)** Results of monitoring line AB.

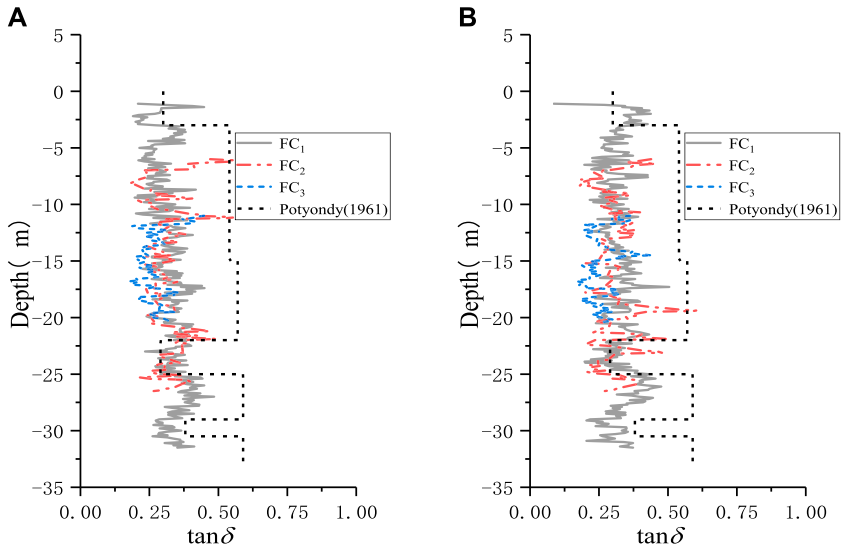

FIGURE 20
Variation of interface friction angle with depth: **(A)** Results of monitoring line A; **(B)** Results of monitoring line B.

gradually decreased, i.e., the strain loss increased. When a silicone structure (E_s=0.5 MPa) was utilized for sealing, the strain loss was 10%, which had a relatively small impact on the sensitivity of the sensor.

(3) The calibration results showed that the two decoupling methods could filter out the influence of normal stress on the test results, and the ball decoupling method exhibited higher sensitivity. After sealing the calibration results of the SFR sensor indicated that there was a good overlap during the loading and unloading processes within the measurement range, with a linear correlation coefficient R^2 greater than 0.996 and a sensitivity coefficient of 4.885 με/kPa. The SFR sensor was able to work continuously and stably under 0.7 MPa water pressure environments, which satisfied meeting the requirements of engineering applications.

(4) The high survival rate of the SFR sensor in field applications was corroborated by its monitoring results, which demonstrate that the SFR increases with the increase of soil depth and the fluctuation of SFR test values are basically consistent with that

of earth pressure test values, thus verifying the reasonableness of the monitoring results from the SFR device.

(5) The friction coefficient from direct shear test for the construction of caisson will overestimate the side friction resistance. It is necessary to use direct test method to obtain the SFR for the design and construction of embedded foundation.

Data availability statement

The original contributions presented in the study are included in the article/Supplementary Material, further inquiries can be directed to the corresponding author.

Author contributions

WT: Writing–original draft, Funding acquisition. PC: Conceptualization, Writing–review and editing. JL: Conceptualization, Methodology, Writing–review and editing. FJ: Investigation, Supervision, Writing–review and editing.

Funding

The author(s) declare that financial support was received for the research, authorship, and/or publication of this article. National key Research and Development Program of China 2022YFB2302500.

Conflict of interest

Authors WT, PC, JL, and FJ were employed by CCCC Second Harbor Engineering Company, Ltd.

Publisher's note

All claims expressed in this article are solely those of the authors and do not necessarily represent those of their affiliated organizations, or those of the publisher, the editors and the reviewers. Any product that may be evaluated in this article, or claim that may be made by its manufacturer, is not guaranteed or endorsed by the publisher.

References

Ali, J. S. M., and Madhav, M. R. (2013). Analysis of axially loaded short rigid composite caisson foundation based on continuum approach. *Int. J. geomechanics* 13 (5), 636–644. doi:10.1061/(asce)gm.1943-5622.0000185

Allenby, D., Waley, G., and Kilburn, D. (2009). Examples of open caisson sinking in Scotland. *Proc. Institution Civ. Engineers-Geotechnical Eng.* 162 (1), 59–70. doi:10.1680/geng.2009.162.1.59

Arshak, K. I., Ansari, F., McDonagh, D., and Collins, D. (1997). Development of a novel thick-film strain gauge sensor system. *Meas. Sci. Technol.* 8 (1), 58–70. doi:10.1088/0957-0233/8/1/009

Cao-Jiong, L., Huang, R., and Yuan-Gang, M. (2022). Researchon caisson sinking resistance in clay-sand intersected stratum. *Bridge Constr.* 52 (04), 61–67. doi:10.3969/j.issn.1003-4722.2022.04.009

Chakrabarti, S. K., Chakrabarti, P., and Krishna, M. S. (2006). Design, construction, and installation of a floating caisson used as a bridge pier. *J. Waterw. port, Coast. ocean Eng.* 132 (3), 143–156. doi:10.1061/(asce)0733-950x(2006)132:3(143)

Craig, R. R., Jr, and Taleff, E. M. (2020). *Mechanics of materials*. John Wiley & Sons.

Dong, X., Tu, J., Xu, J., Cai, L., Wu, B., and Cai, L. (2023). "Based on Abaqus finite element analysis software to assist the construction of super large caisson," in *2023 international Seminar on computer Science and engineering Technology (SCSET)* (IEEE), 627–631.

Gan, F., Ye, X., Yin, K., Li, M., Yang, J., and Xiao, Y. (2018). Experimental study on progressive failure of soil-structure interfaces based on a new measuring method of local stress and displacement. *Chin. J. Rock Mech. Eng.* 37 (3), 734–742. doi:10.13722/j.cnki.jrme.2017.0781

Geonea, I. D., Dumitru, N., Margine, A., Craciunoiu, N., and Copiluși, C. (2020). Design, manufacture and testing of a S type force transducer. *Appl. Mech. Mater.* 896, 255–262. doi:10.4028/scientific.net/amm.896.255

Hjelmstad, K. D. (2007). *Fundamentals of structural mechanics*. Springer Science & Business Media.

Houlsby, G. T., Kelly, R. B., Huxtable, J., and Byrne, B. W. (2006). Field trials of suction caissons in sand for offshore wind turbine foundations. *Géotechnique* 56 (1), 3–10. doi:10.1680/geot.2006.56.1.3

Lai, F., Liu, S., and Deng, Y. (2022). Research progress on mechanical characteristics and environmental effects of Construction process of giant deep buried caisson. *Chin. J. Basic Eng. Sci.* 30 (03), 657–672. doi:10.16058/j.issn.1005-0930.2022.03.012

Li, Z. L., Zhang, X., Dai, G., and Cao, S. (2023). Study on soil parameter evolution during ultra-large caisson sinking based on artificial neural network back analysis. *Sustainability* 15, 10627. doi:10.3390/su151310627

Mitkina, G. V. (1996). Bearing capacity of hollow piles sunk in leader holes. *Soil Mech. Found. Eng.* 33 (3), 105–108. doi:10.1007/bf02361020

Mu, B. G., Bie, Q., Zhao, X. L., and Gong, W. M. (2014). Meso-experiment on caisson load distribution characteristics during sinking. *China J. Highw. Transp.* 27 (09), 49–56. doi:10.19721/j.cnki.1001-7372.2014.09.007

New, B. M., and Bowers, K. H. (1994). "Ground movement model validation at the Heathrow Express trial tunnel," in *Tunnelling'94* (Boston, MA: Springer), 310–329. Proceedings of the 7th International Symposium IMM and BTS, London.

Olujide Ilori, A., Edem Udoh, N., and Umenge, J. I. (2017). Determination of soil shear properties on a soil to concrete interface using a direct shear box apparatus. *Int. J. geo-engineering* 8 (1), 17–14. doi:10.1186/s40703-017-0055-x

Plecanos, L., Soga, K., Chunge, M. P. M., Ouyang, Y., Kwan, V., Kechavarzi, C., et al. (2017). Distributed fibre-optic monitoring of an Osterberg-cell pile test in London. *Geotech. Lett.* 7 (02), 152–160. doi:10.1680/jgele.16.00081

Potyondy, J. G. (1961). Skin friction between various soils and construction materials. *Géotechnique* 11 (4), 339–353. doi:10.1680/geot.1961.11.4.339

Sejia, L., Xu, W., and Zan-Yun, X. (2014). Earth pressure and frictional resistance analysis on open caisson during sinking. *J. Tongji Univ. Nat. Sci. Ed.* 42 (12), 1826–1832. doi:10.11908/j.issn.0253-374x.2014.12.007

Stroud, M. A. (1971). *The behavior of sand at low stress levels in the simple-shear apparatus*. PhD thesis. Cambridge, UK: University of Cambridge.

Tanimoto, K., and Takahashi, S. (1994). Design and construction of caisson breakwaters—the Japanese experience. *Coast. Eng.* 22 (1-2), 57–77. doi:10.1016/0378-3839(94)90048-5

Tehrani, F. S., Han, F., Salgado, R., Prezzi, M., Tovar, R. D., and Castro, A. G. (2016). Effect of surface roughness on the shaft resistance of non-displacement piles embedded in sand. *Geotechnique* 66 (5), 386–400. doi:10.1680/jgeot.15.p.007

Thermann, K., Gau, C., and Tiedemann, J. (2006). Shear strength parameters from direct shear tests–influencing factors and their significance. *The Geological Society of London* 484.

Wang, J., Liu, Y., and Zhang, Y. (2013). Model test on sidewall friction of open caisson. *Rock Soil Mech.* 34 (03), 659–666. doi:10.16285/j.rsm.2013.03.039

Wang, Y., Zhang, M., and Bai, X. (2019). Sinking resistance of jacked piles in clayey soil based on FBG sensing Technology. *J. Vib. Meas. Diagnosis* 39 (5), 1120–1125. doi:10.16450/j.cnki.issn.1004-6801.2019.05.030

Yan, X., Zhan, W., Hu, Z., Xiao, D., Yu, Y., and Wang, J. (2021). Field study on deformation and stress characteristics of large open caisson during excavation in deep marine soft clay. *Adv. Civ. Eng.* 2021, 1–11. doi:10.1155/2021/7656068

Yang, B., Shi, Q., Zhou, H., Qin, C., and Xiao, W. (2023). Study on distribution of sidewall earth pressure on open caissons considering soil arching effect. *Sci. Rep.* 13, 10657. doi:10.1038/s41598-023-37865-9

Zhou, H., Ma, J., Zhang, K., Li, J. T., and Yang, B. (2018). Experimental study of distribution characteristics of frictional resistanceon side wall of open caisson. *Bridge Constr.* 48 (05), 27–32. doi:10.3969/j.issn.1003-4722.2018.05.006

Zhu, J., Qingling, M., Qi, H., and Huang, D. I. (2019). Distribution characteristics of side wall friction of large open caisson foundation. *J. Southeast Univ. Nat. Sci. Ed.* 49 (06), 1136–1143. doi:10.3969/j.issn.1001-0505.2019.06.017

frontiers | Frontiers in Earth Science

TYPE Original Research
PUBLISHED 05 July 2024
DOI 10.3389/feart.2024.1392320

Check for updates

OPEN ACCESS

EDITED BY
Xiaoyu Bai,
Qingdao University of Technology, China

REVIEWED BY
Xiaoding Xu,
China University of Mining and Technology, China
Huajin Li,
Chengdu University, China
Wei Han,
Anhui Polytechnic University, China
Bingbing Chen,
Swansea University, United Kingdom

*CORRESPONDENCE
Menglong Dong,
dongml@hhu.edu.cn

RECEIVED 27 February 2024
ACCEPTED 17 June 2024
PUBLISHED 05 July 2024

CITATION
Teng L, Xing X, Sun C, Liu Z, Li X and Dong M (2024), Research on optimization of grouting treatment for underground mining goaf collapse based on 3-dimensional simulation. *Front. Earth Sci.* 12:1392320. doi: 10.3389/feart.2024.1392320

COPYRIGHT
© 2024 Teng, Xing, Sun, Liu, Li and Dong. This is an open-access article distributed under the terms of the Creative Commons Attribution License (CC BY). The use, distribution or reproduction in other forums is permitted, provided the original author(s) and the copyright owner(s) are credited and that the original publication in this journal is cited, in accordance with accepted academic practice. No use, distribution or reproduction is permitted which does not comply with these terms.

Research on optimization of grouting treatment for underground mining goaf collapse based on 3-dimensional simulation

Lin Teng[1], Xiansen Xing[2], Changze Sun[1], Zujian Liu[2], Xiaoshuang Li[1] and Menglong Dong[2]*

[1]College of Civil Engineering, Qilu Institute of Technology, Jinan, China, [2]School of Earth Science and Engineering, Hohai University, Nanjing, China

The collapse of goaf is one of the most serious geological disasters in cities where underground mineral resources are mined. The ground subsidence caused by the goaf limits the social and economic development of the area, while also endangering the safety of residents and property near the mining area. At present, support and grouting treatment methods are commonly used for the treatment of goaf. The cost of support treatment is relatively high, and it is difficult to control the collapse of the deeper goaf. Grouting treatment is suitable for conducting detailed investigations of underground spaces. The cost of complete grouting is high, and the timing of grouting termination is difficult to control. This paper aims to explore the optimization of grouting efficiency in the treatment of underground subsidence in goaf areas using the reserved pillar mining method. Through the stability calculation of the goaf pillars and roof, it can be concluded that the goaf pillars are unstable pillars under current conditions and are prone to damage under load interference. At present, surface subsidence has occurred in the goaf and requires treatment. Consider the comparison between the collapse control effect under different grouting rates and the complete grouting, and ultimately select the condition of 90% grouting rate to achieve the control effect. This conclusion can provide a certain theoretical reference basis for the treatment of similar goaf collapse, and has certain practical significance.

KEYWORDS

phosphate mine goaf, land subsidence, backfill grouting, surface collapse, three-dimensional finite element method

1 Introduction

According to statistics, there are more than 110,000 non coal mines in China. The extraction of many solid minerals results in millions of cubic meters goaf every year. Failure to deal with goaf effectively makes it still have the hidden danger of ground deformation. Large-scale surface collapse may occur at anytime, which seriously endangers the surrounding environment and the safety of people's property.

The existence of goaf seriously affects the geological environment of the area, mainly in the following. The collapse of the goaf destroys the surface crop land and affects the

agricultural ecology. In plain area, water will accumulate due to concentrated deformation of the goaf. And in arid mountainous area, the goaf will destroy the surface water system and aggravate the problem of water shortage. The ground deformation caused by mining will produce landslides, which pose a great threat to the industrial and civil buildings near the hillside.

The research on the ground deformation of goaf can be traced back to 1838, Gonot put forward the hypothesis of "vertical line theory" of mining subsidence by investigating the surface subsidence accident in Liege. Then many scholars have put forward many hypotheses, such as "normal theory", "second-class line theory", "natural slope theory", "circular arch theory", "zoning theory", *etc.* (Gotsev et al., 2003; Stokes et al., 2003; Ting et al., 2012; Wang XY. et. al, 2017; Zegzulka et al., 2023), which jointly open people's cognition of overburden movement and ground deformation in goaf, and have their geometric theoretical models in different researches. Those researches made the study of goaf stability more systematic and intuitive. The research on the ground deformation of goaf intersected with many adjacent disciplines, infiltrates and complemented each other, gradually evolved into a comprehensive discipline (Xu et al., 2023). According to the long-term research, mining collapse has many characteristics, such as latent, transforming, progressive and sudden. The main influencing factors of surface collapse can be divided into natural geological environment factors and artificial mining activity factors (Wang et al., 2015). The influence radius of surface deformation is related to the depth of coal seam, and the mining method also determines the scale of collapse deformation (Zhang and Yang, 2016). At present, the research of goaf stability focuses on the mechanism and mechanical behavior of roof strata movement and ground deformation (Wang W. et. al, 2017). The research methods can be divided into phenomenological research of goaf deformation and theoretical model research of mechanical mechanism method (Lou et al., 2014). The former is based on the monitoring data of ground deformation in goaf. In the analysis of the data, such as statistical probability integral, section function and other methods are used to summarize the law of surface deformation and failure, and then analyze the change of strata in the mining area (Yavuz, 2004). The other method is based on various mechanical principles and methods. It is applied to goaf analysis. Based on the assumption of continuous medium of rock mass, the mechanical mechanism of rock mass in goaf is studied. Based on the above research, the movement law of overlying strata is analyzed, and the surface deformation model is deduced (Xu et al., 2013). For the complicated geological conditions and influencing factors in actual mining engineering, there is no consistent mechanical model, which is generally applicable to all mining subsidence analysis (Wang et al., 2022). The deformation of underground rock mass determines the characteristics of surface deformation, so the study of rock mass deformation is particularly important in underground mining deformation. The study of rock deformation laws in underground space has become more mature. Yu et al. proposed a numerical model for rock deformation based on microstructure, based on elastic damage mechanics and thermoelastic theory (Yu et al., 2015). Zhu et al. tested the mineral composition of old sandstone in Shanxi Ruineng Coal Mine to elucidate the softening mechanism of rocks after water absorption (Zhu et al., 2021. Yin et al. studied the high-temperature shear mechanical properties and shear dilation deformation characteristics of underground rock masses under different initial normal stresses (Yin et al., 2021).

On the basis of theoretical research on ground deformation of goaf, the methods for stability analysis of goaf can be divided into four types: prediction method, analytical method, semi prediction and semi analysis method and numerical simulation method (Li XB. et. al, 2019; Li PX. et. al, 2019). Each method has its own emphasis and is applicable to the analysis of different problems (Yang et al., 2015). This paper employs the numerical simulation analysis method, which possesses advantages such as high accuracy, speed and efficiency, intuitive visualization, flexibility, and comprehensiveness. These advantages render numerical analysis methods an indispensable and vital tool for the stability evaluation of underground goafs.

To solve the problem of ground deformation in goaf, two methods can be adopted, namely, early design mining method for prevention and late treatment for deformation and damage control (Sergey et al., 2012). The early design mining methods include protective pillar method, strip mining method, pillar mining method, etc. (Guo et al., 2011) This method needs to select an appropriate mining retention ratio in the mining process to achieve the economic benefits of mining while ensuring the stability of the ground. However, it is difficult to ensure the long-term stability of the reserved part, and it is easy to cause multiple collapse accidents due to local damage. The filling methods for goaf treatment can be divided into many types according to the different filling materials, so they have strong adjustability. The filling material can turn waste into treasure. This method has the effect of safety and environmental protection, and is the first choice for goaf treatment. Filling method can be combined with other methods for joint treatment, such as caving filling method and reinforcement filling method, to meet the governance needs of different goaf areas (Xuan and Xu, 2017). By changing the stress distribution of surrounding rock, the filling method can effectively control the deformation of rock stratum and surface, which is applicable to the treatment of goafs under buildings and structures and some goafs that do not allow large deformation (Zhang et al., 2019) Various buildings and traffic facilities can be built above the goaf after filling method treatment (Li et al., 2012).

The existing methods for evaluating the deformation of goaf have their own focuses and shortcomings. For the complex geological conditions and influencing factors in actual mining engineering, there is no consistent mechanical model that is universally applicable to all mining subsidence analysis. In order to reuse the land resources in the goaf and put it into urban construction again, it is necessary to solve the problem of ground deformation and utilization. Under the premise of economic benefit and safety development, and in order to build a project to meet the planning needs, it is full of value to conduct in-depth and systematic research on the ground deformation and control measures of goaf. The existing methods for controlling the collapse of goaf are generally a combination of support and grouting measures. However, this method of controlling goaf collapse has its limitations. Support treatment cannot effectively prevent the collapse and deformation caused by deep mining pits. The problem with grouting lies in its cost, sometimes with a large underground space and high cost of complete filling, and the termination of grouting cannot be effectively controlled. This paper explores the effectiveness of pit

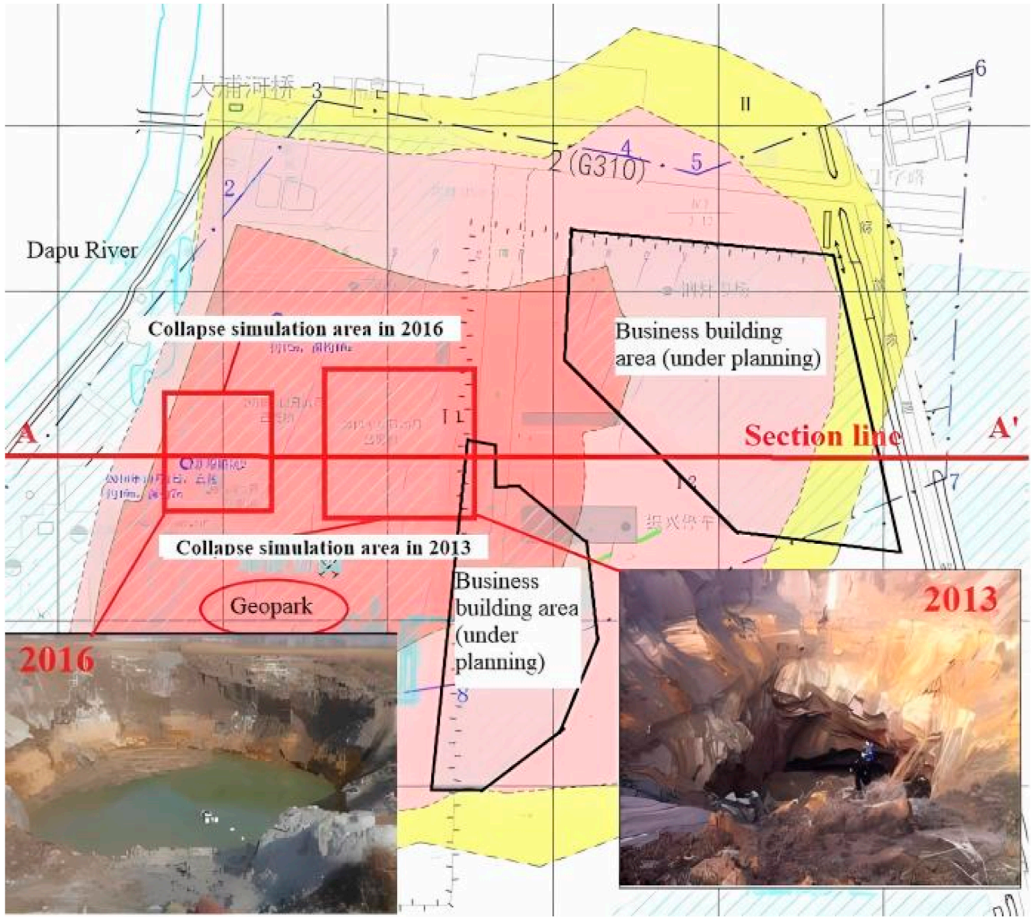

FIGURE 1
Goaf area and collapse pit.

collapse control under incomplete grouting conditions and reserved pillar mining methods.

The phosphate mine goaf studied in this paper is located in Lianyungang China. The existence of goaf seriously restricts the optimal use of land and the development of city. The potential geological disasters threaten the safety of life and property of nearby residents. The treatment of the goaf has practical engineering application significance. At the same time, it can be used as a reference for the analysis and treatment of many goafs that have not been treated. It can provide guidance for the follow-up goaf treatment engineering, and has theoretical significance for the deformation and failure mode, stability analysis method and treatment effect evaluation of goaf.

2 Present situation of collapse deformation in phosphate mine

2.1 Surface collapse

A phosphate mine was designed to be mined in 1966 and closed after a major collapse accident in 2016, with the deepest mining depth of is 440 m underground. On 25 December 2013, affected by underground mining and surrounding construction activities, the overlying strata of the old tunnel collapsed, forming a collapse pit in the upper part of the goaf. The collapse pit is funnel-shaped, with a maximum diameter of about 100 m and a depth of more than 50 m. On 4 March 2016, surface collapse occurred in the middle section, forming an inverted dome collapse pit with a long axis of about 130 m and a short axis of about 100 m, with a collapse area of about 9,400 square meters. On 31 December 2016, a ground collapse occurred about 70 m to the south of the phosphate rock pile in the mining area, and the diameter of the collapse pit was about 100 m. The collapse pits shown in Figure 1. The area circled in red represents the range of impact of collapse deformation. In addition to the formation of collapse pits, cracks have also appeared on the surface and walls of buildings within the scope of collapse impact. Shown as Figure 2. The Quaternary strata in the study area are mainly composed of loose sediments such as terrestrial and marine sand, silty clay, etc., with a thickness of 20.2–34.0 m. According to the exposure of drilling on site, the underlying bedrock strata in the study area are granite mixed with gneiss of Qishan Formation, phosphorus bearing marble of Jinping Formation and dolomitic plagioclase gneiss of Yuntai Formation. Four ore bodies were mined



FIGURE 2
Cracks on the ground and buildings

for phosphate ore, with a main strike of 13°, a dip direction of about 103°, and a dip angle of about 39°. Different stages of mining were carried out using collapse method, open pit method, explosive force transportation method, and stage mining room method. The overall mining was stopped in 2016.

2.2 Ground deformation

Due to the excavation of underground mine room, the upper ground is deformed, and the range of surface movement is called surface movement basin. Since the mining of the phosphate mine, with the expansion of goaf area, the area and maximum subsidence value of the mobile basin were increasing. At that time, there was only one maximum subsidence point in the center of the basin. The old collapse pit had been backfilled, and no obvious large cracks were found in the site. The fracture strikes in the north of this section are 147–162°and in the south are 50°–75°, which are caused by typical tension.

3 Geological modeling of goaf

3.1 Geologic model

The surface range of the model selected in this paper is shown in Figure 1. The schematic diagram of model section A-A ‘is shown in Figure 3.

The original data of three-dimensional finite element calculation model of phosphorite goaf was directly imported into Rhino6.0 from ItasCad, and then imported into ABAQUS in the form of. sat file for modeling. The model is shown in Figure 4A. The three-dimensional finite element software ABAQUS is used to simulate the ground settlement of phosphorus mine goaf. In the field of geotechnical engineering, ABAQUS has irreplaceable analytical advantages compared to other numerical software, and it contains a large number of constitutive models of rock and soil materials. In addition to rich material models, there are also various types of units that can be used to solve various structural problems. In engineering applications, some functions of ABAQUS can facilitate the excavation and backfilling process of rock and soil, and can also automatically generate initial stress for coupled simulation of seepage and stress of fluid solids.

From top to bottom, the horizontal strata are Quaternary strata, strongly weathered rock strata and moderately weathered rock strata. From top right to bottom left are the first member of the lower Yuntai formation of Haizhou group ($Pt_2hay^{1\text{-}1}$), the fourth member of Jinping formation of Haizhou group (Pt_2haj^4), the third member of Jinping formation of Haizhou group (Pt_2haj^3), the second member of Jinping formation of Haizhou group (Pt_2haj^2), the first member of Jinping formation of Haizhou group (Pt_2haj^1) and Qushan formation of Donghai group (Pt_1dhq).

The underground mining chambers are irregular hexahedrons in the actual situation, and the regular hexahedrons of the same scale are used in the model establishment to simplify the calculation. The overall distribution of the chambers is from −120 m to −440 m in depth. The chambers are thin on both sides, and are thick in the middle. The overall size of the model is 1000m × 1000m × 600m, that is, the surface area is one square kilometer, and the calculated depth is 600 m. The chambers formed by mining are generally distributed between the two strata, and the inclination angle of the chambers is roughly consistent with that of the strata. After mining, the rock between the two chambers is the pillar, and the pillar bears the rock pressure after the stress release, shown as Figure 4B.

3.2 Material parameters and boundary conditions

The physical and mechanical parameters of rock mass were obtained by rock mass mechanical tests on samples of different rock strata and ore bodies. Uniaxial compression test, shear test and tensile test were adopted. The parameters are shown in Table 1.

In the three-dimensional finite element model, according to the actual engineering situation, different boundary conditions are set up to realize the settlement of goaf. The displacement and rotation

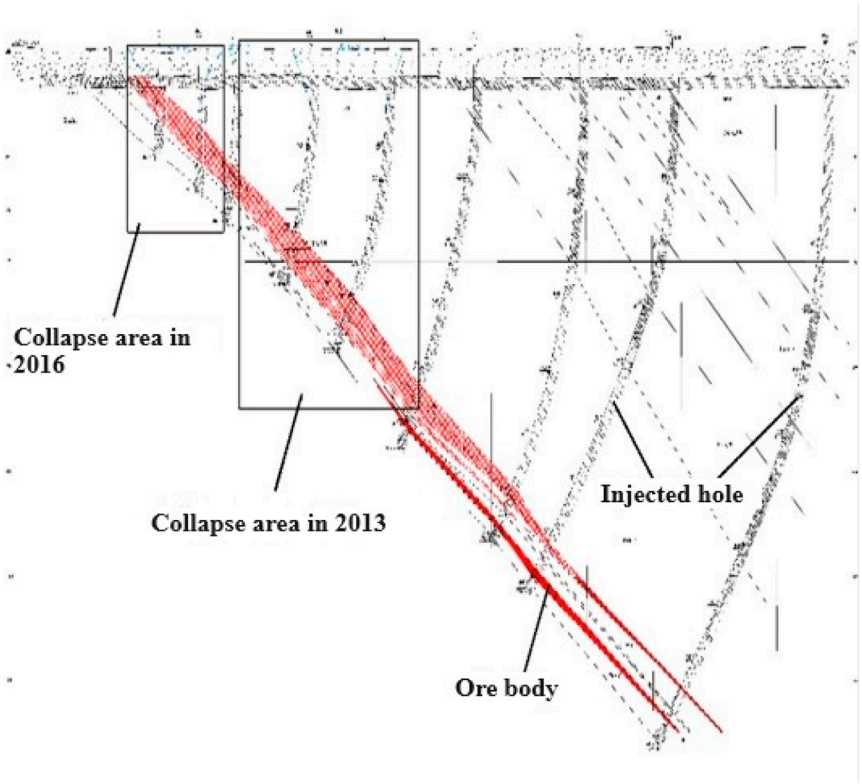

FIGURE 3
Schematic diagram of model section A-A′.

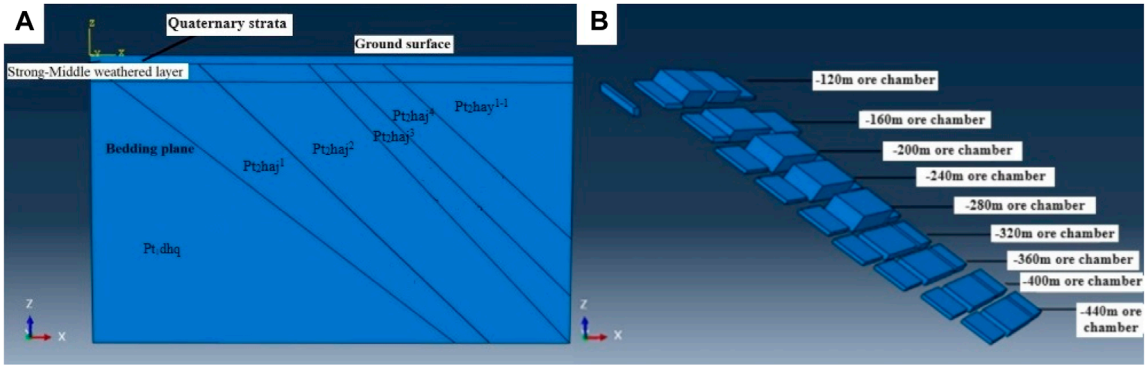

FIGURE 4
Numerical model [**(A)** Three-dimensional calculation model; **(B)** Calculation model of chamber].

angle of the bottom of the model are fixed in *X*, *Y* and *Z* directions. On the left and right sides of the model, that is, the East and west sides of the actual stratum, *X* direction displacement and rotation angle are fixed. *Y* direction displacement and rotation angle are fixed on the front and back sides of the model, that is, the north and south sides of the actual stratum.

The top surface of the model is a free surface boundary condition, and there is no fixed displacement and rotation angle in three directions. In this calculation, the main displacement is the vertical displacement in *Z* direction, that is, the main land subsidence and the vertical displacement of the ground.

4 Analysis of pillar stability

In the mining of the phosphate mine, the pillar was reserved to bear the load of the upper strata. When the load strength of the pillar exceeds the bearing capacity, it may be damaged, making the upper roof partially suspended. It will be easy to produce chain reaction

TABLE 1 Numerical simulation of rock and soil strength parameters in goaf.

Type of rock	Density (kg/m^3)	Bulk modulus (GPa)	Shear modulus (GPa)	Cohesion (MPa)	Friction angle (°)	Tensile strength (MPa)
Quaternary layer	1800	0.01	0.0035	0.04	15	0.015
Strongly weathered rock	2,200	0.53	0.45	0.5	20	0.2
Moderately weathered~ unweathered rock	2,700	3.96	2.03	3.2	40	2
Ore body	2,800	3.05	2.06	2.4	35	1.2

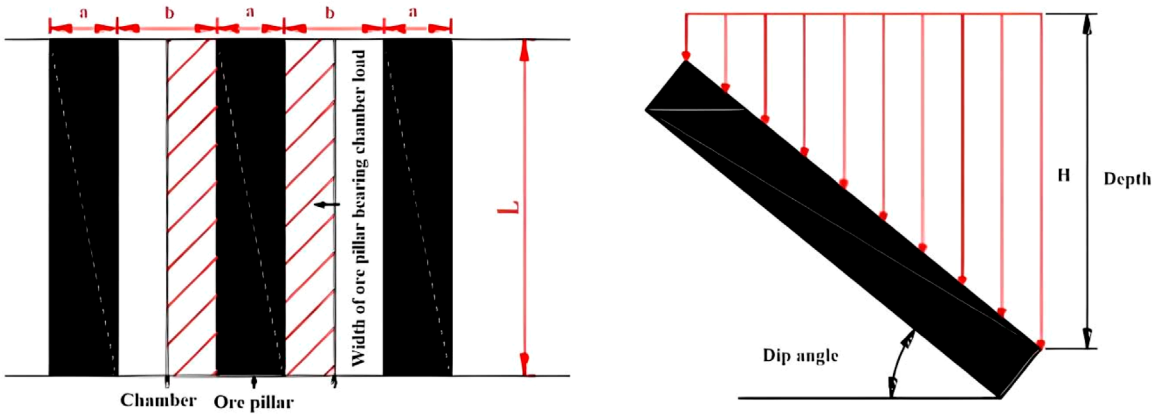

FIGURE 5
Pillar loading mode.

when the roof pressure is transferred to other pillars, which leads to the failure of the pillars in turn.

Therefore, it is necessary to calculate the bearing capacity of the pillars and the relationship between the load and the stability of the pillars. The evaluation of pillar stability is based on the stability coefficient. The calculation formula of mining stability coefficient is as follows Eq. 1.

$$K_Z = P_U / P_Z \tag{1}$$

where: K_Z: Stability coefficient; P_U: Ultimate load of rock pillars, kN; P_Z: Actual load on rock column, kN.

According to the regulations of the safety stability coefficient of mining pillars, when the value reaches between 1.2 and 2.0, it can be said that the mining pillars in the site are basically stable. When the value is greater than 2.0, the pillars of the site reach stability. If the value is less than 1.2, the pillars of the site are considered unstable.

The pillar setting in the goaf of the phosphate mine is special, and the loading condition of the pillar is shown in Figure 5.

According to the load bearing mode, the load formula of pillar section is as follows Eq. 2.

$$P_Z = \gamma_0 H \cos\alpha (a+b) L \tag{2}$$

where: γ_0: Average weight of overlying strata, kN/m^3; H: Buried depth of rock pillar, m; a: Width of retaining rock column, m; b: Width of mining chamber, m; L: Length of retaining rock column, m.

Because the pillar height in the middle section of each layer is the highest, the mining thickness is the largest, and it is most likely to be damaged, so only the pillar stability coefficient in the middle section of each layer needs to be calculated. The specific calculation results are shown in Table 2.

5 Historical deduction and prediction analysis of goaf subsidence

5.1 Establishment of three-dimensional finite element model

At present, the goaf is in the state of no backfilling. In this simulation, taking this as the initial state, the numerical simulation of excavation without backfill is carried out firstly. The initial geostress in the research area is mainly based on the self-weight stress position, and geostress is applied through self-weight.

TABLE 2 Pillar safety factors.

Chamber (m)	Depth (m)	Pillar width (m)	Chamber width (m)	Mining thickness (m)	Stability coefficient
−120	120	2.30 ~ 8.72	5.53 ~ 27.15	0.97 ~ 29.31	0.54 ~ 64.49
−160	160	1.97 ~ 13.74	11.23 ~ 41.33	3.53 ~ 29.99	0.36 ~ 19.24
−200	200	2.10 ~ 8.01	10.89 ~ 22.92	4.49 ~ 35.19	0.21 ~ 3.38
−240	240	4.05 ~ 7.76	10.55 ~ 35.53	3.64 ~ 30.43	0.40 ~ 3.00
−280	280	2.00 ~ 8.79	8.36 ~ 31.12	1.88 ~ 20.45	0.23 ~ 8.93
−320	320	3.64 ~ 9.29	13.03 ~ 27.33	2.75 ~ 24.41	0.41 ~ 5.43
−360	360	4.57 ~ 9.26	8.27 ~ 38.63	2.15 ~ 29.73	0.32 ~ 15.81
−400	400	4.74 ~ 8.00	10.45 ~ 30.00	2.34 ~ 27.08	0.32 ~ 5.13
−440	440	8.82 ~ 24.44	22.79 ~ 33.07	5.00 ~ 22.55	1.15 ~ 17.56

The minimum stability coefficients of pillars are all less than 1.2, which are unstable pillars. It is easy to damage and cause the instability of roof rock mass. If it is not treated, the subsequent surface collapse accident will occur in the goaf. The −120 m chamber and −200 m chamber shown in the table correspond to the location of the collapsed pit.

TABLE 3 Grouting filling type and parameters.

Type of grouting slurry	Water-solid ratio	Solid ratio	Stone rate (%)	Compressive strength (MPa)
Cement fly ash slurry	1:1.0–1:1.1	Cement: Fly ash 3:7	85	2.24
Cement, fly ash, and tailings mixed slurry	1:1.0–1:1.1	Cement: Fy ash: Tailings 3:5:2	85	2.80
Cement, fly ash, and tailings mixed slurry	1:1.0–1:1.1	Cement: Fy ash: Tailings 2:5:3	84	1.85

The numerical analysis is divided into two steps. The first step is to calculate the self-weight stability of the stratum in the original state, and record the stress as the initial stress field. The second step is to excavate the mine chamber under this stress condition, and analyze the stratum settlement after excavation. When calculating the historical ground settlement of the goaf, the calculation steps are set to stop the calculation when the maximum settlement and deformation range of the ground settlement reach the current actual situation. And then the continuous deformation of the goaf ground under the current conditions is simulated. Grouting filling type and parameters are shown in Table 3.

5.2 Simulation of historical deformation

When establishing the model, solid units are selected to simulate the underground rock mass, and the parameters of each layer of rock and soil mainly come from the material strength parameters obtained from on-site measurements and indoor experiments. The underground rock mass is set as an elastic-plastic model and simulated using the Mohr Coulomb yield model built-in in the software.

Submit the calculation task under the above calculation conditions, and output results are analyzed by finite element method. The distribution of current plastic zone in goaf is shown in Figure 6. The plastic zone is mainly distributed in the pillars between the excavation parts of the mine house and the rock mass between the adjacent mine houses at different depths. The overall scale of the plastic zone is small and it does not reach the connection. The mine house will not collapse, and only a small part of the blocks will be deformed and fall off.

According to the displacement nephogram, the displacement values on the surface are distributed in concentric circles. The maximum displacement at the surface is 0.638 m, which is above the mine house from - 120 m to - 400 m depth. According to the east-west and North-South cross-sections, the maximum displacement change occurs at the room with a depth of 280 m, that is, the deformation or shedding of some blocks occurs at the top corner of the room after excavation. The deformation of the room at 280 m is the most obvious under the action of *in situ* stress.

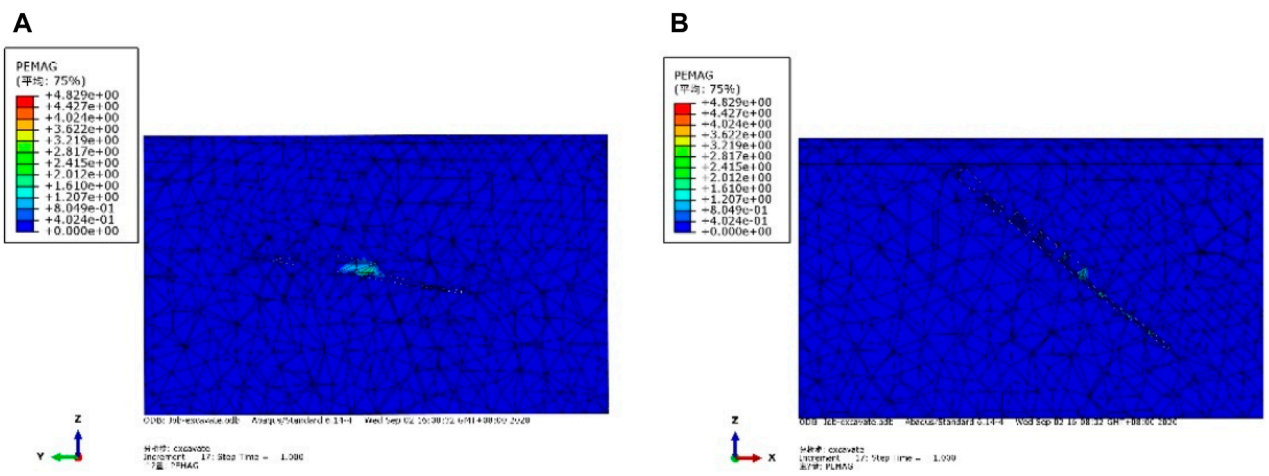

FIGURE 6
Current plastic zone in Goaf [**(A)** Front view; **(B)** Side view].

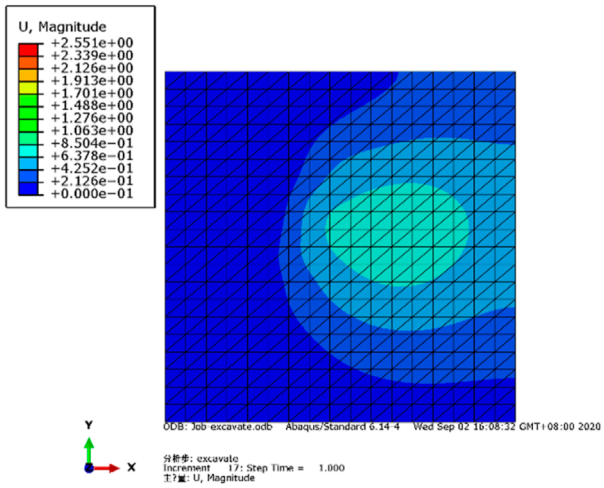

FIGURE 7
Total displacement at current surface of goaf.

The vertical displacement nephogram of the surface and both sides shows that the vertical displacement of the surface is nearly elliptical. A large scale of land subsidence occurred in this area. It is basically consistent with the actual range of building cracks. On the *z*-direction displacement nephogram of the cross sections on both sides, the top of the mine room moves downward due to the self-weight stress of the overlying rock mass, and the bottom of the mine room heaves upward due to the release of excavation stress. The calculated range of land subsidence is small, but the settlement is relatively large, which has a significant impact on the upper buildings. Figure 7 shows the total deformation diagram of the calculation model under the condition of goaf, that is, the changes of various parts in the actual stratum. The results show that the strata change is consistent with the settlement data of the actual project.

5.3 Analysis of collapse control measures

According to the collapse history calculation and current situation analysis results, if the collapse pit is not treated, the collapse disaster in the region will further occur. The requirement of treatment is to eliminate the hidden danger of geological disaster caused by ground collapse. Ensure the safety of roads around the site and completely eliminate the hazard of ground subsidence in the goaf. The site after goaf treatment can meet the requirements of Geological Park, office building and other engineering construction planned in the later stage.

The method of grouting and filling is used to control the mining subsidence in the goaf of phosphate mine. The treatment method is to use the filling material as the geological filling material for phosphate rock mining and fill the mined room. This method can maintain the self-strength of the surrounding rock and the support capacity of the remaining pillars, and prevent the instability or local collapse of the overburden or roadway in the stope.

Grouting body interacts with ore pillar and surrounding rock to form support system to limit displacement of surrounding rock. This changes the stress state of overburden and support system in the stope, reduces the stress difference in surrounding rocks, and relatively improves the strength and bearing capacity of surrounding rocks after mining, thus restricting the movement and alleviating the deformation. At the same time, the stress concentration caused by overburden movement is transferred to the depth of the floor through the filling support system. Therefore, grouting filling can effectively prevent the overall destabilization of overburden rock and significantly reduce the settlement of goaf ground.

Treatment measures to achieve green environmental protection, economic and practical purpose of grouting filling in Phosphate Mine Goaf. According to the principle of material selection for waste utilization and local sampling, the filling materials are mainly tailings sand, fly ash, cement and additives.

In the actual construction process, it is very difficult and expensive to achieve full filling and grouting due to the excessive depths of phosphate rock mining, irregular arrangement of ore

TABLE 4 Deformation calculation results (mm).

Calculation conditions	Maximum total displacement of ground surface	Maximum vertical displacement of ground surface	Maximum horizontal displacement of ground surface	Maximum total underground displacement
Present deformation	637.8	536.8	234.2	1701
Predicted deformation	1,178	900.1	374.2	3,551
70%	712.2	626.4	310.8	2,806

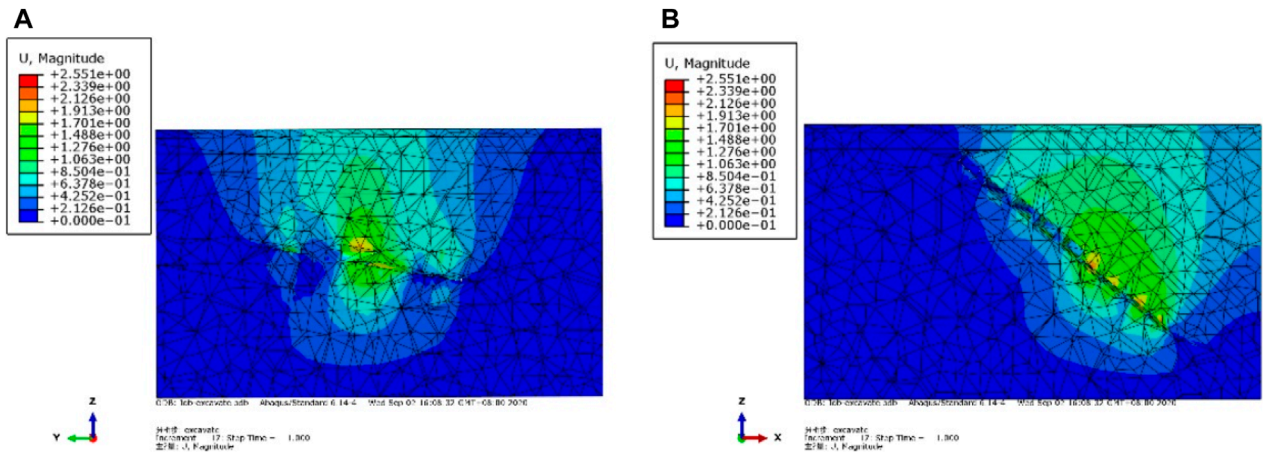

FIGURE 8
Total displacement of current section of goaf. **(A)** Front view; **(B)** Side view.

rooms and the influence of underground pressure and aquifer. In the treatment of room-pillar method, the strength of pillar plays a decisive role in the stability of goaf, so the treatment of goaf can be realized when grouting body accounts for a certain proportion of the room volume. The calculation formula of grouting filling quantity in goaf is as follows Eq. 3.

$$Q_g = \frac{\tau \cdot s \cdot M \cdot N \cdot n \cdot \eta}{c \cdot \cos\alpha} \tag{3}$$

where: Q_g is total filling volume of grouting for goaf treatment, m^3; τ is grout coefficient of losses; s is area of goaf treatment, m^2; M is average mining thickness of ore bed, m; N is Recovery rate of ore bed, %; η is filling coefficient of grouting fluid; c is stone rate of grouting fluid, %; α is dip angle of strata, °.

The volume of the mine room to be treated in the phosphate mine goaf is about 800,000 m^3. Change the grouting fluid filling system while other parameters remain unchanged. The filling coefficient of grouting fluid is set as 70%, 80%, 90% and 100% respectively in the numerical analysis. Through numerical simulation, the ground deformation and stress distribution of goaf under different grouting filling rates are simulated, and the treatment effects under different grouting filling rates are comprehensively compared and analyzed.

The simulation results of displacement under different conditions are shown in Table 4 and Figures 8–12. The treatment effect of different grouting schemes in vertical and horizontal directions will gradually increase with the increase of grouting amount. The vertical settlement reduction and horizontal displacement reduction are the most significant under the condition of complete grouting and filling. The settlement reduction effect under 90% grouting filling rate is close to that of full grouting filling. Overall, the complete grouting and filling treatment not only meets the design requirements, but also has the best effect. This scheme should be preferred without considering the construction difficulty. Based on actual economic benefits, it can be considered to reduce the amount of grouting appropriately to save costs. From the perspective of controlling surface settlement deformation and collapse damage, 90% of the grouting results are close to the complete grouting results, which can effectively control the vertical deformation of the ground.

6 Conclusion

This paper analyzes the treatment effect a phosphate mine under different grouting filling rates, and compares the settlement results of goaf deformation under different calculation conditions. Following conclusions were achieved.

(1) Analyzing the method of mining reserved pillars, it was found that without treatment and filling, the mine cave would

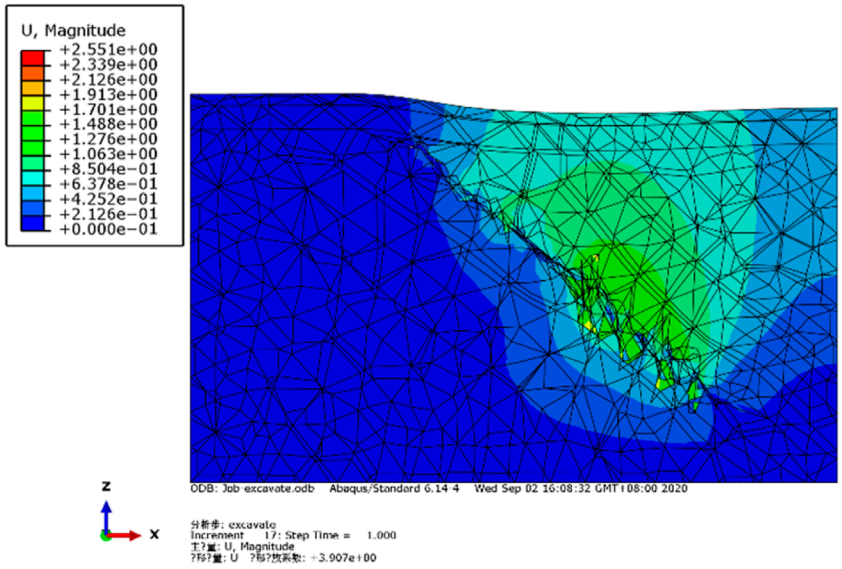

FIGURE 9
Current total deformation diagram of goaf.

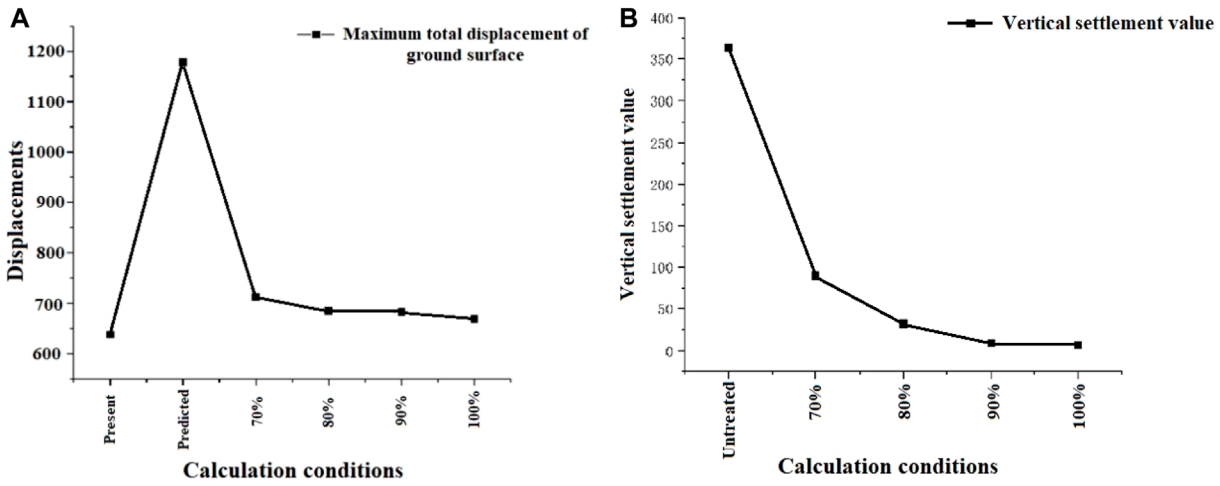

FIGURE 10
(A) Maximum total displacement of ground surface; **(B)** Added value of vertical settlement (mm).

collapse, which is basically consistent with the actual collapse area. After grouting treatment, the bearing capacity of the mine pillar has been improved, the load capacity has been reduced, and the strength is sufficient to bear the overlying rock load without further damage. The goaf after treatment will undergo continuous deformation mainly due to settlement.

(2) Compared to the absence of grouting and filling treatment, each treatment plan has a relatively significant effect on reducing settlement in the goaf, and the effect of reducing deformation increases with the increase of grouting volume. When complete grouting and filling is achieved, the vertical and horizontal deformation of the goaf ground decreases the most. When designing grouting for collapsed mines, starting from the current stage, the ground deformation of the goaf decreases with the increase of grouting filling rate.

(3) The goaf is planned to be treated with grouting, with grouting volume ranging from 70% to 100%. According to simulation results, the total maximum ground displacement, maximum vertical ground deformation, maximum horizontal ground deformation, and maximum underground displacement all decrease with the increase of grouting volume. When the grouting filling amount reaches 100%, the total ground displacement is only 30 mm, and the vertical deformation is only 7.5 mm, which meets the design requirements. There is

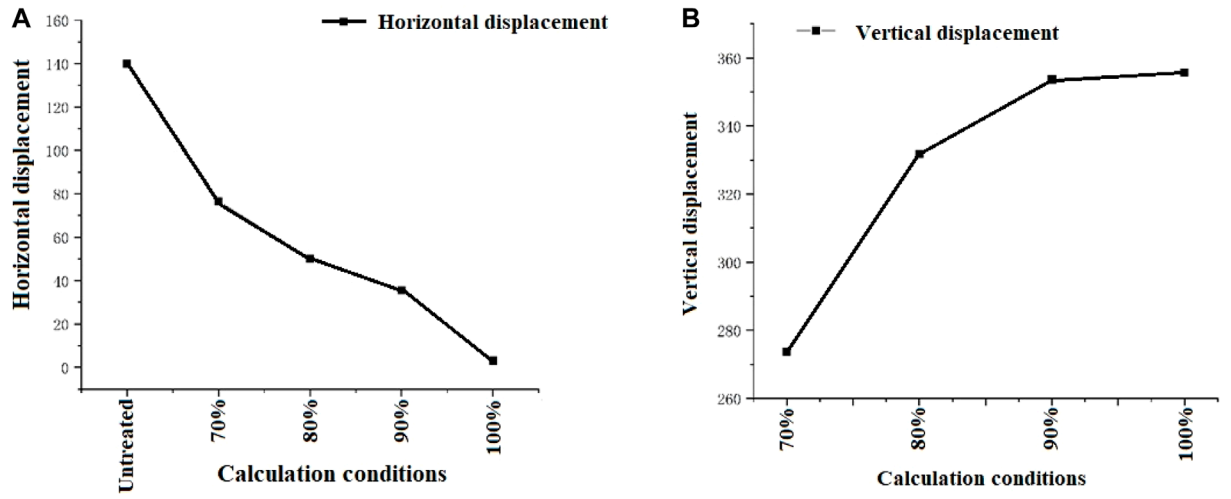

FIGURE 11
(A) Increase value of horizontal deformation (mm); **(B)** Control effect of vertical deformation (mm).

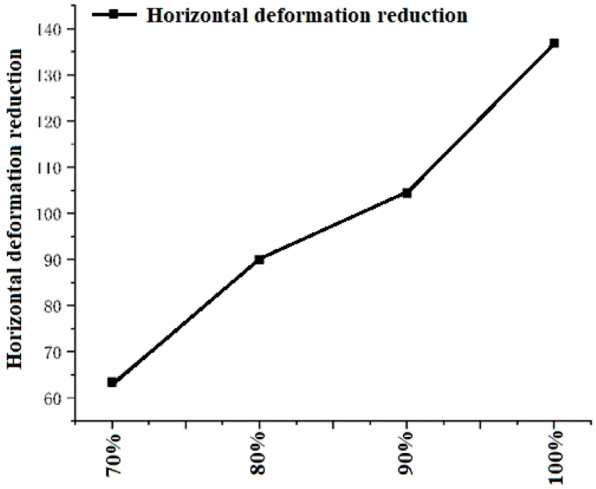

FIGURE 12
Horizontal deformation control effect (mm).

no settlement space inside the mining room, and the effect of subsequent building loads on the treatment area is not significant.

(4) Compared with the ground deformation in the goaf without grouting treatment, the ground settlement under the conditions of 90% grouting amount and complete grouting both meet the design requirements of the upper building load. The vertical reduction effect of the ground under 90% grouting amount is similar to that of complete grouting. Considering the construction difficulty and funding of governance measures, a grouting rate of 90% can also meet the design requirements of subsequent buildings. For the mining method of reserved pillars, if the mining plan is not reasonable, the goaf may collapse. The design of incomplete grouting can save construction costs and reduce construction difficulty, but it is necessary to explore and study the grouting filling rate. This conclusion can provide certain guidance for the treatment of goaf collapse.

Data availability statement

The datasets presented in this study can be found in online repositories. The names of the repository/repositories and accession number(s) can be found in the article/Supplementary Material.

Author contributions

LT: Writing–original draft. XX: Writing–review and editing. CS: Writing–review and editing. ZL: Writing–review and editing. XL: Writing–original draft, Writing–review and editing. MD: Writing–original draft.

Funding

The author(s) declare that financial support was received for the research, authorship, and/or publication of this article. This study is supported by the Research Fund of National Natural Science Foundation of Shandong Province of China (NSFC) (Grant No. ZR2022ME188), Jinan City "new university 20" research leader studio project (Grant No. 20228108), and the project of Slope safety control and disaster prevention technology innovation team of "Youth Innovation Talent Introduction and Education Plan" of

Shandong Colleges and universities [Grant No. Lu Jiao Ke Han (2021) No. 51].

Conflict of interest

The authors declare that the research was conducted in the absence of any commercial or financial relationships that could be construed as a potential conflict of interest.

Publisher's note

All claims expressed in this article are solely those of the authors and do not necessarily represent those of their affiliated organizations, or those of the publisher, the editors and the reviewers. Any product that may be evaluated in this article, or claim that may be made by its manufacturer, is not guaranteed or endorsed by the publisher.

References

Gotsev, D. V., Kovalev, A. V., and Sporykhin, A. N. (2003). Stable equilibrium of the multilayer lining of a vertical mine opening in elastoplastic rock mass. *Int. Appl. Mech.* 39, 286–291. doi:10.1023/A:1024462218891

Guo, W. B., Hou, Q. L., and Zou, Y. F. (2011). Relationship between surface subsidence factor and mining depth of strip pillar mining. *Trans. Nonferrous Metals Soc. China* 21, s594–s598. doi:10.1016/S1003-6326(12)61646-X

Li, L., Hao, G., Wu, K., and Li, R. (2012). New viewpoint of foundation stability of newly building upon goaf. *Energy Procedia* 17, 1717–1723. doi:10.1016/j.egypro.2012.02.303

Li, P. X., Yan, L. L., and Yao, D. H. (2019b). Study of tunnel damage caused by underground mining deformation: calculation, analysis, and reinforcement. *Adv. Civ. Eng.* 2019, 1–18. doi:10.1155/2019/4865161

Li, X. B., Wang, D. Y., Li, C. J., and Liu, Z. X. (2019a). Numerical simulation of surface subsidence and backfill material movement induced by underground mining. *Adv. Civ. Eng.* 2019, 1–17. doi:10.1155/2019/2724370

Lou, S. H., Yang, B., and Luo, Z. Q. (2014). Three-dimensional information acquisition and visualization application in goaf. *Procedia Eng.* 84, 860–867. doi:10.1016/j.proeng.2014.10.507

Sergey, S., Nicolas, O., and Benoît, S. (2012). Ground deformation associated with post-mining activity at the French-German border revealed by novel InSAR time series method. *Int. J. Appl. Earth Observations Geoinformation* 23, 142–154. doi:10.1016/j.jag.2012.12.008

Stokes, T. E., Hocking, G. C., and Forbes, L. K. (2003). Unsteady free-surface flow induced by a line sink. *J. Eng. Math.* 47, 137–160. doi:10.1023/A:1025892915279

Ting, C. H., Sivakugan, N., Read, W., and Shukla, S. K. (2012). Analytical method to determine vertical stresses within a granular material contained in right vertical prisms. *Int. J. geomechanics* 12 (1), 74–79. doi:10.1061/(ASCE)GM.1943-5622.0000110

Wang, F. T., Zhang, C., Zhang, X. G., and Song, Q. (2015). Overlying strata movement rules and safety mining technology for the shallow depth seam proximity beneath a room mining goaf. *Int. J. Min. Sci. Technol.* 25 (1), 139–143. doi:10.1016/j.ijmst.2014.12.007

Wang, T. L., Chen, C. X., Xia, K. Z., Zhang, C. Q., Wang, Y., and Liu, X. T. (2022). Ground surface deformation in the hanging wall of the jinshandian underground iron mine in China. *Front. Earth Sci.* 10, 1–16. doi:10.3389/feart.2022.909466

Wang, W., Jiang, T., and Wang, Z. (2017b). A analytical model for cover stress re-establishment in the goaf after longwall caving mining. *J. South. Afr. Inst. Min. Metallurgy* 117 (7), 670–683. doi:10.17159/2411-9717/2017/v117n7a9

Wang, X. Y., Wang, T. T., Wang, Q., Liu, X. M., Li, R. Z., and Liu, B. J. (2017a). Evaluation of floor water inrush based on fractal theory and an improved analytic hierarchy process. *Mine Water Environ.* 36, 87–95. doi:10.1007/s10230-016-0407-3

Xu, N. X., Kulatilake, PHSW, Tian, H., Wu, X., Nan, Y. H., and Wei, T. (2013). Surface subsidence prediction for the WUTONG mine using a 3-D finite difference method. *Comput. Geotechnics* 48, 134–145. doi:10.1016/j.compgeo.2012.09.014

Xu, Z. C., Xu, W., Zhu, Z. H., and Zhao, J. Y. (2023). Research on monitoring and stability evaluation of ground subsidence in gypsum mine goaf. *Front. Environ. Sci.* 04, 1–20. doi:10.3389/fenvs.2022.1097874

Xuan, D. Y., and Xu, J. L. (2017). Longwall surface subsidence control by technology of isolated overburden grout injection. *Int. J. Min. Sci. Technol.* 27, 813–818. doi:10.1016/j.ijmst.2017.07.014

Yang, Z. Q., Zhai, S. H., Gao, Q., and Li, M. H. (2015). Stability analysis of large-scale stope using stage subsequent filling mining method in Sijiaying iron mine. *J. Rock Mech. Geotechnical Eng.* 7 (1), 87–94. doi:10.1016/j.jrmge.2014.11.003

Yavuz, H. (2004). An estimation method for cover pressure re-establishment distance and pressure distribution in the goaf of longwall coal mines. *Int. J. Rock Mech. Min. Sci.* 41 (2), 193–205. doi:10.1016/S1365-1609(03)00082-0

Yin, Q., Wu, J. Y., Zhu, C., He, M. C., Meng, Q. X., and Jing, H. W. (2021). Shear mechanical responses of sandstone exposed to high temperature under constant normal stiffness boundary conditions. *Geomech. Geophys. Geo-Energy Geo-Resources* 7 (2), 35. doi:10.1007/s40948-021-00234-9

Yu, Q. L., Ranjith, P. G., Liu, H. Y., Yang, T. H., Tang, S. B., Tang, C. A., et al. (2015). A mesostructure-based damage model for thermal cracking analysis and application in granite at elevated temperatures. *ROCK Mech. ROCK Eng.* 48 (6), 2263–2282. doi:10.1007/s00603-014-0679-5

Zegzulka, J., Marsik, F., Necas, J., Hlosta, J., Zurovec, D., and Ivan, I. (2023). Thermodynamic theory of the most energy-efficient natural repose angle. *Continuum Mech. Thermodyn.* 35, 393–412. doi:10.1007/s00161-023-01184-1

Zhang, J. X., Sun, Q., Fourie, A., Ju, F., and Dong, X. J. (2019). Risk assessment and prevention of surface subsidence in deep multiple coal seam mining under dense above-ground buildings: case study. *Hum. Ecol. Risk Assess. Int. J.* 25 (6), 1579–1593. doi:10.1080/10807039.2018.1471579

Zhang, X., and Yang, M. (2016). Influence of dip angle of coal bed to the voidage distribution at goaf area. *J. Resi. Sci. Tech.* 13 (7).

Zhu, C., He, M. C., Jiang, B., Qin, X. Z., Yin, Q., and Zhou, Y. (2021). Numerical investigation on the fatigue failure characteristics of water-bearing sandstone under cyclic loading. *J. Mt. Sci.* 18 (12), 3348–3365. doi:10.1007/s11629-021-6914-0

frontiers | Frontiers in Earth Science

TYPE Original Research
PUBLISHED 29 July 2024
DOI 10.3389/feart.2024.1384143

Check for updates

OPEN ACCESS

EDITED BY
Jianyong Han,
Shandong Jianzhu University, China

REVIEWED BY
Bo Wang,
Southwest Jiaotong University, China
Wengang Dang,
National Sun Yat-sen University, Taiwan

* CORRESPONDENCE
Zhigang Tao,
taozhigang@cumtb.edu.cn

RECEIVED 08 February 2024
ACCEPTED 18 June 2024
PUBLISHED 29 July 2024

CITATION
Sun D, Tao Z, Yang H, Shui H, Lei X, Wang F, Huo S, Shu H, Xia W, Wang Z and He M (2024), Analytical solution for mechanical behavior characterization of sandy dolomite tunneling. *Front. Earth Sci.* 12:1384143.
doi: 10.3389/feart.2024.1384143

COPYRIGHT
© 2024 Sun, Tao, Yang, Shui, Lei, Wang, Huo, Shu, Xia, Wang and He. This is an open-access article distributed under the terms of the Creative Commons Attribution License (CC BY). The use, distribution or reproduction in other forums is permitted, provided the original author(s) and the copyright owner(s) are credited and that the original publication in this journal is cited, in accordance with accepted academic practice. No use, distribution or reproduction is permitted which does not comply with these terms.

Analytical solution for mechanical behavior characterization of sandy dolomite tunneling

Di Sun[1,2,3,4], Zhigang Tao[3,4]*, Hong Yang[5], Haoche Shui[1], Xiaotian Lei[3,4], Fengnian Wang[6,7], Shusen Huo[3,4], Hang Shu[1], Weitong Xia[1], Zhaoxi Wang[1] and Manchao He[1,3,4]

[1]College of Construction Engineering, Jilin University, Changchun, China, [2]Xinhua College of Ningxia University, Yinchuan, China, [3]State Key Laboratory for Tunnel Engineering, Beijing, China, [4]China University of Mining and Technology, Beijing, China, [5]China Railway 12th Bureau Group Co. Ltd, Taiyuan, China, [6]School of Earth Sciences and Engineering, Hohai University, Nanjing, China, [7]Shanxi Provincial Transportation Technology Research and Development Co. Ltd., Taiyuan, China

Tunneling in sandy dolomite strata often faces hazards such as collapse, water inrush, and water–sand inrush, seriously threatening the safety of tunnel construction. There are currently limited studies on the mechanical behaviors of sandy dolomite tunnels. In view of this, an analytical solution for tunneling in sandy dolomite strata is derived in this study, and then parametric analysis is performed to analyze the mechanical response of rock mass in sandy dolomite tunnels. The results demonstrate five tunnel sidewall stress scenarios according to the different lateral pressure coefficients (λ). Varying λ values impact stress distribution and tunnel stability, with extreme values posing risks of instability. Tunnel safety is greatly reduced when rock stress approaches the plastic limit. At different internal friction angles, cohesion, and initial rock stresses, radial stress decreases gradually as the radius increases. The stress values under different conditions tend to be similar, while the effects of internal friction angle, cohesion, and initial rock stress on stress in the elastic zone decrease with increasing distance from the center of the tunnel. Under different internal friction angles and cohesion, the plastic zone radius increases with increasing distance from the excavation surface, and a larger internal friction angle and cohesion lead to an increase in stress. The stress and cohesion of a rock mass significantly affect the plastic zone radius, and an increase in tunnel excavation radius also leads to an increase in the radius of plastic zone. These findings provide a reference and insight for similar geotechnical engineering practices in the future.

KEYWORDS

analytical solution, sandy dolomite tunnel, parametric analysis, mechanical response, mechanical analysis

1 Introduction

The construction of the Central Yunnan Water Diversion Project was outlined in China's 14th Five-Year Plan report. The construction of water conveyance tunnels in sandy dolomite strata faces a variety of challenging engineering geological issues, including significant soft rock deformation, fault zones, rock-bursts under high geo-stress, and water inrush at the tunnel



FIGURE 1
Morphology of dolomite sandy outcrops.

face (Wang et al., 2022). Dolomite sandification is often the most prominent (Figure 1). Taking the Yuxi section of the Central Yunnan water diversion project as an example (Fu et al., 2020; Wu et al., 2021; Wang MQ. et al., 2023), the total length of the Yuxi section of the Central Yunnan Water Conveyance Project is 77.069 km. It has eight water conveyance tunnels with a total length of 72.775 km, accounting for 94.43% of the total project length. The total length of water conveyance tunnels located in the sandy dolomite strata is approximately 14.5 km (19.8% of the total project length). Dolomite sandification not only weakens the strength and quality of the rock mass but also affects the stability of slopes and underground caverns. This can result in challenges such as cavern construction difficulties, poor construction quality, collapse, and large deformation (Figure 2A–C). It can also lead to secondary geological hazards such as surging sand and debris flow in the water-rich tunnel section (Figure 2D–F), complicating the management of engineering hazards and raising safety concerns. This can cause delays and increase investment in the project, thus highlighting the necessity of focusing on rock mass stability in sandy dolomite tunnels.

Dolomite sandification is a unique geological phenomenon which is manifested in the microcrystalline-fine crystalline structure of dolomite gradually weathering into fine sand, gravel, or clasts (Figure 1) by the combined action of dissolution and weathering. This weathering process seriously reduces the quality and stability of the rock mass (Rabajczyk, 2012; Chanyshev, 2023). A series of hazards such as the large deformation of rock mass, underground karst damage, and water inrush and sand gushing are often encountered during the construction of conservancy projects in sandy dolomite strata (Zhang et al., 2023). Jiang et al. (2022) reported extrusion and deformation occurring at the tunnel face during tunneling in a water-rich sandy dolomite stratum, and they proposed a control strategy for preventing sand gushing. Zhou et al. (2022) discussed the challenges and risks of tunnel face instability in terms of mineral composition and its macroscopic and microscopic aspects. Dong et al. (2023) analyzed the main damage modes in a sandy dolomite tunnel and conducted a safety evaluation of it. Diez (2019) analyzed the rock mechanical properties of sandy dolomite after erosion and weathering in the quarry, revealed the mechanism of dissolving gravel in sandy dolomite, and evaluated the safety of rock construction. This literature indicates that dolomite sandification has a great impact on the project, and its safety and reliability must be assessed. If sandy dolomite leads to construction hazards in a water conveyance tunnel, it may force construction progress to slow down and, in serious cases, may also jeopardize the safety of tunnel construction workers and affect the social and economic benefits of the infrastructure.

Currently, there are limited studies on tunneling hazards in sandy dolomite strata. Zarei et al. (2011) analyzed the impact of geological features such as fault zones, open cracks, and dams in sandy dolomite on tunnel safety after the excavation of a water conveyance tunnel in Semnan, Iran. However, they did not assess the impact of mechanical coupling between the tunnel face and sandy dolomite on tunnel safety. Qin et al. (2019) discussed the factors affecting the stability of railway tunnels. They explained the safety problems caused by the desertification of the tunnel rock mass and used a theoretical model to make safety predictions. However, they also did not consider the impact of rock mass desertification. Wu et al. (2013) clarified the maximum horizontal stress generated by rock burst in tunnel engineering and evaluated tunnel safety based on this stress, but they did not address the changes in the mechanical properties of sandy rock mass. Taking a high-speed railway crossing the Taihang Mountain as an example, Di et al. (2020) characterized the rock resistivity distribution of a tunnel by using the controllable source audio magnetotelluric method. They analyzed the safety of the tunnel but did not record its stress condition. Liu et a. (2022) systematically analyzed the hazards and treatment methods of water inrush occurring in a large cross-section filling karst pipeline based on engineering practice, but they did not consider the impact of mechanical problems related to rock mass desertification on water inrush.

The construction of water conveyance tunnels in sandy dolomite strata poses significant challenges due to complex geological issues such as soft rock deformation, fault zones, rock bursts, and water inrush. A key innovation lies in the recognition of dolomite sandification as a primary concern; this weakens the strength and quality of rock mass, thus impacting tunnel stability. This unique geological phenomenon involves the gradual weathering of dolomite into fine sand, gravel, or clasts which reduces rock mass quality. Previous studies have highlighted hazards such as deformation, karst damage, and water inrush, emphasizing the need to assess safety and reliability. Additionally, researchers have identified challenges related to tunnel face instability and proposed control strategies to mitigate risks such as sand gushing. However, there is a lack of comprehensive studies that address the mechanical response of rock mass in sandy dolomite tunnels. Innovative research efforts have focused on developing an analytical solution for the mechanical behaviors of rock mass in sandy dolomite tunnels. The analytical approach adopted here aims to address the limited understanding

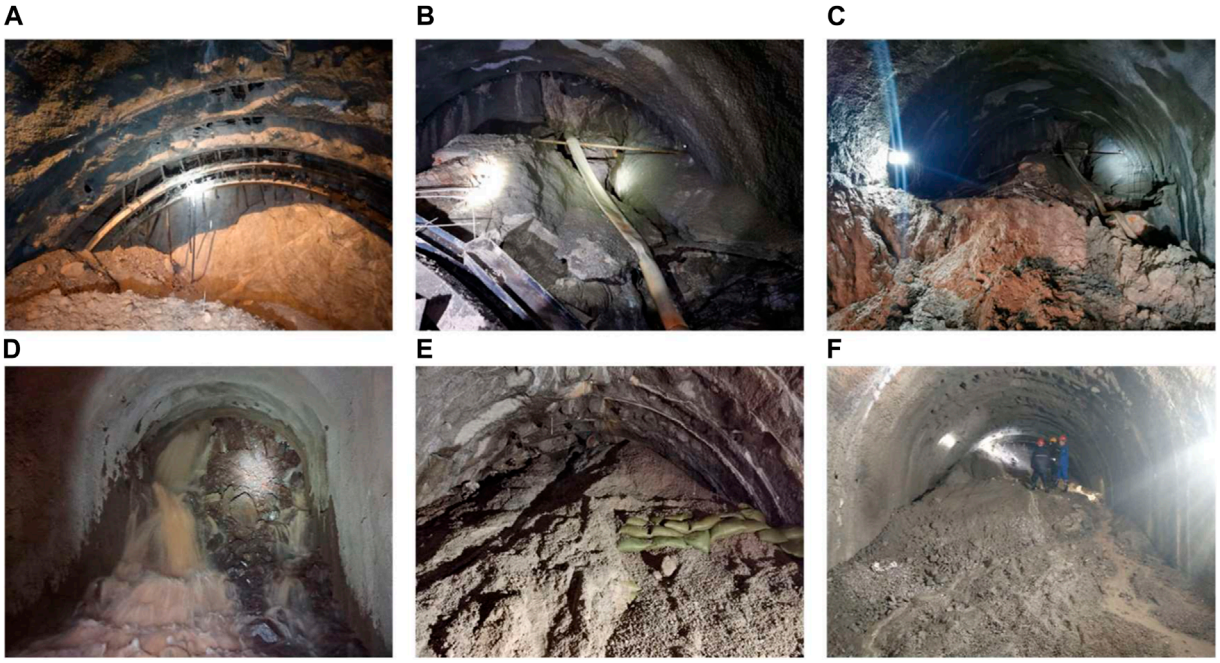

FIGURE 2
Secondary hazards in sandy dolomite tunnels: **(A–C)** Severe sandification and large deformation of support structures, **(D)** Water and sand burst from the tunnel's excavation surface, **(E, F)** Sand and debris flowing inside the cave.

of sandy dolomite tunnel mechanics and to provide insights into enhancing engineering practices. By investigating the impact of dolomite sandification on tunnel stability, this study aims to reduce and prevent instability issues in tunnel construction, ultimately improving project outcomes and safety. The findings not only contribute to the field of geotechnical engineering but also offer valuable guidance for future projects in carbonate rock regions.

2 Statement of the problem

2.1 Tunnel condition

Self-weight and associated geological tectonics are present in natural rock masses (Sperner et al., 2003; Dai et al., 2021; Lu et al., 2024). Generally, a tunnel is subjected to a gravitational (Dong et al., 2019; Wang Q. et al., 2023) and a tectonic stress field (Yale, 2003; Zhou et al., 2023).

$$\sigma = \sigma_z + \sigma_\tau \tag{1}$$

Given the fact that the tectonic stress field is complex and is influenced by many factors, the current study only considers the effect of the gravitational stress field, which is expressed as:

$$\sigma_z = \gamma H \tag{2}$$

$$\lambda = \frac{\mu}{1-\mu} \tag{3}$$

$$\sigma_x = \sigma_y = \frac{\mu}{1-\mu}\sigma_z = \lambda\sigma_z \tag{4}$$

where σ_z is the self-weight stress with a unit of MPa, σ_τ is the tectonic stress with a unit of MPa, γ represents the weight of rock mass with a unit of kN/m^3, H is the depth of rock mass with a unit of m, λ is the lateral pressure coefficient, σ_x, and σ_y are the rock mass stresses with a unit of MPa, and μ is Poisson's ratio of rock mass.

2.2 Basic assumptions

Rock mass during tunnel excavation is mainly in two states. As indicated in Figure 3A, if the rock mass remains elastic after excavation, it is relatively stable and is in a secondary stress state (Aygar and Gokceoglu, 2020). If the excessive stress at the excavated profile exceeds the ultimate strength of rock mass, the rock mass will undergo plastic deformation, which may lead to deformation or a failure of the supporting structure through the relaxation and failure of the rock mass (Zheng and Wei, 2008). However, the rock mass further away from the excavated profile remains in an elastic state, resulting in a plastic zone in the rock mass (Leu and Chang, 2005). The following assumptions have been made to facilitate the elasto-plasticity analysis of rock mass (Wang et al., 2010; Zhang and Sun, 2011; van Bijsterveldt et al., 2021; Guo et al., 2023):

(1) The rock mass is homogeneous, isotropic, and incompressible, and exhibits ideal elastic–plastic mechanical behavior with a constitutive relationship (Figure 3B).
(2) The tunnel is deep-buried, satisfying the ideal plane hole problem, and it has a circular section and infinite length.
(3) Only the self-weight of the rock mass is considered for the initial stress field, with no tectonic stress.

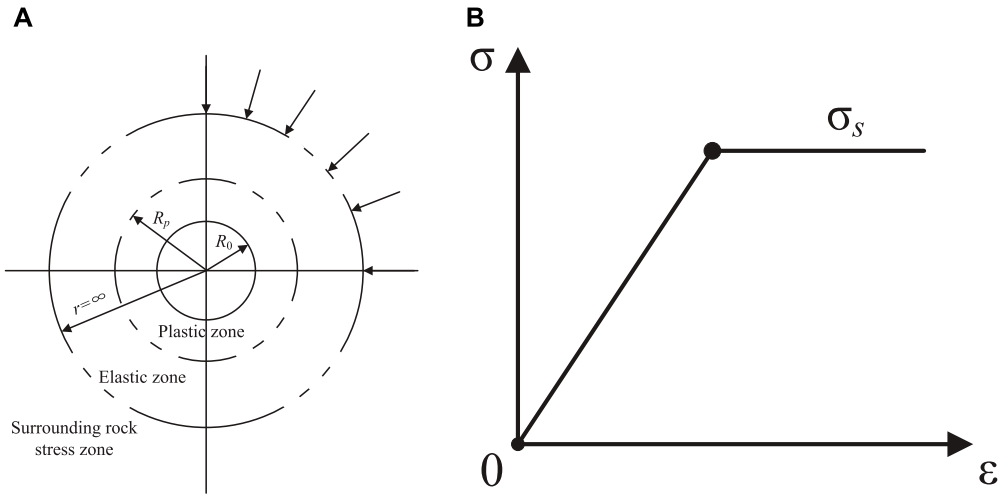

FIGURE 3
Two states of rock mass during tunnel excavation: **(A)** division of the elastic and plastic zones of rock mass; **(B)** constitutive relation diagram.

3 Elasto-plasticity solution for sandy dolomite tunnel

To analyze the mechanical behaviors of a tunnel constructed in sandy dolomite strata, it is simplified into an ideal circular tunnel model based on the principle of small hole stress (Toubal et al., 2005; Schajer, 2010). An elastic-plastic analytical solution of a circular tunnel is then derived to determine the deformation, stress, and radii of plastic zones of tunnel rock mass.

3.1 Solution for rock mass in the elastic zone

If the lateral pressure coefficient λ is not equal to 1, the rock mass stress can be divided into two parts according to the elastic mechanics and then be superimposed to determine the final stress state. Figure 4 illustrates a schematic diagram of the secondary stress in the tunnel rock mass.

Part I: the rock mass is subjected to an initial rock stress of $p = p_0/2$ (1+λ), the vertical stress is equal to the horizontal stress, and the distribution is axisymmetric.

Part II: the rock mass is subjected to an initial rock stress of $p = p_0/2$ (1-λ), the vertical stress is equal to the horizontal stress, and the distribution is antisymmetric.

According to elastic mechanics, the radial σ_r, tangential σ_θ, and shear $\tau_{r\theta}$ stresses can be obtained as:

$$\sigma_r = \frac{p_0}{2}\left[(1+\lambda)\left(1-\frac{R_0^2}{r^2}\right)-(1-\lambda)\left(1-4\frac{R_0^2}{r^2}+3\frac{R_0^4}{r^4}\right)\cos 2\theta\right] \quad (5)$$

$$\sigma_\theta = \frac{p_0}{2}\left[(1+\lambda)\left(1+\frac{R_0^2}{r^2}\right)+(1-\lambda)\left(1+3\frac{R_0^2}{r^4}\right)\cos 2\theta\right] \quad (6)$$

$$\tau_{r\theta} = -\frac{p_0}{2}\left[(1-\lambda)\left(1+2\frac{R_0^2}{r^2}-3\frac{R_0^4}{r^4}\right)\sin 2\theta\right] \quad (7)$$

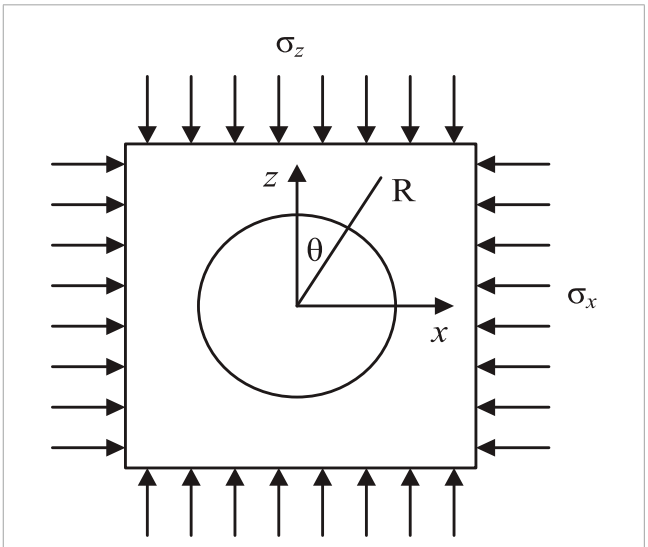

FIGURE 4
Schematic diagram of tunnel model.

The radial displacement u_r and tangential displacement u_θ are expressed as:

$$u_r = \frac{(1+\nu)p_0}{2E}\cdot\frac{R_0^2}{r}\left\{(1+\lambda)+(1-\lambda)\left[2(1-2\nu)+\frac{R_0^2}{r^2}\right]\cos 2\theta\right\} \quad (8)$$

$$u_\theta = \frac{(1+\nu)p_0}{2E}\cdot\frac{R_0^2}{r}\left\{(1-\lambda)\left[2(1-2\nu)+\frac{R_0^2}{r^2}\right]\sin 2\theta\right\} \quad (9)$$

where p_0 is the initial rock stress with a unit of MPa, θ is the angle between the z-axis and the line connecting the computation point to the origin with a unit of °, R_0 is the excavation radius of the tunnel with a unit of m, r is the tunnel radius with a unit of m, ν is the strain coefficient of the rock mass, and E is the elastic modulus of rock mass with a unit of MPa.

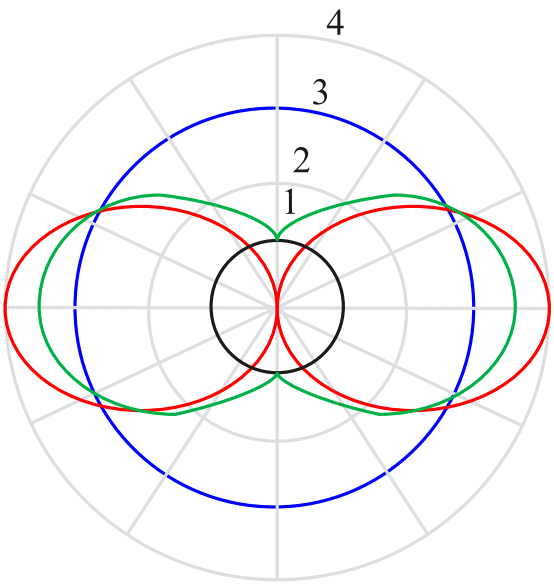

FIGURE 5
Variation of total stress concentration factor of tunnels.

These equations characterize the detailed secondary stress of the rock mass. However, these equations are complicated as they involve not only tangential stress but also tangential displacement. To simplify this problem, the tunnel radius and the excavation radius are assumed to be equal at $r = R_0$.

Thereafter, the equation obtained can be simplified as:

$$\sigma_\theta = p_0[(1+\lambda) + 2(1-\lambda)\cos 2\theta] \tag{10}$$

$$\sigma_r = \tau_{r\theta} = 0 \tag{11}$$

If $1 + 2\cos 2\theta = K_z$, $1 - 2\cos 2\theta = K_x$, then the above equation can be converted to:

$$\sigma_\theta = p_0(K_Z + \lambda K_x) = Kp_0 \tag{12}$$

where K is the total stress concentration factor of the tunnel rock mass, K_z is the vertical stress concentration factor, and K_x is the horizontal stress concentration factor. These parameters are dimensionless.

K varies with θ, p_0, and λ as independent variables (Figure 5). The origin position that is the intersection of the radial line with the tunnel sidewall changes dynamically. The stress value at the origin divided by the initial stress (σ_θ/p_0) is chosen as the scale.

As indicated in Figure 5, when $\lambda = 1$, the stress values of the tunnel wall are all $2p_0$—twice the initial stress. Since the tangential stress is independent of the angle, the stress of the tunnel wall is in the best state, and the tunnel is safer. When $\lambda = 0$, the stress on the tunnel wall is in the most unfavorable state. The left and right sides of the tunnel wall will be subjected to the maximum compressive stress $3p_0$ (three times the initial rock stress), while the upper side of the tunnel wall will be subjected to the maximum tensile stress p_0 (equal to the initial rock stress). When $\lambda = 1/3$, the boundary point of tensile stress appears on the tunnel wall, while the tensile and compressive stresses on the upper side of the tunnel wall is 0. At this point, the tunnel is in stress equilibrium and is safest. When λ is less than ⅓, the tensile stress appears on the upper side of the tunnel wall. The safety of the tunnel is slightly improved, and the risk of tunnel wall damage and leakage is reduced. When λ is greater than ⅓, the compressive stress appears on the upper side of the tunnel wall, and a safety risk to the tunnel will be present.

3.2 Solution for rock mass in the plastic zone

The elastic zone can be expressed thus (Zareifard and Fahimifar, 2016):

$$\begin{matrix}\sigma_r \\ \sigma_\theta\end{matrix} = \mathrm{A} \pm \frac{\mathrm{B}}{r^2} \tag{13}$$

The equilibrium equation is (Wang M. et al., 2023):

$$\frac{\mathrm{d}\sigma_r}{\mathrm{d}r} + \frac{\sigma_r - \sigma_\theta}{r} = 0 \tag{14}$$

The M–C criterion is adopted for the analysis, which is expressed as (Zheng et al., 2005):

$$\sigma_\theta = \frac{1+\sin\Phi}{1-\sin\Phi}\sigma_r + \frac{2C\cos\Phi}{1-\sin\Phi} \tag{15}$$

The stresses in the elastic and plastic zones can be obtained by combining Eqs 13-15.

Stress in elastic zone is expressed as (Oreste et al., 2019):

$$\begin{matrix}\sigma_\theta^e \\ \sigma_r^e\end{matrix} = p_0 \pm (C\cos\Phi + p_0)\left[\frac{(p_0 + C\cot\Phi)(1-\sin\Phi)}{C\cot\Phi}\right]^{\frac{1-\sin\Phi}{2\sin\Phi}}\left(\frac{R_0}{r}\right)^2 \tag{16}$$

$$\sigma_z^e = p_0 \tag{17}$$

Stress in the plastic zone is expressed as (Wang C. et al., 2023):

$$\sigma_\theta^p = C\cot\Phi\left[\left(\frac{r}{R_0}\right)^{\frac{2\sin\Phi}{1-\sin\Phi}} - 1\right] \tag{18}$$

$$\sigma_r^p = C\cot\Phi\left[\frac{1+\sin\Phi}{1-\sin\Phi}\left(\frac{r}{R_0}\right)^{\frac{2\sin\Phi}{1-\sin\Phi}} - 1\right] \tag{19}$$

$$\sigma_z^p = \frac{\sigma_\theta^p + \sigma_r^p}{2} = C\cot\Phi\left[\frac{1}{1-\sin\Phi}\left(\frac{r}{R_0}\right)^{\frac{2\sin\Phi}{1-\sin\Phi}} - 1\right] \tag{20}$$

The radius of the plastic zone can be obtained thus (Singh et al., 2016):

$$R_p = R_0\left[\frac{(p_0 + C\cot\Phi)(1-\sin\Phi)}{C\cot\Phi}\right]^{\frac{1-\sin\Phi}{2\sin\Phi}} \tag{21}$$

where C is cohesion with a unit of MPa, Φ is the internal friction angle with a unit of °, and R_p is the radius of the plastic zone with a unit of m. Eqs 16–21 are derived from Eqs 1–15. The part 4 of the article mainly refers to Eqs 16–21.

4 Parametric analysis on the mechanical behaviors of rock mass

Parameter analysis is performed in this section by utilizing the mechanical parameters of sandy dolomite determined by laboratory

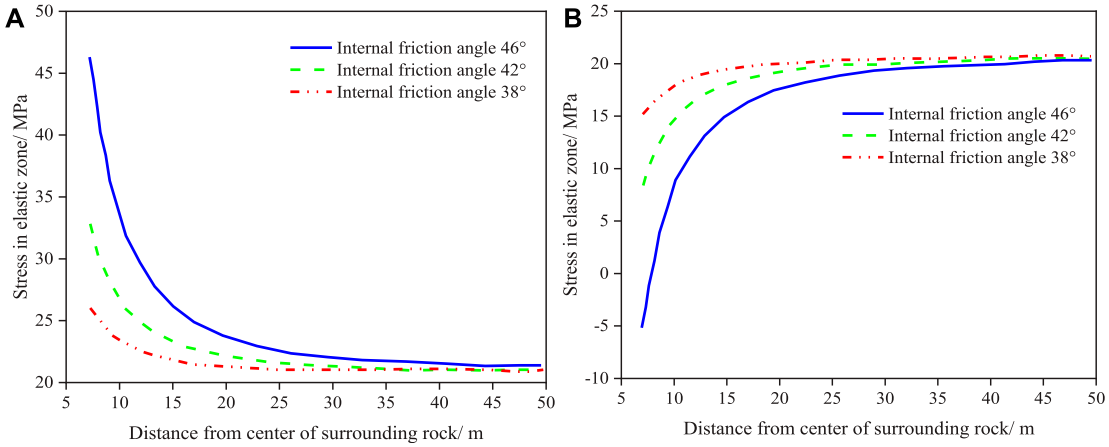

FIGURE 6
Variation of stress in elastic zone under different internal friction angles. **(A)** σ^e_r. **(B)** σ^e_θ.

tests (Dang et al., 2022; Tao et al., 2023b; Tao et al., 2023) which yields various mechanical response curves of rock mass.

4.1 Variation of stress in the elastic zone

4.1.1 Influence of the internal friction angle

Three internal friction angles—38°, 42°and 46°—are selected to explore the variations of stress σ^e_θ (tangential stress) and σ^e_r (radial stress) in the elastic zone. From Eq. 16, the results are presented in Figure 6.

It can be observed from Figure 6 that under different internal friction angles, with an increase in distance from the excavation center, σ^e_r displays a decreasing trend. A larger internal friction angle yields a larger initial σ^e_r value with a greater decline (Figure 6A). An increasing trend is experienced by σ^e_θ as the distance from the excavation surface increases, but the initial value is smaller and the growth rate is larger at a larger internal friction angle (Figure 6B).

4.1.2 Influence of cohesion

Cohesion values of 20, 30, and 40 MPa are selected to explore variations of stress in the elastic zone. From Eq. 16, the results are presented in Figure 7.

Figure 7 confirms that the stress in the elastic zone varies with the distance from the excavation center under different cohesions. It is observed that σ^e_r decreases with an increase in the distance from the excavation center. However, higher cohesion leads to a higher initial σ^e_r and a greater decline (Figure 7A). With an increase in distance from the excavation surface, σ^e_θ experiences an increasing trend, but higher cohesion leads to a smaller initial σ^e_θ and a greater increase (Figure 7B).

4.1.3 Influence of initial rock stress

The initial rock stresses of 21, 25, and 29 MPa are selected to explore the variations of stress in the elastic zone. From Eq. 16, the results are presented in Figure 8.

Figure 8 demonstrates that stress in the elastic zone varies with the distance from the excavation surface under different initial rock stresses. It can be observed that σ^e_r under three initial rock stresses decreases gradually with increased distance from the excavation surface. These three curves have similar shapes, are parallel to each other, and decrease by almost the same amount. Moreover, the initial values of σ^e_r and terminal values of σ^e_θ increase with increasing initial rock stresses. An increasing trend is shown by σ^e_θ under three initial rock stresses with increasing distance from the excavation surface, with very close initial values. However, the greater the initial rock stress, the greater the range of increase in σ^e_θ. When the distance from the excavation surface exceeds 25 m, both σ^e_r and σ^e_θ gently increase or decrease and the curves become almost horizontal.

4.2 Variation of stress in the plastic zone

4.2.1 Influence of the internal friction angle

Three internal friction angles of 38°, 42°, and 46° are selected to explore the variations of stress σ^p_θ (tangential stress) and σ^p_r (radial stress) in the plastic zone. From Eqs 18, 19, the results are shown in Figure 9.

As shown in Figure 9, stress in the plastic zone varies with the distance from the excavation surface under different internal friction angles. It can be observed that σ^p_r and σ^p_θ under the three internal friction angles increase with increased distance from the excavation surface. In addition, the larger the internal friction angle, the greater the increase in value of the two types of stresses. However, the radial stress growth curve consists of three curves with the same starting point; the larger the internal friction angle, the steeper the curve. This indicates that there is little difference in the radial stresses in the plastic zone at different internal friction angles. In contrast, the σ^p_θ curve is composed of three parallel and gentle curves, especially when the distance from the excavation surface is more than 25 m. Furthermore, the rising range of the σ^p_θ curve increases with an increase in the internal friction angle.

4.2.2 Influence of cohesion

Cohesion values of 20, 30, and 40 MPa are selected to explore variations of stress in the plastic zone. From Eqs 18,19, the results are shown in Figure 10.

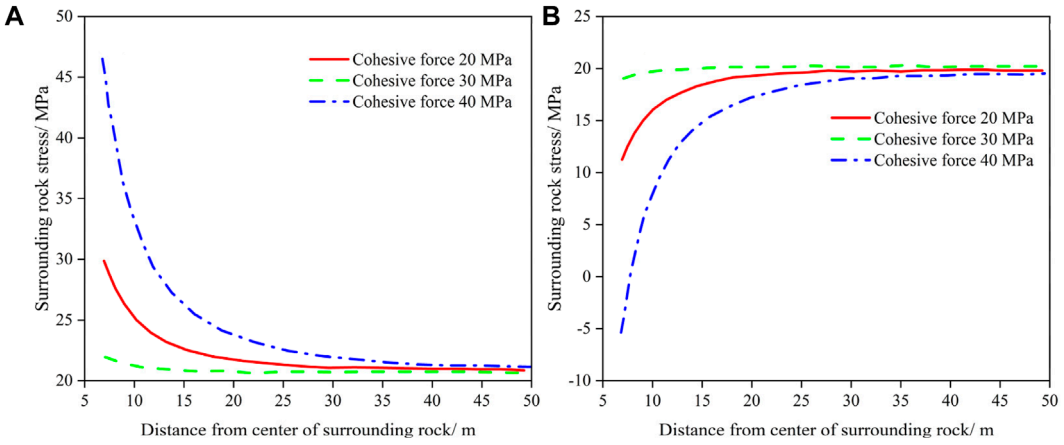

FIGURE 7
Variation of stress in elastic zone under different cohesions. **(A)** $\sigma^e{}_r$. **(B)** $\sigma^e{}_\theta$.

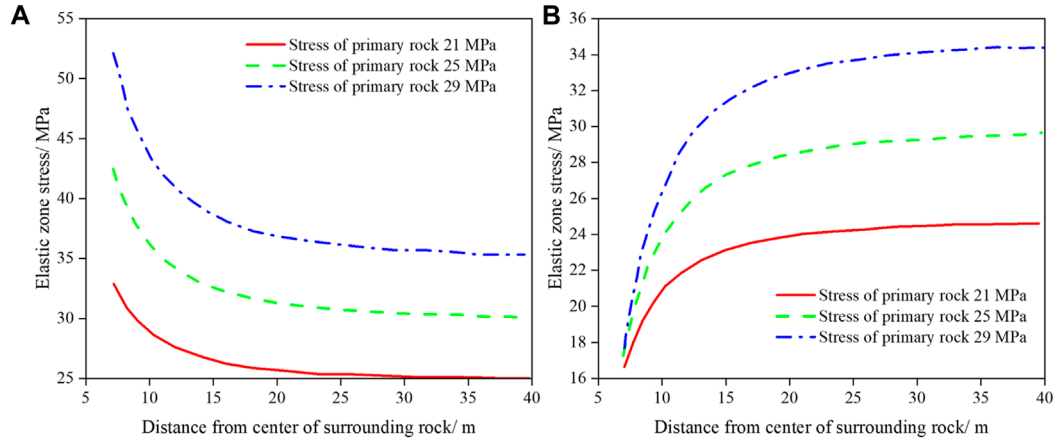

FIGURE 8
Variation of stress in elastic zone under different initial rock stresses. **(A)** $\sigma^e{}_r$. **(B)** $\sigma^e{}_\theta$.

As shown in Figure 10, the stress in the plastic zone varies with the distance from the excavation surface under different cohesions. It is observed that $\sigma^p{}_r$ and $\sigma^p{}_\theta$ under the three cohesion values increase with increased distance from the excavation surface. In addition, the greater the cohesion, the greater the increase in corresponding stress. However, the radial stress growth curve consists of three curves with the same starting point, and the smaller the cohesion, the steeper the curve. This indicates that there is little difference in $\sigma^p{}_r$ in the plastic zone at different cohesions. In contrast, the $\sigma^p{}_\theta$ growth curve consists of three parallel and gentle curves. Furthermore, the rising range of the $\sigma^p{}_\theta$ growth curve with increasing cohesion is smaller, indicating that $\sigma^p{}_\theta$ hardly varies with the distance from excavation surface when cohesion and initial rock stress are constant.

5 Discussion

(1) Influence on stress in elastic zone

Based on the analysis above, it is evident that both the $\sigma^e{}_r$ and $\sigma^e{}_\theta$, curves at different internal friction angles and cohesions are close and almost overlap when the distance from the excavation surface exceeds 40 m. This indicates that within a certain range, the internal friction angle and cohesion have less influence on stress in the elastic zone as the distance from the excavation surface increases.

(2) Variation of the radius of the plastic zone

Cohesion values of 20, 30, and 40 MPa are selected to explore variations in the radius of the plastic zone under different initial rock stresses and tunnel excavation radii. From Eq. 21, the results are shown in Figure 11.

Figure 11 indicates that the radius of the plastic zone varies with the initial rock stress and tunnel excavation radius at different cohesions. The radius of the plastic zone nonlinearly increases with the initial rock stress. Higher cohesion results in a decrease in the radius of plastic zone, and an increase in radius of the plastic zone is dependent on an increase in the initial rock stress at different cohesions. Furthermore, an increase in tunnel excavation radius also leads to an increase in the radius of the plastic zone, and an increase in radius of plastic zone is

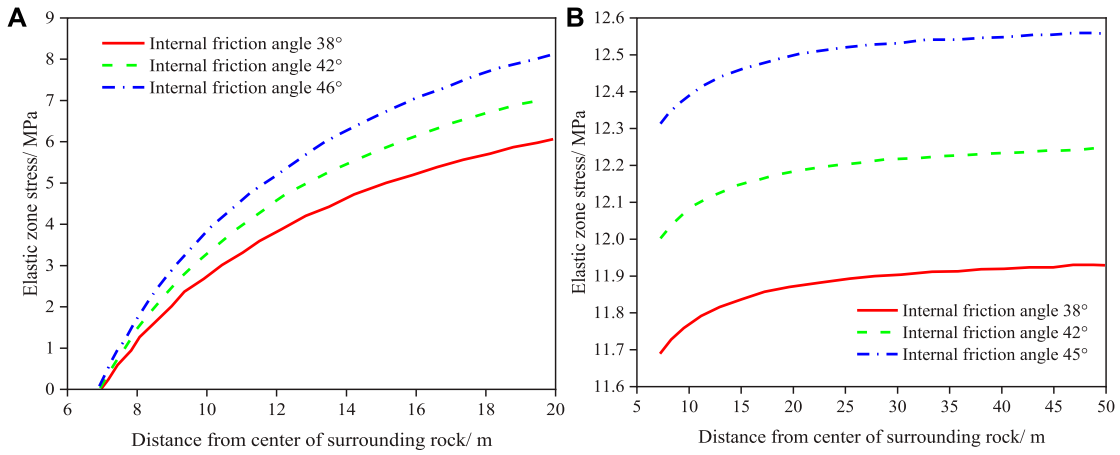

FIGURE 9
Variation of stress in plastic zone under different internal friction angles. **(A)** σ^{p}_{r}. **(B)** σ^{p}_{θ}.

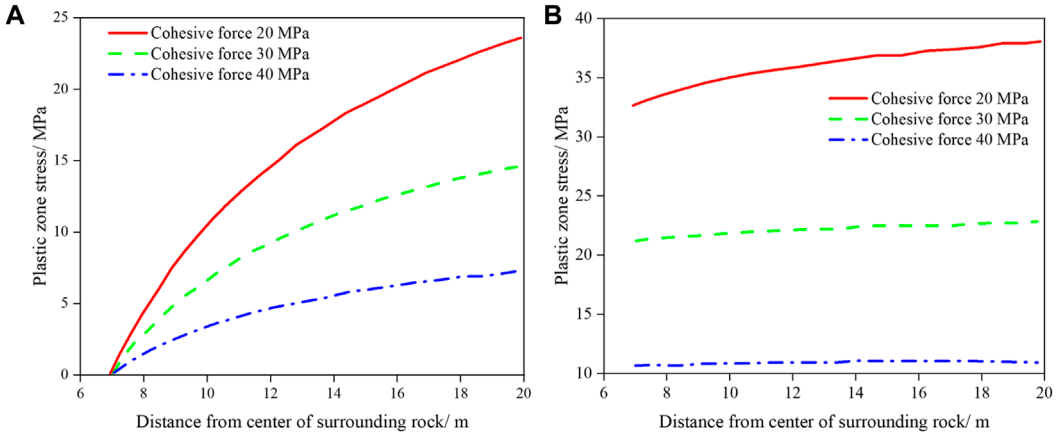

FIGURE 10
Variation of stress in plastic zone under different cohesions. **(A)** σ^{p}_{r}. **(B)** σ^{p}_{θ}.

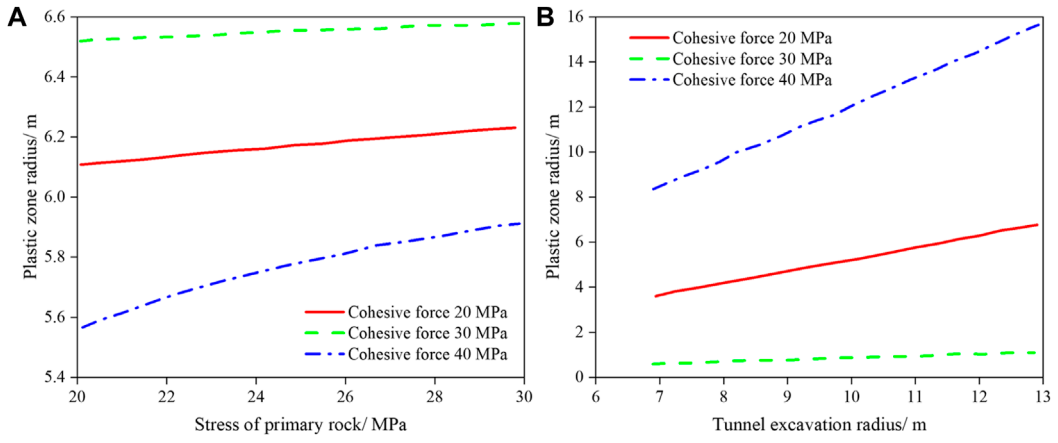

FIGURE 11
Variation of radius of plastic zone under different cohesions. **(A)** The initial rock stress. **(B)** Tunnel excavation radius.

associated with an increase in excavation radius at different cohesion conditions.

Therefore, initial rock stress has a significant impact on the radius of the plastic zone. Higher initial rock stress results in a larger plastic zone radius which demonstrates a significant effect on the rock plasticity. Cohesion also plays a significant role in determining the radius of the plastic zone, with higher cohesion leading to a smaller radius. This suggests that increasing cohesion will greatly enhance the resistance of rock mass to plastic failure. Furthermore, an increase in tunnel excavation radius correlates with an increase in plastic zone radius, highlighting the significant impact of tunnel excavation on the plastic zone of rock mass. This should be fully considered in engineering design and practice. These research results serve as an important theoretical reference for rock mechanical properties and have significant guiding implications for geotechnical engineering practice.

6 Conclusion

This study develops an analytical solution for sandy dolomite tunneling, and then conduct parametric analysis to investigate the mechanical response of rock mass in sandy dolomite tunnels. It draws the following analytical conclusions.

(1) The stress of tunnel sidewalls under different λ values exhibits different characteristics. Varying λ values impacts stress distribution and tunnel stability, with extreme values posing instability risks. When the stress of a rock mass approaches the plastic limit, the deformation rate of rock mass increases. A smaller plastic zone radius leads to lower safety for a tunnel.

(2) In cases of varying internal friction angles, cohesion, and initial rock stress, radial stress exhibits a gradually decreasing trend with increasing distance from the excavation surface. Higher values lead to a greater decline of radial stress. Stress values increase with distance from the excavation surface but become similar within a certain range. The effects on stress in elastic zone decrease as distance from the excavation surface increases.

(3) The plastic zone size increases with a larger tunnel excavation radius, while the internal friction angle and cohesion determine the corresponding stress increase value. The initial rock stress significantly affects the plastic zone radius, with a higher initial rock stress resulting in a larger plastic zone radius while higher cohesion leading to a smaller plastic zone radius. Increased tunnel excavation radius also contributes to the expansion of the plastic zone, demonstrating the significant influence of tunnel excavation on rock mass. These findings provide important reference and guidance for geotechnical engineering practice.

Data availability statement

The original contributions presented in the study are included in the article/Supplementary Material; further inquiries can be directed to the corresponding author.

Author contributions

DS: Conceptualization, Investigation, Methodology, Writing–original draft. ZT: Conceptualization, Methodology, Validation, Writing–review and editing. HY: Funding acquisition, Resources, Supervision, Writing–original draft. HS: Data curation, Investigation, Visualization, Writing–original draft. XL: Formal Analysis, Investigation, Supervision, Writing–original draft. FW: Formal Analysis, Investigation, Supervision, Writing–original draft. SH: Formal Analysis, Investigation, Supervision, Writing–original draft. HS: Data curation, Investigation, Visualization, Writing–original draft. WX: Data curation, Investigation, Visualization, Writing–original draft. ZW: Data curation, Investigation, Visualization, Writing–original draft. MH: Conceptualization, Methodology, Validation, Writing–review and editing.

Funding

The author(s) declare financial support was received for the research, authorship, and/or publication of this article. The research received the financial support provided by the Major Science and Technology Special Plan of Yunnan Province Science and Technology Department (Grant No. 202002AF080003), the Fundamental Research Funds for the Central Universities (Grant No. 2022YJSSB04).

Acknowledgments

Many thanks are due to China Institute of Water Resources and Hydropower Research, Yunnan Institute of Water & Hydropower Engineering Investigation, Design and Research, China Railway No.5 Engineering Group Co., Ltd, and China Railway Tunnel Group Co., Ltd. The authors gratefully acknowledge the financial support provided by the Major Science and Technology Special Plan of Yunnan Province Science and Technology Department (Grant Nos.202002AF080003) and the Fundamental Research Funds for the Central Universities (Grant Nos.2022YJSSB04).

Conflict of interest

Author HY was employed by China Railway 12th Bureau Group Co. Ltd.

Author FW was employed by Shanxi Provincial Transportation Technology Research and Development Co. Ltd.

The remaining authors declare that the research was conducted in the absence of any commercial or financial relationships that could be construed as a potential conflict of interest.

Publisher's note

All claims expressed in this article are solely those of the authors and do not necessarily represent those of their affiliated organizations, or those of the publisher, the editors and the reviewers. Any product that may be evaluated in this article, or claim that may be made by its manufacturer, is not guaranteed or endorsed by the publisher.

References

Aygar, E. B., and Gokceoglu, C. (2020). Problems encountered during a railway tunnel excavation in squeezing and swelling materials and possible engineering measures: a case study from Turkey. *Sustainability-Basel* 12 (3), 1166. doi:10.3390/su12031166

Chanyshev, A. (2023). A way to determine the positive direction of the shear force on the elemental area. *Geohazard Mech.* 1 (2), 179–184. doi:10.1016/j.ghm.2023.04.004

Dai, L. P., Pan, Y. S., Li, Z. H., Wang, A. W., Xiao, Y. H., Liu, F. Y., et al. (2021). Quantitative mechanism of roadway rockbursts in deep extra-thick coal seams: theory and case histories. *Tunn. Undergr. Space Technol.* 111, 103861. doi:10.1016/j.tust.2021.103861

Dang, W., Tao, K., and Chen, X. (2022). Frictional behavior of planar and rough granite fractures subjected to normal load oscillations of different amplitudes. *J. Rock Mech. Geotech. Eng.* 14 (3), 746–756. doi:10.1016/j.jrmge.2021.09.011

Di, Q. Y., Fu, C. M., An, Z. G., Wang, R., Wang, G., Wang, M., et al. (2020). An application of CSAMT for detecting weak geological structures near the deeply buried long tunnel of the Shijiazhuang-Taiyuan passenger railway line in the Taihang Mountains. *Eng. Geol.* 268, 105517. doi:10.1016/j.enggeo.2020.105517

Diez, J. A. (2019). "Analysis of the alterability of quarry rock used in the Alcorlo rock fill dam (Guadalajara, Spain)," in *14th ISRM congress* (Foz do Iguaçu, Brazil: ISRM). ISRM-14CONGRESS-2019-208.

Dong, J. X., Shen, Z. L., Cao, L., Mi, J., Li, J., Zhao, Y., et al. (2023). Water-sand inrush risk assessment method of sandy dolomite tunnel and its application in the Chenaju tunnel, southwest of China. *Geomatics Nat. Hazard. Risk* 14 (1), 2196369. doi:10.1080/19475705.2023.2196369

Dong, W., Song, S. Z., Zhang, B. S., and Yang, DJEFM (2019). SIF-based fracture criterion of rock-concrete interface and its application to the prediction of cracking paths in gravity dam. *Eng. Fract. Mech.* 221, 106686. doi:10.1016/j.engfracmech.2019.106686

Fu, P., Yin, J. M., Ding, X. L., and Liu, Y. K. (2020). "Deformation-strain field characteristics and fault activities in central Yunnan water diversion project area," in IOP Conference Series: Earth and Environmental Science, 570 October 23–26, 2020 (Beijing, China: IOP Publishing). doi:10.1088/1755-1315/570/6/062029

Guo, W., Shui, H. C., Liu, Z., Wang, Y., and Tu, J. W. (2023). Reliability analysis of elastic graphite packer in heat injection well during oil shale *in-situ* conversion. *Adv. Geo-Energy Res.* 7 (1), 28–38. doi:10.46690/ager.2023.01.04

Jiang, Y. F., Zhou, P., Zhou, F. C., Lin, J. Y., Li, J. Y., Lin, M., et al. (2022). Failure analysis and control measures for tunnel faces in water-rich sandy dolomite formations. *Eng. Fail. Anal.* 138, 106350. doi:10.1016/j.engfailanal.2022.106350

Leu, S. S., and Chang, S. L. (2005). Digital image processing based approach for tunnel excavation faces. *Autom. Constr.* 14 (6), 750–765. doi:10.1016/j.autcon.2005.02.004

Liu, N., Pei, J. H., Cao, C. Y., Liu, X. Y., Huang, Y. X., Mei, GXJT, et al. (2022). Geological investigation and treatment measures against water inrush hazard in karst tunnels: a case study in Guiyang, southwest China. *Tunn. Undergr. Space Technol.* 124, 104491. doi:10.1016/j.tust.2022.104491

Lu, B., Sheil, B. B., Zhao, W., Jia, P. J., Bai, Q., and Wang, W. T. (2024). Laboratory testing of settlement propagation induced by pipe-roof pre-support deformation in sandy soils. *Tunn. Undergr. Space Technol.* 146, 105645. doi:10.1016/j.tust.2024.105645

Oreste, P., Hedayat, A., and Spagnoli, G. (2019). Effect of gravity of the plastic zones on the behavior of supports in very deep tunnels excavated in rock masses. *Int. J. Geomech.* 19 (9), 04019107. doi:10.1061/(asce)gm.1943-5622.0001490

Qin, S. W., Ma, Z. J., Jiang, C. D., Lin, J., Bai, M., Lin, T., et al. (2019). Application of magnetic resonance sounding to tunnels for advanced detection of water-related disasters: a case study in the Dadushan Tunnel, Guizhou, China. *Tunn. Undergr. Space Technol.* 84, 364–372. doi:10.1016/j.tust.2018.11.032

Rabajczyk, A. (2012). *The relationship between metal forms found in river bottom sediments and land development (review)*. Rijeka: Water Pollut. InTech, 189–202.

Schajer, G. S. (2010). Advances in hole-drilling residual stress measurements. *Exp. Mech.* 50, 159–168. doi:10.1007/s11340-009-9228-7

Singh, A., Rao, K. S., and Ayothiraman, R. (2016). "Effect of intermediate principal stress on cylindrical tunnel in an elasto-plastic rock mass," in 11th International Symposium on Plasticity and Impact Mechanics (IMPLAST) (New Delhi, INDIA: Indian Inst Technol), 1056–1063.

Sperner, B., Müller, B., Heidbach, O., Delvaux, D., Reinecker, J., and Fuchs, K. (2003). Tectonic stress in the Earth's crust: advances in the World Stress Map project. *Geol.Soc.London Spec. Publ.* 212 (1), 101–116. doi:10.1144/gsl.sp.2003.212.01.07

Tao, K., Dang, W., and Li, Y. (2023). Frictional sliding of infilled planar granite fracture under oscillating normal stress. *Int. J. Min. Sci. Technol.* 33 (6), 687–701. doi:10.1016/j.ijmst.2022.12.001

Tao, K., Dang, W., Liao, X., and Li, X. (2023b). Experimental study on the slip evolution of planar fractures subjected to cyclic normal stress. *Int. J. Coal Sci. Technol.* 10 (1), 67. doi:10.1007/s40789-023-00654-w

Toubal, L., Karama, M., and Lorrain, B. (2005). Stress concentration in a circular hole in composite plate. *Compos. Struct.* 68 (1), 31–36. doi:10.1016/j.compstruct.2004.02.016

van Bijsterveldt, C. E., van Wesenbeeck, B. K., Ramadhani, S., Raven, O. V., van Gool, F. E., Pribadi, R., et al. (2021). Does plastic waste kill mangroves? A field experiment to assess the impact of macro plastics on mangrove growth, stress response and survival. *Sci. Total Environ.* 756, 143826. doi:10.1016/j.scitotenv.2020.143826

Wang, C., Liu, X., Song, D., Wang, E., and Zhang, J. (2023d). Elasto-plastic analysis of the surrounding rock mass in circular tunnel using a new numerical model based on generalized nonlinear unified strength theory. *Comput. Geotech.* 154, 105163. doi:10.1016/j.compgeo.2022.105163

Wang, M., Zhang, Z., Ren, L., Zhang, R., Zheng, L., Zhang, L., et al. (2023c). Analysis of rock mass parameters and plastic zone of a tunnel in southwest mountainous area. *KSCE J. Civ. Eng.* 27 (12), 5448–5459. doi:10.1007/s12205-023-0886-2

Wang, M. Q., Xu, W., Mu, H. Y., Mi, J., Wu, Y. H., and Wang, Y. X. (2022). Study on construction and reinforcement Technology of dolomite sanding tunnel. *Sustainability-Basel* 14 (15), 9217. doi:10.3390/su14159217

Wang, M. Q., Zhang, C. X., Song, B. H., Liu, H. M., and Xu, W. (2023a). Study on the mechanical properties of anisotropic red sandstone under point load strength test and uniaxial compression strength. *J. Civ. Eng. Environ. Sci.* 9 (1), 025–032. doi:10.17352/2455-488x.000064

Wang, Q., Wang, Y. C., Jiang, B., Jiang, Z. H., and Xue, H. J. (2023b). Geomechanics model test research on large deformation control mechanism of roadway disturbed by strong dynamic pressure. *Geohazard Mech.* 1 (2), 140–152. doi:10.1016/j.ghm.2023.06.002

Wang, S. L., Yin, X. T., Tang, H., and Ge, X. R. (2010). A new approach for analyzing circular tunnel in strain-softening rock masses. *Int. J. Rock Mech. Min. Sci.* 47 (1), 170–178. doi:10.1016/j.ijrmms.2009.02.011

Wu, K., Chen, J. M., Su, J. G., Gao, R., and Gu, S. (2021). "Optimal allocation and integrated dispatch of regional water resources in Yunnan Province—problems and countermeasures," in IOP Conference series: earth and environmental science 7th International Conference on Advances in Energy, Environment and Chemical Engineering. 831. Chengdu, China. July 9-11, 2011. (Beijing, China: IOP Publishing). doi:10.1088/1755-1315/831/1/012065

Wu, L., Xu, C. M., Wu, S. L., and Shi, LJAM (2013). Materials, geostress measurement and rock burst prediction analysis for a deep-buried long and large high-speed railway tunnel. *Appl. Mech. Mater.* 256, 1359–1364. doi:10.4028/www.scientific.net/AMM.256-259.1359

Yale, D. P. (2003). Fault and stress magnitude controls on variations in the orientation of *in situ* stress. *Geol.Soc.London Spec. Publ.* 209 (1), 55–64. doi:10.1144/gsl.sp.2003.209.01.06

Zarei, H., Uromeihy, A., Sharifzadeh, M. J. T., and Technology, U. S. (2011). Evaluation of high local groundwater inflow to a rock tunnel by characterization of geological features. *Tunn. Undergr. Space Technol.* 26 (2), 364–373. doi:10.1016/j.tust.2010.11.007

Zareifard, M. R., and Fahimifar, A. (2016). Analytical solutions for the stresses and deformations of deep tunnels in an elastic-brittle-plastic rock mass considering the damaged zone. *Tunn. Undergr. Space Technol.* 58, 186–196. doi:10.1016/j.tust.2016.05.007

Zhang, B. Y., Liu, G., Li, Y. C., and Lin, Z. B. (2023). Experimental study on the seepage mutation of natural karst collapse pillar (KCP) fillings over mass outflow. *Environ. Sci. Pollut. Res.* 30 (51), 110995–111007. doi:10.1007/s11356-023-30230-3

Zhang, Z. Z., and Sun, Y. Z. (2011). Analytical solution for a deep tunnel with arbitrary cross section in a transversely isotropic rock mass. *Int. J. Rock Mech. Min. Sci.* 48 (8), 1359–1363. doi:10.1016/j.ijrmms.2011.10.001

Zheng, G., and Wei, S. W. (2008). Numerical analyses of influence of overlying pit excavation on existing tunnels. *J. Cent. South Univ. Sci. Technol.* 15, 69–75. doi:10.1007/s11771-008-0438-4

Zheng, H., Lui, D. F., Lee, C. F., and Ge, X. R. (2005). Principle of analysis of brittle-plastic rock mass. *Int. J. Solids Struct.* 42 (1), 139–158. doi:10.1016/j.ijsolstr.2004.06.050

Zhou, P., Jiang, Y. F., Zhou, F. C., Wu, F., Qi, Y., and Wang, ZJEFA (2022). Disaster mechanism of tunnel face with large section in sandy dolomite stratum. *Eng. Fail. Anal.* 131, 105905. doi:10.1016/j.engfailanal.2021.105905

Zhou, X. P., Long, Y. D., and Ye, W. (2023). Experimental investigations on the cracking and mechanical responses of PMMA samples with two 3D embedded elliptic flaws under uniaxial compression. *Geohazard Mech.* 1 (1), 77–85. doi:10.1016/j.ghm.2022.11.004

frontiers | Frontiers in Earth Science

TYPE Original Research
PUBLISHED 06 August 2024
DOI 10.3389/feart.2024.1404153

Check for updates

OPEN ACCESS

EDITED BY
Pengjiao Jia,
Soochow University, China

REVIEWED BY
Juan Yang,
Shanghai Institute of Technology, China
Guo Xiaolong,
Shijiazhuang Tiedao University, China

*CORRESPONDENCE
Lin Zhang,
linz65830@gmail.com

RECEIVED 20 March 2024
ACCEPTED 24 July 2024
PUBLISHED 06 August 2024

CITATION
Zhao Y, Hu K, Han D, Lang Y and Zhang L (2024), Multifactor-coupled study on freeze-thaw forces of rocks in cold regions. *Front. Earth Sci.* 12:1404153. doi: 10.3389/feart.2024.1404153

COPYRIGHT
© 2024 Zhao, Hu, Han, Lang and Zhang. This is an open-access article distributed under the terms of the Creative Commons Attribution License (CC BY). The use, distribution or reproduction in other forums is permitted, provided the original author(s) and the copyright owner(s) are credited and that the original publication in this journal is cited, in accordance with accepted academic practice. No use, distribution or reproduction is permitted which does not comply with these terms.

Multifactor-coupled study on freeze-thaw forces of rocks in cold regions

Yonghui Zhao[1], Kun Hu[1], Deming Han[1], Yongxian Lang[1] and Lin Zhang[2]*

[1]Qinghai Traffic Construction Management Co., Ltd., Xining, China, [2]Guizhou Geological Engineering Investigation Design and Research Institute Co., Ltd., Xining, China

This study delves into the mechanical properties of steep and rocky slopes subjected to long-term freeze-thaw actions. Considering the unique climatic conditions in cold regions, especially the significant impact of seasonal and diurnal temperature variations on slope excavation, the research focuses on a high-cold region iron ore mine. Four types of rocks commonly found in the mining area are thoroughly examined, taking into account the hydrogeological conditions of the mining area. The study systematically analyzes the mechanisms of various factors such as weathering, freeze-thaw cycles, and ice-water phase changes on the stability of cold region fractured rock masses. The research reveals that under prolonged freeze-thaw actions, crack water within the rock continuously undergoes ice-water phase changes, generating substantial freeze expansion forces that result in structural damage to the rock mass. This damage is evident not only in the development of existing microcracks but also leads to the generation of new fractures, ultimately causing deterioration in the rock mass structure. The study of the evolution patterns of freeze-thaw forces contributes to a better understanding of slope stability issues in cold region mineral resource extraction, offering crucial insights for the design, construction, and operation of related engineering projects.

KEYWORDS

high-cold region, rock mechanics, freeze-thaw action, freeze expansion force, rock crack

1 Introduction

In the domain of cold region mineral resource exploitation, open-pit mining faces a significant impact from environmental climate conditions, particularly with respect to the pronounced effects of freeze-thaw cycles on steep and rocky slopes (Koide et al., 2016; Timofejeva et al., 2017; Wang et al., 2017). Over an extended period of freeze-thaw action, the rock mass strength diminishes, and structural weathering intensifies, especially in the case of steep rocky slopes composed of high-grade rocks (Wang et al., 2017). Furthermore, the cumulative influence of mining disturbances and seismic events contributes to an increased frequency and scale of disasters such as collapse, land-slides, and rockfalls, thereby heightening the challenges associated with prevention and mitigation (Kia et al., 2016; Yang et al., 2016; Yang et al., 2017; Li et al., 2023).

Jointed fracture rock formations are widely encountered in mining engineering, encompassing slopes, bedrock, underground projects, coal seams, and oil and gas developments (Wang et al., 2019; Dianursanti and Hafidzah, 2021; Profido et al., 2021;

Sun et al., 2022). Within these formations, microcracks and joint planes directly influence the stability of the rock mass (Le Gallo et al., 2018). In the destabilization and failure process of fractured rock formations, various factors interact, including weathering, freeze-thaw cycles, ice-water phase changes, atmospheric precipitation, acid rain, engineering excavation, mining explosions, and seismic events (Hong, 2017; Yang et al., 2017; Le Gallo et al., 2018; Nittayacharn et al., 2019). Under external loading, the deformation of the rock mass and the stability of surrounding rocks exhibit complex and variable states, promoting the development of pre-existing micro-cracks within the rock mass (Ramazanov et al., 2016; Yang et al., 2016; Yevdokimov et al., 2016; Josset et al., 2017). This directly affects the design, construction, implementation, and operation of rock engineering projects and may even lead to engineering accidents. Particularly in the fractured rock formations of high-cold regions, due to the unique environmental conditions, they face prolonged and intricate challenges associated with freeze-thaw disasters (Yu et al., 2018). Under the long-term influence of freeze-thaw actions, water within the rock fractures undergoes continuous ice-water phase changes, generating substantial freeze-thaw forces that persistently drive the expansion of fractures or the formation of new cracks. As micro-cracks gradually widen and propagate, the strength of the rock diminishes, deformation increases, leading to the deterioration of the rock mass structure, ultimately exerting a significant and unavoidable impact on the stability of the entire engineered rock mass.

At present, the academic community primarily focuses on studying the characteristics of rocks under freeze-thaw conditions, centering around factors influencing their freeze-thaw damage. These factors can be broadly categorized into two types: firstly, the internal intrinsic factors of rocks, which directly determine the mechanical properties of the rock mass; secondly, external environmental factors, encompassing the complex and variable conditions that promote alterations in the mechanical properties of rocks (Ou et al., 2017). Typically, these studies aim to reflect the freeze-thaw damage to rocks by analyzing their physical properties, chemical status, mechanical characteristics, and degree of weathering. As freeze-thaw cycles progress and damage accumulates, there is a transformative shift in the rock's characteristics, eventually leading to its failure. This process of deterioration represents a complex and nuanced evolution that warrants in-depth research to unveil its underlying mechanisms.

Yamabe conducted mechanical tests under freezing conditions on rock samples subjected to saturated and dry states. The study results indicate that the loading-unloading process of dry specimens exhibits linear behavior similar to that of elastic materials, with minimal strain deformation. However, for saturated specimens, the induced deformation is larger and not fully recoverable, implying that frozen rocks are not purely elastic mate-rials (Yu et al., 2017). Additionally, the Young's modulus and uniaxial compressive strength values of dry specimens are significantly greater than those of wet samples. Mutluturk et al. per-formed freeze-thaw tests on various rocks, noting that the integrity of rock mass gradually diminishes with an increasing number of freeze-thaw cycles. Furthermore, there are variations in the mechanical properties of rocks (or saturated frozen rocks) under different temperature conditions (Zhang et al., 2018; Guo et al., 2021). Yamabe further investigated the uniaxial compressive strength of dry and saturated samples of Sirahama sandstone at five temperatures: 20°C, −5°C, −7°C, −10°C, and −20°C. The results show that the uniaxial compressive strength of dry samples is significantly greater than that of wet samples, and the strength increases progressively with decreasing temperature.

Xu et al. conducted compressive strength tests on saturated and dry red sandstone and shale within the temperature range of −20°C to 20°C (Adjonu et al., 2023). They found that as the temperature decreases, the compressive strength and elastic modulus of the rocks gradually increase. Particularly in the temperature range of −5°C to −20°C, there is a significant increase in compressive strength and elastic modulus. Argandofta et al. utilized X-ray tomography to observe changes in pore structure characteristics of limestone under freezing-thawing conditions from −15°C to −10°C (Wang et al., 2022). They observed that the rock samples produced granular fragments after seven freeze-thaw cycles, and through-going cracks after 12 freeze-thaw cycles. Mutlütürk et al. conducted freeze-thaw integrity tests on 10 different types of rocks, indicating significant differences in the progressive breakdown rates of different types of rocks under the same number of freeze-thaw cycles (Li et al., 2021). Tan carried out damage deterioration characteristic tests on muscovite granite from Tibet for 0 to 150 freeze-thaw cycles (temperature cycling from +40°C to −40°C) (Zhang et al., 2022). The research findings reveal that with an increase in the number of freeze-thaw cycles, compressive strength, elastic modulus, and cohesion exhibit exponential decay, while axial peak strain gradually increases. It is noteworthy that the internal friction angle remains relatively stable during the freeze-thaw cycles.

Numerous studies have been dedicated to measuring freeze-thaw forces within rock fractures, but most of these investigations have focused on individual influencing factors. A comprehensive and in-depth understanding of how multiple factors collectively influence the evolution of freeze-thaw forces is still lacking in the current academic literature. This study, set against the engineering backdrop of an iron ore mine in a high-cold region, selects four common rock types prevalent in the mining area as the subject of investigation. Considering the hydrogeological conditions, seasonal temperature fluctuations, and diurnal temperature variations at the mining site, the aim is to explore in-depth the changing patterns of freeze-thaw forces under the combined influence of multiple factors. The goal is to provide a more accurate and comprehensive theoretical basis for relevant engineering practices.

2 Methods

2.1 Geological overview

This study focuses on the Beizhan openpit iron ore mine located in a high-cold region, as shown in Figure 1. The specific geographic coordinates of the mining area range from 85°32′52″ to 85°33′46″ east longitude and 43°14′44″ to 43°15′04″ north latitude, covering a total area of 0.72 square kilometers. To facilitate transportation, a 17-km gravel-hardened road has been constructed between the mining area and the Beizhan iron ore living area.

In the vicinity of the mining area, the Tianshan mountain ridge is clearly visible, characterized by steep slopes and perennial

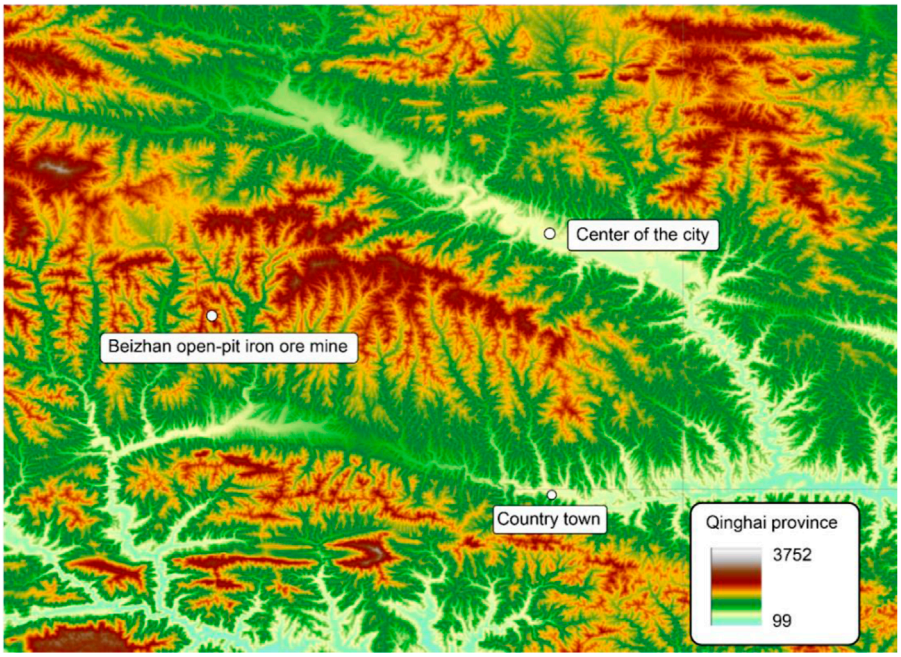

FIGURE 1
Preparation for iron ore remote sensing geographic location map.

glacier coverage. Distinctive features of glacial topography, such as sharp-edged iceeroded cliffs and glacier Ushaped valleys, are widespread. The Beizhan mining area falls within a continental temperate semiarid climate zone, surrounded by permanent glaciers of the Quaternary period, resulting in a cold climate with year-round snow accumulation. The climate is characterized by frequent rain and snow throughout the year, long and extremely cold winters with strong winds. Temperature fluctuations are significant, ranging from a minimum of −40°C to a maximum of 20°C.

The mining area has well-developed water systems, with the surrounding rivers classified as alpine juvenile rivers. These rivers flow year-round, rarely freezing, and their primary sources include snowmelt and atmospheric precipitation, ensuring abundant water supply due to the convergence in the mountain valleys.

In terms of engineering geology, the rock formations in the mining area are categorized into three major types based on stratigraphic characteristics: Quaternary loose soil layers, Carboniferous stratified rock layers, and blocky rock layers. The rock structures surrounding the magnetite ore body exhibit significant development of structural surfaces, leading to poor rock mass integrity. The internal cohesion of the roof and floor rocks is relatively weak, with interlayer bonding forces also being comparatively low.

In the context of engineering geology in the mining area, the division of lithological units is based on a detailed analysis of their stratigraphic characteristics. According to the geological characteristics of the strata, the engineering geological lithological units within the mining area can be classified into three major categories: Quaternary loose soil units, Carboniferous layered rock units, and block rock units. To describe the engineering geological characteristics of each lithological unit more accurately, we further subdivide the lithological units into five specific units based on geological epoch types, stratigraphic divisions, and the engineering geological characteristics of the surrounding rocks, and assign corresponding codes:

(1) Quaternary loose layer lithological unit (Code A): This unit is mainly composed of Quaternary loose sediments, with low density and high porosity. Its engineering geological properties mainly manifest as looseness and susceptibility to deformation.
(2) Lower Carboniferous layered rock lithological unit (Code B): This unit consists of layered rocks formed in the early Carboniferous period, characterized by well-developed bedding and relatively homogeneous rock properties. Its engineering geological properties manifest as stable layered structures.
(3) Block rock lithological unit (Code C): This unit is composed of rock with blocky structures, lacking distinct bedding or layered structures. Its engineering geological properties typically manifest as overall stability, but local discontinuities such as fractures or faults may exist.
(4) Siliceous schist lithological unit at the top and bottom of the magnetite orebody (Code D): This unit specifically refers to the siliceous schist located at the top and bottom of the magnetite orebody. Its engineering geological properties are influenced by the magnetite orebody, typically exhibiting high hardness and brittleness, and may be accompanied by geological phenomena such as hydrothermal alteration.
(5) Magnetite ore block rock lithological unit (Code E): This unit is composed of blocky rocks within the magnetite orebody. Its engineering geological properties mainly manifest as high hardness, high density, and good overall stability. However, attention should be paid to its potential magnetic characteristics and corresponding magnetic effects.

TABLE 1 Stratigraphic subdivision data.

Identification number	Lithology	Stability
A	Sands, gravels, and associated soils	Distributed at the forefront of quaternary glaciation, valley bottoms, slopes, exhibiting fragmented shoulders, extremely loose, unconsolidated, mixed particle deposits, prone to subsidence, susceptible to slope collapse, belonging to extremely unstable solid formations
B	Purple-red conglomerate, agglomerate, Arenaceous greywacke, metamorphic marble, bedded limestone and ying'anite, dolomitic limestone	Distributed in the northern part of the mining area, with a relatively wide range, it belongs to the sub-hard rock category. Within the weathering zone, rocks are extensively weathered and fragmented, with well-developed joint fissures, presenting a fragmented appearance, and exhibiting relatively poor stability. Conversely, within the slightly weathered zone, the rocks demonstrate stronger weathering resistance and better stability
C	Diorite, gabbro, diorite, and monzonite	In the southern and central parts of the mining area, the rocks are dense and hard, exhibiting good integrity and stability
D	Chlorite-epidote-quartz schist, sericite-quartz schist and chlorite-quartz schist	In the central and southern parts of the mining area, there is significant variation in the integrity of the top and bottom plates of the magnetite bodies
E	Massive magnetite, magnetite, angular gravel-like and impregnated	Similarly situated in the central and southern parts of the mining area, the rocks are dense, with relatively few fractures, resulting in relatively good rock quality

For a detailed engineering geological classification and stability assessment of each lithological unit, refer to Table 1. This table systematically summarizes and evaluates the engineering geological characteristics of each lithological unit based on field surveys and laboratory analyses, providing important reference data for engineering design and construction in the mining area.

Additionally, the terrain in the mining area is steep with significant slope gradients, and the rocks are fragmented with distinct joint development, accompanied by small-scale rock layer fractures. Due to insufficient vegetation, the overall geological features of the mining area present a morphology of two slopes enclosing a valley: the east and west slopes forming the mining area's excavation slopes, while the north and south slopes constitute the spoil disposal area.



FIGURE 2
Rock collected at the mine.

2.2 Specimen preparation

In the open-pit slope area of the Beizhan iron ore mine, rock core collection and statistical work were carried out. During this process, several large rock blocks with a diameter of 0.5 m were obtained, as shown in Figure 2. To ensure the integrity of the rock samples and the accuracy of subsequent experiments, the rock blocks were deeply marked, briefly described, and wrapped in plastic foam for preservation.

Following the relevant requirements of the "Code for Rock Testing in Hydraulic and Hydroelectric Engineering," we conducted detailed processing of the large rock samples collected on-site. Through drilling, cutting, and grinding steps, we processed the rock samples into standard cylindrical specimens with dimensions of 50 × 100 millimeters (diameter × height), as shown in Figure 3. To ensure the precision of the specimens, their dimensions were al-lowed to deviate within a range of ±0.3 mm. Simultaneously, we smoothed the side surfaces of the specimens, ensuring their verticality, with a maximum vertical deviation angle of ±0.25°. Additionally, the

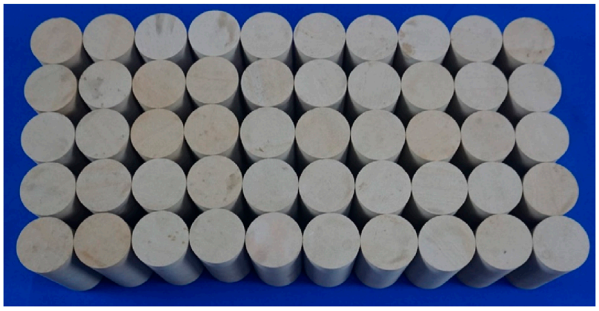

FIGURE 3
Prepared rock specimens.



FIGURE 4
Preparation of rock specimen cracks by cutting.

roughness of the two end faces of the rock samples was strictly controlled within 0.02 mm.

For an in-depth study of the strength evolution of different open-type cracks under freeze-thaw action, we employed high-pressure water jet technology to treat standard cylindrical granite specimens, as shown in Figure 4. By using high-pressure nozzles with diameters of 0.75, 1.5, and 2 mm, we successfully cut through the rock samples to create cracks of different size specifications. Specifically, we generated prefabricated cracks with widths of 1, 2, and 3 mm, and under the same crack width conditions, further cut cracks with lengths of 12, 24, and 36 mm. This precise processing method provided a reliable experimental foundation for subsequent freeze-thaw strength research.

2.3 Experiment

Following the preparation of rock specimens containing prefabricated cracks, we subjected the rock samples to a 24-hour vacuum saturation treatment using a vacuum saturator, followed by freeze-thaw cycling experiments. To accurately monitor the evolution of freeze-thaw forces during the water-ice phase transition, we employed an 8-channel freeze-thaw measurement



FIGURE 5
Freeze-thaw strength testing machine.

system for real-time measurements, as shown in Figure 5. The system consisted of an ultra-low temperature freezer, real-time freeze-thaw force monitoring software, FSR400 thin-film pressure sensors (sized 38 mm in length × 6 mm in width), and temperature sensors as core components.

The FSR400 thin-film pressure sensor served as a crucial component of this system, constructed from flexible nano-functional materials, providing both waterproof and pressure-sensitive capabilities. Its operating principle involved the conversion of pressure to resistance through the thin-film pressure pad, enabling high-sensitivity pressure measurements. As the pressure on the thin-film pressure pad increased, the resistance value of the pressure pad gradually decreased. The sensor's driving force was 0.2 N, with a sensitivity range from 0.2 N to 20 N, and an operating temperature range from −50°C to 85°C. During the testing process, the data acquisition frequency for freeze-thaw forces was set to 5 Hz, while the temperature sensor utilized a waterproof metal probe with an accuracy of ±0.2°C, a recording range of −200°C to 80°C, and a data acquisition frequency of 5 Hz as well.

In the design and selection of pressure measurement systems, the FSR400 thin film pressure sensor has become a critical component due to its unique advantages. This sensor is meticulously crafted from flexible nanomaterials, offering not only outstanding waterproof performance but also pressure-sensitive capabilities, allowing it to operate stably and reliably in various environments. Particularly in applications requiring highly sensitive and durable pressure detection, the FSR400 thin film pressure sensor is the preferred choice. The operating principle of the FSR400 thin film pressure sensor is based on the piezoresistive effect. When external pressure acts on the thin film pressure pad on the sensor surface, the film undergoes slight deformation. This deformation causes a change in the resistance network structure within the film, resulting in a change in resistance value. Specifically, as the pressure on the thin film pressure pad increases, the resistance value decreases, and this change can be precisely measured by the circuit. Through this method, the FSR400 thin film pressure sensor achieves high-sensitivity pressure measurement and finds extensive applications in various scenarios requiring precise pressure control.

The driving force and sensitivity range of the sensor are among its key performance parameters. To ensure the accuracy of the FSR400 thin film pressure sensor in testing, the driving force of the FSR400 thin film pressure sensor is 0.2 N, with a sensitivity range from 0.2 N to 20 N, meaning it can provide accurate measurements across a wide pressure range. To monitor the real-time impact of environmental temperature on sensor performance, we employ a waterproof metal probe as a temperature sensor. This temperature sensor boasts high precision (±0.2°C) and a wide recording range (−200°C to 80°C), ensuring accurate understanding of temperature variations in the sensor's operating environment. During testing, we set the data acquisition frequency of the temperature sensor to 5 Hz, matching the data acquisition frequency of the FSR400 thin film pressure sensor, to ensure simultaneous acquisition of pressure and temperature data for comprehensive analysis.

To ensure the precision of the experiments, we connected all testing instruments to a computer and continuously collected freeze-thaw force and temperature data during the freezing and thawing processes of crack water. The specific experimental steps are outlined below:

Firstly, the rock samples underwent water saturation treatment. The rock specimens with prefabricated cracks were immersed in water naturally for 48 h to achieve water saturation. Subsequently, high-viscosity waterproof tape was applied to seal and water-proof one end of the through cracks. The FSR400 thin-film pressure sensors were also waterproofed.

Secondly, pressure calibration for freeze-thaw forces was conducted. Prior to freeze-thaw force testing, channels 1 to 8 were sequentially connected to the sensors, and a known standard pressure of 100 N was applied to each sensor. The software system displayed a specific pressure value. By inputting the pressure calibration coefficient, the system desktop showed the calibrated 100 N pressure. Saving the calibration coefficients completed the mechanical conversion relationship calibration for the software.

Next, the rock specimens underwent freezing treatment. The test samples were placed in an ultra-low-temperature environmental chamber, and water was injected into the cracks of the specimens. After water injection, the natural state of water-filled cracks in natural conditions was simulated. Subsequently, the waterproofed thin-film pressure sensors and temperature sensor probes were placed in the middle of the crack in the specimen. The freeze-thaw force acquisition software and temperature recorder were activated to record and observe the freeze-thaw force curve and temperature trend during the freezing process. When the freeze-thaw force acquisition system displayed a gradual decrease from high values to a low stable value, it indicated that the water had completely condensed into ice.

Afterward, the rock specimens underwent thawing treatment. The frozen rock samples were taken out and placed at room temperature for natural thawing. Simultaneously, the freeze-thaw force curve and temperature curve were recorded and observed during the melting process, representing the complete melting of ice into water. After completing the experiment, data collection was stopped, and the data were saved.

Finally, by iteratively conducting the third and fourth steps outlined above, we obtained freeze-thaw force and temperature data for crack water under multiple freeze-thaw cycles. These steps collectively constituted the entire process of freezing and melting of crack water, achieving freeze-thaw force testing for one freeze-thaw cycle.

3 Results and discussion

3.1 Effect of single freeze-thaw cycle on freeze-thaw forces

After conducting the freeze-thaw cycle tests, we obtained the typical freeze-thaw force evolution curve for rock prefabricated cracks during a single freeze-thaw process as shown in Figure 6.

Based on the illustrated Figure 6, the evolution of freeze-thaw forces in crack water can be divided into five typical stages, each characterized by specific freeze-thaw evolution features and corresponding freezing mechanisms as described below:

(1) Freeze-thaw Incubation Stage: In this stage, the temperature gradually decreases from 20°C to zero. During this process, crack water begins to transform into a mixture of ice and water, undergoing initial freezing. However, no freeze-thaw force is generated in the prefabricated crack during this stage.

(2) Rapid Increase in Freeze-thaw Force Stage: As the temperature continues to drop, the degree of freezing of the specimen gradually increases. The water-ice phase transition within the crack leads to the generation of significant freeze-thaw forces. In particular, when the temperature drops to approximately −5°C, freeze-thaw forces start to increase significantly. For granite crack water (gap width = 2 mm, gap length = 24 mm), the maximum freeze-thaw force reaches 5.78 MPa.

(3) Steady Decline Stage: In this stage, as the temperature continues to decrease, freeze-thaw forces gradually decrease and tend to stabilize. This is mainly due to two rea-sons: firstly, the density of ice changes with temperature, and during the process where crack ice decreases from 0°C to −40°C, the crystal structure of ice changes, resulting in in-creased density and reduced volume, causing freeze-thaw forces to slowly decrease. Secondly, freeze-thaw leads to cracking of the rock wall, continuous expansion of rock microcracks, causing freeze-thaw forces to gradually disperse and disappear.

(4) Temperature Rise Freeze-thaw Stage: After freeze-thaw forces stabilize, the specimen is removed from the low-temperature chamber and allowed to melt at room temperature. With increasing temperature, secondary freeze-thaw forces are generated within the crack ice, and for granite cracks, the freeze-thaw forces generated during temperature rise reach 5.26 MPa. The mechanism of temperature rise freeze-thaw consists of two parts: the change in ice density as crack ice changes from −40°C to 0°C, and the regelation theory. The latter involves the gradual melting of crack ice during the melting process, migrating towards the rock wall and ice interface under the influence of gravity and hydrostatic pressure, generating secondary freeze-thaw when encountering internally supercooled ice. It is noteworthy that due to the continuous occurrence of regelation, the duration of temperature rise freeze-thaw (approximately 30 min) is significantly longer than the duration of freeze-thaw caused by

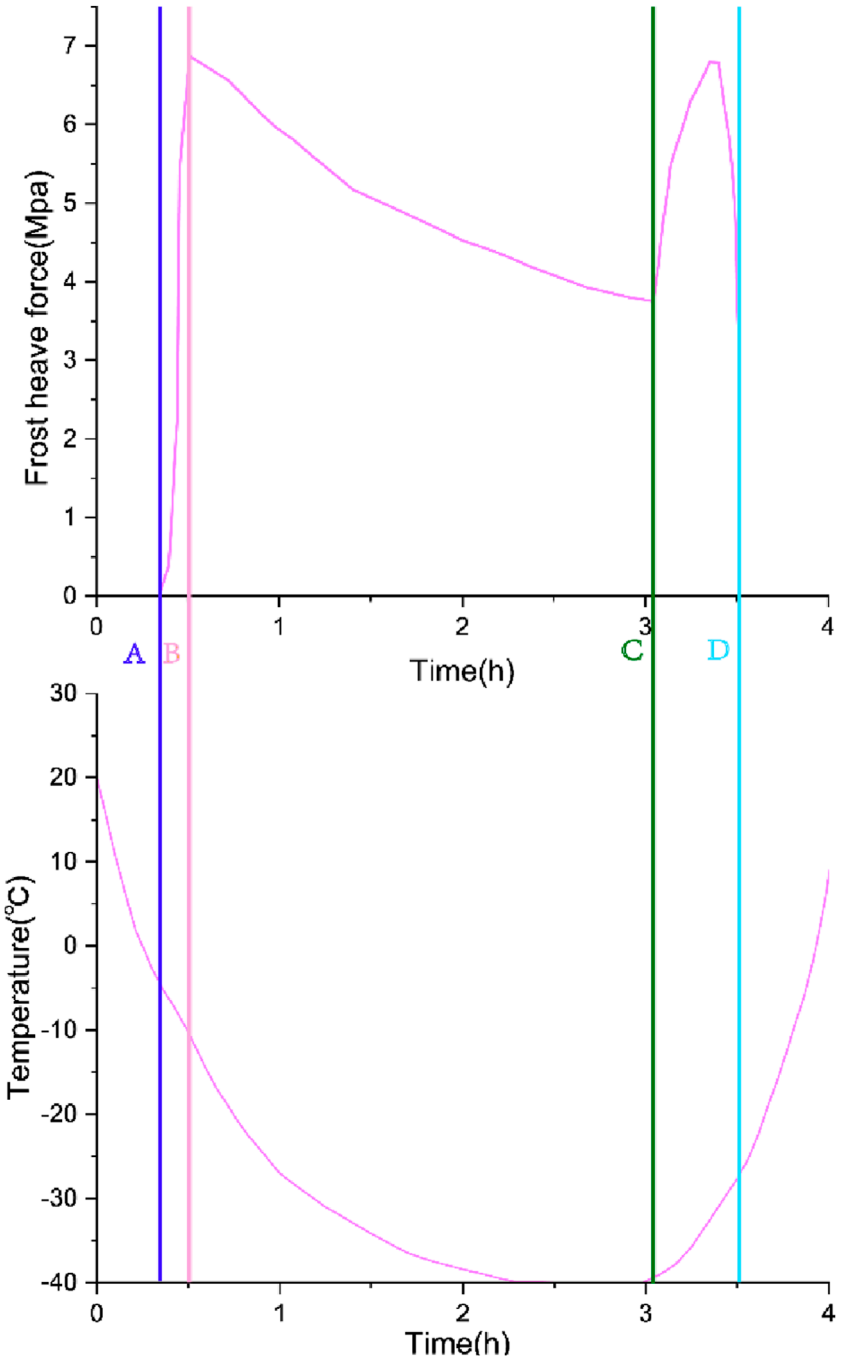

FIGURE 6
Single frost heave force and temperature evolution curve.

water-ice phase transition (approximately 1–2 min). However, temperature rise freeze-thaw forces are usually smaller than the initial peak freeze-thaw forces, which is related to the damage generated on the rock wall during the initial freeze-thaw process.

Figure 7 present the linear expansion coefficients of ice. From the Figure, it can be observed that solid ice exhibits thermal expansion and contraction phenomena below zero degrees. Specifically, the linear expansion coefficient of 0°C ice is 111.2% of that of −40°C ice. Therefore, as the temperature increases, the volume of ice gradually increases, leading to the phenomenon of temperature rise freeze-thaw in crack ice.

(5) Melting Stage: In this stage, the ice in the crack gradually melts, and the freeze-thaw damage phenomenon disappears, with freeze-thaw forces rapidly decreasing to zero. The aforementioned stages collectively constitute the complete evolution process of freeze-thaw forces in crack water, lasting approximately 4 h.

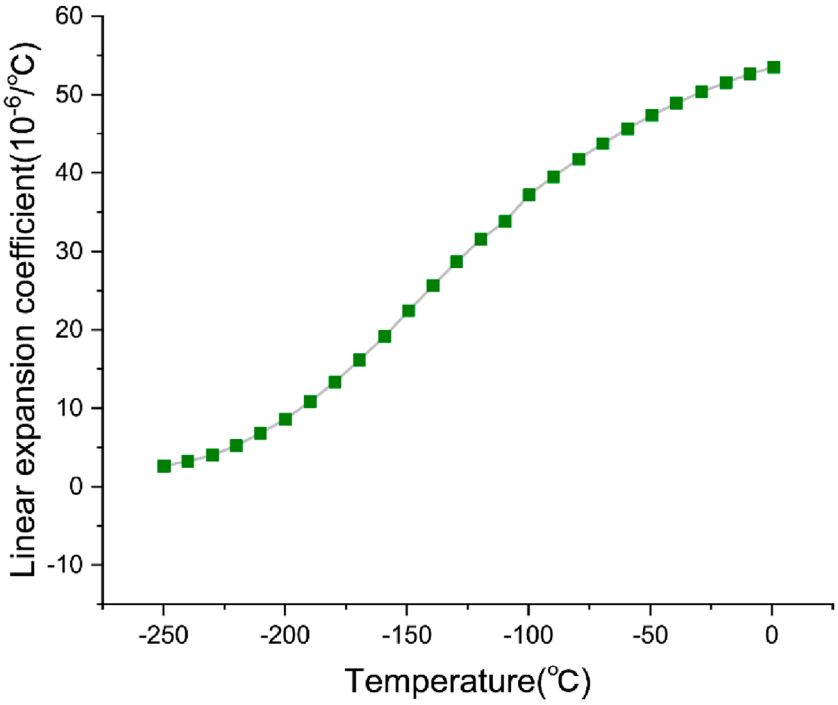

FIGURE 7
The coefficient of linear expansion of ice.

3.2 Effect of crack length on freeze-thaw forces

The study selected prefabricated crack specimens with a constant gap width (2 mm) but varying gap lengths (12, 24, 36 mm) as experimental subjects. Through a care-fully designed experimental procedure, we plotted the curves showing the variation of freeze-thaw forces over time for different crack lengths. Each specimen underwent six rigorous freeze-thaw cycles, and the results are presented in Figures 8–10.

Observing the Figures 8–10, it is evident that there are significant differences in the peak freeze-thaw forces experienced by each specimen during the first freeze-thaw cycle. Specifically, when the gap length is 12 mm, the peak freeze-thaw force is 6.84 MPa; as the gap length increases to 24 mm, the peak freeze-thaw force reaches 7.09 MPa; and when the gap length further extends to 36 mm, the peak freeze-thaw force reaches 7.31 MPa. This trend clearly indicates that with an increase in crack length, the corresponding crack volume increases, allowing for the accommodation of more crack water, resulting in the accumulation of larger freeze-thaw forces.

3.3 Effect of crack width on freeze-thaw forces

The study selected prefabricated crack specimens with a crack length of 24 mm and crack widths of 1, 2, and 3 mm as experimental subjects. Through six freeze-thaw cycles on these specimens, we plotted the freeze-thaw force-duration curves under different crack widths, as shown in Figures 11–13.

Observing the Figures 11–13, it can be observed that the multi-cycle freeze-thaw force evolution patterns of specimens with different crack widths exhibit similar trends to the freeze-thaw force decay patterns of specimens with different crack lengths in previous studies. During the first freeze-thaw cycle, the peak freeze-thaw forces produced by each specimen were 6.21 MPa (width 1 mm), 7.09 MPa (width 2 mm), and 8.45 MPa (width 3 mm). This result indicates that changes in crack width significantly affect the crack volume, thereby influencing the freeze-thaw forces generated by stored crack water. Specifically, the wider the crack width, the greater the peak freeze-thaw force generated by the specimen.

Meanwhile, it can be observed that, under constant gap width conditions, there is no significant trend in the variation of peak freeze-thaw forces with increasing gap length. However, when the gap length remains constant, an evident increasing trend in peak freeze-thaw forces is observed with increasing gap width. Upon further investigation, it is found that the increase in gap width significantly promotes the enlargement of the crack ice volume, a magnitude far surpassing the effect of increased gap length. Consequently, this facilitates the accumulation of larger freeze-thaw forces within the crack.

With an increase in the number of freeze-thaw cycles, the freeze-thaw force decay rates under each width gradually accelerate. Particularly, it is evident from Figures 11–13 that the specimen with a width of 3 mm exhibits the highest peak freeze-thaw force decay rate, indicating a greater susceptibility to freeze-thaw damage for this specimen.

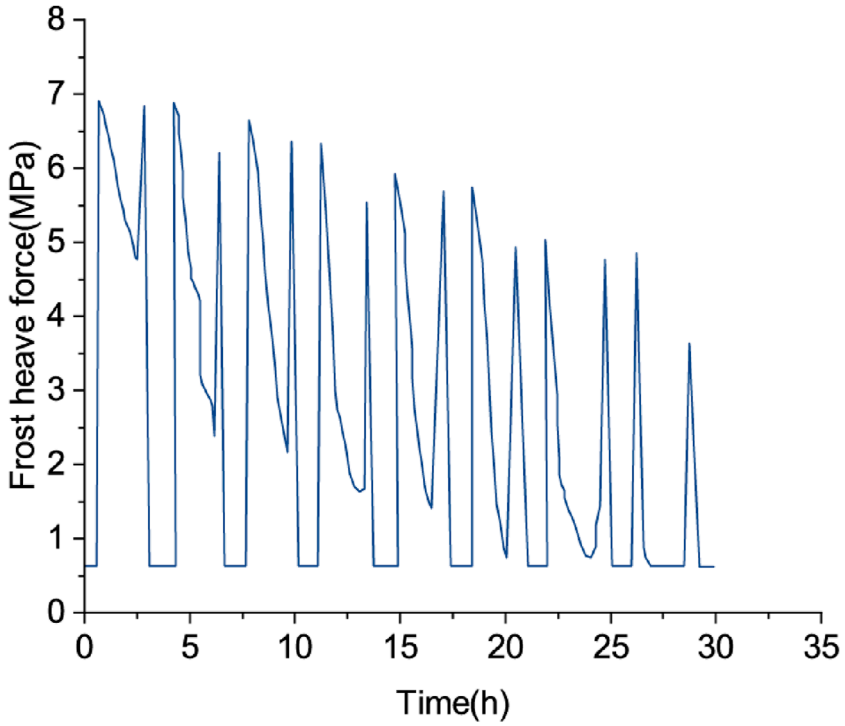

FIGURE 8
Crack length 12 mm frost heave force duration curve.

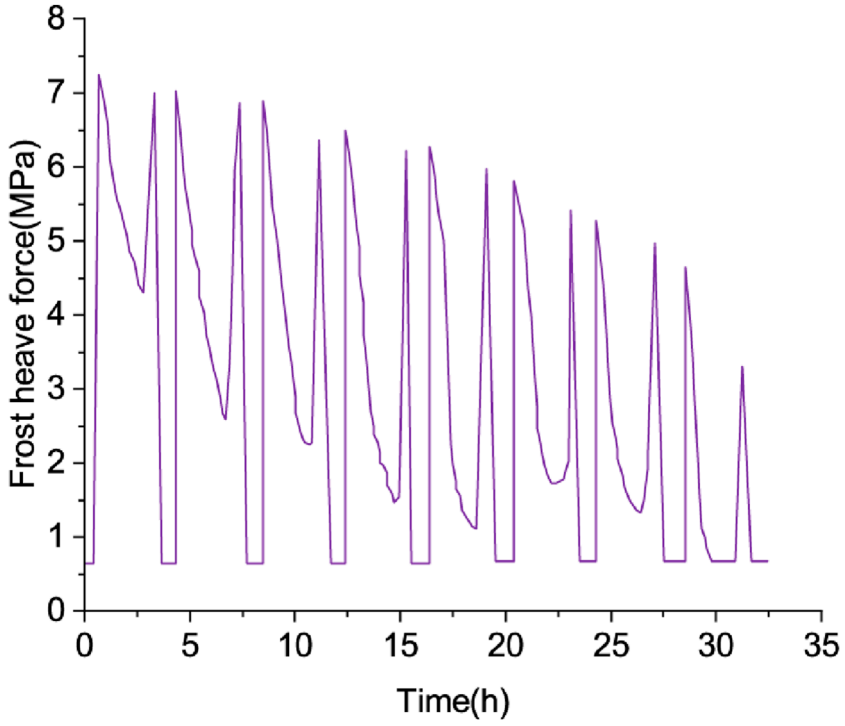

FIGURE 9
Crack length 24 mm frost heave force duration curve.

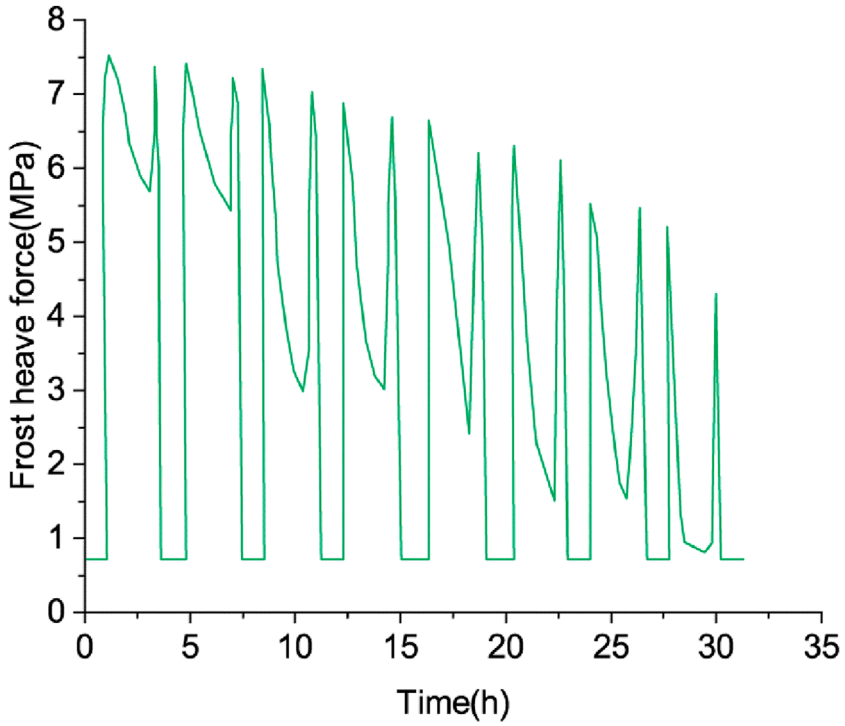

FIGURE 10
Crack length 36 mm frost heave force duration curve.

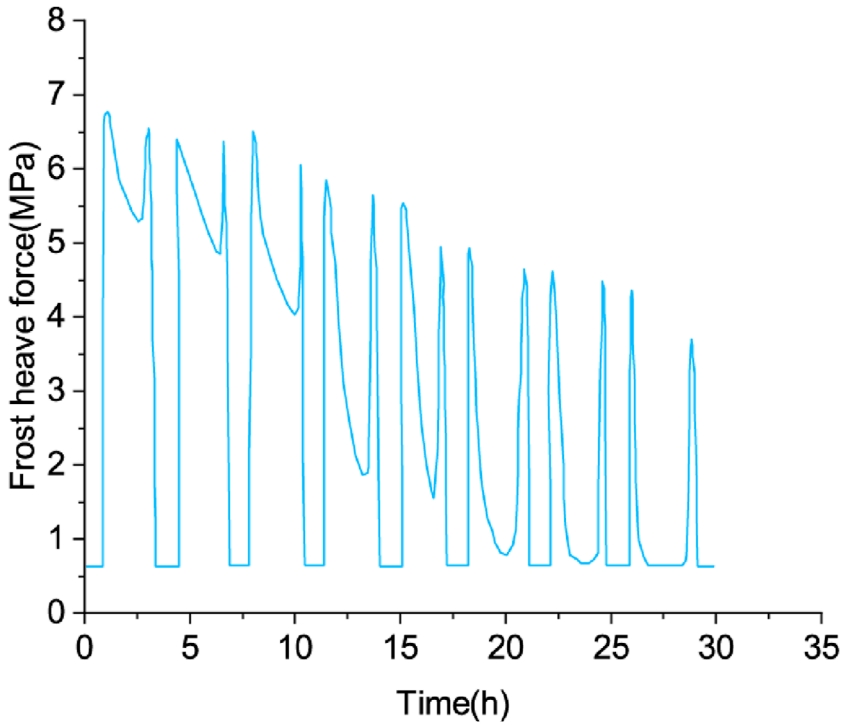

FIGURE 11
Crack width 1 mm frost heave force duration curve.

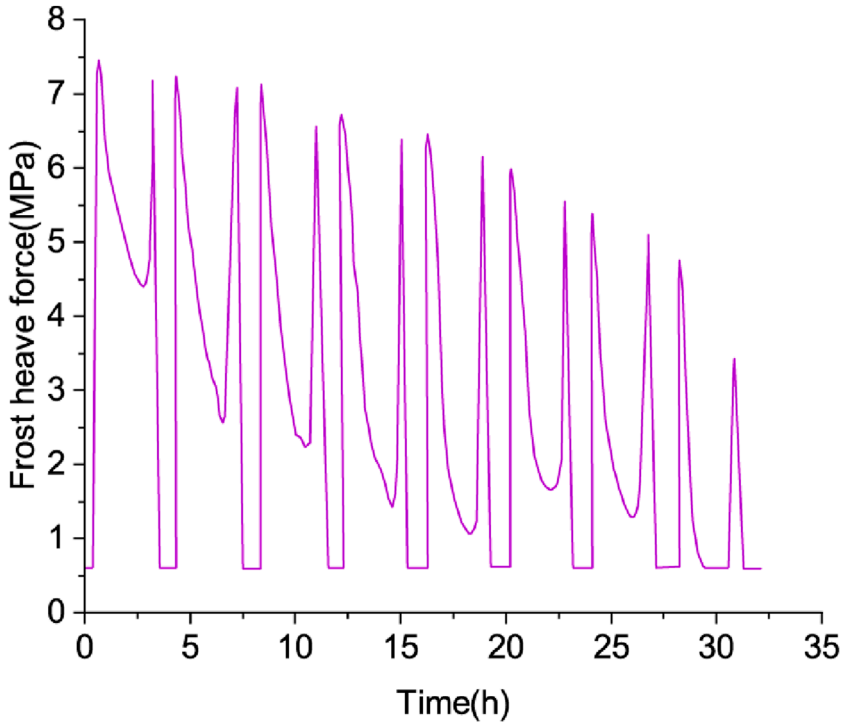

FIGURE 12
Crack width 2 mm frost heave force duration curve.

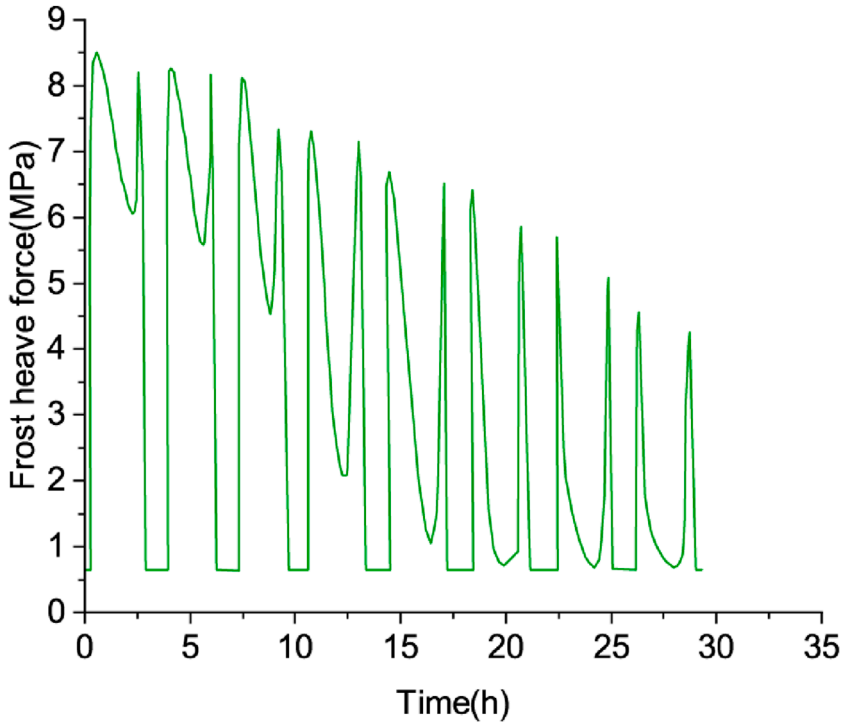

FIGURE 13
Crack width 3 mm frost heave force duration curve.

4 Conclusion

This study revealed five typical stages in the evolution of freeze-thaw forces and identified temperature and crack dimensions as the primary factors influencing the magnitude of freeze-thaw forces, with temperature playing a decisive role. As temperature de-creases and increases, crack water produces peak freeze-thaw forces and secondary warming freeze-thaw forces, respectively. Furthermore, an increase in the water content within cracks enlarges the frozen ice volume, accumulating greater freeze-thaw forces. In this process, the influence of temperature is most significant, followed by crack width and length. Larger freeze-thaw forces promote the expansion of microscopic cracks in rock walls, intensifying damage to large-scale fractured rock masses after multiple freeze-thaw cycles, with a noticeable decline in freeze-thaw forces. This study deepens the under-standing of the freeze-thaw force mechanism in cracks, providing crucial insights for assessing rock mass freeze-thaw damage.

Data availability statement

The original contributions presented in the study are included in the article/Supplementary Material, further inquiries can be directed to the corresponding author.

Author contributions

YZ: Methodology, Writing–original draft. KH: Investigation, Resources, Writing–review and editing. DH: Investigation, Resources, Writing–review and editing. YL: Investigation, Resources, Writing–review and editing. LZ: Formal Analysis, Software, Writing–review and editing.

Funding

The author(s) declare that financial support was received for the research, authorship, and/or publication of this article. This research is financially supported by the Key R$D and Transformation Plan of Qinghai Province (2023-GX-C06).

Conflict of interest

Authors YZ, KH, DH, and YL were employed by Qinghai Traffic Construction Management Co., Ltd. Author LZ was employed by Guizhou Geological Engineering Investigation Design and Research Institute Co., Ltd.

Publisher's note

All claims expressed in this article are solely those of the authors and do not necessarily represent those of their affiliated organizations, or those of the publisher, the editors and the reviewers. Any product that may be evaluated in this article, or claim that may be made by its manufacturer, is not guaranteed or endorsed by the publisher.

References

Adjonu, R., Doran, G., Torley, P., and Agboola, S. (2023). Stability of whey protein bioactive peptide-stabilised nanoemulsions: effect of pH, ions, heating and freeze–thawing. *Int. J. Food Sci. Technol.* 58 (4), 1787–1794. doi:10.1111/ijfs.16292

Dianursanti, D., and Hafidzah, M. A. (2021). The enhancement of phycocyanin yield and purity from Spirulina platensis using freeze-thawing method on various solvents. *AIP Conf. Proc.* 2344 (1). doi:10.1063/5.0047581

Guo, Y. L., Wu, M., Li, R. Q., Cai, Z., and Zhang, H. (2021). Thermostable physically crosslinked cryogel from carboxymethylated konjac glucomannan fabricated by freeze-thawing. *Food Hydrocoll.* 122, 107103. doi:10.1016/j.foodhyd.2021.107103

Hong, K. H. (2017). Polyvinyl alcohol/tannic acid hydrogel prepared by a freeze-thawing process for wound dressing applications. *Polym. Bull.* 74 (7), 2861–2872. doi:10.1007/s00289-016-1868-z

Josset, S., Hansen, L., Orsolini, P., Griffa, M., Kuzior, O., Weisse, B., et al. (2017). Microfibrillated cellulose foams obtained by a straightforward freeze–thawing–drying procedure. *Cellulose* 24, 3825–3842. doi:10.1007/s10570-017-1377-8

Kia, H. D., Razavian, S. M., Dodran, H. V., et al. (2016). Effect of adding Rosa canina extract and Ascorbic Acid as natural and Synthetic antioxidants on freeze-thawing process of ram semen. *Anim. Repord* 13, 567.

Koide, H., Okamoto, A., Tsuchida, H., Ando, H., Ariizumi, S., Kiyokawa, C., et al. (2016). One-step encapsulation of siRNA between lipid-layers of multi-layer polycation liposomes by lipoplex freeze-thawing. *J. Control. Release* 228, 1–8. doi:10.1016/j.jconrel.2016.01.032

Le Gallo, M., de la Motte Rouge, T., Poissonnier, A., Lavoué, V., Tas, P., Leveque, J., et al. (2018). Tumor analysis: freeze–thawing cycle of triple-negative breast cancer cells alters tumor CD24/CD44 profiles and the percentage of tumor-infiltrating immune cells. *BMC Res. Notes* 11, 401–420. doi:10.1186/s13104-018-3504-5

Li, J. H., Sonje, J., and Suryanarayanan, R. (2023). Role of Poloxamer 188 in preventing ice-surface-induced protein destabilization during freeze–thawing. *Mol. Pharm.* 20 (9), 4587–4596. doi:10.1021/acs.molpharmaceut.3c00312

Li, Y., Li, B., Zhang, L., Ma, C., Zhu, J., Li, M., et al. (2021). Chloride ion corrosion pattern and mathematical model for C60 high-strength concrete after freeze-thawing cycles. *Adv. Civ. Eng.* 2021, 1–11. doi:10.1155/2021/5523499

Nittayacharn, P., Dai, K., Therdrattanawong, C., et al. (2019). The effect of freeze/thawing on the physical properties and acoustic performance of perfluoropropane nanobubble suspensions. *IEEE Int. Ultrason. Symp. (IUS)*, 2279–2282. doi:10.1109/ULTSYM.2019.8926224

Ou, K. K., Dong, X., Qin, C. L., Ji, X., and He, J. (2017). Properties and toughening mechanisms of PVA/PAM double-network hydrogels prepared by freeze-thawing and anneal-swelling. *Mater. Sci. Eng. C. Mater. Biogical Appl.* 77, 1017–1026. doi:10.1016/j.msec.2017.03.287

Porfido, C., Rizzo, R. E., Healy, D., Spagnuolo, M., Terzano, R., and Allegretta, I. (2021). Investigating the evolution of fractures in clay–based ceramics during repeated freeze-thawing cycles using X-ray micro-computed tomography and image analysis. *Mat. Charact.* 177, 111185. doi:10.1016/j.matchar.2021.111185

Ramazanov, V. V., Volovelskaya, E. L., and Bondarenko, V. A. (2016). Thromboplastic activity of erythrocytes after freeze-thawing in combined media. *Probl. Kriobiol. Kriomed.* 26 (3), 229–237. doi:10.15407/cryo26.03.229

Sun, J. H., Deng, Y. F., Li, S. H., Xu, W., and Liu, G. (2022). Enhanced efficiency of enzymatic hydrolysis of wheat straw via freeze–thaw pretreatment. *Environ. Sci. Pollut. Res.* 29, 56696–56704. doi:10.1007/s11356-022-18893-w

Timofejeva, A., D'Este, M., and Loca, D. (2017). Calcium phosphate/polyvinyl alcohol composite hydrogels: a review on the freeze-thawing synthesis approach and applications in regenerative medicine. *Eur. Polym. J.* 95, 547–565. doi:10.1016/j.eurpolymj.2017.08.048

Wang, L., Qi, Y., Dong, Y., Peng, Q., Guo, S., He, Y., et al. (2017). Effects and mechanism of freeze-thawing cycles on the soil N2O fluxes in the temperate semi-arid steppe. *J. Environ. Sci.* 56, 192–201. doi:10.1016/j.jes.2016.09.013

Wang, S. Y., Zhang, C., Liu, Q. Q., Wang, Z. J., Wan, K. X., Qian, J. Y., et al. (2022). Modification of potato starch by critical melting pretreatment combined with freeze-thawing: preparation, morphology, structure, and functionality. *LWT* 158, 113109. doi:10.1016/j.lwt.2022.113109

Wang, Z., Zhou, W. W., Zhang, Z. G., et al. (2019). Comparison of pregnancy outcome after D5 and D6 blastocyst under freeze-thawing in two kinds of embryo transfer catheter. *Acta Univ. Med. Anhu*.

Yang, L., Sun, W., Liu, C., Zhang, Y., and Liang, F. (2017). Water absorption and chloride ion penetrability of concrete damaged by freeze-thawing and loading. *J. Wuhan Univ. Technology-Mater. Sci. Ed.* 32 (2), 330–337. doi:10.1007/s11595-017-1599-5

Yang, R. Q., Feng, L., Wang, S., Yu, N., and Gu, Z. (2016). Accumulation of -aminobutyric acid in soybean by hypoxia germination and freeze–thawing incubation. *J. Sci. Food Agric.* 96, 2090–2096. doi:10.1002/jsfa.7323

Yevdokimov, I., Larionova, A., and Blagodatskaya, E. (2016). Microbial immobilisation of phosphorus in soils exposed to dry-ing-rewetting and freeze-thawing cycles. *Biol. Fertil. Soils* 52, 685–696. doi:10.1007/s00374-016-1112-x

Yu, K. K., Zhang, Y., Zhao, R. Y., Zhang, Y., and Zhao, L. (2017). Effect of multiple cycles of freeze–thawing on the RNA quality of lung cancer tissues. *Cell Tissue Bank.* 18, 433–440. doi:10.1007/s10561-016-9600-7

Yu, L., Zhao, A. Q., Yang, M., Wang, C. J., Wang, M. M., and Bai, X. (2018). Effects of the combination of freeze-thawing and enzymatic hydrolysis on the microstructure and physicochemical properties of porous corn starch. *Food Hydrocoll.* 83, 465–472. doi:10.1016/j.foodhyd.2018.04.041

Zhang, C., Han, J. A., and Lim, S. T. (2018). Characteristics of some physically modified starches using mild heating and freeze-thawing. *Food Hydrocoll.* 77, 894–901. doi:10.1016/j.foodhyd.2017.11.035

Zhang, C., Wang, Z. J., Liu, Q. Q., Qian, J. Y., and Lim, S. T. (2022). Improvement of pasting and gelling behaviors of waxy maize starch by partial gelatinization and freeze-thawing treatment with xanthan gum. *Food Chem.* 375, 131656. doi:10.1016/j.foodchem.2021.131656

Frontiers in Earth Science

Investigates the processes operating within the major spheres of our planet

Advances our understanding across the earth sciences, providing a theoretical background for better use of our planet's resources and equipping us to face major environmental challenges.

Discover the latest Research Topics

See more →



Frontiers

Avenue du Tribunal-Fédéral 34
1005 Lausanne, Switzerland
frontiersin.org

Contact us

+41 (0)21 510 17 00
frontiersin.org/about/contact